THE MINISTRY OF SCIENCE AND HIGHER EDUCATION OF THE RUSSIAN FEDERATION

# ST. PETERSBURG STATE POLYTECHNICAL UNIVERSITY

# JOURNAL

## Physics and Mathematics

**VOLUME 16, No. 1.2, 2023**

Peter the Great St. Petersburg
Polytechnic University
2023

**ST. PETERSBURG STATE POLYTECHNICAL UNIVERSITY JOURNAL.**
**PHYSICS AND MATHEMATICS**

**JOURNAL EDITORIAL COUNCIL**

*A.I. Borovkov* – vice-rector for perspective projects;
*V.A. Glukhikh* – full member of RAS;
*V.K. Ivanov* – Dr. Sci.(phys.-math.), prof.;
*A.I. Rudskoy* – full member of RAS, deputy head of the editorial council;
*R.A. Suris* – full member of RAS;
*A.E. Zhukov* – corresponding member of RAS, deputy head of the editorial council.

**JOURNAL EDITORIAL BOARD**

*V.K. Ivanov* – Dr. Sci. (phys.-math.), prof., SPbPU, St. Petersburg, Russia, – editor-in-chief;
*A.E. Fotiadi* – Dr. Sci. (phys.-math.), prof., SPbPU, St. Petersburg, Russia, – deputy editor-in-chief;
*V.M. Kapralova* – Candidate of Phys.-Math. Sci., associate prof., SPbPU, St. Petersburg, Russia, – executive secretary;
*V.I. Antonov* – Dr. Sci. (phys.-math.), prof., SPbPU, St. Petersburg, Russia;
*I.B. Bezprozvanny* – Dr. Sci. (biology), prof., The University of Texas Southwestern Medical Center, Dallas, TX, USA;
*A.V. Blinov* – Dr. Sci. (phys.-math.), prof., SPbPU, St. Petersburg, Russia;
*A.S. Cherepanov* – Dr. Sci. (phys.-math.), prof., SPbPU, St. Petersburg, Russia;
*D.V. Donetski* – Dr. Sci. (phys.-math.), prof., State University of New York at Stony Brook, NY, USA;
*D.A. Firsov* – Dr. Sci. (phys.-math.), prof., SPbPU, St. Petersburg, Russia;
*A.S. Kheifets* – Ph.D., prof., Australian National University, Canberra, Australia;
*O.S. Loboda* – Candidate of Phys.-Math. Sci., associate prof., SPbPU, St. Petersburg, Russia;
*J.B. Malherbe* – Dr. Sci. (physics), prof., University of Pretoria, Republic of South Africa;
*V.M. Ostryakov* – Dr. Sci. (phys.-math.), prof., SPbPU, St. Petersburg, Russia;
*V.E. Privalov* – Dr. Sci. (phys.-math.), prof., SPbPU, St. Petersburg, Russia;
*E.M. Smirnov* – Dr. Sci. (phys.-math.), prof., SPbPU, St. Petersburg, Russia;
*A.V. Solov'yov* – Dr. Sci. (phys.-math.), prof., MBN Research Center, Frankfurt am Main, Germany;
*A.K. Tagantsev* – Dr. Sci. (phys.-math.), prof., Swiss Federal Institute of Technology, Lausanne, Switzerland;
*I.N. Toptygin* – Dr. Sci. (phys.-math.), prof., SPbPU, St. Petersburg, Russia.

The journal is included in the List of leading peer-reviewed scientific journals and other editions to publish major findings of theses for the research degrees of Doctor of Sciences and Candidate of Sciences.

The publications are presented in the VINITI RAS Abstract Journal and Ulrich's Periodical Directory International Database.

The journal is published since 2008 as part of the periodical edition 'Nauchno-tekhnicheskie vedomosti SPb-GPU'.

The journal is registered with the Federal Service for Supervision in the Sphere of Telecom, Information Technologies and Mass Communications (ROSKOMNADZOR). Certificate ПИ № ФС77-52144 issued December 11, 2012.

The journal is distributed through the CIS countries catalogue, the «Press of Russia» joint catalogue and the «Press by subscription» Internet catalogue. The subscription index is **71823.**

The journal is in the **Web of Science** (Emerging Sources Citation Index), **Scopus**, the **Russian Science Citation Index** (RSCI) and the **Directory of Open Access Journals** (DOAJ) databases.

© Scientific Electronic Library (http://www.elibrary.ru).

No part of this publication may be reproduced without clear reference to the source.

The views of the authors may not represent the views of the Editorial Board.

Address: 195251 Politekhnicheskaya St. 29, St. Petersburg, Russia.

Phone: (812) 294-22-85.
http://ntv.spbstu.ru/physics

© Peter the Great St. Petersburg Polytechnic University, 2023

# PREFACE


## International Conference PhysicA.SPb/2022

The International Conference PhysicA.SPb took place in Saint Petersburg, Russia, from October 17 to 21, 2022. The Conference continues the tradition of St. Petersburg Seminars on Physics and Astronomy originating from mid-90s. Since then PhysicA.SPb maintains both scientific and educational quality of contributions delivered to the audience. This is the main feature of the Conference that makes it possible to present the whole spectrum of modern Physics and Astronomy within one event.

PhysicA.SPb/2022 has brought together over 400 academics from many universities and research institutes across Russia as well as from United Kingdom, South Africa, Kazakhstan, Belarus, Azerbaijan, South Korea, Armenia, Germany and France. Oral and poster presentations were organized into well-defined categories among which one should name Astronomy and Astrophysics, Optics and spectroscopy, Physics of ferroics, Nuclear and elementary particle physics, and many others.

This is the second issue of the St. Petersburg State Polytechnical University Journal: Physics and Mathematics presenting the extended contributions from participants of PhysicA.SPb/2022 that were peer-reviewed by expert referees through processes administered by the Presiders of the Organizing and Program Committees to the highest professional and scientific standards. This became possible due to the efforts of the Sectional and Technical Editors of this Issue: Prof. Petr Arseev (Lebedev Physical Institute), Prof. Alexander Ivanchik (Ioffe Institute), Prof. Polina Ryabochkina (Ogarev Mordova State University), Prof. Yuri Kusraev (Ioffe Institute), Dr. Sergey Nekrasov (Ioffe Institute), Prof. Igor Sokolov (Ioffe Institute), Dr. Natalia Teplova (Ioffe Institute), Dr. Nikolay Bert (Ioffe Institute), Dr. Nikita Gordeev (Ioffe Institute), Dr. Grigorii Savchenko (Ioffe Institute), Dr. Prokhor Alekseev (Ioffe Institute), Dr. Mikhail Dunaevskii (Ioffe Institute), Prof. Mikhail Nestoklon (Ioffe Institute), Prof. Andrey Dunaev (Orel State University), Dr. Vadim Evtikhiev (Ioffe Institute), Prof. Alexey Ustinov (St.Petersburg State Electrotechnical University “LETI”), Dr. Alexandra Kalashnikova (Ioffe Institute), Prof. Ivan Mitropolsky (NRC Kurchatov Institute – PNPI), Dr. Evgenia Cherotchenko (Ioffe Institute) and Prof. Dmitry Khokhlov (Moscow State University).

The Editors: **Nikita S. Averkiev, Sergey A. Poniaev and Grigorii S. Sokolovskii**

© Peter the Great St. Petersburg Polytechnic University, 2023

# Contents

## Physical electronics



## Physical optics

## Physical materials technology

## Biophysics and medical physics



## Nuclear physics

## Mathematical physics



## Mechanics



## Astrophysics

## Radiophysics

## Theoretical Physics

PHYSICAL ELECTRONICS

Conference materials
UDC 621.383.51
DOI: https://doi.org/10.18721/JPM.161.201

# Flexible solar cells based on PEDOT:PSS and vertically aligned silicon structures

E.A. Vyacheslavova [1,2]✉, A.V. Uvarov [1,2], V.V. Neplokh [1],
A.A. Maksimova [1,2], A.I. Baranov [1,2], A.S. Gudovskikh [1,2]

[1] Saint Petersburg Alferov University, St Petersburg, Russia;
[2] Saint Petersburg Electrotechnical University, St Petersburg, Russia
✉ cate.viacheslavova@yandex.ru

**Abstract.** Photovoltaic properties of hybrid solar cells based on poly-(3,4 ethylenedioxythiophene): polystyrene sulfonate (PEDOT:PSS) and Si nanowires (SiNWs) are studied. High values of the open circuit voltage ($V_{OC}$) and external quantum efficiency (EQE) at short wavelength region obtained for planar solar cells indicate sufficient passivation properties of *n*-Si/PEDOT:PSS interface. A technology for filling SiNWs (6 μm in height and 1.7 μm in diameter) with PEDOT:PSS has been developed using G-coating. Compared with planar hybrid cell, SiNWs/PEDOT:PSS cell exhibit lower total reflectance (~ 12%) and higher EQE in the long wavelength region. It should be stressed that an increase in the PEDOT:PSS layer thickness by the combination of the G-coating and spin coating methods does not affect the short wavelength region of EQE. This fact is important for development of flexible solar cells based on SiNWs.

**Keywords:** solar cell, silicon nanowires, PEDOT:PSS, flexibility

**Funding:** This work was supported by Ministry of Science and Higher Education of the Russian Federation (research project [0791-2020-0004]).

**Citation:** Vyacheslavova E.A., Uvarov A.V., Neplokh V.V., Maksimova A.A., Baranov A.I., Gudovskikh A.S., Flexible solar cells based on PEDOT:PSS and vertically aligned silicon structures, St. Petersburg State Polytechnical University Journal. Physics and Mathematics. 16 (1.2) (2023) 10–17. DOI: https://doi.org/10.18721/JPM.161.201

This is an open access article under the CC BY-NC 4.0 license (https://creativecommons.org/licenses/by-nc/4.0/)

Материалы конференции
УДК 621.383.51
DOI: https://doi.org/10.18721/JPM.161.201

# Гибкие солнечные элементы на основе PEDOT:PSS и вертикально-ориентированных кремниевых структур

Е.А. Вячеславова [1,2]✉, А.В. Уваров [1,2], В.В. Неплох [1],
А.А. Максимова [1,2], А.И. Баранов [1,2], А.С. Гудовских [1,2]

[1] Академический университет имени Ж.И. Алфёрова РАН, Санкт-Петербург, Россия;
[2] «ЛЭТИ» имени В. И. Ульянова, Санкт-Петербург, Россия
✉ cate.viacheslavova@yandex.ru

**Аннотация.** Изучены фотоэлектрические свойства гибридных солнечных элементов на основе кремниевых нановолокон (SiNWs) и поли(3,4-этилендиокситиофен)-полистиролсульфоната (PEDOT:PSS). Высокие значения напряжения холостого хода ($V_{xx}$) и внешней квантовой эффективности в коротковолновой области, полученные для планарных солнечных элементов, указывают на достаточные пассивирующие свойства интерфейса *n*-Si/PEDOT:PSS. Технология заполнения SiNWs (6 мкм в высоту

© Vyacheslavova E.A., Uvarov A.V., Neplokh V.V., Maksimova A.A., Baranov A.I., Gudovskikh A.S., 2023. Published by Peter the Great St. Petersburg Polytechnic University.

и 1.7 мкм в диаметре) слоем PEDOT:PSS была разработана с использованием метода G-центрифугирования. По сравнению с подобным кремниевым планарным элементом, солнечный элемент с радиальным p–n-переходом демонстрирует гораздо более низкий общий коэффициент отражения (~ 12%) и более высокую квантовую эффективность в диапазоне длин волн 430–1200 нм. Следует подчеркнуть, что увеличение толщины слоя PEDOT:PSS за счет комбинации G- и горизонтального центрифугирования не влияет на коротковолновую область EQE. Этот факт важен для разработки гибких солнечных элементов на основе вертикально-ориентированных структур.

**Ключевые слова:** солнечный элемент, кремниевые нановолокна, PEDOT:PSS, гибкость

**Ссылка при цитировании:** Вячеславова Е.А., Уваров А.В., Неплох В.В., Максимова А.А., Баранов А.И., Гудовских А.С. Гибкие солнечные элементы на основе PEDOT:PSS и вертикально-ориентированных кремниевых структур // Научно-технические ведомости СПбГПУ. Физико-математические науки. 2023. Т. 16. № 1.2. С. 10–17. DOI: https://doi.org/10.18721/JPM.161.201

Статья открытого доступа, распространяемая по лицензии CC BY-NC 4.0 (https://creativecommons.org/licenses/by-nc/4.0/)

## Introduction

Presently, a considerable interest is drawn to the development of renewable energy sources due to the gradual depletion of traditional energy sources and strong requirements to reduce carbon footprint. One of the most promising branches of renewable energy is solar power harvested by photovoltaic devices [1]. Crystalline silicon solar cells dominate the photovoltaic industry. However, these solar cells are rigid and bulky.

Therefore, the transition to the technology of flexible solar cells is promising [2–4]. First, such solar cells have trade-off efficiency and robustness. Besides, expensive glass substrates can be replaced with polymer ones. Secondly, flexible panels are lighter than rigid crystal ones, which makes them easier to transport and install. Third, it is possible to integrate such devices into various surfaces, such as smartphone screens, clothing, the electric car, etc. However, modern flexible solar cells may suffer from several problems. This is due to the use of unstable, expensive or toxic materials. Flexible solar cells based on perovskites are attractive for their increased optical absorption, but they degrade quickly. Flexible III-V tandem solar cells allow expanding the optical absorption spectrum. However, their wide use is limited by the complexity of the technology and the high cost. Promising flexible Copper Indium Gallium Selenide (CIGS) solar cells are includes rare (In) and expensive (Ga) elements may limiting its large-scale usage. Besides, indium-tin-oxide (ITO) is most often used as a transparent electrode of solar cell. ITO can be applied onto flexible plastic substrates [5, 6], but very thin layer and under numerous bending cycles ITO is cracking [7, 8] which significantly reduces of the performance cells. Besides, rare element In may prevent wide implementation of ITO. Hence, new concepts need to be exploited to address these concerns.

An alternative way is to create SiNWs/PEDOT:PSS hybrid solar cells. The SiNWs provides broadband antireflection and have a good light-trapping effect, which can increase the optical absorption of solar radiation in active layers [9–12]. The SiNWs solar cells embedded in polymer matrix have enhanced mechanical stability compared to conventional planar tandem solar cells deposited on flexible substrate. Polymer PEDOT:PSS, in turn, is promising as a transparent electrode material [13]. This layer possess is more flexibility than ITO and can exhibit values of conductivity and transmittance close to those of ITO [7, 14]. Moreover, polymer PEDOT:PSS is a more attractive emitter material for SiNWs compared to *a*-Si:H layer because it is difficult to deposit (*p*)*a*-Si:H/(*i*)*a*-Si:H layer stack with precise thickness control on vertically aligned silicon structures. Besides, using PEDOT:PSS layer is low cost due to low-temperature processing such as spin coating. Thus, combine both of SiNWs and PEDOT:PSS advantages provide a possible simplify production processes and its low costs.

In this work, hybrid solar cells based on PEDOT:PSS with SiNWs structures are reported.

© Вячеславова Е.А., Уваров А.В., Неплох В.В., Максимова А.А., Баранов А.И., Гудовских А.С., 2023. Издатель: Санкт-Петербургский политехнический университет Петра Великого.

## Experimental section

The *n*-type Si (100) wafers with a resistivity of 0.2 Ω·cm and 0.06 Ω·cm were used for solar cells fabrication. The layer of *n*-type doped μc-Si was deposited on the backside of Si substrates by PECVD to form ohmic contact. In order to verify the quality of the hybrid heterojunction, first, the planar Si/PEDOT:PSS solar cell structures were fabricated.

i) Planar Si/PEDOT:PSS solar cell

Previously the Si substrates were dipped in a 10 vol% hydrofluoric (HF) acid solution for 30 s to remove the native silicon oxide at the surface. Two types of PEDOT:PSS based solutions were tested to form emitter layer: 1) PEDOT:PSS with a dispersion content of 1wt% in water mixed with 5 wt% dimethyl sulfoxide (DMSO) to increase conductivity [15]; 2) PEDOT:PSS (DMSO) mixed with 0.25 wt% of Neonol AF 9-12, which was used as a surfactant to improve the adhesion to Si surface. The PEDOT:PSS based solutions were spin coated on Si substrates at a rate of 1000 rpm during 1 min. Then samples were annealed on a hot plate at 120 °C for 2 min in air. The Ag electrodes were applied on the organic PEDOT:PSS layer by vacuum evaporation.

Next, hybrid Si/PEDOT:PSS solar cell were fabricated based on array of Si nanowires.

ii) SiNWs/PEDOT:PSS solar cell

The array of SiNWs was obtained by deep cryogenic etching of Si in a $SF_6/O_2$ plasma using Oxford PlasmaLab System100 ICP380 [16–17]. The SiNWs samples were dipped in a 10 vol% hydrofluoric (HF) acid solution for 30 s to remove the native oxide on the SiNWs surface immediately prior PEDOT:PSS deposition. The both types of PEDOT:PSS based solutions described above for planar structures were used. The PEDOT:PSS layer initially was spin coated on the samples using EZ4 Spin Coater at a rate of 1000 rpm. During spin coating in spinner the PEDOT:PSS layer covered only the tops of the SiNWs (Fig. 1, *a*). It should be noted that reducing the viscosity of the PEDOT:PSS solution (Neonol addition) just slightly improve the process of its penetration between the wires.

Next, we used the G-coating method (Fig. 1, *b*) [18] to fill the area between SiNWs array with the use of swinging bucket centrifuge. It can be noted that during G-coating the PEDOT:PSS layer covers the nanowires along entire length. This is due to the high pressure (G-force) applied to the polymer PEDOT:PSS. Then samples were annealed at 120 °C and Ag electrodes were formed.

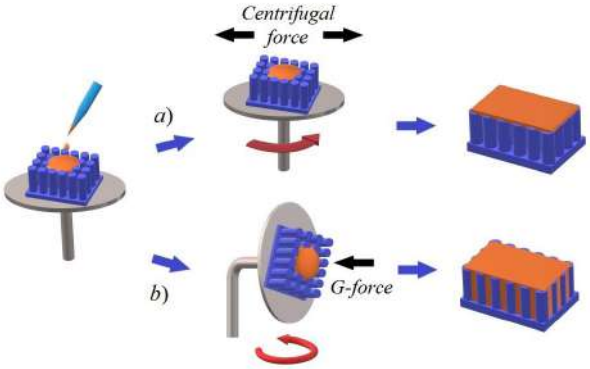


Fig. 1. Schematic of the spin coating (*a*) and G-coating (*b*) of the PEDOT:PSS layer

Besides, we created a structure by a combination of G-coating and spin coating methods. Initially the PEDOT:PSS layer on samples was G-coated on the samples at a rate of 5000 rpm for 5 min. This made it possible to fill the area between SiNWs. Then the PEDOT:PSS layer was spin coated at a rate of 1000 rpm for 1 min. This made it possible to cover the tops of the SiNWs as well.

The current–voltage ($I$–$V$) measurements were performed using an Abet Technologies solar simulator (AM 1.5G, 100 mW/cm$^2$) and a Keithley 2400 electrometer. The external quantum efficiency (EQE) spectra were obtained using an SLS M266 monochromator, a halogen lamp and

a Si reference cell. The total reflectance spectra of the cells were measured using an integrating sphere and spectrometer AvaSpec SensLine.

## Results and Discussion

i) Planar Si/PEDOT:PSS solar cell

Figure 2 compares the total reflectance spectra of the planar Si and SiNWs structures with and without PEDOT:PSS layer. The bare planar Si structure exhibits the total reflectance of more than 23% from 400 to 800 nm. The bare SiNWs structure exhibits the total reflectance at around ~ 15%. Thus, using SiNWs structures can help to improve the light absorption. It should be noted that for the samples with PEDOT:PSS the reflectance is decreased. The SiNWs structure with PEDOT:PSS layer exhibits the reflectance at around ~ 12%. This means that the PEDOT:PSS film exhibits antireflection properties.

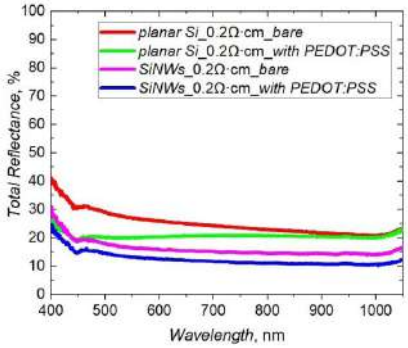


Fig. 2. Measured total reflectance spectra of the Si structures

The current density-voltage ($J$–$V$) curves and photovoltaic parameters of the planar Si/PEDOT:PSS hybrid cells are summarized in Fig. 3, *a* and Table 1, respectively. The photovoltaic parameters such as the open circuit voltage ($V_{OC}$) and the fill factor (FF) were calculated from the illuminated $I$–$V$ curves. The short circuit current density ($J_{SC}$) was extracted from the quantum efficiency spectra.

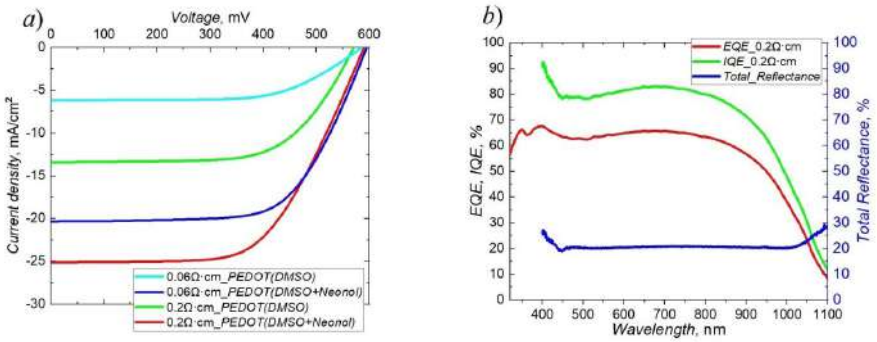


Fig. 3. Measured $J$–$V$ curves (*a*) and quantum efficiency, and total reflectance spectra (*b*) of the planar Si/PEDOT:PSS hybrid cells

Table 1

**Photovoltaic parameters of the planar Si/PEDOT:PSS cell**

| Sample | Wafer resistivity | Co-solvents of PEDOT:PSS | $V_{OC}$, mV | $J_{SC}$, mA/cm² | FF, % |
|---|---|---|---|---|---|
| Planar Si | 0.2 Ω·cm | DMSO | 571 | 13.35 | 64.68 |
| | 0.2 Ω·cm | DMSO + Neonol | 589 | 24.96 | 60 |
| | 0.06 Ω·cm | DMSO | 584 | 6.16 | 63.15 |
| | 0.06 Ω·cm | DMSO + Neonol | 595 | 20.22 | 65.03 |

The structure with a DMSO addition exhibits the $J_{SC}$ of 13.35 mA/cm$^2$, the $V_{OC}$ of 571 mV and the FF of 64.68 %. Compared with this structure, the cell with DMSO and Neonol AF 9-12 addition has improved in all photovoltaic parameters. It inferred that the Neonol AF 9-12 can improve the wettability and conductivity of the PEDOT:PSS layer and thus enhance the photovoltaic parameters of the planar structure.

The $V_{OC}$ at around 589 mV and 595 mV were obtained for Si wafers (PEDOT:PSS with DMSO and Neonol AF 9-12 addition) with a resistivity of 0.2 Ω·cm and 0.06 Ω·cm, respectively. With the decrease of resistivity Si wafers the $J_{SC}$ also decreases to 20.22 mA/cm$^2$. It can be explained by a shorter lifetime of minority carriers in the Si substrate. These results agree well with the results in Sara Jäckle et.al [19].

Figure 3, *b* shows quantum efficiency and reflectance spectra of the planar Si/PEDOT:PSS cells with DMSO and Neonol AF 9-12 addition. Since the total reflectance spectra was measured in the wavelength range from 400 to 1200 nm, the values of the internal quantum efficiency are calculated in the same wavelength range.

Spectral response measurements (Fig. 3, *b*) demonstrate extremely high quantum efficiency in UV region spectrum below 400 nm meaning low absorption losses in PEDOT:PSS layer. Moreover, high values of the $V_{OC}$ and quantum efficiency at short wavelength region indicate low recombination losses at the Si/PEDOT:PSS planar interface. Thus, PEDOT:PSS is a promising candidate to use as an emitter layer for SiNWs structure because of sufficient passivation properties.

ii) SiNWs/PEDOT:PSS solar cell

The $J-V$ curves of the SiNWs/PEDOT:PSS hybrid cells are summarized in Fig. 4, *a*. The photovoltaic parameters such as $V_{OC}$ and FF extracted from the illuminated $I-V$ curves are collected in Table 2. The $J_{SC}$ values were calculated from the quantum efficiency spectrum and are also presented in Table 2. It should be noted that the addition of Neonol AF 9-12 reduced the photovoltaic parameters of the SiNWs/PEDOT:PSS hybrid cells. Besides, the addition of Neonol AF 9-12 reduces the viscosity of the solution, and therefore, it is more difficult to control the process of coating the PEDOT:PSS layer on the SiNWs.

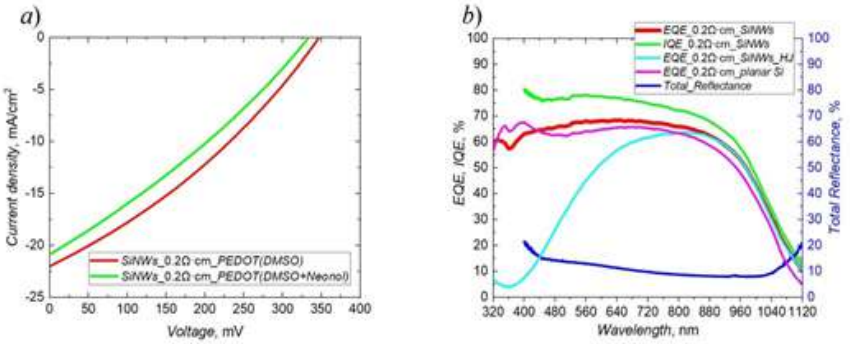


Fig. 4. Measured $J-V$ curves (*a*) and quantum efficiency, and total reflectance spectra (*b*) of the SiNWs/PEDOT:PSS hybrid cells

Table 2

**Summary of photovoltaic parameters of the SiNWs/PEDOT:PSS hybrid cells**

| Sample | Wafer resistivity | Co-solvents of PEDOT:PSS | $V_{OC}$, mV | $J_{SC}$, mA/cm$^2$ | FF, % |
|---|---|---|---|---|---|
| SiNWs | 0.2 Ω·cm | DMSO | 350 | 22.02 | 34 |
| | 0.2 Ω·cm | DMSO + Neonol | 330 | 20.79 | 37.75 |
| HJ (SiNWs) | 0.2 Ω·cm | DMSO | 440 | 20.41 | – |

The SiNWs structure with DMSO addition exhibits the $J_{SC}$ of 22.02 mA/cm$^2$, the $V_{OC}$ of 350 mV and the FF of 34%. The obtained values of $V_{OC}$, $J_{SC}$ and FF are lower than for planar Si cells. It can be explained by the fact that high aspect ratios of SiNWs surface properties

start to define the electrical characteristics. The SiNWs/PEDOT:PSS cell performance could be improved by a better SiNWs surface preparation.

Figure 4, *b* shows quantum efficiency and total reflectance spectra of the SiNWs/PEDOT:PSS cells with DMSO. Compared to planar Si/PEDOT:PSS cell, SiNWs/PEDOT:PSS cell exhibit much higher external quantum efficiency in the wavelength range from 430 to 1200 nm due to enhanced light trapping.

Then, we considered the PEDOT:PSS layer as a transparent electrode material. Silicon heterojunction (HJ) structures based on SiNWs and stack of thin *i*- and *p*- layers amorphous hydrogenated silicon (*a*-Si:H) thin film were fabricated. A strong drop of the EQE in the wavelength range from 350 to 800 nm is observed for heterojunction solar cells (see Fig. 4, *b*). It can be explained by significant absorption, and therefore, recombination losses in the *a*-Si:H layer. However, compared with hybrid SiNWs structure, the heterojunction cell has higher $V_{OC}$ of 440 mV. On the one hand, it can be explained by better passivation properties of *a*-Si:H, which could provide excellent surface passivation [20]. On the other hand, the obtained value of $V_{OC}$ is extremely low compared to that (above 0.7 V) of high-performance heterojunction solar cells. It should be stressed that the planar *a*-Si:H/c-Si solar cells with $V_{OC}$ near to 0.7 V were fabricated using the same deposition conditions. It means that an additional treatment of the SiNWs surface is required to reduce concentration of defects or impurities created during cryogenic etching. Thus, there is a still a room for improvement for hybrid solar cell based on SiNWs. Besides, using thin *a*-Si:H passivation layer improves the wettability of PEDOT:PSS (DMSO). This fact opens a way to combine the advantages of heterojuction and hybrid technology. Deposition of ultra-thin intrinsic *a*-Si:H layer could provide excellent passivation and wettability of SiNWs surface, while PEDOT:PSS provides enhanced quantum efficiency in short wavelength region due to its transparency.

To provide the full filling of the SiNWs array by PEDOT:PSS a combination of the coating techniques was used. For one of the samples after the G-coating, the PEDOT:PSS (DMSO) layer was re-coated on the sample using the spin coating. Then the sample was annealed at 120 °C and Ag electrodes were formed. Figure 5 shows quantum efficiency spectra of the PEDOT:PSS/SiNWs hybrid cells with different methods of coating the PEDOT:PSS layer.

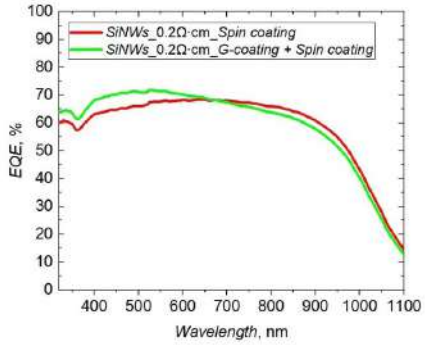


Fig. 5. Measured quantum efficiency of the PEDOT:PSS/SiNWs hybrid cells with different methods of coating the PEDOT:PSS layer

It should be noted that the EQE measurement results indicate that compared with the spin coating the PEDOT:PSS layer, the combination of the G-coating and spin coating methods exhibited a pronounced EQE enhancement in the spectral region of 320–660 nm. An increase in the PEDOT:PSS layer thickness does not affect the short wavelength region of EQE. This fact is important for development of flexible solar cells based on SiNWs.

Next, we examined the structure in relation to flexibility. For mechanical strength, nanowires were filled with Su-8 photoresist. Then the substrate was sunk from the backside first mechanically, and then by etching in plasma. The resulting devices are flexible with a bending radius of 25 mm. The resulting thickness of the substrate was 40 μm.

## Conclusion

In summary, SiNWs/PEDOT:PSS hybrid solar cells where the PEDOT:PSS layer considered both as an emitter material and a transparent electrode were fabricated. It was succeeded to fill the

area between SiNWs with the PEDOT:PSS by using G-coating for a SiNWs solar cells. Compared planar Si/PEDOT:PSS cell, SiNWs/PEDOT:PSS cell exhibit much lower total reflectance and higher EQE in the wavelength range of 430–1200 nm. Besides, SiNWs/PEDOT:PSS flexible structures were successfully fabricated.

**Acknowledgments**

This work was supported by Ministry of Science and Higher Education of the Russian Federation (research project [0791-2020-0004]).

## REFERENCES

1. **Philipps S., et al.,** Photovoltaics Report. Fraunhofer Institute for Solar Energy Systems, ISE with support of PSE Projects GmbH, July 27, 2021.

2. **Kang S.B., Kim J.-H., Jeong M.H., et al.,** Stretchable and colorless freestanding microwire arrays for transparent solar cells with flexibility, J. Light Science & Applications. 8 (1) (2019).

3. **Thiyagu S., Hsueh C.C., Liu C.-T., et al.,** Hybrid organic-inorganic heterojunction solar cells with 12% efficiency by utilizing flexible film-silicon with a hierarchical surface, J. Nanoscale. 6 (6) (2014) 3361–3366.

4. **Li S., Pei Z., Zhou F., et al.,** Flexible Si/PEDOT: PSS hybrid solar cells, J. Nano Research. 8 (10) (2015) 3141–3149.

5. **Choi K.-H., Jeong J.-A., Kang, J. K., et al.,** Characteristics of flexible indium tin oxide electrode grown by continuous roll-to-roll sputtering process for flexible organic solar cells, J. Solar Energy Materials & Solar Cells. 93 (8) (2009) 1248–1255.

6. **Lee S. J., Kim Y., Hwang J.-Y., et al.,** Flexible Indium–Tin Oxide Crystal on Plastic Substrates Supported by Graphene Monolayer, J. Scientific Reports. 7(1) (2017).

7. **Hau S. K., Yip H.-L., Zou J., et al.,** Indium tin oxide-free semi-transparent inverted polymer solar cells using conducting polymer as both bottom and top electrodes, J. Organic Electronics. 10 (7) (2009) 1401–1407.

8. **Inganäs O.,** Avoiding indium, J. Natural Photonics. 5 (2011) 201–202.

9. **Lu W., Chen Q., Wang B., et al.,** Structure Dependence in Hybrid Si nanowire/Poly(3,4-ethylenedioxythiophene): Poly(styrenesulfonate) Solar Cells: Understanding Photovoltaic Conversion in Nanowire Radial Junctions, J. Applied Physics Letters. 100 (2) (2012) 023112.

10. **Thomas J.P., Zhao L., McGillivray D., Leung K.T.,** High-efficiency hybrid solar cells by nanostructural modification in PEDOT: PSS with co-solvent addition, J. Materials Chemistry A. 2 (7) (2014) 2383.

11. **He L., Jiang C., Wang H., et al.,** High efficiency planar Si/organic heterojunction hybrid solar cells, J. Applied Physics Letters. 100 (7) (2012) 073503.

12. **Xia Y., Sun K., Ouyang J.,** Solution-Processed Metallic Conducting Polymer Films as Transparent Electrode of Optoelectronic Devices, J. Advanced Materials 24(18) (2012) 2436–2440.

13. **He L., Jiang C., Wang H., et al.,** Effects of nanowire texturing on the performance of Si/organic hybrid solar cells fabricated with a 2.2 μm thin-film Si absorber, J. Applied Physics Letters. 100 (10) (2012) 103104.

14. **Kim Y. H., Sachse C., Machala M. L., et al.,** Highly conductive PEDOT: PSS electrode with optimized solvent and thermal post-treatment for ITO-free organic solar cells, J. Advances Functional Materials. 21 (6) (2011) 1076–1081.

15. **Pietsch M., Bashouti M., Christiansen S., et al.,** The Role of Hole Transport in Hybrid Inorganic/Organic Silicon/Poly (3, 4- ethylenedioxy-thiophene):Poly(styrenesulfonate) Heterojunction Solar Cells, J. Physical Chemistry C. 117 (18) (2013) 9049–9055.

16. **Morozov I. A., Gudovskikh A.S., Uvarov A. V., et al.,** The study of Latex Sphere Lithography for High Aspect Ratio Dry Silicon Etching, J. Physica Status Solidi (A). 217 (4) (2019) 1900535.

17. **Vyacheslavova E. A., Morozov I. A., Kudryashov D.A., Gudovskikh A.S.,** Formation of $SiO_2$ hard mask using dry etching and nanosphere lithography, J. Physics: Conference Series. 1697 (2020) 012188.

18. **Neplokh V. V., Kochetkov F. M., Deriabin K. V., et al.,** Modified silicone rubber for fabrication and contacting of flexible suspended membranes of n-/p-GaP nanowires with a single-walled carbon nanotube transparent contact, J. Materials Chemistry C. 8 (11) (2020) 3764–3772.

19. **Jäckle S., Mattiza M., Liebhaber M., et al.,** Junction formation and current transport mechanisms in hybrid n-Si/PEDOT: PSS solar cells, J. Scientific Reports. 5(1) (2015).

20. **Adachi D., Hernandes J. L., Yamomoto K.,** Impact of carrier recombination on fill factor for large area heterojunction crystalline silicon solar cell with 25.1% efficiency, J. Applied Physics Letters. 107(23) (2015) 233506.

## THE AUTHORS

**VYACHESLAVOVA Ekaterina A.**
cate.viacheslavova@yandex.ru
ORCID: 0000-0001-6869-1213

**BARANOV Artem I.**
itiomchik@yandex.ru
ORCID: 0000-0002-4894-6503

**UVAROV Alexander V.**
lumenlight@mail.ru
ORCID: 0000-0002-0061-6687

**MAKSIMOVA Alina A.**
deer.blackgreen@yandex.ru
ORCID: 0000-0002-3503-7458

**NEPLOKH Vladimir V.**
vneplox@gmail.com
ORCID: 0000-0001-8158-0681

**GUDOVSKIKH Alexander S.**
gudovskikh@spbau.ru
ORCID: 0000-0002-7632-3194

*Received 18.10.2022. Approved after reviewing 21.11.2022. Accepted 22.11.2022.*

© Peter the Great St. Petersburg Polytechnic University, 2023

Conference materials
UDC 533
DOI: https://doi.org/10.18721/JPM.161.202

# Radiative energy losses of a high-current vacuum arc with an eroding anode

K.K. Zabello [1]✉, Yu.A. Barinov [1], A.A. Logachev [1],
I.N. Poluyanova [2], E.V. Sherstnev [1], S.M. Shkol'nik [1]

[1] Ioffe Institute, St. Petersburg, Russia;
[2] Switchgear design bureau LTD, Sevastopol, Russia
✉ zabellok@mail.ioffe.ru

**Abstract.** The results of measurements of the radiation power of a vacuum ($p \sim 10^{-4}$ Pa) arc in the near infrared, visible and ultraviolet regions of the spectrum (200 nm $\leq \lambda \leq$ 1100 nm) are presented. The arc burned on industrial AMF-electrodes with a diameter of 55 mm. The material of the electrodes was the CuCr30 composition. The arc was fed by a current pulse in the shape close to half of the industrial frequency sine wave ($f = 50$Hz). The radiation was output through one of the side windows of the vacuum chamber. The window was made of quartz KU-1. The radiation receiver was a silicon photodiode with a diameter of 1.2 mm, located outside the vacuum chamber on an axis intersecting with the axis of symmetry of the discharge in the center of the interelectrode gap. The signal from the photodiode was taken through an amplifier and recorded on an oscilloscope. Considering the spectral sensitivity of the diode, two series of measurements were made: measurements without a filter and through a ZhS-10 yellow filter that cuts off radiation with $\lambda \leq 400$ nm. The results obtained made it possible to analyze the dependence of the radiation power on the arc current at different stages of its development. The results showed that at high currents in the developed vacuum arc with anodic activity (eroding anode), a significant part (up to 15%) of the power released in the arc is transferred by radiation.

**Keywords:** vacuum arc, axial magnetic field, radiation power

**Citation:** Zabello K.K., Barinov Yu.A., Logachev A.A., Poluyanova I.N., Sherstnev E.V., Shkol'nik S.M., Radiative energy losses of a high-current vacuum arc with an eroding anode, St. Petersburg State Polytechnical University Journal. Physics and Mathematics. 16 (1.2) (2023) 18–24. DOI: https://doi.org/10.18721/JPM.161.202

This is an open access article under the CC BY-NC 4.0 license (https://creativecommons.org/licenses/by-nc/4.0/)

Материалы конференции
УДК 533
DOI: https://doi.org/10.18721/JPM.161.202

# Излучательные потери энергии сильноточной вакуумной дуги с эродирующим анодом

К.К. Забелло [1]✉, Ю.А. Баринов [1], А.А. Логачёв [1],
И.Н. Полуянова [2], Е.В. Шерстнев [1], С.М. Школьник [1]

[1] Физико-технический институт им. А.Ф. Иоффе РАН, Санкт-Петербург, Россия;
[2] Конструкторское бюро коммутационной аппаратуры, г. Севастополь, Россия
✉ zabellok@mail.ioffe.ru

**Аннотация.** Приведены результаты измерений мощности излучения вакуумной ($p \sim 10^{-4}$ Па) дуги в ближней инфракрасной, видимой и ультрафиолетовой областях спектра (200 нм $\leq \lambda \leq$ 1100 нм). Дуга горела на индустриальных АМП-электродах диаметром 55 мм. Материал электродов – композиция CuCr30. Дуга питалась импульсом

© Zabello K.K., Barinov Yu.A., Logachev A.A., Poluyanova I.N., Sherstnev E.V., Shkol'nik S.M., 2023. Published by Peter the Great St. Petersburg Polytechnic University.

тока по форме близким к половине синусоиды промышленной частоты ($f$ = 50 Гц). Излучение выводилось через одно из боковых окон вакуумной камеры. Окно было изготовлено из кварца КУ-1. Приемником излучения являлся кремниевый фотодиод диаметром 1,2 мм, расположенный вне вакуумной камеры на оси, пересекающейся с осью симметрии разряда в центре межэлектродного промежутка. Сигнал с фотодиода снимался через усилитель и фиксировался на осциллографе. Учитывая вид спектральной чувствительности диода, сделаны две серии измерений: измерения без фильтра и через фильтр ЖС-10, отрезающий излучение с $\lambda \leq 400$ nm. Полученные результаты позволили проанализировать зависимость мощности излучения от тока дуги на разных стадиях ее развития. Результаты показали, что при больших плотностях тока в развившейся вакуумной дуге с анодной активностью (эродирующим анодом) значительная часть мощности переносится излучением.

**Ключевые слова:** вакуумная дуга, магнитное поле, мощность излучения

**Ссылка при цитировании:** Забелло К.К., Баринов Ю.А., Логачёв А.А., Полуянова И.Н., Шерстнёв Е.В., Школьник С.М. Излучательные потери энергии сильноточной вакуумной дуги с эродирующим анодом // Научно-технические ведомости СПбГПУ. Физико-математические науки. 2023. Т. 16. № 1.2. С. 18–24. DOI: https://doi.org/10.18721/JPM.161.202

Статья открытого доступа, распространяемая по лицензии CC BY-NC 4.0 (https://creativecommons.org/licenses/by-nc/4.0/)

## Introduction

A great interest in the research of a high-current vacuum arc is connected not only with the fact that this type of electric discharge is still insufficiently studied, but also with the fact that the results of these studies are widely used. They are used in the creation of vacuum interrupters (VI), which are the main part of various vacuum switching devices. Therefore, high-current vacuum arcs burning under conditions characteristic of arc burning in the VI are intensively studied all over the world. One of the most important areas of work is the study of the energy balance of the arc at high currents.

It is known that in high-current high-pressure gas arcs, a significant part of the energy is transferred by radiation [1]. Radiation plays a more significant role in the energy balance of the arc, the greater the plasma density ($\sim n^2$). Unlike gas arcs, energy transfer by radiation in vacuum arcs has not been practically investigated. In mathematical modeling of vacuum arcs, radiation is most often not taken into account. There are only a few approximate calculations in which radiation was taken into account when considering the energy balance of the arc (for example, [2]). Experimental measurements of the radiation power from a high-current vacuum arc were not carried out before the start of this work.

Our first publication on this topic [3] presents the results obtained in a vacuum arc with artificial ignition, burning on end model electrodes in an external magnetic field. The arc radiation power was measured in the ultraviolet, as well as in the visible and near-infrared regions of the spectrum (200 nm $\leq \lambda \leq$ 1100 nm). This publication presents the results of measurements of radiation coming out of a vacuum arc burning on industrial electrodes generating their own axial magnetic field (such electrodes are called AMF-electrodes). The arc was ignited by opening the electrodes as it happens in the VI. Measurements were carried out in the same spectral intervals.

## Materials and Methods

The experimental setup is described in detail in previous publications [4]. Here we will briefly indicate only the main parameters and make the necessary explanations. The experiments were carried out in a demountable vacuum chamber with continuous pumping ($p \sim 10^{-4}$ Pa). The camera had windows for photographing the arc and output radiation. The electrodes were positioned vertically. The upper electrode (anode) was stationary, and the lower (cathode) could move. In the initial state, the electrodes were closed and spring-loaded. The standard drive detached the lower electrode from the upper one, and it started moving at a mean speed of ~ 1 m/s. When the electrodes were opened, a vacuum arc appeared. The arc was powered by a current pulse having a shape close to half of the industrial frequency sine wave ($f$ = 50 Hz). The opening of the electrodes occurred within the first

© Забелло К.К., Баринов Ю.А., Логачёв А.А., Полуянова И.Н., Шерстнёв Е.В., Школьник С.М., 2023. Издатель: Санкт-Петербургский политехнический университет Петра Великого.

millisecond after the start of the current, so the duration of arc was 9–10 ms. The appearance of the electrodes is shown in Fig. 1. The same figure shows the radial distribution of the $z$-component of the magnetic field generated inside the interelectrode gap when the discharge current flows through the electrode system. The diameter of the electrode is 55 mm, the material of the working part of the electrode is the composition CuCr30. Erosion damage of the electrodes was controlled by periodically opening the vacuum chamber and photographing the working surface of the electrodes. Video recording of the arc was carried out through a side window using a Phantom MIRO M310 camera equipped with a Carl Zeiss 100/2 lens. In order not to overload the camera, dense neutral filters were used.

The window through which the analyzed radiation was output was made of quartz KU-1. The transmission of the window at $\lambda = 200$ nm was 60%. The dusting of the window was monitored and eliminated as needed. The arc radiation was recorded by a photodiode FDUC-1UST (JSC Technoexan). The photosensitive element of the diode had a diameter of $\mathbf{d} = 1.2$ mm. The signal from the photodiode was taken through a trans-impedance amplifier with a conversion factor of 1360 V/A, a bandwidth of 0–300 MHz. The diode was located outside the vacuum chamber on the x axis intersecting with the axis of symmetry of the discharge $z$ in the center of the interelectrode gap. The distance from the $z$ axis to the diode was 1350 mm. Such a large distance is chosen to avoid overloading the diode. The spectral sensitivity of the diode is shown in Fig. 2. Considering the spectral sensitivity of the diode, two series of measurements were made – measurements without a filter and through a ZhS-10 yellow filter that cuts off radiation with $\lambda \leq 400$ nm (Fig. 2). An oscilloscope was used to measure the signal from the diode. Other electrical signals were recorded on the same oscilloscope: the current and voltage of arc, as well as the signal from the sensor of the position of the electrodes. An Agilent DSO 5014A oscilloscope with a differential probe N2772A was used. All recordings from the oscilloscope were transferred to the computer. Before the measurements, the electrodes were cleaned by a series of kiloampere pulses. Fig. 3 shows an example of recording measurement results at close current values with and without the ZhS-10 filter. The maximum current amplitude in these experiments was 47 kA.

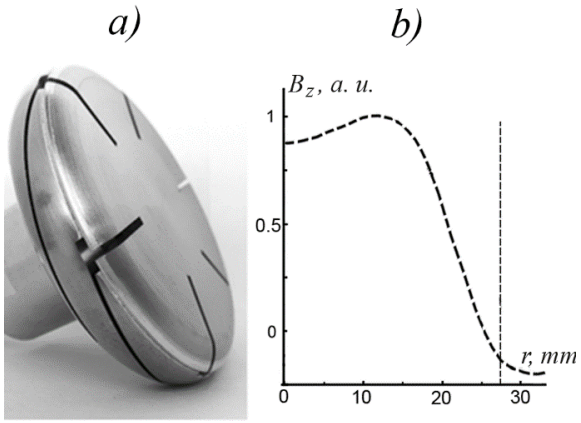


Fig. 1. Photo of the electrode (*a*), Radial distribution of the $z$-components of the magnetic field in the middle of the interelectrode gap (*b*)

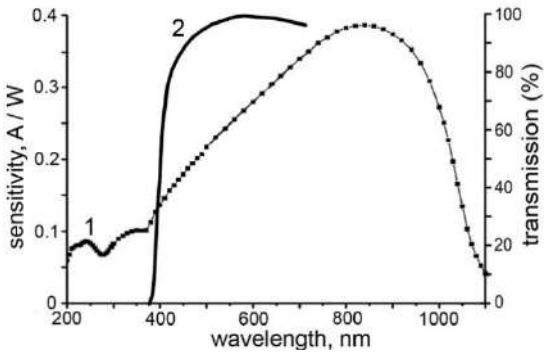


Fig. 2. Spectral sensitivity of the diode (1) and transmission of the ZhS-10 filter (2)

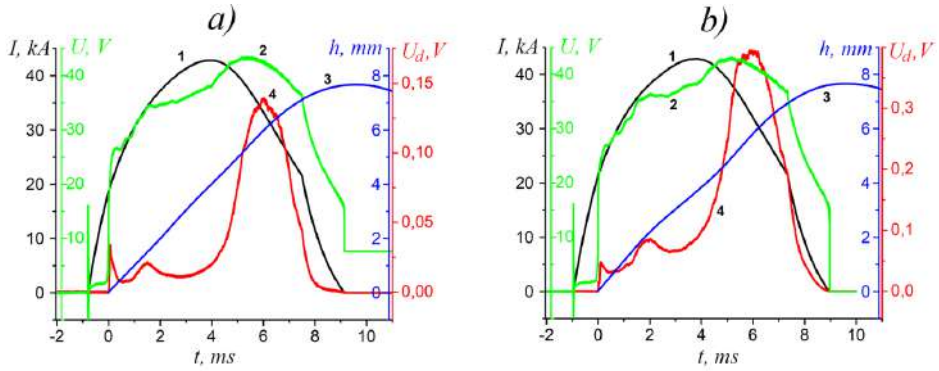


Fig. 3. Examples of recordings of experimental results at close currents when using a filter (*a*) and without a filter (*b*) for current (1), arc voltage (2), arc gap (3), and photodiode voltage (4)

## Results and Discussion

### Description of the discharge

The behavior of the arc on AMF electrodes under similar conditions was described in detail in previous articles [4, 5]. Therefore, here we will describe the arc briefly. Video shooting showed that the arc can be ignited at one point or at several points at once. Ignition at several points usually occurs if the opening of the electrodes began at a current of 8–10 kA or more. Immediately after ignition, the current density in the arc attachment is very high. After ignition, the cathode attachment of the arc increases in size and the current density in the attachment decreases. At some distance from it, new attachments appeared in different directions. The new attachments seem to jump on the surface and are fixed on the cuts of the electrode (see Fig. 1). As the attachment expands and the arc lengthens, the attachment structure and individual cathode spots become visible. The arc moves along the cathode and covers an increasing part of its surface. This process lasts 2–3 ms after ignition, after which the entire working surface of the cathode is covered by an arc. That is, the transition process is being completed.

The arc is symmetrized and centralized. This time corresponds to the penetration time of the AMF created by the electrodes when the arc current flows through them. Further, the arc burns steadily up to zero current. The arc voltage at the stage of its development and establishment (i.e., at the first milliseconds) depends not so much on the current as on the ignition conditions and with single-point ignition significantly exceeds the arc voltage with multipoint ignition. After the arc is established, the voltage is determined by the current (Fig. 4, *a*, curves 1, 2, 3). A gentle voltage maximum is reached approximately (0.5–1.0) ms after the current maximum, which is explained by the lengthening of the arc. This is how the voltage waveform looks at currents up to 32–34 kA. As the current increases, the shape of the waveform begins to change. After ≈ 3 ms after ignition, the voltage begins to grow faster. The maximum voltage becomes more pronounced and is reached after (1.5–2) ms after the maximum current (Fig. 4, *a*, curves 4. 5), or approximately 5.5–6 ms after ignition.

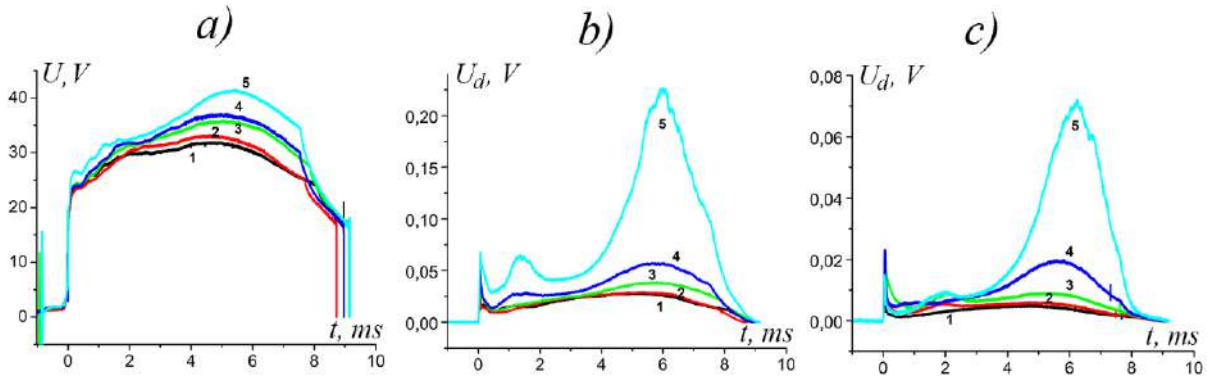


Fig. 4. Experimental time dependencies of arc voltage (*a*), the voltage of the diode without filter (*b*), the voltage of the diode with a filter (*c*) at the current of 24 (1), 28 (2), 32 (3), 37 (4), 41 (5) кА.

To construct the Current-Voltage characteristic (CVC), two characteristic time points were selected during the arc development: 3 ms after ignition, i.e. before the voltage begins to grow faster, and 5.5 ms after ignition, when the voltage reaches a maximum. As you can see, at currents less than 32–34 kA, both CVC are rectilinear. With an increase in the current, the CVC corresponding moment of 3 ms after ignition retains the slope, i.e. remains rectilinear. However, in the CVC corresponding to the time of 5.5 ms after ignition, a change occurs. Its slope increases, but the linearity remains (Fig. 5). A change (increase) in the slope of the CVC indicates that the properties of the arc plasma change, the arc resistance increases.

The signal from the photodiode shows the initial emission corresponding to the glow in sharply contracted cathode attachments. Further, at the initial stage of arc burning, the shape of the signal from the diode is determined by the development of the cathode attachment. In the developed arc, the signal from the diode is determined by the amplitude of the arc current (Fig. 4, *b*, curves 1, 2 ,3). This is typical for currents up to 32–34 kA. At higher currents, the signal from the diode after the arc is established begins to grow rapidly and reaches a maximum about 6 ms after ignition (Fig. 4, *b*, curves 4. 5).

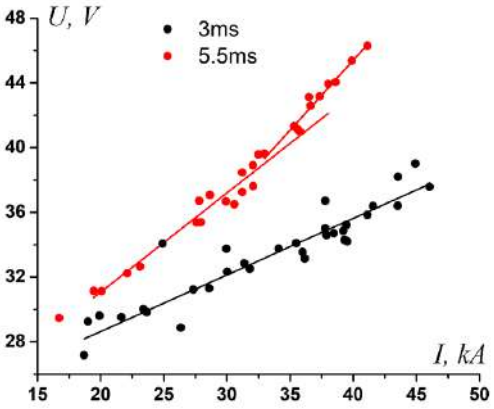


Fig. 5. Volt-ampere characteristics of the arc. The instantaneous values of the voltages and their corresponding currents are given for 3 and 5.5 ms after ignition

Photographing erosion traces on the surface of the electrodes showed that the anode is exposed to greater thermal effects than the cathode [6]. A light surface melt appears on the surface of the anode at moderate currents. At a current of approximately 32–34 kA, a significant part of the anode surface melts, traces of melt movement appear. When the current increases, the entire surface of the anode is melted, traces of intense melt movement are visible (Fig. 6). The dynamics of the melt is clearly visible on the video recordings of the arc and was described in detail in [4, 6], so here, due to the limited space, we will not delve into these issues. The cathode surface, as a whole, is fused weaker. Therefore, it clearly shows traces of deep melting, left by concentrated attachments, in the initial period of arc burning. The initial emissions noted above on the arc glow oscillogram are associated with the formation of the melt and evaporation from its surface.

As you can see (Fig. 4, 6), there are two modes of arc burning after the completion of its development and transition to a stable state. In the first mode, the arc does not glow as brightly as in the second. The thermal effect on the electrodes does not lead to their melting. In the second mode, the arc glows much stronger (by an order of magnitude or more), the electrodes, especially the anode, get very hot and melt, the arc resistance increases. The boundary between the modes passes in the area of current 32–34 kA for electrodes of this geometry. The modes differ in that in the second mode, the anode heats up so much that intense evaporation begins from its surface. The anode vapors entering the plasma are ionized, and the plasma concentration increases. With it, the radiation power increases as the square of the concentration. Such an arc mode is called a mode with anodic activity [5]. As can be seen from Fig. 4, the radiation power in the mode with anode activity increases greatly. Next, we will make estimates of the radiation power at different currents.

**The power of radiation from the plasma.**

In previous works [3, 7], the method of measurements and their processing is described in detail to determine the radiation power. Here we will only briefly recall the result. Using the ZhS-10 filter, we divide the radiation coming to the diode in the studied spectral region ($200 \leq \lambda \leq 1100$) nm into two

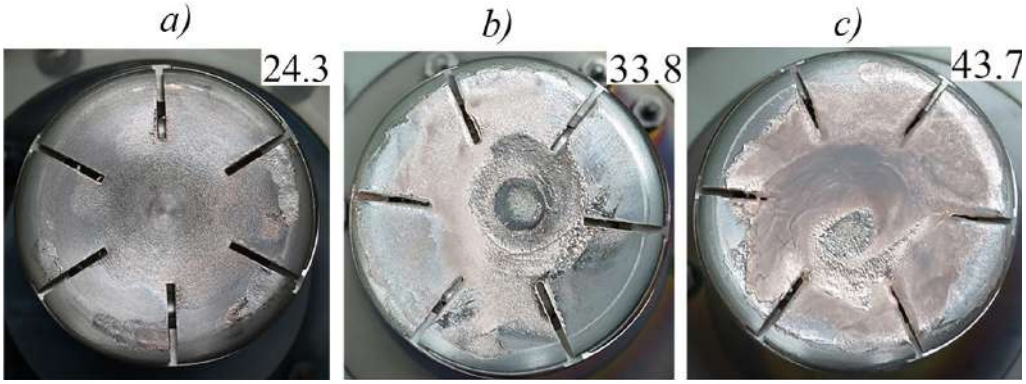


Fig. 6. Photos of anodes after single high-current pulses. The amplitude of the current pulse (kA) is indicated in the upper right corner

parts: radiation in the ultraviolet region ($200 \le \lambda \le 400$) nm and radiation in the visible and infrared regions ($400 \le \lambda \le 1100$) nm. Comparing the measurement results with and without a filter and taking into account the spectral sensitivity of the diode (Fig. 2), we obtain an estimate of the ratio of the power of radiation incident on the diode in the ultraviolet $P_{uv}$ and in the visible and infrared regions of the spectrum $P_v$. In the arc mode with anodic activity, we obtain $P_{uv}/P_v \approx (5-6) >> 1$. It can be seen that the main part of the power is emitted in the ultraviolet region. This is significant, because in the ultraviolet region ($200 \le \lambda \le 400$) nm, the sensitivity weakly depends on the wavelength and we can determine the radiation power with good accuracy without having information about the spectral distribution of radiation. In the visible and infrared regions, the sensitivity significantly depends on the wavelength and for an accurate assessment, information about the spectral distribution is needed. So far, there is no such information, especially at high currents.

Let us make an estimate of the total radiation power of the discharge $P_{uv}$ in the ultraviolet region, which, as we have seen, differs little from the power in the entire range. To do this, it is necessary to make simplifying assumptions. We will consider the plasma optically thin. Note that both the size of the source (discharge) and the receiver (diode) are much smaller than the distance between them. Note that the radiation comes to the receiver from the entire volume of plasma and falls almost normally. Therefore, we can consider the discharge as a point source, radiating uniformly in all directions. The geometry of the discharge does not matter. If the distance between the source and the receiver would not be so large compared to the size of the source or receiver, then the geometry of the source would play a role. Indeed, radiation from the near–axial region of the source would fall on the diode along the normal, and from the peripheral regions at an acute angle and the law of cosine would work.

If we consider the source to be a point, then under the conditions of this experiment, $4.4 \cdot 10^{-8}$ of the total radiation generated in the discharge falls on the receiver. Figure 7 shows the dependence of the radiation power on the current. These calculations take into account the transparency of the window. It can be seen that in modes with anode activity, the radiation power increases exponentially with an

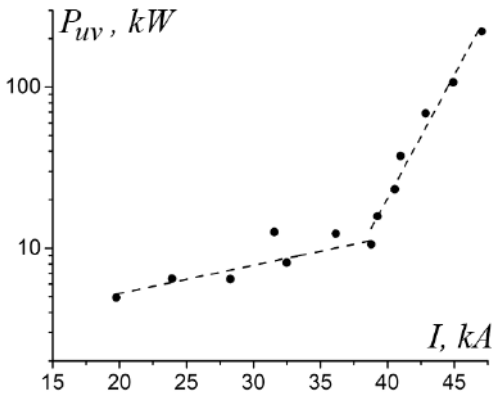


Fig. 7. The maximum radiation power (5.5 ms) in the pulse, depending on the amplitude value of the current

increase in the current amplitude. At a current amplitude of ~ 47 kA, the maximum radiation power (at 5.5 ms) is approximately 14% of the electrical power released at this moment in the discharge. Note that the radiation power in vacuum ultraviolet is not measured by us now. This is planned by us in the future. Taking into account vacuum ultraviolet, the share of radiation power may be significantly higher.

## Conclusion

In modes with anode activity, the radiation power increases exponentially with the current. At extremely high currents, when severe erosion occurs, the radiation power can reach almost 15% of the electrical power released in the discharge.

## REFERENCES

1. **Raizer Yu.P.,** Fizika gazovogo razryada, Dolgoprudny: Izd. Dom. “Intellekt”, chapter 14. 2009.

2. **Wang L., Jia S., Liu .Y, Chen B., Yang D., and Shi Z.,** Modeling and simulation of anode melting pool flow under the action of high-current vacuum arc, J. Appl. Phys. 107 (11) (2010) Art.no.113306.

3. **Barinov Yu.A., Zabello K.K., Logachev A.A., Poluyanova I.N., Sherstnev E.V., Shkol’nik S.M.,** Radiation Power of a High-Current Vacuum Arc Stabilized by an Axial Magnetic Field in the Visible and UV Ranges of the Spectrum, Tech. Phys. Lett. 47 (2) (2021) 118–121.

4. **Zabello K.K., Poluyanova I.N., Logachev A.A., Begal D.I., Shkol’nik S.M.,** Anode Surface State and Anode Temperature Distribution After Current Zero for Different AMF-Contact Systems IEEE. Plasma Sci. 47 (8) (2019) 3563−3571.

5. **Logachev A.A., Poluyanova I.N., and Klochko S.V.,** Arc voltage as a source of information about arc burning on AMF contacts IEEE Trans. Plas. Sci. 47 (8) (2019) 3572−3578.

6. **Zabello K.K., Poluyanova I.N., Logachev A.A., Barinov A.Yu., Shkol`nik S.M.,** Thermal effect on AMF electrodes at different opening speeds IEEE Trans. Plas. Sci. 49 (4) (2021) 1454−1459.

7. **Barinov Yu.A., Zabello K.K., Logachev A.A., Poluyanova I.N., Sherstnev E.V., Bogdanov A.A., and Shkol'nik S.M.,** Measurements of the radiation power of a high-current vacuum arc at high current densities”, Proc. XXIX ISDEIV (Padova: Italy), 2020, pp. 264–267.

## THE AUTHORS

**ZABELLO Konstantin K.**
zabellok@mail.ioffe.ru
ORCID: 0000-0003-4641-9934

**BARINOV Yury A.**
yury@mail.ioffe.ru
ORCID: 0000-0002-0329-5743

**LOGACHEV Alexander A.**
logatchev@mail.ioffe.ru

**POLUYANOVA Irina N.**
pin@tavrida.com

**SHERSTNEV Evgeniy V.**
89045512456@ya.ru

**SHKOL’NIK Sergey M.**
shkolnik@mail.ioffe.ru

*Received 25.10.2022. Approved after reviewing 08.11.2022. Accepted 08.11.2022.*

© Peter the Great St. Petersburg Polytechnic University, 2023

Conference materials
UDC 537.5
DOI: https://doi.org/10.18721/JPM.161.203

# Effect of an external circuit on the stability of thermionic energy converter steady states

A.B. Gerasimenko [1]✉, V.I. Kuznetsov [1]

[1] Ioffe Institute, St. Petersburg, Russia

✉ gerasimenko.alexander@mail.ioffe.ru

**Abstract.** The possibility of creating an alternating current source based on a thermionic energy converter is because, under certain conditions, an electron instability can develop in such a diode in the collisionless mode, leading to a sharp current cut-off. To implement this effect, it is enough to short electrodes through inductance. To select the optimal operation mode of the generator, it is necessary to study external inductance influence on the development of the instability. This problem is theoretically studied in the proposed work, and both over-neutralized and under-neutralized modes are considered. Dispersion equations are obtained. It is shown that when external inductance is included an instability threshold can be moved below the Pierce one. Besides, this type of instability can develop only for inductance values from a limited range.

**Keywords:** thermionic energy converter, plasma diodes

**Funding:** This study was funded by Government project "Physics of elementary, collective and dynamic processes in high-speed gas flows, low-temperature plasma and heterogeneous media" grant number [0040-2019-0022]).

**Citation:** Gerasimenko A.B., Kuznetsov V.I., Effect of an external circuit on the stability of thermionic energy converter steady states, St. Petersburg State Polytechnical University Journal. Physics and Mathematics. 16 (1.2) (2023) 25–31. DOI: https://doi.org/10.18721/JPM.161.203

This is an open access article under the CC BY-NC 4.0 license (https://creativecommons.org/licenses/by-nc/4.0/)

Материалы конференции
УДК 537.5
DOI: https://doi.org/10.18721/JPM.161.203

# Влияние внешней цепи на устойчивость стационарных режимов термоэмиссионного преобразователя энергии

А.Б. Герасименко [1]✉, В.И. Кузнецов [1]

[1] Физико-технический институт им. А.Ф.Иоффе РАН, Санкт-Петербург, Россия

✉ gerasimenko.alexander@mail.ioffe.ru

**Аннотация.** Возможность создания источника переменного тока на основе термоэмиссионного преобразователя энергии обусловлена тем, что в бесстолкновительном режиме в таком диоде при определенных условиях может развиваться электронная неустойчивость, приводящая к резкой отсечке тока. Для выбора оптимального режима работы генератора необходимо изучить влияние внешней индуктивности на развитие неустойчивости. В данной работе рассматриваются перекомпенсированный и недокомпенсированный режимы. Для них получены дисперсионные уравнения и показано, что неустойчивость может развиваться только при значениях внешней индуктивности из ограниченного диапазона.

**Ключевые слова:** электронная неустойчивость, плазменный диод, плазменные колебания

© Gerasimenko A.B., Kuznetsov V.I., 2023. Published by Peter the Great St.Petersburg Polytechnic University.

**Финансирование:** Работа выполнена в рамках Государственного задания «Физика элементарных, коллективных и динамических процессов в высокоскоростных газовых потоках, низкотемпературной плазме и гетерогенных средах» (код темы [0040-2019-0022]).

**Ссылка при цитировании:** Герасименко А.Б., Кузнецов В.И. Влияние внешней цепи на устойчивость стационарных режимов термоэмиссионного преобразователя энергии // Научно-технические ведомости СПбГПУ. Физико-математические науки. 2023. Т. 16. № 1.2. С. 25–31. DOI: https://doi.org/10.18721/JPM.161.203

Статья открытого доступа, распространяемая по лицензии CC BY-NC 4.0 (https://creativecommons.org/licenses/by-nc/4.0/)

## Introduction

Thermionic energy converter (TEC) is used for direct conversion of heat into electrical energy, and is usually a DC source. A concept of AC source based on TEC has been proposed after the study carried out at the Ioffe Institute [1, 2]. This was made possible due to the fact that, under certain conditions, an electron instability develops in the TEC leading to a sharp current cut-off. To implement this effect, the TEC should be in the collisionless (Knudsen) mode, and the electrodes must only be shorted through inductance. The operability of such a device was confirmed experimentally [2]. Thus, both obtaining of electric energy and conversion of DC voltage into AC one are carried out directly in the TEC. There is no need for additional voltage converters. As a result, there are prospects to reduce weight characteristics, to reduce cost as well as to increase reliability of the power plant based on TEC. However, in order to develop the generator it is important to optimize operation modes of the device.

In this paper, we present results of studying the stability features of TEC stationary states and investigate at what values of an external inductance the instability can occur in the diode from external circuit system.

## Materials and Methods

This paper considers a collisionless (Knudsen) diode with surface ionization (KDSI) in which electrons are supplied from the hot emitter by thermal emission and ions are supplied by surface ionization.

There are two modes of operation: over-neutralized and under-neutralized. In the first case, more ions than electrons enter from the emitter (the neutralization parameter $\gamma = n_{i,0} / n_{e,0} > 1$, where $n_{i,0}$ ($n_{e,0}$) is the ion (electrons) density escaping from the emitter surface, at the emitter). As a rule, self-consistent stationary solutions are characterized by potential distributions (PD) that have a broad quasi-neutral plateau in the most part of the inter-electrode gap, while there is potential jump in small near-electrode regions. There is a monotonic potential distribution if $\gamma > 1$. It consists of zone with a sharp potential jump near the emitter, a plateau zone with a zero electric field and a potential jump near the collector that has the same sign as that at the emitter. On the contrary, in the case of $\gamma < 1$ PDs vary non-monotonically: a virtual cathode (VC) is formed near the emitter, reflecting a portion of electrons back to it. There is a strong potential jump and a quasi-neutral plateau region. The potential jump near the collector is of the same sign as that at the VC outside. These are PDs with virtual cathode (VCPD).

At the KDSI, the velocity distribution functions of electrons (EDF) and ions escaping from the emitter surface are semi-Maxwellian with the emitter temperature $T_E$. The charged particle densities in the stationary mode depend only on the potential at the current point and on the potentials at the points of particle reflection from the potential barriers. For the case of KDSI, one can obtain analytical expressions for charged particle densities for any type of PD [4].

For the convenience, we turn to dimensionless quantities, and choose the electron energy at the emitter $W_E = kT_E / 2$ and the Debye-Hückel length $\lambda_D^E = \left[2\tilde{\epsilon}_0 W_E / (e^2 n_{e,0})\right]^{1/2}$ (here $e$ is electron charge and $\tilde{\epsilon}_0$ is vacuum permittivity) as units of energy and length. Then the dimensionless potential $\eta$ is normalized to $kT_E / e$.

© Герасименко А.Б., Кузнецов В.И., 2023. Издатель: Санкт-Петербургский политехнический университет Петра Великого.

In the over-neutralized mode with MPD the particle densities are given by

$$n_e(\eta) = n_{e,0}\, exers(\eta),$$
$$n_i(\eta, \eta_C) = \gamma n_{e,0}\left[2\exp(-\eta) - \exp(-\eta_C) exers(\eta_C - \eta)\right]. \quad (1)$$

Here $\eta_C$ is the potential difference between the electrodes, and the function $exers\,(x) = \exp(x)\,[1-erf(\sqrt{x})]$. The relationship between the neutralization parameter $\gamma$ and the plateau potential $\eta_p$ is determined from the quasi-neutrality condition.

$$exers(\eta_p) - \gamma\left[2\exp(-\eta_p) - \exp(-\eta_C) exers(\eta_C - \eta_p)\right] = 0. \quad (2)$$

In the under-neutralized mode with VCPD the particle densities are given by

$$n_e(\eta, \eta_m) = n_{e,0}\exp(\eta_m) exers(\eta - \eta_m)$$
$$n_i(\eta, \eta_C) = \gamma n_{e,0+}\begin{cases}\left[2exers(-\eta) - \exp(-\eta_C) exers(\eta_C - \eta)\right], & \eta < 0,\\ \left[2\exp(-\eta) - \exp(-\eta_C) exers(\eta_C - \eta)\right], & \eta > 0.\end{cases} \quad (3)$$

We need to solve a system of two equations to calculate the minimum potential $\eta_m$ and plateau potential $\eta_p$. The first of equations corresponds to the condition of quasi-neutrality at the plateau $\eta = \eta_p$, and the second one corresponds to the condition of zero total charge on the VC outer part, i.e. between points $\eta_m$ and $\eta_p$, where the electric field strengths vanish:

$$\exp(\eta_m) exers(\eta_p - \eta_m) - \gamma\left[2\exp(-\eta_p) - \exp(-\eta_C) exers(\eta_C - \eta_p)\right] = 0,$$
$$\exp(\eta_m)\left[iers(\eta_p - \eta_m) - 1\right] - \gamma\left\{2[iers(-\eta_m) - \exp(-\eta_p)] + \right. \quad (4)$$
$$\left. + \exp(-\eta_C)\left[iers(\eta_C - \eta_p) - iers(\eta_p - \eta_m)\right]\right\} = 0.$$

Here, the function $iers\,(x) = (2/\sqrt{\pi})(\sqrt{x}) exers\,(x)$. One can find more detailed consideration of all types of PD in the KDSI in [4].

In our work, we study the electron instability of solutions both with MPD, and with VCPD. In this case, the ions can be considered as immovable. We derive formulas for the diode impedance taking into account the presence of inductance in the external circuit, and use them to study dispersion characteristics of the diode.

In the over-neutralized mode with MPD and in the under-neutralized mode with VCPD, a flow of accelerated electrons with small energy dispersion enters the plasma.

Therefore, we assume that a mono-energetic electron flow enters from the emitter at a velocity which value will be determined below for each mode.

## Results and Discussion

Stability of solutions with MPD in the over-neutralized mode for a diode included in an external circuit without reactive elements was studied in [5]. The PD was represented as

$$\eta(\zeta, \tau) = \eta_0(\zeta) + \tilde{\eta}(\zeta)\exp(-i\Omega\tau), \quad |\,\tilde{\eta}(\zeta)\,| \ll \eta_0(\zeta). \quad (5)$$

Here $\eta_0(\zeta)$, $\tilde{\eta}(\zeta)$ and $\Omega$ are the unperturbed PD, the potential perturbation amplitude, and the complex frequency respectively. Evolution of small potential perturbation was tracked.

In this case, the potential perturbation in the plasma does not affect the EDF at the emitter $f_0(u_0)$ The following equation was obtained for the potential perturbation amplitude:

$$\tilde{\eta}'(\zeta) + \int_0^\infty du_0 u_0 f_e^0(u_0)\int_0^\zeta \frac{dx}{u^3(x,u_0)}\int_0^x dy \exp\{i\Omega[\sigma(\zeta,u_0) - \sigma(y,u_0)]\}\tilde{\eta}'(y) = -\frac{i}{\Omega}\tilde{j}. \quad (6)$$

Here $u(\zeta,u_0)$ and $\sigma(\zeta,u_0)$ are the electron velocity at point $\zeta$ and its motion time from emitter to point $\zeta$ in field with potential $\eta_0(\zeta)$, and $\tilde{j}$ is an amplitude of the total current-density perturbation. At $\eta_p \gg kT_E / W_p$ the EDF at the emitter can be approximated by $\delta$-function: $f_e^0(u_0) = n_E\delta(u_0 - u_E)$ with $n_E = n_{e,0}$, $u_E = \sqrt{(kT_E/m)}$. Then in Eq. 6 one gets rid of one integration. Equation (6) allows

one to find the perturbation potential amplitude for the mode without reflection of electrons from potential barriers at any form of $\eta_0(\zeta)$.

The boundary conditions for perturbations at the emitter are the same as in the Pierce diode, where the monoenergetic electron flow moves through a uniform background of immovable ions, and $\eta_0(\zeta) \equiv 0$:

$$\tilde{\eta}(\zeta)|_{\zeta=0} = 0, \qquad \tilde{j}_e(\zeta)|_{\zeta=0} = 0. \tag{7}$$

Here $\tilde{j}_e$ is a perturbation amplitude of the electron convection current-density.

In studying an effect of the external circuit on stability features of the diode it is convenient to consider the impedance of the diode $Z(\Omega,\sigma) = -\tilde{\eta}(\Omega,\sigma)/\tilde{j}$; here $\tilde{\eta}(\Omega,\sigma)$ is an amplitude of the collector potential perturbation.

When the unperturbed potential of the collector coincides with the plateau potential, the situation is close to the Pierce diode: the electric field in almost the entire gap vanishes. Some differences are that the EDF at the plateau is slightly different from the mono-energetic one, and the near-emitter region, where the potential and charged particle densities vary greatly, has a width although small compared to $\delta$, but finite. When $\eta_p \gg kT_E / W_p$, where $W_p = kT_E/2 + e\Phi_p$ is the kinetic energy of the plasma electrons, the thermal spread of electron velocities can be neglected. In [5] it was shown that the EDF at the emitter should be chosen as following:

$$f_e^0(v) = n_e \delta\left(v - \sqrt{kT_E / m}\right).$$

When deriving an equation for the potential perturbation we follow [5]. The electron energy $W_p$ in plasma and Debye-Hückel length $\lambda_D^p = \left[2\tilde{\epsilon}_0 W_p / (e^2 n_p)\right]^{1/2}$ are used as energy and length units. Note, that plasma energy and Debye-Нькel length parameters are connected with the emitter ones by formulas [5]

$$W_p = W_E + e\Phi_p, \quad \lambda_D^p = \lambda_D^E \left([1 + 2\eta_p(\gamma)] / exers[\eta_p(\gamma)]\right)^{1/2}. \tag{8}$$

Here $\eta_p = e\Phi_p / kT_E$ is the plasma potential calculated in the "emitter" units.

The diode impedance is made up of the impedance $Z_E(\Omega)$ of the emitter region $(0, \zeta_E)$ and one of the plateau region $Z_p(\Omega)$ $(\zeta_E, \delta)$. In the near-emitter region, the unperturbed PD is approximated by a straight line: $\eta_0(\zeta) = \kappa\zeta$. It is found that $\zeta_E$ magnitude is well described by the formula $\zeta_E = 0.62\gamma^{-0.28}(\lambda_D^E/\lambda_D^p)$ for $\gamma$ values from 2 to 10. The following expression is obtained for $Z_E(\Omega)$:

$$Z_E(\Omega,\zeta_E) = \frac{i}{\Omega}\left\{\zeta_E - \frac{\pi}{2\alpha^3}\int_{\alpha\sqrt{u_{em}}}^{\alpha} dy\, y^2 \int_{\alpha\sqrt{u_{em}}}^{y} dx\, x^2 T_{11}(y,x) \exp\left[i\Omega\frac{1}{2\alpha}(y^2 - x^2)\right]\right\}. \tag{9}$$

Here $\alpha = 2/\kappa$, $u_{em} = \sqrt{(W_E/W_p)}$ is a characteristic electron velocity at the emitter, $T_{11}(y,x) = J_1(x)N_1(y) - J_1(y)N_1(x)$, and $J_1$ and $N_1$ are Bessel and Neumann functions of index 1.

The following expression is obtained for $Z_p(\Omega, \delta)$:

$$\begin{aligned} Z_p(\Omega,\delta) = -\frac{1}{2\Omega(1-\Omega^2)}\Bigg[&\frac{1-\Omega}{1+\Omega}(1+g_+)\{1-\exp[i(1+\Omega)(\delta-\zeta_E)]\} - \\ &-\frac{1+\Omega}{1-\Omega}(1+g_-)\{1-\exp[-i(1-\Omega)(\delta-\zeta_E)]\} + 2i\Omega^2(\delta-\zeta_E)\Bigg]. \end{aligned} \tag{10}$$

Here

$$\begin{gathered} g_+ = (1+\Omega)[(1-\Omega)f_1 + if_2], \quad g_- = (1-\Omega)[(1+\Omega)f_1 - if_2], \\ f_1 = -i\Omega Z_E'(\zeta_E) - 1, \quad f_2 = i\Omega Z_E''(\zeta_E), \end{gathered} \tag{11}$$

and $Z'_E(\zeta_E)$ and $Z''_E(\zeta_E)$ are the values of the 1st and 2nd derivatives of the impedance $Z_E$ at the right boundary of the region $(0, \zeta_E)$. In the case under consideration

$$f_s = \frac{\pi}{2a}\int_{\sqrt{V}a}^{a} dx\, x^2 T_{s1}(a,x) \exp\left\{\frac{i\Omega}{2a}(x^2 - a^2)\right\}, \quad s = 1, 2. \tag{12}$$

The matching condition for a diode with an inductive external circuit is

$$Z_E(\Omega,\zeta_E)+Z_p(\Omega,\delta)-i\Omega L=0. \qquad (13)$$

This equation with $L=0$ was solved in [5]. The dispersion curves, i. e. the dependences of the eigen-mode growth rate Γ and frequency Ω on the dimensionless inter-electrode gap δ were plotted. It turned out that both these dependencies are close to the similar dependences for the Pierce diode. The instability threshold is close to that for the Piers diode $\delta_{th}^{P}=\pi$. The picture of the KDSI generation regions is similar to that for the Pierce diode, too [3], but, unlike the latter, in the KDSI the generation regions are localized. This is due to the fact that the real part of the emitter region impedance is positive.

We have studied solutions of the dispersion equation (13) when inductance is present in the external circuit. It is shown that, same as in the Pierce diode [6], an external inductance leads to the appearance of a new instability branch. In addition, it can intersect Γ = 0 axis at δ values below $\delta_{th}^{P}$. This means that by varying the inductance it is possible to change the emission current value at which sharp current cut-off occurs, i.e., to optimize the TEC operation regimes. It is also shown that instability can develop only at values of the external inductance lying in a limited range. For example, at γ = 10 this range is $0 < L < 2.5$ (see Fig.1, *a*). It should be noted, that new branch are corresponded frequencies higher the plasma frequency.

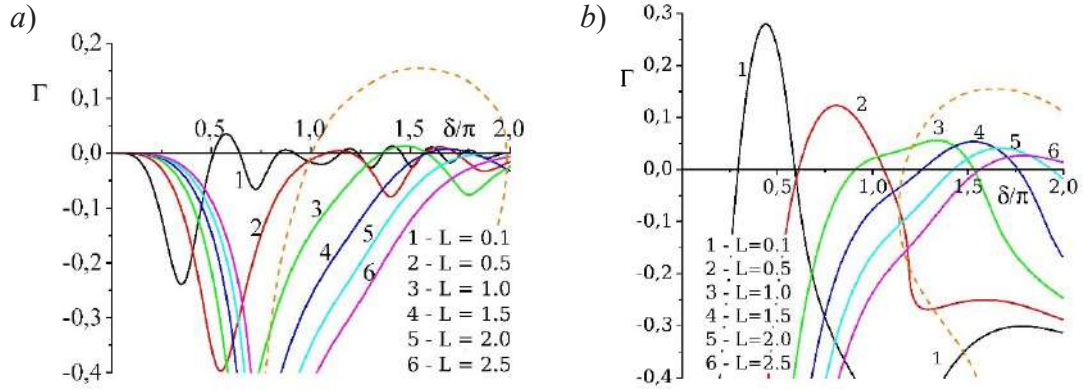


Fig. 1. The growth rate Γ vs δ for various values of an inductance L = 0.1 (1), 0.5 (2), 1.0 (3), 1.5 (4), 2.0 (5), 2.5 (6); dashed curve is the 1st aperiodic Pierce branch in over-neutralized regime, γ = 10 (*a*), and in under-neutralized regime, γ = 0.002 (*b*)

When studying stability of PDs with VC, one can exclude the area between the emitter and the position of VC top $\zeta_m$ due to the small width of this area and study an equivalent problem, when the emitter is placed in a point with coordinates ($\zeta_m$, $\eta_m$). Current supplied by "new" emitter corresponds to flow of the electrons which overcame the potential barrier $\eta_m$ occurring in the stationary field, i.e. the current is $j_m = j_E \exp(\eta_m)$ [7, 8]. In this case, we can assume that during the initial stage of the instability development, perturbation of the VC top position and of the electric field at this top are zero.

The following equation is obtained for the potential perturbation amplitude:

$$\tilde{\eta}'(\zeta)+\int_0^\infty du_1 u_1 f_e^0(u_1)\int_0^\zeta \frac{dx}{u^3(x,u_1)}\int_0^x dy\exp\{i\Omega[\sigma(\zeta,u_1)-\sigma(y,u_1)]\}\tilde{\eta}'(y)=$$
$$=-\frac{i}{\Omega}\tilde{j}\int_0^\infty du_1 u_1 f_e^0(u_1)[\exp\{i\Omega\sigma(\zeta,u_1)\}-1]. \qquad (14)$$

Here $u_1$ is the electron velocity at the "new" emitter. The "current" term in the right part of Eq.(14) is due to the fact that in this case it must be taken into account a perturbation of the lower bound of the velocity region at the emitter, over which the integration takes place when density is calculated. It should be noted, that in this approximation, the potential in the plasma is actually increased by the VC height $|\Phi_m|$, and is $\Delta\Phi = \Phi_p - \Phi_m$. When ΔΦ turns out to be large enough, the thermal velocity spread of electrons in the plasma can be neglected and the EDF at the new emitter can be chosen in the form $f_e^0(u_1) = (j_m/e)\,\delta(u_1)/u_1$.

The boundary conditions for perturbations at the emitter differ from the Peirce-like ones (7) and have the form

$$\tilde{\eta}(\zeta)|_{\zeta=0}=0, \qquad \tilde{\eta}'(\zeta)|_{\zeta=0}=0. \tag{15}$$

When calculating the impedance, we approximate the PD on the external part of the VC by the law, which corresponds to the vacuum diode with zero electric field strength at the emitter:

$$\Phi(z)=\alpha z^{4/3}, \qquad \alpha=\left(\frac{3}{2}\right)^{4/3}\left(\frac{m j_m^2}{2e\epsilon_0^2}\right)^{1/3}. \tag{16}$$

This approximation describes well the behavior of the PD to the right of the VC top [7]. For the position of emitter region boundary $\zeta_E$, electron velocity at the plateau $u_p$ and electron transit time through the emitter layer $\sigma_E$ we have

$$\zeta_E=\left(2^{5/4}/3\right)(\eta_p-\eta_m)^{3/4}, \quad u_p=\left(6^{2/3}/2\right)\zeta_E^{2/3}, \quad \sigma_E=(6\zeta_E)^{1/3}. \tag{17}$$

Here units of length and energy are selected using the emitter parameters, but only with the replacement $\eta_p$ with $\Delta\eta=\eta_p-\eta_m$. To go to plasma units, we need decrease $\zeta_E$ by ratio of the plasma and emitter Debye-Hückel lengths: $\lambda_D^E/\lambda_D^p=(\eta_p-\eta_m)^{-3/4}\exp(-\eta_m/2)$.

To study the diode generation regions and plasma dispersion, let's consider its impedance. As in the over-neutralized mode, it is composed of the impedances of the emitter layer $Z_E(\Omega,\zeta_E)$ and that of the plateau region $Z_p(\Omega,\delta)$. In this case, we have the following expression for $Z_E(\Omega,\zeta_E)$:

$$Z_E(\Omega,\zeta_E)=\frac{1}{\Omega^4}\left[\frac{i}{6}(\Omega\sigma_E)^3+i\Omega\sigma_E+2+\left(i\Omega\sigma_E-2\right)\exp(i\Omega\sigma_E)\right]. \tag{18}$$

The impedance of the plateau region $Z_p(\Omega,\delta)$ is determined by the formulas (10) and (11), but only with other functions $f_1$ and $f_2$:

$$f_1=\frac{1}{\Omega^2\sigma_E^2}\left[1+(i\Omega\sigma_E-1)\exp(i\Omega\sigma_E)\right],$$
$$f_2=\frac{-4}{\Omega^2\sigma_E^5}\left[2+(\Omega^2\sigma_E^2+2i\Omega\sigma_E-2)\exp(i\Omega\sigma_E)\right]. \tag{19}$$

Regions of the KDSI generation for solutions with VCPD in the under-neutralized mode with a purely active external circuit were studied in [7]. It turned out that these regions are localized. This is because the real part of the emitter layer impedance is positive. The $\Omega(\delta)$ dependences turn out to be close to those in the over-neutralized mode. The $\Gamma(\delta)$ dependences are similar to those in the over-neutralized mode, but are shifted in the region of negative $\Gamma$ values. Besides, all bifurcation points on aperiodic branches that are the oscillatory branch start lie below the $\Gamma=0$ axis. The instability threshold is shifted to the right of the $\delta_{th}^P$ point by a value, approximately equal to $\zeta_E$. When there is inductance in the external circuit, new eigen-mode similar to that in over-neutralized mode appears, and it has frequency higher than the plasma frequency. Its $\Gamma(\delta)$ dependence can intersect $\Gamma=0$ axis at $\delta$ values below the Pierce threshold (see Fig.1, *b*). For example, at $\gamma=0.002$ it happens when $L\approx 1.4$.

## Conclusion

In order to create an alternative current directly in the TEC, its electrodes are bridged over an inductance with a magnitude of about several units of $\mu H$ [2]. Feasibility of such a generator is based on the electron instability development in collisionless plasma diodes resulting in the current cut-off effect. We have demonstrated that presence of an external inductance induces a new unstable eigen-mode, which can make the instability threshold lower than the Pierce one. Thus, by varying the external inductance one can control current density magnitude at which the cut-off occurs and affect the generator performance.

In order to calculate the optimum magnitude of the inductance one has to calculate the non-linear time-dependent process in the KDSI plasma taking into account a time variation of the collector potential caused by the presence of an inductance.

## REFERENCES

1. **Babanin V.I., Kuznetsov V.I., Kolyshkin I.N., Sitnov V.I., Ender A.Ya.,** Termoemissionyj sposob preobrazovzniya teplovoj energii v elektricheskuju [Thermoemission method of converting thermal energy into electricity], Russian Federation Patent No. 2030017 (1991).

2. **Babanin V.I., Ender A.Ya., Kolyshkin I.N., Kuznetsov V.I., Sitnov V.I., Paramonov D.V.,** Next generation solar bimodal systems, In: Proceedings of the 32nd IECEC. Honolulu, USA. (1997) 427–429.

3. **Kuznetsov V.I., Ender A.Ya.,** The Q, G-method in physics of collisionless plasma, Plasma Physics Reports. 41 (2015) 240−253.

4. **Ender A.Ya.,** Termoemissionnij preobrazovatel' teplovoi energii v elektricheskuju v knudsenovskon rezhime Diss. kand. fiz.-mat. nauk [Thermionic heat-to-electric converter in the Knudsen regime. Cand. phys. and math. sci. diss.], Leningrad, 1972.

5. **Ender A.Ya., Kuhn S., Kuznetsov V.I.,** The Pierce-diode approximation to the single-emitter plasma diode, Physics of Plasmas. 13 (2006) 113506.

6. **Kuznetsov V.I., Gerasimenko A.B.,** The external circuit effect on the steady states of the Pierce diode, Journal of Physics: Conference Series. 1135 (1) (2018) 012090-012093

7. **Kuznetsov V.I., Ender A.Ya.,** Oscillations in a collisionless thermionic converter, Soviet Physics Technical Physics. 17 (1973) 1859–1867.

8. **Kuznetsov V.I., Ender A.Ya.,** Method of investigating transitional electronic processes in the Knudsen diode. Ioffe Institute Preprint No. 604, 1979.

## THE AUTHORS

**GERASIMENKO Alexander B.**
gerasimenko.alexander@mail.ioffe.ru
ORCID: 0000-0001-8654-8242

**KUZNETSOV Victor I.**
victor.kuznetsov@mail.ioffe.ru
ORCID: 0000-0002-8963-5197

*Received 25.10.2022. Approved after reviewing 21.12.2022. Accepted 21.12.2022.*

© Peter the Great St. Petersburg Polytechnic University, 2023

Conference materials
UDC 533.9
DOI: https://doi.org/10.18721/JPM.161.204

# Stability features of inhomogeneous steady-state potential distributions in diode with counter-streaming electron and ion flows

L.A. Bakaleinikov [1]✉, V.I. Kuznetsov [1], E.Yu. Flegontova [1]

[1] Ioffe Institute, St Petersburg, Russia
✉ bakal.ammp@mail.ioffe.ru

**Abstract.** This paper continues studying stability features of steady states of a diode with counter-streaming electron and ion flows. In our recent paper, an integral-differential equation for the potential perturbation amplitude in the mode without potential barriers reflecting charged particles within the plasma was derived. Its exact solution was found for homogeneous steady-state field distribution. In this paper, we propose a semi-analytical method to solve the integral-differential equation for potential perturbation amplitude in the case of inhomogeneous steady-state solutions. It is based on the use of the piecewise linear approximation of the integral operator kernel and the variable coefficient as well as the potential perturbation distribution. A dispersion equation is obtained and five first dispersion branches are constructed. As a result, we have proved that all steady state potential distributions with the values of dimensionless inter-electrode gap up to $10\pi/\sqrt{2}$ are unstable. Numerical calculations of the potential perturbation development confirm analytical results.

**Keywords:** plasma diode, electron and ion flows, plasma instability

**Funding:** This study was funded by Government project "Physics of elementary, collective and dynamic processes in high-speed gas flows, low-temperature plasma and heterogeneous media", grant number [0040-2019-0022]).

**Citation:** Bakaleinikov L.A., Kuznetsov V.I., Flegontova E.Yu., Stability features of inhomogeneous steady-state potential distributions in diode with counter-streaming electron and ion flows, St. Petersburg State Polytechnical University Journal. Physics and Mathematics. 16 (1.2) (2023) 32–38. DOI: https://doi.org/10.18721/JPM.161.204

This is an open access article under the CC BY-NC 4.0 license (https://creativecommons.org/licenses/by-nc/4.0/)

Материалы конференции
УДК 533.9
DOI: https://doi.org/10.18721/JPM.161.204

# Устойчивость неоднородного стационарного распределения потенциала в диоде со встречными потоками электронов и ионов

Л.А. Бакалейников [1]✉, В.И. Кузнецов [1], Е.Ю. Флегонтова [1]

[1] Физико-технический институт им. А.Ф. Иоффе РАН, Санкт-Петербург, Россия
✉ bakal.ammp@mail.ioffe.ru

**Аннотация.** Статья продолжает исследование устойчивости стационарных состояний диода со встречными потоками электронов и ионов. В предыдущей работе было получено интегро-дифференциальное уравнение для возмущения потенциала в режиме без отражения заряженных частиц от потенциальных барьеров. Для однородного распределения потенциала было найдено его аналитическое решение. В этой статье мы предлагаем полуаналитический метод решения этого уравнения в случае неоднородных распределений потенциала. С помощью этого метода мы исследовали устойчивость стационарных решений для длин диода вплоть до $10\pi/\sqrt{2}$ и показали, что все они неустойчивы. Численное моделирование эволюции возмущения подтвердило результаты, полученные аналитически.

© Bakaleinikov L.A., Kuznetsov V.I., Flegontova E.Yu., 2023. Published by Peter the Great St. Petersburg Polytechnic University.

**Ключевые слова:** плазменный диод, потоки электронов и ионов, плазменная неустойчивость

**Финансирование:** Работа выполнена в рамках Государственного задания «Физика элементарных, коллективных и динамических процессов в высокоскоростных газовых потоках, низкотемпературной плазме и гетерогенных средах» (код темы [0040-2019-0022]).

**Ссылка при цитировании:** Бакалейников Л.А., Кузнецов В.И., Флегонтова Е.Ю. Устойчивость неоднородного стационарного распределения потенциала в диоде со встречными потоками электронов и ионов // Научно-технические ведомости СПбГПУ. Физико-математические науки. 2023. Т. 16. № 1.2. С. 32–38. DOI: https://doi.org/10.18721/JPM.161.204

Статья открытого доступа, распространяемая по лицензии CC BY-NC 4.0 (https://creativecommons.org/licenses/by-nc/4.0/)

## Introduction

The study of the stability of steady states of plasma diodes with counter-streaming electron and ion flows is necessary to understand the mechanism of operation of a high-current plasma diode modulator, which is used to convert a constant voltage of several tens of volts accumulated on a series-connected thermionic energy converters into alternating voltage [1]. In such a diode the flow of electrons coming from the hot emitter and passing through the plasma region is strongly accelerated by a potential jump existing near the collector and ionizes caesium atoms. As a result, a stream of ions moving towards the emitter appears in the narrow collector layer. When studying the stability of steady-state solutions for the diode in the first approximation it can be assumed that the ion flow comes from the collector surface.

Steady-state solutions for such a diode were studied in detail in [2]. It was shown that there are several solutions for fixed inter-electrode gap. They are characterized by different values of the electric field strength at the left electrode. The representation of such solutions on the $(\varepsilon_0,\delta)$ plane, where $\delta$ and $\varepsilon_0$ are the dimensionless inter-electrode gap and electric field strength at the left electrode, respectively, is given in Fig. 4 in Ref.[2]. They belong to two modes: 1) all charged particles move in the inter-electrode gap without reflection and reach the opposite electrodes, 2) the potential distribution has extrema reflecting a portion of the particles. Thus, the problem of determining steady-states in a diode plasma can be considered solved.

Now, one needs consistently study the stability features of each type of steady-state solutions. It is important because non-linear oscillation can develop in plasma instead of stationary states as was reported in Refs. [1], [3]. In Ref.[4], stability features of steady-state solutions of the first type were examined. The method of expanding of potential distribution and charged particles densities into series in powers of small potential perturbation was used. It was assumed that the electrons fly through the interelectrode gap in less time than it takes for the ions to displace to the distance of the order of Debye-Hückel length. This allowed us to believe that perturbations develop with ionic velocities, i.e. to study ionic instability.

An integral-differential equation for the electric field perturbation amplitude was derived. This equation was solved analytically for a homogeneous steady-state solution (branch $n_0$ in Fig. 4 in [2]). The study of dispersion relation showed that there was a threshold in the magnitude of the inter-electrode gap, when exceeded an aperiodic instability developed in the diode plasma.

This paper examines stability features of steady-state solutions with inhomogeneous electric field distribution. For this purpose we have proposed a new original method for solving the equation for the field perturbation amplitude obtained in [4], which is suitable for studying stability of any potential distribution without potential barriers which can reflect charged particles. Applying this method, we have investigated stability features of the solutions belonging to the $n_j$ branches with $j > 0$ (see Fig. 4 in [2]). In addition, we performed numerical calculations of the perturbation evolution for these steady-state solutions. It has been established that all inhomogeneous steady-state solutions of this type are unstable.

© Бакалейников Л.А., Кузнецов В.И., Флегонтова Е.Ю., 2023. Издатель: Санкт-Петербургский политехнический университет Петра Великого.

**Solution of the equation for the electric field perturbation amplitude**

We consider a diode of planar geometry. We assume that a mono-energetic flow of electrons enters the plasma from the left electrode with velocity $v_{e,0}$ and density $n_{e,0}$, while ions enter from the right electrode with a velocity $-v_{i,0}$ and density $n_{i,0}$. Charged particles move without collisions, and when reaching any electrode, they are absorbed. We assume also that electrons and ions enter into inter-electrode gap with the same kinetic energies, i.e. $W_0 \equiv mv_{e,0}^2/2 = Mv_{i,0}^2/2$ (here $m$ and $M$ are the electron and ion masses). As in Ref.[4] we assume that electrons fly through the inter-electrode gap in less time than it takes for ions to move the distance of the order of the Debye-Hückel length $\lambda_D$. This is equivalent to the condition $L/\lambda_D \ll \sqrt{(M/m)}$. In this case, the electrons "instantly" adjust to the existing electric field, and to study the time-dependent problem it is necessary to take into account only the ion movement effects.

For the consideration convenience, we turn to dimensionless quantities, choosing $W_0$ and $\lambda_D = [2\epsilon_0 W_0/(e^2 n_{e,0})]^{1/2}$ as units of energy and length; here $e$ is the electron charge, and $\epsilon_0$ is the vacuum permeability. The electron velocity is measured in units $v_{e,0}$, while ion one is measured in units $v_{i,0} = v_{e,0}\sqrt{(m/M)}$.

When studying the stability features of steady-state solutions, we track evolution of small potential perturbation presenting the potential distribution (PD) as

$$\eta(\zeta,\tau) = \eta_0(\zeta) + \tilde{\eta}(\zeta)\exp(-i\Omega\tau), \quad |\tilde{\eta}(\zeta)| << \eta_0(\zeta). \tag{1}$$

Here $\eta_0(\zeta)$, $\tilde{\eta}(\zeta)$ and $\Omega$ are the unperturbed PD, the potential perturbation amplitude, and the complex frequency respectively. In Ref.[4], integral-differential equation for $\tilde{\eta}(\zeta)$ was derived

$$\begin{aligned}\tilde{\eta}''(\zeta) = -u_e^{-3}(\zeta)\tilde{\eta}(\zeta) + u_i^{-3}(\zeta)\int_\zeta^\delta dx \exp\{i\Omega[\sigma_i(\zeta)-\sigma_i(x)]\}\tilde{\eta}'(x) + \\ + i\Omega u_i^{-1}(\zeta)\int_\zeta^\delta dx u_i^{-3}(x)\int_x^\delta dy \exp\{i\Omega[\sigma_i(\zeta)-\sigma_i(y)]\}\tilde{\eta}'(y).\end{aligned} \tag{2}$$

Here $u_e(\zeta) = [1 + 2\eta_0(\zeta)]^{1/2}$ and $u_i(\zeta) = [1 - 2\eta_0(\zeta) + 2V]^{1/2}$ are the electron and ion undisturbed velocities corresponding to the mono-energetic particle velocity distributions, and $\sigma_i(\zeta) = \int_\zeta^\delta dx[u_i(x)]^{-1}$ is the ion time of flight from the right boundary to the point $\zeta$.

Boundary condition for $\tilde{\eta}(\zeta)$ at the right boundary is $\tilde{\eta}(\delta) = 0$. On the other hand, $\tilde{\eta}'(\delta)$ is considered to be an arbitrary parameter.

A special case $\eta_0(\zeta) \equiv 0$ was considered in [4]. An analytical solution of Eq. 2 was found. In this paper, we study the stability features of inhomogeneous steady-state solutions without potential barriers so that all charged particles move in the inter-electrode gap without reflection and reach the opposite electrodes. The PDs typical for such solutions are shown in Fig. 1. As in the case of homogeneous solution we use Eq. 2 for this purpose. After calculating the first integral on the right-hand side of Eq. 2 in parts and substituting the result into the second term, we can rewrite this equation as

$$\begin{aligned}\tilde{\eta}''(\zeta) + \left[u_e^{-3}(\zeta) + u_i^{-3}(\zeta)\right]\tilde{\eta}(\zeta) = \\ = -i\Omega\int_\zeta^\delta dx\left[u_i^{-1}(x)u_i^{-3}(\zeta) + u_i^{-3}(x)u_i^{-1}(\zeta)\right]\exp\{i\Omega[\sigma_i(\zeta)-\sigma_i(x)]\}\tilde{\eta}(x) + \\ + \Omega^2 u_i^{-1}(\zeta)\int_\zeta^\delta dy u_i^{-1}(y)\exp\{i\Omega[\sigma_i(\zeta)-\sigma_i(y)]\}\tilde{\eta}(y)\int_\zeta^y dx u_i^{-3}(x) = \int_\zeta^\delta dx K(\zeta,x)\tilde{\eta}(x).\end{aligned} \tag{3}$$

The RHS of Eq. 3 is the Volterra integral operator with a degenerate kernel. To solve this equation, we propose the numerical-analytical method. It is as follows. We divide the entire interval $[0, \delta]$ into subintervals with boundaries at the $\zeta_k$ points: $0 = \zeta_0 < \zeta_1 < \cdots < \zeta_{N-1} < \zeta_N = \delta$, and approximate Eq. 3 in each subinterval, replacing the functions $u_e^{-3}(\zeta)$, $u_i^{-3}(\zeta)$, $u_i^{-1}(\zeta)$, $u_e^{-3}(\zeta) + u_i^{-3}(\zeta)$ with their linear approximations. We solve the equations sequentially in intervals $[\zeta_{k-1},\zeta_k]$ starting from the right boundary. We designate an approximation for the perturbation amplitude $\tilde{\eta}(\zeta)$ in the interval $[\zeta_{k-1},\zeta_k]$ as $\tilde{\eta}_k(\zeta)$ . The integral on the RHS of Eq. 3 is represented as

$$\int_\zeta^\delta dx K(\zeta,x)\tilde{\eta}(x) \approx \int_\zeta^{\zeta_k} dx \tilde{K}_k(\zeta,x)\tilde{\eta}_k(x) + \sum_{j=k+1}^{N}\int_{\zeta_j-1}^{\zeta_j} dx \tilde{K}_j(\zeta,x)\tilde{\eta}_j(x) \equiv F_k(\zeta) + H_k(\zeta), \tag{4}$$

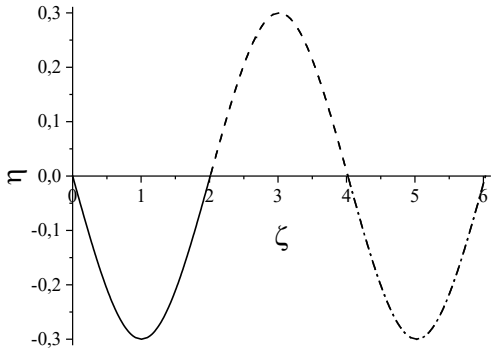


Fig. 1. PDs specific to inhomogeneous steady-state solutions: solid curve corresponds to $n_1$, solid + + dashed one to $n_2$ and solid + dashed + dash-dotted one to $n_3$ branches; $\varepsilon_0 = 0.453$

$$F_k(\zeta) = \int_{\zeta}^{\zeta_k} dx \tilde{K}_k(\zeta, x)\tilde{\eta}_k(x), \quad H_k(\zeta) = \sum_{j=k+1}^{N} \int_{\zeta_{j-1}}^{\zeta_j} dx \tilde{K}_j(\zeta, x)\tilde{\eta}_j(x). \tag{4}$$

Here the kernels $\tilde{K}_j(\zeta, x)$ are given by the same formulas as the kernel $K(\zeta, x)$, but instead of the functions $u_i^{-3}(\zeta)$, $u_i^{-1}(\zeta)$ and $\sigma_i(\zeta)$ their linear approximations on the interval $[\zeta_{j-1},\zeta_j]$ are used. Thus, the function $\tilde{\eta}_k(x)$ obeys the following equation

$$\tilde{\eta}_k''(\zeta)\left[R_k + Q_k(\zeta - \zeta_k)\right]\tilde{\eta}_k(\zeta) = F_k(\zeta) + H_k(\zeta). \tag{5}$$

$$\tilde{\eta}_k(\zeta_k) = y_k, \quad \tilde{\eta}_k'(\zeta_k) = z_k. \tag{6}$$

Here, $R_k$ and $Q_k$ are the coefficients of the linear approximation of the function $u_e^{-3}(\zeta) + u_i^{-3}(\zeta)$ on the $k$th interval. Note that by the moment the problem is solved on the interval $[\zeta_{k-1},\zeta_k]$, functions $\tilde{\eta}_j(x)$, $j = k+1,...,N$ have already been found. Therefore the term $H_k(\zeta)$ on the RHS of (5) is known. Due to the smallness of the interval $[\zeta_{k-1},\zeta_k]$, the term $F_k(\zeta)$ is small. Therefore, the solution to problem (5), (6) within each interval $[\zeta_{k-1},\zeta_k]$ can be obtained using iterations. Assuming the RHS to be known, one can find the solution to problem (5), (6). When $Q_k \neq 0$ its general solution is

$$\tilde{\eta}_k(\zeta) = c_k^1 Ai(\psi(\zeta)) + c_k^2 Bi(\psi(\zeta)) - \pi \int_{\psi_k}^{\psi(\zeta)} d\varphi \left[\tilde{F}_k(\varphi) + \tilde{H}_k(\varphi)\right]\left[Ai(\psi(\zeta))Bi(\varphi) - Bi(\psi(\zeta))Ai(\varphi)\right]. \tag{7}$$

Here $\psi(\zeta) = -\left[R_k + Q_k(\zeta - \zeta_k)\right]Q_k^{-2/3}$, $\psi_k = -R_k Q_k^{-2/3}$, $\tilde{F}_k(\psi) = Q_k^{-2/3}F_k(\chi_k(\psi))$, $\tilde{H}_k(\psi) = Q_k^{-2/3}H_k(\chi_k(\psi))$, $\chi_k(\psi) = \zeta_k - \left(\psi Q_k^{2/3} + R_k\right)/Q_k$. When $Q_k = 0$ the general solution is

$$\tilde{\eta}_k(\zeta) = c_k^1 \cos\left(\sqrt{R_k}(\zeta - \zeta_k)\right) + c_k^2 \sin\left(\sqrt{R_k}(\zeta - \zeta_k)\right) - \int_{\zeta_k}^{\zeta} d\psi \left[F_k(\psi) + H_k(\psi)\right] \times$$
$$\times\left[\cos\left(\sqrt{R_k}(\zeta - \zeta_k)\right)\sin\left(\sqrt{R_k}(\psi - \zeta_k)\right) - \sin\left(\sqrt{R_k}(\zeta - \zeta_k)\right)\cos\left(\sqrt{R_k}(\psi - \zeta_k)\right)\right]\Big/\sqrt{R_k}. \tag{8}$$

The constants $c_k^1$ and $c_k^2$ in Eqs. (7), (8) are determined using conditions (6). Due to the weak dependence of the functions $F_k(\zeta)$ on $\tilde{\eta}_k(\zeta)$ the solution $\tilde{\eta}_k(\zeta)$ can be sequentially refined using the iterations on the base of solution (7) or (8).

Using the described algorithm for a given value of the inter-electrode gap $\delta$, it is possible to calculate an amplitude of the potential perturbation $\tilde{\eta}_k(\zeta)$ for a number of values $\Omega = \omega + i\Gamma$, and, in particular, to build a dependence $\tilde{\eta}(0)$ on $\Omega$. Having the boundary condition on the left boundary $\tilde{\eta}(0, \Omega)$ satisfied, one can determine the eigen-frequencies. (Note that the value of the $\tilde{\eta}'(\delta)$ does not affect the solution of the equation $\tilde{\eta}(0, \Omega) = 0$; the value $\tilde{\eta}'(\delta) = 1$ was used in the calculations). Thus, we calculate dependencies $\Omega(\delta)$, i.e. dispersion branches corresponding to steady-state branches $n_k$ for $k > 0$.

We have implemented the described approach in the study of the aperiodic stability features

of the $n_k$ branches for $k > 0$ at zero electrode potential difference. The unperturbed PDs, $\eta_0(\zeta)$, for the solutions belonging to these branches at $\delta = 2, 4$ and 6 are represented in Fig. 1. The PDs for $\varepsilon_0 < 0$ can be obtained from the ones shown in the figure by reflection about $\zeta$ axis. The dependences of the aperiodic mode growth rate $\Gamma(\delta)$ for the $n_1$ and $n_2$ branches are shown in Fig. 2. It can be seen that the steady-state solutions relevant to these branches turn out to be unstable with respect to small aperiodic perturbations both for $\varepsilon_0 > 0$ and $\varepsilon_0 < 0$. We have also shown that $n_j$ branches with $j = 3$, 4 and 5 are also unstable. At points $\varepsilon_0 = 0$, $\delta_k = \pi k\sqrt{2}$ the growth rate vanishes, which corresponds to the bifurcation at the points, found in Ref. [4] when studying the stability features of the solution corresponding to homogeneous steady states.

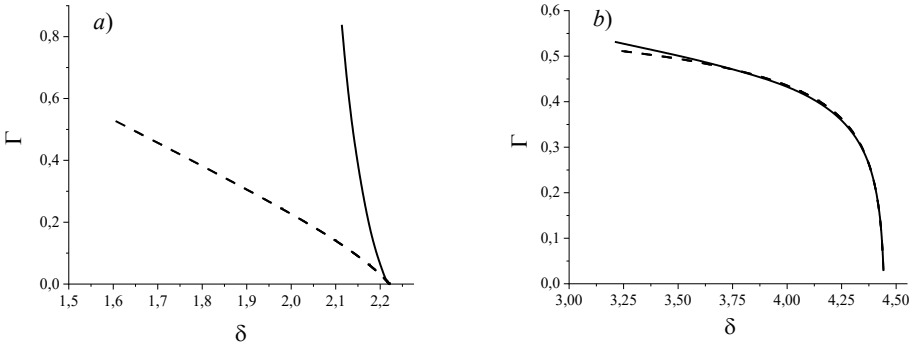


Fig. 2. Aperiodic mode growth rate $\Gamma$ vs. $\delta$ for $n_1$ (*a*), $n_2$ (*b*) branches: solid (dashed) curves correspond to the values $\varepsilon_0 > 0$ ($\varepsilon_0 < 0$)

Thus, we have established that in a diode with counter flows of electrons and ions, steady states corresponding to the $n_j$ branches with $j = 1,...,5$ cannot exist. It should be noted that investigation of the stability features of homogeneous steady-state solution by the developed method produces the same results as in Ref.[4].

**Numerical study of the steady-state solutions stability features**

We also studied the stability features of inhomogeneous steady-state solutions numerically using the code described in [4, 5]. In the simulations, as in the above analytical study, it was assumed that at each time moment $\tau_s$ the electrons instantly adjust to the electric field distribution existing at that moment. Therefore, in the calculations, the electron density was determined by stationary formulas. We simulated the time evolution of a small perturbation introduced to the electric field stationary distribution.

The calculation was carried out for two gap lengths: $\delta = 2.15$ and 2.2 and both signs of $\varepsilon_0$. In all cases, the instability developed. For $\delta = 2.2$ and $\varepsilon_0 > 0$ the value of the growth rate $\Gamma$ turned out to be 0.060, while the analytical result is $\Gamma = 0.0616$. We also compared the shape of the aperiodic eigen-mode of the potential perturbation amplitude obtained analytically with that obtained in the simulation. These curves coincide within the calculation error. For $\delta = 2.15$ and $\varepsilon_0 > 0$ it was found impossible to obtain the value of $\Gamma$ from the results of simulation, since the instability develops too quickly and the time interval in which the transient process is still observed, goes directly into the region of $\tau$ values, where the linear theory is no longer applicable. On the other hand, at $\varepsilon_0 < 0$, we obtained $\Gamma = 0.029$ for $\delta = 2.2$ and $\Gamma = 0.086$ for $\delta = 2.15$. Analytical calculation gives in these cases the values of 0.032 and 0.091, respectively.

After the process leaves the area where the linear theory is applicable, the PD extremum starts to decrease monotonically in absolute value in all cases considered. The rate of its change initially increases and then starts to decrease as the homogeneous solution is approached. In all cases, the evolution of the field distribution at last stage shows that it tends asymptotically to a homogeneous solution (Fig. 3). We found the values of the growth rate $\Gamma$ when approaching to a homogeneous solution and compared them with those found analytically in [4]. For $\delta = 2.2$, numerical calculations gave $\Gamma = -0.0222$, while the analytical value of the growth rate was $-0.0216$. In the case of $\delta = 2.15$, $\Gamma = -0.074$ is obtained both numerically and analytically.

Thus, we have traced the evolution of the perturbed steady-state solutions from the $n_1$ branch to reaching a stable homogeneous stationary solution. In addition, we have validated both the analytical results and the numerical ones.

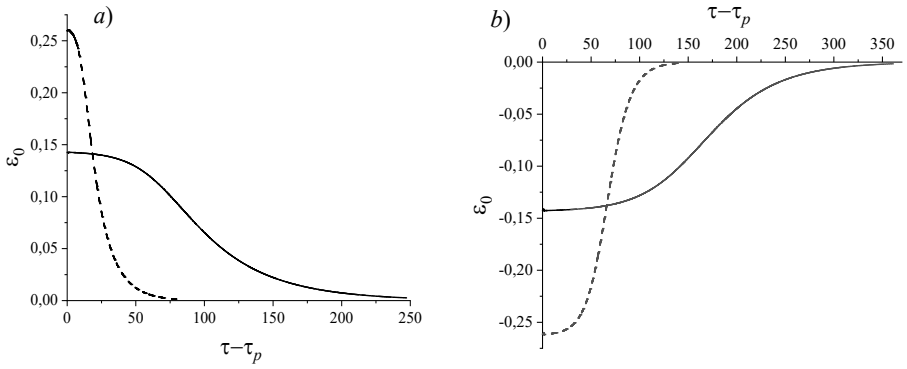


Fig. 3. The electric field strength at the left electrode $\varepsilon_0$ evolution during the process of perturbation development at diode lengths $\delta = 2.15$ (dashed lines) and 2.2 (solid lines) for steady-state solutions with $\varepsilon_0 > 0$ (*a*) and $\varepsilon_0 < 0$ (*b*)

## Conclusion

We have studied the inhomogeneous steady-state solutions stability features for a diode with counter-streaming electron and ion flows for the mode without reflection of charged particles from potential barriers, using the equation for the amplitude of the electric field perturbation derived in [4]. To perform the investigation, we have developed an original semi-analytical method for solving this equation, which works for any undisturbed potential distribution. It is shown that the inhomogeneous steady-state solutions corresponding to the $n_k$ branches with $0 < k \leq 5$ are unstable. The results of the theory are confirmed by numerical calculations using a high-precision numerical code. Based on our analysis we can suppose that in a diode with counter streams of electrons and ions, inhomogeneous stationary solutions in the mode without particle reflection cannot exist. Earlier [4], we found that for homogeneous steady-state solutions there is a threshold in the value of the inter-electrode gap $\delta_{th}$ above which the steady-state solutions become unstable; the steady-state solutions without reflection can exist only when $\delta < \delta_{th}$. It is shown that in the mode without particle reflection, the main instability mode is aperiodic.

The stability of some solutions with reflection of particles from potential barriers was studied numerically in our previous paper [5]. It turned out that for the solutions corresponding to the branch $d_0$ (see Fig. 4 in [2]), there is a threshold in $\delta$, above which the solutions turn out to be unstable, and non-linear periodic oscillations develop. In this case, the main instability mode is oscillatory one. To obtain a complete picture of solutions that are implemented in a diode with counter-streaming electron and ion flows, it is necessary to develop a stability theory for the mode with reflection of charged particles from potential barriers. Besides, to describe the operation of real plasma switches, it is necessary to take into account also the scattering of ions by atoms, i.e. take into account the ion charge exchange [1, 3].

## REFERENCES

1. **Babanin V.I., Kolyshkin I.N., Kuznetsov V.I., Paschina A.S., Sitnov V.I., Ender A.Ya.,** Development of structures in a bounded collisionless plasma and complete modulation of the current in a Knudsen discharge, Technical Physics. 39 (6) (1994) 552–563.

2. **Ender A.Ya., Kuznetsov V.I., Gruzdev A.A.,** Steady states of a diode with counterstreaming electron and positron beams, Plasma Physics Reports. 32 (10) (2016) 936–946.

3. **Klinger T., Greiner F., Rohde T., Piel A.,** Nonlinear dynamical behavior of thermionic low pressure discharges. II. Experimental, Physics of Plasmas. 2 (6) (1995) 1822–1836.

4. **Bakaleinikov L.A., Kuznetsov V.I., Flegontova E.Yu.,** Stability theory of plasma diodes with counterstreaming electron and ion flows, Physics of Plasmas. 28 (12) (2021) 122108.

5. **Kuznetsov V.I., Flegontova E.Yu., Bakaleinikov L.A.,** Occurrence of oscillatory modes in a diode with counter-streaming electron and ion flows, Physics of Plasmas. 27 (9) (2020) 092304.

## THE AUTHORS

**BAKALEINIKOV Leonid A.**
bakal.ammp@mail.ioffe.ru
ORCID: 0000-0001-7293-0264

**FLEGONTOVA Ekaterina Yu.**
fl.xiees@mail.ioffe.ru
ORCID: 0000-0002-3313-3534

**KUZNETSOV Victor I.**
ORCID: 0000-0002-8963-5197

*Received 26.10.2022. Approved after reviewing 10.11.2022. Accepted 10.11.2022.*

© Peter the Great St. Petersburg Polytechnic University, 2023

Conference materials
UDC 537.533.2
DOI: https://doi.org/10.18721/JPM.161.205

# Methods for processing field emission glow patterns to obtain the I–V characteristics of individual emission sites

A.G. Kolosko [1]✉, S.V. Filippov [1], E.O. Popov [1]

[1] Ioffe Institute, St.-Petersburg, Russia

✉ agkolosko@mail.ru

**Abstract.** The work describes the features of processing glow patterns of the field emission projector when obtaining local I–V characteristics of individual emission sites. The features of constructing such dependencies are shown with the example of an experiment with a nanocomposite field emitter. The main factors influencing the analysis of glow patterns are discussed: the illumination effect, the halo effect, adsorption-desorption processes, vacuum discharges, burnout and contamination of the phosphor screen. Algorithms for reducing these effects with the computer processing of experimental data are described.

**Keywords:** field emission, emission glow patterns, local current-voltage characteristics

**Citation:** Kolosko A.G., Filippov S.V., Popov E.O., Methods for processing field emission glow patterns to obtain the I–V characteristics of individual emission sites, St. Petersburg State Polytechnical University Journal. Physics and Mathematics. 16 (1.2) (2023) 39–46. DOI: https://doi.org/10.18721/JPM.161.205

This is an open access article under the CC BY-NC 4.0 license (https://creativecommons.org/licenses/by-nc/4.0/)

Материалы конференции
УДК 537.533.2
DOI: https://doi.org/10.18721/JPM.161.205

# Методы обработки полевых эмиссионных картин свечения для получения I–V характеристик отдельных эмиссионных центров

А.Г. Колосько [1]✉, С.В. Филиппов [1], Е.О. Попов [1]

[1] Физико-технический институт им. А.Ф. Иоффе РАН, Санкт-Петербург, Россия

✉ agkolosko@mail.ru

**Аннотация.** В работе описаны особенности обработки картин свечения полевого эмиссионного проектора при получении локальных ВАХ отдельных эмиссионных центров. Особенности построения таких зависимостей показаны на примере эксперимента с нанокомпозитным полевым эмиттером. Обсуждаются основные факторы, влияющие на анализ картин свечения: эффект засветки, эффект гало, процессы адсорбции-десорбции, вакуумные разряды, выгорание и загрязнение люминофорного экрана. Описаны алгоритмы уменьшения этих эффектов с помощью компьютерной обработки экспериментальных данных.

**Ключевые слова:** полевая эмиссия, эмиссионные картины свечения, локальные вольт-амперные характеристики

**Ссылка при цитировании:** Колосько А.Г., Филиппов С.В., Попов Е.О. Методы обработки полевых эмиссионных картин свечения для получения ВАХ отдельных эмиссионных центров // Научно-технические ведомости СПбГПУ. Физико-математические науки. 2023. Т. 16. № 1.2. С. 39–46. DOI: https://doi.org/10.18721/JPM.161.205

Статья открытого доступа, распространяемая по лицензии CC BY-NC 4.0 (https://creativecommons.org/licenses/by-nc/4.0/)

© Kolosko A.G., Filippov S.V., Popov E.O., 2023. Published by Peter the Great St.Petersburg Polytechnic University.

## Introduction

With the development of electronics and materials science in the field of nanoscale structures, vacuum electronics acquired new perspectives, which once gave way to solid-state semiconductor devices. The new vacuum nanoelectronics is capable of surpassing classical devices in terms of speed and reliability. The developed devices are based on sources of free electrons, which are multitip emission systems – LAFE (large area field emitters), in which the current load is distributed over an array of nanosized emitters. For the formation of sufficiently powerful and stable LAFE, a directed technological optimization is required. One of the options for such optimization is a detailed study of individual emission sites in the LAFE array.

There are several methods for obtaining the emission characteristics of individual emission sites: SAFEM (scanning anode with a hole) [1], STM (scanning with a tunneling microscope needle) [2], ILMS (analysis of the glow patterns of a field emission projector) [3]. The digital processing of glow patterns is based on the assumption that the brightness of the image of each emission site in the glow pattern is directly proportional to its current load. These brightnesses are used as weighting factors to calculate the corresponding local currents from the total emission current.

Usually, when observing individual emission sites, their field enhancement factor (FEF) is estimated at a fixed voltage level. However, the local current-voltage characteristic (IVC) has more complete information. It can be used to estimate not only FEF, but also the field emission area (FEA), as well as the dependence of these parameters on the voltage level.

Earlier in the ref. [4], we presented three methods for obtaining local emission characteristics using ILMS technique. The first method is based on processing the IVC in semi-logarithmic Fowler-Nordheim coordinates to obtain the effective FEF ($\gamma_{eff}$) and the effective FEA of one site ($S_1 = S_{eff} / N_{sites}$, where $S_{eff}$ is the effective FEA of the entire cathode, $N_{sites}$ is the number of sites) [5]. These two effective parameters are in some way an average of the actual emission characteristics of individual sites of the cathode surface.

The second method uses a fixed value of the emission area of one site (obtained, for example, by computer simulation [6]) and plots a histogram of the maximum emission currents of individual emission sites based on the processing of the glow patterns of the field projector at a constant voltage level. From these currents, the local FEFs are found.

The third method is based on a smooth change in the level of the applied voltage and continuous registration of local currents of all found emission sites (as mentioned above, the local currents are obtained by glow patterns processing). As a result, local IVCs are obtained. Further, these IVCs are processed in semi-logarithmic Fowler-Nordheim coordinates and the local FEF and FEA are estimated.

The construction of local IVCs encounters a number of difficulties in processing glow patterns. In this paper, we consider the features of obtaining local IVCs by the computerized ILMS technique with the example of experiments with a nanocomposite field cathode based on carbon nanotubes in a polystyrene (CNT/PS).

## Experimental

To record experimental data, a complex technique for studying the properties of field emitters was used [7]. The experimental setup is a vacuum chamber (vacuum no worse than $10^{-7}$ Torr) with a plane-parallel system of electrodes, one of which has emission properties (in this work, this is a CNT/PS nanocomposite with a nanostructured surface). The voltage is applied in half-sine pulses, so that the emission current also has a pulsed character. During the experiment, IVCs are recorded one for every 20 ms (fast IVCs), as well as the time dependences of the amplitudes of the voltage and emission current pulses (I-V(t)). Registration is performed using a computerized system based on the NI DAQ PCIe-6351 multi-channel data acquisition board.

The distribution patterns of emission sites over the cathode surface (glow patterns) are recorded using a field projector system: the anode is made in the form of a transparent glass plate with an ITO layer coated with a phosphor. Patterns are registered using a long-focus USB microscope (Levenhuk DTX 90), which is located outside the vacuum chamber opposite the transparent window.

For registration and online data processing, we used a special multi-module program “Hephaestus” which is written on the LabVIEW graphical programming platform.

© Колосько А.Г., Филиппов С.В., Попов Е.О., 2023. Издатель: Санкт-Петербургский политехнический университет Петра Великого.

The software is equipped with modules that make it possible to continuously record voltage and current pulses, as well as the vacuum level, into a ".txt" file and simultaneously record glow patterns into an ".avi" file. A separate module "Morpheus" allows to repeatedly reproduce experiment data in the processor modules of "Hephaestus" in the passive experiment mode [8]. The use of this module makes it possible to study in detail and improve the software mechanism for obtaining information from the glow patterns in conjunction with the analysis of electrical characteristics (fast IVCs and I-V(t)).

Figure 1 shows the time dependences of the current, voltage and vacuum levels, as well as the averaged fast IVC, obtained during the experiment with the CNT/PS nanocomposite in the constant voltage mode (1 minute at 1.98 kV with current level 1 mA). This experiment is necessary to collect data on the emission surface before plotting local IVCs.

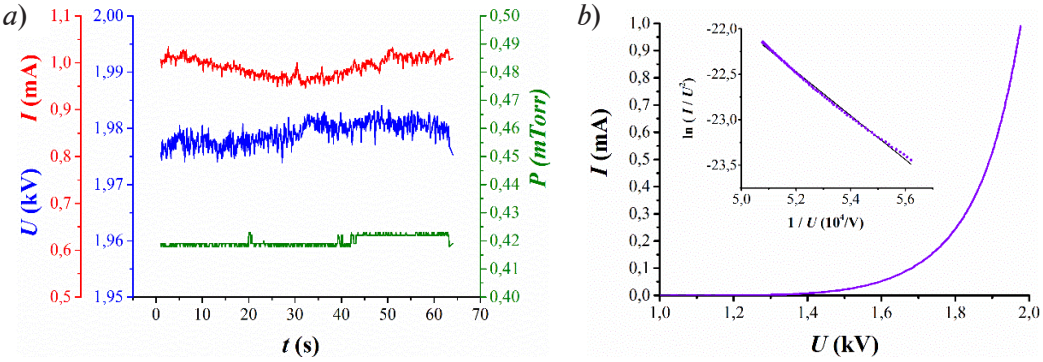


Fig. 1. Results of experiment with constant voltage level: time dependences of current, voltage and vacuum levels (*a*), averaged fast IVC and its analysis in the Fowler-Nordheim coordinates (*b*)

Estimation of the effective parameters of the cathode using IVC analysis in the classical Fowler-Nordheim coordinates gave the values $\gamma_{eff} = 979$ и $S_{eff} = 0.209$ μm².

Figure 2 shows the time dependences of the current, voltage, and vacuum levels, as well as the local IVC of the brightest site, obtained in the mode of a smoothly varying voltage level. Estimated values $\gamma_{local} = 1391$ и $S_{local} = 2.1$ nm².

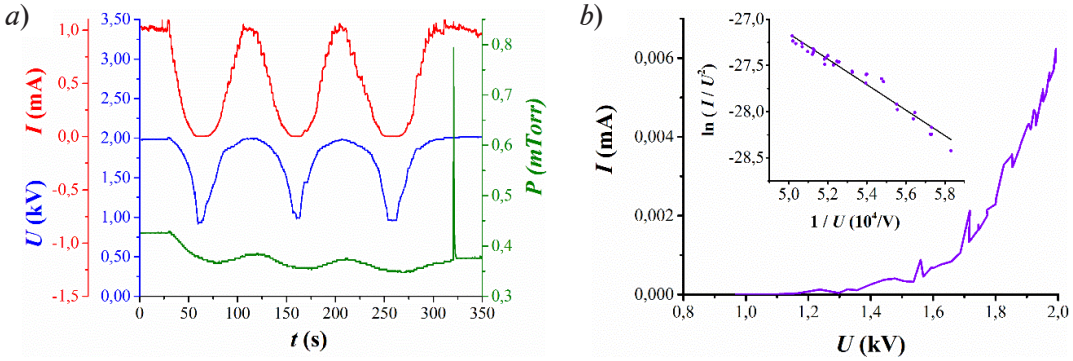


Fig. 2. Results of the experiment with a smoothly varying voltage level: time dependences of current, voltage and vacuum levels (*a*), local IVC of the brightest emission site (*b*)

## Glow pattern analysis

A number of technical difficulties prevent obtaining adequate information about the emitter surface from the "glow pattern".

**A. Overexposure effect**

Overexposure effect is the effect of individual emission sites in the glow pattern exceeding the maximum brightness that a microscope can register. To control the appearance of an overexposure effect in the experiment, a module is built into the program for processing glow patterns, which converts the picture to gray tones online and builds a histogram of the distribution of pixels on the shades of gray (from 0 to 255). The overexposure effect appears as excess number of pixels at the edge of the range (Fig. 3, *a*). To eliminate this effect, a light filter is installed between the microscope and the window of the vacuum chamber. Note that the use of a light filter practically removes from

the glow pattern the dimmest emission sites (reduces them to the noise level), which can make a significant contribution to the total emission current.

Note that similar histograms are sometimes used by experimenters to estimate numerically the quality of the distribution of emission sites over the cathode surface [9]. On the other hand, the overexposure effect can be used to determine the FEA of an emission site (given as an overexposure area) [10], however, the correlation of this emission area with classical definitions raises many questions.

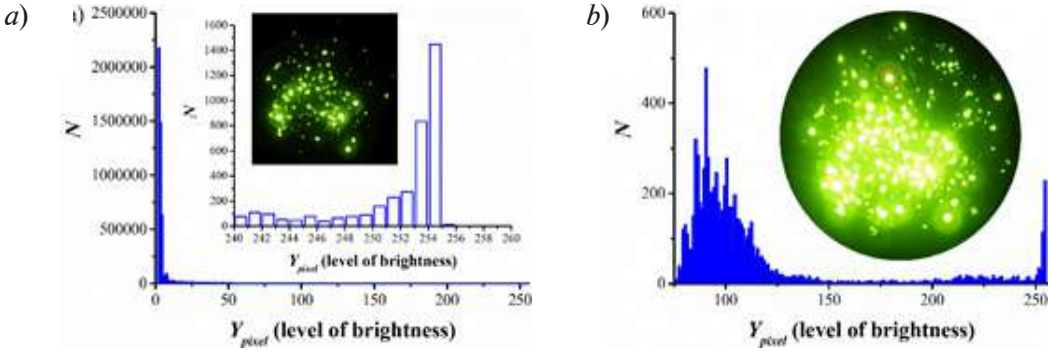


Fig. 3. Parasitic effects in glow patterns: pixel distribution histogram at the overexposure effect (*a*), pixel distribution histogram in a halo ring (*b*)

**B. Scattering of electrons**

The movement of electrons from the emission site to the anode is not linear: they move slightly at an angle and still repel each other in flight. Therefore, the site images are somewhat blurred [11]. The center of the emission site image (position with the maximum brightness) can be considered sufficiently reliable, because of electrons in this place fly along the shortest trajectory. The program "Hephaestus" searches for maxima in the glow pattern using a 3×3 pixels window, displays them on a black-and-white diagram in the form of white spots and highlights them with rectangular zones (the so-called ROI). In the Fig. 4, *a*, these zones are superimposed on the glow pattern.

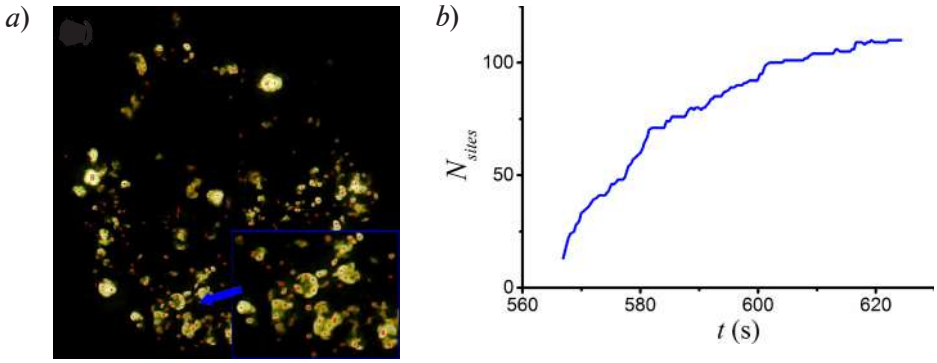


Fig. 4. Collection of information on the emission sites position on the cathode surface: finding emission sites in one frame of the glow pattern (*a*), time dependence of the number of emission sites found (*b*)

Further, the program monitors the detected zones and continuously searches for the pixels with maximum brightness $Y^{i}_{\max}$ in them. This brightness values are used as a weighting factors for distributing the total emission current to the individual emission sites. A smooth increase in the overall voltage level makes it possible to build a local IVC for each of emission site.

Note that the application of pattern filtering (in fact, its smoothing) makes it possible to eliminate digital noise from the search for brightness maxima. The program "Hephaestus" uses the Gaussian Kernels filter (a tool called IMAQ GetKernel VI). Details of the processing are described in [12].

**C. Fluctuations of adsorbates**

The second problem in the analysis of glow patterns is the instability in time. Some effects, which we consider below, can shift the position of the maximum brightness of the emission sites. However, the strongest influence on the stability is exerted by adsorption-desorption processes, which significantly change the work function of individual emission sites, causing them to practically disappear from the

glow pattern and then reappear. This leads to the fact that each frame with the glow pattern coming from the microscope must be processed for search a new set of emission sites. At the online data processing mode, this significantly slows down the analyze of the cathode surface, and also makes it impossible to build the time dependences of the local currents of the individual emission sites.

The solution to this problem is to follow the cathode surface for some time in order to find the positions of all (or at least the main) flickering sites. The "Hephaestus" program finds the positions of the sites by adding new positions of the brightness maxima to the overall black-and-white diagram. Each white spot in this diagram corresponds to the fluctuation region of one emission site. In the process of accumulation, the program builds a time dependence of the number of spots. When this curve reaches a relatively constant level, the collection of sites can be considered complete (Fig. 3, *b*).

This method has disadvantages: at a high density of sites, the effect of merging their spots on the black-and-white diagram occurs, as well as the effect of overlapping their resulting rectangular ROI (the program even has a built-in module for estimating the number and area of such ROI). The influence of these effects decreases with a decrease in the emission current level, as well as with the installation of a stronger light filter. Also, the effect is leveled by raising the threshold brightness level $Y_{th}$. In all three cases, dim sites are excluded (lost) from the analysis.

**D. Galo effect**

Another factor is the inability to distinguish the least bright emission sites from digital noise (pixel-sized bright dots) and from halo-type glows. Halo effects can be caused by the presence of parasitic conductive protrusions in the emission system (on the anode surface), which pull the electron flow towards themselves [11], as well as by the emission of secondary electrons from the anode surface, which scatter to the sides and bombard the phosphor away from the main electron flow, creating glowing rings in the pattern [14]. These glowing reflections are superimposed on the images of emission sites, blur these images, shift them to the side, and so change the brightness level. Moreover, due to halo effects, false peaks of brightness appear in the pattern (usually they located in the glowing rings around the sites images).

This effect can be neutralized by adding a current-carrying grid (the third electrode) to the system, located near the anode [15]. However, this grid will distort the emission pattern and may even lead to spurious diffraction effects if the grid cell size and the interelectrode spacing satisfy the diffraction conditions. Another variant is to use a phosphor with a low secondary emission coefficient [15].

Counteracting the appearance of spurious glows with the computer processing of glow patterns can be carried out in a rather complicated way: by searching for a symmetrical brightness profile of the brightest sites and subtracting the corresponding nonlinear correction from the pattern (Fig. 3, *b* shows the distribution of pixels in a halo-type ring, which has a customary asymmetric peak).

A simpler approach is to cut off the area of the pattern corresponding the cathode surface using a mask, as well as setting the threshold brightness $Y_{th}$, below which pixels should be excluded from the analysis. On the other hand, the application of the technique of virtual repeated experiment allows to create a certain pattern of threshold brightness (each pixel of the pattern has its own $Y_{th}$). Application of this threshold brightness pattern can include in the analysis fainter sites, which were previously excluded due to the influence of halo effects at the region of bright sites.

Fig. 5 shows the found sets of emission sites for direct processing of glow patterns, for pattern processing with Gaussian Kernels filter, and for processing with the filter and the threshold brightness pattern. Fig. 5, *a* – 764 sites, too many into each glowing spot at the pattern. Fig. 5, *b* – 138 sites, only the brightest. Fig. 5, *c* – 409 sites including dim sites. Corresponding current-voltage characteristics of this experiment are presented in Fig. 1.

**E. Microscope and luminophore resolution**

The resolution of the microscope matrix limits the resolution of the emission projector. Dividing the cathode diameter $D_C$ (in our experiments, the metal substrate of the nanocomposite has a diameter of 1 cm) by the number of pixels in the diameter of corresponding cathode surface image $N_p$ ("Hephaestus" determined it automatically by the mask size) gives size of pixel $D_p$. Microscope Levenhuk DTX 90 (matrix 2592 × 1944, 5 Mp) in our measuring system allows us to obtain $D_p = D_C / N_p \sim 10$ μm per pixel. That is, one luminous pixel can image a number of individual carbon nanotubes. Increasing the resolution of the microscope leads to an increase in the amount of data and to a slowdown in the speed of online processing, which is quite critical when constructing local IVCs.

The phosphor coating usually consists of grains of powder, which is applied to the anode surface in the suspension form. The size of these grains, as well as the resolution of the matrix, limits the

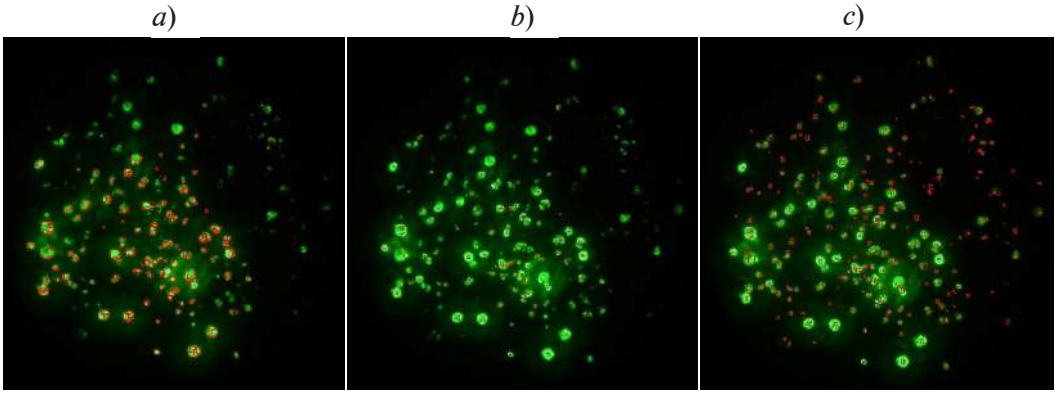


Fig. 5. Sets of emission sites obtained at: direct processing with threshold brightness $Y_{th} = 150$ (*a*), processing with Gaussian Kernels filter (10 times for each frame) (*b*), processing with the filter and the threshold brightness pattern ($\max Y_{th} = 150$, $\min Y_{th} = 50$ for the summary filtered pattern) (*c*)

resolution of the field emission projector. In our experiment, the grain size is less than 5 μm, that is comparable to the size of a pixel. At a sufficiently high density of the emission sites (the density generally increases with the applied voltage), they become indistinguishable, since the distance between sites becomes smaller than the phosphor grain [16].

The non-uniformity of the phosphor coating can also lead to an error in the calculations of the emission sites current load and, accordingly, to the incorrect building of local IVCs. This irregularity can result from local burning of the phosphor by electron beams of sufficiently high power, as well as from the transfer of particles from the cathode to the anode, which is especially often observed in experiments with a fresh emitter (the so-called high-voltage training of the emission surface).

On the other hand, the surface of the nanocomposite emitter is rough and may have macroscopic protrusions, on top of which there may be several emission sites (nanoemitters). A fairly close location of these sites can lead to the fact that in the glow pattern they will be represented by one spot with a common glow halo ring around this spot (Fig. 6, *a*). It is difficult to separate these sites inside this spot using a field projector (some of them merge into one spot in the black-and-white diagram), therefore, from an experimental point of view, it is advantageous to represent them as a single emission site with an increased FEA and an average FEF.

In the case of a sufficiently large distance between the emission sites on a common macroscopic ledge (so that even the halo glow around them is not round), they can be quite clearly separated from each other by the software processing (Fig. 6, *b*).

Note that there is an alternative to phosphor powders – luminescent crystals, for example YAG. However, just like powder, it is subject to the influence of electron bombardment and can degrade over time [17].

It is also worth mentioning the nonlinearity of the dependence of the phosphor brightness on the emission current $Y(I)$ (Fig. 6, *c*). In general, the dependence of the phosphor brightness on the current can have both a concave and a convex form [18]. This nonlinearity must be taken into account when comparing sets of emission sites and their corresponding local characteristics obtained at different current levels. It is possible to change the threshold brightness $Y_{th}$ according to the empirical curve $Y(I)$.

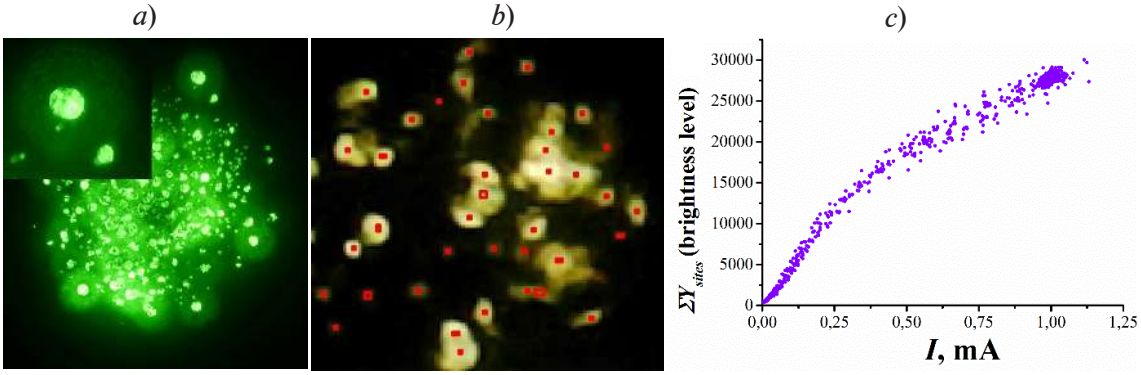


Fig. 6. Parasitic effects in the glow patterns: phosphor inhomogeneity (*a*), finding the emission sites position (*b*), dependence of the total emission current on the total brightness of the emission sites (*c*)

**F. Irreversible processes**

Another variant of changing the structure of the emission sites can be irreversible changes in the cathode surface under the influence of such factors as the pulling forces of the electric field [19] or microscopic vacuum discharges, which can both destroy the longest sites and generate new ones, deforming the surface.

Long-term observation of the nanocomposite cathode surface shows that new sites appear during the entire experiment. In this case, the analysis of glow patterns should be performed in the mode of a repeated virtual experiment, which is provided to the experimenter by the Morpheus software module described above. For the first pass, one can find the position of all sites, and on the next – to analyze their properties.

## Conclusion

We have considered the features of processing glow patterns of the computerized field projector. Today, the world's leading laboratories that study field emission are equipped with such projectors made in USA [11, 17], Brazil [3], and Germany [20]. The main task is to obtain local emission characteristics of a multipoint field cathode and study its relationship with the features of macroscopic emission characteristics. Knowing the relationship between the shape and location of an individual emission sites in the common array of a multi-tip field cathode and the characteristics of the emission current (magnitude and stability) allows targeted optimization of the cathode surface. Optimization is necessary to obtain competitive devices for vacuum nanoelectronics, which already today exceed semiconductor analogues in terms of inertia, radiation resistance and energy efficiency.

## REFERENCES

1. **Nilsson L., Groening O., Groening P., Kuettel O., Schlapbach L.,** Characterization of thin film electron emitters by scanning anode field emission microscopy, Journal of Applied Physics. 90 (2) (2001) 768–780.

2. **Xu Z., Bai X.D., Wang E.G., Wang Z.L.,** Field emission of individual carbon nanotube with in situ tip image and real work function, Applied Physics Letters. 87 (16) (2005) 163106-1–3.

3. **Kopelvski M.M., Ramirez-Fernandez F.J., Galeazzo E., Dantas M.O.S., Peres H.E.M.,** Potentialities of a new dedicated system for real time field emission devices characterization: a case study, 4th International Symposium on Instrumentation Systems, Circuits and Transducers (INSCIT), At Sro Paulo, Brazil, august (2019) 1–5.

4. **Popov E.O., Kolosko A.G., Filippov S.V., Ponyaev S.A.,** Methods for measuring the local emission characteristics of CNT based multi-tip emitters, Journal of Physics: Conference Series. 2103 (1) (2021) 012116-1–6.

5. **Popov E.O., Kolosko A.G., Filippov S.V.,** A Test for Compliance with the Cold Field Emission Regime Using the Elinson–Schrednik and Forbes–Deane Approximations (Murphy–Good Plot), Technical Physics Letters. 46 (9) (2020) 838–842.

6. **de Assis T.A., Dall'Agnol F.F., Andrade R.F.S.,** The consequences of dependence between the formal area efficiency and the macroscopic electric field on linearity behavior in Fowler–Nordheim plots, Journal of Physics D: Applied Physics. 49 (2016) 355301-1–11.

7. **Popov E.O., Kolosko A.G., Filippov S.V., Terukov E.I., Ryazanov R.M., Kitsyuk E.P.,** Comparison of macroscopic and microscopic emission characteristics of large area field emitters based on carbon nanotubes and graphene, Journal of Vacuum Science & Technology B, Nanotechnology and Microelectronics: Materials, Processing, Measurement, and Phenomena. 38 (4) (2020) 043203-1–10.

8. **Kolosko A.G., Chernova V.S., Filippov S.V., Popov E.O.,** Method for Recording and Reproducing an Experimental Research into the Field Emitter Properties Based on Carbon Nanotubes, Advanced Materials and Technologies. 3 (2020) 18–27.

9. **Fursey G.N., Novikov D.V., Dyuzhev G.A., Kotcheryzhenkov A.V., Vassiliev P.O.,** The field emission from carbon nanotubes, Applied surface science. 215 (1-4) (2003) 135–140.

10. **Patra R., Singh A., Vankar V. D., Ghosh S.,** Field emission image analysis: Precise determination of emission site density and other parameters, Advanced Materials Letters. 7 (10) (2016) 771–776.

11. **Fursey G.N.,** Field emission, Soros Educational Journal. 6 (11) (2000) 96–103.

12. **Filippov S.V., Popov E.O., Kolosko A.G., Vinnichek R.N.,** Evaluation of numerical characteristics

of the current load distribution on the surface of multi-tip field emitters, Journal of Physics: Conference Series. 917 (9) (2017) 092022-1–6.

13. **Posos T.Y., Fairchild S.B., Park J., Baryshev S.V.,** Field emission microscopy of carbon nanotube fibers: Evaluating and interpreting spatial emission, Journal of Vacuum Science & Technology B, Nanotechnology and Microelectronics: Materials, Processing, Measurement, and Phenomena. 38 (2) (2020) 024006-1–6.

14. **Nikolski K.N., Baturin A.S., Knyazev A.I., Tchesov R.G., Sheshin E.P.,** Formation of Rings around a Field-Emission Image and Possible Applications of This Effect, Technical Physics. 49 (2) (2004) 250–253.

15. **Il'ichev E.A., Kuleshov A.E., Petrukhin G.N., Minakov P.V., Rychkov G.S., Sen V.V., Teverovskaya E.G.,** Diamond Photocathodes As Field-Emission Electrodes for Vacuum Microelectronics, Technical Physics Letters. 47 (7) (2021) 503–506.

16. **Lyashenko S.A., Volkov A.P., Ismagilov R.R., Obraztsov A.N.,** Field electron emission from nanodiamond, Technical Physics Letters. 35 (3) (2009) 249–252.

17. **Baturin S.S., Baryshev S.V.,** Electron emission projection imager, Review of Scientific Instruments. 88 (3) (2017) 033701-1–7.

18. **Ozol D., Eliseev A., Garkusha M., Pavlenko A.,** Measurement Method of the Distribution of Field Emission Current, 2019 International Vacuum Electronics Conference (IVEC), april (2019) 1–2.

19. **Jung H., An S.Y., Jang D. M., Kim J. M., Park J. Y., Kim D.,** A multi-wall carbon nanotube/polymethyl methacrylate composite for use in field emitters on flexible substrates, Carbon. 50 (3) (2012) 987–993.

20. **Serbun P., Porshyn V., Müller G., Lützenkirchen-Hecht D.,** Advanced field emission measurement techniques for research on modern cold cathode materials and their applications for transmission-type X-ray sources, Review of Scientific Instruments. 91 (8) (2020) 083906-1–19.

## THE AUTHORS

**KOLOSKO Anatoly G.**
agkolosko@mail.ru
ORCID: 0000-0002-6073-6808

**POPOV Eugeni O.**
e.popov@mail.ioffe.ru
ORCID: 0000-0003-2226-6304

**FILIPPOV Sergey V.**
s.filippov@mail.ioffe.ru
ORCID: 0000-0001-5325-2226

*Received 27.10.2022. Approved after reviewing 11.12.2022. Accepted 12.12.2022.*

© Peter the Great St. Petersburg Polytechnic University, 2023

Conference materials
UDC 620.91
DOI: https://doi.org/10.18721/JPM.161.206

# Energy–informational hybrid photovoltaic converter of laser radiation

V.S. Kalinovskii ✉, E.I. Terukov, E.V. Kontrosh, V.S. Yuferev,
K.K. Prudchenko, E.E. Terukova, I.A. Tolkachev, E.G. Koksharov,
E.G. Pavlova, A.V. Chekalin, S.E. Goncharov

Ioffe Institute, St. Petersburg, Russia
✉ vitak.sopt@mail.ioffe.ru

**Abstract.** The possibility of efficient conversion of constant laser radiation using α−Si:H/c−Si structures in the transparency window of the Earth's atmosphere at wavelength 1.06 μm is shown for the first time. A hybrid photovoltaic converter based on α−Si:H/c−Si cells and AlGaAs/GaAs photodetectors has been developed and manufactured. The photoelectric converter provides simultaneous conversion of radiation from two types of laser sources in the photovoltaic mode: continuous at a wavelength of 1.06 μm with an efficiency of ~ 26% and pulsed at a wavelength of 0.78 μm of ≤ 900 ps FWHM.

**Keywords:** laser radiation, transparency window, hybrid photovoltaic converter, AlGaAs/GaAs photodetectors, α−Si:H/c−Si structures

**Citation:** Kalinovskii V.S., Terukov E.I., Kontrosh E.V., Yuferev V.S., Prudchenko K.K., Terukova E.E., Tolkachev I.A., Koksharov E.G., Pavlova E.G., Chekalin A.V., Goncharov S.E., Energy−informational hybrid photovoltaic converter of laser radiation, St. Petersburg State Polytechnical University Journal. Physics and Mathematics. 16 (1.2) (2023) 47−51. DOI: https://doi.org/10.18721/JPM.161.206

This is an open access article under the CC BY-NC 4.0 license (https://creativecommons.org/licenses/by-nc/4.0/)

Материалы конференции
УДК 620.91
DOI: https://doi.org/10.18721/JPM.161.206

# Энерго-информационный гибридный фотоэлектрический преобразователь лазерного излучения

В.С. Калиновский ✉, Е.И. Теруков, Е.В. Контрош, В.С. Юферев,
К.К. Прудченко, Е.Е. Терукова, И.А. Толкачев, Е.Г. Кокшаров,
Е.Г. Павлова, А.В. Чекалин, С.Е. Гончаров

Физико-технический институт им. А.Ф. Иоффе РАН, Санкт-Петербург, Россия
✉ vitak.sopt@mail.ioffe.ru

**Аннотация.** Впервые показана возможность эффективного преобразования постоянного лазерного излучения с использованием α−Si:H/c−Si структур в окне прозрачности земной атмосферы на длине волны 1.06 μm. Разработан и изготовлен гибридный фотоэлектрический преобразователь на основе α−Si:H/c−Si и AlGaAs/GaAs элементов. Фотоэлектрический преобразователь обеспечивает одновременное преобразование излучения от двух типов лазерных источников: непрерывного на длине волны 1.06 μm с эффективностью ~ 26% и импульсного, на длине волны 0.78 μm с ≤ 900 ps FWHM.

**Ключевые слова:** лазерное излучение, окно прозрачности, гибридный фотоэлектрический преобразователь, AlGaAs/GaAs фотодетектор, α−Si:H/c−Si структура

© Kalinovskii V.S., Terukov E.I., Kontrosh E.V., Yuferev V.S., Prudchenko K.K., Terukova E.E., Tolkachev I.A., Koksharov E.G., Pavlova E.G., Chekalin A.V., Goncharov S.E., 2023. Published by Peter the Great St.Petersburg Polytechnic University.

**Ссылка при цитировании:** Калиновский В.С., Теруков Е.И., Контрош Е.В., Юферев В.С., Прудченко К.К., Терукова Е.Е., Толкачев И.А., Кокшаров Е.Г., Павлова Е.Г., Чекалин А.В., Гончаров С.Е. Энерго-информационный гибридный фотоэлектрический преобразователь лазерного излучения // Научно-технические ведомости СПбГПУ. Физико-математические науки. 2023. Т. 16. № 1.2. С. 47–51. DOI: https://doi.org/10.18721/JPM.161.206

Статья открытого доступа, распространяемая по лицензии CC BY-NC 4.0 (https://creativecommons.org/licenses/by-nc/4.0/)

## Introduction

Currently, free space optical communication (FSO) is becoming more widely used. FSO is used to provide wireless high–speed communication channels transmitting a signal over a distance up to 15 km at a speed up to 1 Gbit/s [1].

To ensure the autonomy of FSO operation in hard–to–reach areas, the creation of energy independent receiving and transmitting stations is promising. This paper presents the results of a study of a hybrid photovoltaic converter (HPVC). The HPVC is a prototype of energy independent receiving device created on the basis of an α–Si:H/c–Si heterojunction technology (HJT) cells and an information photoconverter (PC) assembled of four p–i–n AlGaAs/GaAs photodetectors (PDs) of laser radiation respectively, at wavelengths of 1.06 μm and 0.78 μm [2–4].

## Experiment

The structures of the HJT cells were manufactured by deposition of native amorphous silicon (α-Si:H) 5–10 nm thick on a textured single–crystal silicon n–type substrate of 125 μm thick, n–α–Si:H (on the front surface) and p–α–Si:H (on the back surface) layers 10–15 nm thick and indium tin oxide (ITO) layers 100 nm thick. In the experiments, the HJT cells with a size of 156×156 mm$^2$ were used. On the surface of the ITO layers, silver contact tires with a width of 40 μm and a pitch of 1.2 mm are formed by screen printing.

The structure of p–i–n AlGaAs/GaAs PDs included: n–$Al_{0.2}G_{0.8}As$ – back potential barrier, n–GaAs ($N_n$=5·10$^{17}$ cm$^{-3}$)/i–GaAs ($N_n$=1·10$^{15}$ cm$^{-3}$) layers 0.5/1 μm thick and 0.7 μm p–GaAs emitter ($N_p$=2·10$^{18}$ cm$^{-3}$), p–$Al_{0.12}Ga_{0.88}As$ wide gap window 2 μm thick ($N_p$=5·10$^{19}$ cm$^{-3}$). PDs were formed using the post–growth technology with a photosensitive surface diameter of 500 μm with a grid frontal contact.

Fig. 1 presents the spectral characteristics of the external quantum efficiency of the grown α–Si:H/c–Si power cells and AlGaAs/GaAs PDs structures. The spectral sensitivity of the HJT cell at room temperature is in the range of 300 nm–1200 nm, and AlGaAs/GaAs p–i–n PD is 700 nm–900 nm respectively.

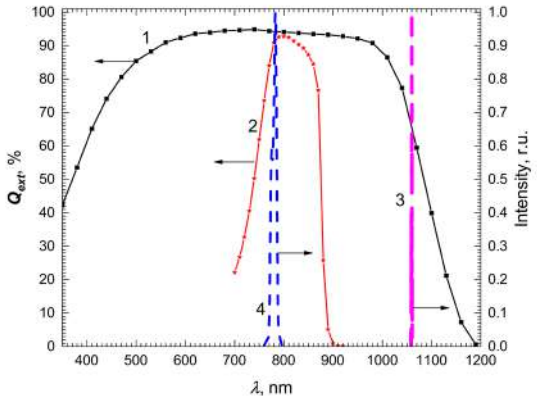


Fig.1. Spectral characteristics of the external quantum efficiency of α-Si:H/c-Si HJT cell (1) and AlGaAs/GaAs p-i-n PD (2), as well as emission intensity spectra of energy constant (3) and information pulsed (4) laser sources

© Калиновский В.С., Теруков Е.И., Контрош Е.В., Юферев В.С., Прудченко К.К., Терукова Е.Е., Толкачев И.А., Кокшаров Е.Г., Павлова Е.Г., Чекалин А.В., Гончаров С.Е., 2023. Издатель: Санкт-Петербургский политехнический университет Петра Великого.

According to the method described in [3], samples of the HJT cells and AlGaAs/GaAs p–i–n PDs were selected and the HPVC was created based on them. The photo of the HPVC is shown in Fig. 2. The assembly of the information PC is made in the form of a quadrature of four series connected p–i–n AlGaAs/GaAs PDs. Silicone microlenses were mounted on the photoactive surface of each p–i–n AlGaAs/GaAs PD. Mounting and electrical connection of the p–i–n PDs is performed on an AlN heat sink base. The information PC with an optical concentrator (focon) is mounted directly in the center of the photosensitive surface of the energy HJT cell.

Measurements of the photovoltaic characteristics of the HPVC (Fig. 3) were carried out with simultaneous illumination by continuous laser radiation with a power density of ~ 51 mW/cm$^2$ at a wavelength of 1.06 μm and pulsed at a wavelength of 0.78 μm of ≤ 10 ps full width at half maximum (FWHM) and the 71 MHz frequency at an average power of ~ 120 mW. The illumination of the energy HJT cell was carried out from a multimode optical fiber with a homogenizer (200/400 μm) with a radiation intensity distribution close to the Gaussian distribution, simulating the scattering of laser radiation in the atmosphere. Fig. 3 shows the load current-voltage (I–V) characteristic of the HJT cell (curve 1) and photoresponse pulses of the information PC (curves 2–4). According to the measured load I–V characteristic, the efficiency of the HJT cell with the AlGaAs/GaAs p–i–n PC mounted on its frontal surface was ~ 26%.

To simulate the displacement of the signal source from the information receiver, the photoresponse pulses of the AlGaAs/GaAs p–i–n PC were measured under laboratory conditions when irradiated from an optical fiber with a divergence angle of 10° at different light spot areas.

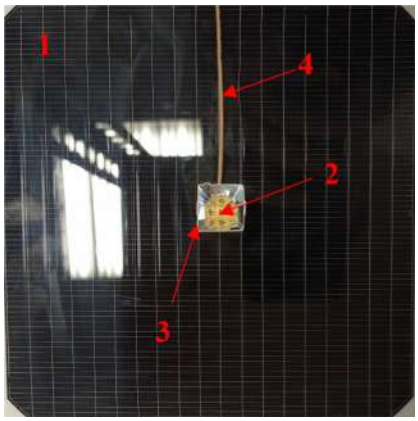


Fig. 2. A photograph of the developed and created energy–informational HPVC, where 1 is the energy HJT cell, 2 is informational AlGaAs/GaAs p–i–n photoconverter with silicone microlenses, 3 is focon, 4 is microwave cable

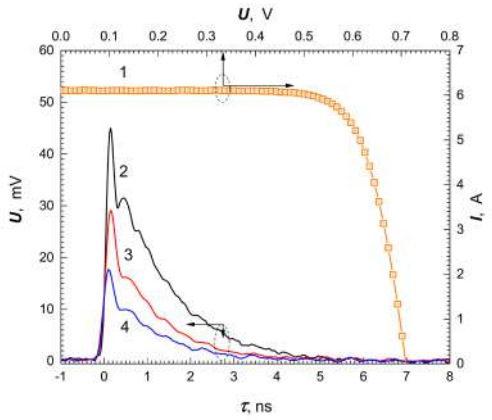


Fig. 3. Characteristics of the HPVC. Load I–V characteristics of the α-Si:H/c–Si HJT cell (continuous, 1.06 μm, ~ 51 mW/cm$^2$) with an informational AlGaAs/GaAs p–i–n PC mounted on it (1), photoresponse pulses of AlGaAs/GaAs p–i–n PC with a focon at the laser spot area of 0.2 (2), 0.8 (3), 2 (4) cm$^2$, (pulse: 0.78 μm, ≤ 10 ps FWHM, $P_c$ = 120 mW)

The measured time parameters are shown in Table 1. According to the results obtained by increasing the area of the laser irradiation spot from 0.2 cm$^2$ to 2 cm$^2$, the maximum amplitude of the signal voltage at a 50 Ohm load drops by 60% (Fig. 3, curves 2–4). The photoresponse rise time ($\tau_{rise}$) of the AlGaAs/GaAs p–i–n PC increased by 22%, the fall time ($\tau_{fall}$) decreased by 7% and FWHM decreased by 22%. With an illumination spot area of 0.2 cm$^2$, the maximum value of the information photoelectric cell amplitude was 45 mV with the following parameters: $\tau_{rise} \sim 140$ ps; $\tau_{fall} \sim 3.0$ ns; ~ 900 ps FWHM (Fig. 3, curve 2). With an illumination spot area of 2 cm$^2$, FWHM was 700 ps, which corresponds to a bandwidth of ≤ 1.25 GHz (Fig. 3, curve 4).

Table 1

**The measured time parameters**

| $S_{laser\ spot}$, cm$^2$ | $U_{max}$, mV | $\tau_{rise}$, ns | $\tau_{fall}$, ns | FWHM, ns |
|---|---|---|---|---|
| 0.2 | 45 | 0.14 | 2.8 | 0.9 |
| 0.8 | 29 | 0.19 | 2.3 | 0.7 |
| 2 | 18 | 0.18 | 2.6 | 0.7 |

The inhomogeneity of the laser radiation profile is one of the factors limiting the effectiveness of the HJT cell needed to build an energetically independent laser channel in FSO. Therefore, an important task is to assess the effect of a not uniform illumination of the HJT cell photoactive surface on its photovoltaic characteristics. The load I–V characteristics of the HJT cell have been measured depending on the shading degree of the photosensitive surface of the element at a uniform power density of 100 mW/cm$^2$ of collimated optical radiation (AM1.5). Fig. 4 shows the dependences of FF and efficiency calculated from the load I–V characteristics on the shading degree of the photosensitive surface of HJT cells.

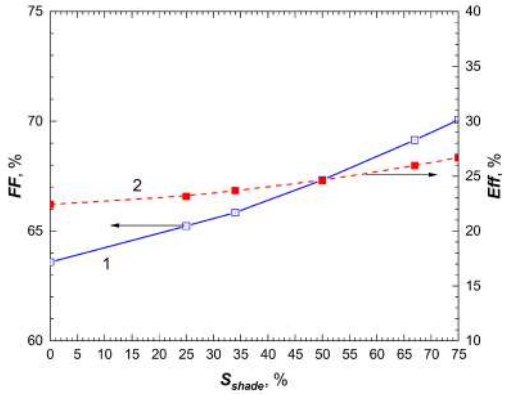


Fig. 4. Fillfactor (1) and efficiency (2) at different degrees of sample shading during pulsed excitation, at the power density 100 mW/cm$^2$ of the collimated optical flux AM1.5.

According to the obtained result, the HJT cells had demonstrated an increase of FF and efficiency with an increase in the shaded area. With an increase in the shaded area of the photoactive surface from 0% to 75%, the efficiency of the HJT cells increased from 22% to 26%. This change in FF and efficiency as well as a 4% decrease in the efficiency value at AM1.5 compared to laser radiation, is associated to the influence of the HJT cells surface spread resistance and thermal losses in short-wave radiation.

## Conclusions

The hybrid photovoltaic converter was developed and manufactured based on the energy α–Si:H/c–Si HJT cell and information AlGaAs/GaAs p–i–n PC. In photovoltaic mode the hybrid photovoltaic converter provides simultaneous conversion of continuous laser radiation with a power density of ~ 51 mW/cm$^2$ at a wavelength of 1.06 μm with an efficiency of ~ 26%, and pulsed laser radiation at a wavelength of 0.78 μm of ≤ 900 ps FWHM.

The corresponded results were obtained with the financial support by the Ministry of Science and Education of the Russian Federation.

## REFERENCES

1. Moctkom. url: http://www.moctkom.ru/optical-ground-stations/. accessed Oct. 26, 2022.
2. **Abramov A.S., Andronikov A., Abolmasov S.N., Terukov E.I.,** Springer series in optical sciences, 140 (2020) 113–132.
3. **Kalinovskii V.S., Kontrosh E.V., Klimko G.V., Tabarov T.S., Ivanov S.V., Andreev V.M.,** Tech. Phys. Lett., 44 (2018) 1013−1016.
4. **Kalinovskii V.S., Kontrosh E.V., Andreeva A.V., Ionova E.A., Malevskaya A.V., Andreev V.M., Malutina-Bronskaya V.B., Zalesskiy V.B., Lemeshevskaya A.M., Kuzoro V.I., Khalimanovich V.I., Zayceva M.K.,** AIP Conference Proceedings, 2149 030003, 2019.

## THE AUTHORS

**KALINOVSKII Vitaliy S.**
vitak.sopt@mail.ioffe.ru

**TERUKOV Evgeny I.**
eug.terukov@mail.ioffe.ru

**KONTROSH Evgeny V.**
kontrosh@mail.ioffe.ru
ORCID: 0000-0003-1812-3714

**YUFEREV Valentin S.**
valyuf.ammp3@mail.ioffe.ru
ORCID: 0000-002-6843-8530

**PRUDCHENKO Kseniia K.**
prudchenkokk@mail.ioffe.ru
ORCID: 0000-0003-4437-2984

**TERUKOVA Ekaterina E.**
eug.terukov@mail.ioffe.ru

**TOLKACHEV Ivan A.**
TolkachevIA@mail.ioffe.ru
ORCID: 0000-0001-8202-7087

KOKSHAROV Egor G.
egor.koksharov.99@mail.ru

**PAVLOVA Ekaterina G.**
kate.pavlova99@yandex.ru

**CHEKALIN Alexander V.**
Chekalin@mail.ioffe.ru

**GONCHAROV Sergey E.**
Goncharov@mail.ioffe.ru

*Received 26.10.2022. Approved after reviewing 10.11.2022. Accepted 10.11.2022.*

© Peter the Great St. Petersburg Polytechnic University, 2023

Conference materials
UDC 620.92, 621.382
DOI: https://doi.org/10.18721/JPM.161.207

# Photovoltaic characteristics of HJT photo converters of laser radiation at a wavelength of 1064 nm

K.K. Prudchenko [1]✉, E.E. Terukova [1], E.V. Kontrosh [1], I.A. Tolkachev [1],
E.G. Koksharov [1], E.G. Pavlova [1], V.S. Kalinovskii [1], E.I. Terukov [1,2]

[1] Ioffe Institute, St. Petersburg, Russia;
[2] St. Petersburg Electrotechnical University "LETI", St. Petersburg, Russia
✉ prudchenkokk@mail.ioffe.ru

**Abstract.** The possibility of efficient conversion of continual infrared laser radiation by heterojunction technology *a*-Si:H/*c*-Si photovoltaic converters is demonstrated. The photovoltaic characteristics of eight different types of heterojunction structures were investigated. The photovoltaic converters of the *n*-α-Si/*n*-*c*-Si/*p*-α-Si heterojunction structure with contact grid Ag turned out to be the best in terms of dark currents, external quantum efficiency, I-V characteristics, and conversion efficiency of laser radiation with 1064 nm wavelength at a power density up to 2 kW/m$^2$. The maximum efficiency ~ 24.5% of this structure was reached at power density of 1 kW/m$^2$.

**Keywords:** heterojunction technology solar cells, free space optics, high-power laser radiation converters, region of optical transparency of the atmosphere.

**Citation:** Prudchenko K.K., Terukova E.E., Kontrosh E.V., Tolkachev I.A., Koksharov E.G., Pavlova E.G., Kalinovskii V.S., Terukov E.I., Photovoltaic characteristics of HJT photo converters of laser radiation at a wavelength of 1064 nm, St. Petersburg State Polytechnical University Journal. Physics and Mathematics. 16 (1.2) (2023) 52–58. DOI: https://doi.org/10.18721/JPM.161.207

This is an open access article under the CC BY-NC 4.0 license (https://creativecommons.org/licenses/by-nc/4.0/)

Материалы конференции
УДК 620.92, 621.382
DOI: https://doi.org/10.18721/JPM.161.207

# Фотовольтаические характеристики HJT фотопреобразователей лазерного излучения на длине волны 1064 нм

К.К. Прудченко [1]✉, Е.Е. Терукова [1], Е.В. Контрош [1], И.А. Толкачев [1],
Е.Г. Кокшаров [1], Е.Г. Павлова [1], В.С. Калиновский [1], Е.И. Теруков [1,2]

[1] Физико-технический институт им. А.Ф. Иоффе РАН, Санкт-Петербург, Россия;
[2] Санкт-Петербургский государственный электротехнический университет «ЛЭТИ» им. В.И. Ульянова, Санкт-Петербург, Россия
✉ prudchenkokk@mail.ioffe.ru

**Аннотация.** Показана возможность эффективного преобразования постоянного лазерного излучения инфракрасного диапазона фотоэлектрическими преобразователями на основе гетеропереходных *a*-Si:H/*c*-Si структур. Исследованы фотовольтаические характеристики образцов из восьми различных типов гетеропереходных структур. Наилучшей по вольт-амперным характеристикам и параметрам темновых токов, внешней квантовой эффективности, эффективности преобразования лазерного излучения на длине волны 1064 нм с плотностью мощности до 2 кВт/м$^2$, оказалась *n*-α-Si/*n*-*c*-Si/*p*-α-Si гетеропереходная структура. Максимальный КПД данной структуры достигался при плотности мощности 1 кВт/м$^2$ и составил ~ 24.5%.

© Prudchenko K.K., Terukova E.E., Kontrosh E.V., Tolkachev I.A., Koksharov E.G., Pavlova E.G., Kalinovskii V.S., Terukov E.I., 2023. Published by Peter the Great St. Petersburg Polytechnic University.

**Ключевые слова:** гетеропереходные солнечные элементы, атмосферные оптические линии связи, преобразователи мощного лазерного излучения, область оптической прозрачности атмосферы.

**Ссылка при цитировании:** Прудченко К.К., Терукова Е.Е., Контрош Е.В., Толкачев И.А., Кокшаров Е.Г., Павлова Е.Г., Калиновский В.С., Теруков Е.И. Исследование фотовольтаических характеристик HJT преобразователей при воздействии лазерного излучения на длине волны 1064 нм // Научно-технические ведомости СПбГПУ. Физико-математические науки. 2023. Т. 16. № 1.2. С. 52–58. DOI: https://doi.org/10.18721/JPM.161.207

Статья открытого доступа, распространяемая по лицензии CC BY-NC 4.0 (https://creativecommons.org/licenses/by-nc/4.0/)

## Introduction

The best *a*–Si:H/*c*–Si photovoltaic converters (PVCs) made by heterojunction technology (HJT) have an efficiency of more than (25–26) % at solar radiation (AM1.5) [1–3]. In addition to solar energy conversion, HJT modules can find their application as high-power laser radiation converters, for example, in free space optics (FSO). Currently, FSO systems depend on reliable external power sources. For this reason, the HJT PVCs can be used as a power supply for the receiving and transmitting stations of FSO [4]. This makes it possible to significantly simplify and autonomize the operation of FSO systems, as well as expand the sphere of their application.

Taking into account the region of optical transparency of the atmosphere, it is important to evaluate the efficiency of the HJT PVCs when illuminated by high-power laser radiation in the near infrared range. In this work, a laser with a wavelength of 1064 nm was used, which has good spatial coherence, low beam divergence and a wavelength that coincides with the transparency window of the atmosphere in the near infrared range. To evaluate the maximum conversion efficiency of PVCs depending on the temperature and an incident laser radiation power, as well as stability and from the point of view of economic feasibility, all currently available HJT structures were used.

In total, eight different types of HJT PVCs structures were considered in this work (Table 1). To identify structures with the best parameters, the following dependences were measured and analyzed: direct dark current-voltage ($I–V$) characteristics in the voltage range from 0 to 1.0 V and characteristics of external quantum efficiency in the wavelength range (350–1200) nm. Further, studies of the PVCs characteristics were carried out on the basis of the selected most promising structure with the best characteristics. Load $I–V$ characteristics in the power density range from 0.06 to 2 kW/m$^2$ with continuous laser radiation at a wavelength of 1064 nm, as well as load $I–V$ characteristics in the temperature range from 25 °C to 80 °C at a power density of 1 kW/m$^2$ were measured.

## Experiment

**The structures of HJT photo converters.** The general scheme of the studied structures of the HJT PVCs is shown in Fig. 1. The studied samples (Table 1) were formed on textured *c*–Si *n*– or *p*–type substrates with a thickness of ~ 125 μm with a charge carrier concentration of ~ $10^{15}$ cm$^{-3}$. A layer of intrinsic amorphous silicon (*i*–α–Si:H) with a thickness of 5–10 nm was deposited on a c–Si substrate. Then, an amorphous or microcrystalline layer of n– or p–type silicon with a thickness of 10–20 nm and layers of indium-tin oxide (ITO) with a thickness of 100 nm were deposited on the front and back sides of the substrate. To create a contact grid on the surface of ITO layers, two manufacturing methods were used. The first is the production of silver (Ag) contact busbars with a width of 40 μm and a pitch of 1.2 mm by screen printing.

The second is the manufacture of copper (Cu) contact busbars by electroplating. The experiments used samples with an area of ~ 1 cm$^2$ with bilateral photosensitivity, which is an additional advantage in the presence of albedo. Samples with an area of 1 cm$^2$ were formed by laser cutting from the original full-size HJT photo converter with a size of 15.6 cm × 15.6 cm. The side surfaces of the cut samples were not subjected to special treatment and did not have additional passivating coatings.

© Прудченко К.К., Терукова Е.Е., Контрош Е.В., Толкачев И.А., Кокшаров Е.Г., Павлова Е.Г., Калиновский В.С., Теруков Е.И., 2023. Издатель: Санкт-Петербургский политехнический университет Петра Великого.

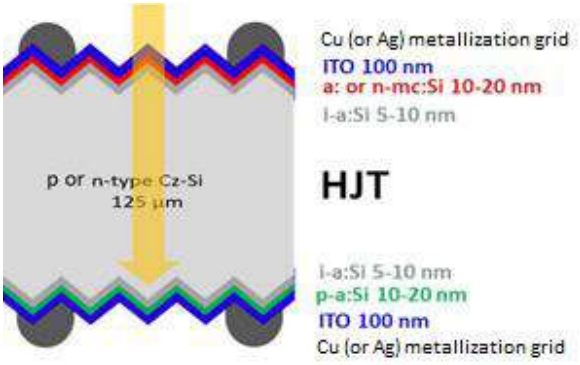


Fig. 1. A schematic sketch of the HJT PVCs on *n*- or *p*-type wafer

**Dark *J*–*V* characteristics of structures (A-H).** According to the method described in [5–6], the experimental direct "dark" *J*–*V* characteristics of the best samples of HJT structures (A-H) were measured and analyzed. The method is applicable to semiconductor *p*–*n* structures and consists in dividing the direct "dark" *J*–*V* characteristic into several exponential sections corresponding to different current flow mechanisms.

Table 1

**The types of *n*– and *p*–type HJT photovoltaic converters structures with dimensions of 1 cm²**

| Structure | Wafer type | Configuration | Front n-layer | Fabrication of a contact grid |
|---|---|---|---|---|
| A | *n* | Rare (back) emitter [3] | Amorphous | Ag paste screen printed |
| B | *n* | Rare (back) emitter | Microcrystalline | Ag paste screen printed |
| C | *n* | Rare (back) emitter | Amorphous | Cu galvanic metallization grid |
| D | *n* | Rare (back) emitter | Microcrystalline | Cu galvanic metallization grid |
| E | *p* (Si doped with B) | – | Amorphous | Ag paste screen printed |
| F | *p* (Si doped with B) | – | Microcrystalline | Ag paste screen printed |
| G | *p* (Si doped with Ga) | – | Amorphous | Ag paste screen printed |
| H | *p* (Si doped with Ga) | – | Microcrystalline | Ag paste screen printed |

There are tunnel-trap (excessive) with diode ideality coefficient $A_t > 2$ (Esaki), recombination with $A_r = 2$ (Sah-Noyce-Shockley) and diffusion with $A_d = 1$ (Shockley). Fig. 2 shows the experimental direct "dark" *J*–*V* characteristics of the best samples of HJT structures (A-H) – (*a*) and the values of "saturation" currents calculated from them – (*b*). According to the calculated experimental curves, all three current flow mechanisms with values of "saturation" currents – $J_{0t}$, $J_{0r}$, $J_{0d}$ are extracted. The lower the "saturation" currents, the higher the efficiency of the laser radiation PVC.

Structure A in total has the lowest values of "saturation" currents, determined by the direct dark *J*–*V* characteristic, namely: $J_{0t} = 2.2 \cdot 10^{-7}$ A/cm²; $J_{0r} = 1.2 \cdot 10^{-10}$ A/cm²; $J_{0d} = 3.8 \cdot 10^{-14}$ A/cm².

**Spectral characteristics of structures (A-H).** In addition to the dark characteristics, the spectral characteristics were studied, which are the main ones for determining the photosensitivity of the investigated structures of the HJT PVCs. In particular, it can be seen from Fig. 3 that in the long-wavelength sensitivity edge of the HJT PVCs, the highest values of quantum efficiency are

achieved in structures on an n-type substrate. The maximum value of the quantum efficiency $Q_{ext}$ = 64% at a wavelength of 1064 nm had the structure A. At the same time, it should be noted that structures on p-type substrates doped with gallium also have relatively high quantum efficiency values. The *p*-type structures doped with boron had the lowest quantum efficiency values. The results obtained are a consequence of the formation of additional recombination centers effect associated with the formation of B-O bonds under the action of light in p-silicon doped with boron [7–8]. This, in turn, leads to a significant reduction in the lifetime of minority charge carriers.

In the long-wavelength region of the spectrum, the maximum difference in quantum efficiency between the structure F and the structure H was 20%. In this case, the higher the values of the external quantum efficiency at a wavelength of 1064 nm, the more preferable the structure is for creating the HJT PVC operating in photovoltaic mode at these wavelengths. The difference in quantum efficiency at a wavelength of 1064 nm between structure F and structure A was 24%.

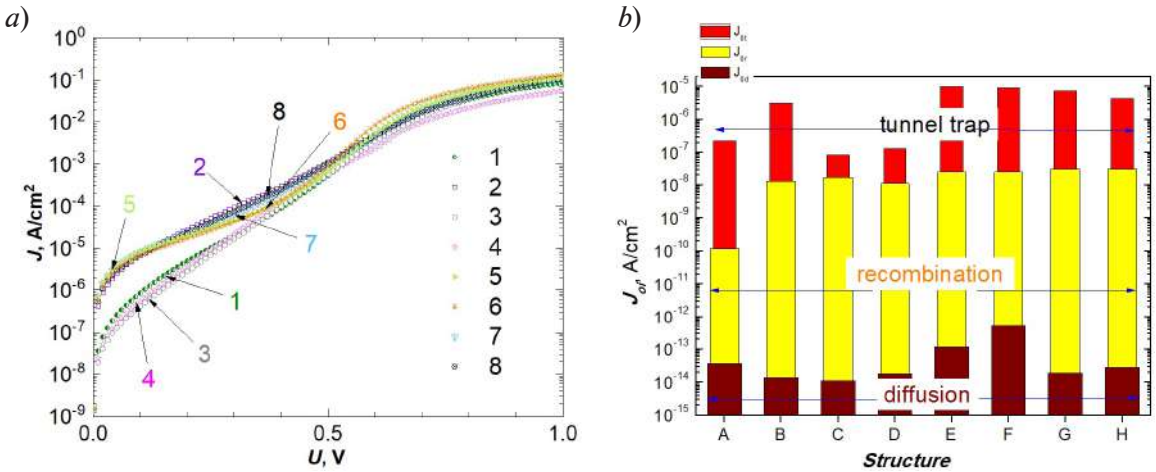


Fig. 2. Dark *J–V* characteristics (a) of HJT PVCs structures A (1), B (2), C (3), D (4), E (5), F (6), G (7), H (8) (Table 1) at $T$ = 300 K, and the calculated values of "saturation" currents (*b*) for HJT structures of A–H types, $J_{0t}$, $J_{0r}$, and $J_{0d}$ are tunnel-trap, recombination, and diffusion components of current flow mechanism, respectively

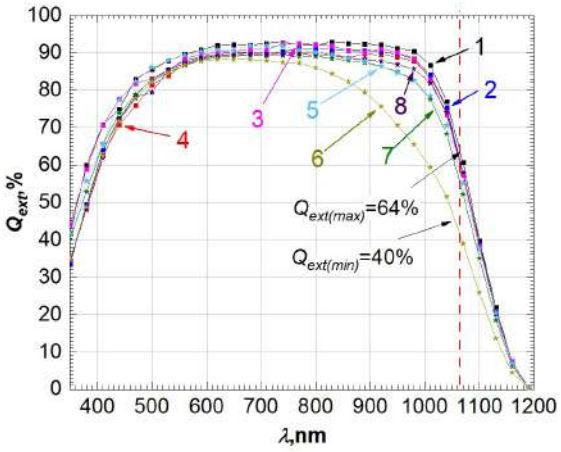


Fig. 3. Spectral characteristics of the external quantum efficiency of HJT PVC structures structures A (1), B (2), C (3), D (4), E (5), F (6), G (7), H (8) (Table 1) at $T$ =300 K

**Load *I–V* characteristics of structures (A–H).** According to the results obtained, the structure A with the lowest dark losses and the highest quantum efficiency at a wavelength of 1064 nm can be chosen as the most preferred structure for an energy-informational PVC of FSO. The study of the effect of a not uniform illumination by radiation on the photovoltaic parameters of structure A was carried out. It has been established that at maximum shading, the fill factor and efficiency retain their original values with high accuracy.

The load $I-V$ characteristics of the HJT PVC (structure A) were measured when it was exposed to laser radiation with a wavelength of 1064 nm, which has a relatively small beam divergence in the setup shown in Fig. 4. Fig. 5 shows the load $I-V$ characteristics measured at laser radiation in the power density range up to 2 kW/m$^2$ and at a temperature of 300 K. The values of photovoltaic parameters and their dependences on the power of incident laser radiation were determined from the obtained curves. Fig. 6 shows the dependences of the fill factor and efficiency calculated values on the power density of the incident radiation.

Fig. 7 shows the load $I-V$ characteristics of the n-α-Si/n-c-Si/p-α-Si:Ag HJT PVC (structure A), measured in the temperature range from 25 °C to 80 °C at a fixed power of continual laser radiation of 1 kW/m$^2$.

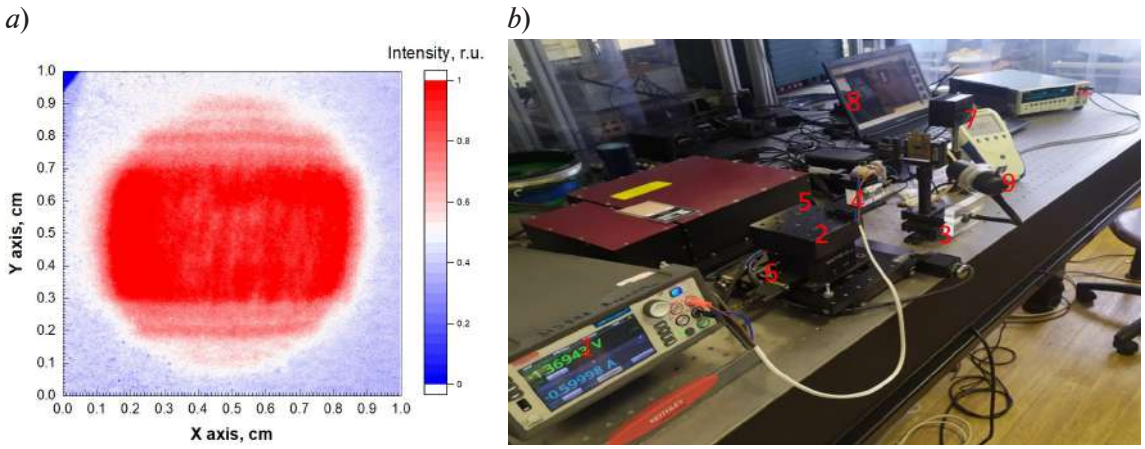


Fig. 4. Distribution of the laser radiation intensity (a) on the photosensitive 1 cm$^2$ surface of the HJT photo converter (structure A); Stand for measuring load I-V characteristics (*b*) of HJT PVC, 1 – source-meter Keithley 2460; 2 – laser (λ = 1064nm) with fiber optic radiation output; 3 – USB camera; 4 – the HJT PVC 1cm x 1cm; 5, 6 – precision three-axis motorized stage; 7 – source-meter Keithley 2430; 8 – PC; 9 – optical table "Standa"

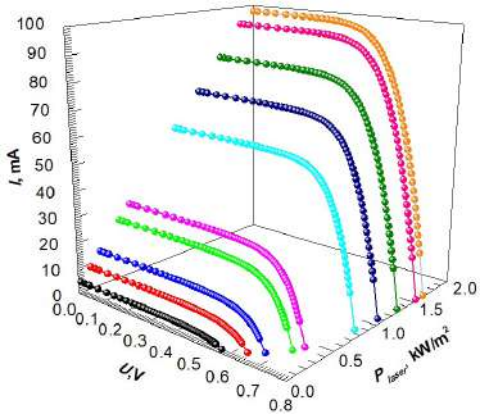


Fig. 5. Load I-V characteristics of HJT photo converter (structure A) in the range of laser radiation power densities 0.06–2 kW/m$^2$, $T$ = 300 K

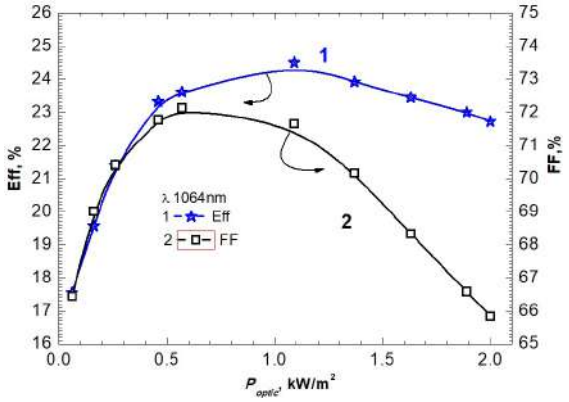


Fig. 6. Dependences of efficiency (1) and fill factor (2) of HJT photoconverter (structure A) on the power of laser radiation (λ = 1064 nm), $T$ = 300 K

Fig. 8 shows the temperature dependences of the fill factor and efficiency, determined from the load $I-V$ characteristics.

From the temperature dependences of the load $I-V$ characteristics and photovoltaic parameters, it can be seen that heating the test sample to 80°C contributes to an almost linear decrease in the open-circuit voltage by 13% and the fill factor by 7%. The efficiency reached a maximum value of ~ 24.8% at temperature of about 50 °C. This is explained by an increase in the short-circuit current (Fig. 6) due to an increase in the quantum efficiency ($Q_{ext}$), caused by the shift of

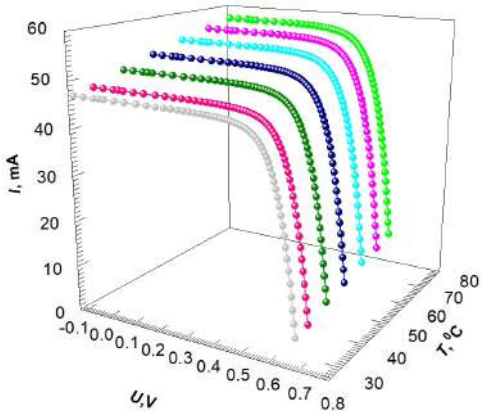


Fig. 7. Load I-V characteristics of HJT photo converter (structure A) in the temperature range from 250 °C to 800 °C, $P_{laser}$ = 1 kW/m²

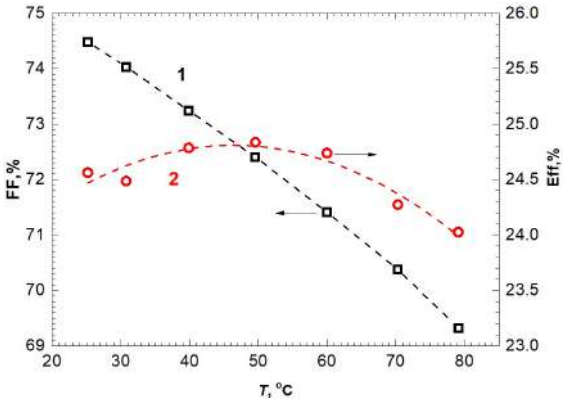


Fig. 8. Dependences of the fill factor (1) and efficiency (2) of HJT photo converter (structure A) on temperature when excited by laser radiation at λ = 1064 nm

the long-wavelength absorption edge to the infrared region when the HJT PVC is heated. Thus, the test sample (HJT, structure A) worked most efficiently at the power density of the incident laser radiation (λ =1064 nm) ~ 1.2 kW/m² with intensity distribution (Fig. 4, *a*) and the heating temperature ~ T = 50 °C (Fig. 6, 8).

## Conclusion

Thus, the samples of the n-α-Si/n-c-Si/p-α-Si:Ag HJT PVC had the lowest "saturation" currents $J_{0i}$ and the best external quantum efficiency $Q_{ext}$ at the long wave edge. Therefore, this structure provided the maximum laser radiation conversion efficiency ~ 24.5% (λ = 1064 nm) at a power density ≤ 2 kW/m² in the atmospheric transparency window. The efficiency of the PVC at the laser radiation power density of ~ 1 kW/m² and when the temperature changed from 293 K to 353 K increased up to 24.8%. The HJT PVC had demonstrated good temperature stability in this range, and the efficiency varied within ± 4%.

The corresponded results have been obtained with the financial support by the Ministry of Science and Education of the Russian Federation.

## Acknowledgments

The authors are grateful to Abolmasov S.N. for the manufactured and provided samples of HJT PVCs.

## REFERENCES

1. **Masuko K., Shigematsu M., Hashiguchi T., Fujishima D., Kai M., Yoshimura N., Yamaguchi T., Ichihashi Y., Mishima T., Matsubara N., Yamanishi T., Takahama T., Taguchi M., Maruyama E., Okamoto S.,** Achievement of More Than 25% Conversion Efficiency With Crystalline Silicon Heterojunction Solar Cell, IEEE Journal of Photovoltaics 4 (6) (2014) 1433–35.

2. **Yoshikawa K., Kawasaki H., Yoshida W., Irie T., Konishi K., Nakano K., Uto T., Adachi D., Kanematsu M., Uzu H.I., Yamamoto K.,** Silicon heterojunction solar cell with interdigitated back contacts for a photoconversion efficiency over 26%, Nature Energy 2 (5) (2017) 17032.

3. **Abramov A.S., Andronikov D.A., Abolmasov S.N., Terukov E.I.,** Chapter 7. High-Efficient Low-Cost Photovoltaics, Silicon Heterojunction Technology: A Key to High Efficiency Solar Cells at Low Cost, Springer Series in Optical Sciences 140 (2020) 113–32.

4. **Kognovitsky S.O., Malevsky D.A., Kalinovsky V.S.,** RF Patent No. RU 2021137224, Photovoltaic receiver of an optical communication line, 2021.

5. **Andreev V.M., Evstropov V.V., Kalinovsky V.S., Lantratov V.M., Khvostikov V.P.,** Current Flow and Potential Efficiency of Solar Cells Based on GaAs and GaSb *p–n* Junctions, Semiconductors 43 (5) (2009) 671–78.

6. **Kalinovskii V.S., Terukov E.I., Kontrosh E.V., Verbitskii V.N., Titov A.S.,** Radiation Resistance of α-Si:H/Si Heterojunction Solar Cells with a Thin i-α-Si:H Inner Layer, Technical Physics Letters 44 (2018) 801–3.

7. **Bothe K., Schmidt J.,** Electronically activated boron-oxygen-related recombination centers in crystalline silicon, J. Appl. Phys. 99 (2006) 013701.

8. **Chen D., Kim M., Shi J., Vicari Stefani B., Yu Z. (J.), Liu S., Einhaus R., Wenham S., Holman Z., Hallam B.,** Defect engineering of p-type silicon heterojunction solar cells fabricated using commercial-grade low-lifetime silicon wafers, Prog. Photovolt. Res. Appl. 29 (11) (2021) 1165–79.

## THE AUTHORS

**PRUDCHENKO Kseniia K.**
prudchenkokk@mail.ioffe.ru
ORCID: 0000-0003-4437-2984

**TERUKOVA Ekaterina E.**
e.terukova@hevelsolar.com

**KONTROSH Evgeny V.**
kontrosh@mail.ioffe.ru
ORCID: 0000-0003-1812-3714

**TOLKACHEV Ivan A.**
TolkachevIA@mail.ioffe.ru
ORCID: 0000-0001-8202-7087

**KOKSHAROV Egor G.**
egor.koksharov.99@mail.ru

**PAVLOVA Ekaterina G.**
kate.pavlova99@yandex.ru

**KALINOVSKII Vitaliy S.**
vitak.sopt@mail.ioffe.ru
ORCID: 0000-0003-4858-7544

**TERUKOV Evgeny I.**
eug.terukov@mail.ioffe.ru

*Received 27.10.2022. Approved after reviewing 06.12.2022. Accepted 07.12.2022.*

© Peter the Great St. Petersburg Polytechnic University, 2023

Conference materials
UDC 536.416, 536.2.022
DOI: https://doi.org/10.18721/JPM.161.208

# Structural stresses and temperature budget in III-V photoconverters with a thin Ge substrate

A.N. Panchak ✉, M.Z. Shvarts

Ioffe Institute, Saint-Petersburg, Russia

✉ a.panchak@mail.ioffe.ru

**Abstract.** In high illumination conditions for photovoltaic converters, it is possible to stabilize the temperature of the photoactive region using a heatsink with high thermal conductivity, and by thinning the substrate that is a holder for semiconductor structure. However, the use of both methods together can lead to significant increase of the possible fragility of the converter. This work is devoted to the searching of balance between brittleness and overheating of GaAs/Ge solar cells installed on a copper heatsink with ceramic intermedia. Such composite heatsink, on the one hand, reduces mechanical stresses in the semiconductor, but, on the other hand, makes better the heat removal mode.

**Keywords:** photovoltaic cells, temperature overheating, mechanical stress, thinning substrate

**Citation:** Panchak A.N., Shvarts M.Z., Structural stresses and temperature budget in III-V photoconverters with a thin Ge substrate, St. Petersburg State Polytechnical University Journal. Physics and Mathematics. 16 (1.2) (2023) 59–63. DOI: https://doi.org/10.18721/JPM.161.208

This is an open access article under the CC BY-NC 4.0 license (https://creativecommons.org/licenses/by-nc/4.0/)

Материалы конференции
УДК 536.416, 536.2.022
DOI: https://doi.org/10.18721/JPM.161.208

# Структурные напряжения и температурный баланс в фотопреобразователях A3B5 с тонкой Ge подложкой

А.Н. Паньчак ✉, М.З. Шварц

Физико-технический институт им. А.Ф. Иоффе РАН, Санкт-Петербург, Россия

✉ a.panchak@mail.ioffe.ru

**Аннотация.** В условиях высокой освещенности для фотоэлектрических преобразователей стабилизировать температуру фотоактивной области можно с помощью радиатора с высокой теплопроводностью и утончения подложки, являющейся держателем полупроводниковой структуры. Однако совместное использование обоих методов может привести к значительному увеличению хрупкости преобразователя. Настоящая работа посвящена поиску баланса между хрупкостью и перегревом солнечных элементов GaAs/Ge, установленных на медном радиаторе с керамической прокладкой. Такой композитный радиатор, с одной стороны, снижает механические напряжения в полупроводнике, а с другой стороны, улучшает режим отвода тепла.

**Ключевые слова:** фотоэлектрические преобразователи, температура, перегрев, механические напряжения, утончение подложки

**Ссылка при цитировании:** Паньчак А.Н., Шварц М.З. Структурные напряжения и температурный баланс в фотопреобразователях A3B5 с тонкой Ge подложкой // Научно-технические ведомости СПбГПУ. Физико-математические науки. 2023. Т. 16. № 1.2. С. 59–63. DOI: https://doi.org/10.18721/JPM.161.208

Статья открытого доступа, распространяемая по лицензии CC BY-NC 4.0 (https://creativecommons.org/licenses/by-nc/4.0/)

© Panchak A.N., Shvarts M.Z., 2023. Published by Peter the Great St. Petersburg Polytechnic University.

## Introduction

In concentrator photovoltaic modules [1] and transducers of high-power laser radiation [2], the operation of photovoltaic converters (PVC) is associated with significant heating. Therefore, to stabilize the temperature and prevent overheating of the PVC, it is necessary to provide efficient heat removal [3] or a mode of temperature-controlled operation [4]. Thus, the efficiency of solar PVC can exceed 45% under concentrated (400–1000 X) irradiation and at cell temperature of 25 °C [5]. Outdoors, the temperature of the PVCs in concentrator module depends on the type and material of the heatsink and environmental conditions. In practice the most widely used heatsinks are based on materials with high thermal conductivity (copper, ceramics).

Additionally, the operating temperature of the photoactive region (p-n junction) can be further reduced by thinning the PVC's substrate. In this case, if the thermal conductivity of the heatsink is higher than of the semiconductor, the temperature gradient between the active region and the heatsink decreases (the thermal flow takes away from the semiconductor volume). However, together with this, the mechanical strength of the sample also decreases. In the process of high-temperature assembly (soldering), the PVC crystal is mounted on the heatsink. After solidification and cooling up to room temperature, significant mechanical stresses arise in the semiconductor structure. It is caused by the difference in the coefficients of thermal expansion (CTE) of the PVC and the heatsink materials. Thus, at thinning Ge substrate from 200 down to 3 μm the temperature of the GaAs active region can decreases from 41 to 30 °C at 1000X irradiation condition and if copper is used as a heatsink. But if the thickness of the substrate is less than 100 μm, mechanical stress will overcomes the flow stress of Ge if PVC is directly attached on copper holder.

## PVC substrate thinning and heatsink selection

This contradiction can be resolved by selecting a heatsink material with a CTE close to the semiconductor. Such materials include aluminum oxide and aluminum nitride ceramics [7]. Since mounting directly on ceramics is difficult, a thin technological copper layer is preliminary deposited on the ceramic base. Thus, in a solar cell soldered on a copper coating of a ceramic heatsink, lower mechanical stresses occur. However, the thermal conductivity of the ceramic material is lower than that of copper. The conditions for heat removal can be improved by using composite systems. In such heatsinks, the main part consists of copper, whereas a thin ceramic with top copper layer is located just below the solar cell. So the ceramic layer compensates the linear expansion of the thin copper layer.

In this work, it was assumed that the semiconductor crystal is rigidly fixed just on the copper layer, in spite of that in practice the mounting of the crystal is carried out using solder. However, the introduction of an additional SnPbAg layer with a thickness of 10 μm does not significantly change the stress distribution inside the semiconductor crystal (the difference in the absolute values of the von Mises stress maximum is less than 2%).

The temperature and mechanical stress in the GaAs layer were studied as a function of the Ge substrate and/or ceramic thicknesses. The simulation of the equilibrium thermal mode and the process of thermal contraction was carried out using COMSOL Multiphysics accounting data given in [8, 9].

## Simulation conditions

Figure 1 represents the modeled structure. The dimensions of the semiconductor crystal and heatsink were 3 mm × 3 mm and 10 mm × 10 mm, correspondingly. The thickness of the GaAs photoactive layer was 5 μm, the copper coating was 127 μm, and the copper heatsink was 1 mm. The thicknesses of the Ge substrate and ceramic intermedia were varied.

In the model, temperature and mechanical stresses were calculated separately. In the first part of the calculations, the maximum temperature at the center of the GaAs layer was determined. The irradiance distribution within the PVC designated illumination area (DIA) of a 2.8 mm in diameter was assumed to be Gaussian. The integrated light power was 1.6 W (corresponds to solar irradiance of 1000 W/m$^2$ concentrated by a Fresnel lens of 40×40 mm$^2$ optical aperture on the PVC). It was assumed that all light power is absorbed in GaAs layer and converted into heat. The temperature of the rear side of the heatsink was taken equal to the ambient temperature (25 °C).

© Паньчак А.Н., Шварц М.З., 2023. Издатель: Санкт-Петербургский политехнический университет Петра Великого.

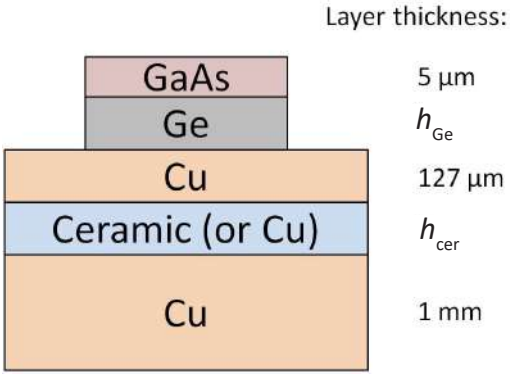


Fig. 1. Model of the structure of a mounted solar cell

In the thermal contraction part, the initial temperature of the PVC crystal and the heatsink was taken equal to 160 °C. At this temperature, their total fixture is ensured. After that, the temperature of the entire system decreased to room temperature (25 °C). Stresses only because of cooling were considered. The effects associated with radiative heating are not considered and will be discussed in the separate paper.

**Simulation results**

The overheating values of the GaAs layer relative to the environment were calculated. The results on Figure 2 show the maximum overheat values in the center of the structure.

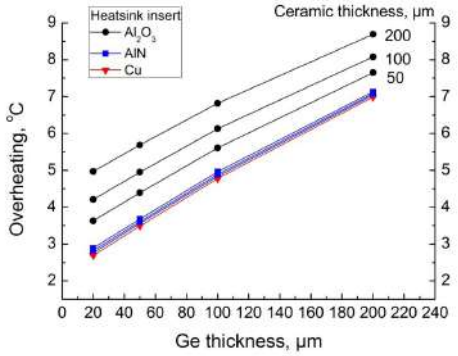


Fig. 2. Overheating relative to the environment in the GaAs layer depending on the thickness of the Ge layer and the thickness of the ceramic insert in the heatsink

Materials with high thermal conductivity significantly reduce overheating of the photoreceiver or solar cell. So a copper thermal dissipation body or a heatsink with an aluminum nitride insert reduce the overheating of the GaAs region from 7 to 2.7 °C if the Ge layer is thinned from 200 to 20 μm. In this case, the variation in the thickness of the AlN intermedia (200, 100, 50 μm) does not significantly affect the overheating value of the GaAs layer. The thermal conductivity of $Al_2O_3$ is noticeably lower than that of copper or AlN. Therefore, an increase in the thickness of the alumina insert in the heatsink from 50 to 200 μm increases the overheating of GaAs by 1 °C for any thickness of the Ge layer.

In the mechanical stress calculations part, the maximum von Mises values in the GaAs layer are given. This representation allows direct comparison with the flow stress parameter. For example, the flow stress of Ge is ~ 2 GPa [10], while that of GaAs is ~ 10 MPa [11]. In the Ge part, the maximum stress does not exceed 20 MPa. Thus, the GaAs layer should be considered the most fragile part of the structure. In addition, it should also be noted that the localization of the maximum stress in the structure in each simulated case is different: with a decrease in the thickness of the Ge layer, it is located closer to the edge of the crystal.

Figure 3 shows the results of modeling the maximum mechanical stress in the GaAs layer.

A copper heatsink produces significant mechanical stresses in the semiconductor structure.

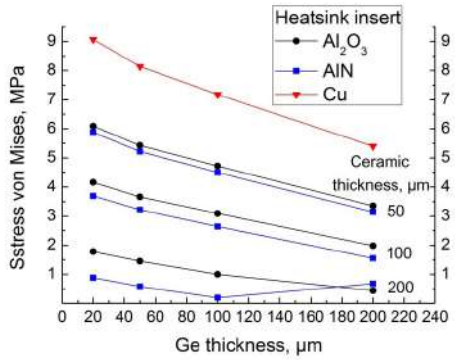


Fig. 3. Von Mises stresses in the GaAs layer depending on the thickness of the Ge layer and the thickness of the ceramic insert in the heatsink

When the Ge layer is thinned, the maximum stress approaches the flow stress. It should be taken into account during operation or in the process of mounting. The solar cell can be additionally stressed from the side of the photoactive region with attached contact grid: for example, when contacting with a measuring probe or during the wiring to the top current-spreading busbar. So it is necessary to provide a factor of safety by optimizing the thickness of the germanium substrate.

The ceramic intemedia in the heatsink significantly reduces mechanical stress directed to the semiconductor crystal. Moreover, an increase in ceramic thickness decreases the effect of a thin copper layer on the PVC and particularly on the GaAs photoactive region. Thus, at a Ge layer thickness of 20 μm, the stress decreases from 9 to 1 MPa if a heatsink with a 200 μm AlN ceramic intermedia is used instead of a full-copper-bodied heatsink.

## Conclusion

In this paper, methods for thermal stabilization of a GaAs/Ge PVC for high irradiance conditions were considered. The main approach discussed is to thin the Ge substrate together with the use of a heatsink with high thermal conductivity. The issue of increasing the fragility of a sample is also considered. It appears in process of mounting the cell on a heatsink. The mechanical stress appears because of the difference in the CTE of a metal and a semiconductor. Modifications of the heatsink for increasing the factor of safety of the solar cell are discussed.

The decrease in the thickness of the Ge substrate from 200 to 20 μm reduces the radiative (1.6W) overheating in GaAs from 7 to 2.7 °C relative to the environment. However, in this case, the maximum mechanical stress in GaAs increases from 5 to 9 MPa (in case Cu heatsink), approaching the flow stress (10 MPa) for semiconductor material. The increase in efficiency from the total effect of reducing the operating temperature and reducing the series resistance of the substrate is about 1%.

The implementation of ceramic intermedia into the heatsink directly underneath the PVC crystal significantly reduces mechanical stresses in the GaAs layer. By using aluminium nitride intermedia with 100 μm thickness, mechanical stresses in GaAs are 0.2 MPa that is not critical for effective photoreceiver operation.

## REFERENCES

1. **Algora C., Rey-Stolle I.,** Handbook on Concentrator Photovoltaic Technology, J. Wiley & Sons, New York, 2016.

2. **Algora C., García I., Delgado M., Peca R., Vázquez C., Hinojosa M., Rey-Stolle I.,** Beaming power: Photovoltaic laser power converters for power-by-light, Joule, 6 (2) (2022) 340.

3. **Daviduk N.Yu., Andreeva A.V., Malevsky D.A., Pokrovsky P.V., Sadchikov N.A., Chekalin A.V., Andreev V.M.,** Electroinsulated Heat Sinks for Concentrated Photovoltaic Solar Cells Technical Physics Letters, 46 (5) (2020) 436.

4. **Shvarts M.Z., Emelyanov V.M., Malevskiy D.A., Mintairov M.A., Mintairov S.A., Nakhimovich M.V., Pokrovskiy P.V., Salii R.A., Kalyuzhnyy N.A.,** Temperature Tweaking of the

Output Photovoltaic Parameters of Laser Power Converters, IEEE Electron Device Letters, 41 (9) (2020) 1324.

5. **Geisz J.F., France R.M., Schulte K.L., Steiner M.A., Norman A.G., Guthrey H.L.,** Young M. R., Song T., Moriarty T., Six-junction III–V solar cells with 47.1% conversion efficiency under 143 Suns concentration, Nature Energy, 5 (2020) 326.

6. **Panchak A.N., Shvarts M.Z.,** Temperature modes and mechanical stresses in photovoltaic converters of concentrated sunlight, Technical Physics, 3 (2022) 373.

7. **Scheuermann U.,** Advanced Power Modules with AlN-Substrates – Extending Current Capability and Lifetime, PCIM Europe, Nuremberg, (2003) 309.

8. **Deng Y., Tang S., Tung D.,** Stress and thermal modeling of microbolometer using COMSOL multiphysics simulator, Proc. Conf. IEEE International Conference on Applied System Invention, Chiba (2018) 1149.

9. V**ajdi M., Moghanlou F., Sharifian Jazi F., Shahedi Asl. M., Shokouhimehr M.,** A review on the Comsol Multiphysics studies of heat transfer in advanced ceramics, Journal of Composites and Compounds, 2 (2020).

10. **Milman Yu.V., Gridneva I.V., Golubenko A.A.,** Construction of Stess-Strain Curves for Brittle Materials by Indentation in a Wide Temperature Range, Sci.of Sintering, 39 (2007) 67.

11. **Yonenaga I., Sumino K.,** Impurity effects on the mechanical behavior of GaAs crystals J. of Appl. Phys. 71 (1992) 4249.

## THE AUTHORS

**PANCHAK Alexander N.**
a.panchak@mail.ioffe.ru
ORCID: 0000-0003-1277-6749

**SHVARTS Maxim Z.**
shvarts.scell@mail.ioffe.ru
ORCID: 0000-0002-2230-7770

*Received 31.10.2022. Approved after reviewing 08.11.2022. Accepted 15.11.2022.*

© Peter the Great St. Petersburg Polytechnic University, 2023

Conference materials
UDC 537.533.2
DOI: https://doi.org/10.18721/JPM.161.209

# Functional dependence of the notional area of field emission

S.V. Filippov [1]✉, E.O. Popov [1], A.G. Kolosko [1]

[1] Ioffe Institute, St. Petersburg, Russia

✉ s.filippov@mail.ioffe.ru, f_s_v@list.ru

**Abstract.** Concepts and basic methods for extracting notional, formal and effective emission areas are considered. A functional dependence of the notional emission area on the field is obtained, taking into account the shape of the emitter. An analysis of the current-voltage characteristics in semi-logarithmic coordinates $\ln(I/U^k)$ vs $1/U$, called "k-power plot", is proposed, which makes it possible to take into account the shape of the emitter, to linearize the dependence, and, therefore, to obtain effective values of the field enhancement independent of the voltage range.

**Keywords:** field emission, effective parameters, emission area, field enhancement factor

**Citation:** Filippov S.V., Popov E.O., Kolosko A.G., Functional dependence of the notional area of field emission, St. Petersburg State Polytechnical University Journal. Physics and Mathematics. 16 (1.2) (2023) 64–69. DOI: https://doi.org/10.18721/JPM.161.209

This is an open access article under the CC BY-NC 4.0 license (https://creativecommons.org/licenses/by-nc/4.0/)

Материалы конференции
УДК 537.533.2
DOI: https://doi.org/10.18721/JPM.161.209

# Функциональная зависимость условной площади полевой эмиссии

С.В. Филиппов [1]✉, Е.О. Попов [1], А.Г. Колосько [1]

[1] Физико-технический институт им. А.Ф. Иоффе РАН, Санкт-Петербург, Россия

✉ s.filippov@mail.ioffe.ru, f_s_v@list.ru

**Аннотация.** Рассмотрены концепции и основные методы извлечения условной, формальной и эффективной площади эмиссии. Получена функциональная зависимость условной площади излучения от напряженности поля с учетом формы эмиттера. Предложен анализ ВАХ в полулогарифмических координатах $\ln(I/U^k)$ vs $1/U$, названный «график k-степени», позволяющий учесть форму эмиттера, линеаризовать зависимость и, следовательно, получить эффективные значения усиления поля, не зависящие от диапазона приложенного напряжения.

**Ключевые слова:** полевая эмиссия, эффективные параметры, площадь эмиссии, коэффициент усиления поля

**Ссылка при цитировании:** Филиппов С.В., Попов Е.О., Колосько А.Г. Функциональная зависимость условной площади полевой эмиссии // Научно-технические ведомости СПбГПУ. Физико-математические науки. 2023. Т. 16. № 1.2. С. 64–69. DOI: https://doi.org/10.18721/JPM.161.209

Статья открытого доступа, распространяемая по лицензии CC BY-NC 4.0 (https://creativecommons.org/licenses/by-nc/4.0/)

## Introduction

Optimization of field emission sources is impossible without extracting reliable quantitative information about the main parameters of emission structures from current-voltage characteristics (IVC). As is known, emitters are characterized by three main parameters that are

© Filippov S.V., Popov E.O., Kolosko A.G., 2023. Published by Peter the Great St. Petersburg Polytechnic University.

included in the main field emission equation. They are the work function φ, the field enhancement factor γ (FEF) and the emission area $A$ (EA).

Most of the experimental works indicate the inadequacy of determining the work function from plotting the IVC in semi-logarithmic Fowler-Nordheim coordinates (FN-plot), based on visual observations of the geometry of potential emission sites according to scanning electron microscopy (SEM) [1–3]. Without considering adsorption processes, the work function for carbon nanostructures is assumed to be 4.6 eV.

The second parameter, FEF, is quite easily extracted from the processing (slope $S^{fit}$) of experimental and 3D modeling data in FN-plot and Murphy-Good (MG-plot) coordinates [4, 5]. Besides, its effective values weakly depend on the range of applied voltage. It is clear that in the case of a stable emitter geometry, its geometric field enhancement does not depend on the magnitude of the field itself. Given the notion that emission obeys a field emission (satisfies the field emission test), the $S^{fit}$ value automatically determines the field on the emitter surface (more precisely, in the selected characteristic point "C").

Now the most discussed issue in the literature is how to determine the emission area (or area-like) parameter, both from the point of view of the conceptual apparatus and the search for the functional dependence of FEA on the applied voltage.

## The concept of notional and effective emission parameters

It is worth to note that the theory of field emission was developed for a fundamentally flat case (planar case). First, it concerns the derivation of the formula for the transparency of the potential barrier when the Schrödinger equation in Cartesian coordinates is used in one-dimensional form along the chosen coordinate axis. Secondly, a flat surface of a solid body is considered to derive Sommerfeld's constant, when the flow of particles through the energy space with energy components normal and parallel to the surface is considered.

Another problem concerns the concept of emission area. In theoretical premises, there is no talk about the dimensions of the emitter surface (there is no concept of "emission area"). The particle flux is indeed defined in terms of the surface area of a unit quantity. In this case, the number of particles is determined by the volume and velocity of the outflow from this volume, that is, their kinetic energy. However, the ratio of the number of particles (states) to the outflow area leads to a reduction in the area. Therefore, only the energy characteristics of the particles remain in the expression for the density. As a result, the current density is determined by the energy window, the area in the energy space by the field at a given field value, which acts as a parameter or constant. The concept of current density is akin to the concept of substance density, that is, a value that does not depend on the size of the object, for example, on the size of the considered body surface.

The lack of a clear understanding of emission area leads to problems in the perception of the concept of current density, causing confusion between local (theoretical) and macroscopic current densities. In radio engineering the current density is a value determined from the flowing current divided by the cross-sectional area of the conductor. On the contrary, in field emission the area of emission will be recovered by the size of the surface having the same magnitude of the electric field. As a result, this surface will provide the emission current measured by the instruments.

In general, it is believed that the emission area serves to formally link the magnitude of the emission current and the theoretical current density. Among the two dozen variants of writing the theoretical types of current density [6], the structure of the formula stands out, called "kernel", in which there are no functional dependencies in the pre-exponential factor, with the exception of the pre-exponential field factor to the power of $k$ ($k = 2$):

$$J_k = a\varphi^{-1}F^2\exp\left(-\nu b\varphi^{3/2} / F\right), \quad (1)$$

where $a$ and $b$ are the first and second Fowler-Nordheim constants, $v$ is the barrier "correction factor" or first barrier factor, φ is the work function.

© Филиппов С.В., Попов Е.О., Колосько А.Г., 2023. Издатель: Санкт-Петербургский политехнический университет Петра Великого.

Taking into account such representations, the total current density can be represented as:

$$J = \lambda J_k \ , \tag{2}$$

where in the multiplier λ is the pre-exponential correction factor (various physical corrections are taken into account, e.g., temperature contribution $\pi p/\sin(\pi p)$, $p$ is the Swanson-Bell parameter, the correcting barrier factor τ or the second barrier factor, etc.).

Two main definitions of the emission area are used in the literature – notional $A_n$ and formal $A_f$:

$$I \equiv A_n J, \tag{3}$$

$$I \equiv A_f J_k. \tag{4}$$

As can be seen from eq. (3), the notional area fully corresponds to the definition of the emission area, since it describes a surface with the same fields and temperature (all this in a flat case). The formal area, on the other hand, formally includes all functional dependences on the field, temperature, and so on. A number of theoretical papers consider only the situation $\lambda = 1$, assuming $I = A_n J_k$.

In the experiment, we are dealing with measured quantities - current and voltage. At this stage, it is useful to introduce the concept of effective parameters – FEF $\alpha_{eff}$ ($F = \alpha U$) and emission area $A_{eff}$. These parameters are extracted from the processing of the current-voltage characteristic in a certain range of applied voltages (fields). The main way to extract these parameters is to process dependences in semilogarithmic coordinates. Thus, the effective values of FEF and emission area depend on the extraction method (most often along the trend line) and on the range (number of points) of the data being processed. The effective parameters obtained in such way, as shown in the ref. [7], coincide with the given notional values $A_n = A_{eff}$ and $\alpha = \alpha_{eff}$ only in two cases (and only in the planar case): using the current density equation (Shrednik equation) in the ref. [8] and processing in quadratic coordinates FN plot, and the equation in the form of MG kernel and processing in MG plot coordinates, respectively:

$$\ln\left(I / U^2\right) = \ln\left(R^{ES,Fit}\right) + S^{ES,Fit}\left(1/U\right), \tag{5}$$

$$\alpha_{ES,eff} = -0.95 b\varphi^{3/2} / S^{ES,Fit}, \tag{6}$$

$$A_{ES,eff} = R^{ES,Fit} / \left[\tau^{-2} a\varphi^{-1} \exp\left(1.03\eta\right)\alpha_{ES,eff}^2\right], \tag{7}$$

$$\eta = b\varphi^{3/2} / F_R = bc_S^2\varphi^{-1/2}, \tag{8}$$

where $c_S$ is Schottky constant, $F_R = \varphi^2 c_S^{-2}$ is reference field or barrier removal field, $\tau^2 \approx 1.1$, $v = 0.95–1.03f^2$, $f = F/F_R$ is scaled barrier field.

$$\ln\left(I / U^{2-\eta/6}\right) = \ln\left(R^{MG,Fit}\right) + S^{MG,Fit}\left(1/U\right), \tag{9}$$

$$\alpha_{MG,eff} = -b\varphi^{3/2} / S^{MG,Fit}, \tag{10}$$

$$A_{MG,eff} = R^{Fit} / \left[\tau^{-2} a\varphi^{-1} F_R^{\eta/6} \exp\left(\eta\right)\alpha_{MG,eff}^{2-\eta/6}\right], \tag{11}$$

where $\tau^2 = 1$, $v = 1 - f + (f/6)\ln f$.

Earlier, to take into account the curvature of dependences when plotting in the FN plot coordinates, it was proposed to use correction factors $r_t$ and $s_t$ ("RS" method) at point $t$, as shown in [9]:

$$\alpha_{eff} = -s_t b\varphi^{3/2} / S^{fit}, \tag{12}$$

$$A_{eff} = R^{fit} / \left[a\varphi^{-1}\alpha^2 r_t\right]. \tag{13}$$

However, this method turned out to be very cumbersome for processing experimental data.

Of all the methods, the MG plot method seems to be the most productive since it rectifies the theoretical dependence.

### Functional dependence of the emission area

Real field emitters have a curved surface. There are a number of models that are used to describe the most commonly used field emitters. These models include the semi-ellipsoid model for describing metal emitters (tungsten, molybdenum tips), the hemisphere on a cone for some spiked silicon structures, and the hemisphere on the cylinder model (HCP), which most closely resembles carbon nanotubes in shape.

The question arises about the correctness of the description of emitters having the above shapes, using the effective values of the area and FEF. These effective values turn out to be very strongly dependent on the increase in the applied voltage.

The idea is, as before, to use the basic formula for the field emission for the field at a selected point on the surface (at the apex of the tip), and for the notional emission area to set a functional dependence on the value of the field at this point.

Thus, the curved surface of the emitter is replaced by a flat disk lying on the apex of the tip, the area of which increases according to a certain law with an increase in the applied voltage.

In a number of theoretical works, such functional dependences were obtained, for example, for a hemisphere on a plane [10], a paraboloid [11], a semiellipsoid [12, 13]. However, for processing the IVC in semilogarithmic coordinates, the proposed analytical formulas are practically not applicable.

In the refs [14, 15] studies of the power-law dependence of the pre-exponential voltage factor for emitters of various shapes were carried out. In the work [14], three-dimensional modeling of electrostatic fields was carried out and the model I–V characteristics of emitters of various shapes were obtained. This made it possible to determine the characteristic shifts in the degree of pre-exponential filed factor. Characteristic and stable shift values $k_A$ were found, depending on the shape of the emitter tip. For example, for nanotubes, the shift values are, depending on the IVC processing method, in the range $k_A = 0.5–0.7$. In [15], a hypothesis was put forward about the direct proportionality of the notional emission area to the voltage in the corresponding degree $A_n \sim U_k$.

Based on 3D modeling of electrostatic fields for the tip in the form of HCP, we obtained the dependence $A_n = I/J_k$ for given values of the field at the apex of the tip $f_a = F/F_R$. Next, we used the expression for the dimensionless notional area $g_n$ for a hemisphere with radius $r_a$: $g_n = A_n / [2\pi r_a^2]$. The dependence of $g_n$ on $f_a$ was plotted in an extended range of fa values from 0.1 to 1. Plot (A) in Fig. 1, a shows the calculated dependence of the notional area $A_n = [2\pi r_a^2]\, g_n$.

To determine the power dependence, a solution was sought in the form of a simple approximation formula of the form $y = cx^d$. As a result of the approximation, the value $b = 0.62$ was obtained. According to the normalization conditions, the maximum value $g_n = cf_a^{0.62}$ will take at $f_a = 1$, hence $c = g_{n,\max}(1) = 0.552$. The power dependence of the notional emission area on the dimensionless field at the apex of the tip will take the form (B) in Fig.1, *a*.

As a result, simple dependences of the notional area on the applied voltage were obtained, allowing the processing of the I–V characteristics in semi-logarithmic coordinates (Fig. 1, *b*):

$$A_n = \left[2\pi r_a^2\right] g_n(1) f_a^{k_A} = A_{n,max} f_a^{k_A}, \tag{14}$$

$$I = [2\pi r_a^2 g_n(1)](\alpha U)^{k_A} / F_R^{k_A}]\, a\varphi^{-1}(\alpha U)^{2-\eta/6} F_R^{\eta/6} \exp(\eta) \exp\left(-b\varphi^{3/2} / (\alpha U)\right), \tag{15}$$

$$I = [A_{n,\max}]\alpha^{2-\eta/6+k_A} a\varphi^{-1} F_R^{\eta/6-k_A} \exp(\eta) U^{2-\eta/6+k_A} \exp\left(-b\varphi^{3/2} / (\alpha U)\right), \tag{16}$$

$$\ln\left(I / U^{2-\eta/6+k_A}\right) = \ln\left(R^{kpower,Fit}\right) + S^{kpower,Fit}(1/U), \tag{17}$$

$$\alpha = -b\varphi^{3/2} / S^{kpower,Fit}, \tag{18}$$

$$A_c = a\varphi^{-1} F_R^{\eta/6-k_A} \exp(\eta), \tag{19}$$

$$R^{kpower,Fit} = A_{n,max} A_c \alpha^{2-\eta/6+k_A} = A_{n,max} A_c \alpha^{k_t}, \tag{20}$$

$$A_{n,max} = R^{kpower,Fit} / \left(A_c \alpha^{k_t}\right), \tag{21}$$

$$r_a = \sqrt{R^{kpower,Fit} / [2\pi g_n(1) A_c \alpha^{k_t}]}. \tag{22}$$

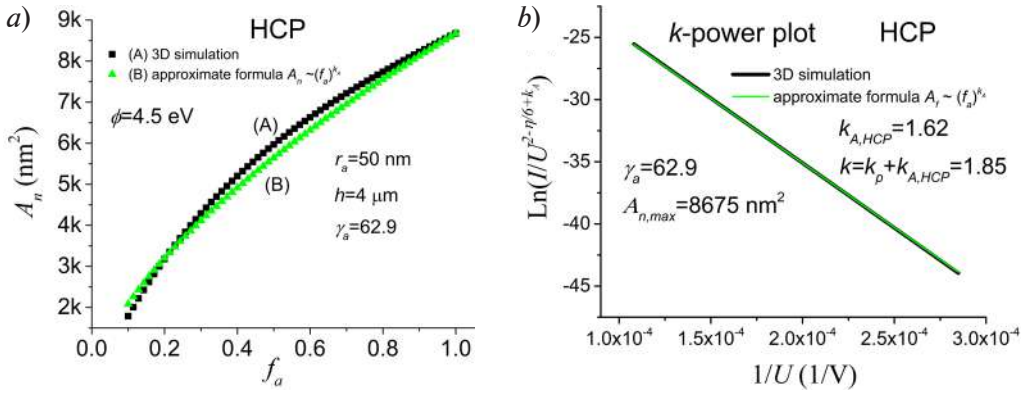


Fig.1. Functional dependences of the notional area on the field: calculated and approximate dependences (*a*), determination of the main emission parameters in k-power plot coordinates (*b*)

## Conclusion

A functional dependence of the notional emission area on the field is obtained. Analysis of the I-V characteristics in semi-logarithmic coordinates $\ln(I/U^k)$ vs $1/U$, called "k-power plot", allows you to linearize the dependence and obtain FEF that is independent of the voltage range. The second parameter, intercept $R^{fit}$, makes it possible to determine the maximum emission area under the condition of the field of complete removal of the barrier. Which, in turn, allows you to determine the radius of the emitter rounding.

## REFERENCES

1. **Eletskii A.V.,** Carbon nanotube-based electron field emitters, Physics-Uspekhi, 53 (9) (2010) 863–892.

2. **Obraztsov A.N., Pavlovsky I.Y., Volkov A.P.,** Low-voltage electron emission from chemical vapor deposition graphite films, Journal of Vacuum Science & Technology B, 17 (2) (1999) 674–678.

3. **Bonard J.M., Dean K.A., Coll B.F., Klinke C.,** Field emission of individual carbon nanotubes in the scanning electron microscope, Physical review letters, 89 (19) (2002) 197602-1–4.

4. **Forbes R.G.,** The Murphy–Good plot: a better method of analysing field emission data, Royal Society open science, 6 (12) (2019) 190912-1–13.

5. **Allaham M.M., Forbes R.G., Knápek A., Sobola D., Burda D., Sedlák P., Mousa M.S.,** Interpretation of field emission current–voltage data: Background theory and detailed simulation testing of a user-friendly webtool, Materials Today Communications, 31 (2022) 103654-1–16.

6. **Forbes R.G., Deane J.H.,** Comparison of approximations for the principal Schottky–Nordheim barrier function $v(f)$, and comments on Fowler–Nordheim plots. Journal of Vacuum Science & Technology B, 28 (2) (2010) C2A33–C2A42.

7. **Popov E.O., Filippov S.V., Kolosko A.G., Knápek A.,** Comparison of the effective parameters of single-tip tungsten emitter using Fowler–Nordheim and Murphy–Good plots, Journal of Vacuum Science & Technology B, 40 (2) (2022) 024201-1–8.

8. **Elinson M.I.,** Cold Cathodes, Sovetskoe Radio, Moscow, 1974.

9. **Forbes R.G., Deane J.H.,** Refinement of the extraction-parameter approach for deriving formal emission area from a FN plot, 30th International Vacuum Nanoelectronics Conference, Regensburg, IEEE (2017) 234–235.

10. **Jensen K.L.,** Introduction to the Physics of Electron Emission, Wiley, Chichester, 2017.

11. **Biswas D.,** Field emission from parabolic tips: Current distributions, the net current, and effective emission area, Physics of Plasmas, 25 (4) (2018) 043105-1–7.

12. **Jensen K.L.,** Field Emission - Fundamental Theory to Usage, Wiley Encyclopedia of Electrical and Electronics Engineering, (2014) 1–29.

13. **Biswas D.,** Interpreting the field emission equation for large area field emitters. Journal of Vacuum Science & Technology B, 40 (2) (2022) 023201-1–6.

14. **Filippov S.V., Kolosko A.G., Popov E.O., Forbes R.G.,** Behavior of notional cap-area efficiency

(g n) for hemisphere-on-plane and related field emitters, 34th International Vacuum Nanoelectronics Conference, Leon, IEEE (2021) 1–2.

15. **Forbes R.G., Popov E.O., Kolosko A.G., Filippov S.V.,** The pre-exponential voltage-exponent as a sensitive test parameter for field emission theories. Royal Society open science, 8 (3), (2021), 201986-1–19.

## THE AUTHORS

**FILIPPOV Sergey V.**
s.filippov@mail.ioffe.ru
ORCID: 0000-0001-5325-2226

**KOLOSKO Anatoly G.**
agkolosko@mail.ru
ORCID: 0000-0002-6073-6808

**POPOV Eugeni O.**
e.popov@mail.ioffe.ru
ORCID: 0000-0003-2226-6304

*Received 27.10.2022. Approved after reviewing 21.11.2022. Accepted 23.11.2022.*

© Peter the Great St. Petersburg Polytechnic University, 2023

Conference materials
UDC 53.043
DOI: https://doi.org/10.18721/JPM.161.210

# Mechanisms leading to thermal quantum efficiency droop in green InGaN/GaN LEDs

E.I. Shabunina [1]✉, A.E. Ivanov [1,3], N.A. Talnishnikh [2], A.P. Kartashova [1],
D.S. Poloskin [1], N.M. Shmidt [1], A.L. Zakgeim [2], A.E. Chernyakov [2],

[1] Ioffe Institute RAS, St. Petersburg, Russia;
[2] Submicron Heterostructures for Microelectronics Research and Engineering Center RAS, St. Petersburg, Russia;
[3] Saint Petersburg Electrotechnical University "LETI", St. Petersburg, Russia
✉ jenni-85@mail.ru

**Abstract.** The contribution of several mechanisms into the external quantum efficiency (EQE) droop in green InGaN/GaN LEDs over a temperature increase from 300 to 400 K is clarified. One of them is the ionization of atoms localized at disordered hetero-interfaces in InGaN/GaN MQWs situated at the depletion region around a p-n junction at $j < 10$ A/cm$^2$ and $U < U_{tr}$ (turn on voltage). The ionized atoms capture tunneling charge carriers, which leads to EQE decrease. Another mechanism is the capture of charge carriers tunneling in 3D spaces of MQWs situated outside of a depletion region at $U > U_{tr}$ and 10 A/cm$^2$ < $j$ < 30 A/cm$^2$. Growing thermalized carriers concentration reduces the band fluctuation potential which results in vertical diffusion transport of carriers and crowding effect.

**Keywords:** InGaN/GaN, LEDs, external quantum efficiency

**Citation:** Shabunina E.I., Ivanov A.E., Talnishnikh N.A., Kartashova A.P., Poloskin D.S., Shmidt N.M., Zakgeim A.L., Chernyakov A.E., Mechanisms leading to thermal quantum efficiency droop in green InGaN/GaN LEDs, St. Petersburg State Polytechnical University Journal. Physics and Mathematics. 16 (1.2) (2023) 70–76. DOI: https://doi.org/10.18721/JPM.161.210

This is an open access article under the CC BY-NC 4.0 license (https://creativecommons.org/licenses/by-nc/4.0/)

Материалы конференции
УДК 53.043
DOI: https://doi.org/10.18721/JPM.161.210

# Механизмы, приводящие к температурному падению квантовой эффективности в зеленых InGaN/GaN светодиодах

Е.И. Шабунина [1]✉, А.Е. Иванов [1,3], Н.А. Тальнишних [2], А.П. Карташова [1],
Д.С. Полоскин [1], Н.М. Шмидт [1], А.Л. Закгейм [2], А.Е. Черняков [2]

[1] Физико-технический институт им. А.Ф. Иоффе РАН, Санкт-Петербург, Россия;
[2] Научно-технологический центр микроэлектроники и субмикронных гетероструктур РАН, Санкт-Петербург, Россия;
[3] Санкт-Петербургский государственный электротехнический университет «ЛЭТИ», Санкт-Петербург, Россия
✉ jenni-85@mail.ru

**Аннотация.** Выяснен вклад нескольких механизмов в падение квантовой эффективности зеленых InGaN/GaN светодиодов по мере роста температуры в диапазоне 300–400 K. Один из них – ионизация атомов, локализованных на разупорядоченных гетерограницах в InGaN/GaN квантовых ямах, расположенных вне области объемного заряда (ООЗ) при $j < 10$ А/см$^2$ and $U < U_{tr}$ (напряжение открытия p-n перехода). Ионизованные атомы захватывают туннелирующих носителей заряда, что приводит к снижению квантовой

© Shabunina E.I., Ivanov A.E., Talnishnikh N.A., Kartashova A.P., Poloskin D.S., Shmidt N.M., Zakgeim A.L., Chernyakov A.E., 2023. Published by Peter the Great St. Petersburg Polytechnic University.

эффективности. Другой механизм связан с захватом носителей заряда, туннелирующих в трехмерных неоднородностях квантовых ям, расположенных вне ООЗ при $U > U_{tr}$ and 10 А/см$^2$ < $j$ < 30 А/см$^2$. Растущая концентрация термолизованных носителей снижает величину зонного флуктуационного потенциала, что приводит к вертикальному диффузионному транспорту носителей и эффекту шнурования.

**Ключевые слова:** InGaN/GaN, светодиоды, внешняя квантовая эффективность

**Ссылка при цитировании:** Шабунина Е.И., Иванов А.Е., Тальнишних Н.А., Карташова А.П., Полоскин Д.С., Шмидт Н.М., Закгейм А.Л., Черняков А.Е. Механизмы, приводящие к температурному падению квантовой эффективности в зеленых InGaN/GaN светодиодах // Научно-технические ведомости СПбГПУ. Физико-математические науки. 2023. Т. 16. № 1.2. С. 70–76. DOI: https://doi.org/10.18721/JPM.161.210

Статья открытого доступа, распространяемая по лицензии CC BY-NC 4.0 (https://creativecommons.org/licenses/by-nc/4.0/)

## Introduction

The thermal droop of external quantum efficiency (EQE) in power InGaN/GaN LEDs, i.e. an EQE decrease over a temperature growth in a wide range (15–450 K), has been studied for many years. However, it is still a subject of many discussions [1, 2]. This effect limits LED usage at high temperatures. It reduces the efficiency of solid-state lighting. Its impact on green LEDs is more severe than in blue ones. Several mechanisms have been proposed to explain the phenomenon [1, 2]. They include Auger recombination, trap-assisted Auger recombination, Shockley-Read-Hall non-radiative recombination, polarization effects, fluctuations of alloy and quantum well (QW) width, and carrier delocalization. However, there is no clear interpretation of thermal EQE droop in green InGaN/GaN LEDs at $j$ < 30 A/cm$^2$ in a practically important temperature range 300–400 K.

It is possible that an approach commonly used to describe wide QWs with homogeneously distributed non-radiative centers might be the issue. An approach based on atomic [3] and localization landscape [4] models seems to give a new perspective to the understanding of thermal EQE droop in green LEDs. These models take into account quantum-mechanical tunneling of charge carriers in non-uniform nanomaterials, fluctuations in the thickness of wells in vertical and lateral directions [5], and indium atoms penetrating in GaN barriers [6] related to random In fluctuations [1, 3]. These phenomena lead to a percolative transport through paths of minimal energy in the two-dimensional (2D) landscape of disordered energies in multiple 2D quantum wells. Such an approach is in good agreement with peculiarities of reverse and forward $I$-$U$ characteristics and optical properties of LEDs based on nitrides.

In this work, we show an experimental study of the mechanisms related to disordered hetero-interfaces in QWs and band fluctuation potential (BFP) leading to thermal EQE droop in green LEDs at $j$ < 30 A/cm$^2$ in the 300–400 K temperature range in accordance to the approach suggested in [3–5].

## Materials and Methods

We studied commercially-available green LEDs based on InGaN/GaN MQW nanostructures with EQE (η) in the range of 35–37% at 530–535 nm. The LEDs under the study had active area of 1 mm2. We investigated $I$-$U$ characteristics, electroluminescence spectra (EL), EQE at direct current (dc) and in pulse mode (pm) (100 ns pulse at 50 Hz) at 50–400 K, distribution of peak EQE values over wavelengths at each value of voltage (U) and current (I), full width at half maximum (FWHM) of EL spectra versus current, low-frequency noise versus frequency and current. $I$-$U$ characteristics were measured by KEITHLEY 6487 power source. Low-frequency noise was measured in the range of 1 Hz–50 kHz. For noise measurements, the studied samples were connected in series with a low-noise load resistor RL whose resistance varied from 100 Ω to 13 kΩ depending on the current through the chip. The voltage fluctuations SU at the resistors RL were amplified by a low-noise preamplifier SR560 (Stanford Research Systems, USA) and subsequently measured by SR770 FET NETWORK Analyzer (Stanford Research

© Шабунина Е.И., Иванов А.Е., Тальнишних Н.А., Карташова А.П., Полоскин Д.С., Шмидт Н.М., Закгейм А.Л., Черняков А.Е., 2023. Издатель: Санкт-Петербургский политехнический университет Петра Великого.

Systems, USA). The background noise of the preamplifier does not exceed 4 nV/√Hz at 1 kHz, which is approximately equivalent to Johnson–Nyquist noise of 1000 Ω resistance. The pulse mode during measurements was provided by an Agillent 8114A generator with PicoLAS LDPV 80-100 V3.3 amplifier. Optical power and emission spectra were recorded using the OL 770-LED Highspeed LED Test and Measurement System in cryostat "CCS-450 Standard Optical Closed-cycle Refrigerator Systems".

## Results and Discussion

The EQE dependences in green InGaN/GaN LEDs as a function of injection current at various temperatures are shown in Fig. 1, *a*. It correlates with the results published in [7, 8]. It is known that maximum EQE at low current densities ~ 1–20 A/cm$^2$ in nitride-based LEDs is determined by the radiative recombination of charge carriers tunneling through QWs [9] located in the space charge region (SCR) around a p-n junction. The EQE droop is observed at a fairly low current corresponding to $j < 1$ A/cm$^2$ where the influence of self-heating effect is negligible. As the temperature increases, EQE values fall gradually. At the same time, the peak-efficiency current is temperature insensitive. The quantum efficiency degradation over increasing temperature is observed in two regions of current: at $j < 10$ A/cm$^2$ when $U < U_{tr}$ and at 10 A/cm$^2$ $< j <$ 30 A/cm$^2$ when $U > U_{tr}$. $U_{tr}$ in green LEDs at 300 K, 350 K, and 420 K is derived from forward *I-U* characteristics shown on the insert to Fig. 1, *b*. Its values are 2.87, 2.82, and 2.68 V, correspondingly. At the same time, $U_{tr}$ significantly exceeds the voltages corresponding to the radiation wavelength ($U_r$) at all temperatures. $U_r$ values for 300, 350, and 420 K are 2.302, 2.298, and 2.284 V, respectively. Such a difference between $U_{tr}$ and $U_r$ is typical for green LEDs. According to [10], it might be caused by non-adiabatic carrier injection when part of the carrier energy is spent on phonon emission (a voltage drop across a series resistance of less than 0.5 Ω does not make a significant contribution to $U_{tr}$).

Figure 1, *a* shows that the shapes of EQE($j$) on the left and right from the current value ~ 10 A/cm$^2$, corresponding to $U_{tr}$, differ noticeably. On the left, we can see a slight EQE reduction, while there is a remarkable EQE droop over a current growth on the right. This hints on the different nature behind these phenomena. The mechanisms of radiative and non-radiative recombination at $j < 10$ A/cm$^2$ occur in QWs in SCR. However, at when the p-n junction opens at $j > 10$ A/cm$^2$, these mechanisms take place in QWs situated outside of SCR as well as at a defect system across the entire active area of LED. The contribution of thermal carries in these current ranges is also different. These phenomena are going to be discussed further below.

Figure 1, *b* shows *I-U* characteristics of the green LEDs at 300–420 K. Reverse and low forward currents clearly show a steady growth as a function of temperature that is caused by the activation of a new defect-related tunneling component. The ideality factor ($n$) of LEDs is $n > 2$ in the same temperature range, which is in agreement with the enhanced leakage current. According to [11], $n > 2$ does not originate from the homogeneous distribution of defects. It is related to inhomogeneously distributed local areas of high defect density, shunting of p-n junction, and presence of charged centres at a depletion region around the p-n junction. The presence of these centres in the space-charge region around p-n junction in green LEDs was detected by DLTS [12]. Thus, we may assume that non-radiative loss at $U < U_{tr}$ is associated with these localized centres. This conclusion is supported by the study of low-frequency noise (Fig. 2, *a*).

Figure 2, *a* shows the noise spectra in green LEDs at 300 K in the current range $4 \cdot 10^{-6}$–$10^{-3}$ A. The similar shape of noise spectra in green LEDs at 300 K shows that the properties of noise source do not change over a current growth at $U < U_{tr}$. The study shows that noise spectra lacks of region that does not depend on frequency at $f > 100$ Hz (the generation-recombination noise) identifying that Shockley-Rea-Hall (SRH) centres uniformly distributed across the active area are not the predominant source of noise in this current range. Therefore, it is unlikely that uniformly distributed SRH centres cause non-radiative losses at $U < U_{tr}$. The 1/*f*-like spectrum might be due the system of defects related to grain boundaries, dislocations piercing the p-n junction, and disordered hetero-interfaces in QWs. It was shown earlier that an increase in surface disorder of LED structures results in a growth in tunneling current as well as ideality factor of *I-U* characteristics, and an EQE decrease [13].

A temperature growth from 300 to 420 K is accompanied by an increase in tunneling current (Fig. 1, *b*). The shape of forward *I-U* characteristics at 300 and 420 K correlates with the one

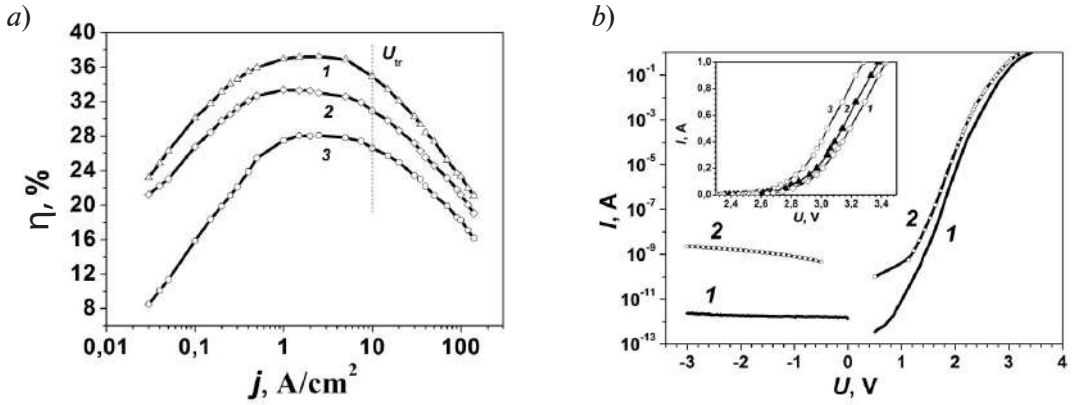


Fig. 1. External quantum efficiency versus current density in green LEDs at various temperatures: 300 (1), 350 (2), 420 (3) K (*a*). Temperature-dependent *I-U* characteristics of green LEDs at various temperatures: 300 (1), 420 (2) K (*b*). On the insert: *I-U* characteristics in a linear scale in the same green LEDs as in Fig. 1, *a* at various temperatures: 300 (1), 350 (2), 420 (3) K

described in the framework of the semi-classical trap assisted multiphonon tunneling (multiphonon TAT) model [14]. Thus, we may suggest that an increase in charge centres concentration through ionization of atoms localized at disordered hetero-interfaces at QWs in the depletion region around the p-n junction. This assumption correlated with a growth in FWHM of EL spectra from 26 to 32 nm at 300–400 K. The ionized centres whose energy is around 50–60 meV in green LEDs were observed by DLTS [15]. The influence of thermalized carriers on the EQE droop continues at current density 10 A/cm$^2$ < $j$ < 30 A/cm$^2$ when $U > U_{tr}$. Peculiarities of peak EQE value distribution over wavelengths at $10^{-2} < j < 100$ A/cm$^2$ as well as the data on $U_{tr}$ provides the information on the mechanisms in MQWs. The vertical arrows indicate wavelengths corresponding to $U_{tr}$.

The sections of the dependences to the right of the arrows (Fig. 2, *b*), corresponding to $U < U_{tr}$, demonstrate a growth in EQE at fixed wavelengths at $j \sim 2$ A/cm$^2$ and, as shown in [16], depict the mechanism of radiative recombination localized at QWs with a well-ordered hetero-junction. Let us consider the distribution features for green LED at 300 K (Fig. 2, *b*, curve 1).

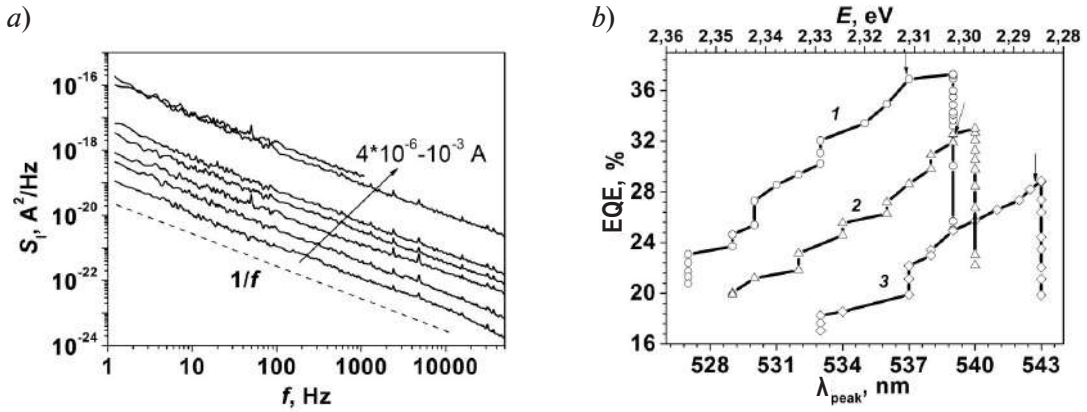


Fig. 2. Low-frequency noise spectra in green LED at 300 K in the current range $4 \cdot 10^{-6}$–$10^{-3}$ A (*a*) and peak EQE distribution on wavelength at various temperatures: 300 (1), 350 (2), 420 (3) K (*b*)

The horizontal section shows regions of disordered alloy ~ 2 nm in QWs or micro-QWs, leading to the loss of carriers because EQE does not increase despite the growth in the tunnel current by several times in this section. When the p-n junction opens at $U > U_{tr}$, lateral random alloy fluctuations get filled by carriers. The mechanism becomes non-equilibrium because it is accompanied by EL spectra broadening from 26 to 38 nm. It appears that the observed pattern of distribution reflects this process. Moreover, the region of significant changes in EQE and wavelengths (from 537 to 528 nm) corresponds to the energy of 40 meV. This value correlates

with the BFP value (40–50 meV for InGaN with 10–30% of In) predicted by the landscape model [4]. Lateral quantum tunneling occurs in the BFP field. The mechanism is typical for non-uniform nano-materials [4]. Moreover, we may assume that each quantum well in the lateral direction consists of tunnel connected nano- and micro-QWs due to fluctuations in the InGaN alloy. The tunneling (migration) of injected carriers along InGaN layers in the field of BFP is accompanied by the gradual filling of nano- and micro-QWs by carriers. The filling starts at the regions of large In content and is followed by non-radiative losses at disordered hetero-interfaces and local regions of disordered alloy. This leads to the EQE droop at 10 A/cm$^2$ < $j$ < 30 A/cm$^2$. An increase in the concentration of thermalized carriers and a decrease in Utr result in the smoothing of BFP and its decrease to 25 meV as well as the onset of an earlier transition from the tunneling carrier transport to predominantly vertical diffusion. At current densities above 30 A/cm$^2$, the concentration of injected carriers is higher than the concentration of thermally induced ones at 420 K. The thermal droop is absent. The change in the carrier transport mechanism leads to the development of the crowding effect [17] and non-radiative recombination related to extended defects [18]. It should be noted that along with main mechanisms leading to the thermal droop in green LEDs an EQE reduction is more prominent than in blue LEDs due to poorer quality of hetero-interface and higher BFP [19]. Lateral BFP for green LEDs with 38% and 30% EQE are 34 meV and 38 meV, respectively. For blue LEDs, BFP is 24 meV.

## Conclusion

The relative contribution of several mechanisms into thermal EQE droop in green InGaN/GaN LEDs occurs in different areas of LEDs at various current densities and voltages applied to the p-n junction. The significant thermal EQE droop is observed at $j$ < 10 A/cm$^2$ in InGaN/GaN MQWs situated in the depletion region around the p-n junction at $U < U_{tr}$. It is caused by an increase in tunneling current involving the trap assisted multiphonon tunneling mechanism and possible carrier losses due to the non radiative multiphonon scattering, as well as carrier capture by ionized atoms localized at disordered hetero-interfaces of InGaN/GaN MQWs. To a lesser extent, a temperature growth has an influence on a EQE decrease in InGaN/GaN MQWs situated outside of the depletion region around the p-n junction at 10 A/cm2 < $j$ < 30 A/cm$^2$ when $U > U_{tr}$. Non-radiative losses are related to charge carriers tunneling in the field of lateral band fluctuation potential and the capture of carriers at disordered hetero-interfaces. An increase in the concentration of thermally treated carriers and a decrease in $U_{tr}$ lead to a smoothing of the band fluctuation potential with an increase in temperature. As a result, there is a transition from tunnel transport of carriers to diffusion. At current densities above 30 A/cm$^2$, the concentration of injected carriers is higher than the concentration of thermally induced ones at 420 K and thermal droop is absent. The change in the mechanism of carrier transport leads to the development of the crowding effect and non-radiative recombination at extended defects. The mechanism of loss associated with the non-radiative multiphonon scattering as well as its contribution to the thermal EQE droop needs to be studied in more detail.

## REFERENCES

1. **Meneghini M., De Santi C., Tibaldi A., Vallone M., Bertazzi F., Meneghesso G., Zanoni E., Goano M.,** Thermal droop in III-nitride based light-emitting diodes: Physical origin and perspectives, Journal of Applied Physics. 127 (2020) 211102.

2. **De Santi C., Meneghini M., La Grassa M., Galler B., Zeisel R., Goano M., Dominici S., Mandurrino M., Bertazzi F., Robidas D., Meneghesso G., Zanoni E.,** Role of defects in the thermal droop of InGaN based light emitting diodes, Journal of Applied Physics. 119 (2016) 094501.

3. **Schulz S., Caro M.A., Coughlan C., O'Reilly E.P.,** Atomistic analysis of the impact of alloy and well-width fluctuations on the electronic and optical properties of InGaN/GaN quantum wells, Physical Review. B 91 (2015) 035439.

4. **Li Ch-K., Piccardo M., Lu L-Sh., Mayboroda S., Martinelli L., Peretti J., Speck J.S., Weisbuch C., Filoche M., Wu Yu-R.,** Localization landscape theory of disorder in semiconductors. III. Application to carrier transport and recombination in light emitting diodes, Physical Review B. 95 (2017) 144206.

5. **Filoch M., Piccardo M., Wu Yu-R., Li Ch-K., Weisbuch C., Mayboroda S.,** Localization landscape theory of disorder in semiconductors. I. Theory and modeling, Physical Review B. 95 (2017) 144204.

6. **Butte R., Lahourcade L., Uždavinys T.K., Callsen G., Mensi M., Glauser M., Rossbach G., Martin D., Carlin J-F., Marcinkevičius S., Grandjean N.,** Optical absorption edge broadening in thick InGaN layers: Random alloy atomic disorder and growth mode induced fluctuations, Applied Physics Letters. 113 (2018) 032106.

7. **Auf der Maur M., Pecchia A., Penazzi G., Rodrigues W., Di Carlo A.,** Efficiency Drop in Green InGaN/GaN Light Emitting Diodes: The Role of Random Alloy Fluctuations, Physical review letters. 116 (2016) 027401.

8. **Rong J., Lu H., Chen D-J., Ren F-F., Yan D-W., Zhang R., Zheng Y-D.,** Temperature-dependent efficiency droop behaviors of GaN-based green light-emitting diodes, Chinese Physics B. 22 (2013) 047805.

9. **Bochkareva N.I., Rebane Y.T., Shreter Y.G., E**fficiency droop and incomplete carrier localization in InGaN/GaN quantum well light-emitting diodes, Applied Physics Letters. 103 (2013) 191101.

10. **Shubert E.F.,** Light Emitting Diodes, UK: Cambridge University Press, Cambridge, 2004.

11. **Steingrube S., Breitenstein O., Ramspeck K., Glunz S., Schenk A., Altermatt P.P.,** Explanation of commonly observed shunt currents in c-Si solar cells by means of recombination statistics beyond the Shockley-Read-Hall approximation, Journal of Applied Physics. 110 (2011) 014515.

12. **Bagutdinov M.L., Yunovich A.E.,** Emission spectra of InGaN/AlGaN/GaN quantum well heterostructures: Model of the two-dimensional joint density of states, Semiconductors. 42 (2008) 429–438.

13. **Petrov V.N., Sidorov V.G., Talnishnikh N.A., Chernyakov A.E., Shabunina E.I., Shmidt N.M., Usikov A.S., Helava H., Makarov Yu.N.,** On the fractal nature of light-emitting structures based on III−N nanomaterials and related phenomena, Semiconductors. 50 (2016) 1173–1179.

14. **Mandurrino M., Goano M., Vallone M., Bertazzi F., Ghione G., Verzellesi G., Meneghini M., Meneghesso G., Zanoni E.,** Semiclassical simulation of trap-assisted tunneling in GaN-based light-emitting diodes, Journal of Computational Electronics. 14 (2015) 444–455.

15. **Polyakov A.Y., Shmidt N.M., Smirnov N.B., Shchemerov I.V., Shabunina E.I., Tal'nishnih N.A., Lagov P.B., Pavlov Yu.S., Alexanyan L.A., Pearton S.J.,** Defect States Induced in GaN-Based Green Light Emitting Diodes by Electron Irradiation, ECS Journal of Solid State Science and Technology. 7 (2018) 323–328.

16. **Talnishnikh N.A., Shabunina E.I., Shmidt N.M., Ivanov A.E.,** Several processes participating in a decrease and the droop of external quantum efficiency in green InGaN/GaN MQW structures, Journal of Physics: Conference Series. 2086 (2021) 012104.

17. **Zakgeim A.L., Ivanov A.E., Chernyakov A.E.,** Features of Operation of High-Power AlInGaN LEDs at High Pulse Currents, Technical Physics Letters. 47 (2021) 834–837.

18. **Aleksiejūnas R., Nomeika K., Miasojedovas S., Nargelas S., Malinauskas T., Jarašiūnas K., Tuna Ö., Heuken M.,** Carrier dynamics in blue and green emitting InGaN MQWs, Physica Status Solidi (B). 252 (2015) 977−982.

19. **Shabunina E.I., Chernyakov A.E., Ivanov A.E., Kartashova A.P., Talnishnikh N.A., Shmidt N.M., Zakgeim A.L.,** Thermal quantum efficiency droop in blue InGaN/GaN LEDs, Journal of Physics: Conference Series. 1697 (2020) 012173.

## THE AUTHORS

**SHABUNINA Evgeniia I.**
jenni-85@mail.ru
ORCID: 0000-0003-4457-8149

**KARTASHOVA Anna P.**
anna_kartashova@mail.ru
ORCID: 0000-0001-5535-0858

**IVANOV Anton E.**
a-e-ivano-v@yandex.ru
ORCID: 0000-0003-2819-1534

**POLOSKIN Dmitry S.**
Dmitrii.Poloskin@mail.ioffe.ru
ORCID: 0000-0002-1576-2572

**TALNISHNIKH Nadezhda A.**
nadya.fel@mail.ru
ORCID: 0000-0003-1127-0973

**SHMIDT Natalia M.**
natalia.shmidt@mail.ioffe.ru
ORCID: 0000-0003-3585-5116

**ZAKGEIM Alexander L.**
zakgeim@mail.ioffe.ru
ORCID: 0000-0002-1887-2064

**CHERNYAKOV Anton E.**
chernyakov.anton@yandex.ru
ORCID: 0000-0002-8153-9512

*Received 27.10.2022. Approved after reviewing 08.11.2022. Accepted 09.11.2022.*

© Peter the Great St. Petersburg Polytechnic University, 2023

Conference materials
UDC 620.3, 620.9, 539.23, 621.315.592
DOI: https://doi.org/10.18721/JPM.161.211

# Dominant recombination in a GaAs solar cell through a compressed GaAs/$In_{0.4}Ga_{0.6}As$/GaAs quantum well

M.A. Mintairov [1]✉, V.V. Evstropov [1], S.A. Mintairov [1],
M.Z. Shvarts [1], N.A. Kalyuzhnyy [1]

[1] Ioffe Institute, St. Petersburg, Russia
✉ mamint@mail.ioffe.ru

**Abstract.** The paper is devoted to the study of the reasons for the increase in the saturation current of a p-n junction when quantum objects (quantum dots, wells, and others) are introduced into it. An assumption has been made and verified that quantum objects create additional recombination centers in the matrix material of *p*—*n* junction. For this case, a model is presented that describes the behavior of the electroluminescence quantum yield. It is shown that the model is applicable to the description of the experimental temperature dependence of electroluminescence intensity when constant current passing through a *p*—*n* junction with quantum objects. The experiment was carried out for GaAs solar cells with different numbers (1, 5, 10) of $Ga_{0.6}In_{0.4}As$ compressed well-like (hybrid) quantum objects. The fundamental parameters of the studied quantum objects are determined. In was shown that the assumption about additional recombination centers can be one of the explanations for the experimentally observed increase in the saturation current of the p-n junction with quantum objects

**Keywords:** solar cells, quantum wells, saturation current

**Citation:** Mintairov M.M., Evstropov V.V., Mintairov S.A., Shvarts M.Z., Kalyuzhnyy N.A., Dominant recombination in a GaAs solar cell through a compressed GaAs/$In_{0.4}Ga_{0.6}As$/GaAs quantum well, St. Petersburg State Polytechnical University Journal. Physics and Mathematics. 16 (1.2) (2023) 77—82. DOI: https://doi.org/10.18721/JPM.161.211

This is an open access article under the CC BY-NC 4.0 license (https://creativecommons.org/licenses/by-nc/4.0/)

Материалы конференции
УДК 620.3, 620.9, 539.23, 621.315.592
DOI: https://doi.org/10.18721/JPM.161.211

# Доминирующая рекомбинация в арсенид-галлиевом солнечном элементе через сжатую квантовую яму GaAs/$In_{0.4}Ga_{0.6}As$/GaAs

М.А. Минтаиров [1]✉, В.В. Евстропов [1], С.А. Минтаиров [1],
М.З. Шварц [1], Н.А. Калюжный [1]

[1] Физико-технический институт им. А.Ф. Иоффе РАН, Санкт-Петербург, Россия
✉ mamint@mail.ioffe.ru

**Аннотация.** Статья посвящена изучению причин увеличения тока насыщения *p*—*n* перехода с включенными в него квантовыми объектами (квантовыми ямами и др.). Сделано и проверено предположение о том, что квантовые объекты создают дополнительные рекомбинационные центры в матричном материале *p*—*n* перехода. Для этого представлена модель, объясняющая поведение квантового выхода электролюминесценции. Показано, что модель применима для описания экспериментальной зависимости интенсивности электролюминесценции от температуры при условиях постоянного тока, пропускаемого через *p*—*n* переход с квантовыми объектами. Эксперимент был проведен для GaAs солнечных элементов с различным количеством квантовых объектов (1, 5, 10). В качестве квантовых объектов были использованы сжатые GaAs/$In_{0.6}Ga_{0.4}As$/GaAs квантовые ямы, являющиеся гибридными, ямо-подобными квантовыми объектами. Фундаментальные

© Mintairov M.M., Evstropov V.V., Mintairov S.A., Shvarts M.Z., Kalyuzhnyy N.A., 2023. Published by Peter the Great St. Petersburg Polytechnic University.

параметры исследуемых образцов были определены. Было показано, что предположение о наличии дополнительных рекомбинационных центров может являться одним из объяснений увеличения тока насыщения *p*–*n* переходов с квантовыми объектами.

**Ключевые слова:** солнечные элементы, квантовые ямы, электролюминисценция

**Ссылка при цитировании:** Минтаиров М.А., Евстропов В.В., Минтаиров С.А., Шварц М.З., Калюжный Н.А. Доминирующая рекомбинация в арсенид-галлиевом солнечном элементе через сжатую квантовую яму GaAs/$In_{0.4}Ga_{0.6}As$/GaAs // Научно-технические ведомости СПбГПУ. Физико-математические науки. 2023. Т. 16. № 1.2. С. 77–82. DOI: https://doi.org/10.18721/JPM.161.211

Статья открытого доступа, распространяемая по лицензии CC BY-NC 4.0 (https://creativecommons.org/licenses/by-nc/4.0/)

## Introduction

The introduction of various types of quantum objects (quantum dots [1–3], quantum wells [4–6], and other related objects [7–11]) into a p-n junction is a promising way for developing photovoltaic and electroluminescent semiconductor devices. In particular, the improvement of solar cells performance can be achieved by the expansion of their spectral sensitivity due to the introduction of quantum objects (QOs). It has been found, however, that the achieved expansion of the spectral sensitivity is accompanied by an increase in the *p*–*n* junction saturation current resulting in a drop in the open circuit voltage and, accordingly, a decrease in the efficiency of solar cells [3, 9–11].

There are several possible explanations of such behavior of saturation current when QOs are introduced in a p-n junction. One of them, considered in this work, is the generation of additional dominant recombination defects (for example, structural defects) outside the QO (in the matrix) which relate to the introduction of QOs. The paper analyzes in detail the assumption that the QO itself is a two-dimensional recombination defect, i.e., the dominant recombination channel is located inside the QO [8]. Based on this assumption, a model has been developed that describes the temperature dependences of the electroluminescence (EL) quantum yield of *p*–*n* junctions with QOs. The aim of this work is to determine the applicability of this model to a single-junction gallium arsenide solar cell with well-like QOs (compressed GaAs/$In_{0.4}Ga_{0.6}As$/GaAs quantum wells) and to explain the reasons for the increase of saturation current. For this, the temperature dependence of the EL spectra of the GaAs solar cell were studied for a different number of the rows of QOs. The novelty of the proposed analysis lies in the fact that the model developed for a single recombination center is transferred to a quantum well.

## Recombination model of the process of current flow

According to the model, the total current in the p-n junction is the sum of (radiative and non-radiative) recombination through the QO. The model was experimentally applied to a compressed GaAs/$In_{0.4}Ga_{0.6}As$/GaAs quantum well. This well-like QO was previously called as well-dots or as hybrid QO [13]. This name is due to the fact that both quantum wells and quantum dots were observed in the photoluminescence spectra of these structures. The model proposed in the work (Fig. 1) applies only to quantum wells. It follows from previous works [8, 11] that recombination through QO begins to dominate over recombination in the matrix when the number of the QO rows is more than fifteen. This recombination is composed of radiative and non-radiative (Fig. 1) ones. Accordingly, the solar cell current is the sum of radiative $J_R = q \cdot L$ and non-radiative $J_{NR} = q \cdot U$ currents:

$$J = J_R + J_{NR},$$

where q is the electron charge, $L$ and $U$ are the intensities of radiative recombination (luminescence) and non-radiative recombination, respectively.

Each current is proportional to a number of physical quantities, and in general, radiative and non-radiative currents can be represented by the following expressions:

© Минтаиров М.А., Евстропов В.В., Минтаиров С.А., Шварц М.З., Калюжный Н.А., 2023. Издатель: Санкт-Петербургский политехнический университет Петра Великого.

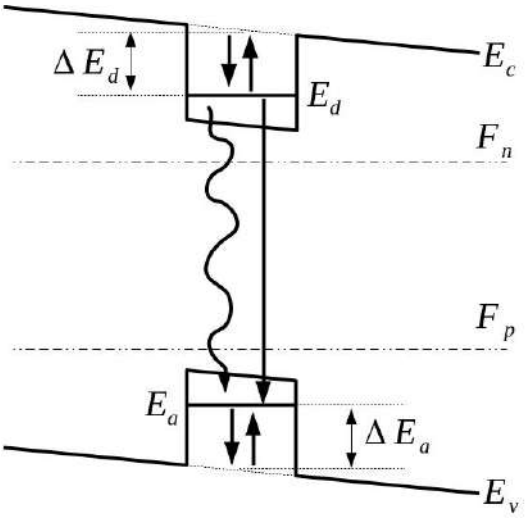


Fig. 1. Recombination transitions in a QO located in the space charge region of p-n junction

$$J_R = k \cdot \alpha_R,$$
$$J_{NR} = k \cdot \alpha_{NR},$$

where the proportionality coefficient $k$ consists of several factors that are the same for both currents (for example, it includes the density of states of 2D electrons and 2D holes, the number of rows, which is equal to this number at a small value [11], and the population of 2D levels). The coefficients $\alpha_R$ and $\alpha_{NR}$ are the corresponding recombination coefficients. When implementing the experiment, we measured the EL spectra at the same current density passing through the structure of the solar cell. Under these conditions, the registered EL intensity of QOs $L$ is proportional to the EL quantum yield.

$$\theta = \frac{J_R}{J_R + J_{NR}} = \frac{\alpha_R}{\alpha_R + \alpha_{NR}}. \quad (1)$$

If the quantum well is interpreted as a lattice defect (in this case, a 2D defect), then the configuration coordinate method [14, 15] gives the existence of a thermal activation barrier $\delta E_b$ for non-radiative recombination and, consequently, an exponential temperature dependence of the non-radiative recombination coefficient

$$\alpha_{NR} = B \cdot \exp\left(\frac{-\delta E_b}{kT}\right). \quad (2)$$

The emissivity $\alpha_R$ does not depend exponentially on temperature. Substituting (2) into (1), we obtain the temperature dependence of the EL quantum yield of QO at a fixed constant current:

$$\theta = \frac{1}{1 + b \cdot \exp\left(\frac{-\delta E_b}{kT}\right)}, \quad (3)$$

where $b = \alpha_R / \alpha_{NR}$.

This temperature dependence has two sections: a plateau at low temperatures and an exponential decline at high temperatures. Formula (3) also gives the temperature dependence of the EL intensity at a fixed current.

## Results and Discussion

The objects of study were three solar cells containing GaAs p-n junctions with different numbers of rows ($r = 1$, $r = 5$, $r = 10$) of GaAs/$In_{0.4}Ga_{0.6}As$/GaAs well-like QOs. All $p$–$n$ junctions were grown by metal-organic vapor phase epitaxy. EL spectra were measured for all samples in the temperature range 80–300 K (Fig. 2).

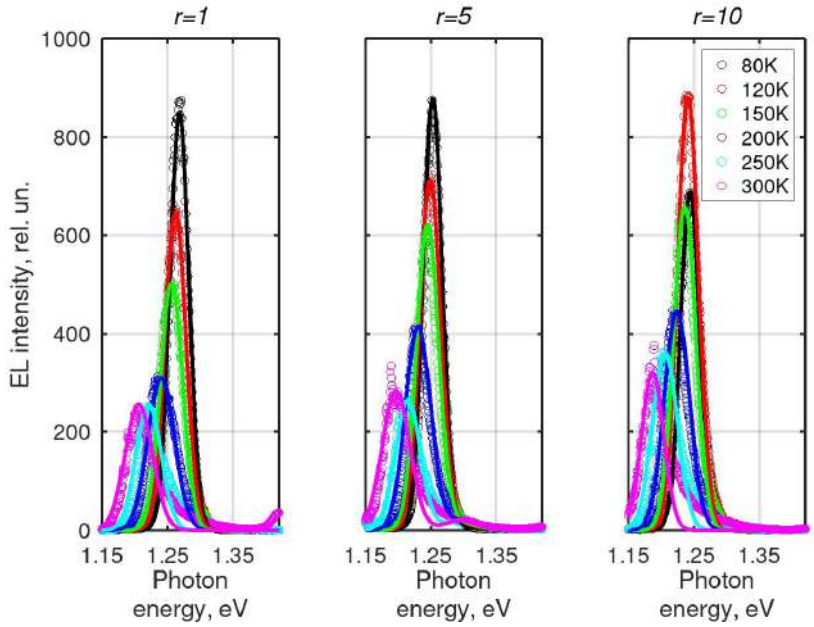


Fig. 2. Electroluminescence intensity spectra for GaAs SCs with different number of quantum objects ($r = 1$, $r = 5$, $r = 10$)

A dominating maximum clearly appears on all spectra, which refers to the radiative transition inside the QO (wave line in Fig. 1). As shown in [13], this peak is due to recombination in the quantum well. The remaining peaks are related to quantum dots. Electroluminescence from them is not dominant. In this case, the performed approximation was focused mainly on the peaks from the quantum well. Electrons inside the electron well and holes inside the hole well are thermalized (in thermal equilibrium with free electrons and holes, respectively). This situation is depicted in Figure 1 by short, oppositely directed arrows. Radiative and non-radiative transitions are under the same conditions (thermal velocities, 2D density of states, and the population of levels), therefore, according to the model, they differ only in recombination coefficients. Accordingly, the radiative and non-radiative current components differ only in these coefficients. In this case, the ratio of the radiative current to the total current (EL quantum yield) is determined by two recombination coefficients (radiative $\alpha_R$ and non-radiative $\alpha_{NR}$) and is described by expression (3). Since the current passed through the structures was constant during the measurements of the spectra, expression (3) can be used to describe the temperature dependence of the EL intensity. The intensity value was determined as the height of the EL peak of QOs. For this the peaks were approximated by the Gaussian function for all measured spectra. The approximation is shown by solid lines in Fig. 2.

Fig. 3 shows the experimental (symbols) and calculated (lines) dependences of peak heights on temperature. It is clearly seen that the experimental dependences contain an inclined section and a tendency to transition to a horizontal one (plateau), which, in accordance with the simulation, is observed at $1/T$ values greater than $\approx 0.015$ 1/K, i.e. at temperatures below 67 K. Using the above approximation, we determined the barrier height with respect to nonradiative recombination $\delta E_b = 0.003$ eV. The parameter $b$ which is equal to the ratio of the radiative recombination coefficient to the non-radiative recombination coefficient is 10.

The dependence of the EL intensity on the number of QO rows is weak and increasing (Fig. 3). If it is interpreted by the recombination model (Fig. 1), then it can be concluded that the complete dominance of recombination through a well-like QOs over recombination in the matrix is not achieved for the solar cells under study. With complete dominance, the independence of the quantum yield of EL on the number of QOs has to be observed. However, in the case of 10 rows of QOs, the EL peak intensity is clearly higher than in case of 5 rows of QOs. In general, the presented experimental data are in good agreement with the consequences of the model that the total current flow can be considered as recombination through QOs.

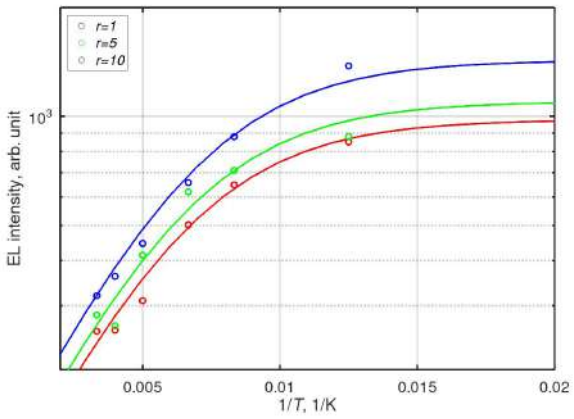


Fig. 3. Experimental (symbols) and calculated (lines) dependences of the electroluminescence intensity on the inverted temperature ($1/T$), for GaAs SCs with different numbers of quantum objects ($r = 1$, $r = 5$, $r = 10$)

## Conclusion

The type of temperature dependence of the EL quantum yield has been established. It corresponds to the proposed model in which all (radiative and non-radiative) recombination in the p-n junction goes through the introduced QOs

The experimental data was approximated using the model expression and the validity of the assumption is shown that the QO introduced into the p-n junction is itself a recombination defect, which can dominate over recombination in the matrix. Therefore, the current in the p-n junction containing a sufficient amount of QOs flows due to recombination through them. It should be expected that such a conclusion is valid not only for the compressed quantum wells studied in this work, but also for other types of QOs. In practical terms, for solar cells, this means that the QOs introduction leads not only to the desired expansion of the spectral sensitivity but also to an occurring another dominant recombination channel leading to a noticeable increase in the saturation current and to a drop in the open-circuit voltage of solar cell.

## REFERENCES

1. **Bailey C., Hubbard S., Polly J.P., Forbes D.V., Raffaelle R.P.,** Quantum Dot Spectral Tuning of Multijunction III-V Solar Cells MRS Online Proceedings Library (OPL) Volume 1121: Symposium N – Next-Generation and Nano-Architectured Photovoltaics 2008 1121-N10–02

2. **Bailey C., Forbes D.V., Raffaelle R.P., Hubbard S.M.,** Near 1 V open circuit voltage InAs/GaAs quantum dot solar cells Appl. Phys. Lett. 98 (2011) 163105.

3. **S. Chan D., Kim A.M., Sanchez Y., Zhang M., Tang J., Wu H. Liu,** InAs/GaAs quantum dot solar cells with quantum dots in the base region IET Optoelectron 13 (2019) p. 215.

4. **Fujii H., Toprasertpong K., Wang Y., Watanabe K., Sugiyama M., Nakano Y.,** 100-period 1.23-eV bandgap InGaAs/GaAsP quantum wells for high-efficiency GaAs solar cells: toward current-matched Ge-based tandem cells Prog. Photovoltaic 22 (2014) 784–795.

5. **Toprasertpong K., Fujii H., Thomas T., Fьhrer M., Alonso-Ељvarez D., Farrell D. J., Watanabe K., Okada Y., Ekins-Daukes N.J., Sugiyama M., Nakano Y.,** Absorption threshold extended to 1.15eV using InGaAs/GaAsP quantum wells for over-50%-efficient lattice-matched quad-junction solar cells Prog. Photovoltaic, (2016), 24, 533–542.

6. **Ekins-Daukes N.J., Barnes J.M., Barnham K.W.J., Connolly J.P., Mazzer M., Clark J.C., Grey R., Hill G., Pate M.A., Roberts J.,** Strained and strain-balanced quantum well devices for high-efficency tandem solar cells Solar Energy Materials & Solar Cells (2001) 68 71–87.

7. **Sugiyama M., Fujii H., Katoh T., Toprasertpong K., Sodabanlu H., Watanabe K., Alonso-Álvarez D., Ekins-Daukes N.J., Nakano Y.,** Quantum wire-on-well (WoW) cell with long carrier lifetime for efficient carrier transport Progress in Photovoltaics: Research and Applications (2016) 24 1606–1614.

8. **Mintairov M.A., Evstropov V.V., Shvarts M.Z., Mintairov S.A., Salii R.A., Kalyuzhnyy N.A.,** Current flow mechanism in GaAs solar cells with GaInAs quantum dots AIP Conf. Proc. 1748 (2016) 050003.

9. **Mintairov M.A., Evstropov V.V., Mintairov S.A., Shvartя M.Z., Kalyuzhnyy N.A.,** Dethermalization of carriers in GaAs solar cells with quantum objects Applied Physics Express, 12 (2019) 035005.

10. **Mintairov M.A, Evstropov V.V, Mintairov S.A, Salii R.A, Shvarts M.Z., Kalyuzhnyy N.A.,** Recombination in GaAs p–i–n Structures with InGaAs Quantum-Confined Objects: Modeling and Regularities Semiconductors, 52 (2018) 1244–1248.

11. **Mintairov M.A, Evstropov V.V, Mintairov S.A, Nadtochii A.M, Salii R.A, Shvarts M. Z., Kalyuzhnyi N.A.,** The influence of the number of rows of gainas quantum objects on the saturation current of gaas photoconverters Technical Physics Letters, 46 (2020) 599–602.

12. **Mintairov S.A., Kalyuzhnyy N.A., Lantratov V.M., Maximov M.V., Nadtochiy A.M., Rouvimov S., Zhukov A.E.,** Hybrid InGaAs quantum well-dots nanostructures for light-emitting and photo-voltaic applications. Nanotechnology, 26 (2015) 385202.

13. **Auth J., Genzow D., Herrmann K.H.,** Photoelektrische Erscheinungen, Berlin Academie-Verloc, 2017.

14. **Ridley B.K.,** Quantum Processes in Semiconductors, Oxford Clarendon Press, 1982.

## THE AUTHORS

**MINTAIROV Mikhail A.**
mamint@mail.ioffe.ru
ORCID: 0000-0002-3481-477X

**SHVARTS Maxim Z.**
shvarts@scell.ioffe.ru
ORCID: 0000-0002-2230-7770

**EVSTROPOV Valerii V.**
vvevstropov@gmail.com
ORCID:

**KALYUZHNYY Nikolay A.**
nickk@mail.ioffe.ru
ORCID: 0000-0001-8443-4663

**MINTAIROV Sergei A.**
mintairov@scell.ioffe.ru
ORCID: 0000-0002-6176-6291

*Received 31.10.2022. Approved after reviewing 09.12.2022. Accepted 16.01.2023.*

© Peter the Great St. Petersburg Polytechnic University, 2023

Conference materials
UDC 53.03, 53.04, 538.9
DOI: https://doi.org/10.18721/JPM.161.212

# Current-voltage characteristics of Cr/SiC(4H) Schottky diodes

A.M. Strel'chuk ✉, E.V. Kalinina

Ioffe Institute, St. Petersburg, Russia

✉ anatoly.strelchuk@mail.ioffe.ru

**Abstract.** Forward and reverse current-voltage characteristics ($I-V$) of Cr/SiC(4H) Schottky diodes (SDs) manufactured using the same technology based on a single weakly-doped ($\sim 4\cdot10^{14}$ cm$^{-3}$) epilayer are investigated. SDs are close to ideal, but a significant spread of $I-V$ and excess current which sometimes unstable were found, unrelated to the difference in the area of the SDs. Investigation in the temperature range 20–210 °C revealed the annealing effect and allowed to estimate the potential barrier height of different diodes before and after annealing. It is suggested that the main diode is shunted by a parasitic diode, which determines forward $I-V$ in the region of $I-V$ exponential dependence.

**Keywords:** SiC, Schottky diodes, current-voltage characteristics, spread, defects

**Funding:** This study was supported in part by RSF grant number [22-12-00003].

**Citation:** Strel'chuk A.M., Kalinina E.V., Current-voltage characteristics of Cr/SiC(4H) Schottky diodes, St. Petersburg State Polytechnical University Journal. Physics and Mathematics. 16 (1.2) (2023) 83–89. DOI: https://doi.org/10.18721/JPM.161.212

This is an open access article under the CC BY-NC 4.0 license (https://creativecommons.org/licenses/by-nc/4.0/)

Материалы конференции
УДК 53.03, 53.04, 538.9
DOI: https://doi.org/10.18721/JPM.161.212

# Вольт-амперные характеристики Cr/SiC(4H) диодов Шоттки

А.М. Стрельчук ✉, Е.В. Калинина

Физико-технический институт им. А.Ф. Иоффе РАН, Санкт-Петербург, Россия

✉ anatoly.strelchuk@mail.ioffe.ru

**Аннотация.** Исследованы прямые и обратные вольт-амперные характеристики ($I-V$) Cr-SiC(4H) диодов Шоттки (SDs), изготовленных по одной и той же технологии на основе одного слаболегированного ($\sim 4\cdot10^{14}$ см$^{-3}$) эпислоя. SDs близки идеальным, но был обнаружен значительный разброс $I-V$ и избыточный ток, который иногда нестабилен, не связанный с разницей в площади SDs. Исследование в диапазоне температур 20–210 °C выявило эффект отжига и позволило оценить высоту потенциального барьера различных диодов до и после отжига. Предполагается, что основной диод во всех случаях шунтируется паразитным диодом, который определяет прямые $I-V$ в области экспоненциальной зависимости тока от напряжения.

**Ключевые слова:** SiC, диоды Шоттки, вольт-амперные характеристики, разброс, дефекты

**Финансирование:** Работа частично поддержана РНФ грантом [22-12-00003].

**Ссылка при цитировании:** Стрельчук А.М., Калинина Е.В. Вольт-амперные характеристики Cr/SiC(4H) диодов Шоттки // Научно-технические ведомости СПбГПУ. Физико-математические науки. 2023. Т. 16. № 1.2. С. 83–89. DOI: https://doi.org/10.18721/JPM.161.212

Статья открытого доступа, распространяемая по лицензии CC BY-NC 4.0 (https://creativecommons.org/licenses/by-nc/4.0/)

© Strel'chuk A.M., Kalinina E.V., 2023. Published by Peter the Great St. Petersburg Polytechnic University.

## Introduction

The study of semiconductor SiC began, apparently, just with the description of the properties of Schottky diodes (SDs) (letter to the editors in 1907 [1] and a series of studies starting in 1923 [2]). Studies of metal-semiconductor contact are summarized, for example, in [3]. The most widely used method for determining Schottky barrier height $\varphi_b$ has long been the study of capacitance-voltage characteristics (CVs; for SiC SDs see, for example, the review in [4]) and some regularities of the change in $\varphi_b$ were established when the metal in contact with SiC varied [4]. An attempt to conduct a similar experiment using current-voltage characteristics ($I$–$V$) to determine $\varphi_b$ showed that in many cases the current $I$ in a significant range of small currents depends on the voltage $U$ exponentially $I = I_{0exp}(qU/(nkT))$ (n is the ideality coefficient), at high currents the dependence becomes linear, but, at the same time along with other effects, there is a significant spread of $I$–$V$ of completely identical SDs (manufactured under absolutely identical conditions on the same SiC monocrystal) (E-MRS 1996, [5]). For diodes characterized by approximately the same value of n, the effect is expressed in a parallel shift of the $I$–$V$ in the region of exponential $I$–$V$ dependence. With the n close to 1, the shift of the $I$–$V$ of different SDs is probably caused by a different value of $\varphi_b$ (assuming the same area). In [5], strongly doped 6H-SiC Lely monocrystals and epilayers were studied (uncompensated donors concentration (doping level) was $N_d$-$N_a \sim (0.6–3)\cdot10^{18}$ cm$^{-3}$). The improvement of the technology allowed to reduce the doping level of SiC. A study of the $I$–$V$ of SDs based on 4H-SiC epilayers with $N_d$-$N_a \sim 3\cdot10^{15}$ cm$^{-3}$ revealed similar effects [6, 7]. This work continues the research [6, 7] with the use of an even weaker doped 4H-SiC; in addition, compared with [7], the number of small-area SDs studied has been increased.

## Materials and Methods

All SDs are made on the basis of one commercial 4H-SiC epitaxial layer N339 with $N_d$-$N_a \approx 4\cdot10^{14}$ cm$^{-3}$ and with a thickness of 5 μm, grown on a substrate with $N_d$-$N_a \gg 10^{18}$ cm$^{-3}$. The Cr films for Schottky contact (with Cr thickness of 0.1 μm) and Cr/Al films for ohmic contact to substrate were deposited by thermal evaporation in a vacuum at a substrate temperature close to room temperature (RT) (before metal deposition, the same standard chemical treatment in acetone, toluene and hydrofluoric acid was carried out). The diameter of the SDs was in range 0.2–8 mm. Annealing of diodes was performed in air for 1–3 hours in increments from 20° to 40°, starting from a temperature of 60 °C to 210 °C. After each annealing, the diodes were cooled to RT. $I$–$V$ were measured in DC mode at RT before annealing, at all annealing temperatures (first heating), at RT after each annealing (annealed diodes) as well as (after annealing at highest temperature 210 °C) the characterization of the SDs was carried out again with monotonous reheating in the same temperature range (second heating). The $I$–$V$ were measured with a KEITHLEY 6485 picoammeter using a clamped contact and a tungsten probe.

## Results and Discussion

Figure 1, *a* shows at RT the forward $I$–$V$ of SDs of different areas on one epilayer. In the region of exponential I(V) dependence almost all $I$–$V$ are characterized by $n$ close to 1 (mostly $n \approx 1.1$ with the exception of curve 1, for which $n \approx 1.25$). However, the spread of $I$–$V$ is very large, even for diodes of the same area (see curves 5–7). Reducing the $I$–$V$ to the unit of area (of the Cr-SiC contact area) does not solve the problem: the spread of $J$–$V$ at the same current density $J$ reaches 0.6 V (Fig. 1, *b*). The number of the investigated SDs of different diameters, shown in Figure 1, *a*, *b*, is relatively small. In order to increase the reliability of the conclusions, SDs were manufactured in an amount of more than 70 pieces with a SD diameter $D$ of 0.3 mm. Almost all forward $I$–$V$ of these diodes in the low-current region are exponential and are characterized by $n = 1.05–1.1$, but the spread of $I$–$V$ at the same current reaches 0.3 V (Fig. 1, *c*). For comparability of these results with the results presented in [5], we present a histogram of the SDs voltage drop distribution at a forward current of 1 μA, however, for some SDs at a current of 1 μA, a deviation from the exponential $I$–$V$ dependence is already noticeable (Fig. 1, *c*). Therefore, we also present a histogram at a forward current of 1 nA (Fig. 1, *d*). An estimate of $n$ of an artificial $I$–$V$ constructed from the coordinates of the maxima of the distribution gives a

© Стрельчук А.М., Калинина Е.В., 2023. Издатель: Санкт-Петербургский политехнический университет Петра Великого.

value of $n \approx 1.25$, which reflects the mentioned deviation at a 'large' current (1 μA), which also manifests itself in a certain broadening of the distribution. Since $n$ is close to 1, the spread of the $I-V$ apparently reflects mainly the spread of the $\varphi_b$, however, the temperature dependence of the forward and reverse currents gives more definite information about the $\varphi_b$ ([3]).

For temperature measurements, 6 SDs were selected, characterizing both the edges and the center of the distributions (Fig. 1, *d*). Figures 2, *a*, *b*, *c* show the temperature dependences of the forward and reverse $I-V$, as well as the effect of annealing on the forward $I-V$ for SD N5 on the right edge of the distribution (Fig. 1, *c*, *d*) and also shows (Fig. 2, *d*) the temperature dependences of the parameters $I_0$, $n$, $I_{rev}$(10 V) at $U_{rev}$ = 10 V for SD N5, as well as for SD N1 on the left edge of the distribution (Fig. 1, *c*, *d*). The situation is complicated by the fact that in some cases, with an increase in the number of measurements of the $I-V$ of one diode, a kind of 'bistability' of the $I-V$ position is observed. An example is shown in Figure 2, a for SD N5, for which out of 10 measurements, in 8 cases, the $I-V$ represented by curve 0a was observed, and in 2 cases – by curve 0b. In both cases, there are significant areas of exponential $I(V)$ dependence and n close to unity ($n$ = 1.05–1.1). The reverse current start to be registered at elevated temperatures, it is characterized by power-law dependences on the voltage $I \sim U^m$ with an exponent $m$ close to 0.25 (Fig. 2, *c*), characteristic of high-quality diodes [3]; the value of reverse current and it activation energy at high temperatures correlates with the corresponding characteristics of the parameter $I_0$ of the forward current. The current represented by the curve 0b (Fig. 2, *a*) can be considered as excess in relation to the current represented by the curve 0a ('main' diode), and caused by a barrier-type shunt. Thus, there is no complete certainty whether the $I-V$ at elevated temperatures and after annealing characterize the 'main' diode, shunt, or both diodes together. Nevertheless, the general trend for all 6 SDs investigated at RT–210 °C temperatures range is that annealing leads to a decrease in the 'initial' activation energy (which reaches ~ 1.7 eV before annealing, and stabilizes at ~ 1 eV after annealing (for example, $E_a \approx 1.7$ eV for SD N5 and ≈ 1.1 eV for SD N1

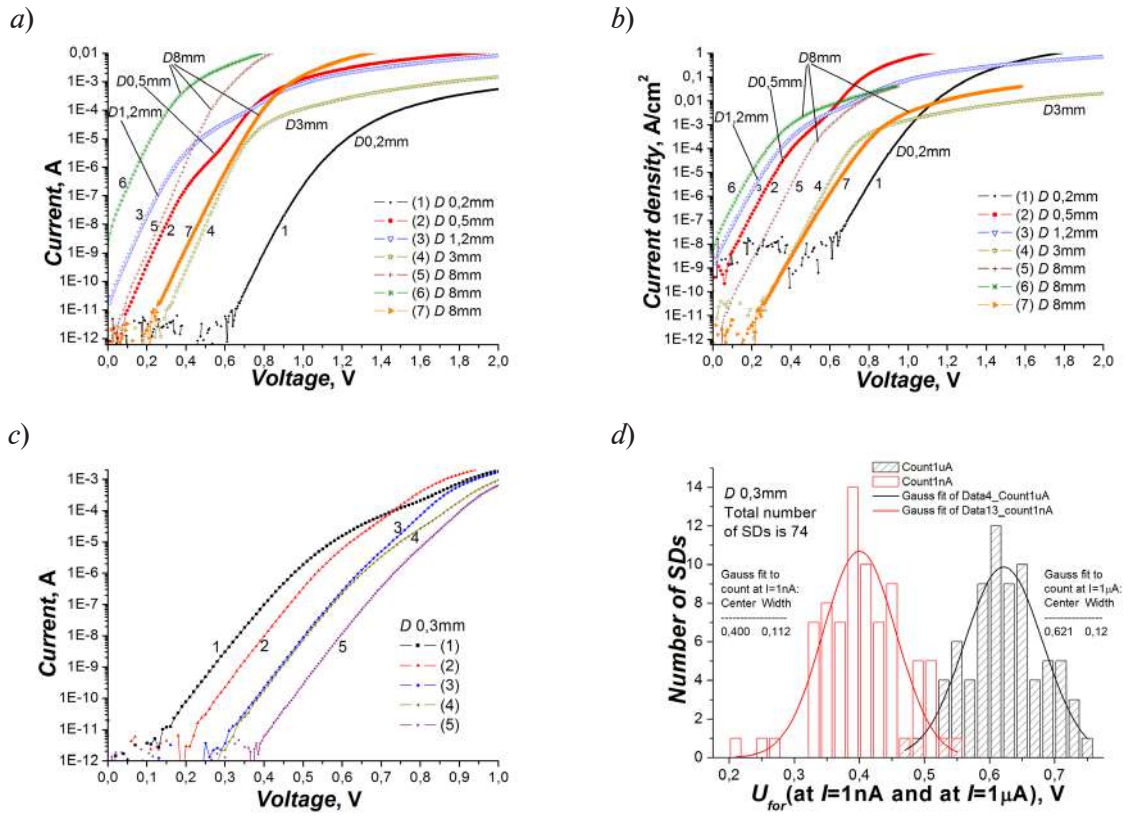


Fig. 1. Forward current-voltage (*a*, *c*) and current density-voltage (*b*) characteristics at RT of 7 SDs (curves 1–7) of different diameters $D$ in the range 0,2–8 mm (*a*, *b*) and of 5 different SDs (curves 1–5) of $D$ = 0,3 mm (*c*) and also the forward voltage drop (at 1 nA and 1 μA forward currents) histograms for SDs of $D$ = 0.3 mm (*d*). The results of the first measurement of the $I-V$ are presented

before annealing, and $E_a \approx 1.04$ eV for SD N5 and $\approx 0.88$ eV for SD N1 after annealing (Fig. 2, *d*)). The activation energy of forward and reverse currents of ideal SDs roughly corresponds to the metal- semiconductor contact barrier height $\varphi_b$ [3]. Thus, the $\varphi_b$ of different Cr-SiC (4H) SDs manufactured under the same conditions on the same epitaxial layer can vary greatly and decrease in some cases even with low-temperature annealing (see also [6, 7]).

Thus, when studying the *I*–*V* characteristics of SDs manufactured by the same method based on a single 4H-SiC epitaxial layer with an doping level of $N_d$-$N_a \approx 4 \cdot 10^{14}$ cm$^{-3}$, it was found that:

A) For some diodes, the *I*–*V* curve is exponential at low currents and turning into a power-law (approaching linear) at high currents, while there is a significant spread of *I*–*V* of identical SDs regardless of the metal-semiconductor contact area (Fig. 1, *a*, *b*, curves 1, 4–7). This is an effect similar to that previously observed in diodes based on more strongly doped SiC ($3 \cdot 10^{15}$ cm$^{-3}$– $3 \cdot 10^{18}$ cm$^{-3}$) [5–7] (see Introduction). This effect of the spread of *I*–*V* will be called the N1 effect ('spread' or 'shift').

B) For the other part of the SDs (Fig. 1, *a*, *b*, curves 2, 3 and Fig. 1, *c*, curves 1, 3, 4), the dependence of current on voltage, in contrast to the one described above, in addition to the exponential section, is characterized by the presence of a more or less pronounced additional power section and an inflection point, which is a characteristic sign of excess current and the presence of barrier-type shunts. In this case, when the current increases, before the inflection point, the current is mostly excess (through the shunt), and after the inflection point it is mostly the current of the main diode.

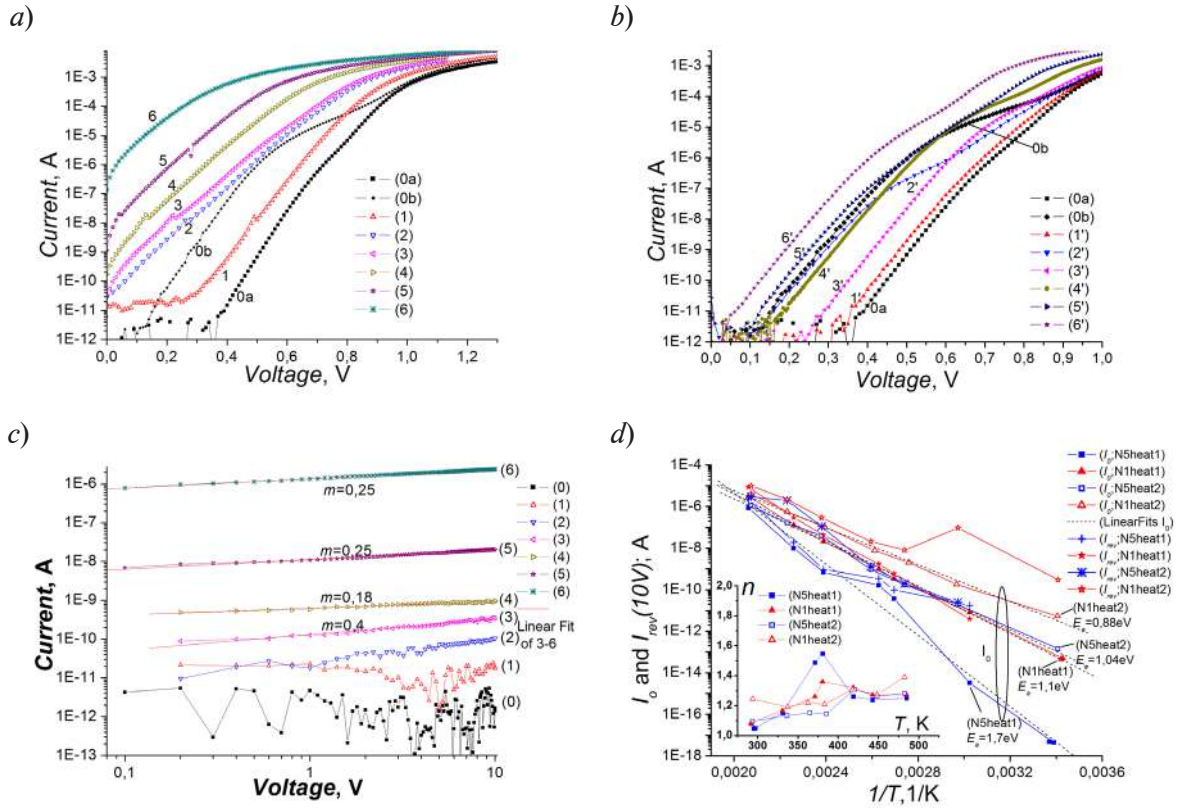


Fig. 2. Forward (*a*) and reverse (*c*) *I*–*V* of the SD N5 at temperatures: RT = 289–295 K (curves 0), 331 K (curves 1), 371 K (curves 2), 380 K (curves 3), 419 K (curves 4), 443 K (curves 5), 485 K (curves 6); *m* is an exponent of power-law dependence of reverse current versus voltage. Forward *I*–*V* (*b*) at RT = 289–296 K (curves 1'–6') of the annealed SD N5 after cooling from the corresponding elevated temperatures (1–6). Curves 0a and 0b in Fig. 2, *a*, *b*, show results of two measurements of the *I*–*V* of the SD N5 at RT before heating. Temperature dependencies (*d*) of the parameters $I_0$ and *n* (inset) of the forward *I*–*V* and reverse current $I_{rev}$(10 V) of the SDs N5 and N1 during first heating (heat1) and second heating (heat2). SDs diameter is 0.3 mm

The position of the inflection point along the axis of currents characterizes the shunt resistance; it different for different diodes and can be quite high. Apparently for the first time in SiC-based diodes, barrier-type shunts identified by forward $I-V$ are described in 6H-SiC p-n structures (E-MRS 1996, [8]). The characteristic size of the shunt (~ 1μm) was estimated by the magnitude of the shunt series resistance, taking into account the spreading effect in the substrate [9], and the potential barrier height of the barrier-type shunt (~ (1−1.3) eV) was estimated by the temperature dependence of the current exponentially dependent on voltage. The presence of such excess forward current will be called the N2 effect ('shunt'). Later, similar effect was observed in 3C-SiC [10] and 4H-SiC [11−15] pn structures, as well as in SDs based on 4H-SiC [16−22] and 6H-SiC [23, 24].

C) For some SDs (Fig. 2, *a*, curves 0a, 0b), a 'bistable' state of the forward $I-V$ is observed in the region of exponential $I(V)$ dependence, when the current in the second stable state (curve 0b in Fig. 2, *a*) is excess at relatively small currents (up to the inflection point), and at high current it is equal to the current through the same diode in the first stable state (curve 0a in Fig. 2, *a*). Such an excess current is a characteristic feature of a barrier-type shunt, i.e. a parasitic diode connected in parallel to the main diode (with $n$ close to 1 in both cases). Previously, similar effects of instability were observed in 4H-SiC pn structures [13, 14], as well as in SDs based on 4H-SiC [25, 22]. The presence of unstable excess forward current will be called the N3 effect ('instability').

In addition, previously, the effects of:

D) the appearance of excess current and a barrier-type shunt in 6H-SiC [8] and 4H-SiC [11, 12] p-n structures as a result of partial degradation of the diode when operating under extreme conditions (when applying a relatively large reverse voltage and/or when operating at elevated temperatures), the N4 effect ('diode degradation');

E) a variation in the series resistance of the SDs, reaching 12 orders of magnitude, as a result of $He^+$-irradiation and fully compensation of epilayer in 4H-SiC SDs with shunts [22], the N5 effect ('resistance spread'); and

F) a suppression (and then recovery after annealing) of the forward and reverse excess currents after electron and proton irradiation for 6H-SiC pn structures with shunts [26], the N6(7) effect ('shunt degradation' ('shunt restoration')) were found.

Interpretation of the effect N1 ('spread') is generally difficult due to the likely manifestation of several effects at once, however, in the particular case of SDs close to ideal ($n$ is close to 1), the most likely explanation of the effect N1 is the spread of the $\varphi_b$ (assuming the same area). When explaining the effect of N2 ('shunt') in p-n structures, we consistently moved from the hypothesis of the inclusion of the second phase (3C-SiC, Si) to the hypothesis of a shunt in the form of a parasitic Schottky diode formed due to 'hole'-type structural defects [8, 10−14] (pits, open core dislocations, see also [16−18]) with the possible participation of carbon as a metal substitute in the formation of the Schottky barrier (it is well-known that the nonstoichiometric sublimation of SiC leads to graphitization of the SiC surface, is currently used to form graphene on the SiC surface and can form a Schottky barrier [27]; by the way the shunting of the SiC pn junction with a carbon particle was proposed already in [28]). The estimate of the barrier height of a parasitic diode in 6H- and 4H-SiC pn structures (1.3−1.4 eV [8, 11]) is close to the typical barrier height of Schottky diodes based on SiC (1−1.5 eV). The effects of N3 ('instability'), N4 ('diode degradation') and N6 ('shunt degradation') in pn structures, as well as the effects of N2 ('shunt'), N3 ('instability') and N5 ('resistance spread') in SDs, it seems to us, closely tied and also can be explained by the hypothesis of a parasitic Schottky diode, considering the conductivity as percolation through carbon-coated surfaces of penetrating structural defects in the form of 'holes' of small cross-section and/or complex shape. Moreover, the results of present study, as well as [5, 12, 13], allow to assume that the effect of N1 ('spread') differs from the effect of N2 ('shunt') only by the 'power' of the shunt (first of all, by the defect area, as well as by the value of $\varphi_b$). Thus, in our opinion, all 6 effects in SiC-based diodes (both in SDs and p-n structures) are related and can be explained from a single position. This is difficult to do with the help of the models [29−31], which are usually used to explain the appearance of excess currents in Schottky diodes (in these models a potential relief on the surface of the semiconductor is considered, which leads to a spread in the Schottky barrier height). In addition, according to [29−31], the $\varphi_b$ spread decreases when using a weaker doped semiconductor, which is not confirmed by our observations

in case of SiC-based SDs. In *CV* measurements, in the presence of a barrier-type shunt, the main diode of a large area will most likely dominate and also, considering the spread of the $\varphi_b$ determined by *CV* [4], it is necessary to take into account the methodological complexity of the exact determination of $\varphi_b$ associated with the need to use a highly-uniform doped semiconductor.

## Conclusion

The study of forward and reverse *I*–*V* of Cr-SiC SDs based on weakly doped (~$4 \cdot 10^{14}$ $cm^{-3}$) 4H-SiC showed that SDs are close to ideal, however, there is a spread of *I*–*V*, not related to the difference in the area of the diodes (of the Cr-SiC contact area). There are also specific excess currents, sometimes unstable. Even a slight heating leads to an irreversible change in the properties of the SDs. It is suggested that the main Schottky diode is shunted in all cases by a parasitic diode, which manifests itself in forward *I*–*V* in the region of exponential current on voltage dependence.

## REFERENCES

1. **Round H.J.,** A note on carborundum, Electrical World 49 (1907) 309.

2. **Losev O.V.,** The effect of contact detectors; the effect of temperature on the generating contact, Wireless Telegraphy and Telephony („T. i T. b. p.“) 18 (1923) 45–62 (in Russian).

3. **Rhoderick E.H.,** Metal-Semiconductor Contacts, Moscow, 1982 (Russian translation).

4. **Andreev A.N., Lebedev A.A., Rastegaeva M.G., Snegov F.M., Syrkin A.L., Chelnokov V.E., Shestopalova L.N.,** Barrier height in n-SiC-6H based Schottky diodes, Semiconductors 29 (1995) 957–962.

5. **Strel'chuk A.M., Rastegaeva M.G.,** Characterization of Schottky barriers occurring at the metal-6H-SiC contact based on results of studies of current-voltage characteristics, Materials Science and Engineering B46 (1997) 379–382.

6. **Strel'chuk A.M., Kalinina E.V., Konstantinov A.O., Hallen A.,** Features of current-voltage characteristics of Cr Schottky diodes based on low-doped 4H-SiC, V Intern. Seminar on SiC, Velikiy Novgorod, Russia (2004) 116-117, and also Strel'chuk A.M., Kalinina E.V., Konstantinov A.O., Hallen A., Current-voltage characteristics of Cr Schottky diodes based on low-doped 4H-SiC, II Ukrainian Scientific Conf. on Semiconductor Physics, Chernivtsi, Ukraine (2004) 216–217.

7. **Strel'chuk A.M., Kalinina E.V.,** Schottky diodes based on 4H-SiC epitaxial layers, Journal of Physics: Conference Series 2103 (2021) 012235.

8. **Strel'chuk A.M., Evstropov V.V., Rastegaeva M.G., Kuznetsova E.P.,** Shunting patterns occurring in epitaxial 6H-SiC p-n structures for high-voltage rectifier, Materials Science and Engineering B46 (1997) 231–235.

9. **Strel'chuk A.M., Gresserov B.N.,** Serial resistance of epitaxial p-n structures based on 6H-SiC, Technical Physics Letters 22 (1996) 304–306.

10. **Strel'chuk A.M., Kiselev V.S., Avramenko S.F.,** Thermal injection current in 3C-SiC pn structures, Materials Science and Engineering B61-62 (1999) 437–440.

11. **Strel'chuk A.M., Savkina N.S.,** Ideal 4H-SiC pn junction and its characteristic shunt, Materials Science and Engineering B80 (2001) 378–382.

12. **Strel'chuk A. M., Kalinina E.V.,** Recombination and excess currents in 4H-SiC structure with low-doped n-region, Materials Science Forum 740–742 (2013) 565–568.

13. **Strel'chuk A.M., Kalinina E.V., Lebedev A.A., Boricheva I.K., Pavshukov V.V.,** Variant of excess current in 4H-SiC pn structures, Materials Science Forum 778-780 (2014) 859-862.

14. **Strel'chuk A.M., Yakimov E.B., Lavrent'ev A.A., Kalinina E.V., Lebedev A.A.,** Characterization of 4H-SiC pn structures with unstable excess current, Materials Science Forum 821-823 (2015) 648–651.

15. **Megherbi M.L., Pezzimenti F., Dehimi L., Rao S., Della Corte F.G.,** Analysis of different forward current–voltage behaviours of Al implanted 4H-SiC vertical p–i–n diodes, Solid-State Electronics 109 (2015) 12–16.

16. **Defives D., Noblanc O., Dua C., Brylinski C., Barthula M., Meyer F.,** Electrical characterization of inhomogeneous Ti:4H-SiC Schottky contacts, Materials Science and Engineering B61-62 (1999) 395-401, and also Defives D., Noblanc O., Dua C., Brylinski C., Barthula M., Aubry-Fortuna V.,

Meyer F., Barrier Inhomogeneities and Electrical Characteristics of Ti/4H–SiC Schottky Rectifiers, IEEE Transactions on Electron Devices 46 (1999) 449–455.

17. **Skromme B.J., Luckowski E., Moore K., Bhatnagar M., Weitzel C.E., Gehoski T., Ganser D.,** Electrical Characteristics of Schottky Barriers on 4H-SiC: The Effects of Barrier Height Nonuniformity, Journal of Electronic Materials (2000) 29 376–383.

18. **Ewing D.J., Wahab Q., Ciechonski R.R., Syvajarvi M., Yakimova R., Porter L.M.,** Inhomogeneous electrical characteristics in 4H–SiC Schottky diodes, Semiconductor Science and Technology 22 (2007) 1287–1291, and also Ewing D.J., Porter L. M., Wahab Q., Ma X., Sudharshan T.S., Tumakha S., Gao M., Brillson L.J., Inhomogeneities in Ni/4H - SiC Schottky barriers: Localized Fermi-level pinning by defect states, Journal of Applied Physics 101 (2007) 114514.

19. **Bolen M.L., Capano M.A.,** Defect Analysis of Barrier Height Inhomogeneity in Titanium 4H-SiC Schottky Barrier Diodes, Journal of Electronic Materials 38 (2009) 574–580.

20. **Nakamura M., Hashino Y., Furusho T., Kinoshita H., Shiomi H., Yoshimoto M.,** Characterization of Schottky diodes on 4H-SiC with various off-axis angles grown by sublimation epitaxy, Materials Science Forum 600-603 (2009) 967–970.

21. **Ivanov P.A., Il'inskaya N.D., Potapov A.S., Samsonova T.P., Afanas'ev A.V., Il'in V.A.,** Effect of Rapid Thermal Annealing on the Current–Voltage Characteristics of 4H_SiC Schottky Diodes, Semiconductors 47 (2013) 81–84.

22. **Strel'chuk A.M., Zelenin V.V., Kuznetsov A.N., Tringe J., Davydov A.V., Lebedev A.A.,** Anomalous scatter of forward current – voltage characteristics of $He^+$ - irradiated Ni/4H-SiC Schottky diodes, Materials Science Forum 858 (2016) 749–752.

23. **Im H.-J., Ding Y., Pelz J.P., Choyke W.J.,** Nanometer-scale test of the Tung model of Schottky-barrier height inhomogeneity, Physical Review B 64 (2001) 075310.

24. **Duman S., Dogan S., Gurbulak B., Turut A.,** The barrier-height inhomogeneity in identically prepared Ni/n-type 6H-SiC Schottky diodes, Applied Physics A 91 (2008) 337–340.

25. **Abdelwahed N., Troudi M., Sghaier N., Souifi A.,** Impact of defect on I(V) instabilities observed on Ti/4H–SiC high voltage Schottky diodes, Microelectronics Reliability 55 (2015) 1169–1173.

26. **Strel'chuk A.M., Kozlovski V.V., Lebedev A.A., Smirnova N.Yu.,** Influence of Irradiation on Excess Currents in SiC pn Structures, Materials Science Forum 483–485 (2005) 1001-1004, and also Strel'chuk A.M., Kozlovski V.V., Smirnova N.Yu., Pil'kevich J.P., Rastegaeva M.G., Effect of Irradiation on Excess Currents in 6H-SiC p-n Structures, Third European Conference on High Temperature Electronics (Berlin, HITEN1999; IEEE Cat. No.99EX372) (1999) doi:10.1109/hiten.1999.827474.

27. **Tongay S., Lemaitre M., Miao X., Gila B., Appleton B.R., Hebard A.F.,** Rectification at Graphene-Semiconductor Interfaces: Zero-Gap Semiconductor-Based Diodes, Physical Review X 2 (2012) 011002.

28. **Patrick L.,** Structure and characteristics of silicon carbide light-emitting junctions, Journal of Applied Physics 28 (1957) 765–776.

29. **Werner J.H., Guttler H.H.,** Barrier inhomogeneities at Schottky contacts, Journal of Applied Physics 69 (1991) 1522–1533.

30. **Sullivan J., Tung R.T., Pinto M., Graham W.R.,** Electron transport of inhomogeneous Schottky barriers: A numerical study, Journal of Applied Physics 70 (1991) 7403-7424.

31. **Tung R.T.,** The physics and chemistry of the Schottky barrier height, Applied Physics Reviews 1 (2014) 011304.

## THE AUTHORS

**STREL'CHUK Anatoly M.**
anatoly.strelchuk@mail.ioffe.ru
ORCID: 0000-0001-5321-0237

**KALININA Evgenia V.**
evk@mail.ioffe.ru

*Received 28.10.2022. Approved after reviewing 08.11.2022. Accepted 10.11.2022.*

© Peter the Great St. Petersburg Polytechnic University, 2023

Conference materials
UDC 544.6, 621.382
DOI: https://doi.org/10.18721/JPM.161.213

# *In situ* conductance studies of electrochemically doped polymer thin films based on nickel-salen complexes

E.A. Smirnova ✉, I.A. Chepurnaya

Ioffe Institute, St. Petersburg, Russia

✉ esmirnova@mail.ioffe.ru

**Abstract.** Modulation of the electron transport properties of metallopolymers based on nickel-salen complexes N,N′-bis(salicylidene)ethylenediaminonickel(II) and N,N′-bis(3-methoxysalicylidene)ethylenediaminonickel(II) upon electrochemical p-doping was studied by *in situ* conductance measurements in an organic electrochemical transistor configuration. Both polymers showed bell-shaped conductance profiles upon positive voltage bias; the results were interpreted using the mixed-valence conductivity model. The electrochemical doping of the methoxy-substituted polymer film resulted in a change in its electrical conductance by four orders of magnitude, which indicates its potential suitability as a channel material for electrochemical transistors. Electrochemical quartz crystal microbalance studies confirmed mixed ionic-electronic transport in this polymer film and revealed different regimes of ion and solvent transfer in the polymer at different doping levels.

**Keywords:** conducting metallopolymer, electrochemical doping, nickel-salen complex, *in situ* conductance measurements, electrochemical quartz crystal microbalance, organic electrochemical transistor

**Citation:** Smirnova E.A., Chepurnaya I.A., *In situ* conductance studies of electrochemically doped polymer thin films based on nickel-salen complexes, St. Petersburg State Polytechnical University Journal. Physics and Mathematics. 16 (1.2) (2023) 90–95. DOI: https://doi.org/10.18721/JPM.161.213

This is an open access article under the CC BY-NC 4.0 license (https://creativecommons.org/licenses/by-nc/4.0/)

Материалы конференции
УДК 544.6, 621.382
DOI: https://doi.org/10.18721/JPM.161.213

# Исследование проводимости электрохимически легированных тонких полимерных пленок на основе саленовых комплексов никеля

Е.А. Смирнова ✉, И.А. Чепурная

Физико-технический институт им. А.Ф. Иоффе РАН, Санкт-Петербург, Россия

✉ esmirnova@mail.ioffe.ru

**Аннотация.** Влияние электрохимического легирования на особенности электронного транспорта в полимерных формах саленовых комплексов никеля N,N′-бис(салицилиден)этилендиаминоникель(II) и N,N′-бис(3-метоксисалицилиден)-этилендиаминоникель(II) исследовано *in situ* методом измерения проводимости на экспериментальной установке, моделирующей условия функционирования органического электрохимического транзистора. Для обоих полимеров получены колоколообразные кривые зависимости проводимости от напряжения. При электрохимическом легировании метокси-замещенной полимерной пленки ее проводимость увеличивается на четыре порядка величины, что указывает на принципиальную возможность использования этого материала в каналах электрохимических транзисторов. Методом электрохимических кварцевых микровесов подтвержден смешанный электронно-ионный транспорт в данном полимере, а также

© Smirnova E.A., Chepurnaya I.A., 2023. Published by Peter the Great St. Petersburg Polytechnic University.

обнаружены различные режимы переноса ионов и растворителя в пленках с различным уровнем легирования

**Ключевые слова:** проводящий полимерный металлокомплекс, электрохимическое легирование, саленовый комплекс никеля, *in situ* измерения проводимости, электрохимические кварцевые микровесы, органический электрохимический транзистор

**Ссылка при цитировании:** Смирнова Е.А., Чепурная И.А. Исследование проводимости электрохимически легированных тонких полимерных пленок на основе саленовых комплексов никеля // Научно-технические ведомости СПбГПУ. Физико-математические науки. 2023. Т. 16. № 1.2. С. 90–95. DOI: https://doi.org/10.18721/JPM.161.213

Статья открытого доступа, распространяемая по лицензии CC BY-NC 4.0 (https://creativecommons.org/licenses/by-nc/4.0/)

## Introduction

Thin films of polymeric mixed ionic-electronic semiconductors have attracted a great deal of attention in the past few decades as functional materials for a broad range of promising applications in energy storage and conversion, electrocatalysis, smart displays, actuators for soft robotics, and organic electronics [1]. An interesting example of conducting polymer-based electronic devices is the organic electrochemical transistor (OECT) used in chemical sensors and biosensors, circuits, memory and neuromorphic systems, wearable and implantable devices [2, 3]. In contrast to more well-known field-effect transistors, an OECT polymer channel bridging the source and drain electrodes is permeable to the ions of the electrolyte layer between the channel and the gate electrode. The working principle of an OECT involves bulk electrochemical doping of the channel material. Upon application of a gate voltage, electrolyte ions are injected into the channel to compensate the charge carrier formation. The doping state and conductivity of the polymer film is modulated by the amount of injected ions throughout its entire volume [4].

To be able to support the switching and amplification functions of an OECT, the channel materials are required to demonstrate a significant (over several orders of magnitude), fast, and reversible change in electronic conductivity upon electrochemical doping. In order to do that, a competitive OECT channel material should exhibit fast electronic transport in the horizontal direction (between the source and the drain) and effective ion penetration in the vertical direction (from the electrolyte into the channel) [5]. However, electronic and ionic transport in most known organic semiconductors cannot be improved simultaneously, which makes it difficult to maximize the device performance [6]. There is an ongoing search for novel polymers that efficiently transport and couple ionic and electronic charge and exhibit drastic variation in conductivity upon electrochemical doping.

Polymeric nickel(II) complexes with salen-type ligands are main-chain metallopolymers, in which oligomers formed by covalently linked monomer units (Fig. 1) can assemble into supramolecular structures. Nickel-salen polymers are undoped in their pristine state and can be electrooxidized (p-doped) in a supporting electrolyte. Unlike many other metallopolymers bearing redox-active metal sites, the electroactivity of nickel-salen polymers is centered at phenolate moieties while nickel(II) ions act as redox-innocent sites that mediate the electronic coupling between the phenolates [7]. In this work, the effect of electrochemical doping on the electrical conductivity of polymer films derived from N,N′-bis(salicylidene)ethylenediaminonickel(II) (poly-[NiSalen]) and N,N′-bis(3-methoxysalicylidene)ethylenediaminonickel(II) (poly-[$NiCH_3OSalen$]) (Fig. 1) was investigated to preliminary evaluate the suitability of these polymers as OECT channel materials.

## Materials and Methods

Monomeric complexes [NiSalen] and [$NiCH_3OSalen$] were synthesized as previously reported [8]. Polymer films were obtained by oxidative electropolymerization of corresponding monomers. The electrodeposition of polymers and subsequent measurements were performed in an argon atmosphere in three-electrode setups with a working electrode (WE), a glassy carbon counter electrode and a non-aqueous $Ag/Ag^+$ reference electrode (+0.3 V versus Ag/AgCl/sat'd NaCl, which

© Смирнова Е.А., Чепурная И.А., 2023. Издатель: Санкт-Петербургский политехнический университет Петра Великого.

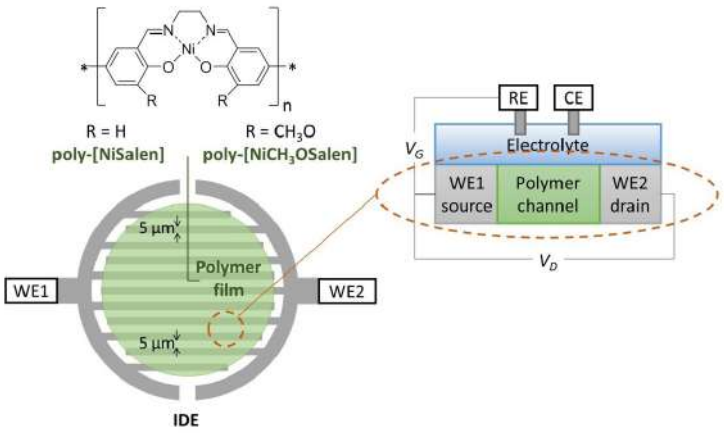


Fig. 1. The structures and abbreviations of the polymers, schematic representation of an interdigitated electrode (IDE), and an OECT-like experimental setup

is used to report the values of electrode potentials in this study) operated by the VSP potentiostat (BioLogic Science Instruments). Two-terminal platinum interdigitated electrodes (IDE) with a comb distance of 5 μm (MicruX Technologies) or platinum-coated quartz crystal substrates were used as working electrodes. A 0.1 M solution of tetraethylammonium tertafluoroborate ($Et_4NBF_4$) in acetonitrile (MeCN) was used as an electrolyte. The electropolymerization was performed by scanning the WE potential between 0.0 V and +1.6 V at 10 mV/s using 1 mM monomer solution in 0.1 M $Et_4NBF_4$/MeCN.

*In situ* conductance measurements were performed on polymer-coated IDEs; two IDE combs constituted two working electrodes (WE1 and WE2) (Fig. 1). By using the potentiostat in a bipotentiostat mode, the working electrode potentials were biased with respect to the RE at a constant rate of 10 mV/s, while keeping a 10 mV difference between WE1 and WE2. The currents on each WE were monitored and used to calculate the conductance of the polymer from Ohm's law as described in [9].

Electrochemical quartz crystal microbalance measurements were performed using a QCM100 (Stanford Research Systems) equipped with an MXC-1600 frequency counter (Metex). A positive bias sweep between 0.0 V and +1.6 V at a 10 mV/s rate was applied to the polymer-modified crystal as the working electrode. The change in the frequency of the crystal oscillation was converted to a change in mass using the Sauerbrey equation [10].

## Results and Discussion

To evaluate electronic transport properties of poly-[NiSalen] and poly-[$NiCH_3OSalen$] films, their conductance was measured in situ [11] in an OECT-like setup shown in Fig. 1. In this configuration, two platinum terminals of a polymer-coated IDE (WE1 and WE2) constitute the source and drain electrodes. The drain bias $V_D$ is defined as the constant potential difference maintained between WE1 and WE2. The combination of a counter electrode (CE) and a reference electrode (RE) constitute the gate. The gate voltage $V_G$ is the potential of the source electrode versus the reference so it is equal in magnitude but opposite in sign to the gate voltage in the solid state field-effect transistors. In this contribution, the data are presented using the $V_G$ scale relative to Ag/AgCl.

Fig. 2 shows the conductance ($G$) versus gate voltage characteristics for poly-[NiSalen] and poly-[$NiCH_3OSalen$] (curve *1* in Fig. 2, *a*, and curve *1′* in Fig. 2, *b*, respectively) in OECT-like setups operated in 0.1 M $Et_4NBF_4$ in MeCN at $V_D$ = 10 mV. In both cases, the pristine polymer film is virtually non-conductive (*OFF* state). Upon application of a positive gate bias, the polymer conductance sharply increases at a threshold voltage $V_T$, reaches a maximum at $V_M$ (*ON* state), and then decreases, i.e. both films show rather bell-shaped conductance profiles. Simultaneously with conductance measurements, the current flowing between the working and counter electrodes $I_W$ was also monitored as a function of gate voltage (curve *2* in Fig. 2, *a* and curve *2′* in Fig. 2, *b*

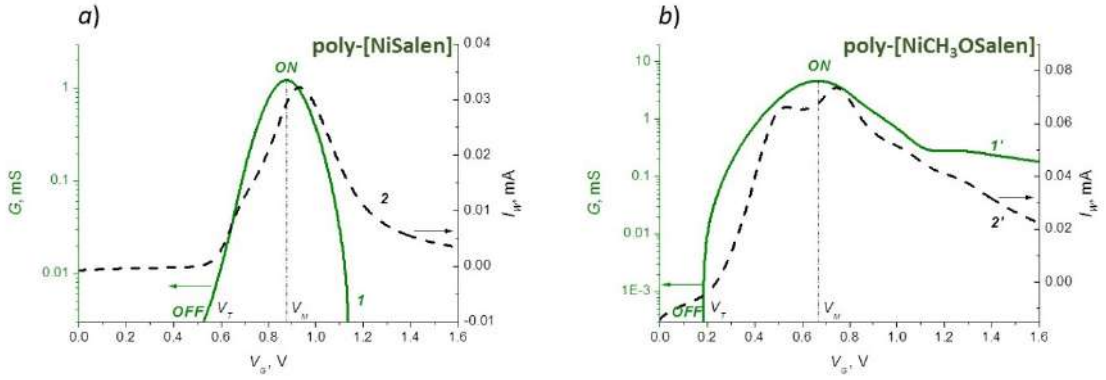


Fig. 2. Variation of conductance $G$ (curves *1* and *1′*) and current $I_W$ (curves *2* and *2′*) with gate voltage for poly-[NiSalen] (*a*) and poly-[NiCH$_3$OSalen] (*b*)

for poly [NiSalen] and poly-[NiCH$_3$OSalen], respectively). This current primarily arises from the electrochemical oxidation of the polymer film resulting in its conversion from the charge-neutral to the p-doped form. The $I_W = f(V_G)$ curves show several broad redox processes with oxidation onsets closely matching the values of $V_T$, and the oxidation current peaks associated with the conductance maxima. Depicted changes in conductance therefore result from the electrochemical doping of polymer films at $V_G > V_T$.

The conductance changes with gate voltage obtained for both polymers do not exhibit a sigmoidal shape typical for highly conjugated intrinsically conducting polymers; rather, they are reminiscent of bell-shaped conductance profiles observed for redox systems and organic oligomer networks [11]. Taking into account the small length of poly-[NiSalen] and poly-[NiCH$_3$OSalen] chains [12], it is feasible to apply the mixed-valence conductivity model [13] for the analysis of the experimental results. According to this model, the electronic transport in electrochemically doped polymers can be described as electron hopping between isoenergetic sites of the overlapping redox states available in the polymer film. The conductivity is proportional to the ratio of the occupied and unoccupied sites of a redox state and should reach a maximum when half the sites are charged. The main conductance maxima in $G = f(V_G)$ plots (curves *1* and *1′* in Fig. 2) are reached at gate voltages equal to the half-wave potentials of the redox couples exhibiting the highest oxidation current peaks in $I_W = f(V_G)$ curves (curves *2* and *2′* in Fig. 2). Based on the literature data [7], this conductivity regime can be attributed to the polymer conversion from the neutral to the radical cation state. For both polymers, the conductance increases in the voltage range between $V_T$ and $V_M$ following an increase in the concentration of mobile charge carriers generated in the polymer backbone. After reaching the maximum value, the conductance decreases due to the smaller number of sites available for hopping. In a highly doped poly-[NiSalen] film, the values of $G$ quickly drop below $10^{-3}$ mS, which points out to the limited amount of redox states in the polymer. On the contrary, the $G = f(V_G)$ plot obtained for the methoxy-substituted film features several shoulders at $V_G > V_M$, which are indicative of the generation of additional (e.g., dicationic [7]) overlapping redox states, which contribute to a non-negligible (above $10^{-1}$ mS) polymer conductance at high doping levels.

The polymer composition has a pronounced effect of the parameters of $G = f(V_G)$ curves (Table 1). Compared to poly-[NiSalen], the poly-[NiCH$_3$OSalen] film shows lower threshold voltage and wider conductivity window (the voltage range in which the polymer is in the conductive state) due to the presence of electron-donating methoxy substituents in the ligand phenyl rings that increase the overall electron density in the polymer backbone and apparently enable charge carrier mobility over extended voltage range. Poly-[NiCH$_3$OSalen] demonstrates a conductance modulation by four orders of magnitude between *ON* and *OFF* states upon electrochemical doping, which indicates its potential suitability as an OECT channel material. For this polymer film, the variation of the conductance with gate voltage is reversible and stable for $V_G$ in the range from 0 V to $V_M$ = 0.67 V, which is the voltage range of interest for OECT applications. If the polymer is biased above $V_M$, a hysteresis in the conductance response and a gradual decrease in the $G$ values are observed upon doping-dedoping.

Table 1

**Parameters of $G = f(V_G)$ curves for studied polymers**

| Polymer | $V_T$ (V) | $V_M$ (V) | Conductivity window (V) | $G_{ON}/G_{OFF}$ |
|---|---|---|---|---|
| poly-[NiSalen] | 0.52 | 0.88 | 0.62 | ~$10^{-3}$ |
| poly-[$NiCH_3OSalen$] | 0.18 | 0.67 | 1.42 | ~$10^{-4}$ |

Table 2

**Apparent dopant masses during oxidation of poly-[$NiCH_3OSalen$]**

| $V_G$ range (V) | Apparent mass (g/mol) |
|---|---|
| 0.18 – 0.70 | 38 |
| 0.70 – 0.97 | 93 |
| 0.97 – 1.18 | 170 |
| 1.18 – 1.35 | 260 |
| 1.35 – 1.6 | 80 |

The in situ conductance studies of poly-[$NiCH_3OSalen$] were complemented by electrochemical quartz crystal microbalance (EQCM) measurements to gain more insight into the ion uptake process during electrochemical doping of the polymer. A positive voltage bias was applied to the polymer film on the surface of a Pt-coated quartz crystal in the same $V_G$ range and at the same rate as in the in situ conductance tests. A continuous non-monotonic increase in the polymer mass was observed, which may be indicative of the charge-compensating electrolyte ions ($BF_4^-$) moving into the polymer film upon its oxidation. To confirm this assumption, the apparent molar mass of the dopant counterions was calculated from the EQCM data, as previously described [14]. The results summarized in Table 2 show that the mechanism of charge compensation is voltage dependent. In the $V_G$ ranges for which the apparent molar mass of the dopant is significantly smaller than the molar mass of the pure $BF_4^-$ anion (87 g/mol), the dopant entry apparently requires concurrent solvent transfer in the opposite direction. And vice versa, values of the apparent dopant mass greater than 87 g/mol are consistent with simultaneous ingress of ions and solvent into the polymer film. Comparison of the data presented in Table 2 with the results of in situ conductance measurements (Fig. 2, *b*) indicates that the initial increase in the poly-[$NiCH_3OSalen$] conductance results from the doping of solvated polymer domains and is accompanied by solvent egress from the polymer film whereas the decrease in the conductance at high polymer doping levels is associated with excessive solvent uptake.

The integration of current with respect to time in EQCM measurements shows that when the poly [$NiCH_3OSalen$] film is biased to $V_M$, the amount of charge consumed in the doping process is nearly equal to the amount of charge extracted during the dedoping process and corresponds to half the total charge that can be extracted from the fully doped polymer. It confirms that the main conductance maximum is observed at equal concentrations of neutral and charged redox sites of the polymer film.

## Conclusions

In this work, we presented a study on the electronic conductivity of nickel-salen type metallopolymers poly-[NiSalen] and poly-[$NiCH_3OSalen$]. The electrochemical doping of these polymer films in an OECT-like setup gives bell-shaped conductance profiles. Experimental results can be explained by mixed-valence conductivity between isoenergetic sites of redox states generated in the polymers, with the main conductance maxima observed at equal concentration of occupied and unoccupied sites in a neutral-radical cation mixed-valence systems. The poly-[$NiCH_3OSalen$] film shows a threshold voltage of 0.18 V, a wide conductivity window (over 1.4 V), and a conductance modulation by four orders of magnitude upon increasing the gate bias voltage, which makes it a preferred candidate for OECT applications. Electrochemical quartz

crystal microbalance studies confirm mixed-ionic electronic transport in this polymer film and reveal different regimes of ion and solvent transfer in the polymer at different doping levels. The elucidated structure-property relationships for mixed ionic-electronic transport in nickel-salen polymers can also be useful to other potential applications of these materials, for example, in the field of energy storage.

## REFERENCES


1. **Paulsen B.D., Tybrandt K., Stavrinidou E., Rivnay J.,** Organic mixed ionic-electronic conductors, Nat. Mater. 19 (2020) 13–26.

2. **Rivnay J., Inal S., Salleo A., Owens R.M., Berggren M., Malliaras G.G.,** Organic electrochemical transistors, Nat. Rev. Mater. 3 (2018) 17086.

3. **Paudel P.R., Tropp J., Kaphle V., Azoulay J.D. Lüssem B.,** Organic electrochemical transistors – from device models to a targeted design of materials, J. Mater. Chem. C. 9 (2021) 9761–9790.

4. **Zeglio E., Inganдs O.,** Active Materials for Organic Electrochemical Transistors, Adv. Mater. 30 (2018) 1800941.

5. **Inal S., Malliaras G.G., Rivnay J.,** Benchmarking organic mixed conductors for transistors, Nat. Commun. 8 (2017) 1767.

6. **Rivnay J., Inal S., Collins B., Sessolo M., Stavrinidou E., Strakosas S., Tassone C., Delongchamp D.M., Malliaras G.G.,** Structural control of mixed ionic and electronic transport in conducting polymers, Nat. Commun. 7 (2016) 11287.

7. **Chepurnaya I.A., Karushev M.P., Alekseeva E.V., Lukyanov D.A., Levin O.V.,** Redox-conducting polymers based on metal-salen complexes for energy storage applications, Pure Appl. Chem. 92 (8) (2020) 1239–1258.

8. **Pfeiffer P., Breith E., Lübbe E. Tsumaki T.,** Tricyclische orthokodensierte Nebenvaenzringe, Justus Liebigs Ann. Chem. 503 (1933) 84–130.

9. **Karlsson C., Huang H., Strшmme M., Gogoll A., Sjödin M.,** Ion- and Electron Transport in Pyrrole/Quinone Conducting Redox Polymers Investigated by in Situ Conductivity Methods, Electrochim. Acta. 179 (2015) 336–342.

10. **Sauerbrey G.,** The Use of Quartz Oscillators for Weighing Thin Layers and for Microweighing, Z. Phys. 155 (2) (1959) 206–222.

11. **Salinas G., Frontana-Uribe B.A.,** Analysis of Conjugated Polymers Conductivity by in situ Electrochemical-Conductance Method, ChemElectroChem. 6 (2019) 4105–4117.

12. **Alekseeva E.V., Chepurnaya I.A., Malev V.V., Timonov A.M., Levin O.,** Polymeric nickel complexes with salen-type ligands for modification of supercapacitor electrodes: impedance studies of charge transfer and storage properties, Electrochim. Acta. 225 (2017) 378–391.

13. **Heinze J., Frontana-Uribe B.A., Ludwigs S.,** Electrochemistry of Conducting Polymers–Persistent Models and New Concepts, Chem. Rev. 110 (2010) 4724–4771.

14. **Vilas-Boas M., Henderson M.J., Freire C., Hillman A.R., Vieil E.,** A Combined Electrochemical Quartz-Crystal Microbalance Probe Beam Deflection (EQCM-PBD) Study of Solvent and Ion Transfers at a Poly[Ni(saltMe)]-Modified Electrode During Redox Switching, Chem. Eur. J. 6 (2000) 1160–1167.


## THE AUTHORS


**SMIRNOVA Evgenia A.**
esmirnova@mail.ioffe.ru
ORCID: 0000-0002-5570-6794

**CHEPURNAYA Irina A.**
ichepurnaya@mail.ioffe.ru
ORCID: 0000-0002-8236-577X


*Received 28.10.2022. Approved after reviewing 08.11.2022. Accepted 13.11.2022.*

© Peter the Great St. Petersburg Polytechnic University, 2023

Conference materials
UDC 538.9
DOI: https://doi.org/10.18721/JPM.161.214

# Change of radiative and low-frequency noise characteristics of UV LEDs based on InGaN/GaN quantum wells at liquid nitrogen temperature

A.M. Ivanov ✉, A.V. Klochkov

Ioffe Institute, St. Petersburg, Russia
✉ post@mail,ioffe.ru

**Abstract.** The results of temperature studies of UV-band LEDs based structures with InGaN/GaN quantum wells are presented. At room temperature and liquid nitrogen temperature, volt-ampere characteristics, frequency dependences of low-frequency noise density, external quantum efficiency, and optical power were measured. The performed studies showed differences in the characteristics of UV LEDs at temperatures $T = 77.4$ K from those at $T = 295$ K. The possible physical mechanisms of the formation of low-frequency current noise, carrier transport, and the effect on the external quantum efficiency of the processes of radiative and non-radiative recombination at two temperatures are considered.

**Keywords:** the external quantum efficiency, the density of current noise, the tunneling current

**Citation:** Ivanov A.M., Klochkov A.V., Change of radiative and low-frequency noise characteristics of UV LEDs based on InGaN/GaN quantum wells at liquid nitrogen temperature, St. Petersburg State Polytechnical University Journal. Physics and Mathematics. 16 (1.2) (2023) 96–102. DOI: https://doi.org/10.18721/JPM.161.214

This is an open access article under the CC BY-NC 4.0 license (https://creativecommons.org/licenses/by-nc/4.0/)

Материалы конференции
УДК 538.9
DOI: https://doi.org/10.18721/JPM.161.214

# Изменение излучательных и низкочастотных шумовых характеристик УФ светодиодов на основе InGaN/GaN квантовых ям при температуре жидкого азота

А.М. Иванов ✉, А. В. Клочков

Физико-технический институт им. А.Ф. Иоффе РАН, Санкт-Петербург, Россия
✉ post@mail.Ioffe.ru

**Аннотация.** Представлены результаты температурных исследований светодиодов УФ диапазона на основе структур с InGaN/GaN квантовыми ямами. При комнатной температуре и температуре жидкого азота измерялись вольт-амперные характеристики, частотные зависимости плотности низкочастотного шума, внешней квантовой эффективности, оптической мощности. Рассмотрены возможные физические механизмы формирования низкочастотного токового шума, транспорта носителей, и влияние на внешнюю квантовую эффективность процессов излучательной и безызлучательной рекомбинации при двух температурах.

**Ключевые слова:** внешняя квантовая эффективность, плотность токового шума, туннельный ток

**Ссылка при цитировании:** Иванов А.М., Клочков А.В. Изменение излучательных и низкочастотных шумовых характеристик УФ светодиодов на основе InGaN/GaN квантовых ям при температуре жидкого азота // Научно-технические ведомости

© Ivanov A.M., Klochkov A.V., 2023. Published by Peter the Great St. Petersburg Polytechnic University.

СПбГПУ. Физико-математические науки. 2023. Т. 16. № 1.2. С. 96–102. DOI: https://doi.org/10.18721/JPM.161.214

Статья открытого доступа, распространяемая по лицензии CC BY-NC 4.0 (https://creativecommons.org/licenses/by-nc/4.0/)

## Introduction

Optoelectronic devices based on nitride materials are currently widely used in various manufacturing industries. A significant increase in the production of UV LEDs (and lasers) based on InGaN/GaN and AlGaN/GaN is associated with the areas of application of light-emitting devices in this range. UV LEDs and lasers are used in industrial and agricultural production, as well as in criminology, banking and solid-state lighting. Of particular importance is the use of these optoelectronic devices in medicine, biology and sanitation.

The modern literature presents works aimed at improving the light-emitting characteristics (often only in the form of mathematical modeling), operability and reliability of semiconductor optoelectronic devices. Temperature measurements more affect the region of elevated temperatures [1–3]. Therefore, the change at reduced temperatures of radiative and noise characteristics [4–7] is of research interest.

With a decrease in temperature, the optical power increases and the degradation of LEDs slows down; the noise density of semiconductor diodes decreases. It has been experimentally established that external quantum efficiency in the range of low pumping current densities (less than 30 A/cm$^2$) increases monotonically with temperature decrease [8]. The radiative recombination increases due to an improvement in the distribution of carriers in the phase space.

Studies of noise density, its spectral composition are used to study degradation processes and forecast service life [9], for comparative studies of UV LEDs and LEDs in visible range [10, 11], improve the reliability of designed optoelectronic, semiconductor devices, and improve their production technology.

Comparative studies performed in this work at room temperature and nitrogen temperature were aimed at identifying differences in the operation of UV LEDs and the possibility of improving their characteristics under conditions of reduced temperatures. Mechanisms of formation of low-frequency current noise and recombination, transport of carriers to active area of InGaN/GaN quantum structures are considered.

## Experimental

The experiments were carried out on commercially manufactured UV (UV-A) LEDs from Betlux with InGaN/GaN quantum well (X: BL-L563VC with peak radiation energy $h_{QW} = 3.06$ eV or radiation wavelength $\lambda = 405$ nm, nominal current $I = 20$ mA, luminous intensity of 100 mcd and Y: BL-L522VC with the same parameters and luminous intensity of 180 mcd). The actual area of LEDs is ~ $10^{-3}$ cm$^2$. Also, control measurements were carried out on blue indicator LEDs from Nichia NSPB300, $h_{QW} = 2.36$ eV, $\lambda = 465$ nm, external quantum efficiency $\eta = 15\%$, luminous intensity is 2300 mcd. Measurements of current, photocurrent and density of low frequency current noise were made at room ($T = 295$ K) and nitrogen temperatures ($T = 77.4$ K). The silicon photodiode FD-24K was located at a strictly fixed distance from the LED and was used to measure only relative changes in the emission intensity (photocurrent) and external quantum efficiency. The power source was a GPS-4303 DC device; the voltage was set using a high-precision Agilent 34401A multivoltmeter. The photocurrent in the short-circuit mode was measured by a digital ammeter.

The time dependence of voltage deviations at the load resistance $R_L = 100$ Ω in the range of three decades of frequency (with a maximum frequency of 7.3 kHz) was measured using an analog–to-digital converter (own noise level 1 μV). The semi-automatic installation was used to measure the density of low-frequency current noise (in four bands with central frequencies of 20, 70, 270 and 1000 Hz) and its frequency dependence. The computer program remembered $2 \cdot 10^6$ samples with a sampling frequency of 16 kHz. A detailed description of the experimental setup is given in [12].

© Иванов А.М., Клочков А.В., 2023. Издатель: Санкт-Петербургский политехнический университет Петра Великого.

## Results and Discussion

Figure 1, *a* shows the results of measuring the optical power (photodiode current) as a function of the current at forward bias $I$ for LED X. At $T = 295$ K, the dependence of the photocurrent has the character of $I_{ph} \propto I^{1.5}$ at $I \leq 100$ μA, at $I \geq 1$ mA it is close to $I_{ph} \propto I$. At $T = 77.4$ K at $0.1 \leq I \leq 1$ mA, there is a significant slowdown in the growth of the photocurrent, followed by its acceleration at high currents. The dependence of the photocurrent at low temperature first exceeds the photocurrent at room temperature, and after the deceleration section becomes less than it.

Figure 1, *b* represents the dependences of the external quantum efficiency of LED X on the current $\eta(I)$ for two temperatures. At $T = 295$ K, the curve has a traditional character with saturation and a slight drop at nominal current. At $T = 77.4$ K at $I \leq 0.1$ mA, the quantum efficiency greatly exceeds the efficiency at room temperature. A significant decrease in efficiency coincides with the region of currents slowing down the growth of photocurrent. The subsequent increase in the efficiency at $I \geq 4$ mA corresponds to the region of a rapid increase in the photocurrent (at $T = 77.4$ K) and saturation and an insignificant drop in the quantum efficiency (at $T = 295$ K).

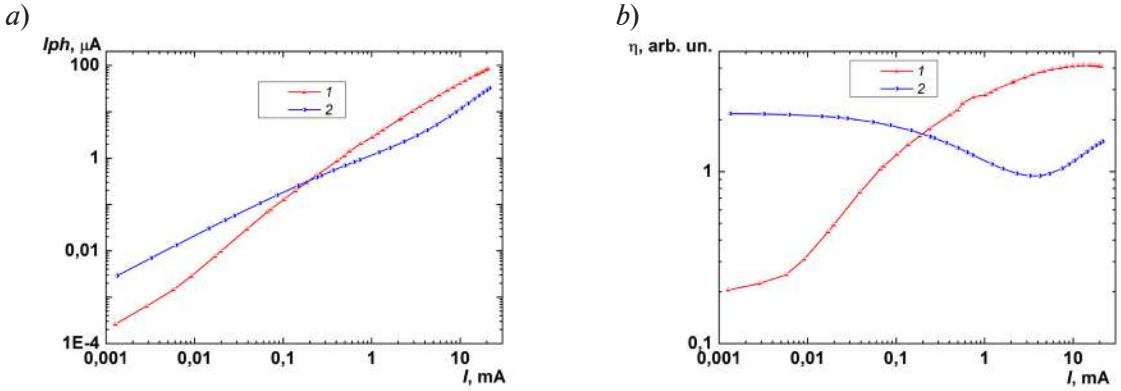


Fig. 1. Photocurrent (*a*), external quantum efficiency (*b*) of UV LED at $T = 295$ (1) and 77.4 (2) K at forward bias for LED X

For comparative studies, measurements of photocurrent and external quantum efficiency in blue LEDs were carried out. Fig. 2, *a* shows the dependence of the optical power on the current at forward bias. At $T = 295$ K, the dependence is close to $I_{ph} \propto I$. And at $T = 77.4$ K, the threshold current $I_{th} = 0.24$ μA; at $I = 0.1 \div 2.0$ mA, the growth of the photocurrent slows down (sublinear dependence) and it becomes less than at $T = 295$ K. Fig. 2, *b* represents graphs of current dependences $\eta(I)$ of a blue LED. Dependencies qualitatively repeat the picture of Fig. 1, *b*. The efficiency of the blue LED at $T = 77.4$ K at $I \geq 0.04$ mA begins to decrease and becomes less than the efficiency at $T = 295$ K. At nominal current, a slight increase in η is manifested, which was not observed before [13].

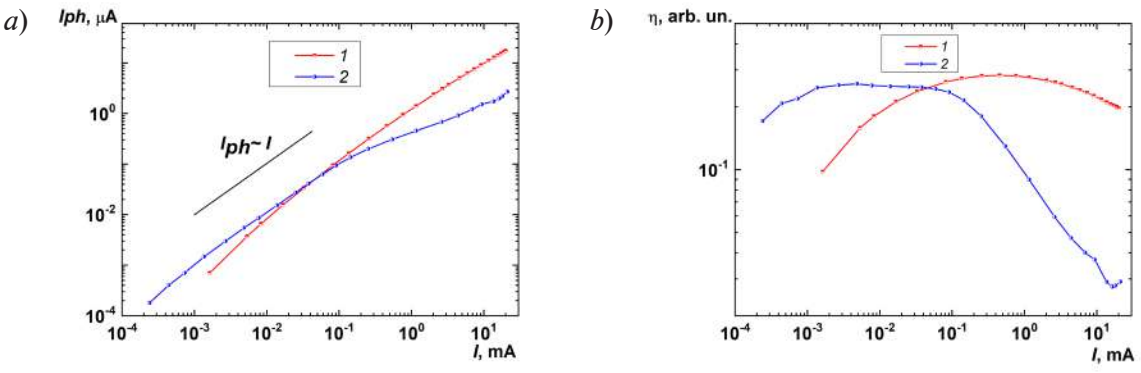


Fig. 2. Photocurrent (*a*) and external quantum efficiency (*b*) of blue LED at T = 295 (1) and 77.4 (2) K at forward bias

When the temperature drops below room temperature, the external quantum efficiency increases (in the case of UV LEDs at $I \leq 0.2$ mA), which is explained by *a*) a decrease in the rate of non-radiative recombination; *b*) an increase in the rate of radiative recombination due to greater overlap of the wave functions of the electron and the hole. The change in the filling of the phase dk space with a decrease in temperature contributes to this, because the number of carriers per interval dk in k-space decreases with an increase in temperature [14] and increases with a decrease in temperature. *c*) At low temperatures ($T < 80$ K), the movement of carriers into quantum wells QWs becomes ballistic or quasi-ballistic [5]. In general, the transport of electrons and holes to the active zones is improving; d) tunnel leakages of charge carriers from QWs to the space charge region are reduced [15, 16].

In the studies performed with a slowdown in the growth of photocurrent at liquid nitrogen temperature, a significant drop in the external quantum efficiency at this temperature is observed. In contrast to [8], where a monotonous increase in efficiency was observed with a decrease in temperature to $T = 160$ K in the same current range, in the presented work the quantum efficiency at $T = 77.4$ K becomes less than the efficiency at $T = 295$ K (for $I \geq 0.2$ mA).

In the ABC model [17], the internal quantum efficiency is $\eta_{int} = Bn^2/\{An + Bn^2 + Cn^3 + F(n)\}$, where $n$ is the carrier concentration, $A$, $B$, $C$ are the coefficients of non-radiative Shockley-Reed-Hall recombination, radiative recombination and non-radiative Auger recombination, respectively. The fourth term in the denominator $F(n)$ is added to take into account the possible outflow of carriers from the QW to the barriers [18]. The temperature dependences of $A$, $B$, $C$ are presented in [2], and in [19] the current dependences of recombination rates are given for various mechanisms. Based on these articles, it can be concluded that *a*) as the temperature decreases, $B$ and $C$ coefficients decrease; *b*) as the current increases, the concentration of n increases, which leads to an increase in $A$ and a decrease in $B$. The coefficient $C$ (Auger recombination) seems to change little in this range of currents. Associated with these changes is the decreasing part of the current dependence of the quantum efficiency at $T = 77.4$ K (Fig. 1, *b*). The subsequent increase in efficiency ($I > 4$ mA) is determined by the superiority of the rate of radiative recombination over the rates of non-radiative recombination [19].

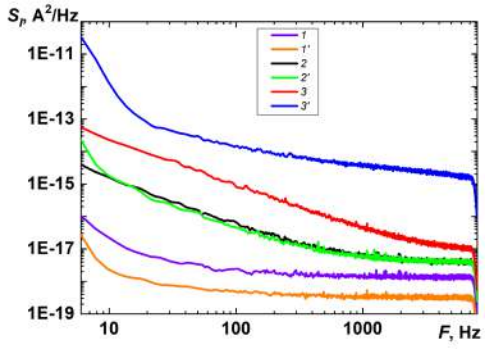


Fig. 3. Frequency dependence of the spectral density of current noise for LEDs X – 1,2, 1',2'; Y – 3, 3' at $T = 295$ (1, 2, 3) and 77.4 (1', 2', 3') K at a current of 2.2 (1), 2.0 (1'), 20.7 (2), 20.3 (2'), 21.0 (3), 20.0 (3') mA

Figure 3 shows the frequency dependences of the current noise density for the UV LEDs X and Y. These dependences have a sharper slope ($\infty 1/f^{\alpha}$) in the low-frequency part of the spectrum, $1 < \alpha \leq 4$. This is most clearly manifested for the dependences at $T = 77.4$ K, where both LEDs X and Y have the highest $\alpha$ value. This may be due to the addition of two or more low-frequency noise mechanisms. An increase in noise density with an increase in the magnitude of the current (dependence 1, 1', 2, 2') at frequencies > 3000 Hz indicates an increase in frequency independent noise. Noise with a "white" spectrum at these frequencies is associated with shot noise due to random photon radiation [9] and increases with current growth at forward bias to the value ~ $10^{15}$ A/Hz.

The observed increase in noise density in the low frequency region suggests the participation of several types of noise in the formation of frequency dependencies. These can be flicker noise,

telegraph noise, generation recombination noise, and noise related with the defect-assisted tunneling.

The high density of defects in InGaN/GaN-based LEDs provides tunneling transport of charge carriers (trap-assisted tunneling (TAT), model [20]) to the active region through potential barriers. In the TAT mechanism, the determining factor is the distance between the centers, since tunneling in the space charge region SCR occurs along deep centers and tails of the density of states of the bands. Near the QW, their density is minimal. At low temperatures, this type of carrier transport becomes predominant [21]. The dual role of defects in the SCR is manifested in the provision of carrier transport and participation in recombination processes.

The low-frequency tunnel resistance noise associated with charge fluctuations at the levels during horizontal jumps (model [12]) is represented by the same mathematical description as the generation-recombination noise [22]. The latter is determined by vertical transitions between centers and free bands. In tunneling transport, the low-frequency current noise is determined by the random distribution of centers over the SCR at the tunneling level. The hopping frequency depends exponentially on the distance between the centers, which is determined by their density [23]. An increase in the tunneling transport of carriers through barriers in a QW is possible due to a change in the spectrum of defects during the flow of current, unevenly distributed over the cross section of the LED [7, 24]. These changes can be caused by non-radiative recombination processes. The amount of energy released in them is close to the semiconductor band gap [19, 25].

The calculated dependences of current on voltage at the $p$-$n$-junction $I(V_I)$ were approximated by the exponential function $I = I_0 \exp(qV_I/n_I(V_I)kT)$, where $kT$ is the thermal energy, $q$ is the elementary charge, and $n_I(V_I)$ is the ideality factor, which determines the features of the current flow, was calculated as $n_I = (q/kT)/(\mathrm{d}lnI/\mathrm{d}V_I)$. The obtained values $n_I(I) \geq 2$ (for $T = 295$ K) only for $I \leq 10$ μA. In the rest of the current range, the values $n_I(I) < 2$. This suggests that the above-barrier injection of carriers into the QW is dominant in almost the entire measured range of currents, while the fraction of the tunneling current is insignificant. At liquid nitrogen temperature, $n_I > 2$ in the current range $I \leq 3$ mA, i.e. hopping conductivity (tunneling) through defects predominates. Consequently, at $T = 77.4$ K, the contribution of noise associated with tunneling through defects is significant, while at $T = 295$ K, other types of noise are mainly manifested.

## Conclusion

The performed studies showed differences in the characteristics of UV LEDs at low temperatures ($T = 77.4$ K) from room temperatures. Despite the increase in the external quantum efficiency at low currents (< 0.2 mA) at $T = 77.4$ K, at high currents there was a drop in efficiency compared to the external quantum efficiency at room temperature. At the temperature of liquid nitrogen in the transport of carriers the role of tunneling by defects increases. The spectrum of defects can change due to the energy released during recombination. A manifestation of this is a sharp increase in noise at the lowest frequencies ≤ 20 Hz, which is due to the addition of several noise mechanisms. The behavior of the external quantum efficiency and density of low-frequency current noise at intermediate temperatures is interesting.

## REFERENCES

1. **Peng Z., Guo W., Wu T., Guo Z., Lu Y., Zheng Y., Lin Y., Chen Z.,** Temperature-Dependent Carrier Recombination and Efficiency Droop of AlGaN Deep Ultraviolet Light-Emitting Diodes, IEEE Photonics Journal. 12 (1) (2020) 8200108.

2. **Tian P., McKendry J.J.D., Herrnsdorf J., Watson S., Ferreira R., Watson I.M., Gu E., Kelly A.E., Dawson M.D.,** Temperature-dependent efficiency droop of blue InGaN micro-light emitting diodes, Applied Physics Letters. 105 (2014) 171107.

3. **Monti D., Meneghini M., De Santi C., Meneghesso G., Zanoni E.,** Degradation of UV-A LEDs: Physical Origin Dependence on Stress Conditions, IEEE Transactions on Device and Materials Reliability. 16 (2) (2016) 213–219.

4. **Marcinkevicius S., Yapparov R., Kuritzky L.Y., Wu Y-R., Nakamura S., Speck J.S.,** Low-temperature carrier transport across InGaN multiple quantum wells: Evidence of ballistic hole transport, Physical Review B. 101 (2020) 075305.

5. **Arteev D.S., Sakharov A.V., Nikolaev A.E., Lundin W.V., Tsatsulnikov A.F.,** Temperature-dependent luminescent properties of dual-wavelength InGaN, Journal of Luminescence. 234 (2021) 117957.

6. **Bochkareva N.I., Voronenkov V.V., Gorbunov R.I., Zubrilov A.S., Lelikov Y.S., Latyshev F.E., Rebane Y.T., Tsyuk A.I., Shreter Y.G.,** Mechanism of efficiency droop in GaN light-emitting diodes, Semiconductors. 44 (6) (2010) 794–800.

7. **Emtsev V.V., Gushchina E.V., Petrov V. NTal'nishnih., N.A., Chernyakov A.E., Shabunina E.I., Shmidt N.M., Usikov A.S., Kartashova A.P., Zybin A.A., Kozlovski V.V., Kudoyarov M.F., Saharov A.V., Oganesyan A.G., Poloskin D.S., Lundin V.V.,** Diversity of Properties of Device Structures Based on Group-III Nitrides, Related to Modification of the Fractal-Percolation System, Semiconductors. 52 (7) (2018) 942–949.

8. **Pavluchenko A.S., Rozhansky I.V., Zakheim D.A.,** Manifestation of the injection mechanism of efficiency droop in the temperature dependence of the external quantum efficiency of AlInGaN-based light-emitting diodes, Semiconductors. 43 (10) (2009) 1351–1356.

9. **Šaulys B., Matukas J., Palenskis V., Pralgauskaite S., Kulikauskas G.,** Light-Emitting Diode Degradation and Low-Frequency Noise Characteristics, Acta Physica Polonica A. 119 (2011) 514–520.

10. **Sawyer S., Rumyantsev S.L., Pala N., Shur M.S., Bilenko Yu., Gaska R., Kosterin P., Salzberg M.,** Noise characteristics of 340 nm and 280 nm GaN-based light emitting diodes, International Journal of High Speed Electronics and Systems. 14 (3) (2004) 702–707.

11. **Rumyantsev S.L., Sawyer S., Shur M.S., Pala N., Bilenko Yu., Zhang J.P., Hu X., Lunev A., Deng J., Gaska R.,** Low-frequency noise of GaN-based ultraviolet light-emitting diodes, Journal of Applied Physics. 97 (2005) 123107.

12. **Bochkareva N.I., Ivanov A.M., Klochkov A.V., Shreter Y.G.,** Current noise and efficiency droop of light-emitting diodes due to defect-related tunneling of carriers from InGaN/GaN quantum well, Semiconductors. 53 (1) (2019) 99–105.

13. **Bochkareva N.I., Zhirnov E.A., Efremov A.A., Rebane Y.T., Gorbunov R.I., Shreter Y.G.,** Tunnel-Recombination Currents and Electroluminescence Efficiency in InGaN/GaN LEDs, Semiconductors. 39 (5) (2005) 594–599.

14. **Schubert F.E.,** Light − Emitting Diodes, Cambridge University Press, Cambridge, 2006.

15. **Bochkareva N.I., Voronenkov V.V., Gorbunov R.I., Latyshev F.E., Lelikov Y.S., Rebane Y.T., Tsyuk A.I., Shreter Y.G.,** Tunnel Injection and Power Efficiency of InGaN/GaN Light-Emitting Diodes, Semiconductors. 47 (1) (2013) 127–134.

16. **Bochkareva N.I., Shreter Y.G.,** Localization of Charge Carriers in InGaN/GaN Quantum Wells Limited by Space Charge, Solid State Physics. 64 (3) (2022) 371–378 (In Russ.).

17. **Karpov S.Yu.,** ABC-model for interpretation of internal quantum efficiency and its droop in III-nitride LEDs: a review, Optical Quantum Electronics. 47 (2015) 1293–1303.

18. **Lv Q., Gao J., Tao X., Zhang J., Mo C., Wang X., Zheng C., Liu J.,** Analysis of dominant non-radiative recombination mechanisms in InGaN green LEDs grown on silicon substrates, Journal Luminecsence. 222 (2020) 117186.

19. **Renso N., De Santi C., Caria A., Dalla Torre F., Zecchin L., Meneghesso G., Zanoni E., Meneghini M.,** Degradation of InGaN-based LEDs: Demonstration of a recombination-dependent defect-generation process, Journal of Applied Physics. 127 (2020) 185701.

20. **Auf der Maur M., Galler B., Pietzonka I., Strassburg M., Lugauer H., Di Carlo A.,** Trap-assisted tunneling in InGaN/GaN single-quantum-well light-emitting diodes, Applied Physics Letters. 105 (2014) 133504.

21. **Molnar R.J., Lei T., Moustakas T.D.,** Electron transport mechanism in gallium nitride, Applied Physics Letters. 62 (1993) 72–76.

22. **D'yakonova N.V., Levinshtein M.E., Rumyantsev S.L.,** Nature of 1/*f* volume noise in GaAs and Si, Soviet Physics Semiconductors 25 (1991) 1241–1275.

23. **Bochkareva N.I., Ivanov A.M., Klochkov A.V., Shreter Y.G.,** Gaussian impurity bands in GaN and weakening of carrier confinement in InGaN/GaN quantum wells, Journal of Physics: Conference Series 1697 (2020) 012203.

24. **Chernyakov A.E., Levinshtein M.E., Talnishnikh N.A., Shabunina E.I., Shmidt N.M.,** Low-frequency noise in diagnostics of power blue InGaN/GaN LEDs, Journal of Crystal Growth. 401 (2014) 302–304.

25. **Yassievich I. N.,** Recombination-induced defect heating and related phenomena, Semiconductor Science and Technology. 9 (8) (1994) 1433–1453.

## THE AUTHORS

**IVANOV Aleksandr M.**
alexandr.ivanov@mail.ioffe.ru
ORCID: 0000-0003-4824-0364

**KLOCHKOV Aleksandr V.**
alex.klo@mail.ioffe.ru
ORCID: 0000-0002-2931-4607

*Received 31.10.2022. Approved after reviewing 14.11.2022. Accepted 15.11.2022.*

© Peter the Great St. Petersburg Polytechnic University, 2023

# PHYSICAL OPTICS

Conference materials
UDC 681.7.069.24
DOI: https://doi.org/10.18721/JPM.161.215

## Fabrication of silicon optical nanoantennas by ultrahigh vacuum STM lithography

V.A. Shkoldin [1,2]✉, D.V. Lebedev [1,3,4], D.V. Permyakov [2], A.O. Golubok [4], A.V. Arkhipov [5], A.K. Samusev [2], I. S. Mukhin [1,5]

[1] St. Petersburg Academic University, St. Petersburg, Russia;
[2] Dept. of Physics and Engineering, ITMO University, St. Petersburg, Russia;
[3] St. Petersburg State University, St. Petersburg, Russia;
[4] Institute for analytical instrumentation RAS, St. Petersburg, Russia;
[5] Peter the Great St. Petersburg Polytechnic University, St. Petersburg, Russia
✉ shkoldin@spbau.ru

**Abstract.** The paper reports on experiments on the observation of scanning tunnel microscope (STM)-induced light emission (STM-LE) from bare silicon surfaces and modified with STM lithography. We produced nanoscale hillocks (nanokhobs) on a crystalline Si substrate, which can be considered as nanoantennas enhancing STM-LE effect. Our experiments show that the nanoknobes formed on the surface of the original substrate did not provide the achievement of the goal. However, in-situ deposition of a 10 nm thick additional layer of undoped Si resulted in the increase of STM-LE quantum efficiency by an order of magnitude in comparison with original substrate. This effect paves the way for the fabrication of nanoscale electrically-driven light sources required for hybrid optoelectronic chips.

**Keywords:** scanning tunneling microscopy, tunnel contact, emission from a tunnel contact, silver film, photonics, ultrahigh vacuum

**Funding:** This study was funded by Russian Science Foundation, grant number 21-79-10346.

**Citation:** Shkoldin V.A., Lebedev D.V., Permyakov D.V., Golubok A.O., Arkhipov A.V., Samusev A.K., Mukhin I.S., Fabrication of silicon optical nanoantennas by ultrahigh vacuum STM lithography, St. Petersburg State Polytechnical University Journal. Physics and Mathematics. 16 (1.2) (2023) 103–107. DOI: https://doi.org/10.18721/JPM.161.215

This is an open access article under the CC BY-NC 4.0 license (https://creativecommons.org/licenses/by-nc/4.0/)

Материалы конференции
УДК 681.7.069.24
DOI: https://doi.org/10.18721/JPM.161.215

## Изготовление кремниевых оптических наноантенн методом сверхвысоковакуумной СТМ-литографии

В.А. Школдин [1,2]✉, Д.В. Лебедев [1,3,4], Д.В. Пермяков [2], А.О. Голубок [4], А.В. Архипов [5], А.К. Самусев [2], И.С. Мухин [1,6]

[1] Алферовский Университет, Санкт-Петербург, Россия;
[2] Физический Факультет, Университет ИТМО, Санкт-Петербург, Россия;
[3] Санкт-Петербургский государственный университет, Санкт-Петербург, Россия;
[4] Санкт-Петербургский политехнический университет Петра Великого, Россия
✉ shkoldin@spbau.ru

**Аннотация.** В статье сообщается об исследовании эмиссии света, индуцированной СТМ-контактом с чистой кремниевой поверхностью и модифицированной методом

© Shkoldin V.A., Lebedev D.V., Permyakov D.V., Golubok A.O., Arkhipov A.V., Samusev A.K., Mukhin I.S., 2023. Published by Peter the Great St. Petersburg Polytechnic University.

СТМ-литографии. На поверхности кремния были созданы нанохолмы, выступающие в роли наноантенн, усиливающие эффект эмиссии света. Однако, они не обеспечили достижение поставленной цели. Тем не менее, осаждение дополнительного слоя нелегированного кремния толщиной 10 нм привело к увеличению квантовой эффективности по сравнению с исходной подложкой. Этот эффект позволит изготавливать наноразмерные электрически управляемые источники света, необходимые для гибридных оптоэлектронных чипов.

**Ключевые слова:** сканирующая туннельная микроскопия, туннельный контакт, излучение из туннельного контакта, серебряная пленка, фотоника

**Финансирование:** Работа выполнена при поддержке Российского Научного Фонда проект № 21-79-10346.

**Ссылка при цитировании:** Школдин В.А., Лебедев Д.В., Пермяков Д.В., Голубок А.О., Архипов А.В., Самусев А.К., Мухин И.С. Изготовление кремниевых оптических наноантенн методом сверхвысоковакуумной СТМ-литографии // Научно-технические ведомости СПбГПУ. Физико-математические науки. 2023. Т. 16. № 1.2. С. 103–107. DOI: https://doi.org/10.18721/JPM.161.215

Статья открытого доступа, распространяемая по лицензии CC BY-NC 4.0 (https://creativecommons.org/licenses/by-nc/4.0/)

## Introduction

The growing importance of information technologies requires the continuous increase of data processing capabilities. The most common way to enhance computing performance consists in the use of multicore systems, which also helps to overcome the problem of the heat produced by processor chips. However, the total performance of multicore systems is often limited by the efficiency of interconnections [1], and this restriction becomes more severe with the increase in the number of cores. Conventional interconnections made of metal wires or cables have inherent limitations in bandwidth, transferred power density, and their length is restricted due to relatively high resistance. Interconnections based on optical links have no such limitations [2]. This approach is not yet widely used mostly due to the unsolved acute problem of miniaturization of optical sources, while other advanced small-size components of optical links are already developed and commercially available [3–5].

One of the possible ways to develop compact light sources is to use the phenomenon of light emission by tunneling electrons [6]. Tunnel junctions have sizes of the order of several nanometers [7] and they are capable to support high-frequency modulation. Until recently, all light sources based on metal-insulator-metal tunnel junctions had a critical drawback, i.e. their quantum yield was very low: typical values corresponded to the range of $10^{-6}$–$10^{-5}$ photons per electron. However, for the last decade it has been demonstrated that optical nanoantennas placed near a tunnel junction can substantially enhance the light emission, which renewed interest of researchers to this type of light sources.

In this paper, we report on the study of a method for the fabrication of silicon hillocks (nanoknobs) on silicon substrates. We have suggested that such features can act as nanoantennas enhancing light emission from tunnel contacts based on the metal tip of scanning tunnel microscope (STM) and the studied silicon features. The obtained results are essential for the development of complementary metal-oxide-semiconductor (CMOS) compatible electrically driven compact light sources.

## Experiment

The experiments were performed in ultra-high vacuum (UHV) conditions in the chamber of a VT AFM XA 50/500 microscope (Scienta Omicron, Germany) which has been upgraded with optical scheme to allow the direct measurements of light emission from STM tunnel junctions (STM-LE). For STM experiments, we employed commercially available Pt/Ir-tips DPT10 (Bruker, USA). Single photon counter ID120 (IDQuantique, Switzerland) with spectral sensitivity in the range of 450–960 nm was used as an optical detector. The used experimental setup has been described in detail elsewhere [8].

© Школдин В.А., Лебедев Д.В., Пермяков Д.В., Голубок А.О., Архипов А.В., Самусев А.К., Мухин И.С., 2023. Издатель: Санкт-Петербургский политехнический университет Петра Великого.

The studied structures were formed on a silicon wafer with (001) surface orientation and high doping level (ca. $10^{19}$ – $10^{20}$ $cm^{-3}$). Before being loaded to STM chamber the substrate was cleaned in 20% HF solution for 5 minutes and then annealed in UHV vacuum at 120 °C for 45 minutes.

In our studies, the original silicon wafer showed STM-induced luminescence with the estimated quantum efficiency not higher than $5 \cdot 10^{-7}$ photons per electron (this result has been previously reported in [9]). This value can be improved by modification of tunnel gap morphology [10] or by introduction of an optical nanoantenna into the tunnel junction [8, 11]. We produced hillocks (nanoknobs) on the Si substrate by applying series of short voltage pulses with deactivated microscope feedback: STM lithography (see STM images in Fig. 1). The bias pulses have triangle shape with an amplitude from –7 V to +7 V and reversal. The duration of each pulse was 200 ms. Initial setpoint was 0.1 nA at 2 V and it was maintained between repetitions. It should be mentioned that nanoknobs are known to operate as optical nanoantennas enhancing STM-LE response [12]. However, our studies did not prove any notable change in the optical emission after surface modification.

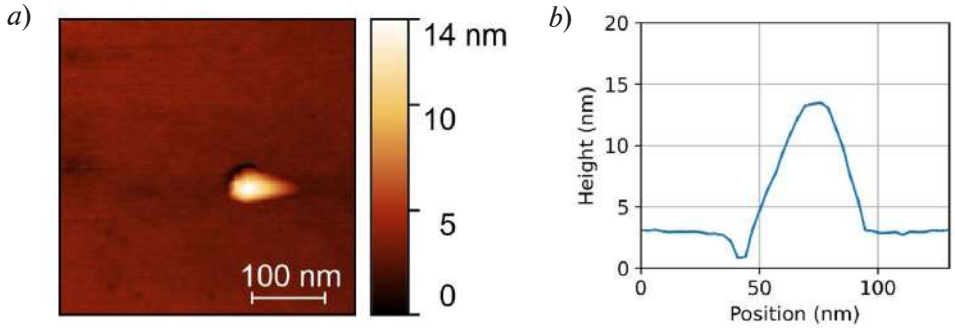


Fig. 1. Typical STM image of the obtained single nanoknob (white spot) on a Si substrate surface (a). Cross-section of single nanoknob topography corresponding to olive line on topography (*b*)

On the next step, inside the STM chamber, a 10 nm layer of undoped Si was thermally deposited on the patterned substrate and the set of nanoknobs was produced with the same STM lithography settings. The fabricated nanoknobs had the approximately the same shape as for the case of bare Si substrate.

Then, the STM-LE measurements were repeated, with bias voltage ramped between −10 V and +10 V while the tip position feedback was deactivated. In these experiments, quantum efficiency at 4.4 V bias was estimated as ca. $4 \cdot 10^{-6}$ photons per electron, which is approximately an order of magnitude higher than that for the sample without additional silicon layer (Fig. 2). We attribute this effect to STM-LE improvement caused by the enhancement of local density of optical states in nanoknobs [12]. The second peak at higher bias values observed in the quantum efficiency dependence in Figure 2 can have a different nature: we explain it by silicon nanostructuring

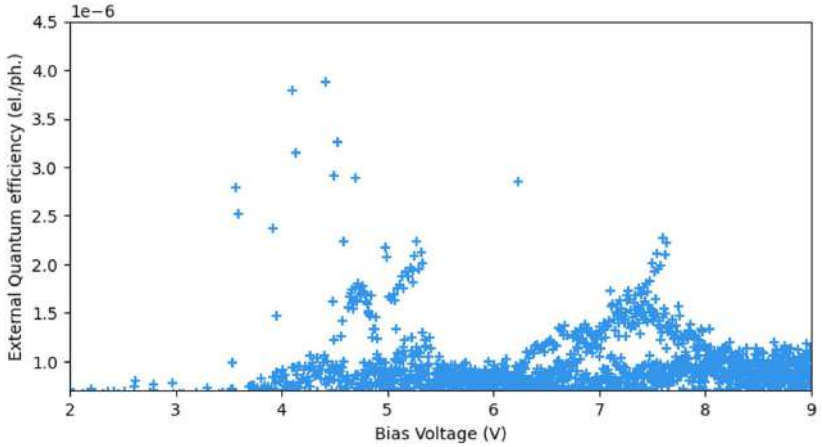


Fig. 2. A plot of estimated STM-LE quantum efficiency vs bias voltage for Si nanoknobs, measured for a tunnel junction between Pt/Ir STM tip and Si substrate with additional 10 nm Si layer

in the nanoknob improving its electroluminescence. At relatively high bias (exceeding 5.5 V) nanocrystals in Si can demonstrate electroluminescence in the visible spectral range due to direct charge carriers' injection and their recombination [13, 14].

## Conclusion

The experiments performed have shown that quantum efficiency of the STM-LE on silicon surface can by increased by nanoscale local modification of the material. This technique can be used for the fabrication of CMOS-compatible nanoscale light sources demanded for the development of electro-optical integrated circuits.

## Acknowledgments

This work was supported by the Russian Science Foundation (project no. 21-79-10346 of the Russian Science Foundation). The studies were carried out using the equipment of the St. Petersburg State University Research Park "Centre for Physical methods of surface investigation".

## REFERENCES

1. **Mattsson P.P.,** Why Haven't CPU Clock Speeds Increased in the Last Few Years?, (2014). https://www.comsol.com/blogs/havent-cpu-clock-speeds-increased-last-years/.

2. **Sun C., Wade M.T., Lee Y., Orcutt J.S., Alloatti L., Georgas M.S., Waterman A.S., Shainline J.M., Avizienis R.R., Lin S., Moss B.R., Kumar R., Pavanello F., Atabaki A.H., Cook H.M., Ou A.J., Leu J.C., Chen Y.H., Asanović K., Ram R.J., Popović M.A., Stojanović V.M.,** Single-chip microprocessor that communicates directly using light, Nature. 528 (2015) 534–538.

3. **Maram R., Kaushal S., Azaca J., Chen L.R.,** Recent Trends and Advances of Silicon-Based Integrated Microwave Photonics, Photonics. 6 (2019).

4. **Xu X., Tan M., Corcoran B., Wu J., Nguyen T.G., Boes A., Chu S.T., Little B.E., Morandotti R., Mitchell A., Hicks D.G., Moss D.J.,** Photonic Perceptron Based on a Kerr Microcomb for High-Speed, Scalable, Optical Neural Networks, Laser Photon. Rev. 14 (2020) 2000070.

5. **Alexoudi T., Kanellos G.T., Pleros N.,** Optical RAM and integrated optical memories: a survey, Light Sci. Appl. 9 (2020) 91.

6. **Lambe J., McCarthy S.L.,** Light Emission from Inelastic Electron Tunneling, Phys. Rev. Lett. 37 (1976) 923–925.

7. **Kuhnke K., Große C., Merino P., Kern K.,** Atomic-Scale Imaging and Spectroscopy of Electroluminescence at Molecular Interfaces, Chem. Rev. 117 (2017) 5174–5222.

8. **Lebedev D.V., Shkoldin V.A., Mozharov A.M., Permyakov D.V., Dvoretckaia L.N., Bogdanov A.A., Samusev A.K., Golubok A.O., Mukhin I.S.,** Scanning Tunneling Microscopy-Induced Light Emission and I (V) Study of Optical Near-Field Properties of Single Plasmonic Nanoantennas, J. Phys. Chem. Lett. 12 (2021) 501–507.

9. **Liu Y., Chua S.-J., Gao S., Hu W., Guo Y.,** Electroluminescence in plasmonic actuator based on $Au/SiO_2$/n-Si tunnel junction, Nanophotonics. 10 (2021) 3487–3496.

10. **Shkoldin V.A., Permyakov D.V., Ladutenko K.S., Zhukov M.V., Vasiliev A.A., Golubok A.O., Uskov A.V., Bolshakov A.D., Bogdanov A.A., Samusev A.K., Mukhin I.S.,** Crucial Role of Metal Surface Morphology in Photon Emission from a Tunnel Junction at Ambient Conditions, J. Phys. Chem. C. 123 (2019) 8813–8817.

11. **Parzefall M., Novotny L.,** Optical antennas driven by quantum tunneling: a key issues review, Reports Prog. Phys. 82 (2019) 112401.

12. **Lebedev D.V., Shkoldin V.A., Mozharov A.M., Larin A.O., Permyakov D.V., Samusev A.K., Petukhov A.E., Golubok A.O., Arkhipov A.V., Mukhin I.S.,** Nanoscale Electrically Driven Light Source Based on Hybrid Semiconductor/Metal Nanoantenna, J. Phys. Chem. Lett. 13 (2022) 4612–4620.

13. **Ledoux G., Gong J., Huisken F., Guillois O., Reynaud C.,** Photoluminescence of size-separated silicon nanocrystals: Confirmation of quantum confinement, Appl. Phys. Lett. 80 (2002) 4834–4836.

14. **Vladimirov A., Korovin S., Surkov A., Kelm E., Pustovoy V.,** Synthesis of luminescent Si Nanoparticles using the laser-induced pyrolysis, Laser Phys. 21 (2011) 830–835.

## THE AUTHORS

**SHKOLDIN Vitaliy A.**
shkoldin@spbau.ru
ORCID: 0000-0002-1014-5401

**LEBEDEV Denis V.**
denis.v.lebedev@gmail.com
ORCID: 0000-0001-5389-2899

**PERMYAKOV Dmitry V.**
d.permyakov@metalab.ifmo.ru
ORCID: 0000-0003-2708-9140

**GOLUBOK Alexander O.**
aogolubok@mail.ru
ORCID: 0000-0001-9970-9172

**ARKHIPOV Alexander V.**
arkhipov@rphf.spbstu.ru

**SAMUSEV Anton K.**
a.samusev@metalab.ifmo.ru
ORCID: 0000-0002-3547-6573

**MUKHIN Ivan S.**
imukhin@yandex.ru
ORCID: 0000-0001-9792-045X

*Received 29.09.2022. Approved after reviewing 14.11.2022. Accepted 25.11.2022.*

© Peter the Great St. Petersburg Polytechnic University, 2023

Conference materials
UDC 538.958
DOI: https://doi.org/10.18721/JPM.161.216

# Thermal characteristics of III-V microlasers bonded onto silicon board

A.S. Dragunova [1]✉, N.V. Kryzhanovskaya [1,2], F. I. Zubov [1,2], E. I. Moiseev [1], A.M. Nadtochiy [1,3], N.A. Fominykh [1], K.A. Ivanov [1], M.V. Maximov [1,2], A.A. Vorobyev [2], A.M. Mozharov [2], N.A. Kalyuzhnyy [3], S.A. Mintairov [3], N.Yu. Gordeev [3], Yu.A. Guseva [3], M.M. Kulagina [3], A.E. Zhukov [1]

[1] HSE University, St. Petersburg, Russia;
[2] Alferov University, St. Petersburg, Russia;
[3] Ioffe Institute, St Petersburg, Russia
✉ anndra@list.ru

**Abstract.** In this work, we study the characteristics of semiconductor microlasers based on the heterostructure with two coupled waveguides intended to improve heat dissipation in cw regime. We analysed total output optical loss of the microlasers, their spectral characteristics, output power, emission pattern and thermal resistance. We observed that the use of the principle of two coupled resonant planar waveguides, active and passive, as well as p-side down bonding, significantly reduces the thermal resistance of microlasers and improves their performance.

**Keywords:** hybrid integration, microlaser, quantum well dots, thermal resistance

**Funding:** This study was supported by Russian Science Foundation grant 18-12-00287, https://rscf.ru/project/18-12-00287/. Support of optical measurements was implemented in the framework of the Basic Research Program at the National Research University Higher School of Economics (HSE University).

**Citation:** Dragunova A.S., Kryzhanovskaya N.V., Zubov F.I., Moiseev E. I., Nadtochiy A.M., Fominykh N.A., Ivanov K. A., Maximov M.V., Vorobyev A.A., Mozharov A. M., Kalyuzhnyy N. A., Gordeev N. Yu, Guseva Yu. A., Kulagina M. M., Zhukov A.E., Thermal characteristics of III-V microlasers bonded onto silicon board, St. Petersburg State Polytechnical University Journal. Physics and Mathematics. 16 (1.2) (2023) 108–113. DOI: https://doi.org/10.18721/JPM.161.216

This is an open access article under the CC BY-NC 4.0 license (https://creativecommons.org/licenses/by-nc/4.0/)

Материалы конференции
УДК 538.958
DOI: https://doi.org/10.18721/JPM.161.216

# Тепловые характеристики микролазеров III-V, перенесенных на кремниевую подложку

А.С. Драгунова [1]✉, Н.В. Крыжановская [1,2], Ф.И. Зубов [1,2], Э.И. Моисеев [1], А.М. Надточий [1,3], Н.А. Фоминых [1], К.И. Иванов [1], М.В. Максимов [1,2], А.А. Воробьев [2], А.М. Можаров [2], Н.А. Калюжный [3], С.А. Минтаиров [3], Н.Ю. Гордеев [3], Ю.А. Гусева [3], М.М. Кулагина [3], А.Е. Жуков [1]

[1] Национальный исследовательский университет «Высшая школа экономики», Санкт-Петербург, Россия;
[2] Академический университет им. Ж.И. Алфёрова, Санкт-Петербург, Россия;
[3] Физико-технический институт им. А.Ф. Иоффе РАН, Санкт-Петербург, Россия;
✉ anndra@list.ru

© Dragunova A.S., Kryzhanovskaya N.V., Zubov F.I., Moiseev E.I., Nadtochiy A.M., Fominykh N.A., Ivanov K.A., Maximov M.V., Vorobyev A.A., Mozharov A.M., Kalyuzhnyy N.A., Gordeev N.Yu, Guseva Yu.A., Kulagina M.M., Zhukov A.E., 2023. Published by Peter the Great St. Petersburg Polytechnic University.

**Аннотация.** В данной работе исследуются характеристики полупроводниковых микролазеров на основе гетероструктуры с двумя связанными волноводами, предназначенных для улучшения теплоотвода в непрерывном режиме. Были проанализированы полные выходные оптические потери микролазеров, их спектральные характеристики, выходная мощность, диаграмма направленности излучения и тепловое сопротивление. Отметим, что использование принципа двух связанных резонансных планарных волноводов, активного и пассивного, а также соединения p-стороной вниз значительно снижает тепловое сопротивление микролазеров и улучшает их характеристики.

**Ключевые слова:** гибридная интеграция, микролазер, квантовые яма-точки, тепловое сопротивление

**Финансирование:** Исследование выполнено при поддержке гранта РНФ18-12-00287, https://rscf.ru/project/18-12-00287/. Оптические измерения осуществлены в рамках Программы фундаментальных исследований НИУ ВШЭ.

**Ссылка при цитировании:** Драгунова А.С., Крыжановская Н.В., Зубов Ф.И., Моисеев Э.И., Надточий А.М., Фоминых Н.А., Иванов К.А., Максимов М.В., Воробьев А.А., Можаров А.М., Калюжный Н.А., Гордеев Н.Ю., Гусева Ю.А., Кулагина М.М., Жуков А.Е. Исследование тепловых характеристик микролазеров III-V, перенесенных на кремниевую подложку // Научно-технические ведомости СПбГПУ. Физико-математические науки. 2023. Т. 16. № 1.2. С. 108–113. DOI: https://doi.org/10.18721/JPM.161.216

Статья открытого доступа, распространяемая по лицензии CC BY-NC 4.0 (https://creativecommons.org/licenses/by-nc/4.0/)

## Introduction

The self-heating effects of cw-operating diode lasers, associated with the incomplete conversion of the supplied electric power into light power, are especially critical for devices with a small surface area, such as microdisk lasers [1]. The active region is the main source of Joule heat in a semiconductor lasers. Depending on the bonding side, heat can be removed mainly in two directions: towards the relatively thin upper epitaxial layers and towards the substrate. One option to reduce thermal resistance is to optimize the design of the laser structure. The standard total thickness of the upper contact layer, the upper p-cladding layer and the upper part of waveguide layer is about 2–2.5 μm. The upper p-cladding layer makes the largest contribution to this thickness (about 1.5 μm). It must effectively confine the fundamental optical mode within the vertical waveguide. As the cladding layer thickness decreases, the mode begins to penetrate into the highly doped upper contact layer, that leads to a catastrophic increase in internal optical losses up to the disruption of lasing. The solution to the problem is to use the principle of two coupled resonant planar waveguides, of which one is active and another is passive [2]. An active waveguide contains an active region and fundamental mode. High-order modes resonantly tunnels into an optically coupled passive waveguide. Also, to reduce further the thermal resistance and ensure maximum heat dissipation, one can mount lasers on a metal or ceramic heat sink with epitaxial layers down (p-side down).

In this work, we study the characteristics of microlasers developed from the heterostructure with two coupled resonant planar waveguides, active and passive. The effect of thermal resistance reduction on the output power before and after bonding was investigated.

## Materials and Methods

Growth of the laser structure was carried out using metalorganic vapour-phase epitaxy on n+-GaAs substrate misoriented by 6o towards [111] direction. The laser structure consisted of an $Al_{0.25}Ga_{0.75}As$ n-cladding layer with a thickness of 1.2 μm, a passive n-GaAs waveguide with a thickness of 0.55 μm, an n-$Al_{0.25}Ga_{0.75}As$ optical barrier, a main undoped GaAs waveguide with a thickness of 1.37 μm, an upper p-$Al_{0.25}Ga_{0.75}As$ cladding layer of 0.5 μm and upper p-GaAs contact

© Драгунова А.С., Крыжановская Н.В., Зубов Ф.И., Моисеев Э.И., Надточий А.М., Фоминых Н.А., Иванов К.А., Максимов М.В., Воробьев А.А., Можаров А.М., Калюжный Н.А., Гордеев Н.Ю., Гусева Ю.А., Кулагина М.М., Жуков А.Е., 2023. Издатель: Санкт-Петербургский политехнический университет Петра Великого.

layer 0.15 μm thick (Fig. 1). The active region consisted of 5 layers of InGaAs quantum well dots. Within the waveguide layer, the active region was shifted towards the upper cladding layer and was located at a distance of 220 nm from it. Its location was chosen to be in the minimum of the second-order vertical mode. Lasing via the first-order mode (green line in Fig. 1) is suppressed due to its resonant leakage into the optically coupled passive waveguide. Thus, we managed to locate the active region at a distance of only 870 nm from the top surface of the heterostructure.

To support the effect of optical tunneling between the two waveguides it is necessary that the effective refractive indices of the interacting modes coincide, and the distance between the waveguides be comparable to the depth of mode penetration into the waveguide cladding. The effective refractive index of the mode increases with the thickness of the waveguide and/or the contrast of the refractive index between the materials of the waveguide layer and the cladding. Therefore, it is possible to design waveguides in such a way that one of the high-order modes of the wide, main waveguide will coincide in effective refractive index with the fundamental mode of the narrow, additional waveguide. If the active medium is located in a multimode (active) waveguide, then a high-order mode resonantly tunnels into a single-mode waveguide and is excluded from laser generation due to a decrease in the optical confinement factor, as well as additional losses in the passive waveguide. The fundamental mode of the multimode waveguide does not change in this case. The advantage of this approach is the possibility of expanding the waveguide thickness in the vertical direction and selective suppression of high-order modes, as well as a decrease in the thickness of the p-emitter layer.

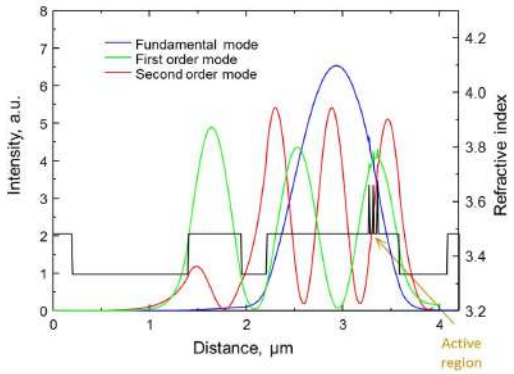


Fig. 1. Structure's refractive index profile and transverse optical modes intensity profiles

Laser mesas were formed with a diameter of 30–50 μm using plasma etching through the active region to the buffer layer. Metal contacts were formed using AuGe/Ni/Au and AgMn/Ni/Au for n- and p-contacts, respectively. Four different types of laser mesas with contacts were formed: microdisk lasers (D), microring lasers with 50 and 30 μm outer diameter and 30 μm (assigned as RB) and 18 μm (assigned as RS) inner diameter. The Au-Au thermocompression bonding of microdisk lasers to the silicon surface was performed using a Finetech FINEPLACERlambda2 setup. Electroluminescence spectra were recorded using a 20x objective, Horiba FHR 1000 monochromator and InGaAs CCD (spectral resolution 30 pm) or, for measurements over a wide spectral range, a Yokogawa AQ6370C optical spectrum analyser was used. The far field emission pattern was obtained using a setup for measuring the spectral-angular dependences of the lasing intensity.

## Results and Discussion

First, broad-area (BA) lasers with a stripe width of 100 μm and a stripe length ($L$) of 200–4000 μm were formed from the grown epitaxial structure. BA lasers operating in the CW-mode at room temperature have a lasing wavelength that strongly depends on the stripe length (Fig. 2, *a*). Such a change in wavelength is associated with losses in the laser. We have studied the dependence of the differential quantum efficiency on the length of the resonator, and we determined the internal optical losses $\alpha_{in}$, which amounted to only 0.7 $cm^{-1}$ and a high internal quantum efficiency of stimulated emission $\eta_{in} = 79\%$. According to the formula $\alpha_{in} + (1/L) \ln(1/R)$, where $R = 0.3$ is the facet reflectivity, we calculated the dependences of the total optical losses in a laser depending on

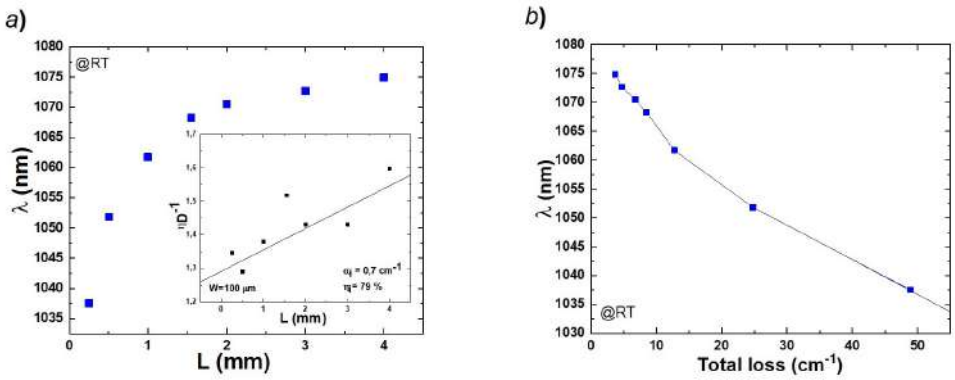


Fig. 2. Dependence of the lasing wavelength on the stripe length, inset: dependence of the external differential efficiency on the stripe length (*a*), dependence of the total optical losses on the lasing wavelength for BA lasers (*b*)

the lasing wavelength (Fig. 2, *b*). From the experimental dependence of the lasing wavelength on the total loss we can estimate the total optical loss for microlasers using their emission wavelength.

We have studied, lasing spectra of the microlasers at room temperature without bonding. Example of the lasing spectra obtained for microdisk lasers are presented in Fig. 3. With decreasing of the microdisk laser diameter we observe the tendency toward a decrease in the lasing wavelength and an increase in the threshold current density (Fig. 4), which is explained by an increase in losses in the microdisk laser. In accordance with the data of Fig. 2, *b* and 3, the total optical loss for a microdisk laser increases from 13.6 $cm^{-1}$ for a diameter of 50 μm to 58 $cm^{-1}$ for a diameter of 30 μm.

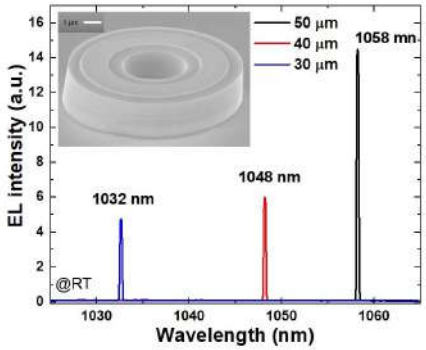


Fig. 3. Electroluminescence spectra for microdisk lasers with a diameter of 30, 40, and 50 μm

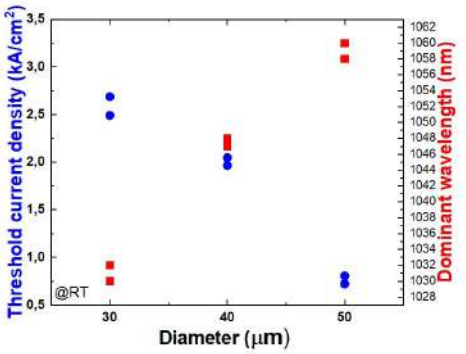


Fig. 4. Lasing wavelength and threshold current vs microdisk diameter (data was obtained for two microlasers of each diameter)

Next we compared the thermal resistance for different types of microlasers with a diameter of 30 and 50 μm before and after bonding to a Si substrate (Fig. 5). For microlasers with a diameter of 30 μm, the thermal resistance was observed at a level of 0.55 K/mW for all types of microlasers before bonding. The value of the thermal resistance for a single-waveguide microdisk laser with a diameter of 30 μm was obtained in [3] to be 0.59 K/mW, which is slightly larger than the value obtained for our microdisk laser with the same diameter. After bonding a decrease in thermal resistance by a factor of about 2–3 is observed for all the microlasers. In our microdisk lasers, the value of thermal resistance after bonding decreased to 0.22 K/mW, while for a single-waveguide microdisk laser, this value decreased to 0.32 K/mW. Based on this comparison, we can conclude that the use of the principle of two coupled resonant active and passive planar waveguides makes it possible to reduce the thermal resistance of microlasers.

We also studied the dependence of thermal resistance on the microlaser type for lasers with a diameter of 50 μm before bonding. Fig. 5, *b* shows that, the thermal resistance of the microlaser increases with a decrease of its area. After bonding, regardless of the type of microlaser, the thermal resistance decreases to ~ 0.15 K/mW.

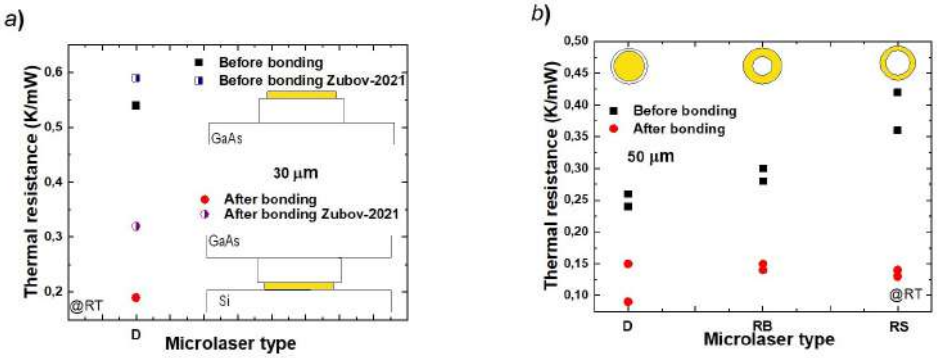


Fig. 5. Thermal resistance before and after bonding against microlaser type for 30 μm (*a*) and 50 μm (*b*)

Reducing thermal resistance improves various characteristics of microlasers. Increase of the output power after bonding was observed for all the devices studied. An example of a change in the output optical power is shown in Figure 6. Also, a decrease in thermal resistance after bonding led to an increase in the output power with the slope of power dependence and increase of the bias current of the thermal roll-over.

Next the far-field emission pattern was obtained for a microdisk laser with a diameter of 50 μm at various injection currents (Fig. 7). To study the far-field emission pattern, a different detector was used than the detector for collecting the output optical power, thus only a fraction of the output signal in a small azimuth angle was collected. We observe an interference pattern with the maximum emission power concentrated in the first two fringes with polar angles of 2° and 8°. This pattern is due to the interference of the direct and reflected from the planar etched GaAs surface output light of the microlaser. The angular position of the fringes depends only on the active region height above the bottom GaAs surface [4]. By fitting this dependence with a model that represents the output as a Gaussian beam, we can estimate the waist radius to be $r_0 \approx 0.9$ μm and thus the aperture (beam divergence) calculated with a well-known formula is $2\alpha = 2\lambda/(\pi r_0) \approx 40°$.

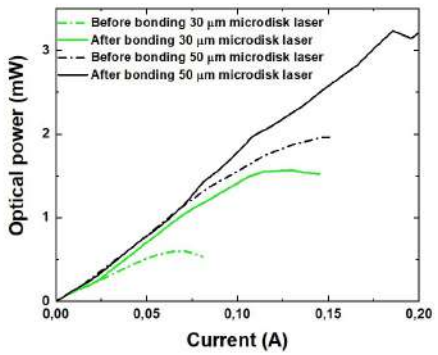


Fig. 6. The dependence of the output optical power on a threshold

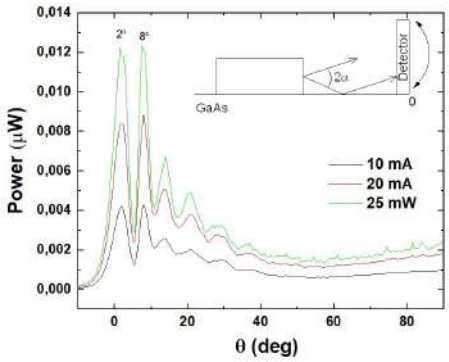


Fig. 7. The vertical far-field emission pattern for 50 μm microdisk laser

## Conclusion

The total optical loss for microlasers with different diameters was calculated. The intensity peak positions on the emission pattern of 50 μm microlaser stayed unchanged with the increase of the injection current. The use of the principle of two coupled resonant planar waveguides active and passive, as well as p-side down bonding, can significantly reduce the thermal resistance of microlasers. A decrease in thermal resistance leads to an improvement in the characteristics of microlasers, including an improvement in the maximum optical power.

## Acknowledgments

This study was supported by Russian Science Foundation grant 18-12-00287, https://rscf.ru/project/18-12-00287/. Support of optical measurements was implemented in the framework of

the Basic Research Program at the National Research University Higher School of Economics (HSE University).

## REFERENCES

1. **Zhukov A.E., et al.,** Impact of self-heating and elevated temperature on performance of quantum dot microdisk lasers, IEEE Journal of Quantum Electronics. 56 (5) (2020) 1–8.

2. **Gordeev N.Y., et al.,** Transverse single-mode edge-emitting lasers based on coupled waveguides, Optics Letters. 40 (9) (2015) 2150–2152.

3. **Zubov F., et al.,** Improved performance of InGaAs/GaAs microdisk lasers epi-side down bonded onto a silicon board,Optics Letters. 46 (16) (2021) 3853–3856.

4. **Kadinskaya S.A., et al.,** Experimental investigation of the far-field emission pattern of microdisk laser modes, Journal of Physics: Conference Series. – IOP Publishing, 1695 (1) (2020) 012094.

## THE AUTHORS

**DRAGUNOVA Anna S.**
anndra@list.ru
ORCID: 0000-0002-0181-0262

**KRYZHANOVSKAYA Natalia V.**
nataliakryzh@gmail.com
ORCID: 0000-0002-4945-9803

**ZUBOV Fedor I.**
fedyazu@mail.ru
ORCID: 0000-0002-3926-8675

**MOISEEV Eduard I.**
emoiseev@hse.ru
ORCID: 0000-0003-3686-935X

**NADTOCHIY Alexey M.**
al.nadtochy@mail.ioffe.ru
ORCID: 0000-0003-0982-907X

**FOMINYKH Nikita A.**
fominy-nikita@yandex.ru
ORCID: 0000-0003-3919-6410

**IVANOV Konstantin I.**
kivanov1992@gmail.com
ORCID: 0000-0003-2165-1067

**MAXIMOV Mikhail V.**
maximov.mikh@gmail.com
ORCID: 0000-0002-9251-226X

**VOROBYEV Alexandr A.**
alex.spbpu@mail.ru
ORCID: 0000-0003-2077-1243

**MOZHAROV Alexey M.**
alex000090@gmail.com
ORCID: 0000-0002-8661-4083

**KALYUZHNYY Nikolay A.**
Nickk@mail.ioffe.ru
ORCID: 0000-0001-8443-4663

**MINTAIROV Sergey A.**
mintairov@scell.ioffe.ru
ORCID: 0000-0002-6176-6291

**GORDEEV Nikita Yu.**
Gordeev@switch.ioffe.ru
ORCID: 0000-0002-9919-4794

**GUSEVA Yulia A.**
Guseva.Julia@mail.ioffe.ru
ORCID: 0000-0002-7035-482X

**KULAGINA Marina M.**
Marina.Kulagina@mail.ioffe.ru
ORCID: 0000-0002-8721-185X

**ZHUKOV Alexey E.**
zhukale@gmail.com
ORCID: 0000-0002-4579-0718

*Received 29.09.2022. Approved after reviewing 09.11.2022. Accepted 11.11.2022.*

© Peter the Great St. Petersburg Polytechnic University, 2023

Conference materials
UDC 535
DOI: https://doi.org/10.18721/JPM.161.217

# Optical properties of single InGaN nanowires with core-shell structure

S.D. Komarov[1]✉, V.O. Gridchin[2,3], V.V. Lendyashova[2,4], K.P. Kotlyar[2,3], R.R. Reznik[2,3], L.N. Dvoretckaia[2], A.S. Dragunova[1], I.S. Makhov[1], A.M. Nadtochiy[1,4], N.V. Kryzhanovskaya[1], G.E. Cirlin [2,3], A.E. Zhukov[1]

[1] HSE University, St. Petersburg, Russia;

[2] Alferov University, St. Petersburg, Russia;

[3] IAI RAS, St. Petersburg, Russia;

[4] Ioffe Institute, St. Petersburg, Russia

✉ serega.komarow@mail.ru

**Abstract.** In this work, the photoluminescence of single InGaN NWs with a core-shell structure is investigated along their entire length at RT and 77 K. Multicolor emission, covering the spectral range from 380 to 650 nm, was obtained and described in details. Using the modified Vegard's law, the photoluminescence lines were correlated with the InGaN composition. Based on these results, conclusions about the structural properties and homogeneity of the InGaN NWs along their length were carried out._

**Keywords:** nanowires, core-shell structure, III-V semiconductors

**Funding:** The samples were grown under support of Ministry of Science and Higher Education of the Russian Federation (state task 0791-2020-0003). SEM studies of the samples were performed under support of Ministry of Science and Higher Education of the Russian Federation (state task 0791-2020-0002). Support of optical measurements was implemented in the framework of the Basic Research Program at the National Research University Higher School of Economics (HSE University).

**Citation:** Komarov S.D., Gridchin V.O., Lendyashova V.V., Kotlyar K.P., Reznik R.R., Dvoretckaia L.N., Dragunova A.S., Makhov I.S., Nadtochiy A.M., Kryzhanovskaya N.V., Cirlin G.E., Zhukov A.E., Optical properties of single InGaN nanowires with core-shell structure, St. Petersburg State Polytechnical University Journal. Physics and Mathematics. 16 (1.2) (2023) 114–120. DOI: https://doi.org/10.18721/JPM.161.217

This is an open access article under the CC BY-NC 4.0 license (https://creativecommons.org/licenses/by-nc/4.0/)

© Komarov S.D., Gridchin V.O., Lendyashova V.V., Kotlyar K.P., Reznik R.R., Dvoretckaia L.N., Dragunova A.S., Makhov I.S., Nadtochiy A.M., Kryzhanovskaya N.V., Cirlin G.E., Zhukov A.E., 2023. Published by Peter the Great St. Petersburg Polytechnic University.

Материалы конференции
УДК 535
DOI: https://doi.org/10.18721/JPM.161.217

# Оптические свойства одиночных нитевидных нанокристаллов InGaN со структурой «ядро-оболочка»

С.Д. Комаров[1]✉, В.О. Гридчин[2,3], В.В. Лендяшова[2,4], К.П. Котляр[2,3], Р.Р. Резник[2,3], Л.Н. Дворецкая[2], А.С. Драгунова[1], И.С. Махов[1], А.М. Надточий[1,4], Н.В. Крыжановская[1], Г.Э. Цырлин[2,3], А.Е. Жуков[1]

[1]Национальный исследовательский университет «Высшая школа экономики», Санкт-Петербург, Россия;

[2]Академический университет им. Ж.И. Алферова РАН, Санкт-Петербург, Россия;

[3] Институт аналитического приборостроения Российской академии наук, Санкт-Петербург, Россия;

[4] Физико-технический институт им. А.Ф. Иоффе РАН, Санкт-Петербург, Россия

✉ serega.komarow@mail.ru

**Аннотация.** В данной работе исследована фотолюминесценция одиночных InGaN ННК со структурой “ядро-оболочка” вдоль всей их длины при комнатной температуре и при 77 K. Получена и подробно описана многоцветная эмиссия, охватывающая спектральный диапазон от 380 до 650 нм. С помощью модифицированного закона Вегарда линии фотолюминесценции были соотнесены с составом InGaN. На основании этих результатов были сделаны выводы о структурных свойствах и однородности InGaN ННК по их длине.

**Ключевые слова:** нитевидный нанокристалл, структура “ядро-оболочка”, III-V полупроводники

**Финансирование:** Образцы выращены при поддержке Министерства науки и высшего образования Российской Федерации (государственное задание № 0791-2020-0003). СЭМ исследования образцов проводились при поддержке Министерства науки и высшего образования Российской Федерации (государственное задание № 0791-2020-0002). Поддержка оптических измерений осуществлялась в рамках программы фундаментальных исследований Национального исследовательского университета «Высшая школа экономики» (НИУ ВШЭ).

**Ссылка при цитировании:** Комаров С.Д., Гридчин В.О., Лендяшова В.В., Котляр К.П., Резник Р.Р., Дворецкая Л.Н., Драгунова А.С., Махов И.С., Надточий А.М., Крыжановская Н.В., Цырлин Г.Э., Жуков А.Е. Оптические свойства одиночных нитевидных нанокристаллов InGaN со структурой «ядро-оболочка» // Научно-технические ведомости СПбГПУ. Физико-математические науки. 2023. Т. 16. № 1.2. С. 114–120. DOI: https://doi.org/10.18721/JPM.161.217

Статья открытого доступа, распространяемая по лицензии CC BY-NC 4.0 (https://creativecommons.org/licenses/by-nc/4.0/)

## Introduction

InGaN ternary compounds are of considerable interest as materials for creation of solid-state light sources due to the possibility of regulating their emission energy from ultraviolet to near-infrared spectral range by changing the chemical composition [1]. A currently urgent problem is to obtain a compound with a high In content that has an emission energy lying in the green and red spectra. This will make it possible to create a highly efficient white light-emitting diode by mixing the base colors, without using phosphor-based wavelength conversion [2]. However, obtaining high crystal quality InGaN layers is complicated due to solid phase immiscibility of InGaN, which imposes restrictions on obtaining homogeneous layers with In concentration $x_{In} = 0.2–0.8$. This peculiarity is caused by a significant mismatch of lattice constants between InN and GaN [3].

© Комаров С.Д., Гридчин В.О., Лендяшова В.В., Котляр К.П., Резник Р.Р., Дворецкая Л.Н., Драгунова А.С., Махов И.С., Надточий А.М., Крыжановская Н.В., Цырлин Г.Э., Жуков А.Е., 2023. Издатель: Санкт-Петербургский политехнический университет Петра Великого.

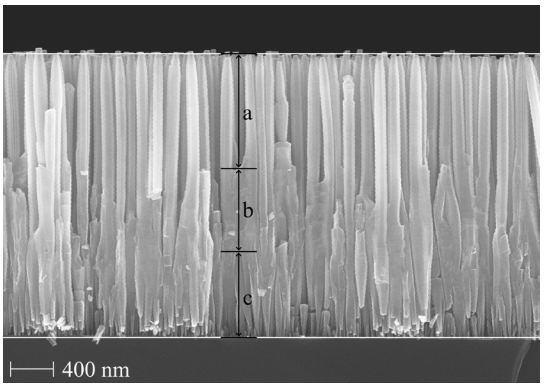


Fig. 1. Cross section SEM image of the InGaN NWs

In addition, the growth of InGaN layers with low density of structural defects is difficult due to the lack of substrates matched to the layer by lattice parameters. These problems can be solved by synthesizing InGaN nanowires (NWs) [4]. It has been shown that synthesis of InGaN NWs is possible over the entire range of chemical composition [5]. In particular, InGaN NWs grown by molecular beam epitaxy (MBE) on a Si substrate can exhibit a spontaneously formed core-shell structure [6]. It should be noted that the chemical composition and morphology of NWs significantly depend on the growth temperature [6]. In particular, the morphology can transform from coalesced nanostructures to spatially separated NWs with the spontaneously formed core-shell structure. However, the literature contains practically no data on the structural and optical properties of InGaN NWs, as well as their homogeneity along the entire length. The study of the optical properties of single NW allows us to estimate their structural and optical properties along the entire length, the presence or absence of localized states within the NWs, the distribution of chemical composition along the NWs.

In this paper photoluminescence of single InGaN NW grown on Si substrate and having core-shell structure is studied along its entire length at different temperatures.

## Samples and Methods

The InGaN nanostructures were grown directly on *p*-type Si(111) substrates using Riber Compact 12 MBE setup, equipped with Ga, In effusion cells, and a nitrogen plasma source. Growth was performed on an atomically clean Si surface under N-rich conditions at equal fluxes of In and Ga and a substrate temperature of 660 °C [7].

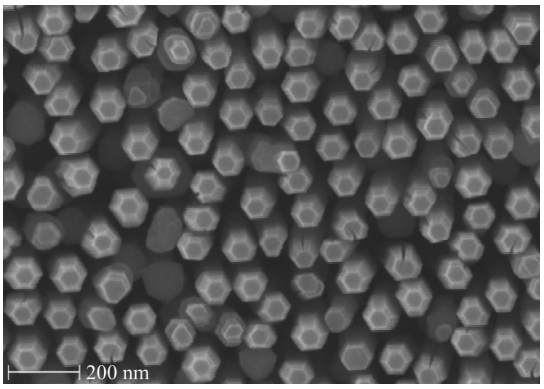


Fig. 2. Plan-view SEM image of the InGaN NWs

The morphology of the samples was studied by scanning electron microscopy (SEM Supra 25 Zeiss). The optical properties of the samples were studied by photoluminescence (PL) microscopy. PL of the samples was excited by a He-Cd laser (CW, $\lambda = 325$ nm), focused into the spot of 0.5 mm using a 50X Mitutoyo Plan Apo NUV HR objective. The positioning of the laser spot at a specific point on the NW was realized by precision objective movement and surface visualization with an external lamp and a video camera. The PL signal was detected using a standard lock-in technique by single-channel Si detector and Stanford Research Systems SR810 Lock-In Amplifier or by Symphony II CCD camera. The light was spectrally separated by SOL instruments MS 5204i monochromator with a 1200 gr/mm grating. The measurements were done at room temperature and at 77 K. For low temperature studies, the sample was mounted into the open-cycle nitrogen cryostat Janis ST-500.

Fig. 1 shows a cross section SEM image of initially grown InGaN NWs. This image shows that the NWs have a maximum length of about 2.6 μm and are morphologically heterogeneous. Along the length of the nanowires, three different regions can be seen: an upper part spatially separated from other NWs (*a*), a middle part coalesced with other NWs (*b*), and a lower part, tapering to the base (*c*). The upper part separated from other NWs have a spontaneously formed core-shell structure, as evidenced by our previous TEM measurements and wedge-shaped cracks at the NWs shown in Fig. 2 [7].

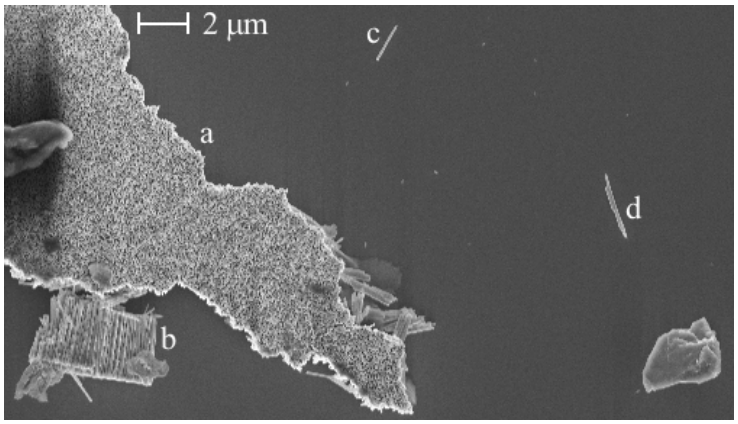


Fig. 3. SEM image of NWs transferred to Si (111) substrate

## Results and Discussion

To study the optical properties of single NW, the NWs were transferred to a pure Si (111) substrate by the method described in [8]. Arrays of InGaN NWs were also transferred to the Si (111) substrate. Fig. 3 shows the SEM image of the transferred NWs. We observe an array of vertically oriented InGaN NWs (*a*), an array of horizontally oriented InGaN NWs (*b*), and individual NWs of different lengths (*c*, *d*). In this work, we studied NWs having a length closest to the maximum for the given sample (*d*). The length of the NW under study (*d*) is ~2.6 mm. The other NWs have smaller length (*c*) due to the damage during the transferring process and they were out of the scope of this work. Fig. 4 shows an optical image of the photoluminescence of NW (*d*) optically pumped by He-Cd laser. Along the length of the NW, we put three points, where its optical properties were investigated. As it is seen from Fig. 4, the photoluminescence color changes continuously from blue to red.

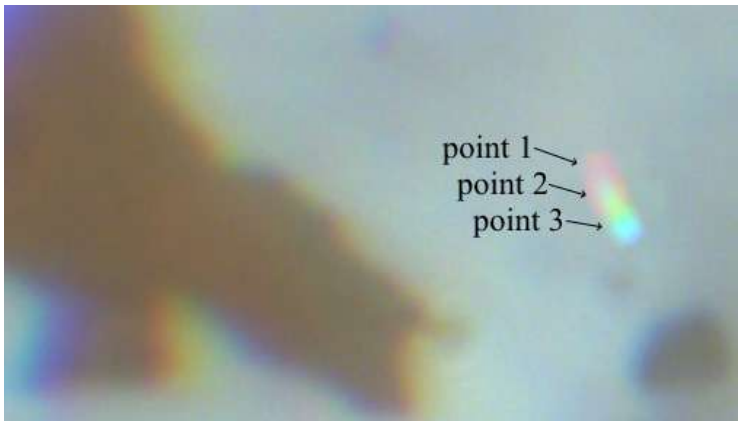


Fig. 4. Optical image of NW under optical pumping

Photoluminescence spectra of the single NW were obtained in three different points, at room temperature (Fig. 6) and at 77 K (Fig. 7). The first point corresponds to the top of the NW, the second to the center, and the third to the bottom. Visually, red color dominates in point 1. In the PL spectrum obtained at this point, the most intense peak has a spectral position of 656 nm (1.89 eV) at RT and 654 nm (1.90 eV) at 77 K. When the laser is focused in point 2, we see PL of different colors from yellow to green. The PL spectrum plot of the second point has two lines, with maxima at 507 nm (2.45 eV) and at 600 nm (2.07 eV) at RT (500 nm (2.48 eV) and 650 nm (1.91 eV) at 77 K), and a lower intensity peak located near 378 nm (3.28 eV) at RT and 77 K. At point 3, the PL has one well-defined peak located at 507 nm (2.45 eV) at RT and at 501 nm (2.48 eV) at 77 K.

It is possible to correlate spectral positions of PL lines with the structural properties of the InGaN NWs. The composition dependence (x) of the bandgap at RT can be described using modified Vegard's law including a quadratic term depending on a bowing parameter $C$:

$$E_g^{InGaN} = xE_g^{InN} + (1-x)E_g^{GaN} - x(1-x)C,$$

where $E_g^{InN}$ is used as 0.7 eV [9], $E_g^{GaN}$ is used as 3.43 eV [10], the bowing parameter $C$ is 1.43 eV [9]. The graph of obtained dependence shown in Fig. 7. The dots indicate the spectral position of obtained PL peaks. The graph shows that there are three $In_xGa_{1-x}N$ compositions with In concentration of 4%, 26%, and 43% in the studied NW, with the In content increasing from the bottom of the NW to its top. In the bottom region, tapering to the base, the In content is ~ 4%. In the middle region, we observe coalescence of the NWs. In this part of the NW, the In content is ~ 26%. In the upper region, where NWs are separated from each other, and core-shell structure is formed the In content in the core is ~ 43%. We assume the alloy variation in the InGaN NWs is explained by a decrease in the effective growth temperature with increasing NW length. This assumption is confirmed by our previous work [6], where small temperature changes had a main influence on both the chemical composition and morphology of InGaN NWs. This is also confirmed by the model proposed in [11] that shows the presence of a nonuniform temperature distribution in GaN/InGaN NWs. Another reason is the huge lattice mismatch between InN and GaN resulting in internal strains and phase separation in InGaN with a high In content [12].

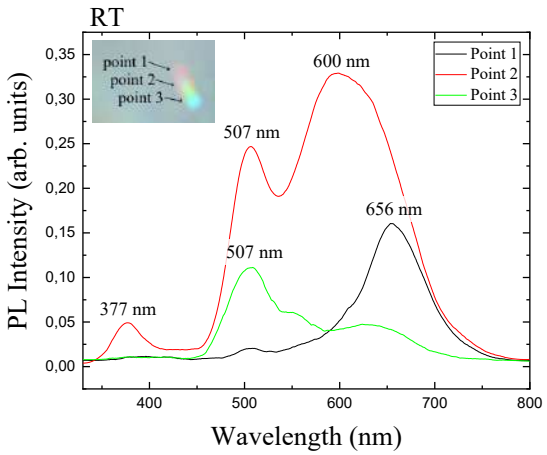


Fig. 5. Photoluminescence spectra obtained at different points of InGaN NW at room temperature

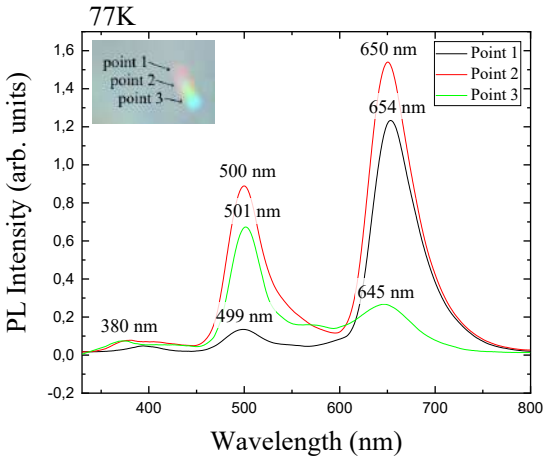


Fig. 6. Photoluminescence spectra obtained at different points of InGaN NW at 77 K

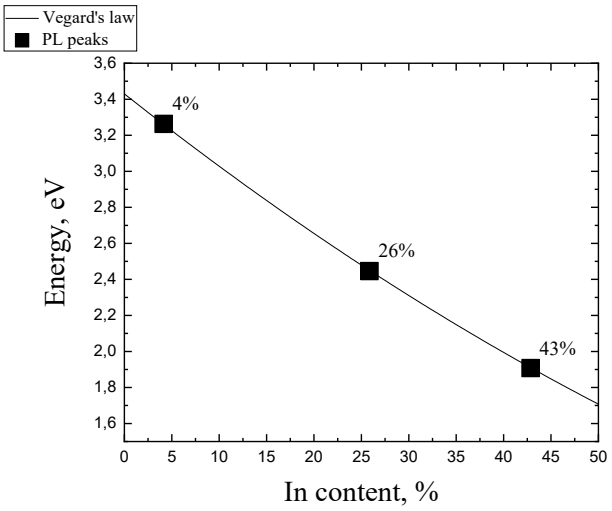


Fig. 7. Composition dependence of the InGaN bandgap at room temperature

## Conclusion

To conclude, for the first time, multicolor emission from a single InGaN NW, covering the spectral range from 380 nm to 650 nm were obtained. Observing the sample under optical pumping, it is visually noticeable that the PL color consistently changes from red to blue. PL spectra for different points of the sample were obtained, and the spectral position of the PL intensity maxima was compared with the InGaN composition. Obtained results correlate well with TEM studies carried out earlier [6].

## Acknowledgments

The samples were grown under support of Ministry of Science and Higher Education of the Russian Federation (state task № 0791-2020-0003). SEM studies of the samples were performed under support of Ministry of Science and Higher Education of the Russian Federation (state task 0791-2020-0002). Support of optical measurements from the Basic Research Program of the National Research University Higher School of Economics is gratefully acknowledged.

## REFERENCES

1. **Bui H. Q.T., et al.,** Full-color InGaN/AlGaN nanowire micro light-emitting diodes grown by molecular beam epitaxy: A promising candidate for next generation micro displays //Micromachines. 10(8) (2019) 492.

2. **der Maur M.A., et al.,** Unraveling the" Green Gap" problem: The role of random alloy fluctuations in InGaN/GaN light emitting diodes //arXiv preprint arXiv:1510.07831. (2015).

3. **Stringfellow G.B., Chen G.S.,** Atomic ordering in III/V semiconductor alloys //Journal of Vacuum Science & Technology B: Microelectronics and Nanometer Structures Processing, Measurement, and Phenomena. 9(4) (1991) 2182—2188.

4. **Dubrovskii V.G., Cirlin G.E., Ustinov V.M.,** Semiconductor nanowhiskers: synthesis, properties, and applications //Semiconductors. 43(12) (2009) 1539-1584.

5. **Roche E., et al.,** Circumventing the miscibility gap in InGaN nanowires emitting from blue to red //Nanotechnology. 29(46) (2018) 465602.

6. **Gridchin V.O., et al.,** Multi-colour light emission from InGaN nanowires monolithically grown on Si substrate by MBE //Nanotechnology. 32(33) (2021) 335604.

7. **Soshnikov I.P., et al.**, Specific Features of Structural Stresses in InGaN/GaN Nanowires // Semiconductors. 55(10) (2021) 795—798.

8. **Lendyashova V.V., et al.,** Separation of III-N partially-coalesced nanowire arrays from Si substrate //Journal of Physics: Conference Series. – IOP Publishing, 2086(1) (2021) 012191.

9. **Orsal G., et al.,** Bandgap energy bowing parameter of strained and relaxed InGaN layers // Optical Materials Express. 4(5) (2014) 1030-1041.

10. **Al Humayun M.A., et al.,** A Comparative Analysis Of Effect Of Temperature On Band-Gap Energy Of Gallium Nitride And Its Stability Beyond Room Temperature Using Bose–Einstein Model And Varshni'S Model //IIUM Engineering Journal. 18(2) (2017) 151—157.

11. **Kim S.U., Ra Y.H.,** Modeling and Epitaxial Growth of Homogeneous Long-InGaN Nanowire Structures //Nanomaterials. 11(1) (2020) 9.

12. **Niu X., Stringfellow G.B., Liu F.,** Phase separation in strained epitaxial InGaN islands //Applied Physics Letters. 99(21) (2011) 213102.

## THE AUTHORS

**KOMAROV Sergey D.**
serega.komarow@mail.ru
ORCID: 0000-0002-7025-3527

**DRAGUNOVA Anna S.**
anndra@list.ru
ORCID: 0000-0002-0181-0262

**GRIDCHIN Vladislav O.**
gridchinvo@yandex.ru
ORCID: 0000-0002-6522-3673

**MAKHOV Ivan S.**
imahov@hse.ru
ORCID: 0000-0003-4527-1958

**LENDYASHOVA Vera V.**
erilerican@gmail.com
ORCID: 0000-0001-8192-7614

**NADTOCHIY Alexey M.**
al.nadtochy@mail.ioffe.ru
ORCID: 0000-0003-0982-907X

**KOTLYAR Konstantin P.**
konstantin-kt21@rambler.ru
ORCID: 0000-0002-0305-0156

**KRYZHANOVSKAYA Natalia V.**
nataliakryzh@gmail.com
ORCID: 0000-0002-4945-9803

**REZNIK Rodion R.**
moment92@mail.ru
ORCID: 0000-0003-1420-7515

**CIRLIN George E.**
cirlin.beam@mail.ioffe.ru
ORCID: 0000-0003-0476-3630

**DVORETCKAIA Lilia N.**
liliyabutler@gmail.com
ORCID: 0000-0002-4172-940X

**ZHUKOV Alexey E.**
zhukale@gmail.com
ORCID: 0000-0002-4579-0718

*Received 14.10.2022. Approved after reviewing 14.11.2022. Accepted 28.11.2022.*

© Peter the Great St. Petersburg Polytechnic University, 2023

Conference materials
UDC 535.215.6
DOI: https://doi.org/10.18721/JPM.161.218

# Estimation of the coupling efficiency of optically induced waveguides in a lithium niobate crystal

D.K. Romanenko[1], A.V. Shchukin[1], V.E. Bodrenin[1], A.S. Perin[1, 2]✉

[1] Tomsk State University of Control Systems and Radioelectronics, Tomsk, Russia;

[2] V.E. Zuev Institute of atmospheric optics Russian academy of sciences, Siberian branch, Tomsk, Russia

✉ anton.s.perin@tusur.ru

**Abstract.** The paper presents the results of an experimental study of the efficiency of coupling of waveguide structures formed in a lithium niobate crystal by the optical induction method. The waveguides were produced by soliton laser beams with wavelengths of 532 and 457 nm at different optical powers. Estimation of the efficiency of coupling of the obtained structures for infrared radiation with a wavelength of 850 nm was more than 70%.

**Keywords:** lithium niobate, optical waveguide, photorefractive effect, pyroelectric effect, coupling efficiency.

**Funding:** The study regarding the development of the experimental setup was supported by the Ministry of Science and Higher Education of the Russian Federation (122041500075-5). The study of estimation of the coupling efficiency of the waveguides was financial supported by the Ministry of Science and Higher Education of the Russian Federation (FEWM-2022-0004).

**Citation:** Romanenko D.K., Shchukin A.V., Bodrenin V.E., Perin A.S., Estimation of the coupling efficiency of optically induced waveguides in a lithium niobate crystal, St. Petersburg State Polytechnical University Journal. Physics and Mathematics. 16 (1.2) 2023 121–125. DOI: https://doi.org/10.18721/JPM.161.218

This is an open access article under the CC BY-NC 4.0 license (https://creativecommons.org/licenses/by-nc/4.0/)

Материалы конференции
УДК 535.215.6
DOI: https://doi.org/10.18721/JPM.161.218

# Оценка эффективности оптически индуцированных волноводов в кристалле ниобата лития

Д.К. Романенко[1], А.В. Щукин[1], В.Е. Бодренин[1], А.С. Перин[1, 2]✉

[1] Томский государственный университет систем управления и радиоэлектроники, г. Томск, Россия;

[2] Институт оптики атмосферы имени В. Е. Зуева СО РАН, Томск, Россия

✉ anton.s.perin@tusur.ru

**Аннотация.** В работе приведены результаты экспериментального исследования эффективности связи волноводных структур, сформированных в кристалле ниобата лития методом оптического индуцирования. Волноводы были получены солитонными лазерными пучками с длинами волн 532 и 457 нм при разных оптических мощностях. Оценка эффективности связи полученных структур для инфракрасного излучения с длиной волны 850 нм составила более 70 %.

**Ключевые слова:** ниобат лития, оптический волновод, фоторефрактивный эффект, пироэлектрический эффект, эффективность связи.

© Romanenko D.K., Shchukin A.V., Bodrenin V.E., Perin A.S., 2023. Published by Peter the Great St. Petersburg Polytechnic University.

**Финансирование:** Работа в части разработки экспериментальной установки выполнена при поддержке Министерства науки и высшего образования Российской Федерации в рамках Государственного задания № 122041500075-5. Исследование по оценке эффективности связи волноводов выполнено при поддержке Министерства науки и высшего образования Российской Федерации в рамках Государственного задания № FEWM-2022-0004.

**Ссылка при цитировании:** Романенко Д.К., Щукин А.В., Бодренин В.Е., Перин А.С. Оценка эффективности оптически индуцированных волноводов в кристалле ниобата лития // Научно-технические ведомости СПбГПУ. Физико-математические науки. 2023. Т. 16. № 1.2. С. 121–125. DOI: https://doi.org/10.18721/JPM.161.218

Статья открытого доступа, распространяемая по лицензии CC BY-NC 4.0 (https://creativecommons.org/licenses/by-nc/4.0/)

## Introduction

The rapid development of fiber-optic technologies stimulates the need for further improvement of the component base based on the use of elements and devices of integrated optics and photonic integrated circuits (PIC), and the possibility of optical nonlinearity in some crystalline materials is of practical interest from the point of view of their application in these areas.

Some crystalline materials have pronounced piezoelectric, pyroelectric, electro-optical and ferroelectric properties, which makes it possible to modulate the parameters of light waves by external fields. In such nonlinear optical media, it is possible to form optical inhomogeneities that can play the role of waveguide elements. One of these materials is a lithium niobate crystal ($LiNbO_3$), which is the base for creating many different optical devices [1, 2].

To create waveguide circuits in lithium niobate, the methods of diffusion [3], ion implantation [4], and proton exchange [5] are successfully applied. There is also a method of optical induction, the essence of which is to modulate the refractive index by known physical phenomena - photorefractive and pyroelectric effects, the combination of which achieves a soliton mode of propagation of narrow monochromatic light beams by compensating for their linear and nonlinear diffractions. This technique is used both in bulk [6, 7] and thin-film materials [8].

The method of formation of structures is implemented due to the electro-optical effect, which causes a change in the refractive index of a substance under the action of an electric field. The photorefractive effect is due to the appearance of an electric field from light entering the ferroelectric medium, which, in turn, causes a redistribution of charges that affect the refractive index of the illuminated area. Laser beams passing through the crystal undergo diffraction divergence caused by a drop in the refractive index. The pyroelectric effect causes a change in the refractive index under the influence of a pyroelectric field arising from a change in temperature. But, unlike the photovoltaic one, the pyroelectric field arising from heating has the opposite direction. Since the two fields are opposite to each other, there is no change in the refractive index in the region of their interaction. In the unlight of the heated region, the refractive index decreases due to the self-defocusing nonlinearity of $LiNbO_3$. As a result, a structure is formed that is capable of channeling light due to the induced difference in the refractive indices. In the previously illuminated region, the refractive index is higher than that in the unilluminated region, which is the main condition for the existence of an optical waveguide.

For the practical application of waveguide elements in integrated optics, it is necessary to solve the problem of efficient light transmission and optical connection of waveguides with each other and with optical fibers. The solution of this problem involves the choice of a technique for creating optical waveguides and the optimal matching of various waveguide structures. A large number of works have been devoted to this problem, but the number of publications on this issue continues to grow, and this shows that the problem of creating efficient waveguide structures and their matching, including various types, still needs to be solved.

This paper presents an experimental study of the coupling efficiency of waveguide structures formed by optical induction in a lithium niobate crystal.

© Романенко Д. К., Щукин А. В., Бодренин В. Е., Перин А. С., 2023. Издатель: Санкт-Петербургский политехнический университет Петра Великого.

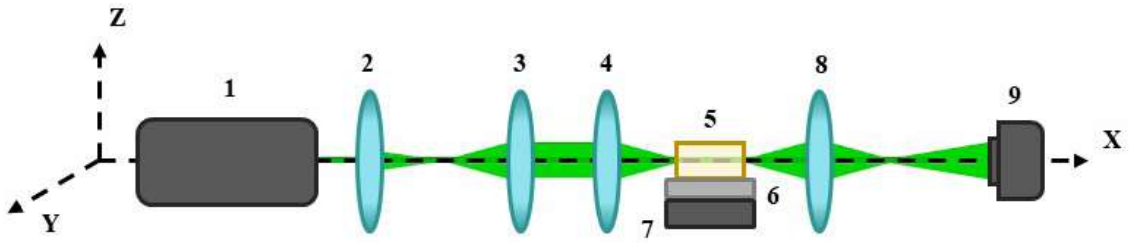


Fig. 1. Scheme of the experimental setup for the formation of optical waveguides: source of laser radiation *1*; focusing lenses *2*, *3*, *4*; $LiNbO_3$ crystal sample *5*; Peltier element *6*; linear translator *7*; imaging lens *8*; laser beam analyzer *9*

## Experimental setups and conditions

An undoped $LiNbO_3$ Z-cut sample was used in the experiments. The sample dimensions were 20×7×1 $mm^3$ along the X, Y, Z axes, respectively. The light beam forming the waveguide propagated in the sample in the direction of the X axis, and its polarization corresponded to an extraordinary wave in the crystal.

Fig. 1 shows a scheme of an experimental setup for the formation of optical waveguides. Radiation sources *1* in the experiments were YAG:$Nd^{3+}$ lasers with a wavelength of 532 nm and KLM-457/50 with a wavelength of 457 nm, both with linear light polarization. The photorefractive sensitivity of $LiNbO_3$ is maximum in the blue-green region of the visible spectrum [9, 10], so optical induction of photonic elements is most effective at these wavelengths. The system of lenses *2*, *3*, *4* set the diameter of the laser beam and focused it on the input face of the crystal. Imaging lens *8* was used to scale the intensity distribution patterns on the front (input) and rear (output) surfaces of the sample, which were studied using a laser beam analyzer *9* coupled to a personal computer.

In the experiments, the diameter of the light beam at the input face of the crystal was ~10 μm at full width at half maximum (FWHM). Sample *5* was able to move in the transverse direction relative to the laser beam using a linear translator *7* with micrometric positioning accuracy. The $LiNbO_3$ crystal was fixed on a Peltier element *6*, which uniformly heated the sample. During the experiments, the sample was heated to the required temperature, which was monitored and controlled by an electronic sensor.

To evaluate the efficiency of optical waveguides, the setup was reduced to the form shown in Fig. 2. Tapered fiber LEN-T-1-Y(47/56-90-SMF28) *2*, which focused infrared (IR) radiation with a wavelength of 850 nm, was fed to the entrance of the structures formed in the crystal *3*. At the output, as close as possible to the sample, an optical power meter *4* was installed, which recorded the parameters of the output radiation. Based on the data obtained, the coupling efficiency was calculated.

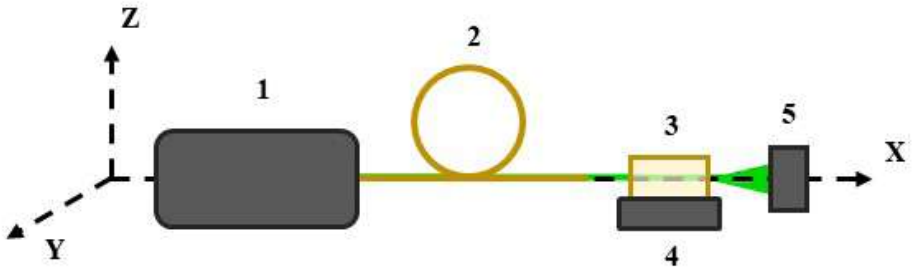


Fig. 2. Scheme of the experimental setup for evaluating the efficiency of optical waveguides: source of IR radiation *1*; conical fiber *2*; $LiNbO_3$ crystal sample *3*; linear translator *4*; optical power meter *5*

## Experimental results and discussions

To evaluate the coupling efficiency, groups of waveguides were first recorded at different wavelengths and at different optical powers. Studies comparing recording with blue and green laser radiation already exist [8, 9]. Of these, it is known that $LiNbO_3$ has a greater sensitivity to the blue optical range, because waveguide structures are recorded faster at a wavelength of 457 nm than at 532 nm and require less radiation power. Based on this, for recording a wavelength of 532 nm, the powers were 0.1, 0.5 and 1 mW; and for a wavelength of 457 nm 0.05, 0.1 and 0.2 mW. For both wavelengths, the diameter of the laser radiation focused on the input face of the crystal was reduced to a size of 10 μm. The temperature of the recording sample was raised by $\Delta T = 10$ °C, for all the cases taken, it was sufficient to compensate for linear and nonlinear diffractions. Further, IR radiation (a wavelength of 850 nm) was introduced into the structures formed by us, and its optical power was measured at the output. The power of IR radiation at the input was 2.87 μW.

The coupling efficiency of the formed waveguide structures was calculated from the ratio of the input power of the IR radiation coming out of the cone-shaped fiber and focused on the input face of the crystal into the recorded structures, and the output power of the radiation transmitted through the waveguides. Losses due to Fresnel reflections were not considered. According to the calculations obtained, tables 1 and 2 were compiled.

From the results, it can be seen that the radiation power equal to 0.1 mW for both wavelengths showed the best communication efficiency, therefore, for the formation of waveguide structures, this optical power can be considered optimal in our case.

From the coupling efficiencies obtained, it can be seen that waveguides recorded at 457 nm have slightly better results than waveguides recorded at 532 nm.

This result is probably due to the fact that a lower photoelectric field at shorter wavelengths leads to lower requirements for the pyroelectric field [9]. A smaller photoelectric field, in turn, makes it possible to detect narrower laser beams in a crystalline medium [10], and, together with a lower field applied for compensation, contributes to a finer and clearer formation of the structure.

## Conclusion

Thus, we experimentally studied the coupling efficiency in waveguide structures formed by optical induction in a lithium niobate crystal. It has been experimentally found that structures formed at a wavelength of 457 nm have a better coupling efficiency than at a wavelength of 532 nm.

Table 1

**Coupling efficiency of waveguides recorded at wavelength 532 nm**

| Recording power, $P$ (mW) | Output IR power, $P_{out}$ (μW) | Coupling efficiency, $T$ (%) |
|---|---|---|
| 0.1 | 2.12 | 73.9 |
| 0.5 | 2.118 | 73.8 |
| 1 | 2.09 | 72.8 |

Table 2

**Coupling efficiency of waveguides recorded at wavelength 457 nm**

| Recording power, $P$ (mW) | Output IR power, $P_{out}$ (μW) | Coupling efficiency, $T$ (%) |
|---|---|---|
| 0.05 | 2.137 | 74.5 |
| 0.1 | 2.158 | 75.2 |
| 0.2 | 2.133 | 74.3 |

## REFERENCES

1. **Diebel F., Leykam D., Boguslawski M., Rose P., Denz C., Desyatnikov A.S.,** All-optical switching in optically induced nonlinear waveguide couplers *Applied Physics Letters* 104 (26) (2014) 261111.

2. **Alibart O., D'Auria V., Micheli M., Doutre F., Kaiser F., Labonté L., Lunghi T., Picholle E., Tanzilli S.,** Quantum photonics at telecom wavelengths based on lithium niobate waveguides *Journal of Optics* 18 (10) (2016) 104001.

3. **Armenise M.N.,** Fabrication techniques of lithium niobate waveguides *IEE Proceedings J*-Optoelectronics 135 (2) (1988) 85–91.

4. **Jiang Y., Wang K.M., Wang X.L., Chen F., Jia C.L., Wang L., Jiao Y., Lu F.,** Model of refractive-index changes in lithium niobate waveguides fabricated by ion implantation *Physical* Review *B* 75 (19) (2007) 195101.

5. **De Micheli M., Botineau J., Sibillot P., Ostrowsky D.B., Papuchon M.,** Fabrication and characterization of titanium indiffused proton exchanged (TIPE) waveguides in lithium niobate *Optics Communications* 42 (2) (1982) 101–113.

6. **Safioui J., Devaux F., Chauvet M.,** Pyroliton: pyroelectric spatial soliton *Optics express* 17 (24) (2009) 22209–22216.

7. **Perin A.S., Shandarov V.M., Ryabchenok V.Y.,** Photonic waveguide structures in photorefractive lithium niobate with pyroelectric mechanism of nonlinear response *Phys. of Wave Phenomena* 24 (1) (2016) 7–10.

8. **Chauvet M., Bassignot F., Henrot F., Devaux F., Gauthier-Manuel L., Maillotte H., Ulliac G., Sylvain B.,** Fast-beam self-trapping in LiNbO3 films by pyroelectric effect *Optics letters* 40 (7) (2015) 1258–1261.

9. **Popescu S.T., Petris A., Vlad V.I.,** Fast writing of soliton waveguides in lithium niobate using low-intensity blue light *Applied Physics B* 108 (4) (2012) 799–805.

10. **Popescu S.T., Petris A., Vlad V.I.,** Recording of self-induced waveguides in lithium niobate at 405 nm wavelength by photorefractive–pyroelectric effect *J. Appl. Phys.* 113 (21) (2013) 213110.

## THE AUTHORS

**ROMANENKO Dmitry K.**
romanenko_dima1999@mail.ru

**BODRENIN Victor E.**
vebodrenin@inbox.ru

**SHCHUKIN Alexander V.**
mr.avshchukin@gmail.com

**PERIN Anton S.**
anton.s.perin@tusur.ru
ORCID: 0000-0002-9597-3088

*Received 10.10.2022. Approved after reviewing 15.11.2022. Accepted 15.11.2022.*

© Peter the Great St. Petersburg Polytechnic University, 2023

Conference materials
UDC 535.015
DOI: https://doi.org/10.18721/JPM.161.219

# Microring lasers with a waveguide coupler

N.A. Fominykh[1]✉, F.I. Zubov[1, 2], K.A. Ivanov[1], E.I. Moiseev[1], A.M. Nadtochiy[1, 3], S.A. Mintairov[3], N.A. Kalyuzhnyy[3], I.A. Melnichenko[1], V.V. Pirogov[2], S.A. Scherbak[2], B.D. Urmanov[4], A.V. Nahorny[4], N.V. Kryzhanovskaya [1], A.E. Zhukov[1]

[1] HSE University, St. Petersburg, Russia;
[2] Alferov University, St. Petersburg, Russia;
[3] Ioffe Institute, St. Petersburg, Russia;
[4] Institute of Physics of NAS of Belarus, Minsk, Belarus
✉ fominy-nikita@yandex.ru

**Abstract.** In the present work, we study the possibility of the emission output of a semiconductor microring laser through a radially coupled optical waveguide. Room temperature lasing has been achieved in continuous wave regime with the wavelength of ~1090 nm. The characteristics of microlasers with and without waveguide have been compared. We have performed a spatial scanning with simultaneous detection of the laser radiation at an injection current above the threshold. We have observed an increase in the output power up to two times due to the use of a coupled waveguide.

**Keywords:** microlaser, microring resonator, quantum well-dots, coupled optical waveguide

**Funding:** The study of the output power was implemented in the framework of the Basic Research Program at the National Research University Higher School of Economics (HSE University), mounting and soldering are supported by the Ministry of Science and Higher Education of the Russian Federation under project 0791-2020-0002, the development and modelling of structures was funded by RFBR and BRFBR project number 20-52-04016.

**Citation:** Fominykh N.A., Zubov F.I., Ivanov K. A., Moiseev E.I., Nadtochiy A.M., Mintairov S.A., Kalyuzhnyy N.A., Melnichenko I.A., Pirogov V.V., Scherbak S.A., Urmanov B.D., Nahorny A.V., Kryzhanovskaya N.V., Zhukov A.E., Microdisk lasers with a waveguide coupler, St. Petersburg State Polytechnical University Journal. Physics and Mathematics. 16 (1.2) 2023 126–132. DOI: https://doi.org/10.18721/JPM.161.219

This is an open access article under the CC BY-NC 4.0 license (https://creativecommons.org/licenses/by-nc/4.0/)

© Fominykh N.A., Zubov F.I., Ivanov K. A., Moiseev E.I., Nadtochiy A.M., Mintairov S.A., Kalyuzhnyy N.A., Melnichenko I.A., Pirogov V.V., Scherbak S.A., Urmanov B.D., Nahorny A.V., Kryzhanovskaya N.V., Zhukov A.E., 2023. Published by Peter the Great St. Petersburg Polytechnic University.

Материалы конференции
УДК 535.015
DOI: https://doi.org/10.18721/JPM.161.219

# Микрокольцевые лазеры с волноводным ответвителем

Н.А. Фоминых[1]✉, Ф.И. Зубов[1, 2], К.А. Иванов[1], Э.И. Моисеев[1], А.М. Надточий[1, 3], С.А. Минтаиров[3], Н.А. Калюжный[1], И.А. Мельниченко[1], В.В. Пирогов[2], С.А. Щербак[2], Б.Д. Урманов[4], А.В. Нагорный[4], Н.В. Крыжановская[1], А.Е. Жуков[1]

[1] Национальный исследовательский университет «Высшая школа экономики», Санкт-Петербург, Россия

[2] Академический университет им. Ж.И. Алфёрова, Санкт-Петербург, Россия

[3] ФТИ им. А.Ф. Иоффе, Санкт-Петербург, Россия

[4] Институт физики Б.И. Степанова, Минск, Беларусь

✉ fominy-nikita@yandex.ru

**Аннотация.** В данной работе исследуется возможность вывода излучения полупроводникового микрокольцевого лазера через радиально связанный оптический волновод. Лазерная генерация при комнатной температуре исследованных структур была реализована в непрерывном режиме на длине волны ~1090 нм. Проведено сравнение характеристик микролазеров с волноводом и без него. Реализовано пространственное сканирование с одновременной регистрацией лазерного излучения при токе накачки выше порогового. Мы наблюдали увеличение выходной мощности до двух раз за счет использования связанного волновода.

**Ключевые слова:** микролазер, микрокольцевой резонатор, квантовые яма-точки, связанные оптические волноводы.

**Финансирование:** Исследование выходной мощности выполнено в рамках программы фундаментальных исследований НИУ ВШЭ (Университет ВШЭ), монтаж и пайка поддержаны Министерством науки и высшего образования РФ по проекту № 0791-2020-0002, разработка и моделирование структур финансировались РФФИ и БРФФИ проект № 20-52-04016.

**Ссылка при цитировании:** Фоминых Н.А., Зубов Ф.И, Иванов К.А., Моисеев Э.И., Надточий А.М., Минтаиров С.А., Калюжный Н.А., Мельниченко И.А., Пирогов В.В., Щербак С.А., Урманов Б.Д, Нагорный А.В, Крыжановская Н.В., Жуков А.Е. е ведомости СПбГПУ. Физико-математические науки. 2023. Т. Микродисковые лазеры с волноводным ответвителем // Научно-технически 16. № 1.2. С. 126–132. DOI: https://doi.org/10.18721/JPM.161.219

Статья открытого доступа, распространяемая по лицензии CC BY-NC 4.0 (https://creativecommons.org/licenses/by-nc/4.0/)

## Introduction

Today the vast majority of integrated circuits are produced by complementary metal-oxide-semiconductor (CMOS) technology based on silicon [1]. Currently, increasing density of transistors on a chip by CMOS technology attracts a lot of attention. A way to achieve this goal is to reduce the transistor size. Thus, problems of scaling and problems with heat dissipation in currently used conductive interconnects have led to the search for their alternative [2]. One of the promising methods is high-speed optical communication [3]. Whispering gallery mode (WGM) semiconductor lasers with microdisk (MD) or microring (MR) optical cavity have high quality factor and low output loss [4]. Other useful properties of WGM microlasers are lateral light output, simplicity of the fabrication, and possibility to use a non-native substrate without complex technological steps [5]. All mentioned above makes microlasers of this design promising candidates for the implementation of compact radiation sources for high-speed optical communication. However, there is a problem of direct and controllable output of the emission from MR and MD lasers [6].

© Фоминых Н.А., Зубов Ф., Иванов К.А., Моисеев Э.И., Надточий А.М., Минтаиров С.А., Калюжный Н.А., Мельниченко И.А., Пирогов В.В., Щербак С.А., Урманов Б.Д., Нагорный А.В., Крыжановская Н.В., Жуков А.Е., 2023. Издатель: Санкт-Петербургский политехнический университет Петра Великого.

Direct and controllable emission output of WGM microlasers may be achieved by various modifications of MR and MD resonators. It was shown, that small harmonic perturbation of the resonator surface (with amplitude less than 0.01 of the MD radius) leads to more directional output of laser emission [7]. More radical modifications of microlasers, such as a pierced hole in the resonator near its edge may result in a single-mode and narrowly focused emission [8]. However, such destructive modifications can only be used with optically pumped microlasers and also can negatively affect laser characteristics (lasing threshold, heat dissipation, etc.). Another effective method of organizing the directional emission output of MD and MR lasers is optical coupling with other optical elements. Such coupling with plasmonic [9] and dielectric [10] antennas has already been investigated. Generally, the laser emission from such structures is not concentrated in the lateral plane. Also, optical coupling between the MD and MR laser and the optical waveguide (WG) is of great interest. Structures of this type can be integrated on a chip, since light propagates in the lateral direction. Here, we present a study of the implementation of optical coupling between semiconductor lasers with a MR optical cavity and a radially coupled optical WG.

## Materials and Methods

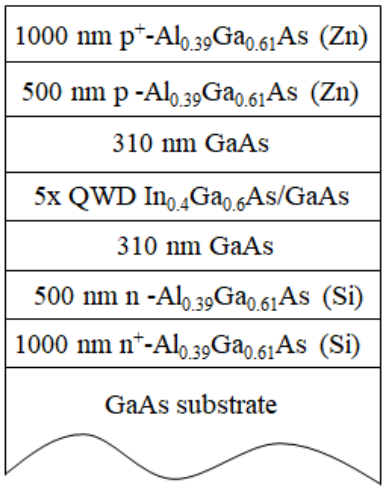


Fig. 1. Scheme of layout of the studied structures

The studied diode MR lasers were fabricated from an AlGaAs/GaAs laser heterostructure synthesized on a *n*+-GaAs substrate with an active region consisting of a 5-layer array of InGaAs quantum wells-dots (QWDs). Photolithography and plasma-chemical etching were used to form MR resonators with a height of about 5 μm and a diameter of 100 and 50 μm radially coupled with multimode WG. The scheme of layout of the structures is presented in Fig. 1. We used AgMn/Ni/Au metallization to form ring contacts to the p+-GaAs layer at the tops of the mesas. The GaAs substrate was thinned to approximately 100 μm, and a solid electrical AuGe/Ni/Au *n*-contact was fabricated on its reverse surface (Fig. 2). More detailed description of the epitaxial structure and fabrication details may be found elsewhere [11].

The absolute value of the output power of the MR laser was estimated by using a Thorlabs FDG1010 1 cm × 1 cm photodiode placed next to the laser under study. To study the spatial distribution of MR laser radiation we formed an electrical contact with a gold wire welded to the *p*-metallization of the laser. The lasers were tested at room temperature in continuous wave regime.

A numerical model of the optical coupling of a MR resonator with an optical WG radially connected to it was developed in COMSOL Multiphysics environment via the finite element method [6]. The optical power output was maximized under conditions when the WG width fits an integer number of the WGM intensity peaks inside the MR. In this work we use 15 μm wide radially coupled WG to support multimode operation.

## Results and Discussion

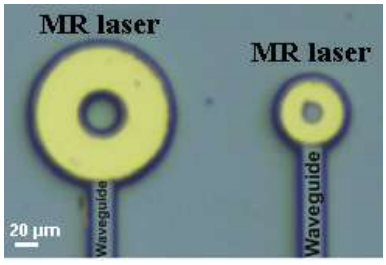


Fig. 2. Photo of injection MR lasers with a diameter of 100 and 50 μm coupled with a WG

The lasing spectra above the threshold of the studied MR lasers with WG are presented in Fig. 3. In order to determine threshold currents, we studied dependences of non-directional lasing line intensity versus injection current (inset to Fig. 3). These dependencies were obtained from the evolution of the emission spectra of the microlasers with and without WG with increasing injection current. Threshold currents for 100 and 50 μm MR lasers with WG were 67.7 mA and 39.4 mA. In the case of microlasers without WG, threshold currents were 32.1 mA and 19.7 mA, respectively. Observed increase of the threshold current for MR lasers with WG we attributed to the growth of the emission output losses.

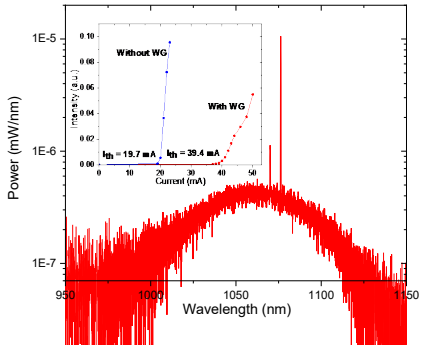


Fig. 3. Emission spectrum above the threshold current of 50 μm MR laser with radially coupled WG

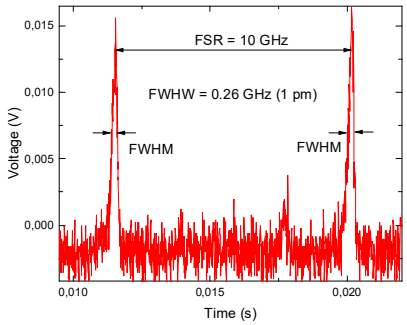


Fig. 4. Signal maxima of 100 μm MR laser obtained by the scanning Fabry–Perot interferometer method

The inset shows an evolution of non-directional lasing line intensity versus injection current of 50 μm MR laser with and without radially coupled WG

The spectral linewidth of MR lasers with WG was studied by the scanning Fabry–Perot interferometer Thorlabs SA210-8B (Fig. 4). The free spectral range (FSR) of the interferometer was 10 GHz. The time scale of the oscilloscope was calibrated to observe two signal maxima to measure spectral linewidth in terms of optical frequency. The linewidth (full width at the half maximum) of the lasing resonance is about 1 pm. The obtained value of the linewidth is comparable to the MR lasers of the same diameter without WG [12]. Thus, the increased output loss introduced by a radially coupled WG do not affect the quality factor (~$10^6$) of the MR resonator within our experimental resolution.

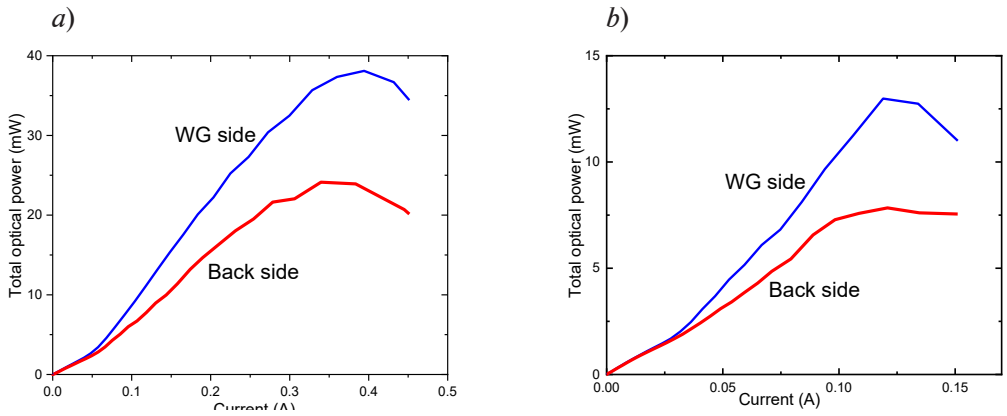


Fig. 5. Watt-ampere characteristics of 100 μm (*a*) and 50 μm (*b*) MR lasers measured from the side of the WG and from the back side

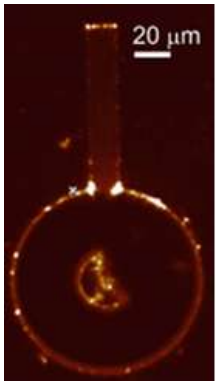


Fig. 6. Spatial distribution
of 100 μm MR laser emission

We measured the values of the absolute output power of MR lasers with a 50 and 100 μm diameter as a function of the injection current (Fig. 5). The dependencies were obtained from the WG side of microlaser and from the opposite side (back side). We observe an increase in the output power from the WG side up to two times, from 24 to 38 mW (peak values) for 100 μm in diameter MR laser and from 7 to 13 mW for 50 μm in diameter MR laser. The maximum power value is limited by the self-heating of the active region and subsequent thermal roll-over. Increase of the laser diameter from 50 to 100 μm results in better heat dissipation and thus in higher output power obtained.

Next, we studied spatial distribution of the laser emission by a confocal scanning optical microscopy in 100 μm microlaser at the injection current ($J$ = 140 mA) above the threshold ($J_{th}$ = 67.7 mA). The image of the output light distribution at wavelength (λ = 1103 nm) is presented in Fig. 6.

The light output from the MR laser was observed along the periphery of the resonator with local intensity maxima caused by roughness on the surface of the resonator. Other two local intensity maxima in the corners between the laser edge and the WG are due to non-directional scattering of light, previously predicted by the numerical analysis of such lasers with WG [6]. We also observe the light distribution along the WG and its output at the cleaved WG edge. The spectra obtained from the edge of the coupled WG and from the laser back side are compared in Fig. 7. We observe higher intensity for the case of WG point. Though the WG contains the same active region as in the laser, its absorption is low at the lasing wavelength, since the lasing occurs at the long-wavelength side of the InGaAs QWD absorption spectra (inset in Fig. 7). Thus, the mentioned above growth of the total optical power from the WG side is not caused only by the scattering of light at the interface between the laser and the WG, but also by the more effective emission from the coupled WG.

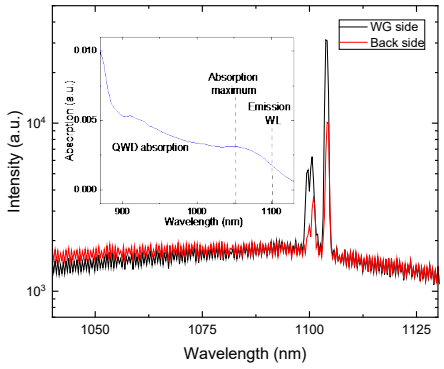


Fig. 7. Lasing spectra of 100 μm MR laser from the point at the end
of the coupled WG and from the opposite point at the back side,
an inset shows the typical absorption spectrum for QWD active region

## Conclusion

The output of radiation from the MR laser with a radially coupled WG was demonstrated. The spectral analysis of the radiation of the MR lasers does not reveal any degradation of quality factor in case of radial WG coupling. An increase in the output power up to two times was observed due to the use of the WG. The presence of undesirable omnidirectional light scattering in the region of the interface between the laser and the WG can probably be excluded by an adiabatic coupling of WG and MR laser. Thus, in the future works we suppose to optimise the joint point of the WG and MR laser for the further optimization of the light output.

## Acknowledgments

The study of the output power was implemented in the framework of the Basic Research Program at the National Research University Higher School of Economics (HSE university), mounting and soldering are supported by the Ministry of Science and Higher Education of the Russian Federation under project 0791-2020-0002, the development and modelling of structures was funded by RFBR and BRFBR project number 20-52-04016.

## REFERENCES

1. **Kunert B., et al.,** How to control defect formation in monolithic III/V hetero-epitaxy on (100) Si? A critical review on current approaches, Semiconductor Science and Technology. 33 (9) (2018) 093002.

2. **Ramirez J. M., et al.,** III-V-on-silicon integration: from hybrid devices to heterogeneous photonic integrated circuits, IEEE Journal of Selected Topics in Quantum Electronics. 26 (2) (2019) 1–13.

3. **Tang M., et al.,** Integration of III-V lasers on Si for Si photonics, Progress in Quantum Electronics. 66 (2019) 1–18.

4. **Kryzhanovskaya N.V., et al.,** Evaluation of energy-to-data ratio of quantum-dot microdisk lasers under direct modulation, Journal of Applied Physics. 126 (6) (2019) 063107.

5. **Zubov F.I., et al.,** Laser characteristics of an injection microdisk with quantum dots and its free-space outcoupling efficiency, Semiconductors. 50 (10) (2016) 1408–1411.

6. **Pirogov V.V., et al.,** Numerical simulation of optical coupling between a microring resonator and a directly connected straight waveguide, Journal of Physics: Conference Series – IOP Publishing. 2086 (1) (2021) 012162.

7. **Liew S.F., et al.,** Active control of emission directionality of semiconductor microdisk lasers, Applied Physics Letters. 104 (23) (2014) 231108.

8. **Tian Z.-N., et al.,** Single-mode unidirectional microcavity laser, Optics Letters. 42 (8) (2017) 1572–1575.

9. **Moiseev E.I., et al.,** Light outcoupling from quantum dot-based microdisk laser via plasmonic nanoantenna, Acs Photonics. 4 (2) (2017) 275–281.

10. **Kryzhanovskaya N.V., et al.,** Enhanced light outcoupling in microdisk lasers via Si spherical nanoantennas, Journal of Applied Physics. 124 (16) (2018) 163102.

11. **Maximov M.V., et al.,** Light emitting devices based on quantum well-dots, Applied Sciences. 10 (3) (2020) 1038.

12. **Kryzhanovskaya N.V., et al.,** Direct modulation characteristics of microdisk lasers with InGaAs/GaAs quantum well-dots, Photonics Research. 7 (6) (2019) 664–668.

## THE AUTHORS

**FOMINYKH Nikita A.**
fominy-nikita@yandex.ru
ORCID: 0000-0003-3919-6410

**ZUBOV Fedor I.**
fedyazu@mail.ru
ORCID: 0000-0002-3926-8675

**IVANOV Konstantin A.**
kivanov1992@gmail.com
ORCID: 0000-0003-2165-1067

**MOISEEV Eduard I.**
emoiseev@hse.ru
ORCID: 0000-0003-3686-935X

**NADTOCHIY Alexey M.**
al.nadtochy@mail.ioffe.ru
ORCID: 0000-0003-0982-907X

**MINTAIROV Sergey A.**
mintairov@scell.ioffe.ru
ORCID: 0000-0002-6176-6291

**KALYUZHNYY Nikolay A.**
Nickk@mail.ioffe.ru
ORCID: 0000-0001-8443-4663

**MELNICHENKO Ivan A.**
ivankomel550@gmail.com
ORCID: 0000-0003-3542-6776

**PIROGOV Vladimir V.**
vladimir.pirogov@metalab.ifmo.ru
ORCID: 0000-0002-8640-1707

**SCHERBAK Sergey A.**
sergeygtn@yandex.ru
ORCID: 0000-0002-0507-5621

**URMANOV Boris D.**
boris-urmanov@mail.ru

**NAHORNY Aliaksei V.**
a.nahorny@ifanbel.bas-net.by

**KRYZHANOVSKAYA Natalia V.**
nataliakryzh@gmail.com
ORCID: 0000-0002-4945-9803

**ZHUKOV Alexey E.**
zhukale@gmail.com
ORCID: 0000-0002-4579-0718

*Received 13.10.2022. Approved after reviewing 09.11.2022. Accepted 09.11.2022.*

© Peter the Great St. Petersburg Polytechnic University, 2023

Conference materials
UDC 535.215.6
DOI: https://doi.org/10.18721/JPM.161.220

# Interference pattern analysis approach for sensory applications

I.V. Kuznetsov[1]✉, A.S. Perin[1]

[1] Tomsk State University of Control Systems and Radioelectronics, Tomsk, Russia

✉ kuznetsov.i.159@e.tusur.ru

**Abstract.** This paper presents the results of a new approach to the analysis of interference patterns in the modulator output waveguide in a Mach-Zehnder interferometer configuration based on lithium niobate thin films. Interference patterns that occur in the output waveguide have been demonstrated. An approach of analysis of the patterns has been described. The method allows us to obtain information about the value of voltage applied to the arm of the interferometer and to double upper limit of measuring electric field strength using MZI based electro-optic modulator.

**Keywords:** Mach-Zehnder interferometer, interference pattern, electro-optic sensor

**Funding:** The research was carried out within the state assignment of Ministry of Science and Higher Education of the Russian Federation (No. FEWM-2022-0004).

**Citation:** Kuznetsov I.V., Perin A.S., Interference pattern analysis approach for sensory applications, St. Petersburg State Polytechnical University Journal. Physics and Mathematics. 16 (1.2) 2023 133–138. DOI: https://doi.org/10.18721/JPM.161.220

This is an open access article under the CC BY-NC 4.0 license (https://creativecommons.org/licenses/by-nc/4.0/)

Материалы конференции
УДК 535.215.6
DOI: https://doi.org/10.18721/JPM.161.220

# Подход к анализу интерференционных картин для сенсорных приложений

И.В. Кузнецов[1]✉, А.С. Перин[1]

[1] Томский государственный университет систем управления и радиоэлектроники, г. Томск, Россия

✉ kuznetsov.i.159@e.tusur.ru

**Аннотация.** В данной работе представлен новый подход к анализу интерференционных картин в выходном волноводе интегрального интерферометра Маха-Цендера, сформированного из гребенчатых волноводов на основе тонкой пленки ниобата лития. Использование представленного подхода может двухкратно увеличить динамический диапазон электрооптических сенсоров электрического поля.

**Ключевые слова:** интерферометр Маха-Цендера, интерференционные картины, электрооптический сенсор

**Финансирование:** Работа выполнена в рамках государственного задания Министерства науки и высшего образования Российской Федерации (№ FEWM0004-2022-).

**Ссылка при цитировании:** Кузнецов И.В., Перин А.С. Подход к анализу интерференционных картин для сенсорных приложений // Научно-технические ведомости СПбГПУ. Физико-математические науки. 2023. Т. 16. № 1.2. С. 133–138. DOI: https://doi.org/10.18721/JPM.161.220

Статья открытого доступа, распространяемая по лицензии CC BY-NC 4.0 (https://creativecommons.org/licenses/by-nc/4.0/)

© Kuznetsov I.V., Perin A.S., 2023. Published by Peter the Great St. Petersburg Polytechnic University.

## Introduction

Currently, integrated optoelectronic devices are widely used. They are characterized by compact size, high noise immunity and wide bandwidth due to the use of light as a carrier wave.

Due to its low cost and wide transparency window, lithium niobate remains one of the main materials in optoelectronics. It is possible to manufacture integrated optical circuits by the method of titanium diffusion into a lithium niobate crystal [1]. The advantage of this method is the possibility of providing a single-mode waveguide due to the small physical dimensions of the resulting waveguides and the small difference between the refractive indices of the waveguide core and its cladding, which can be important for use in telecommunication systems. The disadvantage of this method is the need to use centimeter-sized lithium niobate crystals, which does not meet modern trends in miniaturization of devices. Also the use of the titanium diffusion method is associated with the risk of cracking in the lithium niobate crystal, since the technology involves heating the crystal to temperatures above 1000 °C.

The compact dimensions of the optoelectronic device can be achieved by using thin films of lithium niobate. The method of applying thin films of lithium niobate by Radio frequency magnetron sputtering (RFMS) is promising. RFMS makes it possible to deposit thin films of lithium niobate up to 100 nm thick on semiconductor substrates at a temperature of 500 °C [2]. The ability to deposit a thin film on a semiconductor substrate at such temperatures makes it possible to implement potentially a device that has an optical and electronic integrated circuit on the same chip. The disadvantage of RFMS is that the deposited thin films have a polycrystalline structure. Such a structure can cause high optical losses during light propagation through the film. Controlling of the crystallites orientations of the RFMS thin film is also a problem.

Thin films made using the Lithium Niobate on Insulator (LNOI) method are more widespread. LNOI also allows one to deposit a thin film with a thickness of less than one micron. It is possible to choose the orientation of the film. The disadvantage of LNOI is the technological need to heat the film sample to temperatures above 900 °C, which can cause cracking and destruction of a thin film [3].

The Mach-Zehnder interferometer (MZI) is one of the basic components of integrated optoelectronics. It is possible to create electric field sensors, electro-optical switches, optical radiation intensity modulators and other optoelectronic devices based on MZI [1, 4–9].

One of the promising applications of the MZI is the electric field sensor systems. Various configurations of MZI based electric field sensors are known [1, 10]. Their upper limits of the range of measuring electric field strength are different depending on electrodes length. However, the presented sensors use the same method of analyzing output optical signal: calculating modulator transmission coefficient. This method limits upper range of the measuring electric field strength to the strength corresponding to the half-wave voltage of the modulator.

Hence, the purpose of this work is to study a new approach of analyzing output optic signal of an electro-optical modulator in the configuration of a Mach-Zehnder interferometer based on ridge waveguides made of a thin film of lithium niobate, using FFT BPM.

To perform the study, a simulation of the operation of an electro-optical intensity modulator based on MZI based on FFT BPM was carried [11–14].

## FFT-BPM

The beam propagation method (BPM) is a method for approximating the solution of the Helmholtz equation. As part of this work, a program has been implemented that realizes an FFT based on the fast Fourier transform (FFT) [11, 13].

BPM considers the propagation of an electromagnetic field on a plane as a function of two coordinates u($x$, $z$), where $x$ is a coordinate of a point along the axis of the transverse axis of light propagation, $z$ is coordinate along the axis of light propagation. If the value of the field at the point ($x$, $z_0$), is known then the value of the field at the point ($x$, $z_0+\Delta z$) can be found as:

$$u(x, z_0 + \Delta z) = \Psi(x, z_0 + \Delta z)\exp(i\Gamma), \tag{1}$$

where $\Psi$ is the wave function, $\Gamma$ is phase factor, calculated as:

© Кузнецов И. В., Перин А. С., 2023. Издатель: Санкт-Петербургский политехнический университет Петра Великого.

$$\Gamma = \frac{k^2 - \beta^2}{2\beta} dz,$$

where $k$ is the wavenumber, β is the propagation constant. We apply the discrete Fourier transform to the wave function and get:

$$\Psi_n(x_i, z) = \frac{1}{N} \sum_{n=-N/2}^{N/2} \Psi_n(z) \exp(ik_n x_i), \tag{2}$$

where $k_n = 2\pi n / N\Delta x$ and $N$ is the number of samples, obtaining

$$\Psi_n(x_i, z) = \frac{1}{N} \sum_{n=-N/2}^{N/2} \Psi_n(z) \exp(ik_n x_i). \tag{3}$$

Hence, the problem of calculating the propagation of light is solved by the following algorithm:

1. Perform the discrete Fourier transform to the wave function $\Psi(x,z_0)$, to get $\Psi_n(z_0)$.
2. Calculate $\Psi_n(x, z_0+\Delta z)$ from (1.1).
3. Perform the inverse discrete Fourier transform to the $\Psi_n(z_0 + \Delta z)$, to get $\Psi(x, z_0 + \Delta z)$.
4. If the coordinate $(z_0 + \Delta z)$ does not correspond to the point at which the calculation should stop, then, then $z_0 = z_0 + \Delta z$ and return to the point 1.

## MZI Configuration

In this paper, we will consider a modulator based on a Mach–Zehnder interferometer, made of ridge waveguides made of Z-cut lithium niobate thin film. The geometric parameters of the interferometer are shown in Fig. 1.

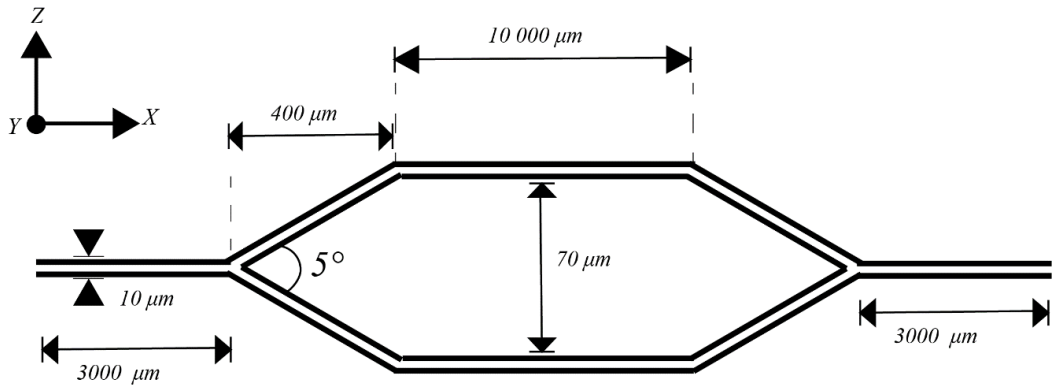


Fig. 1. MZI configuration and orientation of the thin film

Half wave voltage of a MZI modulator is determined by:

$$U_{\frac{\lambda}{2}} = \frac{\lambda d}{n_e^3 r_{33} L}, \tag{4}$$

where λ = 633 nm is the wavelength of the light, $d$ = 10 μm is the width of the waveguides, $n_e$ = 2.2139 is the extraordinary refractive index of the lithium niobate thin film, $L$ is length of the electrodes. Thus, half-wave voltage of represented modulator is 1.93 V.

This simulation was performed using 2D model. Some parameters including waveguide highness and film thickness were not taken into account. However, we note that modern integrated ridge waveguides have highness in range of hundreds of nanometers [15, 16].

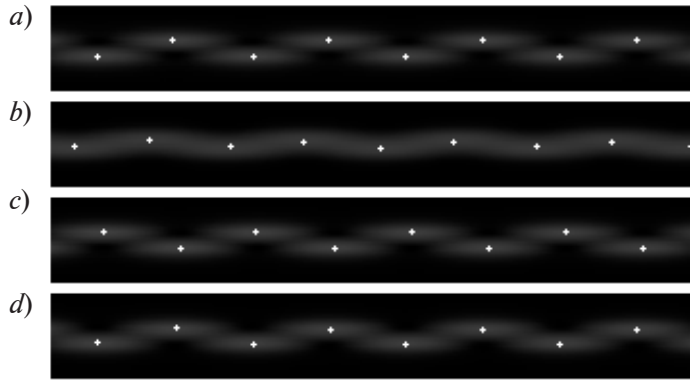


Fig. 2. Interference patterns at various applied voltages:
0.5 V (*a*); 1.5 V (*b*); 2.43 V (*c*); 4.36 V (*d*)

## Simulation parameters and results

The wavelength of light was taken to be 633 nanometers, the light was extraordinary polarized, the refractive index of the core of the waveguides was 2.2139, the refractive index of the environment was taken to be 1, the electro-optical coefficient $r_{33}$ was taken to be 30.8 pm·V$^{-1}$ [17-19]. The geometric parameters of the interferometer are shown in Fig. 1.

As a result of simulation, interference was observed in the output waveguide. Images of parts of the interference patterns (top view) at various values of the applied voltage are shown in Fig. 2, where the white dots indicate the interference maxima.

As can be seen from Fig. 2, at applied voltages of 0.5 V and 4.36 V, the distribution of interference maxima has an identical character. Also, in the interference patterns corresponding to applied voltages of 0.5 V and 2.43 V, there is a change in places of the maxima and minima of the interference relative to each other. Thus, patterns corresponding to voltages differing by 1.93 V are in antiphase, and patterns corresponding to voltages differing by 3.86 V are in the same phase. This confirms the above calculation of the half-wave voltage for the given configuration of the interferometer.

Also the presence of this cycle is confirmed by the dependence of the distance between the maxima of the interference pattern on the applied voltage, presented graphically in Fig. 3.

As can be seen from Fig. 3, the same distance between the interference maxima is repeated with a frequency of 3.86 V. This also confirms that the interference patterns spaced 3.86 V apart are in the same phase, and the half-wave voltage is 1.93 V.

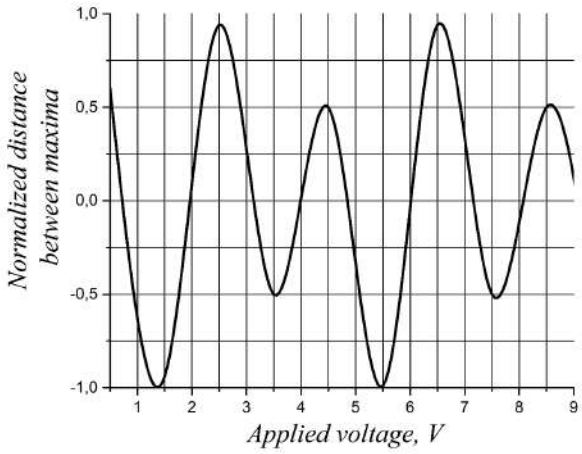


Fig. 3. Dependence of distance between interference maxima on applied voltage

To analyze such interference patterns, in order to extract information about the magnitude of the applied electric field, it is possible to use detectors that determine the distances between adjacent maxima and their position relative to each other. This approach makes it possible to double the measurement range of the electric field strength compared to the measurement of the modulator transmission coefficient.

### Conclusion

Thus, the FFT BPM method was used to study a new approach to the analysis of interference patterns of output waveguide of an electro-optical modulator based on a Mach–Zehnder interferometer made based on ridge waveguides made of thin films of lithium niobate. The simulation of the modulator with a given configuration was carried out. According to the results of the simulation, the considered configuration has a half-wave voltage equal to 1.93 V. Interference patterns arising in the output waveguide of the modulator were presented and considered, and an approach for their analysis was also proposed, based on determining the distance between the interference maxima. Determined that the proposed approach allows to double upper limit of measuring electric field strength in case of MZI-based electric field sensor.

## REFERENCES

1. **Jung H.,** An integrated photonic electric-field sensor utilizing a 1×2 YBB Mach–Zehnder interferometric modulator with a titanium-diffused lithium niobate waveguide and a dipole patch antenna, Crystals. 9 (9) (2019) 459.

2. **Dybov V.A., Serikov D.V., Ryzhkova G.S.,** Growth and substructure of lithium niobate films, Condensed media and interfaces. 21 (1) (2019) 51–59.

3. **Soham S., Siew S. Y., Deng J., Aaron D., Mankei T.,** Fabrication and characterization of optical devices on lithium niobate on insulator chips, Procedia Engineering. (140) (2016) 183–186.

4. **Xiaobo Xie, Khurgin J., Kang J., Chow F.,** Linearized Mach-Zehnder intensity modulator, IEEE Photonics Technology Letters. 15 (4) (2003) 531–533.

5. **Nikolajsen T., Leosson K., Bozhevolnyi S.I.,** Surface plasmon polariton based modulators and switches operating at telecom wavelengths, Applied Physics Letters. 85 (24) (2004) 5833–5835.

6. **Petraru A., Schubert J., Schmid M., Trithaveesak O., Buchal Ch.,** Integrated optical Mach Zehnder modulator based on polycrystalline BaTiO 3, Optics letters. 28 (24) (2003) 2527–2529.

7. **Ran H., Wei D., Hongsheng C., Xiaofeng J., Longzhi Y., Erping L.,** Ultra-compact optical modulator by graphene induced electro-refraction effect, Applied Physics Letters. 103 (6) (2013) 061116.

8. **Singh G., Yadav R. P., Janyani V.,** Ti indiffused lithium niobate (Ti: LiNbO3) Mach-Zehnder interferometer all optical switches: a review, New Advanced Technologies. (2010).

9. **Wang C., Zhang M., Chen X., Bertrand M., Shams-Ansari A., Sethumadhavan Ch, Winzer P., Lončar M.,** Integrated lithium niobate electro-optic modulators operating at CMOS-compatible voltages, Nature. 562 (7725) (2018) 101–104.

10. **Zhang J., Yang L., Li Y.,** Non-invasive measurement of intensive power-frequency electric field using a LiNbO3-integrated optical waveguide sensor, IET Science, Measurement & Technology. 15 (1) (2021)101-108.

11. **Samra A., Yousif B.B.,** Beam Propagation Method Based on Fast Fourier Transform and Finite Difference Schemes and its Application to Optical Diffraction Grating. (Dept. E), MEJ. Mansoura Engineering Journal.31 (1) (2020) P. 67–81.

12. **Devi P., Maddila R.K.,** Modeling of lithium niobate based Mach-Zehnder modulator for visible light communication system with BER analysis, Optical and Quantum Electronics. 53 (6) (2021) 1-15.

13. **Singh G., Janyani V., Yadav R.P.,** Modeling of a 2× 2 electro-optic Mach-Zehnder Interferometer optical switch with s-bend arms, Photonics letters of Poland. 3 (3) (2011) 119–121.

14. **Van Roey J., Van der Donk J., Lagasse P.E.,** Beam-propagation method: analysis and assessment, Josa. 71 (7) (1981) 803-810.

15. **Poberaj G. Hu. H., Sohler W.,Guenter P.,** Lithium niobate on insulator (LNOI) for micro-photonic devices, Laser & photonics reviews. 6 (4) (2012) 488–503.

16. **Wang Y., Chen Z., Hu H.,** Analysis of waveguides on lithium niobate thin films, Crystals. 8 (5) (2018) 191.

17. **Smith D.S., Riccius H.D., Edwin R.P.,** Refractive indices of lithium niobate, Optics communications. 17 (3) (1976) 332–335.

18. **Turner E.H.,** High-frequency electro-optic coefficients of lithium niobate, Applied Physics Letters. 8 (11) (1966) 303-304.

19. **Han H., Cai L., Hu H.,** Optical and structural properties of single-crystal lithium niobate thin film, Optical Materials. 42 (2015) 47-51.

## THE AUTHORS

**KUZNETSOV Igor V.**
kuznetsov.i.159@e.tusur.ru
ORCID: 0000-0002-4226-0500

**PERIN Anton S.**
anton.s.perin@tusur.ru
ORCID: 0000-0002-9597-3088

*Received 18.10.2022. Approved after reviewing 14.11.2022. Accepted 15.11.2022.*

© Peter the Great St. Petersburg Polytechnic University, 2023

Conference materials
UDC 537.874
DOI: https://doi.org/10.18721/JPM.161.221

# High-index waveguides for propagation of electromagnetic waves with high transversal angular momentum

N.G. Iukhtanov[1]✉, M.V. Rybin[1, 2]

[1] ITMO University, St. Petersburg, Russia;

[2] Ioffe Institute, St. Petersburg, Russia

✉ nikita.yuhtanov@metalab.ifmo.ru

**Abstract.** We study periodic waveguides of silicon cylinders for an optical isolator in the configuration of a Mach–Zehnder interferometer, as one of the possible applications in silicon photonics. Magneto-optical effect in silicon is considered under application of external magnetic field normal to the waveguide in the on-chip configuration that is Voight geometry. External magnetic field remains perpendicular to the direction of propagation of the electromagnetic wave for any direction of the waveguide on the surface, which allows us using a serpentine folding of waveguides. The nonzero integral electric field rotation in the plane of the waveguide is demonstrated. Our results uncover the possibility of using bare silicon as a magneto-optical material for optical isolators.

**Keywords:** electric field rotation, optical isolator, Voigt geometry

**Funding:** This study was funded by the Russian Scientific Foundation (grant 21-19-00677).

**Citation:** Iukhtanov N.G., Rybin M.V., High-index waveguides for propagation of electromagnetic waves with high transversal angular momentum, St. Petersburg State Polytechnical University Journal. Physics and Mathematics. 16 (1.2) 2023 139–145. DOI: https://doi.org/10.18721/JPM.161.221

This is an open access article under the CC BY-NC 4.0 license (https://creativecommons.org/licenses/by-nc/4.0/)

Материалы конференции
УДК 537.874
DOI: https://doi.org/10.18721/JPM.161.221

# Высокоиндексные волноводы для распространения электромагнитных волн с большим поперечным угловым моментом

Н.Г. Юхтанов[1]✉, М.В. Рыбин[1, 2]

[1] Университет ИТМО, Санкт-Петербург, Россия;

[2] Физико-технический институт им. А. Ф. Иоффе РАН, Санкт-Петербург, Россия

✉ nikita.yuhtanov@metalab.ifmo.ru

**Аннотация.** В настоящей работе мы предложили новую конфигурацию волновода для реализации кремниевого оптического изолятора (ОИ) на микрочипе с использованием магнитооптического эффекта в удобной для практической реализации геометрии Фойта. При разработке волновода мы основывались на структуре с нарушением зеркальной симметрии. Благодаря нарушению симметрии в продольной плоскости центрального сечения рассматриваемой волноводной структуры и магнитному полю, приложенному перпендикулярно волновому вектору, можно получить необходимую удельную фазу для конструирования ОИ на основе интерферометра Маха–Цендера. Главное отличие данной работы от известных подходов состоит в реализации ОИ только на кремнии и использование магнита, который не требует источников питания.

© Iukhtanov N.G., Rybin M.V., 2023. Published by Peter the Great St. Petersburg Polytechnic University.

**Ключевые слова:** вращение электрического поля, оптический изолятор, геометрия Фойгта

**Финансирование:** Работа выполнена при поддержке Российского Научного Фонда (номер гранта 21-19-00677).

**Ссылка при цитировании:** Юхтанов Н.Г., Рыбин М.В. Высокоиндексные волноводовы для распространения электромагнитных волн с большим поперечным угловым моментом // Научно-технические ведомости СПбГПУ. Физико-математические науки. 2023. Т. .16 1.2 №. С. 139–145. DOI: https://doi.org/10.18721/JPM.161.221

Статья открытого доступа, распространяемая по лицензии CC BY-NC 4.0 (https://creativecommons.org/licenses/by-nc/4.0/)

## Introduction

In the recent years, researchers have been working on the problem of miniaturization of integrated optical devices, such as optical isolators, circulators, etc. [1]. An optical isolator is an analog of regular diodes designed for light, a device that allows for waves to pass but only in one direction. Obtaining an optimal and affordable device on a microchip leads to opportunities for developing promising integrated photonic circuits.

To date there are several approaches to the implementation of non-reciprocal on-chip devices, which are mainly based on electro-optical, nonlinear and magneto-optical effects. Electro-optical effects make it possible to break the time-reversal symmetry (T-symmetry) due to the modulation of the effective refractive index in time [2], which provides a different transmission coefficient for electromagnetic waves in the forward and backward directions. Besides, nonlinear effects, in particular, the nonlinear Kerr effect is exploited in possible devices for a non-reciprocal transfer of pulses [3]. In addition, magneto-optical effects are often used for structures with yttrium iron garnet (YIG) [4], the material with a high magnetic to optical response. Common materials among magneto-optical garnets, which are used to accumulate a non-reciprocal phase in the structure, are cerium substituted yttrium iron garnet (Ce:YIG). These materials show high Faraday rotation rates [5] and a low absorption coefficient in the infrared region of the spectrum [6]. The integration of silicon waveguides fabricated by silicon on insulator (SOI) technology, structures with YIG films is the outstanding technological problem in this approach. The discrepancy between the physical properties of garnets and $A_3B_5$ semiconductors provides difficulties in the epitaxial growth of such structures. Thus, magneto-optical garnet was not grown on semiconductors with sufficiently good crystallinity and the expected high effect indicators were not demonstrated yet [7, 8].

Recently, approach to creating an optical isolator on-chip based on Faraday effect in silicon waveguide structures were proposed [9]. However, the experimental confirmation is challenging since the necessary conditions for optical isolation due to the residual anisotropy of the waveguide, which is difficult to compensate in appropriate degree.

Here we study a silicon-based periodic structure as a two-dimensional (2D) problem that can be used to design an optical isolator in a Mach–Zehnder interferometer (MZI) configuration [10], where the magnetic field is applied perpendicular to the plane of a transverse rotation element (TRE). The advantage of such Voigt geometry [11] lies in the possibility of changing the photonic structure in the plane of the wave vector (Fig. 1). In this way, it is possible to fold the waveguide structure into a compact on-chip geometry.

## Design

In this paper, we consider an array of silicon cylinders in air background. Geometric dimensions are optimized for the telecom wavelength around $\lambda = 1.5$ μm. Note that due to the scalability of the Maxwell equations, the operating wavelength can be shifted by changing the geometric parameters to the near or even far infrared range. Our structure has the following geometric dimensions. The lattice constant is a = 590 nm. Cylinders with radii $R = 142$ nm and $r = 154$ nm, respectively, are shifted relative to their central axes by $l = 89$ nm and $d = 348$ nm in the $y$ and $z$ directions, respectively (Fig. 2). The refractive index for silicon cylinders is $n = 3.48$ based on [12] for the telecom wavelength $\lambda = 1.5$ μm.

© Юхтанов Н. Г., Рыбин М. В., 2023. Издатель: Санкт-Петербургский политехнический университет Петра Великого.

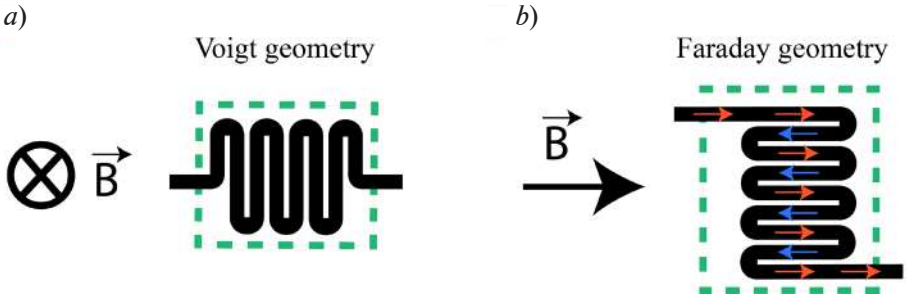


Fig. 1. Schematic comparison of Voigt (*a*) and Faraday (*b*) geometries: (*a*) there is no effect compensation in the Voigt geometry, (*b*) red arrows indicate the effect in one direction, and blue arrows in the opposite direction with the opposite effect, which leads to compensation of the Faraday effect along the entire length of the waveguide

We consider modes with TM polarization, where the electric field vector E lies in the *yz* plane, since we are interested in the integral rotation of electric field in this plane for the subsequent use of a configuration where an external magnetic field $B = 1$ T is applied perpendicular to the *yz* plane (Voigt geometry). This configuration makes it possible to consider silicon as a magneto-optical material with a permittivity tensor containing off-diagonal components $\varepsilon_{yz}$ and $\varepsilon_{zy}$, respectively (1).

$$\hat{\varepsilon} = \hat{\varepsilon}_0 + \Delta\hat{\varepsilon} = \begin{pmatrix} \varepsilon_0 & 0 & 0 \\ 0 & \varepsilon_0 & 0 \\ 0 & 0 & \varepsilon_0 \end{pmatrix} + \begin{pmatrix} 0 & 0 & 0 \\ 0 & 0 & -i\Delta\varepsilon \\ 0 & i\Delta\varepsilon & 0 \end{pmatrix}, \quad (1)$$

where coupling between $\Delta\varepsilon$ and Verdet constant in silicon $V_{Si}$ is $\Delta\varepsilon = \nu_{Si} n\lambda B/180°$.

It is important to note that we use the Voigt configuration but not the similarly named Voigt effect. The Voigt effect is quadratic on the applied magnetic field and cannot help for isolation. Nevertheless, if we assume that the quadratic term in the permittivity tensor will be comparable in magnitude with the linear terms of the tensor, then it will only lead to a slight change in transmission constant in both directions and will practically not affect the calculation results. The proposed periodic structure of silicon cylinders provides the non-zero integral rotation of electric field, as shown in Fig. 3.

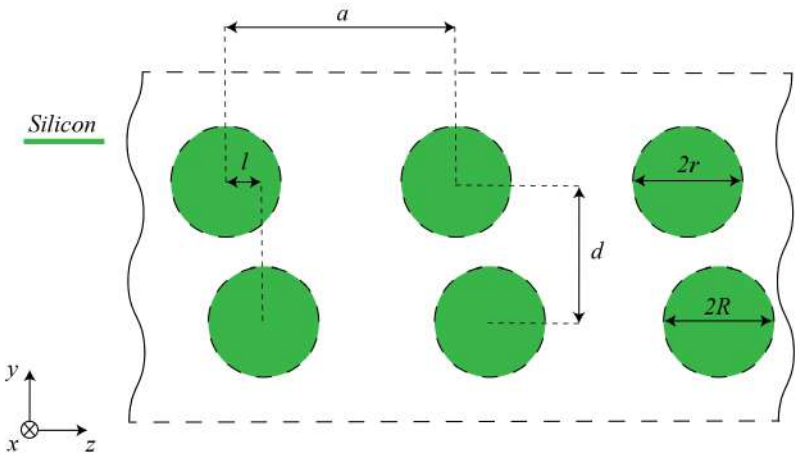


Fig. 2. Schematic view of silicon cylinders array. Infinite rods (along the *x* axis) with radii $R = 142$ nm and $r = 154$ nm. The displacement values between the central axes of the cylinders are $l = 89$ nm and $d = 348$ nm in the *y* and *z* directions, respectively. The refractive index of silicon is $n = 3.48$ and lattice constant is $a = 590$ nm. TM polarization is considered

### Calculation of the specific phase

For the isolator, we consider a structure with finite length $L$. In this structure of silicon cylinders, the specific additional phase accumulates due to magneto-optical effect over the length of the waveguide structure $L$ is expressed in terms of the phase φ (rotation of the vector **E**), Verdet constant in silicon $V_{Si}$, and the magnitude of the magnetic field B:

$$\Delta\varphi = \Delta\beta L, \tag{2}$$

where the Verdet constant for silicon is 15° $cm^{-1}\cdot T^{-1}$ [13].

To calculate the specific phase in Eq. (2), we use the time-independent perturbation theory [14], since the external magnetic field B is assumed to be constant in time. Below is the wave-equation for the electric field **E**:

$$\nabla\times\nabla\times\mathbf{E} - \mu\hat{\varepsilon}\frac{\omega^2}{c^2}\mathbf{E} = 0. \tag{3}$$

where $\mu = 1$, ω is the eigenfrequency and $c$ is the speed of light in vacuum.

We use the known solution of the generalized eigenvalue problem [14] with periodic boundary conditions in our case. Thus, the final expression for the correction to the eigenfrequency Δω due to applied magnetic field is expressed as follows

$$\Delta\omega_j = \frac{\omega_j}{2}\frac{\iint_S \mathbf{E}_\mathbf{j}^* \cdot \Delta\hat{\varepsilon}\cdot\mathbf{E}_\mathbf{j} dydz}{\iint_S \mathbf{E}_\mathbf{j}^* \cdot \hat{\varepsilon}_0\cdot\mathbf{E}_\mathbf{j} dydz}, \tag{4}$$

where are $\mathbf{E}_j$ the electric field of the $j$th mode and $S$ is the area of the periodic unit cell.

So the group velocity of the eigenmode is the power over the linear energy density (energy per unit length) which can be calculated as follows:

$$V_{g,j} = \frac{\iint_S \mathbf{z}(\mathbf{E}_\mathbf{j}\times\mathbf{H}_\mathbf{j}^*) dydz}{\iint_S \mathbf{E}_\mathbf{j}^* \cdot \hat{\varepsilon}_0\cdot\mathbf{E}_\mathbf{j} dydz}, \tag{5}$$

where $z$ is the unit vector along $z$ direction and $\mathbf{H}_j$ is the magnetic field of the $j$th mode.

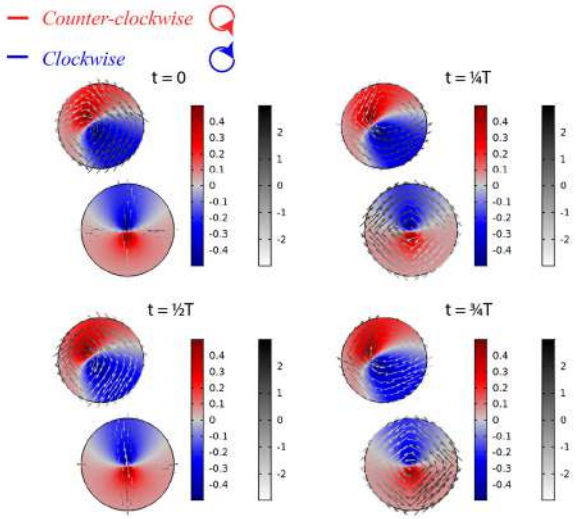


Fig. 3. Snapshots of electric field distribution at four consecutive time intervals. The red marks are the areas where the rotation is counterclockwise, and the blue is ones with clockwise, where the values of rotation are defined as the upper integral of rotation in Eq. (4) normalized by $|\mathbf{E}|^2$. $T$ is the period of electromagnetic oscillations. The black-and-white gradient scale shows the normalization of electric field on $|\mathbf{E}|^2$

Then the specific phase $\Delta\beta_j$ will be expressed in terms of $\Delta\omega$ (Eq. (4)) and $V_{g,j}$ (Eq. (5)) as follows:

$$\Delta\beta_j = \frac{\Delta\omega_j}{V_{g,j}} = \frac{1}{2}\omega_j \frac{\iint_S \mathbf{E}_\mathbf{j}^* \cdot \Delta\hat{\varepsilon} \cdot \mathbf{E}_\mathbf{j} dydz}{\iint_S \mathbf{z}(\mathbf{E}_\mathbf{j} \times \mathbf{H}_\mathbf{j}^*) dydz}. \quad (6)$$

The eigenmode was optimized and calculated in COMSOL Multiphysics for the considered structure at the wavenumber $k = 0.42\ \pi/a$ and frequency of 200 THz ($\lambda = 1.5$ μm) $\Delta\beta \approx 0.11$ cm$^{-1}$ (Fig. 4). It is important to note that the calculated value $\Delta\beta = 0.11$ cm−1 is achieved due to the low group velocity $V_g$, which is $0.004c$ for the considered mode in the dispersion branch.

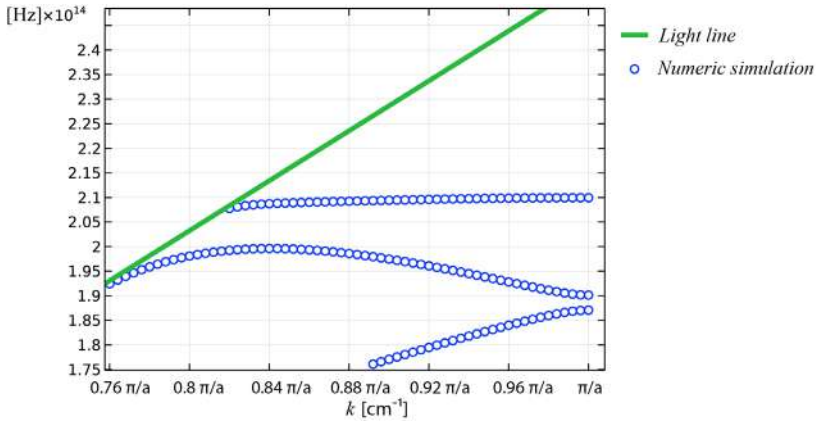


Fig. 4. Dispersion relation for silicon cylinder array (Fig. 2). The operating wavenumber is $k = 0.42\ \pi/a$ and frequency is 200 THz ($\lambda = 1.5$ μm). Calculated indicator $\Delta\beta \approx 0.11$ cm$^{-1}$

## Concept of an optical isolator

In this paragraph, we propose to use a periodic structure of silicon cylinders as TRE with the accumulated phase $\varphi = \pi/4$ in the upper arm and $\varphi = -\pi/4$ in the lower arm and $\varphi = -\pi/4$ and $\varphi = \pi/4$ in the backward direction correspondingly (Fig. 5). The length of the structure of silicon cylinders to achieve the value of the specific phase $\Delta\beta = 0.11$ cm$^{-1}$ is $L \approx 7.14$ cm according to (2). Y-splitters divide the input and output signals into two identical propagating waves in one direction. An additional phase $\varphi_a = -\pi/2$ is required for the implementation of a non-reciprocal device, that is, the transmission of the input signal and the forbidden transmission of the backward signal due to the constructive interference of waves propagating along two Mach–Zehnder interferometer arms in forward direction and destructive interference in the opposite direction. Note that the waveguide in the lower arm is flipped to get an opposite phase of the waveguide in the upper arm (Fig. 5).

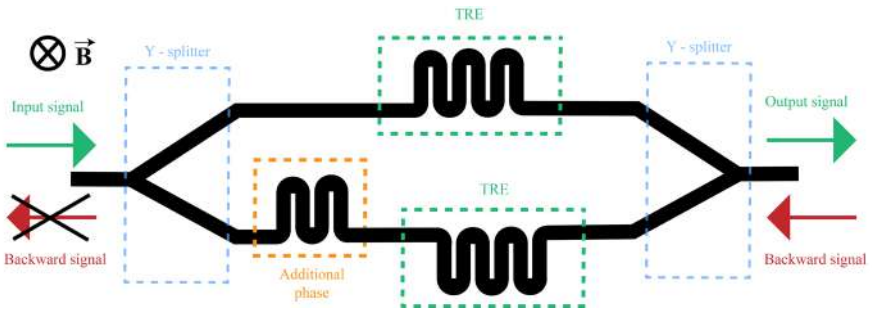


Fig. 5. Optical isolator based on Mach–Zehnder interferometer. Transverse Rotation Elements (TRE) accumulate phase $\varphi = \pi/4$ and $\varphi = -\pi/4$, respectively. Additional phase is $\varphi_a = -\pi/2$. The signal is transmitted in one direction and not transmitted in the opposite direction

Since in our work we consider the silicon waveguide with length of the order of several centimeters, then in such a line the losses due to light propagation will increase. Based on reported data [15], the loss is approximately 17.85 dB at 7.14 cm. This value of losses allows us to count on the registration of the effect under study. Thus, the tendency to reduce the propagation loss in SOI waveguides due to improved manufacturing technology allows us to expect for the use of our proposed concept of an optical isolator in the novel devices. It should be noted that the main objective of our work is that we are studying the very effect of polarization rotation in the Voigt geometry. In addition, the concept of an optical isolator acts as a possible example.

## Conclusion

We have studied the 2D periodic structure of silicon cylinders, which can be used as a TRE in MZI configuration. According to our calculations, the effective length of waveguide in TRE is $L = 7.14$ cm at the value of the specific phase $\Delta\beta = 0.11$ cm$^{-1}$. The optimization of the geometric parameters of the silicon cylinders structure in the COMSOL Multiphysics program was carried out to shift the mode to wavelength $\lambda = 1.5$ μm, which satisfies the telecom wavelength. We have achieved a non-zero integral rotation of the electric field of the longitudinal plane ($yz$ plane) of the considered structure.

## Acknowledgments

We are thankful to Alexander Petrov for fruitful discussions.

This work was supported by the Russian Science Foundation (grant 21-19-00677).

## REFERENCES

1. **Stadler Bethanie J.H., Tetsuya Mizumoto**, Integrated magneto-optical materials and isolators: a review: IEEE Photonics Journal 6.1 (2013): 1–15.

2. **Lira, Hugo, et al.**, Electrically driven nonreciprocity induced by interband photonic transition on a silicon chip: Physical review letters 109.3 (2012): 033901.

3. **Kittlaus, Eric A., Peter O. Weigel, William M. Jones,** Low-loss nonlinear optical isolators in silicon: Nature Photonics 14.6 (2020): 338–339.

4. **Shoji, Yuya, Tetsuya Mizumoto,** Silicon waveguide optical isolator with directly bonded magneto-optical garnet: Applied Sciences 9.3 (2019): 609.

5. **Gomi Manabu, Kensuke Satoh, Masanori Abe.**, Giant Faraday rotation of Ce-substituted YIG films epitaxially grown by RF sputtering: Japanese journal of applied physics 27.8A (1988): L1536.

6. **Onbasli Mehmet C., et al.**, Optical and magneto-optical behavior of cerium yttrium iron garnet thin films at wavelengths of 200−1770 nm: Scientific reports 6.1 (2016): 1-10.

7. **Stadler Bethanie J.H., Anand Gopinath**, Magneto-optical garnet films made by reactive sputtering: IEEE transactions on magnetics 36.6 (2000): 3957–3961.

8. **Stadler Bethanie J.H., et al.**, Integration of magneto-optical garnet films by metal-organic chemical vapor deposition: IEEE transactions on magnetics 38.3 (2002): 1564–1567.

9. **Jalas Dirk, et al.**, Faraday rotation in silicon waveguides: 2017 IEEE 14th International Conference on Group IV Photonics (GFP). IEEE, 2017.

10. **Fujita J., et al.**, Waveguide optical isolator based on Mach−Zehnder interferometer: Applied Physics Letters 76.16 (2000): 2158-2160.

11. **Elmzughi F.G., Tilley D.R.**, Surface and guided-wave polariton modes of magnetoplasma films in the Voigt geometry: Journal of Physics: Condensed Matter 6.23 (1994): 4233.

12. **Li H. H.**, Refractive index of silicon and germanium and its wavelength and temperature derivatives: Journal of Physical and Chemical Reference Data 9.3 (1980): 561-658.

13. **Petrov A.Yu, et al**., Nonreciprocal silicon waveguides and ring resonators with gyrotropic cladding: 7th IEEE International Conference on Group IV Photonics. IEEE, 2010.

14. **Sakurai J.J., Napolitano J.**, Modern Quantum Mechanics (2nd ed.), Addison Wesley ISBN 978-0-8053-8291-4. Chapter 5.

15. **Ghosh Samir, et al.**, Ce: YIG/Silicon-on-Insulator waveguide optical isolator realized by adhesive bonding: Optics express 20.2 (2012): 1839-1848.

## THE AUTHORS

**IUKHTANOV Nikita G.**
nikita.yuhtanov@metalab.ifmo.ru
ORCID: 0000-0003-4071-9047

**RYBIN Mikhail V.**
m.rybin@metalab.ifmo.ru
ORCID: 0000-0001-5097-4290

*Received 21.10.2022. Approved after reviewing 08.11.2022. Accepted 08.11.2022.*

© Peter the Great St. Petersburg Polytechnic University, 2023

Conference materials
UDC 53.082.52
DOI: https://doi.org/10.18721/JPM.161.222

# Seasonal variations in optical attenuation spectra of some urban water bodies

V.S. Goryainov[1]✉, K.G. Antonenko[1], M. Khasenova[1], M.A. Malyga[1], I. A. Prosolov[1]

[1] St. Petersburg Electrotechnical University "LETI", St. Petersburg, Russia

✉ vsgoriainov@etu.ru

**Abstract.** Water samples were taken once a month from several urban water bodies, and using a laboratory setup with two concave mirrors and a fiber optic spectrometer attenuation spectra were obtained in visible and near infrared spectral range. Spectra approximation by a power law gave better fit, indicating the primary influence of scattering by non-algal particles on the total attenuation. Seasonal maximums of attenuation were observed in November and late in summer, attributed to detritus scatterings and algal bloom correspondingly. A negative correlation was found between the spectral slope parameter and the attenuation value at 550 nm, which means that spectra for more turbid samples were spectrally flatter in general.

**Keywords:** urban water bodies, minor water bodies, light attenuation spectra, seasonal variations_

**Funding:** The study was carried out as part of project FSEE-2020-0008, which was carried out as part of the state task of the Ministry of Science and Higher Education of the Russian Federation.

**Citation:** Goryainov V.S., Antonenko K.G., Khasenova M., Malyga M.A., Prosolov I.A., Seasonal variations in optical attenuation spectra of some urban water bodies, St. Petersburg State Polytechnical University Journal. Physics and Mathematics. 16 (1.2) 2023 146–152. DOI: https://doi.org/10.18721/JPM.161.222

This is an open access article under the CC BY-NC 4.0 license (https://creativecommons.org/licenses/by-nc/4.0/)

Материалы конференции
УДК 53.082.52
DOI: https://doi.org/10.18721/JPM.161.222

# Сезонные изменения оптических спектров ослабления в нескольких городских водоемах

В.С. Горяинов[1]✉, К.Г. Антоненко[1], М. Хасенова[1], М. А. Малыга[1], И.А. Просолов[1]

[1] Санкт-Петербургский государственный электротехнический университет «ЛЭТИ» им. В. И. Ульянова (Ленина), Санкт-Петербург, Россия

✉ vsgoriainov@etu.ru

**Аннотация.** Малые городские и пригородные водоемы являются важными объектами для регулярного экологического мониторинга, в том числе при помощи мониторинга их оптических свойств. В данном исследовании ежемесячно определялись спектры коэффициента ослабления излучения для нескольких водоемов при помощи оптоволоконного спектрометра и лабораторной установки с двумя вогнутыми зеркалами, установленными по бокам стеклянной кюветы. Наблюдалось различие в форме спектров между стоячими и проточными водоемами, а также резкое увеличение значений ослабления в стоячих водах в октябре и ноябре.

**Ключевые слова:** городские водоемы, малые водоемы, спектры ослабления света, сезонные изменения

© Goryainov V.S., Antonenko K.G., Khasenova M., Malyga M.A., Prosolov I.A., 2023. Published by Peter the Great St. Petersburg Polytechnic University.

**Финансирование:** Исследование проводилось в рамках проекта № FSEE0008-2020-, который выполнялся в рамках государственного задания Министерства науки и высшего образования Российской Федерации.

**Ссылка при цитировании:** Горяинов В.С., Антоненко К.Г., Хасенова М., Малыга М.А., Просолов И.А. Сезонные изменения оптических спектров ослабления в нескольких городских водоемах // Научно-технические ведомости СПбГПУ. Физико-математические науки. 2023. Т. 16. № 1.2. С. 146–152. DOI: https://doi.org/10.18721/JPM.161.222

Статья открытого доступа, распространяемая по лицензии CC BY-NC 4.0 (https://creativecommons.org/licenses/by-nc/4.0/)

## Introduction

Minor urban and suburban water bodies are subject to a number of anthropogenic stress factors, including pollution by sewage waters, roadway runoff and pesticides, recreational load, as well as negative effects from redevelopment, draining and other artificial transformations. Slow water exchange makes such water bodies more prone to algal bloom and eutrophication as compared to natural waters [1]. All of the above increases the importance of regular ecological monitoring of urban and suburban water bodies.

Contemporary remote methods intended for studying natural waters rely mostly on the data obtained from spaceborne passive radiometers, spectrometers and hyperspectral cameras. However, the spatial resolution for most of such devices ranges from tens of meters to several kilometers [2, 3], which leaves out urban and suburban ponds, minor lakes, rivers and creeks. Consequently, other techniques are developed to study the properties of such water bodies, including the use of portable spectrometers [4] as well as sampling for subsequent hydro-optical measurements or chemical analysis [5].

In this study, spectra of the beam attenuation coefficient $c(\lambda)$, $m^{-1}$ of water samples in the visible and near infrared (NIR) regions were measured. The attenuation coefficient is a principal hydro-optical parameter that describes the total attenuation of solar irradiation in the water and the consequent limitations on photosynthesis and green algae distribution. Using the spectra obtained, several problems were targeted by the study: (1) assessing the total turbidity of natural waters in question, (2) suggesting the optical phenomena that determine the shape of the spectra, (3) trying to distinguish between stagnant and flowing waters by their attenuation spectra, and (4) observing and analyzing the seasonal variations in the spectra.

## Methods and Means of the Experiment

**Objects of the study.** The samples were taken once a month, from March to November 2021 altogether, from five water bodies in St. Petersburg, of which three were park ponds and two belonged to the Neva delta. Table 1 summarizes the sampling sites along with their latitude and longitude (obtained using GPS) and months (in Roman numerals) for which the samples were available.

Table 1

**Sampling sites**

| Abbreviation | Water body | GPS coordinates | Months |
|---|---|---|---|
| BN | Bolshaya Nevka | 59.97402, 30.32733 | III, VI, IX – XI |
| RK | Karpovka | 59.96752, 30.33002 | IV, VI, IX – XI |
| IP | Iordanskiy pond | 59.99366, 30.33595 | VII – XI |
| SP | Serdobolskiy pond | 59.99527, 30.33198 | VII – XI |
| TsP | Tsvetochniy pond | 59.99184, 30.34155 | VII – XI |

© Горяинов В.С., Антоненко К.Г., Хасенова М., Малыга М.А., Просолов И.А., 2023. Издатель: Санкт-Петербургский политехнический университет Петра Великого.

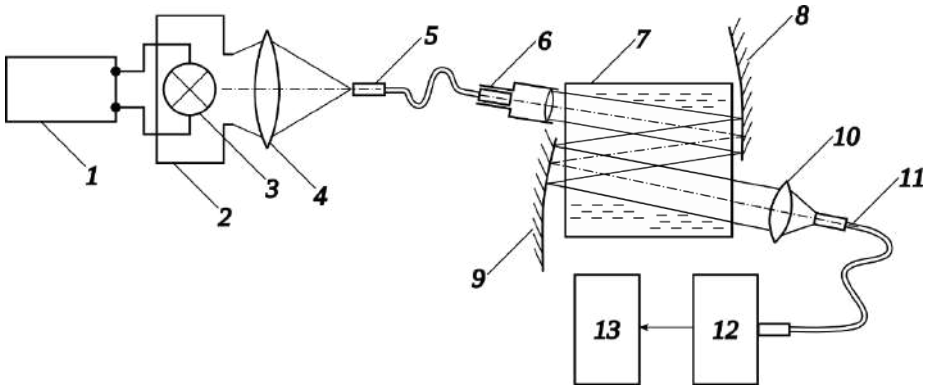


Fig. 1. Scheme of the laboratory setup: stabilized power supply *1*; opaque casing *2*; incandescent lamp *3*; converging lens *4*, *10*; fiber waveguide *5*, *11*; collimator *6*; glass cuvette *7*; concave mirror; *12* — fiber optic spectrometer *8*, *9*; computer *13*

**The laboratory setup.** The setup used for laboratory measurements relied on the well-known idea of extending the path traveled by light in water (Fig. 1). For this purpose, two concave mirrors *8* and *9* were installed on both sides of a 50 mm glass cuvette *7*. Earlier version of the setup used a concave mirror and a plane one, with light passing through the cuvette twice [6]. Some attempts at measuring scattering were also made using that setup, but then the current one was introduced, in which light passes through the cuvette three times, in order to highlight the spectral features more clearly.

The fiber optic spectrometer used for the measurements was an Ocean Insight's USB650 Red Tide. Its crossed Czerny-Turner optical design provided spectral resolution of 2 nm FWHM in the wavelength range from 350 to 1000 nm. The integration time was generally from 10 to 100 ms depending on the sample's turbidity.

For every sample, the following sequence of measurements was performed. First the cuvette was filled with distilled water, and after the necessary adjustments, the spectral intensity distribution ($I_0(\lambda) - I_{D1}(\lambda)$) was registered, with $I_{D1}(\lambda)$ being the noise spectrum (spectrometer's CCD dark current) recorded with the lamp shut off, stored and subtracted internally by the spectrometer's control software. After that, the cuvette was filled with water from the sample under study, the integration time was adjusted if necessary, and the second intensity distribution ($I_T(\lambda) - I_{D2}(\lambda)$) was recorded. In case of very clear sample, both spectra could be recorded using the same integration time, with $I_{D1}(\lambda) = I_{D2}(\lambda)$, obviously. Every measurement was repeated 20 times to enable averaging and estimating the accuracy.

**Processing the experimental data.** Using the aforementioned data, the attenuation coefficient spectrum was calculated by the following formula:

$$c(\lambda) = \frac{1}{3d} \ln\left[\frac{I_0(\lambda) - I_{D1}(\lambda)}{I_T(\lambda) - I_{D2}(\lambda)}\right], \tag{1}$$

where $d$ is the cuvette length.

To approximate the spectrum's shape, two models were used: a decreasing exponent [7]:

$$c_e(\lambda) = c_e(\lambda_0)\exp\left[-S_e\left(\lambda - \lambda_0\right)\right], \tag{2}$$

and a decreasing power function [8]:

$$c_p(\lambda) = c_p(\lambda_0)\left[\lambda / \lambda_0\right]^{-S_p}, \tag{3}$$

where $\lambda_0$ is a reference wavelength and $S_e$, $S_p$ are the spectral slope parameters.

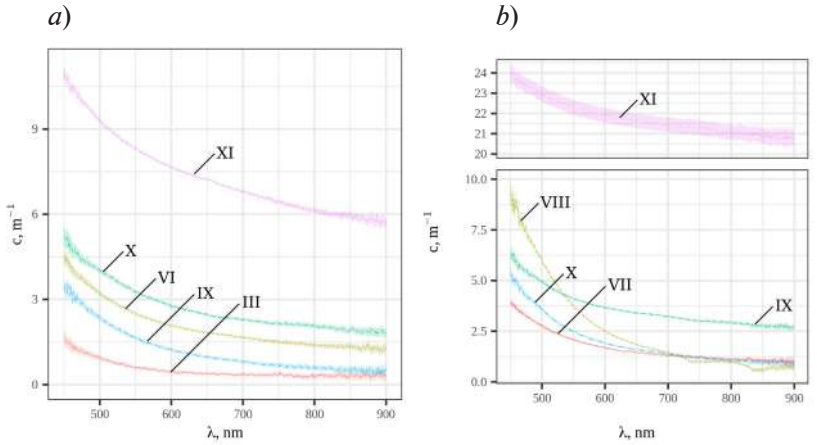


Fig. 2. Attenuation spectra for two water bodies: BN (flowing) (*a*), SP (stagnant) (*b*). Roman numerals denote months. The vertical axis in plot (*b*) is broken due to high attenuation values in November

Since both models are based on a nonlinear function, instead of the coefficient of determination $R^2$, the Bayesian information criterion (BIC) was used to estimate the quality of approximation [9]:

$$BIC = k\ln(n) - 2\ln\left(\hat{L}\right), \tag{4}$$

where $\hat{L}$ is the maximized likelihood of the model, $n$ the number of points in a spectrum, and $k = 1$ is the number of parameters estimated by the model.

All the calculations were performed using the R language and software for statistical computing [10–12].

## Results

As an example of obtained results, Fig. 2 shows the averaged attenuation spectra for two of the water bodies, representing both running waters (BN) and stagnant ones (SP), with Roman numerals denoting months. Semitransparent ribbons along the plot lines show the standard deviation σ.

The power function model (3) gave overall lower BIC values, indicating better fit. Fig. 3 shows the seasonal variations of the spectral slope parameter $S_p$ obtained from approximation (*a*), and of the attenuation coefficient value at 550 nm $c(550)$ (*b*).

Due to relatively low color temperature of the halogen incandescent lamp used as a source of radiation, only the spectral range from 450 to 900 nm was taken into account during approximation. Table 2 contains the Bayesian information criterion (4) values averaged over all the corresponding spectra for each of the water bodies.

Table 2

**Comparison of average BIC values for the two approximation models**

| Water body | Exponential | Power |
|---|---|---|
| BN | 239.66 | –130.69 |
| RK | 553.87 | 139.43 |
| IP | 435.73 | –367.36 |
| SP | 613.60 | 4.96 |
| TsP | 1152.53 | 141.63 |

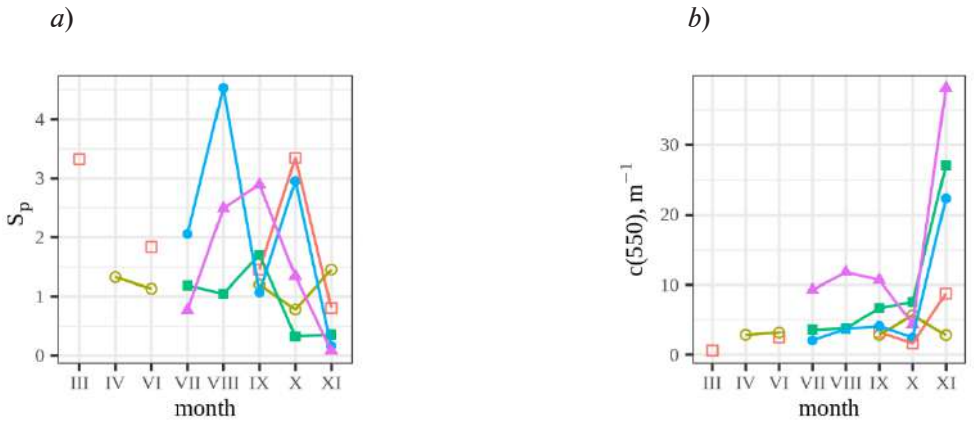


Fig. 3. Seasonal dependence of the spectral slope parameter $S_p$ (*a*) and of the attenuation coefficient value at 550 nm (*b*). The symbols denote the water bodies: □ corresponds to BN, ○ corresponds to RK, ■ corresponds to IP, ● corresponds to SP, ▲ corresponds to TsP

To consider the possible correlation between $S_p$ and $c(550)$, a scatter plot of the two parameters is presented in Fig. 4. Disregarding the separation by water body, Spearman rank correlation coefficient was $\rho = -0.62$. Separate calculations for each of the water bodies gave $\rho$ of $-0.9$ for BN and RK, $-0.6$ for IP and SP, and $-0.2$ for TsP. In other words, higher $c(550)$ values (more turbid samples) corresponded to slower decrease of attenuation with wavelength increasing, and to flatter spectra.

## Discussion

All the spectra obtained in the study showed attenuation decreasing from the blue region to NIR. The models considered for spectral approximation describe absorption of radiation by detritus and non-algal particles [7], and scattering by the same components [8]. With the second model fitting better to experimental data, scattering by detritus might be suggested as the primary process determining the spectra shape. The authors in [8] give an average spectral slope parameter $S_p = 0.938$, which is comparable to the values obtained for RK, or IP and TsP in midsummer months.

The samples from flowing waters (BN and RK) were generally clearer, resulting in lower attenuation values, as Fig. 3,*b*, and the distribution of points along the horizontal axis in Fig. 4 show. The spectral slope parameter, on the other hand, varied more or less widely for all the water bodies, so from the data available, no universal rule can be produced to distinguish between stagnant and flowing waters by the shape of their attenuation spectra. However the two classes of waters showed different seasonal patterns in $S_p$ and c(550) values.

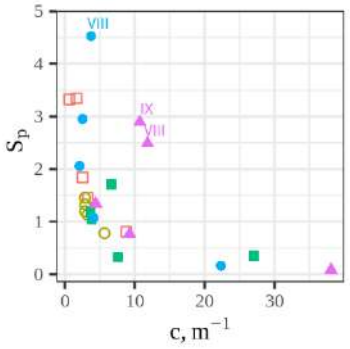


Fig. 4. Interrelation between the spectral slope parameter and the attenuation coefficient value at 550 nm. The symbols denote the water bodies: □ corresponds to BN, ○ corresponds to RK, ■ corresponds to IP, ● corresponds to SP, ▲ corresponds to TsP.
Some notable points are marked by Roman numerals denoting months.

The absolute attenuation maximums for all the water bodies except RK were observed in November (Fig. 3,*b*). The corresponding samples were taken from under the ice edge, near the bank, and appeared visually as very turbid suspension of detritus and mineral particles. The high random error in measurements of attenuation (a wide ribbon along the XI line in Fig. 2, *b*) can be attributed to sedimentation of suspended matter during the measurement reducing turbidity of the sample.

Another maximums for the stagnant waters were observed in late summer (lack of data for flowing waters prevents the comparison between the two classes of water bodies). Rising and decreasing attenuation can be seen for TsP and less prominently, for SP (Fig. 3, *b*). In addition, these points do not follow the general negative correlation between $c(550)$ and $S_p$ stated at the end of the Results section, and appear as outliers with respect to the main trend in Fig. 4, marked with Roman numerals. Such results can be attributed to algae blooming in these two ponds. In the third pond (IP), the same effect appeared in September and to a lesser extent.

Several study limitations arise from its design and conditions. Firstly, comparing the spectra obtained to some results of hydrochemical analysis of the samples could have been very valuable.

Secondly, minor water bodies are prone to rapid ecological changes due to relatively small water mass. For example, chlorophyll concentration in a small pond can follow not only seasonal changes in solar irradiance, but also weather changes and time of day. Studying such processes requires frequent sampling which can be time-consuming, or using submersible probes capable of autonomous operation [13].

## REFERENCES

1. **Bondarenko E.A., Starkov V.A., Andrianova M.Ju.**, Fluorimetric tracing of sewage effluents in the Murinsky creek, Construction of Unique Buildings and Structures. 9 (24) (2014) 27–38.

2. **Krueger J.K., Selva D., Smith M.W., Keesee J.**, Spacecraft and constellation design for a continuous responsive imaging system in space, In: AIAA SPACE 2009 Conference & Exposition, Pasadena, USA, 2009. 6773.

3. **Zhu L., Suomalainen J., Liu J., Hyyppa J., Kaartinen H., Haggren H.**, A review: remote sensing sensors, In: Multi-purposeful Application of Geospatial Data, IntechOpen, London, 2017. 71049.

4. **Liang Q., Zhang Y., Ma R, Loiselle S., Li J., Hu M.**, A MODIS-based novel method to distinguish surface cyanobacterial scums and aquatic macrophytes in lake Taihu, Remote Sensing. 2 (9) (2017) 133.

5. **Andrianova M.J., Bondarenko E.A., Krotova E.O., Chusov A.N.**, Comparison of chemical and optical parameters in monitoring of urban river Okhta, In: EESMS 2014 – 2014 IEEE Workshop on Environmental, Energy and Structural Monitoring Systems, Proceedings. 2014. 198–202.

6. **Горяинов В.С., Хасенова М., Антоненко К.Г., Бузников А.А.**, Лабораторный измеритель гидрооптических характеристик на основе волоконно-оптического спектрометра, Известия СПбГЭТУ «ЛЭТИ». 2 (2021) 5–14.

7. **Bricaud A., Morel A., Babin M., Allali K., Claustre H.**, Variations of light absorption by suspended particles with chlorophyll a concentration in oceanic (case 1) waters: analysis and implications for bio-optical models, Journal of Geophysical Research. C13 (103) (1998) 31033–31044.

8. **Sun D., Li Y., Wang Q., Lv H., Le C., Huang C., Gong S.**, Partitioning particulate scattering and absorption into contributions of phytoplankton and non-algal particles in winter in Lake Taihu (China), Hydrobiologia. 644 (2010) 337–349.

9. **Spiess A.-N., Neumeyer N.**, An evaluation of $R^2$ as an inadequate measure for nonlinear models in pharmacological and biochemical research: a Monte Carlo approach, BMC Pharmacology. 10 (2010) 6.

10. **R Core Team**, R: A Language and Environment for Statistical Computing, R Foundation for Statistical Computing, Vienna, 2020.

11. **Wickham H.**, ggplot2: Elegant Graphics for Data Analysis. Springer-Verlag, New York, 2016.

12. **Xu S., Chen M., Feng T., Zhan L., Zhou L., Yu G.,** Use ggbreak to effectively utilize plotting space to deal with large datasets and outliers, Frontiers in Genetics. 12 (2021) 774846.

13. **Leeuw T., Boss E.S., Wright D.L.**, In situ measurements of phytoplankton fluorescence using low cost electronics, Sensors. 6 (13) (2013) 7872–7883.

## THE AUTHORS

**GORYAINOV Viktor S.**
vsgoriainov@etu.ru
ORCID: 0000-0003-2864-8717

**ANTONENKO Kseniya G.**
kgantonenko@yandex.ru
ORCID: 0000-0002-5776-877X

**KHASENOVA Mariyam**
mariyam-98@mail.ru
ORCID: 0000-0002-9352-7121

**MALYGA Mikhail A.**
mmalyga@list.ru
ORCID: 0000-0003-1844-4104

**PROSOLOV Igor A.**
prosolovigor@gmail.com
ORCID: 0000-0002-9443-7427

*Received 09.11.2022. Approved after reviewing 15.11.2022. Accepted 17.11.2022.*

© Peter the Great St. Petersburg Polytechnic University, 2023

Conference materials
UDC 621.373.826
DOI: https://doi.org/10.18721/JPM.161.223

# 1300 nm VCSELS with active region based on InGaAs/InGaAlAs superlattice for long-distance transmission

V.V. Andryushkin[1]✉, S.A. Blokhin[2], M.A. Bobrov[2], A.A. Blokhin[2],
A.V. Babichev[1], A.G. Gladyshev[1], I.I. Novikov[1], L.Ya. Karachinsky[1],
E.S. Kolodeznyi[1], K.O. Voropaev[3], A.Yu. Egorov[1]

[1] ITMO University, St. Petersburg, Russia;
[2] Ioffe Institute, RAS, St. Petersburg, Russia;
[3] JSC OKB-Planeta, Veliky Novgorod, Russia
✉ vvandriushkin@itmo.ru

**Abstract.** We present the comprehensive study of laser performance of 1300 nm wafer-fused vertical-cavity surface-emitting lasers. Lasers with 5μm buried tunnel junction diameter demonstrate a stable single mode operation in the wide temperature range with maximal output optical power of 6 mW and above 1.5 mW at 20 °C and 80 °C respectively. Based on small-signal analysis the maximal modulation frequency of 8 GHz at 20 °C was estimated. Further increase of the temperature up to 85 °C led to dropping of maximal small-signal modulation frequency down to ~6 GHz at -3dB level despite of remaining of rather high current modulation efficiency about ~2.7 GHz/mA$^{0.5}$._

**Keywords:** vertical-cavity surface-emitting lasers, molecular-beam epitaxy, buried tunnel junction

**Funding:** The authors from ITMO University acknowledge the support in part by the Ministry of Science and Higher Education of the Russian Federation, research project 2019-1442 (project reference number FSER-2020-0013) for the static characteristics measurements and in part by Priority 2030 program for the small-signal modulation experiments. S.A. Blokhin acknowledges the support of the Russian Foundation of Basic Research (Project 20-52-12006) for the spectral characteristics measurements and the part of large-signal modulation experiments.

**Citation:** Andryushkin V.V., Blokhin S.A., Bobrov M.A., Blokhin A.A., Babichev A.V., Gladyshev A.G., Novikov I.I., Karachinsky L.Ya., Kolodeznyi E.S., Voropaev K.O., Egorov A.Yu., 1300 nm VCSELS with active region based on InGaAs/InGaAlAs superlattice for long-distance transmission, St. Petersburg State Polytechnical University Journal. Physics and Mathematics. 16 (1.2) 2023 153–159. DOI: https://doi.org/10.18721/JPM.161.223

This is an open access article under the CC BY-NC 4.0 license (https://creativecommons.org/licenses/by-nc/4.0/)

© Andryushkin V.V., Blokhin S.A., Bobrov M.A., Blokhin A.A., Babichev A.V., Gladyshev A.G., Novikov I.I., Karachinsky L.Ya., Kolodeznyi E.S., Voropaev K.O., Egorov A.Yu., 2023. Published by Peter the Great St. Petersburg Polytechnic University.

Материалы конференции
УДК 621.373.826
DOI: https://doi.org/10.18721/JPM.161.223

# Вертикально-излучающие лазеры спектрального диапазона 1300 нм с активной областью на основе сверхрешетки InGaAs/InGaAlAs для передачи данных на большие расстояния

В.В. Андрюшкин[1]✉, С.А. Блохин[2], М.А. Бобров[2], А.А. Блохин[2], А.В. Бабичев[1], А.Г. Гладышев[1], И.И. Новиков[1], Л.Я. Карачинский[1], Е.С. Колодезный[1], К.О. Воропаев[3], А.Ю. Егоров[1]

[1] Университет ИТМО, Санкт-Петербург, Россия;
[2] ФТИ им. А.Ф. Иоффе, Санкт-Петербург, Россия;
[3] АО ОКБ Планета, Великий Новгород, Россия
✉ vvandriushkin@itmo.ru

**Аннотация.** Представлены результаты комплексных исследований статических и динамических характеристик вертикально-излучающих лазеров спектрального диапазона 1300 нм, созданных по технологии спекания пластины оптического резонатора с пластинами распределенных отражателей, выращенных методом молекулярно-пучковой эпитаксии. Лазеры с диаметром мезы заращенного туннельного перехода 5 мкм продемонстрировали одномодовую лазерную генерацию в широком температурном диапазоне с максимальной выходной мощностью 6 мВт и 1,5 мВт при 20 °С и 85 °С соответственно. Достигнута максимальная частота модуляции 8 ГГц при температуре 20 °С. Дальнейшее увеличение температуры до 85 °С приводит к уменьшению максимальной частоты модуляции до ~6 ГГц на уровне модуляции -3дБ.

**Ключевые слова:** вертикально-излучающие лазеры, молекулярно-пучковая эпитаксия, заращенный туннельный переход_

**Финансирование:** Работа авторов из Университета ИТМО выполнена при поддержке Министерства науки и высшего образования Российской Федерации, проект тематики научных исследований № 1442-2019 (код научной темы FSER-2020-0013) в части исследований статических характеристик, при финансовой поддержке программы «Приоритет 2030» в части экспериментов по исследованию малосигнальной модуляции, а также САБ благодарит за поддержку Российский фонд фундаментальных исследований (Проект № 20-52-12006) в части измерения спектральных характеристик и в части экспериментов по прямой модуляции лазеров большим сигналом.

**Ссылка при цитировании:** Андрюшкин В.В., Блохин С.А., Бобров М.А., Блохин А. А., Бабичев А.В., Гладышев А.Г., Новиков И.И., Карачинский Л.Я., Колодезный Е.С., Воропаев К.О., Егоров А.Ю. Вертикально-излучающие лазеры спектрального диапазона 1300 нм с активной областью на основе сверхрешетки InGaAs/InGaAlAs для передачи данных на большие расстояния // Научно-технические ведомости СПбГПУ. Физико-математические науки. 2023. Т. 16. № 1.2. С. 153–159. DOI: https://doi.org/10.18721/JPM.161.223

Статья открытого доступа, распространяемая по лицензии CC BY-NC 4.0 (https://creativecommons.org/licenses/by-nc/4.0/)

© Андрюшкин В.В., Блохин С.А., Бобров М.А., Блохин А. А., Бабичев А.В., Гладышев А.Г., Новиков И.И., Карачинский Л.Я., Колодезный Е.С., Воропаев К.О., Егоров А.Ю., 2023. Издатель: Санкт-Петербургский политехнический университет Петра Великого.

## Introduction

Nowadays, there has been a significant increase in the volume of digital data requires to be long-distance transmitted. In this regard, the increase in the number of optical communication channels and information processing lead to a significant growth in energy consumption in the world due to necessity to maintain the quantity and quality of transmitted information at high level [1]. The solution of this problem can be found through the development of the new effective laser sources and a vertical-cavity surface-emitting lasers (VCSELs) looks very perspective for this goal. VCSELs in the telecommunication spectral range of 1300 nm can be widely used for optical data transmission over long distances (more than 1 km). Gas sensors [2] and Light Detection and Ranging systems (LIDAR) [3,4] are also belonged to the perspective field of application of these lasers. Development an effective 1300 nm VCSELs requires combining an active region with a high optical gain and a high quality distributed Bragg reflectors (DBR) with a reflection coefficient close to 100%. However, now there are several problems associated with InGaAlAs/GaAs and InGaAlAsP/InP material systems. These problems include insufficient electron localization energy in the InGaAsP quantum well (QW) of the active region [5], large thickness and low thermal conductivity of the InGaAlAsP DBR layers. All these factors lead to weak temperature stability of the output laser's characteristics. One of the ways to solve this problem is to use a wafer-fused (WF) technology for of the active region heterostructures grown on InP substrate and DBRs grown on GaAs substrates, [6, 7], together with the use of a buried tunnel junction (BTJ) as a current and optical confinement [8, 9]. The most important challenge in the development of this approach, to create the very high efficient active gain media based on InP substrates which is able to provide data transfer speeds of tens of Gbit/s.

In this work we present a studies of static and dynamic performance of 1300 nm VCSELs with original design of active gain media based on InGaAs/InGaAlAs superlattice that were fabricated using of molecular-beam epitaxy (MBE) and wafer-fusion technologies.

## Materials and Methods

The active region and top/bottom DBRs heterostructures for 1300 nm VCSELs were grown using MBE Riber 49 system. The active region with optical cavity and active gain media was grown on the InP substrate. It consisted of (see Fig. 1) a bottom intracavity n-InP contact layer with a thin heavy n-doped InGaAs contact layer inside, an active gain media based on a 24-period InGaAs/InAlGaAs SL, a *p*+-InAlAs emitter and composite *n*++-InGaAs/*p*++-InGaAs/*p*++-InAlGaAs BTJ.

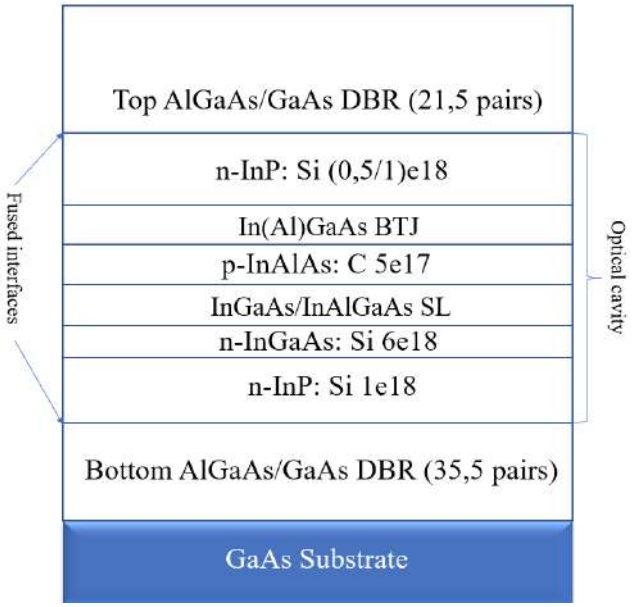


Fig. 1. Schematic representation of the resulting 1300 nm VCSEL heterostructure

The tunnel junction mesa was regrown by *n*-InP layer to form the BTJ. The thickness of the InGaAs layer in SL was 0.8 nm thick, and 2 nm thick for InAlGaAs barrier layers. These values were selected to achieve the photoluminescence peak at a wavelength of 1280 nm at room temperature. The DBR heterostructures were formed by MBE on GaAs substrates. Bottom DBR consisted of 35.5 pairs of $Al_{0.91}Ga_{0.09}As$/GaAs quarter-wave layers and the top DBR consisted of 21.5 pairs. Double wafer fusion of heterostructures at 600°C was carried out using a EVG 510 bonding system under high vacuum conditions. The contact force about 7 kN was applied during the whole bonding process. All thicknesses of the layers were corresponded with the calculated values to ensure resonance peak at 1300 nm. Fig. 2 shows the refractive index profile of the resulting heterostructure. The fabrication of VCSEL chips was carried out by an inductive coupled plasma etching of the top DBR mesa and a selective wet etching of optical cavity layers. Passivation with a SiN dielectric layer was carried out by a plasma-enhanced chemical vapor deposition. The diameter of BTJ mesa was 5 μm.

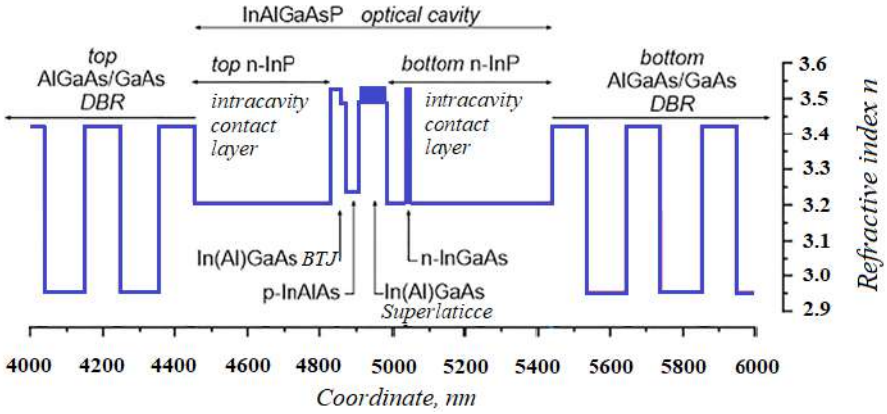


Fig. 2. Refractive index profile of the resulting 1300 nm VCSEL heterostructure

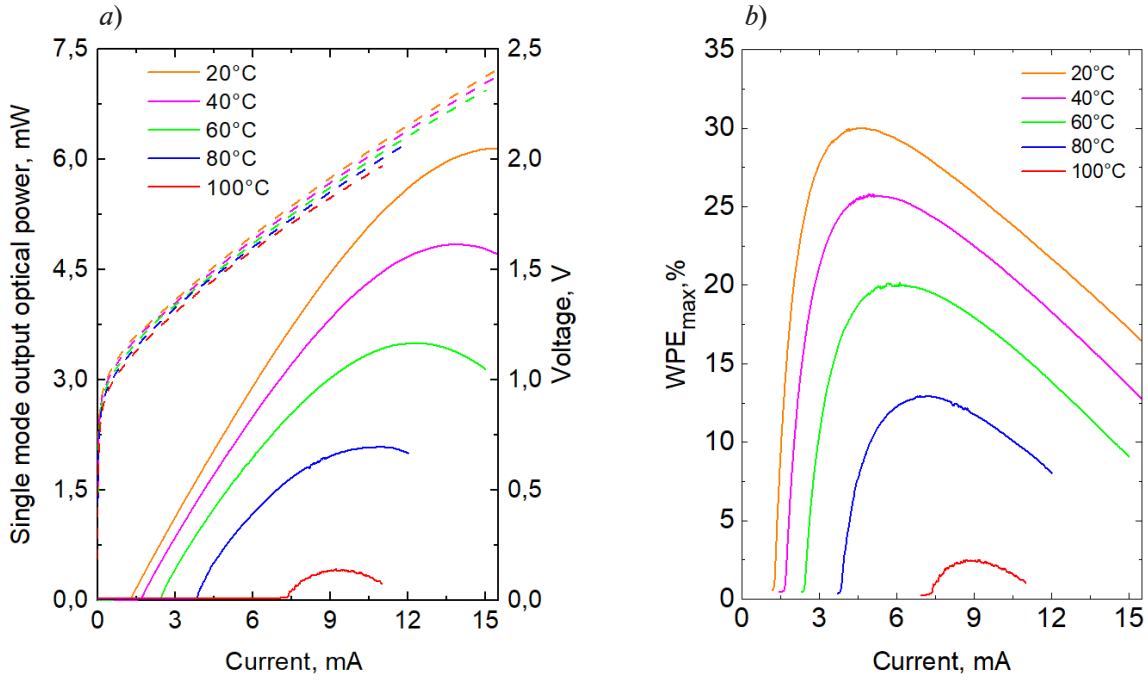


Fig. 3. LIV characteristics of the 1300 nm VCSEL measured at different temperatures (*a*), and dependence of wall-plug efficiency on current (*b*)

## Results and Discussion

The statistic characteristics of the fabricated VCSELs were investigated. The continuous-wave (CW) light-current-voltage (LIV) characteristics of 1300 nm wafer-fused VCSEL were measured in a temperature range 20–100 °C (see Fig. 3,*a*). Lasers have shown the threshold current below 1.5 mA, slope efficiency more than 0.6 W/A and wall-plug efficiency about 30% at room temperature. Analysis of the optical losses in 1300 nm WF VCSELs was discussed in detail early in [10].

The threshold current growths at higher temperatures above the room temperature. At temperatures above 60 °C, an abrupt growth of the threshold current with temperature appears. Moreover, one can see that slope efficiency become the function of the pumping current and this effect increases with the temperature. This may be due to optical absorption at the resonant wavelength of the resonator in the non-pumped parts of the active region. The maximal achieved values of wall-plug efficiency ($WPE_{max}$) were (see Fig. 3,*b*): 30% at room temperature and 9% at 100 °C.

An emission spectra analysis (see Fig. 4) revealed that the VCSELs show stable single-mode lasing for the entire operating range of drive currents and temperatures. As a result, the 1300 nm VCSELs demonstrate a single-mode output optical power more than 6 mW and 1.5 mW at a temperature of 20 °C and 85 °C, respectively, with a side mode suppression ratio more than 40 dB.

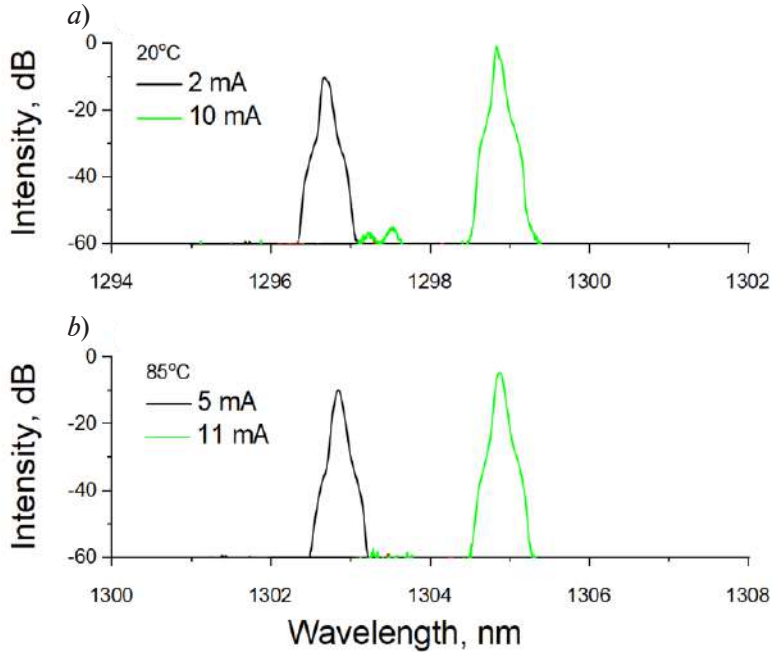


Fig. 4. Optical spectra at different drive current measured at temperatures of 20 °C (*a*), 85 °C (*b*)

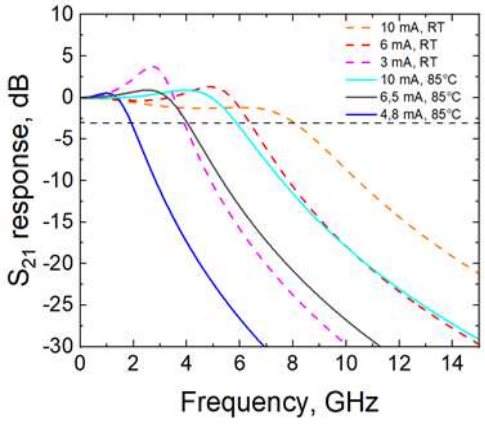


Fig. 5. Small-signal modulation response $S_{21}(f)$ measured at 20 °C and 85 °C

To estimate the dynamic VCSELs performance, the investigation of the frequency response on the small-signal amplitude modulation was carried out. The DC current was combined with the RF-signal through a 45 GHz high frequency bias-tee and was applied to VCSELs via a 40 GHz high-frequency electrical probe. The small-signal frequency response ($S_{21}$) was measured at temperatures of 20 °C and 85 °C (see Fig. 5). At room temperature, the extracted value of -3 dB modulation bandwidth has reached more 8 GHz at 10 mA and drops to 4-5 GHz at higher currents. At 85 °C temperature, the extracted value of -3 dB modulation bandwidth was only 6 GHz despite of maintaining the reasonable high current modulation efficiency about ~2.7 GHz/mA$^{0.5}$. As mentioned previously [10, 11], the electrical parasitics limit the modulation bandwidth of the studied VCSELs.

## Conclusion

The 1300 nm VCSELs with InGaAs/InAlGaAs superlattice acting as active gain media were fabricated using of MBE and wafer-fusion as main technologies for fabrication. Static and dynamic characteristics of developed VCSELs at different temperatures were studied. The lasers with BTJ diameter of 5 μm demonstrated single-mode lasing with side mode suppression ratio more than 40 dB at all investigated temperatures. At temperatures above 60 °C, an abrupt growth of threshold current o temperature appeared, and accompanied by nonlinear behavior of slope efficiency with current, what can be attributed to the optical absorption at the cavity resonance wavelength in the non-pumped parts of the active region (cavity). The maximal modulation frequency reached of 8 GHz at 20 °C. Further increase of the temperature up to 85 °C led to a drop of modulation frequency down to ~6 GHz at -3 dB level despite of remaining of rather high current modulation efficiency value of ~2.7 GHz/mA$^{0.5}$.

## REFERENCES

1. **Masanet E., Shehabi A., Lei N., et al.**, Recalibrating global data center energy-use estimates, Science. 367 (6481) (2020) 984–986.

2. **Kakuma S., Noda K.**, Practical and Sensitive Measurement of Methane Gas Concentration Using a 1.6 μm Vertical-Cavity-Surface-Emitting-Laser Diode, Sensors and Materials. 22(7) (2010) 365–375.

3. **Rablau C.**, LIDAR–A new (self-driving) vehicle for introducing optics to broader engineering and non-engineering audiences, In: Proceedings of Fifteenth Conference on Education and Training in Optics and Photonics: ETOP 2019, Quebec, Canada, 21 – 24 May 2019; Proceedings of SPIE. 2019. Vol. 11143 (2019) 111430C-1.

4. **Steinle G., Ramakrishnan A., Supper D., et. al.**, VCSEL technologies and applications, In: Proceedings of ITCom 2002: The Convergence of Information Technologies and Communications, Boston, USA, 11 July 2002; Proceedings of SPIE. 2002. Vol. 4870 (2002) 419.

5. **Yano M., Imai H., Takusagawa M.**, Analysis of electrical, threshold, and temperature characteristics of InGaAsP/InP double-heterojunction lasers, IEEE Journal of Quantum Electronics. 17(9) (1981) 1954–1963.

6. **Sirbu A., Iakovlev V., Mereuta A., et. al.**, Wafer-fused heterostructures: application to vertical cavity surface-emitting lasers emitting in the 1310 nm band, Semiconductor Science and Technology. 26(1) (2010) 014016.

7. **Ellafi D., Iakovlev V., Sirbu A., et. al.**, Effect of cavity lifetime variation on the static and dynamic properties of 1.3-μm wafer-fused VCSELs, IEEE Journal of Selected Topics in Quantum Electronics. 21 (2015) 414–422.

8. **Onishi Y., Saga N., Koyama K., et. al.**, High power and low resistive GaInNAs-VCSELs with buried tunnel junctions, In Proceedings of 2008 IEEE 21st International Semiconductor Laser Conference, Sorrento, Italy, 14 – 18 September 2008; 53.

9. **Cheng J., Shieh C., Huang X., et. al.**, Efficient CW lasing and high-speed Modulation of 1.3-μm AlGaInAs VCSELs with good high temperature lasing performance, IEEE Photonics Technology Letters. 17 (2005) 7–9.

10. **Blokhin S.A., Babichev A.V., Gladyshev A.G., et. al.**, High power single mode 1300-nm superlattice based VCSEL: impact of the buried tunnel junction diameter on performance, IEEE Journal of Quantum Electronic, 58 (2022) 1–15.

11. **Blokhin S.A., Babichev A.V., Gladyshev A.G., et. al.**, 20-Gbps 1300-nm range wafer-fused vertical-cavity surface-emitting lasers with InGaAs/InAlGaAs superlattice-based active region, Optical Engineering. 61(9) (2022) 196109.

## THE AUTHORS

**ANDRYUSHKIN Vladislav V.**
vvandriushkin@itmo.ru
ORCID: 0000-0002-7471-8627

**BLOKHIN Sergei A.**
blokh@mail.ioffe.ru
ORCID: 0000-0002-5962-5529

**BOBROV Mikhail A.**
bobrov.mikh@gmail.com
ORCID: 0000-0001-7271-5644

**BLOKHIN Aleksey A.**
Aleksey.Blokhin@mail.ioffe.ru
ORCID: 0000-0002-3449-8711

**BABICHEV Andrey V.**
a.babichev@itmo.ru
ORCID: 0000-0002-3463-4744

**GLADYSHEV Andrey G.**
andrey.gladyshev@connector-optics.com
ORCID: 0000-0002-9448-2471

**NOVIKOV Innokenty I.**
innokenty.novikov@itmo.ru
ORCID: 0000-0003-1983-0242

**KARACHINSKY Leonid Ya.**
lkarachinsky@itmo.ru
ORCID: 0000-0002-5634-8183

**KOLODEZNYI Evgenii S.**
evgenii_kolodeznyi@itmo.ru
ORCID: 0000-0002-3056-8663

**VOROPAEV Kirill O.**
kirill.voropaev@novsu.ru
ORCID: 0000-0002-6159-8902

**EGOROV Anton Yu.**
anton.egorov@connector-optics.com
ORCID: 0000-0002-0789-4241

*Received 26.10.2022. Approved after reviewing 10.11.2022. Accepted 10.11.2022.*

© Peter the Great St. Petersburg Polytechnic University, 2023

Conference materials
UDC 535.231.11
DOI: https://doi.org/10.18721/JPM.161.224

# Power-communicating photo-receiving device

S.O. Kognovitskii[1]✉, D.A. Malevskiy[1], E.I. Terukov[1, 2], S.A. Yakovlev[1]

[1] Ioffe Institute, St. Petersburg, Russia;

[2] St. Petersburg Electrotechnical University "LETI", St. Petersburg, Russia

✉ kogn@mail.ioffe.ru

**Abstract.** The work is devoted to the creation of a power-communicating photo-receiving device for an autonomous laser communication unit, designed to receive energy from powerful laser radiation and convert it into electricity, as well as for simultaneous registration of information high-frequency optical signals. The presented results demonstrate the possibility of photo-receiving device practical use in laser communication system, including power supplying of the active equipment.

**Keywords:** wireless power transmission, laser beam, photo-receiving device, photovoltaic cell, high-speed photodiode

**Citation:** Kognovitskii S.O., Malevskiy D.A., Terukov E.I., Yakovlev S.A., Power-communicating photo-receiving device, St. Petersburg State Polytechnical University Journal. Physics and Mathematics. 16 (1.2) 2023 160–164. DOI: https://doi.org/10.18721/JPM.161.224

This is an open access article under the CC BY-NC 4.0 license (https://creativecommons.org/licenses/by-nc/4.0/)

Материалы конференции
УДК 535.231.11
DOI: https://doi.org/10.18721/JPM.161.224

# Энергоинформационное фотоприемное устройство

С.О. Когновицкий[1]✉, Д.А. Малевский[1], Е.И. Теруков[1, 2], С.А. Яковлев[1]

[1] Физико-технический институт им. А.Ф. Иоффе РАН, Санкт-Петербург, Россия;

[2] Санкт-Петербургский государственный электротехнический университет «ЛЭТИ» им. В.И. Ульянова (Ленина)

✉ kogn@mail.ioffe.ru

**Аннотация.** Работа посвящена созданию энергоинформационного фотоприемного устройства для автономного узла лазерной связи, предназначенного для приема энергии мощного лазерного излучения и преобразования ее в электроэнергию, а также для одновременной регистрации информационных высокочастотных оптических сигналов.

**Ключевые слова:** беспроводная передача энергии, лазерный луч, фотоприемное устройство, фотоэлектрический преобразователь, быстродействующий фотодиод

**Ссылка при цитировании:** Когновицкий С.О., Малевский Д.А., Теруков Е.И., Яковлев С.А. Энергоинформационное фотоприемное устройство // Научно-технические ведомости СПбГПУ. Физико-математические науки. 2023. Т. 16. № 1.2. С. 160–164. DOI: https://doi.org/10.18721/JPM.161.224

Статья открытого доступа, распространяемая по лицензии CC BY-NC 4.0 (https://creativecommons.org/licenses/by-nc/4.0/)

© Kognovitskii S.O., Malevskiy D.A., Terukov E.I., Yakovlev S.A., 2023. Published by Peter the Great St. Petersburg Polytechnic University.

## Introduction

The data transmission by modulated laser radiation propagating in the optical fiber line has become widespread. Technologies for simultaneous transmission of optical power and data by the laser radiation in an optical fiber have been earlier investigated [1]. Optical power of several watts through the fiber for a distance up to 200 m can be transmitted to the electricity with the 20% efficiency: electricity conversion cycle, due to limitations of the transmitted power caused by overheating of the fiber at high power up to self-destruction [2].

Optical systems for data transmitting through open atmospheric or space channels have also been developed and implemented. For example, in Russia, the transceiver apparatus of atmospheric optical communication lines is mass-produced by two companies, Mostkom CJSC (Ryazan) (Artrolink), and Catharsis NPK LLC (St. Petersburg) (Lantastica TZR).

Contactless and wireless transmission of laser radiation power pass through the open channel, followed by its photoelectric conversion at the terminal device [3]. This power transmission method has obvious advantages: the power can be increased (up to hundreds of kW) compared to the power transmission through an optical fiber; the power density and data transfer rate can be improved, narrower beam focus and smaller diameters of the transmitter and receiver can be achieved compared to the method of power transmission using microwave radiation [4]. The main applications of laser power transmission technology through an open channel are the following:

- remote power for the industrial and specialized mobile terrestrial equipment;
- remote power organization for the repeaters of 5G data transmission networks;
- cargo delivery to Earth orbit;
- generated power transmission from space stations to ground-based consumers or to the lunar surface, including for powering lunar rovers and stationary research vehicles;
- wireless charging of household devices;
- in medical technology – wireless power transmission of the laser IR radiation through the skin directly into the patient's body for recharging biosensor batteries and smart implants.

In the next decennary, wireless power transmission could become an important part of power grids.

The development of laser power transmission systems has recently been intensified [5] due to the appearance of efficient photovoltaic cell and powerful efficient compact lasers with low beam divergence.

For example, the Russian Rocket and Space Corporation Energia has developed a Pelican laser power transmission system [6]. This system can be used to power, for example, microrovers, research stations with drilling rigs, light beacons to provide landings of automatic and manned spacecraft on the shaded side of the moon. The maximum distance from the source to the receiver is about 300 km. The system is capable to transmit 750 W of electric power at 3000 W of optical power.

The Japanese Aerospace Exploration Agency develops a laser system for power transmission from space to Earth and at interorbital optical communication over long distances. Laser wireless power transmission system investigation by a continuous fiber optic laser (emission wavelength 1070 nm and 500 W power) has been reported [7]. The ability of the beam alignment with an accuracy of 1 μrad has been demonstrated.

A laser system recently developed by PowerLight powered one of Ericsson's 5G cellular base stations, which was not connected to any other power source [8]. The system supplied more than 480 W of electrical power at 300 m. At an early date, the system will be improved to transmit 1 kW over a distance of more than 1 km. The wireless power of 5G stations can improve systems portability, stations can be quickly temporarily deployed in places with increased traffic, for example, at festivals, exhibitions, conferences, or during natural disasters when other communication infrastructure were disrupted.

Laser system for transmitting through an atmospheric channel and converting laser radiation achieved 11.6% efficiency (electricity-electricity) at transmission range 100 m, and generated electrical power 9.7 W [9]. Multi-cell semiconductor photovoltaic (PV) converters with an optimized *p*++-GaAs/*p*-InGaP/*p*-GaAs/*n*-GaAs/*n*-AlGaAs/*n*-GaAs/*n*-Ge structure and with 40.4% efficiency at standard test conditions (STC) (60 kW/m2laser intensity, 24 W laser optical power, wavelength 793 nm) was used in the system.

© Когновицкий С.О., Малевский Д.А., Теруков Е.И., Яковлев С.А., 2023. Издатель: Санкт-Петербургский политехнический университет Петра Великого.

The problem of the space antenna reflecting surface transforming can be solved by curtain deforming with the help of actuators. Power and data are supplied to the actuators by laser beam through the open channel from a semiconductor laser to a photoconverter located directly on the actuator [10]. So antenna weight can be reduced, function reliability can be increased, transformation of antenna shape in order to change radiation diagram can be controlled. A test sample integrating laser source and a photodetector module including four combined PV cells for modeling the power transmission through an open channel were developed in the Ioffe Institute. The photoconversion efficiency 26.3% (1 W) was achieved.

## Photo-receiving device construction

Compact full-size photo-receiving device for simultaneously receiving power and data transmission through an open laser atmosphere channel was developed and manufactured in the presented work. The main criteria for the device design were construction simplicity and low cost.

The created photo-receiving device (Fig. 1) includes five photovoltaic converters (PVC) based on a silicon HJT structure (157×157 mm$^2$ each), and one low response time photodiode based on a lattice-matched InGaAs PIN semiconductor structure (wavelength 1.55 μm), located in the focus of a concentrator. The concentration system includes a conical reflecting secondary optics (hollow aluminum focon and eight mirrors) and Fresnel lens. Four PVCs are placed around the central PVC cell. The central PVC is transparent to information optical signal 1.55 μm wavelength. Low response time InGaAs photodiode with concentrator is located behind the central photoelectric converter. Centrosymmetric beam (for example Gaussian distributed) in Si photosensitivity spectral range falls to the photo-receiving panel: central and peripheral PVCs. Four peripheral PVCs have eight mirrors to reflect peripheral laser radiation to them and the intensity of peripheral radiation increases. Photocurrent values of central and peripheral PVCs align and all Si cells can be series connected without electrical losses to increase the photo-receiving panel efficiency. The spectral range for 'power' laser radiation conversion for Si photo-receiving device is 0.6–1 μm. Due to the human eye invisibility requirement and the presence of atmospheric transparency windows, it should be in the ranges of 0.85–0.9 μm or 0.95–1 μm. The wavelength of the information high frequency modulated radiation should be in the range of 1.3–1.6 μm due to the Si cell transmission spectra.

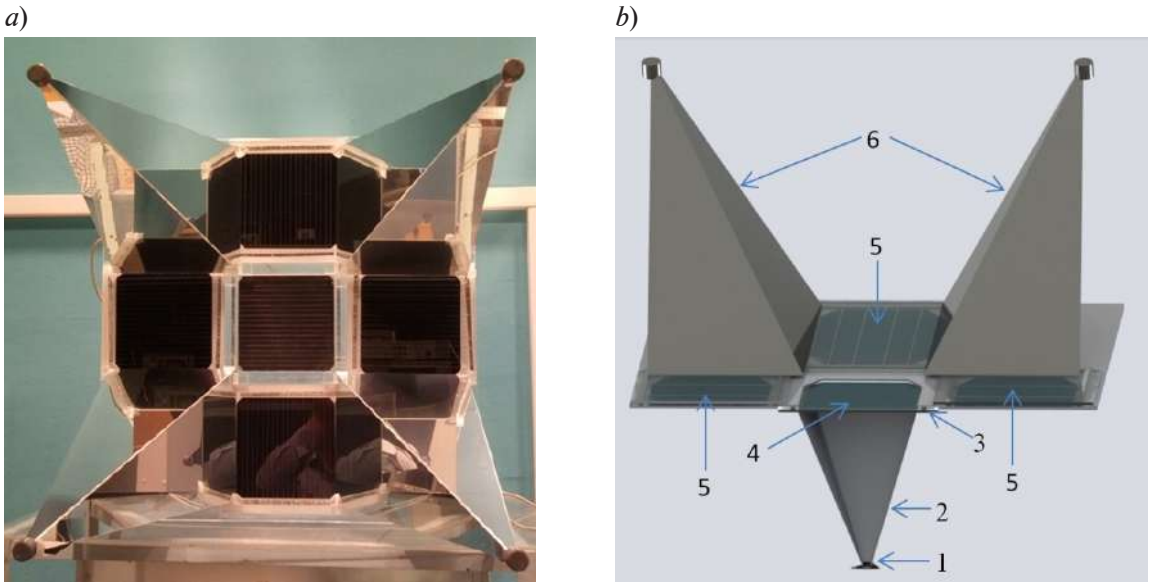


Fig. 1. Power-communicating photo-receiving device (*a*), sectional view (*b*).
InGaAs PIN photodiode *1*, hollow focon *2*, Fresnel Lens *3*, two-sided photosensitivity Si cell *4*, transparent to information optical signal, Si photovoltaic converters *5*, reflectors *6*

## Experimental results

A comparative analysis of the Si cell transmission spectra and the low response time photodiode photosensitivity is shown in Fig. 2. Overlap of InGaAs PIN photodiode photosensitivity and the transmission spectra of Si PVCs is observed. It is necessary to protect the low response time photodiode from solar radiation, for example, by an interference filter. The complex shape of the PVCs transmission spectrum has two minima at about 0.12 μm and 0.14 μm, related to the multilayer construction of the central PVC cell. It includes the multilayer silicon HJT structure, the glass on the one side of silicon structure and a transparent laminating film on the other side.

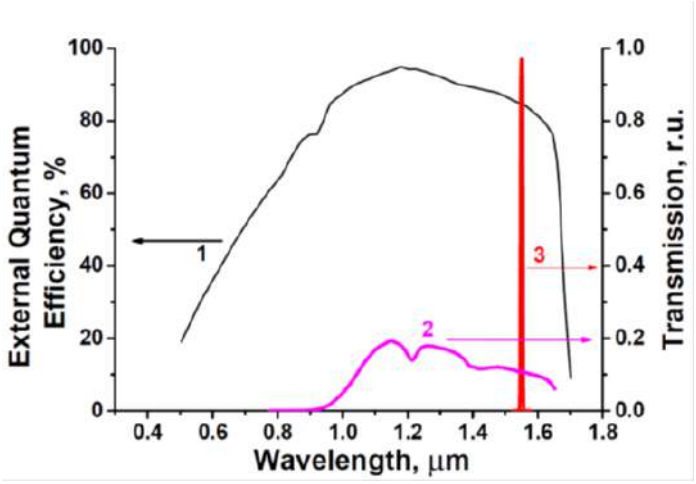


Fig. 2. External quantum efficiency of a low response time photodiode (*1*), the transmission spectra of a silicon solar cell (*2*), the transmission of an interference filter (*3*)

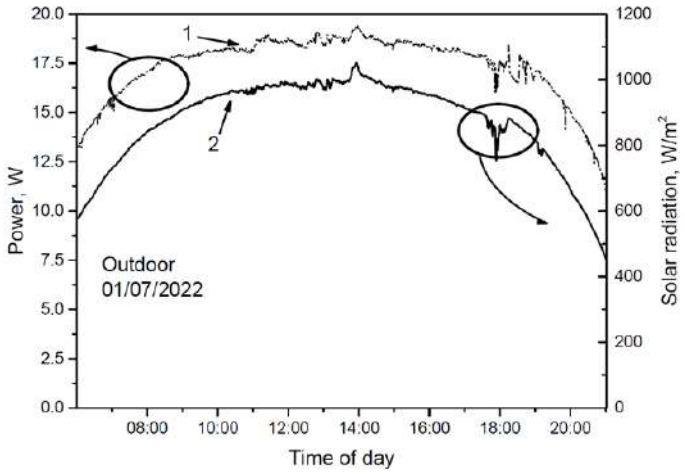


Fig. 3. Photoreceiving device power generation (*1*) of and daily solar radiation (*2*)

At the daytime, the photo-receiving device can generate additional electricity by converting solar radiation (Fig. 3).

Photo-receiving device was installed on the solar tracking system during the solar day. The generated power and the global solar irradiation were measured by photovoltaic monitoring complex [11] (generated power during the day is 270 W·h, all day solar irradiance is 12088 W·h/m$^2$).

### Conclusion

The technical and organizational aspects for the photo-receiving device have been designed. Method of simultaneously registration of information high-frequency optical signal and powerful laser energy conversion is presented.

The main technical parameters of the developed photo-receiving device are as follows:

- electrical power is 80 W;
- data receiver cut-off frequency is 600 MHz;
- dimensions (LxWxH) are 570×614×600 mm.

## REFERENCES

1. **Emelyanov V.M. et al.**, Photovoltaic optical sensors for high-power conversion and information transmission, Optical Sensors. 10231 (2017) 1–12.

2. **Garkushin A.A. et al.**, Sistema peredachi energii po opticheskomu voloknu [Optical fiber energy transferring systems], Scientific Communications Bulletin. 25 (2020) 48–53.

3. **Summerer L., Purcell O.**, Concepts for wireless energy transmission via laser, Int. Conf. Space Optical Syst. Appl. (2009) 1.

4. **Boichuk E.S.**, Peredacha energii lazernym izlucheniem v svobodnom prostranstve [Energy transfer by laser radiation through free space], Scientific Communications Bulletin. 25 (2020) 91–102.

5. **Baranika, et al.**, Wireless Laser Power Transmission: A Review of Recent Progress, Int. Journal of Engineering Research & Technology (IJERT). 6 (2018) 1–13.

6. **Evdokimov R.A., et al.**, Distantsionnoe energosnabzhenie potrebitelei na poverkhnosti Luny [Remote Power Supply of Consumers on the Moon Surface], Bulletin of the Russian Academy of Sciences: Energy. 5 (2019) 3–19.

7. https://www.kenkai.jaxa.jp/eng/research/ssps/ssps-lssps.html

8. https://newatlas.com/energy/wireless-power-transmission-ericsson-powerlight/

9. **He T., et al.**, High-Power High-Efficiency Laser Power Transmission at 100m Using Optimized Multi-Cell GaAs Converter, Chinese Physics Letters. 31 (2014) 104203.

10. **Kochin L.B., et al.**, Peredacha energii i informatsii po opticheskomu kanalu dlia upravleniia formoi kosmicheskoi antenny [Transmission of energy and information through optical communication channel to control the form of space antenna], Reshetnev readings. 1 (2017) 129–130.

11. **Shvarts M.Z., et al.**, Monitoring complex for concentrator photovoltaic installation with a tracking system, IOP Conf. Ser.: Earth Environ. Sci. 578 (2020) 012054.

## THE AUTHORS

**KOGNOVITSKII Sergei O.**
kogn@mail.ioffe.ru

**TERUKOV Evgenii I.**
evgenii.terukov@metalab.ifmo.ru

**MALEVSKIY Dmitrii A.**
dmalevsky@scell.ioffe.ru

**YAKOVLEV Sergei A.**
yakovlev@gvg.ioffe.ru

*Received 27.10.2022. Approved after reviewing 09.11.2022. Accepted 09.11.2022.*

© Peter the Great St. Petersburg Polytechnic University, 2023

Conference materials
UDC 535.415
DOI: https://doi.org/10.18721/JPM.161.225

# Decorative protective coatings produced by atomic layer deposition and calculation of their spectral characteristics

V.V. Aksenova[1, 2✉], M.V. Mesh [3], D.S. Kolokolov[3],
T.Yu. Kartseva[3], N.A. Fedorov[4], A.S. Pavlyuchenko[2]

[1] Peter the Great St. Petersburg Polytechnic University, St. Petersburg, Russia;
[2] Ioffe Institute, St. Petersburg, Russia;
[3] JSC Koltsov's Design Bureau, St. Petersburg, Russia;
[4] ITMO University, St. Petersburg, Russia
✉ valeriyaakse@gmail.com

**Abstract.** In this paper, we consider the possibilities of using the atomic layer deposition process for producing decorative coatings based on aluminum oxide and titanium oxide on steel parts. The parameters of coatings based on aluminum oxide and titanium oxide of different colors were calculated. The calculations of the coating color and its optical characteristics are shown, and it is found that the developed software allows you to calculate the color of the coating. The properties of the resulting coatings have been studied and it has been experimentally established that these coatings can be used for chemical protection of surfaces.

**Keywords:** aluminium oxide, protective coating, atomic layer deposition, titanium oxide, decorative coating

**Citation:** Aksenova V.V., Mesh M.V., Kolokolov D.S., Kartseva T.Yu., Fedorov N.A., Pavlyuchenko A.S., Decorative protective coatings produced by atomic layer deposition and calculation of their spectral characteristics, St. Petersburg State Polytechnical University Journal. Physics and Mathematics. 16 (1.2) 2023 165–171. DOI: https://doi.org/10.18721/JPM.161.225

This is an open access article under the CC BY-NC 4.0 license (https://creativecommons.org/licenses/by-nc/4.0/)

© Aksenova V.V., Mesh M.V., Kolokolov D.S., Kartseva T.Yu., Fedorov N.A., Pavlyuchenko A.S., 2023. Published by Peter the Great St. Petersburg Polytechnic University.

Материалы конференции
УДК 535.415
DOI: https://doi.org/10.18721/JPM.161.225

# Декоративные защитные покрытия, наносимые методом атомно-слоевого осаждения, и расчет спектральных характеристик таких покрытий

В.В. Аксенова[1, 2] ✉, М.В. Меш[3], Д.С. Колоколов[3],
Т.Ю. Карцева[3], Н.А. Федоров[4], А.С. Павлюченко[2]

[1] Санкт-Петербургский политехнический университет Петра Великого, Санкт-Петербург, Россия;
[2] Физико-технический институт им. А.Ф. Иоффе РАН, Санкт-Петербург, Россия;
[3] АО «СКТБ Кольцова», Санкт-Петербург, Россия;
[4] Университет ИТМО, Санкт-Петербург, Россия
✉ valeriyaakse@gmail.com

**Аннотация.** В данной работе рассмотрены возможности применения процесса атомно-слоевого осаждения для нанесения декоративных покрытий на основе оксида алюминия и оксида титана на стальные детали. Были рассчитаны параметры покрытий на основе оксида алюминия и оксида титана разных цветов. Показаны результаты по разработке программного обеспечения для расчета цвета покрытия и его оптических характеристик и установлено, что разработанное программное обеспечение позволяет рассчитать цвет покрытия. Изучены свойства получаемых покрытий и экспериментально установлено, что эти покрытия можно использовать в качестве защитных.

**Ключевые слова:** атомно-слоевое осаждение, оксид титана, оксид алюминия, защитное покрытие, декоративное покрытие

**Ссылка при цитировании:** Аксенова В.В., Меш М.В., Колоколов Д.С., Карцева Т.Ю., Федоров Н.А., Павлюченко А.С. Декоративные защитные покрытия, наносимые методом атомно-слоевого осаждения, и расчет спектральных характеристик таких покрытий // Научно-технические ведомости СПбГПУ. Физико-математические науки. 2023. Т. 16. № 1.2. С. 165–171. DOI: https://doi.org/10.18721/JPM.161.225

Статья открытого доступа, распространяемая по лицензии CC BY-NC 4.0 (https://creativecommons.org/licenses/by-nc/4.0/)

## Introduction

One of the most common ways to protect a metal from corrosion is to isolate its surface from the external environment by depositing a protective coating. The use of atomic layer deposition to create anti-corrosion coatings is not yet widespread, but it is an up-to-date and promising method that has all the advantages necessary in this area, namely, the possibility of a wide range of materials deposition with atomic precision [1] to products of complex geometry with high uniformity of the obtained films.

This process can be used to create a protective and decorative coating on metals; this is especially important for processing products of complex shape, because the atomic layer deposition process will allow uniform coating of the entire surface of sample [2]. Due to the ability to precisely control the thickness, any color of the coating can be obtained by changing the thickness. Interference coatings used in the visible region of the range are characterized not only by optical parameters, but also by color [3]. Chromaticity coordinates are used to describe the color properties of interference coatings. They cover all colors visible to a standard observer and form the CIE chromaticity diagram.

© Аксенова В.В., Меш М.В., Колоколов Д.С., Карцева Т.Ю., Федоров Н.А., Павлюченко А.С., 2023. Издатель: Санкт-Петербургский политехнический университет Петра Великого.

The possibility of using atomic layer deposition as a method for creating anticorrosive and decorative coatings was approved in articles [4–6]. In [4], $Al_2O_3$ and $TiO_2$ coatings proved to be effective in protecting stainless steel substrates from corrosion and increasing the thickness of the coating increased its corrosion resistance. In [5] deposited layers of $Al_2O_3$ and $TiO_2$ were used to create ultra-thin protective coatings on copper to prevent water corrosion, and it turned out that the coating formed by a layer of titanium oxide on a layer of aluminum oxide was very resistant to water corrosion. $TiO_2$ layers 20 nm thick on $Al_2O_3$ layers 5 nm thick protected the copper substrate for 90 days in water at 90°C. Paper [6] systematically investigated the detailed processes for growing $Al_2O_3$ and $TiO_2$ thin films at a growth temperature of 80°C and their applicability for functional color coatings. Using the scheme $TiO_2$ (162 nm)/$Al_2O_3$ (48 nm)/$TiO_2$ (80 nm)/$Al_2O_3$ (60 nm), a pink coating was obtained on a stainless steel substrate with an intermediate layer of TiN, in addition, the colors were determined after finishing deposition of each of the layers.

## Materials and Methods

The process of atomic layer deposition was carried out on a PICOSUN P-300B ALD system. The Picosun-300B unit can operate in the temperature range from 20 to 500 °C. In this work, trimethylaluminum (TMA) + water vapor for $Al_2O_3$ and water vapor + titanium tetrachloride for $TiO_2$ were used from sources. The working pressure was 600 Pa.

For the calculation, a software package was developed that provides access to data on the refractive and absorption indices aggregated in the refractiveindex.info library [7] (for the studied coatings we used refractive indices spectra reported in the following papers: [8] for $TiO_2$, [9] for $Al_2O_3$, [10] for Mo; refractive index spectrum of the glass substrate was determined from our own experiments), based on which the transmission, reflection, and absorption spectra of layered thin films were calculated using the matrix method [11]. The resulting reflection spectrum is converted to color in the CIE XYZ system using analytical approximations of the addition functions of the three-color colorimetric system obtained in [12].

When calculating, the incidence of light was assumed to be normal, the spectrum of the incident light was taken to be the emission spectrum of a black body at a temperature of 5777 K, scattering, as well as surface irregularities, were not taken into account in the calculation.

The transmission and reflection spectra of the samples were studied on an Optronic Laboratories OL 770 spectroradiometer. The radiation was incident on the sample from the side of the film, normal to its surface.

## Results and Discussion

A coating of aluminum oxide and titanium oxide in combination $Al_2O_3/TiO_2/Al_2O_3/TiO_2$ 60/60/60/60 nm with a total thickness of 240 nm was deposited by atomic layer deposition on a glass sample pre-coated with a 100 nm layer of molybdenum (Fig. 1). The reflection spectrum of the resulting coating is shown in Fig. 2. The transmission of a 100-nm-thick molybdenum layer is zero in the optical radiation range, which makes it possible to use such a coating as a test one.

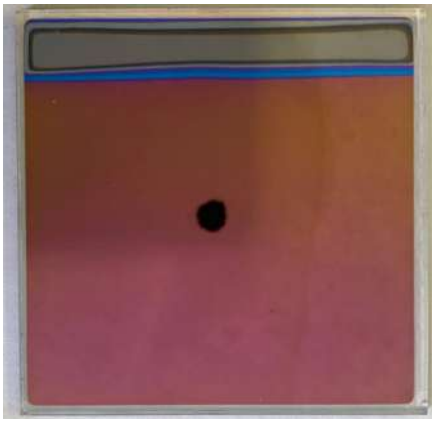

Fig. 1. Glass sample with a layer of molybdenum after atomic layer deposition

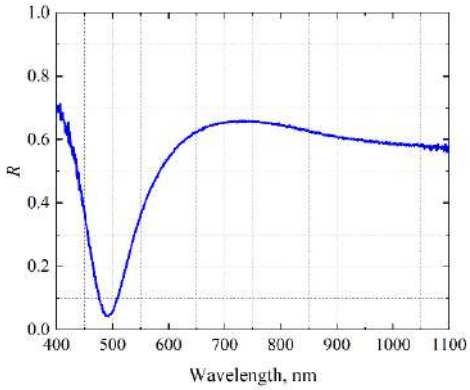


Fig. 2. Experimentally obtained reflection spectrum

In the case of comparing the experimentally obtained spectrum with the previously obtained calculated one, one can see a significant agreement (Fig. 3), which confirms the correctness of the used model for calculating the spectral characteristics of the coating. Visual inspection of the sample also confirms the correspondence of the calculated color characteristics to the color of the experimentally obtained coating (Fig. 4).

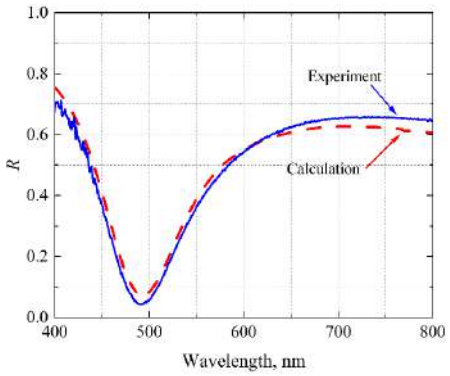


Fig. 3. Comparison of calculated and experimental reflection spectra

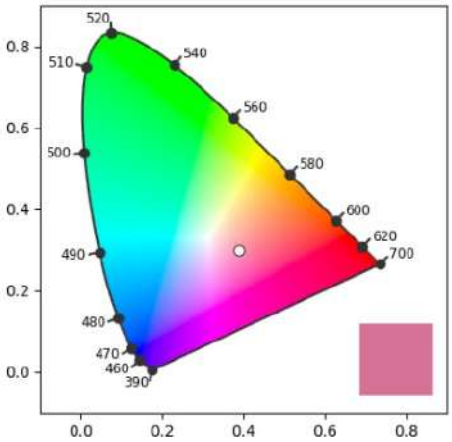


Fig. 4. Calculated color of the coating in normal light incidence

After that a similar coating was deposited on the surface of steel ring (Fig. 5). During the process, part of the sample was masked, which made it possible to obtain a two-color coating on the sample.

Fig. 5. Steel ring after atomic layer deposition

After that, SEM images of two parts of the sample of different colors were obtained (Fig. 6). The surface of the ring, on which the decorative coating was deposited, has a significant roughness obtained during metalworking operation. Although the atomic layer deposition method allows coatings on uneven surfaces, the layer thickness may vary depending on the nature of the roughness. In addition, the resulting color of the coating varies due to the reflection of light at different angles.

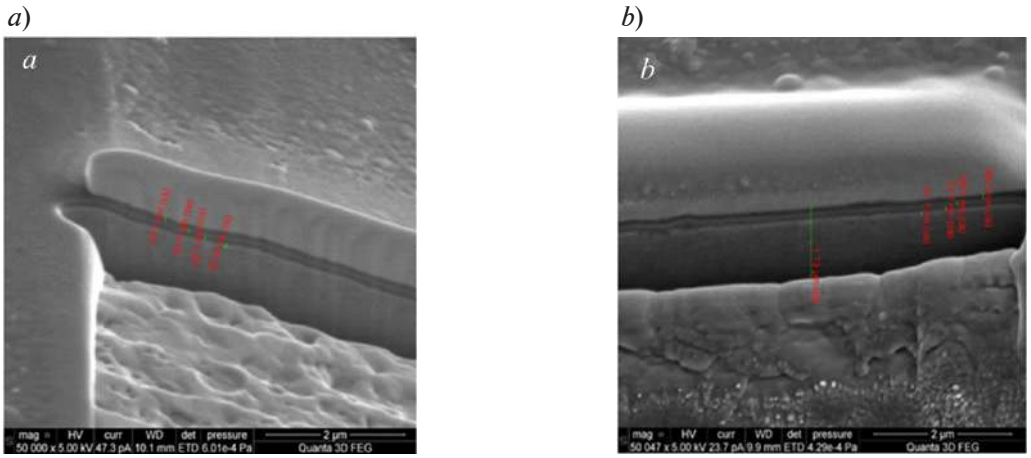


Fig. 6. SEM-image of the blue (*a*) and violet (*b*) parts of sample 1

A steel plate was also coated, which was then sent for a moisture test in a moisture chamber to check their corrosion properties along with a similar uncoated plate. They were exposed to high humidity in the moisture chamber. The test consisted of 9 cycles, each of them was carried out in two stages: 12 hours at a temperature of 55 °C and a humidity of 93 %, then 12 hours at a temperature of 25 °C and a humidity of 95 %.

After the test, no corrosion was found on inspection on the coated sample (Fig. 7, *b*), in contrast to the uncoated sample (Fig. 7,*a*). Tests in a climatic chamber showed that the resulting decorative coating based on aluminum and titanium oxides is corrosion resistant. This makes it possible to further use this type of coating in the field of protection of steel products from corrosion.

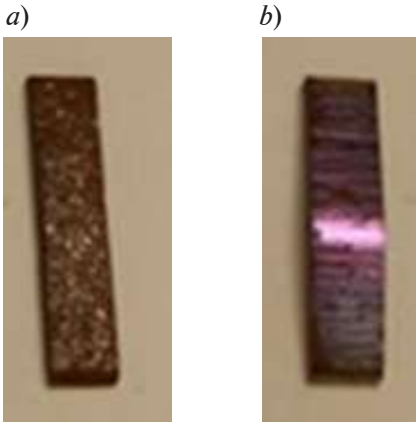


Fig. 7. Photos of uncoated (*a*) and coated (*b*) samples after testing in a climatic chamber

## Conclusion

In this work, decorative protective coatings obtained by the ALD method on metal surfaces were developed. It was experimentally established that the developed coatings have protective properties that are not inferior to traditional protective films.

The use of atomic layer deposition to create decorative coatings is just beginning in industry and research. And this work proposes to use interference coatings with a periodic structure to give decorativeness to metal structural elements. The possibility of obtaining uniform coatings with controlled thickness and the developed method for calculating color will expand the possibilities of using color coatings in optical systems and the electronics industry.

## Acknowledgements

The optical measurements in this work were carried out with the equipment of the Center of Multi-User Facilities "Element Base of Microwave Photonics and Nanoelectronics: Technology, Diagnostics, and Metrology".

## REFERENCES

1. **Malygin A.A., Dubrovensky S.D.,** Quantum-chemical approaches to the identification of nanostructures synthesized by molecular deposition, Rossiyskiy Khimicheskiy Zhurnal. 53 (2) (2009) 98–110.

2. **Malygin A.A., Drozd V.E., Malkov A.A., Smirnov V.M.**, From VB Aleskovskii's "Framework" hypothesis to the method of molecular layering/atomic layer deposition, Chemical Vapor Deposition. 21(10-11-12) (2015) 216–240.

3. **Azamatov M.H., Gajnutdinov I.S., Mihajlov A.V., Sabirov R.S., Safin R.G.**, Determining the color difference of interference coatings, Journal of Optical Technology. 74 (3) (2007) 68–71.

4. **Marin E., Guzman L., Lanzutti A., Ensinger W., Fedrizzi L.**, Multilayer $Al_2O_3/TiO_2$ Atomic Layer Deposition coatings for the corrosion protection of stainless steel, Thin Solid Films. 522 (2012) 283–288.

5. **Abdulagatov A.I., Yan Y., Cooper J.R., Zhang Y., Gibbs Z.M., Cavanagh A.S., Yang R.G., Lee Y.C., George S.M.**, $Al_2O_3$ and $TiO_2$ atomic layer deposition on copper for water corrosion resistance, ACS applied materials & interfaces. 3(12) (2011) 4593–4601.

6. **Kim W. H., Kim H., Lee H. B. R.**, Uniform color coating of multilayered $TiO_2/Al_2O_3$ films by atomic layer deposition, Journal of Coatings Technology and Research. 14(1) (2017) 177.

7. **Polyansky M.N.**, "Refractive index database", https://refractiveindex.info

8. **Sarkar S., Gupta V., Kumar M., Schubert J., Probst P. T., Joseph J., Kцnig T.A.F.**, Hybridized guided-mode resonances via colloidal plasmonic self-assembled grating, ACS applied materials & interfaces. 11(14) (2019) 13752–13760.

9. **Boidin R., Halenkovič T., Nazabal V., Beneљ L., Němec P.**, Pulsed laser deposited alumina thin films, Ceramics International. 42(1) (2016) 1177–1182.

10. **Werner W.S.M., Glantschnig K., Ambrosch-Draxl C.**, Optical constants and inelastic electron-scattering data for 17 elemental metals, Journal of Physical and Chemical Reference Data. 38(4) (2009) 1013–1092.

11. **Born M., Wolf E.**, 1999 Principles of Optics: Electromagnetic Theory of Propagation, Interference and Diffraction of Light (7th ed.) (Cambridge: Cambridge University Press)

12. **Wyman C., Sloan P.P., Shirley P.**, Simple analytic approximations to the CIE XYZ color matching functions, J. Comput. Graph. Tech 2(2) (2013) 11.

## THE AUTHORS

**AKSENOVA Valeriya V.**
valeriyaakse@gmail.com
ORCID: 0000-0002-9202-6165

**KOLOKOLOV Daniil S.**
k.d@koltsov-kb.ru
ORCID: 0000-0002-9624-6579

**PAVLYUCHENKO Alexey S.**
alexey.pavluchenko@gmail.com
ORCID: 0000-0001-5390-276X

**MESH Maxim V.**
mesh@koltsov-kb.ru

**FEDOROV Nikifor A.**
nfedorov@niuitmo.ru

**KARTSEVA Tatyana Yu.**
karceva.t@koltsov-kb.ru

*Received 28.10.2022. Approved after reviewing 10.11.2022. Accepted 10.11.2022.*

© Peter the Great St. Petersburg Polytechnic University, 2023

Conference materials
UDC 535
DOI: https://doi.org/10.18721/JPM.161.226

# Properties of the squared Laguerre–Gaussian vortices

A.A. Savelyeva[1, 2]✉, A.A. Kovalev[1, 2], E.S. Kozlova[1, 2], V.V. Kotlyar[1, 2]

[1] IPSI RAS – branch of the FSRC "Crystallography and Photonics" RAS, Samara, Russia;

[2] Samara National Research University, Samara, Russia

✉ lexis2450@gmail.com

**Abstract.** In this paper, a new type of optical vortex called the squared Laguerre–Gauss $(LG)^2$ vortex beam has been investigated. Theoretical conclusions and numerical experiment confirm that these beams are Fourier-invariant and retain their structure at the focus of a spherical lens. In the Fresnel diffraction zone, such a beam is transformed into a superposition of conventional LG beams, the number of which is equal to the number of rings in the $(LG)^2$ beam. The presented beams are structurally stable in the case of one intensity ring.

**Keywords:** optical vortex, topological charge, Laguerre–Gauss mode, Fourier invariance, Fourier transform, Fresnel diffraction

**Funding:** The work was supported by the Russian Science Foundation, grant 22-22-00265.

**Citation:** Savelyeva A.A., Kovalev A.A., Kozlova E.S., Kotlyar V.V., Properties of the squared Laguerre–Gaussian vortices, St. Petersburg State Polytechnical University Journal. Physics and Mathematics. 16 (1.2) 2023 172–178. DOI: https://doi.org/10.18721/JPM.161.226

This is an open access article under the CC BY-NC 4.0 license (https://creativecommons.org/licenses/by-nc/4.0/)

Материалы конференции
УДК 535
DOI: https://doi.org/10.18721/JPM.161.226

# Свойства квадратичных вихрей Лагерра–Гаусса

А.А. Савельева[1, 2]✉, А.А. Ковалев[1, 2], Е.С. Козлова[1, 2], В.В. Котляр[1, 2]

[1] ИСОИ РАН – филиал ФНИЦ «Кристаллография и фотоника» РАН, Самара, Россия;

[2] Самарский национальный исследовательский университет имени академика С.П. Королёва, г. Самара, Россия

✉ lexis2450@gmail.com

**Аннотация.** В данной работе исследовался новый тип оптического вихря, названный квадратным вихревым пучком Лагерра-Гаусса $(ЛГ)^2$. Теоретические выводы и численный эксперимент подтверждают, что эти пучки Фурье-инвариантны и сохраняют свою структуру в фокусе сферической линзы. В зоне дифракции Френеля такой пучок трансформируется в суперпозицию обычных пучков ЛГ, количество которых равно количеству колец в пучке $(ЛГ)^2$. Представленные пучки структурно устойчивы в случае одного кольца интенсивности.

**Ключевые слова:** оптический вихрь, топологический заряд, мода Лагерра-Гаусса, Фурье-инвариантность, преобразование Фурье, дифракция Френеля

**Финансирование:** работа поддержана Российским научным фондом, грант № 11 22-22-00265.

© Savelyeva A.A., Kovalev A.A., Kozlova E.S., Kotlyar V.V., 2023. Published by Peter the Great St. Petersburg Polytechnic University.

**Ссылка при цитировании:** Савельева А.А., Ковалев А.А., Козлова Е.С., Котляр В.В. Свойства квадратичных вихрей Лагерра-Гаусса // Научно-технические ведомости СПбГПУ. Физико-математические науки. 2023. Т. 16. № 1.2. С. 172–178. DOI: https://doi.org/10.18721/JPM.161.226

Статья открытого доступа, распространяемая по лицензии CC BY-NC 4.0 (https://creativecommons.org/licenses/by-nc/4.0/)

## Introduction

A large number of studies and publications by scientists from all over the world are devoted to optical vortices [1–3], methods for their generation [4–5], and limited circles of applied problems where they are used [6–7]. One of the priority research areas is the search for new types of beams with certain properties [8–9]. For example, in [8], the authors proposed a new type of noncanonical optical vortex, called the "exponential-order phase vortex". In our study [9], a new type of Bessel beams was proposed, which have the property of Fourier invariance and, therefore, are called Fourier–Bessel beams.

However, despite the many methods for creating and describing new types of beams, the well-known Laguerre–Gauss (LG) beams do not lose their relevance [10–12]. Based on the LG modes, new types of optical beams are being developed with various useful properties [13–15]. The authors of [13], using LG modes, generated a vector beam with spatially dependent polarization in the cross section by means of nonlinear magneto-optical rotation. In [15], a new type of partially coherent beam with an unconventional correlation function, called the elliptic correlated Laguerre–Gauss Shell model (LGShM), was theoretically and experimentally investigated. The intensity of such beams in the far field (or in the focal plane) has an elliptical annular profile. Let us give examples of laser beams that differ from conventional Laguerre–Gauss beams and are not structurally stable, since they do not retain the shape of the intensity distribution during propagation.

It is also possible to give examples of laser beams that differ from conventional Laguerre–Gauss beams and are not structurally stable, since they do not retain the shape of the intensity distribution during propagation. For example, in [16] non-structurally stable Laguerre–Bessel–Gauss laser beams are considered. New exact solutions of the paraxial wave equation were obtained in the form of a product of Laguerre polynomials, Bessel functions and Gaussian functions. In [17], Laguerre–Gauss beams with radial and azimuthal polarizations are considered. Complete characteristics of the propagation of several types of azimuthally polarized Laguerre–Gauss beams through optical systems represented by complex ABCD matrices were obtained. In next paper Hermite-sinusoidal-Gaussian laser beams are considered [18]. Hermitian-sinusoidal-Gaussian solutions of the wave equation were obtained. In the limit of a large Hermite–Gaussian beam size, sinusoidal factors dominate and are reduced to ordinary rectangular waveguide modes. In the opposite limit, the rays reduce to the well-known Hermite–Gauss form. The beams that are described by the product of three Airy functions are considered in [19]. Propagation of the product of three Airy beams in a Fresnel zone is investigated numerically. It is shown that the Fourier image of this field has a cubic phase and a radially symmetric intensity with a super-Gaussian decrease.

It should be noted that LG beams and similar beams are of high practical importance for optical communications [20–22], micromanipulation [23], and atoms photoexcitation [24].

In this study, we have proposed a new type of optical beams, whose amplitude is proportional to the squared Laguerre polynomial. These beams extend the LG modes basis. Their theoretical and numerical research was carried out, which showed their Fourier invariance.

## Materials and Methods

In this paper, numerical simulation of the generation and propagation of a Gaussian Laguerre beam in the square is implemented. The complex amplitude of this beam in the initial plane has the form:

© Савельева А.А., Ковалев А.А., Козлова Е.С., Котляр В.В., 2023. Издатель: Санкт-Петербургский политехнический университет Петра Великого.

$$E_{2,n,m}(r,\varphi) = E_2 \exp\left(-\frac{r^2}{w^2} + i2n\varphi\right)\left(\frac{r}{w}\right)^{2|n|}\left[L_m^{|n|}\left(\frac{r^2}{w^2}\right)\right]^2, \quad (1)$$

where $E_2$ is the constant. For numerical simulation, author's Matlab scripts were used in which the Fourier integral and the Fresnel integral are realized.

Let us consider a beam, which we have called the squared LG beam or $(LG)^2$. Beam (1) is not a mode. It does not retain its structure in the Fresnel diffraction zone, but does it in the far field. It means, that the $(LG)^2$ beam is Fourier-invariant, and its complex amplitude at the focus of an ideal spherical lens with focal length $f$ has the form:

$$\begin{aligned} E_{2n,m}(\rho,\theta) &= \frac{-iz_0}{f} E_2 (-1)^n \exp(2in\theta) \int_0^\infty x^n \exp(-x)\left[L_m^{|n|}(x)\right]^2 J_{2n}\left(y\sqrt{x}\right) dx = \\ &= \frac{-iz_0}{f} E_2 (-1)^n \exp\left(2in\varphi - \frac{y^2}{4}\right)\left(\frac{y}{2}\right)^{2|n|}\left[L_m^{|n|}\left(\frac{y^2}{4}\right)\right]^2, \end{aligned} \quad (2)$$

where $x = (r/w)^2$, $y = kw\rho/f$, $(\rho, \theta)$ are polar coordinates in the Fourier plane. For obtaining Eq. (5), a reference integral was used from [2].

Comparing the complex amplitudes in the initial plane (1) and in the focus of the spherical lens (2) it can be seen that they coincide up to a constant. In the Fresnel diffraction zone, the $(LG)^2$ beam is a finite superposition of conventional LG beams, since the complex beam amplitude (1) at any $z$ is calculated using the Fresnel trans-form and is equal to:

$$\begin{aligned} E_{2,n,m}(\rho,\theta,z) &= \frac{-iz_0}{z}(-1)^n \exp\left(\frac{ik\rho^2}{2z} + 2in\theta\right) \int_0^\infty x^n \exp(-px)\left[L_m^{|n|}(x)\right]^2 J_{2n}\left(y\sqrt{x}\right) dx = \\ &= \frac{-iz_0}{z}(-1)^n \exp\left(\frac{ik\rho^2}{2z} + 2in\theta\right)\left(\frac{y}{2}\right)^{2|n|} \frac{\Gamma(|n|+m+1)}{\pi m!\, p^{2n+1}} \times \\ &\times \exp\left(-\frac{y^2}{4p}\right) \sum_{s=0}^{m} \frac{(-1)^s}{(m-s)!} \frac{\Gamma(m-s+1)\Gamma(s+1/2)}{\Gamma(|n|+s+1)} \times \\ &\times \left(\frac{p-2}{2}\right)^{2s} L_{2s}^{2|n|}\left(\frac{y^2}{2p(2-p)}\right), \end{aligned} \quad (3)$$

where $x = (r/w)^2$, $y = kw\rho/z$, $p = 1 - iz_0/z$, $\Gamma(x)$ is the Gamma function. For obtaining Eq. (6), a reference integral was used from [2].

The number of terms in the sum (3) coincides with the number of rings in the ordinary LG beam. It follows from (3) that for $m = 0$ (the radial mode index is zero) the LG beam has one ring $\left(L_0^n(x) = 1\right)$ and the sum in (3) reduces to one first term. Therefore, the ordinary LG beam with squared amplitude is conserved on propagation. It also follows from the general expression for the complex amplitude of structurally stable beams [3], which in the initial plane $z = 0$ is given by

$$E(\xi,\eta,0) = \exp(-\xi^2 - \eta^2) f(\xi + i\eta), \quad (4)$$

where $(\xi, \eta) = (x/w, y/w)$ are the transverse Cartesian coordinates normalized by the waist radius, and $f(.)$ is any entire analytic function of finite growth.

Next, we carried out numerical simulation of the $(LG)^2$ beam structure with a spherical lens using MATLAB templates. The author's script of the Fourier transform in the focal plane was implemented. After that, Fresnel diffraction was considered, which was realized through several Fourier transforms. The program was also implemented in the MATLAB package.

## Results and Discussion

Fig. 1 shows the initial intensity and phase distribution for $(LG)^2$ with the following parameters: $\lambda = 532$ nm, $w = 0.5$ mm, $n = 5$, $m = 4$.

Focusing with a spherical lens is described by the Fourier transform. The simulation results for this beam in the focus are shown in Fig. 2.

Fig. 1 and 2 differ only by a constant and clearly demonstrate the Fourier invariance of $(LG)^2$ beams proved in the first section.

The simulation results at different distances are shown in Figs. 3–5.

Fig. 3 shows the intensity (*a*), its cross section (*b*) and the phase (*c*) of the $(LG)^2$ beam shown in Fig. 1, but at a half of the Rayleigh length. It can be seen in Fig. 3 that instead of five intensity rings (Fig. 1), seven intensity rings appear in the beam. In addition, the brightest ring is no longer the first one (Fig. 1). It is the second, instead.

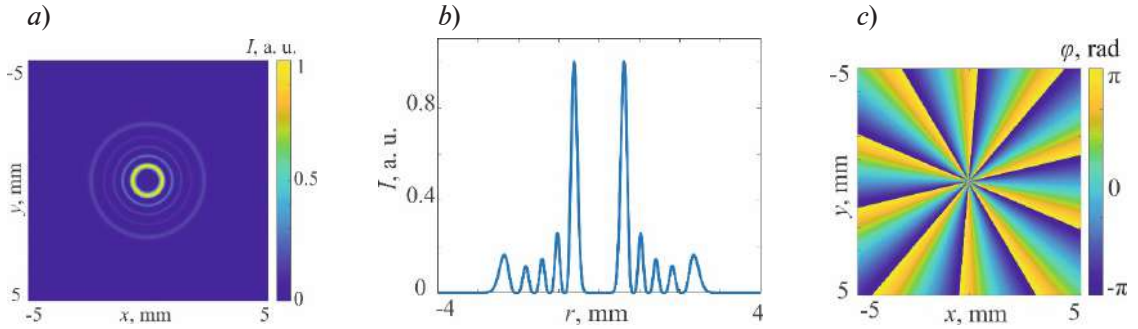


Fig. 1. Initial $(LG)^2$ beam: 2D intensity distribution (*a*); intensity cross section along the radius (*b*); 2D phase distribution (*c*)

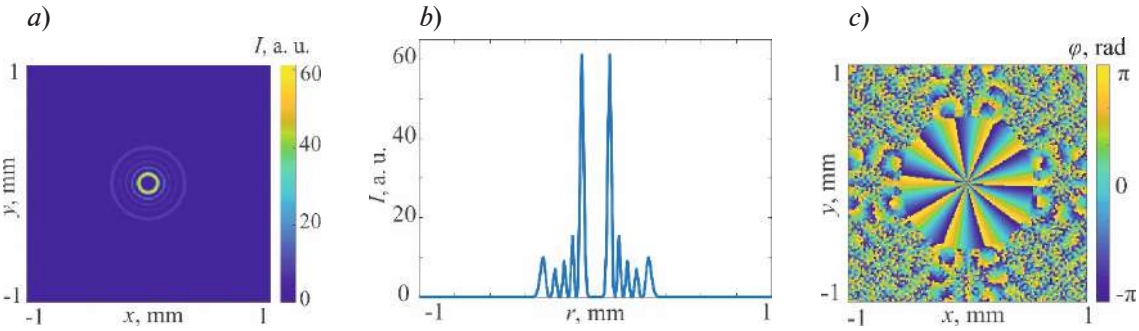


Fig. 2. Field at the focus of a spherical lens after focusing the initial beam from Fig. 1: 2D intensity distribution (*a*); intensity cross section along the radius (*b*); 2D phase distribution (*c*)

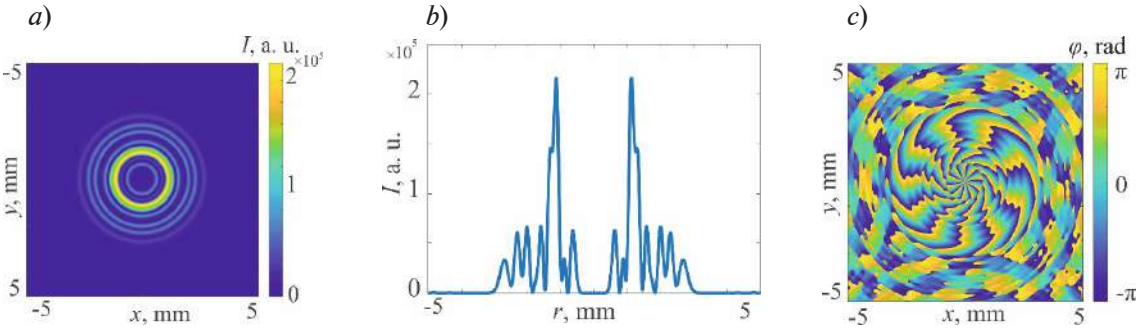


Fig. 3. Fresnel-transformed field of the initial $(LG)^2$ beam ($I$) at a distance $z = z_0/2$ ($z_0 \approx 1.476$ m): 2D intensity distribution (*a*); intensity cross section along the radius (*b*); 2D phase distribution (*c*)

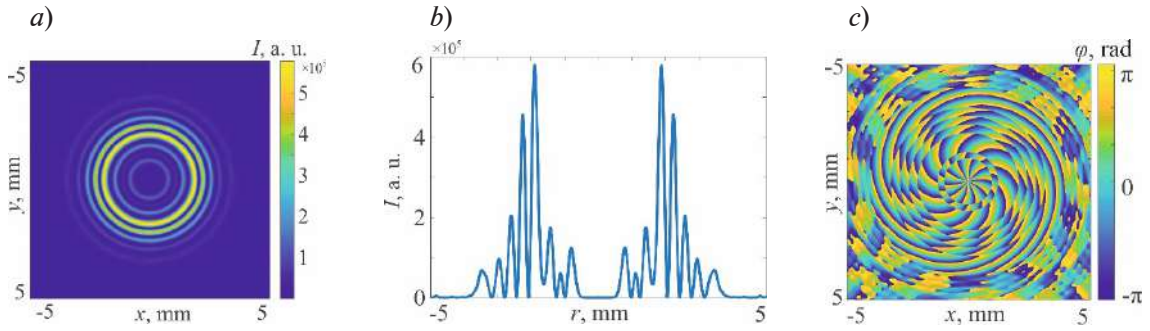


Fig. 4. Transformed field of the initial $(LG)^2$ beam (1) at a distance $z = z_0$ ($z_0 \approx 1.476$ m): 2D intensity distribution (*a*); intensity cross section along the radius (*b*); 2D phase distribution (*c*)

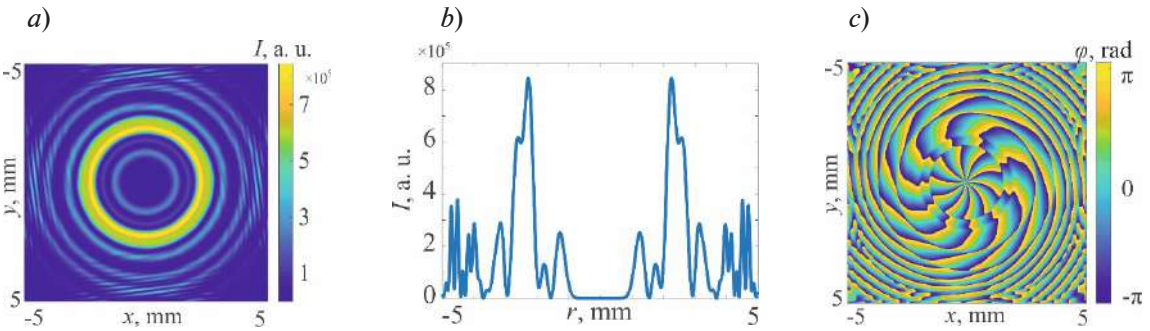


Fig. 5. Transformed field of the initial $(LG)^2$ beam (1) at a distance $z = 2z_0$ ($z_0 \approx 1.476$ m): 2D intensity distribution (*a*); intensity cross section along the radius (*b*); 2D phase distribution (*c*)

Fig. 4 shows the intensity (*a*), its cross section (*b*), and phase (*c*) of the same beam (Fig. 1), but at the Rayleigh distance. It can be seen in Fig. 4 that the beam has eight bright rings, but the energy distribution between them differs from that presented in Fig. 3.

Fig. 5 shows the same as Figs. 3–4, but at a distance of two Rayleigh lengths. There are still 7 rings in the intensity distribution.

## Conclusion

In this paper, a new type of vortex beams was considered, which intersects with a family of well-known Laguerre–Gaussian (LG) beams. The complex amplitude of these beams is proportional to squared Laguerre polynomial and thus they are called squared Laguerre–Gaussian beams $(LG)^2$. Conventional LG beams with zero radial index and with even azimuthal index coincide with $(LG)^2$ beams. It is theoretically and numerically shown that the squared LG vortex beams are Fourier-invariant and retain their structure at the focus of a spherical lens or in the far diffraction field. In the Fresnel diffraction zone, such a beam is transformed into an axial superposition of conventional LG beams, the number of which is equal to the number of rings in the $(LG)^2$ beam. If there is only one ring, then the beam is structurally stable (propagation invariant). The results of this study can find their application in optical communications [16–18].

## Acknowledgments

The work was supported by the Russian Science Foundation, grant 22-22-00265.

## REFERENCES


1. **Shen Y., Wang X., Xie Z., Min C., Fu X., Liu Q., Gong M., Yuan X.,** Optical vortices 30 years on: OAM manipulation from topological charge to multiple singularities, Light Sci Appl. 8 (90) (2019) 1-29. https://doi.org/10.1038/s41377-019-0194-2.

2. **Zhang H., Li X., Ma H., Tang M., Li H., Cai Y.,** Centrosymmetric Optical Vortex, Applied Sciences. 9 (7) (2019) 1429. https://doi.org/10.3390/app9071429.

3. **Kotlyar V.V., Kovalev A.A., Porfirev A.P.,** Vortex Laser Beams, Boca Raton: CRC Press, 2018, ISBN: 9781351009607, 418.

4. **Lian Y., Qi X., Wang Y., Bai Z., Wang Y., Lu Z.,** OAM beam generation in space and its appli-cations: A review, Optics and Lasers in Engi-neering. 151 (2022) 106923. https://doi.org/10.1016/j.optlaseng.2021.106923.

5. **Zhang K., Wang Y., Yuan Y., Burokur S.N.,** A Review of Orbital Angular Momentum Vortex Beams Generation: From Traditional Methods to Metasurfaces, Appl. Sci. 10 (2020) 1015. https://doi.org/10.3390/app10031015.

6. **Liang Y., Lei M., Yan S., Li M., Cai Y., Wang Z., Yu X., Yao B.,** Rotating of low-refractive-index microparticles with a quasi-perfect optical vortex, Appl. Opt. 57 (2018) 79–84.

7. **Yang Y., Ren Y., Chen M., Arita Y., Rosales-Guzman C.,** Optical trapping with structured light: a review, Advanced Photonics. 3 (3) (2021) 034001. https://doi.org/10.1117/1.AP.3.3.034001.

8. **Li P., Liu S., Peng T., Xie G., Gan X., Zhao J.,** Spiral autofocusing Airy beams carrying power-exponent-phase vortices, Opt. Express, 22, (2014) 7598–7606.

9. **Kotlyar V.V., Kovalev A.A., Kalinkina D.S., Kozlova E.S.** Fourier-Bessel beams of finite energy, Computer Optics. 45 (4) (2021) 506-511. DOI: 10.18287/2412-6179-CO-864

10. **Wang M., Ma Y., Sheng Q., He X., Liu J., Shi W., Yao J., Omatsu T.,** Laguerre−Gaussian beam generation via enhanced intracavity spherical aberration, Opt. Express. 29 (2021) 27783–27790.

11. **Rafayelyan M., Brasselet E.,** Laguerre−Gaussian modal q-plates, Opt. Lett. 42 (2017) 1966-1969.

12. **Mao H., Ren Y.-H., Yu Y., Yu Z., Sun X., Zhang S., Wong K.K.Y.,** Broadband meta-converters for multiple Laguerre−Gaussian modes, Photon. 9 (2021) 1689–1698.

13. **Ghaderi Goran Abad M., Mahmoudi M.,** La-guerre-Gaussian modes generated vector beam via nonlinear magneto-optical rotation, Sci Rep. 11 (2021) 5972.

14. **Huang S., Miao Z., He C., Pang F., Li Y., Wang T.,** Composite vortex beams by coaxial superpo-sition of Laguerre−Gaussian beams, Optics and Lasers in Engineering. 78 (2016) 132−139.

15. **Chen Y., Liu L., Wang F., Zhao C., Cai Y.,** Elliptical Laguerre−Gaussian correlated Schell-model beam, Opt. Express. 22 (2014) 13975–13987.

16. **Tovar A.A.,** Propagation of Laguerre−Bessel−Gaussian beams, J. Opt. Soc. Am. A. 17 (2000) 2010-2018.

17. **Tovar A.A.,** Production and propagation of cylindrically polarized Laguerre−Gaussian laser beams, J. Opt. Soc. Am. A. 15 (1998) 2705–2711

18. **Tovar A.A., Casperson L.W.,** Production and propagation of Hermite−sinusoidal-Gaussian laser beams, J. Opt. Soc. Am. A. 15 (1998) 2425–2432.

19. **Abramochkin E., Razueva E.,** Product of three Airy beams, Opt. Lett. 36 (2011) 3732–3734.

20. **Pang K., Liu C., Xie G., Ren Y., Zhao Z., Zhang R., Cao Y., Zhao J., Song H., Song H., Li L., Willner A.N., Tur M., Boyd R.W., Willner A.E.,** Demon-stration of a 10 Mbit/s quantum communication link by encoding data on two Laguerre−Gaussian modes with different radial indices, Opt. Lett. 43 (2018) 43 5639–5642.

21. **Zeng J., Liu X., Zhao C., Wang F., Gbur G., Cai Y.,** Spiral spectrum of a Laguerre−Gaussian beam propagating in anisotropic non-Kolmogorov turbulent atmosphere along horizontal path, Opt. Express. 27 (2019) 25342–25356.

22. **Cox M.A., Maqondo L., Kara R., Milione G., Cheng L., Forbes A.,** The Resilience of Hermite− and Laguerre−Gaussian Modes in Turbulence, J. Lightwave Technol. 37 (2019) 3911–3917.

23. **Otsu T., Ando T., Takiguchi Y., Ohtake Y., Toyoda H., Itoh H.,** Direct evidence for three-dimensional off-axis trapping with single Laguerre−Gaussian beam, Scientific Reports. 4 (1) (2014) 4579.

24. **Peshkov A.A., Seipt D., Surzhykov A., Fritzsche S.,** Photoexcitation of atoms by Laguerre−Gaussian beams, Physical Review A. 96 (2) (2017) 023407. https://doi.org/10.1103/PhysRevA.96.023407.

## THE AUTHORS

**SAVELYEVA Alexandra A.**
lexis2450@gmail.com
ORCID: 0000-0001-7031-5989

**KOVALEV Alexey A.**
alanko.ipsi@mail.ru
ORCID: 0000-0002-0488-4267

**KOZLOVA El ena S.**
kozlova.elena.s@gmail.com
ORCID: 0000-0001-7031-5989

KOTLYAR Victor V.
kotlyar@ipsiras.ru
ORCID: 0000-0003-1737-0393

*Received 28.10.2022. Approved after reviewing 08.11.2022. Accepted 08.11.2022.*

© Peter the Great St. Petersburg Polytechnic University, 2023

# PHYSICAL MATERIALS TECHNOLOGY

Conference materials
UDC 538.975
DOI: https://doi.org/10.18721/JPM.161.227

## Physical properties of GaN nanowires with core-shell InGaN/GaN insertions grown by PA-MBE on Si substrate

D.N. Bondarenko[1,2]✉, V.O. Gridchin[1,2,3], K.P. Kotlyar[1], R.R. Reznik[1,2,3], D.A. Kirilenko[4], A.I. Baranov[2], A.S. Dragunova[2,5], N.V. Kryzhanovskaya[5], A.A. Maksimova[2], G.E. Cirlin[1,2,3,4]

[1] St. Petersburg State University, St. Petersburg, Russia;
[2] Alferov University, St. Petersburg, Russia;
[3] IAI RAS, St. Petersburg, Russia;
[4] Ioffe Institute, St. Petersburg, Russia;
[5] HSE University, St. Petersburg, Russia
✉ bondarenko.dariya.spb@gmail.com

**Abstract.** An approach to the fabrication of LED structure based on GaN nanowires with thick core-shell InGaN insertions with high indium content is studied. The results of optical measurements demonstrate the photoluminescence from the InGaN insertions in the green spectrum at room temperature. The study of electrical properties shows typical diode dependence. The results can be crucial for the development of light-emitting diodes on Si substrates.

**Keywords:** GaN/InGaN nanowires, micro light-emitting diodes, plasma-assisted molecular beam epitaxy, thick core-shell InGaN insertions.

**Funding:** The samples were grown under financial support of Ministry of Science and Higher Education of the Russian Federation (state task № 0791-2020-0003). Optical studies of grown samples were done under financial support of Russian Science Foundation grant №19-72-30010. Structural and electro-physical properties were studied under financial support of St. Petersburg State University under research grant № 92591131.

**Citation:** Bondarenko D.N., Gridchin V.O., Kotlyar K.P., Reznik R.R., Kirilenko D.A., Baranov A.I., Dragunova A.S., Kryzhanovskaya N.V., Maksimova A.A., Cirlin G.E., Physical properties of GaN nanowires with core-shell InGaN/GaN insertions grown by PA-MBE on Si substrate, St. Petersburg State Polytechnical University Journal. Physics and Mathematics. 16 (1.2) (2023) 179–184. DOI: https://doi.org/10.18721/JPM.161.227

This is an open access article under the CC BY-NC 4.0 license (https://creativecommons.org/licenses/by-nc/4.0/)

© Bondarenko D.N., Gridchin V.O., Kotlyar K.P., Reznik R.R., Kirilenko D.A., Baranov A.I., Dragunova A.S., Kryzhanovskaya N.V., Maksimova A.A., Cirlin G.E., 2023. Published by Peter the Great St. Petersburg Polytechnic University.

Материалы конференции
УДК 538.975
DOI: https://doi.org/10.18721/JPM.161.227

# Физические свойства нитевидных нанокристаллов GaN с вставками структуры «core-shell» InGaN/GaN, выращенных методом МПЭ с плазменной активацией на подложке Si

Д.Н. Бондаренко[1,2]✉, В.О. Гридчин[1,2,3], К.П. Котляр[1], Р.Р. Резник[1,2,3], Д.А. Кириленко[4], А.И. Баранов[2], А.С. Драгунова[2,5], Н.В. Крыжановская[5], А.А. Максимова[2], Г.Э. Цырлин[1,2,3,4]

[1] Санкт-Петербургский государственный университет, Санкт-Петербург, Россия;

[2] Санкт-Петербургский академический университет имени Ж. И. Алферова РАН, Санкт-Петербург, Россия;

[3] Институт аналитического приборостроения РАН, Санкт-Петербург, Россия;

[4] Физико-технический институт имени А. Ф. Иоффе РАН, Санкт-Петербург, Россия;

[5] Национальный исследовательский университет «Высшая школа экономики», Санкт-Петербург, Россия

✉ bondarenko.dariya.spb@gmail.com

**Аннотация.** Исследован подход к созданию светоизлучающей структуры на основе нитевидных нанокристаллов GaN с объемными вставками структуры «core-shell» InGaN с высоким содержанием индия. Результаты оптических измерений демонстрируют фотолюминесценцию вставок InGaN в зеленом спектре при комнатной температуре. Изучение электрических свойств показывает типичную диодную зависимость. Результаты могут иметь решающее значение для разработки светоизлучающих диодов на кремниевых подложках.

**Ключевые слова:** нитевидные нанокристаллы GaN/InGaN, микросветоизлучающие диоды, молекулярно-пучковая эпитаксия с плазменной активацией, объемные вставки структуры «core-shell» InGaN

**Финансирование:** Экспериментальные образцы были синтезированы при финансовой поддержке Министерства науки и высшего образования Российской Федерации (государственное задание № 0791-2020-0003). Оптические исследования выращенных образцов выполнены при финансовой поддержке гранта РНФ №19-72-30010. Структурные и электрофизические свойства изучены при финансовой поддержке СПбГУ в рамках исследовательского гранта № 92591131.

**Ссылка при цитировании:** Бондаренко Д.Н., Гридчин В.О., Котляр К.П., Резник Р.Р., Кириленко Д.А., Баранов А.И., Драгунова А.С., Крыжановская Н.В., Максимова А.А., Цырлин Г.Э. Физические свойства нитевидных нанокристаллов GaN с вставками структуры «core-shell» InGaN/GaN, выращенных методом МПЭ с плазменной активацией на подложке Si // Научно-технические ведомости СПбГПУ. Физико-математические науки. 2023. Т. 16. № 1.2. С. 179–184. DOI: https://doi.org/10.18721/JPM.161.227

Статья открытого доступа, распространяемая по лицензии CC BY-NC 4.0 (https://creativecommons.org/licenses/by-nc/4.0/)

## Introduction

Nowadays, a particular interest of researchers is directed to the creation of micro light-emitting diodes (LEDs) based on InGaN ternary compounds [1]. Among the unique properties of these direct band gap semiconductors, the ability to tune the emission wavelength from the near UV to near IR by changing the chemical composition is highlighted [1]. However, the synthesis of homogeneous InGaN layers in a wide chemical range leads to the internal strains and phase separation («miscibility gap») due to the large lattice mismatch between InN and GaN [2]. In addition, the lack of lattice-matched substrates relative to InGaN remains as an unsolved problem

© Бондаренко Д.Н., Гридчин В.О., Котляр К.П., Резник Р.Р., Кириленко Д.А., Баранов А.И., Драгунова А.С., Крыжановская Н.В., Максимова А.А., Цырлин Г.Э., 2023. Издатель: Санкт-Петербургский политехнический университет Петра Великого.

of the synthesis of InGaN layers with high crystalline quality. As was shown earlier, one of the methods for solving these challenges is the synthesis of nanowires (NWs) [3]. Among advantages of NWs, the possibility of obtaining practically defect-free structures on substrates with different lattice parameters and different thermal expansion coefficients [4]. This advantage allows using low cost and high availability silicon wafers as the substrates for NWs growth. Another advantage of NWs is the possibility to circumvent of «miscibility gap» and obtain InGaN solid solution with any required chemical composition [5]. Generally, InGaN NWs with a high In content are grown in spontaneously formed core-shell structure [6]. In these regards, an approach to the creation of thick core-shell InGaN active area embedded in GaN NWs can be a promising way to obtain high efficiency visible LEDs. In addition, the quantum confinement Stark effect can be negligible due to the using of thick core-shell active area.

In this work, we study the structural and optoelectronic properties of GaN NWs with the thick core-shell InGaN active region grown on n-Si (111) substrates by plasma-assisted molecular beam epitaxy (PA-MBE).

## Materials and Methods

The GaN/InGaN NWs were grown by molecular-beam epitaxy using a Riber Compact 12 MBE setup equipped with Ga, In, Mg, and Si effusion cells and a nitrogen plasma source. We used n-Si(111) substrates with 0.002-0.004 Ω·cm electrical resistivity. The pretreatment of the substrates, necessary for the removal native silicon oxide layer, was carried out using an aqueous solution of hydrofluoric acid. After processing, the substrates were transferred to a growth chamber and heated to a temperature of 950 °C for thermal treatment. Next, the temperature was lowered to a value of 600 °C, and a Ga source was opened for 15 seconds to form droplets on the substrate surface. Then the substrate temperature was raised to 820 °C. After stabilization of the temperature, a nitrogen plasma source with a power of 450 W was ignited, the flux of which was set at 0.4 sccm. At this stage, the effusion cells of Ga and Si were simultaneously opened to form GaN NWs with n-type conductivity. After that, the substrate temperature was decreased to the formation of InGaN active area. Finally, GaN doped by Mg were grown for obtaining p-type conductivity. Total growth time was 17h. The morphological properties of the sample were studied using scanning electron microscopy (SEM supra 25 Zeiss).

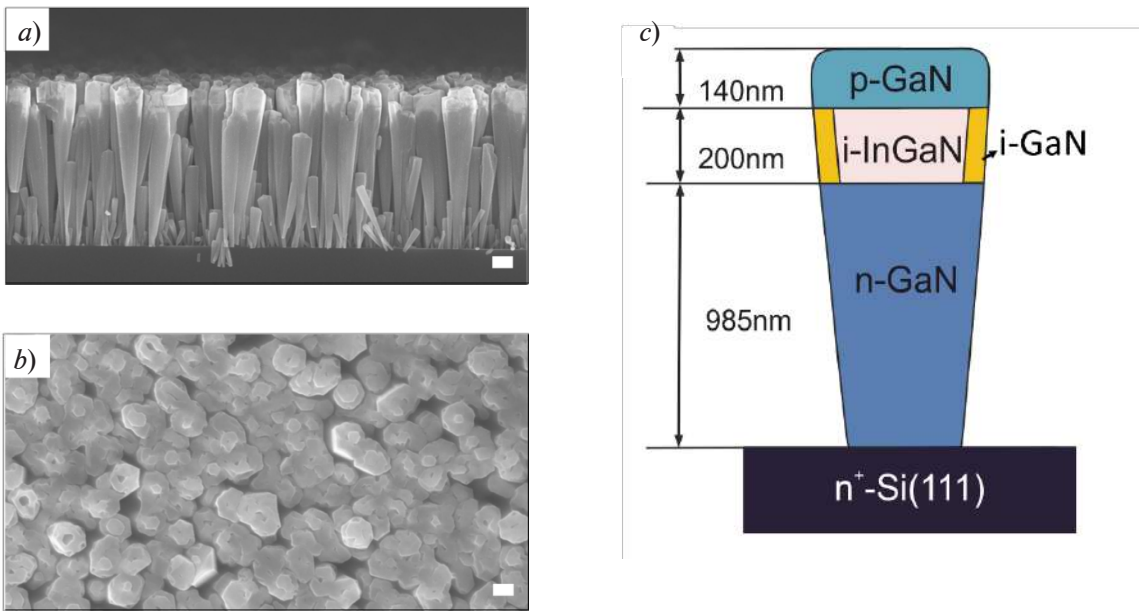


Fig. 1. SEM images of GaN/InGaN NWs: cross-section view (*a*), plane view (PV) (*b*) and schematic image of the NW structure (*c*). The scale bars correspond to 200 nm

The study of optical properties of GaN/InGaN NWs was realized using the photoluminescence (PL) method at the room temperature. To excite the PL, a helium-cadmium (He-Cd) metal-vapor laser with a wavelength of 325 nm and a power of 15.5 mW was used. The microstructure and chemical composition of grown NWs were studied by high-angle annular dark-field scanning transmission electron microscopy (HAADF-STEM, JeolJEM-2100FTEM) with energy-dispersive X-ray (EDX) spectroscopy techniques (XFlash 6TI30, Bruker). The electrical properties of the NWs were studied by measuring the current–voltage (I-V) curves at room temperatures.

## Results and Discussion

Fig. 1 shows SEM images of the obtained GaN/InGaN NWs in two views: a cross-section view (*a*) and a plane view (*b*), as well as a schematic image of the NW structure (*c*).

As can be seen from Fig. 1, the morphology of the grown structures is close-packed GaN/InGaN NWs with an average length of 1.7 μm and the diameters at the base and top of about 100 nm and 300 nm, respectively. Also, it can be seen that the sample consists of both separated and partially coalesced NWs.

The typical PL spectrum is shown in Fig. 2. The results of the PL measurements showed that the sample has a PL spectrum in the visible region (450–650 nm) with a maximum nearly 536 nm. The full width at half maximum is about 67 nm.

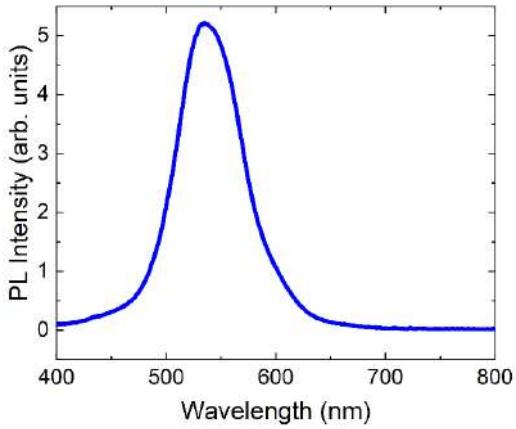


Fig. 2. Typical photoluminescence spectrum of the GaN/InGaN NWs

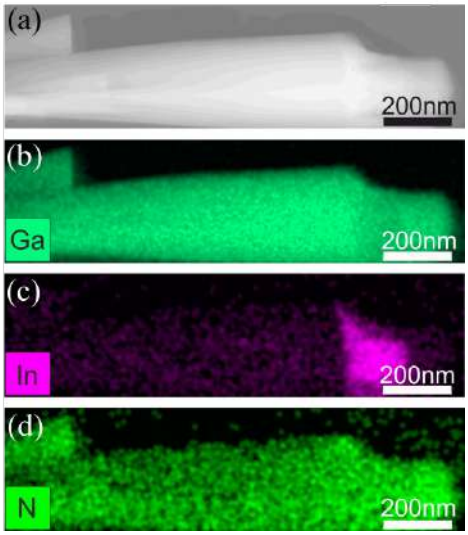


Fig. 3. HAADF-STEM image of an GaN/InGaN NWs (*a*);
the Ga distribution along the NW (*b*); the In distribution along the NW (*c*)

Fig. 3 shows HAADF-STEM image of a single GaN/InGaN NW and the Ga, In distribution along the NW. As can be seen from these results, the InGaN insert exhibits core–shell structure with lateral and vertical sizes about 230 nm and 200 nm, respectively. In accordance with the PL and TEM measurements, the In content in the NWs is about 30%.

To measure the I-V curves the aluminium ohmic bottom contacts were formed on the n-Si substrate. Next, face top contacts were formed on the p-GaN NWs by coating Ag paste (Fig. 4, *a*). Fig. 4, *b* presents the results of the measurements of I-V curves. As can be seen from the figure, the sample demonstrates typical diode dependence with the opening voltage of about 6V. High opening voltage is apparently related to the Schottky barrier on p-GaN/Ag interface [7].

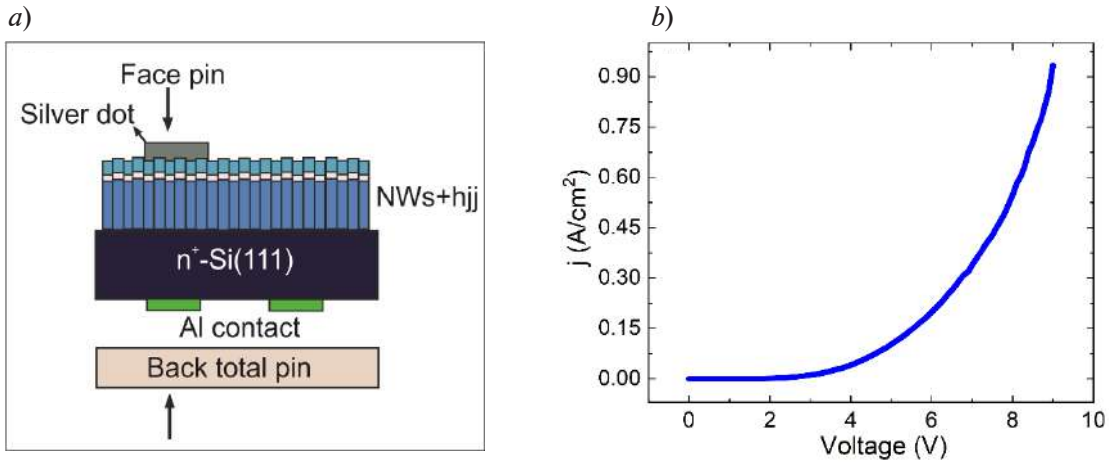


Fig. 4. Scheme of an LED based on an array of GaN/InGaN NWs on the *n*-Si(111) substrate (*a*); the current-voltage curve of GaN/InGaN NWs LED (*b*)

## Conclusion

The experimental results of the growth of the n-GaN/i-InGaN/p-GaN nanowires on the n-Si(111) substrate by the PA-MBE method were presented. It was shown that the photoluminescence of the obtained nanostructure is observed in the visible green region with a maximum of the PL spectrum at about 536 nm. STEM studies showed, that the InGaN inserts have a spontaneously formed core—shell structure with In content in the core about 30 %. The presented results can be promising for creation of green LEDs grown on silicon substrates.

## Acknowledgments

The samples were grown under financial support of Ministry of Science and Higher Education of the Russian Federation (state task 0791-2020-0003). Optical studies of grown samples were done under financial support of Russian Science Foundation grant 19-72-30010. Structural and electro-physical properties were studied under financial support of St. Petersburg State University under research grant 92591131.

## REFERENCES

1. **Bui H.Q.T., Velpula R.T., Jain B., Aref O.H., Nguyen H.-D., Lenka T.R., Nguyen H.P.T.,** Full-Color InGaN/AlGaN Nanowire Micro Light-Emitting Diodes Grown by Molecular Beam Epitaxy: A Promising Candidate for next Generation Micro Displays, Micromachines. 10 (8) (2019) 492.
2. **Ho I., Stringfellow G.B.,** Solid phase immiscibility in GaInN, Applied Physics Letters. 69 (18) (1996) 2701—2703.
3. **Yan R., Gargas D., Yang P.,** Nanowire photonics, Nature Photonics. 3 (10) (2009) 569.
4. **Dubrovskii V.G., Cirlin G.E., Ustinov V.M.,** Semiconductor nanowhiskers: Synthesis, properties, and applications, Semiconductors. 43 (12) (2009) 1539—1584.

5. **Roche E., Andre Y., Avit G., Bougerol C., Castelluci D., Rйveret F., Gil E., Mйdard F., Leymarie J., Jean T., Dubrovskii V. G., Trassoudaine A.,** Circumventing the Miscibility Gap in InGaN Nanowires Emitting from Blue to Red, Nanotechnology. 29 (46) (2018) 465602.

6. **Gridchin V.O., Kotlyar K.P., Reznik R.R., Dragunova A.S., Kryzhanovskaya N.V., Lendyashova V.V., Kirilenko D.A., Soshnikov I.P., Shevchuk D.S., Cirlin G.E.,** Multi-colour light emission from InGaN nanowires monolithically grown on Si substrate by MBE, Nanotechnology. 32 (33) (2021) 335604.

7. **Picozzi S., Continenza A., Satta G., Massidda S., Freeman A. J.,** Metal induced gap states and Schottky barrier heights at non−reactive GaN/noble-metal interfaces, Physical Review B. 61 (24) (2000) 16736.

## THE AUTHORS

**BONDARENKO Daria N.**
bondarenko.dariya.spb@gmail.com
ORCID: 0000-0003-4537-069X

**BARANOV Artem I.**
baranov_art@spbau.ru
ORCID: 0000-0002-4894-6503

**GRIDCHIN Vladislav O.**
gridchinvo@yandex.ru
ORCID: 0000-0002-6522-3673

**DRAGUNOVA Anna S.**
anndra@list.ru
ORCID: 0000-0002-0181-0262

**KOTLYAR Konstantin P.**
konstantin21kt@gmail.com
ORCID: 0000-0002-0305-0156

**KRYZHANOVSKAYA Natalia V.**
nataliakryzh@gmail.com
ORCID: 0000-0002-4945-9803

**REZNIK Rodion R.**
moment92@mail.ru
ORCID: 0000-0003-1420-7515

**MAKSIMOVA Alina A.**
deer.blackgreen@yandex.ru
ORCID: 0000-0002-3503-7458

**KIRILENKO Demid A.**
Kirilenko@mail.ioffe.ru
ORCID: 0000-0002-1571-209X

**CIRLIN George E.**
george.cirlin@mail.ru
ORCID: 0000-0003-0476-3630

*Received 11.10.2022. Approved after reviewing 14.11.2022. Accepted 14.11.2022.*

© Peter the Great St. Petersburg Polytechnic University, 2023

Conference materials
UDC 53.097
DOI: https://doi.org/10.18721/JPM.161.228

# Bottom-up approach to the formation of bi-resonant glass-metal nanocomposite

E.S. Babich[1, 2]✉, E.A. Lubyankina[1, 2], I.V. Reduto[1]

[1] Alferov University, St. Petersburg, Russia;

[2] Peter the Great St. Petersburg Polytechnic University, St. Petersburg, Russia

✉ babich_es@spbstu.ru

**Abstract.** We demonstrate the bottom-up approach to the formation of a glass-metal nanocomposite. The approach is based on simultaneous diffusion of different metal ions in glass and the self-assembly of the reduced ions with the formation of metal nanoparticles. In particularly, the approach includes: sputtering of silver and gold thin films on the surface of the glass, embedding of silver and gold ions in glass via field-assisted ion-exchange (applying DC voltage to metal films) and annealing of the ions-enriched glass at the temperature above the glass transition temperature. The formed nanocomposite is glass substrate with the buried layers of gold and silver nanoparticles, which is characterized by two distinct optical resonances (bi-resonant nanocomposite). The influence of the parameters of the ion exchange (thickness of metal films, ratio of the metals, and applied voltage) and annealing (temperature and duration) on the formation of silver and gold nanoparticles and optical properties of the glass-metal nanocomposite is considered.

**Keywords:** glass-metal nanocomposite, field-assisted ion-exchange, nanoparticles

**Funding:** This study was supported by the Russian Science Foundation (agreement 22-22-20005 dated 23.03.2022) and St. Petersburg Science Foundation (agreement 04/2022 dated 13.04.2022).

**Citation:** Babich E.S., Lubyankina E.A., Reduto I.V., Bottom-up approach to the formation of bi-resonant glass-metal nanocomposite, St. Petersburg State Polytechnical University Journal. Physics and Mathematics. 16 (1.2) 2023 185–190. DOI: https://doi.org/10.18721/JPM.161.228

This is an open access article under the CC BY-NC 4.0 license (https://creativecommons.org/licenses/by-nc/4.0/)

Материалы конференции
УДК 53.097
DOI: https://doi.org/10.18721/JPM.161.228

# Подход «снизу-вверх» для формирования бирезонансных стеклометаллических нанокомпозитов

Е.С. Бабич[1, 2]✉, Е.А. Лубянкина[1, 2], И.В. Редуто[1]

[1] Академический университет им. Ж.И. Алфёрова РАН, Санкт-Петербург, Россия;

[2] Санкт-Петербургский Политехнический университет Петра Великого, Санкт-Петербург, Россия

✉ babich_es@spbstu.ru

**Аннотация.** Мы продемонстрировали подход «снизу-вверх» для формирования бирезонансных стеклометаллических нанокомпозитов, представляющих собой стекло с золотыми и серебряными наночастицами в объеме. Подход заключается во внедрении ионов серебра и золота в стекло посредством электростимулированной диффузии металлов из тонкопленочных многокомпонентных электродов, и в восстановлении ионов и кластеризации атомов с образованием наночастиц при последующей высокотемпературной обработке. В рамках работы изучено влияние параметров диффузии и высокотемпературной обработки на процесс формирования наночастиц и оптические свойства стеклометаллических нанокомпозитов.

© Babich E.S., Lubyankina E.A., Reduto I.V., 2023. Published by Peter the Great St. Petersburg Polytechnic University.

**Ключевые слова:** стеклометаллические нанокомпозиты, электростимулированная диффузия, наночастицы

**Финансирование:** Работа выполнена за счет гранта Российского научного фонда (соглашение № 22-22-20005 от 23.03.2022) при софинансировании Санкт-Петербургским научным фондом (соглашение № 04/2022 от 13.05.2022).

**Ссылка при цитировании:** Бабич Е.С., Лубянкина Е.А., Редуто И.В. Подход «снизу-вверх» для формирования бирезонансных стеклометаллических нанокомпозитов // Научно-технические ведомости СПбГПУ. Физико-математические науки. 2023. Т. 16. № 1.2. С. 185–190. DOI: https://doi.org/10.18721/JPM.161.228

Статья открытого доступа, распространяемая по лицензии CC BY-NC 4.0 (https://creativecommons.org/licenses/by-nc/4.0/)

## Introduction

Media containing metal nanoparticles receive a significant attention due to their unique optical properties related to the phenomenon of localized surface plasmon resonance (LSPR) in the nanoparticles [1]. Engineering spectral position and intensity of LSPR allows enhancement of light emission [2], optimizing photovoltaic structures [3], optical nonlinearity effects [4] and transmission spectra [5], etc. LSPR strongly depends on material, shape and size of nanoparticles, and numerous studies are devoted to the manipulation of fine features of the nanoparticles and precise nanofabrication to adjust LSPR position [6, 7]. Another approach is to combine several LSPRs and, thus, modify/expand the spectral range in which the properties of a material as a whole are significantly affected by the plasmonic properties of the embedded nanoparticles. This possibility has been confirmed by formation of core-shell [8] and alloyed nanoparticles [9], or joining of different types of nanoparticles on a substrate [10]. In this work, we present an approach to manipulate optical properties of a glass embedded with metal nanoparticles that is glass-metal nanocomposite (GMN), which is based on simultaneous diffusion of different metal ions in glass and the self-assembly of silver and gold nanoparticles with the formation of a bi-resonant structure.

## Materials and Methods

Two series of GMNs have been made and optically characterized using SPECORD 50 spectrometer. The depth distribution of the formed nanoparticles was characterized via monitoring absorption spectra of GMN during it step by step etching in HF solution (5 μl HF: 5 g $NH_4F$: 40 g $H_2O$) and measuring thickness of etched glass layer with mechanical profilometer Ambios XP-1.

### *First series*

We embedded gold ions in glass by applying DC voltage, +250 or +1000V, to 50 nm-thick gold film sputtered on the glass surface. During this procedure the glass slide was heated to 300 °C to accelerate diffusion of the ions (field-assisted ion-exchange) [11]. The procedure continued until current flowing through the glass slide decreased down to ~0.1 mA. To form gold nanoparticles, we annealed the glass slide for 30 min at 650 °C.

### *Second series*

Both, silver and gold ions were embedded in glass by the field-assisted ion-exchange. The surface of the glass slide was covered with gold and silver films, each 50 nm thick, and topped with 10 nm-thick gold layer to protect silver from oxidation. We applied DC voltage of +250 or +1000 V to the bi-layer film at elevated temperature of 300 °C until current flowing through the glass slide decreased down to ~0.1 mA and annealed the obtained samples for 30–60 min at 650–700 °C. The bi-layer anode with different ratio of thicknesses of silver/gold layers was also tested. In particular, DC voltage of 1000+ V was applied to the surface of the glass slide covered with 50 nm-thick gold and 30 nm-thick silver films; the glass slide was annealed for 60 min at 700 °C.

© Бабич Е. С., Лубянкина Е. А., Редуто И. В., 2023. Издатель: Санкт-Петербургский политехнический университет Петра Великого.

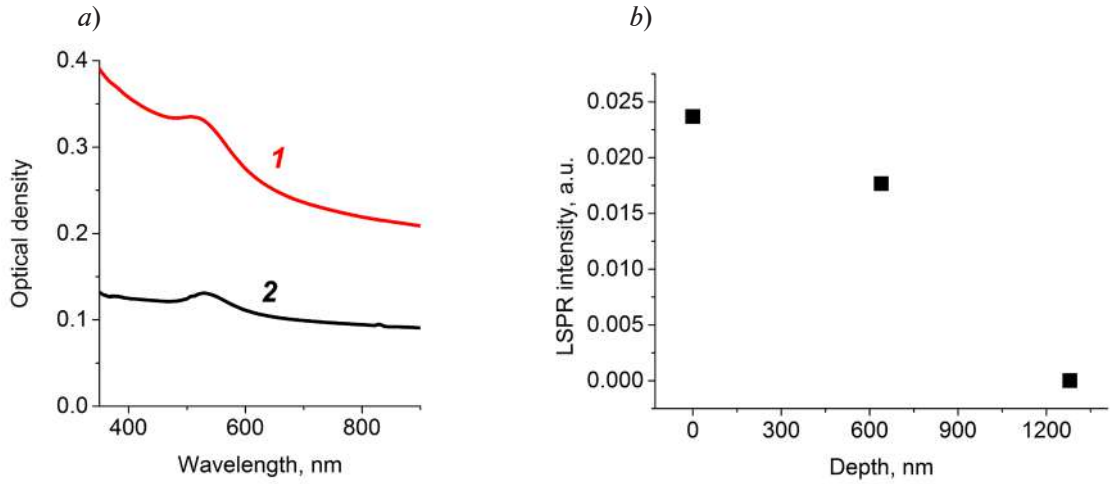


Fig. 1. Optical absorption spectra of GMN (first series) obtained under 1000 V (*1*) and 250 V (*2*) (*a*). Dependence of the intensity of gold LSPR in the spectrum of GMN on thickness of etched glass (the GMN was obtained under 250 V) (*b*)

## Results and Discussion

The absorption spectra of the samples of the first series are presented in Fig. 1,*a*. One can see, gold doping of glass by field-assisted ion-exchange combined with the high-temperature annealing results in the formation of a structure with LSPR at ~525 nm which is characteristic for gold nanoparticles [12]. The concentration of gold nanoparticles is higher in the sample obtained under 1000 V comparatively to the one obtained under 250 V, which follows from the noticeable difference in the LSPR intensity. Note, ultrasonic cleaning of the samples' surface in acetone did not affect the spectra, which evidences formation of gold nanoparticles in the glass bulk that is GMN. To characterize depth distribution of the nanoparticles we step by step etched GMN in HF solution, measured thickness of etched glass and GMN absorption spectra (see section 2 for details). The results for the sample obtained under 250 V are presented in Fig. 1,*b*. Evidently, a thin, ~1300 nm, layer of GMN is formed in anodic subsurface region.

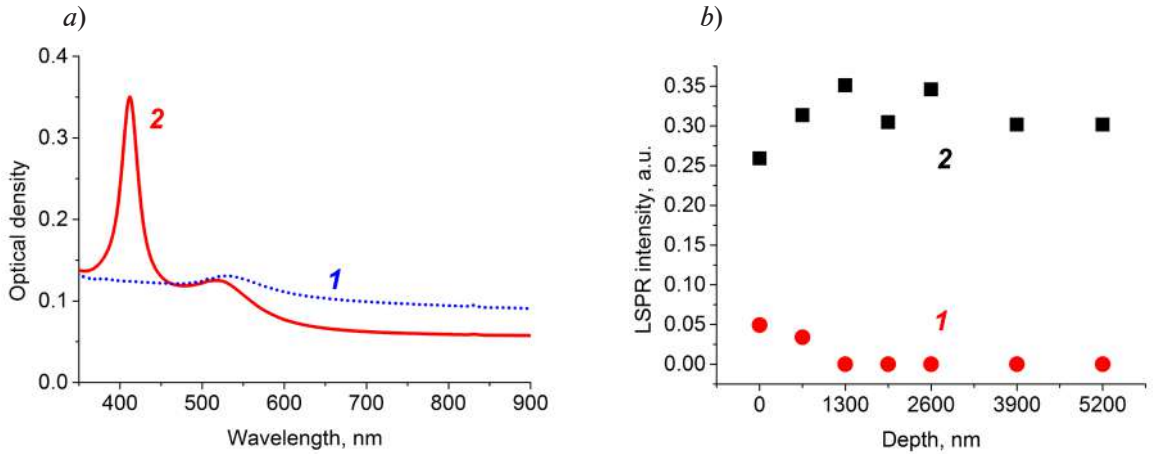


Fig. 2. Comparison of optical absorption spectra of GMN (*1*, first series) and bi-resonant GMN (*2*, second series) obtained under 250 V (*a*). Dependence of the intensity of gold (*1*) and silver (*2*) LSPRs in the spectrum of bi-resonant GMN on thickness of etched glass (*b*)

The absorption spectrum of the sample in the second series obtained under 250 V and annealing for 30 min at 650 °C is presented in Fig. 2,*a* and compared with the spectrum of the sample in the first series obtained under the same conditions. The spectrum of the sample in the second series demonstrates two optical resonances at ~410 and ~525 nm, and does not change after ultrasonic cleaning of the sample surface in acetone. Thus, both silver and gold ions diffused into the glass in the course of the field-assisted ion-exchange with the bi-layer anode, and the high-temperature annealing resulted in reduction of the ions and formation of nanoparticles in the glass bulk that is a bi-resonant GMN. The difference in silver/gold LSPR intensities supposedly indicates a difference in concentrations of silver and gold nanoparticles in the GMN.

Intensity and spectral position of the longer-wavelength LSPR coincide well with ones of LSPR in the GMN formed by the field-assisted ion-exchange with single-layer gold anode and hence presence of silver does not essentially influence gold diffusion and clustering (see Fig. 2,*a*). We assumed that silver nanoparticles form separately from the gold ones.

To determine the burial depth of gold and silver nanoparticles we repeated the step by step etching. The results for the 250 V sample are presented in Fig. 2,*b*. One can see, gold LSPR vanishes from the GMN spectrum when ~1300 nm of glass is etched off, which corresponds with the results of the etching of the sample obtained using single-layer gold anode (see Fig. 1,*b*). Silver LSPR remains in the spectrum, even when ~5000 nm of glass is removed. Note, silver LSPR disappeared from the spectrum when ~15 μm of glass was removed. The results clarify process of ions diffusion in the course of the field-assisted ion-exchange with bi-layer gold-silver anode: the concentration of silver ions in glass increase faster than gold one due to higher mobility of silver ions [13, 14]. However, since ions continue to move from glass surface towards bulk under the electric field, silver ions go deeper in the glass, which results in spatial separation of gold and silver ions. The high-temperature annealing results in reduction and clustering of the ions and formation of bi-resonant structure represented as layered GMN: gold nanoparticles in the subsurface glass layer of the thickness of ~1 μm and silver nanoparticles-containing layer buried deeper in glass by ~ 15 μm.

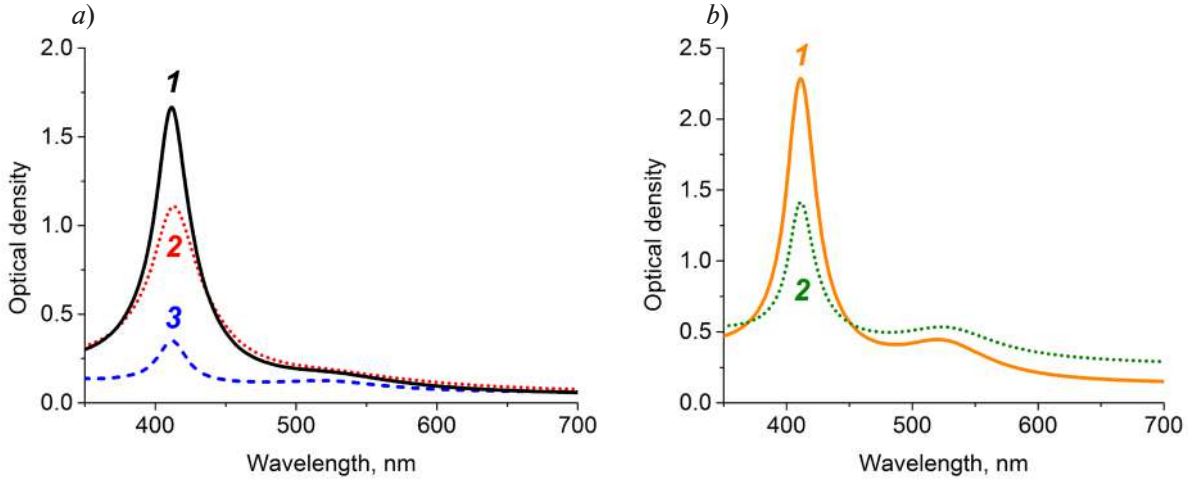


Fig. 3. Optical absorption spectra of bi-resonant GMNs obtained under different applied voltage and annealing duration: 1000 V and 60 min (*1*), 1000 V and 30 min (*2*), 250 V and 30 min (*3*); annealing temperature 650 °C (*a*). Spectra of GMNs obtained under 1000 V, 700 °C and 60 min using bi-layer anodes with different ratio of thicknesses of gold/silver layers (Au:Ag): 1:1 (*1*), 1.5:1 (*2*) (*b*)

The ratio of silver/gold LSPR intensities in the formed bi-resonant GMN can be varied by the ratio of thicknesses of silver/gold layers in bi-layer anode, the applied voltage, temperature or duration of the annealing. For example, increase in the voltage from 250 V to 1000 V or the annealing duration from 30 to 60 min results in the intensification of silver LSPR (Fig. 3,*a*), while increase in the annealing temperature from 650 to 700 °C or decrease in thickness of silver layer in bi-layer anode from 50 to 30 nm results in the intensification of gold LSPR (Fig. 3,*b*).

## Conclusion

Two-step bottom-up approach is demonstrated for fabrication of bi-resonant GMN. The approach includes applying DC voltage to bi-layer gold-silver film sputtered on glass surface and annealing of the glass at 650–700 °C. Obtained GMN contains gold nanoparticles in ~1 μm thick subsurface region and silver nanoparticles in an essentially thicker region. The GMN is characterized by two resonances which spectral positions correspond to LSPR in silver and gold nanoparticles. It is demonstrated that the ratio of silver/gold LSPR intensities can be adjusted by varying the applied voltage, temperature or duration of the annealing.

## Acknowledgments

This study was supported by the Russian Science Foundation (agreement №22-22-20005 dated 23. 03. 2022) and St. Petersburg Science Foundation (agreement №04/2022 dated 13. 04. 2022), project № 22-22-20005.

## REFERENCES

1. **Li J., Liu J., Tian X., Li Z.-Y.**, Plasmonic particles with unique optical interaction and mechanical motion properties, Particle & Particle Systems Characterization. 34 (8) (2017) 1600380.

2. **Zhang K., Zhou D., Qiu J., Long Z., Zhu R., Wang Q., Lai J., Wu H., Zhu C.**, Silver nanoparticles enhanced luminescence and stability of CsPbBr3 perovskite quantum dots in borosilicate glass, Journal of the American Ceramic Society. 103 (4) (2020) 2463–2470.

3. **Long X., Yue W., Su Y., Chen W., Li L.**, Large-Scale, Bandwidth-Adjustable, Visible Absorbers by Evaporation and Annealing Process, Nanoscale Research Letters. 14 (1) (2019) 1–8.

4. **Halonen M., Lipovskii A., Zhurikhina V., Lyashenko D., Svirko Y.**, Spectral mapping of the third-order optical nonlinearity of glass-metal nanocomposites, Optics Express. 17 (19) (2009) 17170–17178.

5. **Lipovskii A. A, Melehin V. G., Petrikov V. D.**, Electric-field-induced bleaching of ion-exchanged glasses containing copper nanoparticles, Technical physics letters. 32 (3) (2006) 275–277.

6. **Chou Chau Y.-F., Syu J.-Y., Chao C.-T. C., Chiang H.-P., Lim C. M.**, Design of crossing metallic metasurface arrays based on high sensitivity of gap enhancement and transmittance shift for plasmonic sensing applications, Journal of Physics D: Applied Physics. 50 (4) (2017) 045105.

7. **Kumar A., Kim S., Nam J. M.**, Plasmonically engineered nanoprobes for biomedical applications, Journal of the American Chemical Society. 138 (44) (2016) 14509–14525.

8. **Li J. F., Zhang Y. J., Ding S. Y., Panneerselvam R., Tian Z. Q.**, Core–Shell Nanoparticle-Enhanced Raman Spectroscopy, Chemical reviews. 117 (7) (2017) 5002–5069.

9. **Nastulyavichus A. A., Kudryashov S. I., Smirnov N. A., Rudenko A. A., Kharin A. Y., Busleev N. I., Zayarny D. A., Ionin A. A., Kirilenko D. A., Brunkov P. N.**, Novel approach of controllable stoichiometric fabrication of alloyed Au/Ag nanoparticles by nanosecond laser ablation of thin bi-layered films in water, Laser Physics Letters. 16 (9) (2019) 096002.

10. **Mathpal M. C., Kumar P., Tripathi A. K., Balasubramaniyan R., Singh M. K., Chung J. S., Agarwal A.**, Facile deposition and plasmonic resonance of Ag–Au nanoparticles in titania thin film, / New Journal of Chemistry. 39 (8) 6522–6530.

11. **Cattaruzza E., Battaglin G., Gonella F., Ali S., Sada C. and Quaranta A.**, Characterization of silicate glasses doped with gold by solid-state field-assisted ion exchange, Materials Science and Engineering: B. 149 (2) (2008) 195–199.

12. **Amendola V., Pilot R., Frasconi M., Maragт O. M., Iatм M. A.**, Surface plasmon resonance in gold nanoparticles: a review, Journal of Physics: Condensed Matter. 29 (20) (2017) 203002.

13. **Najafi S., Suchoski P., Ramaswamy R.**, Silver film-diffused glass waveguides: Diffusion process and optical properties, IEEE journal of quantum electronics. 22 (12) (1986) 2213–2218.

14. **Gonella F., Cattaruzza E., Quaranta A., Ali S., Argiolas N., Sada C.**, Diffusion behavior of transition metals in field-assisted ion-exchanged glasses, Solid State Ionics. 177 (35-36) (2006) 3151–3155.

## THE AUTHORS

**BABICH Ekaterina S.**
babich_es@spbstu.ru
ORCID: 0000-0003-4970-2591

**LUBYANKINA Ekaterina A.**
lubjankina_e_st@spbau.ru
ORCID: 0000-0003-0210-1780

**REDUTO Igor V.**
reduto-igor@mail.ru
ORCID: 0000-0001-7172-5250

*Received 21.10.2022. Approved after reviewing 08.11.2022. Accepted 08.11.2022.*

© Peter the Great St. Petersburg Polytechnic University, 2023

Conference materials
UDC 538.9
DOI: https://doi.org/10.18721/JPM.161.229

# Stimulated emission from asymmetric InAs/InAsSb/InAsSbP LED heterostructures

A.A. Semakova[1]✉, V.V. Romanov[1], N.L. Bazhenov[1],
K.D. Mynbaev[1, 2], K.D. Moiseev[1]

[1] Ioffe Institute, St. Petersburg, Russia;
[2] ITMO University, St. Petersburg, Russia
✉ antonina.semakova@mail.ioffe.ru

**Abstract.** Electroluminescent (EL) properties of asymmetrical InAs/$InAs_{1-y}Sb_y$/InAsSbP heterostructures with the $y = 0.09$ and $y = 0.11$ InSb content in the active layer were studied in wide temperature range $T = 4.2–300$ K. The stimulated emission in the spectral range 4.1–4.2 μm has been observed at low temperatures ($T < 30$ K). It was estimated that EL spectra were formed owing to different channels of radiative recombination depending on the ambient temperature. The influence of the quality of the type II InAsSb/InAsSbP heterojunction on radiative recombination transitions has been considered.

**Keywords:** light-emitting diodes, heterojunctions, InAs, antimonides, stimulated emission

**Citation:** Semakova A.A., Romanov V.V., Bazhenov N.L., Mynbaev K.D., Moiseev K.D., Stimulated emission from asymmetric InAs/InAsSb/InAsSbP LED heterostructures, St. Petersburg State Polytechnical University Journal. Physics and Mathematics. 16 (1.2) 2023 191–195. DOI: https://doi.org/10.18721/JPM.161.229

This is an open access article under the CC BY-NC 4.0 license (https://creativecommons.org/licenses/by-nc/4.0/)

Материалы конференции
УДК 538.9
DOI: https://doi.org/10.18721/JPM.161.229

# Стимулированное излучение в светодиодах на основе асимметричных гетероструктур InAs/InAsSb/InAsSbP

А.А. Семакова[1]✉, В.В. Романов[1], Н.Л. Баженов[1],
К.Д. Мынбаев[1, 2], К.Д. Моисеев[1]

[1] Физико-технический институт им. А.Ф. Иоффе РАН, Санкт-Петербург, Россия;
[2] Университет ИТМО, Санкт-Петербург, Россия
✉ antonina.semakova@mail.ioffe.ru

**Аннотация.** Исследованы электролюминесцентные (ЭЛ) характеристики асимметричных гетероструктур InAs/$InAs_{1-y}Sb_y$/InAsSbP с мольной долей InSb в активной области $y = 0.09$ и $y = 0.11$ в диапазоне температур $T = 4.2–300$ K. При низких температурах ($T < 30$ K) наблюдалось стимулированное излучение в спектральной области 4.1–4.2 мкм. Установлено, что спектры ЭЛ формировались за счет различных каналов излучательной рекомбинации в зависимости от температуры окружающей среды. Рассмотрено влияние качества гетероперехода II типа InAsSb/InAsSbP на излучательные рекомбинационные переходы.

**Ключевые слова:** светодиоды, гетеропереходы, InAs, антимониды, стимулированное излучение

© Semakova A.A., Romanov V.V., Bazhenov N.L., Mynbaev K.D., Moiseev K.D., 2023. Published by Peter the Great St. Petersburg Polytechnic University.

**Ссылка при цитировании:** Семакова А.А., Романов В.В., Баженов Н.Л., Мынбаев К.Д., Моисеев К.Д. Стимулированное излучение в светодиодах на основе асимметричных гетероструктур InAs/InAsSb/InAsSbP // Научно-технические ведомости СПбГПУ. Физико-математические науки. 2023. Т. 16. № 1.2. С. 191–195. DOI: https://doi.org/10.18721/JPM.161.229

Статья открытого доступа, распространяемая по лицензии CC BY-NC 4.0 (https://creativecommons.org/licenses/by-nc/4.0/)

## Introduction

The unflagging interest in heterostructures based on narrow-gap $A^{III}B^{V}$ compounds is due to both their fundamental properties and a wide area of practical use for a broad range of optoelectronic devices operating in the mid-infrared (IR) spectral range (2–6 μm). Light-emitting diode (LED) heterostructures based on InAs(Sb, P) solid solutions are promising sources for environmental control systems and medical diagnostics [1, 2]. A challenge of enhancing the efficiency of mid-IR LEDs has found successful practical solutions [3]. However, optimization of the output characteristics of LEDs is often accompanied by a complication of the design of device structures. At the same time, identification of mechanisms of recombination processes occurring in narrow-gap semiconductor-based heterostructures can assist to discover new possibilities for the improvement in the efficiency of LEDs. The paper reports on getting a stimulated emission caused by interface-related radiative transitions in asymmetric heterostructures *n*-InAs/$InAs_{1-y}Sb_y$/*p*-InAsSbP with an ultimate molar fraction of InSb in the ternary solid solution of the active region ($y > 0.09$).

## Materials and Methods

The InAs/$InAs_{1-y}Sb_y$/InAsSbP heterostructures were grown by the Metal-Organic Vapour-Phase Epitaxy (MOVPE) method on unintentionally doped InAs(001) substrates. The epitaxial deposition of the InAsSb and InAsSbP layers was performed under atmospheric pressure in a horizontal reactor with resistive heating. The active layer based on the InAsSb ternary solution was not intentionally doped during its deposition. Initial electron concentration in the *n*-type $InAs_{1-y}Sb_y$ layer was evaluated to be $n = 3 \times 10^{16}$ cm$^{-3}$ ($T = 300$ K) and caused by the presence of residual impurities. The zinc-doped InAsSbP barrier layer was grown on top of the heterostructure studied and followed the active layer.

Two asymmetric heterostructures with a molar fraction of InSb in the ternary solid solution $y = 0.09$ (structure *A*) and $y = 0.11$ (structure *B*) were studied.

LED chips with round-shaped mesa with 300 μm diameter were fabricated using standard photolithography and wet chemical etching. The electroluminescence (EL) spectra were recorded in the temperature range $T = 4.2$–300 K under pulsed excitation at a frequency of 1 kHz and a pulse width of 2 μs. An InSb photodiode was used as a detector.

## Results and Discussion

Fig. 1 presents EL properties of the structures under study. Fig. 1,*a* displays typical EL spectra at $T = 4.2$ K and the lowest injection current ($i = 0.2$ A) in our experiment. The spectra had the average full width at half maximum (FWHM) about 20–23 meV. The sharp low-energy edge in these spectra at $h\nu \sim 0.29$ eV is due to the absorption of the outcoming emission by molecules of carbon dioxide ($CO_2$) present in the ambient atmosphere. Fig. 1,*b* shows the temperature dependences of the spectral positions for the EL peaks of the heterostructures *A* and *B*, as well as the calculated temperature dependences of the energy gap ($E_g$) of the active layer for $InAs_{1-y}Sb_y$ solid solution with antimony content $y = 0.09$ and $y = 0.11$. The $E_g(T)$ dependences for $InAs_{1-y}Sb_y$ were obtained as a result of the Varshni approximation:

$$E_g = E_0 - \alpha \cdot T^2 \cdot (T + \beta)^{-1}, \quad (1)$$

© Семакова А.А., Романов В.В., Баженов Н.Л., Мынбаев К.Д., Моисеев К.Д., 2023. Издатель: Санкт-Петербургский политехнический университет Петра Великого.

with parameters $\alpha = 2.76 \times 10^{-4}$ eV/K and $\beta = 93$ K typical of the solid solution enriched with InAs [4]. The values of $E_0$ were calculated for the InAsSb solid solutions as an interpolation of the fractions of the binary compounds InAs and InSb in accordance with the expression [5]:

$$E_0 = E_{g\mathrm{InAs}} \cdot (1 - y) + E_{g\mathrm{InSb}} \cdot y - C_{\mathrm{InAsSb}} \cdot y \cdot (1 - y), \quad (2)$$

where $E_{g\mathrm{InAs}} = 0.417$ eV, $E_{g\mathrm{InSb}} = 0.235$ eV, and the bowing parameter $C_{\mathrm{InAsSb}} = 0.61$ eV [6].

As we can see in Fig.1,*b*, an unusual behaviour of the spontaneous luminescence was observed for both structures. In the low temperature range ($T < 100$ K) a large discrepancy between experimental and calculated data was observed and a shift of the spectral position of the EL band maximum towards high energies of photon was revealed with temperature increasing. At high temperatures ($T > 200$ K) the spectral position of the EL band maximum was found to be close to the calculated curve corresponding to the temperature dependence of the energy gap of the ternary solid solution. It means that the temperature shift of the EL band for the structures under study to the low energy region corresponded to the narrowing of the band gap of $InAs_{1-y}Sb_y$ epilayer. Moreover, there is a temperature range $100 < T < 200$ K where experimental data exhibited a trend in temperature dependence similar to the computed curve with some distance from the latter. The revealed energy distance was found to start from 15 meV and decreased to 0 at $T > 200$ K. The observed difference can be explained by the possible diffusion of Zn during growth or post-growth processing of the structures. Thus, it can be suggested that the spontaneous emission spectra in this temperature range were due to radiative recombination involving Zn acceptor states in the bulk of the active layer, as the activation energy of Zn shallow acceptor in InAs-related materials has similar value [6]. One can assume that there are two mechanisms of radiative recombination transitions which are switching from one to another near $T = 100$ K. This is indicative of the fact that with an increase in temperature to 300 K, band-to-band radiative recombination transitions in the active layer of the heterostructures became dominant in EL spectra, whereas the interface-related transitions could be responsible for the low-energy parts of the EL spectra.

As was shown in [7], the $InAs_{1-y}Sb_y$/InAsSbP heterojunction at $y > 0.09$ determines the type II alignment of the energy bands at the heterointerface. Owing to such band alignment, the energy gap between levels of localization for electrons and holes involved in radiative transitions can be smaller than the smallest bandgap of each alloy forming this heterojunction. Moreover, the value of this gap decreased with an increase in a molar fraction of InSb in the ternary solid solution $InAs_{1-y}Sb_y$ in the active region. A significant difference of 40–42 meV between the calculated bandgap of the InAsSb solid solution and the spectral position of the EL band maximum recorded at 4.2 K reveals that interface radiative recombination transitions occur across the $InAs_{1-y}Sb_y$/InAsSbP heteroboundary. As shown for a single type II heterostructure *n*-InGaAsSb/*p*-GaInAsSb, localization of electrons and holes in adjacent potential wells at the type II interface can result in obtaining a lasing mode based on indirect interface-assisted transitions [8].

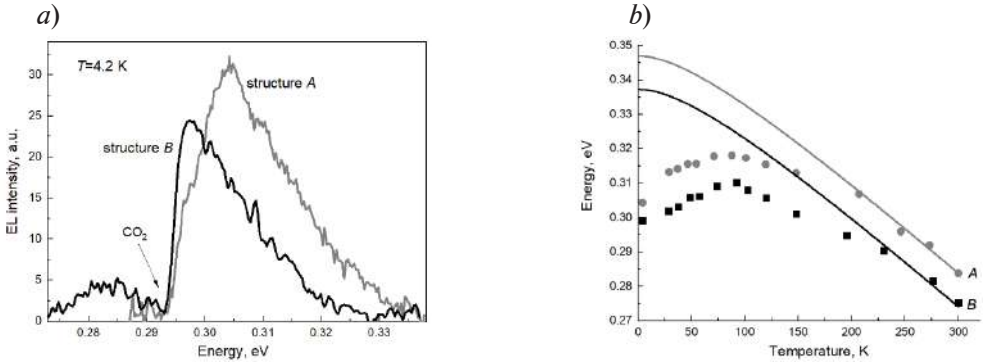


Fig. 1. EL spectra of spontaneous emission measured at $T = 4.2$ K and $i = 0.2$ A (*a*) and the temperature dependences of photon energy at the peak maximum of spontaneous emission (symbols) and calculated $E_g(T)$ dependences of $InAs_{0.91}Sb_{0.09}$ (structure *A*) and $InAs_{0.89}Sb_{0.11}$ (structure *B*) solid solution (curves) (*b*)

Fig. 2 shows the EL spectra of the heterostructures under study at higher injection levels and low temperature ($T = 4.2$ K). The stimulated emission starts at the injection level of $i > 0.2$ A and demonstrates a narrow spectrum with FWHM ~ 2 meV. Increase in the injection level ($i > 0.6$ A) led to the formation of multi-mode spectrum which could be approximated with Lorentz distributions. The resulting intensity of EL spectra reached the saturation level at the injection current characteristic of the appearance of the third mode in the spectra. It should be noted that with an increase in the excitation level, the intensity of individual modes in the EL spectrum changed. The average inter-mode distance was $\Delta\lambda \sim 1.2$ nm corresponded to the cavity length $L = 170$ μm, which was determined mainly by the thickness of the InAs substrate.

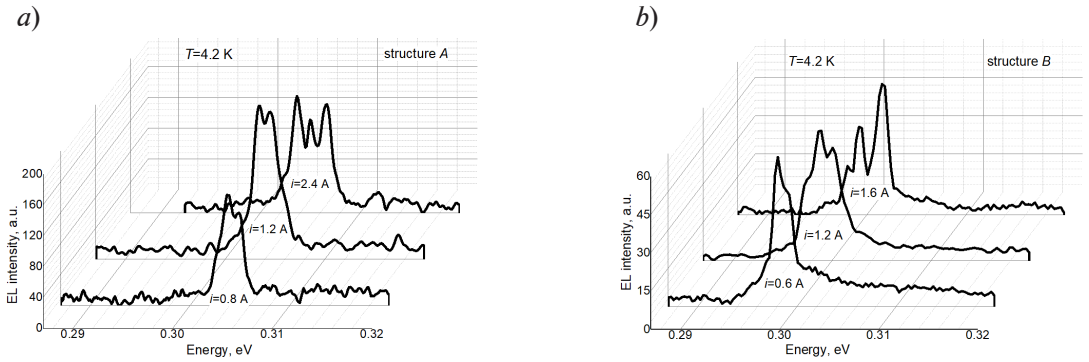


Fig. 2. EL spectra of stimulated emission for the heterostructures $A$ (*a*) and $B$ (*b*) measured at $T = 4.2$ K and different injection currents

As can be seen in Fig. 2, the stimulated emission was generated in the spectral region 0.29–0.31 eV depending on the studied heterostructure and that manifests a good agreement with spontaneous EL data at the given temperature. Therefore, the observed stimulated emission at low temperatures was caused by the interface radiative recombination of holes near the Fermi level with electrons localized in the potential well. The shift towards higher energy of photon with increasing of an injection level can be explained by a shift of localization level for electrons.

It should be noted that the stimulated emission was observed in the temperature range 4.2–30 K for both structures. The transition from stimulated to spontaneous emission occurred at $T \sim 30$ K (not shown in Fig. 1,*b*). The maximum temperature reached here is less than that reported for similar heterostructure based on the InAsSb active layer containing smaller antimony concentration [9]. The amazing fact manifested in this work is that the samples studied had the ultimate content of antimony in the active layer at which the crystalline structure of the layers of the heterostructure was not yet corrupted. It is well known that the crystalline perfection of ternary solid solutions grown on InAs substrates is in close association with a parameter of the lattice mismatch between epitaxial layer and substrate matrix. This parameter for $InAs_{1-y}Sb_y$ epitaxial layers at $y = 0.09$–$0.11$ does not exceed 1%, which is a critical value for thin layers. If the mismatch is greater, a near-surface network of dislocations can be generated, accompanied by an increase in the concentration of extended and point defects, etc., which leads to relaxation of the epitaxial system. Experiments carried out for samples with a higher content of antimony in the active region demonstrated suppression of stimulated emission in similar narrow-gap asymmetric heterostructures based on the InAsSb ternary solid solution.

## Conclusion

Electroluminescence spectra of asymmetrical $InAs/InAs_{1-y}Sb_y/InAsSbP$ LED heterostructures with ultimate concentration of InSb in the active layer $y = 0.09$ and 0.11 were studied in the temperature range $T = 4.2$–300 K. The rearrangement of the contributions of three different mechanisms of radiative recombination was observed with temperature increasing. At low temperatures ($T < 100$ K) the spontaneous luminescence and the stimulated emission were caused by the interfacial radiative transitions at the type-II InAsSb/InAsSbP heterointerface. At higher temperatures ($T > 100$ K) radiative recombination transitions (solely spontaneous) involving zinc acceptor states in the active layer were dominant. At $T > 200$ K and up to 300 K the EL was determined by interband radiative transitions in the bulk of the active layer made of InAsSb ternary solid solution.

## REFERENCES

1. **Ting D.Z., Soibel A., Khoshakhlagh A., Keo S. A., Rafol S. B., Fisher A. M., Pepper B.J., Luong E.M., Hill C.J., Guhapala S.D.,** Advances in III-V semiconductor infrared absorbers and detectors, Infrared Physics and Technology, 97 (2019) 210–216.

2. **Jung D., Bank S., Lee M. L., Wasserman D.,** Next-generation mid-infrared sources, Journal of Optics, 19 (2017) 123001.

3. **Lu Q., Zhou Y., Chen J., He L., Krier A.,** Mid-infrared interband cascade light-emitting diodes with InAs/GaAsSb superlattices on InAs substrates, Smart Photonic and Optoelectronic Integrated Circuits XXII, 11284 (2020) 39.

4. **Varshni Y.P.,** Temperature dependence of the energy gap in semiconductors, Physica, 34(1) (1967) 149–154.

5. **Vurgaftman I., Meyer J.R., Ram-Mohan L.R.,** Band parameters for III-V compound semiconductors and their alloys, Journal of Applied Physics, 89(11) (2001) 5815–5875.

6. **Landolt-Bцrnstein,** Handbook "Numerical Data, Ser. III, Ed. O. Madelung." 17a (1982).

7. **Moiseev K.D., Romanov V.V.,** Band diagram of the $InAs_{1-y}Sb_y$/InAsSbP heterojunction in the composition range $y$<0.2, Physics of the Solid State, 63 (2021) 595–602.

8. **Moiseev K.D., Mikhailova M.P., Yakovlev Yu.P.,** Special features of spontaneous and coherent emission of IR lasers based on a single type-II broken-gap heterojunction, Semiconductors, 37 (2003) 985–991.

9. **Mynbaev K.D., Bazhenov N.L., Semakova A.A., Chernyaev A.V., Kizhaev S.S., Stoyanov N.D., Bougrov V.E., Lipsanen H., Salikhov Kh.M.,** Spontaneous and stimulated emission in InAsSb-based LED heterostructures, Infrared Physics and Technology, 85 (2017) 246–250.

## THE AUTHORS

**SEMAKOVA Antonina A.**
antonina.semakova@mail.ioffe.ru
ORCID: 0000-0002-0741-1895

**MYNBAEV Karim D.**
mynkad@mail.ioffe.ru
ORCID: 0000-0002-9853-8874

**ROMANOV Viacheslav V.**
romanovvv@mail.ioffe.ru
ORCID: 0000-0002-9989-3843

**MOISEEV Konstantin D.**
mkd@iropt2.ioffe.ru
ORCID: 0000-0002-6306-0129

**BAZHENOV Nicolay L.**
bazhnil.ivom@mail.ioffe.ru
ORCID: 0000-0002-3019-2280

*Received 24.10.2022. Approved after reviewing 08.11.2022. Accepted 08.11.2022.*

© Peter the Great St. Petersburg Polytechnic University, 2023

Conference materials
UDC 539.412.1
DOI: https://doi.org/10.18721/JPM.161.230

# Nanostructured high-strength high-modulus film polymer materials: statistical elastic and fracture mechanical properties

Yu.M. Boiko✉, V.A. Marikhin, L.P. Myasnikova

Ioffe Institute, St. Petersburg, Russia

✉ yuri.boiko@mail.ioffe.ru

**Abstract.** The statistical distributions of the mechanical properties (strength σ, strain at break $\varepsilon_b$, and Young's modulus E) of the high-strength high-modulus oriented thin films and fibers of polyamide-6 (PA-6) have been investigated. For this purpose, two types of the PA-6 samples have been selected: single thin threads and multifilament fibers consisting of some hundreds of individual fibers. The statistical analysis has been carried out on a large number of mechanical tests of identical samples (50 testing samples for each of the two sample types) using the Gaussian and Weibull's models. Beside the 'traditional' mechanical properties (σ, $\varepsilon_b$, and E) commonly used for materials characterization, two additional viscoelastic and fracture characteristics have been estimated and introduced when analyzing the stress-strain curve by taking its first derivative. These are the tangent to the linear viscoelastic portion of the stress-strain curve at relatively large strains (6–14%) and the deformation interval between $\varepsilon_b$ and the strain value received by extrapolation of this curve portion to σ = 0, referred to as the apparent viscoelastic modulus ($E_2$) and apparent strain at break ($\varepsilon_{b2}$), respectively. The similarities and differences of the statistical distribution behaviors of σ, $\varepsilon_b$, E, $E_2$, and $\varepsilon_{b2}$ for two PA-6 sample types investigated, including the applicability of the Gaussian and Weibull's models, have been discussed.

**Keywords:** polyamide-6, fibers, mechanical properties, statistics

**Funding:** This study was carried out in the framework of the State Task "Strength Physics Problems: Processes of Fracture of Solids, Principles of Materials Strengthening and Enhancement of Materials Dynamical Strength, Development of Crack- and Wear-Resistant Materials" (theme number 0040-2014-0008).

**Citation:** Boiko Yu.M., Marikhin V.A., Myasnikova L.P., Nanostructured high-strength high-modulus film polymer materials: statistical elastic and fracture mechanical properties, St. Petersburg State Polytechnical University Journal. Physics and Mathematics. 16 (1.2) 2023 196–203. DOI: https://doi.org/10.18721/JPM.161.230

This is an open access article under the CC BY-NC 4.0 license (https://creativecommons.org/licenses/by-nc/4.0/)

Материалы конференции
УДК 539.412.1
DOI: https://doi.org/10.18721/JPM.161.230

# Наноструктурированные высокопрочные высокомодульные пленочные полимерные материалы: статистические упругие и прочностные механические свойства

Ю.М. Бойко✉, В.А. Марихин, Л.П. Мясникова

Физико-технический институт им. А.Ф. Иоффе РАН, Санкт-Петербург, Россия

✉ yuri.boiko@mail.ioffe.ru

**Аннотация.** Исследованы статистические механические свойства высокопрочных высокомодульных ориентированных тонких пленок и волокон полиамида6-. Обсуждается применимость статистических моделей Гаусса и Вейбулла для описания распределений ряда упругих и прочностных характеристик.

© Boiko Yu.M., Marikhin V.A., Myasnikova L.P., 2023. Published by Peter the Great St. Petersburg Polytechnic University.

**Ключевые слова:** полиамид-6, волокна, механические свойства, статистика

**Финансирование:** Работа выполнена в рамках Государственного задания «Проблемы физики прочности: процессы разрушения твердых тел, принципы упрочнения материалов и повышения динамической прочности материалов, создание трещиностойких, износостойких материалов» (код темы [0008-2014-0040]).

**Ссылка при цитировании:** Бойко Ю.М., Марихин В.А., Мясникова Л.П. Наноструктурированные высокопрочные высомодульные пленочные полимерные материалы: статистические упругие и прочностные механические свойства // Научно-технические ведомости СПбГПУ. Физико-математические науки. 2023. Т. 1.2 № .16. С. 196–203. DOI: https://doi.org/10.18721/JPM.161.230

Статья открытого доступа, распространяемая по лицензии CC BY-NC 4.0 (https://creativecommons.org/licenses/by-nc/4.0/)

## Introduction

As is known [1], the orientational drawing behavior of isotropic low-strength polymers is an effective way for producing high-strength high-modulus oriented polymer thin films and multifilament fibers which are the perspective materials in various fields of application. It has been shown that, in the course of orientation, the initial lamellar nanostructure (stacks of folded crystalline lamellae) is transformed into a fibrillar structure (oriented nanofibrils) due to the unfolding of polymer chain folds in the initial lamellae. Such a discrete nanostructural improvement of the material leads to a significant (by an order of magnitude or more) increase in the important mechanical characteristics of the material: Young's (or elastic) modulus ($E$) up to 200 GPa and strength ($\sigma$) up to 6 GPa [1, 2]. However, a negative consequence of this process is the embrittlement of the material, which leads to a sharp increase in the scatter of the measurement results. This behavior is due to the appearance and development of surface nanocracks at the final stages of orientational drawing, the so-called kink bands, which are the initiators of the growth of the main crack during sample failure.

The materials mechanical properties of a common use such as $\sigma$, $E$, and strain at break ($\varepsilon_b$) are important characteristics playing a key role in choosing the most appropriate fields of materials applications. It is generally believed that five tests of identical samples are sufficient to characterize the material by estimating the mean (average) value of $\sigma$, $\varepsilon_b$, or $E$ ($\sigma_{av}$, $\varepsilon_{av}$, or $E_{av}$) [3, 4]. However, in some cases, for high-strength high-modulus oriented polymer materials which are quasi-brittle, the scatter of the measured values of mechanical properties is rather broad. Hence, the test number should be increased markedly, up to some tens or even hundreds, in order to estimate correctly the values of $\sigma_{av}$, $\varepsilon_{av}$, or $E_{av}$ [2, 5–9]. This makes it possible not only to estimate the values of $\sigma_{av}$, $\varepsilon_{av}$ and $E_{av}$ more reliably, but to perform the statistical analysis of the distributions of mechanical properties. Information received from such an analysis, for instance, the conformity to a certain theoretical model (e.g., Gaussian, Weibull's [5–11]), can be helpful for a better understanding of the deformation and fracture mechanisms of materials and making a more proper recommendation on their practical use. Actually, if the *distribution* of a measured *data* set can be represented with a bell curve that is characteristic of the *Gaussian* (*or normal) distribution,* it implies that the data *scatter* is caused by the sum of many independent and equally weighted factors [3, 5]. By contrast, if it obeys the Weibull's statistics, it should have the shape of a linear plot in specific coordinates $\ln\ln[1/(1 - P_j)] - \ln\sigma$, where $P_j$ is the cumulative probability of failure, that is indicative of the dominant role in the sample fracture of the surface cracks and their propagation across the sample cross-section [6–11].

Weibull's statistics, proposed initially for $\sigma$ only, is based on the idea that the fracture of the whole sample is controlled by weakest (local) link [6]. In this approach, the cumulative probability function $P(\sigma)$ describing the probability of failure of identical samples at or below stress $\sigma$ is given by

© Бойко Ю.М., Марихин В.А., Мясникова Л.П., 2023. Издатель: Санкт-Петербургский политехнический университет Петра Великого.

$$P(\sigma) = 1 - \exp\left[-(\sigma/\sigma_0)^m\right], \quad (1)$$

where $m$ is the so-called Weibull modulus (a measure of data dispersion) and $\sigma_0$ is the scale parameter (having the physical meaning of $\sigma_{av}$).

For carrying out Weibull's analysis, a set of test results should be converted into an experimental probability distribution by ordering them from the lowest strength to highest ones. The $j$th result in the set of $n$ samples is assigned a cumulative probability of failure ($P_j$)

$$P_j = (j - 0.5)/n. \quad (2)$$

By rearranging Eq. (1), taking logarithm of its both sides twice and replacing $P(\sigma)$ with $P_j$, Eq. (3) is obtained

$$\ln\ln[1/(1 - P_j)] = -m\cdot\ln\sigma_0 + m\cdot\ln\sigma. \quad (3)$$

In fact, Eq. (3) represents a linear regression

$$y = a + bx, \quad (4)$$

where $y = \ln\ln[1/(1 - P_j)]$, $b$ is the $m$, $x$ is the $\ln\sigma$, and $a = -m\cdot\ln\sigma_0$ is the curve intersect with the $y$ axis. By estimating $m$ as the tangent to the curve $\ln\ln[1/(1 - P_j)] = f(\ln\sigma)$ using a standard procedure of the linear regression analysis, we can calculate $\sigma_0$ by solving Eqs. (5) and (6):

$$\ln\sigma_0 = -a/m, \quad (5)$$

$$\sigma_0 = \exp(-a/m). \quad (6)$$

Earlier [12], it has been suggested to apply this approach, along with $\sigma$, to $\varepsilon_b$ and $E$ as well. So, by replacing the values of $\sigma$ and $\sigma_0$ in Eqs. (1) and (3) by $\varepsilon_b$ and $\varepsilon_0$, and $E$ and $E_0$, we obtain:

$$\ln\ln[1/(1 - P_j)] = m\cdot\ln\varepsilon_b - m\cdot\ln\varepsilon_0, \quad (7)$$

$$\varepsilon_0 = \exp(-a/m), \quad (8)$$

$$\ln\ln[1/(1 - P_j)] = m\cdot\ln E - m\cdot\ln E_0, \quad (9)$$

$$E_0 = \exp(-a/m). \quad (10)$$

Eqs. (7) and (9) can be reduced to Eq. (4), by analogy with $\sigma$, where $x = \ln\varepsilon_b$ or $\ln E$, and $a = -m\cdot\ln\varepsilon_0$ or $a = -m\cdot\ln E_0$.

In order to analyze the stress-strain behavior of high-strength oriented polymers in more detail than traditionally (to analyze $\sigma$, $\varepsilon_b$, and $E$ only), the first derivative of the stress-strain curves should be calculated and specific points found (see [12]). In this work, for the first time, the statistical analysis of other mechanical properties found on the stress-strain curves will be performed for the high-strength fibers of polyamide-6 (PA-6) of two types: single and multifilament fibers. The choice of these two different sample types was motivated by their different statistical natures: 'statistical' multifilament sample (consisting of two hundreds of individual fibers) and 'non-statistical' single fiber.

## Materials and Methods

The commercial PA-6 single filament with a diameter $d$ of 0.20 mm and the PA-6 multifilament consisting of ~200 individual fibers with a linear density of 213 tex, i.e., with an effective sample $d$ = 0.52 mm or individual fiber $d$ = 2.6 μm, have been used. The force-displacement curves were recorded on an *Instron*-1122 tensile tester at ambient temperature at a cross-head speed of 200 mm/min and a distance between the clamps of 500 mm, i.e., at a strain rate of 0.4 $min^{-1}$. In order to receive statistically correct results, 50 identical samples were tested for each of the sample types.

## Results and Discussion

Fig. 1,*a* shows the stress-strain curves for the oriented mono- and multifilament PA-6 fibers. For the two sample types, the slopes of the curves become steeper at ε >6%, indicating that some strengthening takes place. This behavior suggests that the potential of strengthening has not been realized in the course of drawing and its conditions were not optimal. To put it differently, even after drawing the samples by 10% only, the mechanical properties can be enhanced markedly. Let us consider the stress-strain curves in more detail by differentiating them (see Fig. 1,*b*). As is seen, there are two linear curve portions characterizing with the Young's modulus $E_1$ at small strains < 1% and an apparent modulus $E_2$ at large strains >5%. By extrapolating the second curve portion $E_2$ to σ = 0, the value of strain at break $\varepsilon_{b\text{-}2}$ for this range of ε can be estimated.

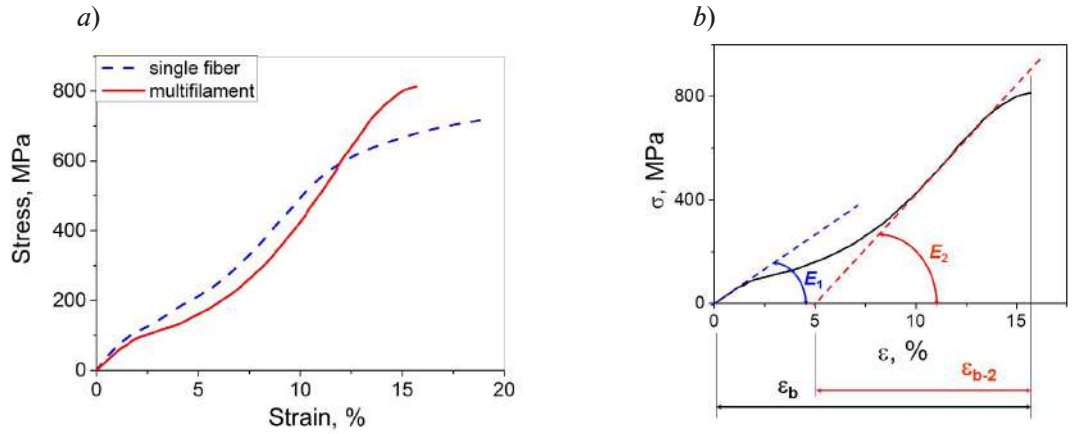


Fig. 1. Stress vs engineering strain for oriented mono- and multifilament PA-6 fibers (*a*), and the scheme of the analysis of the stress-strain curve for the multifilament PA-6 fibers (*b*)

Let us apply the Weibull's and Gaussian models to describe the statistical distributions of the values of $E_2$ and $\varepsilon_{b\text{-}2}$ presented in Figs. 2,*a* and 3,*a*, respectively. For this purpose, the values of $\varepsilon_b$, $\varepsilon_0$, $E$, and $E_0$ in Eqs. (7–10) can be replaced by the corresponding values of $\varepsilon_{b\text{-}2}$, $\varepsilon_{2\text{-}0}$, $E_2$, and $E_{2\text{-}0}$. As a result, one obtains Eqs. (11–14) that will be used for the Weibull's analysis of $E_2$ and $\varepsilon_{b\text{-}2}$.

$$\ln\ln[1/(1-P_j)] = m\cdot\ln\varepsilon_{b\text{-}2} - m\cdot\ln\varepsilon_{2\text{-}0}, \quad (11)$$

$$\varepsilon_{2\text{-}0} = \exp(-a/m), \quad (12)$$

$$\ln\ln[1/(1-P_j)] = m\cdot\ln E_2 - m\cdot\ln E_{2\text{-}0}, \quad (13)$$

$$\ln E_{2\text{-}0} = \exp(-a/m). \quad (14)$$

The results of the Weibull's analysis of the distributions of $E_2$ and $\varepsilon_{b\text{-}2}$ are shown in Fig. 2,*b* and 3,*b*, respectively. By analogy, the statistical distributions of the values of σ, $\varepsilon_b$, and $\mathbf{E}_1$ have been analyzed. The results of this analysis for the five mechanical properties ($p$) under investigation (σ, $\varepsilon_b$, $E_1$, $\varepsilon_{b\text{-}2}$, and $E_2$) are collected in Table 1.

As is seen, all the values of the ratio of the scale parameter to the average value $p_0/p_{av}$ ($E_{2\text{-}0}/E_{2\text{-}av}$, $\varepsilon_{2\text{-}0}/\varepsilon_{2\text{-}av}$, $E_{1\text{-}0}/E_{av}$, $\sigma/\sigma_{av}$, and $\varepsilon_0/\varepsilon_{av}$) presented in Table 1 for the two sample types investigated are close to 1 ($p_0/p_{av} \approx 1$), indicating that the Weibull analysis carried out is correct for all the five mechanical properties investigated. For estimating the effect of the deformation strengthening at the second portion of the stress-strain curve, let us compare statistically correct values of $E_1$ and $E_2$, i.e., the values of $E_{1\text{-}0}$ and $E_{2\text{-}0}$, respectively, calculated from the corresponding Weibull's plots. Since the ratio $E_{2\text{-}0}/E_{1\text{-}0}$ for the single and multifilament PA-6 fibers are 0.98 and 1.55, respectively, it means that the slope of the second portion ($\varepsilon > 6\%$) of the stress-strain curve for the PA-6 multifilament is steeper with respect to its initial portion ($\varepsilon < 1\%$) while those for the single fibers are equal. This suggests a marked effectiveness of strengthening of the PA-6 multifilament. It should also be noted that the applicability of the Weibull's model is more correct for a fracture property ($\varepsilon_{b\text{-}2}$, $R^2 > 0.96$) with respect to a viscoelastic property ($E_2$, $R^2 < 0.94$). This behavior seems to be reasonable since this model has been proposed initially namely for a fracture property ($\sigma$). The values of $m$ for the two sample types investigated are compared in Table 2. It is seen that they are rather close for $E_1$ and $\sigma$ while they are markedly larger for the multifilament, by a factor of 3 to 4, for $E_2$, $\varepsilon_b$, and $\varepsilon_{b\text{-}2}$. It means that the data scatter for the multifilament is substantially smaller with respect to that for the single fiber. This behavior may be explained by an extremely large number of the fractured single fibers per one test for the multifilament sample including 200 single fibers with respect to the monofilament sample (200 against 1), making the results for the former more proper statistically.

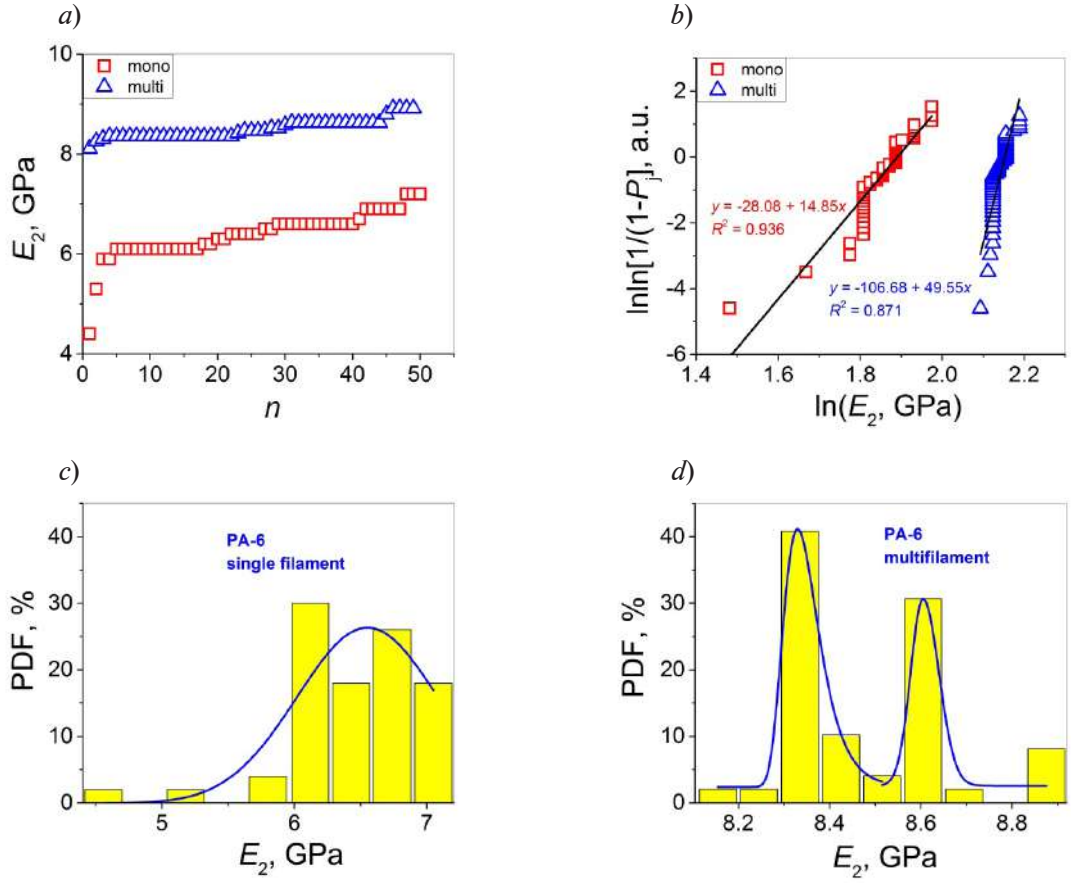


Fig. 2. Modulus $E_2$ vs sample number in ascending order for a single fiber (open squares) and a multifilament (open triangles) of oriented PA 6 (*a*); Weibull plots for the data presented in (*a*) (*b*); the solid lines are linear fits to experimental data; histograms of PDF vs $\varepsilon_{b\text{-}2}$ (*c*, *d*) for a single fiber (*c*) and a multifilament of oriented PA 6 (*d*); the Gaussian fits are shown with bell-shaped solid curves

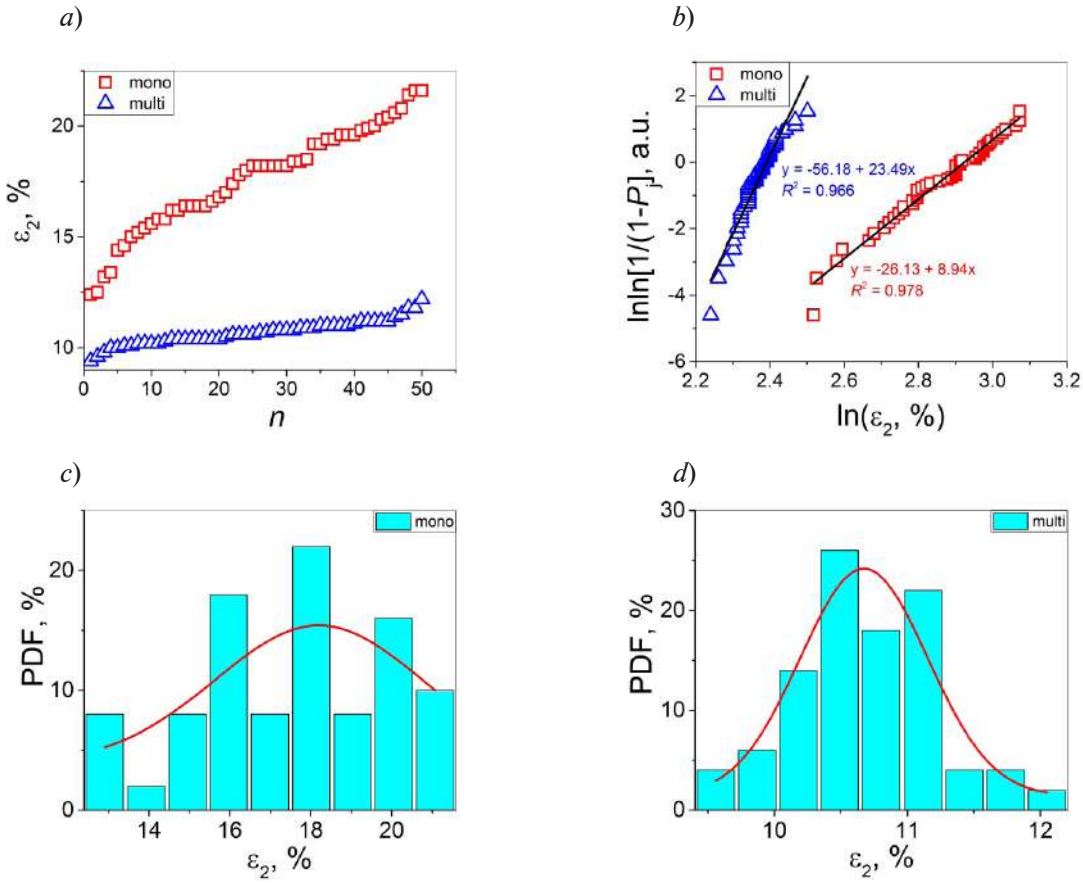


Fig. 3. Extrapolated strain at break $\varepsilon_{b\text{-}2}$ vs sample number in ascending order for a single fiber (open squares) and a multifilament fiber (open triangles) of oriented PA 6 (*a*); its Weibull plots; the solid lines are linear fits to experimental data (*b*); histograms of PDF vs $\varepsilon_{b\text{-}2}$ for a single fiber (*c*) and a multifilament of oriented PA 6 (*d*); the Gaussian fits are shown with bell-shaped solid curves

Table 1

**Results of the Weibull analysis of the distributions of various mechanical properties of high-strength single and multifilament fibers of PA-6**

| Sample type | Property, $p$ | $y = a + bx$ | $R^2$ | m | $p_0$ | $p_{av}$ | $p_0/p_{av}$ |
|---|---|---|---|---|---|---|---|
| single | $E_2$ | $y = -28.08 + 14.85x$ | 0.936 | 14.85 | 6.63 GPa | 6.40 GPa | 1.04 |
| multi | | $y = -106.68 + 49.55x$ | 0.871 | 49.55 | 8.62 GPa | 8.56 GPa | 1.01 |
| single | $\varepsilon_{b\text{-}2}$ | $y = -26.13 + 8.94x$ | 0.978 | 8.94 | 18.6% | 17.6% | 1.06 |
| multi | | $y = -56.18 + 23.49x$ | 0.966 | 23.49 | 10.9% | 10.7% | 1.02 |
| single | $E_1$ | $y = -44.63 + 23.39x$ | 0.907 | 23.39 | 6.75 GPa | 6.60 GPa | 1.02 |
| multi | | $y = -29.55 + 17.24x$ | 0.940 | 17.24 | 5.56 GPa | 5.38 GPa | 1.03 |
| single | σ | $y = -297.94 + 45.32x$ | 0.936 | 45.32 | 0.72 GPa | 0.71 GPa | 1.02 |
| multi | | $y = -291.42 + 43.41x$ | 0.982 | 43.41 | 0.83 GPa | 0.81 GPa | 1.02 |
| single | $\varepsilon_b$ | $y = -28.48 + 9.40x$ | 0.982 | 9.40 | 20.7% | 19.6% | 1.06 |
| multi | | $y = -97.06 + 35.01x$ | 0.958 | 35.01 | 16.0% | 16.1% | 0.99 |

Table 2

**Ratios of *m* for multi- to monofilament PA-6 fibers for a number of mechanical properties**

| Mechanical property | $E_1$ | σ | $\varepsilon_b$ | $E_2$ | $\varepsilon_{b\text{-}2}$ |
|---|---|---|---|---|---|
| *m*(multi)/*m*(single) | 0.74 | 0.96 | 3.72 | 3.34 | 2.63 |

As far as the Gaussian analysis is concerned, the results received turned out to be of various degree of success. Actually, only one (see Fig. 3,*d*, $\varepsilon_{b\text{-}2}$ for multifilament) of the four histograms presented in Figs. 2, *c*, *d* and 3, *c*, *d* can be considered as a bell curve that is characteristic of the normal (Gaussian) distribution. Concerning the distribution of the $E_2$ values, a bell curve is observed for the single fibers (see Fig. 2,*c*). However, it has an asymmetric shape. Moreover, for the multifilament fibers (see Fig. 2,*d*), a set of the $E_2$ values demonstrates bimodal distribution. These two observations indicate that the applicability of the Gaussian model for describing the statistical distributions of $E_2$ and $\varepsilon_{b\text{-}2}$ is rather limited, suggesting that the distributions of $E_2$ and $\varepsilon_{b\text{-}2}$ is not always controlled by the sum of many independent and equally weighted factors.

## Conclusion

The marked effect of strengthening of the PA-6 multifilament in the course of tensile testing has been found, indicating that the enhancement of the mechanical properties proceeded more effectively with respect to the PA-6 single fibers. It has been shown that the Weibull's model is more correct for describing the statistical distributions of the mechanical properties of the high-strength PA-6 fibers than the Gaussian one. It has been shown that the data scatter for some of the mechanical properties ($E_2$, $\varepsilon_b$, and $\varepsilon_{b\text{-}2}$), including those estimated, for the first time, by differentiating the stress-strain curves ($E_2$ and $\varepsilon_{b\text{-}2}$), is substantially smaller for the multifilament with respect to that for the single fibers due to the substantially larger (by two orders of magnitude) number of the fractured single fibers per test in the multifilament samples as compared to the single fibers, making the results received for the former more proper statistically. Basing on the results received in this work and earlier [2, 9–11], we guess that it is necessary to use both the Weibull's and Gaussian models for the correct statistical analysis of the mechanical properties of high-strength materials of various natures, both fragile and ductile.

## REFERENCES

1. **Marikhin V.A., Myasnikova L.P.**, Structural basis of high-strength high-modulus polymers, In: *Oriented Polymer Materials*, Ed. S. Fakirov, Chapter 2 (1996) 38–98, Huthig & Wepf Verlag-Zug, Heidelberg.

2. **Boiko Yu.M., Marikhin V.A., Myasnikova L.P., Moskalyuk O.A., Radovanova E.I.**, Weibull statistics of tensile strength distribution of gel-cast ultra-oriented film threads of ultra-high-molecular-weight polyethylene, Journal of Materials Sciences. 52 (3) (2017) 1727–1735.

3. **Callister W.D., Rethwisch D.G.**, Characteristics, Applications, and Processing of Polymers, In: *Materials Science and Engineering*, 10th ed., (2020) Chapter 15, 523–576, Wiley.

4. **Boiko Yu.M., Kovriga V.V.**, Relaxation behavior of polyethylene oriented by various techniques, International Journal of Polymeric Materials. 22 (1-4) (1993) 209–217.

5. **Thomopoulos N.T.**, Statistical Distributions: Applications and Parameter Estimates (2017) 189 p., Springer International Publishing AG.

6. **Zok F.W.**, On weakest link theory and Weibull statistics. Journal of the American Ceramic Society. 100 (4) (2017) 1265–1268.

7. **Tanaka F., Okabe T., Okuda H., Kinloch I.A., Young R.J.**, Factors controlling the strength of carbon fiber in tension, Composites A. 57 (February) (2014) 88–94.

8. **Baikova L.G., Pesina T.I., Kireenko M.F., Tikhonova L.V., Kurkjian C.R.**, Strength of optical silica fibers measured in liquid nitrogen, Technical Physics. 60 (6) (2015) 869–872.

9. **Boiko Yu.M., Marikhin V.A., Moskalyuk O.A., Myasnikova L.P., Tsobkallo E.S.**, Statistical analysis of the tensile strength of oriented polyamide-6 fibers, Technical Physics Letters. 45 (4) (2019) 404–406.

10. **Boiko Yu.M., Marikhin V.A., Moskalyuk O.A., Myasnikova L.P., Tsobkallo E.S.**, Laws of statistical distribution of the mechanical properties of oriented polyamide-6 fibers, Technical Physics Letters. 45 (7) (2019) 707–710.

11. **Boiko Yu.M., Marikhin V.A., Myasnikova L.P., Radovanova E.I.**, Statistical viscoelastic and fracture mechanical properties of gel-cast ultra-oriented high-strength film threads of ultra-high-molecular-weight polyethylene, Colloid and Polymer Sciences. 296 (10) (2018) 1651–1656.

12. **Boiko Yu.M., Kovriga V.V.**, Deformation properties of self-reinforced polyethylene and their generalized description, Mechanics of Composite Materials. 27 (4) (1991) 392–397.

## THE AUTHORS

**BOIKO Yuri M.**
yuri.boiko@mail.ioffe.ru
ORCID: 0000-0003-3031-5137

**MARIKHIN Vyacheslav A.**
v.marikhin@mail.ioffe.ru
ORCID: 0000-0001-7088-5914

**MYASNIKOVA Liubov' P.**
liu2000@mail.ru
ORCID: 0000-0003-0648-5056

*Received 20.10.2022. Approved after reviewing 15.11.2022. Accepted 15.11.2022.*

© Peter the Great St. Petersburg Polytechnic University, 2023

Conference materials
UDC 538.911
DOI: https://doi.org/10.18721/JPM.161.231

# Glycine and triglycine sulphate crystals doped with croconic acid: crystal structure, UV-VIS absorption, and dielectric properties

E.V. Balashova[1]✉, A.A. Levin[1], A.A. Zolotarev[2], B.B. Krichevtsov[1], H. Zhang[3], F. Li[3], H. Ke[3]

[1] Ioffe Institute, St. Petersburg, Russia;

[2] St. Petersburg State University, St. Petersburg, Russia;

[3] Harbin Institute of Technology, Harbin, China

✉ balashova@mail.ioffe.ru

**Abstract**. Single crystals of amino acid glycine (Gly) and triglycine sulphate (TGS) doped with organic croconic acid (CA) were synthesized by evaporation from aqueous solutions. Depending on the concentration of CA in the solution, Gly:CA crystalizes in structure of γ- (sp.gr. $P3_1$ (144)) or α- ($P2_1/n$ (14)) polymorphs of glycine. TGS:CA crystallizes in ferroelectric ($P2_1$ (4)) TGS structure. X-ray phase analysis of single crystals and powders shows that the introducing of CA does not change the symmetry of the crystal lattices, but only slightly changes the volumes of the unit cells that is possible when small CA molecules enter the pores of crystal structures. Analysis of UV-Vis absorption spectra shows that CA doping leads to the appearance in Gly:CA and TGS:CA of new absorption bands placed in transparency region of pure TGS and Gly crystals. As compared to pure TGS the dielectric hysteresis loops of TGS:CA are characterized by increase of coercive field and decrease of switchable polarization.

**Keywords:** polymorphs, amino acid glycine, croconic acid, crystal structure, Powder XRD analysis, UV-Vis absorption spectra, dielectric properties

**Funding:** The reported study was funded by RFBR and NSFC, project 21-52-53015.

**Citation:** Balashova E.V., Levin A.A., Zolotarev A.A., Krichevtsov B.B., Zhang H., Li F., Ke H., Glycine and triglycine sulphate crystals doped with croconic acid: crystal structure, UV-VIS absorption, and dielectric properties, St. Petersburg State Polytechnical University Journal. Physics and Mathematics. 16 (1.2) 2023 204–211. DOI: https://doi.org/10.18721/JPM.161.231

This is an open access article under the CC BY-NC 4.0 license (https://creativecommons.org/licenses/by-nc/4.0/)

Материалы конференции
УДК 538.911
DOI: https://doi.org/10.18721/JPM.161.231

# Кристаллическая структура, поглощение в УФ и видимой области и диэлектрические свойства кристаллов глицина и триглицинсульфата, легированных кроконовой кислотой

Е.В. Балашова[1]✉, А.А. Левин[1], А.А. Золотарев[2], Б.Б. Кричевцов[1], Х. Чжан[3], Ф. Ли[3], Х. Ке[3]

[1] Физико-технический институт им. А.Ф. Иоффе РАН, Санкт-Петербург, Россия;

[2] Санкт-Петербургский государственный университет, Санкт-Петербург, Россия;

[3] Харбинский технологический институт, Харбин, Китай

✉ balashova@mail.ioffe.ru

**Аннотация.** Монокристаллы аминокислоты глицина (Gly) и триглицинсульфата (TGS), допированные органической кроконовой кислотой (CA), были синтезированы методом испарения из водных растворов. Введение CA не изменяет симметрию кристаллических решеток, незначительно меняя объемы элементарных ячеек, и приводит к появлению

© Balashova E.V., Levin A.A., Zolotarev A.A., Krichevtsov B.B., Zhang H., Li F., Ke H., 2023. Published by Peter the Great St. Petersburg Polytechnic University.

в Gly:CA и TGS:CA новых полос поглощения, расположенных в области прозрачности чистых кристаллов TGS и Gly из-за проникновения малых молекул CA.

**Ключевые слова:** полиморфы, аминокислота глицин, кроконовая кислота, кристаллическая структура, рентгенофазовый анализ, спектры поглощения UV-Vis, диэлектрические свойства

**Финансирование:** Исследование выполнено при финансовой поддержке РФФИ и Государственного фонда естественных наук Китая в рамках научного проекта № 21-52-53015.

**Ссылка при цитировании**: Балашова Е.В., Левин А.А., Золотарев А.А., Кричевцов Б.Б., Чжан Х., Ли Ф., Ке Х. Кристаллическая структура, поглощение в УФ и видимой области и диэлектрические свойства кристаллов глицина и триглицинсульфата, легированных кроконовой кислотой. // Научно-технические ведомости СПбГПУ. Физико-математические науки. 2023. Т. 16. № 1.2. С. 204–211. DOI: https://doi.org/10.18721/JPM.161.231

Статья открытого доступа, распространяемая по лицензии CC BY-NC 4.0 (https://creativecommons.org/licenses/by-nc/4.0/)

## Introduction

Organic and semiorganic crystals are currently the subject of intensive research, since they provide the basis for obtaining new multifunctional materials that can be used to create sensors for various fields, information recording systems, energy harvesters, medical applications, and so on. In this connection, ferroelectric and pyroelectric crystals play an important role because they exhibit a combination of different properties such as the electric polarization switching, pyroelectric and piezoelectric effect, efficient linear and nonlinear optical phenomena. Numerous studies have shown that the properties of organic and semiorganic crystals can be controlled by doping them with various ions. Since many of these crystals are grown from solutions by evaporation or slow cooling, doping can be done by adding substances of interest to the solution.

Crystallization of amino acid Glycine (Gly) $NH_2CH_2COOH$ is characterized by polymorphism. The most stable polymorphs α-Gly and γ-Gly crystallize in centrosymmetric ($P2_1/n$ (14)) and non-centrosymmetric ($P3_2$ (145) or $P3_1$ (144)) crystal lattice correspondingly. Non-centrosymmetric γ-Gly exhibit high optical transparency in wide spectral range, high values of nonlinear optical (NLO) efficiency [1–5], and piezoelectric ($d_{33}$ ~ 8 pC/N) [6] and pyroelectric effect ($p$ ~ 13 μC/m$^2$K). Flexible γ-Gly amino acid-based energy harvesting has been developed [7]. The effect of doping on second-harmonic generation (SHG) efficiency of γ-Gly with cesium chloride, zinc sulphate, formic acid was studied in [8–10].

Triglycine sulphate (TGS), $(NH_2CH_2COOH)_3 \cdot H_2SO_4$, is well known semiorganic ferroelectric with above room temperature (RT) Curie temperature $T_c$ ~ 49 °C [11]. Due to large values of pyroelectric coefficient in vicinity of phase transition ($P2_1/m$ (11) → $P2_1$ (4)) $p \approx 550$ μC/m$^2$·K ($T$ = 35 °C) [12], it found numerical applications in the production of pyroelectric detectors, room temperature infrared detectors, transducers and sensors. For the operation of devices based on the use of TGS, it is highly desirable to obtain a single-domain state without application of an external electric field, which is possible in a unipolar state [13–15] due to the presence of impurities. The effect of doping on the properties of TGS was studied in a number of works using metal ions and nanoparticles [16], amino acids [17, 18], organic acids [19, 20], and inorganic acids and salts [21, 22] as impurities.

Croconic acid (CA) $C_5H_2O_5$ molecule about 0.5 nm in size has flat shape and consists of oxocarbonic anion $C_5O_5^{2-}$ connected with two hydrogen ions. Due to their small size, it can be incorporated in crystal structure and modified physical properties of host substance, in particular, due to a fact that CA molecule has high value of dipole momentum $d$ ~ (9–10) Debye. CA crystallize in non-centrosymmetric structure ($Pca2_1$ (29)) and exhibit large value of spontaneous polarization $Ps$ = 30 μC/cm$^2$ at room temperature [23]. As was shown in [24], doping of α- and γ-Gly crystals with CA molecules results in appearance of strong green luminescence.

© Балашова Е.В., Левин А.А., Золотарев А.А., Кричевцов Б.Б., Чжан Х., Ли Ф., Ке Х., 2023. Издатель: Санкт-Петербургский политехнический университет Петра Великого.

The aim of presented study was examination of crystal and electronic band structure of Gly and TGS single crystals doped with CA, and studying dielectric properties of TGS:CA crystals.

## Materials and Methods

CA doped Gly (Gly:CA) and TGS (TGS:CA) single crystals were grown at RT from aqueous solutions of nominally pure Gly or TGS and CA crystals. For growth of CA crystals, Alfa Aesar reagent (CA 98%) was used. Three different mass ratios (98:2), (90:10) and (80:20) of Gly or TGS and CA in solution were used to obtain crystals with different CA concentrations. Doping of Gly and TGS with CA leads to the appearance of a yellow color characteristic of CA crystals and solutions.

Crystal structure of Gly:CA and TGS:CA was studied by single crystal and powder X-ray diffraction (XRD) methods. Single crystal XRD measurements were carried at RT using a Bruker D8 Venture diffractometer, a Bruker Kappa APEX DUO diffractometer (Bruker AXS Karlsruhe, Germany) using monochromatic Mo$K_\alpha$ radiation, and a Rigaku «XtaLAB Synergy» diffractometer using monochromated CuKα radiation. The structure has been solved by the direct methods by means of the *SHELX* program [25] incorporated in the *OLEX2* program package [26]. Empirical absorption correction was applied in *CrysAlisPro* program complex [CrysAlisPro, Agilent Technologies, Version 1.171.36.32] using spherical harmonics, implemented in SCALE3 ABSPACK scaling algorithm and using the Bruker software APEX2 [Bruker-AXS. APEX2, Version 2014.11-0; Bruker-AXS: Madison, WI, USA, 2014].

Powder XRD measurements of the grinded crystals were carried out using a D2 Phaser X-ray powder diffractometer (Bruker AXS, Karlsruhe, Germany). Radiation of an X-ray tube with a Cu anode filtered by a Ni $K_\beta$ filter (Cu-$K_{\alpha 1,2}$ radiation) was used. XRD patterns were recorded using a semiconductor linear X-ray detector LYNXEYE (Bruker AXS). The measurements were carried out in a symmetric scanning mode $\theta$2-$\theta$. Temperature in sample chamber during the measurements was 313(1) K. The angular corrections of the observed Bragg angles to zero shift and displacement are introduced from the additional XRD measurements with internal XRD standard Si640f (NIST, USA). Program *Celsiz* [27], utilizing least-square technique, is used for calculation of the unit cell parameters, the initial ones for Rietveld fitting the XRD patterns using *TOPAS* program [28].

Absorption spectra in the ultraviolet-visible (UV-Vis) range were obtained using a UV-3600i Plus UV-Vis-NIR spectrophotometer (Shimadzu Corp., Kyoto, Japan) at RT in the wavelength range of 200–2000 nm. The test was conducted in reflection mode using an integrating sphere. $BaSO_4$ was used as reference sample.

Measurements of capacity and dielectric losses in TGS:CA(98:2) crystals were performed in the frequency range $120–10^5$ Hz and temperature interval 297–340 K with LCR-meters MIT 9216A (Protek, USA), and E7-20 (MNIPI, Belarus), using the *LabView* software package (Version 2011, NIST, Gaithersburg, MD, USA). Dielectric hysteresis loops were measured in the Sawyer-Tower circuit. A sinusoidal electric field from a G3-123 oscillator and a TREK 2200 (Trek Inc., Denver, CO, USA) amplifier was applied to the crystals. The measurements were carried out at a frequency of $f = 50$ Hz. The signal was taken from a 0.1 μF reference capacitor and recorded with a GDS-71062A digital oscilloscope.

## Results and Discussion

Single crystal XRD analysis shows that pyramid-like γ-Gly:CA(80:20) crystallize in a lattice typical to γ-Gly (sp. gr. $P3_1$ (144)), and plate-like crystals of Gly:CA(90:10) is characterized by a pure α-Gly-like structure (sp.gr. $P2_1/n$ (14)). γ-Gly:CA crystals contain twins with opposite orientation of screw axis $3_1$. The volume ratio of twins is approximately 50:50. Crystal lattice parameters for α-Gly:CA(90:10) and γ-Gly:CA(80:20) according to single-crystal XRD are presented in Table 1. Comparison with literature data shows that CA doping results in small decrease of unite cell volume of pure γ-Gly $V = 235.719(3)$ E$^3$ [29, 30] to $V = 231.30(2)$ E$^3$ in γ-Gly(80:20). In centrosymmetric α-Gly:CA(90:10) the unit cell volume $V = 309.43(5)$ E$^3$ is little bit more than in pure α-Gly $V = 308.5$ E$^3$ [31].

Powder XRD analysis shows that the α- and γ-Gly samples doped with CA molecules contains two isostructural phases (see Table 1 for the results of unit cell parameters calculations by *Celsiz* program). The unit cell parameters of the Phase 1 in the both α- and γ-Gly:CA powders are close

to the values obtained in single-crystal XRD, while the Phase 2 unit cell parameters differ a little bit, apparently, due to a different CA content. The formation of several closely related phases with different impurity concentrations in organic molecular crystals was observed in [32]. Both WHP and SSP analysis revealed the absence of microstrains for γ-Gly:CA Phase 2 and gave the crystallite size of D = 48(5) nm. The parameters of the unit cell of this Phase 2 (Table 1) are close to the parameters of pure γ-Gly [29,30], which indicates a smaller content of CA. Phase 2 in α-Gly:CA is characterized by a larger unit cell compared to α-Gly:CA Phase 1. The WHP and SSP methods demonstrated the presence of microstrains, $\varepsilon_s$ ~ 0.1% in Phase 2 and crystallite size of D ~50 nm. For the Phase 1 of α- and γ-Gly:CA, the SSP technique, which is more sensitive to the presence of microstrains [33], gave the microstrain value $\varepsilon_s$ ~ 0.1% and crystallite size of *D* ~ 75 nm. Probably, the formation of microstrains is due to the size of CA molecules comparable with the pore sizes ~0.5 nm in the α- and γ-Gly structures.

Analysis of single-crystal XRD data shows that TGS:CA samples crystallize in typical for TGS monoclinic structure (sp.gr. $P2_1$ (4)). Crystal lattice parameters (*a*, *b*, *c)*, angles (α, β, γ) and unit cell volume *V* for TGS:CA samples are presented in Table 2.

Table 1

**Crystal lattice parameters (*a, b, c),* angles (α, β, γ), unit cell volume *V* for α-Gly:CA(90:10) and γ-Gly:CA(80:20) obtained by single-crystal and powder XRD**

| | α- Gly:CA(90:10) | | | γ-Gly:CA(80:20) | | |
|---|---|---|---|---|---|---|
| | single crystal | Powder Phase 1 | Phase 2 | single crystal | Powder Phase 1 | Phase2 |
| *a*, Å | 5.1004(5) | 5.1050(16) | 5.1216(20) | 6.9848(3) | 7.0388(6) | 7.0541(14) |
| *b*, Å | 11.9664(9) | 11.9771(40) | 12.0064(64) | -"- | -"- | -"- |
| *c*, Å | 5.44570(5) | 5.4614(17) | 5.4715(22) | 5.4744(2) | 5.4797(9) | 5.4890(18) |
| α, ° | 90 | 90 | 90 | 90 | 90 | 90 |
| β, ° | 111.714(3) | 111.74(2) | 111.70(3) | 90 | 90 | 90 |
| γ, ° | 90 | 90 | 90 | 120 | 120 | 120 |
| *V*, Å$^3$ | 309.43(5) | 310.18(36) | 312.61(36) | 231.30(2) | 235.12(4) | 236.54(9) |

Table 2

**Crystal lattice parameters (*a*, *b*, *c),* angles (α, β, γ), and unit cell volume *V* for TGS, TGS:CA(90:10), and TGS:CA(80:20) obtained by single-crystal and powder XRD**

| | TGS | TGS:CA(90:10) | | TGS:CA(80:20) |
|---|---|---|---|---|
| | powder | single crystal | powder | single crystal |
| *a*, Å | 9.4323(7) | 9.440(9) | 9.4261(9) | 9.402(2) |
| *b*, Å | 12.6584(3) | 12.646(14) | 12.6516(4) | 12.623 (4) |
| *c*, Å | 5.7514(3) | 5.738(6) | 5.7475(4) | 5.7304 (14) |
| α, ° | 90 | 90 | 90 | 90 |
| β, ° | 110.359(7) | 110.19(5) | 110.349(9) | 110.144(13) |
| γ, ° | 90 | 90 | 90 | 90 |
| *V*, Å$^3$ | 643.8(1) | 642.9(1.2) | 642.6(1) | 638.5(3) |

Powder XRD study shows that samples of TGS and TGS:CA(90:10) contain only one crystalline phase corresponding to TGS structure. Analysis of microstructure parameters obtained from the profiles of XRD reflections by means of WHP and SSP methods indicates an absence of microstrains. The sizes of crystallites in both TGS and TGS:CA(90:10) are of ~70 nm. Rietveld analysis reveals a decrease of unit cell volume caused by CA doping from 643.8(1) $E^3$ in TGS to 642.6(1) in TGS(90:10). So, the CA doping of TGS does not changes crystal lattice structure but results only in small decrease of unit cell volume depending on CA concentration. Apparently, this is due to the smaller size of CA molecules ~0.5 nm compared to the pore sizes of the TGS structure up to ~0.6–1.1 nm.

Absorption spectra of α-Gly:CA(90:10), γ-Gly:CA(80:20) and TGS:CA(80:20) are shown in Fig. 1.

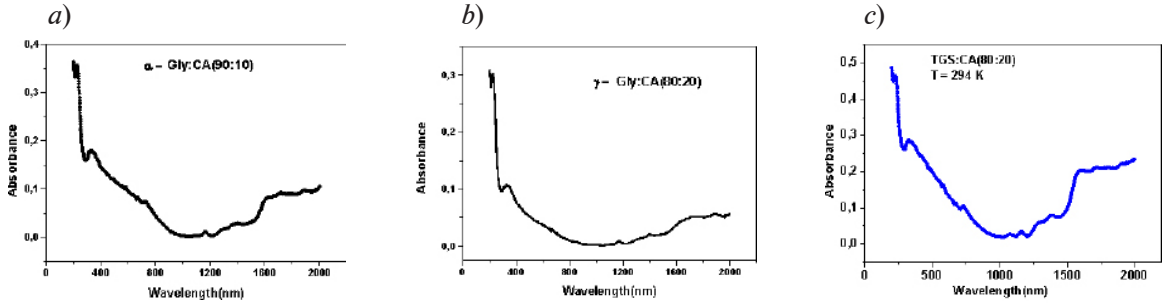


Fig. 1. Absorbance spectra of (*a*) α-Gly:CA(90:10), (*b*) γ-Gly:CA(80:20) and (*c*) TGS:CA(80:20)

Colorless TGS, α- and γ-Gly crystals are transparent in wide spectral range and significant optical absorption is observed only for photons with energies $E_{ph} \geq 5.2$ eV, which is manifests itself in a sharp increase of absorbance below $\lambda = 230–246$ nm. Doping TGS and Gly crystals with CA molecules is accompanied by considerable increase of absorbance for $\lambda < 1000$ nm. Fig. 2 presents Tauc plots for the case of direct allowed optical transitions (dependencies of $(\alpha E_{ph})^2$ on $E_{ph}$, where α is the absorption coefficient and $E_{ph}$ is photon energy).

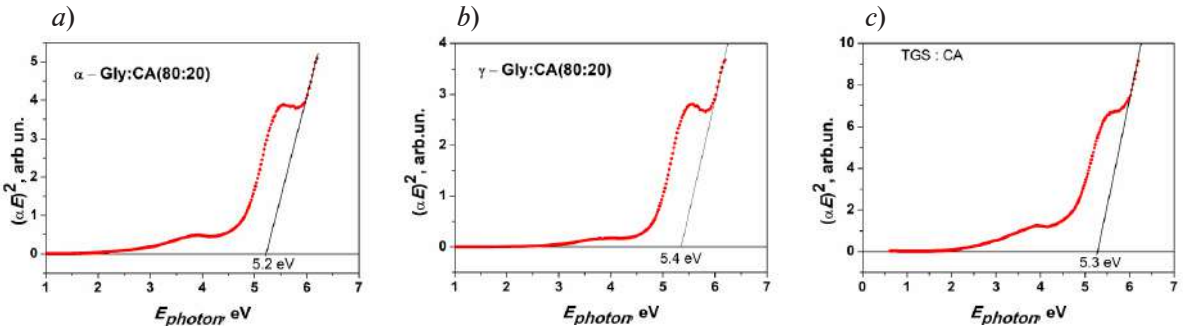


Fig. 2. Tauc plots for case of direct allowed optical transitions
for (*a*) α-Gly:CA(80:20), (*b*) γ-Gly:CA(80:20) and (*c*) TGS:CA(80:20)

Estimates of the band gap $E_g$ in doped crystals $E_g$ ~ 5.2–5.4 eV are very close to those observed in undoped TGS and Gly crystals. Additional absorption bands in doped crystals below $E_g$ can be associated with localized electronic transitions between states caused by the incorporation of CA into the pores of the original crystal.

Study of dielectric properties of TGS:CA(98:2) crystal shows that even small concentration of CA molecules incorporated in TGS results in their remarkable changes. First of all, it manifests in decrease of dielectric anomaly at ferroelectric phase transition. The value of $T_c$ does not change remarkably with doping. The maximum value of the dielectric constant $\varepsilon_b$ at $T = T_c$, decreases from $\varepsilon_b$ ~ 6000 in pure TGS, used for growth of TGS:CA, to $\varepsilon_b$ ~ 500 in TGS:CA(98:2). Comparison of dielectric hysteresis loops shows considerable decrease of switchable polarization from $P_{sw}$ ~ 2.7 μC/cm² to $P_{sw}$ ~ 0.5 μC/cm² and considerable increase of coercive field by a factor of ~ 4. Such behaviour can be related by appearance in TGS crystal structure of doping molecules with high value of dipole momentum $d$ ~ (9–10) D that results in additional pinning of ferroelectric domain walls.

## Conclusion

The present study shows that doping of α-, γ-Gly and TGS crystals with CA molecules is accompanied by very similar changes in the structural and optical properties of the initial crystals. The introduction of CA does not lead to a noticeable change in the crystal structure, but only to very small changes in the volume of the unit cell. This is possible if small CA molecules enter the pores of host crystal structures. Microstrains appear in α- and γ-Gly crystallites where the structure pore sizes are close to the CA molecule sizes. Nevertheless, the interaction of CA molecules with ions of the host crystal significantly changes the electronic structure of materials, leading to the appearance of new absorption bands below the band gap $E_g$ caused most likely by localized optical transitions. Even a small concentration of CA in TGS ferroelectrics cause a strong increase in the coercive field, and a decrease in the switchable polarization and magnitude of dielectric anomaly at ferroelectric phase transition, which indicates that the domain walls are pinned by doping CA molecules with a high dipole momentum.

## Acknowledgments

The authors are grateful to F.B. Svinarev for help in measuring the dielectric properties. The single-crystal XRD experiments for TGS:CA(90:10) and γ-Gly:CA(80:20) were carried out using facilities of the XRD Resource Center of St. Petersburg University. The XRD powder characterizations were performed using equipment and software of the Joint Research Center "Material science and characterization in advanced technology" (Ioffe Institute, St. Petersburg, Russia).

## REFERENCES

1. **Balakrishnan T., Babu R.R., Ramamurthi K.,** Growth, structural, optical and thermal properties of γ-glycine crystal, Spectrochimica Acta Part A: Molecular and Biomolecular Spectroscopy. 69 (2008) 1114-1118.

2. Anis M., Baig M.I., Muley G.G., Rabbani G., Shirsat M. D., Shkir M., Ghramh H.A., Gamma glycine crystal for efficient second harmonic generation of 1064 nm Nd:YAG laser light, Mater. Lett. 233 (2018) 238–241.

3. **Vijayalakshmi V., Dhanasekaran P**., Growth and characterization of γ-glycine single crystals for photonics and optoelectronic device applications, J. Cryst. Growth. 506 (2019) 117–121.

4. **Peter M.E., Ramasamy P.,** Growth of gamma glycine crystal and its characterization, Spectrochim. Acta A. 75 (2010) 1417–1421.

5. **Kumar R.A., Vizhi R.E., Vijayan N., Babu D.R.,** Structural, dielectric and piezoelectric properties of nonlinear optical γ-glycine single crystals, Phys. B. 406 (2011) 2594–2600.

6. **Guerin S., Stapleton A., Chovan D., Mouras R., Gleeson M., McKeown C., Noor M.R., Silien C., Rhen F.M.F., Kholkin A.L., et al.,** Control of piezoelectricity in amino acids by supramolecular packing, Nat. Mater., 17 (2018) 180–186.

7. **Okosun F., Guerin S. Celikin M. Pakrashi V.,** Flexible amino acid-based energy harvesting for structural health monitoring of water pipes, Cell Rep. Phys. Sci. 2 (2021) 100434.

8. **Anis M., Ramteke S.P., Shirsat M.D., Muley G.G., Baig M.I.,** Novel report on g-glycine crystal yielding high second harmonic generation efficiency, Opt. Mater. 72 (2017) 590–595.

9. **Vijayalakshmia V., Dhanasekaran P.,** Growth and characterization study of γ-glycine crystal grown using different mole concentrations of zinc sulphate as structure-directing agents, J. Cryst. Growth. 498 (2018) 372–376.

10. **Justin P., Anitha K.,** Influence of formic acid on optical and electrical properties of glycine crystal, Mater. Res. Express. 4 (2017) 115101.

11. **Matthias B.T., Miller C.E., Remeika J.P.,** Ferroelectricity of glycine sulfate, Phys. Rev. 104 (1956) 849–850.

12. **Whatmore, R.W.,** Pyroelectric devices and materials, Rep. Prog. Phys. 49 (1986) 1335–1386.

13. **Shut V.N., Kashevich I.F**., Formation of the unipolar state in hydrogenous ferroelectric crystals, Ferroelectrics. 350 (2007) 57–64.

14. **Sidorkin A.S., Milovidova S.D., Rogazinskaya O.V., Sidorkin A.A.,** Internal bias field in TGS crystals doped with different impurities, Crystallogr. Reports. 49 (2004) 130–133.

15. **Choudhury R.R., Chitra R., Ramanadham M., Jayavel R**., Prevention of depoling in TGS by alanine substitution: An interpretation based on a neutron-diffraction study, Appl. Phys. A 74 (2002) SUPPL.II 1667–1669.

16. **Belugina N.V., Gainutdinov R.V., Tolstikhina A.L., Ivanova E.S., Kashevich I.F., Shut V.N., Mozzharov S.E.**, Formation of a regular domain structure in TGS–TGS + Cr crystals with a profile impurity distribution, Crystallogr. Reports. 60 (2015) 555–560.

17. **Raghavan C. M., Sankar R., Mohan Kumar R., Jayavel R.,** Effect of amino acid doping on the growth and ferroelectric properties of triglycine sulphate single crystals, Mater. Res. Bull. 43 (2008) 305–311.

18. **Stadnyk V.Y., Romanyuk N.A., Kiryk Y.I.,** Optical properties of TGS crystal with L- valine admixture, Crystallogr. Reports. 55 (2010) 995–999.

19. **Rai C., Narayana Moolya B., Dharmaprakash S.M.,** Iminodiacetic acid doped ferroelectric triglycine sulphate crystal: Crystal growth and characterization, Phys. B Condens. Matter. 406 (2011) 1–7.

20. **Rai C., Sreenivas K., Dharmaprakash S.M.,** Growth of 4-(dimethylamino) benzaldehyde doped triglycine sulphate single crystals and its characterization, Phys. B Condens. Matter 404 (2009) 3886–3889.

21. **Parimaladevi R., Sekar C., Krishnakumar V.,** The effect of nitric acid (HNO3) on growth, spectral, thermal and dielectric properties of triglycine sulphate (TGS) crystal, Spectrochim. Acta A 75 (2010) 617–623.

22. **Deepti P.R., Shanti J.,** Structural and Optical Studies of Potential Ferroelectric Crystal: KDP Doped TGS, J. Sci. Res. 6 (2013) 1–9.

23. **Horiuchi S., Kagawa F., Hatahara K., Kobayashi K., Kumai R., Murakami Y., Tokura Y.,** Above-room-temperature ferroelectricity in a single-component molecular crystal, Nature. 463 (2010) 789–792.

24. **Balashova E.V., Smirnov A.N., Davydov V.Yu., Krichevtsov B.B., Starukhin A.N.,** Raman scattering and luminescence in single crystals of the amino acid glycine C2H5NO2 with an admixture of croconic acid C5H2O5 J. Phys. Conf. Ser. (2021) 012070.

25. **Sheldrick G.M.,** A short history of SHELX, Acta Crystallogr. A 64 (2008) 112–122.

26. **Dolomanov O.V., Bourhis L.J., Gildea R.J., Howard J.A.K., Puschmann H.,** OLEX2: A complete structure solution, refinement and analysis program, J. Appl. Crystallogr. 42 (2009) 339–341.

27. **Maunders C., Etheridge J., Wright N., Whitfield H.J.,** Structure and microstructure of hexagonal Ba3Ti2RuO9 by electron diffraction and microscopy. Acta Crystallogr. B. 61 (2005) 154–159.

28. Brucker AXS, Karlsruhe, TOPAS Version 5, Technical reference. 2014.

29. Zulifiqar Ali Ahamed Sd., Dillip G. R., Raghavaiah P., Mallikarjuna K., Deva Prasad Raju B. Spectroscopic and thermal studies of γ-glycine crystal grown from potassium bromide for optoelectronic applications, Arabian J. Chem. 6 (2013) 429–433.

30. **Dillip G. R., Raghavaiah P., Mallikarjuna K., Madhukar Reddy C., Bhagavannarayana G., Ramesh Kumar V., Deva Prasad Raju B.,** Spectrochim. Acta A. 79 (2011) 1123–1127.

31. Justin P., Anitha K., Basheer Ahamed M., Vijayaraghavan G. V., Enhanced piezoelectric, optical, mechanical, and laser damage threshold studies on creatinine doped glycine single crystals, J. Mater. Sci: Mater. Electron. 30 (2019) 9735–9741.

32. **Balashova E., Levin A.A., Fokin A., Redkov A., Krichevtsov B.,** Structural Properties and Dielectric Hysteresis of Molecular Organic Ferroelectric Grown from Different Solvents, Crystals. 11 (2021) 1278.

33. **Levin A.A.,** Program SizeCr for Calculation of the Microstructure Parameters from X-ray Diffraction Data. Preprint. Available online: https://www.researchgate.net/profile/Alexander-Levin-6/research (accessed on 29 March 2022) DOI:10.13140/RG.2.2.15922.89280.

## THE AUTHORS

**BALASHOVA Elena V.**
balashova@mail.ioffe.ru
ORCID: 0000-0003-4552-6762

**LEVIN Aleksandr A.**
aleksandr.a.levin@mail.ioffe.ru
ORCID: 0000-0001-9258-3204

**ZOLOTAREV Andrey A.**
a.zolotarev@spbu.ru

**KRICHEVTSOV Boris B.**
boris@mail.ioffe.ru
ORCID: 0000-0003-4032-8708

**ZHANG Hongjun**
zhanghj@hit.edu.cn
ORCID: 0000-0003-1719-2179

**LI Fangzhe**
lifangzhe@hit.edu.cn
ORCID: 0000-0001-7270-8057

**KE Hua**
hua_ke@hit.edu.cn
ORCID: 0000-0002-5707-6212

*Received 24.10.2022. Approved after reviewing 21.11.2022. Accepted 21.11.2022.*

© Peter the Great St. Petersburg Polytechnic University, 2023

Conference materials
UDC 535.3, 52-77
DOI: https://doi.org/10.18721/JPM.161.232

# Temperature dependences of terahertz spectra of rutile grown by various methods

K.V. Puzanovskiy[1], V.V. Galutskiy[1], E.V. Stroganova[1]✉

[1] Kuban State University, Krasnodar, Russia

✉ stroganova@phys.kubsu.ru

**Abstract.** The paper presents measurements of the temperature dependence of the refractive index and the absorption coefficient in the THz range for rutile crystals grown by the cold container method. The obtained parameters are compared with the temperature behaviour of lithium niobate crystals, whose matrix allows significant deviations from stoichiometry. The coefficient of the temperature dependence of the refractive index of rutile crystals in the terahertz range is commensurate with that of heavily doped lithium niobate samples and is $3 \cdot 10^{-3}$ $K^{-1}$.

**Keywords:** rutile, THz range, cold container method, stoichiometry._

**Funding:** Financial support from the Kuban science Foundation project № MFI-20.1/129 and the Ministry of Science, RFBR 19-42-230006 r_a and High Education of the Russian Federation (Minobrnauka) (FZEN-2020-0022) is gratefully acknowledged.

**Citation:** Puzanovskiy K.V., Galutskiy V.V., Stroganova E.V., Temperature dependences of terahertz spectra of rutile grown by various methods, St. Petersburg State Polytechnical University Journal. Physics and Mathematics. 16 (1.2) 2023 212–217. DOI: https://doi.org/10.18721/JPM.161.232

This is an open access article under the CC BY-NC 4.0 license (https://creativecommons.org/licenses/by-nc/4.0/)

Материалы конференции
УДК 535.3, 52-77
DOI: https://doi.org/10.18721/JPM.161.232

# Температурные зависимости терагерцовых спектров рутила, выращенного различными методами

К.В. Пузановский[1], В.В. Галуцкий[1], Е.В. Строганова[1]✉

[1] Кубанский государственный университет, Краснодар, Россия

✉ stroganova@phys.kubsu.ru

**Аннотация.** В статье приводятся данные измерений температурной зависимости показателя преломления и коэффициента поглощения в ТГц диапазоне для кристаллов рутила, выращенных методом холодного контейнера. Полученные параметры сравниваются с температурным поведением кристаллов ниобата лития, матрица которого допускает значительные отклонения от стехиометрии. Коэффициент температурной зависимости показателя преломления в терагерцовом диапазоне кристаллов рутила соизмерим с аналогичным значением сильно легированных образцов ниобата лития и составляет $3 \cdot 10^{-3}$ $K^{-1}$.

**Ключевые слова:** рутил, ТГц диапазон, метод холодного контейнера, стехиометрия.

**Финансирование:** Исследования выполнены в рамках проекта КНФ № MFI129/20.1-, РФФИ №230006-42-19 r_a и FZEN-2020-0022.

© Puzanovskiy K.V., Galutskiy V.V., Stroganova E.V., 2023. Published by Peter the Great St. Petersburg Polytechnic University.

**Ссылка при цитировании:** Пузановский К.В., Галуцкий В.В., Строганова Е.В. Температурные зависимости терагерцовых спектров рутила, выращенного различными методами // Научно-технические ведомости СПбГПУ. Физико-математические науки. 2023. Т. 16. № 1.2. С. 212–217. DOI: https://doi.org/10.18721/JPM.161.232

Статья открытого доступа, распространяемая по лицензии CC BY-NC 4.0 (https://creativecommons.org/licenses/by-nc/4.0/)

## Introduction

The development of technologies for producing nonlinear optic materials wield major influence on the advantages of their practical use, the use of devices and components based on them. A promising area of nonlinear optic materials implementation is terahertz devices and technologies. One of the important methods for generating and detecting the THz radiation, along with the frequency up-conversion from the microwave range, is the down conversion using nonlinear optic conversion [1]. Therefore, the question of the effectiveness of such nonlinear optic conversions and the related question of the attenuation of the generated THz radiation in a nonlinear optic material and the temperature dependence of the attenuation is extremely important.

Technologies for the manufacture of gallium nitride, nitride heterostructures, are developing at a tremendous pace, allowing producing more powerful microwave devices that operate at higher temperatures than gallium arsenide [2]. One of the important directions of development of gallium nitride technology is the production and perfection of substrates. In addition to manufacturing substrates directly from gallium nitride, sapphire, which may be an expensive technology, rutile crystals have been also considered. The use of low-cost methods of growing rutile crystals reduces the cost of substrates.

Both of these areas of use of rutile crystals are important in themselves and in their totality. However, the rutile crystal allows significant deviations from stoichiometry, which entails changes in the defective structure and, as a consequence, other physical parameters.

Lithium niobate can also be considered as a nonlinear material with significant deviations from stoichiometry. The measurement of its optical properties, the temperature dependence of optical properties up to the THz range allowed us to conclude about the contribution of the defective structure to the temperature dependence of refractive indices in the THz range, depending on the type and level of its doping [3].

A number of papers are devoted to the research of THz spectra of nonlinear optical materials [4]. The methods used were far-infrared spectroscopy, which allowed us to establish the regularities of the absorption and refraction coefficients in the THz range, but the lens effect did not allow us to achieve unambiguity in the data obtained. Other methods [4] used TDS (time domain sensitive) methods for generating THz radiation by semiconductor antennas after pumping with femtosecond laser pulses. In these works, the temperature dependence of the refractive and absorption coefficients of lithium niobate crystals grown by the traditional Czochralski method is compared with the coactivation of crystals with different amounts of magnesium ions to reduce photorefraction. However, studies of the temperature change of optical properties in the THz range associated with the activation of carriers in the crystal, depending on the method of preparation, have not been conducted. Therefore, in this paper, the THz absorption and refraction spectra of rutile crystals produced by the cold container method are investigated.

## Research method

Titanium dioxide crystals of rutile phase were grown at Kuban State University by the cold container method on a Crystal 400 series installation designed for direct high-frequency melting and crystal growth by directional crystallization with a container load capacity of 12 kg of charge. A metal Mg was used for the initial heating. The resulting crystals were fused druses of dark color. Next, rutile plates were cut out of single crystals, oriented along the direction <001>, and polished to optical quality. The grown rutile crystals allowing significant deviations from stoichiometry were compared with lithium niobate crystals produced by Czochralski method with liquid make-up [5] at Kuban State University.

© Пузановский К. В., Галуцкий В. В., Строганова Е. В., 2023. Издатель: Санкт-Петербургский политехнический университет Петра Великого.

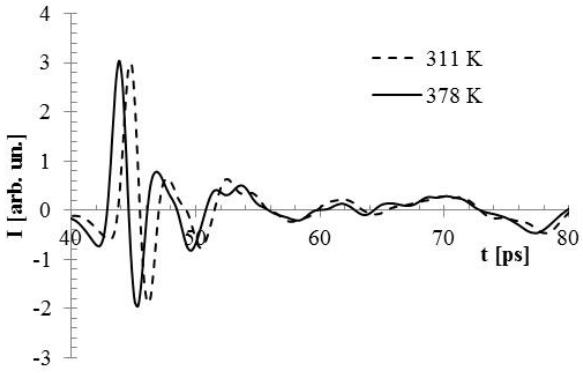


Fig. 1. Laser pulse after passing a rutile crystal at different temperatures

Further, the samples of the grown crystals were placed in a terahertz spectrograph TeraK15Kit with the possibility of changing the temperature of the sample during measurements (Fig. 1).

The spectrograph measurement mode and accumulation time were selected in the range from 10 ms to 100 ms. As a reference signal for measuring the refraction and absorption spectra, a signal recorded through the atmosphere inside the spectrograph was selected. To reduce the influence of water vapor in the atmosphere, the spectrograph space was purged with argon.

Rutile crystal samples obtained by the cold container method and lithium niobate samples obtained by the Czochralski method with liquid make-up were heated using the resistive heating element coupled via the TRM101 controller with a type K thermocouple. The spectra were measured after stabilization of the set sample temperature. Stabilization of the sample temperature was carried out using the built-in PID controller in TRM101 within 1K.

The obtained temperature dependences of the femtosecond laser pulse change after passing the crystal samples are shown in Fig. 1. The figures show that with an increase in temperature, the shape of the pulse is tightened and its amplitude decreases. Further processing of the pulse shape was carried out in the program part of the spectrograph.

## Results and Discussion

A typical view of the obtained dependences of the refractive index on frequency and temperature in the THz range is shown in Fig. 2. It can be seen that as the temperature of the crystals under study increases, the refractive index in the THz range increases, and this applies to the entire range of crystals under study in the temperature range of 290–390 K. However, the rate of increase in the refractive index values with increasing temperature turns out to be different compared to lithium niobate crystals, which allows significant deviations from stoichiometry (Figs. 2, 3). The constructed linear trends over the temperature range at arbitrarily selected frequencies, for example, 0.8 THz, 0.9 THz, 1 THz, have different slope coefficients depending on the following:

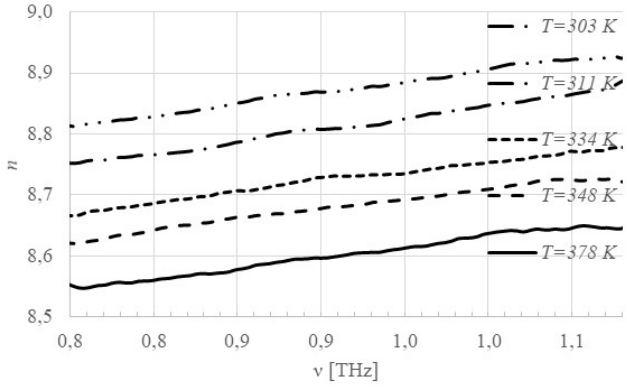


Fig. 2. Spectral dependence of the rutile index grown
by the cold container method in the THz range at different temperatures

the type of crystal matrix (rutile or lithium niobate), the type of crystallographic orientation for lithium niobate (X-slice or Z-slice), the type of impurity (more precisely, its crystallographic radius and the degree of distortion of the crystal lattice of lithium niobate with ions $Yb^{3+}$, $Er^{3+}$) [6].

Fig. 3 shows the temperature dependences of the refractive index for rutile plates. The birefringence for lithium niobate in the THz range [6] is 1.4, 1.5, which is 21–23% compared to the value of the refractive index for an ordinary wave in this range of 6.44. This value of birefringence in the THz range is almost five times greater in percentage terms of birefringence in the visible range.

Another interesting feature of the refractive indices of a rutile single crystal grown by the cold container method presented in Fig. 3 is a higher sensitivity to temperature changes of $3 \cdot 10^{-3}$ $K^{-1}$ than for lithium niobate X-section in the THz range, where the temperature coefficient is $0.7 \cdot 10^{-3}$ $K^{-1}$. In addition, the temperature dependences of the refractive index of rutile grown by the cold container method shown in Fig. 3 have the same slope at frequencies of 0.8, 0.9, 1 THz, which indicates a monotonic temperature spectral dependence of crystals. Compared with the measured coefficients of the temperature dependence of the refractive spectra of lithium niobate crystals ($3.5 \cdot 10^{-3}$ $K^{-1}$) activated by $Yb^{3+}$ and $Er^{3+}$ ions, the ionic radius of which exceeds the radius of the main components of the crystal lattice, the temperature dependence of rutile crystals has a comparable temperature dependence. This dependence may be due to strong stresses in the crystal lattice of rutile, taking into account the inherent deviation of the composition from stoichiometry and the formation of various kinds of defects.

The obtained temperature dependences of refractive indices in the THz range for the studied rutile and lithium niobate crystals grown by the cold container and Czochralski methods with

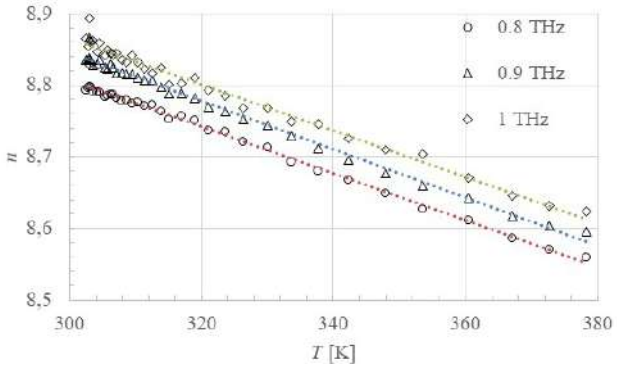


Fig. 3. Temperature dependence of the refractive index of rutile in the THz range grown by the cold container method

liquid make-up are summarized in Table 1. Attention is drawn to the values obtained from the temperature dependence of the refractive index for heavily doped lithium niobate, which are comparable with those for grown rutile.

A similar analysis of the temperature dependence was carried out for the absorption coefficient of the studied samples in the THz range. Fig. 4 shows the temperature dependence of the absorption index in the THz range for the grown rutile crystal.

Table 1

**Refractive index values at $T = 300$ K**

| Crystal | $n$ | ν, THz | $\Delta n/\Delta T$, $\cdot 10^{-3}$ $K^{-1}$ |
|---|---|---|---|
| $LiNbO_3$ | 4.8 | 0.9 | 0.7 |
| Yb,Er:$LiNbO_3$ | 4.4 | 0.7 | 3.5 |
| $TiO_2$ (rutile) | 8.8 | 0.9 | 3.0 |

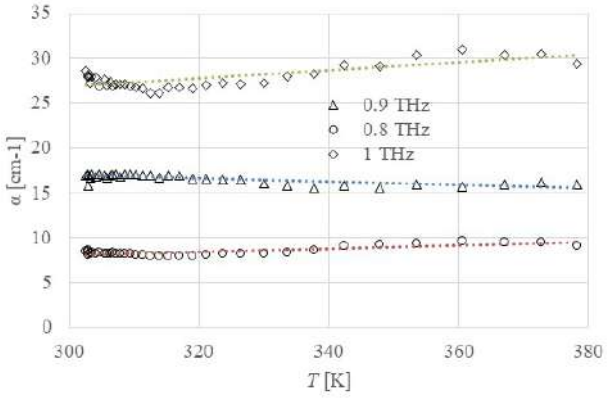


Fig. 4. Temperature dependence of the rutile absorption index in the THz range grown by the cold container method

For grown rutile crystals, there are practically no temperature changes in the absorption spectra in the THz range, the temperature has the strongest effect on the values of the absorption coefficient at a frequency of 1 THz compared to the signal recorded at a frequency of 0.8 THz. A similar dependence of the absorption coefficient is observed for lithium niobate crystals grown by the Czochralski method with liquid make-up. The values of the absorption coefficient in the range of 0.8–1 THz are significant and amount to 7–28 $cm^{-1}$ (Fig. 5).

The measurements of the refractive index spectra made it possible to construct and estimate the temperature conditions for matching interacting waves when working with nonlinear rutile and lithium niobate crystals that allow significant deviations from stoichiometry in the THz range. When pumped by powerful laser sources in the materials used for frequency conversion, the samples are heated. In the case of optical fibers with birefringence [7] to obtain a radiation spectrum in the THz range when interacting waves are matched, temperature relaxation along the direction of propagation of powerful pumping radiation occurs due to the large ratio of the surface area of the waveguide to its volume. The realized frequency shift in this case is 3–4 THz [7]. In the case of crystals, when using high-power pumping radiation to obtain a significant gain in the THz range, it is also necessary to take into account the effect of misalignment due to the heating of the crystal. For the rutile crystal under study, the temperature dependence of the refractive index is $3 \cdot 10^{-3}$ $K^{-1}$ (greater than, for example, for lithium niobate), which reduces the temperature stability of the radiation received. On the other hand, a large value of the temperature dependence of the refractive index will allow four-wave processes to be carried out for a wider range of THz radiation with temperature adjustment for one pump wavelength. It follows from the results obtained that the maximum observed temperature dependence of the refractive index of $3.5 \cdot 10^{-3}$ $K^{-1}$ is comparable to the value of temperature stability for phase matching condition in the IR range for lithium niobate and $3 \cdot 10^{-3}$ $K^{-1}$ for rutile crystals grown by the cold container method.

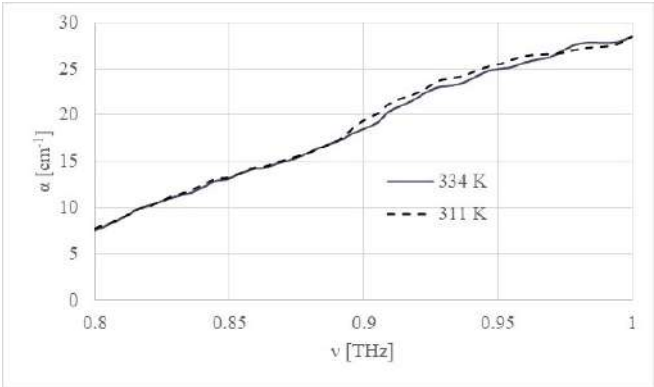


Fig. 5. Spectral dependence of the absorption coefficient of rutile grown by the cold container method in the THz range at different temperatures

## Conclusion

Thus, the use of rutile grown by the technological method of a cold container as a substrate and a nonlinear optical medium for the conversion of radiation in the THz range is characterized by a temperature sensitivity coefficient comparable to the temperature sensitivity coefficient of lithium niobate with a high defect population. The high defect population in lithium niobate is due to the activation of the crystal lattice by large erbium and ytterbium ions. In rutile crystals grown by the cold container method, a strong temperature dependence may be due to significant deviations from stoichiometry during crystal growth. However, the measured values of the absorption coefficient of rutile single crystals (7–28 $cm^{-1}$ in the range of 0.8–1.0 THz) is comparable with similar values for lithium niobate, which allows the use of THz radiation generation mode only in the surface layer.

## Acknowledgments

Financial support from the Kuban science Foundation project MFI-20.1/129 and the Ministry of Science, RFBR 19-42-230006 r_a and High Education of the Russian Federation (Minobrnauka) (FZEN-2020-0022) is gratefully acknowledged.

## REFERENCES

1. **Ravi K., Huang W.R., Carbajo S., Nanni E.A., Schimpf D.N., Ippen E.P., Kärtner F.X.,** Theory of terahertz generation by optical rectification using tilted-pulse-fronts, Optics Express. 23(4) (2015) 5253–5276.

2. **Alfaraj N., Li K.-H., Kang C.H., Braic L., Zoita N.C., Kiss A.E., Ng T.K., Ooi B. S.,** Silicon-integrated monocrystalline oxide–nitride heterostructures for deep-ultraviolet optoelectronics, Optical Materials Express. 11(12) (2021) 4130–4144.

3. **Sidorov N.V., Volk T.R., Mavrin B.N., Kalinnikov V.T.**, Lithium Niobate: Defects, Photorefraction, the Vibrational Spectrum, the Polaritons, Nauka, Moscow, 2003.

4. **Unferdorben M., Szaller Z., Hajdara I., Hebling J., Pőlfalvi L.,** Measurement of Refractive Index and Absorption Coefficient of Congruent and Stoichiometric Lithium Niobate in the Terahertz Range, Journal of Infrared, Millimeter, and Terahertz Waves. 36 (2015) 1203–1209.

5. **Galutskiy V.V., Vatlina M.I., Stroganova E.V.,** Growth of single crystal with a gradient of concentration of impurities by the Czochralski method using additional liquid charging, Journal of Crystal Growth. 311 (4) (2009) 1190–1194.

6. **Galutskiy V.V., Ivashko S.S.,** Temperature dispersions of refractive indices and absorption coefficients of $KNbO_3$ and $LiNbO_3$ crystals in the THz frequency range, Journal of Optical Technology. 87(1) (2020) 50–55.

7. **Agrawal G.**, Nonlinear Fiber Optics, 6th Edition (Academic Press), 2019.

## THE AUTHORS

**PUZANOVSKIY Kirill V.**
puzanovsky.kv@yandex.ru
ORCID: 0000-0003-0840-8089

**STROGANOVA Elena V.**
stroganova@kubsu.ru
ORCID: 0000-0002-3625-3515

**GALUTSKIY Valeriy V.**
galutskiy17v@mail.ru
ORCID: 0000-0002-8837-1011

*Received 26.10.2022. Approved after reviewing 08.11.2022. Accepted 08.11.2022.*

© Peter the Great St. Petersburg Polytechnic University, 2023

Conference materials
UDC 621.38
DOI: https://doi.org/10.18721/JPM.161.233

# Fabrication of nanoscale structures by FIB-induced deposition of materials and study of their electrical properties

A.V. Kotosonova✉, A.S. Kolomiytsev, O.I. Soboleva

Southern Federal University, Taganrog, Russia

✉ alena.kotosonova@gmail.com

**Abstract.** Methods of local formation of nanoscale structures based on the application of focused ion beam open up new possibilities in terms of providing the necessary geometric parameters and ensuring the reproducibility of micro- and nanostructures, which contributes to the development of devices with previously unattainable characteristics. This paper presents the technological modes of formation of nanostructures with a height of 1 μm and diameters from 100 to 500 nm by the FIB method. The structures were formed by ion-induced deposition of carbon and tungsten, as well as electron-induced deposition of tungsten. A method for measuring the electrical parameters of high-aspect ratio structures based on an atomic force microscope (AFM) was proposed. The current value of 25 nA was obtained at 50 V. Threshold voltages for various nanostructures ranged from 7 to 32 V. The stability of structures to the electric field at voltages up to 50 V was investigated. _

**Keywords:** nanotechnology, focused ion beam, beam-induced deposition, nanopatterning

**Funding:** The study was carried out with the financial support of the Russian Science Foundation Grant 22-29-01239 in Southern Federal University.

**Citation:** Kotosonova A.V., Kolomiytsev A.S., Soboleva O.I., Fabrication of nanoscale structures by FIB-induced deposition of materials and study of their electrical properties, St. Petersburg State Polytechnical University Journal. Physics and Mathematics. 16 (1.2) 2023 218–223. DOI: https://doi.org/10.18721/JPM.161.233

This is an open access article under the CC BY-NC 4.0 license (https://creativecommons.org/licenses/by-nc/4.0/)

Материалы конференции
УДК 621.38
DOI: https://doi.org/10.18721/JPM.161.233

# Изготовление наноразмерных структур методом ионно-стимулированного осаждения материалов и изучение их электрических свойств

А.В. Котосонова✉, А.С. Коломийцев, О.И. Соболева

Южный федеральный университет, Таганрог, Россия

✉ alena.kotosonova@gmail.com

**Аннотация.** Методы локального формирования наноразмерных структур, основанные на применении фокусированного ионного пучка (ФИП), открывают новые возможности с точки зрения обеспечения необходимых геометрических параметров и обеспечения воспроизводимости микро- и наноструктур, что способствует разработке устройств с недостижимыми ранее характеристиками. В данной работе представлены технологические режимы формирования наноструктур путем ионно-стимулированного осаждения углерода и вольфрама, а также электронно-стимулированного осаждения вольфрама. Предложен метод измерения электрических параметров структур с высоким соотношением сторон, основанный на атомно-силовой микроскопии (АСМ). При приложении смещения 50 В достигнуто значение тока 25 нА. Для различных наноструктур пороговые значения напряжения варьировались от 7 до 32 В. Исследована устойчивость структур к воздействию электрического поля при напряжениях до 50 В.

© Kotosonova A.V., Kolomiytsev A.S., Soboleva O.I., 2023. Published by Peter the Great St. Petersburg Polytechnic University.

**Ключевые слова:** нанотехнологии, фокусированный ионный пучок, ионно-стимулированное осаждение, нанопрофилирование.

**Финансирование:** Исследование выполнено за счет гранта Российского научного фонда № 22-29-01239 в Южном федеральном университете

**Ссылка при цитировании:** Котосонова А.В., Коломийцев А.С., Соболева О.И. Изготовление наноразмерных структур методом ионно-стимулированного осаждения материалов и изучение их электрических свойств // Научно-технические ведомости СПбГПУ. Физико-математические науки. 2023. Т. 1.2 № .16. С. 218–223. DOI: https://doi.org/10.18721/JPM.161.233

Статья открытого доступа, распространяемая по лицензии CC BY-NC 4.0 (https://creativecommons.org/licenses/by-nc/4.0/)

## Introduction

The development of elements of nanoelectronics requires new nanostructuring methods that ensure the achievement of the specified geometric parameters and electrical characteristics of the created devices. One of the promising methods for creating nanoscale structures on the surface of solids is the technology of local processing of materials with a focused ion beam (FIB). The FIB method allows one to perform operations of local milling and local ion-induced deposition of materials based on various gases. Despite the insufficiently high productivity of the process, the FIB method is effectively used to solve specialized problems in the creation of electronics and micromechanics elements, e.g. for the formation of the tips of atomic force microscopy (AFM) probes [1] and scanning near-field microscopy probes [2], for the formation of micromechanics structures and nanoscale conductors [3]. In a number of studies, the FIB method was used for the manufacturing of field emission cathodes with nanoscale interelectrode gaps [4–6]. An important advantage of the FIB method is its compatibility with the technological processes of traditional microelectronics, which makes it possible to significantly expand the scope of its application. When forming structures for micro- and nanoelectronics, it is often critically important not only to ensure the specified sizes of structures, but also provide their electrical parameters that determine the characteristics of the created devices.

## Experimental details

In this paper, experimental studies were carried out on the formation of nanoscale structures with specified parameters for elements of nanoelectronics by the FIB method.

The objective of this study was to evaluate the effect of the technological parameters of the ion beam on the parameters of structures formed by ion-induced deposition of carbon (i-C) and tungsten (i-W). To increase the objectivity when comparing the characteristics of nanostructures made by the FIB method from various materials, it is necessary to minimize the influence of dimensional factors. In accordance with this, one of the tasks of this experiment was to form structures of identical height and width. The process parameters were selected in order to form 5 structures with a height of 1 μm and diameters of 100, 200, 300, 400 and 500 nm. With ion-induced deposition from the gas phase, the composition of the deposited material will include not only the initial components of the gas, but also gallium atoms from the ion beam [7]. To assess the effect of implanted gallium ions on the electrical properties and durability of the cathode, an additional electron-induced (e-W) deposition of tungsten was carried out, thus excluding the presence of gallium atoms in the deposited material.

The test structures were formed using an electron microscope with the Nova NanoLab 600 FIB system equipped with a gallium ion source. To implement ion-induced deposition of materials, carrier gases of the deposited material, $WCO_6$ and $C_6H_{14}$, were locally supplied into the microscope chamber. The formed structures were studied using Ntegra AFM. After the measurements, the structures were examined by scanning electron microscopy (SEM).

© Котосонова А.В., Коломийцев А.С., Соболева О.И., 2023. Издатель: Санкт-Петербургский политехнический университет Петра Великого.

**Ion-induced deposition of tungsten and carbon.** During the preliminary stage of experimental studies, characteristic irregularities were found on the surface of the i-W structures. Similar irregularities, but much less pronounced, were also present on the i-C structures. It was found that reducing the exposure time at the point and increasing the value of the "Refresh time" parameter makes it possible to reduce this effect. However, just selecting the optimal exposure time at the point and 'Refresh time' is not enough to obtain a smooth surface of the i-W structure. The appearance of this effect may also be conditioned by other factors, for example, the defocusing of the beam at different heights, the influence of residual vacuum level or the scanning trajectory of the beam during the deposition process.

The control i-W and i-C structures (Fig. 1) were formed by ion-induced deposition of tungsten and carbon at the beam energy of 30 keV and a beam current of 10 pA on a $Ti/SiO_2/Si$ structure with a titanium film thickness of 50 nm. The formation of structures with a minimum diameter was carried out by deposition at one point with a single exposure time of 5 μs, the number of passes and 'Refresh time' were 1.4×106 and 15 μs for the i-C structure and 1.8×106 and 150 μs for the i-W. The final diameters were 156 nm for the i-C and 115 nm for the i-W structure.

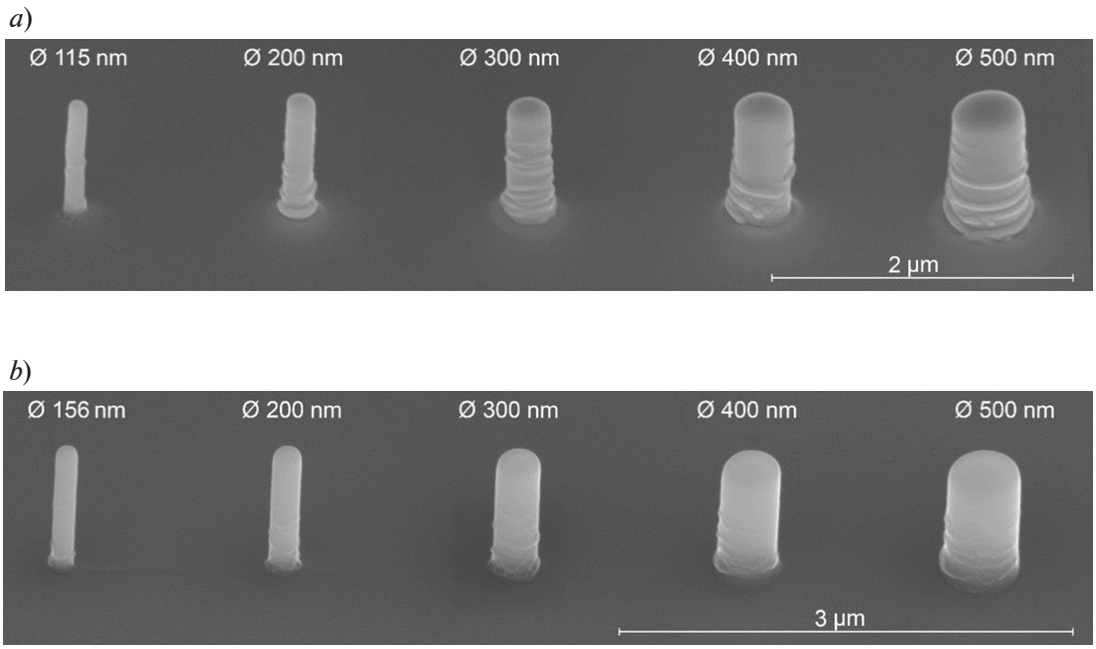


Fig. 1. SEM images of high-aspect ratio nanoscale (*a*) i-W and (*b*) i-C structures formed by the FIB-induced deposition. The figures indicate the value of the structures diameter

For diameter values in the range from 200 to 500 nm, the exposure time at the point was 1 μs. When tungsten was deposited by an ion beam, the 'Refresh time' value for each structure increased proportionally with increasing diameter (600 μs for 200 nm, 900 μs for 300, etc.). The number of points that the beam passes through in one pass depends on the diameter value, which means that the total scanning time increases with increasing diameter, hence it takes more time to replenish the number of gas molecules in the area of interaction with the ion beam. During the carbon deposition, the 'Refresh time' for each structure was equal to 15 μs; this parameter value was optimal for a structure with a diameter of 500 nm, and it was impractical to reduce it for structures with a smaller diameter due to the fact that the total deposition time would change by only a few seconds.

**Electron-induced deposition of tungsten.** The electron-induced deposition of structures was complicated by the presence of electron beam drift, which is manifested in the appearance of a deviation of the structure from the normal with an increase in its height. To eliminate this effect, it is necessary to reduce the total deposition time, which was done by increasing the beam current. e-W structures with a diameter of 200 to 500 nm were formed at an electron beam current of 2.1 nA, the accelerating voltage was 10 keV, the beam exposure time at a point was 1 μs. The

electron beam has a higher resolution compared to the ion beam (due to the nature of electrons, whose diameter is orders of magnitude smaller than those of ions), however, the beam drift present during the experiments did not allow to achieve the best values of the diameter of the structures, and at a current of 2.1 nA the minimum obtained diameter was 200 nm. Based on this, in order to form a structure with a diameter of 100 nm, the current was reduced to 0.54 nA. The resulting array of e-W structures is shown in Fig. 2.

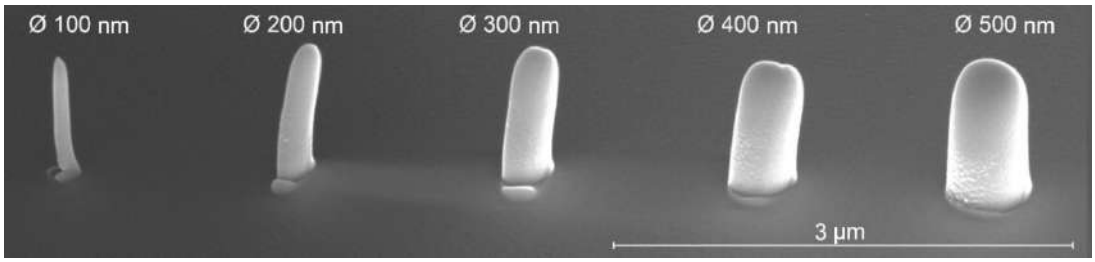


Fig. 2. SEM image of high-aspect ratio nanoscale e-W structures formed by electron-induced deposition. The figures indicate the value of the structures diameter

**Method of measuring electrical parameters.** According to the research methodology, first, a 10 × 10 μm area was scanned in a semi-contact mode, in which the structures under study were located. The probe was brought into contact with the top of the structure, after which it was withdrawn to a distance of 30 nm. The voltage between the probe and the substrate was manually changed from 0 to 50 V with a small step. At the same time, two characteristics of the process were measured – the dependence of voltage on time and the dependence of current on time. If there was no characteristic increase in current with increasing voltage, the distance was reduced to 10 nm. After the measurements, the obtained dependences were digitized and numerically reconstructed into a CVC.

## Results and Discussion

Fig. 3,*a* shows an example of the obtained CVC for the i-W structure with a diameter of 400 nm, measured at a distance probe-surface of 10 nm. The threshold voltage (the voltage at which the current began to exceed the noise level of tens of pA) was 17 V. Fig. 3,*b* shows the time dependence of the current at a constant voltage of 50 V for the same structure.

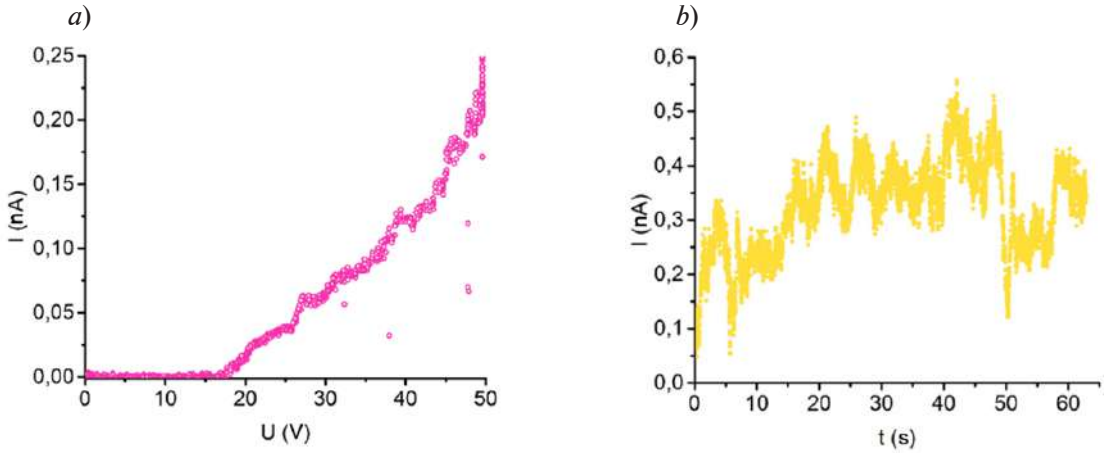


Fig. 3. Results of measuring the electrical parameters of the 400 nm diameter i-W structure at a distance of 10 nm: CVC (*a*) and time dependence (*b*) of the current

The analysis of the obtained dependences showed that, for an i-W structure with a diameter of 500 nm, with a decrease in the distance to the probe from 30 to 10 nm, the threshold voltage decreased from 12 to 8 V; the average value of the current at 50 V increased from 2.5 to 5.1 nA. A comparison of the characteristics of i-W and i-C structures with a diameter of 300 nm showed that the current value on carbon structures was an order of magnitude higher than on tungsten structures, with voltage thresholds equal to 20 and 32 V, respectively. When comparing the parameters of i-W and e-W structures with a diameter of 500 nm, it was found that higher current values were achieved on the e-W structure, while the threshold voltage differed slightly (7 V for e-W and 8 V for i-W). Fluctuation of current values during measurements was observed for all structures.

After the measurements the studied structures were re-examined by SEM. The obtained images are shown in Fig. 4. Image analysis shows that the surfaces of i-C structures with diameters of 100 and 200 nm changed significantly during measurements. The height of the structure with a diameter of 100 nm decreased from 1 μm to 690 nm (Fig. 4,*a*); that of the structure with a diameter of 200 nm decreased from 1 μm to 950 nm (Fig. 4,*b*). Small protrusions appeared on the tops of these and the other structures. The largest number of protrusions is observed on tungsten structures deposited by an ion beam (Fig. 4, *d*, *e*, *f*); for structures formed by electron-induced deposition, the number of protrusions is minimal (Fig. 4, *g*, *h*).

The protrusions that appeared during the measurements could provoke the instability of the current observed during the measurements: some protrusions appeared and others disappeared, which made different contributions to the current.

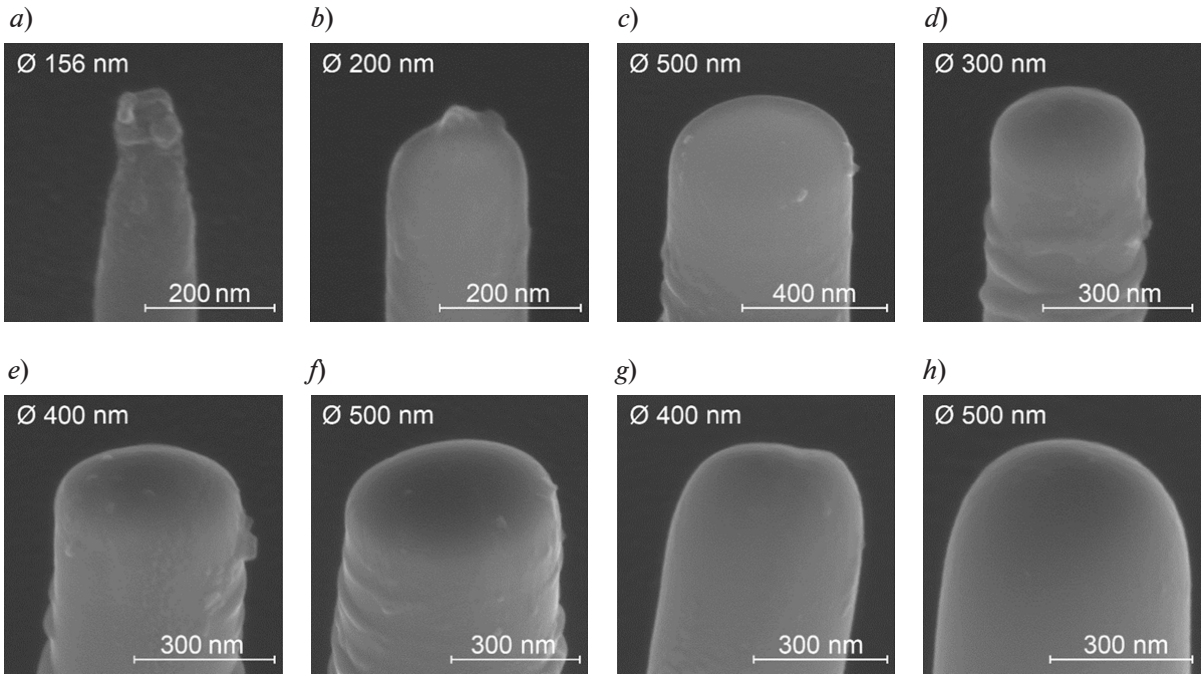


Fig. 4. SEM images of surfaces of (*a*, *b*, *c*) i-C, (*d*, *e*, *f*) i-W and (*g*, *h*) e-W structures after measurements of electrical parameters. The diameters of the structures are given in the panels

## Conclusion

Thus, high-aspect ratio nanoscale structures were formed using electron- and ion-induced deposition of tungsten and carbon. The modes of the process were determined, allowing the formation of structures with a diameter of 100–500 nm and a height of up to 1 μm, which can be used in the formation of various elements of nanoelectronics. The study and comparison of electrical parameters and stability under electric field for structures of various sizes and consisting of various materials was carried out. A strong instability of the current observed during probe measurements was detected, which could be caused by the appearance and disappearance of small protrusions on the surface of structures with a bias voltage of up to 50 V.

We proposed a new method for measuring the electrical parameters using an AFM probe, which can be used to study the electrical properties of high−aspect ratio structures, in particular, field emission properties. When measuring the CVC of the formed structures in the range up to 50 V, the values of the measured currents reached 25 nA, the threshold voltages for various structures ranged from 7 to 32 V.

In the course of the research, it was possible to optimize the shape of nanoscale carbon and tungsten structures by selecting the values of the beam exposure time at the point and the 'Refresh time' parameter, which made it possible to increase the smoothness and uniformity of the structures.

It was shown that the application of the method of local ion-induced deposition of carbon and tungsten from the gas phase allowed to form structures with specified geometric and electrical parameters with high reproducibility for solving problems of creating new components of nanoelectronics and nanosystem technology.

## REFERENCES

1. **Panchenko I.V., Shandyba N.A., Ballouk A., et al.**, Investigation of the influence of the geometric parameters of AFM cantilevers on the resonant frequency of their oscillations, J. Phys. Conf. Ser. IOP Publishing. 1695 (2020) 12182.

2. **Kolomiytsev A.S., Panchenko I.V., Shandyba N. A., et al.**, Fabrication of probes for scanning near-field optical microscopy using focused ion beam, J. Phys. Conf. Ser.: Materials Science and Engineering. IOP Publishing. 443 (1) (2018) 012015.

3. **Aloysius R.P., Husale S., Kumar A., et al.**, Superconducting properties of tungsten nanowires fabricated using focused ion beam technique, Nanotechnology. IOP Publishing. 30 (2019) 405001.

4. **Liu M., Li T., Wang Y.**, Low voltage field emission of Cu nanowire with nanogap in air, IEEE 12th International Conference on Nano/Micro Engineered and Molecular Systems. Institute of Electrical and Electronics Engineers Inc. (2017) 333–336.

5. **Xu J., Wang Q., Tao Z., et al.**, High-Quality and Stable Electron Emission Device with Sub-30-nm Aligned Nanogap Arrays, IEEE Trans. Electron Devices. Institute of Electrical and Electronics Engineers Inc. 64 (5) (2017) 2364-2368.

6. **Liu M., Fu W., Li T., et al.**, Excellent field emission properties of vanadium oxide nanoemitters in air, IEEE 17th International Conference on Nanotechnology. Institute of Electrical and Electronics Engineers Inc. (2017) 351–354.

7. **Gnaser H., Kallmayer C., Oechsner H.**, Focused-ion-beam implantation of Ga in elemental and compound semiconductors, J. Vac. Sci. Technol. B Microelectron. Nanom. Struct. American Inst of Physics. 13 (1) (1995) 19–26.

## THE AUTHORS

**KOTOSONOVA Alena V.**
alena.kotosonova@gmail.com
ORCID: 0000-0002-4382-8698

**SOBOLEVA Olga I.**
osotova@sfedu.ru
ORCID: 0000-0002-0487-7542

**KOLOMIYTSEV Alexey S.**
askolomiytsev@sfedu.ru
ORCID: 0000-0001-7483-0240

*Received 26.10.2022. Approved after reviewing 10.11.2022. Accepted 11.11.2022.*

© Peter the Great St. Petersburg Polytechnic University, 2023

Conference materials
UDC 548.527
DOI: https://doi.org/10.18721/JPM.161.234

# Synthesis of semi-polar GaN(11-22) on a nano-patterned Si(113) substrate

V.N. Bessolov, E.V. Konenkova✉, S.N. Rodin

Ioffe institute, St. Petersburg, Russia

✉ lena@triat.ioffe.ru

**Abstract.** A method for synthesising hexagonal GaN on a Si(113) substrate with a nanostructure of about 75 nm on its surface (NP-Si(113) substrate) is proposed. It has been established that the method of the metal-organic chemical vapor deposition on such a substrate makes it possible to form a semi-polar layer of GaN(11-22) with half-widths of the X-ray diffraction curve $\omega_0$ ~ 30 arcmin.

It is shown that during epitaxy from organometallic compounds in hydrogen atmosphere at the initial stages of growth the layer orientation is given by the direction of Si(111) plane of nanocanals in NP-Si(113) and the growth rate of GaN layer in (11-22) and (0001) planes direction is comparable._

**Keywords:** semi-polar GaN(11-22), nano-patterned Si(113) substrate, epitaxy from the metal-organic chemical vapor deposition

**Citation:** Bessolov V.N., Konenkova E.V., Rodin S.N., Synthesis of semi-polar GaN(11-22) on a nano-patterned Si(113) substrate, St. Petersburg State Polytechnical University Journal. Physics and Mathematics. 16 (1.2) 2023 224–228. DOI: https://doi.org/10.18721/JPM.161.234

This is an open access article under the CC BY-NC 4.0 license (https://creativecommons.org/licenses/by-nc/4.0/)

Материалы конференции
УДК 548.527
DOI: https://doi.org/10.18721/JPM.161.234

# Синтез полуполярного GaN(11-22) на наноструктурированной подложке Si(113)

В. Н. Бессолов, Е. В. Коненкова✉, С. Н. Родин

Физико-технический институт им. А.Ф. Иоффе РАН, Санкт-Петербург, Россия

✉ lena@triat.ioffe.ru

**Аннотация.** Предложен метод синтеза гексагонального GaN на подложке Si(113), на поверхности которой сформирована наноструктура с размером элементов около 75 нм (подложка NP-Si(113)). Установлено, что метод газофазной эпитаксии из металлоорганических соединений на такой подложке позволяет сформировать полуполярный слой GaN(11-22) при минимальной полуширине рентгенодифракционной кривой качания $\omega_0$ ~ 30 arcmin.

Показано, что при эпитаксии из металлоорганических соединений в атмосфере водорода на начальных стадиях роста ориентация слоя задается направлением плоскости Si(111) наноканавок в NP-Si(113), а скорость роста слоя GaN в направлении плоскостей (22-11) и (0001) соизмерима.

**Ключевые слова:** полуполярный GaN(11-22), наноструктурированная подложка Si(113), газофазная эпитаксия из металлоорганических соединений

© Bessolov V.N., Konenkova E.V., Rodin S.N., 2023. Published by Peter the Great St. Petersburg Polytechnic University.

**Ссылка при цитировании:** Бессолов В.Н., Коненкова Е.В., Родин С.Н. Синтез полуполярного GaN(11-22) на наноструктурированной подложке Si(113) // Научно-технические ведомости СПбГПУ. Физико-математические науки. 2023. Т. 16. № 1.2. С. 224–228. DOI: https://doi.org/10.18721/JPM.161.234

Статья открытого доступа, распространяемая по лицензии CC BY-NC 4.0 (https://creativecommons.org/licenses/by-nc/4.0/)

## Introduction

Optoelectronic devices using the polar plane of GaN have a strong internal polarization field, which leads to dimensional separation of electrons and holes in quantum wells and a decrease in their radiative recombination. One of the possible ways to increase the luminescence efficiency of quantum-dimensional structures is to grow the III-nitride emitters along semi-polar orientations [1].

Growing of semi-polar GaN on a Si substrate that will be fully compatible with inexpensive modern Si-based integrated circuit technology is considered a promising direction [2, 3].

The biggest problems in the synthesis of semi-polar GaN-on-Si are, firstly, the lack of epitaxial coupling between the semi-polar GaN on any oriented Si substrate. For this reason, it is impractical to grow semi-polar GaN directly on a flat Si(100) substrate and therefore a structured Si(100) substrate with (1-11) and (-11-1) faces was used for the growing of GaN-on-Si [4, 5]. Secondly, the presence of a reaction between Ga and Si at the initial stage of the synthesis of the layer leads to a disorder of the planarity of the structure and to the defect formation [6]. Usually, to reduce such a reaction, an AlN buffer layer is initially grown. However, for the growth of GaN(11-22) on micro-structured silicon substrates, due to the large number of voids formed in the grooves during nucleation, the GaN layer has a high chance of reacting with Si facets [7].

Recently, to destroy the reaction of Ga and Si, it was proposed a method for the synthesis of GaN(11-22) on a microstructured Si (113) substrate with a special design in the form of additional grooves for ammonia access, and in this way the authors managed to reduce the parasitic reaction of Ga with silicon in the overgrown grooves [7].

This work is dedicated to the epitaxy of GaN(11-22) on a Si(113) substrate, on the surface of which it were formed the nanostructures with element sizes smaller than the free path of the Al adatom over the surface of the buffer layer. In order to achieve this goal, a U-shaped NP-Si(113) nanostructure with a period of 75 nm and a height of inclined narrow rectangular nanochrebs of 75 nm was formed using the technology [8] (Fig. 1).

The structural characteristics of the GaN layers were determined by X-ray diffraction analysis, scanning electron microscopy and atomic force microscopy.

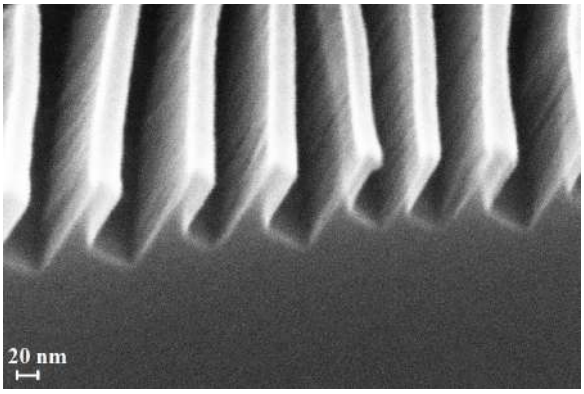


Fig.1. SEM image of NP-Si(113) substrate

© Бессолов В. Н., Коненкова Е. В., Родин С. Н., 2023. Издатель: Санкт-Петербургский политехнический университет Петра Великого.

## Materials and Methods

Initially, a buffer layer of AlN with a thickness of 20 nm was grown on all structures in a hydrogen atmosphere. Then an insular layer of GaN(11-22) with a size of ~ 0.05—0.1 μm and solid layers of GaN(11-22) with a thickness of 0.5—1 μm were grown.

X-ray diffraction analysis of the layers showed that the GaN(11-22) layers have a half-width of the X-ray diffraction curve $\omega_\theta$ ~ 30 arcmin.

To clarify the pattern of the origin of the GaN layer on AlN, an island layer was first deposited (Fig. 2). The results are as follows:

A nanocrystalline layer of AlN with a thickness of about 20 nm completely covers the surface of nanoelements of the NP-Si(113) structure (Fig. 3,*a*). The geometry of nanocrystallites clearly indicates that islands with the GaN(11-22) plane are formed on the surface (Fig. 3, *a*, *b*). It can be seen that the GaN island layer tends to form a continuous one with the surface (11-22) (Fig. 3,*b*).

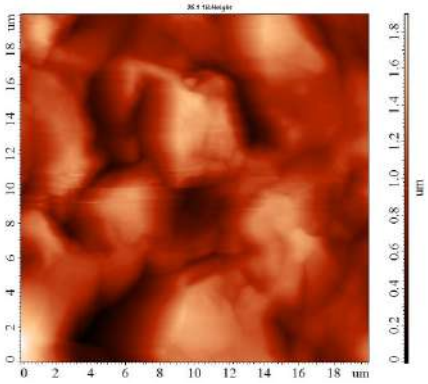


Fig.2. AFM image of GaN(11-22)/NP-Si(113) surface

## Results and Discussion

In our experiments, the edge length Si(111) is 75 nm, that is, the condition is fulfilled when the diffusion length of the Al atom on the surface $L_{Al}$ of 40 nm [9] is commensurate with the edge length of the groove face and the atoms have a high probability of embedding in the crystal lattice on the surface. The origin and growth of the AlN layer occurs under conditions of 'quasi-two-dimensional' growth even at epitaxy temperature no higher than 1030° C for AlN. As it is known, the values of the surface energy for GaN(0001) of 0.185 eV/A2 and for GaN(11-22) of 0.194 eV/A2 [10] are close, so the growth rates of GaN layers on these planes should be almost the same.

The origin of the GaN layer occurs on the surface of the AlN/Si(111) face at higher growth rates than for AlN (Fig. 3, *b*) and after the coalescence stage, a continuous layer with a semi-polar GaN(11-22) surfaces formed. The fact of selective nucleation of nanocrystallites of semi-polar GaN(11-22) in the region of inclined nanochannels of the NP-Si(113) structure has been established.

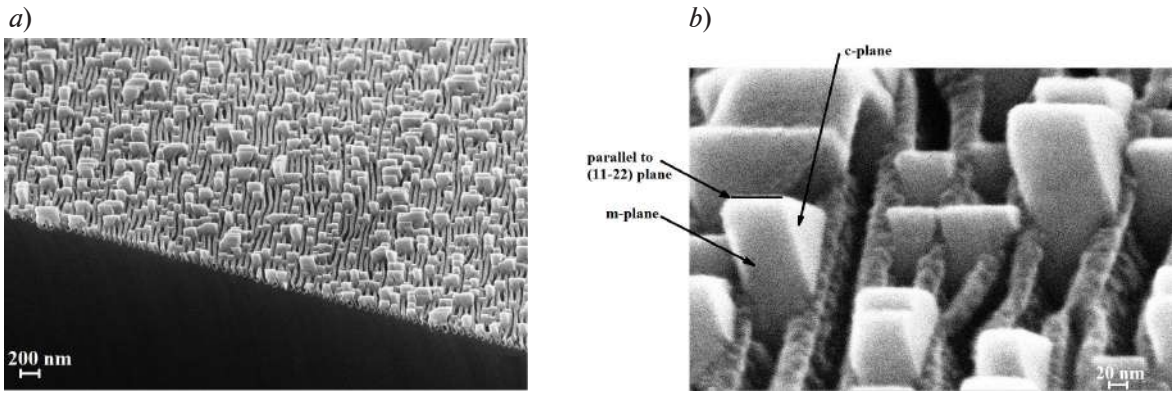


Fig.3. SEM images of GaN of the insular layer (*a*) and crystal faces (*b*)

The shape of the insular nuclei (Fig. 3,*b*) shows the presence of the '*c*-GaN', '*m*-GaN' planes and partially GaN(11-22). The orientation of the nanocrystallites in the array is set by the direction of the plane Si(111) of the nanochannels in NP-Si(113).The thickness of the layer in the direction of growth [0001] was about 50 nm, and it corresponded to the thickness of the layer from the surface of NP-Si(113) to the surface of GaN(11-22).

AFM measurements of the surface of the semi-polar GaN(11-22) layer with on an area of 50 × 50 microns shows the presence of rectangular blocks with a size of 2 × 6 μm between which dips of up to 1.3 microns are observed. The distance between the grooves in the GaN(11-22) layer according to AFM data was about 10 microns (Fig. 2). From the AFM data (Fig. 2), it can be assumed that the sizes of the blocks formed on the surface of NP-Si(113) indicate the diffusion length of Ga atoms at the epitaxy of the GaN layer equal to 3-4 microns, which is less than the authors observed [11].

## Conclusion

It is shown that during GaN(11-22) synthesis by MOCVD method in hydrogen atmosphere at the initial growth stages the layer orientation e is set by the plane direction of Si(111) nanochannels in NP-Si(113) and layer growth rates in (11-22) and (0001) plane directions are comparable. The proposed approach to growing semi-polar GaN(11-22) on a nano-patterned silicon substrate is promising for the integration of gallium nitride and silicon optoelectronics.

## Acknowledgments

The authors are grateful to Quantum Silicon LLC (Moscow, Russia) for providing NP-Si(100) substrates, as well as to V. Smirnov for useful discussions and M. Shcheglov for X-ray structural measurements.

## REFERENCES

1. **Wang T.,** Topical Review: Development of overgrown semi-polar GaN for high efficiency green/yellow emission. Semiconductor Science and Technology. 31(9) (2016) 093003.

2. **Li T.K., Mastro M., Dadgar A.,** III-V Compound Semiconductors: Integration with Silicon-Based Microelectronics. CRC Press, Parkway, NW, 2010.

3. **Selvaraj L.S., Watanabe A., Egawa T.,** Influence of deep-pits on the device characteristics of metal-organic chemical vapor deposition grown AlGaN/GaN high-electron mobility transistors on silicon substrate. Applied Physics Letters. 98(25) (2011) 252105.

4. **Yang M., Ahn H.S., Tanikawa T., Honda Y., Yamoguchi M., Sawaki N.,** Maskless selective growth of semi-polar (112-2) GaN on Si (311) substrate by metal organic vapor phase epitaxy. Journal of Crystal Growth. 311(10) (2009) 2914–2918.

5. **Bessolov V., Zubkova A., Konenkova E., Konenkov S., Kukushkin S., Orlova T., Rodin S., Rubets V., Kibalov D., Smirnov V**., Semipolar GaN(10−11) Epitaxial Layer Prepared on Nano-Patterned SiC/Si(100) Template. Physica Status Solidi B. 256(2) (2019) 1800268.

6. **Ishikawa H., Yamamoto K., Egawa T., Soga T., Jimbo T., Umeno M**., Thermal stability of GaN on (111) Si substrate. Journal of Crystal Growth. 189 (1998) 178–182.

7. **Ni X., Ozgur U., Baski A.A., Morkoc H., Zhou L., Smith D.J., Tran C.A.,** Epitaxial lateral overgrowth of (11-22) semipolar GaN on (1-100) *m*m-plane sapphire by metalorganic chemical vapor deposition. Applied Physics Letters. 90(18) (2007) 182109.

8. **Smirnov K., Kibalov D.S**., Wave-Ordered Structure Induced by Nitrogen Ion Beam on Silicon Surface: A Self-Forming Hard Nanomask and Its Applications, In: Proceedings of the 21st International Conference on Ion-Surface Interactions, Yaroslavl, Russia, 22−26 August 2013; Vol. 1 (2013) p. 62−66.

9. **Bayram C., Ott J.A., Shiu K.T., Cheng Ch.W., Zhu Y., Kim J., Razeghi M., Sadana D.K.,** Gallium Nitride: Cubic Phase GaN on Nano-grooved Si (100) via Maskless Selective Area Epitaxy. *Advanced Functional Materials*. 24(28) (2014) 4492.

10. **Akiyama T., Seta Y., Nakamura K., Ito T.,** Modified approach for calculating individual energies of polar and semipolar surfaces of group-III nitrides. Physcal Review Materials. 3 (2019) 023401.

11. **Rozhavskaya M.M., Lundin W.V., Troshkov S.I., Tsatsulnikov A.F., Dubrovskii V.G.,** Determination of the diffusion lengths of Ga adatoms using GaN stripe profiling. Physica Status Solidi A. 212(4) (2015) 851–854.

## THE AUTHORS

**BESSOLOV Vasily N.**
bes@triat.ioffe.ru
ORCID: 0000-0001-7863-9494

**KONENKOVA Elena V.**
lena@triat.ioffe.ru
ORCID: 0000-0002-5671-5422

**RODIN Sergey N.**
s_rodin77@mail.ru
ORCID: 0000-0003-2236-8642

*Received 27.10.2022. Approved after reviewing 14.11.2022. Accepted 15.11.2022.*

© Peter the Great St. Petersburg Polytechnic University, 2023

Conference materials
UDC 621.382
DOI: https://doi.org/10.18721/JPM.161.235

# Zinc stannate nanostructures for low-temperature gas sensors with improved response and performance

K.N. Punegova[1], S.S. Nalimova[1]✉, V.A. Arkhipenko[1], A.A. Ryabko[2], V.M. Kondratev[3], Z.V. Shomakhov[4], A.M. Guketlov[4]

[1] St. Petersburg Electrotechnical University "LETI", St. Petersburg, Russia;
[2] Ioffe Institute, St. Petersburg, Russia;
[3] Moscow Institute of Physics and Technology, Dolgoprudny, Russia;
[4] Kabardino-Balkarian State University named after H.M. Berbekov, Nalchik, Russia
✉ sskarpova@list.ru

**Abstract**. Nowadays, the development of approaches to increase the sensitivity and reduce the operating temperature of gas sensors based on metal oxides is the important task. In this paper, these problems are solved by forming zinc stannate nanostructures during hydrothermal treatment of zinc oxide nanowires. The microstructure and chemical composition of the synthesized nanostructures were studied by SEM, EDS and XPS. Sensor responses to isopropyl alcohol vapors (1000 ppm) at 120 °C, 180 °C and 250 °C were measured. It was found that the sensor response values of zinc stannate nanostructures significantly exceed the responses of zinc oxide. Moreover, zinc stannate demonstrates the response of 6.3 at 120 °C. Thus, the developed structures can be used to create sensors of reducing gases with low operating temperatures.

**Keywords:** nanostructures, sensitivity, hydrothermal treatment

**Funding:** strategic academic leadership program 'Priority 2030' (Agreement 075-02-2021-1316 30.09.2021), "Development program of ETU "LETI" within the framework of the program of strategic academic leadership" Priority-2030 075-15-2021-1318 on 29 September 2021.

**Citation:** Punegova K.N., Nalimova S.S., Arkhipenko V.A., Ryabko A.A., Kondratev V.M., Shomakhov Z.V., Guketlov A.M., Zinc stannate nanostructures for low-temperature gas sensors with improved response and performance, St. Petersburg State Polytechnical University Journal. Physics and Mathematics. 16 (1.2) 2023 229–235. DOI: https://doi.org/10.18721/JPM.161.235

This is an open access article under the CC BY-NC 4.0 license (https://creativecommons.org/licenses/by-nc/4.0/)

© Punegova K.N., Nalimova S.S., Arkhipenko V.A., Ryabko A.A., Kondratev V.M., Shomakhov Z.V., Guketlov A.M., 2023. Published by Peter the Great St. Petersburg Polytechnic University.

Материалы конференции
УДК 621.382
DOI: https://doi.org/10.18721/JPM.161.235

# Наноструктуры станната цинка для низкотемпературных газовых сенсоров с улучшенным откликом и быстродействием

К.Н. Пунегова[1], С.С. Налимова✉[1], В.А. Архипенко[1], А.А. Рябко[2], В.М. Кондратьев[3], З.В. Шомахов[4], А.М. Гукетлов[4]

[1] Санкт-Петербургский электротехнический университет «ЛЭТИ», Санкт-Петербург, Россия;
[2] Физико-технический институт им. А.Ф. Иоффе РАН, Санкт-Петербург, Россия;
[3]Московский физико-технический институт, г. Долгопрудный, Россия;
[4]Кабардино-Балкарский государственный университет им. Х.М. Бербекова, г. Нальчик, Россия
✉ sskarpova@list.ru

**Аннотация.** В настоящее время важной задачей является разработка подходов к повышению чувствительности и снижению рабочей температуры газовых датчиков на основе оксидов металлов. В данной работе эти проблемы решаются путем формирования наноструктур станната цинка при гидротермальной обработке оксида цинка. Было обнаружено, что значения отклика сенсора наноструктур станната цинка значительно превышают отклики оксида цинка. Таким образом, разработанные конструкции могут быть использованы для создания датчиков восстанавливающих газов с низкими рабочими температурами.

**Ключевые слова: наноструктуры, чувствительность, гидротермальный синтез**

**Финансирование:** программа академического стратегического лидерства «Приоритет 2030» (Соглашение 30.09.2021 1316-2021-02-075), «Программа развития СПбГЭТУ «ЛЭТИ» в рамках программы стратегического академического лидерства» Приоритет-2030 № 075-15-2021-1318 от 29 сентября 2021 г.

**Ссылка при цитировании:** Пунегова К.Н., Налимова С.С., Архипенко В.А., Рябко А.А., Кондратьев В.М., Шомахов З.В., Гукетлов А.М., Наноструктуры станната цинка для низкотемпературных газовых сенсоров с улучшенным откликом и быстродействием // Научно-технические ведомости СПбГПУ. Физико-математические науки. 2023. Т. 16. № 1.2. С. 229–235. DOI: https://doi.org/10.18721/JPM.161.235

Статья открытого доступа, распространяемая по лицензии CC BY-NC 4.0 (https://creativecommons.org/licenses/by-nc/4.0/)

## Introduction

Metal oxide semiconductors are of great interest for chemoresistive gas sensors due to their high sensitivity, ease of manufacture and low cost [1–4]. The approaches for increasing the gas sensitivity of adsorption semiconductor sensors have been developing. The formation of nanostructured materials with a large surface-to-volume ratio, such as hollow nanostructures [5] and one-dimensional nanostructures [6], is among the most promising ones. Hierarchical flower-like ZnO have been demonstrated enhanced ethanol gas-sensing properties [7]. Selective ppb-level ozone gas sensor was developed based on hierarchical branch-like $In_2O_3$ nanostructures [8]. Another approach is the use of multicomponent or composite materials. For example, uniform CuO nanoflakes modified with rGO nanosheets showed ultrahigh response towards $NO_2$ at room temperature [9]. Mesoporous $CdS/PbS/SnO_2$ composites showed high-selective response towards $H_2$. Enhanced properties were explained by a great number of active sites to gas adsorption and diffusion in surface redox reaction. Numerous heterojunctions of the $CdS/PbS/SnO_2$ composites may serve as highly conductive channels to accelerate carrier transfer, thus further leading to an improved performance of the sensors [10].

© Пунегова К.Н., Налимова С.С., Архипенко В.А., Рябко А.А., Кондратьев В.М., Шомахов З.В., Гукетлов А.М., 2023. Издатель: Санкт-Петербургский политехнический университет Петра Великого.

In recent years, triple oxides attract a lot of attention as a new type of sensor materials, since they have a stable and excellent sensing response when detecting various gases [11]. However, the sensitivity of many ternary metal oxides is too low for commercial application due to the small area of interaction with gas and, consequently, poor electron exchange [12]. Among tin-based ternary metal oxides, $ZnSnO_3$ is a typical multifunctional n-type semiconductor oxide with a perovskite structure. Due to its chemical activity and excellent electronic properties, $ZnSnO_3$ is widely used as gas sensing materials [13–15]. A range of $ZnSnO_3$ nanostructures in the form of nanoparticles [16], hollow spheres [17], cubic nanostructures [18], nanofibers [19] with large surface-to-volume ratio have been hollow spheres synthesized.

The aim of the work is the development of zinc stannate nanostructures with excellent and fast sensor response at lower working temperatures. Hydrothermal treatment of preliminary prepared zinc oxide nanowires was chosen to change their composition and to form zinc stannate nanostructures. The microstructure and element composition were studied. The sensor response was analyzed towards isopropyl alcohol vapors.

## Materials and Methods

Gas-sensitive layers of zinc oxide nanowires were synthesized on substrates with interdigitated gold electrodes by hydrothermal method described in details in [20–22]. The resulting layers were further processed to partially replace zinc atoms in the crystal structure of the nanowires with tin atoms and form a triple oxide. A substrate with zinc oxide nanowires were placed in an aqueous alcohol solution of potassium stannate trihydrate and urea. The synthesis was carried out in stainless steel autoclave with Teflon liner at 170 °C for 30 minutes. After that, the samples were washed with distilled water, dried in air and annealed at 500 °C for 15 minutes.

The microstructure was studied by scanning electron microscopy, elemental composition was analyzed by energy dispersive spectroscopy (Zeiss Supra25, Carl Zeiss, Germany). X-ray photoelectron spectroscopy (K-Alpha, Thermo Scientific, USA) using a monochromatized Al Kα X-ray source (hν = 1486.6 eV) was used to acquire the chemical composition and bonding states.

The gas sensor responses of zinc oxide and zinc stannate towards isopropyl alcohol vapors (1000 ppm) were investigated at 120 °C, 180 °C, 250 °C. The current was recorded using a Keithley 6485 picoammeter. The bias voltage was 5 V. The sensor response was calculated using the following equation:

$$S = \frac{R_{air}}{R_{gas}},$$

where $R_{air}$ and $R_{gas}$ are the sample resistances in the air and when exposed to the detected gas (isopropyl alcohol).

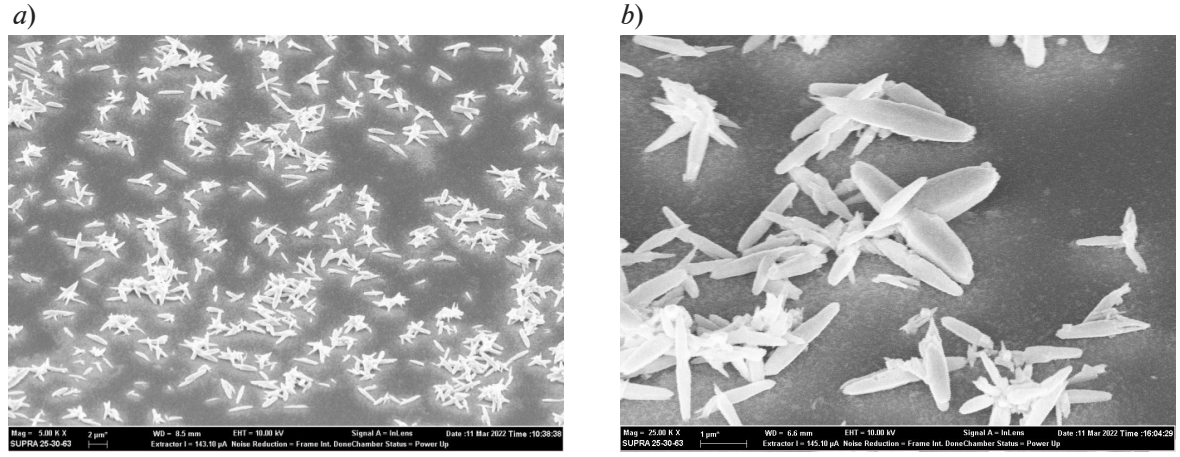


Fig. 1. Scanning electron microscopy images of zinc stannate

## Results and discussion

The surface morphology and elements of the samples were characterized by SEM and EDS. As shown in Fig. 1, *a*, *b*, initial size and shape of zinc oxide nanowires remain the same as a result of hydrothermal treatment and zinc stannate formation. The EDS elemental distribution maps of zinc stannate are presented in Fig. 2, *a*, *b*, *c*, which show the presence of Zn and O elements in nanowires and uniform distribution of Sn on substrate surface.

The chemical composition and valence of zinc stannate nanostructures were analyzed by XPS (Fig. 3). The high-resolution spectrum of Zn 2p was divided into two photoelectron peaks: Zn 2p3/2 (located at 1022.5 eV) and Zn 2p1/2 (located at 1045.6 eV). The spin-orbit split is 23.1 eV, indicating the normal chemical state of $Zn^{2+}$ in $ZnSnO_3$ [23]. The high-resolution spectrum of Sn 3d was divided into two photoelectron peaks: the peaks at 487.3 eV and 495.7 eV were attributed to Sn 3d5/2 and Sn 3d3/2, respectively. The split value of the bimodal spin orbit is about 8.4 eV, indicating the presence of $Sn^{4+}$ cations [24]. The O 1s spectrum was divided into two fitting peaks corresponding to $O^{2-}$ species in the lattice (530.7 eV) and chemically adsorbed hydroxyl groups (532 eV) [25].

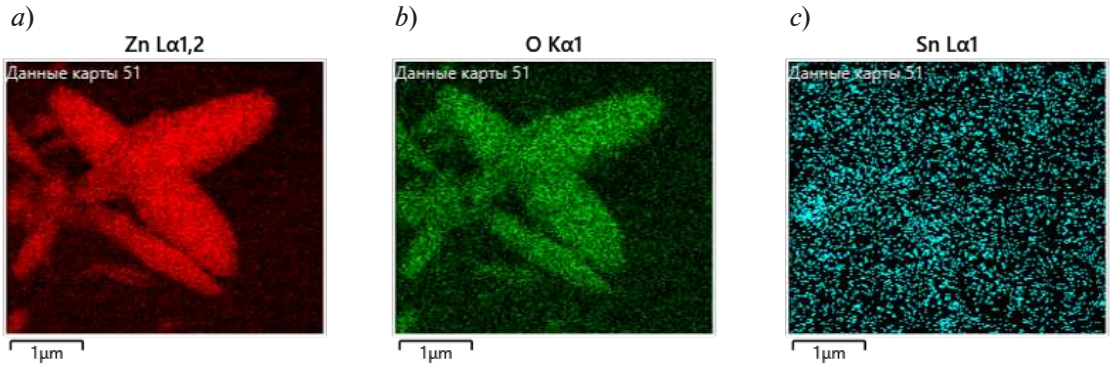


Fig. 2. EDS elemental mapping images of Zn (*a*), O (*b*) and Sn (*c*)

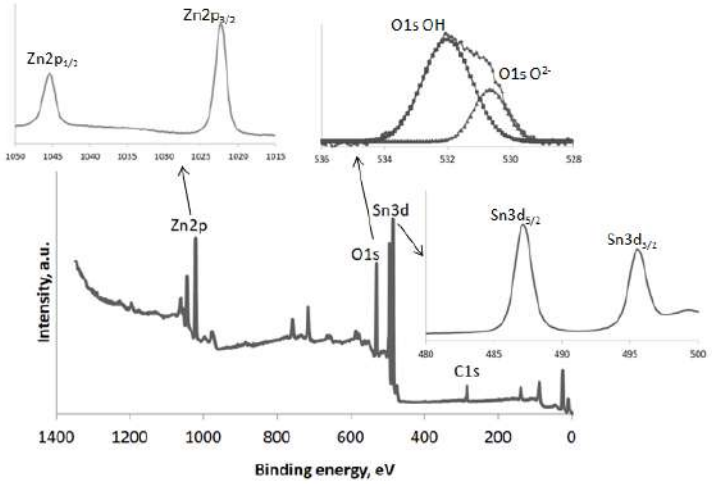


Fig. 3. X-ray photoelectron spectra of zinc stannate

The sensor responses of the layer consisting of zinc oxide nanowires are 1.4, 1.9 and 2.5, while for the zinc stannate layer they are 6.3, 6.7 and 15.6 (at 120 °C, 180 °C and 250 °C, respectively). The study of the interaction of samples with isopropyl alcohol vapors showed that at all temperatures the sensor responses of zinc stannate are much higher than the ones of zinc oxide (Fig. 4).

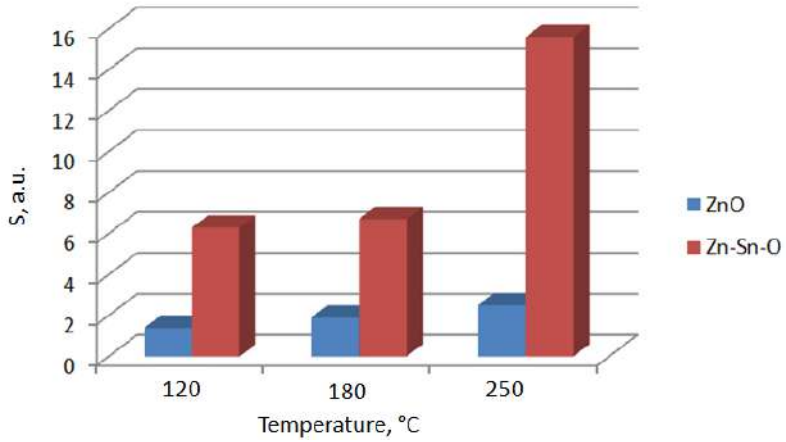


Fig. 4. Sensor responses of zinc oxide and zinc stannate layers

The changes in the sensor responses of zinc stannate sample during the exposure of isopropyl alcohol vapor are shown in Fig. 5. The exposure of isopropyl alcohol starts at 0 s and finished at 600 s. When isopropyl alcohol vapor is supplied, we can observe a decrease in resistance, and when air is supplied, an increase, which corresponds to the processes in the interaction of *n*-type semiconductors with reducing gases. It was found that an increase in temperature from 180 °C to 250 °C leads to a sharp increase in sensitivity. At the same time, the sensitivity values of the sample at measurement temperatures of 120 °C and 180 °C differ slightly. The response values of zinc stannate show that the developed sensor layers can be used at low operating temperatures less than 150 °C.

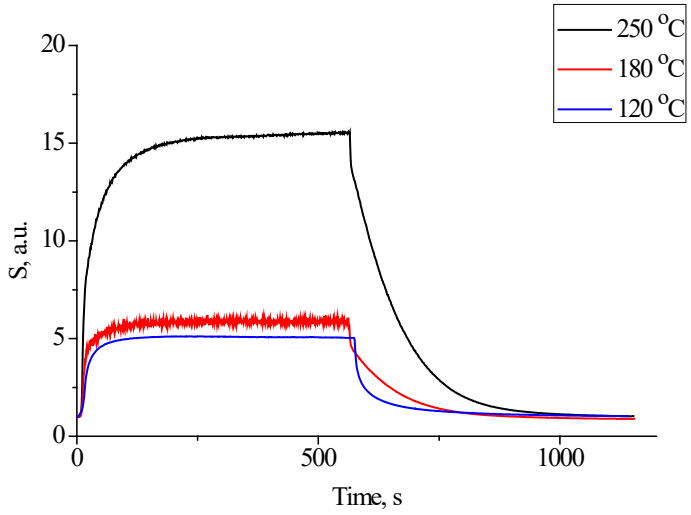


Fig. 5. Time dependences of the sensor responses of zinc stannate sample to isopropyl alcohol vapors at different temperatures

The improvement of the gas-sensitive properties of zinc stannate sample in comparison with ZnO can be explained as follows. The process of metal oxide interaction with the target gas is a complex process including both redox and acid-base catalytic reactions [26, 27]. Therefore, the improvement of the gas-sensitive properties is achieved by the development of materials containing adsorption centers with different redox and acid-base properties. When such sites are situated nearby a new effect of the nanosystem appears providing separate acceleration of the processes of adsorption and oxidation of gas molecules.

## Conclusion

The improvement of the gas-sensitive properties of zinc oxide nanowires when treated in an aqueous alcohol solution of potassium stannate and urea is shown. The surface of resulting zinc stannate nanostructures contains sites of various types participated in the adsorption and oxidation of isopropyl alcohol vapors. Zinc stannate at 120 °C exhibits a response of 6.3, which indicates the prospects of the obtained layers for use in low-temperature gas sensors.

## Acknowledgments

V.M.K. thanks the strategic academic leadership program "Priority 2030" (Agreement 075-02-2021-1316 30.09.2021). S.S.N. and V.A.M. thank the "Development program of ETU "LETI" within the framework of the program of strategic academic leadership" Priority-2030 No 075-15-2021-1318 on 29 September 2021.

## REFERENCES

1. **Korotcenkov G.,** Nanomaterials 10 (2020) 1392.
2. **Moshnikov V.A., Gracheva I.E., Kuznezov V.V., Maximov A.I., Karpova S.S., Ponomareva A.A.,** Journal of Non-Crystalline Solids 356 (2010) 2020.
3. **Staerz A., Weimar U., Barsan N.,** 2022 Sensors and Actuators B 358 131531.
4. **Nalimova S.S., Moshnikov V.A., Myakin S.V.,** 2016 Glass Physics and Chemistry 4 597.
5. **Zhao R., Wang Z., Yang Y., Xing X., Zou T., Wang Z., Wang Y.,** Journal of Physics and Chemistry of Solids 120 (2018) 173.
6. **Kaur N, Singh M and Comini E.,** Langmuir 36 (2020) 6326.
7. **Zhu L., Li Y., Zeng W.,** Applied Surface Science 427 (2018) 281.
8. **Sui N., Zhang P., Zhou T., Zhang T.,** Sensors and Actuators B 336 (2021) 129612.
9. **Bai H., Guo H., Wang J., Dong Y., Liu B., Xie Z., Guo F., Chen D., Zhang R., Zheng Y.,** Sensors and Actuators B 337 (2021) 129783.
10. **Bai H., Guo H., Tan Y., Wang J., Dong Y., Liu B., Xie Z., Guo F., Chen D., Zhang R., Zheng Y.,** Sensors and Actuators B 340 (2021) 129924.
11. **Mongwaketsi N., Khamlich S., Kaviyarasu K., Matinise N., Maaza M.,** Applied Surface Science 446 (2018) 250.
12. **Wang B. S., Yu J. B., Li X. H., Yin J., Chen M.,** RSC Advances 9 (2019) 14809.
13. **Yin Y., Shen Y., Zhou P., Lu R., Li A., Zhao S., Liu W., Wei D., Wei K.,** Applied Surface Science 509 (2020) 145335.
14. **Levkevich E. A., Maksimov A. I., Kirillova S. A., Nalimova S. S., Kondrat'ev V. M.**, IEEE Conference of Russian Young Researchers in Electrical and Electronic Engineering (EIConRus) (2020) 984.
15. **Levkevich E.A., Semenova A.A., Maximov A.I., Nalimova S.S., Kirillova S.A., Moshnikov V.A., Zhukov M.V.,** AIP Conference Proceedings (2020) 0018936.
16. **Feng G., Che Y., Song C., Xiao J., Fan X., Sun S., Huang G., Ma Y.,** Ceramics International 47 (2021) 2471.
17. **Bing Y., Zeng Y., Liu C., Qiao L., Sui Y., Zou B., Zheng W., Zou G.,** Sensors and Actuators B 190 (2014) 370.
18. **Guo W.W., Zhao B.Y., Fu M., Wang C.J., Peng R.,** Results in Physics 15 (2019) 102606.
19. **Chen Q., Wang Y.H., Wang M.X., Ma S.Y., Wang P.Y., Zhang G.H., Chen W.J., Jiao H.Y., Liu L.W., Xu X.L.,** Journal of Colloid and Interface Science **543** (2019) 285.
20. **Ryabko A.A., Maximov A.I., Moshnikov V.A., Terukov E.I., Verbitskii V.N., Levitskii V.S.,** Semiconductors 54 (2020) 1496.
21. **Nalimova S.S., Ryabko A.A., Maximov A.I., Moshnikov V.A.,** Journal of Physics: Conference Series 1697 (2020) 012128.
22. **Bobkov A., Moshnikov V., Varezhnikov A., Plugin I., Fedorov F. S., Goffman V., Sysoev V., Trouillet V., Geckle U., Sommer M.,** Sensors 19 (2019) 4265.
23. **Zhao S., Shen Y., Yan X., Zhou P., Yin Y., Lu R., Han C., Cui B., Wei D.,** Sensors and Actuators B 286 (2019) 501.
24. **Kim R., Jang J.-S., Kim D.-H., Kang J.-Y., Cho H.-J., Jeong Y. J., Kim I.-D.,** Advanced Functional Materials 29 (2019) 1903128.

25. **Jia X., Yu S., Yang J., Wang S., Li Y., Shao D., Song H.,** IEEE Sensors Journal 22 (2022) 1916.
26. **Karpova S.S., Moshnikov V.A., Mjakin S.V., Kolovangina E.S.,** Semiconductors 47 (2013) 392.
27. **Karpova S.S., Moshnikov V.A., Maksimov A.I., Mjakin S.V., Kazantseva N.E.,** Semiconductors 47 (2013) 2016.

## THE AUTHORS

**PUNEGOVA Kseniya N.**
punegova.k@mail.ru

**NALIMOVA Svetlana S.**
sskarpova@list.ru
ORCID: 0000-0003-3065-3961

**ARKHIPENKO Victoriya A.**
va_arkhipenko@mail.ru

**RYABKO Andrey A.**
a.a.ryabko93@yandex.ru
ORCID: 0000-0001-9626-7612

**KONDRATEV Valeriy M.**
kvm_96@mail.ru
ORCID: 0000-0002-3469-5897

**SHOMAKHOV Zamir V.**
shozamir@yandex.ru
ORCID: 0000-0001-5738-2626

**GUKETLOV Aslan M.**
guketlovaslan3@gmail.com
ORCID: 0000-0002-3469-5897

*Received 01.11.2022. Approved after reviewing 10.11.2022. Accepted 17.11.2022.*

© Peter the Great St. Petersburg Polytechnic University, 2023

Conference materials
UDC 539.23, 537.62
DOI: https://doi.org/10.18721/JPM.161.236

# Magnetic properties of heterophase film coatings based on a solid solution of cadmium sulfide and iron

S.V. Stetsyura, P.G. Kharitonova✉

Saratov State University, Saratov, Russia

✉ haritonovapg@gmail.com

**Abstract.** In this work, we measured and analyzed the magnetic susceptibility and the isotherms of magnetization of a semimagnetic material based on CdS: Fe with nanosized inclusions of FeS and $Fe_2O_3$ phases. These measurements made it possible to divide the ferromagnetic and paramagnetic phases. Measurements of magnetic force microscopy showed manifestations of magnetic properties mainly at the boundaries of CdS grains, which is explained by the predominance of the mechanism of diffusion of iron atoms along the boundaries of crystallites. The displacement of Cd atoms with the formation of FeS or the oxidation of Fe to the state of maghemite occurs at the boundaries of these crystallites.

**Keywords:** semimagnetic material, heterogeneous material, magnetic force microscopy, magnetization isotherms, magnetic susceptibility, magnetic hysteresis

**Funding:** The work was carried out at the expense of the Russian Science Foundation (project 22-22-00194, https://rscf.ru/en/project/22-22-00194/).

**Citation:** Stetsyura S.V., Kharitonova P.G., Magnetic properties of heterophase film coatings based on a solid solution of cadmium sulfide and iron, St. Petersburg State Polytechnical University Journal. Physics and Mathematics. 16 (1.2) 2023 236–240. DOI: https://doi.org/10.18721/JPM.161.236

This is an open access article under the CC BY-NC 4.0 license (https://creativecommons.org/licenses/by-nc/4.0/)

Материалы конференции
УДК 539.23, 537.62
DOI: https://doi.org/10.18721/JPM.161.236

# Магнитные свойства гетерофазных пленочных покрытий на основе твердого раствора сульфида кадмия и железа

С.В. Стецюра, П.Г. Харитонова✉

СГУ имени Н.Г. Чернышевского, г. Саратов, Россия

✉ haritonovapg@gmail.com

**Аннотация.** В настоящей работе проведены измерения и анализ изотерм намагниченности и магнитной восприимчивости полумагнитного материала на основе CdS:Fe с наноразмерными включениями фаз FeS и $Fe_2O_3$. Данные измерения позволили разделить ферромагнитную и парамагнитную фазы. Измерения магнито-силовой микроскопии показали проявление магнитных свойств в основном на границах зерен CdS, что объясняется преобладанием механизма диффузии атомов железа по границам кристаллитов, где и происходит замещение атомов Cd с образованием FeS или окисление Fe до состояния маггемита.

**Ключевые слова:** полумагнитный материал, гетерогенный материал, магнито-силовая микроскопия, изотермы намагниченности, магнитная восприимчивость, магнитный гистерезис

**Финансирование:** Исследование выполнено за счет гранта Российского научного фонда № 00194-22-22, https://rscf.ru/project/22-22-00194/.

© Stetsyura S.V., Kharitonova P.G., 2023. Published by Peter the Great St. Petersburg Polytechnic University.

**Ссылка при цитировании:** Стецюра С.В., Харитонова П.Г. Магнитные свойства гетерофазных пленочных покрытий на основе твердого раствора сульфида кадмия и железа // Научно-технические ведомости СПбГПУ. Физико-математические науки. 2023. Т. 16. № 1.2. С. 236–240. DOI: https://doi.org/10.18721/JPM.161.236

Статья открытого доступа, распространяемая по лицензии CC BY-NC 4.0 (https://creativecommons.org/licenses/by-nc/4.0/)

## Introduction

A semimagnetic material can be obtained in the case of partial displacement of metal atoms of the base material (for example, cadmium chalcogenide) by dopant atoms (for example, Fe) [1, 2]. At present, the study of the properties of semimagnetic materials is very important, because the specific properties of these materials significantly depend on the concentration of dopant atoms and their interaction. At the same time, nanoparticles showing ferromagnetic properties are no less interest [3]. Of particular interest are ensembles of such particles included in a semiconductor matrix with paramagnetic or semimagnetic properties.

This paper presents the research results of heterogeneous film samples based on CdS obtained by thermal evaporation in vacuum. Doping with iron atoms from a nanosized film on the back surface of CdS occurred by thermal annealing. During annealing, the diffusion of iron atoms occurs deep into the CdS sample with the formation of a substitutional solid solution $Cd_xFe_{1-x}S$ based on the cubic modification of CdS [4]. Also there is recrystallization of CdS which is attended by a polymorphic transformation of its crystal lattice from sphalerite to wurtzite. The resulting significant differences in the crystal lattices of the photosensitive modification of CdS, iron and its sulfide during annealing lead to a limitation in the solubility of the components and the formation of a heterogeneous material based on a $Cd_xFe_{1-x}S$ solid solution.

A significant change in the electrical and optical properties is observed for heterogeneous CdS: Fe materials under the action of an applied magnetic field. This is of interest for modern micro- and nanoelectronics, and can be used to create semiconductor devices with magnetic field-controlled characteristics [5].

## Materials and Technology

The object of study in this work is thin-film polycrystalline samples of cadmium sulfide doped with iron. There are many ways to obtain CdS films and their doping [6, 7]. For this research, we obtained samples with a multilayer structure created by successive deposition of layers by thermal evaporation in vacuum.

Initially, we deposited a layer of chemically pure iron 30–50 nm thick on a glass substrate at a pressure of $6 \cdot 10^{-5}$ Torr for 5 minutes, then, on top of it, a layer of chemically pure cadmium sulfide 0.6–0.8 μm thick. The mixture of CdS also contained the $CuCl_2$ activator at a ratio of 20 mg $CuCl_2$ per 1 g CdS. Thus, the film, which is the source of iron during diffusion, is located between the glass substrate and the CdS film. Further, the samples were annealed in a furnace in an air atmosphere at a temperature of 450°C for 15 minutes. As a result of such high-temperature annealing of samples consisting of components with low mutual solubility (the solubility of Fe in CdS is less than 9%), one can expect the formation of precipitates from iron atoms, FeS, and iron oxides.

## Results and Discussion

To study the magnetic properties of the obtained heterogeneous CdS: Fe material, we used magnetic force microscopy (MFM) and methods for measuring of magnetization curves and of the dependence of magnetic susceptibility on temperature.

Fig. 1 shows the results of measurements of the magnetization isotherms of heterogeneous materials samples based on $Cd_xFe_{1-x}S$ solid solutions. The measurements were made on a magnetometer with a vibrating sample.

The presence of hysteresis indicates about a ferromagnetic phase, and an increase of the specific magnetization $M_S$ with increasing magnetic field intensity indicates about a paramagnetic phase.

An analysis of the experimental magnetization isotherms makes it possible to separate the ferromagnetic and paramagnetic phases (Fig. 2).

© Стецюра С.В., Харитонова П.Г., 2023. Издатель: Санкт-Петербургский политехнический университет Петра Великого.

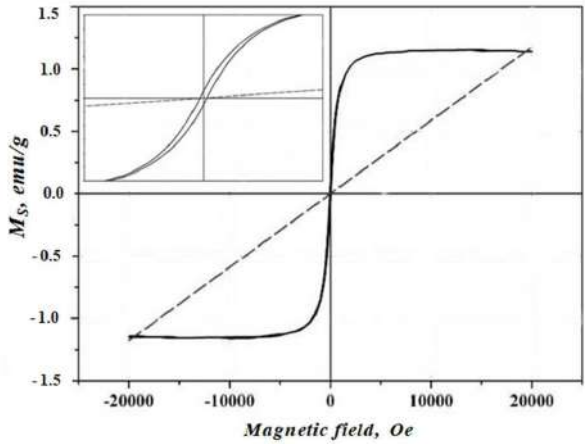


Fig. 1. Experimental magnetization isotherm of an annealed heterophase CdS:Fe sample with a selected hysteresis area in the range from -1500 Oe to +1500 Oe

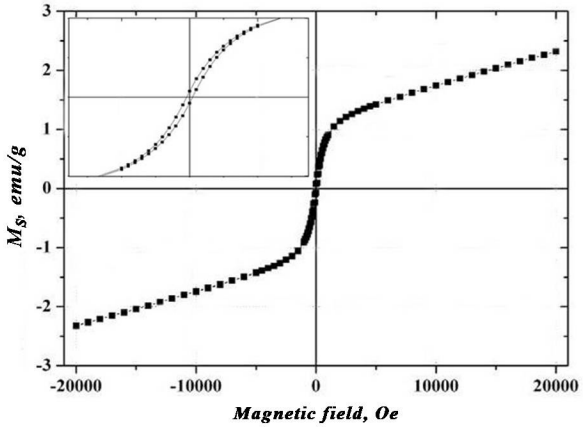


Fig. 2. Separation of paramagnetic (dotted line) and ferromagnetic (solid line) components from the experimental graph in Fig. 1.
The area on the fragment is increased in the range from -1500 Oe to +1500 Oe

The ferromagnetic phase is a soft magnet, characterized by a coercive force $H_C$ = 44 Oe, with a value of specific magnetization $M_S$ = 1.15 emu/g. The area of the hysteresis loop determines the amount of energy losses required to remagnetize the sample, which are used to heat the sample. As we can see, the hysteresis loop is quite "narrow". Narrow magnetic hysteresis loops are observed in soft magnetic materials, which also indicates that this material belongs to the class of soft magnetic materials.

Fig. 3 shows the temperature dependence of the magnetic susceptibility $\chi$ of heterogeneous semiconductor film samples of CdS:Fe. The dependence was obtained using a magnetometer with a vibrating sample under the influence of an external magnetic field of 1500 Oe.

Different classes of substances have different ranges of magnetic susceptibility values. These values are on the order of $10^{-4}$—$10^{-6}$ for diamagnets and paramagnets. But at the same time, diamagnets and paramagnets are practically independent of the intensity of the applied magnetic field. The magnetic susceptibility can reach very large values from several tens to many thousands of units for ferromagnets. Also there is a strong dependence on the intensity of the applied field for ferromagnets. Therefore, for convenience, we use the differential magnetic susceptibility, which is equal to the derivative of the magnetization of a unit volume of a substance on the magnetic field intensity. The magnetic susceptibility of paramagnets decreases with increasing temperature, obeying the Curie—Weiss law. The magnetic susceptibility of ferromagnets, increases with increasing temperature, reaching a sharp maximum near the Curie point.

In our research at room temperature, the sample shows paramagnetic properties, but as the temperature increases, the shape of the curve differs from the curve observed in the Curie–Weiss law. In addition, we observe a local peak at a temperature of about 212 °C, which is characteristic of ferromagnetic samples. These measurements confirm the heterogeneity of the annealed CdS: Fe sample and the presence of paramagnetic and ferromagnetic phases in these samples.

We used magnetic force microscopy (MFM) to characterize the magnetic properties of the

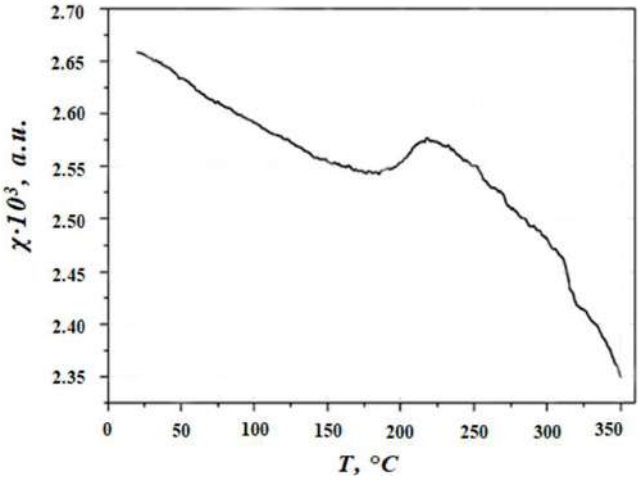


Fig. 3. Temperature dependence of magnetic susceptibility χ for an annealed heterophase CdS:Fe sample

surface of heterophase CdS:Fe samples. Measurements of magnetic force microscopy make it possible to study magnetic domain structures with a high spatial resolution of recording and reading information in a magnetic medium, magnetization reversal processes, etc.

When obtaining MFM images, an external magnetic field was applied to the samples in the range from 0 to 500 Oe with the intensity vector parallel to the plane of the sample. Fig. 4 shows MFM images of the surface of a CdS:Fe sample in the absence and in the presence of an external magnetic field of 500 Oe.

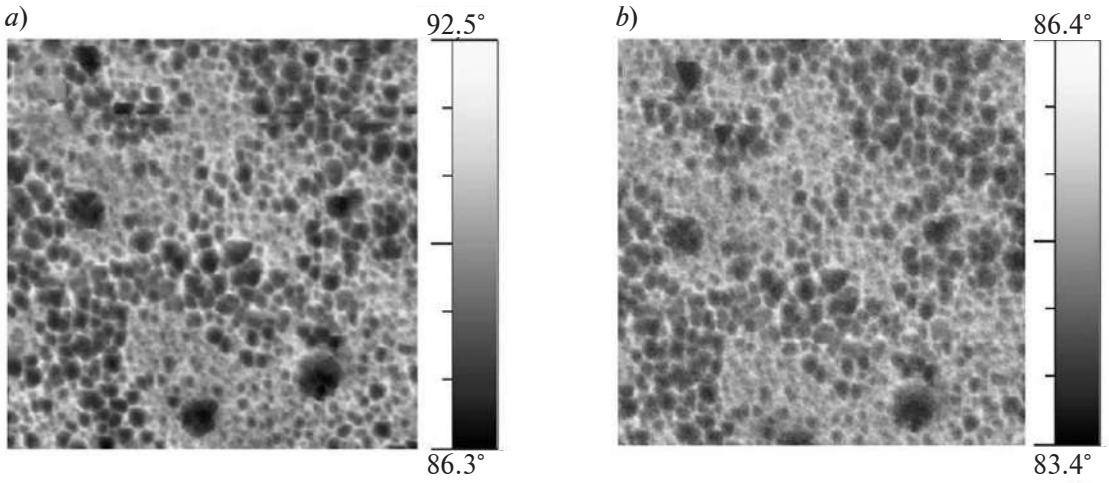


Fig. 4. MFM images of the surface of an annealed heterophase CdS: Fe sample without (*a*) and with (*b*) a magnetic field. The scan size is 10×10 μm

The application of an external magnetic field leads to a decrease in the contrast of the MFM image that can be explained by an increase in the magnetization of the inner regions. That is, there is another ferromagnetic phase inside the film along with a ferromagnetic phase on the surface. The ratio of MFM signals indicates a significant (up to 9.2%) change in the signal for the intercrystalline space and insignificant (1.5%) for large crystallites on the surface. This fact can be explained by the diffusion of iron atoms to the surface during annealing. Iron accumulates at grain boundaries where magnetic particles grow. At the same time, the external magnetic field has a slight attachment on large CdS crystallites.

### Conclusion

Thus, measurements of the magnetic hysteresis and magnetic susceptibility showed the presence of paramagnetic and ferromagnetic phases in a heterogeneous material based on a $Cd_xFe_{1-x}S$ solid solution after high-temperature annealing. Based on the data of magnetic force microscopy, it can be concluded that there are various ferromagnetic phases inside the annealed samples of the heterogeneous CdS:Fe material and on its surface. Magnetic properties mainly appear at the boundaries of CdS grains that is explained by the predominance of the mechanism of diffusion of iron atoms along the boundaries of crystallites. The displacement of Cd atoms with the formation of FeS or the oxidation of Fe to the state of maghemite ($Fe_2O_3$) occurs at the boundaries of these crystallites. The oxidation process dominates on the surface, while the sulfur replacement process dominates inside heterogeneous samples. This circumstance explains the presence of one ferromagnetic phase on the surface and another ferromagnetic phase in the bulk of the sample.

### Acknowledgments

The work was carried out at the expense of the Russian Science Foundation (project 22-22-00194, https://rscf.ru/en/project/22-22-00194/).

## REFERENCES

1. **Thirumala Rao G., Ravikumar R.V.S.S.N.**, Novel Fe-doped ZnO-CdS nanocomposite with enhanced visible light-driven photocatalytic performance, Materials Research Innovations. 25(4) (2021) 215–220.

2. **Mel'nichuk S.V., Nikitin P.I., Savchuk A.I., Trifonenko D.N.**, Faraday effect in semimagnetic $Cd_{1-x}Fe_xTe$ semiconductor, Semiconductors. 30(10) (1996) 959–961.

3. **Matiushkina A.A., Dubavik A.U., Baranov M.A., Maslov V.G., Orlova A.O.**, Optical Properties of Core−Shell $Fe_3O_4$/CdSe/ZnS Nanocomposites, Optics and Spectroscopy. 129 (2021) 780−788.

4. **Khludkov S.S., Prudaev I.A., Tolbanov O.P., Novikov V.V., Ivonin I.V.**, A study of the process of decomposition of supersaturated GaAs:Fe solid solution by scanning probe microscopy, Semiconductors. 44(8) (2010) 975−977.

5. **Kulbachinskii V. A., Maryanchuk P. D., Churilov I. A., Inoue M., Sasaki M., Negishi H., Hara Y.**, Electronic and magnetic properties of the diluted magnetic semiconductor $Hg_{1-x}Mn_xTe_{1-y}Se_y$, Semiconductor Science and Technology. 10(4) (1995) 463–468.

6. **Moualkia H., Hariech S., Aida M.S.**, Structural and optical properties of CdS thin films grown by chemical bath deposition, Thin Solid Films. 518(4) (2009) 1259−1262.

7. **Stetsyura S. V., Glukhovskoy E. G., Kozlowski A. V., Malyar I. V.**, Fabrication of ultrathin impurity source to minimize radiation-induced losses in photosensitive films of CdS, Technical Physics. 60(5) (2015) 746−752.

## THE AUTHORS

**STETSYURA Svetlana V.**
stetsyurasv@mail.ru
ORCID: 0000-0002-4337-012X

**KHARITONOVA Polina G.**
haritonovapg@gmail.com
ORCID: 0000-0003-0591-9908

*Received 28.10.2022. Approved after reviewing 08.11.2022. Accepted 08.11.2022.*

© Peter the Great St. Petersburg Polytechnic University, 2023

Conference materials
UDC 539.234
DOI: https://doi.org/10.18721/JPM.161.237

# $BaTiO_3$ nanocrystalline thin films: synthesis, plasma treatment, and memristive effect

Z.E. Vakulov[1, 2✉], D.A. Dzyuba[2, 3], I.A. Shihovcov[2, 3], N.V. Parshina[3], R.V. Tominov[2, 3], V.S. Klimin[3], V.A. Smirnov[2, 3], O.A. Ageev[3]

[1] Federal Research Centre the Southern Scientific Centre of the RAS, Rostov-on-Don, Russia;

[2] Neuroelectronics and Memristive Nanomaterials Research Laboratory, Southern Federal University, Taganrog, Russia;

[3] Institute of Nanotechnologies, Electronics, and Equipment Engineering, Southern Federal University, Taganrog, Russia

✉ vakulov@ssc-ras.ru

**Abstract.** Here, experimental studies on barium titanate nanocrystalline thin films fabricated by pulsed laser deposition and the influence of the oxygen pressure on the morphological parameters are presented. The average grain size changes from (20.1±1.8) nm to (88.2±7.9) nm with increasing oxygen pressure from $1\times10^{-5}$ Torr to $1\times10^{-2}$ Torr. The effect of plasma treatment on the parameters of $BaTiO_3$ nanocrystalline thin films was studied. It was found that the formation of whisker-like structures is preferred for $BaTiO_3$ when the power of inductively coupled and capacitive plasma sources increases. The results can be applied to the design and development of technological processes for promising lead-free energy converters, eco-friendly energy devices and memristive structures developed based on pulsed laser deposition.

**Keywords:** barium titanate, thin films, pulsed laser deposition, plasma treatment, memristive effect

**Funding:** The reported study was funded by the Russian Foundation for Basic Research, projects 19-38-60052 and 19-29-03041 mk, by the Foundation for Assistance to Small Innovative Enterprises (FASIE) (Agreement 53GURES14/72779), and partially supported by Grant of the President of the Russian Federation MK-6252.2021.4 and by the Government of the Russian Federation (Agreement 075-15-2022-1123).

**Citation:** Vakulov, Z.E., Dzyuba, D.A., Shihovtsov, I.A., Parshina, N.V., Tominov, R.V., Klimin, V.S., Smirnov, V.A. And Ageev, O.A. $BaTiO_3$ nanocrystalline thin films: synthesis, plasma treatment, and memristive effect, St. Petersburg State Polytechnical University Journal. Physics and Mathematics. 16 (1.2) (2023) 241–246. DOI: https://doi.org/10.18721/JPM.161.237

This is an open access article under the CC BY-NC 4.0 license (https://creativecommons.org/licenses/by-nc/4.0/)

© Vakulov Z.E., Dzyuba D.A., Shihovtsov I.A., Parshina N.V., Tominov R.V., Klimin V.S., Smirnov V.A., Ageev O.A., 2023. Published by Peter the Great St. Petersburg Polytechnic University.

Материалы конференции
УДК 539.234
DOI: https://doi.org/10.18721/JPM.161.237

# Тонкие нанокристаллические пленки $BaTiO_3$: синтез, плазменная обработка, мемристивный эффект

З.Е. Вакулов[1, 2✉], Д.А. Дзюба[2, 3], И.А. Шиховцов[2, 3], Н.В. Паршина[3], Р.В. Томинов[2, 3], В.С. Климин[3], В.А. Смирнов[2, 3], О.А. Агеев[3]

[1] Федеральный исследовательский центр Южный научный центр РАН, Ростов-на-Дону, Россия;

[2] Научно-исследовательская лаборатория «Нейроэлектроника и мемристивные наноматериалы» Южного федерального университета, Таганрог, Россия;

[3] Институт нанотехнологий, электроники и приборостроения Южного федерального университета, Таганрог, Россия

✉ vakulov@ssc-ras.ru

**Аннотация.** В работе представлены результаты экспериментальных исследований влияния давления кислорода при импульсном лазерном осаждении и режимов плазменной обработки на морфологические параметры нанокристаллических тонких пленок титаната бария. Полученные результаты могут быть использованы при проектировании и разработке технологических процессов для перспективных бессвинцовых преобразователей энергии и мемристивных структур, созданных на основе импульсного лазерного осаждения.

**Ключевые слова:** титанат бария, тонкие пленки, импульсное лазерное осаждение, плазменная обработка, мемристивный эффект

**Финансирование:** Исследование выполнено при финансовой поддержке РФФИ в рамках научных проектов № 60052-38-19 и № 03041-29-19 мк, поддержано Фондом содействия инновациям (ФСИ) (Договор № 53ГУРЭС7277/149), Грантом Президента Российской Федерации № МК-6252.2021.4 и Правительством РФ (Соглашение № 075-15-2022-1123).

**Ссылка при цитировании:** Вакулов З.Е., Дзюба Д.А., Шиховцов И.А., Паршина Н.В., Томинов Р.В., Климин В.С., Смирнов В.А., Агеев О.А. Тонкие нанокристаллические пленки $BaTiO_3$: синтез, плазменная обработка, мемристивный эффект // Научно-технические ведомости СПбГПУ. Физико-математические науки. 2023. Т. 16. № 1.2. С. 241–246. DOI: https://doi.org/10.18721/JPM.161.237

Статья открытого доступа, распространяемая по лицензии CC BY-NC 4.0 (https://creativecommons.org/licenses/by-nc/4.0/)

## Introduction

Ferroelectric materials attract attention for promising applications such as non-volatile memory devices [1], transducers and actuators [2], and energy harvesters [3]. Barium titanate ($BaTiO_3$) can be used in many applications due to ferroelectricity, high dielectric constant, and large electro-optic coefficients [4]. RF sputtering, molecular beam epitaxy, sol-gel, and pulsed laser deposition (PLD) can be used for $BaTiO_3$ thin film fabrication. Due to the ability to provide stoichiometric growth of multi-component oxide films in reactive environments PLD is one of the prospective techniques for $BaTiO_3$ thin film fabrication [5].

$BaTiO_3$ nanocrystalline films formed by pulsed laser deposition often have rough relief due to the presence of drop-shaped structures on the surface [6]. This issue is common to a wide range of ferroelectric materials and significantly limits the integration of ferroelectric films with silicon technology. Plasma treatment is one of the possible ways to control the modification of the thin film's surface topography [7]. However, the data on plasma treatment of $BaTiO_3$ is fragmentary. Therefore, understanding the processes involved in the micro- and nanofabrication of multicomponent oxide films requires additional research. Thus, the purpose of the experimental studies was to determine the regularities of the influence of capacitive and inductively coupled plasma sources power on the morphological parameters of nanocrystalline $BaTiO_3$ films.

© Вакулов З.Е., Дзюба Д.А., Шиховцов И.А., Паршина Н.В., Томинов Р.В., Климин В.С., Смирнов В.А., Агеев О.А., 2023. Издатель: Санкт-Петербургский политехнический университет Петра Великого.

## Materials and Methods

$BaTiO_3/SiO_2$ structures fabricated by PLD technique in Pioneer 180 module (Neocera LCC, Beltsville, MD, USA) with a KrF excimer laser ($\lambda = 248$ nm) were used as experimental samples. $BaTiO_3$ target (Kurt J. Lesker) was in a vacuum chamber evacuated to $1\times10^{-6}$ Torr. The films were formed in oxygen atmosphere in the pressure range from $1\times10^{-5}$ Torr to $1\times10^{-2}$ Torr. Substrate temperature, laser power density, and pulse repetition rate were 600 °C, 1.7 J/cm$^2$, and 10 Hz, respectively. The etching process was carried out by plasma-chemical processing of materials in a combined capacitive and inductive discharge plasma in STE ICPe68. The power values of the inductively coupled and capacitive plasma sources ranged from 200 W to 600 W and from 10 W to 40 W, respectively.

The morphology of the obtained films was studied by scanning electron microscopy (SEM) and atomic force microscopy (AFM) in the semicontact mode using a Nova Nanolab 600 scanning electron microscope (FEI.Co, Netherlands) and the Ntegra probe nanolab (NT-MDT-SI, Russia) [8]. In order to correctly determine the depth of etching, a protective plasma-resistant layer was applied to the samples. I-V measurements of the $Si/SiO_2/ITO/ZnO/Ti$ structure was carried out using Probe Nanolaboratory Ntegra (NT-MDT-Si, Russia) [9].

## Results and Discussion

Fig. 1 shows AFM images of $BaTiO_3$ nanocrystalline films obtained under different oxygen pressures.

It was found that the samples obtained at an oxygen pressure of $1\times10^{-5}$ Torr have a fine-grained structure compared to the films obtained at higher oxygen pressures. The average grain size changes from (20.1±1.8) nm to (88.2±7.9) nm with increasing oxygen pressure from $1\times10^{-5}$ Torr to $1\times10^{-2}$ Torr (Fig. 2).

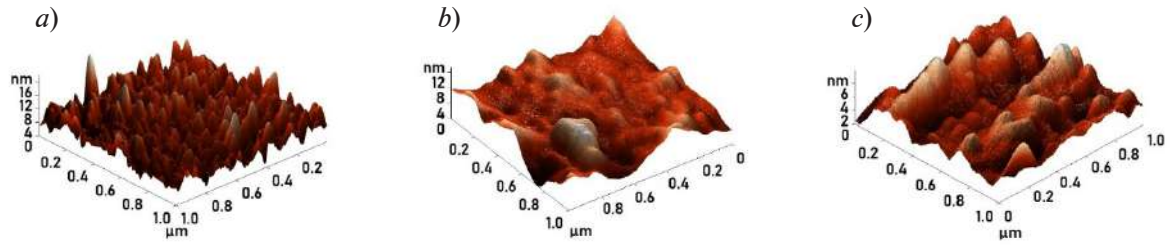


Fig. 1. AFM images of $BaTiO_3$ nanocrystalline films fabricated under different oxygen pressure: $1\times10^{-4}$ Torr (*a*), $1\times10^{-3}$ Torr (*b*), and $1\times10^{-2}$ Torr (*c*)

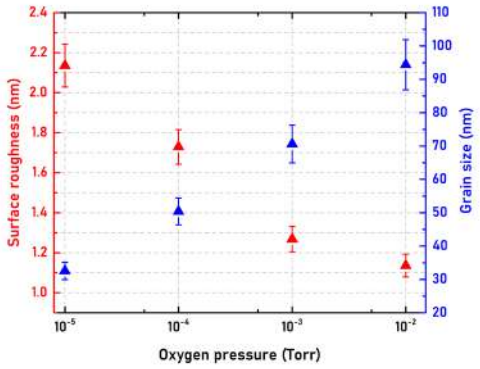


Fig. 2. AFM studies of $BaTiO_3$ nanocrystalline films obtained at different oxygen pressures: surface roughness (red) and grain size (blue)

Thus, at lower oxygen pressures, there is an increase in nucleation density, which leads to the formation of small size grains (Fig. 1), and the reason for the increase in grain size (with increasing oxygen pressure) may be phase separation (formation of clusters on the surface of the film) [10]. In addition, changes in the morphological parameters of the films may be associated with the combined effect of mismatch deformation, the appearance is caused by a mismatch of the crystal lattices of the film and substrate materials and is an indicator of island growth at the initial stage of $BaTiO_3$ film formation [11]. All $BaTiO_3$ films obtained in the pressure range under consideration have a homogeneous structure and no cracks. The surface of $BaTiO_3$ films obtained at an oxygen pressure of $1\times10^{-5}$ Torr is smooth except for small particles, the appearance of which is probably caused by the effect of redeposition of the material from the surface of a heated substrate. As oxygen pressure increases, cluster aggregation is observed due to a decrease in the surface roughness of the films (Fig. 1). In this case, the grain size increases with increasing oxygen pressure since the evaporated particles do not have enough energy to migrate across the substrate surface due to decreased kinetic energy and free path length.

Fig. 3 shows the dependence of the etching depth of $BaTiO_3$ films on the power of inductively coupled and capacitive plasma sources.

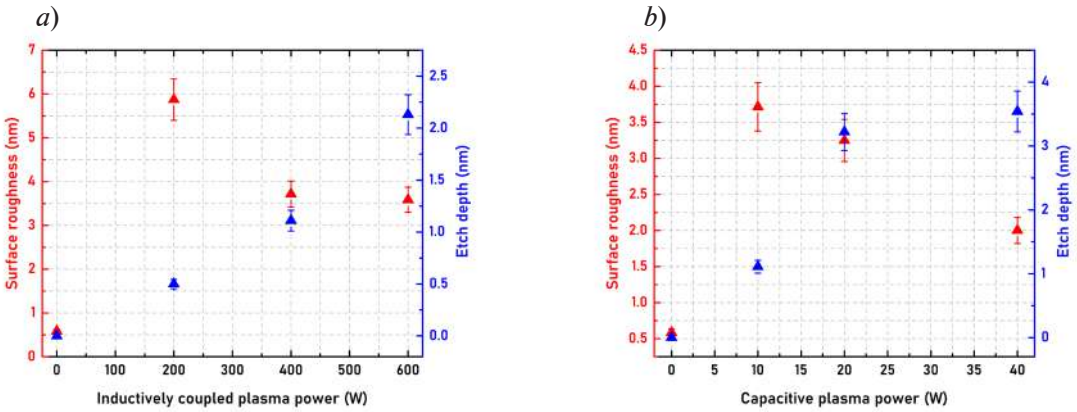


Fig. 3. Dependencies of etch depth (blue) and surface roughness (red) of $BaTiO_3$ nanocrystalline films on power of inductively coupled (*a*) and capacitive (*b*) plasmas

It was found that when the power of the inductively coupled plasma source is increased from 200 W to 600 W, the etching depth of $BaTiO_3$ films increases from (0.52±0.04) nm to (2.14±0.27) nm. When the capacitive plasma power was changed from 10 W to 40 W, the etching depth of $BaTiO_3$ nanocrystalline films increased from (1.1±0.1) nm to (3.5±0.3) nm. The increase in the etching depth can be attributed to the strong influence of the physical component in the etching process when the power of the capacitive plasma source increases.

It was found that the formation of whisker-like structures is a preferred for $BaTiO_3$ films when the power of inductively coupled (from 0 W to 200 W) and capacitive (from 0 W to 10 W) plasma sources increases (Fig. 4), which leads to a sharp increase in surface roughness of $BaTiO_3$ nanocrystalline films from (0.60±0.15) nm to (5.9±0.5) nm when using inductively coupled plasma and to (3.7±0.3) nm when using capacitive plasma.

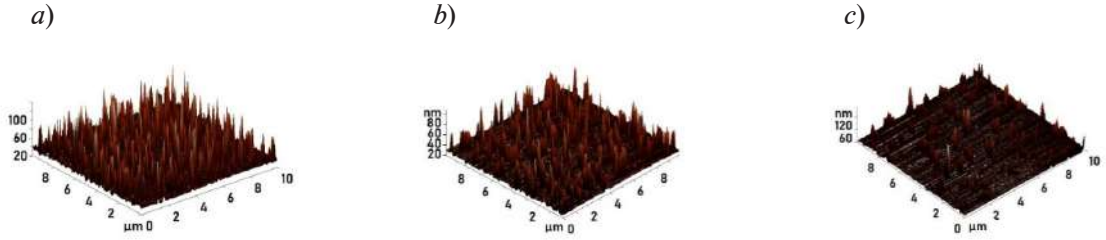


Fig. 4. AFM images of $BaTiO_3$ nanocrystalline films after plasma treatment in inductevely coupled plasma: 200 W (*a*), 400 W (*b*), and 600 W (*c*)

With further increase of plasma source power up to 600 W for inductively coupled plasma and 40 W for capacitive plasma, respectively, a gradual decrease in the surface roughness of $BaTiO_3$ films is observed, which is associated with a decrease in the height and density of nanostructures on the surface of the obtained films.

The I-V sweep in Fig. 5 show bipolar switching characteristic in $BaTiO_3$ nanocrystalline film.

It was found that the obtained $BaTiO_3$ films have a memristive effect. $R_{HRS}/R_{LRS}$ ratio for $BaTiO_3$ films fabricated under $1\times10^{-2}$ Torr was 22, with the low resistance state $R_{LRS} = (0.28\pm0.04)\times10^9$ Ω and high resistance state $R_{HRS} = (6.25\pm0.52)\times10^9$ Ω.

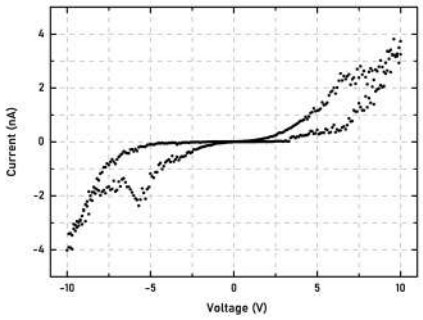


Fig. 5. Current-voltage characteristic of $BaTiO_3$ nanocrystalline film

## Conclusion

It was established that increasing oxygen pressure from $1\times10^{-5}$ Torr to $1\times10^{-2}$ Torr results in an increase in average grain size in the range from (20.1±1.8) nm to (88.2±7.9) nm, and cluster aggregation is observed due to a decrease in the surface roughness of the films. $BaTiO_3$ nanocrystalline thin films have a whisker-like structure after plasma treatment. With the increase in plasma source power up to 600 W for inductively coupled plasma and 40 W for capacitive plasma, a gradual decrease in the surface roughness of $BaTiO_3$ films is observed. The current-voltage characteristic showed a bipolar resistive switching with $R_{LRS} = (0.28\pm0.04)\times10^9$ Ω and $R_{HRS} = (6.25\pm0.52)\times10^9$ Ω. The results can be applied to the design and development of technological processes for promising lead-free energy converters, eco-friendly energy devices, and memristive structure manufacturing based on pulsed laser deposition.

## REFERENCES

1. **Klimin V. S., Tominov R. V., Avilov V. I., Dukhan D. D., Rezvan A. A., Zamburg E. G., Smirnov V. A., Ageev O. A.**, Nanoscale profiling and memristor effect of ZnO thin films for RRAM and neuromorphic devices application, International Conference on Micro-and Nano-Electronics 2018. 11022 (2019) 89–96.

2. **Gao J., Xue D., Liu W., Zhou C., Ren X.**, Recent progress on $BaTiO_3$-based piezoelectric ceramics for actuator applications, Actuators. 3 (6) (2017) 24.

3. **Vakulov Z., Geldash A., Khakhulin D., Il'ina, M. V., Il'in O. I., Klimin V. S., Dzhuplin V. N., Konoplev B. G., He Z., Ageev O. A.**, Piezoelectric energy harvester based on $LiNbO_3$ thin films, Materials. 18 (13) (2020) 3984.

4. **Acosta M., Novak N., Rojas V., Patel S., Vaish R., Koruza J., Rossetti Jr G. A., Rudel J.**, $BaTiO_3$-based piezoelectrics: Fundamentals, current status, and perspectives, Applied Physics Reviews. 4 (4) (2017) 041305.

5. **Vakulov Z., Khakhulin D., Geldash A., Tominov R. V., Klimin V. S., Smirnov V. A., Ageev O. A.**, Impact of laser pulse repetition frequency on nucleation and growth of $LiNbO_3$ thin films, Journal of Advanced Dielectrics. 2 (12) (2022) 2160019.

6. **Liang Y. C., Lee H. Y., Liu H. J., Huang C. K., Wu T. B.**, Real-time X-ray study of roughness scaling in the initial growth of epitaxial $BaTiO_3/LaNiO_3$ superlattices, Journal of crystal growth. 1-2 (279) (2005) 114–121.

7. **Rezvan A. A., Morozova J. V., Klimin V. S.**, Plasma surface treatment of local modify silicon plates, Journal of Physics: Conference Series. 1 (2086) (2021) 012033.

8. **Shandyba N. A., Panchenko I. V., Tominov R. V., Smirnov V. A., Pelipenko M. I., Zamburg E. G., Chu Y. H.**, Size effect on memristive properties of nanocrystalline ZnO film for resistive synaptic devices, Journal of Physics: Conference Series. 8 (1124) (2018) 081036.

9. **Tominov R. V., Smirnov V. A., Avilov V. I., Fedotov A. A., Klimin V. S., Chernenko N. E.**, Formation of ZnO memristor structures by scratching probe nanolithography, IOP Conference Series: Materials Science and Engineering. 1 (443) (2018) 012036.

10. **Kim, K. S., Han, S. H., Kim, J. S., Kim, H. G., Cheon, C. I.**, Effect of working pressure on the properties of $BaTiO_3$-$CoFe_2O_4$ composite films deposited on STO (100) by PLD, Materials Letters. 15 (64) (2010) 1738–1741.

11. **Ahadi K., Mahdavi S. M., Nemati A., Tabesh M., Ranjbar M.**, Electronic structure and morphological study of $BaTiO_3$ film grown by pulsed-laser deposition, Materials Letters. (72) (2012) 107–109.

## THE AUTHORS

**VAKULOV Zakhar E.**
vakulov@ssc-ras.ru
ORCID: 0000-0003-3084-4522

**TOMINOV Roman V.**
tominov@sfedu.ru
ORCID: 0000-0002-1263-2158

**DZYUBA Dmitry A.**
dmdzyuba@sfedu.ru
ORCID: 0000-0002-6028-9518

**KLIMIN Viktor S.**
kliminvs@sfedu.ru
ORCID: 0000-0002-9794-4459

**SHIHOVCOV Ivan A.**
shihovcov@sfedu.ru
ORCID: 0000-0002-0355-9665

**SMIRNOV Vladimir A.**
vasmirnov@sfedu.ru
ORCID: 0000-0001-7130-2194

**PARSHINA Natalia V.**
nparshina@sfedu.ru
ORCID: 0000-0001-5600-5001

**AGEEV Oleg A.**
agevoa@gmail.com
ORCID: 0000-0003-1755-5371

*Received 28.10.2022. Approved after reviewing 09.11.2022. Accepted 10.11.2022.*

© Peter the Great St. Petersburg Polytechnic University, 2023

Conference materials
UDC 621.38-022.532
DOI: https://doi.org/10.18721/JPM.161.238

# Multilevel resistive switching in forming-free nanocrystalline ZnO films for neuromorphic applications

R.V. Tominov[1]✉, I.A. Shikhovtsov[1], D.A. Khakhulin[1], Z.E. Vakulov[2], V.A. Smirnov[1]

[1] Southern Federal University, Taganrog, Russia

[2] Southern Scientific Centre of the Russian Academy of Sciences (SSC RAS), Rostov-on-Don, Russia

✉ tominov@sfedu.ru

**Abstract.** We have experimentally studied the multilevel resistive switching in forming-free nanocrystalline ZnO films. It was shown that potentiation and depression at 0.5 V and –0.5 V for 3000 cycles led to the film resistance increasing by 3 orders of magnitude. In addition, it was shown that ZnO films successfully mimic biological memory through increased pulse number stimulation. Fixing the amplitude of the training pulses makes it possible to achieve different resistive states such as synaptic weight levels of the biological brain. The obtained results can be used for ReRAM elements of neuromorphic artificial intelligence systems fabrication based on forming-free nanocrystalline ZnO films.

**Keywords:** neuromorphic systems, memristor; ReRAM, multilevel resistive switching, forming-free nanocrystalline ZnO, pulsed laser deposition

**Funding:** The reported study was funded by the Russian Foundation for Basic Research according to research project 19-29-03041_mk and project 19-38-60052 (Electrical measurements in forming-free nanocrystalline ZnO film). ZnO thin film samples fabrication was carried out with the financial support of the by grant of the President of the Russian Federation MK6252.2021.4-. Potentiation and depression test was carried out with the financial support of the Russian Federation Government (Agreement 075-15-2022-1123). Investigation of multilevel resistive switching in forming-free nanocrystalline ZnO film was supported by a grant of the Russian Science Foundation 21-79-00216, https://rscf.ru/project/21-79-00216/, in Southern Federal University.

**Citation:** Tominov R.V., Shihovtsov I.A., Khakhulin D.A., Vakulov Z.E., Smirnov V.A., Multilevel resistive switching in forming-free nanocrystalline ZnO films for neuromorphic applications. St. Petersburg State Polytechnical University Journal. Physics and Mathematics. 16 (1.2) (2023) 247–252. DOI: https://doi.org/10.18721/JPM.161.238

This is an open access article under the CC BY-NC 4.0 license (https://creativecommons.org/licenses/by-nc/4.0/)

Материалы конференции
УДК 621.38-022.532
DOI: https://doi.org/10.18721/JPM.161.238

# Многоуровневое резистивное переключение в forming-free нанокристаллических пленках ZnO для нейроморфных приложений

Р.В. Томинов [1]✉, И.А. Шиховцов[1], Д.А. Хахулин[1], З.Е. Вакулов[2], В.А. Смирнов[1]

[1] Южный федеральный университет, Таганрог, Россия

[2] Южный научный центр Российской академии наук (ЮНЦ РАН), Ростов-на-Дону, Россия

✉ tominov@sfedu.ru

**Аннотация.** Мы экспериментально исследовали многоуровневое резистивное переключение в forming-free нанокристаллических пленках ZnO. Было показано, что потенцирование и депрессия при 0,5 В и -0,5 В в течение 3000 циклов привели к

© Tominov R.V., Shihovtsov I.A., Khakhulin D.A., Vakulov Z.E., Smirnov V.A., 2023. Published by Peter the Great St. Petersburg Polytechnic University.

увеличению сопротивления пленки на 3 порядка. Также было показано, что пленки ZnO успешно имитируют биологическую память путем увеличения числа импульсов стимуляции. Фиксация амплитуды обучающих импульсов позволяет достичь различных резистивных состояний, таких как уровни синаптического веса биологического мозга. Полученные результаты могут быть использованы для изготовления элементов ReRAM нейроморфных систем искусственного интеллекта на основе forming-free нанокристаллических пленок ZnO.

**Ключевые слова:** нейроморфные системы, мемристор; ReRAM, многоуровневое резистивное переключение, forming-free нанокристаллический ZnO, импульсное лазерное осаждение

**Финансирование:** Работа выполнена при финансовой поддержке Российского фонда фундаментальных исследований в рамках научно-исследовательского проекта № 19-29-03041_мк и проекта № 19-38-60052 (Электрические измерения в forming-free нанокристаллической пленке ZnO). Изготовление образцов тонкой пленки ZnO проводилось при финансовой поддержке гранта Президента РФ № МК-6252.2021.4. Потенцирование и депрессия пленок ZnO проводились при финансовой поддержке Правительства Российской Федерации (соглашение № 075-15-2022-1123). Исследование многоуровневого резистивного переключения в бесформенной нанокристаллической пленке ZnO проводилось при поддержке гранта Российского научного фонда № 21-79-00216, https://rscf.ru/project/21-79-00216/, в Южном федеральном университете.

**Ссылка при цитировании:** Томинов Р.В., Шиховцов И.А., Хахулин Д.А., Вакулов З.Е., Смирнов В.А. Многоуровневое резистивное переключение в forming-free нанокристаллических пленках ZnO для нейроморфных приложений // Научно-технические ведомости СПбГПУ. Физико-математические науки. 2023. Т. 16. № 1.2. С. 247–252. DOI: https://doi.org/10.18721/JPM.161.238

Статья открытого доступа, распространяемая по лицензии CC BY-NC 4.0 (https://creativecommons.org/licenses/by-nc/4.0/)

## Introduction

In recent years, tasks related to perception, recognition, learning and memory functions have become increasingly important [1–3]. The concept of neuromorphic computing, which mimics the computational primitives of the biological brain, is replacing conventional von Neumann calculations [4–6]. Here, the main functional component is the synapse, which enables the transfer of information between neurons. It is worth noting the extreme complexity of this kind of system, where parallel data processing and information storage take place in a single device consisting of an array of nonvolatile and energy efficient memory elements operating in analog mode [7, 8]. It is important to ensure that any artificial synaptic device correctly recreates the computational primitives of biological synapses before using it in neuromorphic applications. One promising candidate as an element base for neuromorphic systems is non-volatile resistive memory (ReRAM), as it satisfies several important requirements, such as non-volatility, low power consumption and the presence of multiple stable resistive states between the high-resistance and low-resistance states ($R_{HRS}$ and $R_{LRS}$) due to redistribution of oxygen ions and oxygen vacancies in the oxide volume [9, 10]. It is important to note that ReRAM can mimic various biological brain characteristics such as short-term plasticity (STP), long-term plasticity (LTP), spike-rate-dependent plasticity (SRDP), and spike-timing-dependent plasticity (STDP). In addition, ReRAM is bipolar, has a simple metal/dielectric/metal structure, which means it is compatible with conventional semiconductor technology, and offers a high integration density [12, 13].

Various classes of materials such as perovskites, chalcogenides, solid electrolytes, organic compounds, and metal oxides exhibit the memristor effect [14–16]. Among the latter, oxides such as ZnO, $TiO_2$, $HfO_2$, $ZrO_2$, etc. are of particular interest. Literary analysis showed that many scientific publications are devoted to the study of the creation of ReRAM memory elements based on forming-free nanocrystalline ZnO films, largely because this material has only one phase, which

© Томинов Р.В., Шиховцов И.А., Хахулин Д.А., Вакулов З.Е., Смирнов В.А., 2023. Издатель: Санкт-Петербургский политехнический университет Петра Великого.

increases the stability of the neuromorphic systems created. There are many methods for producing metal oxide films, the main ones being atomic layer deposition (ALD), magnetron sputtering, pulsed laser deposition (PLD), etc. [17, 18]. A few studies have shown that ZnO nanocrystalline films grown using PLD exhibit impressive memristor effect parameters, with higher $R_{HRS}/R_{LRS}$ ratios and low operating voltages [19–21]. However, there is still a lack of knowledge in various aspects of the fabrication of ReRAM neuromorphic elements based on this material, such as potentiation and depression processes as well as multi-bit properties, which is the aim of this paper. The results obtained can be used to create ReRAM elements of neuromorphic artificial intelligence systems based on forming-free nanocrystalline ZnO films.

## Materials and Methods

Forming-free nanocrystalline ZnO films were fabricated using a Pioneer 180 pulsed laser deposition system (Neocera LCC, USA) equipped with a KrF excimer laser with a wavelength of 248 nm and an energy of 200 mJ. Silicon wafers with (100) crystallographic orientation was used as substrates. Titanium nitride (TiN) 42.3±5.2 nm films were formed using PLD under the following conditions: substrate temperature 600 °C, number of pulses 30,000, frequency 10 Hz, nitrogen pressure 1 mTorr. Forming-free nanocrystalline ZnO films were prepared on Si/TiN structure under the following conditions: substrate temperature 300 °C, laser frequency 10 Hz, number of pulses: 17,000.

The multilevel resistive switching in forming-free nanocrystalline ZnO films was studied using a Keithley 4200-SCS semiconductor parameter analyser (Keithley Instruments, USA), an EM-6070A submicrometer probe system (Planar, Republic of Belarus), Keithley electrometer/high resistance meter Series 6517B, and Keithley picoammeter/voltage source 6487. MathWorks MATLAB v9.12 (MathWorks, USA) was used for data processing. TiN bottom contact was grounded, and a tungsten probe with diameter about 80 nm was used as the top contact. The compliance current was set to 3 mA to avoid thermal breakdown of the investigated films. As a result, current-voltage curves (CVC) were obtained for the sweep voltage amplitude from 0.5 V to 1.5 V, a potentiation/depression study was performed at 3000 cycles at 0.5 V and –0.5 V, respectively. The resistance dependences on the cycle number were performed at 1000 cycles for the pulse voltage (up) 0.8 V and the read voltage 0.1 V.

## Results and Discussion

Fig. 1 shows the results of experimental studies of electrical measurements in forming-free nanocrystalline zinc oxide films. Analysis of the results obtained showed that an increase in voltage amplitude from 0.5 V to 1.5 V leads to a decrease in the $R_{HRS}/R_{LRS}$ ratio from 100 to 35 (Fig. 1,*a*), to a decrease in $R_{HRS}$ and $R_{LRS}$ from $1.92\times10^6$ Ω to $0.61\times10^6$ Ω and from $19.23\times10^3$ Ω to $16.09\times10^3$ Ω, respectively (Fig. 1,*b*).

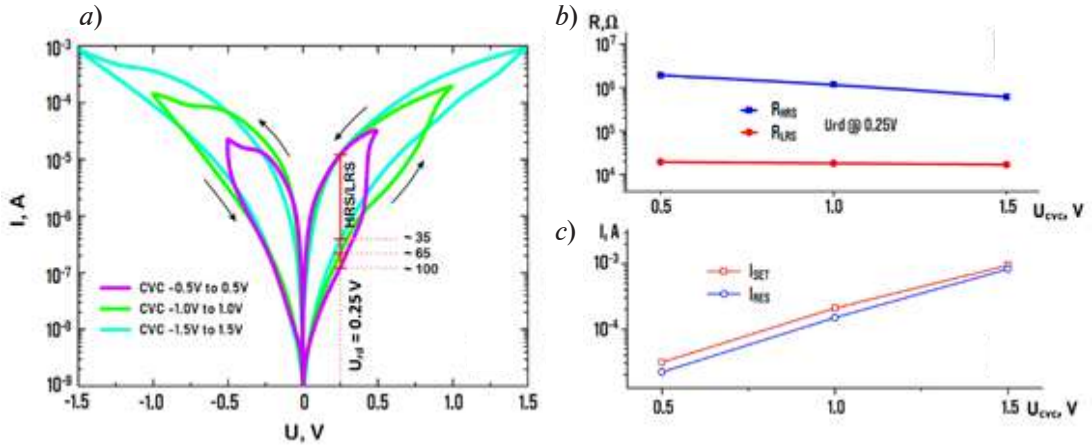


Fig. 1. Electrical measurements in the forming-free nanocrystalline ZnO film: current-voltage characteristic (*a*); dependences of $R_{HRS}$ and $R_{LRS}$ on the CVC voltage amplitude (*b*); dependences of $I_{SET}$ and $I_{RES}$ on the CVC voltage amplitude (*c*)

Additionally, an increase in the amplitude of the CVC voltage from 0.5 V to 1.5 V leads to an increase in $I_{SET}$ and $I_{RES}$ from $0.03\times10^{-3}$ A to $0.92\times10^{-3}$ A and $0.02\times10^{-3}$ A to $0.81\times10^{-3}$ A, respectively. The obtained result can be explained by an increase in the number of electrons due to an increase in the concentration of oxygen vacancies in the bulk of the ZnO film with an increase in the voltage amplitude.

An analysis of the experimental results of the multilevel resistive effect in a forming-free nanocrystalline zinc oxide film showed that the potentiation from 1200 cycles to 1500 cycles led to the film resistance increasing by 3 orders of magnitude. When the polarity of the applied voltage of the training pulse is reversed, the film resistance returns to the initial state from the 1800 cycle to the 1900 cycle. It was shown that potentiation occurs faster than depression because of the different free energies of the metal and the oxide.

Thus, it was shown that the forming-free nanocrystalline zinc oxide film successfully mimics biological memory through increased pulse number stimulation. Fig. 2,*b* shows that fixing the amplitude of the training pulses makes it possible to achieve different resistive states (synaptic weight levels), which is like the biological brain, in which memory changes as the stimulation increases (increasing the number of pulses).

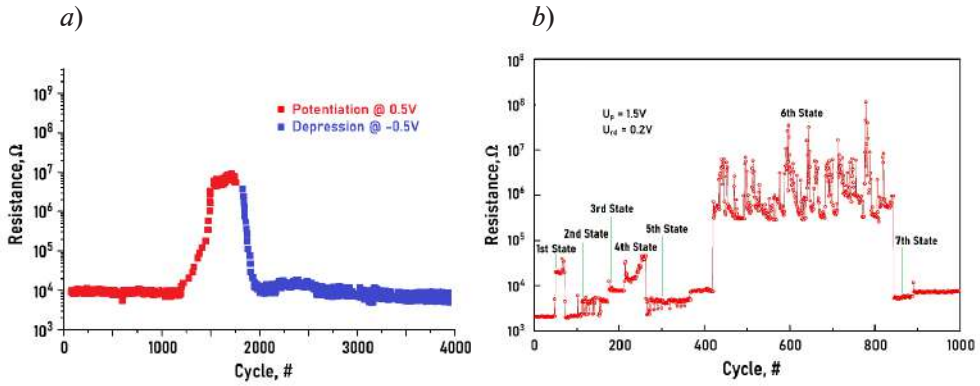


Fig. 2. Resistive switching in forming-free nanocrystalline ZnO film: potentiation and depression (*a*); ZnO film stimulation by training pulses (*b*)

This analog-like behavior with multilevel states is desirable for improving the performance and reliability of a neuromorphic computing systems. The results obtained can be used to create ReRAM elements of neuromorphic artificial intelligence systems based on forming-free nanocrystalline ZnO films.

## Conclusion

In this work, multilevel resistive switching in forming-free nanocrystalline ZnO films has been studied. Potentiation and depression at 0.5 V and –0.5 V for 3000 cycles led to the film resistance increasing by 3 orders of magnitude. It was shown that ZnO films successfully mimic biological memory through increased pulse number stimulation. Fixing the amplitude of the training pulses makes it possible to achieve different resistive states such as synaptic weight levels of the biological brain. The obtained results can be used for ReRAM elements of neuromorphic artificial intelligence systems fabrication based on forming-free nanocrystalline ZnO films.

## REFERENCES

1. **Ismail M., Mahata C., Kim S.,** Forming-free $Pt/Al_2O_3/HfO_2/HfA_1O_x/TiN$ memristor with controllable multilevel resistive switching and neuromorphic characteristics for artificial synapse, Journal of Alloys and Compounds. (892) (2022) 162141.

2. **Dongale T.D., Khot, A.C., Takaloo, A.V., Kim, T.G.,** Facile synthesis of nickel cobaltite quasi-hexagonal nanosheets for multilevel resistive switching and synaptic learning applications, NPG Asia Materials. 13(1) (2021) 1–12.

3. **Das B., Samanta M., Sarkar P., Ghorai U.K., Mallik A., Chattopadhyay K.K.,** Phthalocyanine (CuPc) Based Optoelectronic Memory Device with Multilevel Resistive Switching for Neuromorphic Application, Advanced Electronic Materials. 7(4) (2021) 2001079.

4. **Zhong T., Qin Y., Lv F., Qin H.,** Tian X. Light-activated multilevel resistive switching storage in Pt/Cs2AgBiBr6/ITO/glass devices, Nanoscale research letters. 16(1) (2021) 1–9.

5. **Saini M., Kumar M., Mandal R., Mitra A., Som T.,** Light-activated multilevel resistive switching storage in Pt/Cs2AgBiBr6/ITO/glass devices, Nanoscale research letters. 16(1) (2021) 1–9.

6. **Tominov R.V., Vakulov Z.E., Avilov V.I., Khakhulin D.A., Polupanov N.V., Smirnov V.A., Ageev O.A.,** The effect of growth parameters on electrophysical and memristive properties of vanadium oxide thin films, Molecules. 26(1) (2020) 118.

7. **Tominov R.V., Vakulov Z.E., Polupanov N.V., Saenko A.V., Avilov V.I., Ageev O.A., Smirnov V.A.,** The effect of growth parameters on electrophysical and memristive properties of vanadium oxide thin films, Molecules. 26(1) (2020) 118.

8. **Zou L.,** Multilevel resistive switching performance of TiO2-based flexible memory prepared by low-temperature sol-gel method with UV irradiation, Current Applied Physics. (24) (2021) 32–38.

9. **Swathi S.P., Angappane S.,** Low power multilevel resistive switching in titanium oxide-based RRAM devices by interface engineering, Journal of Science: Advanced Materials and Devices. 6(4) (2021) 601–610.

10. **Patil S.R., Mullani N.B., Kamble B.B., Tayade S.N., Kamat R.K., Park T.J., Dongale T.D.,** Forming-free and multilevel resistive switching properties of hydrothermally synthesized hexagonal molybdenum oxide microrods, Journal of Materials Science: Materials in Electronics. 32(9) (2021) 12490–12502.

11. **Tominov R., Avilov V., Vakulov Z., Khakhulin D., Ageev O., Valov I., Smirnov V.** Forming-Free Resistive Switching of Electrochemical Titanium Oxide Localized Nanostructures: Anodization, Chemical Composition, Nanoscale Size Effects, and Memristive Storage, Advanced Electronic Materials. (2022) 2200215.

12. **Singh R., Kumar M., Iqbal S., Kang H., Kim U., Park J. Y., Seo H.**, Electric Field-Induced Area Scalability toward the Multilevel Resistive Switching, Advanced Materials Interfaces. 8(17) (2021) 2100664.

13. **Shvetsov B.S., Minnekhanov A.A., Emelyanov A.V., Ilyasov A.I., Grishchenko Y.V., Zanaveskin M.L., Demin V.A.**, Parylene-based memristive crossbar structures with multilevel resistive switching for neuromorphic computing, Nanotechnology. 33(25) (2022) 255201.

14. **Ray R., Pal S.K.**, Solution-Processed Photoinduced Multilevel Resistive Switching Devices Based on Lead-Free All-Inorganic Perovskite, IEEE Electron Device Letters. 42(9) (2021) 1284–1287.

15. **Mahata C., Kim S.**, Modified resistive switching performance by increasing Al concentration in $HfO_2$ on transparent indium tin oxide electrode, Ceramics International. 47(1) (2021) 1199–1207.

16. **Fang S.L., Han C.Y., Liu W.H., Li X., Wang X.L., Huang X.D., Geng L.**, Multilevel resistive random access memory achieved by $MoO_3$/Hf/$MoO_3$ stack and its application in tunable high-pass filter, Nanotechnology. 32(38) (2021) 385203.

17. **Yun H.J., Ryu S.Y., Lee H.Y., Park W.Y., Kim S.G., Choi B.J.**, Multilevel operation of $GdO_x$-based resistive switching memory device fabricated by post-deposition annealing, Ceramics International. 47(12) (2021) 16597–16602.

18. **Zhong T., Qin Y., Lv F., Qin H., Tian X.**, Correction to: Light-Activated Multilevel Resistive Switching Storage in Pt/$Cs_2AgBiBr_6$/ITO/Glass Devices, Nanoscale Research Letters. 17(1) (2022) 1–1.

19. **Tominov R.V., Smirnov V.A., Avilov V.I., Fedotov A.A., Klimin V.S., Chernenko N.E.**, Formation of ZnO memristor structures by scratching probe nanolithography, IOP Conference Series: Materials Science and Engineering. – IOP Publishing. (443)1 (2018) 1.

20. **Tominov R.V., Vakulov Z.E., Avilov V.I., Khakhulin D.A., Fedotov A.A., Zamburg E.G., Ageev O.A.** Synthesis and memristor effect of a forming-free ZnO nanocrystalline films, Nanomaterials. 10(5) (2020) 1007.

21. **Smirnov V.A., Tominov R.V., Avilov V.I., Alyabieva N.I., Vakulov Z.E., Zamburg E.G., Ageev O.A.**, Investigation into the memristor effect in nanocrystalline ZnO films, Semiconductors. 53(1) (2019) 72–77.

## THE AUTHORS

**TOMINOV Roman V.**
tominov@sfedu.ru
ORCID: 0000-0002-1263-2158

**VAKULOV Zakhar E.**
zvakulov@sfedu.ru
ORCID: 0000-0003-3084-4522

**SHIKHOVTSOV Ivan A.**
shihovcov@sfedu.ru
ORCID: 0000-0002-0355-9665

**SMIRNOV Vladimir A.**
vasmirnov@sfedu.ru
ORCID: 0000-0001-7130-2194

**KHAKHULIN Daniil A.**
dhahulin@sfedu.ru
ORCID: 0000-0002-0058-0274

*Received 28.10.2022. Approved after reviewing 08.11.2022. Accepted 10.11.2022.*

© Peter the Great St. Petersburg Polytechnic University, 2023

# BIOPHYSICS AND MEDICAL PHYSICS

Conference materials
UDC 532.5, 576.5
DOI: https://doi.org/10.18721/JPM.161.239

## Development of microfluidic devices for experimental study of cell migration activity, use of numerical methods

A.A. Rakhimov [1, 2]✉, A.A. Valiev[1, 2], A.T. Akhmetov[2], K.V. Danilko[1]

[1] Bashkir State Medical University, Ufa, Russia;
[2] Mavlutov Institute of Mechanics UFRC RAS, Ufa, Russia
✉ ragar83@mail.ru

**Abstract.** Assessment of the migration potential of tumor cells, as well as cells of the immune system in tumor foci, is relevant due to the need for highly informative and fast methods for diagnosing and predicting cancer. To study the active movement of cells, a two-level migration cell was developed and fabricated by soft photolithography. It consists of fluid supply channels and two chambers ("gradient" and "storage") 50 μm high, which communicate through "migration" channels 10 μm high. A chemoattractant and nutrient medium were supplied to the "gradient" chamber of the cell. Due to diffusion, mass transfer occurs between the two laminar flows of the chemoattractant and the nutrient medium, a concentration gradient of the chemoattractant is formed perpendicular to the direction of flow, stimulating the movement of cells located in the "storage" chamber. The features of the model are smooth transitions at the junctions of channels and in transition zones; sealed containers of the "storage" chamber, degassing of injected liquids. For cell adhesion, the inner walls of the cell were covered with collagen. With the help of numerical simulation in the Comsol Multiphysics program, taking diffusion into account, the distribution of the velocity field in the supply channels and in the "gradient" chamber was found. The velocities in the center of the channels practically coincide with those obtained during the flow of luminescent latex spherules: 180 μm/s in the supply channels and 150 μm/s in the "gradient chamber". The development of microfluidic devices for monitoring cell migration is an important step towards improving the diagnosis and therapy of cancer.

**Keywords:** cancer cell, microfluidics, migration cell, microchannel, soft photolithography.

**Funding:** The study was supported by a grant from the Russian Science Foundation 22-25-00531, https://rscf.ru/en/project/22-25-00531/.

**Citation:** Rakhimov A.A., Valiev A.A., Akhmetov A.T., Danilko K.V., Development of microfluidic devices for experimental study of cell migration activity, use of numerical methods, St. Petersburg State Polytechnical University Journal. Physics and Mathematics. 16 (1.2) (2023) 253–259. DOI: https://doi.org/10.18721/JPM.161.239

This is an open access article under the CC BY-NC 4.0 license (https://creativecommons.org/licenses/by-nc/4.0/)

© Rakhimov A.A., Valiev A.A., Akhmetov A.T., Danilko K.V., 2023. Published by Peter the Great St. Petersburg Polytechnic University.

Материалы конференции
УДК 532.5, 576.5
DOI: https://doi.org/10.18721/JPM.161.239

# Разработка микрожидкостных устройств для экспериментального изучения миграционной активности клеток, использование численных методов

А.А. Рахимов [1, 2]✉, А.А. Валиев[1, 2], А.Т. Ахметов[2], К.В. Данилко[1]

[1] Башкирский государственный медицинский университет, г. Уфа, Россия;
[2] Институт механики им. Р.Р. Мавлютова УФИЦ РАН, г. Уфа, Россия
✉ ragar83@mail.ru

**Аннотация.** Оценка миграционного потенциала клеток опухоли, а также клеток иммунной системы в опухолевые очаги актуальна в связи с потребностью в высокоинформативных и быстрых методах диагностики и прогнозирования онкозаболеваний. Для изучения активного перемещения клеток разработана и изготовлена методом мягкой фотолитографии двухуровневая миграционная ячейка. Она состоит из подводящих жидкость каналов и двух камер («градиентной» и «накопительной») высотой 50 мкм, которые сообщаются через «миграционные» каналы высотой 10 мкм. К «градиентной» камере ячейки подавались хемоаттрактант и питательная среда. За счет диффузии происходит массообмен между двумя ламинарными потоками хемоаттрактанта и питательной среды, формируется градиент концентрации хемоаттрактанта перпендикулярный направлению течения, стимулирующий движение клеток, расположенных в «накопительной» камере. Особенностями модели являются плавные переходы на стыках каналов и в переходных зонах; герметизированные емкости «накопительной» камеры, дегазация вводимых жидкостей. Для адгезии клеток внутренние стенки ячейки покрывались коллагеном. С помощью численного моделирования в программе Comsol Multiphysics, с учетом диффузии, найдено распределение поля скоростей в подводящих каналах и в «градиентной» камере, скорости в центре каналов практически совпадают с полученными при течении люминесцентных латексных шариков: 180 мкм/с в подводящих каналах и 150 мкм/с в «градиентной камере». Разработка микрожидкостных устройств для наблюдения за миграцией клеток является важным шагом на пути улучшения диагностики и терапии онкологических заболеваний.

**Ключевые слова:** раковая клетка, микрогидродинамика, миграционная ячейка, микроканал, мягкая фотолитография

**Финансирование:** Исследование выполнено за счет гранта Российского научного фонда № 00531-25-22, https://rscf.ru/project/00531-25-22/.

**Ссылка при цитировании:** Рахимов А.А., Валиев А.А., Ахметов А.Т., Данилко К.В. Разработка микрожидкостных устройств для экспериментального изучения миграционной активности клеток, использование численных методов// Научно-технические ведомости СПбГПУ. Физико-математические науки. 2023. Т. 16. № 1.2. С. 253–259. DOI: https://doi.org/10.18721/JPM.161.239

Статья открытого доступа, распространяемая по лицензии CC BY-NC 4.0 (https://creativecommons.org/licenses/by-nc/4.0/)

## Introduction

Currently, microfluidics is widely used in various fields of biology and medicine. Microfluidic devices are used in foreign studies as an effective tool for creating micromodels of cancer cell extravasation [1], studying intercellular interactions, including at the level of the tumor microenvironment [2], and properties of single cells [3]. Despite progress in the development of new drugs and treatments, metastatic cancer remains an incurable disease and one of the leading causes of death in the world [4]. A hallmark of the process of metastasis is the ability of cancer cells to migrate from the primary tumor to distant sites in the body. Currently, there are no effective methods for assessing the metastatic potential of cancer cells, which leads to delayed diagnosis of aggressive forms of cancer or the choice of suboptimal treatment methods [5].

© Рахимов А.А., Валиев А.А., Ахметов А.Т., Данилко К.В., 2023. Издатель: Санкт-Петербургский политехнический университет Петра Великого.

## Materials and Methods
### Development of a migration cell

To study the features of the movement of cancer cells, a two-level migration chamber was made, the prototype of which was the microfluidic cell in [6]. Its schematic view is shown in Fig. 1, and is also given in our previous work [7].

It consists of fluid supply channels, two chambers ("gradient" and "storage") 50 μm high, which communicate through "migration" channels 10 μm high, different widths from 10 to 50 μm and 200 μm long, and cylindrical holes in polydimethylsiloxane (PDMS) with a depth of 5 mm and a diameter of 3 mm, the hole diameter is 6 mm (Fig. 1). Chemoattractant solutions and nutrient medium were supplied to the "gradient" chamber of the cell by hydrostatic pumps. Due to diffusion, mass transfer occurs between the two laminar flows of the chemoattractant and the nutrient medium, a concentration gradient of the chemoattractant is formed perpendicular to the direction of flow, stimulating the movement of cells located in the "storage" chamber.

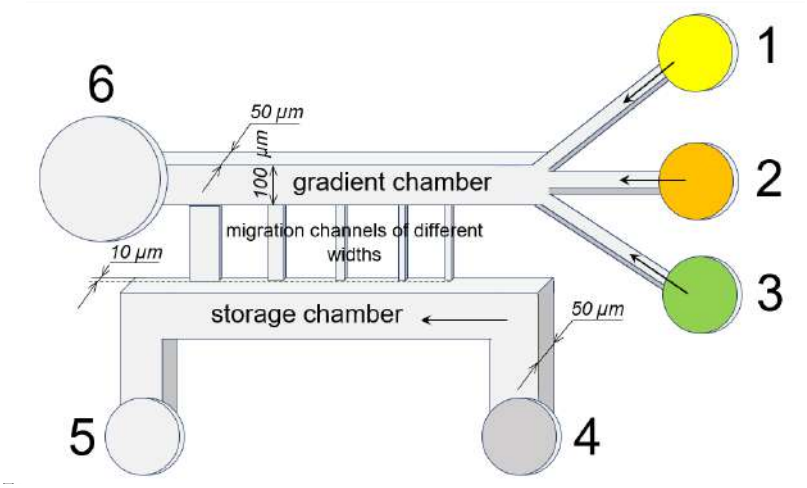


Fig. 1. Schematic representation of a migration cell. 1, 2, 3, 4 are inlets for chemoattractant (1), nutrient medium (2, 3) and cancer cells (4); 5, 6 are outlet holes

When conducting experiments with cells, a number of methodological difficulties were discovered related to the action of capillary forces, the release of gas bubbles from supplied liquid media, and the effect of dynamic blocking [8]. The flow through the stepwise constriction of a suspension containing cancer cells in a nutrient medium, when passing from the inlet container to the microchannel, led to the accumulation of cells at the inlet before the constriction, which practically did not allow the cells to reach the accumulation area in front of the "ladder" being the system of migration channels. The capillary pressure of liquids in the reagent inlet holes with a diameter of 3 mm exceeds the hydrostatic pressure (5 mm w.c.). This prompted us to change slightly the design of the migration cell.

Our two-level migration chamber was made using 2 masks. On one mask there are migration channels through which it is planned to study cell migration, 10 μm high and of various widths, and on the other mask there are supply channels with gradient and storage chambers 50 μm high. For the manufacture of the mask, a vector drawing was developed for printing on a high-resolution printer. The migration chamber mask pattern used in previous experiments [7] has been slightly modified. To prevent the accumulation of microbubbles and cancer cells at the microchannel inlet, the cylindrical containers in the photoresist layer were replaced with containers with a smooth transition, all holes have a smooth expansion, and the junction of the supply channels is rounded. In the middle of storage chamber, an expanded container was made (Fig. 2), due to which the speed drops and the cells are better fixed. Fig. 2 shows the mask alignment area, where it was necessary to combine the second mask with migration channels under the microscope with the first mask at the manufacturing stage. For the convenience of combining the masks, marks were applied, which are clearly visible under a microscope.

Fig. 2. Place where the storage chamber is combined with the mask of migration channels, 3 pieces of the same width (in microns) from left to right: 10, 15, 25, 50, 25, 15, 10

**Migration cell fabrication technique**

Migration cells are designed and manufactured by soft photolithography. According to it, a photoresist was applied to the glass, the layer thickness of which determined the depth of the resulting microchannels, and the photoresist was exposed through the fabricated photomask. The exposed areas became insoluble (negative photoresist) and were used to replicate microchannels in polydimethylsiloxane (PDMS). Since, in our case, the microfluidic device is two-level: the thickness of narrow microchannels ("ladders") is 10 ± 2 μm, and the thickness of the rest of the cell (supply channels) is 50 ± 5 μm, the fabrication was carried out in 2 stages. At the first stage, using a mask of migration channels, a photomask was made on conductive ITO glass (glasses with good adhesion). After obtaining the photomask, it was heated on a tile at 250 °C for 10 minutes with slow cooling for better fixation to the glass, and also so that the developed protrusions serving as a photomask for migration channels darkened and were visible through the photoresist layer during further manufacturing. Further, at the second stage, a photoresist was poured onto the photomask from above, and using the mask for the supply channels, ledges were made on the glass with a thickness of 50 μm. Due to the dark color of the channels, visible through the photoresist layer and the applied marks, it was convenient under a microscope to combine the place of the mask with the expansion of the storage chamber with the protrusions of the migration channels revealed at the first stage (Fig. 2). When washing, both illuminated areas with protrusions of different heights were preserved. Further, using the method of soft photolithography, based on a two-level photomask, a replica was obtained from the solidified PDMS with channels of correspondingly different depths: 10 μm for migration channels and 50 μm for the rest of the cell. After that, holes 3 mm in diameter were made in PDMS with a thickness of 5 mm for containers, and then a replica of PDMS was attached to a glass slide, the microcell was ready. In microfluidic devices, glass and PDMS with replica channels are transparent, which allows the use of imaging techniques. To create conditions for cell adhesion, the channel walls were covered with collagen, which serves as an extracellular matrix.

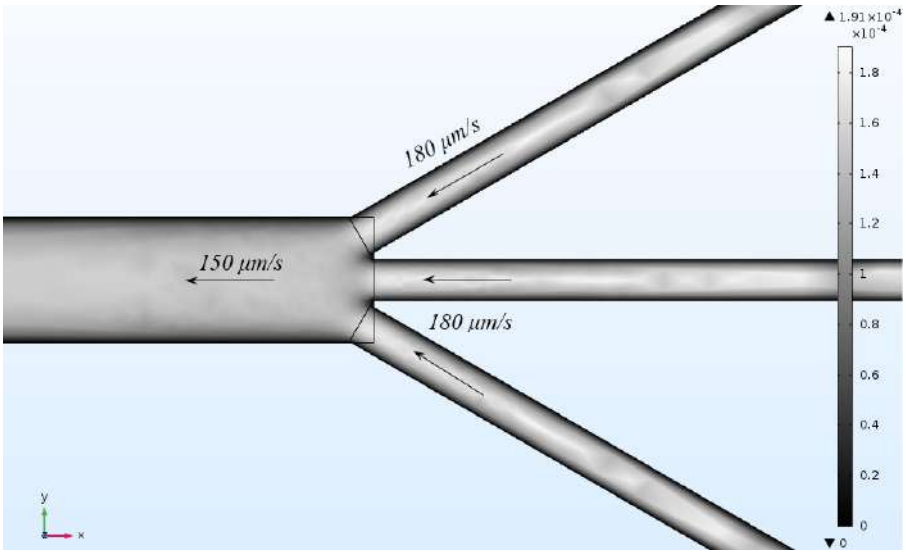


Fig. 3. The distribution of the velocity field in numerical simulation in the Comsol Multiphysics program

## Results and Discussion

### Preparation for the experiment in the migration cell

Cell migration in the cell was studied under a microscope on a thermostatic table with a temperature of 37 °C; under such conditions, the supplied liquid from the input containers and the output container evaporated for 3 hours. An attempt to manufacture chambers for the cell, even with a polycarbonate thermal pack, was not successful, since liquid condensed on the upper surface. Therefore, cone tips from a 1 ml dispenser with a liquid volume of 0.3 ml were used, one of which was filled with DMEM (or RPMI 1640) medium with a chemoattractant, and the other with only a nutrient medium, a cone was also fixed into the outlet. To reduce evaporation, the cone was covered with a "parafilm" film, in which a 500-micron hole was made to equalize the pressure with atmospheric pressure. After filling the storage chamber containers with cells, they were filled with a nutrient solution; the cell container was sealed with a "parafilm" film pressed against a glass plate. Since there is a rather significant difference between the temperature of the liquids in the cones (25 °C) and in the microchannels of the cell (37 °C), gas bubbles were released in the microchannels during heating. In order to avoid bubbling, the inlet liquids were degassed.

Migration cells were tested with distilled water, water with dye or with latex micron spherules. The liquid was supplied due to the pressure difference between the liquid levels in the inlet and outlet containers, which are a hydrostatic pump 5 mm of water column (50 Pa). To test the flow and determine the diffusion erosion of the boundary between tinted and pure water, a blue dye and luminescent latex spherules 1 μm in diameter were used. The boundary between the colored and uncolored laminar jets was blurred due to diffusion in the area in front of the migration channels ("ladder"). During the passage from the confluence of liquids from three supply channels to the beginning of the "ladder" (12 seconds), diffusion mixing led to the formation of a concentration gradient.

The results of numerical simulations obtained in the Comsol Multiphysics program (Fig. 3) showed that the flow velocities corresponded to 180 μm/s at the point where the nutrient medium and chemoattractant were supplied (three supply channels) and 150 μm/s in the widest part of the microchannel. An analysis of the measurement of particle velocities according to video recording using a Canon XM-2 camera mounted on a Zeiss Stemi 2000C microscope give similar values for the flow velocity of liquids.

### Experimental study of the migration activity of cancer cells in a two-level cell

The procedure for preparing the migration cell for the experiment on cell migration was similar to that presented earlier in our work [7] where we used DU145 cell lines. In this work we used cell lines PC-3 (obtained from bone metastasis of a patient with stage IV prostate adenocarcinoma) and HGF (hepatocyte growth factor) chemoattractant. In the presence of HGF the cell lines in the Boyden chamber showed greater migratory activity than in the presence of IL8 (interleukin 8) [7].

Cells in the microfluidic migration system were observed using an AxioObserver D1 inverted microscope (Zeiss, Germany) with A-Plan ×20 and ×10 objectives using the phase contrast method. Microphotography was carried out using an AxioCam MRc5 digital camera (Zeiss, Germany) with ZEN software (Zeiss, Germany). To describe the nature of movements, frame-by-frame shooting of cells was carried out for 2–8 hours with an interval of 5 minutes with ×10 or ×20 lenses. An experiment was carried out on the movement of the PC-3 cancer line. Before the start of the experiment, the cells were located at the entrance to the migration channels.

Fig. 4 shows the displacement of one of the PC-3 cells depending on time. The photographs show that the cell moves at different speeds, and accelerates closer to the exit from the migration channel, which is most likely due to a higher concentration of the chemoattractant at the exit. First, after entering a narrow 15 μm channel, the cell spreads out, the speed in the time interval of 120-180 minutes (Fig. 4) was 16 μm/hour. Then, in the area of 180–240 minutes, the cell speed was 30 microns/hour. In the last section of 250–255 minutes, the speed was 950 microns/hour. The average speed in the area of 120-255 minutes was about 70 microns/hour.

An analysis of the movement of other cells showed that they move at different speeds and also accelerate closer to the exit from the migration channel. The uniqueness of the results obtained is due to the use of the developed new method, which has the ability to study not only the migration characteristics of cells, but also their deformation, which affects movement in spatially constrained conditions under the influence of various types of chemical agents.

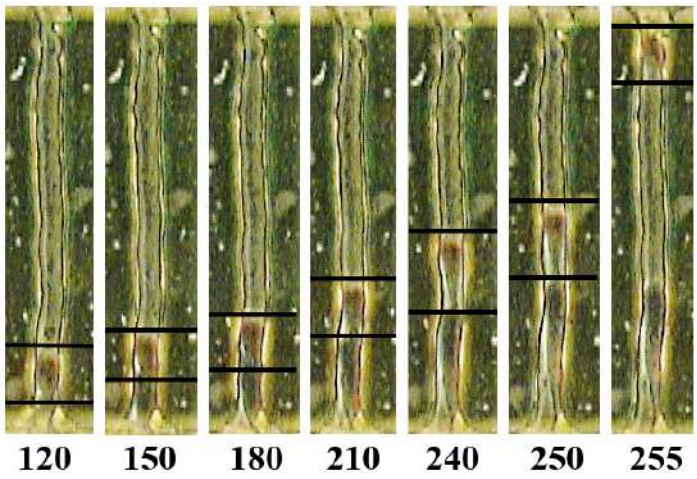


Fig. 4. Microimages of PC-3 cells in the same microchannel 15 μm wide, front and back parts of the examined cell are marked with black lines, the time in minutes from the start of the experiment is shown below the images

## Conclusion

To study the migration potential of cells, a two-level migration cell was developed and fabricated by soft photolithography. The device has been improved compared to the previous one [7], by creating smooth transitions at the channel junctions and transition zones to prevent the dynamic blocking effect associated with the accumulation of microbubbles or cells in the constriction. To reduce the effect of pressure drop when filling the storage chamber with cells, the chamber containers after filling with cells were sealed with a "parafilm" film pressed against a glass plate. To prevent the chemoattractant from getting into other containers and to reduce the effect of capillary forces, cone tips were inserted into the inlet and outlet holes; to reduce evaporation, the cone was covered with a "parafilm" film, in which microscopic holes were made to equalize pressure with atmospheric pressure.

With the help of numerical simulation in Comsol Multiphysics program and taking into account diffusion, velocity field distribution in supply channels and in "gradient" chamber was characterized, velocities in the centre of the channels practically coincide with those obtained by flowing over spherules: 180 μm/s in supply channels and 150 μm/s in the "gradient" chamber.

The ability of PC-3 cancer cells to migrate in the migration microfluidic system developed by us has been experimentally demonstrated. The development of this device is carried out to create a method for accelerated analysis of the migration potential of cancer cells, the differences in the movement of tumor cells compared to normal cells will also allow differentiating healthy and cancer cells. The creation of a device and a method for studying cell migration is an important step towards improving the diagnosis and therapy of oncological diseases.

## Acknowledgments

The study was supported by a grant from the Russian Science Foundation 22-25-00531, https://rscf.ru/en/project/22-25-00531/.

## REFERENCES

1. **Coughlin M.F., Kamm R.D.** The Use of Microfluidic Platforms to Probe the Mechanism of Cancer Cell Extravasation. Advanced Healthcare Materials. 9 (8) (2020) 1901410.

2. **Yu J., Berthier E., Craig A. et al.,** Reconfigurable open microfluidics for studying the spatiotemporal dynamics of paracrine signaling. Nature Biomedical Engineering. 3 (2019) 830–841.

3. **Urbanska M., Mucoz H.E., Shaw Bagnall J. et al.,** A comparison of microfluidic methods for high-throughput cell deformability measurements. Nature Methods. 17 (2020) 587–593.

4. World health organization, data and statistics. URL: http://www.euro.who.int/en/health-topics/noncommunicable-diseases/cancer/data-and-statistics. Accessed Aug. 14, 2020.

5. **Zavadil J., Haley J., Kalluri R., Muthuswamy S.K., Thompson E.,** Epithelial-mesenchymal transition. Cancer Research. 68 (23) (2008) 9574–9577.

6. **Tong Z., Balzer E.M., Dallas M.R., Hung W., Stebe K.J. Konstantopoulos K.** Chemotaxis of Cell Populations through Confined Spaces at Single-Cell Resolution. PLoS ONE. 7 (1) (2012) e29211.

7. **Rakhimov A.A., Akhmetov A.T., Valiev A.A., Danilko K.V., Sametov S.P., Khismatullin D.B.,** To the issue of the mechanism of cell migration. Multiphase Systems. 14 (1) (2019) 17–26.

8. **Akhmetov A.T., Sametov S.P., Rakhimov A.A., Latypova D.R., Khanova M.D., Dokichev V.A.,** Dynamic blocking phenomenon of water-in-oil emulsion solutions based on emulsifier-stabilizer for water-in-oil emulsions SET-1. Petroleum engineering. 11 (2) (2013) 64–70.

## THE AUTHORS

**RAKHIMOV Artur A.**
ragar83@mail.ru
ORCID: 0000-0001-6757-463X

**AKHMETOV Alfir T.**
alfir@anrb.ru
ORCID: 0000-0002-5698-0111

**VALIEV Azat A.**
azatphysic@mail.ru
ORCID: 0000-0001-6856-5065

**DANILKO Ksenia V.**
kse-danilko@yandex.ru
ORCID: 0000-0002-4374-2923

*Received 30.09.2022. Approved after reviewing 08.11.2022. Accepted 09.11.2022.*

© Peter the Great St. Petersburg Polytechnic University, 2023

Conference materials
UDC 536-12
DOI: https://doi.org/10.18721/JPM.161.240

# Quasi-particle description of correlations and statistical memory effects in the discrete time dynamics of complex non-physical systems

A.A. Elenev[1]✉, S.A. Demin[1], V.A. Yunusov[1]

[1] Kazan Federal University, Kazan, Russia;

✉ a.elenev6345@gmail.com

**Abstract.** We present the main provisions and ideas of the quasi-particle description concept of the discrete time dynamics of complex non-physical systems, developed within the frameworks of Memory Functions Formalism. The initial signal generated by a complex system is represented as time variations of the quasiparticle movement coordinate in one-dimensional space. The novelty of the proposed concept lies in the derivation of analytical expressions for chains of finite-difference equations relating time correlation functions and statistical memory functions for a sequence of derivatives of the temporal dynamics of the quasiparticle coordinates: velocity, acceleration, energy, energy flow. The proposed concept was tested for the study of correlations and statistical memory effects, as well as relaxation patterns, in the dynamics of neuromagnetic responses of healthy subjects and a patient with photosensitive epilepsy in response to a red-blue flickering stimulus. The results obtained allow establishing informationally significant sensors and the corresponding zones of localization of the human cerebral cortex for the analysis and diagnosis of photosensitive epilepsy._

**Keywords:** complex systems, time series analysis, Memory Functions Formalism, correlations, statistical memory effects, quasi-particle description, neuromagnetic responses, photosensitive epilepsy

**Funding:** This paper has been supported by the Kazan Federal University Strategic Academic Leadership Program (PRIORITY–2030).

**Citation:** Elenev A.A., Demin S.A., Yunusov V.A., Quasi-particle description of correlations and statistical memory effects in the discrete time dynamics of complex non-physical systems, St. Petersburg State Polytechnical University Journal. Physics and Mathematics. 16 (1.2) (2023) 260–269. DOI: https://doi.org/10.18721/JPM.161.240

This is an open access article under the CC BY-NC 4.0 license (https://creativecommons.org/licenses/by-nc/4.0/)

© Elenev A.A., Demin S.A., Yunusov V.A., 2023. Published by Peter the Great St. Petersburg Polytechnic University.

Материалы конференции
УДК 536-12
DOI: https://doi.org/10.18721/JPM.161.240

# Квазичастичное описание корреляций и эффектов статистической памяти в дискретной временной динамике сложных нефизических систем

А.А. Еленёв[1]✉, С.А. Демин[1], В.А. Юнусов[1]

[1] Казанский федеральный университет, г. Казань, Россия;

✉ a.elenev6345@gmail.com

**Аннотация.** Представлены основные положения и понятия концепции квазичастичного описания дискретной временной динамики сложных нефизических систем, развиваемой в рамках формализма функций памяти. На основе техники проекционных операторов Цванцига–Мори получено аналитическое выражение цепочки конечно-разностных уравнений для набора исходных временных корреляционных функций и функций статистической памяти временных вариаций характеристик перемещения квазичастицы в одномерном пространстве. Проведена апробация предложенной концепции к исследованию корреляций и эффектов статистической памяти, а также релаксационных закономерностей в динамике нейромагнитных откликов здоровых испытуемых и пациента с фоточувствительной эпилепсией в ответ на красно-голубой мерцающий стимул.

**Ключевые слова:** сложные системы, анализ временных серий, формализм функций памяти, эффекты статистической памяти, квазичастичное описание, нейромагнитные отклики, фоточувствительная эпилепсия._

**Финансирование:** Работа выполнена за счет средств Программы стратегического академического лидерства Казанского (Приволжского) федерального университета.

**Ссылка при цитировании:** Еленёв А.А., Демин С.А., Юнусов В.А. Квазичастичное описание корреляций и эффектов статистической памяти в дискретной временной динамике сложных нефизических систем // Научно-технические ведомости СПбГПУ. Физико-математические науки. 2023. Т. 16. № 1.2. С. 260–269. DOI: https://doi.org/10.18721/JPM.161.240

Статья открытого доступа, распространяемая по лицензии CC BY-NC 4.0 (https://creativecommons.org/licenses/by-nc/4.0/)

## Introduction

Currently, there is no strictly established definition of a complex system in the scientific literature. In most cases, a complex system is considered as an object consisting of an infinite (huge) number of interacting components. The interaction between the parts of the whole leads to unique properties that only complex systems possess. To describe the evolution and properties of complex physical and nonphysical (biological, social, economic, financial) systems, methods of statistical analysis of time signals are effectively used [1–3]. Conventionally, such methods can be divided into two large groups: methods of analysis in the time domain [4, 5] and spectral methods [6–8], which are used to study the periodic patterns of signals.

The study of the statistical memory effects in complex physical systems involves the use of the Hamiltonian [9]. The operation of statistical averaging is performed using the Gibbs distribution function or the quantum density operator. The evolution of such systems is described by integro-differential equations with infinitesimal time increments. In contrast, the stochastic dynamics of complex non-physical systems is characterized by discrete sequences of observations recorded by recording equipment with a certain discretization step [10, 11]. The discreteness of observational data leads to difficulties in the theoretical description of complex non-physical systems by classical statistical methods with continuous time. In addition, for such systems there is no possibility of representing the Hamiltonian.

© Еленёв А.А., Демин С.А., Юнусов В.А., 2023. Издатель: Санкт-Петербургский политехнический университет Петра Великого.

In this paper, to study correlations and statistical memory effects of complex non-physical systems, we develop the main relations of the Memory Functions Formalism (MFF) for the case of a quasi-particle description. The initial discrete time dynamics of the experimental parameter is presented as a trajectory of the quasiparticle motion. In comparison with the previously obtained relations [6, 8, 12], in this work, for time sequences of quasi-derivatives (velocity, acceleration, energy, energy flow) of fixed parameters of complex systems, for the first-time systems of finite-difference equations are obtained that relate correlation functions and statistical memory functions. This approach allows extracting information not only from the original signals, but also from sequences of quasi-derivatives of a discrete type.

## Methods. Quasi-particle description of complex systems within the framework of Memory Functions Formalism

Previously, in [6, 8, 12], the main provisions of the MFF were outlined, which is a finite-difference generalization of the Zwanzig-Mori formalism [13, 14]. The technique of Zwanzig and Mori projection operators is used in studying the dynamic properties of liquids and phase transitions, describing Brownian motion, calculating transport coefficients, and analyzing anomalous diffusion. Through the efforts of the Kazan scientific school under the guidance of Professor R.M. Yulmetyev, this technique was generalized to consider the discrete temporal dynamics of complex non-physical systems. The direct purpose of these methods is to study the correlations and statistical memory effects in the investigated non-physical complex systems. In this paper, we develop the MFF for the case of a quasiparticle description.

The dynamics of an experimentally recorded parameter of a complex system as a discrete time series is represented as $\{x_j\}$ of the variable $X$:

$$X = \{x(T), x(T+\tau), x(T+2\tau), \ldots, x(T+(N-1)\tau\}, x_j = X(T+j\tau). \quad (1)$$

where $T$ is the initial moment of time, $(N-1)\tau$ is the total signal registration time, $\tau$ is the time step.

For clarity, the analysis of finite-difference quasi-derivatives of different orders of the original time sequence can be reduced to the following analogy. The sequence of observations $x_j$, recorded at time $t = T + j\tau$, can be considered as the "coordinates" of a quasi-particle with an "effective mass" $m^*$, moving in one-dimensional space.

The sequences of quasi-derivatives of a discrete type will be identified with a set of quantities characterizing the motion of a particle: "velocity" $v_j$, "acceleration" $a_j$, "kinetic energy" , "energy flow" $q_j$. To do this, we use the finite difference method.

For example, the sequence of velocity observations $\{v_j\}$would be defined as:

$$\nu = \{\nu_j\} = \{\nu(T), \nu(T+\tau), \nu(T+2\tau), ..., \nu(T+(N-2)\tau)\}, \nu_j = \nu(T+j2),$$
$$\nu_j = \frac{x_{j+1} - x_j}{\tau}. \quad (2)$$

By analogy, sequences of observations are found for acceleration $\{a_j\}$, energy $\{e_j\}$, energy flow $\{q_j\}$. Generalizing the obtained expressions, we represent the dynamics of the recorded parameter of a complex system in the form:

$$\xi = \{\xi(T), \xi(T+\tau), \xi(T+2\tau), ...\}, \ \xi = \{x, v, a, e, q\}. \quad (3)$$

For a discrete process $\xi$, we determine the average value $\langle\xi\rangle$, fluctuations $\delta\xi_j$, and absolute variance $\sigma^2$.

Next, we introduce a set of normalized time correlation functions (TCF) $X(t)$, $V(t)$, $A(t)$, $E(t)$, $Q(t)$ for sequences of observations $\{x_j\}$, $\{v_j\}$, $\{a_j\}$, $\{e_j\}$, $\{q_j\}$.

For example, for a sequence of observations of velocity $\{v_j\}$, TCF is presented as:

$$V(t)=\frac{1}{(N-m-1)\sigma_V^2}\sum_{j=0}^{N-m-2}\delta\nu(T+j\tau)\delta\nu(T+(j+m)\tau),$$
$$\sigma_V^2=\frac{1}{(N-1)}\sum_{j=0}^{N-1}\delta\nu^2(T+j\tau),\ 1\le m\le N-2. \tag{4}$$

When calculating the TCF, the effective mass is reduced by normalization.
The general expression for the TCF, according to expression (3), will have the form:

$$\Xi(t)=\frac{1}{Z}\frac{\sum_{j=0}^{Z-1}\delta\xi(T+j\tau)\delta\xi(T+(j+m)\tau)}{\sigma_\Xi^2}. \tag{5}$$

Using the Zwanzig–Mori projection operator technique, by analogy with [6, 8, 12], we write down the analytical expression for the chain of finite-difference equations for the set of initial TCF $\Xi(t)$ and obtain relations for higher-order memory functions $M_i^{\Xi}(t), i=1,2,...,$ where $\mathbf{\Xi}$ = {*X*, *V*, *A*, *E*, *Q* }:

$$\begin{cases}\dfrac{\Delta\Xi(t)}{\Delta t}=\lambda_1^{\xi}\Xi(t)-\tau\Lambda_1^{\xi}\sum_{j=0}^{m}M_1^{\Xi}(j\tau)\Xi(t-j\tau),\\ \dfrac{\Delta M_1^{\Xi}(t)}{\Delta t}=\lambda_2^{\xi}M_1^{\Xi}(t)-\tau\Lambda_2^{\xi}\sum_{j=0}^{m}M_2^{\Xi}(j\tau)M_1^{\Xi}(t-j\tau),\\ \dfrac{\Delta M_{n-1}^{\Xi}(t)}{\Delta t}=\lambda_n^{\xi}M_{n-1}^{\Xi}(t)-\tau\Lambda_n^{\xi}\sum_{j=0}^{m}M_n^{\Xi}(j\tau)M_{n-1}^{\Xi}(t-j\tau).\end{cases} \tag{6}$$

Here $\lambda_n^{\xi}$ are the eigenvalues of the Liouville quasi-operator $\hat{L}^{\xi}$, $\Lambda_n^{\xi}$ are the relaxation parameters having the dimension of the squared frequency.

The functions and parameters presented in expression (6) can be obtained using orthogonal dynamic variables $\mathbf{W}_n^{\xi}=\mathbf{W}_n^{\xi}(t)$. The variables $\mathbf{W}_n^{\xi}$ are related to the lower ones $\mathbf{W}_{n-1}^{\xi}$ by the following recursive relations:

$$\mathbf{W}_0^{\xi}=A_k^0(0),\ \mathbf{W}_1^{\xi}=\left(i\hat{L}^{\xi}-\lambda_1^{\xi}\right)\mathbf{W}_0^{\xi},\mathbf{W}_2^{\xi}=\left(i\hat{L}^{\xi}-\lambda_2^{\xi}\right)\mathbf{W}_1^{\xi}-\Lambda_1^{\xi}\mathbf{W}_0^{\xi},..., \tag{7}$$

where

$$A_k^0(0)=\{\delta\xi_0,\delta\xi_1,\delta\xi_2,...,\delta\xi_{k-1}\}.$$

To describe the statistical memory effects in complex non-physical systems, a frequency-dependent generalization is used:

$$\varepsilon_i^{\xi}(\nu)=\left\{\frac{\mu_{i-1}^{\xi}(\nu)}{\mu_i^{\xi}(\nu)}\right\}^{\frac{1}{2}}. \tag{8}$$

Here $\mu_i^{\xi}(\nu)$ is the power spectrum of the corresponding $i$th-order memory function $M_i^{\Xi}(t)$:

$$\mu_i^{\xi}(\nu) = \left| \Delta t \sum_{j=0}^{N-1} M_i^{\Xi}(t_j) \cos(2\pi\nu t_j) \right|^2 . \quad (9)$$

It should be noted that the finite-difference kinetic Eqs. (6) obtained above represent a generalization of the statistical theory of irreversible Zwanzig-Mori processes [13, 14] for the case of analyzing breaks in quasi-derivatives of different orders for the dynamics of complex systems.

## Results and Discussion
### Analysis of quasi-derivatives of the dynamics of evoked neuromagnetic activity in the human cerebral cortex

Approbation of the developed method is carried out on the example of the study of the human cerebral cortex neuromagnetic responses (MEG) [15, 16]. MEG signals were recorded by 61 superconducting quantum interference sensors (SQUID) under the influence of a red-blue flickering stimulus for a group of 9 healthy subjects and a patient with photosensitive epilepsy (PSE).

Fig. 1 and Fig. 2 show phase trajectories for dynamic variables $\{\mathbf{W}_0^{\xi}, \mathbf{W}_1^{\xi}\}$ of neuromagnetic responses recorded by the 10th sensor for a healthy subject and patient. In the case of a healthy subject, phase trajectories line up in quasi-periodic spirals. On all graphs, nuclei that are symmetrical with respect to the origin of coordinates are found. Similar structures were found for all members of the control group. In the case of a patient, an increase in the scale of phase trajectories is observed. For example, the stratification of phase trajectories for a patient in comparison with the control group is increased approximately 10 times for the combination $\{\mathbf{W}_0^{x}, \mathbf{W}_1^{x}\}$, 1000 times for $\{\mathbf{W}_0^{q}, \mathbf{W}_1^{q}\}$.

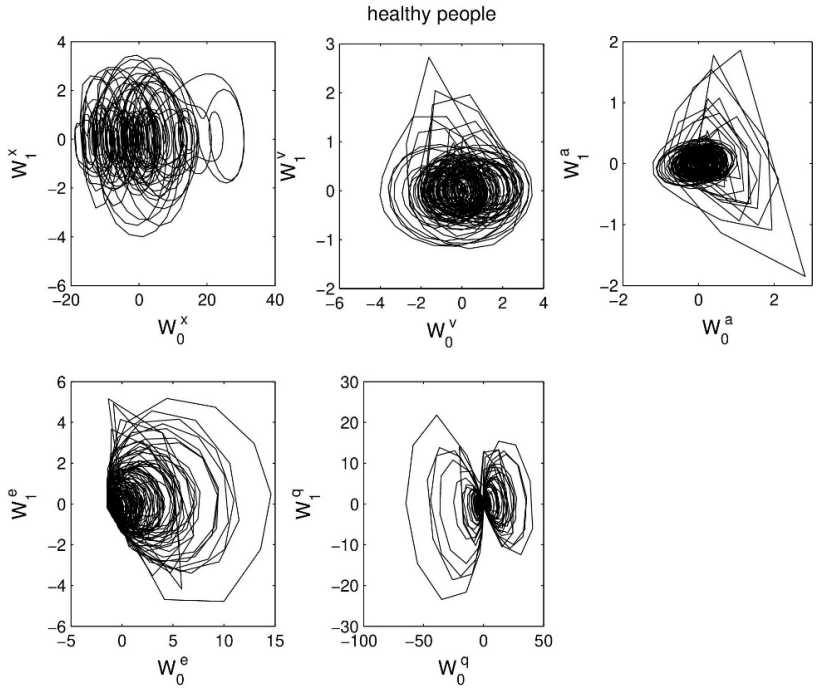


Fig. 1. Phase trajectories of combinations of orthogonal dynamic variables $\{\mathbf{W}_0^{\xi}, \mathbf{W}_1^{\xi}\}$ for the neuromagnetic response recorded by sensor 10 from the cerebral cortex of the seventh healthy subjects under the influence of a red-blue flickering stimulus. Calculation for variations of coordinate $\{x_j\}$, etc.

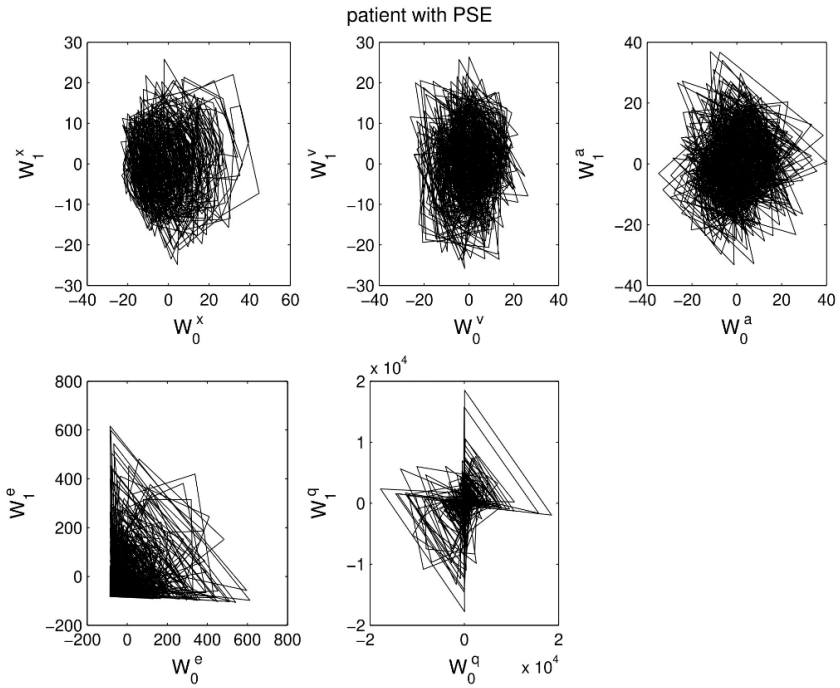


Fig. 2. Phase trajectories of combinations of orthogonal dynamic variables $\left\{\mathbf{W}_0^{\xi}, \mathbf{W}_1^{\xi}\right\}$ for the neuromagnetic response recorded by a 10-sensor from the cerebral cortex of a patient with photosensitive epilepsy when exposed to a red-blue flickering stimulus. Calculation for variations of coordinate $\{x_j\}$, etc.

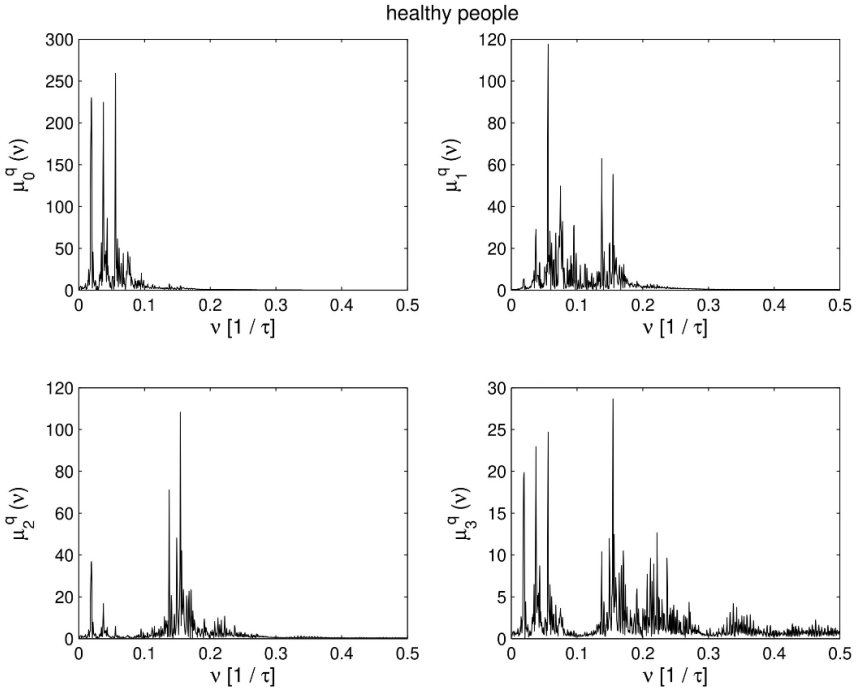


Fig. 3. Power spectra of the initial TCF and memory functions $\mu_i^q(\nu)$ for the neuromagnetic response recorded by sensor 10 from the cerebral cortex of the seventh healthy subjects under the influence of a red-blue flickering stimulus. Frequency dependences are obtained for time variations of the energy flow $\{q_j\}$

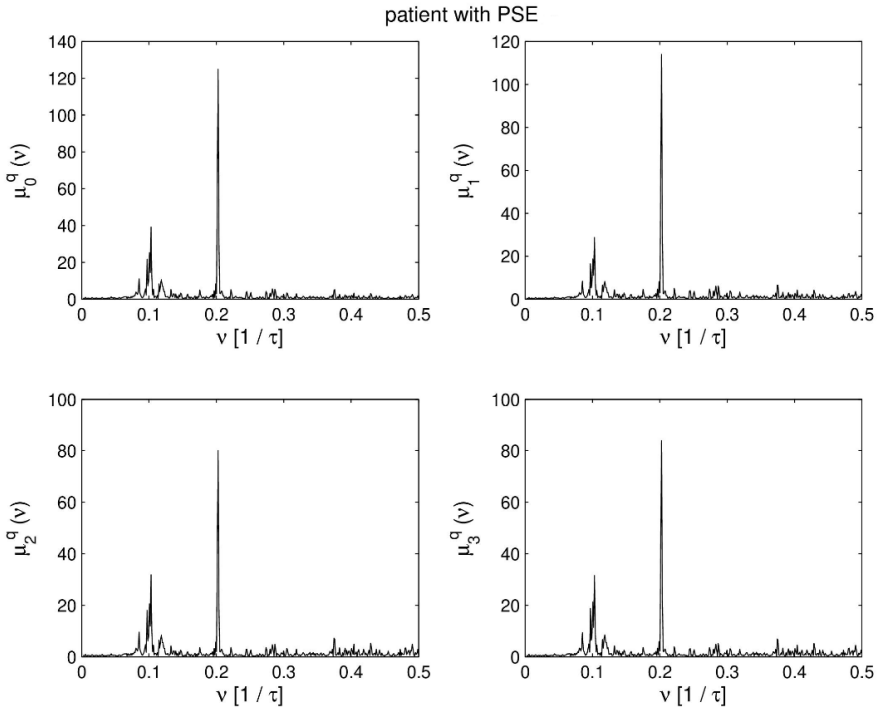


Fig. 4. Power spectra of the initial TCF and memory functions $\mu_i^q(\nu)$ for the neuromagnetic response recorded by the 10th sensor from the cerebral cortex of a patient under the influence of a red-blue flickering stimulus. Frequency dependences are obtained for time variations of the energy flow $\{q_j\}$

Fig. 3 and Fig. 4 show the power spectra of the initial TCF and memory functions $\mu_i^q(\nu)$ for time variations of the energy flow $\{q_j\}$ for neuromagnetic responses recorded by the 10th sensor for a healthy subject and patient. For the power spectrum of the initial TCF of a healthy subject in the region of medium and high frequencies, a fractal dependence $\mu_0^q(\nu) \sim 1/\nu^\alpha$. This indicates the self-similar nature of the MEG signals from healthy subjects. In the low frequency region up to 50 Hz, bursts are observed corresponding to physiological brain rhythms (**α**-, **β**-activity). The power spectra of the memory functions show additional periodic processes in the mid-frequency region. In the case of a patient (Fig. 4), the violation of the fractal dependence is noticeable for the power spectra of the TCF and memory functions over the entire frequency band. Bursts at frequencies of 50 Hz and 100 Hz are dominant. Suppression of normal brain rhythms is a diagnostic criterion for functional disorders in the activity of the patient's cerebral cortex. Exposure to a flickering stimulus provokes abnormal collectivity of neuron activity, for example, in the vicinity of sensor 10.

Fig. 5 shows the frequency dependences of the parameters $\varepsilon_1^e(\nu), \varepsilon_1^q(\nu)$ for the MEG signal of a healthy subject and a patient with PSE under the influence of a flickering stimulus. Visual analysis makes it possible to establish oscillations in the low-frequency region for a healthy subject with resonances characterized by brain rhythms. The values of the parameters $\varepsilon_1^e(0) \approx 4.3,\ \varepsilon_1^q(\nu) \approx 1.8$ for a healthy subject and $\varepsilon_1^{e,q}(0) \approx 1$ for the patient characterize the change in the statistical memory effects in the neuromagnetic activity of the cerebral cortex in pathology. The critical role of statistical memory effects serves as a diagnostic criterion for abnormal activity of neurons near the 10 sensor when exposed to a red-blue flickering stimulus.

Comparative analysis of kinetic $\lambda_1^\xi$ and relaxation parameters $\Lambda_1^\xi$ for MEG signals of a healthy subject and a patient establishes an increase in the decay rate of relaxation processes in pathology. This fact can be explained by the appearance of a significant number of high-frequency resonances in the functional activity of the patient's cerebral cortex in response to exposure to a flickering stimulus.

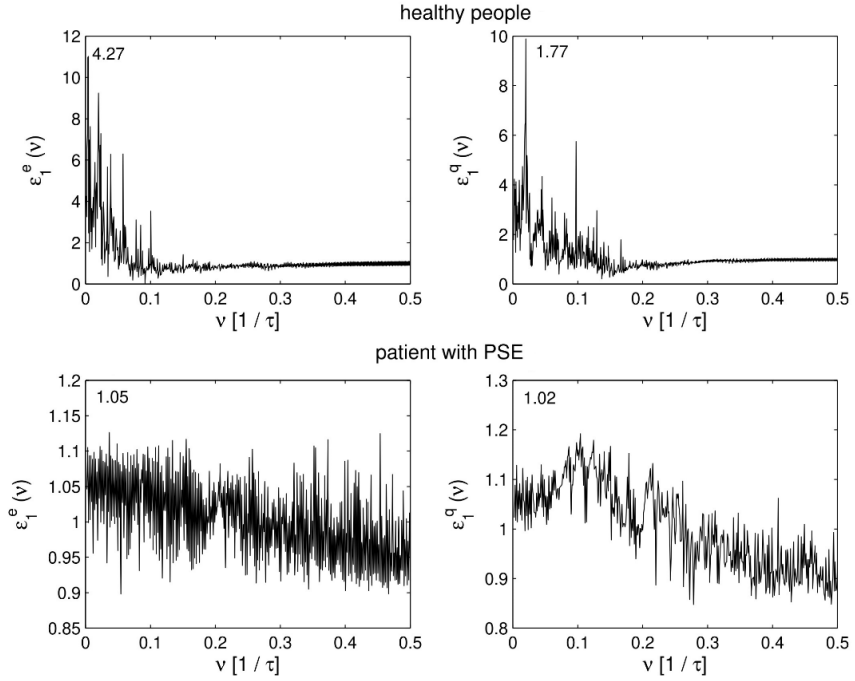


Fig. 5. Frequency dependence of the parameters $\varepsilon_1^e(\nu), \varepsilon_1^q(\nu)$ for the neuromagnetic response recorded by the 10th sensor from the cerebral cortex of the seventh healthy subject and a patient with photosensitive epilepsy when exposed to red-blue flickering stimulus. Frequency dependences are obtained for time variations of energy $\{e_j\}$ and energy flow $\{q_j\}$.
The values of the parameters at zero frequency are numerically presented

## Conclusion

In this paper, we develop the main provisions of the Memory Functions Formalism for the case of studying finite-difference derivatives (velocity, acceleration, energy, energy flow) from initial time signals generated by complex systems of non-Hamiltonian nature. Within the framework of the concept of a quasiparticle description for time sequences of finite-difference derivatives, for the first-time systems of discrete type equations with model representations of statistical memory functions are obtained. The resulting equations determine the normalized time autocorrelation functions, statistical memory functions of different orders, construct their power spectra, calculate orthogonal dynamic variables, kinetic and relaxation parameters, and compare the relaxation times and the existence of memory in the dynamics of finite-difference quasi-derivatives of the original time series. Such a representation allows revealing additional information about spatiotemporal breaks in temporal signals, as well as correlations and memory effects at different levels of statistical description.

The concept was assessed for the analysis of neuromagnetic signals recorded from the cerebral cortex of healthy subjects and a patient with photosensitive epilepsy. The results obtained allow establishing informationally significant SQUIDs (localization of areas of the human cerebral cortex is determined accordingly) for the analysis and diagnosis of photosensitive epilepsy. The development of a quasi-particle description of complex non-physical systems provides effective tools for diagnosing neurological diseases [8, 17, 18], emotional [19, 20] and psychiatric [21, 22] human disorders based on the study of correlation and relaxation features of time dynamics [23–25].

## REFERENCES

1. **Markovsky I., Dörfler F.**, Behavioral systems theory in data-driven analysis, signal processing, and control, Annu. Rev. Control. 52 (2021) 42–64.

2. **Comin C.H., Peron T., Silva F.N., Amancio D.R., Rodrigues F.A., Costa L.F.**, Complex systems: Features, similarity and connectivity, Phys. Rep. 861 (2020) 1–41.

3. **Fan J., Meng J., Ludescher J., Chen X., Ashkenazy Y., Kurths J., Havlin S., Schellnhuber H.J.**, Statistical physics approaches to the complex Earth system, Phys. Rep. 896 (2021) 1–84.

4. **Salcedo-Sanz S., Casillas-Pérez D., Del Ser J., Casanova-Mateo C., Cuadra L., Piles M., Camps-Valls G.**, Persistence in complex systems, Phys. Rep. 957 (2022) 1–73.

5. **Demin S.A., Nefedyev Y.A., Andreev A.O., Demina N.Y., Timashev S.F.**, Non-stationarity and cross-correlation effects in the MHD solar activity, Adv. Space Res. 61 (2018) 639–644.

6. **Panischev O.Y., Demin S.A., Bhattacharya J.**, Cross-correlation markers in stochastic dynamics of complex systems, Physica A. 389 (2010) 4958–4969.

7. **Lahmiri S., Salah Uddin G., Bekiros S.**, Clustering of short and long-term co-movements in international financial and commodity markets in wavelet domain, Physica A. 486 (2017) 947–955.

8. **Demin S.A., Yulmetyev R.M., Panischev O.Y., Hänggi P.**, Statistical quantifiers of memory for an analysis of human brain and neuro-system diseases, Physica A. 387 (8) (2008) 2100–2110.

9. **Piziak R., Mitchell J.**, Hamiltonian formalism and the state of a physical system, Comput. Math. Appl. 42 (2001) 793–805.

10. **Wang X., Lu J., Wang Z., Li Y.**, Dynamics of discrete epidemic models on heterogeneous networks, Physica A. 539 (2020) 122991.

11. **Demin S.A., Panischev O.Y., Nefedyev Y.A.**, Auto- and cross-correlation analysis of the QSOs radio wave intensity, J. Phys. Conf. Ser. 661 (2015) 012003.

12. **Yulmetyev R., Demin S., Emelyanova N., Gafarov F., Hänggi P.**, Stratification of the phase clouds and statistical effects of the non-Markovity in chaotic time series of human gait for healthy people and Parkinson patients, Physica A. 319 (2003) 432–446.

13. **Zwanzig R.**, Memory Effects in Irreversible Thermodynamics, Phys. Rev. 124 (1961) 983–992.

14. **Mori H.**, A Continued-Fraction Representation of the Time-Correlation Function, Prog. Theor. Phys. 34 (1965) 399–416.

15. **Bhattacharya J., Katsumi W., Shinsuke S.**, Nonlinear dynamics of evoked neuromagnetic responses signifies potential defensive mechanisms against photosensitivity, Int. J. Bifurc. Chaos. 14 (8) (2004) 2701–2720.

16. **Bhattacharya J.**, Seeing red: Colour modulation and photosensitive epilepsy, Epilepsy Professional. 18 (2010) 26–29.

17. **Timashev S.F., Polyakov Y.S., Yulmetyev R.M., Demin S.A., Panischev O.Y., Shimojo S., Bhattacharya J.**, Analysis of biomedical signals by flicker-noise spectroscopy: Identification of photosensitive epilepsy using magnetoencephalograms, Laser Phys. 19 (4) (2009) 836–854.

18. **Yulmetyev R.M., Demin S.A., Hänggi P.**, Manifestation of chaos in real complex systems: Case of Parkinson's disease, In: The logistic map and the route to chaos: From the beginnings to modern applications, Understanding Complex Systems, ed. M. Ausloos and M. Dirickx, Springer Science & Business Media, Berlin/Heidelberg. (2006) 175–196.

19. **Wang J., Wang M.**, Review of the emotional feature extraction and classification using EEG signals, Cogn. Robot. 1 (2021) 29–40.

20. **Demin S.A., Panischev O.Y., Demina N.Y.**, Cross MFF–analysis in studying the obsessive-compulsive disorder, J. Phys. Conf. Ser. 741 (2016) 012073.

21. **Tozzi A.**, The multidimensional brain, Phys. Life Rev. 31 (2019) 86–103.

22. **Timashev S.F., Panischev O.Y., Polyakov Y.S., Demin S.A., Kaplan A.Y.**, Analysis of cross-correlations in electroencephalogram signals as an approach to proactive diagnosis of schizophrenia, Physica A. 391 (2012) 1179–1194.

23. **Demin S., Panischev O., Yunusov V., Timashev S.**, The application of statistical methods for the analysis of multi-parameter data of complex composite objects in the field of cyber-physical systems, Stud. Syst. Decis. Control. 350 (2021) 27–38.

24. **Panischev O.Y., Demin S.A., Panischeva S.N., Bhattacharya J.**, How Analyzing the Interictal EEG Can Identify the Epilepsy, Nonlinear Phenom. Complex Syst. 18 (2) (2015) 230–235.

25. **Sobolev M.E., Gorelik A.L., Vlasova O.L.**, A novel physico-mathematical technique of analyzing the quantitative electroencephalograms: development and application, St. Petersburg Polytechnical State University Journal. Physics and Mathematics. 13 (3) (2020) 119–129.

## THE AUTHORS

**ELENEV Alexander A.**
a.elenev6345@gmail.com

**YUNUSOV Valentin A.**
valentin.yunusov@gmail.com
ORCID: 0000-0002-7424-7116

**DEMIN Sergey A.**
serge_demin@mail.ru
ORCID: 0000-0003-3916-7679

*Received 05.10.2022. Approved after reviewing 08.11.2022. Accepted 09.11.2022.*

© Peter the Great St. Petersburg Polytechnic University, 2023

Conference materials
UDC 543.2, 681.2-5, 664.3.032.9
DOI: https://doi.org/10.18721/JPM.161.241

# Intelligent sensor system for ranking the ionic composition of breast milk

A.Yu. Zaitceva[1]✉, M.M. Guzenko[1]

[1] Institute for Analytical Instrumentation, RAS, St. Petersburg, Russia

✉ anna@da-24.ru

**Abstract.** The intelligent sensor system conducts a qualitative and highly accurate medical ranking of breast milk and dairy products based on a personalized approach. It can make the decision-making procedure for medical workers as objective as possible and ensure the implementation of high-quality, effective and safe hardware solutions in the field of artificial intelligence and personalized medicine into medical practice.

**Keywords:** sensory system, breast milk, digital images, biological environment

**Funding:** The study was carried out within the framework of State Task 075-00280-21-00 on the topic "New approaches to the development of analytical systems based on genetic, physico-chemical and immune research methods" SU NIR 0074-2019-0013.

**Citation:** Zaitceva A.Yu., Guzenko M.M., Intelligent sensor system for ranking the ionic composition of breast milk, St. Petersburg State Polytechnical University Journal. Physics and Mathematics. 16 (1.2) (2023) 270–276. DOI: https://doi.org/10.18721/JPM.161.241

This is an open access article under the CC BY-NC 4.0 license (https://creativecommons.org/licenses/by-nc/4.0/)

Материалы конференции
УДК 543.2, 681.2-5, 664.3.032.9
DOI: https://doi.org/10.18721/JPM.161.241

# Интеллектуальная сенсорная система ранжирования ионного состава грудного молока

А.Ю. Зайцева[1]✉, М.М. Гузенко[1]

[1] Институт Аналитического приборостроения РАН, Санкт-Петербург, Россия

✉ anna@da-24.ru

**Аннотация**. Интеллектуальная сенсорная система проводит качественное и высокоточное медицинское ранжирование грудного молока и молочных продуктов на основе персонализированного подхода. Она способна сделать процедуру принятия решений медицинскими работниками максимально объективной и обеспечить внедрение в медицинскую практику качественных, эффективных и безопасных аппаратных решений в области искусственного интеллекта и персонализированной медицины.

**Ключевые слова**: сенсорная система, грудное молоко, цифровые изображения, биологическая среда

**Финансирование**: Исследование выполнено в рамках Государственного задания № 075-00280-21-00 по теме «Новые подходы к разработке аналитических систем на основе генетических, физико-химических и иммунных методов исследования» SU NIR 0074-2019-0013.

**Ссылка при цитировании:** Зайцева А.Ю., Гузенко М.М. Интеллектуальная сенсорная система ранжирования ионного состава грудного молока // Научно-технические ведомости СПбГПУ. Физико-математические науки. 2023. Т. 16. № 1.2. С. 270–276. DOI: https://doi.org/10.18721/JPM.161.241

© Zaitceva A.Yu., Guzenko M.M., 2023. Published by Peter the Great St. Petersburg Polytechnic University.

Статья открытого доступа, распространяемая по лицензии CC BY-NC 4.0 (https://creativecommons.org/licenses/by-nc/4.0/)

## Introduction

The qualitative ionic composition of breast milk is the main factor that determines the fullness of growth, physical and intellectual health of newborns throughout life. The study of a multilevel system of mechanisms that determine and control the ionic composition of milk is an important problem of lactation physiology [1]. Breast milk is a dynamic body fluid; clinical evidence has been presented of changes in the composition of breast milk depending on the changing needs of the infant [2]. Breast milk can also actively stimulate the accelerated development of the newborn's defense systems and suppress excessive inflammation in response to various irritants until the intestine's own immune response develops [3].

The study solves the scientific problem of the complexity of identifying the functional state of the mother-newborn system using standard medical analysis methods. The purpose of this work is fundamental research of a comprehensive solution to the problem of identification and analysis of the state of complex multicomponent biological media: in particular, the qualitative ionic composition of breast milk, based on new intelligent methods of electrochemical analysis. Currently, most medical institutions, due to the lack of the necessary methodological and instrument base, are limited to the subjective interpretation of various types of analyses by medical personnel [4]. Interpretations can vary significantly depending on the specialist studying the results of indirect methods for determining the functional state of the mother-newborn system.

For the first time, a method of noninvasive diagnostics has been developed, it consists in the use of a set of electrochemical sensors with sensitivity to the main significant components of the investigated medium, and analysis using artificial neural-like systems and mathematical methods for processing arrays of multidimensional information, including the method of principal components. The proposed approach differs from existing methods in that it does not require high-precision determination of the content of certain components in biological media, and it is proposed to use a set of sensors that respond to the presence of several components of the analyzed medium at once. The resulting set of multidimensional data requires modern mathematical processing. For this purpose, the machine learning method (the principal component method) is used for data processing.

## Materials and Methods

To solve the problem of controlling the qualitative ionic composition of breast milk, the construction was developed, and the main blocks of the intelligent sensor system were tested [5]. Electrochemical electrodes based on polymer plasticized potentiometric membranes were used as sensors [6]. The polymer base of the membranes in all the membranes was polyvinyl chloride. Di-2-ethylhexylsebacinate, *o*-nitrophenyloctyl ether and 2-fluorophenyl-2-ytrophenyl ether were used as a solvent-plasticizer.

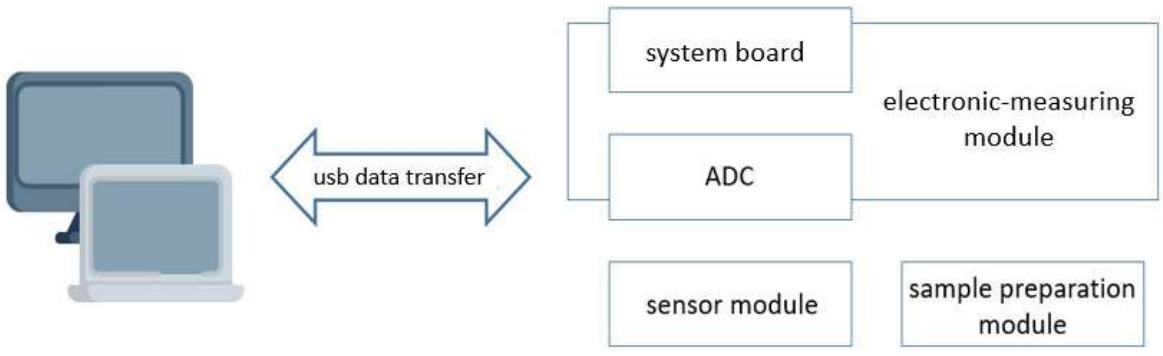


Fig. 1. Block diagram of an intelligent sensor system

© Зайцева А. Ю., Гузенко М. М., 2023. Издатель: Санкт-Петербургский политехнический университет Петра Великого.

The intelligent sensor system consists of two main blocks. The measuring unit includes sample preparation modules, a sensor, a microprocessor-measuring module. The information block includes modules for learning, recognition and visualization of images. The block diagram of the prototype sensor system is shown in Fig. 1.

The sample preparation module includes a device for installing sensors in the test medium, its temperature control and mixing.

The sensor module is represented by a set of polyselective electrochemical sensors with cross-sensitivity to biologically important components.

The learning and recognition module is presented as a mathematical model that implements the training of the system and the recognition of multidimensional "images" formed by the sensor module in the form of arrays of EMF values.

## Experimental studies

At the preparatory phase of the research, the compositions of working solutions for calibration, conditioning, storage of sensors and evaluation of their cross-sensitivity were worked out, as well as methods for preparing sensors for measurement, evaluating their characteristics in control solutions.

The studies were conducted on fourteen female subjects during the second semester of lactation. Also nineteen samples of unpasteurized and whole cow's milk were examined to evaluate and demonstrate the efficiency of the intellectual sensory system for obtaining "digital images" of the milk samples under study and their visual representation. 6 potentiometric polyselective sensors (H+, Na+, K+, NH4+, F+, pH) with cross-sensitivity were used.

## Results and Discussion

*Digital image plotting.*

A visual results representation of two of the most typical subjects during the second semester of lactation is presented in Fig. 2. One of these subjects had a viral infection during the last month of lactation. Visual results are represented in the form of "digital images" of their breast milk: heptahedrons with rays radiating from the center to the points of intersection of the faces. The length of the beam at the points of intersection of the faces corresponds to the result of measurements of the potential generated by each polyselective electrode.

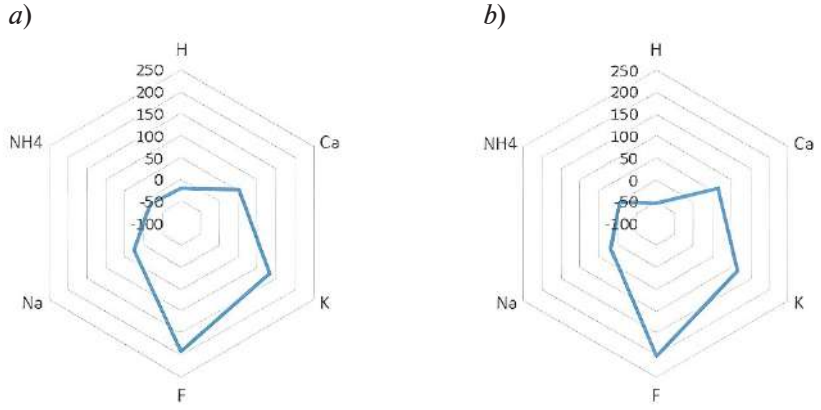


Fig. 2. "Digital images" of breast milk of a healthy woman (*a*) and a woman who has had a viral disease during the last month of lactation (*b*). The readout of electrochemical sensors (sensitive to certain ions) in the content of breast milk are marked on the axes of the radial diagram. It can be noticed that in the breast milk of a healthy woman, the content of hydrogen ions is higher than in the breast milk of a woman who suffered a viral disease in the last month of lactation

Furthermore, "digital images" of breast milk of women who suffered a breast infection during lactation were obtained. The observation of changes in the state of milk before and after taking antibacterial therapy was carried out. Examples of radial diagrams of breast milk in dynamics are shown in Fig. 3.

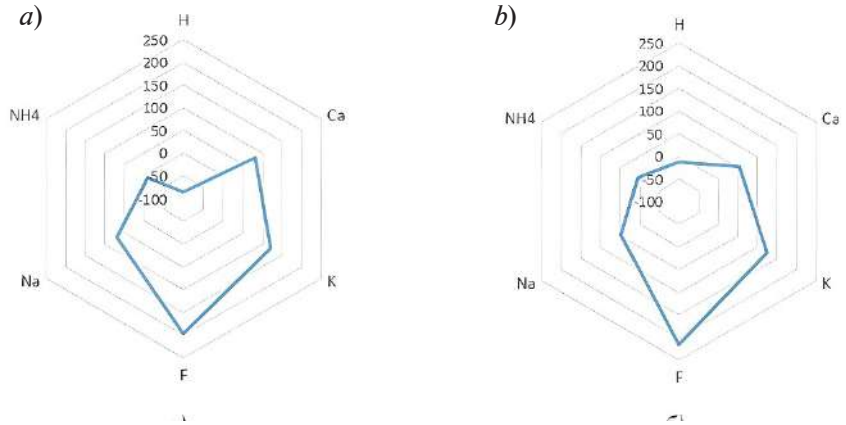


Fig. 3. Visual representation "digital image" of breast milk of a woman with an infectious breast disease before receiving antibacterial therapy (*a*) and after receiving therapy (*b*). The readout of electrochemical sensors (sensitive to certain ions) in the content of breast milk are marked on the axes of the radial diagram. As can be seen from the diagrams, after receiving antibacterial therapy the content of hydrogen ions increased significantly, and a slight increase in the content of fluorine and a decrease in the content of sodium and calcium can also be noted

The results of the conducted studies show that the "digital image" of breast milk of each of the subjects during the second semester of lactation in a healthy state has its own individual characteristics. Diseases modify it. It was found that the "digital images" of breast milk of women who have had diseases differ significantly from the diagrams of breast milk of healthy women. The capabilities of the studied sensory system to form individual "digital images" of the breast milk were used to form algorithms for training the sensory system to recognize the functional state of the mother-newborn system.

**The principal component method.**

Two multidimensional matrices of the form "objects-signs" were formed, where the rows correspond to the test objects, and the columns correspond to the features - the registered numerical standardized readings of each of the seven electrochemical sensors.

The first matrix was made up of breast milk samples, the second matrix contained data from the analysis of ultra-pasteurized and whole cow's milk. Since each test object in the matrix is described by a high-dimension vector, the dimension of the data space should be reduced with minimal loss of their informativeness at the subsequent stage of information analysis [7].

In addition, the task of visualizing multidimensional data was set. Traditionally, dimensionality reduction methods are used for this. Such methods are based on the analysis of the variances of the array data in coordinate directions or methods of finding a vector in the studied multidimensional space, in the direction of which the variance is maximal [8]. Currently, one of the most modern method of solving the problem of compressing amount of information is the principal component method (PCA), which allows the transition from the original coordinate system to a new orthogonal basis in the multidimensional space under consideration [9].

The principal component method is based on the processing of the correlation matrix, namely, the search for eigenvalues and eigenvectors. The selection of the first two components of PC1 and PC2 eigenvectors corresponding to the largest eigenvalues, the construction on the plane (PC1, PC2) as points of "digital images" of milk and the analysis of their relative positions constitute a complete cycle of analysis. The number of components (as well as the sum of all the obtained eigenvalues) is equal to the number of initial features. To calculate the percentage of variance per component, each variance related to each component is divided by the sum of the cumulative total variance for all components. Then the components are discarded so that the proportion of dispersion of the remaining components is 80–90% [10]. All components together make up 100% of the total variance of the initial features.

After calculations, it was found that the first and second main components of PC1 and PC2 together explain 73.1% of the initial data. The visualization of the proportion of the variance explained by different components is shown in Fig. 4.

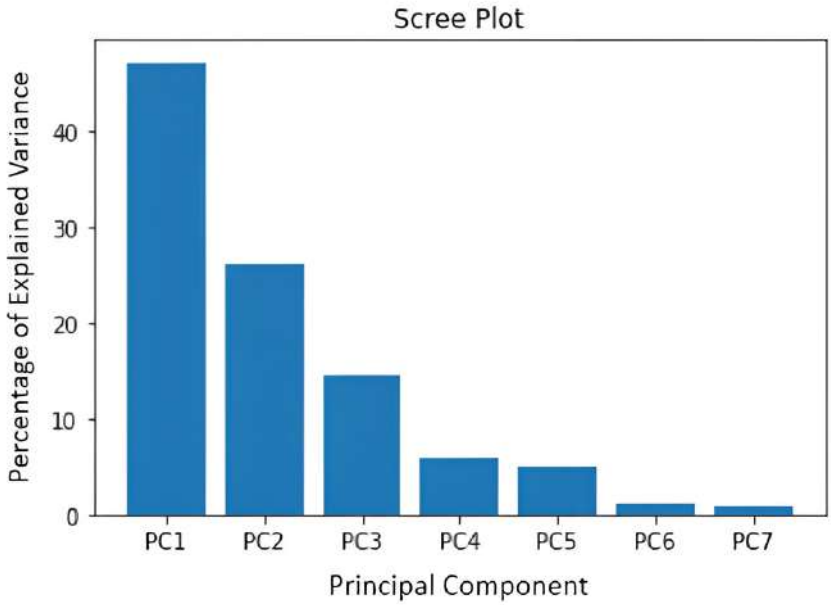


Fig. 4. Contributions of each component to the overall variability of the initial data (features). The first 7 components are presented. The features are registered numerical readings of electrochemical sensors

Obviously, the first and second main components (PC1 and PC2) make the greatest contribution. Thus, only 2 main components can be left.

The observations were visualized in a new space of reduced dimension in the axes of the first two main components. The result is shown in Fig. 5. Each tested biological medium (breast or cow's milk) is characterized by a two-dimensional point in a Cartesian rectangular coordinate system. The resulting point can be attributed to one of the formed clusters.

Fig. 5 shows "digital images" of biological media of breast and cow's milk projected onto the plane of the first two main components, representing the numerical readout of the electrochemical sensors.

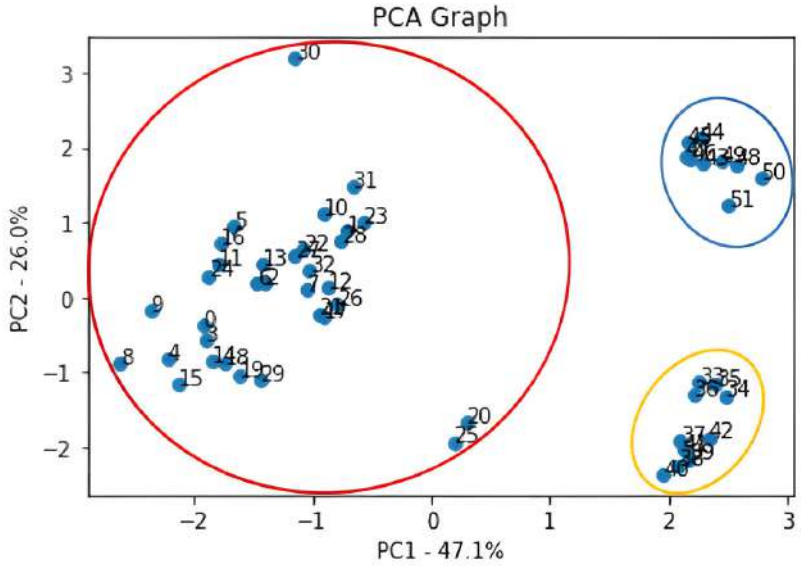


Fig. 5. "Digital images" of biological media of breast and cow's milk projected onto the plane of the first two principal components. The biggest cluster highlighted in red is breast milk, upper blue is whole milk, lower yellow is ultra-pasteurized milk

The cluster highlighted in red is breast milk (milk samples were taken from each subject at the beginning and at the end of feeding), blue is whole milk, yellow is ultra–pasteurized milk.

During the research the following trends were identified:

1. There is a tendency for biological media to group. That indicates their similarity according to certain criteria.

2. The groups of whole and ultra-pasteurized milk are greatly different from each other and from breast milk. This is visually displayed as three different groups of points in the space of the first two main components.

## Conclusion

A model of an intelligent sensor system for imaging biological medium based on the analysis of the output signals of a set of polyselective sensors with cross-sensitivity has been developed, manufactured and tested. It has been experimentally shown that the "digital image" of breast milk of subjects in a healthy state has its own individual characteristics. Diseases modify it. It has been established that the "digital images" of breast milk of women who have had diseases differ significantly from the "digital images" of breast milk of healthy women.

Using of projection methods to build a "digital image" of biological environments is quite promising and allows getting the result in a simple visual form as a set of points on the plane of the first two principal components. The study shows the possibility of ranking milk by similarity groups.

The research results indicate the high efficiency of a new methodological approach to solving the problems of identification and analysis of the state of complex multicomponent biological medium, namely the qualitative ionic composition of breast milk, based on new intelligent methods of electrochemical analysis. The presented intelligent sensor system can be used to create a new generation of diagnostic systems for medical purposes.

## Acknowledgments

The study was carried out within the framework of State Task 075-00280-21-00 on the topic "New approaches to the development of analytical systems based on genetic, physico-chemical and immune research methods" SU NIR 0074-2019-0013.

## REFERENCES

1. **Kislyakova L.P.,** Dynamics of the formation of the water-salt composition of milk. PhD dissertation, St. Petersburg State University. (1996) 33.

2**. Lawrence P.B.**., Breast Milk: Best Source of Nutrition for Term and Preterm Infants, Pediatric Clinics of North America. 41(5) (1994) 925—941.

3.**Walker A.,** Breast Milk as the Gold Standard for Protective Nutrients, J of Pediatrics. 156(2) (2010) S3-S7.

4. **Kislyakova L.P., Bulyanitsa A.L., Kislyakov Yu.Ya., Gulyaev V.I.,** Assessment of the functional state of a person under physical exertion by indicators of exhaled air condensate recorded by polyselective electrochemical sensors using projection methods of multidimensional analysis, J. Scientific Instrumentation. 26(2) (2016) 37—47.

5. **Pechenkina I.A., Mikhelson K.N**., Materials for the ionophore-based membranes for ionselective electrodes: problems and achievements, Russian J. of Electrochemistry. 51(2) (2015) 93—102.

6. **Tenenev V.A., Shaura A.S.,** Application of data dimensionality reduction methods to the construction of fuzzy neural networks, J. Intelligent Systems in Production. 18(4) (2020) 109—116.

7. **Bondarev A.E., Galaktionov V.A.,** Investigation of multidimensional data in multiparametric optimization problems, J. New Information Technologies in Automated systems. 16 (2013) 84—92.

8. **Esbensen K.H.,** Multivariate Data Analysis – in practice 5th ed. (2001) 137—139.

9. **Jolliffe I. T.,** Principal component analysis 2nd ed, New York: Springer Science & Business Media. (2002) 129—155.

## THE AUTHORS

**ZAITCEVA Anna Y.**
anna@da-24.ru
ORCID: 0000-0003-0334-2770

**GUZENKO Maria M.**
maria51m@mail.ru
ORCID: 0000-0003-3116-5812

*Received 25.10.2022. Approved after reviewing 06.12.2022. Accepted 07.12.2022.*

© Peter the Great St. Petersburg Polytechnic University, 2023

Conference materials
UDC 543.51
DOI: https://doi.org/10.18721/JPM.161.242

# Study of exhaled air composition during recovery after respiratory disease by mass spectrometric analysis

A.A. Cherednikova[1]✉, A.G. Kuzmin[1], M.M. Guzenko[1], Yu.A. Titov[1], A.Yu. Zaitceva[1]

[1]Institute for Analytical Instrumentation, RAS, St. Petersburg, Russia

✉ arina4erednikova@yandex.ru

**Abstract.** This article considers the possibility of monitoring recovery after respiratory diseases by mass spectrometric methods. Two groups of test subjects took part in the study: 18 individuals who had had a respiratory viral infection and 31 healthy volunteers in good physical condition. A noninvasive mass spectrometric method of controlling the gas composition of exhaled air was used in the study. The results of the experiment demonstrate the effectiveness of the technique: the differences detected in the mass spectra of healthy people and subjects who had a respiratory viral infection allow the technique to be used to search for pathology markers.

**Keywords:** mass spectrometry, gas composition analysis, exhaled air, acute respiratory viral infection, principal component method

**Funding:** The study was carried out at the Institute for Analytical Instrumentation as part of State Assignment 075-00761-22-00.

**Citation:** Cherednikova A.A., Kuzmin A.G., Guzenko M.M., Titov Yu.A., Zaitceva A.Yu., Study of exhaled air composition during recovery after respiratory disease by mass spectrometric analysis, St. Petersburg State Polytechnical University Journal. Physics and Mathematics. 16 (1.2) (2023) 277–281. DOI: https://doi.org/10.18721/JPM.161.242

This is an open access article under the CC BY-NC 4.0 license (https://creativecommons.org/licenses/by-nc/4.0/)

Материалы конференции
УДК 543.51
DOI: https://doi.org/10.18721/JPM.161.242

# Исследование состава выдыхаемого воздуха в период восстановления после респираторного заболевания методом масс-спектрометрического анализа

А.А. Чередникова[1]✉, А.Г. Кузьмин[1], М.М. Гузенко[1], Ю.А. Титов[1], А.Ю. Зайцева[1]

[1] Институт аналитического приборостроения РАН, Санкт-Петербург, Россия

✉ arina4erednikova@yandex.ru

**Аннотация.** В статье рассматривается возможность мониторинга восстановления после перенесенных респираторных заболеваний методами масс-спектрометрии. В исследовании приняли участие две группы испытуемых: 18 человек, переболевших респираторной вирусной инфекцией, и 31 здоровый доброволец в хорошей физической форме. В исследовании использовалась неинвазивная масс-спектрометрическая методика контроля газового состава выдыхаемого воздуха. Результаты эксперимента показывают эффективность методики: выявленные различия в масс-спектрах здоровых людей и испытуемых, перенесших респираторную вирусную инфекцию, позволяют использовать методику для поиска маркеров патологий.

**Ключевые слова:** масс-спектрометрия, анализ газового состава, выдыхаемый воздух, острая респираторная вирусная инфекция, метод главных компонент

© Cherednikova A.A., Kuzmin A.G., Guzenko M.M., Titov Yu.A., Zaitceva A.Yu., 2023. Published by Peter the Great St. Petersburg Polytechnic University.

**Финансирование:** Работа выполнялась в ИАП РАН в рамках государственного задания 00-22-00761-075.

**Ссылка при цитировании:** Чередникова А.А., Кузьмин А.Г., Гузенко М.М., Титов Ю.А., Зайцева А.Ю. Исследование состава выдыхаемого воздуха в период восстановления после респираторного заболевания методом масс-спектрометрического анализа // Научно-технические ведомости СПбГПУ. Физико-математические науки. 2023. Т. 16. № 1.2. С. 277–281. DOI: https://doi.org/10.18721/JPM.161.242

Статья открытого доступа, распространяемая по лицензии CC BY-NC 4.0 (https://creativecommons.org/licenses/by-nc/4.0/)

## Introduction

Human health and work capacity of individuals are largely determined by metabolic processes in various organs and tissues, the products of which are distributed in various biological media of the body (in cells, blood, exhaled air, urine, etc.) and are indicators of the functional state of the physiological systems of the body. Analysis of the molecular composition of biological media is a possible technology for assessing the degree of deviation of diagnostically significant components from the norm, used for diagnosis, disease prognosis and monitoring the effectiveness of treatment. Human exhaled air contains a wide range of low- and high-molecular weight compounds that change their composition in the presence of pathology. Each person has their own individual "imprint" of the composition of exhaled air, which can be detected by highly sensitive mass spectrometric methods of analysis.

The use of mass spectrometric methods of controlling the gas composition of exhaled air in the diagnosis of diseases will provide a high accuracy of research and rapid analysis results, which is an important criterion in periods of high workload of medical institutions, such as in a pandemic. The method is non-invasive (in contrast to methods requiring the collection of biological material [1]), which also increases the speed and reduces the complexity of sampling, and the lack of the need for special preliminary preparation significantly reduces the likelihood of error in the finished analysis.

The purpose of the work is to implement in practice the new approach proposed earlier [2] to medical and biological research of the functional state of a human by physiologically significant components of exhaled air with the use of mass spectrometric methods of analysis. This will make it possible to determine the presence of respiratory viral infections and, in the future, to identify physiological criteria for the return of workers to work while monitoring the dynamics of recovery after a viral illness.

## Materials and Methods

The composition of exhaled air samples was analyzed on a small-size quadrupole mass spectrometer MS7-200 with direct sample introduction at atmospheric pressure, developed at IAP RAS [2–6].

The analyzed gas at atmospheric pressure is fed into the ionization chamber of the electron impact ion source through a capillary inlet. The resulting ions are injected into a quadrupole mass analyzer. The resulting mass-spectrometric signals are processed using specialized software and compared to spectra in a library of standard mass spectra, then individual spectrum components are identified and their concentrations determined. A heated capillary injection system allows sample flow within a distance of up to 5 meters from the mass spectrometer. The sample flow rate is 2 μl/sec.

Sampling was performed using sampling devices: specially prepared medical syringes with a volume of 20 ml. Predominantly two-component syringes without rubber pistons were chosen. Each sampling device was pre-purified for 3 days. Before sampling, mass-spectrometric checking of the composition of the sampling devices filled with atmospheric air for the absence of background impurities was carried out. The described technique of preparation of sampling devices allows obtaining an accurate undistorted mass-spectrum of the gas composition of the studied sample.

© Чередникова А.А., Кузьмин А.Г., Гузенко М.М., Титов Ю.А., Зайцева А.Ю., 2023. Издатель: Санкт-Петербургский политехнический университет Петра Великого.

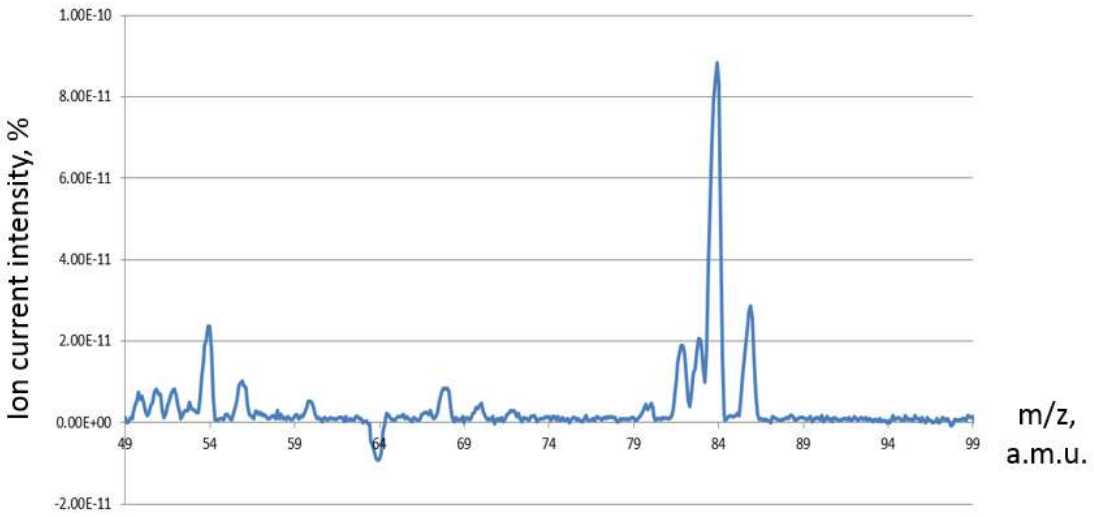


Fig. 1. Mass spectrum of an air sample in the room where exhaled air was collected

Decoding of the mass-spectrum of the analyzed sample allows determining the qualitative composition of the components in the exhaled sample and revealing markers of pathological conditions. The composition of the spectrum can be influenced not only by the subject's health condition, but also by the presence of impurities contained in the atmosphere; therefore, the gas composition of the atmosphere was analyzed before starting the experiment. The resulting mass spectrum obtained during the measurement is the difference of mass spectra of the atmosphere and the sample is shown in Fig. 1.

In mass surveys of public health during a pandemic coronavirus infection, there is usually no prior information about the type of causative agent of the patient. When diagnosing the health status of patients by exhaled air analysis, it is advisable to record the entire spectrum of exhaled gases (disease markers) and then compare it with data from one of the control groups with a known disease.

Table 1

**Comparison table of two subjects from the group of healthy subjects and the group that had had a respiratory viral infection**

| m/z | $I_{ion}$(health) | $I_{ion}$(pathology) |
|---|---|---|
| 53 | 1.70E-11 | 2.17E-12 |
| 55 | –3.98E-13 | 6.14E-12 |
| 56 | 8.10E-12 | 1.07E-11 |
| 57 | 3.16E-13 | 9.58E-12 |
| 58 | 3.95E-11 | 2.20E-11 |
| 60 | 1.39E-11 | 5.11E-12 |
| 67 | 2.63E-11 | 3.62E-12 |
| 68 | 1.52E-11 | -7.01E-13 |

## Experimental studies

49 samples were examined in order to evaluate and demonstrate the performance of the diagnostic system in terms of the ability to obtain mass spectra of the functional state of the subjects and their visual representation.

To work out the methods of experimental study of the effect of viral infection on the subject's mass spectrum, studies of healthy subjects and subjects who had had a viral infection were performed. The samples were taken in the state of physical rest. To create a reference group of healthy subjects, 31 young men aged from 18 to 21 years and the second group of subjects, 18 people with symptoms of respiratory infections from 20 to 50 were recruited and samples were taken during the recovery period after the disease. The subjects were offered a special exhalation technique: deep inhalation, breath-holding for 10 seconds, slow exhalation into the sampling device, involving the lower parts of the lungs. This measurement procedure made it possible to determine the concentration of exhaled air components and form an individual print of each subject.

## Results and Discussion

As a result of the experiment, a preliminary methodology for diagnosing respiratory viral infections was developed, and mass spectra of two groups of subjects were obtained.

Based on the results of the experiment, Table 1 with the masses of substances responsible for the presence or absence of disease was compiled.

The composition of exhaled air of a healthy person contains three main components: isoprene (masses 53, 67, 68), acetone (58), acetic acid (60) [2]. The mass spectra obtained as a result of measurements had significant peculiarities. In the group with symptoms of respiratory viral infection, a significant decrease in the concentration of acetic acid and isoprene was recorded, and some additional components were detected.

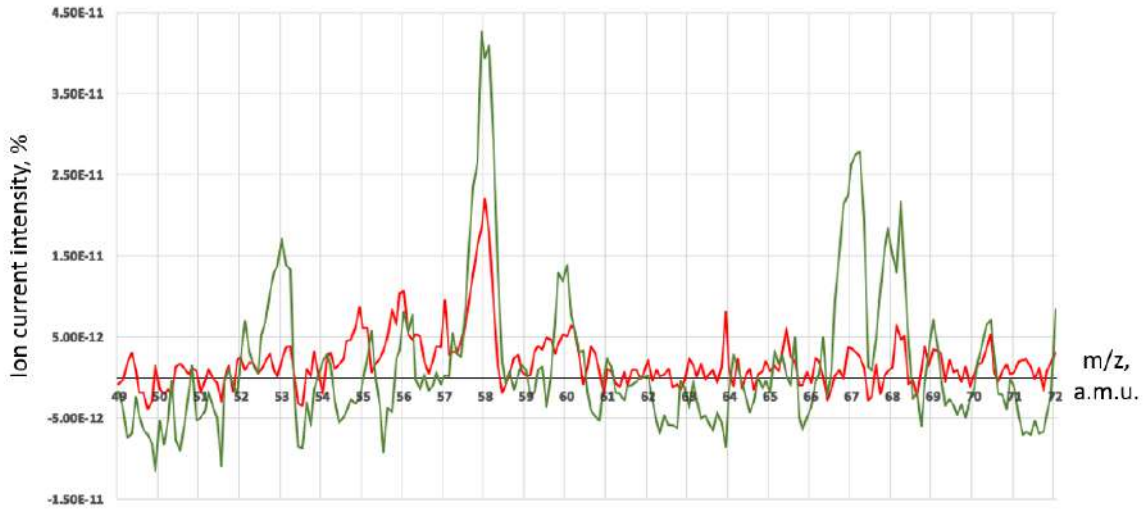


Fig. 2. Two mass spectra are illustrated: of a healthy subject (green line) and of a subject with respiratory viral infection symptoms (red line)

## Conclusion

Thus, the possibility of monitoring recovery from respiratory viral infections using the developed noninvasive high-sensitivity mass spectrometric technique has been shown. Further research in this area is necessary to improve the technique and expand the range of possibilities, such as diagnosis of viral infections in the acute phase.

## REFERENCES

1. **Mazing M.S., Zaitceva A.Y., Kislyakov Y.Y., Davydov V.V., Kondakov N.S., & Avdyushenko S.A.,** Analytical complex for study of the oxygen status of tissues of the human organism. In Journal of Physics: Conference Series (Vol. 1695, No. 1, p. 012065). IOP Publishing. 2020, December.

2**. Kuzmin A., Tkachenko E., Oreshko L., Titov Y. and Balabanov A.**, Medical Academic J. 16 106-107, 2016.

3. **Manoilov V., Kuzmin A. and Titov Y.,** J. of Analytical Chemistry 71(14) 1301–1308, 2016.

4. **Shevchenko A., Kuzmin A., Titov Y.,** Scientific instrumentation 28 62–68, 2018.

6. **Kuzmin A., Titov Y., Suvorov N., Kuropatenko M.,** Scientific Instrumentation 30 84–94, 2020.

7. **Ryabokon A.M., Anaev E.K., Kononikhin A.S., Starodubtseva N.L., Kireeva G.K., Popov I.A., Varfolomeev S.D.,** Comparative proteomic analysis of exhaled breath condensate in patients with lung carcinoma using high resolution mass-spectrometry, Pulmonologiya, (1), 5–11, 2014.

## THE AUTHORS

**CHEREDNIKOVA** Arina A.
arina4erednikova@yandex.ru
ORCID: 0000-0003-4614-7801

**KUZMIN** Aleksey G.
arina_ch@list.ru

**GUZENKO** Maria M.
Maria51m@mail.ru

**TITOV** Yuriy A.
toplm@mail.ru
ORCID: 0000-0002-6970-0916

**ZAITCEVA** Anna Yu.
anna@da-24.ru
ORCID: 0000-0003-0334-2770

*Received 28.10.2022. Approved after reviewing 08.11.2022. Accepted 11.11.2022.*

© Peter the Great St. Petersburg Polytechnic University, 2023

# NUCLEAR PHYSICS

Conference materials
UDC 539.16
DOI: https://doi.org/10.18721/JPM.161.243

## New limit on axion-electron coupling obtained from searching for resonant absorption of solar axions by $^{83}$Kr nuclei

A.V. Derbin[1]✉, I.S. Drachnev[1], A.M. Gangapshev[2], Yu.M. Gavrilyuk[2], V.V. Kazalov[2], V.V. Kuzminov[2], M.S. Mikulich[1], V.N. Muratova[1], D.A. Tekueva[2], E.V. Unzhakov[1], S.P. Yakimenko[2]

[1] Petersburg Nuclear Physics Institute – NRC Kurchatov Institute, Gatchina, Russia;

[2] Institute for Nuclear Research RAS, Moscow, Russia

✉ derbin_av@pnpi.nrcki.ru

**Abstract.** A search for resonant excitation of first nuclear level of $^{83}$Kr nucleus at 9.4 keV by solar axion fluxes that depend on axion-electron coupling constant $g_{Ae}$ have been performed. The search was carried out via gaseous proportional counter that was installed in a low-background experimental setup located at underground facility of Baksan Neutrino Observatory (INR RAS). The measurement yielded new limit on axion-electron coupling constant and axion mass $|g_{Ae}\, m_A| \leq 1.33 \cdot 10^{-9}$ eV.

**Keywords:** solar axion, dark matter

**Funding:** This study was funded by Russian Science Foundation grant number 22-22- 00017.

**Citation:** Derbin A.V., Drachnev I.S., Gangapshev A.M., Gavrilyuk Yu.M., Kazalov V.V., Kuzminov V.V., Mikulich M.S., Muratova V.N., Tekueva D.A., Unzhakov E.V., Yakimenko S.P., New limit on axion-electron coupling obtained from searching for resonant absorption of solar axions by $^{83}$Kr nuclei, St. Petersburg State Polytechnical University Journal. Physics and Mathematics. 16 (1.2) (2023) 282–286. DOI: https://doi.org/10.18721/JPM.161.243

This is an open access article under the CC BY-NC 4.0 license (https://creativecommons.org/licenses/by-nc/4.0/)

Материалы конференции
УДК 539.16
DOI: https://doi.org/10.18721/JPM.161.2

## Новый предел на константу связи аксиона с электроном, полученный в результате поиска резонансного поглощения солнечных аксионов ядром $^{83}$Kr

А.В. Дербин[1]✉, И.С. Драчнев[1], А.М. Гангапшев[2], Ю.М. Гаврилюк[2], В.В. Казалов[2], В.В. Кузьминов[2], М.С. Микулич[1], В.Н. Муратова[1], Д.А. Текуева[2], Е.В. Унжаков[1], С.П. Якименко[2]

[1] Петербургский институт ядерной физики, г. Гатчина, Россия;

[2] Институт ядерных исследований, г. Москва, Россия

✉ derbin_av@pnpi.nrcki.ru

**Аннотация**. Проведен поиск резонансного возбуждения первого ядерного уровня нуклида $^{83}$Kr с энергией 9.4 кэВ потоком солнечных аксионов, образующихся за счет предполагаемого аксион-электронного взаимодействия. Измерения проводились с помощью газонаполненного пропорционального счетчика, установленного в низкофоновой подземной лаборатории Баксанской нейтринной обсерватории (ИЯИ РАН). В результате было получено новое ограничение на константу связи аксиона с электронами и массу аксиона $|g_{Ae}\, m_A| \leq 1.33 \cdot 10^{-9}$ эВ.

© Derbin A.V., Drachnev I.S., Gangapshev A.M., Gavrilyuk Yu.M., Kazalov V.V., Kuzminov V.V., Mikulich M.S., Muratova V.N., Tekueva D.A., Unzhakov E.V., Yakimenko S.P., 2022. Published by Peter the Great St. Petersburg Polytechnic University.

**Ключевые слова:** солнечные аксионы, темная материя

**Финансирование**: Работа выполнена в рамках гранта Российского Научного Фонда № 22-22-00017.

**Ссылка при цитировании:** Дербин А.В., Драчнев И.С., Гаврилюк Ю.М., Гангапшев А.М., Казалов В.В., Кузьминов В.В., Микулич М.С., Муратова В.Н., Текуева Д.А., Унжаков Е.В., Якименко С.П. Новый предел на константу связи аксиона с электроном, полученный в результате поиска резонансного поглощения солнечных аксионов ядром $^{83}$Kr // Научно-технические ведомости СПбГПУ. Физико-математические науки. 2023. Т. 16. № 1.2. С. 282–286. DOI: https://doi.org/10.18721/JPM.161.243

Статья открытого доступа, распространяемая по лицензии CC BY-NC 4.0 (https://creativecommons.org/licenses/by-nc/4.0/)

## Introduction

Intense experimental searches for axions are being motivated by two principal factors. Axion hypothesis was originally designed to solve strong CP-problem in QCD while at the same time axion particles eventually became a well-motivated dark matter candidate. In addition, existence of axions could potentially explain excessive cooling rates of particular stars as well as anomalous transparency of the Universe for high-energy gamma-quanta. Axion interactions with baryonic matter depend on Peccei-Quinn symmetry [1] breaking scale $f_A$ and are defined in terms of effective coupling constants for interactions of axions with photons $g_{A\gamma}$, electrons $g_{Ae}$ and nucleons $g_{AN}$ [2, 3]. Detailed review of theoretical and experimental works in axion field can be found in [4] and references therein.

Stars are expected to be powerful axion sources. Intense axion fluxes can be produced within the Sun due to a number of processes. In particular, axions can appear as a result of electron-nucleus bremsstrahlung $e+Z\rightarrow Z+e+A$, Compton-like process$\gamma+e\rightarrow e+A$or duringatomic de-excitation or recombination. Corresponding axion fluxes $\Phi_{gAe}$ depend on axion-electron coupling $g_{Ae}$ as $\Phi_{gAe}\propto g_{Ae}^2$ and were calculated in [5–9] (see Fig. 1). For this work, we used axion spectrum calculated in [9], which gives the flux value at energy of 9.396 keV (corresponding to the first excited state of $^{83}$Kr) to be equal to $d\Phi/dE = 1.33\cdot10^{11}$ (cm$^2$·s·keV)$^{-1}$ assuming that $g_{Ae} = 10^{-11}$.

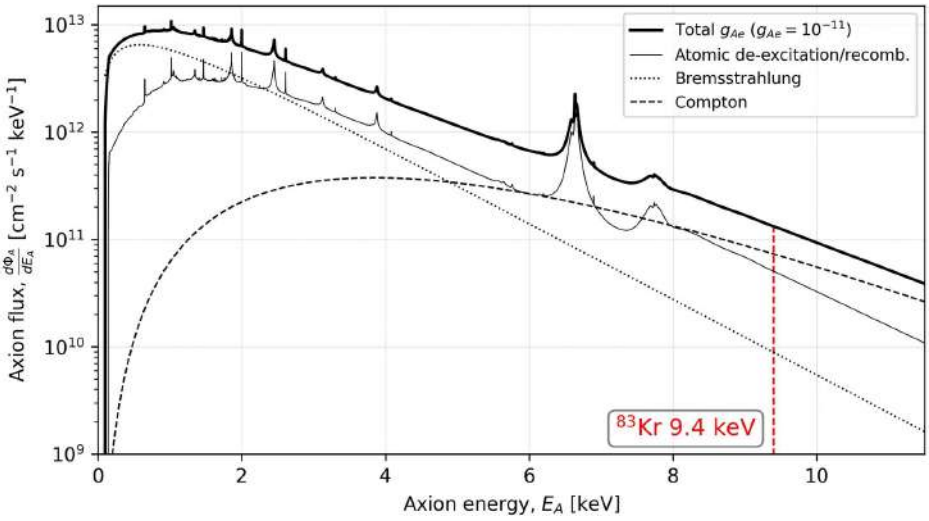


Fig. 1. Spectra of solar axions produced by $g_{Ae}$ related processes calculated assuming $g_{Ae} = 10^{-11}$ for massless axion

© Дербин А.В., Драчнев И.С., Гаврилюк Ю.М., Гангапшев А.М., Казалов В.В., Кузьминов В.В., Микулич М.С., Муратова В.Н., Текуева Д.А., Унжаков Е.В., Якименко С.П., 2022. Издатель: Санкт-Петербургский политехнический университет Петра Великого.

The cross-section of resonant absorption of axion by nucleus is defined in similar fashion to the gamma absorption corrected by ratio between gamma-ray $\omega_\gamma$ or axion $\omega_A$ emitting transition probabilities.

The probability ratio $\omega_A/\omega_\gamma$ depends on isoscalar $g_{AN}^0$ and isovector $g_{AN}^3$ components of axion-nucleon coupling, which can be expressed in terms of axion mass $m_A$ in KSVZ and DFSZ axion models [10, 11].

Expected rate of axion absorption $R_A$ depends on axion flux defined by $g_{Ae}$, and on the cross-section of resonant axion absorption for a given nuclear transition defined by $g_{AN}^0$ and $g_{AN}^3$:

$$R_A = \pi\sigma_{0\gamma}\Gamma\left(d\Phi_A / dE_A\right)\left(\omega_A / \omega_\gamma\right), \tag{1}$$

where $\sigma_{0\gamma}$ is the maximal cross-section for gamma absorption. Experimentally derived value of $\sigma_{0\gamma}$ in case of $^{83}$Kr is $\sigma_{0\gamma} = 1.22\cdot10^{-18}$ cm$^2$. The lifetime of $^{83}$Kr first excited state is $\tau = 223$ ns, thus yielding level width of $\Gamma = 2.95\cdot10^{-12}$ keV.

Consequently, the axion absorption rate $R_A$ expressed in units of (atom·s)$^{-1}$ in model- independent form (i. e. depending exclusively on the values of coupling constants) becomes:

$$R_A = 1.50\times10^{16} g_{Ae}^2\left(g_{AN}^3 - g_{AN}^0\right)^2\left(p_A / p_\gamma\right)^3. \tag{2}$$

Here, $(p_A/p_\gamma)$ is the ratio between momenta of axion and gamma-quanta. Ultimately, by employing the expressions of $g_{AN}^0$ and $g_{AN}^3$ in terms of axion mass $m_A$ described in KSVZ model [2, 3] absorption rate can be presented as a function of $g_A\gamma$ and $m_A$:

$$R_A = 3.53 g_{Ae}^2\left(g_{AN}^3 - g_{AN}^0\right)^2\left(p_A / p_\gamma\right)^3. \tag{3}$$

Total number of registered axion events would depend on the amount of $^{83}$Kr nuclei contained within the target, time of exposure and detector efficiency, while the probability of peak observation at 9.4 keV would be determined by background level of experimental setup.

## Experimental Setup

A dedicated experiment searching for resonant absorption of solar axions by $^{83}$Kr nuclei is underway at Baksan neutrino observatory [10, 11]. The structure of $^{83}$Kr nucleus features a low-lying $7/2^+$ level at 9.4 keV. Magnetic type (M1) transition to the ground state $0^+$ allows for emission or absorption of a pseudoscalar particle. Principal detector construction is based on a copper chamber filled with Kr gas with 99.9% enrichment in $^{83}$Kr isotope. Gaseous counter operates at pressure of 1.8 bar and total mass of $^{83}$Kr gas amounts to 58 g. The chamber is surrounded by passive and active shieldings and is located at underground laboratory with 4900 m of water equivalent overburden. Energy resolution of proportional counter at 9.4 keV is equal to 85%.

## Results and Analysis

The measurements were carried out in separate series during 713 days. The final background spectrum presented in Fig. 2 contains prominent peaks that are associated with Cu and Br characteristic X-rays, and decays of $^{81}$Kr nuclei. Second peak also contains contribution from krypton and bromine X-rays originating from non-sensitive region of the chamber.

Since there is no visible peak within the ROI at 9.4 keV, maximum likelihood method was employed in order to set the upper limit on the number of “axion” events. Analytical description of the spectrum was constructed from Gaussian peaks at fixed known energies and continuous exponential background. The best fit corresponding to the minimum $\chi^2 = 156.7/150$ is shown in Fig. 2 by the solid line.

The determined upper limit on the number of events at 9.4 keV ROI yields the consequent limits on axion couplings $g_{AN}$, $g_{Ae}$ and axion mass $m_A$, in accordance with equations (2, 3). Assuming that momenta ratio $(p_A/p_\gamma)^3 \approx 1$ when $m_A < 2$ keV, one gets:

$$\left|g_{Ae}\left(g_{AN}^3 - g_{AN}^0\right)\right| \le 1.70\cdot10^{-17}, \tag{4}$$

$$\left|g_{Ae} m_A\right| \leq 1.33 \cdot 10^{-9} \text{eV}. \quad (5)$$

The limit (4) is a model-independent bound on couplings of axion (or any other ALP) with electrons and nucleons. The limit (5) sets the region of allowed values in $|g_{A_i}\ m_A|$ parameter space and enables the comparison of current result against other axion experiments (see Fig. 3).

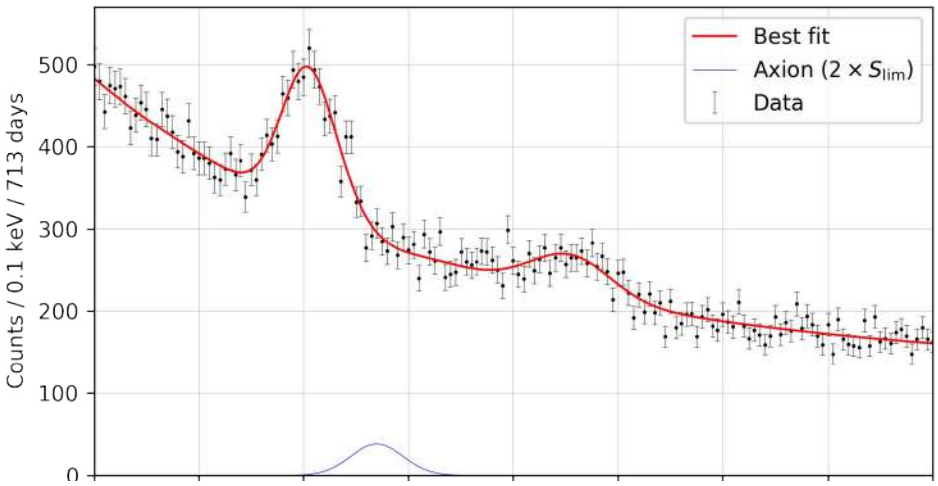


Fig. 2. Spectrum obtained by Kr proportional counter during 713 days and the result of analytical fit. Cu characteristic X-rays (1); $^{81}$Kr decays (2); expected 9.4 keV axion peak (3)

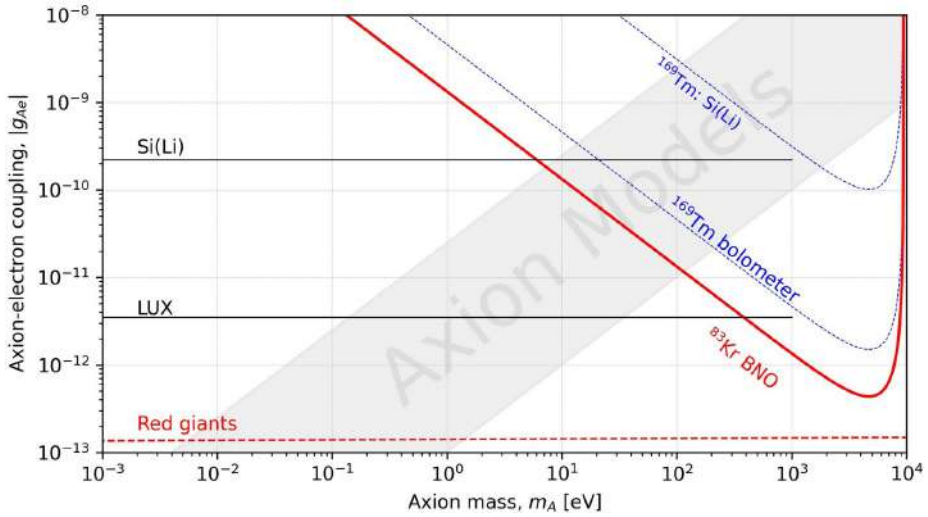


Fig. 3. Upper limits on $g_{Ae}$ coupling constant obtained in current work using $^{83}$Kr proportional counter in comparison with previous experiments: search for axioelectric effect on Si(Li) detector [12], resonant absorption by $^{169}$Tm nucleus [13], LUX experiment [14] and astrophysical bounds [15]

New limit (5) excludes previously unexplored region of $g_{Ae}$ values at relatively high axion masses allowed by KSVZ and DFSZ models and excludes axion masses above $m_A > 120$ eV in terms of KSVZ-axion. Within axion mass range 0.4 keV $< m_A <$ 9 keV the obtained limit on axion-electron coupling is the most stringent among direct laboratory searches and approaches the astrophysical limit of $g_{Ae} \leqslant 1.5 \cdot 10^{-13}$ derived from observation of red giants from a number of globular clusters.

## Conclusion

A search for resonant absorption of solar axions by $^{83}$Kr nuclei leading to excitation of 9.4 keV first nuclear level have been performed. Large proportional counter filled with gaseous $^{83}$Kr was used in order to register X-rays, gammas, conversion and Auger electrons. Low-background experimental setup was located at the underground facility of Baksan neutrino observatory (INR RAS). As the result, a new limit was set on axion-electron coupling and axion mass $|g_{Ae}\, m_A| \leqslant 1.33 \cdot 10^{-9}$.

## REFERENCES


1. **Peccei R.D., Quinn H.R.**, Phys. Rev. Lett., 38(25), (1977) 1440–1443.
2. **Kaplan D.B.**, Nucl. Phys. B, 260, (1985) 215–226.
3. **Srednicki M.**, Nucl. Phys. B, 260 (1985) 689–700.
4. **Zyla P. et al., (Particle Data Group)**, PTEP, 083C01 and 2021 update (2020).
5. **Krauss L.M., Moody J.E., Wilczek F.**, Phys. Lett. B, 144, (1984) 391–394.
6. **Gondolo P., Raffelt G.G.**, Phys. Rev. D, 79(10), (2009) 107301.
7. **Kekez D., Ljubičić A., Krečak Z., Krčmar M.**, Phys. Lett. B, 671, (2009) 345–348.
8. **Derbin A.V., Kayunov A.S., Muratova V.V. et al.**, Phys. Rev. D, 83(2) (2011) 023505.
9. 9. **Redondo J., Raffelt G.**, JCAP, 2013, (2013) 034–034.
10. **Gavrilyuk Y.M., Gangapshev A.N., Derbin A V. et al.** JETP Lett., 101 (2015) 664–669.
11. **Gavrilyuk Y.M., Gangapshev A.N., Derbin A.V. et al.**, JETP Lett., 107 (2018) 589–594.
12. **Derbin A.V., Drachnev I.S., Kayunov A.S. et al.**, JETP Lett., 95 (2012) 339–344.
13. **Abdelhameed A.H., Bakhlanov S.V., Bauer P. et al.**, EPJ C, 80 (2020) 376.
14. **Akerib D.S., Alsum S., Aquino C., et al., (LUX Collaboration)**, Phys. Rev. Lett., 118(26) (2017) 261301.
15. **Straniero O., Pallanca C., Dalessandro E. et al.**, A&A, 644, (2020) A166.


## THE AUTHORS


**DERBIN Alexander V.**
derbin_av@pnpi.nrki.ru
ORCID: 0000-0002-4351-2255

**DRACHNEV Ilia S.**
drachnev_is@pnpi.nrcki.ru
ORCID: 0000-0002-4064-8093

**GAVRILYUK Yuri M.**
gangapsh@list.ru

**GANGAPSHEV Albert M.**
gangapsh@list.ru
ORCID: 0000-0002-6086-0569

**KAZALOV Vladimir V.**
vvk1982@mail.ru
ORCID: 0000-0001-9521-8034

**KUZMINOV Valery V.**
bno_vvk@mail.ru

**MIKULICH Maxim S.**
mikulich_ms@pnpi.nrcki.ru

**MURATOVA Valentina N.**
muratova_vn@pnpi.nrcki.ru
ORCID: 0000-0001-5532-7711

**TEKUEVA Djamilia A.**
gangapsh@list.ru

**UNZHAKOV Evgeniy V.**
unzhakov_ev@pnpi.nrcki.ru
ORCID: 0000-0003-2952-6412

**YAKIMENKO Sergey P.**
yakimenko@inr.ru


*Received 29.09.2022. Approved after reviewing 08.11.2022. Accepted 17.11.2022.*

© Peter the Great St. Petersburg Polytechnic University, 2023

Conference materials
UDC 53.082.79
DOI: https://doi.org/10.18721/JPM.161.244

# Radiation hardness of silicon semiconductor detectors under irradiation with fission products of $^{252}$Cf nuclide

N.V. Bazlov[1,2], A.V. Derbin[1], I.S. Drachnev[1], I.M. Kotina[1], O.I. Konkov[1,3], I.S. Lomskaya[1], M.S. Mikulich[1], V.N. Muratova[1], D.A. Semenov[1], M.V. Trushin[1]✉, E.V. Unzhakov[1]

[1] NRC "Kurchatov Institute"— PNPI, Gatchina, Russia;

[2] St. Petersburg State University, St. Petersburg, Russia;

[3] Ioffe Physical-Technical Institute of the RAS, St. Petersburg, Russia

✉ trushin_mv@pnpi.nrcki.ru

**Abstract.** The influence of the prolonged irradiation by fission products of $^{252}$Cf radionuclide on the operational parameters of silicon-lithium Si(Li) *p-i-n* detectors, Si surface barrier detectors and Si planar $p^+n$ detector was investigated. The obtained results revealed a linear shift of the fission fragment peaks positions towards the lower energies with increase of the irradiation dose for all investigated detectors. The rate of the peaks shift was found to depend strongly on the detector type and the strength of the electric field in the detector's active region, but not on the temperature of irradiation (room or liquid nitrogen temperature). Based on the obtained results, the possibility of integration of the investigated types of Si semiconductor detectors in a radionuclide neutron calibration source is considered.

**Keywords:** silicon detectors, fission fragments, pulse height defect, radiation hardness

**Funding:** The reported study was funded by RFBR, project number 20-02-00571.

**Citation:** Bazlov N.V., Derbin A.V., Drachnev I.S., Kotina I.M., Konkov O.I., Lomskaya I.S., Mikulich M.S., Muratova V.N., Semenov D.A., Trushin M.V., Unzhakov E.V., Radiation hardness of silicon semiconductor detectors under irradiation with fission products of $^{252}$Cf nuclide, St. Petersburg State Polytechnical University Journal. Physics and Mathematics. 16 (1.2) (2023) 287–294. DOI: https://doi.org/10.18721/JPM.161.244

This is an open access article under the CC BY-NC 4.0 license (https://creativecommons.org/licenses/by-nc/4.0/)

© Bazlov N.V., Derbin A.V., Drachnev I.S., Kotina I.M., Konkov O.I., Lomskaya I.S., Mikulich M.S., Muratova V.N., Semenov D.A., Trushin M.V., Unzhakov E.V., 2023. Published by Peter the Great St. Petersburg Polytechnic University.

Материалы конференции
УДК 53.082.79
DOI: https://doi.org/10.18721/JPM.161.244

# Радиационная стойкость кремниевых полупроводниковых детекторов при облучении продуктами деления радионуклида $^{252}$Cf

Н.В. Базлов[1,2], А.В. Дербин[1], И.С. Драчнев[1], И.М. Котина[1], О.И. Коньков[1,3], И.С. Ломская[1], М.С. Микулич[1], В.Н. Муратова[1], Д.А. Семенов[1], М.В. Трушин[1]✉, Е.В. Унжаков[1]

[1] НИЦ «Курчатовский Институт» - ПИЯФ, г. Гатчина, Россия;

[2] Санкт-Петербургский Государственный Университет, Санкт-Петербург, Россия;

[3] Физико-Технический Институт им. А.Ф. Иоффе РАН, Санкт-Петербург, Россия

✉ trushin_mv@pnpi.nrcki.ru

**Аннотация**. Исследовалось влияние длительного облучения продуктами деления радионуклида $^{252}$Cf на параметры работы кремний-литиевых Si(Li) *p-i-n* детекторов, Si поверхностно-барьерных детекторов и Si планарного $p^+n$ детектора. Для всех исследованных типов детекторов был обнаружен линейный сдвиг положения пиков осколков деления в сторону меньших энергий с увеличением дозы облучения. Установлено, что скорость смещения пиков сильно зависит от типа детектора и напряженности электрического поля в активной области детектора, но не от температуры облучения (комнатная или температура жидкого азота). На основании полученных результатов рассматривается возможность применения исследованных детекторов в составе радиоизотопного калибровочного источника нейтронов.

**Ключевые слова**: кремниевые детекторы, осколки деления, амплитудный дефект, радиационная стойкость

**Финансирование**: Работа выполнена при поддержке Российского Фонда Фундаментальных Исследований, номер гранта 20-02-00571.

**Ссылка при цитировании:** Базлов Н.В., Дербин А.В., Драчнев И.С., Котина И.М., Коньков О.И., Ломская И.С., Микулич М.С., Муратова В.Н., Семенов Д.А., Трушин М.В., Унжаков Е.В. Радиационная стойкость кремниевых полупроводниковых детекторов при облучении продуктами деления радионуклида $^{252}$Cf // Научно-технические ведомости СПбГПУ. Физико-математические науки. 2023. Т. 16. № 1.2. С. 287–294. DOI: https://doi.org/10.18721/JPM.161.244

Статья открытого доступа, распространяемая по лицензии CC BY-NC 4.0 (https://creativecommons.org/licenses/by-nc/4.0/)

## Introduction

Heavy nuclides subjected to the spontaneous fission decay accompanied by emission of several fast neutrons can be utilized as a compact neutron calibration source. The most common spontaneous fission source is $^{252}$Cf which undergoes α-decay and spontaneous fission with a branching ratio of 97:3, whereas each spontaneous fission event liberates 3.8 neutrons and 9.7 gamma-ray photons on average [1]. The timing of the moment of neutron production can be fixed by detecting the fission fragments signal with a semiconductor detector.

Semiconductor detectors possess sufficiently high energy resolution for detection of the high-energy heavy ions. The main obstacle for the integration of such detectors in the neutron calibration source could be their limited lifetime under the influence of the nuclide radiation [2]. Degradation of the detector's operational parameters effectively proceeds just in case of irradiation by alpha particles and fission fragments (FF), which are capable of transferring a significant fraction of their energy to the atoms of the detector lattice. Therefore, the degradation of the semiconductor detector will limit the maximal neutron source activity and/or the source expiration period.

© Базлов Н.В., Дербин А.В., Драчнев И.С., Котина И.М., Коньков О.И., Ломская И.С., Микулич М.С., Муратова В.Н., Семенов Д.А., Трушин М.В., Унжаков Е.В., 2023. Издатель: Санкт-Петербургский политехнический университет Петра Великого.

This article is devoted to the investigations of degradation of the operational parameters of several types of silicon semiconductor detectors under prolonged irradiation with fission products of $^{252}$Cf (α-particles and fission fragments). The main issue was to study the rate of degradation of different detector types under irradiation by $^{252}$Cf fission products at various irradiation conditions. Irradiation was performed at room and liquid nitrogen temperatures as well as with different detector's operational biases, i.e. with different electric field strength in the detectors active regions. Results of the preceding investigations were presented in previous articles [3–5].

## Detectors and experimental setup

Three types of silicon semiconductor detectors were under investigations. Detectors of the first type are SiLi *p-i-n* detectors produced from p-type silicon ingot with resistivity of 2.5 kΩ×cm and carrier lifetime of 1000 μs. Two similar detectors with a sensitive region of 20 mm in diameter and 4 mm thick were produced using standard Li drift technology [6]. The thickness of the undrifted *p*-type layer in these detectors (i.e. the entrance window thickness) usually amounts to 300-500 nm [7], which is kept to suppress the excessive growth of the leakage current at high operation reverse voltage [8]. Detectors of the second type were two surface-barrier (SB) detectors fabricated from p-type boron-doped silicon wafer of (111) orientation and 10 mm in diameter. The resistivity and the carrier lifetime were 1 kΩ×cm and 1000 μs, respectively. The front side of the wafers was covered by a thin layer of amorphous silicon which served as a passivation coating [9]. The ohmic contact was made by sputtering of Pd layer on the whole rear side of the wafer, whereas the rectifying one – by evaporation of Al dot with diameter of 7 mm in the center of the wafer's front side. Detector of the third type was $p^+n$ planar detector with the thickness of 300 mm produced in Ioffe Physical-Technical Institute (entrance window thickness was about 50 nm and the voltage of full depletion nearly 150 V).

Irradiation by a $^{252}$Cf source was performed in a vacuum cryostat typically during 10–20 days. The source representing a stainless steel substrate covered by an active layer under the thin protective coating was mounted 1 cm above the detector front surface that was collimated in order to exclude side surface effects of incomplete charge collection. The spectra of the fission products of $^{252}$Cf were recorded continuously during the whole irradiation period in short 1-hour series, what allowed us to observe the spectra evolution directly. Detector reverse current was also monitored during the whole irradiation period on 5-second basis with following averaging on 1-hour measurement series. Details of the measurement setup were presented in [3–5].

## Experimental results

In order to study the influence of temperature of irradiation on the degradation of the detector's parameters, the irradiation of identical SiLi detectors was performed at room (SiLi1 detector) and liquid nitrogen (SiLi2 detector) temperature, respectively. To study the influence of external electric field strength on the detector's parameters degradation, two identical SB detectors were subjected to the irradiation with different applied reverse biases, i.e. with different electric field strengths in their active regions. The operating biases applied to the respective detector during the irradiation period, the corresponding surface electric field strengths and the total exposures are collected in Table 1.

For all investigated detectors the similar signs of operational parameters degradation as a result of the prolonged irradiation by $^{252}$Cf fission products were revealed. As an example, Fig. 1a represents the spectra recorded by SB2 detector at the beginning and at the end of the prolonged irradiation period. The peak at 6.1 MeV corresponding to α-particles and another peak at doubled energy of the α-particles caused by their accidental coincidences were used as reference points for the calibration of the energy scale. Two broad unresolved peaks appearing at higher energies correspond to fission fragments of light and heavy groups, respectively.

The main effect of the detector degradation is a gradual shift of fission fragments visible energy towards the lower values, see Fig. 1,*a*. The positions of the peaks corresponding to heavy (HF) and light (LF) fission fragments were approximated using the Gaussian function for each 1-hour series. The dependences of the peaks positions with exposure by fission fragments can be well described by linear functions (Fig. 1,*b*) for any masses of fission fragments and for all investigated detectors. The obtained slope coefficients are summarized in Table 1. It is interesting to note, that the obtained coefficients for the peaks of light and heavy fission fragments groups differ

approximately by the factor of 2; this holds for all types of investigated detectors and for all irradiation conditions. In more details this fact will be discussed separately in the next paper. A similar approximation of the positions of α-peaks didn't reveal any measurable shift with the irradiation dose for all studied detectors [4–5].

Another sign of the detector's operational parameters degradation under irradiation is the rapid increase of the leakage current which proceeds linearly with the number of absorbed fission products [3]. The obtained slope coefficients of the leakage current growth are also collected in Table 1.

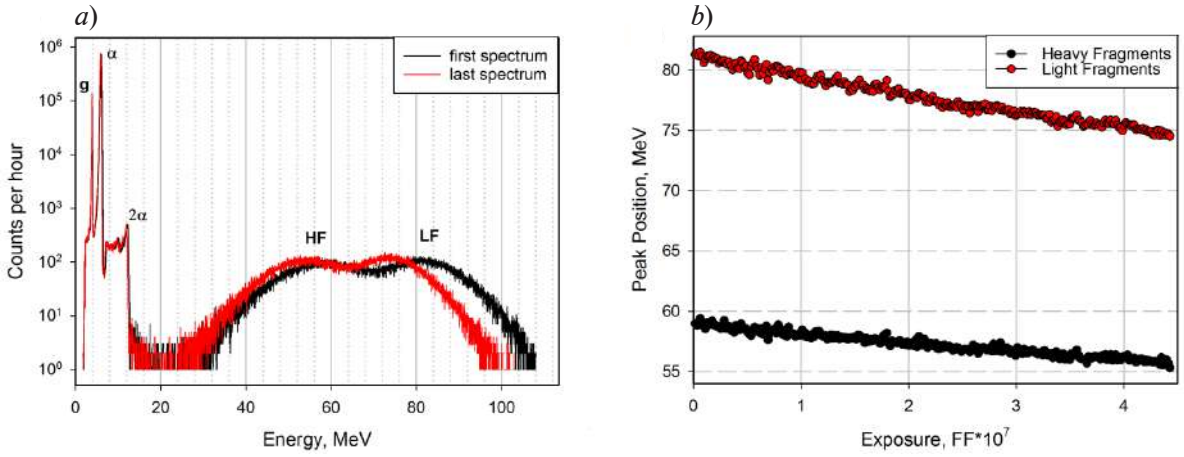


Fig. 1. First and last spectra measured by SB2 detector in the beginning and at the end of the prolonged irradiation period. The following peaks are marked: constant amplitude generator peak (g), peak of α-particles at 6.118 MeV (α), peak at doubled energy of α-particles (2α) and the peaks due to FFs of light (LF) and heavy (HF) groups (*a*). Dependence of the light and heavy FF peaks visible energies on exposure by FFs (*b*)

## Discussion

It could be noted in Fig. 1 that the peak energies of light and heavy groups of fission fragments are below the predicted values of 104 MeV and 79 MeV [10], respectively, even on the spectrum measured by non-irradiated detectors. The same is true for all other investigated detectors. This effect is known as pulse-height defect (PHD) in heavy charged particles spectroscopy by semiconductor detectors implying that the measured pulse height amplitude for heavy charged particles is somewhat lower than that for α-particles of the same energy [1]. It is generally considered that PHD is caused by a combination of energy losses (i) in the detector dead layer/entrance window, (ii) due to the atomic collisions and (iii) due to recombination of the electron-hole pairs created by the incident heavy particle. Whereas the energy losses by (i) and (ii) mechanisms are well understood, the full understanding of the charge losses due to recombination is still missing. Two models were suggested supposing that enhanced carrier recombination proceeds either in the bulk region on the radiation-induced defects created by incident FFs [11], or at the surface states of the semiconductor [12]. The later model is consistent with the TRIM [13] simulation results (Fig. 2) showing that the density of electron-hole pairs generated by fission fragments reaches the maximum in the near-surface region of the detector and then gradually drops down towards the bulk, suggesting therefore that more decisive impact on PHD growth would have the carrier recombination at the surface states.

Previously, the PHD of about 7-10 MeV was reported for $^{252}$Cf fission fragments detection by semiconductor detectors not subjected to the prolonged irradiation [10]. These PHD values are close to those ones obtained for the investigated planar and SB1 detectors operated at high reverse bias (Table 1). We believe, that higher PHD values in non-irradiated SiLi are related with rather thick entrance window in these detectors. Whereas the increase of PHD for SB2 detector operated at lower electric field (Table 1) reflects the influence of the electric field strength on the charge carrier collection efficiency, i.e. on the recombination of the generated electron-hole pairs (note that the active layer thickness in SB2 detector exceeds the projection range of incident FFs even at 30V).

Table 1

**Irradiation conditions and the degradation of operational parameters of the investigated detectors**

| | $p^+n$ planar | SB1 | SB2 | SiLi1 | SiLi2 |
|---|---|---|---|---|---|
| $U_b$, V | 150 | 200 | 30 | 400 | 400 |
| $F_s$, kV/cm | 8.5 | 40 | 17 | 1.5 | 1.5 |
| $PHD_{LF}/PHD_{HF}$, MeV | 8/10 | 9/11 | 18/19 | 28/29 | 35/37 |
| $N_{FF}\times10^8$ | 1.1 | 0.45 | 0.43 | 3.4 | 1 |
| $N_\alpha\times10^{10}$ | 0.5 | 0.20 | 0.19 | 1.5 | 0.44 |
| $\Delta E_{HF}/\Delta N_{FF}\times10^{-5}$, keV/FF | -0.9 | -1.8 | -8.9 | -3.6 | -5.7 |
| $\Delta E_{LF}/\Delta N_{FF}\times10^{-5}$, keV/FF | -1.9 | -3.9 | -20 | -6.2 | -12 |
| $\Delta I/\Delta N\times10^{-16}$, A/ion | 8.9 | 14 | 8.0 | 4.4 | - |
| $N_{FFmax}\times10^8$ | 22 | 12 | 2.2 | 6.9 | 4.7 |
| $t$, years | 11.6 | 6.3 | 1.2 | 3.6 | 2.5 |

Notations: $U_b$ is applied bias during irradiation; $F_s$ is surface electric field strength; $PHD_{LF}/PHD_{HF}$ is pulse-height defects for light and heavy fragments peaks registered by non-irradiated detectors; $N_{FF}$ and $N_\alpha$ are exposure by fission fragments and α-particles, respectively; $\Delta E_{HF}/\Delta N_{FF}$ is slope coefficient describing the linear shift of heavy fission fragment maximum; $\Delta E_{LF}/\Delta N_{FF}$ is slope coefficient describing the linear shift of light fission fragment maximum; $\Delta I/\Delta N$ is rate of the reverse current increase relative to the total number of the registered fission products (was not measured for SiLi2 detector); $N_{FFmax}$ is maximal permissible exposure by fission fragments; $t$ is expected active operation period of the detector in a neutron source.

As a result of the prolonged irradiation by $^{252}Cf$ fission products, the linear shift of FF peaks positions, i.e. the linear increase of PHD for fission fragments peaks, was revealed. Since the task of semiconductor detector operating as a part of neutron calibration source is the reliable detection of fission fragments signal, the irradiated detector could be considered to be "degraded" when the spectrum of the heavy fission fragment overlaps with much more intense signal at double energy of α-peak, what prevents us from discrimination between them [3]. The values of the maximal "permissible" exposure by fission fragments $N_{FFmax}$ corresponding to the beginning of the peaks overlap at three standard deviations from their maxima were estimated for each detector using the corresponding slope coefficients derived for HF peak and the results are presented in Table 1.

Permissible exposure values $N_{FFmax}$ for the investigated detectors appeared to vary approximately by one order of magnitude. The highest $N_{FFmax}$ values were found for planar and SB1 detector operated at 200V. Reduction of the operating bias and thus the electric field strength in case of SB2 detector has led to considerable decrease of the expected permissible exposure value. Therefore, the electric field strength affects not only the PHD on non-irradiated detector, but also the value of the expected maximal exposure. However the $N_{FFmax}$ exposure values for SiLi detectors, which operated with lowest electric field as compared with other detectors, are significantly higher than that for SB2 detector. Thus the expected maximal exposure appeared to be more sensitive to the electric field strength in the surface barrier detectors and less sensitive in SiLi and planar detectors. It follows then that not only the electric field strength, but also a detector's internal structure defines the PHD growth under irradiation and the maximal permissible exposure.

According to TRIM simulations, irradiation of Si detectors by fission fragments will lead to the creation of vacancy-interstitial pairs and therefore to the formation of high density of radiation-induced defects in the region from detector surface till the depth of 17 μm with the maxima at 14–16 μm (Fig. 2). Additionally TRIM indicates, that the energy of FFs is high enough to damage the detector surface by sputtering. Therefore, prolonged irradiation with fission fragments will lead to an increase of the carrier recombination rate both in Si bulk and on the surface of the semiconductor, thus contributing to the PHD growth.

The transition region in the detectors produced by planar and by SiLi technology ($p^+n$ and $p$-$i$ transition regions, respectively) is located inside the crystalline matrix at the typical depths of 50–500 nm from the surface. Apparently, the contribution of the surface recombination to the charge carrier losses will be more significant for surface-barrier detectors than for SiLi and planar ones, whereas the contribution of bulk defects is approximately similar in all detectors, what may be the reason for different sensitivity of $N_{\text{FFmax}}$ exposure to the electric field strength in these detectors. Additional investigations are needed to determine the dominant charge loss channel.

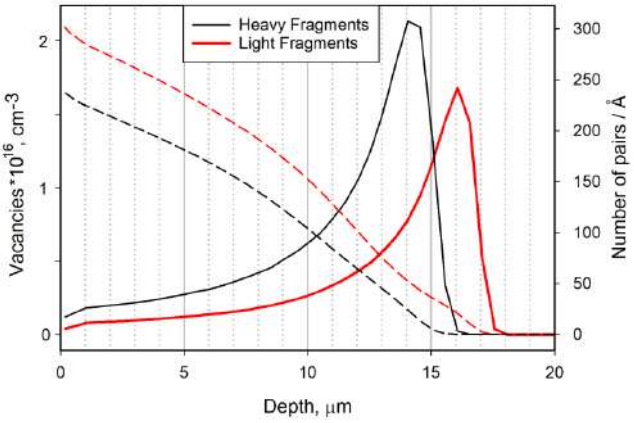


Fig. 2. TRIM simulated vacancies distribution profiles (solid lines) and linear densities of electron-hole pairs (dashed lines) generated by light and heavy FFs with mean energies and masses of 104 MeV and 79 MeV, 106 amu and 142 amu, respectively

Suggested neutron calibration source should operate also at cryogenic temperatures (liquid nitrogen or slightly above). Performed irradiation of SiLi2 detector at liquid nitrogen temperature has shown, that in contrast to the electric field, temperature of irradiation seems to have no or only minor influence on the expected value of maximal exposure as it could be concluded from the comparable $N_{\text{FFmax}}$ values obtained for SiLi detectors irradiated at different temperatures. Somewhat smaller $N_{\text{FFmax}}$ exposure obtained for SiLi2 detector is probably related with thicker entrance window in this detector.

Knowing the maximal expected exposure values $N_{FFmax}$, it is possible to estimate the duration of active "lifetime" of neutron calibration source. For the operation of neutron calibration source the reasonable neutron activity would be the around 20 neutrons/s and taking into account that each spontaneous fission releases in average 3.7 fast neutrons, the activity of 20 neutrons/s would correspond to ~6 spontaneous fissions per second. Therefore, considering the maximal exposure value from Table 1, the duration of active "lifetime" of such neutron calibration source will be 1.2–11.6 years (without taking into account the decay of the radiation source).

During this operation period, a significant increase of leakage current up to ~100 μA can be expected at room temperature, as can be calculated from the obtained coefficients of leakage current growth (Table 1). Such high reverse current is unacceptable and therefore the detector cooling in order to reduce the reverse current during the neutron source operation will be required. The coefficients of current growth upon irradiation by fission products of $^{252}$Cf appeared to be an order of magnitude higher than the corresponding coefficients of $(7–17)\cdot10^{-17}$ A/α determined by us earlier for the identical detectors subjected to long-term irradiation by α-particles [4]. This fact confirms that the prolonged irradiation by FFs leads to the creation of the effective recombination-generation defect centers participating in charge carrier recombination and the reverse current growth.

## Conclusions

Prolonged irradiation of three different types of Si semiconductor detectors by fission products of $^{252}$Cf nuclide has led to a gradual increase of pulse-height defect for the fission fragments peaks in all investigated detectors. This will eventually lead to the overlap with more intense α-peak and therefore to the impossibility of further reliable detection of fission fragments by the semiconductor detector and thus to the limitation of the operation period of neutron calibration source. Obtained experimental results suggest, that in order to assure the longest operation period of the neutron calibration source it is worth to use the semiconductor detectors with lowest surface recombination rate and with highest possible electric field strength in their active region. Among the investigated detectors, the planar one most fully meets these requirements, whereas for relatively thick SiLi detectors it will be difficult to achieve the high electric field and surface-barrier detectors may suffer from high surface recombination. With properly chosen semiconductor detector the expected active operation period of $^{252}$Cf-based neutron calibration source may reach up to 12 years.

## REFERENCES

1. **Knoll G.F.**, Radiation Detection and Measurement, 3rd ed. New York: John Wiley and Sons, 2000.

2. **Moll M.**, Displacement damage in silicon detectors for high energy physics, IEEE Transactions on Nuclear Science 65 (2018) 1561–1582.

3. **Bakhlanov S.V., Derbin A.V., Drachnev I.S., Konkov O.I., Kotina I.M., Kuzmichev A.M., Lomskaya I.S., Mikulich M.S., Muratova N.V., Niyazova N.V., Semenov D.A., Trushin M.V., Unzhakov E.V.**, Degradation of silicon detectors under long-term irradiation by $^{252}$Cf fission products, Journal of Physics: Conference Series 2103 (2021) 012138.

4. **Bakhlanov S.V., Bazlov N.V., Chernobrovkin I.D., Derbin A.V., Drachnev I.S., Kotina I.M., Konkov O.I., Kuzmichev A.M., Mikulich M.S., Muratova N.V., Trushin M.V., Unzhakov E.V.,** Influence of α-particles irradiation on the properties and performance of silicon semiconductor detectors, Journal of Physics: Conference Series 2103 (2021) 012139.

5. **Bazlov N.V., Bakhlanov S.V., Derbin A.V., Drachnev I.S., Izegov G.A., Kotina I.M., Muratova V.N., Niyazova N.V., Semenov D.A., Trushin M.V., Unzhakov E.V., Chmel E.A.,** A Change in the Parameters of Si(Li) Detectors under Exposure to α Particles, Instrum. Exp. Tech. 63(1) (2020) 25.

6. **Bazlov N.V., Bakhlanov S.V., Derbin A.V., Drachnev I.S., Eremin V.K., Kotina I.M., Muratova V.N., Pilipenko N.V., Semenov D.A., Unzhakov E.V., Chmel E.A.,** A Beta Spectrometer Based on Silicon Detectors, Instruments and Experimental Techniques 61 (2018) 323.

7. **Alekseev I.E., Bakhlanov S.V., Derbin A.V., Drachnev I.S., Kotina I.M., Lomskaya I.S., Muratova V.N., Niyazova N.V., Semenov D.A., Trushin M.V., Unzhakov E.V.,** Precision measurement of the 210Bi β spectrum, Physical Review C 102 (2020) 064329.

8. **Kozai M., Fuke H., Yamada M., Perez K., Erjavec T., Hailey C. J., Madden N., Rogers F., Saffold N., Seyler D., Shimizu Y., Tokuda K., Xiao M.,** Developing a mass-production model of large-area Si(Li) detectors with high operating temperatures, Nuclear Inst. and Methods in Physics Research A 947 (2019) 162695.

9. **Kotina I.M., Danishevskii A.M., Konkov O.I., Terukov E.I., Tuhkonen L.M.,** On the collection of photocarriers in high-resistance silicon amorphous-crystalline heterostructures, Semiconductors 48(9) (2014) 1167.

10. **Paasch K., Krause H., Scobel W.,** Fission fragment spectroscopy with large surface barrier detectors, Nuclear Inst. and Methods in Physics Research 221 (1984) 558.

11. **Eremin V.K., Il'yashenko I.N., Strokan N.B., Shmidt B.,** Recombination of nonequilibrium carriers in heavy ion tracks in Si, Fiz. Tekh. Poluprovodn. 29(1) (1995) 79.

12. **Tsyganov Y. S,** Registration of highly ionizing particles: nonlinear phenomena in near-surface layers of silicon detectors, Physics of Particles and Nuclei 44(1) (2013) 92.

13. **Ziegler J.F., Biersack J.P., Ziegler M.D.,** SRIM – Stopping and Range of Ions in Matter. URL: www.srim.org. Accessed: May 2022.

## THE AUTHORS

**BAZLOV Nickolay V.**
nikolay.bazlov@gmail.com
ORCID: 0000-0001-9492-6258

**DERBIN Alexander V.**
derbin_av@pnpi.nrki.ru
ORCID: 0000-0002-4351-2255

**DRACHNEV Ilia S.**
drachnev_is@pnpi.nrcki.ru
ORCID: 0000-0002-4064-8093

**KOTINA Irina M.**
kotina_im@pnpi.nrcki.ru

**KONKOV Oleg I.**
oleg.konkov@mail.ioffe.ru

**LOMSKAYA Irina S.**
lomskaya_is@pnpi.nrcki.ru

**MIKULICH Maxim S.**
mikulich_ms@pnpi.nrcki.ru

**MURATOVA Valentina N.**
muratova_vn@pnpi.nrcki.ru
ORCID: 0000-0001-5532-7711

**SEMENOV Dmitriy A.**
semenov_da@pnpi.nrcki.ru

**TRUSHIN Maxim V.**
trushin_mv@pnpi.nrcki.ru
ORCID: 0000-0001-7620-0955

**UNZHAKOV Evgeniy V.**
unzhakov_ev@pnpi.nrcki.ru
ORCID: 0000-0003-2952-6412

*Received 17.10.2022. Approved after reviewing 08.11.2022. Accepted 25.11.2022.*

© Peter the Great St. Petersburg Polytechnic University, 2023

Conference materials
UDC 539,1,074
DOI: https://doi.org/10.18721/JPM.161.245

# Kinetics of current outflow from electron-hole plasma generated in silicon detectors by relativistic heavy ions

N.N. Fadeeva[1]✉, V. Eremin[1], E. Verbitskaya[1], I. Eremin[1], Yu. Vidimina[1, 2]

[1] Ioffe Institute, St. Petersburg, Russia;
[2] St. Petersburg Electrotechnical University "LETI", St. Petersburg, Russia
✉ fadeeva.nadezda@mail.ioffe.ru

**Abstract.** The investigation is focused on the processes associated with the detection of heavy ions of hundreds GeV energy in silicon $p^+$-$n$-$n^+$ detectors. In the study, the 1D simulation of the electric field and free carrier density evolution in the $^{238}$U ion track during the first nanosecond was carried out, which demonstrated the initial appearance of narrow high electric field regions adjacent to the contacts and a strong reduction of the electric field *in between*. The kinetics of the electron-hole plasma dispersal was assigned to a track polarization within 100 ps followed by a delayed track destruction up to its disappearance. It was shown that the process at the $p^+$ contact was governed by the drift of electrons as a merged fraction of free carriers, which controls the hole current flowing between the track and the $p^+$ contact. The density of the current initiated by the track polarization was evaluated as $8 \cdot 10^3$ A/cm$^2$._

**Keywords:** silicon radiation detector, electron-hole plasma, electric field

**Citation:** Fadeeva N.N., Eremin V., Verbitskaya E., Eremin I., Vidimina Yu., Kinetics of current outflow from electron-hole plasma generated in silicon detectors by relativistic heavy ions, St. Petersburg State Polytechnical University Journal. Physics and Mathematics. 16 (1.2) (2023) 295–301. DOI: https://doi.org/10.18721/JPM.161.245

This is an open access article under the CC BY-NC 4.0 license (https://creativecommons.org/licenses/by-nc/4.0/)

Материалы конференции
УДК 539,1,074
DOI: https://doi.org/10.18721/JPM.161.245

# Исследование кинетики истекания тока из электронно-дырочной плазмы, создаваемой в кремниевых детекторах релятивистскими тяжелыми ионами

Н.Н. Фадеева [1]✉, В. Еремин[1], Е. Вербицкая[1], И. Еремин[1], Ю. Видимина[1, 2]

[1] Физико-технический институт им. А.Ф. Иоффе РАН, Санкт-Петербург, Россия;
[2] СПбГЭТУ «ЛЭТИ» им. В.И.Ульянова, Санкт-Петербург, Россия
✉ fadeeva.nadezda@mail.ioffe.ru

**Аннотация.** Основное внимание в исследовании уделяется процессам, связанным с регистрацией тяжелых ионов с энергией в сотни ГэВ в кремниевых $p^+$-$n$-$n^+$-детекторах. В работе проведено 1D-моделирование эволюции электрического поля и концентрации свободных носителей в треке иона $^{238}$U в течение первой наносекунды, которое продемонстрировало начальное появление узких областей сильного электрического поля, прилегающих к контактам, и сильное снижение электрическое поле между ними. Кинетика разлета электронно-дырочной плазмы связывалась с поляризацией трека в течение 100 пс с последующим замедленным разрушением трека вплоть до его исчезновения. Показано, что процесс на $p^+$-контакте определяется дрейфом электронов как объединенной фракции свободных носителей, который контролирует дырочный ток, протекающий между треком и $p^+$-контактом. Плотность тока, инициируемого поляризацией трека, оценивалась как $8 \cdot 10^3$ А/см$^2$.

© Fadeeva N.N., Eremin V., Verbitskaya E., Eremin I., Vidimina Yu., 2023. Published by Peter the Great St. Petersburg Polytechnic University.

**Ключевые слова:** кремниевый детектор излучений, электронно-дырочная плазма, электрическое поле

**Ссылка при цитировании:** Фадеева Н.Н., Еремин В., Вербицкая Е., Еремин И., Видимина Ю. Исследование кинетики истекания тока из электронно-дырочной плазмы, создаваемой в кремниевых детекторах релятивистскими тяжелыми ионами // Научно-технические ведомости СПбГПУ. Физико-математические науки. 2023. Т. 1.2 № .16. С. 295–301. DOI: https://doi.org/10.18721/JPM.161.245

Статья открытого доступа, распространяемая по лицензии CC BY-NC 4.0 (https://creativecommons.org/licenses/by-nc/4.0/)

## Introduction

The experiments planned in nuclear physics require the use of intense exotic ion beams with the known ion mass and energy [1]. The system for obtaining such beams includes an ion accelerator and the unit for the ion fragmentation. The fragments, i.e., ions with a certain combination of masses, energy and charge are the tool and the object of research and should be characterized in the on-line mode, i.e., directly in the beam. Taking into account high intensity of the primary beam, the ion on-line diagnostic system needs high speed operation. An ion separation system includes time-of-flight (ToF) spectrometers capable of operating at beam intensities up to $10^6$ particles/cm$^2$ per a second and a time resolution of tens of ps, which will ensure the ion mass resolution per unit of atomic mass in the range from light elements to uranium at their energies from tens of MeV/u to several GeV/u.

For light ions of medium and high energy, the choice of Si detectors in this issue is obvious and based on the experience of their use in accelerator complexes, such as Large Hadron Collider at CERN. In this case the detector signal kinetics is predictable since the signal originates from generation of electron-hole (e-h) pairs with a low density inside the particle tracks and their collection. For detecting heavy ions, application of Si detectors requires special study, since the signal arises from a dense e-h plasma, which slows down charge collection and worsens the maximum detection rate of particles and the time resolution of Si detectors as well as and the ToF spectrometer on a whole. This topic was analyzed qualitatively in [2], and it was shown that the detector signal kinetics can be considered as a two-stage process: at the first stage the track is polarized, which creates the conditions for a subsequent slow escape of carriers during the second stage, and the latter determines the duration of the detector response.

In this work, we consider the processes responsible for the formation of a signal in Si detector in the first nanosecond after the charge generation within the ion track, which is essential for advancing the ToF ion spectrometry to the range of picosecond time resolution. The investigation is performed by using original program for simulating the charge transfer in $p^+$-$n$-$n^+$ detector structures. The time interval of the processes in the ion track is within few ps to 1 ns, which does not allow their direct experimental study. Therefore, simulation is considered as an "objective physical experiment" that provides quantitative data for the analysis of ongoing processes.

## Model of ion track

A track of high-energy ion traversing the total detector thickness is the electrical object in the volume of the detector characterized by specific ionization losses and representing geometrically a thin cylinder with a diameter corresponding to the region in which nonequilibrium electrons and holes arise. Although a large number of studies are devoted to the physics of the ion track formation, there are only rough estimates of its geometry yielding the diameter in the range hundredths of a μm to a μm, which results in the ambiguity of the concentration of charge carriers created by the ion [3].

In the simulations performed in this work, a track with a diameter of 1 μm and a uniform distribution of e-h pairs with initial concentrations of electrons and holes $n_0$ and $p_0$ equal to $8 \cdot 10^{15}$ cm$^{-3}$ created by a heavy ion, is considered. This concentration corresponds to $^{238}$U ions with energies in hundreds of GeV.

© Фадеева Н.Н., Еремин В., Вербицкая Е., Еремин И., Видимина Ю., 2023. Издатель: Санкт-Петербургский политехнический университет Петра Великого.

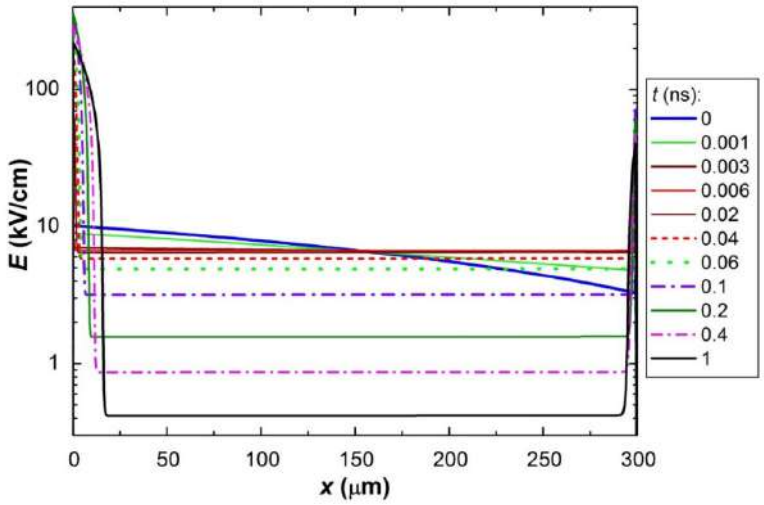


Fig. 1. Distribution of the electric field across the detector thickness. $V = 200$ V

The processes in the track were studied in a 1D model extending along the thickness of the detector (coordinate $x$). Simulations were carried out using original software package applied earlier for calculating the electric field profile $E(x)$ in Si $p^+$-$i$-$n^+$ structures [4]. The package included modeling the processes of carrier drift and diffusion along the $x$-coordinate and allowed tracking the kinetics of the redistributions of $E(x)$ and the electron and hole concentration $n$ and $p$, respectively. The model structure was a silicon detector processed on the wafer with a resistivity of 3 kΩcm, a thickness $d$ of 300 μm and degenerate $p^+$ and $n^+$ contacts. The generation of $e$-$h$ pairs arose from a single heavy ion penetration inside the detector bulk normally to the surface and was uniformly distributed across the track cross-section. The profiles of the electron and hole densities were uniform over the structure thickness, turning into the degenerate layers at $x = 0$ and $x = d$ (the $p^+$ and $n^+$ contacts, respectively). The bias voltage applied to the detector was 200 V, which matches Si detector operation in the experiments with heavy ions at room temperature.

**Evolution of the electric field profile in subnanosecond time range**

Fig. 1 shows the electric field profiles obtained by simulation in the detector sensitive area over its total depth and corresponding to different moments of time from the appearance of the track ($t = 0$) up to $t = 1$ ns. It should be noted that this time interval is of significant importance. Indeed, with a target time resolution of the ToF spectrometer in tens of picoseconds, the electric field redistribution at $t < 1$ ns is vital, since it controls the kinetics of the current response to impinging ions. With that in mind, the study considers the high rate processes of the electric field redistribution in the regions adjacent to the contacts.

Two features are clearly observed in the evolution of the $E(x)$ distribution in the subnanosecond range. At $t \geq 0.01$ ns, sharp electric field maxima $E_{max}$ arise near the detector contacts. This is accompanied by a reduction in the electric field *in between*, i.e., in most of the detector volume that becomes eventually close to uniform and goes down in time.

Fig. 2 shows the details of the electric field rearrangement in the track in the interval 0-1 ns in the region adjacent to the $p^+$ contact. The formation of a region with a maximum electric field occurs within a few picoseconds. $E_{max}$ rises with time and reaches hundreds of kV/cm (maximum value is ~350 kV/cm at ~100 ps), which significantly exceeds the initial $E_{max}$ of $10^4$ V/cm at $t = 0$. The following decay of the electric field from its maximum takes place within the region $x = 0$–16 μm, and the electric field gradient $dE/dx$ is close to linear.

Transformation of the electric field profiles occurs in two time stages showing different tendencies:

- $0 < t < 100$ ps, $E_{max}$ increases, while a subsequent linear decrease of the electric field with an almost constant slope is observed within a region with a width $W$ of few μm (Fig. 2,*a*);
- 100 ps $< t <$ 1 ns, $E_{max}$ drops, and an intensive expansion of the high electric field region takes place near the $p^+$ contact leading to the $dE/dx$ decrease (Fig. 2,*b*).

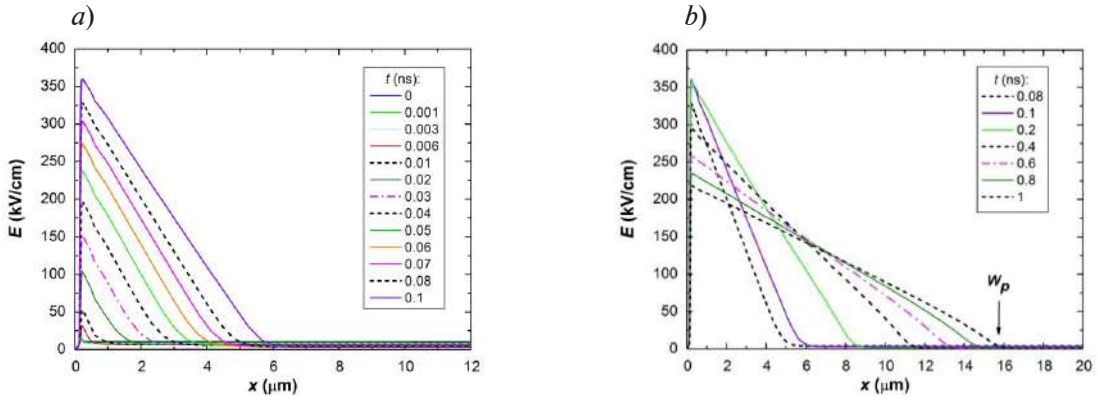


Fig. 2. Distribution of the electric field near the detector $p^+$ contact in the time intervals: 0–0.1 ns (*a*), and 0.08–1 ns. $V = 200$ V (*b*)

The appearance of the electric field maxima near the contacts is accompanied by the formation of a region with a constant field in the main part of the volume, whose value successively decreases with time to $E$ below 1 kV/cm. It should be noted that such a redistribution of the electric field goes on at a constant bias voltage applied to the detector.

The nonmonotonic dependence of $E_{max}$ on time is presented in Fig. 3. The maximal electric field ~350 kV/cm is achieved at $t \approx 150$ ps, and the width of the region with a linear $E(x)$ decay is 16 μm at $t = 1$ ns.

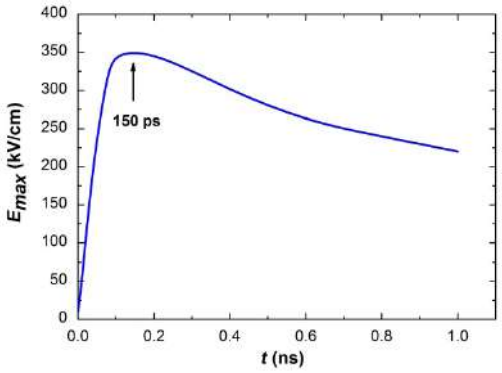


Fig. 3. Time dependence of $E_{max}$

**Evolution of space charge and carrier concentration due to polarization inside the track**

At $t = 0$, the maximum electric field at the $p^+$ contact $E_0$ of 10 kV/cm is determined by the effective space charge concentration $N_{eff0} = 1 \cdot 10^{12}$ cm$^{-3}$ in the sensitive n-type region of the detector. In the track generated by impinging ion, the e-h plasma is electrically neutral and only slightly affects the initial electric field distribution. Further, $E_{max}$ at the $p^+$ contact increases and $dE/dx$ gradient goes down, while remaining close to linear, which evidences a change in $N_{eff}$ with time in the region with a width $W$. The $N_{eff}$ dependence on the width $W$ is determined by the Poisson equation:

$$\frac{dE}{dx} = -\frac{eN_{eff}}{\varepsilon\varepsilon_0}, \tag{1}$$

where $e$ is the elementary charge, $\varepsilon$ and $\varepsilon_0$ are permittivities of Si and vacuum, respectively, and is shown in Fig. 4. The dependence demonstrates two regions. In the first one, in the interval $0 < t < 60$ ps, i.e., at $W \le 3.8$ μm, $N_{eff}$ is positive and equals $4.7 \cdot 10^{15}$ cm$^{-3}$. In the second region, at $t \ge 60$ ps $N_{eff}$ goes down as $W$ rises, which implies changing the mechanism of the electric field distribution.

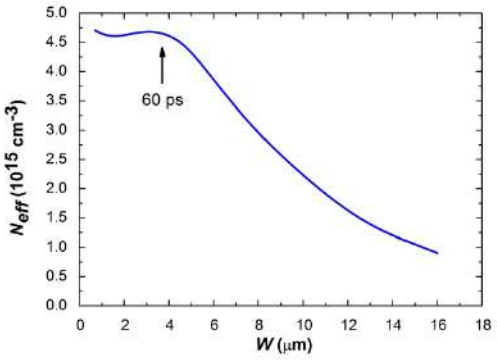


Fig. 4. Dependence of $N_{eff}$ in the region
with a linear electric field gradient on its width $W$

Evolution of the electric field profile at $p^+$ contact originates from the time distribution of the electron and hole concentrations in the region adjacent to the $p^+$ contact. The primary process is the drift of the electron column as a whole in the electric field $E_c$ in the central region of the detector ($E_c \leq 6$ kV/cm at $t \geq 10$ ps). It can be seen that the column border stays sharp and shifts in time (Fig. 5,***a***), which expands the region deeply depleted with electrons; for example, at $x < 5$ μm, the concentration $n$ is below $1 \cdot 10^4$ cm$^{-3}$. In turn, positive charge of free holes in this region (Fig. 5, *b*) determines the distribution of the electric field. Obviously, free holes will drift in the electric field towards the $p^+$ contact, creating conduction current. This process is visualized in the hole concentration distribution as a region with a decrease in $p$ from $8 \cdot 10^{15}$ cm$^{-3}$ to ~$5 \cdot 10^{15}$ cm$^{-3}$ within the interval 40–100 ps. This concentration of holes is still high and comparable with its value in the electrically neutral track.

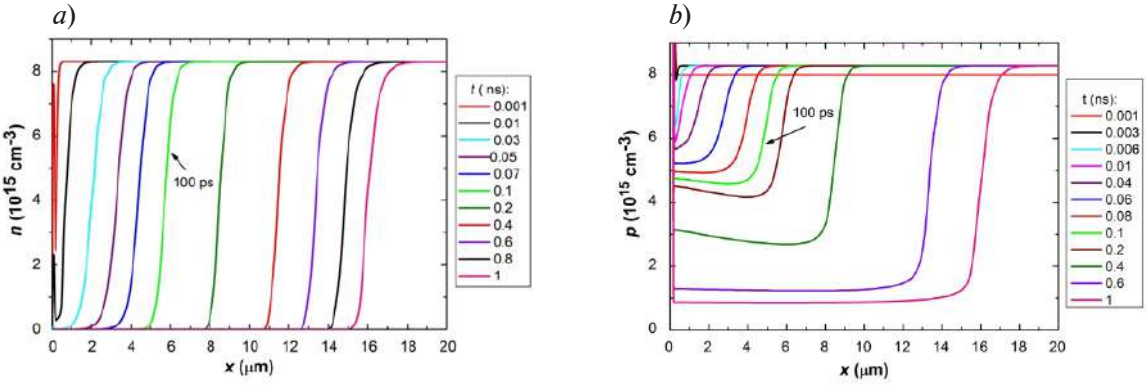


Fig. 5. Evolution of the carrier concentration in the ion track in time:
(*a*) electrons, and (*b*) holes

The process of plasma drift in the electric field can be described by two equations. The first one determines the relation between the displacement velocity of the electron column border $W_e$, $dW_e/dt$, and the density of hole charge $dq_h/dt$ outflowing from the track:

$$\frac{dq_h}{dt} = en\frac{dW_e}{dt}. \tag{2}$$

The second yields the dependence of hole current density $J_h$ on the hole concentration:

$$J = e\mu_h E_p, \tag{3}$$

where $\mu_h$ is the hole mobility. A displacement of the electron column border via its drift is a basic process determining the current $dq_h/dt$ at $t < 100$ ps. Then, at $t = 0.1$ ns, $W_e$ is 5 μm and $n$ equals $8 \cdot 10^{15}$ cm$^{-3}$, while $J$ is $8 \cdot 10^3$ A/cm$^2$ that corresponds to the current of $7.5 \cdot 10^{-5}$ A outflowing from the track with a diameter of 1 μm. It should be noted that this estimation corresponds to the time when the electric field at the $p^+$ contact reaches its maximum of about 350 kV/cm. Then, considering $\mu_h E = v_{sat}$ (where $v_{sat} = 7.5 \cdot 10^6$ cm/s is the hole saturated velocity) and using Eq. (3), the mean hole concentration in the layer $W$ is $6 \cdot 10^{15}$ cm$^{-3}$ that is in the reasonable agreement with $p$ at $t < 100$ ps.

At $t = 1 \cdot 10^{-10}$ s $E_{max}$ starts decreasing, and the expansion of the high electric field region slows down (Figs. 2,*b* and 3). The above two stages in the $E(x)$ transformation can be attributed to two qualitatively different processes:

track polarization which manifesting itself as a rapid change in the electric field distribution, which occurs in the 0—100 ps interval and leads to the formation of the polarization charge layer with a thickness $W_{pol}$. This results in the electric field rise to the maximum $E_{max}$ and is accompanied by a significant decrease in the electric field in the detector volume outside the $W_{pol}$ layer;

slower expansion of the depleted layer to the central part of the detector (Fig. 2,*b* and 5,*a*) that finalizes with the disappearance of the track due to the escape of all nonequilibrium carriers to the contacts.

It should be noted finally that the presented results do not affect the electric field formation at the ohmic $n^+$ contact, whose analysis requires an additional software resource and is included in further research plan. However, the overview $E(x)$ plot (Fig. 1) shows a qualitative similarity of the processes at the $n^+$ contact with those at the $p^+$-$n$ junction, which allows us to consider the current results as a basis for further study.

### Conclusion

The performed simulation of the electric field distribution demonstrated the following.

- In the range of few ps, the track polarization is a dominating process.
- The polarization at the $p^+$ contact is characterized by deep depletion of the narrow layer by electrons, while the concentration of holes only reduces.
- Both processes, electron column shift and the hole current flow, are balanced and characterized by the high current density in the range of thousands A/cm$^2$.
- The hole concentration is nearly constant in time, which predicts the constant current flow during the polarization phase controlled by the hole saturated velocity.
- The modeling enables a physically justified parameterization of the high resolution timing characteristics of Si detectors.

## REFERENCES

1. **Kiselev O. et al.,** Si detectors for nuclear physics experiments with exotic beams, International Symposium on Exotic Nuclei EXON-2014, Kaliningrad, Russia, 8—13 September 2014, World Scientific, pp. 607—618 [ISBN: 978—981—4699—45—7].

2. **Eremin V., Kiselev O., Egorov N., Eremin I., Tuboltsev Yu., Verbitskaya E., Gorbatyuk A.,** Picosecond timing of high-energy heavy ions with semiconductor detectors, Nucl. Instrum. Meth. Phys. Res. A 796 (2015) 158–164.

3. **Colladant T., L'Hoir A., Sauvestre J.E., Flament O.,** Monte-Carlo simulations of ion track in silicon and influence of its spatial distribution on single event effects, Nucl. Instrum. Meth. Phys. Res. B 245 (2006) 464–474.

4. **Eremin V., Fadeeva N., Verbitskaya E.,** The impact of active base on the bulk current in silicon heavily irradiated detectors, JINST 12 P09005 (2017).

## THE AUTHORS

**FADEEVA Nadezda**
fadeeva.nadezda@mail.ioffe.ru
ORCID: 0000-0002-1282-4619

**EREMIN Vladimir**
vladimir.eremin@cern.ch

**VERBITSKAYA Elena**
Elena.Verbitskaia@cern.ch
ORCID: 0000-0002-2313-1789

**EREMIN Igor**
Igor.Pti@mail.ioffe.ru

**VIDIMINA Yulia**
uvidimina@gmail.com

*Received 18.10.2022. Approved after reviewing 08.11.2022. Accepted 08.11.2022.*

© Peter the Great St. Petersburg Polytechnic University, 2023

Conference materials
UDC 539.17
DOI: https://doi.org/10.18721/JPM.161.246

# Nuclear isomers as a tool for studying the influence of zero-point fluctuations of an electromagnetic field on the probability of spontaneous electromagnetic transitions

V.V. Koltsov[1]✉

[1] JSC "Khlopin Radium Institute", St. Petersburg, Russia

✉ vladimir-koltsov@yandex.ru

**Abstract.** A review of works on the influence of zero-point fluctuations of the electromagnetic (EM) field (ZPFs) on EM transitions in atomic nuclei inside metals is presented. In a metal, as well as in a resonator of extremely small dimensions, ZPFs are suppressed in the region of low frequencies ω, for which the reflection of EM waves from the metal surface is still significant ($\hbar\omega$ is less than ~ 1 keV). Based on the concept of the stimulation of spontaneous EM transitions of energy $\hbar\omega_0$ by resonant ZPFs of frequency $\omega_0$, one could expect suppression of transitions of energy up to ~ 1 keV for excited nuclei in a metal matrix. In experiments with nuclear isomers, such an effect was indeed found for conversion transitions of 76, 910, and 2173 eV energy, which cannot be explained only by the deformation of the electron shells of isomeric atoms or by the scattering of conversion electrons by matrix atoms. Qualitatively, the effect corresponds to the suppression of conversion transitions with a decrease in the ZPFs energy density in metals at the transition frequencies.

**Keywords:** nuclear isomers, probability of nuclear transitions, zero-point fluctuations of the electromagnetic field

**Citation:** Koltsov V.V., Nuclear isomers as a tool for studying the influence of zero-point fluctuations of an electromagnetic field on the probability of spontaneous electromagnetic transitions, St. Petersburg State Polytechnical University Journal. Physics and Mathematics. 16 (1.2) (2023) 302–307. DOI: https://doi.org/10.18721/JPM.161.246

This is an open access article under the CC BY-NC 4.0 license (https://creativecommons.org/licenses/by-nc/4.0/)

Материалы конференции
УДК 539.17
DOI: https://doi.org/10.18721/JPM.161.246

# Ядерные изомеры как инструмент для исследования влияния нулевых колебаний электромагнитного поля на вероятность спонтанных электромагнитных переходов

В.В. Кольцов[1]✉

[1] АО «Радиевый институт им. В.Г. Хлопина», Санкт-Петербург, Россия

✉ vladimir-koltsov@yandex.ru

**Аннотация.** Проведен обзор экспериментальных и теоретических работ по влиянию нулевых колебаний электромагнитного (ЭМ) поля (НКП) на вероятность ЭМ переходов малой энергии в атомных ядрах внутри металлов. В металле, как и в резонаторе предельно малых размеров, НКП подавлены в области малых частот ω, для которых еще существенно отражение ЭМ волн от поверхности металла ($\hbar\omega$ меньше ~ 1 кэВ). Исходя из представления о стимуляции спонтанных ЭМ переходов энергии $\hbar\omega_0$ резонансными НКП частоты $\omega_0$, можно было ожидать подавления ЭМ переходов энергии до ~ 1 кэВ для возбужденных ядер в матрице металла. В экспериментах с ядерными изомерами действительно был обнаружен такой эффект для конверсионных переходов энергии 76, 910 и 2173 эВ, который не может быть объяснен только деформацией электронных оболочек изомерных атомов или рассеянием конверсионных электронов на атомах матрицы. Качественно эффект соответствует подавлению конверсионных переходов при уменьшении в металле плотности энергии НКП на частоте перехода.

© Koltsov V.V., 2023. Published by Peter the Great St. Petersburg Polytechnic University.

**Ключевые слова:** ядерные изомеры, вероятность ядерных переходов, нулевые колебания электромагнитного поля

**Ссылка при цитировании:** Кольцов В.В. Ядерные изомеры как инструмент для исследования влияния нулевых колебаний электромагнитного поля на вероятность спонтанных электромагнитных переходов // Научно-технические ведомости СПбГПУ. Физико-математические науки. 2023. Т. 16. № 1.2. С. 302–307. DOI: https://doi.org/10.18721/JPM.161.246

Статья открытого доступа, распространяемая по лицензии CC BY-NC 4.0 (https://creativecommons.org/licenses/by-nc/4.0/)

## Introduction

Immediately after the creation of quantum electrodynamics, the idea arose of stimulating the spontaneous emission of photons by zero-point fluctuations of an electromagnetic (EM) field (ZPFs) [1] (see also references in [2]). This idea was based on the description of the interaction of charged particles according to perturbation theory, when the Hamiltonian of a system of particles and an EM field is divided into the Hamiltonians of particles and fields (photons and ZPFs), that do not interact with each other, and the energy of interaction between them. Then, if we do not consider the processes induced by photons, the interaction of particles is caused by their interaction with ZPFs. The ZPFs energy density $dW_{\text{ZPF}}(\omega)$ in the frequency range $d\omega$ is given by the formula (see, for example, [3])

$$\mathrm{d}W_{\text{ZPF}}(\omega) = \theta^2(\omega)\,\frac{\hbar\omega^3}{\pi^2 c^3}\,\mathrm{d}\omega, \tag{1}$$

where $c$ is the light speed, $\hbar$ is Planck's constant divided by $2\pi$. For the convenience of further analysis, a real function $\theta(\omega)$ is introduced into formula (1), in the free space $\theta(\omega) = 1$.

The matrix element $S^{\text{ph}}(t)$ of spontaneous emission of a photon of energy $\hbar\omega_0$ at moment $t$ is proportional to the following integral (see, for example, [4])

$$S^{\text{ph}}(t) \;\propto\; \int_{-\infty}^{\infty} \mathrm{d}\omega\; \omega^{3/2}\,\theta(\omega)\,J_1(\omega) \underbrace{\int_{t_0}^{t} \mathrm{d}t_1\, \mathrm{e}^{\mathrm{i}(\omega_0-\omega)t_1}}_{\delta(\omega_0-\omega)} \;\propto\; \theta(\omega_0), \tag{2}$$

where $t_0$ is the moment of formation of the excited state, $J_1(\omega)$ is the space integral of the particle transition current. The average photon emission time is of the order of the half-life of the excited state $T_{1/2}$ and $t - t_0 >> 1/\omega_0$. Then the integral over time gives the δ-function and the emission probability is proportional to the $dW_{\text{ZPF}}(\omega_0)$. In a cavity with a diameter of $D$ with ideally reflecting walls (in a resonator), ZPFs do not contain low frequencies $\omega < c/D$. If an emitter is placed in the resonator of $D < c/\omega_0$, then the emission of a photon of energy $\hbar\omega_0$ will be suppressed, which was observed for excited atoms (see references in [2]).

## Dependence of the probability of a nuclear conversion transition on the ZPFs spectrum

It is interesting to study the stimulation of spontaneous EM transitions by ZPFs in a quantum system located inside a medium with photon absorption, for example, inside a metal. For this, however, the emission of photons by atoms is inconvenient, since photons of low energy do not emerge from the metal, and the lifetimes of the atom's excited states are short. For research, it is more convenient to isomeric nuclear states that decay by a low-energy conversion transition, when nuclear excitation is transferred to the electron shell of an atom with electron emission due to inelastic scattering of an atomic electron by an excited nucleus [4]. It was shown in [2] that ZPFs stimulate the nuclear conversion transition in the same resonant manner as the transition with photon emission. Indeed, the matrix element $S^{\text{e}}(t)$ of the conversion transition of energy $\Delta E_{\text{N}} = \hbar\omega_0$ is obtained in the second order of the perturbation theory and has the form

© Кольцов В. В., 2023. Издатель: Санкт-Петербургский политехнический университет Петра Великого.

$$S^{c}(t) \;\propto\; \int_{-\infty}^{\infty} \mathrm{d}\omega\; J_2(\omega)\,\omega\;\theta^2(\omega) \int_{t_0}^{t} \mathrm{d}t_1\, \mathrm{e}^{\mathrm{i}(\omega_e+\omega)t_1} \underbrace{\int_{t_0}^{t_1} \mathrm{d}t_2\, \mathrm{e}^{\mathrm{i}(\omega_0-\omega)t_2}}_{\delta(\omega_0-\omega)} \;\propto\; \theta^2(\omega_0), \tag{3}$$

where $J_2(\omega)$ is the spatial integral of the product of the transition currents of the nucleus and the conversion electron, $\hbar\omega_e$ is the change in the electron energy, the limits of integration over time $t$ and $t_0$ are the same as in formula (2). The interaction duration $t_1 - t_0$ is of the order of $T_{1/2}$ of the isomeric state and always $\Delta E_N\,(t_1 - t_0) >> \hbar$. Then, in formula (3), the integral over time $t_2$ gives the δ-function, which provides the resonance in the stimulation of the conversion transition by ZPFs. In the case of inelastic scattering of free particles, the condition $\Delta E\,(t_1 - t_0) >> \hbar$ is not satisfied and there is no resonance in the transfer of energy $\Delta E$.

### Zero-point fluctuations of the EM field (ZPFs) inside the medium

For nuclei in the resonator, where $\theta(\omega_0) = 0$, according to formula (3), the probability of conversion transitions of energy $\hbar\omega_0$ is equal to zero. For nuclei in a metal, such an effect is possible at $\hbar\omega_0$ less than ~1 keV, when reflection from the metal is still significant for EM waves with a frequency $\omega_0$. Metal is the limiting case of a small collapsing resonator and due to the Doppler effect upon reflection of ZPFs from the approaching walls of the initial resonator, the frequency of ZPFs increases and the energy density $dW_{ZPF}(\omega)$ of low frequency ZPFs inside the metal decreases [5].

For a transparent medium, $dW_{ZPF}(\omega)$ is given by formula (1) at $\theta(\omega) = n_\omega^{3/2}$ [3], the optical refractive index $n_\omega < 1$ [6]. In a medium with absorption of EM radiation, $\theta(\omega) < 1$ as well [3, 5]. Metals seem to play a special role, since ZPFs cannot be absorbed by the medium due to transitions between stationary states of atoms (see, e.g., [7]). But $dW_{ZPF}(\omega)$ can decrease upon interaction with electrons in a continuous energy spectrum, in particular, with conduction electrons in a metal. The absorption of ZPFs in a metal is weaker than the absorption of real photons, and edge effects for ZPFs can affect deeper layers of the metal than for real photons.

Another way to reduce $dW_{ZPF}(\omega)$ inside a medium is possible by increasing the energy of interaction between ZPFs and the electrons of the atoms of the medium, if the region of free states in the continuous electron energy spectrum expands during phase transitions in the medium [8]. Thus, when a crystal is formed from free atoms, the number of allowed electronic states increases when continuous energy bands appear for electrons instead of discrete levels of low energy for free atoms. After the phase transition, the ZPFs spectrum changes with time due to the diffusion of ZPFs into the medium from the free space.

In all considered cases, in the metal $\theta(\omega) < 1$ and $\theta(\omega) \to 1$ with increasing $\omega$. Then, according to formula (3), one can expect suppression of conversion transitions of energy up to ~ 1 keV for nuclei in a metal. This effect was studied at the Khlopin Radium Institute on several nuclear isomers.

### Isomeric transition 76 eV of $^{235m}$U nuclei in silver

The $^{235m}$U isomer is formed in the α-decay of $^{239}$Pu and decays into the $^{235}$U ground state by a conversion transition of energy 76 eV. This transition was studied by many authors; the $^{235m}$U recoil nuclei emitted from the $^{239}$Pu layer were collected in an Ar-atmosphere or in a vacuum onto backings of different metals. It was shown that $T_{1/2} \approx 26$ min and varies within 5% due to deformation of the electron shells of isomer atoms or due to scattering of conversion electrons on backings atoms. The decay of $^{235m}$U in a metal at a depth of $d > 100$ Å was studied only in [9, 10] using the following method. 1) The 1000 Å thick Ag-layer was deposited on the W-backing, then $^{235m}$U recoil nuclei were deposited on this Ag-layer in vacuum or in an Ar-atmosphere, then the preparation was again covered with the 1000 Å Ag-layer. To improve the structure of the U − Ag system, the preparation was annealed and then divided it into several identical samples. 2) Silver was removed from Sample 1 by heating it in vacuum so that the uranium atoms remained on the surface of the W-backing, and the decay curve of Sample 1 was measured by detecting $^{235m}$U conversion electrons with a channel electron multiplier. At this time, $^{235m}$U in other samples remained "buried" in the Ag-layers. 3) Then the silver was removed from Sample 2 and the decay curve

was also measured for it with the same detector. If the isomeric transition is suppressed inside the Ag-layer, then a "step" $\Delta N$ is formed between the decay curves of the samples, caused by different residence times of $^{235m}$U in silver for the samples. The course of the experiments was checked by examining the structure of the deposited Ag-layers and the integral spectrum of conversion electrons from the samples. Together with $^{235m}$U, in the same way $^{237}$U nuclei from the $^{241}$Pu layer were applied to the preparations as an isotopic tag; its activity in the samples was determined by $^{237}$U γ-quanta.

Dozens of experiments were carried out according to the scheme described above. All of them showed an excess activity of $^{235m}$U for the compared samples, in which $^{235m}$U was in silver longer. But with the same difference in $\Delta t$ in the exposure time of Samples 1 and 2 in silver, the magnitude of this excess varied, apparently due to insufficient reproducibility of the structure of the U–Ag system. The greatest effects were obtained when $^{235m}$U nuclei were deposited on the preparations in an Ar-atmosphere (Fig. 1), which was possibly caused by a change in the ZPFs spectrum during phase transitions in the Ag–U oxide layers at the boundary of the Ag-layers upon annealing of the preparations, as was noted in Section 3. When four samples were prepared at the same time, for them the accumulation of the "step" effect was observed with time, however, this accumulation gradually ceased over a time of about 100 min. Whether this saturation was due to the diffusion of $^{235m}$U nuclei onto the surface of the Ag-layers, or, as discussed in Section 3, it was due to the diffusion of ZPFs into the interior of the Ag-layer with $^{235m}$U nuclei after the phase transition upon annealing of the Ag-layer, this question remained unclear and needs further research.

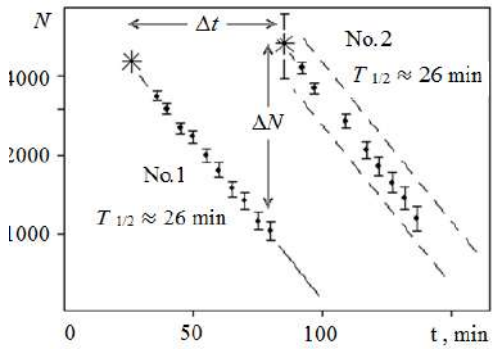


Fig. 1. Example of $^{235m}$U decay curves in Samples 1 and 2. $N$ is the electron count per 60 s, $t$ is the time after the end of $^{235m}$U deposition. Asterisks indicate the moments of silver removal from the samples. Step $\Delta N$ between curves gives $T_{1/2} > 230$ min for $^{235m}$U inside silver. The normalization error for $N$ in Sample 2 (dashed lines) is caused by the $^{237}$U activity measurement in the samples. Here and below, the errors are at the level of one standard deviation

### Isomeric transition 2173 eV of $^{99m}$Tc nuclei in metals

The $^{99m}$Tc isomer with a period $T_{1/2} \approx 6.02$ h decays via a conversion transition of an energy of 2173 eV to the underlying state and then to the ground state of the nucleus, emitting a 140 keV γ-quantum. $T_{1/2}$ can be measured with an accuracy of 0.01%, $T_{1/2}$ variations within 0.1% were observed due to deformation of the electron shell of $^{99m}$Tc atoms. In Ref. [11], an increase in $T_{1/2}$ of the $^{99m}$Tc isomer was found as it deepens into the matrix of Cu, Ag, Sn, Au, and Pb metals. In [11], matrices with $^{99m}$Tc uniformly distributed over them were used. The $^{99m}$Tc matrices of different sizes were compared in terms of the change in the intensity of 140 keV γ-quanta counting with time, using a setup that made it possible to alternately measure γ-spectra from four sources. There always has been $^{99m}$Tc pertechnetate as the reference source. In all cases, the observed $T_{1/2}$ for $^{99m}$Tc increased with an increase in the matrix size and, accordingly, with an increase in the depth of $^{99m}$Tc in the matrix. The decay curves of $^{99m}$Tc in Pb-matrices are shown in Fig. 2.

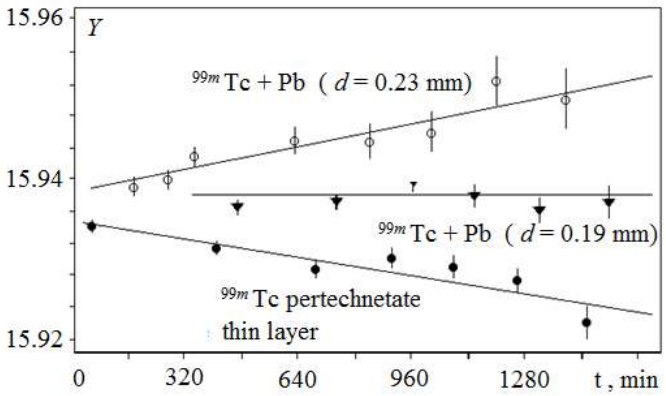


Fig. 2. Decay curves of $^{99m}$Tc in Pb-matrices. $Y = \ln[N(t)\cdot\exp(\ln 2\cdot t/t_o)]$, $t$ is the time, $t_o$ = 6.02 h, $N(t)$ is the count of 140 keV γ-quanta from sources per 3000 s. $d$ is the average depth from which $^{99m}$Tc decay γ-quanta are visible. For the smaller matrix ($d$ = 0.19 mm), $T_{1/2}$ = 6.028 ± 0.002 h, for the larger matrix ($d$ = 0.23 mm) $T_{1/2}$ = 6.043 ± 0.004 h

## Transition 910 eV of $^{154m}$Eu nuclei in tin

The 910 eV transition raising from the decay of the $^{154m}$Eu isomer ($T_{1/2}$ = 46 min) obtained from Sm in the (p, n) reaction at the cyclotron is promising for studying the matrix effect [12]. This transition is at the beginning of one of the competing cascades of ~100 keV γ-transitions, via which the $^{154m}$Eu isomer decays. By measuring the relative yield of these γ-quanta, one can measure 910 eV transition probability for $^{154m}$Eu nuclei directly inside the matrix. Another advantage of this transition is that its energy is less than the energy of the $^{99m}$Tc isomeric transition, and the matrix effect for 910 eV transition should be greater than for $^{99m}$Tc transition. In experiment [12], it actually turned out that when thin flat pieces of an Sm-metal containing $^{154m}$Eu isomers are dissolved in Sn-metal, the probability of 910 eV transition decreases by approximately 20% compared to the probability for $^{154m}$Eu chloride.

## Study of other nuclear isomers in metals

At the Khlopin Radium Institute the $^{229m}$Th, $^{234m}$Pa, and $^{244m}$Np isomers were also studied, but they turned out to be inconvenient for experiments. The isomeric transition in the $^{229m}$Th nucleus has a very low energy $\Delta E \approx 8$ eV, and the transition probability strongly depends on the chemical environment of the isomer; against this background, it is difficult to distinguish the ZPFs effects. For $^{234m}$Pa ($T_{1/2}$ = 1.17 min), it turned out that the isomeric transition has a very high energy $\Delta E \approx 2.5$ keV, and the matrix effects are too small to observe. For the $^{240m}$Np isomer ($\Delta E < 18$ keV, $T_{1/2}$ = 7.22 min), an excess of $T_{1/2}$ for nuclei in the Ag-metal was observed compared to the Np-chloride, but the complexity of the experiment prevented systematic studies.

## Conclusion

The results of the experiments indicate the suppression of conversion transitions of nuclei in metals, which cannot be explained only by the deformation of the electron shells of atoms or by the scattering of conversion electrons in metals. Qualitatively, the effect corresponds to the suppression of these transitions with a decrease in the ZPFs energy density in metals at the transition frequency. Further studies are needed to more accurately elucidate the nature of this effect.

## Acknowledgments

For more than thirty years, dozens of people have participated in these studies, the author was happy to work with them. Late Dr. A.A. Rimskii-Korsakov and Dr. D.N. Suglobov from the Khlopin Radium Institute played a particularly important role, the author is especially grateful to them.

## REFERENCES


1. **Weisskopf V.F., Wigner E.,** Calculation of the natural line breadth on the basis of Dirac's light theory, Zs. Phys. Bd. 63 (1930) 54 – 73.
2. **Koltsov V.V.,** On the resonant character of a nuclear conversion transition and the possibility of its resonant stimulation, Bull. Russ. Acad. Sci.: Phys. 83 (2019) 1144–1148.
3. **Lifshitz E.M., Pitaevskii L.P.,** Statistical Physics, Part 2, Butterworth-Heinemann, Oxford, 1981.
4. **Akhiezer A.I., Berestecky V.B.,** Quantum Electrodynamics, John Wiley and Sons, New-York, 1965.
5. **Koltsov V.V.,** Method for describing the influence of the dielectric properties of the medium on the probability of the isomeric transition $E = 3.5$ eV in the $^{229m}$Th nucleus, Bull. Russ. Acad. Sci.: Phys. 64 (2000) 447–451.
6. **Henke B.L., Gullikson E.M., Davis J.C.,** X-ray interactions: photoabsorption, scattering, transmission, and reflection at E = 50-30000 eV, Z = 1-92, ADNDT **54** (1993) 181–342.
7. **Schiff L.I.,** Quantum Mechanics, McGraw-Hill Inc, New York, 1955.
8. **Koltsov V.V.,** On resonant influence of matrix with isomeric nuclei on isomeric transition probability. Proc. Int. Conf. "Nucleus-2018". Dubna, Russia, July 1-5, (2019) 176.
9. **Koltsov V.V., Rimskii-Korsakov A.A.,** Influence of the electro conducting environment on the decay of the $^{235m}$U isomer, Bull. Acad. Sci. USSR. Phys. Ser. (USA) 53 (1989) 21–24.
10. **Vorjhalov O.V., Zaitzev E.A., Koltsov V.V., Rimskii-Korsakov A.A.,** The study of the decay of the $^{235m}$U isomer inside a conducting medium, Bull. Acad. Sci. USSR. Phys. Ser. (USA) 56 (1992) 30–38.
11. **Koltsov V.V., Suglobov D.N., Masherov L.G. et al.,** New data on the decay constant of the $^{99m}$Tc isomer in tin and lead matrices, Bull. Russ. Acad. Sci.: Phys. 64 (2000) 451–455.
12. **Koltsov V.V., Rimskii-Korsakov A.A., Karasev V.V.,** Influence of a metallic matrix on the probability of the transition at 910 eV in $^{154}$Eu nuclei, Bull. Russ. Acad. Sci.: Phys. 80 (2016) 884–887.


## THE AUTHOR


**KOLTSOV Vladimir V.**
vladimir-koltsov@yandex.ru
ORCID: 0000-0003-1412-2757


*Received 24.10.2022. Approved after reviewing 22.11.2022. Accepted 23.11.2022.*

© Peter the Great St. Petersburg Polytechnic University, 2023

Conference materials
UDC 539.1
DOI: https://doi.org/10.18721/JPM.161.247

# Prospects of light-by-light scattering measurements and axion-like particle searches at the LHC

N.A. Burmasov[1, 2]✉

[1] National Research Center "Kurchatov Institute" – PNPI, Gatchina, Russia;
[2] Moscow Institute of Physics and Technology, Dolgoprudny, Russia
✉ nazar.burmasov@cern.ch

**Abstract.** Ultra-peripheral collisions of heavy ions (UPCs) provide a clean environment for studies of two-photon interactions due to large impact parameters between incoming nuclei at which strong interactions are highly suppressed. In particular, UPCs were used by the ATLAS and CMS collaborations at the LHC to establish the evidence of the light-by-light scattering process (LbyL). In addition, there has been a growing interest to studies of physics beyond the Standard Model (BSM) in photon-induced processes, specifically, to studies of production of axion-like particles (ALPs) that appear in a number of extensions of the Standard Model. The ATLAS and CMS managed to measure differential cross sections of LbyL process and improve limits on ALP-$\gamma$ coupling constant in a range of masses between 5 and 100 GeV, while the region below 5 GeV can be addressed in the future ALICE 3 experiment, the proposed next-generation experiment for LHC Run 5 and beyond. In this work, a review of recent results on LbyL and searches for ALPs at the Large Hadron Collider will be given, and future prospects for the measurements will be discussed.

**Keywords:** heavy-ion collisions, new physics, two-photon interactions

**Funding:** This study was funded by Russian Science Foundation according to the research project 22-42-04405.

**Citation:** Burmasov N.A., Prospects of light-by-light scattering measurements and axion-like particle searches at the LHC, St. Petersburg State Polytechnical University Journal. Physics and Mathematics. 16 (1.2) (2023) 308–314. DOI: https://doi.org/10.18721/JPM.161.247

This is an open access article under the CC BY-NC 4.0 license (https://creativecommons.org/licenses/by-nc/4.0/)

Материалы конференции
УДК 539.1
DOI: https://doi.org/10.18721/JPM.161.247

# Перспективы проведения измерений рассеяния света на свете и поиска аксионоподобных частиц на большом адронном коллайдере

Н.А. Бурмасов[1, 2]✉

[1] Национальный исследовательский центр «Курчатовский институт» – ПИЯФ, г. Гатчина, Россия;
[2] Московский физико-технический институт (национальный исследовательский университет), г. Долгопрудный, Россия
✉ nazar.burmasov@cern.ch

**Аннотация.** Ультра-периферические столкновения тяжелых ядер дают возможность для проведения детальных исследований двухфотонных взаимодействий при значительном подавлении адронных процессов, что достигается благодаря значительным прицельным параметрам между налетающими ядрами. В данной работе рассматриваются перспективы для проведения измерений рассеяния света на свете и поиска аксионоподобных частиц с помощью изучения таких столкновений.

© Burmasov N.A., 2023. Published by Peter the Great St. Petersburg Polytechnic University.

**Ключевые слова:** столкновения тяжелых ионов, новая физика, двухфотонные взаимодействия

**Финансирование:** Работа выполнена при финансовой поддержке Российского научного фонда в рамках проекта № 04405-42-22.

**Ссылка при цитировании:** Бурмасов Н.А. Перспективы проведения измерений рассеяния света на свете и поиска аксионоподобных частиц на Большом адронном коллайдере // Научно-технические ведомости СПбГПУ. Физико-математические науки. 2023. Т. 16. № 1.2. С. 308–314. DOI: https://doi.org/10.18721/JPM.161.247

Статья открытого доступа, распространяемая по лицензии CC BY-NC 4.0 (https://creativecommons.org/licenses/by-nc/4.0/)

## Introduction

Ultra-peripheral collisions of heavy ions (UPCs) provide a unique tool for studies of two-photon interactions [1, 2]. Due to impact parameters being greater than the sum of radii of incoming nuclei, hadronic interactions are strongly suppressed, leading to an increased role of electromagnetic processes. At ultra-relativistic energies electromagnetic field of nuclei is commonly described in terms of the Weizsäcker–Williams formalism and treated as a flux of quasi-real photons with virtualities very close to zero $q^2 < (\hbar c/R)^2$, $R$ being the radius of a nucleus. Photon fluxes depend on the squared nuclear charge $Z^2$, and consequently cross sections of photon-induced processes scale as $Z^4$, therefore one can benefit from much higher interaction probability in the processes of interest in comparison to $pp$ or $e^+e^-$ collisions.

Among all the two-photon interactions that can be studied using UPCs, the light-by-light scattering process (LbyL), $\gamma\gamma \rightarrow \gamma\gamma$, is particularly interesting. This is a process in the Standard Model (SM) proceeding via virtual box-diagrams involving W± bosons and charged fermions (leptons and quarks). The diagrams may include contributions from new virtual charged particles, therefore the process is considered to be sensitive to a number of Standard Model extensions, such as Born-Infeld Theory [3], anomalous gauge couplings [4], supersymmetry [5], monopoles [6], unparticles [7], low-scale gravity [8] and non-commutative interactions [9].

In addition to light-by-light scattering measurements, there has been an increasing interest in searches for axion-like particles (ALPs) in the process $\gamma\gamma \rightarrow a \rightarrow \gamma\gamma$. ALPs are introduced as pseudo Nambu-Goldstone bosons of a new spontaneously broken global symmetry in various extensions of the Standard Model, such as supersymmetry, composite dynamics models and Higgs extension models. Light pseudoscalar ALPs are proposed as dark matter candidates or dark-sector mediators [10–12]. Moreover, there are theories suggesting that ALPs found in the low-mass region below 5 GeV could possibly explain the muon $g - 2$ puzzle [10, 13]. In SM extensions, ALPs couple to photons via the effective Lagrangian:

$$\mathcal{L} = -\frac{1}{4} g_{a\gamma} a F^{\mu\nu} \tilde{F}_{\mu\nu}, \quad (1)$$

where $a$ is the ALP field, $F^{\mu\nu}$ is the photon field strength tensor, and $g_{a\gamma} = 1/\Lambda_a$ the dimensional ALP-$\gamma$ coupling constant related to the high-energy scale $\Lambda$ associated with the broken symmetry. Thus, the production and decay rates of axion-like particles are fully defined in the two-dimensional parameter space of the axion mass ma and the corresponding coupling $g_{a\gamma}$.

In this paper, recent results on measurements of the light-by-light scattering process and searches for axion-like particles at the LHC, as well as future prospects for the measurements are discussed.

## Light-by-light scattering measurements

The first evidence of the light-by-light scattering process was established by the ATLAS and CMS collaborations [14, 15]. Since then, more thorough measurements of differential cross sections were carried out in the region of diphoton invariant masses $m_{\gamma\gamma}$ between 5 and 100 GeV. ATLAS has

© Бурмасов Н.А., 2023. Издатель: Санкт-Петербургский политехнический университет Петра Великого.

reported the total fiducial cross section, $\sigma = 120 \pm 17$ (stat.) $\pm$ 13 (syst.) $\pm$ 4 (lumi.) nb, which is in a good agreement with the value extracted by CMS, $\sigma = 120 \pm 46$ (stat.) $\pm$ 28 (syst.) $\pm$ 12 (theo.) nb. Both results are in accord with theoretical predictions [16]. Unfortunately, accuracy of the measurements is limited by amount of statistics that can be possibly obtained for invariant masses above 5 GeV, and measurements below the threshold are hardly possible due to trigger restrictions in the ATLAS and CMS detectors.

The low-mass region could be addressed in the ALICE 3, the future next-generation experiment at the Large Hadron Collider [17]. The proposed detector design is aimed at measurements of photons at very low transverse momenta down to $p_T \sim 10$ MeV and below.

Considering wide pseudorapidity coverage $|\eta| < 4$ and high particle tracking capabilities, ALICE 3 gives a unique opportunity for precise light-by-light scattering measurements.

However, diphoton measurements at low invariant masses become very challenging due to the presence of a combinatorial background originating from decays of neutral pions $\gamma\gamma \to \pi^0\pi^0 \to \gamma\gamma\gamma\gamma$ [18]. In order to study possible ways of reducing this source of background events, a dedicated Monte Carlo generator for ultra-peripheral collisions, Upcgen [19], was used. For this study, the light-by-light scattering process and production of $\pi^0$ pairs were added to the program. LbyL simulation is based on a dedicated 1-loop calculation that was carried out using FormCalc [20]. Production of neutral pions is based on one of the most complete models of this process that accounts for contribution of intermediate resonance states and QCD mechanisms [21].

We have estimated diphoton invariant mass spectra for LbyL and the $\pi^0$ background in Pb–Pb UPCs at $\sqrt{s_{NN}} = 5.02$ TeV for the case of the ALICE 3 fiducial region considering a proposed integrated luminosity $L = 35$ nb$^{-1}$. As can be seen from Fig. 1, LbyL measurements are hardly possible without a dedicated event selection strategy in the invariant mass range below 3 GeV.

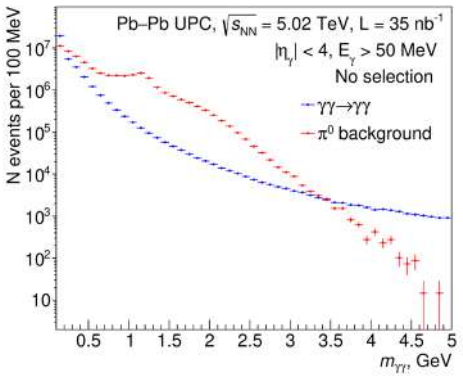


Fig. 1. Diphoton invariant mass spectra of the light-by-light scattering process (blue) and the combinatorial background originating from neutral pion decays (red) for the ALICE 3 acceptance

As proposed in [18], scalar and vector asymmetries of the outgoing photons can be used to reduce background:

$$A_s = \left| \frac{|p_T^1| - |p_T^2|}{|p_T^1| + |p_T^2|} \right|, \quad A_v = \frac{|p_T^1 - p_T^2|}{|p_T^1 + p_T^2|}, \tag{2}$$

where $p_T^1$ and $p_T^2$ are the transverse momenta of the outgoing photons. In the light-by-light scattering process, the majority of the photons have back-to-back topology, therefore their asymmetries are very close to zero, while the relative angular distribution of uncorrelated photons coming from decays of different pions is significantly wider. Indeed, a clear difference in asymmetry distributions can be seen in Fig. 2, where the distributions that were obtained using $10^8$ Upcgen events are shown. In view of the difference in the topology of outgoing photons for the LbyL signal and the combinatorial background, two options for event selection were considered.

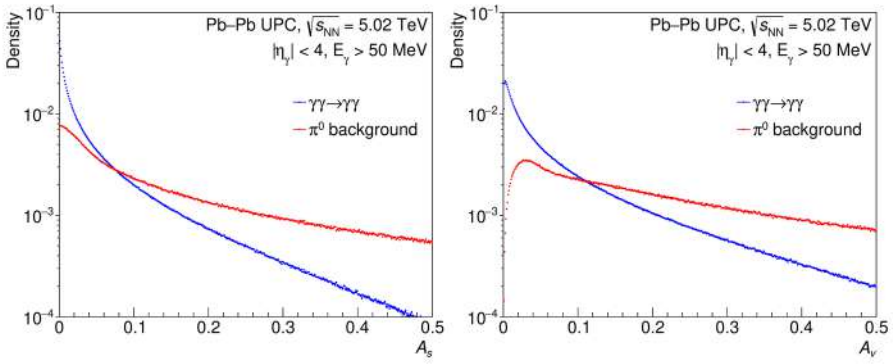


Fig. 2. Normalized scalar (left) and vector (right) asymmetry distributions for LbyL and the combinatorial background

The first approach is based on imposing a simple asymmetry restriction $A_s < 0.02$, as proposed in [18]. Using such criterion, one can effectively suppress background at very low invariant Masses (see Fig. 4, left). However, this rough cut significantly reduces amount of signal events at low invariant masses, which is a major drawback of the approach. In order to improve event selection quality, we applied a machine learning (ML) technique based on the gradient-boosted decision tree algorithm. In this approach, we used a variation of the algorithm implemented by Yandex in their CatBoost library [22]. According to benchmark studies by the CatBoost developers, it provides much faster learning and prediction, up to factors of 30–100, compared to the contemporary gradient boosting libraries, which was verified also in a number of studies in the field of high-energy physics, e.g. [23, 24].

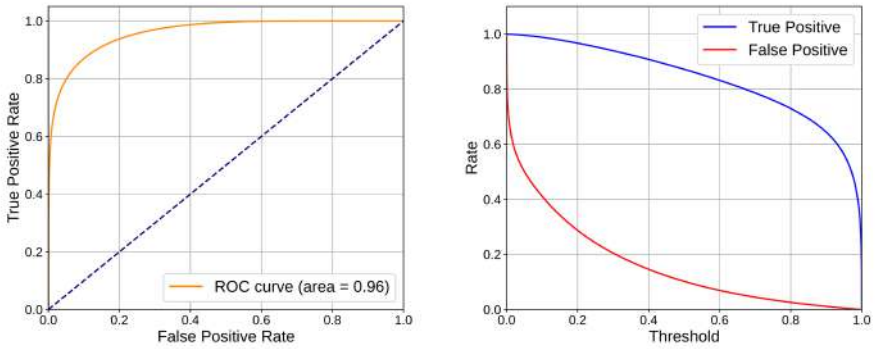


Fig. 3. Characteristic curves for the CatBoost model: ROC-curve (left), true positive and false positive rates as functions of the classification threshold (right)

For model training, all the available kinematic characteristics of the signal and background events were used: four-momenta of the outgoing photons, pair invariant masses and rapidities, as well as scalar and vector asymmetries. The training dataset consisted of $10^8$ LbyL events and $10^8$ uncorrelated photon pairs from the neutral pion decays. The events were generated in Upcgen, and the final state photons were selected using kinematic cuts for the ALICE 3 acceptance: $|\eta_\gamma| < 4$ and $E_\gamma > 50$ MeV.

For quality assurance purposes we have plotted the following characteristic curves using a separate control dataset with the same properties:

true positive rate as a function of the classification threshold (TPR-curve);

false positive rate as a function of the classification threshold (FPR-curve);

receiver operating characteristic (ROC-curve).

The ML model was applied for event selection in the control dataset to estimate diphoton invariant mass spectra for LbyL and the decay photons from $\pi^0$ pair production (see Fig. 4, right). Event selection results were improved drastically in comparison to the simple cut selection: the background was suppressed throughout the mass range, while the majority of signal events were saved.

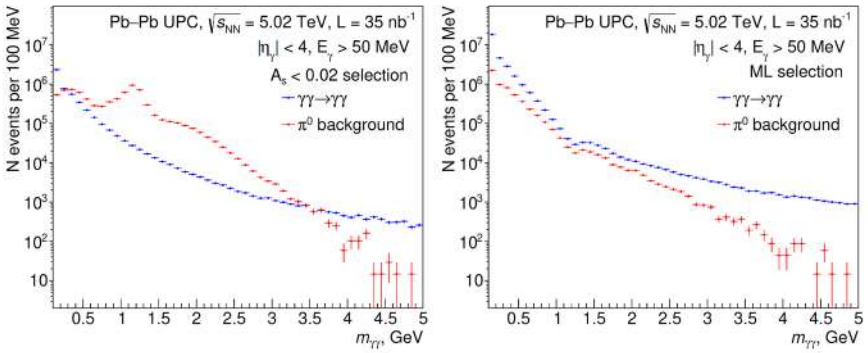


Fig. 4. Diphoton invariant mass spectra for light-by-light scattering process and the combinatorial background with the event selection based on the additional restriction on scalar asymmetry (left) and the machine learning technique (right)

**Searches for axion-like particles**

The strictest limits on ALPs in the mass range between 5 and 100 GeV have been obtained in light-by-light scattering measurements performed in Pb−Pb UPCs by the CMS [15] and ATLAS [14] collaborations. The ALICE experiment has a possibility to improve the limits using data that will be collected during the future Run 3 and Run 4 stages at the LHC [17, 25]. The future ALICE 3 experiment has an opportunity to extend searches to lower ALP masses below 5 GeV.

From the experimental point of view, two-photon interaction with production of an intermediate axion-like particle, $\gamma\gamma \to a \to \gamma\gamma$, is very similar to the light-by-light scattering process [26]. ALP production can be detected by a clear peak in the diphoton invariant mass distribution above background processes. In this measurement, LbyL and decay photons originating from the $\pi^0$ decays are the main sources of background events. In view of the similarity of kinematic properties of ALP production and LbyL scattering, we attempted to improve limits for ALP-γ coupling for the ALICE 3 experiment provided in [17] using ML model, that was previously trained for suppressing the combinatorial background.

To estimate cross section of ALP production and simulate a signal dataset, we upgraded Upcgen and added ALP production channel to the program, with the simulation process based on the narrow-resonance approximation [27]. Event selection was performed using two methods: using a simple asymmetry cut and a combination of the simple asymmetry restriction and the ML technique. Using cross section estimates, Poisson upper limits at confidence level of 95% [28] on $\Lambda_a$ in dependence of ALP mass ma for the case of the ALICE 3 fiducial region were extracted. The limits were obtained for 5% and 100% photon reconstruction efficiencies. A comparison between the limits for the two selection methods obtained in an assumption of the ideal photon

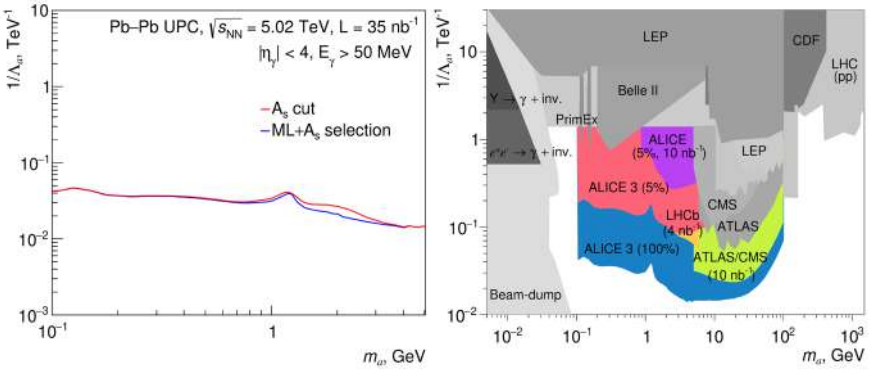


Fig. 5. Left: limits for the ALP-γ coupling obtained using the simple asymmetry cut (red) and using the combination of asymmetry cut with the ML model (blue). Right: limits on ALP-γ coupling constant from existing and future searches for ALPs

reconstruction efficiency is shown in (Fig. 5, left). As can be seen from the figure, only marginal improvement was achieved with ML event selection. Such insignificant change may be due to the fact that in this method only the combinatorial background is suppressed, while LbyL events effectively stay intact.

The results obtained with the combined selection are shown in Fig. 5 (right) in comparison to the existing limits from various experiments (shown in grayscale colors) obtained from [14] and projections for other LHC experiments from [17, 25, 26]. One can see that ALICE 3 has a possibility to reach limits below 1 $TeV^{-1}$ and fill the gap in ALP masses below 5 GeV even with photon reconstruction efficiency of 5% and reach 0.1 $TeV^{-1}$ in the ideal case that can be approached with calorimeter measurements.

## Conclusions

In this paper, an overview of the existing results on the light-by-light scattering process and searches for axion-like particles was given. The future prospects for the measurements were discussed and the results of the feasibility studies for the proposed next-generation experiment at the LHC, ALICE 3, were given.

The study results demonstrated that the ML technique can be used to suppress the $\pi 0$ background dominating in the low invariant mass region much more efficiently in comparison to simple asymmetry cuts, leading to a much higher purity of LbyL signal yield.

The ML technique used for LbyL selection can be also used to select signal events in searches for ALP production due to the similarity of kinematic properties of the two processes. However, the improvement of limits for the ALP-$\gamma$ turned out to be only marginal. It may be explained by the fact that the ML model filtered out only the combinatorial background, leaving LbyL events almost intact. Nevertheless, the projections on the $\Lambda_a$ limits for ALICE 3 obtained in this work proved to be competitive even in the case of photon reconstruction efficiency of 5%.

In continuation of this work, a more thorough study using full simulation framework with realistic detector description for the ALICE 3 experiment will be carried out in order to obtain more precise estimates for the ALP limits and diphoton invariant mass spectra for LbyL measurements.

## Acknowledgments

The author is grateful to Mariola Kłusek-Gawenda for sharing her calculations of $\pi^0$ pair production cross sections that were used to simulate the background in this work.

## REFERENCES

1. **Baltz A.J.**, The physics of ultraperipheral collisions at the LHC. Phys. Rept., 458 (2008) 1–171.
2. **Contreras J.G., Tapia Takaki J.D.**, Ultra-peripheral heavy-ion collisions at the LHC, Int. J. Mod. Phys. A, 30 (2015) 1542012.
3. **Ellis J., Mavromatos N. E., You T.**, Light-by-light scattering constraint on Born-Infeld theory, Phys. Rev. Lett., 118 (2017) 261802.
4. **Brodsky S.J., Zerwas P.M.**, High-energy photon-photon collisions, Nucl. Instrum. Meth. A, 355 (1995) 19–41.
5. **Ohnemus J., Walsh T.F., Zerwas P.M.**, Gamma-gamma production of non-strongly interacting SUSY particles at hadron colliders, Phys. Lett. B, 328 (1994) 369–373.
6. **Ginzburg I.F., Schiller A.**, Search for a heavy magnetic monopole at the Tevatron and CERN LHC, Phys. Rev. D, 57 (1998) 6599–6603.
7. **Cakir O., Ozansoy K.O.**, Unparticle searches through gamma-gamma scattering, Eur. Phys. J. C, 56 (2008) 279–285.
8. **Cheung K.**, Diphoton signals for low scale gravity in extra dimensions, Phys. Rev. D, 61 (2000) 015005.
9. **Hewett J.L., Petriello F.J., Rizzo T.G.**, Signals for noncommutative interactions at linear colliders. Phys. Rev. D, 64 (2001) 075012.
10. **Bauer M., Neubert M., Thamm A.**, Collider Probes of Axion-Like Particles. JHEP, 12 (2017) 044.
11. **Duffy L.D., Bibber K.**, Axions as dark matter particles, New J. Phys., 11 (2009) 105008.
12. **Marsh D.J.E.**, Axion Cosmology. Phys. Rept., (2016) 643:1–79.
13. **Marciano W.J., Masiero A., Paradisi P., and Passera M.**, Contributions of axionlike particles to lepton dipole moments, Phys. Rev. D, 94 (2016) 115033.

14. **Aad G. et al.**, Measurement of light-by-light scattering and search for axion-like particles with 2.2 $nb^{-1}$ of Pb+Pb data with the ATLAS detector, JHEP, 11 (2021) 050.

15. **Sirunyan A.M. et al.**, Evidence for light-by-light scattering and searches for axion-like particles in ultraperipheral PbPb collisions at $\sqrt{s_{NN}} = 5.02$ TeV, Phys. Lett. B, 797 (2019) 134826.

16. **Kłusek-Gawenda M., Lebiedowicz P., Szczurek A.**, Light-by-light scattering in ultraperipheral Pb-Pb collisions at energies available at the CERN Large Hadron Collider, Phys. Rev. C, 93 (2016) 044907.

17. Letter of intent for ALICE 3: A next generation heavy-ion experiment at the LHC, CERN CDS: CERN-LHCC-2022-009.

18. **Kłusek-Gawenda M., McNulty R., Schicker R, Szczurek A.**, Light-by-light scattering in ultraperipheral heavy-ion collisions at low diphoton masses, Phys. Rev. D, 99 (2019) 093013.

19. **Burmasov N., Kryshen E., Buehler P., Lavicka R.**, Upcgen: a Monte Carlo simulation program for dilepton pair production in ultra-peripheral collisions of heavy ions, Comput. Phys. Commun., 277 (2022) 108388.

20. **Hahn T., Perez-Victoria M.**, Automatized one loop calculations in four-dimensions and D-dimensions, Comput. Phys. Commun., 118 (1999) 153–165.

21. **Kłusek-Gawenda M., Szczurek A.**, $\pi^+\pi^-$ and $\pi^0\pi^0$ pair production in photon-photon and in ultraperipheral ultrarelativistic heavy-ion collisions, Phys. Rev. C, 87 (2013) 054908.

22. **Dorogush A. V., Ershov V., Gulin A.**, Catboost: gradient boosting with categorical features support, arXiv: 1810.11363.

23. **Anderlini L. et al.**, Muon identification for LHCb Run 3, JINST, 15 (2020) T12005.

24. **Khairullin E., Ustyuzhanin A.**, Speeding up prediction performance of BDT-based models, J. Phys. Conf. Ser., 1085 (2018) 042009.

25. **Goncalves V.P., Martins D.E., Rangel M.S.**, Searching for axionlike particles with low masses in *p*Pb and PbPb collisions, Eur. Phys. J. C, 81 (2021) 522.

26. **Knapen S., Lin T., Lou H. K., Melia T.**, Searching for axionlike particles with ultraperipheral heavy-ion collisions, Phys. Rev. Lett., 118 (2017) 171801.

27. **Brodsky S.J., Kinoshita T., Terazawa H.**, Two photon mechanism of particle production by high-energy colliding beams, Phys. Rev. D, 4:1532–1557, 1971.

28. **Olive K. A. et al.**, Review of particle physics, Chin. Phys. C, 38 (2014) 090001.

## THE AUTHOR

**BURMASOV Nazar A.**
nazar.burmasov@cern.ch
ORCID: 0000-0002-9962-1880

*Received 30.10.2022. Approved after reviewing 10.11.2022. Accepted 10.11.2022.*

© Peter the Great St. Petersburg Polytechnic University, 2023

MATHEMATICAL PHYSICS

Conference materials
UDC 517.958
DOI: https://doi.org/10.18721/JPM.161.248

# Effects observed in the ballistic-conductive model of heat conduction

S.A. Rukolaine[1]✉

[1] Ioffe Institute, St. Petersburg, Russia

✉ rukol@ammp.ioffe.ru

**Abstract.** In this paper, we study the behavior of solutions to the initial value problem in the framework of the ballistic-conductive (BC) model of heat conduction. As a result of the study, the effect of partial "immobilization" of thermal energy has been found. This effect is unphysical and is a defect of the BC model.

**Keywords:** non-Fourier heat conduction, hyperbolic heat conduction, the ballistic-conductive model

**Citation:** Rukolaine S.A., Effects observed in the ballistic-conductive model of heat conduction, St. Petersburg State Polytechnical University Journal. Physics and Mathematics. 16 (1.2) (2023) 315–321. DOI: https://doi.org/10.18721/JPM.161.248

This is an open access article under the CC BY-NC 4.0 license (https://creativecommons.org/licenses/by-nc/4.0/)

Материалы конференции
УДК 517.958
DOI: https://doi.org/10.18721/JPM.161.248

# Эффект в баллистико-кондуктивной модели теплопроводности

С.А. Руколайне[1]✉

[1] Физико-технический институт им. А.Ф. Иоффе РАН, Санкт-Петербург, Россия

✉ rukol@ammp.ioffe.ru

**Аннотация.** В этой статье мы рассматриваем поведение решений задачи Коши в рамках баллистико-кондуктивной (БК) модели теплопроводности. В результате исследования обнаружен эффект частичной «иммобилизации» тепловой энергии. Этот эффект нефизичен и является дефектом БК модели.

**Ключевые слова:** неклассическая теплопроводность, гиперболическая теплопроводность, баллистико-кондуктивная модель

**Ссылка при цитировании:** Руколайне С.А. Эффект в баллистико-кондуктивной модели теплопроводности // Научно-технические ведомости СПбГПУ. Физико-математические науки. 2023. Т. 16. № 1.2. С. 315–321. DOI: https://doi.org/10.18721/JPM.161.248

Статья открытого доступа, распространяемая по лицензии CC BY-NC 4.0 (https://creativecommons.org/licenses/by-nc/4.0/)

© Rukolaine S.A., 2023. Published by Peter the Great St. Petersburg Polytechnic University.

## Introduction

The heat equation, based on Fourier's law, is commonly used for description of thermal conductivity. However, Fourier's law is valid under the assumption of local equilibrium [1], which is violated in very small dimensions and short timescales, and at low temperatures [2–6]. There are a number of methods for constructing models of non-Fourier thermal conductivity [7–16].

In Ref. [15], a ballistic-conductive (BC) model of heat conduction in the framework of non-equilibrium thermodynamics with internal variables (NET-IV) was developed. The BC model is described by a symmetric hyperbolic system. This provides a finite velocity of thermal energy propagation. However, the finiteness of the propagation velocity is not enough for the model to accurately describe heat transfer. In Ref. [17] this model was tested against experimental data and demonstrated qualitative agreement.

In Refs. [18, 19], we investigated the dual-phase-lag model of heat conduction [4] and showed unphysical effects of this model. In this paper, in order to find out the features of the BC model and to establish its possible limitations, we study the behavior of solutions to the initial value problem in the framework of the BC model. Asymptotic analysis allows us to establish the structure and properties of the solutions without the influence of boundary conditions.

## Statement of the problem

Consider the system of dimensionless equations, describing the ballistic–conductive (BC) model of heat conduction [15, 17]:

$$\begin{gathered}\partial_t T + \partial_x q = f(x,t),\\ \tau_q \partial_t q + q + \partial_x T + k\partial_x Q = 0,\\ \tau_Q \partial_t Q + Q + k\partial_x q = 0,\end{gathered} \tag{1}$$

or, equivalently, $\partial_t \boldsymbol{w} + A\partial_x \boldsymbol{w} + B\boldsymbol{w} = (f,0,0)$, where $\boldsymbol{w} = (T,q,Q)$, $T$ is temperature, $q$ is heat flux, $Q$ is an internal variable, $f \equiv f(x, t)$ is a heat source, $\tau_q$ and $\tau_Q$ are relaxation times, and $k$ is a material parameter. The system (1) is symmetric hyperbolic [20], and the eigenvalues of the matrix $A$ are $\lambda_1 = 0$ and $\lambda_{2,3} = \pm v$, $v = [(k^2 + \tau_Q)/\tau_q\tau_Q]^{1/2}$.

Excluding in the system (1) the variables $q$ and $Q$, we find that temperature satisfies the equation

$$\begin{gathered}\tau_q\tau_Q\partial_t^3 T + \left(\tau_q + \tau_Q\right)\partial_t^2 T + \partial_t T - \partial_x^2 T - \left(k^2 + \tau_Q\right)\partial_t\partial_x^2 T =\\ = \tau_q\tau_Q\partial_t^2 f + \left(\tau_q + \tau_Q\right)\partial_t f + f - k^2\partial_x^2 f,\end{gathered} \tag{2}$$

and we consider the equation on the whole real axis. Note that, if $f = 0$, Eq. (2) takes the form of Eq. (14) in Ref. [17]. We impose the following initial conditions on the system (1): $T|_{t=0} = \varphi(x)$, $q|_{t=0} = 0$, $Q|_{t=0} = 0$. From these conditions and the system (1) we obtain initial conditions for Eq. (2):

$$T\big|_{t=0} = \varphi(x),\ \ \partial_t T\big|_{t=0} = f\big|_{t=0},\ \ \partial_t^2 T\big|_{t=0} = \tau_q^{-1}\varphi''(x) + \partial_t f\big|_{t=0}. \tag{3}$$

## Solution to the initial value problem

In this section we assume that $f = 0$, since below we show that the solution to the initial value problem (2), (3) is the same in the cases $\varphi = \varphi_0(x)$, $f = 0$ and $\varphi = 0$, $f = \varphi_0(x)\delta(t)$, where $\delta(\cdot)$ is the Dirac delta function. If $f = 0$, Eq. (2) takes the form

$$\tau_q\tau_Q\partial_t^3 T + \left(\tau_q + \tau_Q\right)\partial_t^2 T + \partial_t T - \partial_x^2 T - \left(k^2 + \tau_Q\right)\partial_t\partial_x^2 T = 0, \tag{4}$$

and the initial conditions (3) take the form

© Руколайне С. А., 2023. Издатель: Санкт-Петербургский политехнический университет Петра Великого.

$$T\big|_{t=0} = \varphi(x),\ \ \partial_t T\big|_{t=0} = 0,\ \ \partial_t^2 T\big|_{t=0} = \tau_q^{-1}\varphi''(x). \tag{5}$$

The Fourier transform of the temperature distribution is given by

$$\mathcal{F}T = \left\{ \mathrm{e}^{-\mu_1 t} E + \mathrm{e}^{-\mu_2 t} \left[ F\cos Bt + G\frac{\sin Bt}{B} \right] \right\} \mathcal{F}\varphi, \tag{6}$$

(see the derivation in the next section), the coefficients are given by Eqs. (13), (14), (15).

Suppose that $\varphi(x) = \delta(x)$, i.e., all the thermal energy at the initial moment was concentrated at the origin. In this case the Fourier transform of the temperature distribution, which we denote by $T_\delta$, is given by

$$\mathcal{F}T_\delta = \mathrm{e}^{-\mu_1 t} E + \mathrm{e}^{-\mu_2 t} \left[ F\cos Bt + G\frac{\sin Bt}{B} \right].$$

Taking into account the asymptotic behavior of the coefficients, we obtain the asymptotic behavior of the Fourier transform

$$\mathcal{F}T_\delta = \mathrm{e}^{-\mu_{1,\infty} t} E_\infty + \mathrm{e}^{-\mu_{2,\infty} t} \left[ F_\infty \cos v\xi t + G_\infty \frac{\sin v\xi t}{v\xi} \right] + O\left(\frac{1}{\xi^2}\right) \quad \text{as} \quad \xi \to \infty.$$

Performing the inverse Fourier transform we conclude that the temperature distribution has the form $T_\delta(x,t) = T_{\text{sing},1}(x,t) + T_{\text{sing},2}(x,t) + T_{\text{disc}}(x,t) + T_{\text{cont}}(x,t)$, where $T_{\text{sing},1}(x,t) = \mathrm{e}^{-\mu 1,\infty t} E_\infty \delta(x)$ and $T_{\text{sing},2}(x,t) = \mathrm{e}^{-\mu 2,\infty t} F_\infty [\delta(x - vt) + \delta(x + vt)]/2$ are singular terms, $T_{\text{disc}}(x,t) = \mathrm{e}^{-\mu 2,\infty t} G_\infty \mathbf{1}_{(-vt,vt)}/2v$ is a discontinuous term. The term $T_{\text{cont}}$ is a continuous function, since its Fourier transform has the asymptotic behavior $O(1/\xi^2)$ as $\xi \to \infty$.

In the general case the temperature distribution is the convolution of $T_\delta$ with the initial temperature distribution $\varphi$, i.e.,

$$T(x,t) = \int_{-\infty}^{\infty} T_\delta(x-y,t)\varphi(y)\mathrm{d}x \equiv T_1(x,t) + T_2(x,t) + T_3(x,t), \tag{7}$$

where

$$T_1(x,t) = \int_{-\infty}^{\infty} T_{\text{sing},1}(x-y,t)\varphi(y)\mathrm{d}x \equiv \mathrm{e}^{-\mu_{1,\infty} t} E_\infty \varphi(x), \tag{8}$$

$$T_2(x,t) = \int_{-\infty}^{\infty} T_{\text{sing},2}(x-y,t)\varphi(y)\mathrm{d}x \equiv \mathrm{e}^{-\mu_{2,\infty} t} F_\infty \frac{1}{2}\Big[\varphi\big(x-vt\big) + \varphi\big(x+vt\big)\Big], \tag{9}$$

and $T_3$ is the convolution of $T_{\text{disc}} + T_{\text{cont}}$ with $\varphi$. The term $T_1$ means that part of the initial thermal energy does not spread anywhere, though this part decreases exponentially with time. This is an unphysical effect of the BC model. The mathematical reason for this effect is the zero eigenvalue of the matrix $A$ of the system (1). The term $T_2$ means that equal parts of the initial thermal energy propagate in opposite directions with the velocity $v$, while exponentially decaying. The term $T_2$ corresponds to ballistic phonons.

Fig. 1 presents solution (7) to problem (4), (5). The values of the parameters $\tau_q$, $\tau_Q$ and $k$ have been taken from Ref. [21]. We take the function $\varphi_\sigma(x) = [(2\pi)^{1/2}\sigma]^{-1} \exp(-x^2/2\sigma^2)$ as an initial temperature distribution. The figure clearly shows the unphysical term (8) and the "ballistic" term (9). The figure also shows that the portion of thermal energy contained in the unphysical term is comparable to that in the "ballistic" term.

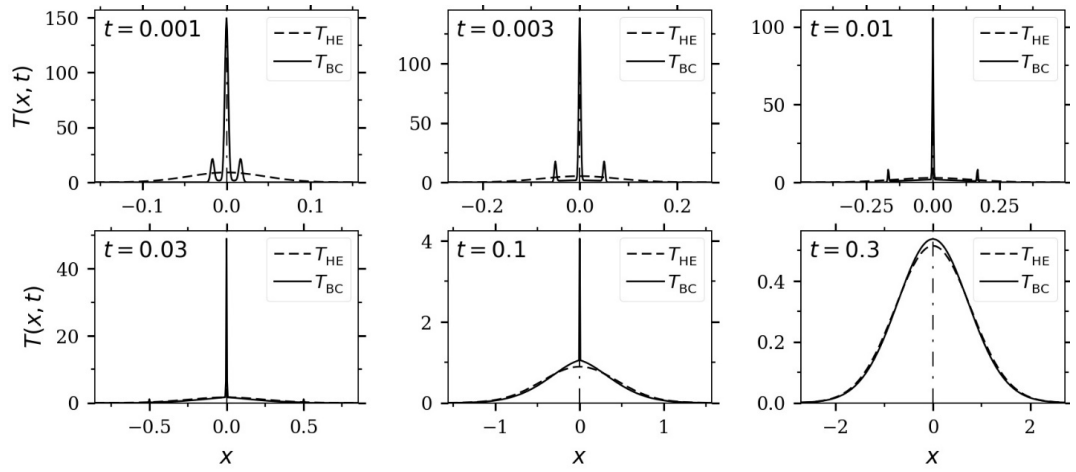


Fig. 1. Solution $T_{\mathrm{BC}}$ to the initial value problem in the framework of the ballistic-conductive model in comparison with the solution $T_{\mathrm{HE}}$ to the initial value problem for the heat equation. The parameters are $\tau_q$ =0.0156, $\tau_Q$ =0.0058 and $k$ =0.140, $\sigma$ =0.002

The solution (7) is compared in the figures with the solution to the initial value problem for the heat equation

$$\partial_t T - \partial_x^2 T = 0, \;\; T\big|_{t=0} = \varphi(x).$$

**Derivation of the solution to the initial value problem**

The Fourier transform of the problem (2), (3) results in the equation

$$\begin{aligned}\tau_q\tau_Q\partial_t^3\mathcal{F}T + \left(\tau_q+\tau_Q\right)\partial_t^2\mathcal{F}T + \partial_t\mathcal{F}T + \xi^2\mathcal{F}T + \left(k^2+\tau_Q\right)\xi^2\partial_t\mathcal{F}T = \\ = \tau_q\tau_Q\partial_t^2\mathcal{F}f + \left(\tau_q+\tau_Q\right)\partial_t\mathcal{F}f + \mathcal{F}f + k^2\xi^2\mathcal{F}f\end{aligned} \tag{10}$$

with initial conditions

$$\mathcal{F}T\big|_{t=0} = \mathcal{F}\varphi, \;\; \partial_t\mathcal{F}T\big|_{t=0} = \mathcal{F}f\big|_{t=0}, \;\; \partial_t^2 T\big|_{t=0} = -\xi^2\tau_q^{-1}\mathcal{F}\varphi + \partial_t\mathcal{F}f\big|_{t=0}. \tag{11}$$

The Laplace transform of the problem (10), (11) results in the equation

$$\begin{aligned}\tau_q\tau_Q\left(s^3\mathcal{L}\mathcal{F}T - s^2\mathcal{F}\varphi + \frac{\xi^2}{\tau_q}\mathcal{F}\varphi\right) + \left(\tau_q+\tau_Q\right)\left(s^2\mathcal{L}\mathcal{F}T - s\mathcal{F}\varphi\right) + \left(s\mathcal{L}\mathcal{F}T - \mathcal{F}\varphi\right) + \\ + \xi^2\mathcal{L}\mathcal{F}T + \left(k^2+\tau_Q\right)\xi^2\left(s\mathcal{L}\mathcal{F}T - \mathcal{F}\varphi\right) = \left[\tau_q\tau_Q s^2 + \left(\tau_q+\tau_Q\right)s + 1 + k^2\xi^2\right]\mathcal{L}\mathcal{F}f.\end{aligned}$$

Hence, the Laplace–Fourier transform of the temperature distribution is given by

$$\mathcal{L}\mathcal{F}T = \frac{\tau_q\tau_Q s^2 + \left(\tau_q+\tau_Q\right)s + 1 + k^2\xi^2}{\tau_q\tau_Q s^3 + \left(\tau_q+\tau_Q\right)s^2 + \left[1 + \left(k^2+\tau_Q\right)\xi^2\right]s + \xi^2}\left(\mathcal{F}\varphi + \mathcal{L}\mathcal{F}f\right). \tag{12}$$

One can see that the solution is the same in the cases $\varphi = \varphi_0(x)$, $f = 0$ and $\varphi = 0$, $f = \varphi_0(x)\,\delta(t)$, where $\delta(\cdot)$ is the Dirac delta function. Therefore, hereafter we assume that $f = 0$. If $f = 0$, Eq. (12) takes the form

$$\mathcal{LF}T = \frac{s^2 + as + (\tau_q\tau_Q)^{-1}\left(1 + k^2\xi^2\right)}{s^3 + as^2 + bs + c}\mathcal{F}\varphi = \left[\frac{E}{u - 2A} + \frac{F(u + A) + G}{\left(u + A\right)^2 + B^2}\right]\mathcal{F}\varphi, \tag{13}$$

where

$$a = \tau_q^{-1} + \tau_Q^{-1},\ b = (\tau_q\tau_Q)^{-1} + v^2\xi^2,\ c = (\tau_q\tau_Q)^{-1}\xi^2,$$
$$s = u - a/3,$$
$$p \equiv p(\xi) = -(a^2/3) + b,\ q \equiv q(\xi) = 2\left(a/3\right)^3 - (ab/3) + c,$$
$$\alpha = \sqrt[3]{-(q/2) + \sqrt{\Delta}},\ \beta = \sqrt[3]{-(q/2) - \sqrt{\Delta}},\ \Delta = \left(p/3\right)^3 + \left(q/2\right)^2,$$
$$A = (\alpha + \beta)/2,\ B = \sqrt{3}(\alpha - \beta)/2,\ C = a/3,\ D = -2\left(a/3\right)^2 + (\tau_q\tau_Q)^{-1}(1 + k^2\xi^2),$$

the roots α and β are chosen so that the equality $\alpha\beta = -p/3$ is valid and the value $A$ is real, and

$$E = \frac{4A^2 + 2AC + D}{9A^2 + B^2},\ F = 1 - E,\ G = \frac{-3A^3 + AB^2 + 3A^2C + B^2C - 3AD}{9A^2 + B^2}. \tag{14}$$

We can conclude that the inverse Laplace transform is equal to

$$\mathcal{L}^{-1}\left[\frac{E}{u - 2A} + \frac{F(u + A) + G}{\left(u + A\right)^2 + B^2}\right] = \mathrm{e}^{-\mu_1 t}E + \mathrm{e}^{-\mu_2 t}\left[F\cos Bt + G\frac{\sin Bt}{B}\right],$$

where

$$\mu_1 \equiv \mu_1(\xi) = -2A + \left(\tau_q^{-1} + \tau_Q^{-1}\right)/3,\ \mu_2 \equiv \mu_2(\xi) = A + \left(\tau_q^{-1} + \tau_Q^{-1}\right)/3. \tag{15}$$

As a result, we obtain that the Fourier transform of the temperature distribution is given by Eq. (6).

**Asymptotic behavior of the coefficients as $\xi \to \infty$**

The asymptotic behavior of the coefficients $p$ and $q$ is given by

$$p = C_p\xi^2\left[1 + O\left(\xi^{-2}\right)\right] \text{ and } q = C_q\xi^2\left[1 + O\left(\xi^{-2}\right)\right],$$

where

$$C_p = v^2,\ C_q = (\tau_q\tau_Q)^{-1} - \left(\tau_q^{-1} + \tau_Q^{-1}\right)v^2/3.$$

Therefore,

$$\sqrt{\Delta} = \left(C_p/3\right)^{3/2}|\xi|^3\left[1 + O\left(\xi^{-2}\right)\right],$$

and the asymptotic behavior of the radicals α and β is given by

$$\alpha = \left(C_p/3\right)^{1/2}|\xi|\left[1 - \left(C_p/3\right)^{-3/2}(C_q/6)|\xi|^{-1} + O\left(\xi^{-2}\right)\right],$$

$$\beta = -\left(C_p/3\right)^{1/2}|\xi|\left[1 + \left(C_p/3\right)^{-3/2}(C_q/6)|\xi|^{-1} + O\left(\xi^{-2}\right)\right].$$

The asymptotic behavior of the coefficients $A$, $B$ and $D$ follows from the above asymptotics and is given by

$$A = (\tau_q^{-1} + \tau_Q^{-1})/6 - (k^2 + \tau_Q)^{-1}/2 + O\left(|\xi|^{-1}\right),\ B = v|\xi|\left[1 + O\left(\xi^{-2}\right)\right]$$

and

$$\text{and } D = k^2 \tau_q^{-1} \tau_Q^{-1} \xi^2 \left[1 + O\left(\xi^{-2}\right)\right].$$

Therefore, the asymptotic behavior of the coefficients $E$, $F$ and $G$ is given by

$$E = E_\infty \left[1 + O\left(\xi^{-2}\right)\right],\ F = F_\infty \left[1 + O\left(\xi^{-2}\right)\right] \text{ and } G = G_\infty \left[1 + O\left(|\xi|^{-1}\right)\right],$$

where

$$E_\infty = \frac{k^2}{k^2 + \tau_Q},\ F_\infty = 1 - E_\infty,\ G_\infty = \frac{2k^2 - \tau_Q}{2(k^2 + \tau_Q)^2}.$$

The asymptotic behavior of the coefficients $\mu_1$ and $\mu_2$ is given by

$$\mu_1 = \mu_{1,\infty} + O\left(\xi^{-2}\right),\ \mu_2 = \mu_{2,\infty} + O\left(\xi^{-2}\right).$$

where

$$\mu_{1,\infty} = (k^2 + \tau_Q)^{-1},\ \mu_{2,\infty} = \left[\tau_q^{-1} + \tau_Q^{-1} - (k^2 + \tau_Q)^{-1}\right]/2.$$

## Conclusions

As a result of the study, the effect of partial “immobilization” of thermal energy was found, when part of the initial thermal energy does not spread anywhere, though this part decreases exponentially with time. This is the defect of the BC model. This effect is similar to that previously established for particles in the mass transfer model, which is described by the Jeffreys-type equation [22].

## REFERENCES


1. **de Groot S.R., Mazur P.,** Non-Equilibrium Thermodynamics, Dover, 1984.
2. **Joseph D.D., Preziosi L.,** Heat waves, Rev. Mod. Phys., 61 (1989) 41–73.
3. **Guo Y., Wang M.,** Phonon hydrodynamics and its applications in nanoscale heat transport. Phys. Rep., 595 (2015) 1–44.
4. **Zhang Z.M.,** Nano/Microscale Heat Transfer. Springer, Cham, 2020.
5. **Chen G.,** Non-Fourier phonon heat conduction at the microscale and nanoscale. Nat. Rev. Phys., 3 (2021) 555–569.
6. **Zhmakin A.I.,** Heat conduction beyond the Fourier law. Tech. Phys., 66 (2021) 1–22.
7. **Guyer R.A., Krumhansl J.A.,** Solution of the linearized phonon Boltzmann equation. Phys. Rev., 148 (1966) 766–778.
8. **Dreyer W., Struchtrup H.,** Heat pulse experiments revisited. Continuum Mech. Thermodyn., 5 (1993) 3–50.
9. **Tzou D.Y.,** Macro- to Microscale Heat Transfer: The Lagging Behavior. Taylor & Francis, Washington, 1997.
10. **Muller I., Ruggeri T.,** Rational Extended Thermodynamics. Springer, New York, 1998.

11. **Ottinger H.C.,** Beyond Equilibrium Thermodynamics. Wiley, Hoboken, 2005.
12. **Jou D., Casas-Vazquez J., Lebon G.,** Extended Irreversible Thermodynamics. Springer, New York, 2010.
13. **Dong Y., Cao B.-Y., Guo Z.-Y.,** Generalized heat conduction laws based on thermomass theory and phonon hydrodynamics. J. Appl. Phys., 110(6) (2011) 063504.
14. **Ma Y.,** A transient ballistic-diffusive heat conduction model for heat pulse propagationin nonmetallic crystals. Int. J. Heat Mass Transf., 66 (2013) 592–602.
15. **Kovacs R., Van P.,** Generalized heat conduction in heat pulse experiments. Int. J. Heat Mass Transf., 83 (2015) 613–620.
16. **Mohammadzadeh A., Struchtrup H.,** A moment model for phonon transport at roomtemperature. Continuum Mech. Thermodyn., 29 (2017) 117–144.
17. **Kovacs R., Van P.,** Models of ballistic propagation of heat at low temperatures. Int. J. Thermophys., 37 (2016) 95.
18. **Rukolaine S.A.,** Unphysical effects of the dual-phase-lag model of heat conduction. Int. J. Heat Mass Transf., 78 (2014) 58–63.
19. **Rukolaine S.A.,** Unphysical effects of the dual-phase-lag model of heat conduction: higher-order approximations. Int. J. Therm. Sci., 113 (2017) 83–88.
20. **Courant R., Hilbert D.,** Methods of Mathematical Physics. Volume II. Partial Differential Equations. Wiley, Singapore, 1962.
21. **Kovacs R., Van P.,** Second sound and ballistic heat conduction: NaF experiments revisited. Int. J. Heat Mass Transf., 117 (2018) 682–690.
22. **Rukolaine S. A., Samsonov A. M.,** Local immobilization of particles in mass transfer described by a Jeffreys-type equation. Phys. Rev. E, 88 (2013) 062116.

## THE AUTHOR

**RUKOLAINE Sergey A.**
rukol@ammp.ioffe.ru

*Received 21.10.2022. Approved after reviewing 14.11.2022. Accepted 15.11.2022.*

© Peter the Great St. Petersburg Polytechnic University, 2023

Conference materials
UDC 53:51
DOI: https://doi.org/10.18721/JPM.161.249

# Electromagnetic fields of regular rotating electrically charged objects in nonlinear electrodynamics minimally coupled to gravity

I.G. Dymnikova[1], E.V. Galaktionov[1]✉

[1] Ioffe Institute, St. Petersburg, Russia

✉ galakt@ammp.ioffe.ru

**Abstract.** We present a brief overview of the main properties of electromagnetic fields of regular rotating electrically charged objects in non-linear electrodynamics minimally coupled to gravity (NED-GR). The basic features of electromagnetic fields follow from the analysis of the regular solutions to the NED-GR dynamic equations. For NED-GR regular objects the Lagrangian inevitably branches at a single minimum of the field invariant $F$. The study of the asymptotic of the solutions of the field equations at $r \to 0$ reveals the fundamental features of the electromagnetic dynamics on the de Sitter vacuum disk ($r = 0$) in the deep interiors of rotating NED-GR objects. The disk has the properties of a perfect conductor and an ideal diamagnetic, zero magnetic induction, and is confined by a ring with a superconducting current, which replaces the Kerr ring singularity, serves as a non-dissipative source of electromagnetic fields of NED-GR regular objects and provides the origin of their intrinsic magnetic momenta.

**Keywords:** non-linear electrodynamics, Lagrangian, asymptotic of the solutions

**Citation:** Dymnikova I.G., Galaktionov E.V., Electromagnetic fields of regular rotating electrically charged objects in nonlinear electrodynamics minimally coupled to gravity, St. Petersburg State Polytechnical University Journal. Physics and Mathematics. 16 (1.2) (2023) 322–329. DOI: https://doi.org/10.18721/JPM.161.249

This is an open access article under the CC BY-NC 4.0 license (https://creativecommons.org/licenses/by-nc/4.0/)

Материалы конференции
УДК 53:51
DOI: https://doi.org/10.18721/JPM.161.249

# Электромагнитные поля регулярных вращающихся электрически заряженных объектов в нелинейной электродинамике, минимально связанной с гравитацией

И.Г. Дымникова[1], Е.В. Галактионов[1]✉

[1] Физико-технический институт им. А.Ф. Иоффе РАН, Санкт-Петербург, Россия

✉ galakt@ammp.ioffe.ru

**Аннотация.** Приведен краткий обзор основных свойств электромагнитных полей регулярных вращающихся электрически заряженных объектов в нелинейной электродинамике, минимально связанной с гравитацией (NED-GR). Основные черты электромагнитных полей следуют из анализа регулярных решений динамических уравнений NED-GR. Для обычных объектов NED-GR Лагранжиан неизбежно разветвляется в единственной точке минимума инварианта поля F. Изучение асимптотики решений уравнений поля при $r$, стремящемся к нулю, раскрывает основные черты электромагнитной динамики на вакуумном диске де Ситтера ($r = 0$) в глубоких недрах вращающихся объектов NED-GR. Диск обладает свойствами идеального проводника и идеального диамагнетика с нулевой магнитной индукцией и ограничен кольцом со сверхпроводящим током, заменяющим сингулярность кольца Керра, и, кроме того, служит недиссипативным источником электромагнитных полей для регулярных объектов NED-GR и обеспечивает возникновение их собственных магнитных моментов.

© Dymnikova I.G., Galaktionov E.V., 2023. Published by Peter the Great St. Petersburg Polytechnic University.

**Ключевые слова:** нелинейная электродинамика, Лагранжиан, асимптотика решений

**Ссылка при цитировании:** Дымникова И.Г., Галактионов Е.В. Электромагнитные поля регулярных вращающихся электрически заряженных объектов в нелинейной электродинамике, минимально связанной с гравитацией // Научно-технические ведомости СПбГПУ. Физико-математические науки. 2023. Т. 16. № 1.2. С. 322–329. DOI: https://doi.org/10.18721/JPM.161.249

Статья открытого доступа, распространяемая по лицензии CC BY-NC 4.0 (https://creativecommons.org/licenses/by-nc/4.0/)

## Introduction

Electrically charged objects related by electromagnetic and gravitational interactions are described in general setting by nonlinear electrodynamics coupled to gravity (NED-GR). Nonlinear electrodynamics (NED) was proposed by Born and Infeld in 1934 with the aim to describe electromagnetic field and particles in the unique common frame which provides finite values for physical quantities, and presents an appropriate model of the electron [1]. In their theory electromagnetic energy has made finite by imposing an upper limit on the electric field related to the electron size, but geometrical quantities remained singular.

The Born-Infeld program can be realized in the frame essentially including gravity. Source-free NED-GR equations admit the class of regular axially symmetric solutions asymptotically Kerr-Newman for a distant observer [2–4], which describe not only electromagnetic spinning solitons [5] (for a review see [6]) but also regular rotating electrically charged black holes.

Axially symmetric metrics are typically obtained from the spherical metrics of the Kerr–Schild class [7] by applying the Gürses–Gürsey formalism [8]. For this class of metrics the source terms have the algebraic structure [5]

$$T_t^t = T_r^r \ \ (p_r = -\rho). \tag{1}$$

In the Boyer–Lindquist coordinates the axially symmetric metric reads [8]

$$ds^2 = \frac{2f-\Sigma}{\Sigma}dt^2 + \frac{\Sigma}{\Delta}dr^2 + \Sigma d\theta^2 - \frac{4af\sin^2\theta}{\Sigma}dtd\phi + \\ + \left(r^2 + a^2 + \frac{2fa^2\sin^2\theta}{\Sigma}\right)\sin^2\theta d\phi^2. \tag{2}$$

Here $a$ is the angular momentum, the Lorentz signature is [- + + +], $\Sigma = r^2 + a^2\cos^2\theta$, $\Delta = r^2 + a^2 - 2f(r)$, and $f(r) = r\int_0^r \tilde{\rho}(x)x^2dx$ where $\tilde{\rho}$ is the density profile of a related spherical solutions. The surfaces of constant $r$ are the oblate confocal ellipsoids $r^4 - (x^2 + y^2 + z^2 - a^2)r^2 - a^2z^2 = 0$ which degenerate, for $r = 0$ to the equatorial disk $x^2 + y^2 \le a^2$, $z = 0$ bounded by the ring $x^2 + y^2 = a^2$, $z = 0$.

Spacetime can have at most two horizons defined by $\Delta(r) = 0$, and at most two ergospheres which are surfaces of a static limit $g_{tt} = 0$ [2]. Ergospheres confine ergoregions where $g_{tt} < 0$ which makes possible extraction of rotational energy. Geometrical structure of a regular rotating object with the metric (2) is determined by the weak energy condition (WEC) which requires $\rho > 0$ and $\rho + p_\perp \ge 0$. The density and pressures are related by [2]

$$\rho(r,\theta) + p_\perp(r,\theta) == \frac{r^2}{\Sigma}\left[2\left(\frac{r^2}{\Sigma} - 1\right)\tilde{\rho}(r) - \frac{r}{2}\tilde{\rho}'\right] = \\ = \frac{r|\tilde{\rho}'|}{2\Sigma^2}S(r,z);\ S(r,z) = r^4 - \frac{2a^2z^2}{r|\tilde{\rho}'|}(\tilde{\rho} - \tilde{p}_\perp). \tag{3}$$

© Дымникова И.Г., Галактионов Е.В., 2023. Издатель: Санкт-Петербургский политехнический университет Петра Великого.

The prime denotes the derivative with respect to $r$. In the equatorial plane $r^2/\Sigma = 1$, and $(p_\perp + \rho) = -r\tilde{\rho}'(r)/2$. For regular spherical solutions satisfying WEC $\tilde{\rho}' \le 0$ and $r\tilde{\rho}'(r) \to 0$ at $r \to 0$. Equation of state takes the form $p = -\rho$ and describes the de Sitter vacuum in the co-rotating frame. The interior de Sitter vacuum disk is the generic feature of all regular rotating objects of this class [5, 2].

If the function $S(r,z)$ in (3) vanishes only on the disk $r = 0$, WEC is satisfied. This type of structure is shown in Fig. 1 (Left) together with the horizons $r_+$, $r_-$ and the ergosphere. There can exist an additional surface of the de Sitter vacuum $p_\perp + \rho = 0$, $S$-surface which incorporates the de Sitter disk as a bridge [2]. Then WEC is violated in the cavities between the $S$-surface and the disk, filled with an anisotropic phantom fluid, $p_r = -\rho$; $p_\perp = w_\perp \rho$ with $w_\perp < -1$ [3]. This type of interiors is shown in Fig. 1 (Middle) for the case $\alpha < \pi\beta^2/8$, and in Fig. 1 (Right) for the case $\alpha > \pi\beta^2/8$, where $\alpha = a/m$ is the specific angular momentum and $\beta = q/m$ is the specific charge. The parameter $r_q$ denotes the characteristic radius $r_q = \pi q^2/8m$ for the regularized Newtonian/Coulomb profile applied for pictures [2].

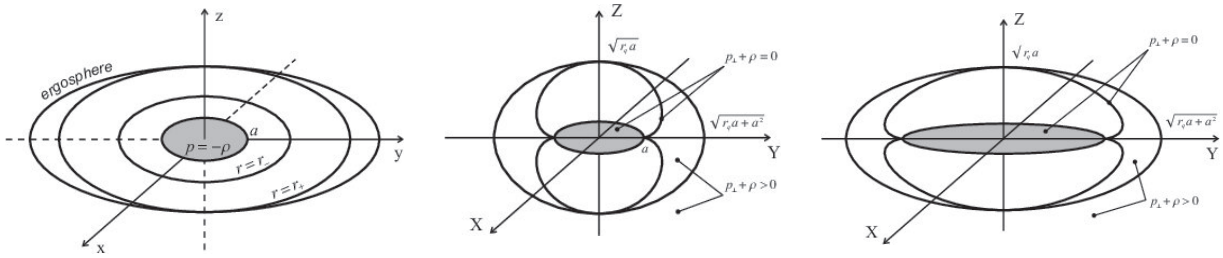


Fig. 1. Typical structure satisfying WEC (Left), and two cases of typical structure violating WEC: the cases with $\alpha < \pi\beta^2/8$ (Middle) and $\alpha > \pi\beta^2/8$ (Right)

NED-GR solutions for electrically charged objects belong to this class automatically since for any gauge-invariant Lagrangian $L(F)$ stress-energy tensor of an electromagnetic field, $T^\mu_\nu = -2\mathcal{L}_F F_{\nu\alpha} F^{\mu\alpha} + 0.5\delta^\mu_\nu \mathcal{L}$ has the algebraic structure specified by (1) [9, 5]. In the Maxwell weak field limit the metric tends to the Kerr–Newman metric with $f(r) = mr - q^2/2$, where $m$ is the mass of an object and $q$ its electric charge.

The first problem encountered by regular electrically charged NED-GR objects, is the problem of their existence itself, which appears forbidden by "the nonexistence theorems" [10].

This existential problem is addressed in Section 2 where we outline the typical behavior of Lagrangians. Section 3 presents the basic features of regular solutions for electromagnetic fields in the limit $r \to 0$ and $r \to \infty$, and Section 4 contains conclusions.

## Typical behavior of the Lagrangian for NED-GR regular objects

In the minimally coupled NED-GR the action is given (in geometrical units $c = G = 1$) by

$$S = \frac{1}{16\pi}\int d^4x\sqrt{-g}\,[R - \mathcal{L}(F)];\; F = F_{\mu\nu}F^{\mu\nu}. \tag{4}$$

Here $R$ is the scalar curvature, $F_{\mu\nu} = \partial_\mu A_\nu - \partial_\nu A_\mu$ is the electromagnetic field, and $A_\mu$ is the Maxwell limit of electromagnetic potential. The gauge-invariant electromagnetic Lagrangian $\mathcal{L}(F)$ should have the Maxwell limit, $\mathcal{L} \to F$, $\mathcal{L}_F = d\mathcal{L}/dF \to 1$ in the weak field regime. Variation with respect to $A_\mu$ and the Bianchi identities yield the dynamic field equations

$$\nabla_\mu(L_F F^{\mu\nu}) = 0;\; \nabla_\mu {}^*F^{\mu\nu} = 0, \tag{5}$$

where ${}^*F^{\mu\nu} = 1/2\eta^{\mu\nu\alpha\beta}F_{\alpha\beta}$, and the antisymmetric unit tensor is defined as $\eta_{0123} = \sqrt{-g}$.

In the spherically symmetric cases the only essential component of $F_{\mu\nu}$ describes a radial electric field $F_{01} = -E(r)$. Dynamical Eqs. (5) give $r^2\mathcal{L}_F F^{01} = q$ [10] where $q$ is constant of integration identified as an electric charge. The field invariant $F$ is given by

$$F = 2F_{01}F^{01} = -\frac{2q^2}{\mathcal{L}_F^2 r^4}. \tag{6}$$

For electrically charged NED-GR structures the density and pressures are given by [9]

$$\rho = -p_r = (\mathcal{L}/2 - F\mathcal{L}_F);\ p_\perp = -\mathcal{L}/2;\ p_\perp + \rho = -F\mathcal{L}_F. \tag{7}$$

WEC imposes two general constraints on the Lagrangian $\mathcal{L}(F)$. Equation (7) leads to

$$\mathcal{L}_F \geq 0;\ \mathcal{L}(F) \geq 2F\mathcal{L}_F. \tag{8}$$

The theorem of non-existence of electrically charged structures with the regular center [10] requires the Maxwell behavior at the center, $\mathcal{L} \to F$, $\mathcal{L}_F \to 1$ as $F \to 0$ [10]. The proof is that regularity of stress-energy tensor requires $|F\mathcal{L}_F| < \infty$ as $r \to 0$, while $F\mathcal{L}_F^2 \to -\infty$ by virtue of (6). It follows that $\mathcal{L}_F \to 0$, while $F \to 0$ which is not compatible with the Maxwell behavior.

In fact, regularity and WEC suggest existence of regular electrically charged structures without the Maxwell limit in the center. Regularity requires $\rho < \infty$. WEC requires $\rho \geq 0$ and $\rho + p_\perp \geq 0$ which leads to $\rho' \leq 0$ since the tangential pressure satisfies $\rho + p_\perp = -r\rho'/2$. As a result, the electromagnetic density $T^t_t = \rho$ achieves its maximum, and one cannot expect the weak field behavior in the region of the maximal density. De Sitter vacuum in the centers of regular solutions implies $p_\perp + \rho = 0$ which leads to $F\mathcal{L}_F = 0$ at $r = 0$. It follows, taking into account (8) and (6), that $\mathcal{L}_F \to +\infty$ while $F \to -0$ when $r \to 0$.

Conditions for a Lagrangian and its derivative in the regular center are thus

$$\mathcal{L}(0) = 2\rho(0);\ \mathcal{L}_F \to \infty. \tag{9}$$

The Maxwell asymptotic at $r \to +\infty$ imposes two conditions on Lagrangian in the limit $F \to -0$

$$\mathcal{L} \to F \to -0;\ \mathcal{L}_F \to 1. \tag{10}$$

The invariant $F$ evolving between $F = -0$ at the center and at infinity, is not monotonic function, which leads unavoidable to branching of a Lagrangian [10, 9]. Lagrangian on its way from (9) to (10) must change its sign; according to (7), it is opposite to the sign of the pressure $p_\perp$ which can vanish only once for the case of one de Sitter vacuum scale [9].

As a result a Lagrangian has two branches, and the action takes the form [11]

$$S = S_{int} + S_{ext} = \\ = \frac{1}{16\pi}\left[\int_{\Omega_{int}} (R - \mathcal{L}_{int}(F))\sqrt{-g}\, d^4x + \int_{\Omega_{ext}} (R - \mathcal{L}_{ext}(F))\sqrt{-g}\, d^4x\right]. \tag{11}$$

Each region of the manifold, $\Omega_{int}$ and $\Omega_{ext}$, is confined by the space-like hypersurfaces $t = t_{in}$ and $t = t_{fin}$ and by the time-like 3-surface at infinity, where electromagnetic fields vanish in the Maxwell limit. Internal boundary between $\Omega_{int}$ and $\Omega_{ext}$ is defined as a time-like hypersurface $\Sigma_c$ at which the field invariant $F$ achieves its minimum. In the case of the minimal coupling variation in the action (11) results in the dynamical Eqs. (5) in both regions $\Omega_{int}$ and $\Omega_{ext}$, and in the boundary conditions on the surface $\Sigma_c$ [11].

$$\int_{\Sigma_c} \left(\mathcal{L}_{F\,(int)} F_{\mu\nu\,(int)} - \mathcal{L}_{F\,(ext)} F_{\mu\nu\,(ext)}\right)\sqrt{-g}\, \delta A^\mu d\sigma^\nu = 0, \tag{12}$$

$$\mathcal{L}_{(int)} - 2\mathcal{L}_{F\,(int)} F_{int} = \mathcal{L}_{(ext)} - 2\mathcal{L}_{F\,(ext)} F_{ext}. \tag{13}$$

Eq. (6) defines in the first approximation the derivative $d\mathcal{L}_F/dF$ in the minimum $r = r_c$ of the invariant $F$ by $\mathcal{L}_{FF} = -2\mathcal{L}_F/(Fr_c)$. In accordance with (8), $\mathcal{L}_F$ has the same finite limit as $F \to F_c + 0$ and $F \to F_c - 0$, while $F$ changes its sign, so that $\mathcal{L}_{FF}$ tends to infinities of opposite signs, and a Lagrangian $\mathcal{L}(F)$ has the cusp at $F = F_c$.

According to (8), the Lagrangian $\mathcal{L}(F)$ is a monotonic function of $F$ which decreases smoothly along the first branch from its maximal value $\mathcal{L}(0) = 2\rho(0)$ to its value in the cusp $\mathcal{L}_c$ at $F = F_{min} = F_c$, and then increases along the second branch from its minimal value $\mathcal{L}_c < 0$ to its Maxwell limit $\mathcal{L} \to F \to -0$ as $F$ increases from $F_c$ to $F \to -0$ as $r \to \infty$. Typical behavior of the Lagrangian and its derivatives dependently on $F$ is shown in Fig. 2 [3].

Similar behavior of $\mathcal{L}(F)$ is generic for regular axially symmetric solutions where the invariant $F$ evolves between $F = -0$ on the disk $r = 0$ [2] and in the Maxwell limit at $r \to \infty$ [12].

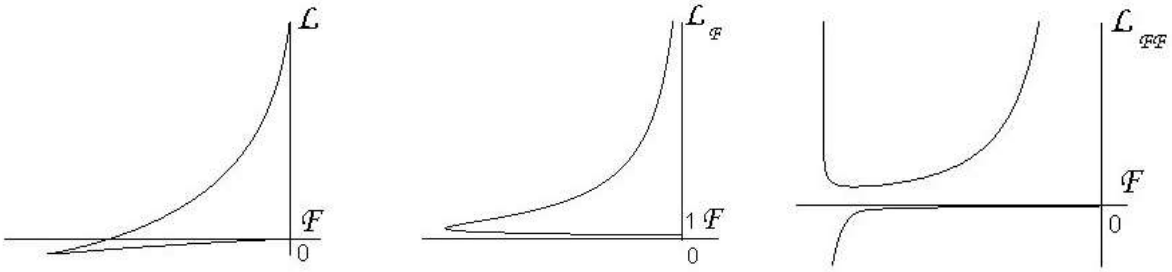


Fig. 2. Typical behavior of the Lagrangian (Left), Lagrangian derivative (Middle), and the second Lagrangian derivative (Right)

## Electromagnetic fields

In the axially symmetric geometry the non-zero field components are $F_{01}$, $F_{02}$, $F_{13}$, $F_{23}$, related in the metric (2) by $F_{31} = a\sin^2\theta F_{10}$; $F_{23} = (r^2 + a^2)F_{02}$. As a result, Eqs. (5) form the system of four equations for two independent functions [2]

$$\frac{\partial}{\partial r}[(r^2+a^2)\sin\theta\mathcal{L}_F F_{10}] + \frac{\partial}{\partial\theta}[\sin\theta\mathcal{L}_F F_{20}] = 0;$$
$$\frac{\partial}{\partial r}\left[\frac{\mathcal{L}_F F_{31}}{\sin\theta}\right] + \frac{\partial}{\partial\theta}\left[\frac{\mathcal{L}_F F_{32}}{(r^2+a^2)\sin\theta}\right] = 0; \tag{14}$$

$$\frac{\partial F_{23}}{\partial r} + \frac{\partial F_{31}}{\partial\theta} = 0;\ \frac{\partial F_{01}}{\partial\theta} + \frac{\partial F_{20}}{\partial r} = 0. \tag{15}$$

Solutions to this system should satisfy the compatibility condition [2]

$$\frac{\partial}{\partial r}\left(\frac{1}{\mathcal{L}_F}\frac{\partial\mathcal{L}_F}{\partial\theta}\right)\frac{\partial}{\partial\theta}\left(\frac{1}{\mathcal{L}_F}\frac{\partial\mathcal{L}_F}{\partial r}\right) + \frac{4a^2\sin^2(\theta)}{\Sigma^2}\frac{1}{\mathcal{L}_F^2}\left[r\frac{\partial\mathcal{L}_F}{\partial r} + \cot(\theta)\frac{\partial\mathcal{L}_F}{\partial\theta}\right]^2 = 0, \tag{16}$$

as the necessary and sufficient condition of compatibility of Eqs. (14)–(15) and the necessary condition for the existence of solutions [2].

Equations (14–15) and compatibility condition (16) are satisfied by the functions [5]

$$\Sigma^2(\mathcal{L}_F F_{01}) = -q(r^2 - a^2\cos^2\theta);\ \Sigma^2(\mathcal{L}_F F_{02}) = qa^2 r\sin 2\theta; \tag{17}$$

$$\Sigma^2(L_F F_{31}) = aq\sin^2\theta\,(r^2 - a^2\cos^2\theta);\ \ \Sigma^2(L_F F_{23}) = aqr(r^2+a^2)\sin 2\theta \tag{18}$$

in the weak field limit $\mathcal{L}_F = 1$, where they coincide with the solutions to the Maxwell-Einstein equations [13, 14, 15], and in the strongly nonlinear regime as the asymptotic solutions in the limit $\mathcal{L}_F \to \infty$ [2]. In terms of the field intensities defined as $E_j = \{F_{j0}\}$; $D^j = \{\mathcal{L}_F F^{0j}\}$; $B^j = \{{}^*F^{0j}\}$; $H_j = \{\mathcal{L}_F {}^*F_{0j}\}$; $j = 1, 2, 3$ [16, 5], the dynamical Eqs. (5) take the form of the source-free Maxwell equations

$$\nabla \cdot \mathbf{D} = 0;\ \nabla \times \mathbf{H} = \frac{\partial \mathbf{D}}{\partial t};\ \nabla \cdot \mathbf{B} = 0;\ \nabla \times \mathbf{E} = -\frac{\partial \mathbf{B}}{\partial t}. \tag{19}$$

The electric induction **D** and the magnetic induction **B** are related with the field intensities by $D^j = \varepsilon^j_k E^k$; $B^j = \mu^j_k H^k$ where $\varepsilon^k_j$ and $\mu^k_j$ are the tensors of the electric and magnetic permeability given by [5]

$$\varepsilon^r_r = \frac{(r^2 + a^2)}{\Delta}\mathcal{L}_F;\ \varepsilon^\theta_\theta = \mathcal{L}_F;\ \mu^r_r = \frac{(r^2 + a^2)}{\Delta \mathcal{L}_F};\ \mu^\theta_\theta = \frac{1}{\mathcal{L}_F}. \tag{20}$$

The relation connecting density and pressure with the electromagnetic fields reads [5]

$$p_\perp + \rho = 2\mathcal{L}_F \left( F^2_{10} + \frac{F^2_{20}}{a^2 \sin^2 \theta} \right). \tag{21}$$

According to (20) and (21), WEC should be satisfied for NED-GR structures, since $\mathcal{L}_F$ defines the electric permeability, which cannot be negative in electrodynamics of continuous media.

Applying (17, 18) in the limit $\mathcal{L}_F \to \infty$ we obtain

$$p_\perp + \rho = \frac{2q^2}{\mathcal{L}_F \Sigma^2}. \tag{22}$$

It follows that $L_F \to \infty$ at the *S*-surface, including disk where $\rho + p_\perp = 0$. This testifies for zero magnetic permeability and infinite electric permeability, i.e., for the properties of a perfect conductor and an ideal diamagnetic of the disk and *S*-surface. On these surfaces the magnetic induction **B** vanishes [17].

The surface current on the disk is obtained, with taking into account (17, 18) and (20), as [17]

$$j_\phi = -\frac{q}{2\pi a}\sqrt{1 + q^2/a^2}\ \sin^2 \xi \frac{\mu}{\cos^3 \xi}, \tag{23}$$

where $\xi$ is the intrinsic coordinate on the disk, $0 \le \xi \le \pi/2$. The magnetic permeability $\mu = 0$ on the disk by virtue of (20). As a result, the current $j_\phi$ is zero throughout the disk except the ring $\xi = \pi/2$, where both terms in the second fraction go to zero independently and the current on the ring can be any and amount to a non-zero value, which means that the basic condition for superconducting state [18] is satisfied.

The superconducting current (23) replaces the ring singularity of the Kerr–Newman geometry, represents a non-dissipative source of the exterior fields and of the intrinsic magnetic momentum [19], and can in principle provide a practically unlimited life time of an object [17].

## Conclusions

Analysis of regular axially symmetric solutions to the NED-GR dynamic equations, which describe electrically charged regular rotating black holes and spinning electromagnetic solitons, allows us to reveal the fundamental features of electrically charged regular rotating NED-GR objects. They can have two types of interiors suggested by geometry, whose detailed properties are determined by behavior of electromagnetic fields and by the weak energy condition involving dependence on the electric permeability which is regulated by the basic requirements of electrodynamics of continuous media. Their obligatory basic features are as follows:

For regular solutions the electromagnetic invariant $F$ is non-monotonic function evolving between $F = -0$ at $r = 0$ and at $r \to \infty$. This results in branching of a Lagrangian in the minimum of the invariant $F$. The basic generic feature of the regular electrically charged NEDGR structures is the existence of a characteristic surface separating regions described by different branches of Lagrangians in the non-uniform variational problem.

All NED-GR electrically charged regular rotating objects have in their deep interiors de Sitter vacuum disks $r = 0$ with the properties of a perfect conductor and an ideal diamagnetic, and zero magnetic induction.

De Sitter disk is confined by the ring with a superconducting current which serves as a non-dissipative source of electromagnetic fields of a NED-GR regular object, and provides the origin of its intrinsic magnetic momentum.

There can exist additional interior de Sitter vacuum $S$-surfaces with de Sitter disk as a bridge and with the properties of a perfect conductor and an ideal diamagnetic and zero magnetic induction over the whole surface.

Violation of WEC is prevented by the basic requirement of non-negativity of the electric permeability in electrodynamics of continuous media, which prefers the NED-GR structures without $S$-surfaces, and distinguishes admissible models for interiors of NED-GR objects with $S$-surfaces: shell-like models with the flat vacuum and zero fields in the cavities between $S$-surfaces and disks, and models with the de Sitter vacuum cores within $S$-surfaces, with the properties of a perfect conductor and an ideal diamagnetic and zero magnetic induction over the whole core [2, 3]. Such models require further research.

## REFERENCES

1. **Born M., Infeld L.,** Foundation of the New Field Theory, Proceedings of the Royal Society of London A. 852 (144) (1934) 425–451.

2. **Dymnikova I.G., Galaktionov E.V.,** Regular rotating electrically charged black holes and solitons in non-linear electrodynamics minimally coupled to gravity, Class. Quant. Gravity. 16 (32) (2015), 165015.

3. **Dymnikova I.G., Galaktionov E.V.,** Dynamics of electromagnetic fields and structure of regular rotating electrically charged black holes and solitons in nonlinear electrodynamics minimally coupled to gravity, Universe. 5 (205) (2019) 14.

4. **Dymnikova I.G., Galaktionov E.V.,** Regular electrically charged objects in nonlinear electrodynamics coupled to gravity, J. Phys.: Conf. Ser. 1 (2103) (2021) 012080.

5. **Dymnikova I. G.,** Spinning superconducting electrovacuum soliton, Phys. Lett. B. 3-4 (639) (2006) 368–372.

6. **Dymnikova I.G.,** Image of the electron suggested by nonlinear electrodynamics coupled to gravity, Particles. 2 (4) (2021) 129–145.

7. **Kerr R.P., Schild A.,** Some algebraically degenerate solutions of Einstein's gravitational field equations, Proc. Symp. Appl. Math. (17) (1965) 199–209.

8. **Gürses M., Gürsey F.,** Lorentz covariant treatment of the Kerr-Schild geometry, J. Math. Phys. 12 (16) (1975) 2385–2390.

9. **Dymnikova I. G.,** Regular electrically charged vacuum structures with de Sitter centre in nonlinear electrodynamics coupled to general relativity, Class. Quant. Gravity. 18 (21) (2004) 44174428.

10. **Bronnikov K.A.,** Regular magnetic black holes and monopoles from nonlinear electrodynamics, Phys. Rev. D. 4 (63) (2001) 044005.

11. **Dymnikova I.G., Galaktionov E.V., Tropp E.A.,** Existence of electrically charged structures with regular center in nonlinear electrodynamics minimally coupled to gravity, Advances in Mathematical Physics. (2015) (2015) 496475.

12. **Dymnikova I.G., Galaktionov E.V.,** Basic generic properties of regular rotating black holes and solitons, Advances in Mathematical Physics. (2017) (2017) 1035381.

13. **Newman E.T., Couch E., Chinnapared K., Exton A., Prakash A., Torrence R.,** Metric of a rotating, charged mass, J. Math. Phys. (6) (1965) 918-919.

14. **Carter B.,** Global structure of a Kerr family of gravitational fields, Phys. Rev. 5 (174) (1968) 1559–1571.

15. **Tiomno J.,** Electromagnetic field of rotating charged bodies, Physical Review D. 4 (7) (1973) 992-997.

16. **Burinskii A.Y., Hildebrandt S.R.,** New type of regular black holes and particle-like solutions from nonlinear electrodynamics, Physical Review D. 10 (65) (2002) 104017.

17. **Dymnikova I. G.,** Electromagnetic source for the Kerr-Newman geometry, Int. J. Mod. Phys. D. (24) (2015) 1550094.

18. **Landau L.D., Lifshitz E.M.,** Electrodynamics of continuous media, Pergamon Press, 1993.

19. **Dymnikova I.G.,** Origin of the magnetic momentum for regular electrically charged objects described by nonlinear electrodynamics coupled to gravity, Int. J. Mod. Phys. D. (28) (2019) 1950011.

## THE AUTHORS

**DYMNIKOVA Irina G.**
igd.ammp@mail.ioffe.ru
ORCID: 0000-0003-2612-2893

**GALAKTIONOV Evgeniy V.**
galakt@ammp.ioffe.ru
ORCID: 0000-0002-6752-4787

*Received 27.10.2022. Approved after reviewing 10.11.2022. Accepted 10.11.2022.*

© Peter the Great St. Petersburg Polytechnic University, 2023

# MECHANICS

Conference materials
UDC 532.529.5
DOI: https://doi.org/10.18721/JPM.161.250

## Formation of supersonic steam-water jets accompanied by generation of acoustic pulsations

R.Kh. Bolotnova✉, V.A. Korobchinskaya

Mavlyutov Institute of Mechanics UFRC RAS, Ufa, Russia

✉ bolotnova@anrb.ru

**Abstract.** The features of supersonic steam-water jets formation under outflow through a thin nozzle from a high-pressure chamber are considered. The modes of emerging vibration processes are investigated, depending on variation of initial saturation states determined by pressure and temperature. The proposed system of model equations for steam-water mixture in three-dimensional formulation, in two-temperature, single-pressure, and single-velocity approximations, takes into account the interphase heat exchange, evaporation and condensation phenomena. The numerical implementation of this problem is carried out by the authors developed solver in the OpenFOAM package. The process of supersonic jet development with the formation of Mach disk is studied and the causes of acoustic pressure pulsations are investigated. The analysis of influence of initial saturation states of vapor-water fluid located in a high-pressure chamber on intensity and frequency of acoustic vibrations is given. To validate the numerical method using the OpenFOAM package, the obtained numerical solution is compared with an experimental picture of a supersonic nitrogen jet flowing through a cylindrical nozzle from a high-pressure reservoir.

**Keywords:** thin nozzle, fluid outflow, Mach disk, acoustic pressure pulsations, numerical modeling, OpenFOAM package

**Funding:** The research work was supported by the state budget funds for State Assignment 0246-2019-0052.

**Citation:** Bolotnova R.Kh., Korobchinskaya V.A., Formation of supersonic steam-water jets accompanied by generation of acoustic pulsations, St. Petersburg State Polytechnical University Journal. Physics and Mathematics. 16 (1.2) (2023) 330–336. DOI: https://doi.org/10.18721/JPM.161.250

This is an open access article under the CC BY-NC 4.0 license (https://creativecommons.org/licenses/by-nc/4.0/)

© Bolotnova R.Kh., Korobchinskaya V.A., 2023. Published by Peter the Great St. Petersburg Polytechnic University.

Материалы конференции
УДК 532.529.5
DOI: https://doi.org/10.18721/JPM.161.250

# Формирование сверхзвуковых пароводяных струй, сопровождающееся генерацией акустических пульсаций

Р.Х. Болотнова✉, В.А. Коробчинская

Институт механики им. Р.Р. Мавлютова УФИЦ РАН, г. Уфа, Россия

✉ bolotnova@anrb.ru

**Аннотация.** Рассмотрены особенности формирования сверхзвуковых пароводяных струй, истекающих через тонкое сопло из камеры высокого давления. Исследованы режимы возникающих вибрационных процессов в зависимости от изменения начальных состояний насыщения, определяемых давлением и температурой. Предлагаемая система модельных уравнений пароводяной смеси в трехмерной постановке включает двухфазные уравнения динамики в двухтемпературном, однодавленческом, односкоростном приближениях с учетом межфазного теплообмена, явлений испарения и конденсации. Численная реализация поставленной задачи проведена с применением разработанного авторами решателя в среде открытого пакета OpenFOAM. Изучен процесс развития сверхзвуковой струи с образованием диска Маха и исследованы причины образования акустических пульсаций давления. Дан анализ влияния исходных состояний насыщения водного флюида, находящегося в камере высокого давления, на интенсивность и частоту возникающих акустических колебаний. Для обоснования достоверности используемого численного метода с применением пакета OpenFOAM проведено сравнение полученного численного решения с экспериментальной фотографией сверхзвуковой струи азота, истекающей через цилиндрическое сопло из резервуара высокого давления.

**Ключевые слова:** тонкое сопло, истечение флюида, диск Маха, акустические пульсации давления, численное моделирование, пакет OpenFOAM

**Финансирование:** Работа выполнена средствами государственного бюджета по госзаданию 0246-2019-0052.

**Ссылка при цитировании:** Болотнова Р.Х., Коробчинская В.А. Формирование сверхзвуковых пароводяных струй, сопровождающееся генерацией акустических пульсаций // Научно-технические ведомости СПбГПУ. Физико-математические науки. 2023. Т. 16. № 1.2. С. 330–336. DOI: https://doi.org/10.18721/JPM.161.250

Статья открытого доступа, распространяемая по лицензии CC BY-NC 4.0 (https://creativecommons.org/licenses/by-nc/4.0/)

## Introduction

Recently, it has been of interest the studying of processes that occur during jet supersonic flows, the consequence of which is the generation of acoustic disturbances in the form of noise or sound vibrations. The mentioned phenomena are associated with the need to solve noise reduction problems on industrial devices of various technological productions. Among the studies in this direction, it should be note the work of [1], in which various aspects of modeling the noise of pulsed jets owing from a conical nozzle are considered. In the work [2], the analysis of gas injection into closed volume with liquid at periodic pressure pulsations in the gas volume was studied. The initial stage of boiling liquid outflow during sudden depressurization of a high-pressure chamber using the numerical method of movable Lagrangian grids was carried out in [3] for the conditions of experiments series [4]. In [3] the influence of initial equilibrium water state and the frequency of nucleation on the evolution of steam-water jet shape were analyzed. In the work [5] the dynamics of vapor jet formation with supercritical state parameters outflowing from a high-pressure vessel through a thin nozzle was investigated by numerical approach implemented in the OpenFOAM package.

© Болотнова Р.Х., Коробчинская В.А., 2023. Издатель: Санкт-Петербургский политехнический университет Петра Великого.

The proposed work is continuing of investigations [3–5] which is aimed to analysis of a spatial axisymmetric outflow through a thin nozzle of a steam-water jet in the modes of supersonic flow velocities under experimental conditions [4], in order to study the initial conditions influence for the formation of pulsation pressure disturbances with evaluation of their intensity and oscillation frequencies.

## Problem statement and model equations

For solving the considered process a two-phase model of gas-liquid mixture is used with one-pressure, one-velocity, and two-temperature approximations, taking into account interfacial heat exchange, evaporation and condensation phenomena. The system of differential equations in three-dimensional Cartesian coordinate system includes the equations of continuity, momentum and energy conservation of phases [6, 7]:

$$\frac{\partial(\alpha_i\rho_i)}{\partial t}+\operatorname{div}(\alpha_i\rho_i\vec{v})=\Gamma_i,$$

$$\frac{\partial(\alpha_i\rho_i\vec{v})}{\partial t}+\operatorname{div}(\alpha_i\rho_i\vec{v}\vec{v})=-\alpha_i\nabla p+\operatorname{div}(\alpha_i\boldsymbol{\tau}_i)+\Gamma_i\vec{v},$$

$$\boldsymbol{\tau}_i=\mu_i\left(\nabla\vec{v}+\vec{v}^{\mathrm{T}}\right)-\frac{2}{3}\left(\mu_i\operatorname{div}\vec{v}\right)\mathbf{I}, \tag{1}$$

$$\frac{\partial(\alpha_i\rho_i(e_i+K_i))}{\partial t}+\operatorname{div}(\alpha_i\rho_i(e_i+K_i)\vec{v})=-p\frac{\partial\alpha_i}{\partial t}-\operatorname{div}(\alpha_i\vec{v}p)+$$

$$+\operatorname{div}(\alpha_i\gamma_{i,eff}\nabla h_i)+K_{ht}(T_j-T_i)+L_i\Gamma_i,\ \ \gamma_{i,eff}=\frac{c_{p_i}}{c_{V_i}}\gamma_i.$$

The mass transfer rate $\Gamma_i = dm_i/dt$ is determined by the intensity of evaporation (condensation) process in the equilibrium saturation state described by Arden Buck equation [8].

$$p_s\left(T\right)=6.1121\exp\left(\left(18.678-\frac{T}{234.5}\right)\left(\frac{T}{257.14+T}\right)\right). \tag{2}$$

The following notations were used in the above equations: $\vec{v}$ is mass velocity vector, $p$ is pressure, $\rho_i$ is the density, $\alpha_i$ is volume fraction content, $\mathbf{I}$ is unit tensor, $\mu_i$ is dynamic viscosity, $c_{pi}$, $c_{Vi}$ is specific heat capacities at constant pressure and volume, respectively, $\gamma_i$, $\gamma_{i,eff}$ is true and effective thermal diffusivities, respectively, $e_i$ is internal energy, $K_i$ is kinetic energy, $h_i$ is enthalpy, $T_i$ is temperature, $L_i$ is latent heat of vaporization/condensation, $K_{ht}$ is heat transfer coefficient. The subscript $i = l, g$ corresponds to liquid and vapor phases. The thermodynamic properties of water and vapor are described by perfect equations of state. For isobaric heat capacity $c_p$ the temperature dependence in form of polynomial function JANAF [8] was applied.

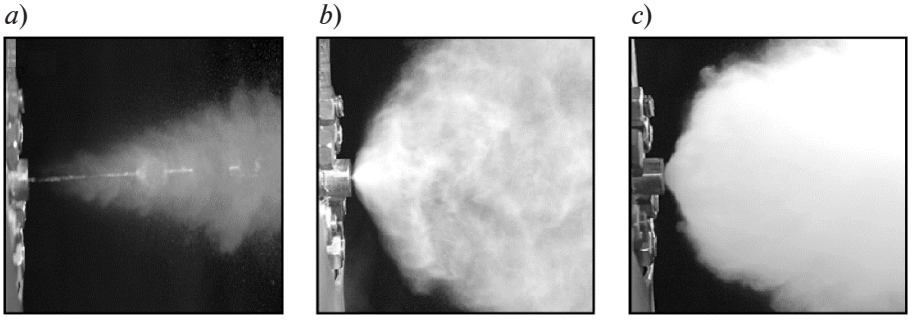


Fig. 1. Photographs of boiling water jets under outflow through a thin cylindrical nozzle at various initial states [4]. $T_0$ = 422 K (*a*), 490 K (*b*), 650 K (*c*)

In this article, the numerical simulation of experiments [4] was carried out. In [4] is assumed, that at the initial time moment in cylindrical high-pressure tank of length $x_h$ = 10 mm and radius $y_h$ = 10 mm there is a vapor-water mixture. The depressurization process resulting from the rupture of the diaphragm located at the right end of the cylindrical nozzle of length $x_s$ = 0.5 mm and radius $y_s$ = 0.25 mm, leads to outflow of boiling water with jet formation. The photographs of water jets outflow for various initial conditions [4], is shown in Fig. 1.

**Reliability of numerical implementation method**

The computer implementation of the proposed gas-vapor-liquid mixture model was carried out using the reactingTwoPhaseEulerFoam solver modified by the authors in OpenFOAM package [5, 9] in an axisymmetric formulation by an adaptive grid.

To justify the reliability of the numerical modeling method by OpenFOAM package, a comparative analysis of calculations with the experiment of [10] was carried out. In [10], the process of formation of a supersonic nitrogen jet when outflowing through a cylindrical nozzle with a diameter of $d$ = 10 mm from a high-pressure tank with a length of $l$ = 38 mm, at an initial pressure of $p_{0r}$ = 4 MPa and a temperature of $T_{0r}$ = 300 K in to the environment with $p_b$ = 0.1 MPa, $T_b$ = 300 K was investigated. Below, a system of equations is given for compressible medium describing the dynamics of simulated experiment, which includes the equations of conservation of mass, momentum and energy in a single-phase approximation, numerically implemented in the package OpenFOAM [8]:

$$\frac{\partial \rho}{\partial t} + \mathrm{div}\left(\rho \vec{v}\right) = 0, \quad \frac{\partial (\rho \vec{v})}{\partial t} + \mathrm{div}(\rho \vec{v}\vec{v}) = -\nabla p + \mathrm{div}\boldsymbol{\tau}, \tag{3}$$

$$\frac{\partial \left(\rho \left(e + K\right)\right)}{\partial t} + \mathrm{div}(\rho \left(e + K\right)\vec{v}) = -\mathrm{div}(\vec{v}p). \tag{4}$$

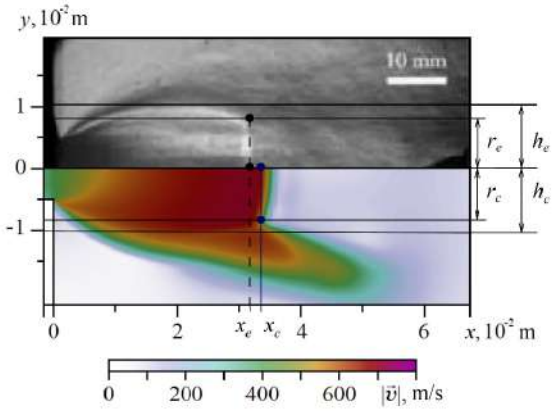


Fig. 2. Experimental photograph of nitrogen gas outflow [10] at the time moment $t$ = 0.2 ms for initial pressure ratio $p_{0r}/p_b$ = 40/1 (upper fragment). The calculated velocity magnitude field for the same experiment [10] obtained using the OpenFOAM package (lower fragment)

Fig. 2 shows a photograph of a nitrogen jet at time $t$ = 0.2 ms from the beginning of outflow process [10] (upper fragment). In the lower fragment of the same Fig. the results of the numerical solution are presented at the time under consideration, in the form of the velocity magnitude field $\left|\vec{v}(x,y)\right|$ using the Eqs. (3–4) in a problem statement similar to the experiment [10]. In numerical solution, as in the experiment, a supersonic axisymmetric gas jet acquires a barrel shape with the formation of normal (Mach disk) and hanging (along the boundary of the 'barrel') compression jumps and has a degree of incalculability $n = p_a/p_b > 2$, where $p_a$ is the pressure at the nozzle slice, $p_b$ is ambient pressure. The distance from the nozzle outlet to Mach disk on the axis of gas jet was estimated by the formula [11]:

$$x_M = 0.67d\left(\frac{p_\text{a}}{p_\text{b}}\right)^{0.5}. \quad (5)$$

The analytical value $x_M = 33.58$ mm (5) corresponds to the calculated values of the simulated experiment $p_a = 2.5$ MPa, $p_b = 0.1$ MPa. The visualization of computed results (Fig. 2) showed the coincidence of the distances under consideration: $x_c = x_M$. The value $x_e = 33.2$ mm obtained from the experimental photo has an error compared to (5): $\delta_x = (|x_e - x_M|/x_M)\cdot 100\% \approx 1\%$. The estimates of the relative error for experimental (subscript *e*) and calculated values (subscript *c*) for the radius of Mach disk $r_e \approx 7.8$ mm, $r_c \approx 7.5$ mm, have the following values: $\delta_r = (|r_e - r_c|/r_c)\cdot 100\% < 5\ \%$, and the height of the barrel: $h_c = h_e \approx 20$ mm. The analysis showed a satisfactory agreement between the experimental data [10] and the numerical solutions obtained using the OpenFOAM package.

## Analysis of numerical results

The results of numerical simulation of main problem about jet flow formation of a steam-water mixture are presented in Fig. 3 at time $t = 35$ μs in the form of velocity magnitude fields $|\vec{v}(x,y)|$ (left fragment) and volumetric water content $\alpha_l$ (right fragment). The calculated pressure dependences on time $p(t)$ at selected points of the studied experiments [4], located on the axis of symmetry of the jet are presented on Fig. 4. The notations (*a*, *b*, *c*) in Figs. 3, 4 correspond to the experimental photographs are shown in Fig. 1.

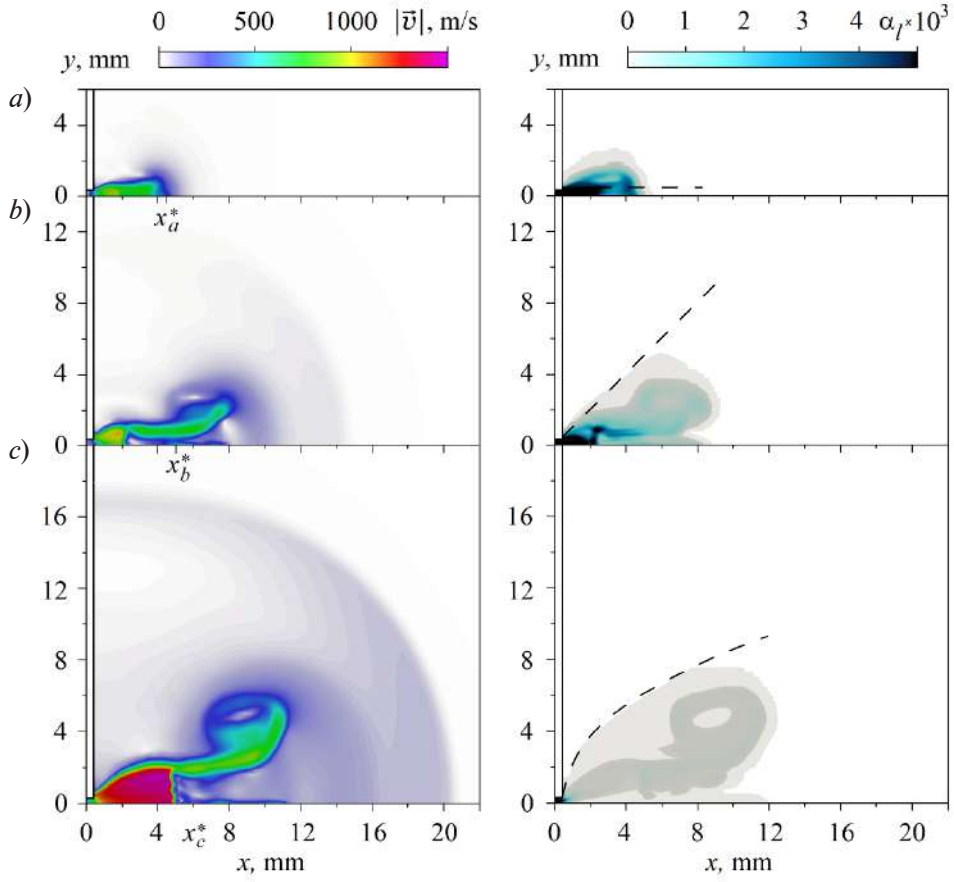


Fig. 3. The calculated velocity magnitude field $|\vec{v}(x,y)|$ (left fragment) and volumetric water content $\alpha_l$ (right fragment) of jet formation process at time moment $t = 35$ μs for different initial conditions shown in Fig. 1, *a*, *b*, *c*

Fig. 3, *a* shows the results of simulation of the outflow process for the initial values of saturation pressure $p_0$ = 0.43 MPa and temperature $T_0$ = 422.6 K [4]. As in the experiment [4] (Fig. 1, *a*), in the calculations it is not jet expansion, and subsonic outflow regime is maintained with Mach number M ≈ 0.8. The time dependence of calculated pressure $p(t)$ in control point $x_a^*$ = 4.5 mm on the jet axis fixes a single pressure pulse due to the moment of arrival of the jet leader. Periodic pressure pulsations were also not detected in this case (Fig. 4, *a*).

The process of forming a vapor-water jet at initial values of saturation pressure $p_0$ = 2.14 MPa and temperature $T_0$ = 490.1 K in accordance with the experiment [4] (Fig. 1,*b*) is shown in Fig. 3,*b*. In this case, as in [4], the jet acquires a close to conical shape, which is shown in the right fragment of Fig. 3,*b* as a dashed line skirting the boundary of existence the volumetric water content in jet stream. In this outflow regime a supersonic jet with a maximum value of velocity $|\vec{v}|$ ≈ 900 m/s (M ≈ 1.7) is formed.

In Fig. 3,*c*, the results of calculation are given for the outflow regime with an initial temperature of $T_0$ = 650 K and pressure $p_0$ = 22.73 MPa, which corresponds to the initial state near critical point of the vapor-water fluid. As noted in the experiment [4], under the given initial conditions, there is an intense expansion of the jet, which acquires a shape close to parabolic, shown in the right fragment of Fig. 3, *c* by the dashed line. Supersonic (M ≈ 2.22) expiration velocity of $|\vec{v}|$ ≈ 1200 m/s are achieved here.

At the boundary of expanding supersonic jets (see the left fragment of Fig. 3, *b*, *c*) hanging and normal (Mach disk) compression jumps are formed. The lateral boundaries of jet are also characterized by a supersonic flow mode. The formed jet supersonic flow in the near zone of the axis of symmetry forms regions of periodically changing pressure (Fig. 4).

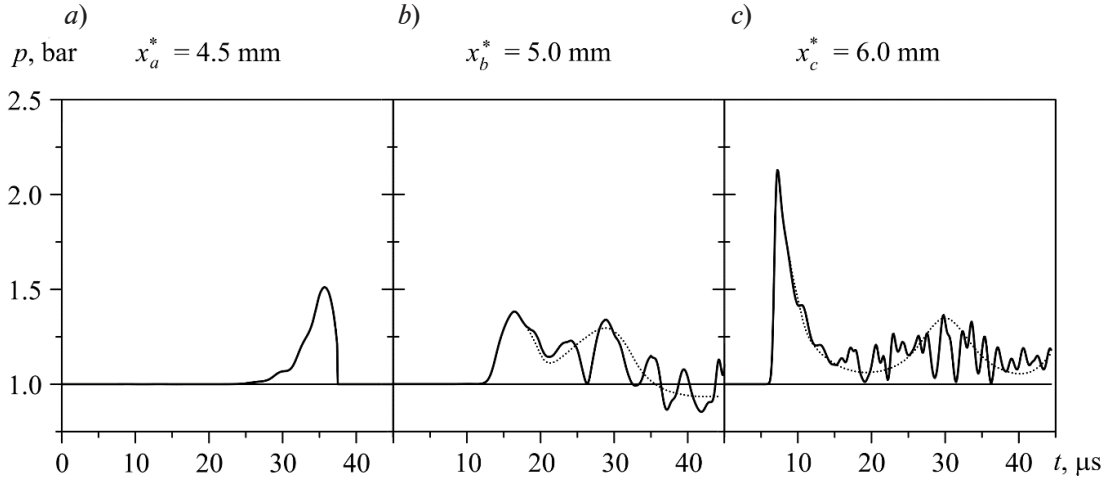


Fig. 4. Calculated pressure time dependences $p(t)$ on the points $x^*$ for different initial conditions shown in Fig. 1, *a*, *b*, *c*

The calculated small-scale high-frequency pressure pulsations have a characteristic oscillation period of $\tilde{T}$ ≈ 8 μs, which correspond to frequency of $\tilde{\upsilon}$ ≈ 125 kHz for outflow regime at $T_0$ = 490.1 K (Fig. 4, *b*) and $\tilde{T}$ ≈ 2 μs ($\tilde{\upsilon}$ ≈ 500 kHz) at $T_0$ = 650 K (Fig. 4,*c*).

On Fig. 4, *b*, *c* by dotted lines marked the initial stage on formation of large-scale and low-frequency pressure pulsations with $\tilde{T}$ ≈ 30 μs ($\tilde{\upsilon}$ ≈ 33 kHz) (Fig. 4,*b*) and with $\tilde{T}$ ≈ 20 μs ($\tilde{\upsilon}$ ≈ 50 kHz) (Fig. 4,*c*).

## Conclusion

The non-stationary process of the outflow of a vapor-water mixture from a high-pressure chamber through a thin nozzle on basis of developed two-phase model in two-temperature, one-pressure, one-velocity approximations with take into account interphase heat exchange, evaporation and condensation phenomena was investigated. Numerical modeling of considered problem using by the authors solver developed in the OpenFOAM package was carried out. The calculations the influence of initial saturation states of aqueous fluid on the formation of the jet flow were estimated.

It is shown that with an increase the initial saturation temperature and pressure, the outflow process transformed from subsonic for supersonic regime. Supersonic outflow regimes was accompanied by the formation of conical and then parabolic jet shapes, and are characterized by supersonic pressure pulsations in a range of 30–50 kHz. It was not the jet pulsations when the initial temperature decreases.

The calculations obtained are in qualitative agreement with the photographs of experiments on the boiling water outflow, and with the experiment on outflow of nitrogen jet, confirming the reliability of used numerical simulation method.

The results will be important and useful as recommendations in solving issues related to noise reduction problems in various industrial plants.

## REFERENCES

1. **Volkov K.N., Emelyanov V.N., Tsvetkov A.I., Chernyshov P.C., Koverda V.P.,** Modeling impulse flow noise using eddy-resolving methods, Noise Theory and Practice. 5(1) (2019) 27–38.

2. **Alekseev M.V., Vozhakov I.S., Lezhnin S.I.,** Pressure pulsations during gas injection into a liquid-filled closed vessel with a high pressure drop, T and A. 26(5) (2019) 781–784.

3. **Bolotnova R.Kh., Korobchinskaya V.A.,** Boiling water jet outflow from a thin nozzle: spatial modeling, T and A. 24(5) (2017) 761–771.

4. **Reshetnikov A.V., Busov K.A., Mazheiko N.A., Skokov V.N., Koverda V.P.,** Transient behavior of superheated water jets boiling, T and A. 19 (2) (2012) 329–336.

5. **Bolotnova R.Kh., Korobchinskaya V.A., Faizullina E.A.,** Analysis the dynamic formation of a vapor supersonic jet under outflow from thin nozzle, J Phys Conf Ser. 2103 (2021) 012219.

6. **Nigmatulin R.I.,** Dynamics of Multiphase Media, Hemisphere, New York, 1990.

7. **Landau L.D., Lifshitz E.M.,** Fluid Mechanics, Vol. 6, Pergamon, Oxford,1987.

8. OpenFOAM. The Open Source Computational Fluid Dynamics (CFD) Toolbox. URL: http: // www.openfoam.com. Accessed Apr. 10, 2022.

9. **Bolotnova R.Kh., Gainullina E.F.,** Supercritical steam outflow through a thin nozzle: forming a hollow jet, T and A. 25(5) (2018) 751–757.

10. **Orescanin M.M., Austin J.M., Kieffer S.W.,** Unsteady high-pressure flow experiments with applications to explosive volcanic eruptions, Journal of geophysical research. 115 (2010) B06206.

11. **Abramovich G.N.,** Applied gas dynamics, Vol. 1, Nauka, Moscow, 1991.

## THE AUTHORS

**BOLOTNOVA Raisa Kh.**
bolotnova@anrb.ru
ORCID: 0000-0001-5847-7328.

**KOROBCHINSKAYA Valeria A.**
buzina_lera@mail.ru
ORCID: 0000-0001-5755-7561.

*Received 21.10.2022. Approved after reviewing 14.11.2022. Accepted 15.11.2022.*

© Peter the Great St. Petersburg Polytechnic University, 2023

Conference materials
UDC 532.529:5
DOI: https://doi.org/10.18721/JPM.161.251

# Analysis the influence of aqueous foam rheological properties on the structure of wave impulse

R.Kh. Bolotnova✉, E.F. Gainullina

Mavlyutov Institute of Mechanics UFRC RAS, Ufa, Russia

✉ bolotnova@anrb.ru

**Abstract.** The dynamics of a low-intensity plane shock wave during its propagation into a foam layer is numerically investigated for experimental data conditions performed in a horizontal shock tube. To describe the behavior of aqueous foam under weak impact, the model of aqueous foam developed by the authors was used, describing it as an elastic-viscoplastic system taking into account elastic properties in accordance with Hooke's law, and describes viscoplastic behavior by the Herschel-Bulkley conditions. The model was numerically implemented by creating the new solver in the OpenFOAM software. The analysis of the wave flow dynamics during the propagation of a weak air shock wave into the foam layer is carried out. The features of the elastic precursor formation are shown. Based on the results of calculations, the influence of the initial liquid volume fraction on the elastic-viscoplastic properties of the aqueous foam, on which the structure of the shock wave profile, its intensity and propagation velocity depend, is estimated. The reliability of the obtained calculations is confirmed by satisfactory agreement of numerical solutions with experimental data.

**Keywords:** aqueous foam, weak shock wave, elastic-viscous-plastic properties, numerical modeling, OpenFOAM software

**Funding:** This study was funded by the state budget funds for State Assignment 0246-2019-0052.

**Citation:** Bolotnova R.Kh., Gainullina E.F., Analysis the influence of aqueous foam rheological properties on the structure of wave impulse, St. Petersburg State Polytechnical University Journal. Physics and Mathematics. 16 (1.2) (2023) 337–342. DOI: https://doi.org/10.18721/JPM.161.251

This is an open access article under the CC BY-NC 4.0 license (https://creativecommons.org/licenses/by-nc/4.0/)

Материалы конференции
УДК 532.529:5
DOI: https://doi.org/10.18721/JPM.161.251

# Анализ влияния реологических свойств водной пены на структуру и интенсивность слабых ударных волн

Р.Х. Болотнова✉, Э.Ф. Гайнуллина

Институт механики им. Р.Р. Мавлютова УФИЦ РАН, Уфа, Россия

✉ bolotnova@anrb.ru

**Аннотация.** Изучена динамика волнового течения при распространении в пенный слой слабых воздушных ударных волн различной интенсивности для условий литературных экспериментальных данных. При численном исследовании рассматриваемых процессов использована модель водной пены, описывающая ее поведение с учетом упруго-вязко-пластических свойств и численно реализованная в решателе, созданном авторами в пакете OpenFOAM. Проанализировано влияние начального объемного водосодержания пены на скорости распространения и амплитуды давлений упругого предвестника и основной волны сжатия. Достоверность полученных решений подтверждена их сравнительным анализом с экспериментальными осциллограммами давлений в пене.

© Bolotnova R.Kh., Gainullina E.F., 2023. Published by Peter the Great St. Petersburg Polytechnic University.

**Ключевые слова:** водная пена, слабая ударная волна, упруго-вязко-пластические свойства, численное моделирование, пакет OpenFOAM

**Финансирование:** Работа выполнена при поддержке средствами госбюджета по госзаданию 0246-2019-052.

**Ссылка при цитировании:** Болотнова Р.Х., Гайнуллина Э.Ф. Анализ влияния реологических свойств водной пены на структуру и интенсивность слабых ударных волн // Научно-технические ведомости СПбГПУ. Физико-математические науки. 2023. Т. .16 1.2 №. С. 337–342. DOI: https://doi.org/10.18721/JPM.161.251

Статья открытого доступа, распространяемая по лицензии CC BY-NC 4.0 (https://creativecommons.org/licenses/by-nc/4.0/)

## Introduction

Study of aqueous foams as media with damping properties is the important area of scientific research, since the development of impact protection methods is of great scientific and practical importance.

Aqueous foam in a quasi-static state exhibits elastic properties at small deformations with the structure preservation [1]. When describing the dynamic response of the foam to a weak impact load, the existing theoretical models are mainly limited to specifying its viscoplastic behavior. The new experimental data, concerning shock impact on aqueous foam [2, 3], indicate the elastic precursor formation ahead of main wave. In this regard, the studies aimed at modeling and investigating wave processes in aqueous foam, taking into account its rheological features, namely, elastic-viscoplastic properties, are of interest [4, 5].

In the present work, dynamics of low intensity plane air shock wave (SW) during its interaction with the aqueous foam layer under experimental data conditions [3] is studied in order to analyze the effect of the foam elastic-viscous-plastic properties on the wave profile structure formation.

## Governing equations

The proposed two-phase model of aqueous foam is based on the use of approaches [6, 7] and includes the conservation equations for phases mass and energy, mixture momentum and equation of the liquid volume fraction dynamics of the foam:

$$\begin{gathered}
\frac{\partial(\alpha_i\rho_i)}{\partial t}+\operatorname{div}(\alpha_i\rho_i\vec{v})=0,\\
\frac{\partial(\alpha_i\rho_i(u_i+K_i))}{\partial t}+\operatorname{div}(\alpha_i\rho_i(u_i+K_i)\vec{v})=-p\frac{\partial\alpha_i}{\partial t}-\operatorname{div}(\alpha_i\vec{v}p)+\operatorname{div}(\alpha_i\vec{v}\cdot\boldsymbol{\tau})+\\
+\operatorname{div}(\alpha_i\vec{v}\cdot\boldsymbol{s})+\operatorname{div}(\alpha_i\gamma_{i,eff}\nabla h_i),\\
\frac{\partial(\rho\vec{v})}{\partial t}+\operatorname{div}(\rho\vec{v}\vec{v})=-\nabla p+\operatorname{div}\boldsymbol{\tau}+\operatorname{div}\boldsymbol{s},\\
\frac{\partial\alpha_1}{\partial t}+\operatorname{div}(\alpha_1\vec{v})-\alpha_1\operatorname{div}\vec{v}=\alpha_1\alpha_2\left(\frac{1}{\rho_2}\frac{d\rho_2}{dt}-\frac{1}{\rho_1}\frac{d\rho_1}{dt}\right),
\end{gathered}\tag{1}$$

where $\alpha_i$, $\rho_i$, $u_i$, $K_i$, $\gamma_{i,eff}$, $h_i$ are volume fraction, density, internal and kinetic energy, effective thermal conductivity and enthalpy for $i$-th phase ($i = 1$ corresponds to water, $i = 2$ corresponds to air), respectively; $t$ is time, $p$ is pressure, $\rho = \alpha_1\rho_1+\alpha_2\rho_2$ is aqueous foam density, $\boldsymbol{s}$ is stress tensor deviator.

Viscous stress tensor $\boldsymbol{\tau}$ is related to the mass velocity vector $\vec{v}$ by the ratio [7]:

$$\boldsymbol{\tau}=\mu_{eff}(\nabla\vec{v}+\nabla\vec{v}^{T})-\frac{2}{3}(\mu_{eff}\operatorname{div}\vec{v})\boldsymbol{I},$$

where $\mu_{eff}$ is effective viscosity, $\boldsymbol{I}$ is unit tensor.

© Болотнова Р.Х., Гайнуллина Э.Ф., 2023. Издатель: Санкт-Петербургский политехнический университет Петра Великого.

The system of equations (1) is closed by the perfect equations of state for liquid and gas.

To describe the elastic properties of aqueous foam in the case when the shear stresses do not exceed the elastic limit $s_0$, it is proposed to use Hooke's elasticity law [6]:

$$\boldsymbol{s} = \mu_s(\nabla\vec{e} + \nabla\vec{e}^T) - \frac{2}{3}(\mu_s \mathrm{div}\vec{e})\boldsymbol{I},$$

where $\mu_s$ is shear modulus, $\vec{e}$ is deformation vector.

The foam transition from the elastic to viscoplastic state occurs when the shear stress limit is exceeded and is determined by the von Mises yield fluidity criterion [8] with correction the components of stress tensor deviator $\boldsymbol{s}$:

$$\begin{cases} \left|I_2(\boldsymbol{s})\right| - \frac{1}{3}s_0^2 \le 0, \quad \tilde{s}_{kl} = s_{kl}, \\ \left|I_2(\boldsymbol{s})\right| - \frac{1}{3}s_0^2 > 0, \quad \tilde{s}_{kl} = s_{kl}\frac{s_0}{\sqrt{3\left|I_2(\boldsymbol{s})\right|}}. \end{cases}$$

To describe the viscoplastic properties of aqueous foam as a non-Newtonian fluid, the Herschel–Bulkley model with effective viscosity $\mu_{eff}$ is used [10]:

$$\mu_{eff} = k\left|\dot{\gamma}\right|^{n-1} + \tau_0\left|\dot{\gamma}\right|^{-1}.$$

Here $k$ is consistency index, $\dot{\gamma}$ is shear rate, $n$ is flow index [10], $\tau_0$ is yield stress.

Numerical implementation of the model (1) was performed in the new solver created by the authors in OpenFOAM software [9].

## Problem definition

The weak air SW dynamics in a shock tube containing the aqueous foam layer is studied in accordance with experiments [3]. The shock tube 3.79 m long consists of high pressure (HP, 0.75 m) and low pressure (LP, 2.0 m) chambers, filled with air, and movable tube segment with aqueous foam (FS, 1.04 m). The used foams of two types differ in the initial liquid volume fraction: $\alpha_{10}^1 = 0.0125$ and $\alpha_{10}^2 = 0.0333$. Pressure oscillograms on the SW were recorded by sensors $l_1$ and $l_2$ located in the foam layer at a distance of 3.52 m and 3.19 m from the left boundary of the experimental setup, respectively. Scheme of the experiment is shown in Fig. 1.

Process of the air SW formation with amplitude $p_{air}$ occurs after the rupture of diaphragm ($t = 0$) located between the high and low pressure chambers. As in experiments [3], in this work two types of compression wave formation in the aqueous foam under the impact of SW, initiated in the gaseous region, were studied. Table 1 shows the values of pressure $p_{air}$ and velocity of SW propagation $D_{air}$ in air for the Mach numbers M = 1.3 (I) and M = 1.5 (II), as well as the location of pressure sensors $l$ in the corresponding experiments. To determine the SW pressure amplitude in gas by Mach number $\mathrm{M} = D_{air}/c_{air}$ ($c_{air}$ = 346 m/s is local speed of sound), the relations, following from the conservation laws of mass, momentum, and energy flows when passing through a shock jump, were used [7]:

$$\frac{p_{air}}{p_0} = \frac{2\gamma}{\gamma+1}\mathrm{M}^2 - \frac{\gamma-1}{\gamma+1},$$

where $p_0$ = 1 bar is pressure in undisturbed medium, $\gamma$ = 1.4 is air adiabatic index.

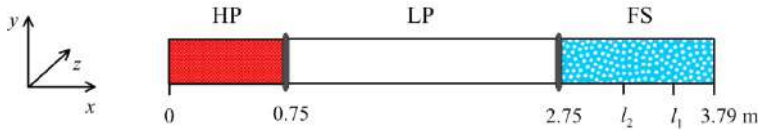


Fig. 1. Experiment scheme [3]: HP, LP are high and low pressure chambers, FS is the tube segment filled with aqueous foam, $l_1$ = 3.52 m, $l_2$ = 3.19 m are pressure sensors

Table 1

**SW parameters in air for the considered experiments [3]**

| No | M | $D_{air}$, m/s | $p_{air}$, bar | $l$, m |
|---|---|---|---|---|
| **I** | 1.3 | 450 | 1.8 | 3.52 |
| **II** | 1.5 | 520 | 2.5 | 3.19 |

## Modeling results

The compression waves dynamics in aqueous foam, initially initiated in air for Mach numbers M = 1.3 ( $p^{I}_{air} \approx 1.8$ bar) with $\alpha^{1}_{10} = 0.0125$, $\alpha^{2}_{10} = 0.0333$ (**I**) and M = 1.5 ( $p^{II}_{air} \approx 2.5$ bar) with $\alpha^{1}_{10} = 0.0125$ (**II**) (see Table 1) was numerically studied. The computed results and corresponding experiments [3] are presented in Fig. 2 as pressure oscillograms at the sensor locations $l_1 = 3.52$ m (2*a*) and $l_2 = 3.19$ m (2*b*) (see Fig. 1). Solid (*1*) and dashed (*2*) black lines indicate calculations with (*1*) and without (*2*) elastic properties of the foam, colored lines indicate experimental data [3].

Numerical solutions obtained on the basis of the elastic-viscous-plastic model of aqueous foam demonstrate two-stage structure of compression wave in the foam, consisting of the main wave and elastic precursor ahead of it, which is consistent with the experimental data [3].

Fig. 2,*a* shows the first series of calculations (**I**). In this case, the pressure amplitude of the main wave, recorded by the sensor $l_1$ located in the far zone from the gas-foam contact boundary, reaches $p_{foam} \approx 1.9$ bar in the foam with initial liquid volume fraction $\alpha^{1}_{10} = 0.0125$ and $p_{foam} \approx 1.85$ bar in the foam with $\alpha^{2}_{10} = 0.0333$.

The pressure amplitudes of elastic precursors are defined by the elastic limit $s_0$ and equal to $p^{1}_{prec} = s^{1}_{0} = 0.19$ bar and $p^{2}_{prec} = s^{2}_{0} = 0.23$ bar, respectively. When the compression wave moves through the foam layer, its velocity decreases by ~2.4 ($\alpha^{1}_{10} = 0.0125$) and ~3.9 ($\alpha^{2}_{10} = 0.0333$) times compared to the SW velocity in air. The elastic precursor velocity in a less dense foam layer ($\alpha^{1}_{10} = 0.0125$) is $D^{1}_{prec} \approx 233$ m/s, which is ≈ 1.6 times higher than the velocity $D^{2}_{prec} \approx 142$ m/s in the foam of high initial liquid volume fraction $\alpha^{2}_{10} = 0.0333$.

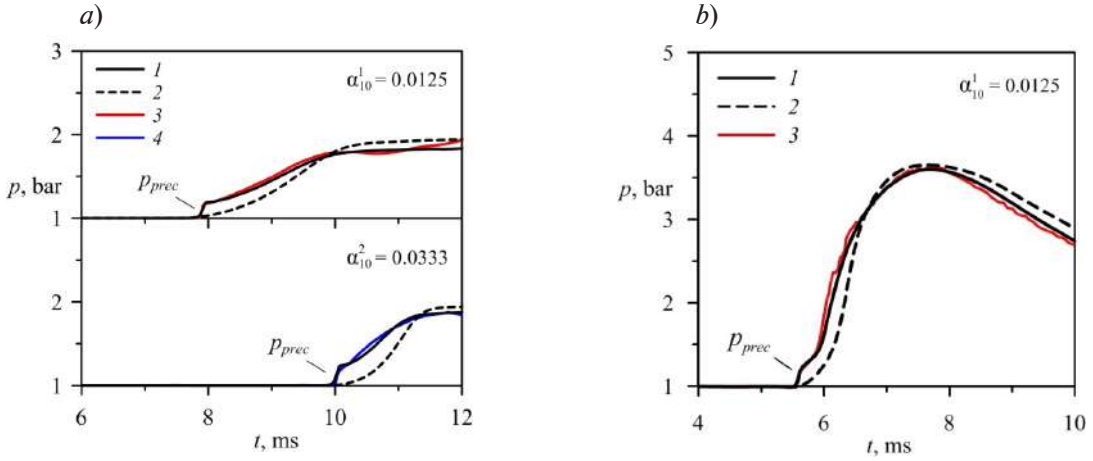


Fig. 2. Time dependencies of pressure $p(t)$ in aqueous foam for the first (**I**, *a*) and second (**II**, *b*) series of experiments, recorded by the sensor in positions $l_1$ (*a*) and $l_2$ (*b*). *1*, *2* correspond to calculations with and without taking into account elastic properties of the foam, *3*, *4* correspond to experimental data [3]; $p_{prec}$ is elastic precursor. Approximation dependencies of the elastic precursor velocity (*1*) and main compression wave average velocity (*2*) on the initial liquid volume fraction of the foam $\alpha_{10}$ for calculation series **I** (blue curves) and **II** (black curves); points *3*, *4* correspond to calculated and experimental data

Fig. 2,*b* presents the comparative analysis of calculations (**II**) and the corresponding experimental data [3] obtained from the sensor $l_2$ = 3.19 m, located in the near zone from the boundary of foam layer and gas (see Fig. 1). This case matches the air SW propagation with Mach number M = 1.5 and amplitude $p_{air}^{II} \approx 2.5$ bar into the foam with $\alpha_{10}^1 = 0.0125$. As in **I**, the compression wave in the foam has a two-stage structure. The main wave pressure amplitude reaches $p_{foam} \approx 3.6$ bar, the elastic precursor amplitude in the considered case **II**, as in **I**, is $p_{prec}^1 = s_0^1 = 0.19$ bar (Fig. 2).

The calculated parameters of simulated problems and obtained values of pressures, main wave average propagation velocities $D_w$ and elastic precursor velocities $D_{prec}$ are summarized in Table 2.

To analyze the effect of foam initial liquid fraction on the dynamics of wave flow, additional calculations were performed for the case of air SW ( $p_{air}^{II} \approx 2.5$ bar) interaction with the foam layer of $\alpha_{10}^2 = 0.0333$. Fig. 3 shows the obtained approximation curves for the elastic precursor velocity $D_{prec}$ (solid lines *1*) and average velocity of the main compression wave $D_w$ (dashed lines *2*) depending on the foam initial liquid volume fraction $\alpha_{10}$, calculated (*3*) and experimental (*4*) points [3]. Given in Fig. 3 numerical solutions correspond to series of experiments **I**, **II** (see Table 1) initiated in the air zone for SW velocities $D_{air}$ = 450 m/s (M = 1.3) and $D_{air}$ = 520 m/s (M = 1.5). The analysis of results showed that increase in the density of foam layer leads to a slowdown in velocities of elastic precursor and the main compression wave, which is consistent with the experimental data [3]. Extrapolation of obtained solutions and experimental data (see Fig. 3) shows that in the studied modes of dynamic action on aqueous foams, with a further increase in the initial liquid volume fraction the velocities of the elastic precursor and the main wave slow down, which can lead to a single-stage structure of compression wave front.

Table 2

**Parameters of the wave flow formed during the air SW propagation in aqueous foam**

| $p_{air}$, bar | $x$, m | $\alpha_{10}$,% | $\tau_0$, bar | $\mu_s$, bar | $p_{foam}$, bar | $D_w$, m/s | $D_{prec}$, m/s |
|---|---|---|---|---|---|---|---|
| 1.8 | 3.52 | 1.25 | 0.19 | 0.16 | 1.7 | 187 | 233 |
| 2.5 | 3.19 | | | 0.22 | 3.6 | 200 | 275 |
| 1.8 | 3.52 | 3.33 | 0.23 | 0.03 | 1.8 | 115 | 142 |
| 2.5 | 3.19 | | | 0.04 | 3.8 | 120 | 160 |

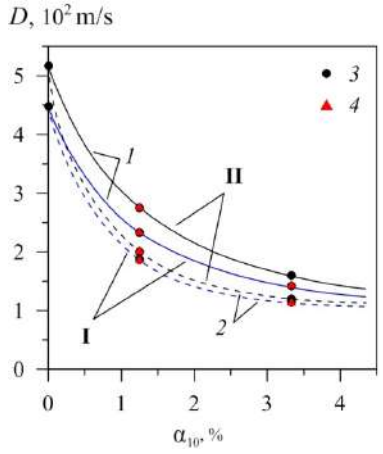


Fig. 3. Approximation dependences of the elastic precursor velocity (*1*) and main compression wave average velocity (*2*) on the initial liquid volume fraction of the foam $\alpha_{10}$ for calculation series **I** (blue curves) and **II** (black curves); points *3*, *4* correspond to calculated and experimental data

## Conclusion

The propagation process of different intensity air SW in a shock tube containing the aqueous foam layer is studied in accordance with the experimental conditions [3]. The behavior of aqueous foam under a weak impact is described by the model of gas-liquid elastic-viscous-plastic medium developed by the authors, which takes into account the elastic properties of the foam in accordance with Hooke's law and the viscoplastic behavior by using the Herschel – Bulkley conditions. Numerical implementation of the model equations is carried out in the author's solver of the OpenFOAM package. The calculation results revealed a two-stage structure of the compression wave front in aqueous foam, caused by the elastic precursor formation ahead of the main wave. It has been established, that the pressure amplitude of elastic precursor is determined by the initial liquid volume fraction of the foam and does not depend on the initial intensity of the impact, limited by the condition of preserving the foam structure. The extrapolation of obtained solutions for the conditions of shock wave initiation in air with Mach numbers M = 1.3, 1.5 showed that velocities of the elastic precursor and main compression waves in aqueous foam decrease as the initial density of the foam increases, which can lead to equalization of their velocities, i.e. to the elastic precursor degeneration. Reliability of the obtained solutions is confirmed by their satisfactory agreement with the corresponding experimental data.

## REFERENCES

1. **Vetoshkin A.G.,** Physics and technology of foam separation processes, Infra-Ingeneria, Moscow, 2016.

2. **Monloubou M., Le Clanche J., Kerampran S.,** New experimental and numerical methods to characterise the attenuation of a shock wave by a liquid foam, Actes 24eme Congres Francaisde Mecanique. Brest: AFM. (2019) 255125.

3. **Jourdan G., Mariani C., Houas L. Chinnayya A., Hadjadj A., Del Prete E., Haas J.-F., Rambert N., Counilh D., Faure S.,** Analysis of shock-wave propagation in aqueous foams using shock tube experiments, Phys. Fluids, 27 (2015) 056101.

4. **Bolotnova R.Kh., Gainullina E.F.,** Modeling of weak shock waves propagation in aqueous foam layer, J. Phys.: Conf. Series, 2103 (2021) 012217.

5. **Bolotnova R.Kh., Gainullina E.F.,** Influence of the dissipative properties of aqueous foam on the dynamics of shock waves, Journal of Applied Mechanics and Technical Physics, 61(4) (2020) 510–516.

6. **Nigmatulin R.I.,** Dynamics of multiphase media, Hemisphere, New York, 1990.

7. **Landau L.D., Lifshitz E.M.,** Fluid mechanics, Vol. 6, Pergamon Press, Oxford, 1987.

8. **Wilkins M.L.,** Calculation of elastic-plastic flow, Methods in computational physics, Vol. 3, Academic Press, New York (1964) 211–263.

9. OpenFOAM. The Open Source Computational Fluid Dynamics (cfd) Toolbox 2021. URL: http://www.openfoam.com. Accessed Apr. 15, 2022.

10. **Dollet B., Raufaste C.,** Rheology of aqueous foams, Comptes Rendus Physique, (15) (2014) 731–747.

## THE AUTHORS

**BOLOTNOVA Raisa Kh.**
bolotnova@anrb.ru
ORCID: 0000-0001-5847-7328

**GAINULLINA Elina F.**
elina.gef@yandex.ru
ORCID: 0000-0001-6625-2815

*Received 21.10.2022. Approved after reviewing 09.11.2022. Accepted 10.11.2022.*

© Peter the Great St. Petersburg Polytechnic University, 2023

Conference materials
UDC 532.1
DOI: https://doi.org/10.18721/JPM.161.252

# Determination of correlation dependences of emulsion viscosity on the concentration of water droplets under non-isothermal conditions

V.I. Valiullina[1]✉, A. A. Musin[1], Yu. S. Zamula[1], L. A. Kovaleva[1]

[1] Bashkir State University, Ufa, Russia

✉ valiullina.vilena @mail.com

**Abstract.** There are several factors that affect the rheological properties of an emulsion. Because heavier oils are highly viscous, determining this property plays a special role in the oil industry. Viscous oils can cause many problems throughout the system and can also cause difficulties in pumping and transportation. In this paper, the experimental values were approximated by an exponential viscosity-temperature relationship in which the empirical coefficients are a function of concentration. At low concentrations, the pre-exponential multiplier is described by the Taylor formula; at concentrations greater than 2.5%, the curve is described by a power function. The dependence of the temperature coefficient of viscosity on concentration is described by a linear function.

**Keywords:** disperse system, viscosity, emulsion, correlation dependences

**Funding:** The reported study was funded by the grant of the Russian Science Foundation (project 19-11-00298).

**Citation** Valiullina V.I., Musin A.A., Zamula Yu.S., Kovaleva L.A., Determination of correlation dependences of emulsion viscosity on the concentration of water droplets under non-isothermal conditions, St. Petersburg State Polytechnical University Journal. Physics and Mathematics. 16 (1.2) (2023) 343–348. DOI: https://doi.org/10.18721/JPM.161.252

This is an open access article under the CC BY-NC 4.0 license (https://creativecommons.org/licenses/by-nc/4.0/)

Материалы конференции
УДК 532.1
DOI: https://doi.org/10.18721/JPM.161.252

# Определение корреляционных зависимостей вязкости эмульсии от концентрации капель воды в неизотермических условиях

В.И. Валиуллина[1]✉, А.А. Мусин[1], Ю.С. Замула[1], Л.А.Ковалева[1]

[1] Башкирский государственный университет, г. Уфа, Россия

✉ valiullina.vilena @mail.com

**Аннотация.** Существует несколько факторов, влияющих на реологические свойства эмульсии. Поскольку более тяжелые масла обладают высокой вязкостью, определение этого свойства играет особую роль в нефтяной промышленности. Вязкие масла могут создавать множество проблем во всей системе, а также могут вызывать трудности при перекачке и транспортировке. В настоящей работе экспериментальные значения были аппроксимированы экспоненциальной зависимостью вязкости от температуры. При низких концентрациях предэкспоненциальный множитель описывается формулой Тейлора, при концентрациях более %2,5 кривая описывается степенной функцией. Зависимость температурного коэффициента вязкости от концентрации описывается линейной функцией.

© Valiullina V.I., Musin A.A., Zamula Yu.S., Kovaleva L.A., 2023. Published by Peter the Great St. Petersburg Polytechnic University.

**Ключевые слова**: дисперсная система, вязкость, эмульсия, корреляционные зависимости

**Финансирование**: Работа выполнена при поддержке гранта РНФ (тема №19-11-00298).

**Ссылка при цитировании:** Валиуллина В.И., Мусин А.А., Замула Ю.С., Ковалева Л.А. Определение корреляционных зависимостей вязкости эмульсии от концентрации капель воды в неизотермических условиях // Научно-технические ведомости СПбГПУ. Физико-математические науки. 2023. Т. 1.2 № .16. С. 348–343. DOI: https://doi.org/10.18721/JPM.161.252

Статья открытого доступа, распространяемая по лицензии CC BY-NC 4.0 (https://creativecommons.org/licenses/by-nc/4.0/)

## Introduction

Water-in-oil emulsions occur in a variety of natural and industrial systems. In particular, the formation of emulsions causes many serious problems in the oil industry. The presence of emulsions in crude oil causes resistance to flow, especially in arctic thermal conditions, due to rather complex rheology of the fluid [1]. Changes in rheological properties have a significant impact on the entire hydrodynamics of emulsions. For example, the structure of flows during thermal convection of emulsion systems has features that are associated with changes in rheological characteristics during gravitational stratification of the emulsion [2]. In industrial systems, the rheological properties of emulsions are important for modeling energy requirements, process equipment and pipeline design, as well as for assessing flow quality during transportation [3]. Highly efficient computational methods for modeling a large volume of a dispersed system are required to more accurately determine the rheological parameters of such systems based on the calculated properties of its components [4]. There are several factors that influence the rheological properties of emulsions, such as water volume fraction, temperature, shear stress and shear rate. Studying the rheological behavior of emulsions, including their viscosity properties during shear flow, as well as determining the correlation dependences of emulsion viscosity on system parameters is of both theoretical and practical importance.

There are various formulas for calculating the viscosity of disperse systems. In the case of dilute suspensions (particle concentration less than 5%), in which the dispersed phase is particles, the formula published in Einstein's work [5], which started the experimental study of liquids with solid inclusions, can be used to calculate the viscosity:

$$\eta = \eta_c(1 + 2.5C), \tag{1}$$

where $\eta$ is the viscosity of the suspension, $\eta_c$ is the viscosity of the dispersion medium, C is the volume content of the dispersed phase.

The expression derived by Einstein is true for spherical particles and can also be used to determine viscosity when droplet deformation is almost non-existent, such as for microemulsions. It is necessary to correct the formula for inclusions of other shapes, for example, flattened or elongated. In order to expand the field of application of the Einstein formula, a different formula for calculating the viscosity of the disperse system was proposed in Taylor's work [6]:

$$\eta = \eta_c\left(1 + 2.5C\left(\frac{\eta_d + 0.4\eta_c}{\eta_d + \eta_c}\right)\right), \tag{2}$$

where $\eta_d$ is the viscosity of the dispersed phase. Here it is assumed that instead of particles, the inclusions are droplets of another liquid.

The viscosity model presented in [10] is applicable to both Newtonian and non-Newtonian fluids:

© Валиуллина В.И., Мусин А.А., Замула Ю.С., Ковалева Л.А., 2023. Издатель: Санкт-Петербургский политехнический университет Петра Великого.

$$\eta = \eta_c (1 - K_0 K_f(\gamma) C)^{-2.5}, \tag{3}$$

where $K_0$ is the hydration coefficient, which depends on the nature of the emulsifier, $K_f$ is the flocculation coefficient, which depends on the shear rate and is used only in non-Newtonian fluids.

The formula for emulsion viscosity proposed in [11] is true for any volume concentration of droplets and has the form:

$$\left(\frac{\eta}{\eta_c}\right)^{2/5} \left(\frac{2\eta + 5\eta_d}{2\eta_c + 5\eta_d}\right)^{3/5} = (1 - C)^{-1}. \tag{4}$$

If we take solid particles instead of droplets, i.e. droplet viscosity $\eta_d \to \infty$, we get a formula for the viscosity of a polydisperse system with spherical particles.

Pal has proposed many different formulas in his works, one of them being an extension of the Taylor formula for modeling the viscosity of concentrated emulsions [12]:

$$\left(\frac{\eta}{\eta_c}\right)\left(\frac{2\eta + 5\eta_d}{2\eta_c + 5\eta_d}\right)^{3/2} = \left(1 - \frac{C}{C_{\max}}\right)^{-2.5 C_{\max}}, \tag{5}$$

where $C_{max}$ is the maximum concentration of droplets.

The author also compared the calculated viscosity according to the formula with the experimental data in his work and obtained a good agreement of the results.

It is necessary to take into account the temperature dependence of viscosity in addition to the dependence of viscosity on concentration when studying the dynamics of emulsion systems under nonisothermal conditions. The present work is devoted to the study of emulsion viscosity changes depending on the temperature and concentration of water droplets in it, as well as to the determination of the correlation dependence.

## Materials and Methods

The object of the study in the presented work is water-oil emulsion. Medical Vaseline oil (GOST 3164-78) was used as the dispersed phase. Dispersion medium was deionized water (Milli-Q). Nonionic surfactant sorbitan monooleate (Span 80) was used to obtain a stable emulsion. The manufacturing procedure was as follows: 0.5% Span 80 (by weight) was added to Vaseline oil and stirred for 5 min at 300 rpm using an ES 8300D top drive stirrer (Ecros), then deionized water was added depending on the desired concentration during the stirring process, the water-oil stirring process continued for 5 min. As a result, a stable inverse (water in oil) emulsion was obtained.

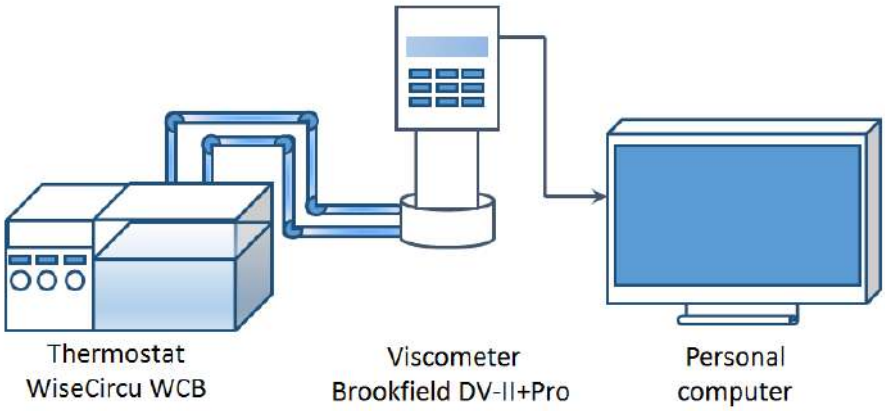


Fig. 1. Schematic of the experimental setup

An experimental setup was assembled, the scheme of which is shown in Fig. 1. The main part of the setup is a Brookfield DV-II+Pro viscometer with a sample bowl, a cone spindle and a thermowell with liquid circulation holes, connected to a WCB (WiseCircu) thermostat. The emulsion to be tested was placed inside the sample bowl in a volume of 0.5 mL.

The principle of the rotational viscometer is to measure the torque of the rotor generated by the liquid under test. This measurement is performed by the rotation angle sensor by the twist of the measuring spring.

The cell was heated over a temperature range of 20 to 70°C in 10°C increments. The concentration of water in the emulsion varied from 1 to 20%. All data were acquired with the Rheocalc software, which provides data acquisition and automatic computer control. Shear stresses from the shear rate (torque) of the emulsions at different media temperatures were measured, allowing the viscosity to be further calculated and its dependence on temperature and concentration to be plotted.

## Results and Discussion

To determine viscosity values, the experimental shear stress versus shear rate dependencies for an emulsion with a concentration of C = 1–20% in the temperature range 20–70 °C were approximated by the Bingham model, since it includes two components: the Newtonian viscosity takes into account all flow resistance, and the plastic one does not take into account structural strength, but reflects the fracture rate.

According to the results of the experimental studies, the viscosity dependences on the difference of the current and initial temperature for different concentrations were plotted (Fig. 2). It can be seen that as the temperature of the emulsion increases, its viscosity decreases. At the same time, the viscosity dependence on the concentration becomes less noticeable at temperatures above 40 °C.

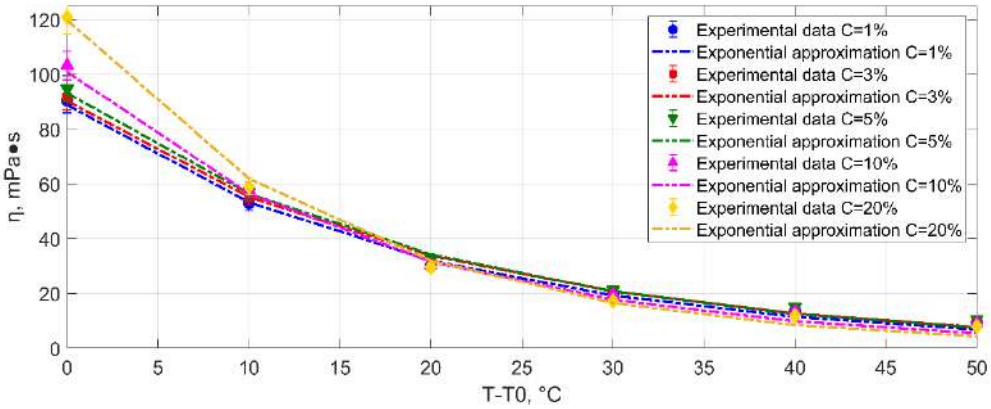


Fig. 2. Experimental dependences of viscosity on temperature for concentrations C=1, 3, 5, 10 and 20 %

The studies were conducted at different concentrations and temperatures. To obtain an empirical curve, the experimental values were approximated by an exponential relationship in which the empirical coefficients are a function of concentration:

$$\eta = \eta_0(C) \cdot e^{(-\gamma(C)\cdot(T-T_0))}, \quad (6)$$

where η is the dynamic viscosity of the emulsion at temperature $T$; $\eta_0(C)$ is the dynamic viscosity of the emulsion at temperature $T_0$; $\gamma(C)$ is the temperature viscosity coefficient; $T$, $T_0$ are the current and initial temperatures of the emulsion.

The dependences of the temperature coefficient of viscosity on the emulsion concentration and the pre-exponent on the emulsion concentration are shown in Table 1.

Table 1

**Dependencies of the emulsion dynamic viscosity at temperature $T_0$ and the temperature coefficient of viscosity on the emulsion concentration**

| $C$, % | $\eta_0$, mPa·s | $\gamma$ |
|---|---|---|
| 1 | 88.8 | 0.051 |
| 3 | 90.23 | 0.052 |
| 5 | 93.12 | 0.054 |
| 10 | 100.9 | 0.058 |
| 20 | 119.8 | 0.066 |

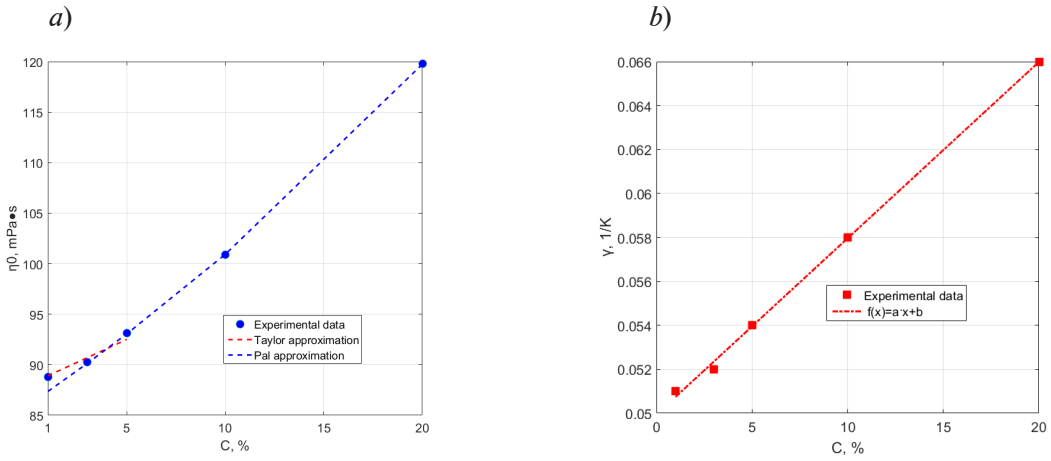


Fig. 3. Experimental concentration dependences of emulsion dynamic viscosity at temperature $T_0$ (*a*); temperature viscosity coefficient (*b*)

The dependence of emulsion viscosity on concentration at temperature $T_0$ obtained during the experiments (Table 1) was analyzed by means of empirical dependences (2) and (3). It was obtained that at low concentrations (less than 5%), the results agreed well with the Taylor formula (red curve in Fig. 3,*a*, $\eta_{c1} = 88$ mPa·s. At concentrations over 2.5%, the curve is described by function (3) with coefficient $K_0K_f = 0.62$ (blue curve in Fig. 3, *a*), $\eta_{c2} = 86$ mPa·s. A weak dependence of the temperature coefficient of viscosity on concentration was observed. The dependence has a linear character and is described by the equation $\gamma(C) = \gamma_0 + \alpha \cdot C$, where $\gamma_0 = 0.04994$ 1/K, $\alpha = 8 \cdot 10^{-4}$ 1/K (Fig. 3,*b*).

Finally, we obtain an empirical relationship for the viscosity of the water in vaseline oil emulsion:

$$\eta = \eta_0(C) \cdot e^{(-\gamma(C)\cdot(T-T_0))}, \; 20°C \le T \le 70°C,$$

$$\eta_0(C) = \begin{cases} \eta_{c1}\left(1 + 2.5C\left(\dfrac{\eta_d + 0,4\eta_{c1}}{\eta_d + \eta_{c1}}\right)\right), 0 \le C \le C_s, \\ \eta_{c2}\left(1 - K_0K_fC\right)^{-2.5}, C_s < C \le 20\%, \end{cases} \tag{7}$$

$$\gamma(C) = \gamma_0 + \alpha \cdot C.$$

Dependence (7) is valid for concentrations from 0 to 20% and for temperatures from 20 to 70 °C. It can be used, for example, to estimate the viscosity of emulsions in process systems, as well as in the simulation of processes related to heating and stratification of concentrated emulsions.

## Conclusion

Experimental studies of the viscosity of water-in-oil emulsion as a function of temperature and concentration of water droplets in it using a Brookfield DV-II+Pro viscometer were conducted. The experimental values are approximated by an exponential dependence of viscosity on temperature, in which the empirical coefficients are a function of concentration. At low concentrations, the pre-exponential multiplier is described by the Taylor formula; at concentrations over 2.5%, the curve is described by a power function. The dependence of the temperature coefficient of viscosity on concentration is described by a linear function

## Acknowledgments

The reported study was funded by the grant of the Russian Science Foundation (project 19-11-00298).

## REFERENCES

1. **Wong, Siew Fan, et al.** Miri light crude water-in-oil emulsions characterization—Rheological behaviour, stability and amount of emulsions formed. Journal of Petroleum Science and Engineering. (165) (2018) 58—66.
2. **Valiullina, V. I., et al.** Experimental study of the stratification of polydisperse emulsions in a cell with heated walls. Journal of Physics: Conference Series. Vol. 2057. (1) IOP Publishing, 2021 012041.
3. **Omer, Ali, and Rajinder Pal.** Pipeline flow behavior of water-in-oil emulsions with and without a polymeric additive in the aqueous phase. Chemical Engineering & Technology: Industrial Chemistry-Plant Equipment-Process Engineering-Biotechnology. 33 (6) (2010) 983—992.
4. **Pityuk, Yulia A., et al.** BEM based numerical approach for the study of the dispersed systems rheological properties." International Conference on Information Technologies. Springer, Cham, 2019 338—352.
5. **Einstein, Albert.** Eine neue bestimmung der molekьldimensionen. Diss. ETH Zurich, 1905.
6. **Taylor G. I.** The viscosity of a fluid containing small drops of another fluid //Proceedings of the Royal Society of London. Series A, Containing Papers of a Mathematical and Physical Character. 138 (834) (1932) 41—48.
7. **Brinkman, H.** The viscosity of concentrated suspensions and solutions. J. Chem. Phys. 20 (4) (1952) 571—584.
8. **Roscoe R.** The viscosity of suspensions of rigid spheres //British journal of applied physics. 3(8) (1952) 267.
9. **Pal R., Rhodes E.** Viscosity/concentration relationships for emulsions //Journal of Rheology. 33(7) (1989) 1021—1045
10. **Phan-Thien N., Pham D. C.** Differential multiphase models for polydispersed suspensions and particulate solids //Journal of Non-Newtonian Fluid Mechanics. 72 (2-3) (1997) 305—318.
11. **Pal R.** Novel viscosity equations for emulsions of two immiscible liquids //Journal of Rheology. 45 (2) (2001) 509—520.

## THE AUTHORS

**VALIULLINA Vilena I.**
valiullina.vilena@mail.ru
ORCID: 0000-0001-6277-9783

**ZAMULA Yuriy S.**
yuriyzamula@gmail.com
ORCID: 0000-0002-7910-3023

**MUSIN Airat A.**
mus-airat@yandex.ru

**KOVALEVA Liana A.**
liana-kovaleva@yandex.ru
ORCID: 0000-0001-8953-6490

*Received 26.10.2022. Approved after reviewing 10.11.2022. Accepted 10.11.2022.*

© Peter the Great St. Petersburg Polytechnic University, 2023

Conference materials
UDC 532.5
DOI: https://doi.org/10.18721/JPM.161.253

# Dynamics of branching blood flows at artery-bypass junctions with and without tissue overgrowth: patient-specific CFD simulation

Y.F. Ivanova[1, 2]✉, L.G. Tikhomolova[1, 2], A.D. Yukhnev[1, 2], E.M. Smirnov[1], A.A. Vrabiy[2], A.A. Suprunovich[2], A.N. Morozov[2], G.G. Khubulava[2], V.N. Vavilov[2]

[1] Peter the Great St. Petersburg Polytechnic University, St. Petersburg, Russia;
[2] Pavlov First St. Petersburg State Medical University, St. Petersburg, Russia
✉ radfn94@mail.ru

**Abstract.** The article presents the results of numerical study of hemodynamics in proximal femoral-popliteal anastomoses of real patients in case of neointimal hyperplasia. Geometric models of anastomoses were based on the clinical data obtained by computer tomography. The neointimal hyperplasia causes changes in the blood flow structure and in stagnant zones after the suture area. Due to the cross-section narrowing, the time-averaged wall shear stresses (TAWSS) in this region increase and the oscillatory shear index (OSI) decreases, and the combined index known as relative residence time (RRT) increases as well. Low values of TAWSS and high values of OSI and RRT are observed in the stagnant zone. High RRT values indicate areas with a high risk of neointimal hyperplasia.

**Keywords:** patient-specific simulation, femoral-popliteal anastomoses, neointimal hyperplasia, wall shear stress, oscillatory shear index, relative residence time

**Funding:** this study was funded by the Russian Science Foundation, grant 20-65-47018.

**Citation:** Ivanova Y.F., Tikhomolova L.G., Yukhnev A.D., Smirnov E.M., Vrabiy A.A., Suprunovich A.A., Morozov A.N., Khubulava G.G., Dynamics of branching blood flows at artery-bypass junctions with and without tissue overgrowth: patient-specific CFD simulation, St. Petersburg State Polytechnical University Journal. Physics and Mathematics. 16 (1.2) (2023) 349–355. DOI: https://doi.org/10.18721/JPM.161.253

This is an open access article under the CC BY-NC 4.0 license (https://creativecommons.org/licenses/by-nc/4.0/)

Материалы конференции
УДК 532.5
DOI: https://doi.org/10.18721/JPM.161.253

# Динамика разветвляющегося кровотока в местах соединения артерии с шунтом при гиперплазии ткани и без нее: пациент-ориентированное численное моделирование

Я.Ф. Иванова[1, 2]✉, Л.Г. Тихомолова[1, 2], А.Д. Юхнев[1, 2], Е.М. Смирнов[1], А.А. Врабий[2], А.А. Супрунович[2], А.Н. Морозов[2], Г.Г. Хубулава[2], В.Н. Вавилов[2]

[1] Санкт-Петербургский политехнический университет Петра Великого, Санкт-Петербург, Россия;
[2] Первый Санкт-Петербургский государственный медицинский университет им. акад. И.П. Павлова, Санкт-Петербург, Россия
✉ radfn94@mail.ru

**Аннотация.** В работе представлены результаты численного моделирования кровотока в проксимальных анастомозах бедренно-подколенных шунтов реальных пациентов в случае гиперплазии неоинтимы. Геометрические модели анастомозов построены на основе клинических данных компьютерной томографии. Результаты показали,

© Ivanova Y.F., Tikhomolova L.G., Yukhnev A.D., Smirnov E.M., Vrabiy A.A., Suprunovich A.A., Morozov A.N., Khubulava G.G., 2023. Published by Peter the Great St. Petersburg Polytechnic University.

что из-за гиперплазии неоинтимы и, соответственно, сужения поперечного сечения увеличиваются осредненные по времени сдвиговые напряжения (TAWSS), уменьшается индекс их колебаний (OSI) и увеличивается относительное время пребывания частиц на стенке (RRT). Низкие значения TAWSS и высокие значения OSI и RRT наблюдаются в застойных зонах. Высокие значения RRT указывают на области с высоким риском гиперплазии неоинтимы.

**Ключевые слова:** пациент-ориентированное моделирование, бедренно-подколенное шунтирование, гиперплазия неоинтимы, сдвиговые напряжения, индекс колебания сдвиговых напряжений, относительное время пребывания

**Финансирование:** работа выполнена при поддержке Российского Научного Фонда, грант № 20-65-47018.

**Ссылка при цитировании:** Иванова Я.Ф., Тихомолова Л.Г., Юхнев А.Д., Смирнов Е.М., Врабий А.А., Супрунович А.А., Морозов А.Н., Хубулава Г.Г. Динамика разветвляющегося кровотока в местах соединения артерии с шунтом при гиперплазии ткани и без нее: пациент-ориентированное численное моделирование // Научно-технические ведомости СПбГПУ. Физико-математические науки. 2023. Т. 1.2 № .16. С. 349–355. DOI: https://doi.org/10.18721/JPM.161.253

Статья открытого доступа, распространяемая по лицензии CC BY-NC 4.0 (https://creativecommons.org/licenses/by-nc/4.0/)

## Introduction

Synthetic vascular grafts are most often used in surgery for femoral artery bypass. However, unlike vein graft, they are more susceptible to process of excessive tissue overgrowth (neointimal hyperplasia) in the suture area [1], especially during the first year after implantation [2]. If the cross-section of the graft is occluded, new bypass implementation operation is necessary.

Assessment of hemodynamics of the anastomosis (a branch of the vascular graft from the artery) of a real patient can play an important role in predicting the neointimal hyperplasia risk. Currently, patient-specific numerical modeling is actively used for this purpose [3-5], mostly to evaluate the hemodynamic parameters that affect the neointimal hyperplasia. The main of these parameters known in the literature are the time-averaged wall shear stress (TAWSS) and the oscillatory shear index (OSI) [3]. For simplifying flow analysis, some authors use the RRT (relative residence time) [6] being a combination of the OSI and TAWSS parameters. An important task is to analyze local changes of these parameters due to the neointimal hyperplasia at the anastomoses for a sample of patients being under specific observations. This can promote finding correlations between the neointimal hyperplasia and the distributions of wall shear stress parameters.

The aim of the work is to compare the blood flow patterns obtained on the base of patient-specific simulation for femoral artery anastomoses with and without neointimal hyperplasia.

## Methods

**Geometric models.** The present study deals with models of real anastomoses after femoral-popliteal bypass surgery. A scheme of proximal femoral-popliteal anastomosis is shown in Fig. 1. A graft is installed bypassing the occluded superficial femoral artery (SFA). The blood flow from the common femoral artery (CFA) is divided into a graft and a deep femoral artery (DFA).

Among 10 patients under common observation, four had an neointimal hyperplasia during 12–30 months after bypass surgery. The maximum neointima thickness, ranging from 1 to 4 mm, was measured using the ultrasound technique. Anastomosis geometries of these four patients were obtained from the clinical data provided by computer tomography. The inner diameter of CFA in the studied models was in the range of 5.5 to 8.0 mm, and the graft inner diameter was 8-9 mm. Models of anastomoses with and without neointimal hyperplasia were constructed for each patient of the four selected.

© Иванова Я.Ф., Тихомолова Л.Г., Юхнев А.Д., Смирнов Е.М., Врабий А.А., Супрунович А.А., Морозов А.Н., Хубулава Г.Г., 2023. Издатель: Санкт-Петербургский политехнический университет Петра Великого.

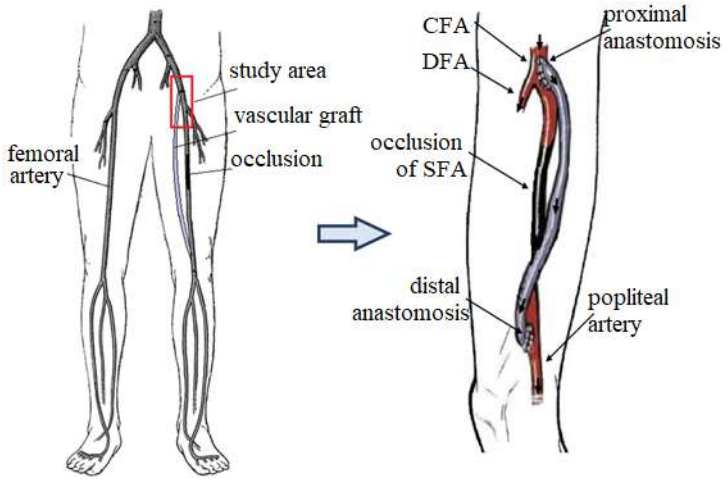


Fig. 1. Area of studied proximal anastomosis
and the blood flow scheme in femoral-popliteal bypass

**Mathematical model and computational aspect.** Numerical simulation was carried out by solving non-stationary three-dimensional Navier-Stokes equations. The ANSYS CFX fluid dynamics package was used. Quasi-laminar flow of viscous incompressible fluid with density of 1050 kg/m$^3$ and dynamic viscosity of 0.0035 Pa·s was considered, that is typical for modeling hemodynamics in large vessels. The walls elasticity was not taken into account. A typical grid consisted of about 2.5 mln elements. Spatial and temporal discretizations were of second-order accuracy. The time step was 0.01 s.

At the inlet of the CFA velocity curves were set in accordance to clinical ultrasound measurements, time-average inlet flows ranged from 300 to 800 ml/min. Inlet velocity profiles were flat. At the outlet of the graft the part of the input flow (50–70%) was set in accordance with the ultrasound personalized data. The no-slip condition was set on the walls, where velocity components are equal zero. The maximum values of the inlet Reynolds number were in the range from 1200 to 3000. The inlet Womersley number ranged from 8.5 to 14.0.

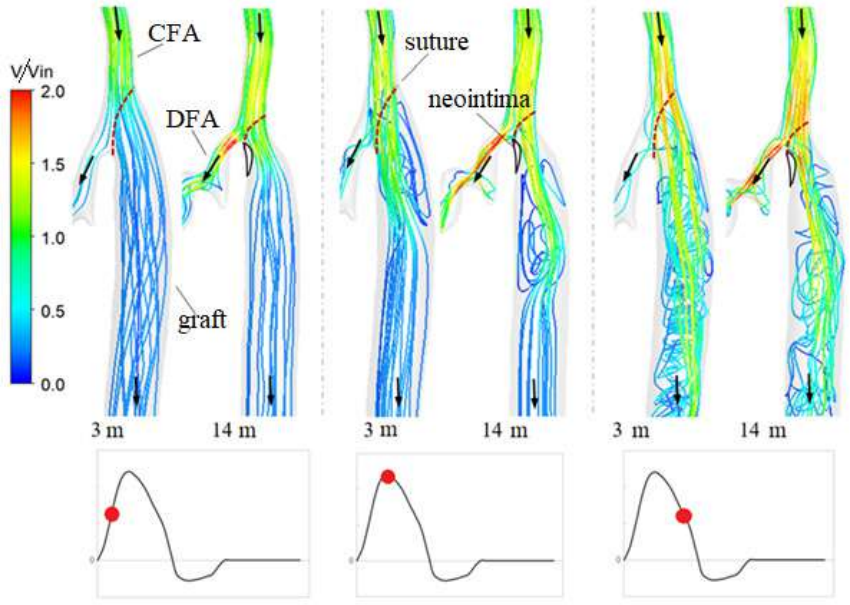


Fig. 2. Streamlines at three instances after 3 (left)
and 14 (right) months after bypass surgery (patient 1)

## Results and Discussion

Fig. 2 shows streamlines at three cycle-time moments for one of the selected patients. Two constructed anastomosis models correspond to 3 and 14 months after bypass. After 11 months there have been changes in the anastomosis geometry: namely, the cross-section in the suture area has decreased and the neointima has grown in the graft inlet. The section narrowing led to a slight flow deviation (relative to the flow in the 3-month model) in the graft and a significant increase in the stagnant zone size after neointimal hyperplasia area.

The presence of stagnant zones, seen clearly at the maximum flow instant, is interconnected with areas of low values of time-averaged wall shear stress (TAWSS) and high values of the oscillatory shear index (OSI). This, in turn, points to an increase in the risk of neointimal hyperplasia.

Comparisons of shear stress parameters in the models with and without neointimal hyperplasia were carried out. In addition to the TAWSS (1) and OSI (2), the RRT parameter (3) was also considered.

$$TAWSS = \frac{1}{T}\int_0^T \left|\vec{\tau}_w\right| dt, \tag{1}$$

$$OSI = \frac{1}{2}\left(1 - \left|\int_0^T \vec{\tau}_w dt\right| \Big/ \int_0^T \left|\vec{\tau}_w\right| dt\right), \tag{2}$$

$$RRT = \frac{1}{TAWSS(1-2\cdot OSI)}, \tag{3}$$

where $\vec{\tau}_w$ is wall shear stress vector, $T$ is cycle time, $t$ is time.

Figs. 3–6 show the distributions of the TAWSS, OSI, and RRT for each of the four selected patients with and without neointimal hyperplasia. In the figures, areas of neointimal hyperplasia are marked in gray. It can be seen that almost in all cases shear stress values in this area increase and oscillatory index decrease. This is due to an increase in the blood flow velocity in the narrowed section. The cross-section area narrowing, evaluated for the considered models as 5-20%, led to increase of time-average wall shear stresses by 50–130 %, to decrease of the oscillatory shear index by 20-30% and to decrease the relative residence time by 25–100 %. High RRT values in Figs. 3–6 (c) indicate areas with higher risk of neointimal hyperplasia (low shear stresses values and high oscillatory shear index).

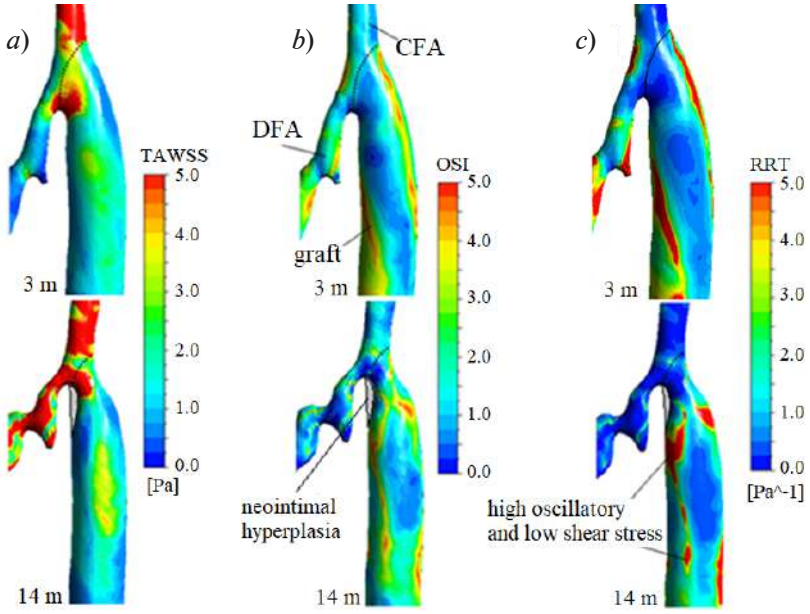


Fig. 3. Time-average wall shear stress (*a*), oscillatory shear index (*b*) and relative residence time (*c*) for 3 (top) and 14 (bottom) months after bypass surgery (patient 1)

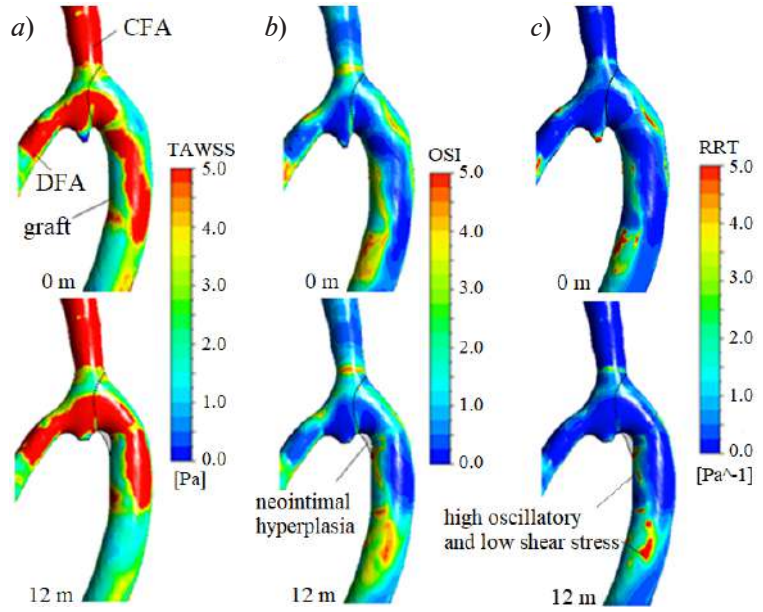


Fig. 4. Time-average wall shear stress (*a*), oscillatory shear index (*b*) and relative residence time (*c*) for 0 (top) and 12 (bottom) months after bypass surgery (patient 2)

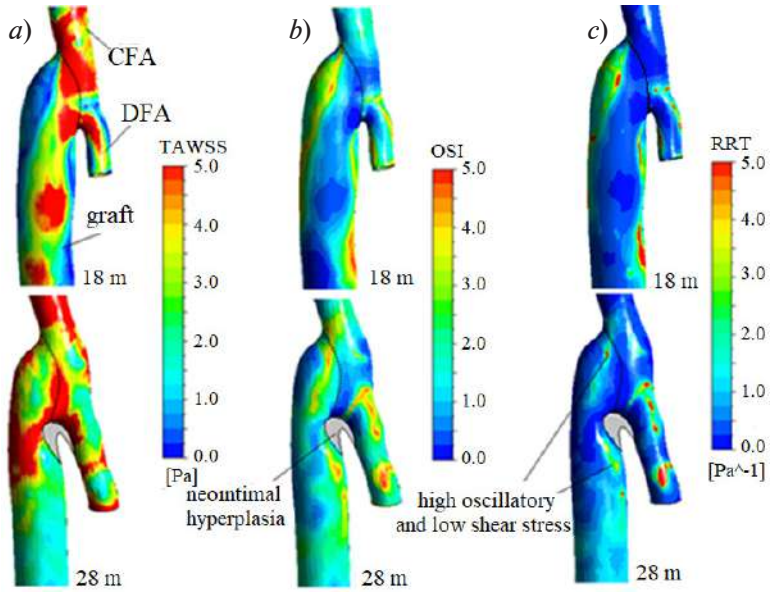


Fig. 5. Time-average wall shear stress (*a*), oscillatory shear index (*b*) and relative residence time (*c*) for 18 (top) and 28 (bottom) months after bypass surgery (patient 3)

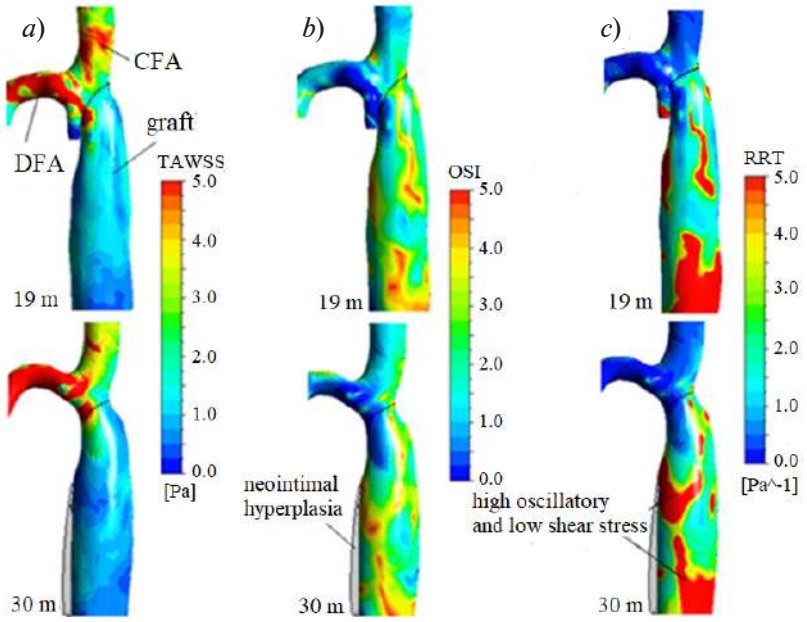


Fig. 6. Time-average wall shear stress (*a*), oscillatory shear index (*b*) and relative residence time (*c*) for 19 (top) and 30 (bottom) months after bypass surgery (patient 4)

## Conclusion

Numerical study of the neointimal hyperplasia effects on hemodynamics in proximal femoral--popliteal anastomoses of real patients was carried out. It has been revealed that the neointimal hyperplasia led to an increase in stagnant zones downstream the anastomosis area.

Comparison of blood flow patterns in the models with and without neointimal hyperplasia has shown that, due to the cross-section narrowing, time-averaged wall shear stresses in this region increase, the oscillatory shear index decreases and the relative residence time decreases. In the stagnant zone, values of these parameters are worsen in terms of neointimal hyperplasia risk.

## Acknowledgments

Simulations were performed on the Polytechnic RSC Tornado cluster of the Polytechnic Supercomputer Center (http://www.scc.spbstu.ru).

## REFERENCES

1. **Lemson M.S., Tordoir J.H. M., Daemen M.J.A.P., Kitslaar P.J.E.H.M.**, Intimal Hyperplasia in Vascular Grafts, Eur. J. Vasc. Endovasc. Surg.19 (2000) 336–350.

2. **Tishchenko I.S., Zolkin V.N., Tarabrin A.S., Maksimov N.V., Korotkov I.N., Barzaeva M.A.**, Remote results of infrainguinal bypass graft procedures for critical lower limb ischaemia, Angiology and vascular surgery. 27(1) (2021) 121–125.

3. **Donadoni F., Pichardo-Almarza C., Bartlett M., Dardik A., Homer-Vanniasinkam S.,Диаz-Zuccarini V.**, Patient-Specific, Multi-Scale Modeling of Neointimal Hyperplasia in Vein Grafts, Front. Physiol.8 (2017) 20.

4. **Singh J., Brunner G., Morrisett J. D., Ballantyne C. M., Lumsden A. B., Shah D. J.,Decuzzi P.**, Patient-specific flow descriptors and normalised wall index in peripheral artery disease: a preliminary study, Computer Methods in Biomechanics and Biomedical Engineering: Imaging and Visualization. 6(2) (2016) 9.

5. **Ivanova Y.F., Tikhomolova L.G., Yukhnev A.D., Smirnov E.M., Kalmikova R.V., Morozov A.N., Suprunovich A.A., Vrabiy A.A., Khubulava G.G., Vavilov V.N.**, Influence of the femoral artery-graft junction patient-specific geometry on blood flow structure and wall shear stress, J. Phys.: Conf. Ser. 2103 (2021) 6.

6. **Meirson T., Orion E., Di Mario C., Webb C., Patel N., Channon K. M., Ben Gal Y., Taggart D. P.**, Flow patterns in externally stented saphenous vein grafts and development of intimal hyperplasia, The Journal of Thoracic and Cardiovascular Surgery. 150(4) (2015) 871–879.

## THE AUTHORS

**IVANOVA Yana F.**
radfn94@mail.ru
ORCID: 0000-0002-6671-9451

**TIKHOMOLOVA Ludmila G.**
ludmila060495@mail.ru
ORCID: 0000-0002-5719-5959

**YUKHNEV Andrey D.**
a.yukhnev@mail.ru

**SMIRNOV Evgeny M.**
smirnov_em@spbstu.ru
ORCID: 0000-0002-7218-6372

**VRABIY Andrey A.**
dock1@yandex.ru
ORCID: 0000-0003-4923-605X

**SUPRUNOVICH Andrey A.**
doctoras@mail.ru

**MOROZOV Alexey N.**
alexx-vma@mail.ru
ORCID: 0000-0003-3051-6334

**KHUBULAVA Gennady G.**
ggkh07@rambler.ru
ORCID: 0000-0001-9093-8024

*Received 01.11.2022. Approved after reviewing 08.11.2022. Accepted 09.11.2022.*

© Peter the Great St. Petersburg Polytechnic University, 2023

Conference materials
UDC 532.546:536.421
DOI: https://doi.org/10.18721/JPM.161.254

# Formation of carbon dioxide hydrate in a closed volume of a water-saturated porous medium

G.R. Rafikova[1]✉

[1]Mavlyutov Institute of Mechanics of UFRC of RAS, Ufa, Russia

✉ rafikova_guzal@mail.ru

**Abstract.** In the present work, a mathematical model is constructed for the formation of carbon dioxide hydrate in a closed volume of a porous medium saturated with water and carbon dioxide. The thermobaric parameters of the system correspond to the conditions for the existence of gaseous carbon dioxide and $CO_2$ hydrate at positive temperatures. The system of basic equations includes mass conservation equations for phase components, energy and state equations. An analysis was made of the influence of the initial parameters of the system (water saturation, pressure, temperature, porosity) on the intensity of hydrate formation. A decision map has been constructed illustrating the possible modes of hydrate formation, in particular, when water completely or partially passes into the composition of the gas hydrate._

**Keywords:** formation of carbon dioxide hydrate, porous medium, water saturation

**Funding:** The work was done using the state budget funds for the state assignment for 2019-2022 (0246-2019-0052).

**Citation:** Rafikova G.R., Formation of carbon dioxide hydrate in a closed volume of a water-saturated porous medium, St. Petersburg State Polytechnical University Journal. Physics and Mathematics. 16 (1.2) (2023) 356–361. DOI: https://doi.org/10.18721/JPM.161.254

This is an open access article under the CC BY-NC 4.0 license (https://creativecommons.org/licenses/by-nc/4.0/)

Материалы конференции
УДК 532.546:536.421
DOI: https://doi.org/10.18721/JPM.161.254

# Образование гидрата углекислого газа в замкнутом объеме водонасыщенной пористой среды

Г.Р. Рафикова[1]✉

[1] Институт механики им.Р.Р. Мавлютова УФИЦ РАН, г. Уфа, Россия

✉ rafikova_guzal@mail.ru

**Аннотация.** В настоящей работе построена математическая модель образования гидрата углекислого газа в замкнутом объеме, заполненном пористой средой, насыщенной водой и диоксидом углерода. Термобарические условия системы соответствуют условиям существования газообразного диоксида углерода и гидрата $CO_2$ при положительных температурах. Система основных уравнений состоит из уравнений сохранения массы для всех компонентов, уравнения энергии и уравнения состояния газа. Проведен анализ влияния начальных параметров системы (водонасыщенности, давления, температуры, пористости) на интенсивность гидратообразования.

**Ключевые слова:** образование газогидрата углекислого газа, пористая среда, водонасыщенность

**Финансирование:** Работа выполнена в рамках Государственного задания «Численные, аналитические и экспериментальные методы в многофазных, термовязких и микродисперсных системах газогидродинамики» (код темы 0246-2019-0052).

© Rafikova G.R., 2023. Published by Peter the Great St. Petersburg Polytechnic University.

**Ссылка при цитировании:** Рафикова Г.Р. Образование гидрата углекислого газа в замкнутом объеме водонасыщенной пористой среды // Научно-технические ведомости СПбГПУ. Физико-математические науки. 2023. Т. 16. № 1.2. С. 356–361. DOI: https://doi.org/10.18721/JPM.161.254

Статья открытого доступа, распространяемая по лицензии CC BY-NC 4.0 (https://creativecommons.org/licenses/by-nc/4.0/)

## Introduction

In the past few decades, much attention has been paid around the world to the problem of excessive carbon dioxide emissions as a result of the work of a large number of enterprises that contribute to the pollution of the Earth's atmosphere. Sufficiently safe and reliable way to store greenhouse gases is their storage in the gas hydrate state, since the method of such conservation will save not only large volumes of carbon dioxide, but also a fairly large amount of fresh water [1, 2]. In this connection, the study of the theoretical foundations of underground utilization of carbon dioxide by converting it into a gas hydrate state is an important and urgent task.

Mathematical modeling of carbon dioxide hydrate formation in a porous formation saturated with methane and water is considered in [3, 4]. Experimental work on the study of the formation of carbon dioxide hydrate in rocks was carried out in [5]. The influence of temperature, water and ice saturation, and the composition of soil samples on the kinetics of hydrate formation was assessed, and the course of the process at positive and negative temperatures was compared. The effect of surfactants and porous material on the intensity of $CO_2$ hydrate formation was studied in [6–8].

In the present work, the process of formation of carbon dioxide hydrate in an isolated porous medium saturated with water and carbon dioxide is studied.

## Problem statement

We consider a porous medium that is in a sealed and thermally insulated container and in its initial state is saturated with water and carbon dioxide. The initial pressure and temperature correspond to the thermobaric conditions for the formation of a hydrate and the existence of gaseous carbon dioxide. Let us assume that at will be the formation of $CO_2$ hydrate at positive temperatures, and taking into account the homogeneity of the initial thermobaric conditions and the tightness of the container, the filtration flow of gas in a porous medium will be neglected. The porous medium, water and gas hydrate will be assumed to be incompressible and motionless. The accepted statement of the problem means that during the characteristic time of filling the container until the pressure value is reached, hydrate formation in a porous medium can be neglected. For this, it is necessary that the porous medium has a sufficiently high permeability, and the characteristic dimensions of the container must be small. This statement of the problem is the theoretical basis of one of the methods for experimental study of the kinetics of hydrate formation.

Let us write the mass conservation equations for water, hydrate and gas, taking into account the above assumptions:

$$\frac{d\left(mS_w\rho_w\right)}{dt} = -J_w,\ \frac{d\left(mS_h\rho_h\right)}{dt} = J_h,\ \frac{d\left(mS_g\rho_g\right)}{dt} = -J_g. \tag{1}$$

Here $m$ and $S_i$ are, respectively, the porosity of the skeleton and the volume saturation of pores with water, hydrate, and gas, $J_w$ and $J_g$ are the intensities of water and gas consumption for hydrate formation with the intensity $J_h$ per unit volume of the porous medium. Here and in what follows, the subscripts $w$, $h$, $g$, correspond to the parameters related to water, carbon dioxide gas hydrate, and carbon dioxide.

For the intensities $J_w$, $J_g$ and $J_h$ we write the stoichiometry conditions [9]:

$$J_w = \left(1-G\right)J_h,\ J_g = GJ_h. \tag{2}$$

© Рафикова Г.Р., 2023. Издатель: Санкт-Петербургский политехнический университет Петра Великого.

Taking into account Eqs. (1) and relations (2), we obtain expressions for determining the saturation of hydrate, water and gas:

$$S_h = \frac{\left(1 - S_{w0} - S_g\right)}{\left(1 - \rho_h\left(1-G\right)/\rho_w\right)},\ S_w = S_{w0} - \frac{\rho_h}{\rho_w}\left(1-G\right)S_h. \tag{3}$$

Assuming that the temperature for all components of the system is the same, we write the heat balance equation:

$$\rho c \frac{dT}{dt} = J_h l,\ \ \rho c = \left(1-m\right)\rho_{sk} c_{sk} + m \sum_{j=w,g,h} \rho_j S_j c_j. \tag{4}$$

Here $c_j$ and $\rho c$ are the specific heat capacity of the phases and $l$ is the specific volumetric heat capacity of the system, and is the specific heat per unit mass of the hydrate released during its formation. Due to the fact that the largest contribution to the value of the volumetric heat capacity is made by the corresponding parameters of the skeleton of the porous medium, we will consider them to be constant values.

For carbon dioxide, we write the equation of state of the gas:

$$p = \rho_g R_g T. \tag{5}$$

For the kinetics of the formation of carbon dioxide hydrate, we accept the scheme of phase transitions considered in [9, 10]. According to this scheme, we consider a porous medium as a system of porous micro channels with radius a, water covers the walls of these channels ($a < r < a_w$), carbon dioxide hydrate will form on top of this layer ($a_w < r < a_h$), and in the remaining annular layer ($r > a_g$)) the gas mixture will flow. The rate of hydrate formation will be determined by the diffusion of carbon dioxide through the $CO_2$ hydrate layer formed between the gas and water.

For the intensity of formation of carbon dioxide hydrate, we write the expression:

$$J_h = \frac{4m\rho_g D}{aG\ln\left(1 + S_h/S_g\right)}, \tag{6}$$

where $a$ is the microchannel radius in a porous medium, $D$ is the diffusion coefficient of carbon dioxide through the $CO_2$ hydrate layer.

The permeability of a porous medium is related to the radius of the channels by the following relation:

$$a = \left(k/m\right)^{1/2}. \tag{7}$$

The system of Eqs. (1−5), taking into account (6, 7), is reduced to a system of ordinary differential equations for changing pressure, temperature and hydrate saturation:

$$\frac{d\left(pS_g\right)}{dt} = -\frac{GJ_h R_g T}{m}, \frac{dT}{dt} = \frac{J_h l}{\rho c}, \frac{dS_h}{dt} = \frac{J_h}{m\rho_h}.$$

## Result of calculation

For the parameters characterizing the system porous medium - gas hydrate $CO_2$ - carbon dioxide, the following values are taken [11]: $m = 0.1$, $k = 10^{-11}$ m, $\rho c = 2.5 \cdot 10^6$ J/(m$^3$·K), $l = 10 \cdot 4.8^5$ J/kg, $\rho_h^0 = 1117$ kg/m$^3$, $\rho_w^0 = 1000$ kg/m$^3$, $G = 0.29$, $R_g = 189$ J/(kg·K), $D = 10^{-16}$ m$^2$/s.

For determination of the equilibrium temperature for system "$CO_2$ + water + gas hydrate" for the current pressure during the hydrate formation process, we write the phase equilibrium condition for temperature and pressure [9]:

$$T_s(p) = T_{s0} + T_* \ln(p/p_{s0}),$$

where $T_{s0}$ is the equilibrium temperature at pressure value $p_{s0}$, $T_*$ is an empirical parameter having the dimension of temperature. These parameters are defined for carbon dioxide as $T_{s0}$=280 $K$, $p_{s0}$ = 2.88 MPa, $T_*$ = 7.1 $K$ [11].

Fig. 1 shows the dynamics of pressure (*a*), temperature (*b*), and hydrate and water saturation (*c*) at different values of the initial water saturation $S_{w0}$ = 0.3 (line 1) and 0.05 (line 2). The initial values of pressure and temperature are taken respectively $p_0$= 3 MPa, $T_0$=274 $K$. The dotted line corresponds to the water saturation value. Here and below, the dashed line corresponds to the equilibrium temperature for the current pressure values.

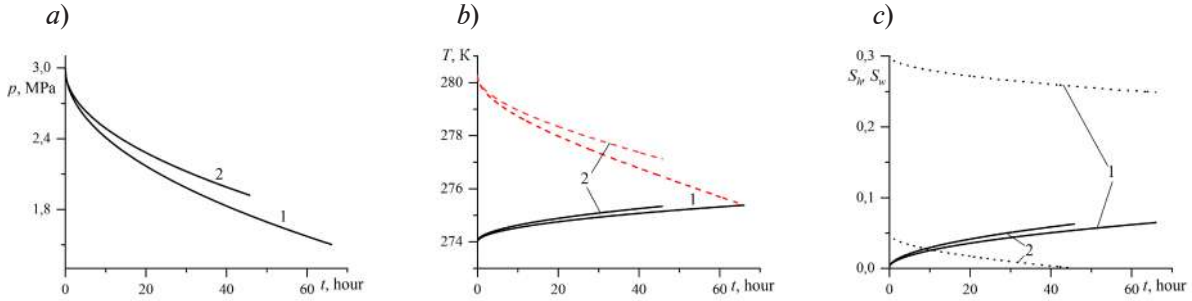


Fig. 1. Dynamics of pressure $p$ (*a*), temperature $T$ (*b*), hydrate and water saturations $S_h$, $S_w$ (*c*) versus time at different values of initial water saturation (1 – $S_{w0}$ = 0.3, 2–0.05)

It is shown that due to the consumption of gas for the formation of hydrate and the release of energy due to the phase transition, the pressure of the system decreases and the temperature rises. The end of the process of hydrate formation is either the complete transition of water into the composition of the hydrate (line *1*), or the achievement of an equilibrium temperature of the system (line *2*), corresponding to the current pressure in the porous medium. A higher intensity of hydrate formation is observed at lower values of the initial water saturation, which is associated with a higher specific contact surface between the hydrate and water.

Fig. 2 shows the dependences of pressure, temperature and hydrate saturation of the system on time. Lines 1 and 2 correspond to the values of the skeleton porosity $m$ = 0.1 and 0.2. The intensity of hydrate formation increases approximately 2 times with growing porosity. This effect is explained by an increase in the specific area of the porous medium, which contributes to the intensification of the process.

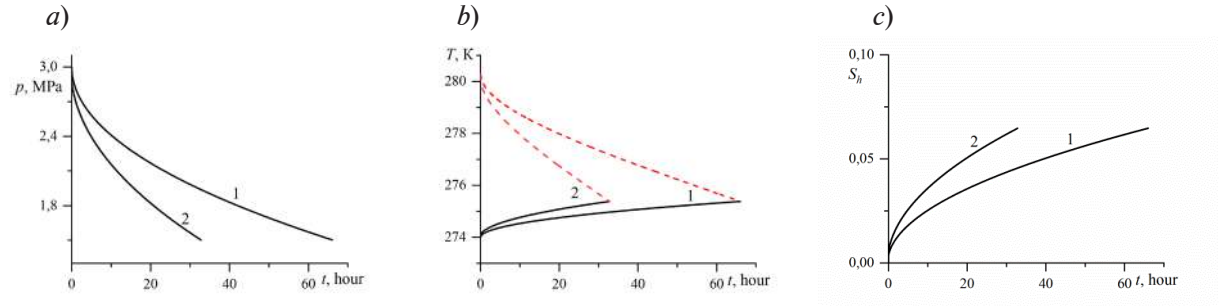


Fig. 2. Dynamics of pressure $p$ (a), temperature $T$ (*b*), hydrate saturation $S_h$ (*c*) versus time at different values of porosity (1 – $m$ = 0.1, 2–0.2)

Fig. 3 illustrates the dependences of the relative hydrate saturation after the termination of the hydrate formation process on the initial static pressure (*a*) at $S_{w0}$ = 0.3, and on the initial water saturation at $T_0$ = 273 $K$ (*b*). In Fig. 3,*a*, lines *1* and *2* correspond to the temperature values $T_0$ = 273 $K$ and 277 K. In Fig. 3,*b*, lines *1* and *2* correspond to pressure values $p_0$= 2 and 3.5 MPa.

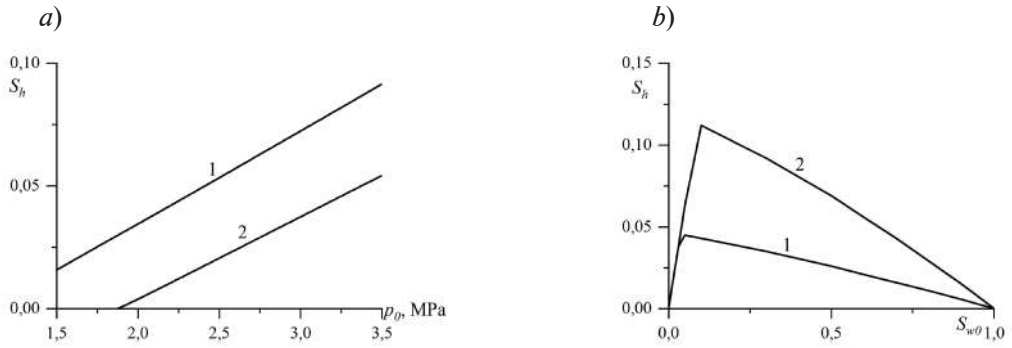


Fig. 3. Influence of initial pressure values (*a*), initial water saturation (*b*) on the final value of hydrate saturation $S_h$

It is established that the higher the initial pressure and the lower the initial temperature, the greater the proportion of water passes into the gas hydrate state (Fig. 3, *a*). It is revealed that there is a certain value of the initial water saturation, which depends on the initial pressure and the initial temperature at which the greatest hydration saturation is achieved by the end of the process (Fig. 3,*b*). At low values of the initial water saturation, a complete transition of water into the hydrate occurs, and at high values of the initial water saturation, the temperature of the equilibrium value is reached and the water does not completely enter the hydrate state.

## REFERENCES

1. **Makogon Y.F.,** Gas hydrates. History of study and prospects of development, Geology and minerals of the World Ocean 2 (2010) 5–21.

2. **Belova S.V., Chiglintseva A.S., Khasanov M.K., Shagapov V.S., Dudareva O.V.,** Simulation of CH4 recovery from hydrate deposits by injection of CO2, Thermal science. 23 (S2) (2019) S447–S454.

3. **Gubaidullin A.A., Musakaev N.G., Hai D.N., Borodin S.L., Thai N.Q., Thang N.T.,** Theoretical modeling of the carbon dioxide injection into the porous medium saturated with methane and water taking into account the $CO_2$ hydrate formation, Vietnam Journal of Mechanics. 40 (3) (2018) 233–242.

4. **Khasanov M.K.,** Mathematical modeling of carbon dioxide injection into the reservoir taking into account hydrate formation, Scientific and Technical Bulletin of the Volga region 3 (2017) 139.

5. **Chuvilin E.M., Guryeva O.M.,** Experimental study of the formation of co2 hydrates in the pore space of freezing and frozen rocks, Cryosphere of the Earth XIII 3 (2009) 70–79.

6. **Roosta H., Varaminian F., Khosharay Sh.,** Experimental study of CO2 hydrate formation kinetics with and without kinetic and thermodynamic promoters, Scientia Iranica 21 (3) (2014) 753–762.

7. **Sarlak H., Azimi A., Ghomshe M., Mirzaei M.,** Thermodynamic study of CO2 hydrate formation in the presence of SDS and graphene oxide nanoparticles. Advances in environmental science and technology 4 (2018) 233–240.

8. **Jia Liu, Yajuan Wei, Wei Meng, Pei-Zhou Li, Yanli Zhao, Ruqiang Zou.** Understanding the Pathway of Gas Hydrate Formation with Porous Materials for Enhanced Gas Separation, Research 2019 (2019) 3206024.

9. **Shagapov V.Sh., Rafikova G.R., Khasanov M.K.** On the theory of formation of gas hydrate in partially water-saturated porous medium when injecting methane, High Temperature 54 (6) (2016) 858−866.

10. **Shagapov V.Sh., Chiglintseva A.S., Rafikova G.R.,** On the applicability of a quasi-stationary solution of the diffusion equation for the hydrate layer formed at the gas−ice (water) interface, Theor. Found. of Chem. Engin. 52 (4) (2018) 560–567.

11. **Shagapov V.Sh., Rafikova G.R., Khasanov M.K.,** The theory of the replacement of methane by carbon dioxide in gas hydrates, Theor. Found. of Chem. Engin. 53 (1) (2019) 64–74.

## THE AUTHOR

**RAFIKOVA Guzal R.**
rafikova_guzal@mail.ru
ORCID: 0000-0003-3305-8586

*Received 30.10.2022. Approved after reviewing 09.11.2022. Accepted 10.11.2022.*

© Peter the Great St. Petersburg Polytechnic University, 2023

ASTROPHYSICS

Conference materials
UDC 52
DOI: https://doi.org/10.18721/JPM.161.255

# Asymmetry study of the mixed-morphology supernova remnant G 18.95-1.1

A.M. Bykov[1], Yu.A. Uvarov[1]✉

[1] Ioffe Institute, St. Petersburg, Russia

✉ uv@astro.ioffe.ru

**Abstract.** Radio and X-ray maps of supernova remnants (SNRs) in many cases revealed an asymmetric global structure. This may reflect the inhomogeneity of the circumstellar/ambient matter, anisotropic energy release or both. Given a growing sample of the observed SNRs some techniques to characterize the global asymmetry are needed to identify old SNRs in sky surveys among other observed extended structures of low surface brightness. We discuss here the applications of modified power-ratio technique to quantify the global asymmetry of the mixed-morphology SNR G 18.95-1.1 using its recent mapping with SRG and compare results with the well-studied SNRs IC 443 and Cas A.

**Keywords:** supernova remnants, SNR, power-ratio method

**Funding:** Modeling by A.M. Bykov at RAS JSCC was supported by RSF grant 21-72-20020. Data analysis by Yu.A. Uvarov was supported by theme 0040-2019-0025 at Ioffe Institute.

**Citation:** Bykov A.M., Uvarov Yu.A., Asymmetry study of the mixed-morphology supernova remnant G 18.95-1.1, St. Petersburg State Polytechnical University Journal. Physics and Mathematics. 16 (1.2) (2023) 362–369. DOI: https://doi.org/10.18721/JPM.161.255

This is an open access article under the CC BY-NC 4.0 license (https://creativecommons.org/licenses/by-nc/4.0/)

Материалы конференции
УДК 52
DOI: https://doi.org/10.18721/JPM.161.255

# Исследование асимметрии остатка сверхновой смешанной морфологии G 18.95-1.1

А.М. Быков[1], Ю.А. Уваров[1]✉

[1] Физико-технический институт им. А.Ф. Иоффе РАН, Санкт-Петербург, Россия

✉ uv@astro.ioffe.ru

**Аннотация.** Радио и рентгеновские наблюдения остатков сверхновых (ОСН) во многих случаях выявили их асимметричную глобальную структуру. Эта асимметрия может отражать неоднородность окружающего вещества, анизотропное выделение энергии взрыва или и то, и другое. Учитывая растущее число обнаруженных ОСН, необходимы методы для измерения и классификации их наблюдаемой асимметрии, в том числе для идентификации старых ОСН в обзорах неба среди других наблюдаемых протяженных структур с низкой поверхностной яркостью. Мы обсуждаем применение модифицированного метода отношений моментов для количественной оценки глобальной асимметрии ОСН смешанного типа G 18.95-1.1, на основе его недавних наблюдений обсерваторией СРГ, и сравниваем полученные результаты с результатами анализа хорошо изученных ОСН IC 443 и Cas A.

**Ключевые слова:** остатки сверхновых, ОСН, метод отношения моментов

**Финансирование:** Компьютерное моделирование А.М. Быкова с использованием ресурсов МСЦ РАН было поддержано грантом РНФ 20020-72-21. Работа Ю.А. Уварова была поддержана госзаданием 0025-2019-0040.

© Bykov A.M., Uvarov Yu.A., 2023. Published by Peter the Great St. Petersburg Polytechnic University.

**Ссылка при цитировании:** Быков А.М., Уваров Ю.А. Исследование асимметрии остатка сверхновой смешанной морфологии G 18.95-1.1 // Научно-технические ведомости СПбГПУ. Физико-математические науки. 2023. Т. 16. № 1.2. С. 362–369. DOI: https://doi.org/10.18721/JPM.161.255

Статья открытого доступа, распространяемая по лицензии CC BY-NC 4.0 (https://creativecommons.org/licenses/by-nc/4.0/)

## Introduction

Mixed-morphology SNRs comprise a subclass of more than 40 SNRs with shell-type radio images and a central-filled thermal X-ray maps (see [1–3] for a review). A mixed-morphology supernova remnant G 18.95-1.1 was studied in a broad energy range from radio to X-rays. It was discovered by Fuerst et al. [4] in the radio survey of the galactic plane [5]. In $H_\alpha$ it was studied in [6]. X-ray observations with ROSAT [7, 8], ASCA [9], Chandra [10] and recently SRG [11] established a highly anisotropic shape with a bunch of bright emission clumps in the south with a prominent line emission, dim north part and a likely pulsar wind nebula (PWN) in the center elongated to the north. Bright southern clumps line emission shows an excess of element abundances over the solar values which is typical for ejecta fragments [11]. These features can be understood if G18.95-1.1 is a result of the asymmetric supernova explosion with a progenitor star interior material ejected to the south and a pulsar kick directed to the north. An asymmetric mass ejection right after the supernova core collapse was modelled, e.g., in [12] while the subsequent sphericization of the remnants in the isotropic interstellar medium was discussed earlier in [13]. To quantify the global asymmetric morphology of SNRs in [14] was proposed the power-ratio technique which modified version we apply here to the recent detailed maps of SNR G18.95-1.1 [11] obtained with SRG X-ray observatory [15]. A similar analyses of the asymmetry of IC443 and Cas A SNRs are also discussed for a comparison.

IC 443 (G189.1+3.0) is an extended and old SNR (~ 45′ size at a distance of 1.5 kpc [16]). In radio bands it shows two half shell structure [17]. This is considered to be an effect of an interaction with a torus-like molecular cloud [18, 19] that separates two half-shells. In X-rays it was studied with ROSAT [20], ASCA [21, 22], BeppoSAX [23], Chandra [24–26], XMMNewton [27, 28, 19], and RXTE [29]. XMM-Newton mosaic exposure corrected X-ray image in the 0.4–8.0 keV energy range is shown in Fig. 1. X-ray emission morphology is center-filled with maximum emission in the north and a bright clump of the emission in the south (1SAX J0618.0+2227). This southern source is considered to be a PWN [24, 25, 27]. There is a bunch of clump-like sources in the southern part that could be considered as interaction cites of the ejecta fragments and a molecular cloud [28, 30].

Cas A is a young and bright SNR that was studied in depth in all of the spectral bands: radio [31–33], optical [34], infrared [35, 36], X-rays [37, 38]. The total Chandra exposure used for observation of this remnant exceeds 1 Ms that allows construction of high resolution X-ray image of the SNR (Fig. 1) that shows a remarkable source structure.

To analyze morphology of the discussed above SNRs shown in Fig. 1 we apply a modified power-ratio technique. This technique was developed in [39, 40] for studies of galactic clusters.

Then it was successfully applied to study asymmetric structure of a set of SNRs in [14, 41–44]. The method is described in the next section.

## Methods

The power-ratio method is based on the multipole expansion of the 2D gravitation potential within the circular aperture with radius $R$:

$$\Psi\left(R,\phi\right) = -a_0 ln\left(1/R\right) - \sum_{m=1}^{\infty}\left(a_m cos\left(m\phi\right) + b_m sin\left(m\phi\right)\right)/mR^m,$$

$$a_m = \int_{r'<R} \Sigma\left(r',\phi\right) cos\left(m\phi\right) r'^{m+1}\, dr'\, d\phi,$$

$$b_m = \int_{r'<R} \Sigma\left(r',\phi\right) sin\left(m\phi\right) r'^{m+1}\, dr'\, d\phi,$$

© Быков А.М., Уваров Ю.А., 2023. Издатель: Санкт-Петербургский политехнический университет Петра Великого.

Here $\Sigma(r,\phi)$ is the surface mass density inside the aperture. In practice the surface mass density is not known and a X-ray brightness distribution is used instead. Thus $\Sigma(r,\phi)$ is not directly connected with the surface mass density and actually this method is no more than the multipole expansion for the surface brightness filtered by aperture that allows one to make a classification of the structure of studied objects. The power of the multipole expansion is calculated as:

$$P(R)=\frac{1}{2\pi}\int_0^{2\pi}\Psi_m(R,\phi)\Psi_m(R,\phi)d\phi,$$
$$P_0=\left(a_0 ln(R)\right)^2,\ P_m=\frac{a_m^2+b_m^2}{2m^2R^{2m}}. \quad (1)$$

Usually the dimensionless ratio $P_m/P_0$ is measured and the origin of coordinate system is chosen in the center of brightness so $P_1 = 0$. However, $P_m/P_0 \sim 1/R^{2m}ln^2(R)$ is aperture size dependent value that makes a comparison of these ratios for objects with different sizes not straightforward. We suggest instead calculating amplitudes $\tilde{a}_m, \tilde{b}_m$ of multipole expansion in the dimensionless coordinates $r/R_*$ where $R_*$ is a characteristic radius of the studied object. We define $R_*$ to be the radius of the minimum circle aperture fully enclosing the object. In this case, $a_m = R_*^{m+2}\tilde{a}_m, b_m = R_*^{m+2}\tilde{b}_m$. We also suggest using ratios $\tilde{P}_m / \tilde{a}_0^2$ for the analyses which are dimensionless, don't depend on object size and reflects the object structure. We use these notations below for study G18.95-1.1, IC 443 and Cas A SNRs.

However, usually SNR outer borders are not sharp enough and some diffuse background emission is present that allows a systematic error in the definition of $R_*$. It also should be mentioned that the integrand expressions for $a_m$, $b_m$ are growing as $r^{m+1}$ with $r$ and thats why even small background emission far outside the source can dramatically spoil the moment estimations if it is included in the integration. So clearing the emission map from background point sources and diffuse emission is essential. This is made in tree steps. At first point sources are filtered out. Then the diffuse background emission outside the $R_*$ aperture is estimated and subtracted from the image. At last the emission outside the aperture is set to zero. After this the values $\tilde{P}_m / \tilde{a}_0^2$ are independent from the aperture size $R > R_*$ enclosing the circle $R_*$ if the value $R_*$ is used for R in the Eq. (1). However, these values are dependent on the position of the origin of coordinate system. In particular, $\tilde{P}_1 = 0$ if and only if the origin coincides with the center of brightness.

The systematic errors arising from the uncertainty of $R_*$ can be estimated by comparison of the results obtained for different values of $R_*$. The stochastic errors arising because of the Poisson nature of the incoming photons can be calculated with the Monte-Carlo simulation of a set of X-ray images as was done in [41].

## Results

We demonstrate the application of the power-ratio method for study G18.95-1.1, IC 443 and Cas A SNRs. Cas A has an almost spherically symmetric shell. However there is a special structure in the north-east part of the shell that is considered to be a trace of the jet formed during SN explosion. IC 443 is a well-known example of the SNR interacting with a molecular cloud. G18.95-1.1 is considered to be an example of an asymmetric SN explosion [11].

Fig. 1 shows X-ray maps of the studied SNRs and demonstrates the analyses used. G18.95-1.1 map was constructed as a result of SRG/eROSITA observations (panel (*a*), [11]). Panel (*b*) shows the same map with point sources filtered out including pulsar candidate (P) and bright source (1) associated with a star [11]. IC 443 map is constructed as a mosaic image of XMM-Newton observations using ESAS[1] software (panel (*c*)). Panel (*d*) shows the same map with point sources filtered out together with PWN candidate that with some probability belongs to an other SNR G189.6+3.3 [24–27] overlapping with IC 443. Cas A X-ray image was obtained using Chandra data. The center point source was filtered out in the analyses. O and X points show the geometrical center of the apertures and the center of brightness. Apertures $R_*$ that were used for estimation of the systematic errors of momentum estimations are also shown for all studied remnants.

[1] http://www.cosmos.esa.int/web/xmm-newton/xmm-esas

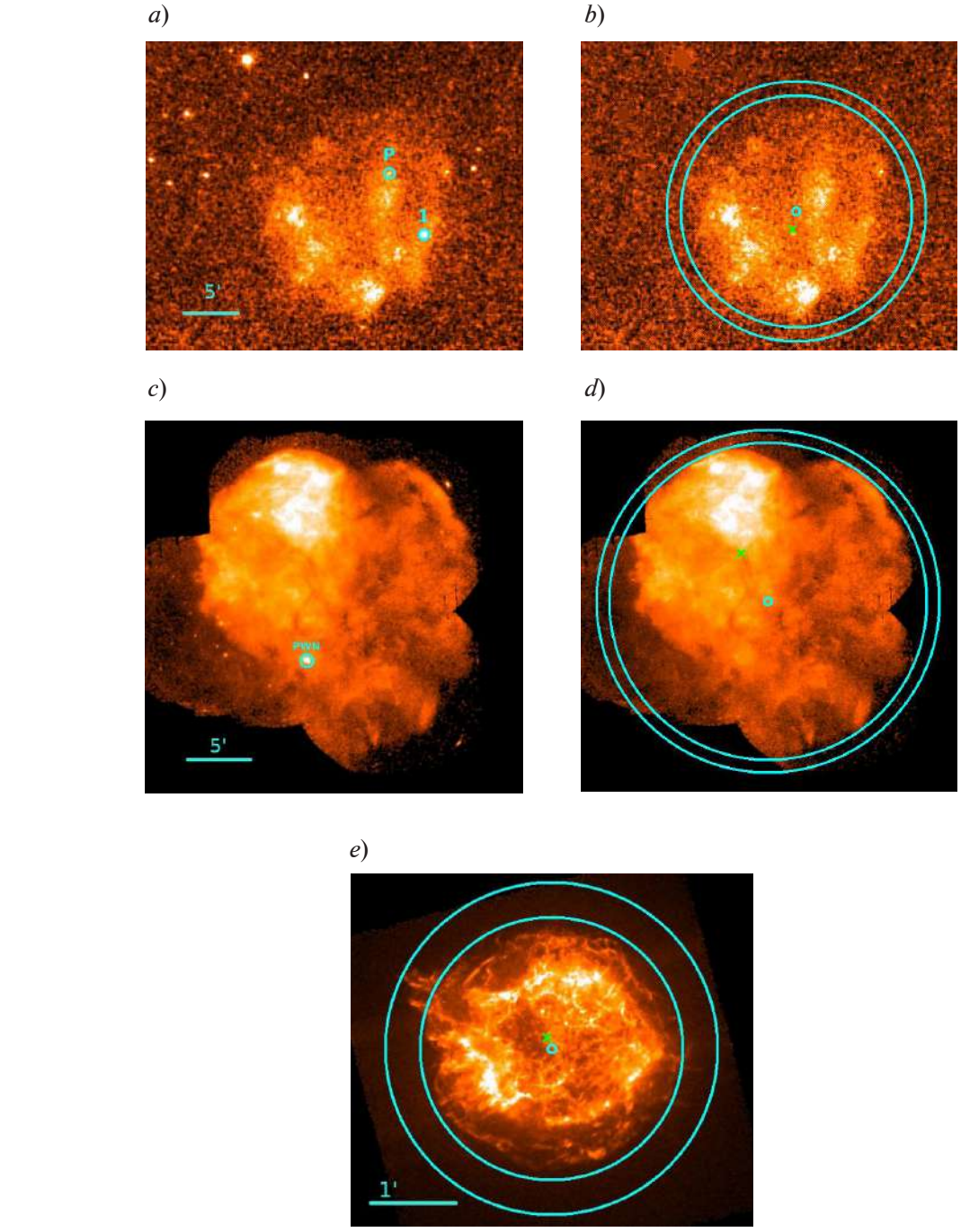


Fig. 1. X-ray maps of studied SNRs. Upper panels show SRG/eROSITA map (0.5–2.3 keV) of the G18.95-1.1 with (*a*) and without (*b*) filtering of point sources. Middle panels show XMMNewton map (0.4–8.0 keV) of the IC443 produced with ESAS software with (*c*) and without (*d*) filtering of point sources and PWN region. Lower panel (*e*) shows Chandra map (0.4–8.0 keV) of the Cas A. Different apertures $R_*$ used for systematic errors estimations are shown as cyan circles whose radius values are listed in Tables 1,2. O and X points show the geometrical center of the apertures and the center of brightness

Tables 1, 2 list calculated values $\tilde{P}_m / \tilde{a}_0^2$ for $m$ = 1, 2, 3, 4 for each values of $R_*$ used. Table 1 lists the results for the case when the origin of coordinate system coincides with the center of brightness so $\tilde{P}_1 = 0$. Table 2 lists the results for the case when the origin coincides with the center of aperture. 1σ statistical error due to Poisson statistic of the incoming photons, listed in the Tables, was calculated in Monte-Carlo simulations of the emission maps with 1000 iterations and subsequent image smoothing with the same criteria that was used to construct an initial map.

Table 1

**Values of $\tilde{P}_m / \tilde{a}_0^2$ for $m$ = 2, 3, 4**
**Center of brightness coordinate system**

| object | $R_*$, arcmin | $\tilde{P}_2 / \tilde{a}_0^2$ | $\tilde{P}_3 / \tilde{a}_0^2$ | $\tilde{P}_4 / \tilde{a}_0^2$ |
|---|---|---|---|---|
| G 18.95-09 | 21.6 | $(8.0\pm0.4)\cdot10^{-5}$ | $(3.9\pm0.2)\cdot10^{-5}$ | $(4.2\pm0.3)\cdot10^{-6}$ |
| | 19.2 | $(5.6\pm0.3)\cdot10^{-5}$ | $(3.3\pm0.1)\cdot10^{-5}$ | $(2.8\pm0.2)\cdot10^{-6}$ |
| IC 443 | 27.0 | $(9.50\pm0.05)\cdot10^{-4}$ | $(4.75\pm0.05)\cdot10^{-5}$ | $(1.85\pm0.01)\cdot10^{-4}$ |
| | 25.0 | $(9.20\pm0.05)\cdot10^{-4}$ | $(4.85\pm0.05)\cdot10^{-5}$ | $(1.75\pm0.01)\cdot10^{-4}$ |
| Cas A | 3.9 | $(4.03\pm0.04)\cdot10^{-4}$ | $(2.70\pm0.03)\cdot10^{-5}$ | $(2.60\pm0.03)\cdot10^{-6}$ |
| | 3.1 | $(3.60\pm0.01)\cdot10^{-4}$ | $(3.42\pm0.01)\cdot10^{-5}$ | $(1.14\pm0.01)\cdot10^{-6}$ |

Note: 1σ statistical error due to Poisson photon distribution is listed in the Table.

Table 2

**Values of $\tilde{P}_m / \tilde{a}_0^2$ for $m$ = 1, 2, 3, 4**
**Center of aperture coordinate system**

| object | $R_*$ | $\tilde{P}_1 / \tilde{a}_0^2$ | $\tilde{P}_2 / \tilde{a}_0^2$ | $\tilde{P}_3 / \tilde{a}_0^2$ | $\tilde{P}_4 / \tilde{a}_0^2$ |
|---|---|---|---|---|---|
| | arcmin | $\times10^{-3}$ | $\times10^{-3}$ | $\times10^{-3}$ | $\times10^{-6}$ |
| G 18.95-09 | 21.6 | 10.2±0.1 | $(9.8\pm0.4)\cdot10^{-2}$ | $(1.5\pm0.1)\cdot10^{-2}$ | 1.7±0.2 |
| | 19.2 | 9.8±0.1 | $(7.7\pm0.3)\cdot10^{-2}$ | $(1.4\pm0.1)\cdot10^{-2}$ | 1.0±0.1 |
| IC 443 | 27.0 | 91.9±0.1 | 9.11±0.01 | 1.44±0.01 | 730±1 |
| | 25.0 | 93.2±0.1 | 9.20±0.01 | 1.45±0.01 | 700±1 |
| Cas A | 3.9 | 3.45±0.01 | $(3.10\pm0.01)\cdot10^{-1}$ | $(2.36\pm0.01)\cdot10^{-2}$ | 5.42±0.04 |
| | 3.1 | 3.28±0.01 | $(2.77\pm0.01)\cdot10^{-1}$ | $(2.97\pm0.01)\cdot10^{-2}$ | 3.57±0.02 |

Note: 1σ statistical error due to Poisson photon distribution is listed in the Table. Multiplication factors listed in the first row should be applied to the table values of the corresponding columns.

**Discussion and Conclusions**

In this work three anisotropic SNRs were considered: G18.95-1.1, IC 443 and Cas A. Cas A image has a possible trace of the jet formed during SN explosion, IC 443 is an example of SNR interacting with a molecular cloud and G18.95-1.1 is considered to be a result of an asymmetric SN explosion. We modified the power-ratio method for analyses of the objects with different sizes and applied it for listed SNRs using two different coordinate systems. One of which coincides with the center of brightness and the other with the geometrical center of the object. A center of minimal circular aperture fully enclosing the object was chosen as the geometrical center of SNR.

For both systems of coordinates asymmetry of IC443, which is interacting with a molecular cloud, is characterized by greater values of all 4 moments $\tilde{P}_1, \tilde{P}_2, \tilde{P}_3, \tilde{P}_4$. While G18.95-1.1, that was born in an asymmetric explosion, has higher value of $\tilde{P}_1$ and lower values of $\tilde{P}_2$ and $\tilde{P}_4$, than Cas A, which has more symmetric shell with a trace of a jet. We demonstrate that a modified power-ratio method can be used for the comparative analysis of SNR anisotropy even if angular sizes of studied remnants differ.

## REFERENCES


1. **Rho J., Petre R.,** Mixed-Morphology Supernova Remnants, Astrophysical Journal Letters. 503 (1998) L167–L170.
2. **Slane P., et al.,** Supernova Remnants Interacting with Molecular Clouds: X-Ray and Gamma-Ray Signatures, Space Science Reviews. 188 (2015) 187–210.
3. **Vink J.,** Physics and Evolution of Supernova Remnant. Springer, 2020.
4. **Fuerst E., et al.,** A new non-thermal galactic radio source with a possible binary system. Nature, 314 (1985) 720–721.
5. **Reich W., et al.,** A radio continuum survey of the galactic plane at 11cm wavelenght. I. The area 357.4 < or = L < or = 76, - 1.5 < or = B < or = 1.5, Astronomy and Astrophysics Supplement Series. 58 (1984) 197–248.
6. **Stupar M., Parker Q.A.,** Catalogue of known Galactic SNRs uncovered in Halpha light, Monthly Notices of the RAS. 414 (2011) 2282–2296.
7. **Aschenbach B., et al.,** Observation of soft X-ray emission from the supernova remnant G 18.95-1.1, Astronomy and Astrophysics. 246 (1991) L32–L35.
8. **Fuerst E., Reich W., Aschenbach B.,** New radio and soft X-ray observations of the supernova remnant G 18.95-1.1, Astronomy and Astrophysics. 319 (1997) 655–663.
9. **Harrus I.M., et al.,** An X-Ray Study of the Supernova Remnant G18.95-1.1, Astrophysical Journal. 603 (2004) 152–158.
10. **Tüllmann R., et al.,** Searching for the Pulsar in G18.95-1.1: Discovery of an X-ray Point Source and Associated Synchrotron Nebula with Chandra, Astrophysical Journal. 720 (2010) 848–852.
11. **Bykov A.M., et al.,** Spatially resolved X-ray spectra of the Galactic SNR G18.95-1.1: SRG/eROSITA view, Astronomy and Astrophysics. 661 (2022) A19–28.
12. **Janka H.T.,** Neutron Star Kicks by the Gravitational Tug-boat Mechanism in Asymmetric Supernova Explosions: Progenitor and Explosion Dependence, Astrophysical Journal. 837 (2017) 84.
13. **Bisnovatyj-Kogan G.S., Blinnikov S.I.,** Sphericization of the Remnants of an Asymmetric Supernova Outburst in a Homogeneous Medium, Soviet Astronomy. 26 (1982) 530–537.
14. **Holland-Ashford T., et al.,** Comparing Neutron Star Kicks to Supernova Remnant Asymmetries, Astrophysical Journal. 844 (2017) 84–99.
15. **Sunyaev R., et al,** SRG X-ray orbital observatory. Its telescopes and first scientific results, Astronomy and Astrophysics. 656 (2021) A132.
16. **Fesen R.A., Kirshner R.P.,** Spectrophotometry of the supernova remnant IC 443, Astrophysical Journal. 242 (1980) 1023–1040.
17. **Green D.A.,** Constraints on the secular decrease in the flux density of CAS A at 13.5, 15.5 and 16.5 GHz, Monthly Notices of the RAS. 221 (1986) 473–482.
18. **Burton M.G., et al,** Shocked molecular hydrogen in the supernova remnant IC 443, Monthly Notices of the RAS. 231 (1988) 617–634.
19. **Troja E., Bocchino F., Reale F.,** XMM-Newton Observations of the Supernova Remnant IC 443. I. Soft X-Ray Emission from Shocked Interstellar Medium, Astrophysical Journal. 649 (2006) 258–267.

20. **Asaoka I., Aschenbach B.,** An X-ray study of IC443 and the discovery of a new supernova remnant by ROSAT, Astronomy and Astrophysics. 284 (1994) 573–582.
21. **Keohane J.W., et al.,** A Possible Site of Cosmic Ray Acceleration in the Supernova Remnant IC 443, Astrophysical Journal. 484 (1997) 350–359.
22. **Kawasaki M.T., et al.,** ASCA Observations of the Supernova Remnant IC 443: Thermal Structure and Detection of Overionized Plasma, Astrophysical Journal. 572 (2002) 897–905.
23. **Bocchino F., Bykov A.M.,** Hard X-ray emission from IC443: evidence for a shocked molecular clump?, Astronomy and Astrophysics. 362 (2000) L29–L32.
24. **Olbert C.M., et al.,** A Bow Shock Nebula around a Compact X-Ray Source in the Supernova Remnant IC 443, Astrophysical Journal. 554 (2001) L205–L208.
25. **Gaensler B.M., et al.,** The X-Ray Structure of the Pulsar Bow Shock G189.22+2.90 in the Supernova Remnant IC 443, Astrophysical Journal. 648 (2006) 1037–1042.
26. **Weisskopf M.C., et al.,** Chandra observations of neutron stars: an overview, Astrophysics and Space Science. 308 (2007) 151–160.
27. **Bocchino F., Bykov A.M.,** The plerion nebula in IC 443: The XMM-Newton view, Astronomy and Astrophysics. 376 (2001) 248–253.
28. **Bocchino F., Bykov A.M.,** XMM-Newton study of hard X-ray sources in IC 443, Astronomy and Astrophysics. 400 (2003) 203–211.
29. **Sturner S.J., Keohane J.W., Reimer O.,** Observation of non-thermal emission from the supernova remnant IC 443 with RXTE, Advances in Space Research. 33 (2004) 429–433.
30. **Bykov A.M., et al.,** Isolated X-Ray-Infrared Sources in the Region of Interaction of the Supernova Remnant IC 443 with a Molecular Cloud, Astrophysical Journal. 676 (2008) 1050–1063.
31. **Anderson M.C., Rudnick L.,** Sites of Relativistic Particle Acceleration in Supernova Remnant Cassiopeia A, Astrophysical Journal. 456 (1996) 234.
32. **Kassim N.E., et al.,** Evidence for Thermal Absorption inside Cassiopeia A, Astrophysical Journal. 455 (1995) L59.
33. **O'Sullivan C., Green D.A.,** Constraints on the secular decrease in the flux density of CAS A at 13.5, 15.5 and 16.5 GHz, Monthly Notices of the RAS. 303 (1999) 575–578.
34. **Fesen R.A., et al.,** Ejecta Knot Flickering, Mass Ablation, and Fragmentation in Cassiopeia A, Astrophysical Journal. 736 (2011) 109.
35. **Koo B.C., et al.,** A Deep Near-infrared [Fe II] + [Si I] Emission Line Image of the Supernova Remnant Cassiopeia A, Astrophysical Journal. 866 (2018)139.
36. **Vogt F.P.A., et al.,** Probing Interstellar Dust with Infrared Echoes from the Cas A Supernova, Astrophysical Journal. 750 (2012) 155.
37. **Gotthelf E.V., et al.,** Chandra Detection of the Forward and Reverse Shocks in Cassiopeia A, Astrophysical Journal. 552 (2001) L39–L43.
38. **Sato T., et al.,** X-Ray Measurements of the Particle Acceleration Properties at Inward Shocks in Cassiopeia A, Astrophysical Journal. 853 (2018) 46.
39. **Buote D.A., Tsai J.C.,** Quantifying the Morphologies and Dynamical Evolution of Galaxy Clusters. I. The Method, Astrophysical Journal. 452 (1995) 522.
40. **Buote D.A., Tsai J.C.,** Quantifying the Morphologies and Dynamical Evolution of Galaxy Clusters. II. Application to a Sample of ROSAT Clusters, Astrophysical Journal. 458 (1996) 27.
41. **Lopez L.A., et al.,** Typing Supernova Remnants Using X-Ray Line Emission Morphologies, Astrophysical Journal. 706 (2009) L106–L109.
42. **Lopez L.A., Fesen R.A.,** The Morphologies and Kinematics of Supernova Remnants, Space Science Reviews. 214 (2018) 44.
43. **Holland-Ashford T., Lopez L.A., Auchettl K.,** Asymmetries of Heavy Elements in the Young Supernova Remnant Cassiopeia A, Astrophysical Journal. 889 (2020) 144–152.
44. **Picquenot A., et al.,** Three-dimensional morphological asymmetries in the ejecta of Cassiopeia A using a component separation method in X-rays, Astronomy and Astrophysics. 646 (2021) A82–A94.

## THE AUTHORS

**UVAROV Yury A.**
uvy@mail.ru
ORCID: 0000-0002-4962-5437

**BYKOV Andrei M.**
byk@astro.ioffe.ru
ORCID: 0000-0003-0037-2288

*Received 14.10.2022. Approved after reviewing 22.11.2022. Accepted 22.11.2022.*

© Peter the Great St. Petersburg Polytechnic University, 2023

Conference materials
UDC 524.354.6
DOI: https://doi.org/10.18721/JPM.161.256

# Middle-aged gamma-ray pulsar J0554+3107 in X-rays

A.S. Tanashkin✉, A.V. Karpova, Yu.A. Shibanov, A.Yu. Potekhin, D.A. Zyuzin

Ioffe Institute, St. Petersburg, Russia

✉ artyom.tanashkin@gmail.com

**Abstract.** We present some results of X-ray observations of the middle-aged γ-ray pulsar J0554+3107 with *XMM-Newton*. For the first time, we detected X-ray pulsations with the J0554+3107 spin period from the presumed X-ray counterpart, thus confirming its pulsar nature. The pulsed fraction in the 0.2–2 keV band is 25±6%. The pulsar spectrum can be fitted by the model consisting of thermal and non-thermal components. To describe the former, we created and applied hydrogen atmosphere models for neutron stars with dipole magnetic fields. In addition, an absorption feature at 0.34 keV is required to fit the spectrum. The spectral analysis implies that J0554+3107 has the effective temperature of ~47±2 eV. The analysis also indicates that J0554+3107 may be a rather heavy neutron star with the mass of ~1.9±0.2 $M_{\odot}$. Implementing the relation between the interstellar absorption and the distance in the pulsar direction, we obtained the distance to the pulsar to be about 2 kpc. Implications of the results for cooling scenarios of neutron stars and the equation of state of supra-dense matter in their cores are briefly discussed.

**Keywords:** neutron stars, pulsars, neutron star cooling, supra-dense matter

**Citation:** Tanashkin A.S., Karpova A.V., Shibanov Yu.A., Potekhin A.Yu., Zyuzin D.A., Middle-aged gamma-ray pulsar J0554+3107 in X-rays, St. Petersburg State Polytechnical University Journal. Physics and Mathematics. 16 (1.2) (2023) 370–376. DOI: https://doi.org/10.18721/JPM.161.256

This is an open access article under the CC BY-NC 4.0 license (https://creativecommons.org/licenses/by-nc/4.0/)

Материалы конференции
УДК 524.354.6
DOI: https://doi.org/10.18721/JPM.161.256

# Рентгеновские наблюдения гамма-пульсара J0554+3107

А.С. Танашкин✉, А.В. Карпова, Ю.А. Шибанов, А.Ю. Потехин, Д.А. Зюзин

Физико-технический институт им. А.Ф. Иоффе РАН, Санкт-Петербург, Россия

✉ artyom.tanashkin@gmail.com

**Аннотация.** В работе представлены результаты рентгеновских наблюдений гамма-пульсара среднего возраста J3107+0554, выполненных при помощи обсерватории *XMM-Newton*. Нами впервые обнаружены пульсации излучения с периодом J0554+3107 от предполагаемого рентгеновского двойника, что подтверждает его пульсарную природу. Доля пульсирующей составляющей в диапазоне 0,2–2 кэВ равна 25±6%. Спектр пульсара хорошо аппроксимируется моделью, включающей в себя тепловую и нетепловую компоненты. Для описания первой нами были рассчитаны сетки моделей водородных атмосфер нейтронных звезд с сильными магнитными полями. Кроме того, для корректного описания наблюдаемого спектра требуется включение в модель линии поглощения на энергии 0,34 кэВ. По результатам спектрального анализа эффективная температура J0554+3107 составляет ~47±2 эВ. Из него также следует, что масса нейтронной звезды равна ~1,9±0.2 $M_{\odot}$. Используя соотношение между межзвездным поглощением и расстоянием в направлении на пульсар, мы получили оценку на расстояние до него около 2 кпк. В свете полученных результатов кратко обсуждается проблема остывания нейтронных звезд и уравнений состояния сверхплотного вещества в их ядрах.

© Tanashkin A.S., Karpova A.V., Shibanov Yu.A., Potekhin A.Yu., Zyuzin D.A., 2023. Published by Peter the Great St. Petersburg Polytechnic University.

**Ключевые слова:** нейтронные звезды, пульсары, остывание нейтронных звезд, сверхплотное вещество

Ссылка при цитировании: Танашкин А.С. и др. Рентгеновские наблюдения гамма-пульсара J0554+3107 // Научно-технические ведомости СПбГПУ. Физико-математические науки. 2023. Т. 16. № 1.2. С. 370–376. DOI: https://doi.org/10.18721/JPM.161.256

Статья открытого доступа, распространяемая по лицензии CC BY-NC 4.0 (https://creativecommons.org/licenses/by-nc/4.0/)

## Introduction

The middle-aged pulsar J0554+3107 (hereafter J0554) discovered in $\gamma$-rays with the *Fermi* observatory has the spin period $P$ = 465 ms, the characteristic age $t_c$ = 52 kyr, the spin-down luminosity $\dot{E} = 5.6 \cdot 10^{34}$ erg s$^{-1}$ and the characteristic magnetic field $B_c = 8.2 \cdot 10^{12}$ G [1]. In the radio, only upper limits on the pulsar flux density were set [1–3]. J0554 is likely associated with the shell-type supernova remnant (SNR) G179.0+2.6 [1]. The distance to the latter is not well constrained: different relations between the radio surface brightness and the SNR diameter (so-called $\Sigma$–$d$ relations) result in about 3–6 kpc [4–6]. On the other hand, studies of the interstellar extinction along the line of sight to the remnant suggest a smaller distance of ~0.9 kpc, according to the model of Zhao et al. [7]. These estimates roughly agree with the 'pseudo--distance' to J0554 of 1.9 kpc, which is derived from the empirical correlation between the distance and the pulsar $\gamma$-ray flux [8] and is uncertain within a factor of 2–3. The likely pulsar X-ray counterpart was found in the *Swift* data [9]. This is a soft source whose spectrum can be described by the black body or hydrogen neutron star (NS) atmosphere models with effective temperatures of ~50–100 eV. Since only 17 counts were detected, an accurate spectral analysis is impossible. Detection of pulsations with the J0554 spin period from the presumed X-ray counterpart would directly confirm its pulsar nature. Here we briefly report some results of our deeper X-ray observations of J0554 with *XMM-Newton*.

## *XMM-Newton* data and imaging

The observations were performed on 2021 October 7 (ObsID 0883760101, PI A. Karpova) with a total exposure of about 45 ks. Two MOS detectors were operated in the Full Frame mode while the Large Window mode was chosen for the pn camera. The data were reprocessed using the *XMM-Newton* Science Analysis Software v.19.1.0 package. We filtered out the periods of flaring background activity that resulted in exposures of 44.3, 44.5 and 38.8 ks for MOS1, MOS2 and pn detectors. The exposure-corrected combined (MOS+pn) image of the J0554 field, constructed utilizing the 'images' script [10], is shown in Fig. 1. A bright X-ray point-like source is clearly seen at the $\gamma$-ray position of J0554 [1], thus confirming the *Swift* X-ray counterpart at much higher significance. We derived its coordinates R.A. = $05^h54^m05.^s067(10)$ and Dec. = $+31°07'41.''40(13)$ with the EDETECT_CHAIN tool (errors in parentheses are 1$\sigma$ pure statistical uncertainties). We found no evidence of extended emission (e.g. the pulsar wind nebula) around J0554. Due to the wide wings of the *XMM-Newton* point spread function (PSF) it can be blurred with the pulsar. However, the brightness radial profile of the source is in agreement with the PSF shape and, therefore, no extended emission is resolved.

## Timing

To search for pulsations with the pulsar spin period, we used the pn data whose time resolution was ~48 ms. We extracted events in the 0.2–2 keV band from the 22″-radius circle and applied the barycentric correction using the DE405 ephemeris. The selected aperture contains 1026 source counts. We then ran $Z^2_n$-test [11] in the 2.1501–2.1509 Hz range, where the number of harmonics $n$ was varied from 1 to 5. It revealed pulsations at the frequency of 2.150474376(14) Hz. The contribution from harmonics higher than 2 is not statistically significant. The maximum $Z^2_2$ of 42.7 corresponds to the detection confidence level of ~4.7 $\sigma$.

© Танашкин А.С., Карпова А.В., Шибанов Ю.А., Потехин А.Ю., Зюзин Д.А., 2023. Издатель: Санкт-Петербургский политехнический университет Петра Великого.

The obtained frequency is slightly higher than the value of 2.150474376(14) Hz predicted from the *Fermi* timing solution [1] at the epoch of the *XMM-Newton* observations. About 8 years passed between the $\gamma$-ray and X-ray observations so the discrepancy could arise from the pulsar timing noise or glitches. The detected pulsations firmly establish the pulsar nature of the X-ray source.

The J0554 folded light curve in the 0.2–2 keV band is shown in Fig. 2. We calculated the pulsed fraction (PF) using the method from [12]. The resulting background corrected value is 25±6%. Above 2 keV there are only $\lesssim$2% of the total number of source counts, which precludes any definite conclusions about pulsations in the hard band.

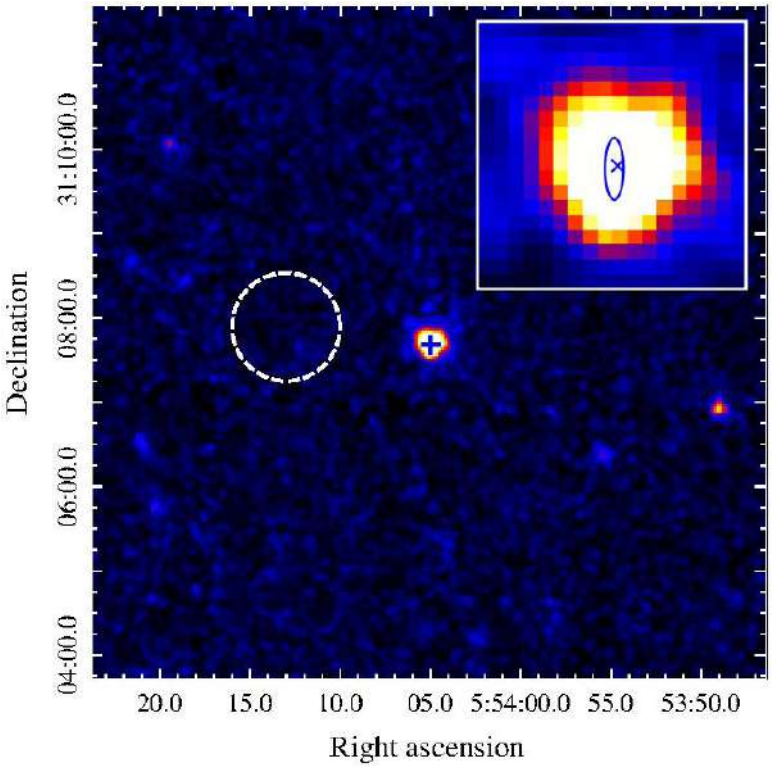


Fig. 1. 8′×8′ *XMM-Newton* exposure-corrected combined image of the J0554 field in the 0.2–2 keV band. The pulsar $\gamma$-ray position [1] is marked by the cross. The dashed circle encloses the region used for the background. The inset shows the zoomed-in 0.6′×0.6′ region around the J0554 X-ray counterpart, whose position is shown by the 'X' symbol. The ellipse shows 1$\sigma$ position uncertainties of the pulsar in $\gamma$-rays, which is a combination of the *Fermi* position uncertainties and the *XMM-Newton* absolute pointing accuracy of 1.″2 (see https://xmmweb.esac.esa.int/docs/documents/CAL-TN-0018.pdf)

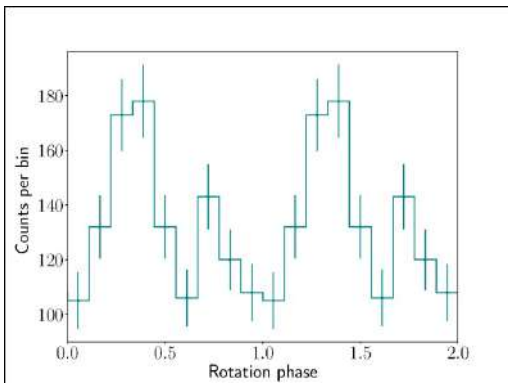


Fig. 2. J0554 pulse profile in the 0.2–2 keV band

## Spectral analysis

We extracted the J0554 spectra from the MOS and pn data using 19″-radius aperture. For the background, we used the circle region shown in Fig. 1. We fitted the spectra simultaneously in the 0.2–10 keV band utilizing the X-Ray Spectral Fitting Package (XSPEC) v.12.11.1 [13]. To account for the interstellar medium (ISM) absorption, we applied the TBABS model with the WILM abundances [14].

As a preliminary step, all spectra were grouped to ensure at least 25 counts per energy bin to use the $\chi^2$-statistics. At first, we tried the POWERLAW (PL) model which can represent the non-thermal emission of the NS magnetosphere origin. Though it resulted in a statistically acceptable fit, it requires the photon index $\Gamma \approx 7$, while the typical values for pulsars are $\lesssim 3$ [15]. Such an unrealistically high $\Gamma$ may indicate the presence of a thermal component. To fit the latter, we created an NS hydrogen atmosphere model NSMDINTB, which was computed using an advanced version of the code described in [16]. This model takes into account the effects of incomplete ionization of plasma, atomic center-of-mass motion across the magnetic field and polarization of vacuum (see, e.g., [17] for review and references). The phase-averaged spectra of radiation from the entire surface, as seen by a distant observer, were computed assuming a dipole magnetic field and taking into account the effects of General Relativity, using the same approach as described in Appendix A of [18]. The magnetic field at the pole $B_p$ was set to $10^{13}$ G, which is close to the J0554 spin-down field. The following model parameters are variable: the NS mass $M$ and the radius $R$, the angle $\alpha$ between the rotation and the magnetic axes, the angle $\zeta$ between the rotation axis and the line of sight, the distance $D$, and the redshifted effective temperature $T^{\infty} = T / (1+z_g)$, where $z_g$ is the gravitational redshift. This model describes the spectra poorly with $\chi^2$/d.o.f. $= 62/39$ (d.o.f. ≡ degrees of freedom). The fit becomes statistically acceptable ($\chi^2$/d.o.f. $= 41/36$) if we add the absorption Gaussian line at ~0.35 keV. For the latter, we used the model GABS. However, the residuals show slight flux excess over the model in the hard band ($\gtrsim$2 keV). Thus, we included the PL component in the model and obtained $\chi^2$/d.o.f. $= 39/34$.

Table 1

**Best-fitting parameters for the (NSMDINTB+PL)×GABS model**

| $N_H$, $10^{21}$ cm$^{-2}$ | $D$, kpc | $M$, $M_\odot$ | $R$, km | $T^{\infty}$, eV | $\Gamma$ | log $L_X$, erg s$^{-1}$ | $E_0$, eV | EW, eV |
|---|---|---|---|---|---|---|---|---|
| $1.62^{+0.08}_{-0.06}$ | $2.0^{+0.2}_{-0.4}$ | $1.9^{+0.2}_{-0.2}$ | $13.5^{+1.2}_{-1.7}$ | $47^{+2}_{-2}$ | $2.2^{+0.6}_{-0.4}$ | $30.21^{+0.15}_{-0.30}$ | $340^{+40}_{-40}$ | $150^{+120}_{-40}$ |

Notes: Errors correspond to 68 % credible intervals. $L_X$ is the non-thermal luminosity in the 2–10 keV band, $E_0$ and EW are the center and equivalent width of the Gaussian absorption line. Angles $\alpha$ and $\zeta$ are poorly constrained and thus not presented. $W$/d.o.f. $= 228/211$ and $\chi^2$/d.o.f. $= 43/34$.

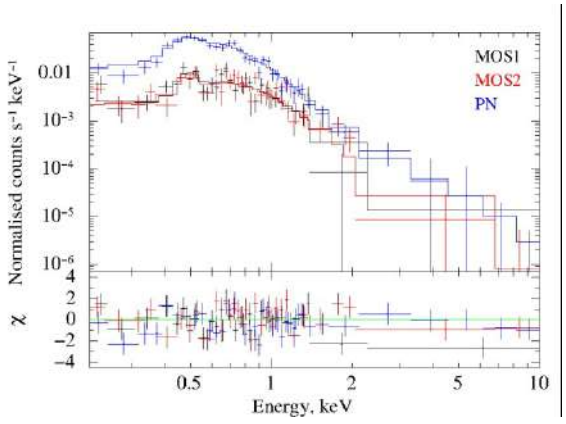


Fig. 3. J0554 spectra, best-fitting model and residuals

Since the number of counts from the pulsar is not large, to robustly constrain model parameters we rebinned the spectra to have at least 1 count per energy bin and applied the *W*-statistics [19], which is suitable for the Poisson data. We then performed the Bayesian parameter estimation using the python package EMCEE [20], an implementation of affine-invariant ensemble sampler for Markov chain Monte Carlo (MCMC) [21]. Such a method makes it possible to include some prior information in the fitting procedure. We used the 3D extinction map [22] to estimate the distance to the pulsar. The selective reddening $E(B-V)$ was transformed to the equivalent hydrogen column density $N_{\rm H}$, which is responsible for the ISM absorption in X-rays, using the relation from [23]. Finally, we constrained the photon index $\Gamma$ between 0.5 and 3, as appropriate for pulsars [15].

The best-fitting parameters, corresponding to the maximum values of probability density, are presented in Table 1 while the J0554 spectrum with the best-fitting model is shown in Fig. 3. We checked the fit quality by calculating the $\chi^2$-statistics value for the spectra grouped to ensure at least 25 counts per bin. Inclusion of the priors in the fitting procedure led to some deviation of this value from the preliminary one.

## Discussion and conclusions

Using *XMM-Newton* we have confirmed the *Swift* X-ray counterpart candidate of J0554 and surely established its pulsar nature by revealing the X-ray pulsations with the pulsar spin period. We found that the J0554 time-integrated spectrum in the 0.2–10 keV band is well fitted by the model containing the thermal and non-thermal components and the absorption line. The thermal component can be produced by the hydrogen magnetized atmosphere of an NS with the mass of $1.9\pm0.2$ $M_\odot$ and the redshifted effective temperature of $47\pm2$ eV. Using the extinction–distance relation, we estimated the distance to J0554 to be in the range of 1.6–2.2 kpc, which is compatible with the 'pseudo-distance' of 1.9 kpc. The pulsar non-thermal X-ray luminosity in the 2–10 keV range $L_X = (1.6\pm0.7)\cdot10^{30}$ erg s$^{-1}$. The corresponding efficiency of generation of X-ray photons from the pulsar rotation energy losses is $\eta_X = L_X/\dot{E} \sim 10^{-5}$, where $\dot{E} = 1.4\cdot10^{35}$ erg s$^{-1}$ is calculated for the best-fitting NS mass and radius. These values are in agreement with the empirical relations $L_X(t_c)$ and $\eta_X(t_c)$ obtained for other pulsars [24].

As for the absorption feature at 0.34 keV, its origin is unclear. If it is produced near the NS surface, its unredshifted energy should be ~ 0.4 – 0.5 keV. If this is a cyclotron absorption line produced by electrons, the corresponding magnetic field is $\sim4\cdot10^{10}$ G, which is much lower than the characteristic field $B_c = 8.2\cdot10^{12}$ G. This implies that such a line should be created in NS radiation belts [25]. On the other hand, if it is the proton cyclotron line, the magnetic field is $\gtrsim7\cdot10^{13}$ G, an order of magnitude higher than $B_c$ and the $B$ values used in our atmosphere modeling. Such a proton cyclotron line might indicate the presence of strong non-dipolar field components (cf. [26, 27]; also see [28] and references therein). The absorption feature can be also produced by atomic transitions in the NS atmosphere composed of heavier chemical elements (e.g., see Fig. 16 in [29] for neon). One explanation that is more possible is an instrumental artifact. The feature is not prominent in the MOS spectra likely due to the much lower count statistics. We could check the presence of the line in pn spectra of other sources in the J0554 field, but, unfortunately, they are not bright enough for such analysis.

The best-fitting atmosphere model provides the PF in the 0.2–2 keV band up to ~20%, which is compatible with the observed value of $25\pm6$%. Because of the low count statistics, we cannot make definite conclusions about pulsations in the hard band where the PL component dominates in the pulsar spectrum. Though the PL contribution to the pulsar flux in the 0.2–2 keV band is less than that of the thermal component, the former can increase the model predicted PF and lead to apparent asymmetry of the observed pulse profile.

The derived bolometric thermal luminosity of J0554 $L_{\rm bol} \approx 1.8\cdot10^{32}$ erg s$^{-1}$ appears to be significantly lower than the values predicted for a 52 kyr old NS by the so-called 'minimal cooling' scenario [30,31], which assumes that the heat losses mainly occur via neutrino generated by modified Urca processes in the NS core. On the other hand, it is much higher than the values predicted for this age by the enhanced cooling scenario, which involves direct Urca processes operating when the NS mass $M$ exceeds some threshold value $M_{\rm DU}$ (see, e.g., [17] for review and references). The derived $L_{\rm bol}$ can be brought to an agreement with the enhanced cooling scenario, if the true age of J0554 is much smaller than $t_c$, which is not unusual for the pulsars (see [32]). An alternative is that $M$ only slightly exceeds the threshold, so that the direct Urca processes are working only in a small central part of the NS core. Another possibility is that $M$ is only slightly smaller than $M_{\rm DU}$. In this case, the modified

Urca processes are strongly enhanced, so that the NS cools faster, as recently shown by Shternin et al. [33]. The value of $M_{DU}$ is currently uncertain: it depends on the composition and equation of state of the NS matter and strongly varies from one theoretical model to another. For example, the modern model BSk24 predicts $M_{DU} \approx 1.6\ M_{\odot}$ [34], while another widely used model APR gives $M_{DU} \approx 2.0\ M_{\odot}$ [35]. Both values lie within the $2\sigma$ uncertainty interval of the $M$ value given in Table 1.

Deeper X-ray observations are required to better constrain the shape of the pulse profile, to perform the phase-resolved spectral analysis and thereby to establish the nature of the low energy spectral feature and the pulsar geometry.

**Acknowledgements**

We are grateful to V.F. Suleimanov for providing calculations of specific spectral fluxes from hydrogen atmospheres of NSs with strong magnetic fields. DAZ thanks Pirinem School of Theoretical Physics for hospitality.

## REFERENCES

1. **Pletsch H. J., et al.**, Einstein@Home Discovery of Four Young Gamma-Ray Pulsars in Fermi LAT Data, Astrophys. J. 779 L11 (2013).

2. **Tyul'bashev S.A., Kitaeva M.A., Tyulbasheva G.E.**, Search for Periodic Emission from Five Gamma-Ray Pulsars at the Frequency of 111 MHz, Astronomy Reports 65 (2021) 819–25.

3. **Griesmeier J.M., Smith D.A., Theureau G., Johnson T.J., Kerr M., Bondonneau L., Cognard I., Serylak M.**, Follow-up of 27 radio-quiet gamma-ray pulsars at 110-190 MHz using the international LOFAR station FR606, Astron. Astrophys. 654 A43 (2021).

4. **Case G.L., Bhattacharya D.**, A New -D Relation and Its Application to the Galactic Supernova Remnant Distribution, Astrophys. J. 504 (1998) 761–72.

5. **Guseinov O.H., Ankay A., Sezer A., Tagieva S.O.**, The relation between the surface brightness and the diameter for galactic supernova remnants, Astronomical and Astrophysical Transactions 22 273 (2003).

6. **Pavlovic M.Z., Dobardzic A., Vukotic B., Urosevic D.**, Updated Radio Sigma-D Relation for Galactic Supernova Remnants, Serbian Astronomical Journal 189 (2014) 25–40.

7. **Zhao H., Jiang B., Li J., Chen B., Yu B., Wang Y.**, A Systematic Study of the Dust of Galactic Supernova Remnants. I. The Distance and the Extinction, Astrophys. J. 891 137 (2020).

8. **Saz Parkinson P. M. et al.**, Eight γ-ray Pulsars Discovered in Blind Frequency Searches of Fermi LAT Data, Astrophys. J. 725 (2010) 571–84.

9. **Zyuzin D.A., Karpova A.V., Shibanov Y.A.**, X-ray counterpart candidates for six new -ray pulsars, Mon. Not. R. Astron. Soc. 476 (2018) 2177–85.

10. **Willatt R., Ehle M.**, Guide for use of the images script. URL: https://www.cosmos.esa.int/documents/332006/641121/README.pdf. Accessed Oct. 9, 2022.

11. **Buccheri R., et al.**, Search for pulsed gamma-ray emission from radio pulsars in the COS-B data, Astron. Astrophys. 128 (1983) 245–51.

12. **Swanepoel J.W.H., de Beer C.F., Loots H.**, Estimation of the Strength of a Periodic Signal from Photon Arrival Times, Astrophys. J. 467 261 (1996).

13. **Arnaud K.A.**, Astronomical Data Analysis Software and Systems V, In: Astronomical Society of the Pacific Conference Series vol. 101 ed. Jacoby G. H. and Barnes J. (1996) 17.

14. **Wilms J., Allen A., McCray R.**, On the Absorption of X-Rays in the Interstellar Medium, Astrophys. J. 542 (2000) 914–24.

15. **Kargaltsev O., Pavlov G.G.**, 40 Years of Pulsars: Millisecond Pulsars, Magnetars and More, In: American Institute of Physics Conference Series vol. 983 ed. Bassa C., Wang Z., Cumming A. and Kaspi V.M. (2008) 171–85.

16. **Suleimanov V., Potekhin A.Y. and Werner K.**, Models of magnetized neutron star atmospheres: thin atmospheres and partially ionized hydrogen atmospheres with vacuum polarization, Astron. Astrophys. 500 (2009) 891–9.

17. **Potekhin A.Y., De Luca A., Pons J.A.**, Neutron StarsThermal Emitters, Space Sci. Rev. 191 (2015) 171–206.

18. **Zyuzin D.A., Karpova A.V., Shibanov Y.A., Potekhin A.Y., Suleimanov V.F.**, Middle aged -ray pulsar J1957+5033 in X-rays: pulsations, thermal emission, and nebula, Mon. Not. R. Astron. Soc. 501 (2021) 4998–5011.

19. **Wachter K., Leach R., Kellogg E.**, Parameter estimation in X-ray astronomy using maximum likelihood, Astrophys. J. 230 (1979) 274–87.

20. **Foreman-Mackey D., Hogg D.W., Lang D., Goodman J.**, emcee: The MCMC Hammer, Publ. Astron. Soc. Pacific 125 306 (2013).

21. **Goodman J., Weare J.**, Ensemble samplers with affine invariance, Communications in Applied Mathematics and Computational Science 5 (2010) 65–80.

22. **Green G.M., Schlafly E., Zucker C., Speagle J.S., Finkbeiner D.**, A 3D Dust Map Based on Gaia, Pan-STARRS 1, and 2MASS, Astrophys. J. 887 93 (2019).

23. **Foight D.R., Güver T., Özel F. and Slane P.O.**, Probing X-Ray Absorption and Optical Extinction in the Interstellar Medium Using Chandra Observations of Supernova Remnants, Astrophys. J. 826 66 (2016).

24. **Zharikov S., Mignani R.P.**, On the PSR B1133+16 optical counterpart, Mon. Not. R. Astron. Soc. 435 (2013) 2227–33.

25. **Luo Q., Melrose D.**, Pulsar radiation belts and transient radio emission, Mon. Not. R. Astron. Soc. 378 (2007) 1481–90.

26. **Bilous A.V., et al.**, A NICER View of PSR J0030+0451: Evidence for a Global-scale Multipolar Magnetic Field, Astrophys. J. 887 L23 (2019).

27. **Lockhart W., Gralla S. E., Özel F., Psaltis D.**, X-ray light curves from realistic polar cap models: inclined pulsar magnetospheres and multipole fields, Mon. Not. R. Astron. Soc. 490 (2019) 1774–83.

28. **Mereghetti S., Pons J.A., Melatos A.**, Magnetars: Properties, Origin and Evolution, Space Sci. Rev. 191 (2015) 315–38.

29. **Mori K., Ho W.C.G.**, Modelling mid-Z element atmospheres for strongly magnetized neutron stars, Mon. Not. R. Astron. Soc. 377 (2007) 905–19.

30. **Gusakov M.E., Kaminker A.D., Yakovlev D.G., Gnedin O.Y.**, Enhanced cooling of neutron stars via Cooper-pairing neutrino emission, Astron. Astrophys. 423 (2004) 1063–71.

31. **Page D., Lattimer J.M., Prakash M., Steiner A.W.**, Minimal Cooling of Neutron Stars: A New Paradigm, Astrophys. J. Suppl. Ser. 155 (2004) 623–50.

32. **Potekhin A.Y., Zyuzin D.A., Yakovlev D.G., Beznogov M.V., Shibanov Y.A.**, Thermal luminosities of cooling neutron stars, Mon. Not. R. Astron. Soc. 496 (2020) 5052–71.

33. **Shternin P.S., Baldo M., Haensel P.**, In-medium enhancement of the modified Urca neutrino reaction rates, Physics Letters B 786 (2018) 28–34.

34. **Pearson J.M., Chamel N., Potekhin A.Y., Fantina A.F., Ducoin C., Dutta A.K., Goriely S.**, Unified equations of state for cold non-accreting neutron stars with Brussels-Montreal functionals - I. Role of symmetry energy, Mon. Not. R. Astron. Soc. 481 (2018) 2994–3026.

35. **Akmal A., Pandharipande V.R., Ravenhall D.G.**, Equation of state of nucleon matter and neutron star structure, Phys. Rev. C 58 (1998) 1804–28.

## THE AUTHORS

**TANASHKIN Artyom S.**
artyom.tanashkin@gmail.com
ORCID: 0000-0002-3340-0938

**POTEKHIN Alexander Y.**
palex@astro.ioffe.ru
ORCID: 0000-0001-9955-4684

**KARPOVA Anna V.**
karpann@astro.ioffe.ru
ORCID: 0000-0002-4211-5856

**ZYUZIN Dmitry A.**
da.zyuzin@gmail.com
ORCID: 0000-0002-8521-9233

**SHIBANOV Yury A.**
shib@astro.ioffe.ru

*Received 27.10.2022. Approved after reviewing 10.11.2022. Accepted 11.11.2022.*

© Peter the Great St. Petersburg Polytechnic University, 2023

Conference materials
UDC 537.867
DOI: https://doi.org/10.18721/JPM.161.257

# Mathematical modeling of effects of plasma and gravitational inhomogeneities in the structure of electromagnetic signals

D.S. Lukyantsev[1]✉, N.T. Afanasiev[1], A.B. Tanaev[1]

[1] Irkutsk State University, Irkutsk, Russia

✉ cmeofs1997@mail.ru

**Abstract.** The three-dimensional algorithm of calculation of the trajectory characteristics of electromagnetic signals in a random-inhomogeneous space plasma placed in the gravity field of difficult configuration has been suggested. The influence of the gravity on the signal propagation has been taken into account by the use of efficient index of refraction. The inhomogeneities of plasma have been defined by the model of spatial correlation function of fluctuations of index of refraction. Results of mathematical modeling of lensing of electromagnetic signals in the gravity field from several space objects have been provided. It is shown that, a significantly different spatial structure of ray field can occur in picture plane of the observer depending on the properties of the gravitational field and parameters of random plasma inhomogeneities.

**Keywords:** mathematical modeling, lensing effect, geometrical optics approximation, gravitational field

**Funding:** Scientific work is supported by Irkutsk State University (project 091−22−307), the Russian Federation Ministry of Science and High Education (project FZZE−2020−0024). The work was performed at the UNU "Astrophysical Complex of MSU−ISU" (agreement 075-15-2021-675).

**Citation:** Lukyantsev D.S., Afanasiev N.T., Tanaev A.B., Mathematical modeling of effects of plasma and gravitational inhomogeneities in the structure of electromagnetic signals, St. Petersburg State Polytechnical University Journal. Physics and Mathematics. 16 (1.2) (2023) 377−382. DOI: https://doi.org/10.18721/JPM.161.257

This is an open access article under the CC BY-NC 4.0 license (https://creativecommons.org/licenses/by-nc/4.0/)

Материалы конференции
УДК 537.867
DOI: https://doi.org/10.18721/JPM.161.257

# Математическое моделирование эффектов плазменных и гравитационных неоднородностей в структуре электромагнитных сигналов

Д.С. Лукьянцев[1]✉, Н.Т. Афанасьев[1], А.Б. Танаев[1]

[1] Иркутский государственный университет, г. Иркутск, Россия

✉ cmeofs1997@mail.ru

**Аннотация**. Предложен трехмерный алгоритм расчета траекторных характеристик электромагнитных сигналов в случайно-неоднородной космической плазме, помещенной в гравитационное поле сложной конфигурации. Влияние гравитации на распространение сигнала учтено путем введения эффективного показателя преломления вакуума. Неоднородности плазмы заданы моделью пространственной корреляционной функции флуктуаций показателя преломления. Приведены результаты математического моделирования линзирования электромагнитных сигналов в гравитационном поле от нескольких космических объектов. Показано, что в зависимости от свойств гравитационного поля и параметров случайных неоднородностей плазмы может возникать существенно разная пространственная структура лучевого поля в картинной плоскости наблюдателя.

© Lukyantsev D.S., Afanasiev N.T., Tanaev A.B., 2023. Published by Peter the Great St. Petersburg Polytechnic University.

**Ключевые слова**: математическое моделирование, линзирующий эффект, приближение геометрической оптики, гравитационное поле

**Финансирование**: Данная работа была выполнена при поддержке Иркутского Государственного Университета (проект № 307–22–091), Министерства Науки и Высшего Образования Российской Федерации (проект FZZE–2020–0024). Научная работа выполнена в рамках УНУ "Астрофизический комплекс МГУ–ИГУ" (соглашение № 675–2021–15–075).

**Ссылка при цитировании:** Лукьянцев Д.С., Афанасьев Н.Т., Танаев А.Б. Математическое моделирование эффектов плазменных и гравитационных неоднородностей в структуре электромагнитных сигналов // Научно-технические ведомости СПбГПУ. Физико-математические науки. 2023. Т. 16. № 1.2. С. 377–382. DOI: https://doi.org/10.18721/JPM.161.257

Статья открытого доступа, распространяемая по лицензии CC BY-NC 4.0 (https://creativecommons.org/licenses/by-nc/4.0/)

## Introduction

As known [1], when interpreting data of measurements of electromagnetic signals of remote space sources, it is necessary to take into account the influence of inhomogeneities of medium, through which they have propagated. In particular, the plasma of the Solar system and interstellar space can significantly distort spatial-time structure of received signals. The electromagnetic signals propagating near massive space objects are also affected by the gravity fields of these objects at interstellar distances. Analysis of the collective influence of the plasma and gravity disturbance on the propagation of the signals of the space sources is important.

In complex gravity field created by system of stars, analytical calculation of the characteristics of received signals distorted by interstellar space is the great problem [2, 3]. Meanwhile, as follows from the theory of relativity [4, 5], the propagation of electromagnetic waves in the gravity field can be considered as task of waves in the Euclidian space. At the same time it is necessary to take into account, that gravity field changes in the certain way index of refraction of vacuum. Since the typical scales of such index of refraction are usually large is comparison to the wavelength the direction of wave propagation can be calculated with high accuracy in the ray approximation [6]. When the interstellar distances are considered then intersection of rays is possible leading to the effect of gravity lensing [7, 8]. One of these examples can be lensing of the radiation of the quasar on galaxies located on the propagation path. Random inhomogeneities of space plasma hide the effects of the gravity field and impose restrictions on wavelength of electromagnetic waves for observations of the gravity focusing. Thus effect of lensing of the gravity field in the electromagnetic waves propagation in random-inhomogeneous media can be realized for certain range of the electromagnetic scale.

## Mathematical tool

To analyze the effect of influence of plasma and gravitational inhomogeneities on the trajectory characteristics of signals from remote space sources, a stochastic system of ray differential equations in the spherical case was used:

$$\frac{dR}{d\varphi} = R\cot\beta;\ \ \frac{d\delta}{d\varphi} = \tan\alpha;$$

$$\frac{d\beta}{d\varphi} = \left(1+\sin^2\beta\tan^2\alpha\right)\left(\frac{1}{\tilde{n}}\frac{\partial\tilde{n}}{\partial\varphi}\cot\beta - \frac{R}{\tilde{n}}\frac{\partial\tilde{n}}{\partial R} - 1\right); \tag{1}$$

$$\frac{d\alpha}{d\varphi} = \left(1+\cot^2\beta\cos^2\alpha\right)\left(\frac{1}{\tilde{n}}\frac{\partial\tilde{n}}{\partial\delta} - \frac{1}{\tilde{n}}\frac{\partial\tilde{n}}{\partial\varphi}\tan\alpha\right);$$

© Лукьянцев Д.С., Афанасьев Н.Т., Танаев А.Б., 2023. Издатель: Санкт-Петербургский политехнический университет Петра Великого.

where $R$, φ, δ are spherical coordinates of the ray, α, β are the angles of the refraction accordingly at the vertical and horizontal planes.  is the efficient index of refraction of random-inhomogeneous medium in presence of the gravity field. Let us present as a sum:

$$\tilde{n} = n_0 + \tilde{n}_1, \tag{2}$$

where  characterizes index of refraction of vacuum in conditions of influence of deterministic gravity field,  describes the random inhomogeneities of space plasma. In the case of a single gravitational object, the function  is represented as [9]:

$$n_0 = 1 + R_g / R, \tag{3}$$

where $R_g$ is gravity radius of the space objects being researched.

The following model for  is used at the research of propagation electromagnetic waves in the presence of several gravity objects:

$$\begin{gathered} n_0 = 1 + R_g / R + \\ + \sum_{i=1}^{N} A_i \exp\left[ -b1_i \left(\varphi - \varphi 0_i\right)^2 - b2_i \left(\delta - \delta 0_i\right)^2 - b3_i \left(R - R0_i\right)^2 \right], \end{gathered} \tag{4}$$

where $N$ is quantity of the additional objects, $A_i$, $\varphi 0_i$, $\delta 0_i$, $R0_i$, $b1_i$, $b2_i$, $b3_i$ are intensity, coordinates of localization and scales of inhomogeneity of index of refraction, accordingly, appearing due to influence of gravity object $i$.

To estimate collective influence of gravity field and random inhomogeneities of plasma on the propagation of the electromagnetic waves system (1) was solved by the perturbation method at . As a result the generating system of the equations was obtained (system (1) at ). It describes trajectories of rays in the gravity field in absence of the influence of random plasma inhomogeneities.

Also system of equations for calculating of fluctuations of trajectory characteristics of electromagnetic waves was obtained. The second statistic moments of ray trajectories were modeled by this system. In particular, we have the following system of equations to calculating of deviation of refraction of δ in case of the Gaussian correlation function of plasma inhomogeneities:

$$\begin{gathered} \frac{d\sigma_\delta^2}{d\varphi} = \frac{\mu}{4}\sqrt{\frac{\pi}{Q}}\left( \frac{DP^2}{Q} + 16\left( D - \frac{K}{Q} \right)\left(\varphi J_1 - J_2\right) \right); \\ \frac{dJ_1}{d\varphi} = P^2; \ \frac{dJ_2}{d\varphi} = \varphi P^2. \end{gathered} \tag{5}$$

where $P(\varphi) = \left( \frac{1}{\cos^2 \alpha_0} + \cot^2 \beta_0 \right)$; $D = \frac{\tan^2 \alpha_0}{a_\varphi^2} + \frac{1}{a_\delta^2}$; $K = \left( \frac{1}{a_\varphi^2} - \frac{1}{a_\delta^2} \right)^2 \tan^2 \alpha_0$; $Q = \frac{1}{a_\varphi^2} + \frac{1}{a_\delta^2}\tan^2 \alpha_0 + \frac{R_0^2}{a_R^2}\cot^2 \beta_0$,

μ, $a_\varphi$, $a_\delta$, $a_R$ are intensity and scales of random plasma inhomogeneities, respectively. Characteristics $\alpha_0$, $\beta_0$, $R_0$, $\delta_0$ are defined by numerical integration of system (1) at $\tilde{n}_1 = 0$.

One can estimate the influence of the random inhomogeneities of plasma on the gravity lensing solving obtained system of equations (5) together with generating system (system (1) at $\tilde{n}_1 = 0$).

**Results of mathematical modelling and their discussion**

The generating system was numerically solved at the various parameters of index of refraction (4). The results of the calculations of density of points of arrival of ray trajectories on fix distance $R = R_k$ are shown on the picture plane of the observer in coordinates (δ, φ). For example, in Figs. 1, 2, accordingly, the results of modeling of ray trajectories and density of rays in picture plane of the observer in presence of two gravity objects are shown. The localization of the objects relatively source is schematically shown in Fig. 3. Parameters of objects amounted: $R_g$=1 cul, $A_1$=0.5,

$R0_1$ = 10 cul, $\delta 0_1$ = 0 rad, $\varphi 0_1$ = 0.6 rad, scales $b1_1$ = 0.5, $b2_1$ = 0.5, $b3_1$ = 0.5(1/cul$^2$). Here cul is conventional unit of length. Initial states: $R(\varphi = 50$ = (0 cul, $\delta(\varphi = 0) = 0$. Angle α belonged to the range [—0.14; 0.14] rad with step 0.006 rad, angle β belonged to the range [—0.3; -0.21] rad and [0.21; 0.3] rad with step 0.004 rad. The calculated points of arrival or rays are provided in the picture plane (fig.2) for mentioned sectors of angles α, β around gravity objects. Also here the end angles φ are noticed, under which the ray arrives the distance $R_k$=50 cul. The lack of the values of φ from 0 till 2± rad occurs due to the impossibility of passing of rays through gravity objects. It is easy to see that the trajectory picture significantly distorts in gravity field of objects, and phenomenon of gravity focusing is possible. The closer an electromagnetic wave propagates near a gravitational object, the stronger the refraction effect. Also one can notice that the form of the trajectories of rays between two gravitational objects is non-monotone for some sector of the angles (Fig. 1). The results of the calculating of trajectories and density of distribution of the points of arrival of rays at picture plane in Euclidean space at $n_0$ = 1 are shown to estimate in Figs. 4, 5. In this situation the points of arrival of rays evenly distribute at the picture plane in researched sector of the angles α (0), β (0).

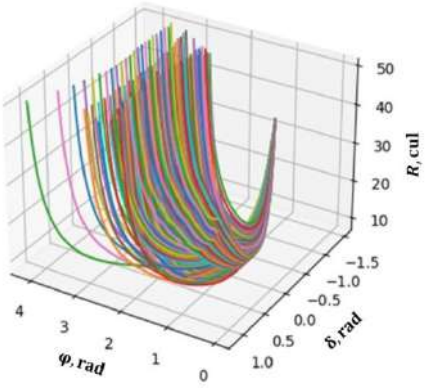


Fig. 1. Trajectories of propagation of electromagnetic waves in gravity field of two space objects

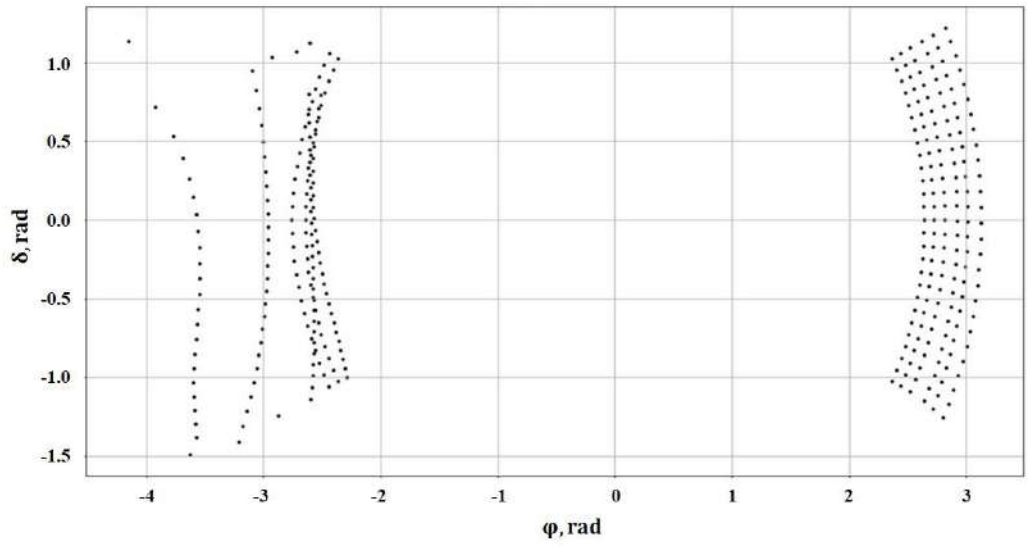


Fig. 2. The gravity lensing in the observer plane

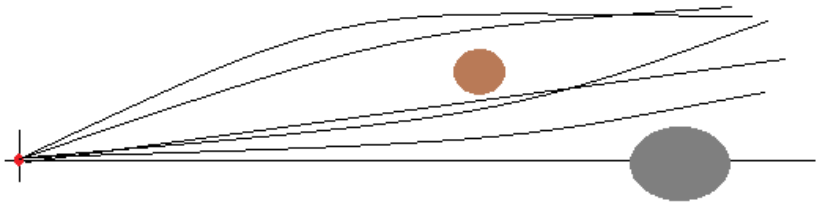

Fig. 3. Location of the source and gravity space objects. Side projection

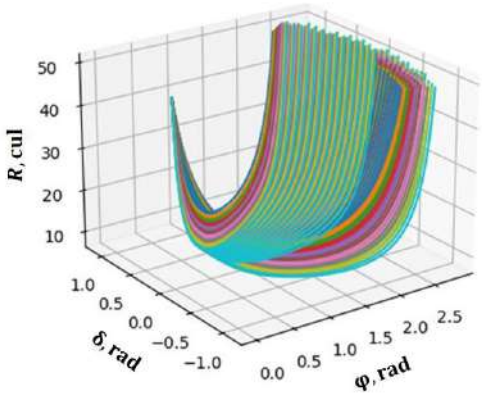


Fig. 4. The trajectories of electromagnetic waves in the absence of the gravity space object

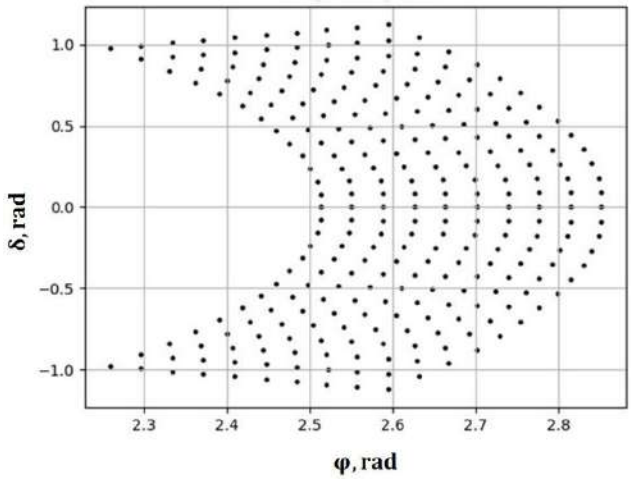


Fig. 5. Picture plane of the observer in the absence of the gravity space object

The results of the calculating of the fluctuations of the density of points of arrival of rays in picture plane are shown on fig.6. Here the calculated mean points of arrival of rays are shown for mentioned sectors of angles α, β in coordinates (δ, φ) for the same parameters of model (4) as on fig.2. Vertical lines demonstrate the standard deviations of obtained points of arrival in the picture plane triggered plasma random inhomogeneities. Parameters of plasma inhomogeneities amounted: $\mu = 10^{-6}$, $a_\varphi = 10^{-3}$, $a_\delta = 10^{-3}$, $a_R = 10^{-3}$ cul. One can notice that in the picture plane of the observer the statistical blurring of the gravity focusing appears. The smaller the path of propagation of electromagnetic radiation, the smaller the scatter of the point on the observer picture plane is observed.

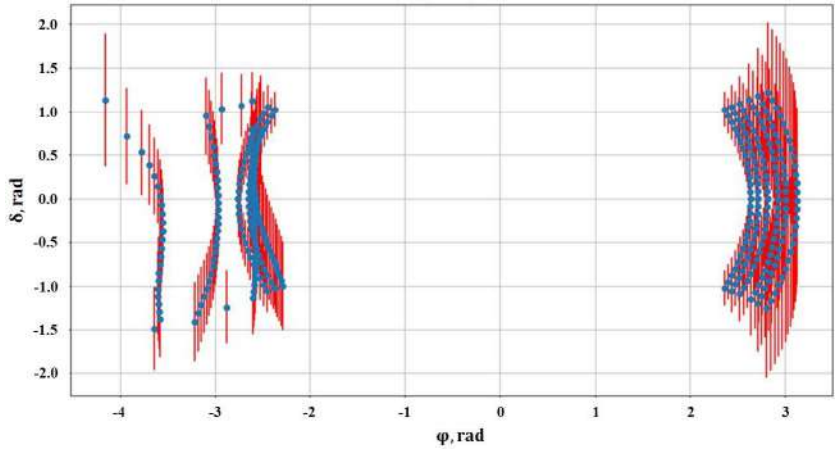


Fig. 6. Statistical blurring of gravity lensing in the observer plane

## Conclusion

Mathematical modeling of the trajectory characteristics of the electromagnetic signals in difficult gravity field of several space objects has been performed by created three-dimensional algorithm. The random-inhomogeneous plasma has been taken into account in the calculations of this algorithm. The conditions of the appearance of the effect of the gravity lensing in picture plane of the observer have been showed. Calculation of standard deviation values of side deviations of rays under the influence of random inhomogeneities of plasma has been completed. Example of statistical blurring of effect of gravity focusing of rays on several space objects due to the refraction scattering on inhomogeneities of space plasma have been provided.

## REFERENCES

1. **Verschuur G.L., Kellerman K.I.,** Galactic and extragalactic radioastronomy. Berlin: Springer, 1976.
2. **Fok V.A.,** Theory of spatial, time and gravity. Moscow: Science, 1969.
3. **Zeldovich Ya.B., Novikov I.D.,** Theory of gravity and evolution of stars. Moscow: Science, 1971.
4. **Volkov A.M., Izmestiev A.A., Skrockiy G.V.,** Journal of Experemental and Theoretical Physics (JETP), 59 (10) (1970) 1254.
5. **Plebanski I.,** Electromagnetic Waves in Gravitational Fields. Phys.Rev, 118 (5) (1960) 1396.
6. **Kravtsov Yu.A., Orlov Yu.I.,** Geometrical Optics of Inhomogeneous Medium. Berlin: Springer-Verlag, 1990.
7. **Blioh P.V., Minakov A.A.,** Gravity lenses. Kiev: Scientific thought, 1989.
8. **Zaharov A.F.,** Gravity lenses and micro-lenses. Moscow: Yanus-K, 1997.
9. **Yakovlev O.I.,** Space Radio Science. Boca Raton: CRC Press, 2002.

## THE AUTHORS

**LUKYANTSEV Dmitriy S.**
cmeofs1997@mail.ru
ORCID: 0000-0001-8649-4387

**TANAEV Andrey B.**
tanaev.ab@yandex.ru
ORCID: 0000–0002–9217–8185

**AFANASIEV Nikolay T.**
spacemaklay@gmail.com
ORCID: 0000-0002-7902-4448

*Received 13.10.2022. Approved after reviewing 08.11.2022. Accepted 08.11.2022.*

© Peter the Great St. Petersburg Polytechnic University, 2023

Conference materials
UDC 537.867
DOI: https://doi.org/10.18721/JPM.161.258

# Diagnostics of CME cavity using data of multiwave measurements of behind-the-limb solar radio bursts

S.O. Chudaev[1]✉, N.T. Afanasiev[2], D.S. Lukyantsev[2]

[1] Institute of Solar-Terrestrial Physics of Siberian Branch of RAS, Irkutsk, Russia;

[2] Irkutsk State University, Irkutsk, Russia.

✉ ch45st@gmail.com

**Abstract.** Mathematical modeling of the behind-the-limb radio bursts propagation characteristics at the second harmonic of the local plasma frequency of the solar corona was performed for analytical models of the electron density of the circumsolar plasma and CMEs. The features of the bursts trajectories are studied depending on the parameters of the CMEs and the initial coordinates of solar radio sources. The conditions for the strong effect of CME on radio bursts are determined. The possibility of determining the CME cavity's parameters from the data of multiwave measurements of the group delays of behind-the-limb radio bursts is shown.

**Keywords:** mathematical modeling, geometrical optics approximation, behind-limb source, near-Sun plasma

**Funding:** Scientific work has performed at support Irkutsk State University (project 091-22-307), Ministry of Science and High Education (project FZZE-2020-0024, agreement 075-15-2021-675).

**Citation:** Chudaev S.O., Afanasiev N.T., Lukyantsev D.S., Diagnostics of CME cavity using data of multiwave measurements of behind-the-limb solar radio bursts, St. Petersburg State Polytechnical University Journal. Physics and Mathematics. 16 (1.2) (2023) 383–388. DOI: https://doi.org/10.18721/JPM.161.258

This is an open access article under the CC BY-NC 4.0 license (https://creativecommons.org/licenses/by-nc/4.0/)

Материалы конференции
УДК 537.867
DOI: https://doi.org/10.18721/JPM.161.258

# Диагностика полости КВМ по данным многоволновых измерений залимбовых солнечных радиовсплесков

С.О. Чудаев[1]✉, Н.Т. Афанасьев[2], Д.С. Лукьянцев[2]

[1] Институт Солнечно-Земной Физики СО РАН, г. Иркутск, Россия;

[2] Иркутский государственный университет, г. Иркутск, Россия

✉ ch45st@gmail.com

**Аннотация.** Для аналитических моделей электронной концентрации околосолнечной плазмы и КВМ выполнено математическое моделирование характеристик распространения залимбовых радиовсплесков на второй гармонике локальной плазменной частоты короны. Изучены особенности траекторий всплесков в зависимости от параметров КВМ и начальных координат солнечных радиоисточников. Определены условия существенного воздействия КВМ на распространение радиовсплесков. Показана возможность определения параметров полости CME по данным многоволновых измерений групповых задержек залимбового всплеска.

**Ключевые слова:** математическое моделирование, приближение геометрической оптики, залимбовый источник, околосолнечная плазма

© Chudaev S.O., Afanasiev N.T., Lukyantsev D.S., 2023. Published by Peter the Great St. Petersburg Polytechnic University.

**Финансирование:** Данная работа была выполнена при поддержке Иркутского Государственного Университета (проект № 307–22–091), Министерства Науки и Высшего Образования (проект FZZE–2020–0024, соглашение № 075–15–2021–675).

**Ссылка при цитировании:** Чудаев С.О., Афанасьев Н.Т., Лукьянцев Д.С. Диагностика полости КВМ по данным многоволновых измерений залимбовых солнечных радиовсплесков // Научно-технические ведомости СПбГПУ. Физико-математические науки. 2023. Т. 16. № 1.2. С. 383–388. DOI: https://doi.org/10.18721/JPM.161.258

Статья открытого доступа, распространяемая по лицензии CC BY-NC 4.0 (https://creativecommons.org/licenses/by-nc/4.0/)

## Introduction

The mechanisms of generation and propagation of coronal mass ejections (CMEs) are of great interest. Passing through the interplanetary medium, these plasma disturbances can have a significant effect on the condition of near-earth space and can be the cause of the magnetosphere deformation, geomagnetic storms and other phenomena [1]. CME observations are usually carried out with white light coronagraphs installed on spacecraft board. In particular, the source of such data is the LASCO coronagraph that located on spacecraft named SOHO [2]. Coronographs provide two-dimensional CME's images, which allow direct determination of some characteristics of plasma ejections in the celestial plane, for example, the angular size of the ejection in latitude and the velocity of its elements. At the same time, the determination of the electron density in CME from two-dimensional images (that was obtained at one point) is possible only with the use of a priori assumptions about the structure of the plasma ejection [3]. In addition, white light coronagraphs are used in the STEREO space mission (SECCHI). These devices make it possible to study the processes of solar activity in a 3D image, which contributes to the determination of additional parameters, including the propagation direction of the plasma emission. However, these devices are located far enough from the solar photosphere. Great hopes are pinned on the next-generation satellites: SolO and Parker Solar Probe. These devices will be located near the solar photosphere, which will allow studying the processes of solar activity in more detail. The results of distant radio sounding by sources of natural origin are used to research the Sun atmosphere. One of the possibilities for studying CMEs can be observations of the Sun's own radio emission passing through the corona. There is a well-known type of solar radio emission called bursts. The bursts are generated at the second harmonic of the local plasma frequency of the solar corona. The radio bursts with the sources located on the opposite side of the Sun (in relation to the observer in the Earth's orbit) are of great interest. It is noted that ground based observations of the behind-the-limb (BTL) bursts were possible in the presence of CMEs from active regions near the solar limb in the frequency range of 25–44 MHz [4]. Physical interpretation this effect had been considered in [5, 6].

In this work, mathematical modeling of the coronal plasma formation's effect on the solar radio emission's propagation is carried out and the possibility of estimation of the CME cavity parameters by the characteristics of radio bursts from sources located on the reverse side of the Sun is shown.

## Numerical simulation of characteristics of radio emission propagation in a disturbed solar corona

Calculations of the CMEs' effect on the propagation of solar radio emission were carried out in the approximation of geometric optics [7]. It was assumed that the source of the radio burst is isotropic, point-like and radiates at the second harmonic of the local plasma frequency of the corona. A two-dimensional case was considered. A polar heliocentric coordinate system was used. The geometry of the case is shown in Fig. 1. The small circle (continuous line) represents the Sun's photosphere. The middle circle (dash-dotted line) is the area of background concentration near the solar photosphere, extending to level $R = R_m$ relative to the center of the Sun. The large circle (dashed line) is responsible for the Earth's orbit with a radius $R_z$ = 1AU. The dotted curve characterizes the trajectory connecting the source and receiver of the radio burst.

© Чудаев С.О., Афанасьев Н.Т., Лукьянцев Д.С., 2023. Издатель: Санкт-Петербургский политехнический университет Петра Великого.

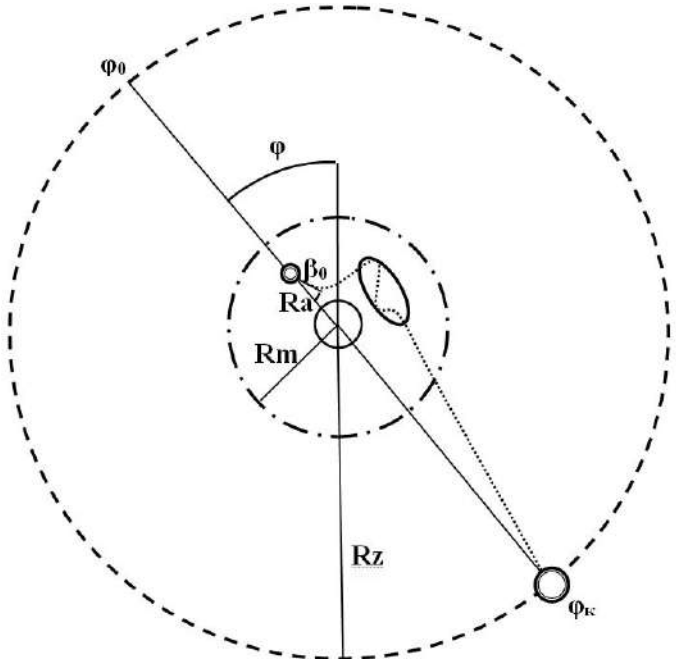


Fig. 1. Geometric diagram of radiation propagation from a BTL radio burst
$R_a$ is the radial coordinate of the position of the radio emission source relative to the center of the Sun, $\varphi_0$ is the angular coordinate of the radio burst source relative to the Sun, $\varphi_k$ is the receiver angular coordinate, $\beta$ is the radiation angle

To calculate the trajectory characteristics of radio emission in the disturbed solar corona, we used the system of ray equations [8]:

$$\frac{dR}{d\phi} = R\cot\beta; \quad \frac{d\beta}{d\phi} = \frac{1}{2\varepsilon}\left(\frac{\partial\varepsilon}{\partial\phi}\cot\beta - R\frac{\partial\varepsilon}{\partial R}\right) - 1, \tag{1}$$

where: $\varepsilon(R, \varphi) = \varepsilon_0(R) + \varepsilon_1(R, \varphi)$ is dielectric constant of the medium, $\varepsilon_0$, $\varepsilon_1$ characterize the regular condition and disturbed condition of the corona, $\varphi$ is independent variable (angle relative to the center of the coordinate system associated with the Sun), $\beta(\varphi)$ is beam refraction angle, $R(\varphi)$ is the current radial coordinate of the beam. We used the following equation a model of the dielectric constant of the regular corona [9]:

$$\varepsilon_0 = 1 - \left(\frac{f_{pl}}{f}\right)^2 \left(\frac{R_m}{R}\right)^2, \tag{2}$$

where: $R_m = 5R_s$; $f_{pl}$ is plasma frequency at level $R_m$; $f$ is operating frequency. Coronal plasma formation was described using the function:

$$\varepsilon_1 = \mu \exp\left[-\left(\frac{\varphi - \varphi_l}{a}\right)^2 - \left(\frac{R - R_l}{b}\right)^2\right], \tag{3}$$

where $R_l$, $\varphi_l$ are radial and angular coordinates of the CME localization center, $a$, $b$ are radial and angular scales of CME, $\mu$ is parameter characterizing the electron concentration of plasma inside the CME cavity.

Based on system (1), numerical modeling of the CME effects on the solar radio bursts trajectory characteristics was carried out. The following initial conditions were set. It was assumed that the source of radio emission is at an altitude $R_a = 3\ R_s$, where $R_s \approx 7 \cdot 10^5$ km is the solar photosphere radius, $\varphi_0 = 0$ rad, $\beta_n = 2.07$ rad is the initial radiation angle. The radiation of BTL radio sources was considered in the frequency range of 25–44 MHz. CME parameters were: $a = 0.06\ R_s$, $b = 0.15$ rad, $\mu = 1$. The localization center of the coronal disturbance had coordinates $\varphi_l = 0.8$ rad, $R_l = 3\ R_s$. Fig. 2 shows the dependences of the refraction angles of radio emission on the angular variable, calculated using the system of Eqs. (1), for regular (Fig. 2,*a*) and disturbed (Fig. 2,*b*) conditions. It follows from the obtained graphs disturbance of depleted electron density appears in the solar corona, the overall propagation path of radio bursts also increases in the entire range of the considered operating frequencies. At the same time, non-monotonic sections appear in the dependences of the refraction angles. This unusual behavior of the curves is associated with the emerging possibility of leakage of decameter radio bursts at low frequencies over long distances.

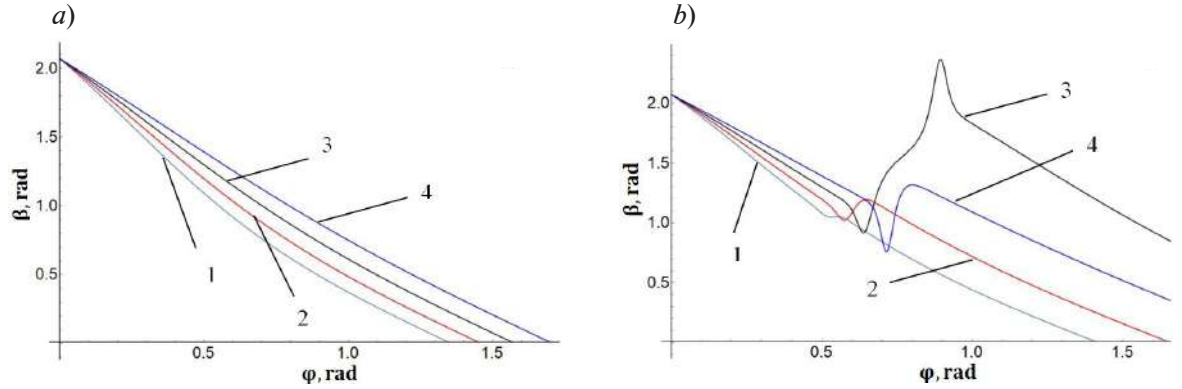


Fig. 2. Refraction angles of decameter radio bursts at different operating frequencies in the absence (*a*) and in the presence (*b*) of a cavity with a reduced electron concentration

Fig. 3 shows the results of calculations of the corresponding trajectories of radio bursts:

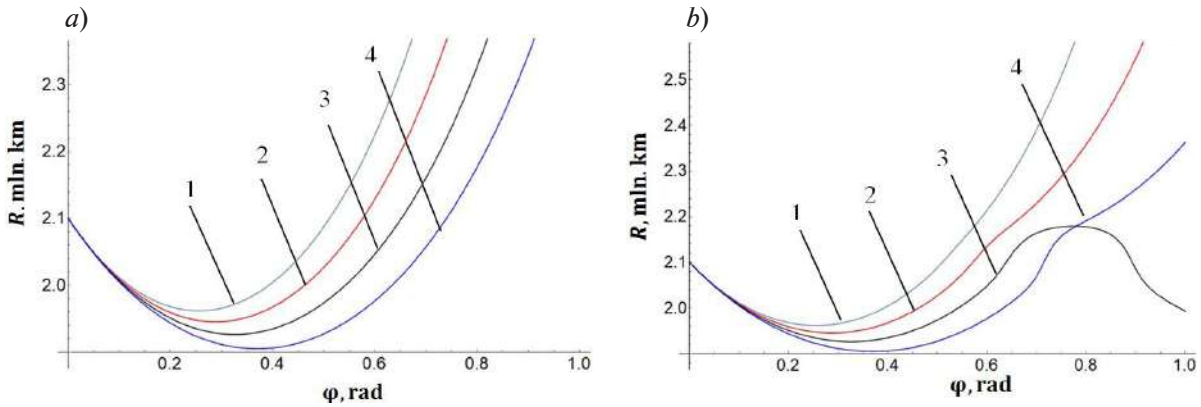


Fig. 3. Trajectories of radio bursts at different operating frequencies in the absence (*a*) and in the presence (*b*) of a cavity with depleted electron density

As follows from Fig. 3, the appearance of a CME-type coronal plasma formation contributes to a significant curvature of the radio burst trajectory and an increase in its propagation path. The trajectory of the radio burst, the angle of refraction of which manifested itself in an unusual way, becomes much longer due to the propagation of radio emission in the CME. In the presence of CME in the corona, along with the variation of the trajectory of the radio burst, its group delay changes. The additional equation was introduced into system (1) to calculate this delay:

$$\frac{d\tau}{d\phi} = \frac{R}{c\sqrt{\varepsilon}\sin\beta}, \tag{4}$$

where $c$ is speed of light.

Mathematical modeling of the radio bursts group delays at various frequencies was performed, based on Eqs. (1), (4), The coordinates of the radio burst source and the receiver relative to the Sun were: $\varphi_0 = 0$ rad, $\varphi_k = 1.995$ rad. The following dependence was considered as a model of the disturbed solar corona:

$$\varepsilon = 1 - \left(\frac{f_{pl}}{f}\right)^2 \left(\frac{R_m}{R}\right)^2 \left(1 - \mu \exp\left[-\left(\frac{\varphi - \varphi_l}{a}\right)^2 - \left(\frac{R - R_l}{b}\right)^2\right]\right), \tag{5}$$

where $f_{pl} = 14$ MHz, $R_m = 5\ R_s$, $a = 0.05\ R_s$, $b = 0.4$ rad, $\varphi_l = 0.7$ rad, $R_l = 3\ R_s$.

The ranging was carried out at the observation point of the ray trajectories for different transmission frequencies in the process of numerically calculating the frequency dependence of the radio bursts' group delay in the disturbed corona. Fig. 4 shows the results of calculations of the difference between the group delays of radio bursts at different frequencies and the delay at a frequency $f = 25$ MHz.

It is easy to see that at low frequencies (26–30 MHz), when refraction is most significant,

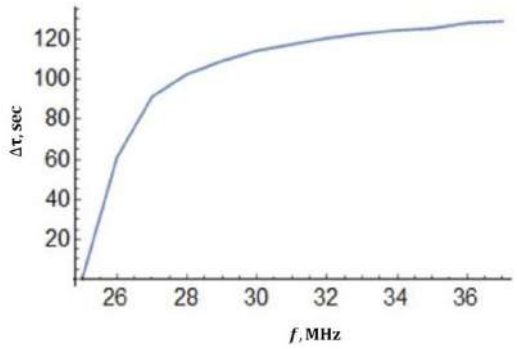


Fig. 4. Difference in the group delays of radio bursts in a disturbed corona at different frequencies

there is a strong difference in the group delays of radio bursts at different frequencies. At high frequencies (30–36 MHz) this dependence becomes slower and reaches the saturation level. The calculated group delay difference can be used to reconstruct the CME parameters from the measured relative delays of radio bursts at different frequencies along the path between the emitting source and the observer. It is possible to equalize the calculated and measured dependences on the frequency of the radio bursts' group delays using the regular corona model and information on the CME's spatial parameters from the data of optical observations, by fitting the parameter μ. This will determine the contrast parameter of the CME cavity.

## Conclusion

The mathematical modeling of the characteristics of the BTL solar radio bursts propagation through the solar corona was carried out. The conditions for the significant effect of coronal plasma formations on the trajectories of radio bursts are determined. The possibility of reliable ground-based observations of the radio emission beyond the limb in the presence of CME is shown. The possibility of determining the parameters of the CME cavity from the data of multi-wave measurements of the solar radio bursts' group delays is shown. The developed apparatus for mathematical modeling can be used to interpret the experimental data of the CME BTL transmission from spacecraft. It is also applicable in the analysis of observational data of planetary radar signals and radio emission from discrete space sources passing through the heliosphere.

## REFERENCES

1. **Zeleny L.M., Veselovsky I.S**., Plasma Heliogeophysics. Moscow: Fizmatlit, 2008, p 672.
2. **Aschwanden M.J.,** Physics of the Solar Corona. An Introduction with Problems and Solutions. London: Springer, 2005, p 908.
3. **Thernisien A.F.R., Howard R.A., Vourlidas A.,** Modeling of flux rope coronal mass ejections. The Astrophysical Journal, 2006, 652, p 763–773.
4. **Brazhenko A.I., Melnik V.N., Konovalenko A.A., Dorovskyy V.V., Frantsuzenko A.V., Rucker H.O., Panchenko M.I., Stanislavsky A.A.,** An unusual Solar burst decameter vawe-length. 1. Observations. Radio Physics and Radio Astronomy, 2012, V.17, №2, p 90–105.
5. **Brazhenko A.I., Melnik V.N., Konovalenko A.A., Dorovskyy V.V., Frantsuzenko A.V., Rucker H.O., Panchenko M.I., Stanislavsky A.A.**, An unusual Solar burst decameter vawe-length. 2. Interpretation. Radio Physics and Radio Astronomy, 2012, V.17, №3, p 199–206.
6. **Stanislavsky A.A.,** The role of radio wave propagation effects in the solar corona to interpret the behind-limb bursts Radioastronomy and Astrophysics, 2016, 21**,** p 3–13.
7. **Ginzburg V.L.,** Propagation of Electromagnetic Waves in Plasma. New-York: Gordon and Breach Pub., 1961, p 684.
8. **Kravtsov Yu.A., Orlov Yu.I.,** Geometrical Optics of Inhomogeneous Medium. Berlin: Springer-Verlag, 1990, p 312.
9. **Yakovlev O.I.**, Space Radio Science. Boca Raton: CRC Press, 2002, p 320.

## THE AUTHORS

**CHUDAEV Stanislav O.**
ch45st@gmail.com
ORCID: 0000-0002-9699-8420

**LUKYANTSEV Dmitriy S.**
cmeofs1997@mail.ru
ORCID: 0000-0001-8649-4387

**AFANASIEV Nikolay T.**
spacemaklay@gmail.com
ORCID: 0000-0002-7902-4448

*Received 16.10.2022. Approved after reviewing 22.11.2022. Accepted 22.11.2022.*

© Peter the Great St. Petersburg Polytechnic University, 2023

Conference materials
UDC 524.1
DOI: https://doi.org/10.18721/JPM.161.259

# Technique for reconstructing the parameters of EAS and primary cosmic rays based on experimental data of the Tunka-Grande scintillation array

A.L. Ivanova [1, 2]✉, TAIGA Collaboration

[1] Novosibirsk State University, Novosibirsk, Russia;

[2] Irkutsk State University, Irkutsk, Russia

✉ annaiv.86@mail.ru

**Abstract.** The Tunka-Grande scintillation array is a part of a single TAIGA experimental complex located in the Tunka Valley, 50 km from the Lake Baikal. It consists of 19 observation stations deployed on an area of about 0.5 km$^2$. The main aim of the Tunka-Grande facility is a detailed study of the energy spectrum and mass composition of cosmic rays in the energy range from 10 PeV to 1 EeV by detecting the charged and muon component of EAS. The article presents a method for reconstructing the parameters of the EAS and primary cosmic rays, the cosmic rays energy spectrum based on 4 measurement seasons, and compares the results obtained with the data of the Tunka-133 and TAIGA-HiSCORE Cherenkov arrays._

**Keywords:** Primary Cosmic Rays, EAS, scintillation detectors, Tunka-Grande scintillation array

**Funding:** The work was performed at the UNU "Astrophysical Complex of MSU-ISU" (agreement EB-075-15-2021-675). The work is supported by Russian Foundation for Basic Research (grant 19-32-60003), the Russian Science Foundation (grants 23-72-00016 (Section 3), 23-72-00054 (Sections 4, 5)), the Ministry of Science and Higher Education of the Russian Federation (projects FZZE-2020-0024, FZZE-2023-0004, FSUS-2020-0039, FSUS-2022-0015).

**Citation:** Ivanova A.L., Taiga collaboration, Technique for reconstructing the parameters of EAS and primary cosmic rays based on experimental data of the Tunka-Grande scintillation array.– St. Petersburg State Polytechnical University Journal. Physics and Mathematics. 16 (1.2) (2023) 389–394. DOI: https://doi.org/10.18721/JPM.161.259

This is an open access article under the CC BY-NC 4.0 license (https://creativecommons.org/licenses/by-nc/4.0/)

Материалы конференции
УДК 524.1
DOI: https://doi.org/10.18721/JPM.161.259

# Методика реконструкции параметров шал и первичного космического излучения по экспериментальным данным сцинтилляционной установки Tunka-Grande

А.Л. Иванова [1, 2]✉, Коллаборация TAIGA*

[1] Новосибирский национальный исследовательский государственный университет, г. Новосибирск, Россия;

[2] Иркутский государственный университет, Научно-исследовательский институт прикладной физики, г. Иркутск, Россия

✉ annaiv.86@mail.ru

**Аннотация.** Сцинтилляционная установка Tunka-Grande является частью единого экспериментального комплекса TAIGA, расположенного в Тункинской долине, в 50 км от оз. Байкал. Она состоит из 19 станций наблюдения, развернутых на площади около 0.5 км$^2$. Основной целью установки является детальное исследование энергетического спектра и массового состава космических лучей в диапазоне энергий от 10 ПэВ до 1 ЭэВ методом регистрации заряженного и мюонного компонента ШАЛ.

© Ivanova A.L., Taiga collaboration, 2023. Published by Peter the Great St. Petersburg Polytechnic University.

В докладе представлены методика реконструкции параметров, зарегистрированных ШАЛ и первичного космического излучения, энергетический спектр космических лучей, набранный за первые 4 сезона измерений, а также приводится сравнение полученных результатов с данными черенковских установок Тунка133- и TAIGA-HiSCORE.

**Ключевые слова:** первичные космические лучи, ШАЛ, сцинтилляционные детекторы, сцинтилляционная установка Tunka-Grande

**Финансирование:** Работа выполнена на УНУ «Астрофизический комплекс МГУ-ИГУ» (соглашение ЕВ-075-15-2021-675), поддержана Министерством науки и высшего образования Российской Федерации (проекты FZZE-2020-0024, FZZE-2023-0004, FSUS-2020-0039, FSUS-2022-0015), РНФ (гранты 23-72-00016 (раздел 3), 23-72-00054 (разделы 4, 5)), РФФИ (грант 19-32-60003).

**Ссылка при цитировании:** Иванова А.Л., Коллаборация TAIGA, Методика реконструкции параметров шал и первичного космического излучения по экспериментальным данным сцинтилляционной установки Tunka-Grande // Научно-технические ведомости СПбГПУ. Физико-математические науки. 2023. Т. 16. № 1.2. С. 389–394. DOI: https://doi.org/10.18721/JPM.161.259

Статья открытого доступа, распространяемая по лицензии CC BY-NC 4.0 (https://creativecommons.org/licenses/by-nc/4.0/)

## Introduction

The study of energy spectrum and mass composition of primary cosmic ray particles in the energy range of $10^{16}$–$10^{18}$ eV is of crucial importance for the understanding of the origin of cosmic rays and their propagation in the Galaxy. It seems the maximum energy of cosmic rays accelerated in SN remnants to be in this energy domain [1]. As it was pointed out in [2], in this energy range the transition from Galactic to extragalactic cosmic rays occur.

One of the cosmic ray studies methods in the energy range of $10^{16}$–$10^{18}$ eV is the detection of charged particles from Extensive Air Showers (EAS). It is based on the property of primary particles to generate a cascade of secondary particles in the Earth's atmosphere. To realization (implementation) of this method, scintillation detectors or water Cherenkov detectors of charged particles are usually used.

## Tunka-Grande scintillation array

The cosmic ray's studies by detecting of the EAS charged and muon component began in the Tunka Valley in 2015, when the Tunka-Grande scintillation array was put into operation.

The Tunka-Grande scintillation array contains 19 scintillation stations located on the area of the Cherenkov Tunka-133 array in a circle with a radius of ~ 400 m. The total area of the Tunka-Grande is about 0.5 sq.km.

Each scintillation station consists of surface and underground detector. The first detects all EAS charged particles at the level of array and consists of 12 counters united in 2 parts, 6 counters in each. The second, located under a layer of soil ~1.5 m thick and designed to detect muon component of EAS, consist of 8 counters, united into 4 pairs. The surface detector total area is about 8 $m^2$, the underground detector total area is about 5 $m^2$. A detailed description of the Tunka-Grande array is presented in [3, 4]. The energy and time resolution of the scintillators and description of the employed electronics are provided in [5, 6].

## Data processing and reconstructing EAS parameters

During the four seasons from 2017 to 2021, there were 691 days of Tunka-Grande operation. The array trigger condition was a coincidence of any three surface detectors within 5 μs. During this period, about 3 409 000 triggering events were detected on the Tunka-Grande area over 8900 h of operation. The scintillation array also operated using triggers of the Tunka-133 Cherenkov array [7]. There were 850 h of joint operations and about 250 000 events were selected.

The first step of reconstruction from the primary data is extraction of pulse amplitude $A$, front delay $t$, and pulse area $Q$. The measured values of $Q$ are used to determine a particle density in detectors and a shower core position.

© Иванова А.Л., ТАЙГА, 2023. Издатель: Санкт-Петербургский политехнический университет Петра Великого.

The particles density in surface and underground detectors of each station is defined by the formulas:

$$\rho_e = \frac{1}{S_e} \cdot \sum_{i=1}^{2} \frac{Q_i}{Q_{MPV_i}}, \ \rho_\mu = \frac{1}{S_\mu} \cdot \sum_{i=1}^{4} \frac{Q_i}{Q_{MPV_i}}, \quad (1)$$

where $i$ is the number of the surface detector part or number of a counter pair of the underground detector, $Q_i$ is the pulse area, $Q_{MPV_i}$ is the most probable value of the pulse area corresponding to the one particle level, $S_i$ is the total area of the counters of the surface detector, $S_\mu$ is the total area of the counters of the underground detector.

The shower arrival direction parametrized by the shower axis's zenith and azimuth angles is determined by fitting the measured pulse front delay using a curved shower front formula, which is obtained in a KASCADE-Grande experiment [8]:

$$T_i - T_{th} = a \cdot \left(1 + \frac{R_i}{30}\right)^b, \quad (2)$$

where $T_{th}$ is the theoretical delay time for a flat shower front, $R_i$ is the perpendicular distance from the shower axis in meters. The values of the variable parameters $a$ and $b$ were obtained by analyzing artificial showers generated by the CORSIKA program [9]. The zenith and azimuthal angles are determined using the triangle method by the trigger times of 3 surface detectors with highest detected particle density and optimal geometry.

To reconstruct the lateral distribution of charged particles, the LDF from the EAS MSU experiment [10, 11] is used. This function takes into consideration experimental data on the distribution of particles over the distance from the EAS core position, obtained with the EAS MSU array [12]. The lateral distribution of muons is described using the Greisen function [11].

The shower core coordinates, number of muons and charged particles, and slope of the LDF are calculated in minimizing the functional using independent variables.

An effective method for estimating the energy of primary particles for an array of detectors spaced over longer distances is based on a measure of the density of charged particles at distance form EAS core close to distance between nearby measure stations. Since the typical distance between the Tunka-Grande observation stations is about 200 m as a measure of energy we use the charged particles density at a core distance of 200 meters $-\rho_{200}(\theta)$. The parameter $\rho_{200}(\theta)$ is rescaled relative to the measured zenith angle as:

$$\rho_{200}(0) = \rho_{200}(\theta) \cdot \exp\left(\frac{x_0}{\lambda} \cdot (\sec\theta - 1)\right), \quad (3)$$

where $x_0 = 960$ g/sm$^2$ is the atmospheric depth from sea level for the Tunka Valley, $\lambda = 260$ g/sm$^2$ is the average value of absorption path length obtained from experimental data.

The value of $\rho_{200}(0)$ relative to the energy can be rescaled as:

$$E_0 = 10^b \cdot (\rho_{200}(0))^a, \quad (4)$$

where $a = 0.84 \pm 0.01$, $b = 15.99 \pm 0.01$. Correlation $\rho_{200}(0)$ with the primary energy is determined using the experimental results of Tunka-133 [7] and TAIGA-HiSCORE [3] Cherenkov arrays (Fig. 1, *a*, *b*).

### Comparison of the Tunka-Grande and Cherenkov facilities experimental data

The accuracy of the reconstructed shower parameters can be estimated using analysis of joint events with Tunka-133 and TAIGA-HiSCORE Cherenkov facilities (Fig. 2, *a*, *b*).

The search for joint events was performed within the time range of [–10 μs; +10 μs] in showers, detected in a circle with $R < 350$ m and the zenith angles range from 0 to 35 degrees.

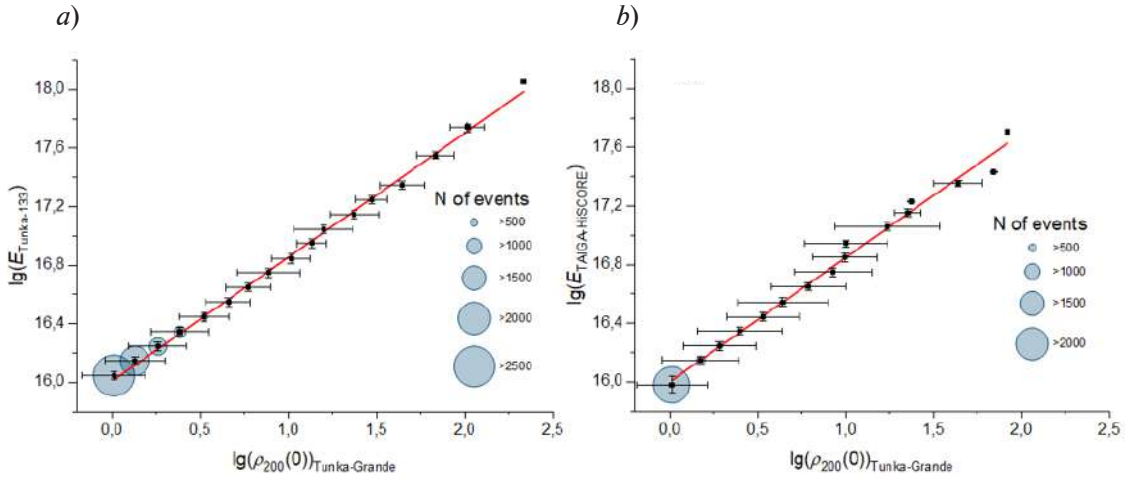


Fig. 1. Correlation $\rho_{200}(0)$ with the primary energy from the Tunka-133 (*a*) and TAIGA-HiSCORE (*b*) experimental data

The mean value of angle between EAS arrival directions reconstructed from Tunka-Grande and TAIGA-HiSCORE experimental data is about 2.5 degrees. The median value is 1.65 degrees, the most probably value of angle is 1.15 degrees (Fig. 2,*a*). The angle resolution of the Tunka-Grande array can be obtained from the distribution of the angle $\psi$ between reconstructed by Tunka-Grande and TAIGA-HiSCORE EAS arrival directions, being defined by 68% of the events having deviations less than it does. It is 2.25 degrees.

A detailed analysis of the Tunka-Grande and Cherenkov facilities joint events is presented in [13].

## The energy spectrum

To plot the spectrum events with zenith angle $\theta \leq 35$ degrees and core position in a circle with radius $R < 350$ m were selected. The number of recorded events with energies above 10 PeV was about 260 000. Approximately 2100 events from them had energies above 100 PeV. The best quality of recovery of the EAS parameters and the primary energy is achieved for events inside the geometrical area of the array. The volume of statistics accumulated over 4 seasons allowed us to limit events inside the Tunka-Grande facility and exclude events whose core position was on the border and outside the array The threshold energy of 100% registration efficiency for chosen area and zenith angles is 10 PeV.

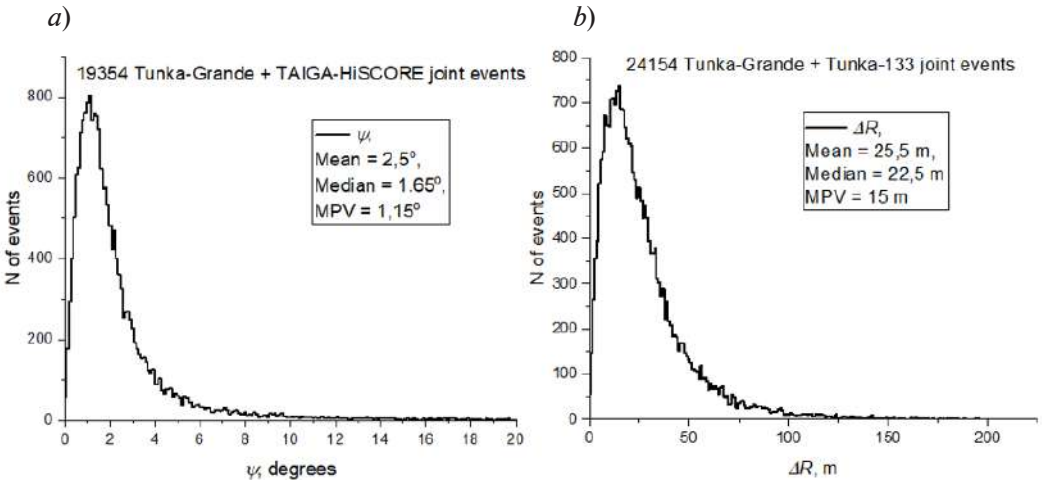


Fig. 2. The accuracy of the EAS arrival direction reconstruction by the Tunka-Grande array in comparison with data of TAIGA-HiSCORE array (*a*) and the accuracy of the EAS core position reconstruction by the Tunka-Grande array in comparison with data of Tunka-133 facility (*b*)

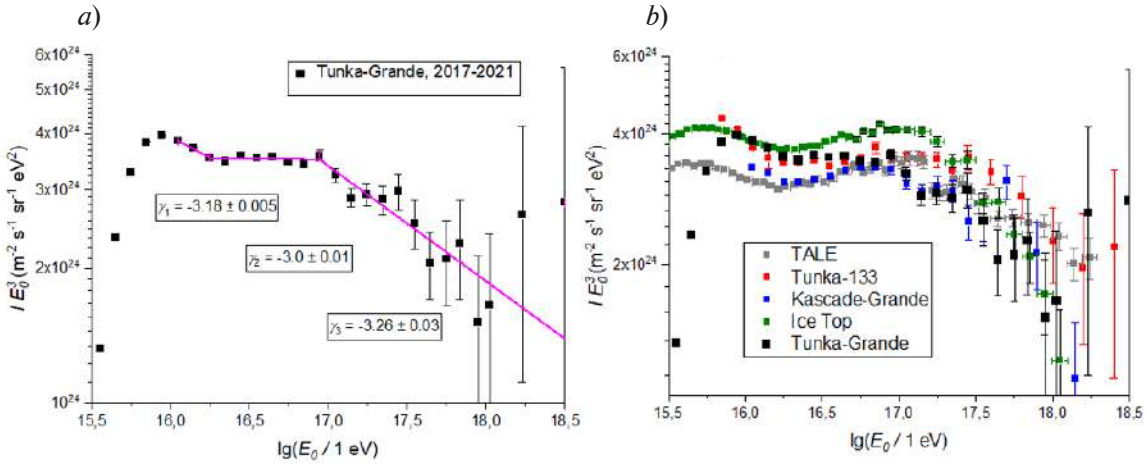


Fig. 3. Differential primary cosmic-ray energy spectrum with a fit of a doubly broken power law (*a*) and comparison of energy spectrum obtained at Tunka-Grande with some other experimental results (TALE [14], Tunka-133 [7], Kascade-Grande [15], Ice Top [16]) (*b*)

The energy spectrum beyond the first "knee" looks rather complicated. One can see that the spectrum can be fitted by power laws with three different power law indexes (Fig. 3,*a*). The value of power law index below 2 PeV is $\gamma_1 = -3.18 \pm 0.005$ and above this energy is $\gamma_2 = -3.0 \pm 0.01$. The spectrum becomes much steeper with $\gamma_3 = -3.26 \pm 0.03$ above 100 PeV (the second "knee").

Fig. 3,*b* compiles the energy spectra obtained by different experiments. Tunka-Grande all-particle energy spectrum are compatible with the findings of most of the other experiments.

## Conclusion

Applying above reconstruction method to the Tunka-Grande data, we obtained the all-particle energy spectrum based on 4 measurement seasons. The energy spectrum demonstrates the good agreement with data of large terrestrial facilities. Comparison of the Tunka-Grande array data with the data of the Cherenkov facilities confirmed the sufficient quality of the reconstructed events for their further use in joint analysis for the gamma-hadron separation.

## Acknowledgments

We are grateful to the Irkutsk Supercomputer Center of SB RAS for providing computational resources of the HPC-cluster "Akademik V.M. Matrosov" that made it possible to carry out our tasks.

## REFERENCES

1. **Ptuskin V.S., Zirakashvili V.N.**, Limits on diffusive shock acceleration in supernova remnants in the presence of cosmic-ray streaming instability and wave dissipation, Astron. Astroph. 403 (2003) 1–10.
2. **Aloisio R. et al.**, A dip in the UHECR spectrum and the transition from galactic to extragalactic cosmic rays, Astropart. Phys. 27 (2007) 76–91.
3. **Budnev N.M. et al.**, TAIGA - an advanced hybrid detector complex for astroparticle physics, cosmic ray physics and gamma-ray astronomy, PoS ICRC2021. 395 (2021) 731.
4. **Ivanova A.L. et al.**, Tunka-Grande scintillation array: resent results, J.Phys.Conf.Ser. 1690 (2020) 012014.
5. **Likiy O.I. et al.**, Investigating the Characteristics of Scintillation Detectorsfor the NEVOD-EAS Experiment, Instrum. Exp. Tech. 59 (6) (2016) 781–788.
6. **Monkhoev R.D. et al**, The Tunka-Grande experiment, JINST. 12 (06) (2017) C06019.
7. **Budnev N.M. et al.**, The primary cosmic-ray energy spectrum measured with the Tunka-133 array, Astroparticle Physics. 117 (2020) 102406.
8. **Glasstetter R. et al.**, Shower Size Reconstruction at KASCADE-Grande, 29th International Cosmic Ray Conference Pune. 6 (2005) 293-296.

9. **Heck D. and Pierog T**. https://web.iap.kit.edu/corsika/usersguide/usersguide.pdf.
10. **Fomin Yu.A. et al.**, Nuclear composition of primary cosmic rays in the 'knee' region according MSU EAS array data, J. Phys. G: Nucl. Part. Phys. 22 (1996) 1839-1849.
11. **Monkhoev R.D. et al.**, The Tunka-Grande experiment: Status and prospects, Bull. Russ. Acad. Sci. 81 (4) (2017) 468-470.
12. **Kalmykov N.N. et al.**, Estimating the fraction of gamma quanta in the primary cosmic ray flux with energies of $\sim 10^{17}$ eV from the MSU EAS array data, Bull. Russ. Acad. Sci. 77 (5) (2013) 626-628.
13. **Ivanova A.L. et al.**, Tunka-Grande array for high-energy gamma-ray astronomy and cosmic-ray physics: preliminary results, PoS ICRC2021. 395 (2021) 361.
14. **Abbasi R.U. et al.**, The Cosmic Ray Energy Spectrum between 2 PeV and 2 EeV Observed with the TALE Detector in Monocular Mode, Astrophysical Journal. 865 (2018) 74.
15. **Apel W.D. et al.**, The spectrum of high-energy cosmic rays measured with KASCADE-Grande, Astropart. Phys. 36 (2012) 183.
16. **Rawlins K. et al.**, Cosmic ray spectrum and composition from three years of IceTop and IceCube, J. Phys. Conf. Ser. 718 (5) (2016) 052033.

## THE AUTHORS

**IVANOVA Anna I.**
annaiv.86@mail.ru
ORCID: 0000-0001-8057-4722

***TAIGA Collaboration**
Astapov I.I., Bezyazeekov P.A., Bonvech E.A., Borodin A.N., Budnev N.M., Bulan A.V., Chernov D.V., Chiavassa A., Dyachok A.N., Gafarov A.R., Garmash A.Yu., Grenebyuk V.M., Gres E.O., Gres O.A., Gres T.I., Grinyuk A.A., Grishin O.G., Ivanova A.D., Ilushin M.A., Kalmykov N.N., Kindin V.V., Kiryukhin S.N., Kokoulin R.P., Kompaniets K.G., Korosteleva E.E., Kozhin V.A., Kravchenko E.A., Kryukov A.P., Kuzmichev L.A., Lagutin A.A., Lavrova M.V., Lemeshev Yu.E., Lubsandorzhiev B.K., Lubsandorzhiev N.B., Malakhov S.D., Mirgazov R.R., Monkhoev R.D., Okuneva E.A., Osipova E.A., Pakhorukov A.L., Pankov L.V., Pan A., Panov A., Petrukhin A.A., Podgrudkov D.A., Popova E.G., Postnikov E.G., Prosin V.V., Ptuskin V.S., Pushnin A.A., Raikin R.I., Razumov A.Yu., Rubtsov G.I., Ryabov E.V., Samoliga V.S., Satyshev I., Sidorenkov A.Yu., Silaev A.A., Silaev A.A., Tarashchansky B.A., Tkachev L.G., Tanaev A.B., Ternovoy M.Yu., Ushakov N.A., Volchugov P.A., Volkov N.V., Voronin D.M., Zagorodnikov A.V., Zhurov D.P., Yashin I.I., Vaidyanathan A.

*Received 18.10.2022. Approved after reviewing 14.11.2022. Accepted 15.11.2022.*

© Peter the Great St. Petersburg Polytechnic University, 2023

Conference materials
UDC 524.7
DOI: https://doi.org/10.18721/JPM.161.260

# Formation of spiral dwarf galaxies: observational data and results of numerical simulation

S.S. Khrapov[1]✉, A.V. Khoperskov[1]✉, N.A. Zaitseva[3], A.V. Zasov[2,3], A.V. Titov[1]

[1] Volgograd State University, Volgograd, Russia;
[2] Lomonosov Moscow State University, Moscow, Russia;
[3] Sternberg Astronomical Institute, Moscow, Russia
✉ khrapov@volsu.ru, khoperskov@volsu.ru

**Abstract.** Recent studies show the possibility of the formation of fairly regular and global spiral patterns in dwarf galaxies (dS type). Our sample of observed dwarf objects of this class also includes galaxies with a central stellar bar. The analysis of the observational data provides a small rotation velocity and a small disk component mass for dS galaxies, which is in poor agreement with the spiral structure generation mechanism in isolated dwarfs due to the development of disk gravitational instability. Numerical simulation of the stellar–gaseous disks self-consistent dynamics imposes restrictions on the stellar disk thickness and the maximum gas rotation velocity, at which the gravitational mechanism of spiral formation can still be effective.

**Keywords:** dwarf galaxies, spiral structure, N-body simulation

**Funding:** The work was supported by the Ministry of Science and Higher Education of the Russian Federation (SSK, AVK and AVT, state assignment, project 0633-2020-0003, implementation of all numerical simulations) and by Russian Foundation for Basic Research (NAZ, project 20-02-00080 A, observational data analysis).

**Citation:** Khrapov S.S., Khoperskov A.V., Zaitseva N.A., Zasov A.V., Titov A.V., Formation of spiral dwarf galaxies: observational data and results of numerical simulation, St. Petersburg State Polytechnical University Journal. Physics and Mathematics. 16 (1.2) (2023) 395–402. DOI: https://doi.org/10.18721/JPM.161.260

This is an open access article under the CC BY-NC 4.0 license (https://creativecommons.org/licenses/by-nc/4.0/)

© Khrapov S.S., Khoperskov A.V., Zaitseva N.A., Zasov A.V., Titov A.V., 2023. Published by Peter the Great St. Petersburg Polytechnic University.

Материалы конференции
УДК 524.7
DOI: https://doi.org/10.18721/JPM.161.2

# Особенности формирования спиральных карликовых галактик: данные наблюдений и результаты численного моделирования

С.С. Храпов[1]✉, А.В. Хоперсков[1]✉, Н.А. Зайцева[3], А.В. Засов[2],[3], А.В. Титов[1]

[1] Волгоградский государственный университет, г. Волгоград, Россия;

[2] Московский государственный университет имени М.В. Ломоносова, Москва, Россия;

[3] Государственный астрономический институт имени П.К. Штернберга, Москва, Россия

✉ khrapov@volsu.ru, khoperskov@volsu.ru

**Аннотация**. Последние исследования указывают на возможность формирования в карликовых галактиках (dS) достаточно правильных и глобальных спиральных узоров. Наша выборка наблюдаемых объектов этого класса включает также галактики с центральной перемычкой. Анализ данных наблюдений дает маленькую скорость вращения и маленькую массу дисковой компоненты у dS-галактик, что плохо согласуется с гравитационным механизмом генерации спиральной структуры у изолированных карликов. Численное моделирование динамики звездно-газовых дисков дает ограничения на толщину звездного диска и максимальную скорость вращения газа, при которых гравитационный механизм образования спиралей может являться еще эффективным.

**Ключевые слова**: карликовые галактики, спиральные структуры, N-body моделирование

**Финансирование**: Работа выполнена в рамках госзадания Министерства науки и высшего образования Российской Федерации (проект № 0633-2020-0003, все результаты на основе численного моделирования получены С.С.Х., А.В.Х., А.В.Т.) и гранта РФФИ №20-02-00080 А (Н.А.З. провела обработку данных наблюдений карликов).

**Ссылка при цитировании:** Храпов С.С., Хоперсков А.В., Зайцева Н.А., Засов А.В., Титов А.В. Особенности формирования спиральных карликовых галактик: данные наблюдений и результаты численного моделирования // Научно-технические ведомости СПбГПУ. Физико-математические науки. 2023. Т. 16. № 1.2. С. 395–402. DOI: https://doi.org/10.18721/JPM.161.260

Статья открытого доступа, распространяемая по лицензии CC BY-NC 4.0 (https://creativecommons.org/licenses/by-nc/4.0/)

## Introduction

Dwarf galaxies are small in size and mass compared to classical spiral galaxies (S or SB types) and are usually considered structureless, irregular objects (Irr). Some late-type dwarfs (Sd–Sm types) have a rotating stellar disk without any regular and developed spiral structure. Such galaxies exhibit flocculent type of spirals, which are discontinuous and consist of short regions [1]. Gravitational instability in large massive disks is able to provide a regular spiral pattern covering the entire disk, so Grand Design spiral structure is common for Sa–Sc galaxy types [2–6].

Only a small part of dwarf galaxies shows a global, relatively regular spiral pattern in their disk, and such objects belong to the fairly rare dS type [7–9]. The observations comparative analysis of normal S- and dS-galaxies represents that such dwarfs are more than just smaller copies of large objects, since their spectral characteristics are similar to Irr galaxies [10]. The small size and mass of dwarf galaxies appear to be a theoretical problem for the formation of extended spirals due to gravitational instability [5, 6].

Here we consider the observed properties of the sample of dS galaxies compared to dwarf galaxies without a regular spiral structure [7]. The numerical simulation of the dynamics of the dwarf stellar disks with a rich gaseous component makes it possible to determine the conditions under which gravitational instability can generate sufficiently extended spiral patterns in dS galaxies, which morphology is similar to Grand Design galaxies.

© Храпов С.С., Хоперсков А.В., Зайцева Н.А., Засов А.В., Титов А.В., 2023. Издатель: Санкт-Петербургский политехнический университет Петра Великого.

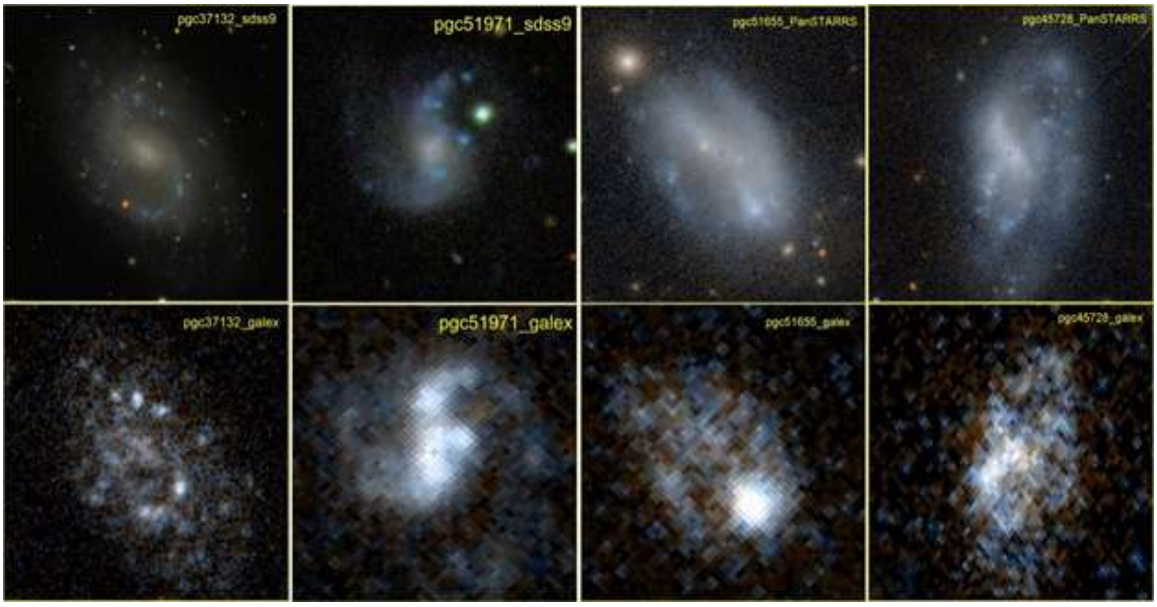


Fig. 1. Dwarf galaxies with a spiral pattern from our sample

**Sample of dS-galaxies and its properties**

Our sample is limited to objects (usually type Sc – Irr) with the absolute magnitude $M_B > -18^m$, the optical diameter $D_{25} < 12$ kpc, $m_B < 15^m$, the inclination angle $i < 75^\circ$ [7]. It is also important to have images in different spectral ranges for deeper study (Figures 1, 2). The logarithm of isolation index log(*ii*) characterizes the degree of environmental influence [11] and we do not consider both Virgo, UMa, Fornax clusters and peculiar galaxies with signs of strong interaction.

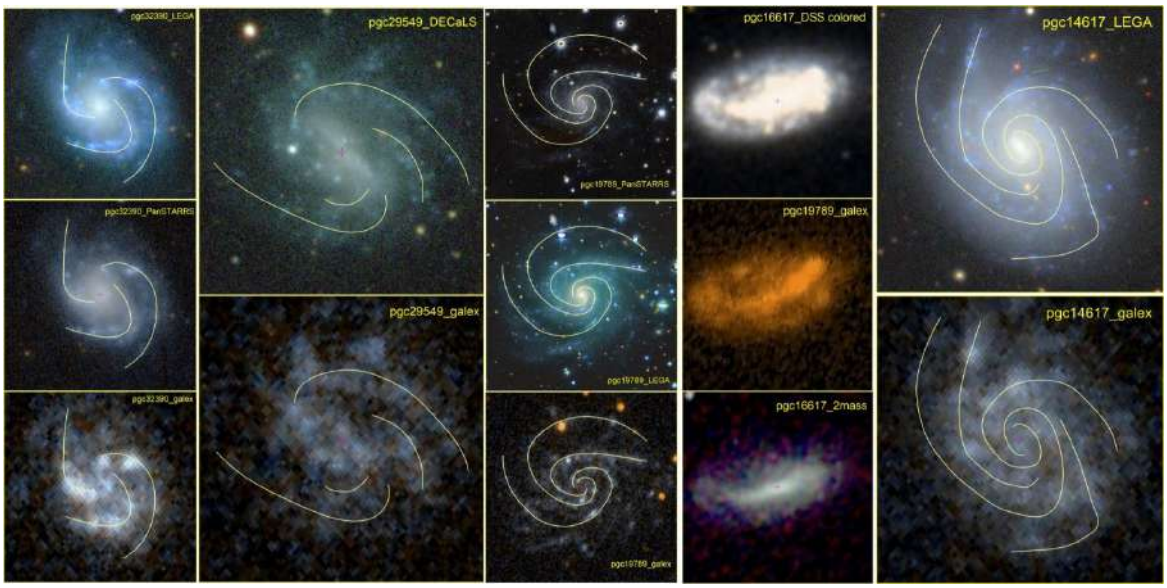


Fig. 2. Dwarf galaxies with a spiral pattern from our sample (continued)

Our sample of spiral dwarf galaxies includes 43 objects, which are compared with the sample of dwarfs without spirals (119 objects of Sm and Irr types, see detailed description in [7]). Fig. 1 shows dwarf galaxies with bars and two distinct arms. The images of SDSS 9 (the Sloan Digital Sky Survey), DECaLS (the Dark Energy Camera Legacy Survey), DSS (the Digitized Sky Survey), PanSTARRS (the Panoramic Survey Telescope and Rapid Response System), LEGA (the DESI Legacy Imaging Surveys) [12] characterize the distributions of the stellar components.

The bottom rows in Figs. 1, 2 show the distributions of gas and young stars according to GALEX data (the Galaxy Evolution Explorer). Fig. 2 demonstrates galaxies with a more complex spiral structure, where the yellow lines highlight the positions of the spiral arms. Moreover, the spirals in the stellar and gaseous components are in good agreement with each other. Three-arm patterns indicate a rather massive dark halo.

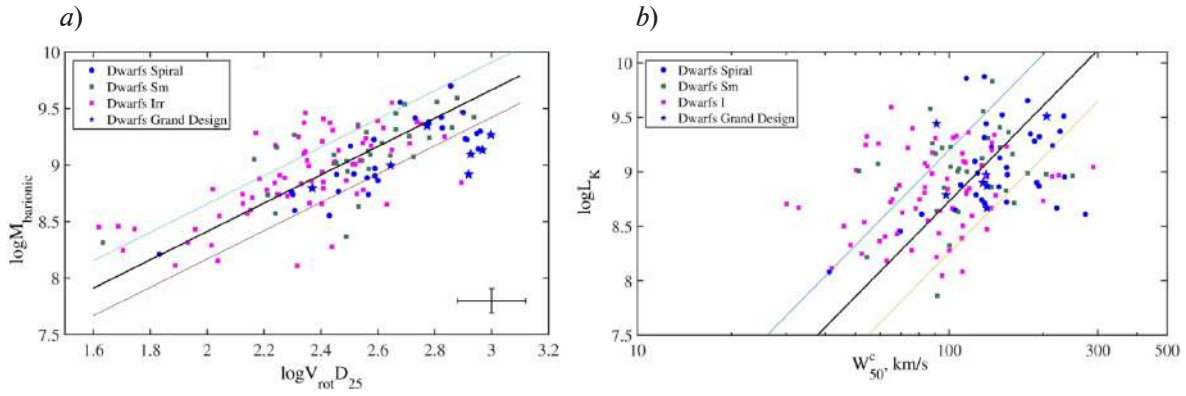


Fig. 3. Positions of various dwarf galaxies: blue icons are spirals, green squares are Sm-type, pink squares are irregular objects. In-plane distribution of the ''baryon mass – momentum'' parameters compared to the regression for isolated galaxies of the AMIGA sample [13] (black line), colored lines show deviation 1σ, $M_{barionic} = \Upsilon_K^* L_K + \eta M_{HI}$, where $\Upsilon_K^* = 0.6$ [14] and $\eta = 1.33$(*a*). Tully-Fisher relation for the K-band compared to those obtained by Karachentsev et al. [15] for the sample of Local Volume dwarf galaxies (black line, colored lines show 1σ deviation) (*b*)

Each galaxy in our two samples is characterized by the systemic velocity $V_{sys}$, the diameter $D_{25}$ the maximum rotation velocity $V_{rot}$, the HI mass $M_{HI}$, the estimate of the total gravitating mass $M_{dyn}$, the luminosities $L_K$ according to the K-magnitudes of 2MASS catalog [16]. Statistical analysis gives the following conclusions (See also [7]).

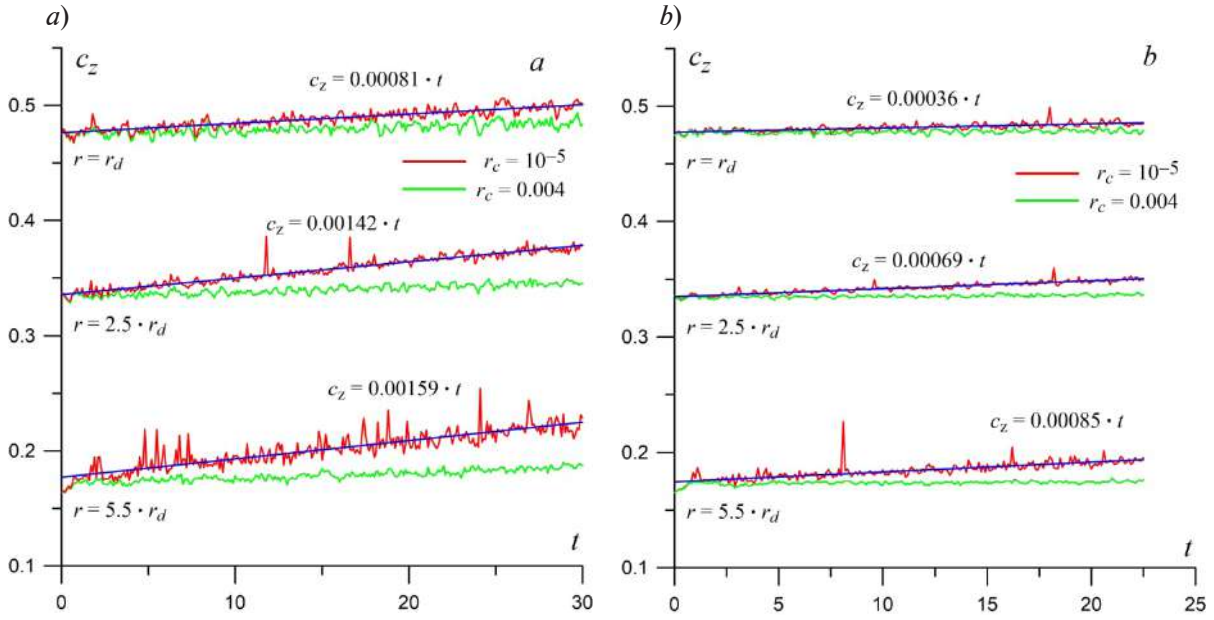


Fig. 4. Dispersion dynamics of stellar vertical velocities in disk models for different gravitational potential cutoff radii ($r_c$), the number of particles in the disk ($N^{(*)}$) and the live halo ($N^{(h)}$). $N^{(*)} = N^{(h)} = 2^{18}$, $r_c = 10^{-5}$ (red lines), $r_c = 4 \cdot 10^{-3}$ (green lines), for different radii ($r_d$ is the radial exponential scale of stellar disk) (*a*); $N^{(*)} = N^{(h)} = 2^{20}$, $r_c = 10^{-5}$ (red lines), $r_c = 4 \cdot 10^{-3}$ (green lines), for different radii (*b*)

— Dwarf galaxies with developed spiral structure are the most massive objects in the sample.

— The distributions of dS galaxies and objects without spirals indicate the absence of very significant differences for various pairs of parameters, for example $L_K - M_{dyn}$, $L_K - M_{HI}$, $D_{25} - M_{HI}$, $M_{dyn} - M_{HI}$, $V_{rot} - M_{HI}$, and others (Fig. 3).

— The HI mass in dS galaxies is, on average, about two times less than in dwarf non-spiral galaxies, although the dynamical and photometric parameters are close for both samples.

— The central stellar bar is found both in dS-type objects and in non-spiral galaxies.

— Tidal influence is apparently not an essential factor of the formation in considered galaxies.

— The proportion of baryonic matter in spiral dwarfs is, on average, lower than in objects with irregular structure and in giant spiral galaxies, which may indicate the influence of the dark halo on the formation of the spiral patterns in dS-dwarfs.

— Remote dwarf galaxies follow the same Tully-Fisher relation as Local Volume dwarfs, but their physical parameters are determined with larger uncertainties due to the low brightness of these objects, which significantly increases the points scatter on the diagram.

## Numerical modeling of the galactic disk

The numerical models are based on the self-consistent dynamics of the N-body gravitating system for the stellar disk and the gaseous component, which is described by the hydrodynamic equations [3, 7]. We used direct method to calculate self-gravity forces (each particle interacts with each other), which is the most accurate modeling approach [17]. The GPUs application for parallel code makes it possible to perform fast numerical experiments with $2^{20}$—$2^{23}$. The numerical model should ensure the collisionlessness of the stellar component [7, 18], which is achieved by cutting off the Newtonian potential at small radii $r_c$. Surface density of the stellar exponential disk $\sigma(r) = \sigma_0 \exp(-r/r_d)$ characterized by the radial scale $r_d$. We use dimensionless units of length $r = 1 \rightarrow 4$ kpc, velocity $V = 1 \rightarrow 47$ km sec$^{-1}$ and time $t = 1 \rightarrow 80$ Myr.

Fig. 4 demonstrates the presence or absence of the stellar disk heating for the corresponding values of $r_c$ and $N = N^{(*)} + N^{(h)}$ (where $N^{(*)}$ is the number of particles in the stellar disk, $N^{(h)}$ is the number of particles that form dark live halo).

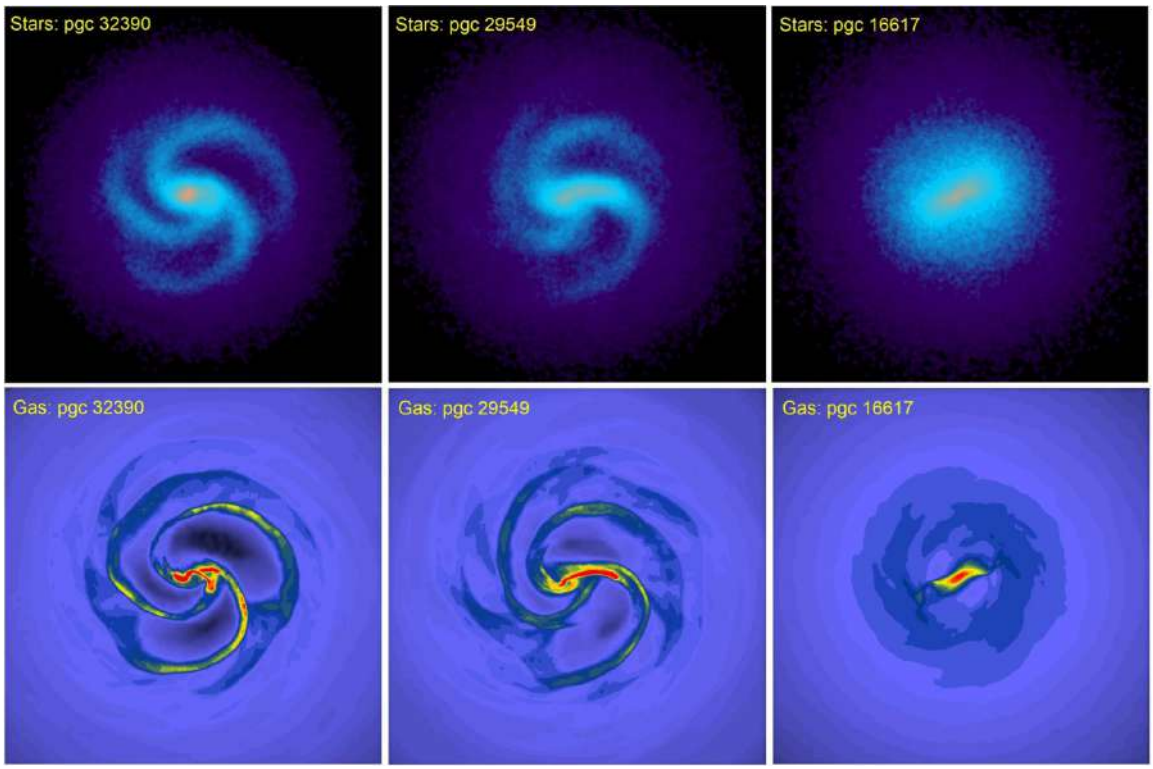


Fig. 5. Examples of spiral patterns in numerical models of galaxies PGC 32390, PGC 29549, PGC 16617. Top row: stellar disk, bottom row: gaseous disk.

We see a noticeable linear increase in vertical velocity dispersion at very small cutoff radii due the absence of collisionlessness in such a model. The value $r_c = 0.004$ ensures the almost stationary behavior of the velocity dispersions (green lines). The heating is stronger for a smaller values of the number of particles $N^{(*)}$ and $N^{(h)}$ (comparison of Fig. 4,*a*, and Fig. 4,*b*).

Fig. 5 shows various spiral structures in dwarf galaxies models. We obtain different stellar and gaseous disks morphology in numerical models by varying the relative masses of stars, gas, and dark halo, as well as the radial and vertical scales that determine the distributions of subsystem parameters. The model structures in gaseous and stellar disks are close to the observed patterns of the corresponding galaxies (See Fig. 1, 2). Other calculation examples are given in [7].

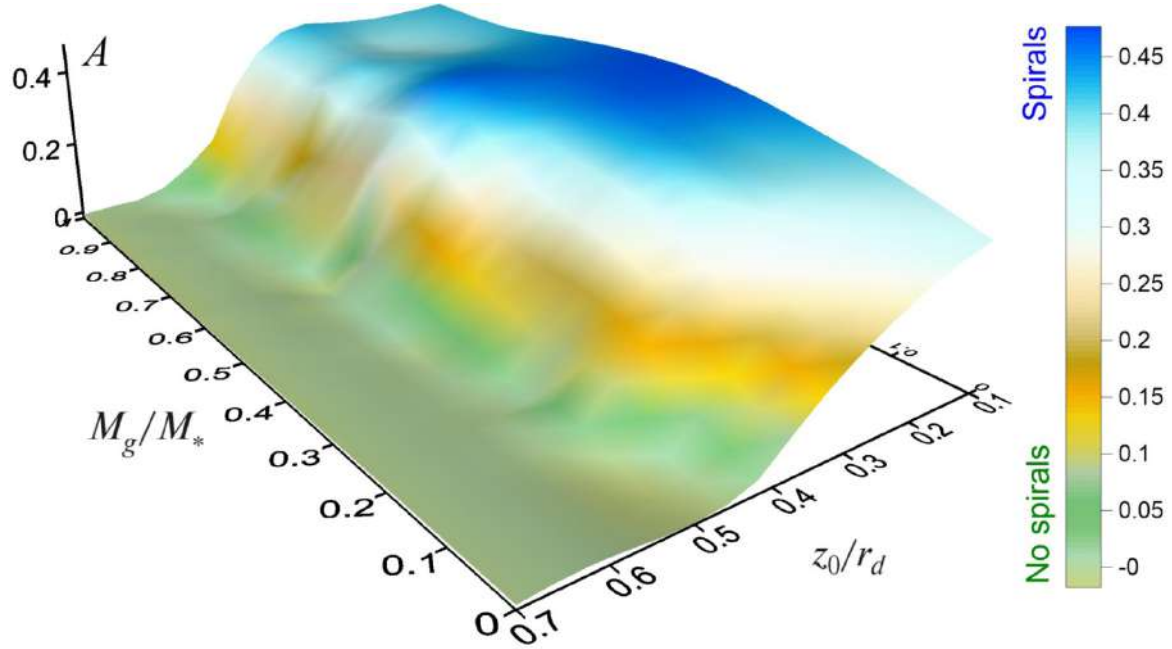


Fig. 6. Distribution of the Fourier harmonics maximum amplitude $A$ on the plane of dimensionless parameters (where $M_g/M_*$ is the relative gas mass, $z_0$ is the vertical disk scale, $r_0$ is the radial disk scale)

## Conclusion

Photometric and kinematic observational data do not allow us to identify confidently the factors that ensure the formation of a global spiral patterns in dwarf galaxies, which are a rather rare phenomenon. There is only some gas deficit in dS galaxies as compared to dIrr objects.

We have studied the possibility of the global spiral structure formation in numerical models of isolated dwarf galaxies due to the development of gravitational instability in the stellar disk rich in gas. The presence of a spiral pattern in dwarf models imposes some restrictions on the disks thickness, the radial velocity dispersion profiles in stellar disk, the sound speed in gas and the gas density. The results of numerical simulations show that the maximum gas rotation velocity must be higher than 60 km $sec^{-1}$ in order to excite spiral waves with significant amplitude. Thicker stellar disk requires more gas to form the spiral pattern.

## Acknowledgments

This research has made use of Aladin Sky Atlas developed at CDS, Strasbourg Observatory, France.

## REFERENCES

1. **Mondal C., Subramaniam A., George K., Postma J. E., Subramanian S., Barway S.,** Tracing young star-forming clumps in the nearby flocculent spiral galaxy NGC 7793 with UVIT imaging, The Astrophysical Journal. 909 (2) (2021) 203.

2. **Kormendy J., Falcyn-Barroso J., Knapen J. H.,** Secular evolution in disk galaxies, Secular Evolution of Galaxies. (2013) 1.

3. **Khrapov S., Khoperskov A., Korchagin V.,** Modeling of spiral structure in a multi-component Milky Way-like galaxy, Galaxies. 9 (2) (2021) 29.

4. **Griv E., Jiang I. G., Hou L. G.,** The nearby spiral density-wave structure of the Galaxy, Monthly Notices of the Royal Astronomical Society. 468 (3) (2017) 3361-3367.

5. **Dobbs C., Baba J.,** Dawes review 4: spiral structures in disc galaxies, Publications of the Astronomical Society of Australia. 31 (2014) e035.

6. **Buta R.,** Galaxy morphology, Secular Evolution of Galaxies, Cambridge University Press, Cambridge, (2013) 155–258.

7. **Zasov A.V., Khoperskov A.V., Zaitseva N.A., Khrapov S.S.,** On the formation of spiral arms in dwarf galaxies, Astronomy Reports. 65 (12) (2021) 1215–1232.

8. **Serrano M., Hidalgo Gámez A. M., Vega-Acevedo I., Castaceda H. O.,** Star Formation Rate in Late-Type Galaxies: I-The Hα and FUV Integrated Values, Revista mexicana de astronomía y astrofísica. 56 (1) (2020) 39–54.

9. **Edmunds M.G., Roy J.R.**, The co-existence of spiral structure and abundance gradients, Monthly Notices of the Royal Astronomical Society. 261 (1) (1993) L17–L19.

10. **Hidalgo-Gamez A. M.,** Dwarf and normal spiral galaxies: are they self-similar?, Revista mexicana de astronomía y astrofísica. 40 (1) (2004) 37–51.

11. **Makarov D., Karachentsev I.,** Galaxy groups and clouds in the local (z ~ 0.01) Universe, Monthly Notices of the Royal Astronomical Society. 412 (4) (2011) 2498–2520.

12. **Dey A., Schlegel D.J., Lang D., Blum R., et. al.,** Overview of the DESI legacy imaging surveys, The Astronomical Journal. 157 (5) (2019) 168.

13. **Lisenfeld U., Verdes-Montenegro L., Sulentic J., et. al.,** The AMIGA sample of isolated galaxies-III. IRAS data and infrared diagnostics, Astronomy & Astrophysics. 462 (2) (2007) 507–523.

14. **McGaugh S.S., Schombert J.M.,** Color–Mass-to-light-ratio relations for disk galaxies, The Astronomical Journal. 148 (5) (2014) 77.

15. **Karachentsev I.D., Kaisina E.I., Kashibadze O.G.,** The local tully–fisher relation for dwarf galaxies, The Astronomical Journal. 153 (1) (2016) 6.

16. **Huchra J.P., Macri L.M., Masters K.L., et. al.,** The 2MASS Redshift Survey–description and data release, The Astrophysical Journal Supplement Series. 199 (2) (2012) 26.

17. **Khrapov S.S., Khoperskov S.A., Khoperskov A.V.,** New features of parallel implementation of N-body problems on GPU, Bulletin of the South Ural State University. Ser. Mathematical Modelling, Programming & Computer Software. 11 (1) (2018) 124–136.

18. **Smirnov A.A., Sotnikova N.Y.,** What determines the flatness of X-shaped structures in edge-on galaxies?, Monthly Notices of the Royal Astronomical Society. 481 (3) (2018) 4058–4076.

## THE AUTHORS

**KHRAPOV Sergey S.**
khrapov@volsu.ru
ORCID: 0000-0003-2660-2491

**KHOPERSKOV Alexander V.**
khoperskov@volsu.ru
ORCID: 0000-0003-0149-7947

**ZAITSEVA Natalia A.**
edera@list.ru
ORCID: 0000-0001-7871-5805

**ZASOV Anatoly V.**
zasov@sai.msu.ru
ORCID: 0000-0001-9914-4466

**TITOV Alexander V.**
alexandr.titov@volsu.ru
ORCID: 0000-0001-6373-9708

*Received 25.10.2022. Approved after reviewing 09.11.2022. Accepted 10.11.2022.*

© Peter the Great St. Petersburg Polytechnic University, 2023

Conference materials
UDC 523.44, 52-17, 521.3
DOI: https://doi.org/10.18721/JPM.161.261

# Gravitational and non-gravitational effects in the orbital motion of asteroid 2022 AE1

A.A. Martyusheva[1]✉, A.V. Devyatkin[1], V.N. L'vov[1]

[1] The Central Astronomical Observatory of the RAS, St. Petersburg, Russia

✉ alex.mart13@gmail.com

**Abstract.** Asteroid 2022 AE1 with a diameter of about 70 m, discovered at the very beginning of 2022, approached the Earth on December 31, 2021 at a minimum distance of 0.0664 au. The potential hazard of a collision with the Earth during the next close approach in 2023 was estimated by astronomers at 1 in 1700, which raised widespread public concern. Subsequent observations made it possible to refine the asteroid's orbit and showed that the collision will be avoided. However, the upcoming close encounters of this asteroid with the Earth and, especially, with Venus, as well as possible approaches with the main belt asteroids, require not to weaken the attention to this object. Gravitational and non-gravitational effects can have a significant impact on its orbit and, as a consequence, lead to a collision with one of the inner planets. In this work, the displacements of asteroid 2022 AE1 under the influence of solar radiation pressure were calculated over several time intervals for various values of the average density of the object. Furthermore, the diurnal and seasonal components of the Yarkovsky effect were calculated for various rotation periods and axial tilt angles of the asteroid. As a result of the simulation, possible orbits of the asteroid were obtained and a probability estimation of the asteroid collision with the Earth was made.

**Keywords:** potentially hazardous asteroids, solar radiation pressure, the Yarkovsky effect

Citation: Martyusheva A.A., Devyatkin A.V., L'vov V.N., Gravitational and non-gravitational effects in the orbital motion of asteroid 2022 AE1, St. Petersburg State Polytechnical University Journal. Physics and Mathematics. 16 (1.2) (2023) 403–409. DOI: https://doi.org/10.18721/JPM.161.261

This is an open access article under the CC BY-NC 4.0 license (https://creativecommons.org/licenses/by-nc/4.0/)

Материалы конференции
УДК 523.44, 52-17, 521.3
DOI: https://doi.org/10.18721/JPM.161.261

# Гравитационные и негравитационные эффекты в орбитальном движении астероида 2022 AE1

А.А. Мартюшева[1]✉, А.В. Девяткин[1], В.Н. Львов[1]

[1] Главная (Пулковская) астрономическая обсерватория РАН, Санкт-Петербург, Россия

✉ alex.mart13@gmail.com

**Аннотация**. В данной работе были вычислены отклонения астероида 2022 AE1 под действием светового давления, а также сезонные и суточные составляющие эффекта Ярковского. В результате моделирования получены возможные орбиты астероида и сделана оценка вероятности столкновения астероида с Землей.

**Ключевые слова**: потенциально опасные астероиды, световое давление, эффект Ярковского.

© Martyusheva A.A., Devyatkin A.V., L'vov V.N., 2023. Published by Peter the Great St. Petersburg Polytechnic University.

**Ссылка при цитировании:** Мартюшева А.А., Девяткин А.В., Львов В.Н. Гравитационные и негравитационные эффектов в орбитальном движении астероида 2022 AE1 // Научно-технические ведомости СПбГПУ. Физико-математические науки. 2023. Т. 16. № 1.2. С. 403–409. DOI: https://doi.org/10.18721/JPM.161.261

Статья открытого доступа, распространяемая по лицензии CC BY-NC 4.0 (https://creativecommons.org/licenses/by-nc/4.0/)

## Introduction

Asteroid 2022 AE1 was discovered by astronomers from the Mount Lemmon Observatory (USA) at the very beginning of 2022. It approached the Earth on December 31, 2021 at a minimum distance of 0.0664 au, with an apparent magnitude of 20.6. This fairly large object of about 70 m in size [1] came close (at a distance of 0.0173 au) to the Earth for the last time on July 4, 1966. Despite the apparent magnitude of 18.0, it was not discovered then due to unfavorable observing conditions.

Initial observations of this asteroid, undertaken by observatories around the world after its discovery, have revealed a high chance of a collision with the Earth in July 2023, which raised major concern. Collision hazard has been confirmed by the AstOD (Asteroid Orbit Determination) automated system, which is used to calculate the orbits of discovered asteroids and assess their potential hazard on the Palermo Scale. Thus, the asteroid 2022 AE1 was assigned one of the highest ratings. Then the asteroid had disappeared from the field of view due to the full moon for some time, and thereafter the resumed observations made it possible to improve the initial calculations. In fact, it turned out that the asteroid will avoid colliding with the Earth by flying past at a safe distance of about 9 Mkm.

Considering all of the above, the study of both gravitational and non-gravitational effects in orbital motion of asteroid 2022 AE1 is of great interest.

## Features of Orbital Motion

The EPOS software package [2] developed at the Pulkovo Observatory has been used to study the orbit of asteroid 2022 AE1. New elements of the orbit, based on all the latest world observations, make it possible to correct the forecast of close encounters of this asteroid with the planets. Table 1 contains data for two centuries.

Table 1

**Upcoming close encounters of asteroid 2022 AE1 for two centuries**

| Date | Distance (au) | Planet |
|---|---|---|
| 01.07.2023 | 0.0595 | Earth |
| 15.08.2039 | 0.0245 | Venus |
| 02.09.2055 | 0.0645 | Venus |
| 03.10.2071 | 0.0432 | Venus |
| 10.06.2089 | 0.0527 | Venus |
| 12.06.2105 | 0.0326 | Venus |
| 04.10.2119 | 0.0664 | Venus |
| 17.09.2135 | 0.0598 | Venus |
| 07.07.2151 | 0.0076 | Earth |
| 21.08.2151 | 0.0606 | Venus |
| 21.07.2169 | 0.0525 | Venus |
| 05.07.2176 | 0.0049 | Earth |
| 06.04.2187 | 0.0561 | Venus |

© Мартюшева А.А., Девяткин А.В., Львов В.Н., 2023. Издатель: Санкт-Петербургский политехнический университет Петра Великого.

Two closer approaches to the Earth will occur in the next century. Not so close, but more numerous and, most importantly, almost periodic encounters with Venus are expected. It can be assumed that in the end this object will either collide with one of the inner planets (probably Venus), or its movement will become more chaotic.

The aphelion distance of asteroid 2022 AE1 is $Q = 2.273$ au. Consequently, its orbit is partially located in the main asteroid belt, where encounters with tens of thousands of other objects (more than 630000 with a perihelion distance of less than 2.28) are possible. Therefore, one can speak confidently about the stability of its orbit only after studying its motion in this region of the solar system.

Potentially hazardous objects for asteroid 2022 AE1, i.e. all those whose interorbital distance does not exceed 0.05 au, have been found using the EPOS software package. At the same time, no restrictions have been imposed on the absolute magnitude $H$, and, consequently, on the size. The number of such objects have turned out to be 30393. The search for close encounters is a very time-consuming task, especially if one looks for encounters for years and decades to come. Therefore, we have limited ourselves to larger objects, although the picture will be incomplete under this condition. Fig. 1 shows a histogram of the sizes of objects from this list. It can be seen that the vast majority of the sizes do not exceed 6 km. However, there are also 243 larger asteroids: Lamberta (147 km), Desiderata (109 km), Chaldaea (71 km), Dike (67 km) and others.

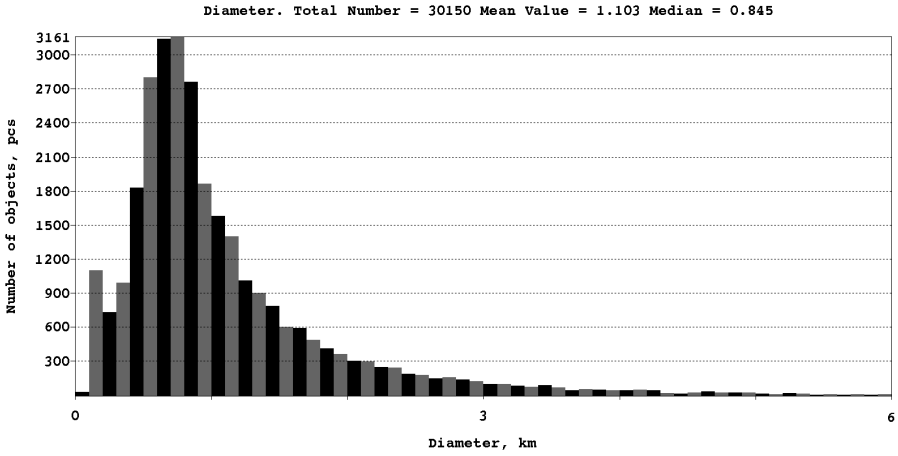


Fig . 1. Size distribution of potentially hazardous objects for asteroid 2022 AE1

Fig. 2 shows the distribution by perihelion distance and orbital inclination. Clusters corresponding to families of asteroids (from top to bottom: Phocaea, Eunomia, Flora) are seen.

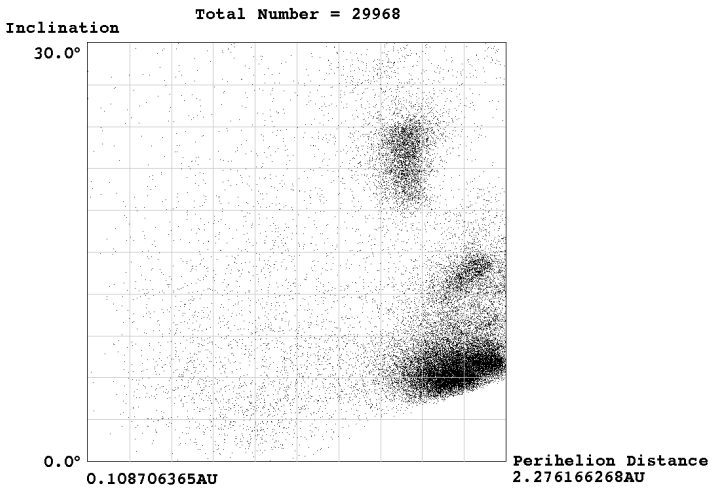


Fig. 2. Distribution of potentially hazardous objects for asteroid 2022 AE1 by perihelion distance and orbit inclination

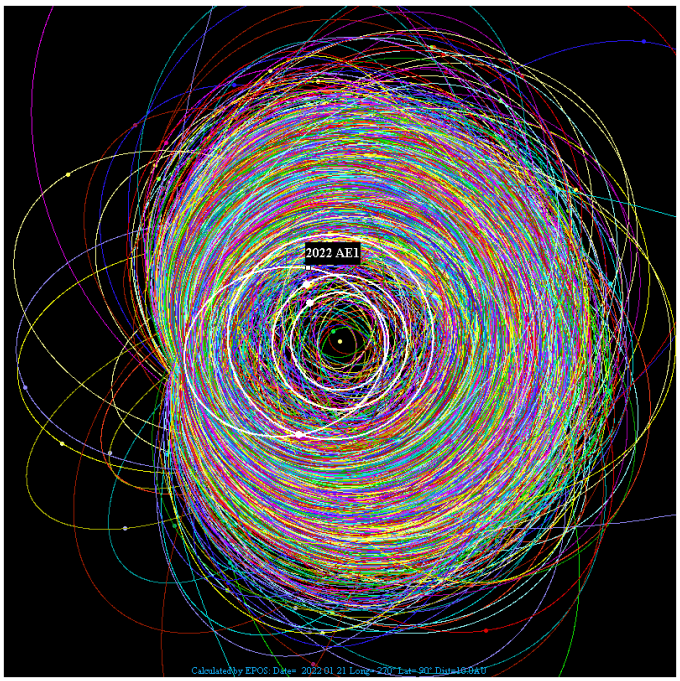


Fig. 3. Orbits and positions of Venus, the Earth, Mars, asteroid 2022 AE1 and potentially hazardous objects to it on January 21, 2022

Fig. 3 shows the orbits of three planets (Venus, the Earth, Mars), asteroid 2022 AE1 and identified potentially hazardous asteroids larger than 1 km, as well as their positions on January 21, 2022.

## Estimation of Non-Gravitational Effects

Model calculations of the influence of such non-gravitational effects as solar radiation pressure and the Yarkovsky effect, which is a non-gravitational acceleration in motion caused by anisotropic re-emission of solar radiation by the surface of an asteroid, were performed for asteroid 2022 AE1.

The calculations have been carried out for the following initial data for the epoch 2459600.5 (2022-01-21):

$e$ = 0.54592866 is the eccentricity [3],
$a$ = 1.470237 au is the semi-major axis [3],
$H_v$ = 23.50 is the absolute magnitude in $V$ band [3],
$D$ = 70 m is the diameter [1],
$n$ = 0.55287027°/d is the mean motion [3],
$M$ = 39.444720° is the mean anomaly [3],
$P_{rev}$ = 651.1473 d is the sidereal orbital period [3],
$\delta$ = 0.14 is the geometric albedo derived from the formula [4]

$$\lg D = 3.122 - 0.5\lg\delta - 0.2H_v, \quad (1)$$

$k$ = 1.06 is the optical coefficient derived from the formula [5]

$$k = 1 + 4\delta/9. \quad (2)$$

Some unknown characteristics of the asteroid have been taken as average, namely, $\varepsilon$ = 0.9 is the emission coefficient, $K = 10^{-2}$ W/m·K is the thermal conductivity, $C$ = 500 J/kg·K is the heat capacity [6]. The following rounded values of 5, 10, 15 h acceptable for an asteroid of this size and the standard angle values of 0°, 45°, 90°, 135°, 180° have been taken as the rotation period $P_{rot}$ and the axial tilt angle $\gamma$ in the absence of real ones, respectively.

Table 2

**Displacements of asteroid 2022 AE1 for 1, 129 and 154 years at various density values**

| ρ (kg/m³) | \|Δ*r*\| (km) | | | \|Δ*l*\| (km) | | | \|Δ*d*\| (km) | | |
|---|---|---|---|---|---|---|---|---|---|
| | 1 (yr) | 129 (yr) | 154 (yr) | 1 (yr) | 129 (yr) | 154 (yr) | 1 (yr) | 129 (yr) | 154 (yr) |
| 1380 | 0.63 | 445.98 | 504.81 | 0.54 | 1192.02 | 1384.38 | 0.83 | 1215.60 | 1402.27 |
| 2710 | 0.32 | 227.10 | 257.06 | 0.27 | 607.00 | 704.96 | 0.42 | 619.02 | 714.07 |
| 3137 | 0.28 | 196.19 | 222.07 | 0.24 | 524.38 | 609.00 | 0.36 | 534.76 | 616.88 |
| 5320 | 0.16 | 115.69 | 130.95 | 0.14 | 309.21 | 359.11 | 0.22 | 315.33 | 363.75 |

Since the asteroid density is also unknown, the solar radiation pressure calculations have been performed for three different mean densities ρ of the main spectral types of asteroids: C-type carbonaceous asteroids (1380 kg/m³), S-type silicaceous asteroids (2710 kg/m³), and M-type metallic asteroids (5320 kg/m³) [7]; as well as for their arithmetic mean (3137 kg/m³). The Yarkovsky effect has been calculated only for the arithmetic mean of the density of the main spectral types (3137 kg/m³).

The solar radiation pressure calculations have been carried out using the numerical integration of the motion equations by the Everhart method on three time intervals: 1, 129 and 154 years, which corresponds to close encounters of the asteroid with the Earth in 2023, 2151 and 2176. The calculation process has been described in detail in [8]. As a result, the following values have been obtained: the asteroid displacement along the heliocentric radius vector Δ*r*, the asteroid displacement along the longitude Δ*l*, and the total asteroid displacement Δ*d*. The calculation results are presented in Table 2. It should be noted that the displacements Δ*r,* Δ*l*, Δ*d* are non-linear in time and decrease with increasing density.

Calculations of the rate of change in the semi-major axis of the orbit *a* of asteroid 2022 AE1 under the influence of the diurnal $(da/dt)_d$ and seasonal $(da/dt)_s$ components of the Yarkovsky effect $(da/dt)_{d+s}$ depending on the rotation period $P_{rot}$ , and the axial tilt angle γ of the asteroid have been conducted using the Gauss-Everhart integrator [9] and the model taken from [6]. The calculation results are presented in Table 3.

Table 3

**Rate of change in the semi-major axis of the orbit *a* of asteroid 2022 AE1 under the influence of the diurnal $(da/dt)_d$ and seasonal $(da/dt)_s$ components of the Yarkovsky effect $(da/dt)_{d+s}$ depending on the rotation period $P_{rot}$ and the axial tilt angle γ of the asteroid**

| $P_{rot}$ (h) | γ (°) | $(da/dt)_d \cdot 10^{-6}$ (au/Myr) | $(da/dt)_s \cdot 10^{-8}$ (au/Myr) | $(da/dt)_{d+s} \cdot 10^{-6}$ (au/Myr) |
|---|---|---|---|---|
| 5 | 0 | 4.1180 | 0 | 4.1180 |
| | 45 | 2.9119 | –3.5710 | 2.8762 |
| | 90 | 0 | –7.1421 | –0.0714 |
| | 135 | –2.9119 | –3.5710 | –2.9476 |
| | 180 | –4.1180 | 0 | –4.1180 |
| 10 | 0 | 3.5104 | 0 | 3.5104 |
| | 45 | 2.4822 | –3.5710 | 2.4465 |
| | 90 | 0 | –7.1421 | –0.0714 |
| | 135 | –2.4822 | –3.5710 | –2.5179 |
| | 180 | –3.5104 | 0 | –3.5104 |
| 15 | 0 | 3.1241 | 0 | 3.1241 |
| | 45 | 2.2090 | –3.5710 | 2.1733 |
| | 90 | 0 | –7.1421 | –0.0714 |
| | 135 | –2.2090 | –3.5710 | –2.2447 |
| | 180 | –3.1241 | 0 | –3.1241 |

The influence of the diurnal component $(da/dt)_d$ on the semi-major axis $a$ is maximum when the rotation axis is perpendicular to the orbit plane at 0° and 180°, and is equal to 0 at 90°, which fits the case when the rotation axis lies in the orbit plane. The effect of the seasonal component $(da/dt)_s$, on the contrary, is maximum at 90°, and becomes zero at 0° and 180°. The maximum heating of a hemisphere is reached sometime after the summer solstice due to the thermal inertia of matter. Therefore, the resulting reactive impulse has a component directed opposite to the motion direction of an asteroid and leading to a decrease in the semi-major axis $a$. At the same time, the change in the rotation period of the asteroid $P_{rot}$ has not been affected the seasonal component $(da/dt)_s$. The Yarkovsky effect is the result of the action of both components $(da/dt)_{d+s}$. It can induce both an acceleration of the orbital motion, that is an increase in the semi-major axis $a$ at $\gamma < °90$, and a deceleration, that is a decrease in the major semi-axis $a$ at $\gamma \geq 90°$, depending on the direction of rotation of an asteroid with respect to the direction of orbital motion.

## Conclusion

Future close encounters of asteroid 2022 AE1 with the Earth and, especially, with Venus, as well as possible approaches with the main belt asteroids, require further high-precision astrometric observations and improvement of its orbit. Gravitational and non-gravitational effects can significantly change the asteroid orbit and, consequently, lead to a collision with one of the inner planets.

Calculations have shown that the maximum displacements of asteroid 2022 AE1, caused by solar radiation pressure, can be 0.22-0.83 km per 1 year (which corresponds to a close approach in 2023), 315.33-1215.60 km per 129 years (close approach in 2151) and 363.75-1402.27 km per 154 years (close approach in 2176), depending on its density.

The rate of change in the semi-major axis of the orbit of asteroid 2022 AE1 under the influence of the Yarkovsky effect can be from -4.1180·$^{6-}$10 to 4.1180·$^{6-}$10 au/Myr, depending on the assumed rotation period and the axial tilt angle of the asteroid.

From the data obtained, it can be seen that solar radiation pressure has a more noticeable effect on the motion of a given asteroid with the given physical characteristics in a fairly short period of time than the Yarkovsky effect.

## REFERENCES

1. Near-Earth Objects Coordination Centre. URL: https://web.archive.org/web/20220121022739/https://neo.ssa.esa.int/search-for-asteroids?sum=1&des=2022AE1. Accessed Oct. 21, 2022.

2. **L'vov V.N., Tsekmeister S.D.**, The use of the EPOS software package for research of the solar system objects, Solar System Research. 46 (2) (2012) 177–179.

3. JPL Small Body Database. URL: https://ssd.jpl.nasa.gov/tools/sbdb_lookup.html#/?sstr=2022%20AE1. Accessed Oct. 21, 2022.

4. **Vinogradova T.A., Zheleznov N.B., Kuznetsov V.B., Chernetenko Yu.A., Shor V. A.**, Catalogue of potentially hazardous asteroids and comets, Transactions of IAA RAS. 9 (2003) 43.

5. **Polyakhova E.N., Shmyrov A.S.**, The physical model of the solar radiation pressure on a sphere and a plane, Vestnik of SPbSU. 2 (8) (1994) 87–104.

6. **Panasenko A.I., Chernetenko Yu.A.**, Simulation of the Yarkovsky effect in the motion of asteroids, Transactions of IAA RAS. 31 (2014) 59–65.

7. **Krasinsky G.A., Pitjeva E.V., Vasilyev M.V., Yagudina E.I.**, Hidden mass in the asteroid belt, Icarus. 158 (1) (2002) 98–105.

8. **Martyusheva A.A., Petrov N.A., Polyakhova E.N.**, Solar radiation pressure effects on asteroid motions, including near-Earth objects, Vestnik of SPbSU. 2 (1) (2015) 135–47.

9. **Avdyushev V.A.**, Gauss-Everhart integrator, Computational Technologies. 15 (4) (2010) 31–46.

## THE AUTHORS

**MARTYUSHEVA Alexandra A.**
alex.mart13@gmail.com
ORCID: 0000-0001-7491-2772

**DEVYATKIN Alexander V.**
a9kin@mail.ru
ORCID: 0000-0001-5095-664X

**L'VOV Victor N.**
epos-gao@mail.ru
ORCID: 0000-0002-1547-3674

*Received 24.10.2022. Approved after reviewing 09.11.2022. Accepted 10.11.2022.*

© Peter the Great St. Petersburg Polytechnic University, 2023

Conference materials
UDC 520.2
DOI: https://doi.org/10.18721/JPM.161.262

# Development of detector cluster based on silicon photomultipliers for the Cherenkov gamma-ray telescope TAIGA-IACT

A.A. Bogdanov[1]✉, G.A. Repman[1], Yu.V. Tuboltsev[1],
Yu.V. Chichagov[1], E.E. Kholupenko[1], A.M. Krassilchtchikov[1]

[1] Ioffe Institute, St. Petersburg, Russia

✉ Alexander.A.Bogdanov@mail.ioffe.ru

**Abstract.** A new experimental detector cluster for the TAIGA-IACT telescope has been developed. The cluster contains 28 pixels based on MicroFJ-60035 silicon photomultipliers, whose signal is digitized with an analog memory chip (switched capacitor array) DRS4 at a frequency of up to 5 GHz. The paper describes the device and the operation principles of the detector cluster, reveals the peculiarities encountered in the development process. Dark chamber tests of the cluster with a point source of short pulses of ultraviolet light have allowed us to obtain dependencies of the cluster conversion coefficient and the maximum value of the recorded signal on the overvoltage of the silicon detectors.

**Keywords:** SiPM, silicon photomultipliers, readout electronics, IACT

**Funding:** This research has been supported by the Russian Science Foundation via grant 197220045.

**Citation:** Bodganov A.A., Repman G.A., Tuboltsev Yu.V., Chichagov Yu.V., Kholupenko E.E., Krassilchtchikov A.M., Development of detector cluster based on silicon photomultipliers for the cherenkov gamma-ray telescope TAIGA-IACT, St. Petersburg State Polytechnical University Journal. Physics and Mathematics. 16 (1.2) (2023) 410–416. DOI: https://doi.org/10.18721/JPM.161.262

This is an open access article under the CC BY-NC 4.0 license (https://creativecommons.org/licenses/by-nc/4.0/)

Материалы конференции
УДК 520.2
DOI: https://doi.org/10.18721/JPM.161.262

# Разработка детекторного кластера на кремниевых фотоумножителях для черенковского гамма-телескопа TAIGA-IACT

А.А. Богданов[1]✉, Г.А. Репман[1], Ю.В. Тубольцев[1],
Ю.В. Чичагов[1], Е.Е. Холупенко[1], А.М. Крассильщиков[1]

[1] Физико-технический институт им. А.Ф. Иоффе РАН, Санкт-Петербург, Россия

✉ Alexander.A.Bogdanov@mail.ioffe.ru

**Аннотация.** Создан новый экспериментальный детекторный кластер для телескопа TAIGAIACT. Кластер содержит 28 пикселей с кремниевыми фотоумножителями MicroFJ-60035, сигнал с которых оцифровывается с применением микросхемы аналоговой памяти DRS4 с частотой до 5 GHz. В работе описывается устройство и принцип работы детекторного кластера, раскрываются сложности, с которыми пришлось столкнуться в процессе разработки. Также в работе описывается проведение испытаний в темной камере с точечным источником коротких импульсов ультрафиолетового света, в результате которых были получены зависимости коэффициента преобразования кластера и максимальной величины регистрируемого сигнала от величины перенапряжения кремниевых детекторов.

**Ключевые слова:** SiPM, кремниевые фотоумножители, считывающая электроника, IACT

© Bodganov A.A., Repman G.A., Tuboltsev Yu.V., Chichagov Yu.V., Kholupenko E.E., Krassilchtchikov A.M., 2023. Published by Peter the Great St. Petersburg Polytechnic University.

**Финансирование:** Работа выполнена в рамках гранта Российского научного фонда № 197220045.

**Ссылка при цитировании:** Богданов А.А., Репман Г.А., Тубольцев Ю.В., Чичагов Ю.В., Холупенко Е.Е., Красильщиков А.М. Разработка детекторного кластера на кремниевых фотоумножителях для черенковского гамма-телескопа TAIGA-IACT

// Научно-технические ведомости СПбГПУ. Физико-математические науки. 2023. Т. 16. № 1.2. С. 410–416. DOI: https://doi.org/10.18721/JPM.161.262

Статья открытого доступа, распространяемая по лицензии CC BY-NC 4.0 (https://creativecommons.org/licenses/by-nc/4.0/)

## Introduction

Currently, the TAIGA Observatory [1] designed to study cosmic sources of gamma-ray emission and cosmic rays is actively developing in the Tunka Valley. This observatory includes an array of Cherenkov imaging gamma-ray telescopes TAIGA-IACT [2], whose detecting chamber is based on vacuum photomultipliers [3]. However, development of microelectronics makes it possible to create detection systems based on silicon photomultipliers, which are superior to vacuum photomultipliers in a number of important parameters. For example, silicon photomultipliers operate at lower supply voltages, are not sensitive to magnetic fields, are more compact and resistant to illumination.

In recent years, the Ioffe Institute has been developing a detector cluster for the camera of TAIGA-IACT based on silicon photomultipliers (SiPM) MicroFJ-60035, sensitive to radiation in both visible (300–600 nm) and ultraviolet (250–300 nm) ranges. The choice of this type of SiPM is due to their high detection efficiency (PDE) both in the visible range (25–50% at an overvoltage of 6 V, depending on the wavelength) and in the ultraviolet range (5–20%, depending on the wavelength). The latter circumstance is important, since the design of the upgraded chamber assumes the possibility of performing rough spectrometry of the Cherenkov radiation of extensive atmospheric showers (EAS) [4], which can increase the efficiency of determining the type of the primary particle (the so-called gamma-hadron separation). In addition, an important feature of these detectors is the presence of a fast output that allows one to obtain a signal length of the order of several nanoseconds, which is important for revealing a low-amplitude signal against a highly noisy background created in the detecting cameras by the night sky radiation.

The development of a new detector cluster is at the final stage; this article describes the final version of the cluster and its testing in a dark chamber.

## Description of the cluster

A simplified block diagram of the detector cluster is shown in Fig. 1. The cluster contains 28 pixels based on silicon photomultipliers (SiPM) MicroFJ-60035. The final scheme for removing the signal from the detectors is somewhat different from that described in paper [5]. Each pixel contains four SiPMs. The signals from their fast outputs are fed to the emitters of the BFT93 transistors employed in the scheme with a common base. This switching scheme ensures formation of a short signal. The transistor collectors are connected together, which allows summing up the signals from the detectors before amplifying them and this significantly reduces the number of preamp components, its power consumption and heat dissipation. The pixel preamp has a fixed gain of 100, which is achieved using two gain stages based on AD8099 operational amplifiers with a gain of 10 for each stage. The gain of the entire pixel is changed by adjusting the overvoltage of the silicon photomultipliers.

The signal from each pixel is transmitted via a coaxial cable through high-frequency miniature MMCX connectors and is received by an amplifier stage based on an AD8099 operational amplifier with a total gain of 0.33, which allows the signal to be scaled to the input range of the DRS4 analog memory chip (from 0 V to 1 V).

© Богданов А.А., Репман Г.А., Тубольцев Ю.В., Чичагов Ю.В., Холупенко Е.Е., Красильщиков А.М., 2023. Издатель: Санкт-Петербургский политехнический университет Петра Великого.

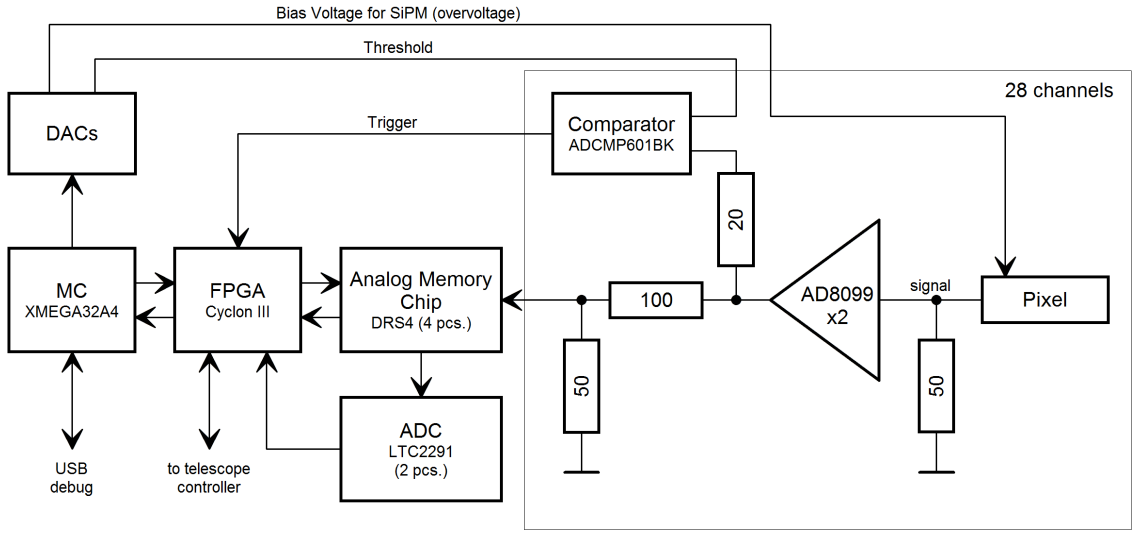


Fig. 1. Block diagram of the detector cluster

Four DRS4 analog memory chips are installed into the cluster. In every DRS4 chip seven channels out of nine are employed. DRS4 is capable of storing a signal with a frequency of up to 5 GHz. Frequency control was tested using a reference frequency and an internal PLL. However, with such a control, some DRS4 chips under the same conditions worked unstable. Therefore, frequency control was implemented by applying a controlled voltage from a digital-to-analog converter (DAC) to the DSPEED input, and this solution was shown to allow a reliable control of the DRS4 frequency and reduce the number of digital signals that can negatively affect the quality of the analog signal from the pixels.

To digitize the signals recorded in the analog memory, two 12-bit two-channel analogtodigital converters (ADC) LTC2291 operating at a frequency of 20 MHz are used. Each ADC digitizes signals from two DRS4 chips.

The control of the DRS4 chip and of accumulation of the digitized signals from the four ADCs is done with a field-programmable gate array (FPGA) Cyclone III, operating at a reference frequency of 100 MHz, while its individual parts operate at a frequency of 400 MHz. The internal memory capacity of the FPGA allows one to record 1024 values with a bit depth of 12 bits for each of the 28 registration channels. However, it is worth noting that each memory cell of the DRS4 chip is characterized by an individual base offset of the zero level different from other memory cells, which can be corrected, and that significantly improves the accuracy of the digitized signal. Tests have shown that without the offset correction, the standard deviation of the channel noise track on average across all the channels is 34 ADC code units, and with the offset correction it reduces to only about 12.5 ADC codes, that is, the noise parameters are improved almost by the factor of 3. However, in order to make such a correction in the FPGA memory, it is necessary to have an array of 1024 numbers for each channel with an individual offset value in order to compensate the values in the real time during signal processing. Unfortunately, the internal memory of the Cyclone III is not enough to store the offset correction values of all the 28 channels, but this can be done at a post-processing step while analyzing the recorded wavea forms on a computer.

The data recorded in the FPGA memory are read using an XMEGA microcontroller operating at a frequency of 32 MHz. The microcontroller performs the general command control of the clusters, and also calculates the signal amplitude for each pixel after measurement, and stores the amplitude data in its memory. On a demand from an external computer, the microcontroller transmits the 28 amplitude values. This makes it possible to significantly reduce the amount of data transmitted, since it is not necessary to transmit the channel waveforms. The microcontroller also controls digital-to-analog converters (DACs) over SPI, which set the bias voltage of the detectors, the voltage that determines the frequency of operation of the DRS4, and the threshold voltage of the comparators.

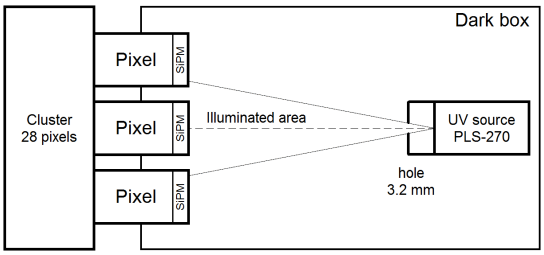


Fig. 2. Scheme of the experiment in the dark chamber

Each of the 28 channels has an ADCMP601BK comparator, which generates a trigger signal when the software-set threshold is exceeded by a signal from a pixel. Each trigger signal of the channel enters the FPGA, which forms a time window of 10 ns for each trigger signal and counts the number of overlaps of the time windows of the channels with each other. If the number of such overlays exceeds a predetermined number, the FPGA generates a stop signal with some delay necessary to write the signal to the memory of the DRS4 chips and starts reading the DRS4 chips. After reading, the FPGA notifies the microcontroller of the completion of the measurement, which either reads the waveforms to determine the amplitudes of the signals, or transmits the waveforms to the computer via an USB connection.

To test the entire cluster in conditions close to working conditions, a dark chamber was developed (Fig. 2).

There is an LED source of UV radiation PLS-270 in the dark chamber, which emits weak pulses of UV radiation at the wavelength of 277 nm, duration of 600 ps and frequency of 5 MHz. A spatial filter with a ⌀3.2 mm hole is installed on the source, which allows one to illuminate certain pixels of the cluster by changing the distance between the silicon detectors and the source. The main part of the cluster is located outside the dark chamber, which contributes to the natural cooling of the electronics. An example of visualization of the data received from the cluster is shown in Fig. 3.

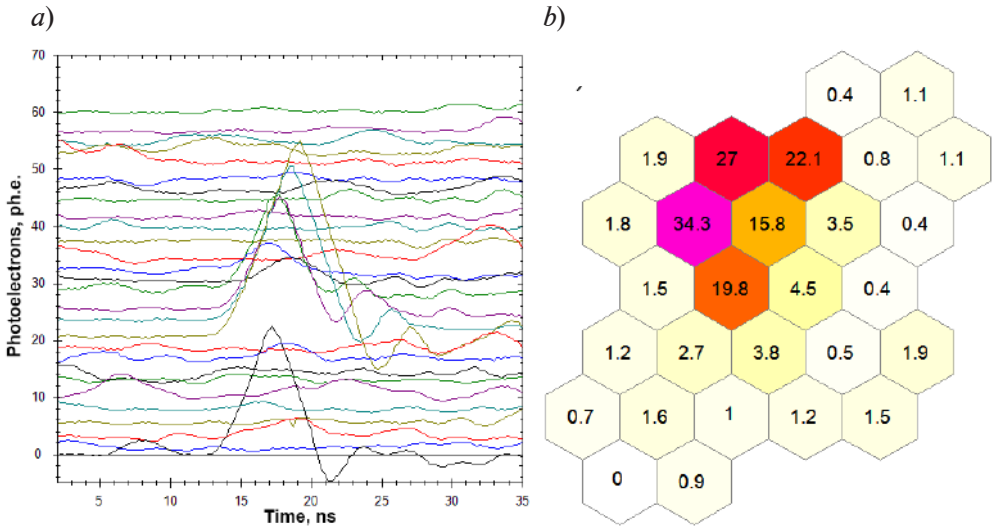


Fig. 3. An example of waveforms (*a*) and an image (*b*) of a UV radiation pulse from a PLS-270 source. The waveforms are artificially shifted relative to each other for clarity. The numbers inside the pixels are the signal amplitudes in photoelectrons (ph.e.)

## Calibration of the cluster

The purpose of calibration of the detector cluster is to determine the conversion coefficient of the ADC value (hereinafter code) into the number of photons per pixel, as well as to determine the value of the maximum recorded signal - the maximum range of the cluster. The registration efficiency of silicon photomultipliers, as the ratio of the number of photons registered by the detector to the number of photons that hit the detector, depends on the temperature conditions [6] and on the overvoltage of the detector. Hence, it is advisable to determine the conversion coefficient relative to the number of registered photons (hereinafter referred to as photoelectrons or ph.e.).

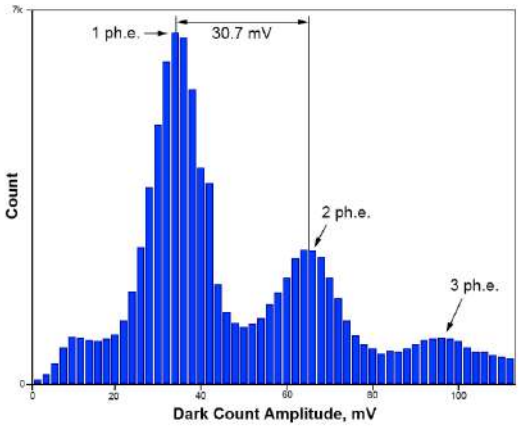


Fig. 4. The amplitude spectrum of the dark count at an overvoltage of 6 V

The detector converts photoelectrons into the signal amplitude in voltage units. This signal is amplified later by the amplifying path and eventually digitized on the ADC, which converts the voltage into a digital code. The described transformation can be reduced to the following formula:

$$K = k_{SiPM} \cdot k_{PA} \cdot k_{Amp} \cdot k_{ADC},$$

where $K$ is the conversion coefficient of the cluster, code/ph.e., $k_{SiPM}$ is the conversion coefficient of silicon photomultipliers in mV/ph.e., $k_{PA}$ is the pixel conversion coefficient (the preamp part of the amplifying path) equal to 100, $k_{Amp}$ is the conversion coefficient of the amplifying path equal to 1/3, $k_{ADC}$ is the conversion coefficient of ADC LTC2291, equal to 4.096 code/mV.

To find the SiPM conversion coefficient at high overvoltage values (above 4.5 V), it is sufficient to measure the difference between the dark count pulses with an amplitude of 1 ph.e. and 2 ph.e., i.e. a single signal that is numerically equal to the conversion coefficient of a silicon photomultiplier. An example of the amplitude spectrum for an overvoltage of 6 V is shown in Fig. 4.

However, when the overvoltage value decreases, the amplitude peaks corresponding to pulses of 1 ph.e. and 2 ph.e. merge, which does not allow one to obtain the value of a single signal directly at low overvoltage values (below 4.5 V). At the same time, it is known that the dependence of the avalanche photodiode gain on overvoltage is linear and can be found in the datasheet of the SiPM from the manufacturer [7]. Therefore, it is possible to extrapolate the trend of the SiPM conversion coefficient to the region of low overvoltage values. Fig. 5 shows the directly measured values of single signals (blue crosses) and a graph of the dependence of the gain of the silicon photomultiplier (red line) on the overvoltage.

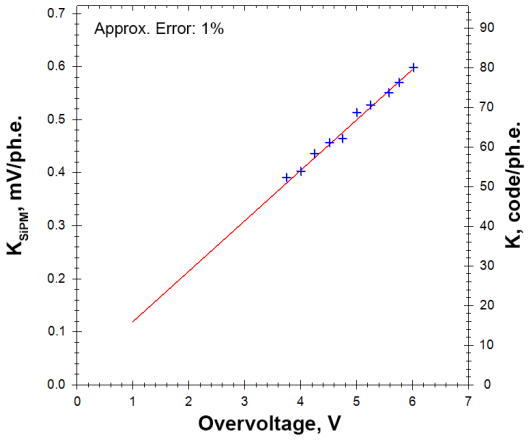


Fig. 5. Dependence of the conversion coefficient of the SiPM and the cluster as a whole on the overvoltage of the detectors

The gain in this graph is renormalized relative to the magnitude of a single signal at an overvoltage of 6 V. The average approximation error of the measured points to the line is 1%. Thus, the cluster conversion factor is 16 code/ph.e. at 1 V of overvoltage and 80 code/ph.e. at 6 V.

Taking into account that the maximum range of the ADC is 4096 codes, and the base signal level of each pixel is shifted by 750 codes, it is possible to determine the maximum range of signals recorded by the cluster in photoelectrons. However, when the overvoltage changes, the registration efficiency (PDE) and the probability of crosstalk also change, therefore, when considering the maximum range of the cluster, it is also important to consider it in photons that have hit the detector. In the silicon photomultiplier datasheet, the manufacturer provides a linear dependence of the PDE on overvoltage, the dependence of the crosstalk on overvoltage is not directly given, but it is reasonable to believe that it is linear based on studies of an analogous MPPC manufactured by Hamamatsu [8].

Fig. 6 shows the dependencies of the maximum range of the cluster in the units of photoelectrons (red line) and in the units of photons (blue line), with account of the PDE and of the crosstalk probability at a given overvoltage. It is worth noting that the microcells of a silicon photomultiplier triggered by a crosstalk can also generate crosstalk events, but here such chains of crosstalk events are not considered.

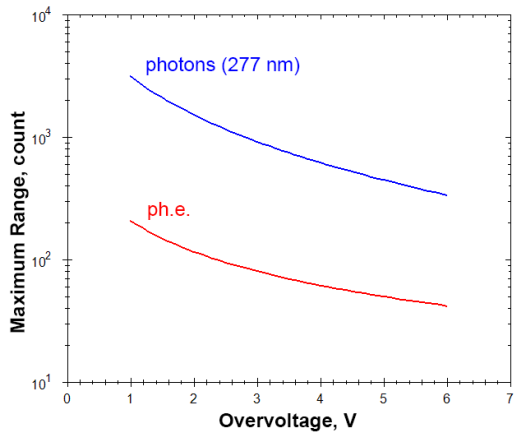


Fig. 6. Dependence of the maximum recorded signal value on the overvoltage of the detectors

At an overvoltage of 6 V, the maximum range of the cluster is 42 ph.e., or 340 photons with a wavelength of 277 nm, and at 1 V is 210 ph.e., or 3200 photons. With a further decrease in the overvoltage below 1 V, a further increase in the range is also expected, however, the approximation of the bias voltage to the breakdown voltage of the silicon photomultiplier may affect the dependencies of the SiPM characteristics and requires a separate dedicated study.

## Conclusion

A new experimental detector cluster based on silicon photomultipliers has been developed for the TAIGA-IACT Cherenkov gamma-ray telescope. The signal readout and preprocessing scheme has been worked out. In the calibration process, the dependency of the cluster conversion coefficient on the overvoltage of the silicon detectors was obtained in order to calculate the number of registered photons. The dependency of the magnitude of the maximum recorded signal on the overvoltage of the detectors is obtained as well.

The performed studies complete the stage of development and construction of the detector cluster. In the near future, it is planned to install the cluster into the camera of the currently operating TAIGAIACT unit and carry out observations of the background signal and the signal from bright cosmic gamma-ray sources.

## Acknowledgements

This research has been supported by the Russian Science Foundation via grant 197220045.

The results of the presented research will be also used at UNU “Astrophysical complex MSU-ISU” (the complex is supported by the agreement 13.UNU.21.0007 between the ISU and the Ministry of Science and Higher education of Russia).

## REFERENCES

1. **Kuzmichev L. A. et al.,** TAIGA Gamma Observatory: Status and Prospects, Physics of Atomic Nuclei. 81 4 (2018) 497–507.

2. **Sagan Y. et al.,** TAIGA observatory: IACT fabrication and tests, ICRC2019. 36 (2019) 776.

3. **Budnev N.M. et al.,** TAIGA: a complex of hybrid systems of cooperating detectors for gamma astronomy and cosmic ray physics in the Tunka valley, Bulletin of the Russian Academy of Sciences: Physics. 83 (8) (2019) 951−4.

4. **Kholupenko E.E. et al.,** The Application Potential of Silicon Photomultipliers for a Camera of a Small-Size Cherenkov Gamma-Ray Telescope for Reducing the Detection Threshold, Tech. Phys. 65 (6) (2020) 886–95.

5. **Bogdanov A.A. et al.,** Development of detector pixels based on silicon photomultipliers for the Cherenkov gamma-ray telescope TAIGA-IACT, J. Phys.: Conf. Ser. 2103 (2020) 012026.

6. **Bogdanov A.A. et al.,** Temperature Dependence of the Sensitivity of Silicon Photomultipliers in the Regime of Single-Photon Detection of Ultraviolet Radiation, Tech. Phys. *66* (2021) 699–704.

7. SiPM Datasheet MicroJ Series. URL: https://www.onsemi.com/pdf/datasheet/microj-series-d.pdf.

8. **Li S., Smoot G.**, Characterization of a silicon photomultiplier for the Ultra-Fast Astronomy telescope, Proc. SPIE 11115, UV/Optical/IR Space Telescopes and Instruments: Innovative Technologies and Concepts IX. (2019) 111150A.

## THE AUTHORS

**BODGANOV Alexander A.**
Alexander.A.Bogdanov@mail.ioffe.ru
ORCID: 0000-0002-5275-5603

**REPMAN Georgiy A.**
repman.gast@mail.ru

**TUBOLTSEV Yuri V.**
tuboltsev@mail.ioffe.ru
ORCID: 0000-0001-9770-0158

**CHICHAGOV Yuriy V.**
chichagov@mail.ioffe.ru
ORCID: 0000-0002-2679-6380

**KHOLUPENKO Evgeny E.**
eug_khol@mail.ru

**KRASSILCHTCHIKOV Alexander M.**
kra@astro.ioffe.ru
ORCID: 0000-0001-7681-4316

**BOGDANOV Alexander A.**
Alexander.A.Bogdanov@mail.ioffe.ru
ORCID: 0000-0002-5275-5603

*Received 24.10.2022. Approved after reviewing 08.11.2022. Accepted 08.11.2022.*

© Peter the Great St. Petersburg Polytechnic University, 2023

Conference materials
UDC 537.591.15
DOI: https://doi.org/10.18721/JPM.161.263

# Design of an optical concentrators array for the camera of a small-size Cherenkov gamma-ray telescope

A.S. Antonov[1]✉, A.A. Bogdanov[1], A.M. Krassilchtchikov[1]

[1] Ioffe Institute, St. Petersburg, Russia

✉ andrey.antonov@mail.ioffe.ru

**Abstract.** Quantitative modeling of a system of optical concentrators based on an improved design of Winston hexagonal cones, providing a possibility of using light filters and intended for the registration camera of a small-size Cherenkov gamma-ray telescope, has been performed. The transmission of the cones is calculated, and the intensity distributions of the photon flux in the detector plane are given. Based on the results obtained, an optimal configuration of optical concentrators is proposed with an account for design features of the TAIGA-IACT mount, mirror, and camera, as well as of new detector units. The results obtained for the considered system are compared with the previously published models.

**Keywords:** Cherenkov gamma-ray telescope, Winston cone, numerical simulation, TAIGA-IACT

**Funding:** This research has been supported by the Russian Science Foundation via grant 19-72-20045. The results of the presented research will be also used at UNU "Astrophysical complex MSU-ISU" (the complex is supported by the agreement 13.UNU.21.0007 between the ISU and the Ministry of Science and Higher education of Russia).

**Citation:** Antonov A.S., Bodganov A.A., Krassilchtchikov A.M., A Design of an optical concentrators array for the camera of a small-size Cherenkov gamma-ray telescope, St. Petersburg State Polytechnical University Journal. Physics and Mathematics. 16 (1.2) (2023) 417–422. DOI: https://doi.org/10.18721/JPM.161.263

This is an open access article under the CC BY-NC 4.0 license (https://creativecommons.org/licenses/by-nc/4.0/)

Материалы конференции
УДК 537.591.15
DOI: https://doi.org/10.18721/JPM.161.263

# Разработка системы оптических концентраторов для камеры малоразмерного черенковского гамма-телескопа

А.С. Антонов[1]✉, А.А. Богданов[1], А.М. Красильщиков[1]

[1] Физико-технический институт им. А.Ф. Иоффе РАН, Санкт-Петербург, Россия

✉ andrey.antonov@mail.ioffe.ru

**Аннотация.** Выполнено количественное моделирование системы оптических концентраторов на основе массива шестиугольных конусов Уинстона, предназначенной для камеры регистрации малоразмерного черенковского гамма-телескопа. Определена трансмиссия конусов, а также распределение интенсивности потока фотонов в плоскости детектора.

**Ключевые слова:** черенковский гамма-телескоп, конус Уинстона, численное моделирование, TAIGA-IACT

**Финансирование:** Авторы благодарят Российский научный фонд (РНФ) за поддержку в рамках проекта 20045-72-19.

© Antonov A.S., Bodganov A.A., Krassilchtchikov A.M., 2023. Published by Peter the Great St. Petersburg Polytechnic University.

**Ссылка при цитировании:** Антонов А.С., Богданов А.А., Красильщиков А.М. Разработка системы оптических концентраторов для камеры малоразмерного Черенковского гамма-телескопа // Научно-технические ведомости СПбГПУ. Физико-математические науки. 2023. Т. 16. № 1.2. С. 417–422. DOI: https://doi.org/10.18721/JPM.161.263

Статья открытого доступа, распространяемая по лицензии CC BY-NC 4.0 (https://creativecommons.org/licenses/by-nc/4.0/)

## Introduction

Currently, Cherenkov gamma-ray telescopes are the main type of astronomical instruments in the energy range above 0.1 TeV. Having a very large (~$10^4$–$10^5$ $m^2$) effective detection area they make it possible to measure rather weak fluxes of teravolt range gamma radiation from a number of cosmic sources (see, for example, [1, 2]). Such a large detection area is due to the fact that observations are carried out not by a direct method but by registering Cherenkov radiation of electrons and positrons of extensive air showers (EAS) initiated by primary cosmic gamma rays during their interaction with the Earth's atmosphere. The characteristic transverse size of an EAS is of the order of 200–500 m. The large detection area and the relatively low cost of Cherenkov gamma-ray telescopes provide such significant competitive advantages that, most likely, in the foreseeable future they will remain the main instruments of gamma-ray astronomy in the energy range above 0.1 TeV. Projects of new (IV) generation Cherenkov telescopes [3, 4] are in an active phase, and the existing (III generation) Cherenkov telescopes are being continuously modernized [5, 6].

Since 2019 a team from the Ioffe Institute is carrying out a project aimed at upgrading the camera of the TAIGA-IACT Cherenkov gamma-ray telescope (SINP MSU, Irkutsk University) [7, 8]. The main goal of the project is the development of new detector clusters for the TAIGA-IACT camera based on silicon photomultipliers (SiPM), which would improve the efficiency of this telescope by reducing the threshold detection energy and increasing the duty cycle [9, 10]. The detector cameras of Cherenkov gamma-ray telescopes usually consist of several hundred photomultipliers (PMTs) [11, 12], each equipped with a light concentrator (usually, a Winston cone) which performs several functions [13, 14], such as:

1) transition from the pixel size which is determined by the size of the focal plane area where the image of a Cherenkov flash is formed, and the number of camera pixels, to the size of the input window of the selected photocell, i.e., the additional concentration of source photons;

2) transition from the pixel shape (usually, a hexagon), which should ensure filling of the detector plane without gaps and overlaps in order to reduce the area of "dead" (non-recording) areas of the camera, to the shape of the input window of the selected photocell (in the case of a traditional vacuum PMT, it is usually a circle)

3) reduction of the noise background made of photons from the night sky and reflected background photons.

Such a device is typically an off-axis paraboloid of revolution, which collects a set of rays, allowing the off-axis rays to repeatedly reflect when passing from the entrance to the exit aperture. At present, Winston cones with windows in the shape of regular hexagons are used in the TAIGA-IACT telescope cameras, the exit window size (the diameter of the inscribed circle) is about 14.8 mm, which corresponds to the size of the 15 mm round entrance window of the XP1911 PMTs [15]. The planned modernization of this camera involves the employment of an assembly of four OnSemi MicroFJ-60035 SiPMs with a square-shaped entrance window with a size of about 12.8 mm as photocells [9]. Such differences would require the development of new light concentrators. In order to assess the need for changes in the design of light concentrators (Winston cones) for the upgraded TAIGA-IACT camera compared to those currently used, preliminary modeling of Winston cones was carried out using the ZEMAX package [16]. Some results of these simulations are presented below.

© Антонов А.С., Богданов А.А., Красильщиков А.М., 2023. Издатель: Санкт-Петербургский политехнический университет Петра Великого.

## Materials and Methods

The main characteristic of a Winston cone is the viewing angle θ equal to the angle of inclination of the parabola axis to the axis of the cone. This value determines the area of transmission of the cone in the space of angles, as well as the ratio of the areas of the input and output windows. A simplified (polygonal) construction of cones, consisting of a set of parabolic surfaces, is considered. Thus, the inlet and outlet of the cones are polygons. Fig. 1 shows a drawing of a modified design of an array of Winston cones with flanges for attaching light filters. The prototype of these cones with a reflective film applied to the inner surface was made for the new TAIGA-IACT camera. Based on the requirements for the design of the telescope registration camera for numerical simulation, hexagonal Winston cones were chosen, whose characteristics are close to the ideal case of a paraboloid of revolution. The calculations of [18] showed that the transmission of a hexagonal Winston cone does not differ significantly from its axisymmetric counterpart at cone angles of about 30 degrees or more. The transmission of a cone refers to the percentage ratio of the number of photons that have passed through the cone to the number of photons that have arrived at the input window of the cone.

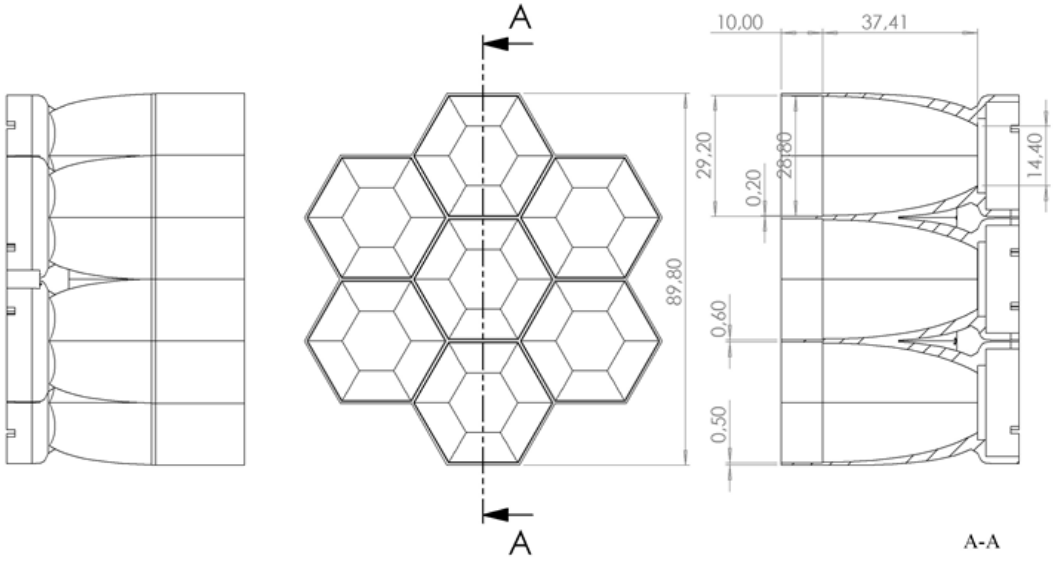


Fig. 1. Design of an array of modified Winston cones

Numerical simulations were carried out using the ZEMAX software package designed for the calculation of optical systems and optoelectronic devices. To solve problems of geometric optics, this package employs Monte Carlo ray tracing, the essence of which is to track the trajectory of rays and calculate interactions with the objects lying on the trajectories. According to the specification, the reflection coefficient of the inner surface of the Winston cones must be at least 0.95 in the wavelength range of 300–700 nm. This is the value used in the simulations.

The numerical model included a parabolic telescope mirror, a single Winston cone, and a set of 4 detectors located near the exit window of the cone. The geometrical parameters of the telescope mirror were taken as follows: the radius of the mirror, 2.16 m, and the focal length, 4.75 m. Each of the 4 detectors has the shape of a square with a side of 6.13 mm, the centers of the detectors are located in the corners of a square with a side of 6.33 mm. When determining the geometric parameters of the cone, the following relations were used:

$$\frac{R_2}{R_1} = \sin\theta, \quad h = \frac{R_1 + R_2}{\operatorname{tg}\theta},$$

where $R_1$ and $R_2$ are the radii of the inscribed circle for the input and output windows respectively, θ is the angle of the cone, $h$ is the height of the cone.

## Results and Discussion

Three variants of the cone design were considered, differing in the angle θ equal to 26.56, 30 and 35 degrees, respectively. In particular, when the angle $\theta = 30^\circ$, the ratio of the areas of the input and output windows of the cone is 4. Based on the simulation results, the angular size of a pixel of the telescope mirror and a single cone system was determined, which is a hexagonal area on the celestial sphere with an inscribed circle angular radius of 10.8′.

In the numerical simulation, the photons started from plane 2 (Fig. 2) in the direction of the telescope mirror with a uniform distribution in the coordinate space within the region bounded by a circle with a radius equal to the radius of the telescope mirror, and in the space of angles within a circle with an angular radius of 10.8′. This value corresponds to the found angular size of the pixel of the telescope mirror and a single cone system. The detectors were located at a distance of 1 mm from the output window of the cone, which made it possible to minimize signal losses. Due to the imperfection of the cone, namely to the polygonal structure, some of the photons did not pass through it and were reflected in the opposite direction. These photons were recorded on plane 2 (Fig. 2) which made it possible to determine the signal loss caused by the imperfection of the cone. Calculations have shown that the best transmission is obtained in the case of a cone angle of 30 degrees. The most significant reason for the decrease in the signal was the loss of photons in the area of the detectors. Losses due to reflection from the inner surfaces of the cones were no more than 10%. At the same time, for the construction of a cone with an angle of 26.56 degrees (at such an angle, the radius of the circumscribed circle of the output hexagon is 2 times less than the radius of the inscribed circle of the input hexagon), noticeable losses in the photon flux were associated with their reflection in the opposite direction.

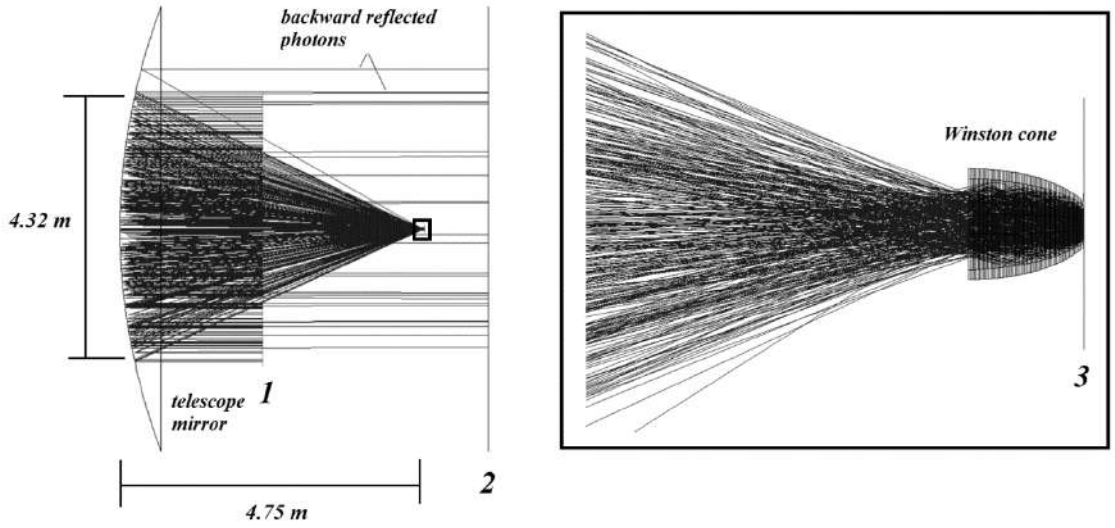


Fig. 2. Numerical model in the Zemax package including a telescope mirror and a single Winston cone: *1* is the plane of the start of photons, *2* is the plane of registration of photons reflected in the opposite direction, *3* is the plane of the detectors

The calculation of the normalized intensity distribution of the of the photon flux in the plane of the detectors (Fig. 3, *a*) showed that, despite the hexagonal shape of the cones, this distribution is generally symmetrical with respect to the axis of the cone. The intensity distribution of photons reflected in the opposite direction in plane 2 is shown in Fig. 3,*b*.

For a Winston cone with an angle of 30 degrees, a numerical simulation of a modified design with a 10 mm flange was carried out. Two variants of the reflective surface of the flange were considered: an ideally absorbing surface and a surface with a reflection coefficient of 0.95. Calculations showed that in the case of a cone model without a flange, the transmission was equal to 73.57%. At the same time, even in the case when the surface of the cone flange was ideally absorbent the transmission only decreased to 67.91%. In a realistic case, when the reflection coefficient of the cone flange was 0.95, the transmission turned out to be 72.41%.

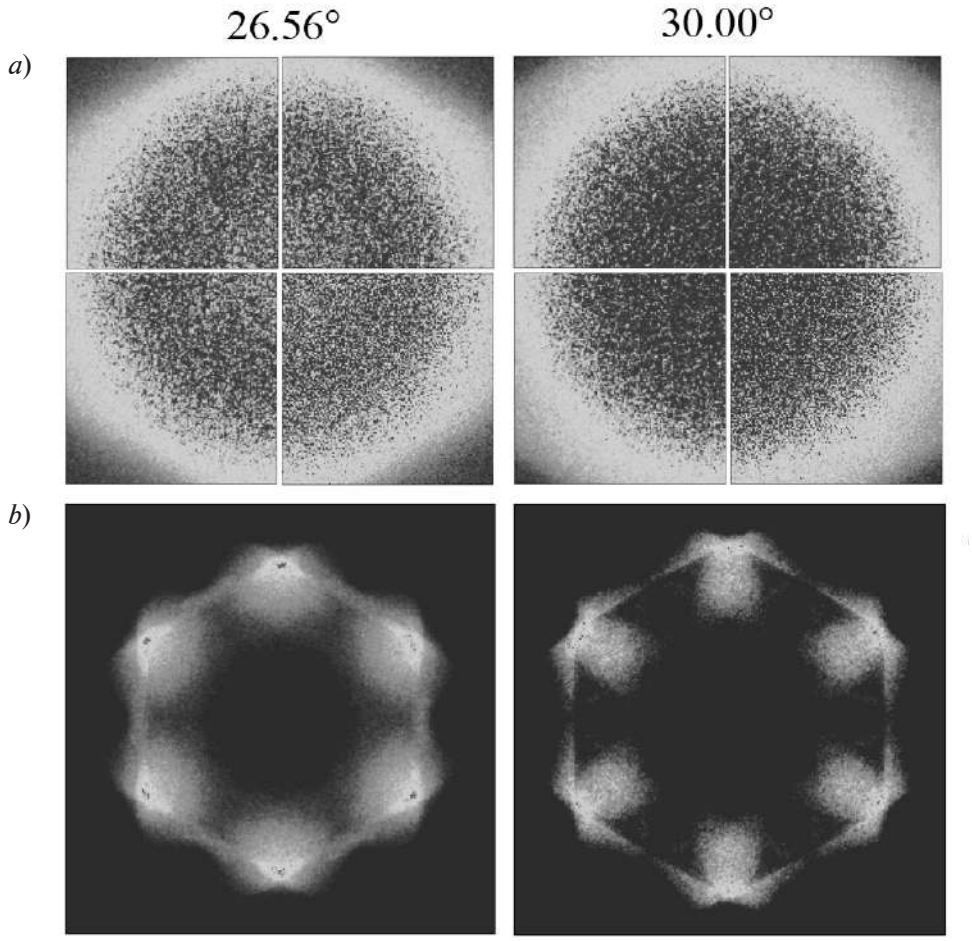


Fig. 3. Distribution of the normalized intensity of the photon flux for different cone angles: in the plane of the detectors (*a*), in the plane of registration of photons reflected in the opposite direction (*b*)

## Conclusion

Quantitative modeling of an optical concentrator array based on modified Winston hexagonal cones for a small-size Cherenkov gamma-ray telescope showed that of the 3 designs considered, a cone with a viewing angle of 30 degrees has the best performance when using a given configuration of 4 detectors. According to the results of the numerical simulation, the losses during reflection from the inner surfaces of the cone amounted to 7.43%, and the losses caused by the discrepancy between the exit window of the cone and the detectors amounted to 17.53%. Thus, the numerically found transmission of this cone was above 73%. At the same time, the addition of a filter attachment flange to the design of the cone results in only a slight reduction in transmission.

## Acknowledgments

This research has been supported by the Russian Science Foundation via grant 19-72-20045. The results of the presented research will be also used at UNU "Astrophysical complex MSU-ISU" (the complex is supported by the agreement 13.UNU.21.0007 between the ISU and the Ministry of Science and Higher education of Russia).

## REFERENCES


1. **Becherini Y., Djannati-Atai A., Punch M., Bernlцhr K. et al.,** AIP Conference Proceedings 1085 (2008) 738.
2. **Ansoldi S. et al**, Teraelectronvolt pulsed emission from the Crab Pulsar detected by MAGIC, A&A 585 (2016) A133.
3. **Barres de Almeida U.**, Status of the Cherenkov Telescope Array project, Astronomische Nachrichten 336 (8-9) (2015) 795.
4. **Bykov A. M., Aharonian F.A., Krassilchtchikov A.M. et al.**, Journal of Technical Physics 62 (2017) 819−836.
5. **Aleksic J., Ansoldi S., Antonelli L. A. et al.,** Astroparticle Physics 72 (2016) 61-75.
6. **Giavitto G., Ashton T., Balzer A. et al.**, Nuclear Instruments and Methods in Physics Research Section A 876 (2017) 35-38.
7. **L.A. Kuzmichev L.A., Astapov I.I., Bezyazeekov P.A. et al.,** Physics of Atomic Nuclei 81 (4) (2018) 497–507.
8. **Lubsandorzhiev N., Astapov I., Bezyazeekov P. et al.,** In 35th International Cosmic Ray Conference (ICRC2017) 301 (1) (2017) 757.
9. **Bogdanov A.A., Kholupenko E.E., Tuboltsev Yu.V., Chichagov Yu.V.,** Latvian J. Phis. and Tech. Science 1 (2020) 13.
10. **Kholupenko E.E., Krassilchtchikov A.M., Badmaev D.V., Bogdanov A.A., Tuboltsev Y.V., Chichagov Y.V., Antonov A.S., Kuleshov D.O., Khil'kevich E.M.,** The Application Potential of Silicon Photomultipliers for a Camera of a SmallSize Cherenkov GammaRay Telescope for Reducing the Detection Threshold, Journal of Technical Physics 65(6) (2020) 886–895.
11. **Aharonian F.A. Akhperjanian A.G. Kankanian A.S. Mirzoyan R.G. et al**., Proceedings of the 22nd International Cosmic Ray Conference. 11-23 August, 1991. Dublin, Ireland 2, (1991) 615.
12. **Bolmont J., Corona P., Gauron P. et al.,** Instrumentation and Methods for Astrophysics, Res. Sec. A 761 (2014) 46–57.
13. **Aguilar J.A., Basili A., Boccone V. et al**., Astroparticle Physics 60 (2015) 32-40.
14. **Henault F., Petrucci P.-O., Jocou L. et al.,** Proc. SPIE 8834, Nonimaging Optics: Efficient Design for Illumination and Solar Concentration X, 883405 (18 September 2013) 883405.
15. XP1911, product specification, http://www.hzcphotonics.com/products/XP1911.pdf, http://www.isuzuoptics.com.tw/data/product/photonis/pmt/19mm-1.pdf.
16. URL: http://www.zemax.com.
17. **Winston R., Jiang L., Ricketts M.**, Adv. Opt. Photonics 10 (2) (2013) 484.
18. **Coopera T., Dählera F., Ambrosetti G., Pedretti A., Steinfeld A.,** Performance of compound parabolic concentrators with polygonal apertures, Solar Energy 95 (2013) 308–318.


## THE AUTHORS


**ANTONOV Andrei S.**
andrey.antonov@mail.ioffe.ru
ORCID: 0000-0001-9356-5841

**KRASSILCHTCHIKOV Alexander M.**
kra@astro.ioffe.ru
ORCID: 0000-0001-7681-4316

**BODGANOV Alexander A.**
Alexander.A.Bogdanov@mail.ioffe.ru
ORCID: 0000-0002-5275-5603


*Received 24.10.2022. Approved after reviewing 21.11.2022. Accepted 21.11.2022.*

© Peter the Great St. Petersburg Polytechnic University, 2023

Conference materials
UDC 520.2
DOI: https://doi.org/10.18721/JPM.161.264

# Modeling of performance enhancement of the TAIGA-IACT Cherenkov gamma-ray telescope equipped with semiconductor photomultipliers

A.M. Krassilchtchikov[1]✉, E.E. Kholupenko[1], D.V. Badmaev[1], A.A. Bodganov[1]

[1] Ioffe Institute, St. Petersburg, Russia

✉ kra@astro.ioffe.ru

**Abstract.** We present modeling of effective area and count rates of a TAIGA-IACT Cherenkov gamma-ray telescope unit with an upgraded camera based on semiconductor photo detectors (SiPM) OnSemi MicroFJ-60035 and optical filters SL 290–590 and SL 280-390. In comparison with the current configuration of TAIGA-IACT where classic vacuum photomultipliers are employed, the threshold detection energy of cosmic gamma-quanta by a TAIGA-IACT unit equipped with a SIiPM-based camera and a wide-band optical filter SL 290590 would be reduced down to about 0.4 TeV, and with a narrower filter SL 280-390 down to about 0.7 TeV. Application of semiconductor photo detectors, which are stable against excess illumination, and optical filters of the near-UV band allows one to substantially increase the duty cycle of a Cherenkov gamma-ray telescopes due to the possibility to carry out observations during moonlit nights and at twilight even without a need to substantially increase the trigger threshold. Hence, one may conclude that a TAIGA-IACT unit with an upgraded camera with SiPM detectors will be an efficient instrument for studies of TeV-range emission from space gamma-ray objects.

**Keywords:** Cherenkov gamma-ray astronomy, silicon photomultipliers, TAIGA observatory

**Funding:** This research was supported by the Russian Science Foundation with the project 19-72-20045.

**Citation:** Krassilchtchikov A.M., Kholupenko E.E., Badmaev D.V., Bodganov A.A., Modeling of performance enhancement of the TAIGA-IACT Cherenkov gamma-ray telescope equipped with semiconductor photomultipliers, St. Petersburg State Polytechnical University Journal. Physics and Mathematics. 16 (1.2) (2023) 423–428. DOI: https://doi.org/10.18721/JPM.161.264

This is an open access article under the CC BY-NC 4.0 license (https://creativecommons.org/licenses/by-nc/4.0/)

© Krassilchtchikov A.M., Kholupenko E.E., Badmaev D.V., Bodganov A.A., 2023. Published by Peter the Great St. Petersburg Polytechnic University.

Материалы конференции
УДК 520.2
DOI: https://doi.org/10.18721/JPM.161.264

# Моделирование параметров черенковского гамма-телескопа TAIGA-IACT с камерой на полупроводниковых фотодетекторах

А.М. Красильщиков[1]✉, Е.Е. Холупенко[1], Д.В. Бадмаев[1], А.А. Богданов[1]

[1] Физико-технический институт им. А.Ф. Иоффе РАН, Санкт-Петербург, Россия

✉ kra@astro.ioffe.ru

**Аннотация.** В работе представлены результаты моделирования эффективной площади и скоростей счета черенковского телескопа TAIGA-IACT с модернизированной камерой, оснащенной полупроводниковыми фотодетекторами SiPM OnSemi MicroFJ-60035 и светофильтрами SL 290-590 и SL 280-390. Показано, что по сравнению текущей конфигурацией телескопа TAIGA-IACT, где используются классические вакуумные фотоэлектронные умножители, пороговая энергия регистрации космического гамма-излучения телескопом TAIGA-IACT с камерой на SiPM и широким фильтром SL 290–590 будет снижена и составит около 0.4 ТэВ, а с более узким фильтром SL 280–390 – около 0.7 ТэВ. Применение устойчивых к засветке полупроводниковых фотодетекторов и светофильтров УФ-диапазона позволяет существенно увеличить рабочий цикл черенковского гамма-телескопа за счет наблюдений в лунные ночи и в сумерках даже без значительного увеличения порога регистрации. Таким образом, можно сделать вывод, что телескоп TAIGA-IACT с модернизированной камерой на SiPM будет перспективным инструментом для исследования теравольтного излучения космических гамма-источников.

**Ключевые слова:** черенковская гамма-астрономия, полупроводниковые фотодетекторы, обсерватория TAIGA

**Финансирование:** Исследование выполнено при поддержке РНФ, проект № 19-72-20045.

**Ссылка при цитировании:** Красильщиков А.М., Холупенко Е.Е., Бадмаев Д.В., Богданов А.А. Моделирование параметров черенковского гамма-телескопа TAIGA-IACT с камерой на полупроводниковых фотодетекторах // Научно-технические ведомости СПбГПУ. Физико-математические науки. 2023. Т. 16. № 1.2. С. 423–428. DOI: https://doi.org/10.18721/JPM.161.264

Статья открытого доступа, распространяемая по лицензии CC BY-NC 4.0 (https://creativecommons.org/licenses/by-nc/4.0/)

## Introduction

The TAIGA-IACT gamma-ray telescope is an array of small-size imaging atmospheric Cherenkov gamma-ray telescopes (IACTs) operated as part of the multipurpose TAIGA observatory located in the Tunka valley of Republic of Buryatia [1–6]. Recently a new detector cluster (28 pixels) for a TAIGA-IACT unit was developed at the Ioffe Institute [7–11]. The new cluster is based on silicon photomultipliers (SiPM) OnSemi MicroFJ-60035. Development of the new hardware is accompanied by numerical modeling of its characteristics. Such modeling has been performed both for individual blocks of the new detector [12, 13] and for the telescope as a whole [14, 15]. Here we present the results of quantitative modeling of the effective area of the upgraded TAIGA-IACT unit, as well as of the count rate and of the threshold detection energy for various types of energetic primaries (gamma-quanta, cosmic ray protons).

© Красильщиков А.М., Холупенко Е.Е., Бадмаев Д.В., Богданов А.А., 2023. Издатель: Санкт-Петербургский политехнический университет Петра Великого.

## Modeling and results

Formation and propagation of Cherenkov emission of extensive air showers (EASs) triggered by energetic primaries was modeled with the standard CORSIKA package [16]. We have modeled EASs induced by vertically incident gamma-quanta and protons at logarithmically scaled energies 0.32, 0.5, 0.7, 1.0, 3.2, 10.0, 32 TeV. A typical model spectrum of EAS Cherenkov emission is shown in Fig. 1. Modeling of optical night sky background was carried out with a Monte Carlo code TAIGA Soft [15], where a set of local parameters was adopted from [17–20] and the global integral intensity in the 300-600 nm band was normalized to $3 \cdot 10^{12}$ phot/m$^2$/s/srad. A typical night sky background spectrum is also shown in Fig. 1.

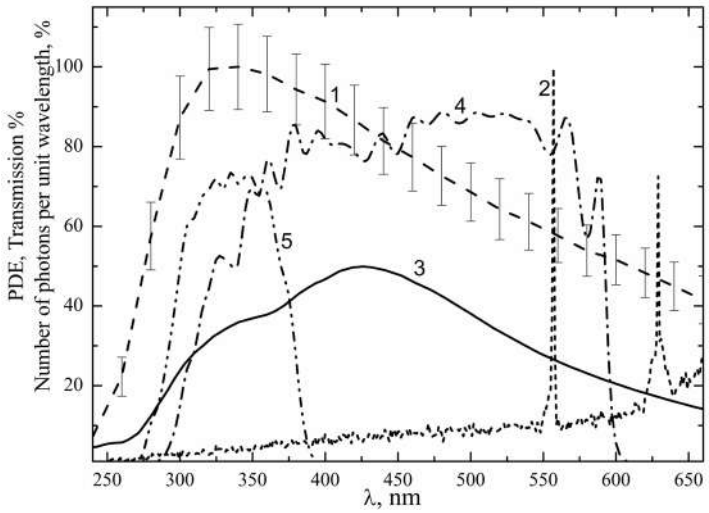


Fig. 1. Curve (1) corresponds to the averaged Cherenkov emission spectrum from and EAS induced by a 1 TeV gamma-quantum, normalized to 100% at its maximum at ~330 nm (long dash); (2) is an example of particular Monte-Carlo realization of the night sky background spectrum (normalized to 100% at its maximum at ~557 nm, short dash); curve (3) is the photon detection efficiency of the SiPM OnSemi MicroFJ-60035 photomultipliers (solid curve); curve (4) is the transmission of the SL 290-590 optical filter (dot-dashed curve); curve (5) is the transmission of the SL 280-390 optical filter (double dot-dashed curve)

With the TAIGA Soft package, we were also able to model the photon transport of the telescope and its registration within its camera. A significant difference from the algorithm described in [15] is the modification allowing a realistic approximation for the segmented mirror structure, where the effective camera mirror radius $R_T^{eff} = (S_m / \pi)^{1/2} = 1.75\,m$ ($S_m$ is the reflecting area) was replaced by the real mirror radius value $R_T = 2.15m$ and the probability of a particular photon hitting the mirror segment was $\zeta \le S_m / (\pi R_T^{\,2})$, where $\zeta$ is a random value evenly distributed over the [0; 1] interval. Within this modeling such data as wavelength dependencies of the filter transmission [22] and photon detection efficiency (PDE) of the SiPM detectors [23] were employed. The transmission of the Winston cones was conservatively set to 0.7 [13]. The triggering conditions were formulated as signal over the threshold in any three neighboring pixels; the threshold was set at the level of 10 photo electrons for the wideband filter SL 290-590 and 4 photo electrons for the medium band filter SL 280-390. Such a trigger choice reflected the balance between a relatively low false count rate ($\le 10^3$ Hz) required in order not to overload the read out chains and a relatively high percentage (~10%) of the triggered events caused by EAS emission.

The effective area of the telescope was defined as

$$S^{MC}(E) = 2\pi \int_0^{\infty} P(E,r) r dr,$$

where $P(E,r)$ is the probability to register emission of a cosmic primary of energy $E$ at the distance $r$ from the EAS axis, estimated within a Monte Carlo approach [15].

The results of effective area calculations and their approximations are shown in Fig. 2. There results show that effective areas in regards of gamma-quanta triggering are larger than those for the protons (for both filters), while the cutoff energy, where the areas begin to rapidly decline with energy, is about 2 times higher for the protons. For the highest considered energies (above 100 TeV), the modeled effective area for the protons was found to be about 0.9–1 km$^2$ and for the gamma-quanta 1.3–1.4 km$^2$. For the medium-band filter SL 280-390 the effective areas are expectedly lower. Once the effective areas are modeled with the already measured parameters of the cosmic ray spectrum [24] and typical parameters of some classes of space gamma-ray sources [25, 26], one may estimate the total count rates as integrals over energy of the product of the spectral flux (measured, e.g., in [phot m$^{-2}$s$^{-1}$TeV$^{-1}$]) and the effective area, and the threshold energies as the maxima of these products. The modeled values of a modified TAIGA-IACT camera triggering rate are ~212 Hz from proton-induced EASs and ≈ 0.13 Hz for gamma-ray induced EASs from a 1 Crab Unit object [25, 26]. The corresponding detection thresholds would be ~0.94 TeV for the protons and ~0.4 TeV for the gamma-quanta. With the medium-band filter SL 280-390 the triggering rates would decrease to ~106 Hz for the protons and to ~0.06 for the gamma-quanta, and the threshold energies increase to ~1.2 TeV and ~0.7 TeV, correspondingly.

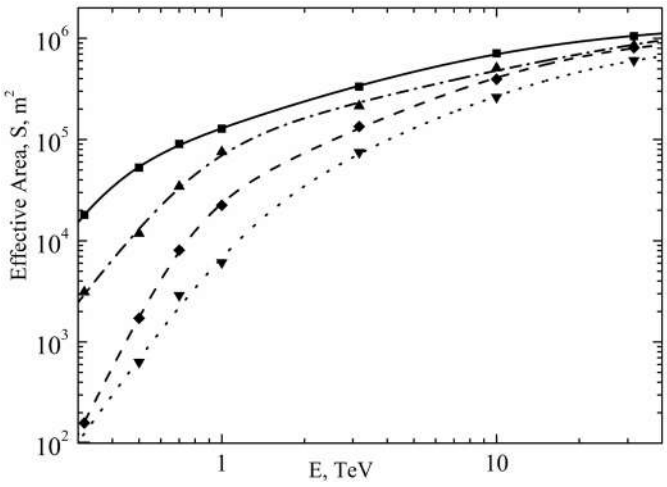


Fig. 2. Modeled effective areas of a TAIGA-IACT unit and their approximations (shown as separate symbols and curves) for various types of energetic primaries and various optical filters. The square symbols: gamma-quanta and the SL 290–590 filter; the rhomb symbols: cosmic ray protons and the SL 290–590 filter; the downward-directed triangles: gamma-quanta and the SL 280–390 filter; the upward-directed triangles: cosmic ray protons and the SL 280–390 filter.

## Conclusions

The undertaken modeling has shown that at the chosen triggering conditions the count rates in an upgraded TAIGA-IACT camera would be low enough so that the read-out electronics would not be overloaded. With an SL 290–590 filter, the threshold triggering energy can be decreased down to ~0.4, which is somewhat lower than the currently obtained threshold of the TAIGA-IACT camera based on vacuum photo multipliers (0.5 TeV, [27]).

With a medium filter SL 280–390 the threshold would be ~0.7 TeV, which is quite acceptable for small-size (about 10 sq. m mirror) IACTs. At the same time, unlike vacuum photo multipliers, which are damaged by excess illumination, the SiPM detectors are stable and can operate normally during moonlit nights and at twilight. Hence, a simultaneous application of SiPM detectors and near-UV band filters would substantially (up to 30%) increase the duty cycle of an IACT without a dramatic increase of the detection threshold.

This research was supported by the Russian Science Foundation with the project 19-72-20045. The obtained results can be applied for modernization of UNU “The Astrophysical Complex MSU-ISU” carried out within the contract 13.UNU.21.0007 between the Ministry of Science and Higher Education of Russia and the Irkutsk State University.

## REFERENCES


1. **Budnev N.M., Ivanova A.L., Kalmykov N.N., et al.,** The Tunka-Grande scintillator array of the TAIGA Gamma Ray Observatory, Bulletin of the Russian Academy of Sciences. Physics. 79(3) (2015) 395–396.

2. **Astapov I.I., Barbashina N.S., Bogdanov A.G., et al.,** The TAIGA-HiSCORE array prototype: Status and first results, Bulletin of the Russian Academy of Sciences. Physics. 81(4) (2017) 460–463.

3. **Borodin A.N., Grebenyuk V.M., Grinyuk A.A., et al.,** The IACT Optical System of the TAIGA Observatory Complex, Bulletin of the Russian Academy of Sciences. Physics. 83(8) (2019) 945–947.

4. **Prosin V.V., Astapov I.I., Bezyazeekov P.A., et al.,** Depth of the Maximum of Extensive Air Showers (EASes) and the Mean Mass Composition of Primary Cosmic Rays in the 1015−1018 eV Range of Energies, According to Data from the TUNKA-133 and TAIGA-HiSCORE Arrays for Detecting EAS Cherenkov Light in the Tunkinsk Valley, Bulletin of the Russian Academy of Sciences. Physics. 85(4) (2021) 395–397.

5. **Bezyazeekov P.A., Budnev N.M., Chernykh D.O., et al.,** Precise Reconstruction of a Shower Maximum in the Tunka Radio Extension Experiment, Bulletin of the Russian Academy of Sciences. Physics. 83(8) (2019) 998–1000.

6. **Kuzmichev L.A., Astapov I.I., Bezyazeekov P.A., et al.,** TAIGA Gamma Observatory: Status and Prospects, Physics of Atomic Nuclei. 81(4) (2018) 497-501.

7. **Bogdanov A.A., Tuboltsev Y.V., Chichagov Y. V., et al.,** Measurements of the 277 nm photon detection efficiency of the OnSemi MicroFJ-60035 silicon photomultiplier, Journal of Physics Conference Series. 1697(1) (2020) id. 012015.

8. **Bogdanov A.A., Tubol'tsev Y.V., Chichagov Y.V., et al.,** Temperature Dependence of the Sensitivity of Silicon Photomultipliers in the Regime of Single-Photon Detection of Ultraviolet Radiation, Technical Physics. 66(5) (2021) 699–704.

9. **Bogdanov A.A., Tuboltsev Y.V., Chichagov Y.V., et al.,** Development of detector pixels based on silicon photomultipliers for the Cherenkov gamma-ray telescope TAIGA-IACT, Journal of Physics: Conference Series. 2103(1) (2021) article id. 012026.

10. **Kuleshov D.O., Simonyan V.A., Bogdanov A.A., et al.,** Measurement of the photon detection efficiency of silicon photomultipliers for the new detector cluster of the Cherenkov gamma-ray telescope TAIGA-IACT equipped with UV filters, Journal of Physics Conference Series. 2103(1) (2021) article id. 012036.

11. **Bogdanov A.A., Repman G.A., Tubol'tsev Y.V., et al.,** Development of detector cluster based on silicon photomultipliers for the Cherenkov gamma-ray telescope TAIGA-IACT, Journal of Physics Conference Series. (2022), accepted for publication.

12. **Bogdanov A.A., Kholupenko E.E., Tuboltsev Y.V., Chichagov Y.V.,** Modelling of SiPM performance for detection of Cherenkov radiation from extensive air showers in UV and visible ranges for application at the TAIGA-IACT telescope, Latvian Journal of Physics and Technical Sciences. 57(1-2) (2020) 13–21.

13. **Antonov A.S., Bogdanov A.A., Krasilshchikov A.M., Kholupenko E.E.,** Modelirovanie opticheskih kontsentratorov dlya modernizirovannoj kamery cherenkovskogo gamma-teleskopa TAIGA-IACT, Zhurnal tekhnicheskoj fiziki. 91(11) (2021) 1601–1607.

14. **Kholupenko E.E., Krassilchtchikov A.M., Badmaev D.V., et al.,** The Application Potential of Silicon Photomultipliers for a Camera of a Small-Size Cherenkov Gamma-Ray Telescope for Reducing the Detection Threshold, Technical Physics. 65(6) (2020) 886–895.

15. **Kholupenko E.E., Badmaev D.V., Antonov A.S., et al.,** Small-Size Cherenkov Telescope with an SiPM-Based Camera: Full-Particle Modeling of the Cosmic gamma-Ray Source Detection Threshold, Technical Physics. 67(2) (2022) 80–103.

16. **Heck D., Knapp J., Capdevielle J. N., Schatz G., Thouw T.,** CORSIKA: a Monte Carlo code to simulate extensive air showers. Forschungszentrum Karlsruhe GmbH, Karlsruhe (Germany), (1998).

17. **Leinert C., Bowyer S., Haikala L. K., et al.,** The 1997 reference of diffuse night sky brightness, Astronomy and Astrophysics Supplement. 127(1) (1998) 1–99.

18. **Benn C.R., Ellison S.L.,** Brightness of the night sky over La Palma, New Astronomy Reviews. 42(6-8) (1998) 503-507.

19. **Mikhalev A.V., Medvedeva I.V., Beletsky A.B., Kazimirovsky E.S.,** An investigation of the upper atmospheric optical radiation in the line of atomic oxygen 557.7 nm in East Siberia, Journal of Atmospheric and solar-terrestrial physics. 63(9) (2001) 865–868.

20. **Mirzoyan R., Lorenz E.,** Internal report of the HEGRA collaboration. MPI-PhE/94-35, Muenchen (1994).

21. **Budnev N., Astapov I., Bezyazeekov P., et al.,** The TAIGA experiment: from cosmic ray to gamma-ray astronomy in the Tunka valley, Journal of Physics: Conference Series. 718(5) (2016) article id. 052006.

22. **Zabudko M.A.,** Specifications of optical filters SL 280 - 390 and SL 290 - 590. Photooptic Ltd., Moscow (2021).

23. ON Semiconductor J-Series SiPM Sensors. Silicon Photomultipliers (SiPM), High PDE and Timing Resolution Sensors in a TSV Package. (2017).

24. **Alfaro R., Alvarez C., Alvarez J. D., et al.,** All-particle cosmic ray energy spectrum measured by the HAWC experiment from 10 to 500 TeV, Physical Review D. 96(12) (2017) article id. 122001.

25. **Nigro C., Deil C., Zanin R., et al.,** Towards open and reproducible multi-instrument analysis in gamma-ray astronomy, Astronomy & Astrophysics. 625 (2019) article id. A10 .

26. **Abeysekara A.U., Albert A., Alfaro R., et al.,** Measurement of the Crab Nebula Spectrum Past 100 TeV with HAWC, The Astrophysical Journal. 881(2) (2019) article id. 134.

27. **Tluczykont M., Budnev N., Astapov I., et al.,** Connecting neutrino Astrophysics to Multi-TeV to PeV gamma-ray astronomy with TAIGA, Proceedings of Magellan Workshop: Connecting Neutrino Physics and Astronomy, Deutsches Elektronen-Synchrotron, DESY: Magellan Workshop, Hamburg, Germany, 17 Mar 2016 - 18 Mar 2016.

## THE AUTHORS

**KRASSILCHTCHIKOV Alexander M.**
kra@astro.ioffe.ru
ORCID: 0000-0001-7681-4316

**BADMAEV Danr V.**
danir1996@mail.ru

**KHOLUPENKO Evgeny E.**
eugene@astro.ioffe.ru

**BODGANOV Alexander A.**
Alexander.A.Bogdanov@mail.ioffe.ru
ORCID: 0000-0002-5275-5603

*Received 25.10.2022. Approved after reviewing 08.11.2022. Accepted 15.11.2022.*

© Peter the Great St. Petersburg Polytechnic University, 2023

Conference materials
UDC 524.8
DOI: https://doi.org/10.18721/JPM.161.265

# Positron production due to interaction of cosmological background photons

A.N. Popov[1], D.P. Barsukov[1]✉, A.V. Ivanchik[1], S.V. Bobashev[1]

[1] Ioffe Institute, St. Petersburg, Russia

✉ bars.astro@mail.ioffe.ru

**Abstract.** The interaction of photons of the cosmological background radiation with producing electron-positron pairs is considered. It is shown that main input in positron production is given by interaction of cosmological gamma-ray background photons with photons of extragalactic background light, although taking into account the interaction of cosmological gamma-ray background photons with cosmological ultraviolet background photons may substantially increase the pair production rate.

**Keywords:** positron, photon, cosmology radiation background

**Citation:** Popov A.N., Barsukov D.P., Ivanchik A.V., Bobashev S.V., Positron production due to interaction of cosmological background photons, St. Petersburg State Polytechnical University Journal. Physics and Mathematics. 16 (1.2) (2023) 429–435. DOI: https://doi.org/10.18721/JPM.161.265

This is an open access article under the CC BY-NC 4.0 license (https://creativecommons.org/licenses/by-nc/4.0/)

Материалы конференции
УДК 524.8
DOI: https://doi.org/10.18721/JPM.161.265

# Генерация позитронов при взаимодействии фотонов космологического фона

А. Н. Попов[1], Д. П. Барсуков[1]✉, А. В. Иванчик[1], С. В. Бобашев[1]

[1] Физико-технический институт им. А.Ф. Иоффе РАН, Санкт-Петербург, Россия

✉ bars.astro@mail.ioffe.ru

**Аннотация**. Рассматривается взаимодействие фотонов космологического фонового излучения с рождением пар. Показано, что основной вклад в рождение пар дает взаимодействие фотонов космологического гамма-фона с фотонами внегалактического оптического излучения, хотя учет взаимодействия фотонов космологического гамма-фона с фотонами космологического ультрафиолетового фона может существенно увеличить темп рождения позитронов.

**Ключевые слова**: позитрон, фотон, космологическое фоновое излучение

Ссылка при цитировании: Попов А.Н., Барсуков Д.П., Иванчик А.В., Бобашев С.В. Генерация позитронов при взаимодействии фотонов космологического фона // Научно-технические ведомости СПбГПУ. Физико-математические науки. 2023. Т. 16. № 1.2. С. 429–435. DOI: https://doi.org/10.18721/JPM.161.265

Статья открытого доступа, распространяемая по лицензии CC BY-NC 4.0 (https://creativecommons.org/licenses/by-nc/4.0/)

© Popov A.N., Barsukov D.P., Ivanchik A.V., Bobashev S.V., 2023. Published by Peter the Great St. Petersburg Polytechnic University.

## Introduction

The cosmological background radiation (CB) is homogeneous, isotropic radiation that fills all Universe. The main component of CB is cosmological microwave background radiation (CMB) which is a relict of the epoch of reionization and it gives us a knowledge about process in this epoch [1]. The second most important [1] component of CB is optical extragalactic background light (EBL). It is mainly created by radiation of stars and consequently it contains a history of star formation [1–3]. The cosmological gamma-ray background radiation (CGB) is mainly created by supernovae and active galactic nuclei and hence it gives us an information about evolution of activity of galactic nuclei and star formation rate [1, 4]. The cosmological X-ray background radiation (CXB) is mainly created by radiation of accretion disks in the galactic nuclei [1, 5]. And the cosmological ultraviolet background radiation (CUB) is mainly radiated by hot young stars and interstellar nebulae [1] and consequently gives us an information about evolution of these objects. In this paper we consider the production of electron-positron pairs due to interaction of high energetic but not numerous CGB photons with numerous but low energetic EBL and CUB photons.

## Photon-photon interaction

Let us consider the interaction of two photons producing electron-positron pair. The cross-section σ of this process is given by the following expression [6]:

$$\sigma = \sigma(s) = \frac{\pi}{2} r_e^2 \cdot \left(1 - v^2\right) \times \times \left( \left(3 - v^2\right) \ln\left(\frac{1+v}{1-v}\right) - 2v\left(2 - v^2\right) \right) \cdot h\left(s - 1\right), \tag{1}$$

where $r_e = e^2/mc^2$ is classical electron radius, $m$ is the rest mass of electron, $h(x)$ is Heaviside function ($h(x) = 1$ at $x > 0$ and $h(x) = 0$ at $x < 0$),

$$v = \sqrt{1 - 1/s} \text{ and } s = \frac{1}{2} \frac{\varepsilon_1 \varepsilon_2}{m^2 c^4} \left(1 - \cos \Psi\right), \tag{2}$$

$\varepsilon_1$ and $\varepsilon_2$ are photons energies and $\Psi$ is angle between the momenta of the two photons, see Fig. 1. In the case of isotropic photon distribution the pair production rate is given by the following expression:

$$Q_{tot} = \int_0^{+\infty} Q \cdot d\varepsilon_1 d\varepsilon_2 = \int_0^{+\infty} c\Sigma\left(\frac{\varepsilon_1 \cdot \varepsilon_2}{m^2 c^4}\right) \cdot \frac{dn_1}{d\varepsilon_1}(\varepsilon_1) \cdot \frac{dn_2}{d\varepsilon_2}(\varepsilon_2) \cdot d\varepsilon_1 d\varepsilon_2, \tag{3}$$

where $Q_{tot}$ is total number of pairs produced in 1 cm$^3$ per 1 s, $dn_i = \frac{dn_i}{d\varepsilon_i}(\varepsilon_i) \cdot \mathrm{d}\varepsilon_i$ is the number density of photons of kind $i$ with energy $\varepsilon_i \in d\varepsilon_i$, $i = 1, 2$ and functions $Q$ and $\Sigma(s)$ are defined as

$$Q = c\Sigma\left(\frac{\varepsilon_1 \cdot \varepsilon_2}{m^2 c^4}\right) \cdot \frac{dn_1}{d\varepsilon_1}(\varepsilon_1) \cdot \frac{dn_2}{d\varepsilon_2}(\varepsilon_2), \text{ and } \Sigma(s) = \frac{2}{s^2} \cdot \int_1^s \sigma(\tilde{s}) \cdot d\tilde{s}, \tag{4}$$

so $dN = Q \cdot d\varepsilon_1 d\varepsilon_2$ is number of pairs produced in 1 cm$^3$ per 1 s by interaction of photons with energies $\varepsilon_1$ and $\varepsilon_2$, which lies in intervals $d\varepsilon_1$ and $d\varepsilon_2$correspondingly and $\Sigma(s)$ may be considered as averaged cross-section. The graphics of functions $\sigma(s)$ and $\Sigma(s)$ are presented in left panel of Fig. 2.

© Попов А.Н., Барсуков Д.П., Иванчик А.В., Бобашев С.В., 2023. Издатель: Санкт-Петербургский политехнический университет Петра Великого.

In the case of "power-law" photon spectrum $\frac{dn_1}{d\varepsilon_1}(\varepsilon_1) = \mathrm{K}\,\varepsilon_1^{-\gamma_1} \cdot h\left(\varepsilon_1 - \varepsilon_1^{\min}\right)$ and $\frac{dn_2}{d\varepsilon_2}(\varepsilon_2) = \mathrm{K}\,\varepsilon_2^{-\gamma_2} \cdot h\left(\varepsilon_2^{\max} - \varepsilon_2\right) \cdot h\left(\varepsilon_2 - \varepsilon_2^{\min}\right)$ and with the assumptions $\gamma_1 > 2$ and $\varepsilon_1^{\min} \cdot \varepsilon_2^{\max} \le m^2c^4$ the total pair production rate is equal to

$$Q_{tot} = c\Sigma_{\gamma_1} \cdot n_1 \cdot n_2 \cdot 2 \cdot \frac{\gamma_1 - 1}{\gamma_1 + 1} \cdot \frac{1 - \gamma_2}{\gamma_1 - \gamma_2} \cdot \frac{1 - r_2^{\gamma_1 - \gamma_2}}{1 - r_2^{1-\gamma_2}} \cdot \left( \frac{\varepsilon_1^{\min} \cdot \varepsilon_2^{\max}}{m^2c^4} \right)^{\gamma_1 - 1}, \qquad (5)$$

where $r_2 = \varepsilon_2^{\min} / \varepsilon_2^{\max}$, $\Sigma_\gamma = \int_1^{+\infty} \sigma(s) \cdot s^{-\gamma} \cdot ds$ and $n_i = \int_0^{+\infty} \frac{dn_i}{d\varepsilon_i}(\varepsilon_i) \cdot d\varepsilon_i$ is the number density of photons of kind $i$, $i$ = 1, 2. The dependence of $\Sigma(s)$ on $\gamma$ is presented on right panel of Fig. 2.

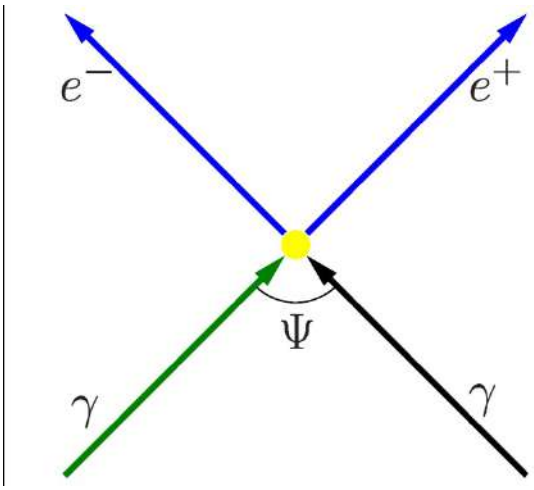


Fig. 1. Sketch to illustrate the interaction of two photons producing electron-positron pair

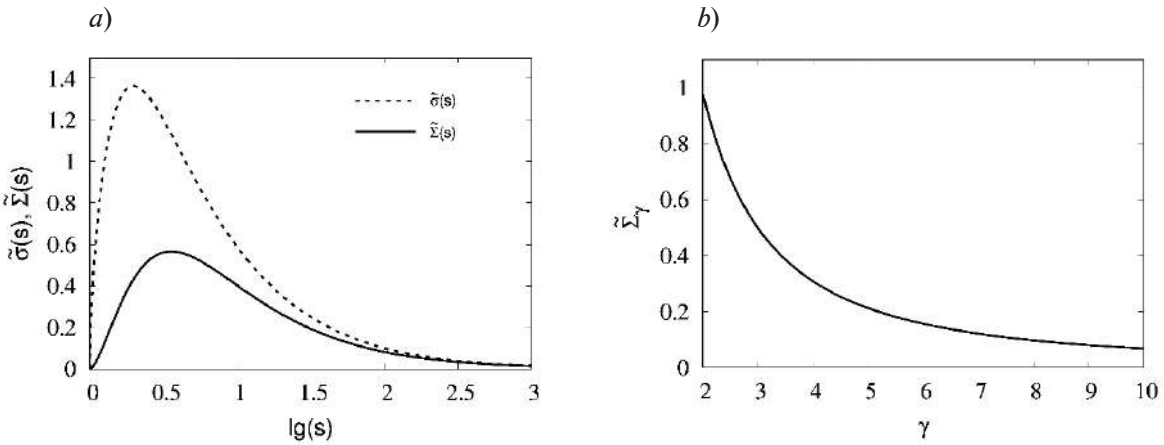


Fig. 2. Graphs of functions $\sigma(s)$ and $\Sigma(s)$ are presented on left panel (*a*).
Dashed line corresponds to normalized cross-section of pair production $\tilde{\sigma}(s) = 2 \cdot \sigma(s) / (\pi r_e^2)$
and solid line corresponds to normalized averaged cross-section $\tilde{\Sigma}(s) = 2 \cdot \Sigma(s) / (\pi r_e^2)$.
The dependence of $\tilde{\Sigma}_\gamma = 2 \cdot \Sigma_\gamma / (\pi r_e^2)$ on parameter $\gamma$ is presented on right panel (*b*)

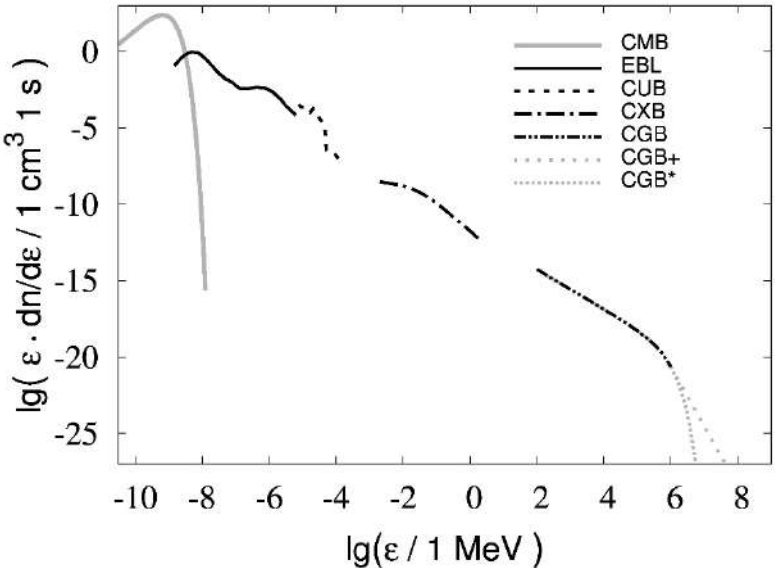


Fig. 3. CB spectrum used in calculation are presented. The CMB spectrum is shown with the solid gray line. The EBL spectrum taken from [3] is shown with the solid black line, the upper limit on the CUB spectrum taken from [1] is shown with the dashed black line, the CXB spectrum taken from [5] is shown with the dot-dashed black line and the CGB spectrum taken from [4] is shown with the double dot-dashed black line. The extrapolations of the CGB spectrum up to 100 TeV are shown with the dotted gray lines

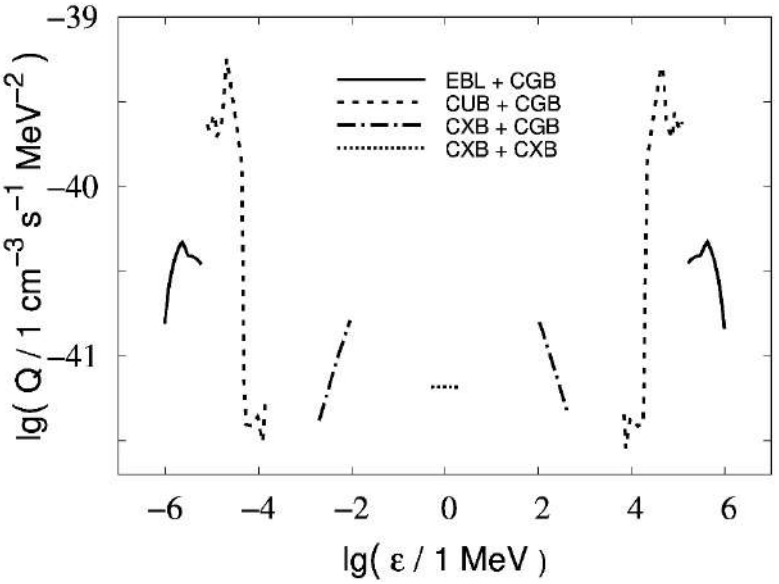


Fig. 4. The dependence of pair production rate $Q$ (in units of $1\text{cm}^{-3}\,\text{s}^{-1}\,\text{MeV}^{-2}$) on photon energy ε is presented. The solid line corresponds to the interaction of the CGB photons with the EBL photons, the dashed line corresponds to the interaction of the CGB photons with the CUB photons, the dot-dashed line corresponds to the interaction of the CGB photons with the CXB photons and the dotted line corresponds to the interaction of the CXB photons with itself

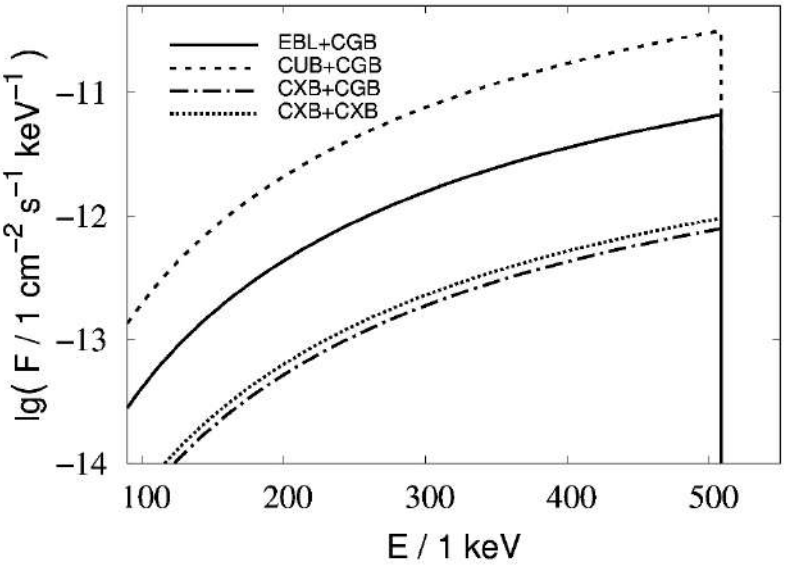


Fig. 5. Here $F$ is annihilation photon flux (at $z$ =0) in units of 1 cm$^{-2}$ s$^{-1}$ keV$^{-1}$, $E$ is annihilation photon energy. The lines mean the same as in Fig. 4

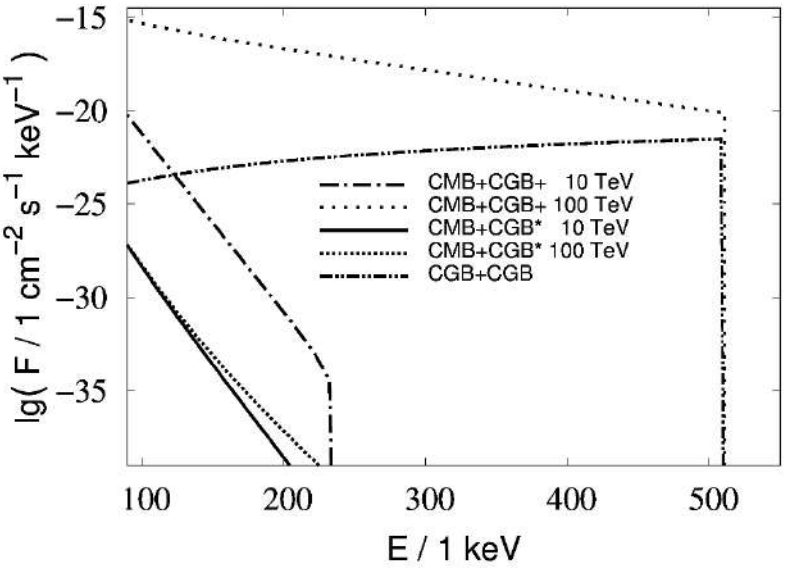


Fig. 6. Same as Fig. 5, but the case of the interaction of the CMB photons with the CGB photons is presented. The solid and the dot-dashed lines correspond to extrapolation of the CGB spectrum up to 10 TeV, the dotted lines correspond to extrapolation of the CGB spectrum up to 100 TeV. The double dot-dashed line corresponds to the interaction of the CGB photons with itself

## Results

We have considered the interaction of CGB photons with CXB and EBL photons. Spectrum of CGB, CXB and EBL photons used in calculation taken from [4], [5] and [3] correspondingly are presented in Fig. 3. The resulting pair production rate $Q_{tot}$ values are presented in table 1. In order to estimate pair production rate due to the interaction of CGB photons with CUB photons we also consider the case when CUB photons spectra coincides with its upper limits taken from [1]. In this paper we neglect the interaction of CGB photons with itself because of it gives negligible pair production rate.

Table 1

**Pair production rate $Q_{tot}$ in units of 1 cm$^{-3}$ s$^{-1}$.**

| | EBL+CGB | CUB+CGB | CXB+CGB | CGB+CGB | CXB+CXB |
|---|---|---|---|---|---|
| $Q_{tot}$ | $5.0\cdot10^{-37}$ | $2.4\cdot10^{-36}$ | $6.0\cdot10^{-38}$ | $2.3\cdot10^{-47}$ | $7.3\cdot10^{-38}$ |

In calculation of the pair production rate $Q_{tot}$ the EBL spectrum is taken in range 1.5 meV–3 eV, the CXB spectrum is taken in range 2 keV-1.5 MeV, the CGB spectrum is taken in range 100 MeV–1 TeV and the upper limit of the CUB spectrum is taken in range 7.5–120 eV

The dependence of pair production rate $Q$ on photon energies is presented in Fig. 4. Here we assume that photon energies are related as $\varepsilon_1\cdot\varepsilon_2=\varepsilon_0^2$ where $\varepsilon_1$ is the energy of EBL, CUB or CXB photon correspondingly, $\varepsilon_2$ is energy of CGB photon and $\varepsilon_0\approx 1$ MeV. A such value of $\varepsilon_0$ corresponds to the maximum of averaged cross-section $\Sigma$. This figure shows that the interaction of CGB photons with EBL photons gives main input in electron-positron pairs production although the taking into account the interaction of CGB photons with CUB photons may substantially increase the pair production rate.

The positrons created due to these interactions will slow down and annihilate later producing two or three photons. In this paper we, for simplicity, assume that all positrons annihilate immediately and neglect of annihilation photon absorption. Also we neglect the input of three photon annihilation and suppose that CB spectrum do not depend on red shift $z$. In this case the observed (at $z = 0$) distribution of annihilation photons may be written as

$$\frac{dN}{dVdEd\Omega}=\frac{Q_{tot}}{4\pi}\cdot\frac{1}{H_0}\cdot\frac{1}{mc^2}\cdot\left(\frac{E}{mc^2}\right)^2\cdot\frac{1}{\tilde{F}(mc^2/E)}\cdot h\left(mc^2-E\right), \tag{6}$$

where $E$ is energy of annihilation photon (at $z = 0$), $E=mc^2/(1+z)$ and $H_0=67.8$ km s$^{-1}$ Mpc$^{-1}$ is Hubble constant at present epoch ($z = 0$) [7]. In case of standard $\Lambda$CDM-cosmological model (at $z\ll z_{eq}$ where $z_{eq}\approx 3365$ is the redshift of the transition from a radiation-dominated to a matter-dominated Universe) the function $\tilde{F}(x)$ is equal to $\tilde{F}(x)=\sqrt{\Omega_\Lambda+\Omega_M\cdot x^3}$, where coefficients $\Omega_\Lambda=0.692$ and $\Omega_M=0.308$ describe relative fractions of dark energy and dark matter correspondingly [7]. The resulting profile of annihilation line is presented in figure 5. The width of this "line" is very large $\Delta E\sim 100-150$ keV and the line flux is about $F\sim 10^{-12}$ cm$^{-2}$ s$^{-1}$ keV$^{-1}$ without taking into account the interaction of CGB and CUB photons and may achieve $F\sim 10^{-11}$ cm$^{-2}$ s$^{-1}$ keV$^{-1}$ with taking into account this interaction.

We also consider the interaction of photons of the extrapolated CGB spectrum with the CMB photons. The resulted profiles of annihilation line are presented in figure 6. In calculation only the CMB photons with frequencies $\nu\le 3$ THz are taken in account because of the EBL radiation has already totally dominated at $\nu\sim 3$ THz, see Fig. 3. We consider two variants of extrapolation. The CGB+ spectrum corresponds to power law extrapolation by using last two point, the CGB* spectrum corresponds to extrapolation by using approximation formula $\varepsilon\cdot\frac{dn}{d\varepsilon}(\varepsilon)=I_{100}\cdot\left(\frac{\varepsilon}{100MeV}\right)^{-\gamma+1}\cdot\exp\left(-\frac{\varepsilon}{\varepsilon_{cut}}\right)$ where $\gamma\approx 2.3$, $I_{100}\approx 5.4\cdot10^{-14}$ cm$^{-3}$ and $\varepsilon_{cut}\approx 366$ GeV [4], see Fig. 3. The two cases of extrapolation up to 10 TeV and up to 100 TeV correspondingly are considered. Also the profile of annihilation line due to the interaction of the CGB photons with itself is presented in figure 6. It is easy to see that the positron production due to the interaction of the CMB photons with the CGB photons is comparable to the production by the interaction of the CGB photons with itself. So its input to the total positron production is negligible too. The cutoff of annihilation line in the case of the CGB+ spectrum extrapolated up to 10 TeV at $E\approx 230$ keV is artificial and is related to our restriction on the considered CMB photons energies $\nu\le 3$ THz.

**Acknowledgments**

We sincerely thank D.S. Svinkin for comments and useful discussions.

## REFERENCES

1. **Hill R., Masui K. W., Scott D.**, The spectrum of Universe, Applied Spectroscopy, 72 (5) (2018) 663—688.

2. **Cooray A.**, Extragalactic background light measurement and applications, Royal Society Open Science, 3 (3) (2016) 150555.

3. **Franceschini A., Rodighiero G., Vaccari M.**, Extragalactic optical-infrared background radiation, its time evolution and the cosmic photon-photon opacity, Astronomy and Astrophysics, 487 (3) (2008) 837—852.

4. **Ackermann M. et al**, The spectrum of isotropic diffuse gamma-ray emission between 100 MeV and 820 GeV, Astrophysical Journal, 799 (1) (2015) 86.

5. **Ajello M., Greiner J., Sato G., Willis D.R., Kanbach G., Strong A. W., Diehl R., Hansinger G., Gehrels N., Markwardt C.B., Tueller J.**, Cosmic X-ray background and Earth albedo spectra with Swift BAT, Astrohysical Journal, 689 (2) (2008) 666—677.

6. **Gould R. J., Schreder G. P.**, Opacity of the Universe to high-energy photons, Physical Review, 155 (5) (1967) 1404—1407.

7. **Ade P. A. R. et al**, Planck 2015 results. XIII. Cosmological parameters, Astronomy and Astrophysics, 594 (2016) A13.

## THE AUTHORS

**POPOV Alexandr N.**
alexander.popov@mail.ioffe.ru
ORCID: 0000-0002-5112-3452

**IVANCHIK Alexandre V.**
iav.astro@mail.ioffe.ru
ORCID: 0000-0003-2155-0813

**BARSUKOV Dmitry P.**
bars.astro@mail.ioffe.ru
ORCID: 0000-0002-3358-2014

**BOBASHEV Sergey V.**
S.Bobashev@mail.ioffe.ru
ORCID: 0000-0003-2648-8895

*Received 27.10.2022. Approved after reviewing 08.11.2022. Accepted 08.11.2022.*

© Peter the Great St. Petersburg Polytechnic University, 2023

Conference materials
UDC 524.7
DOI: https://doi.org/10.18721/JPM.161.266

# HD molecules in the Magellanic Clouds

D.N. Kosenko[1]✉, S.A. Balashev[1]

[1] Ioffe Institute, St. Petersburg, Russia

✉ kosenkodn@yandex.ru

**Abstract.** We present the detection of HD absorption lines in the Magellanic Clouds using FUSE space telescope archival data. We found HD in five (including one known) absorption systems in the Large Magellanic Cloud and three systems in the Small Magellanic Cloud. The measured HD column densities, N(HD), vary from $2{\cdot}10^{13}$ to $2{\cdot}10^{15}$ $cm^{-2}$ for associated $H_2$ column densities, $NH_2$, in the range $3{\cdot}10^{19}$ to $5{\cdot}10^{20}$ $cm^{-2}$. Using Hubble Space Telescope archival data, we also determined the population of CI fine-structure levels and metallicities in these systems. The modelling of obtained observational data for HD, $H_2$ and C I allow us to estimate physical conditions in the interstellar medium of the Magellanic Clouds associated with these absorption systems, namely, the cosmic ray ionization rate, ultraviolet field intensity and number density.

**Keywords:** galaxies, ISM, molecules, cosmic rays

**Funding:** RSF grant 18-12-00301.

**Citation:** Kosenko D.N., Balashev S.A., HD molecules in the Magellanic Clouds. St. Petersburg State Polytechnical University Journal. Physics and Mathematics. 16 (1.2) (2023) 436–441. DOI: https://doi.org/10.18721/JPM.161.266

This is an open access article under the CC BY-NC 4.0 license (https://creativecommons.org/licenses/by-nc/4.0/)

Материалы конференции
УДК 524.7
DOI: https://doi.org/10.18721/JPM.161.266

# Молекулы HD в Магеллановых Облаках

Д.Н. Косенко[1]✉, С.А. Балашев [1]

[1] Физико-технический институт им. А.Ф. Иоффе РАН, Санкт-Петербург, Россия

✉ kosenkodn@yandex.ru

**Аннотация**. Мы представляем детектирование абсорбционных линий молекул HD в Магеллановых Облаках в архивных данных космического телескопа FUSE. Мы нашли HD в пяти (включая одну уже известную) абсорбционных системах в Большом Магеллановом Облаке и в трех системах в Малом Магеллановом Облаке. Полученные лучевые концентрации HD, N(HD), варьируются от $2{\cdot}10^{13}$ до $2{\cdot}10^{15}$ $см^{-2}$, концентрации $N(H_2)$ находятся в диапазоне от $3{\cdot}10^{19}$ до $5{\cdot}10^{20}$ $см^{-2}$. Используя архивные данные космического телескопа «Хаббл», мы также оценили относительную населенность уровней тонкой структуры C I и металличность в этих системах. Моделирование полученных результатов для HD, $H_2$ и C I позволило оценить физические условия в межзвездной среде в Магеллановых Облаках, а именно, скорость ионизации космическими лучами, интенсивность УФ поля и объемную концентрацию.

**Ключевые слова**: галактики, МЗС, молекулы, космические лучи

**Финансирование:** грант РНФ №18-12-00301.

**Ссылка при цитировании:** Косенко Д.Н., Балашев С.А. Молекулы HD в Магеллановых Облаках // Научно-технические ведомости СПбГПУ. Физико-математические науки. 2023. Т. 16. № 1.2. С. 436–441. DOI: https://doi.org/10.18721/JPM.161.266

Статья открытого доступа, распространяемая по лицензии CC BY-NC 4.0 (https://creativecommons.org/licenses/by-nc/4.0/)

© Kosenko D.N., Balashev S.A., 2023. Published by Peter the Great St. Petersburg Polytechnic University.

## Introduction

One of the most important constituent of the galaxies is the interstellar medium (ISM) due to its tight connection to galaxy evolution and star formation processes. The cold phase of ISM, which is an important step of the medium on its way to gravitational collapse, can be in principle traced by molecular hydrogen $H_2$, which is the most abundant molecule in the Universe. In case when $H_2$ abundance is large enough, one can detect its isotopoloque, deuturated hydrogen (HD), see e.g. [1–3] and references therein. However, the detection of $H_2$ and HD in emission is a quite challenging task even in our Galaxy, so the main way of learning about these molecules is the absorption line spectroscopy. The resonant HD and $H_2$ absorption lines are located in ultraviolet domain, so a bit paradoxically, their observations are simplified at high redshifts, $z \gtrsim 2$, since the lines are shifted in the optical domain and quasar can be used as a background sources, that allow to exploit large ground telescopes with high resolution spectrographs (see e.g. [4, 5]). Nevertheless, UV space telescopes (e.g. Copernicus, Far Ultraviolet Spectroscopic Explorer (FUSE)) were extensively used for the measurements of $H_2$ and HD in the Milky Way [1, 6, 7] and in the local galaxies, mostly including Magellanic Clouds [8].

The Large and Small Magellanic Clouds are one of the closest galaxies to ours (with distance ~50 and ~60 kpc, respectively) have significantly lower metallicities, ~0.5 and 0.2 of solar, respectively. The distance to Magellanic Clouds allows one to observe individual bright stars, that were used by [8] to obtain a sample of the $H_2$ absorption systems with FUSE. We recently showed [9], that HD abundance may significantly enhance at low metallicities (that is corroborated by observations at high redshifts), therefore the Magellanic Clouds may provide as important test to further study this behaviour. Additionally, $HD/H_2$ ratio is sensitive to physical conditions in the cloud, especially, to the cosmic ray ionization rate (CRIR) [9], which was exhaustively studied in Milky Way, but is quite poorly known in other galaxies. Finally, obtained estimates [3] were performed only towards individual sightlines within each remote galaxy, at the same time, the proximity of the Magellanic Clouds gives a good opportunity to study CRIR towards multiple sightlines within the galaxy.

Therefore, we decided to make an extensive search for HD absorption lines in the Magellanic Clouds. We present four and three new detection of HD in the LMC and SMC, respectively, and we reanalysed one already known system in the LMC. To derive physical conditions in the absorption systems we used the observed abundances of HD as well as C I fine-structure and $H_2$ rotational levels and Zn II column density.

## Data and analysis

We used FUSE archival spectra to search for HD in the sample of known $H_2$ absorption systems associated in the Magellanic Clouds [8]. We considered the systems with $H_2$ column densities $\log N_{H_2} > 18$ (here and in the following text column densities are expressed in $cm^{-2}$). HD detection was previously reported in the system towards Sk-69 246 [10], but we reanalyzed HD and $H_2$ to make the analysis homogeneous. In general, we identified HD in four and three sightlines towards the LMC and SMC, respectively. We also independently reanalysed $H_2$ absorption lines to constrain the population of $H_2$ rotational levels. Metal lines were analysed in the spectra obtained using STIS and COS spectrographs on board of the Hubble Space Telescope (HST). To model line profiles we performed standard multicomponent Voigt profile fitting using the Monte Carlo Markov Chain sampler, that allow us to obtain the posterior distribution function of absorption system parameters. To report the values of fit parameters and its uncertainties we used maximum aposterior probability estimate and highest posterior density 68.3% credible intervals, respectively.

## FUSE data

The sample of spectra obtained by the FUSE telescope [11, 12] towards stars in Magellanic Clouds is available in the FUSE Magellanic Clouds Legacy Project [13]. We used spectra from 1A LiF channel, as they cover most of HD and $H_2$ lines. Unfortunately, most of FUSE spectra have low S/N and are not properly wavelength calibrated, so we decided to improve the quality of calibration. First, we obtained a zero order coadded solution by alignment of exposures from the individual sightlines using cross-correlation procedure [14, 15] to find achromatic shift between

© Косенко Д.Н., Балашев С.А., 2023. Издатель: Санкт-Петербургский политехнический университет Петра Великого.

exposures. Then we used the $H_2$ synthetic spectrum as a template to obtain wavelength dependent shifts for individual $H_2$ lines individually for each exposure. We selected narrow unblended $H_2$ lines and calculated cross-correlation function with the corresponding lines from the synthetic template. We fitted the wavelength dependency of the estimated shifts using piece-wise linear functions, that was finally used to correct the individual exposures before the final coadding. In most cases this procedure improves a quality of calibration.

The nominal FUSE resolution is $R = \lambda/\Delta\lambda = 20000$, but we notice that it can be likely reduced by the procedure of coadding of individual exposures, calibration routine and other systematics effects of observations. Therefore we assumed $R$ as an independent fitting parameter. We also allowed Doppler parameters for all rotational levels to vary independently, but used the penalty function to obtain the proper $H_2$ excitation diagram (for details see [3, 16]).

## HST data

Since, most of the metal and C I lines are not covered by FUSE, to estimate C I column densities and metallicities in the HD/$H_2$ absorption systems we used archival data obtained by the STIS/COS at HST and downloaded from the MAST archive[1]. Some of the systems have already been analyzed by [17, 18], but we reanalyzed them to get independent results. We fitted C I absorption lines from three fine-structure levels where we tied Doppler parameters. To obtain metallicity[2] we fitted Zn II absorption lines and used $N_{\mathrm{H\,I}}$ values obtained by [8] and solar values of $\log(\mathrm{X/H})_\odot$ from [19].

## Results

We summarize our measurements of HD, $H_2$ and C I in Table 1. We report four and three new HD detections in the LMC and SMC, respectively. In Fig. 1 we compare the values of HD and $H_2$ column densities measured in the Magellanic Clouds with already known systems (at high redshifts and in the Milky Way) and D/H isotopic ratio. One can see that Galactic measurements of HD/ $H_2$ are well below the D/H isotopic ratio, while the measurements at high redshifts do not show such tendency. As we showed in [9], it can be explained by the difference in physical conditions, primarily by systematically lower metallicity for systems at high redshifts. Measurements in the Magellanic Clouds show the same tendency as in our Galaxy despite they have lower metallicity that is comparable (in case of the SMC) with the average of high-z values. In principle, since the HD is sensitive to the other physical conditions (e.g. CRIR, UV field intensity and column density), it can be partly explained by a higher UV field intensity (see the next section).

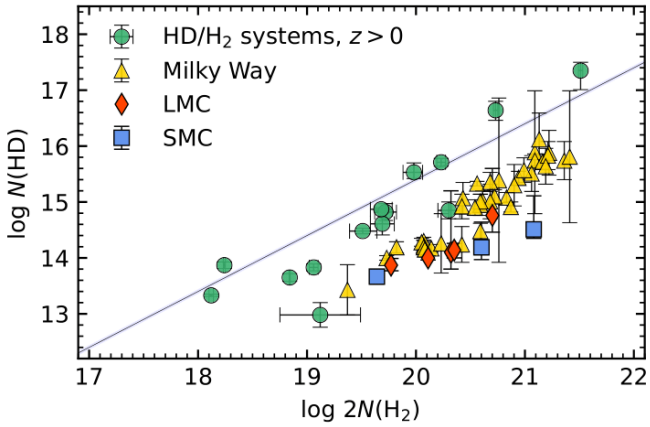


Fig. 1. Relative abundance of HD and $H_2$ molecules. The red diamonds and blue squares correspond to measurements in the LMC and SMC, respectively, obtained in this work. The green circles are detections at high redshifts (for references see [3]), yellow triangles are measurements in our Galaxy. The solid blue line shows the D/H primordial isotopic ratio [20].

[1] https://archive.stsci.edu/

[2] metallicity relative to solar is $Z = [\mathrm{X/H}] = \log(\mathrm{X/H}) - \log(\mathrm{X/H})_\odot$

Table 1

**Summary of measured HD, $H_2$, C I and Zn II column densities in the absorption systems in the Magellanic Clouds**

| Star | HI* | $H_2$ | HD | C I | ZnII |
|---|---|---|---|---|---|
| Sk-67 5 | 21.00 | $19.470^{+0.001}_{-0.001}$ | $13.87^{+0.12}_{-0.10}$ | $15.04^{+0.01}_{-0.01}$ | $12.80^{+0.02}_{-0.01}$ |
| Sk-70 79 | 21.18 | $20.04^{+0.03}_{-0.04}$ | $14.76^{+0.84}_{-0.30}$ | $14.39^{+0.01}_{-0.01}$ | $13.09^{+0.02}_{-0.02}$ |
| Sk-68 135 | 21.60 | $20.02^{+0.01}_{-0.01}$ | $14.1^{+1.1}_{-0.3}$ | $14.44^{+0.01}_{-0.01}$ | $13.31^{+0.01}_{-0.01}$ |
| Sk-69 246 | 21.41 | $19.81^{+0.01}_{-0.01}$ | $14.00^{+0.04}_{-0.04}$ | $14.25^{+0.03}_{-0.02}$ | $13.38^{+0.01}_{-0.01}$ |
| BI 253 | 21.60 | $20.05^{+0.01}_{-0.01}$ | $14.14^{+0.12}_{-0.14}$ | $15.31^{+0.40}_{-0.77}$ | $13.49^{+0.01}_{-0.01}$ |
| AV 80 | 21.81 | $20.30^{+0.01}_{-0.01}$ | $14.19^{+0.45}_{-0.22}$ | $13.70^{+0.03}_{-0.02}$ | $13.22^{+0.02}_{-0.01}$ |
| AV 488 | 21.15 | $19.340^{+0.001}_{-0.020}$ | $13.67^{+0.09}_{-0.08}$ | $13.36^{+0.03}_{-0.03}$ | $12.99^{+0.02}_{-0.02}$ |
| Sk 191 | 21.51 | $20.78^{+0.03}_{-0.03}$ | $14.51^{+0.60}_{-0.16}$ | $13.87^{+0.02}_{-0.02}$ | $12.55^{+0.03}_{-0.04}$ |

*values taken from [8]

## Physical conditions

To obtain physical conditions in the systems we followed method described by [3] and based on the balance equation of HD formation and destruction processes. We have showed that this relatively simple formalism gives result close to that calculated by Meudon PDR code [21] which takes into account a large chemical network. The fit parameters of the model (that was compared with the observed HD/ $H_2$ ratio) are the cosmic ray ionization rate (CRIR, ξ) UV field intensity (χ), number density (*n*) and metallicity (Z).

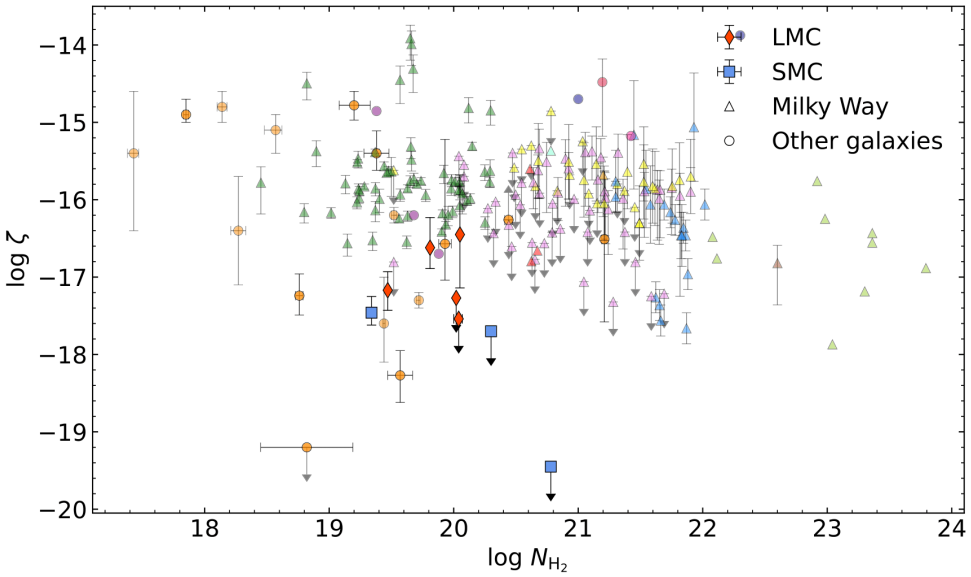


Fig. 2. Cosmic ray ionization rate as a function of H2 column density. The red squares and blue diamonds show to measurements in the Magellanic Clouds obtained in this work. The triangles are values from our Galaxy, circles are high redshifts measurements (see [3])

We used estimated Zn II and H I (measured by [8]) column densities to obtain metallicity (provided in Table 2), which was fixed in following calculations. Using the same methodology as was done in [5, 22], we consequently used the population of $H_2$ rotational and C I fine-

structure levels to constrain the number density and UV field intensity. Finally, we used these estimates as priors (with additional flat prior for $\xi$) during Markov Chain Monte Carlo sampling to derive posterior probability distributions on the model parameters. The obtained parameters are shown in Table 2 and in Fig. 2 we present CRIR as a function of $N_{H2}$ (which is connected to cloud depth). One can see that found CRIR values are lower than on average in our Galaxy, therefore HD formation rate is not enough to produce sufficient HD for self-shielding from UV radiation and hence HD column density is found to be quite low. Also the upper limit in the system towards Sk 191 may be treated as an outlier, since the system has exceptionally low metallicity, so this system requires additional study.

Table 2

**Derived physical conditions in the absorption systems in the Magellanic Clouds**

| Star | Z[†] | log*n* | log$\chi$ | log$\xi$ |
|---|---|---|---|---|
| Sk-67 5 | $-0.76^{+0.05}_{-0.05}$ | $2.45^{+0.25}_{-0.11}$ | $0.55^{+0.13}_{-0.12}$ | $-17.17^{+0.24}_{-0.26}$ |
| Sk-70 79 | $-0.65^{+0.05}_{-0.05}$ | $3.02^{+0.27}_{-0.31}$ | $1.17^{+0.16}_{-0.11}$ | $\lesssim -17.54$ |
| Sk-68 135 | $-0.85^{+0.05}_{-0.05}$ | $2.52^{+0.22}_{-0.15}$ | $2.1^{+0.6}_{-0.4}$ | $\lesssim -17.27$ |
| Sk-69 246 | $-0.59^{+0.05}_{-0.05}$ | $2.24^{+0.21}_{-0.15}$ | $1.85^{+0.21}_{-0.31}$ | $-16.64^{+0.41}_{-0.25}$ |
| BI 253 | $-0.67^{+0.05}_{-0.05}$ | $0.87^{+0.49}_{-0.46}$ | $1.58^{+0.24}_{-0.21}$ | $-16.45^{+0.77}_{-0.69}$ |
| AV 80 | $-1.15^{+0.05}_{-0.05}$ | $1.97^{+0.14}_{-0.23}$ | $1.89^{+0.31}_{-0.24}$ | $\lesssim -17.70$ |
| AV 488 | $-0.72^{+0.05}_{-0.05}$ | $2.16^{+0.18}_{-0.28}$ | $0.53^{+0.13}_{-0.12}$ | $-17.46^{+0.21}_{-0.16}$ |
| Sk 191 | $-1.51^{+0.06}_{-0.06}$ | $2.60^{+0.20}_{-0.16}$ | $0.83^{+0.17}_{-0.11}$ | $\lesssim -19.45$ |

[†] Uncertainties of solar values $N_{Zn}$ from [19] dominate over uncertainties of Zn II column densities in the presented systems, therefore almost all metallicity uncertainties are the same

## Conclusions

We present a detection of HD in five (four new) systems in LMC and three systems in SMC. We measured that HD column density varies from ~ $10^{13}$ to ~$10^{15}$ cm$^{-2}$. We also reanalyzed $H_2$ absorption lines, analyzed C I lines and estimated metallicity to constrain physical conditions in the systems using population of C I fine structure and $H_2$ rotational levels. Using our formalism [9] we obtained the cosmic ray ionization rate in LMC and SMC to have typical values of $\xi \sim 10^{-17}$ s$^{-1}$.

## REFERENCES

1. **Snow T.P. et al.,** A New FUSE Survey of Interstellar HD, Astroph.J., 2008, vol. 688, 1124—36.

2. **Varshalovich D.A. et al.,** HD Molecular Lines in an Absorption System at Redshift z = 2.3377, Astronomy Letters, 2001, Vol. 27, 683—5.

3. **Kosenko D.N. et al.,** HD molecules at high redshift: cosmic ray ionization rate in the diffuse interstellar medium, MNRAS, 2021, Vol. 505, 3810—22.

4. **Noterdaeme P., et al.,** HD molecules at high redshift. A low astration factor of deuterium in a solar-metallicity DLA system at z = 2.418, Astron. Astroph., 2008, vol.491, 397—400.

5. **Balashev S.A., et al.,** X-shooter observations of strong $H_2$-bearing DLAs at high redshift, MNRAS, 2019, Vol. 490, 2668—78.

6. **Savage B.D., et al.,** A survey of interstellar molecular hydrogen. I., Astroph. J., 1977, Vol. 216, 291–307.
7. **Shull J.M., et al.,** A Far Ultraviolet Spectroscopic Explorer Survey of Interstellar Molecular Hydrogen in the Galactic Disk, Astroph. J., 2021, Vol. 911, 55.
8. **Welty D.E., et al.,** Interstellar H I and $H_2$ in the Magellanic Clouds: An Expanded Sample Based on Ultraviolet Absorption-line Data, Astroph. J., 2012, Vol. 745, 173.
9. **Balashev S.A., Kosenko D.N.,** HD/$H_2$ ratio in the diffuse interstellar medium, MNRAS, 2020, Vol. 492, L45—9.
10. **Bluhm H., de Boer K.S.,** $H_2$, HD, and CO at the edge of 30 Dor in the LMC: The line of sight to Sk-69 246, Astron. Astroph., 2001, Vol. 379, 82–9.
11. **Moos H.W., et al.,** Overview of the Far Ultraviolet Spectroscopic Explorer Mission, Astroph. J. Lett, 2000, Vol. 538, L1–6.
12. **Sahnow D.J., et al.,** On-Orbit Performance of the Far Ultraviolet Spectroscopic Explorer Satellite, Astroph. J. Lett., 2000, Vol. 538, L7–11.
13. **Blair W.P., et al.,** The Far Ultraviolet Spectroscopic Explorer Legacy in the Magellanic Clouds: An Online Stellar Sight Line Atlas, Pub. Astron. Soc. Paific, 2009, Vol. 121, 634.
14. **Simkin S.M.,** Measurements of Velocity Dispersions and Doppler Shifts from Digitized Optical Spectra, Astron. Astroph., 1974, Vol. 31, 129.
15. **Tonry J, and Davis M.,** A survey of galaxy redshifts. I. Data reduction techniques, Astron. J., 1979, Vol. 84, 1511–25.
16. **Noterdaeme P., et al.,** Down-the-barrel observations of a multi-phase quasar outflow at high redshift. VLT/X-shooter spectroscopy of the proximate molecular absorber at z = 2.631 towards SDSS J001514+184212, Astron. Astroph., 2021, Vol. 646, A108.
17. **Roman-Duval J., et al.,** METAL: The Metal Evolution, Transport, and Abundance in the Large Magellanic Cloud Hubble Program. II. Variations of Interstellar Depletions and Dust-to-gas Ratio within the LMC, Astroph. J., 2021, Vol. 910, 95.
18. **Tchernyshyov K., et al.,** Elemental Depletions in the Magellanic Clouds and the Evolution of Depletions with Metallicity, Astroph. J., 2015, Vol. 811, 78.
19. **Asplund M., et al.,** The Chemical Composition of the Sun, Ann. Rev. Astron. Astroph., 2009, Vol. 47, 481–522.
20. Planck Collaboration, Planck 2018 results. VI. Cosmological parameters, Astron. Astroph, 2020, Vol. 641, A6.
21. **Le Petit F., et al.,** A Model for Atomic and Molecular Interstellar Gas: The Meudon PDR Code, Astroph. J. Suppl., 2006, Vol. 164, 506–29.
22. **Klimenko V.V., Balashev S.A.,** Physical conditions in diffuse interstellar medium of local and high redshift galaxies: measurements based on excitation of $H_2$ rotational and CI fine-structure levels, MNRAS, 2020, Vol. 498, 1531–49.

## THE AUTHORS

**KOSENKO Daria N.**
kosenkodn@yandex.ru
ORCID: 0000-0001-7431-8298

**BALASHEV Sergei A.**
s.balashev@gmail.com

*Received 28.10.2022. Approved after reviewing 09.11.2022. Accepted 10.11.2022.*

© Peter the Great St. Petersburg Polytechnic University, 2023

Conference materials
UDC 52.6, 533.9
DOI: https://doi.org/10.18721/JPM.161.267

# Stability of steady states of plasma diodes with counter-streaming electron and positron flows

V.I. Kuznetsov[1]✉, L.A. Bakaleinikov[1], E.Yu. Flegontova[1]

[1] Ioffe Institute, St. Petersburg, Russia

✉ victor.kuznetsov@mail.ioffe.ru

**Abstract.** Stability of steady states of a planar geometry diode with counter flows of electrons and positrons is studied. The study is related to the elucidation of pulsar RF radiation nature. The equation for the electric field perturbation is derived. Its exact solution is obtained for the case of a homogeneous steady-state field. The study of the dispersion equation obtained has shown that there is a threshold for the inter-electrode gap value, above which steady-state solutions are unstable. The instability threshold turned out to be √2 times higher than the known Pierce threshold._

**Keywords:** plasma diode, electron and positron flows, plasma instability

**Funding:** This study was funded by Government project "Physics of elementary, collective and dynamic processes in high-speed gas flows, low-temperature plasma and heterogeneous media", grant [0040-2019-0022]).

**Citation:** Kuznetsov V.I., Bakaleinikov L.A., Flegontova E.Yu., Stability of steady states of plasma diodes with counter-streaming electron and positron flows, St. Petersburg State Polytechnical University Journal. Physics and Mathematics. 16 (1.2) (2023) 442–448. DOI: https://doi.org/10.18721/JPM.161.267

This is an open access article under the CC BY-NC 4.0 license (https://creativecommons.org/licenses/by-nc/4.0/)

Материалы конференции
УДК 52.6, 533.9
DOI: https://doi.org/10.18721/JPM.161.267

# Устойчивость стационарных состояний плазменного диода со встречными пучками электронов и позитронов

В.И. Кузнецов[1]✉, Л.А. Бакалейников[1], Е.Ю. Флегонтова[1]

[1] Физико-технический институт им. А.Ф. Иоффе РАН, Санкт-Петербург, Россия

✉ victor.kuznetsov@mail.ioffe.ru

**Аннотация.** Исследована устойчивость стационарных состояний плоского вакуумного диода со встречными пучками электронов и позитронов. Исследование связано с выяснением природы радиоизлучения пульсаров. Получено уравнение, описывающее эволюцию малого возмущения электрического поля. В случае однородного стационарного электрического поля найдено его аналитическое решение. Исследование полученного дисперсионного уравнения показало, что существует порог по длине вакуумного зазора, выше которого стационарные состояния неустойчивы. Порог устойчивости оказался в √2 раз выше известного порога Пирса.

**Ключевые слова:** плазменный диод, потоки электронов и позитронов, плазменная неустойчивость_

© Kuznetsov V.I., Bakaleinikov L.A., Flegontova E.Yu., 2023. Published by Peter the Great St. Petersburg Polytechnic University.

**Финансирование:** Работа выполнена в рамках Государственного задания «Физика элементарных, коллективных и динамических процессов в высокоскоростных газовых потоках, низкотемпературной плазме и гетерогенных средах» (код темы [0022-2019-0040]).

**Ссылка при цитировании:** Кузнецов В.И., Бакалейников Л.А., Флегонтова Е.Ю. Устойчивость стационарных состояний плазменного диода со встречными пучками электронов и позитронов // Научно-технические ведомости СПбГПУ. Физико-математические науки. 2023. Т. 16. № 1.2. С. 442–448. DOI: https://doi.org/10.18721/JPM.161.267

Статья открытого доступа, распространяемая по лицензии CC BY-NC 4.0 (https://creativecommons.org/licenses/by-nc/4.0/)

## Introduction

Since the discovery of pulsars in 1967, the understanding of the physical processes responsible for their RF radiation has not advanced much compared to the classical works [1, 2]. Neither the mechanism of this radiation nor the reason for switching between modes have been understood so far. It is only in recent years that astrophysicists have come to understanding that the radiation is associated with collective processes in plasma formed by electrons and positrons in a pulsar diode [3]. In this case, it can be argued that the RF radiation of pulsars is caused by electric field oscillations that occur during the development of instability in the plasma. It is like the Bursian-Pierce instability that is characteristic of diodes with collisionless plasma [4].

Steady-state solutions for a planar geometry diode with counter flows of charged particles of opposite signs moving in plasma without collisions were studied in detail in [5]. It was shown that there are two modes: 1) all charged particles move in the inter-electrode gap without reflection and reach the opposite electrodes, 2) the potential distribution has extrema reflecting the portion of the particles. The paper examines the stability of steady-state solutions of the first type. The equation for the electric field perturbation is derived. Its analytical solution is found for the case of a homogeneous steady-state field. The study of dispersion relation has shown that there is a threshold for the gap value, when exceeded, an aperiodic instability develops in the diode plasma.

## Derivation of equations

We consider a diode of planar geometry. We assume that electrons enter the plasma from the left electrode with a non-relativistic velocity $v_{e,0}$ and density $n_{e,0}$, and positrons enter from the right electrode with a non-relativistic velocity $-v_{p,0}$ and density $n_{p,0}$. Charged particles move without collisions, and when reaching the electrode they are absorbed. We assume that electrons and positrons enter into inter-electrode gap with the same kinetic energies, i.e., $W_0 \equiv m_e v_{e,0}^2/2 = m_p v_{p,0}^2/2$ (here $m_e$ and $m_p$ are the masses of the electron and positron).

For the convenience, we turn to dimensionless quantities, choosing the electron energy at the left boundary $W_0$ and the Debye-Hückel length $\lambda_D = [2\varepsilon_0 W_0/(e^2 n_{e,0})]^{1/2}$ as units of energy and length (here $e$ is the electron charge, and $\varepsilon_0$ is the vacuum permeability).

For the density of electrons entering from the left electrode and moving without reflection in a time-dependent field, the following expression is obtained in Ref. [6]

$$n_e(\eta,\tau) = \left[\left(1+2\eta+2G_e(\eta)\right)^{-1/2} - Q_e(\eta)\right]^{-1}. \quad (1)$$

Here

$$G_e(\zeta,\tau;u_{e,0},\tau_{e,0}) = -\int_{\tau_0}^{\tau} dt\,\frac{\partial}{\partial t}\eta(\zeta,t),$$

$$Q_e(\zeta,\tau;u_{e,0},\tau_{e,0}) = \quad (2)$$

$$= -\int_0^{\tau-\tau_{e,0}} dt(\tau-\tau_{e,0}-t)\frac{d}{d\tau_{e,0}}\varepsilon\left[\zeta(t+\tau_{e,0});u_{e,0},\tau_{e,0}\right]_{u_{e,0}=const}.$$

© Кузнецов В.И., Бакалейников Л.А., Флегонтова Е.Ю., 2023. Издатель: Санкт-Петербургский политехнический университет Петра Великого.

For the density of positively charged particles entering from the right electrode and moving without reflection in a time-dependent field, an expression similar to Eq. (1) is obtained in Ref. [7]

$$n_p(\eta,\tau)=\left\{\left|-\left[1-2(\eta-V)+2G_p(\eta)\right]^{1/2}-Q_p(\eta)\right|\right\}^{-1}. \tag{3}$$

Here

$$G_p(\zeta,\tau;u_{p,0},\tau_{p,0})=\int_{\tau_0}^{\tau}dt\frac{\partial}{\partial t}\eta(\zeta,t),$$

$$Q_p(\zeta,\tau;u_{p,0},\tau_{p,0})= \tag{4}$$

$$=\int_0^{\tau-\tau_{p,0}}dt(\tau-\tau_{p,0}-t)\frac{d}{d\tau_{p,0}}\varepsilon\left[\zeta(t+\tau_{p,0});u_{p,0},\tau_{p,0}\right]_{u_{p,0}=const}.$$

In Eqs. (1–4), $\tau$, $\zeta$, $\eta$ and $\varepsilon$ are dimensionless time, coordinate, potential and electric field strength, while $\tau_{e,0}$, $u_{e,0}$, $\tau_{p,0}$ and $u_{p,0}$ are the time moments and velocities of the departure of electrons and positrons from the corresponding electrodes. Note that in Eqs. (1) and (3), the value of $G$ is equal to the amount of energy that a charged particle acquires ($G>0$) or loses ($G<0$) when moving in a time-dependent field, and the function $Q$ characterizes the additional (compared to motion in a stationary field) compression (or extension) experienced by a group of particles that have left the boundary with velocities within a narrow range.

The potential distribution (PD) at each moment $\tau$ is found as a solution of the second order equation, which is obtained after substituting expressions for the densities of electrons (1) and positrons (3) into Poisson's equation

$$\frac{d^2\eta}{d\zeta^2}=\left[\left(1+2\eta+2G_e(\eta)\right)^{1/2}-Q_e(\eta)\right]^{-1}- \tag{5}$$

$$-\left\{\left[1-2\left(\eta-V\right)+2G_p(\eta)\right]^{1/2}+Q_p(\eta)\right\}^{-1}.$$

Studying the stability features of solutions, we consider small perturbations of PD in the form

$$\eta(\zeta,\tau)=\eta_0(\zeta)+\tilde{\eta}(\zeta)\exp(-i\Omega\tau), \tag{6}$$

$$|\tilde{\eta}(\zeta)|<<\eta_0(\zeta).$$

In this case, we can assume that $G_{e,i}(\zeta,\tau)=\tilde{G}_{e,i}(\zeta)\exp(-i\Omega\tau)$, $Q_{e,i}(\zeta,\tau)=\tilde{Q}_{e,i}(\zeta)\exp(-i\Omega\tau)$, and both of these functions are quantities of the order of $\tilde{\eta}$ [6], [7]. Expanding both parts of Eq. (5) in a power series in small potential perturbation amplitude and taking into account the linear terms only, we get

$$\tilde{\eta}''(\zeta)=-u_{e,0}^{-3}(\zeta)\left[\tilde{\eta}(\zeta)+\tilde{G}_e(\zeta)\right]+u_{e,0}^{-2}(\zeta)\tilde{Q}_e(\zeta)- \tag{7}$$

$$-u_{p,0}^{-3}(\zeta)\left[\tilde{\eta}(\zeta)-\tilde{G}_p(\zeta)\right]+u_{p,0}^{-2}(\zeta)\tilde{Q}_p(\zeta).$$

In Eq. (7),

$$u_{e,0}(\zeta)=\left[1+2\eta_0(\zeta)\right]^{1/2}, \tag{8}$$

$$u_{p,0}(\zeta)=\left[1-2\eta_0(\zeta)+2V\right]^{1/2}$$

are the undisturbed velocities of electrons and positrons corresponding to the monoenergetic particle velocity distributions. The following expressions are obtained for the functions $\tilde{G}_e$, $\tilde{Q}_e$, $\tilde{G}_p$ and $\tilde{Q}_p$ in Refs. [8] and [7]:

$$\tilde{G}_e(\zeta) = -\tilde{\eta}(\zeta) + \int_0^\zeta dx\tilde{\eta}'(x)\exp\left\{i\Omega[\sigma_e(\zeta) - \sigma_e(x)]\right\},$$

$$\tilde{Q}_e(\eta) = -i\Omega u_{e,0}(\zeta)\int_0^\zeta dx[u_{e,0}(x)]^{-3}\int_0^x dy\tilde{\eta}'(y)\exp\left\{i\Omega[\sigma_e(\zeta) - \sigma_e(y)]\right\},$$

$$\tilde{G}_p(\zeta) = \tilde{\eta}(\zeta) + \int_\zeta^\delta dx\tilde{\eta}'(x)\exp\left\{i\Omega[\sigma_p(\zeta) - \sigma_p(x)]\right\}, \quad (9)$$

$$\tilde{Q}_p(\zeta) = i\Omega u_{p,0}(\zeta)\int_\zeta^\delta dx[u_{p,0}(x)]^{-3}\int_x^\delta dy\tilde{\eta}'(x)\exp\left\{i\Omega[\sigma_p(\zeta) - \sigma_p(x)]\right\}.$$

Here

$$\sigma_e(\zeta) = \int_0^\zeta dx[u_{e,0}(x)]^{-1},\ \sigma_p(\zeta) = \int_\zeta^\delta dx[u_{p,0}(x)]^{-1} \quad (10)$$

are times of electron and positron flight from the corresponding electrode to the point $\zeta$ in an undisturbed field.

After substituting (9) into (7), we obtain an integral-differential equation for an amplitude of the potential perturbation, which, after a single integration using the boundary condition for the potential perturbation at the right boundary $\tilde{\eta}(\delta) = 0$ takes the following form:

$$\tilde{\eta}'(\zeta) + \int_0^\zeta dx[u_{e,0}(x)]^{-3}\int_0^x dy\tilde{\eta}'(y)\exp\left\{i\Omega[\sigma_e(\zeta) - \sigma_e(y)]\right\} +$$
$$+\int_\zeta^\delta dx[u_{p,0}(x)]^{-3}\int_x^\delta dy\exp\left\{i\Omega[\sigma_p(\zeta) - \sigma_p(y)]\right\}\tilde{\eta}'(y) = A. \quad (11)$$

Here

$$A = \tilde{\eta}'(\delta) + \int_0^\delta dx[u_{e,0}(x)]^{-3}\int_0^x dy\exp\left\{i\Omega[\sigma_e(\delta) - \sigma_e(y)]\right\}\tilde{\eta}'(y), \quad (12)$$

and the value of the derivative $\tilde{\eta}'(\delta)$ is an arbitrary parameter.

Thus, we have obtained for the first time an equation for the amplitude of the electric field perturbation in a diode with counter flows of electrons and positrons.

**Study of homogeneous steady-state solutions stability**

Consider the special case of $\eta_0(\zeta) \equiv 0$. Here $u_{e,0}(\zeta) = 1$, $u_{p,0}(\zeta) = 1$ (the latter is the velocity absolute value), $\sigma_e(\zeta) = \zeta$, $\sigma_p(\zeta) = \delta - \zeta$. After making simple calculations and getting rid of 2-fold integrals, for the Eq. (11) we get

$$\tilde{\eta}'(\zeta) + \int_0^\zeta dxK_+(\zeta - x)\tilde{\eta}'(x) - \int_\zeta^\delta dxK_-(\zeta - x)\tilde{\eta}'(x) = A. \quad (13)$$

Here

$$A = \tilde{\eta}'(\delta) + \int_0^\delta dxK_+(\delta - x)\tilde{\eta}'(x),\ K_\pm(t) = t\exp(\pm i\Omega t). \quad (14)$$

Eq. 13 is an integral equation of the convolution type. It is solved using the Laplace transform. For the image $f(p)$ of the function $\tilde{\eta}'(\zeta)$ we get the following expression:

$$f(p)=\frac{\left(p^2+\Omega^2\right)^2}{P_4(p)}\left[\frac{g_1}{(p+i\Omega)^2}-\frac{g_2}{p+i\Omega}+\frac{A}{p}\right]=$$
$$=\frac{g_1}{(p+i\Omega)^2}-\frac{g_2}{p+i\Omega}+\frac{A}{p}-\frac{2g_1(p^2-\Omega^2)}{(p+i\Omega)^2P_4(p)}+\frac{2g_2(p^2-\Omega^2)}{(p+i\Omega)P_4(p)}-\frac{2A(p^2-\Omega^2)}{pP_4(p)}. \quad (15)$$

Here

$$P_4(p)=\left(p^2+\Omega^2\right)^2+2\left(p^2-\Omega^2\right),$$
$$g_1=\int_0^\delta dx\exp(i\Omega x)\tilde{\eta}'(x),\quad g_2=\int_0^\delta dx\,x\exp(i\Omega x)\tilde{\eta}'(x), \quad (16)$$

and it is taken into account that the image of $K_\pm$ kernels look like $k_\pm(p)=(p\mp i\Omega)^{-2}$. The polynomial $P_4(p)$ has 4 roots:

$$\alpha_i=\pm\left[-\left(\Omega^2+1\right)\pm\sqrt{4\Omega^2+1}\right]^{1/2},\ i=1,\ldots,4. \quad (17)$$

The function $\tilde{\eta}'(\zeta)$ is found by the inverse Laplace transform using (15–17):

$$\tilde{\eta}'(\zeta)=\left[\sum_{i=1}^4\frac{\left(\alpha_i^2+\Omega^2\right)^2\exp(\alpha_i\zeta)}{\alpha_i\prod\limits_{i\neq j}(\alpha_i-\alpha_j)}+\frac{\Omega^4}{\prod\limits_{i\neq j}(-\alpha_i)}\right]A+\left[\sum_{i=1}^4\frac{\left(\alpha_i-i\Omega\right)^2\exp(\alpha_i\zeta)}{\prod\limits_{i\neq j}(\alpha_i-\alpha_j)}\right]g_1-$$
$$-\left[\sum_{i=1}^4\frac{\left(\alpha_i-i\Omega\right)^2(\alpha_i+i\Omega)\exp(\alpha_i\zeta)}{\prod\limits_{i\neq j}(\alpha_i-\alpha_j)}\right]g_2. \quad (18)$$

It can be seen from Eq. 18 that the function $\tilde{\eta}'(\zeta)$ depends on three values: A, $g_1$ and $g_2$. They, in turn, depend on this function and are the solution of the system of linear equations obtained after substitution of Eq. (18) to Eqs. (14) and (16).

$$\begin{aligned}(1-B_{1,1})\cdot A-B_{1,2}\cdot g_1-B_{1,3}\cdot g_2&=\tilde{\eta}'(\delta),\\ B_{2,1}\cdot A+(B_{2,2}-1)\cdot g_1+B_{2,3}\cdot g_2&=0,\\ B_{3,1}\cdot A+B_{3,2}\cdot g_1+(B_{3,3}-1)\cdot g_2&=0.\end{aligned} \quad (19)$$

Here the coefficients $B_{k,l}$ depend on the roots $\alpha_i$, and the values $\Omega$ and $\delta$. We do not write them out explicitly because of their cumbersomeness. The solution of the system (19) has the form:

$$A=\frac{\Delta_A}{\Delta}\tilde{\eta}'(\delta),\quad g_1=\frac{\Delta_1}{\Delta}\tilde{\eta}'(\delta),\quad g_2=\frac{\Delta_2}{\Delta}\tilde{\eta}'(\delta). \quad (20)$$

Here

$$\Delta_A=(B_{2,2}-1)(B_{3,3}-1)-B_{2,3}B_{3,2},$$
$$\Delta_1=-[B_{2,1}(B_{3,3}-1)-B_{2,3}B_{3,1}],\ \Delta_2=B_{2,1}B_{3,2}-B_{3,1}(B_{2,2}-1),$$
$$\Delta=\begin{vmatrix}1-B_{1,1} & -B_{1,2} & -B_{1,3}\\ B_{2,1} & B_{2,2}-1 & B_{2,3}\\ B_{3,1} & B_{3,2} & B_{3,3}-1\end{vmatrix}. \quad (21)$$

Substituting (20) into (18), we find the function $\tilde{\eta}'(\zeta)$. After integrating the resulting expression over $\zeta$ from 0 to $\delta$ and taking into account $\tilde{\eta}(0) = 0$, we obtain the dispersion equation

$$\frac{1}{\Delta}\left\{\left[\sum_{i=1}^{4}\frac{\left(\alpha_i^2+\Omega^2\right)^2[\exp(\alpha_i\delta)-1]}{\alpha_i^2\prod\limits_{i\neq j}(\alpha_i-\alpha_j)}+\frac{\Omega^4\delta}{\prod\limits_{i\neq j}(-\alpha_i)}\right]\Delta_A+\left[\sum_{i=1}^{4}\frac{\left(\alpha_i-i\Omega\right)^2[\exp(\alpha_i\delta)-1}{\alpha_i\prod\limits_{i\neq j}(\alpha_i-\alpha_j)}\right]\Delta_1-\right.$$
$$\left.-\left[\sum_{i=1}^{4}\frac{\left(\alpha_i-i\Omega\right)^2(\alpha_i+i\Omega)[\exp(\alpha_i\delta)-1]}{\alpha_i\prod\limits_{i\neq j}(\alpha_i-\alpha_j)}\right]\Delta_2\right\}=0. \tag{22}$$

The solutions of Eq. 22 are the dependences of the growth rate $\Gamma$ and the frequency $\omega$ of the eigen mode on the magnitude of the inter-electrode gap $\delta$ (the so-called dispersion branches). We have calculated and constructed some dispersion branches. In particular, several aperiodic branches, i.e. dependencies of $\Gamma(\delta)$ at $\omega = 0$, are shown in Fig. 1. It can be seen that they intersect the axis of $\Gamma = 0$, i.e. solutions corresponding to the values of $\delta$ with $\Gamma > 0$, are unstable. Calculations show that the growth rates of all oscillatory branches lie below the $\Gamma = 0$ axis, i.e., all oscillatory perturbations are stable.

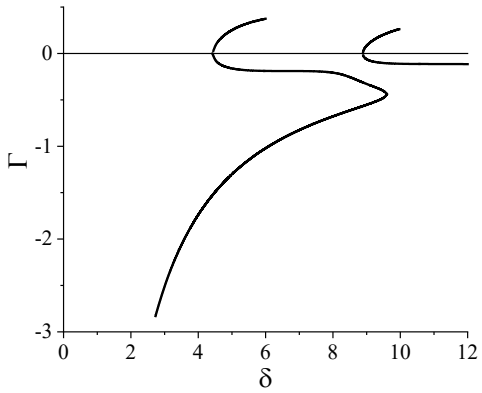


Fig. 1. Dependence of the growth rate on the inter-electrode distance for the first two aperiodic branches

We found the exact $\delta$ values relevant to the points where the growth rate vanishes. For this purpose, the roots $\alpha_i$, as well as the values $\Delta$, $\Delta_A$, $\Delta_1$, and $\Delta_2$ at $|\Gamma| << 1$, $\omega = 0$ were calculated. As a result, the dispersion Eq. (22) was reduced to the form

$$\tan\left(\delta/\sqrt{2}\right)=0. \tag{23}$$

The roots of this equation are $\delta_k = \sqrt{2}\pi k$, $k = 1, 2, 3,\ldots$. The threshold of solution stability with respect to small aperiodic disturbances corresponds to the minimum value of $k$ and is equal to

$$d=\sqrt{2}\pi\lambda_D. \tag{24}$$

This value turned out to be $\sqrt{2}$ times greater than the Pierce threshold. It should be noted that in the Pierce diode, during the development of the disturbance, positively charged particles (ions) are considered immovable. On the other hand, in a diode with counter flows of electrons and positrons, where the masses of positively and negatively charged particles are the same, all particles take part in the process of instability development. This leads to the fact that the instability threshold of such a diode differs from the Pierce one.

## Conclusion

The stability features of steady-state solutions in a diode with counter flows of electrons and positrons in the mode when all charged particles reach the opposite electrode is studied. The equation for the electric field perturbation evolution is derived. For a steady-state solution with a homogeneous field distribution, its analytical solution is found and the dispersion equation is obtained. Solutions of this equation show that there is a threshold for the gap value, when exceeded, an aperiodic instability develops in the diode plasma.

Thus, we have taken the first step towards elucidating the nature of pulsar RF radiation. Further, it is necessary to study the stability features of inhomogeneous steady-state solutions, as well as solutions that have extremes on the potential distribution that reflect a portion of the flow of charged particles. After that, numerical calculations need to be carried out to understand in which states the process of instability development ends. This will allow us to determine the frequencies of the electric field oscillations in the electron-positron plasma, which may be associated with the RF radiation of pulsars.

## REFERENCES

1. **Goldreich P., Julian W.H.,** Pulsar Electrodynamics, The Astrophysical Journal. 157 (2) (1969) 869–880.

2. **Sturrock P.A.,** The model comprises a rotating neutron star (R 106 cm) with a strong magnetic field, The Astrophysical Journal. 164 (3) (1971) 529–556.

3. **Philippov A., Timokhin A., Spitkovsky A.,** Origin of Pulsar Radio Emission, Physical Review Letters. **124** (24) (2020) 245101.

4. **Ender A.Ya., Kuznetsov V.I., Schamel H., Akimov P.V.,** Switching of nonneutral plasma diodes. I. Analytic theory, Physics of Plasmas. 11 (6) (2004) 3212–3223.

5. **Ender A.Ya., Kuznetsov V.I., Gruzdev A.A.,** Steady states of a diode with counterstreaming electron and positron beams**,** Plasma Physics Reports. 32 (10) (2016) 936–946.

6. **Kuznetsov V.I., Ender A.Ya.,** The Q, G-method in physics of collisionless plasma, Plasma Physics Reports. 41 (3) (2015) 240–253.

7. **Bakaleinikov L. A., Kuznetsov V.I., Flegontova E.Yu.,** Stability theory of plasma diodes with counterstreaming electron and ion flows, Physics of Plasmas. 28 (12) (2021) 122108.

8. **Kuznetsov V.I., Ender A.Ya.,** Stability Theory of Knudsen Plasma Diodes, Plasma Physics Reports. **41**(11) (2015) 905–917.

## THE AUTHORS

**KUZNETSOV Victor I.**
victor.kuznetsov@mail.ioffe.ru
ORCID: 0000-0002-8963-5197

**FLEGONTOVA Ekaterina Yu.**
fl.xiees@mail.ioffe.ru
ORCID: 0000-0002-3313-3534

**BAKALEINIKOV Leonid A.**
bakal.ammp@mail.ioffe.ru
ORCID: 0000-0001-7293-0264

*Received 26.10.2022. Approved after reviewing 10.11.2022. Accepted 10.11.2022.*

© Peter the Great St. Petersburg Polytechnic University, 2023

Conference materials
UDC 523.44; 52-17; 521.3
DOI: https://doi.org/10.18721/JPM.161.268

# The Earth trojans

S.N. Petrova[1]✉, A.V. Devyatkin[1], V.N. L'vov[1]

[1] The Central Astronomical Observatory of the RAS, St. Petersburg, Russia

✉ stalkered@yandex.ru

**Abstract**. Asteroids 2010 TK7 and 2020 XL5 are of particular interest because of their behavior, which is similar to the so-called trojan asteroids. In this paper, computer simulations of the orbital evolution of the asteroids in question were carried out using the EPOS software system. The results of the computer simulations suggest that the Earth trojans were not ordinary trojans in the recent past and will most likely shift to another type of orbit in the distant future.

**Keywords:** asteroids, 2010 TK7, 2020 XL5

**Citation:** Petrova S.N., Devyatkin A.V., L'vov V.N., The Earth trojans, St. Petersburg State Polytechnical University Journal. Physics and Mathematics. 16 (1.2) (2023) 449–453. DOI: https://doi.org/10.18721/JPM.161.268

This is an open access article under the CC BY-NC 4.0 license (https://creativecommons.org/licenses/by-nc/4.0/)

Материалы конференции
УДК 523.44; 52-17; 521.3
DOI: https://doi.org/10.18721/JPM.161.268

# Троянцы Земли

С.Н. Петрова[1]✉, А.В. Девяткин[1], В.Н. Львов[1]

[1] Главная (Пулковская) астрономическая обсерватория РАН, Санкт-Петербург, Россия

✉ stalkered@yandex.ru

**Аннотация.** Из-за схожести своего орбитального движения с так называемыми астероидами троянской группы астероиды 2010 TK7 и 2020 XL5 представляют особый интерес для исследования. С помощью пакета программ ЭПОС в рамках задачи двух неподвижных центров проведено исследование движения этих астероидов с помощью интегрирования уравнений их движения на длительных интервалах времени, смоделирована эволюция их орбит. Моделирование позволяет предположить, что с большой вероятностью тип орбит исследуемых астероидов в далеком будущем изменится.

**Ключевые слова:** астероиды, 2010 TK7, 2020 XL5

**Ссылка при цитировании:** Петрова С.Н., Девяткин А.В., Львов В.Н. Троянцы Земли // Научно-технические ведомости СПбГПУ. Физико-математические науки. 2023. Т. 16. № 1.2. С. 449–453. DOI: https://doi.org/10.18721/JPM.161.268

Статья открытого доступа, распространяемая по лицензии CC BY-NC 4.0 (https://creativecommons.org/licenses/by-nc/4.0/)

## Introduction

By the time of this research, the list of trojan minor planets contains more than 11800 objects [1]. The vast majority of them are the so-called Jupiter trojans, and all the small bodies swarming around the Lagrange triangular points at 60° ahead and 60° behind any planet in its orbit are called trojans as well. The leading point $L_4$ and the trailing point $L_5$ are the positions of stable equilibria, and thus they are of prime interest for different space programs.

© Petrova S.N., Devyatkin A.V., L'vov V.N., 2023. Published by Peter the Great St. Petersburg Polytechnic University.

In the 2000s, in the frame of the Interplanetary Solar Stereoscopic Observatory (ISSO) project [2], the observational program devoted to the search of massive bodies in the vicinity of the Sun-Earth triangular Lagrange points ($L_4$ and $L_5$) was performed at the Pulkovo Observatory (CAO RAS) using its two telescopes (ZA-320M and MTM-500M). Installation of two identical space telescopes in these two gravitationally stable areas of the "Sun-Earth+Moon barycenter" system was a part of the ISSO project, so it was necessary to investigate the neighbourhoods of $L_4$ and $L_5$. The software for different computer simulations related to this project was also developed.

However, the discovery of the first Earth trojan asteroid was made only in 2010 by the NASA's WISE infrared astronomy space telescope [3]. A decade later, in 2020, the second Earth trojan was discovered using large telescopes of ground-based observatories [4].

Using the observational data available in the Minor Planet Center database [5, 6], we decided to investigate the orbital evolution and stability of these two asteroids peculiar to our planet.

## Orbital analysis

All the computer simulations of orbit evolutions were carried out by using the EPOS software system created at the Pulkovo Observatory [7].

In the frame of the problem of two fixed centers (Sun-Earth+Moon barycenter), numerical integration of the motion equations of the asteroids in question was performed using DE441 numerical ephemerides [8].

Despite the accumulation of errors during the calculations, some certain features of the orbital behavior of the asteroids can be pointed out.

For a better understanding of peculiarity of the Earth trojans, let us first demonstrate the libration motion of the four big Jupiter $L_4$ and $L_5$ trojans 1143 Odysseus, 588 Achilles, 3317 Paris and 617 Patroclus during the previous two millennia and the next one. The results are presented in Fig. 1 *a*, *b* as examples of a typical trojan behavior. For this simulation, the same software and databases as for the Earth trojans [5–7] were used. Of course, depending on a number of conditions (vicinity to $L_4$ and $L_5$, mass, speed, etc.), the shape of the trojan's orbit may differ, which results in its stabilitv or instabilitv.

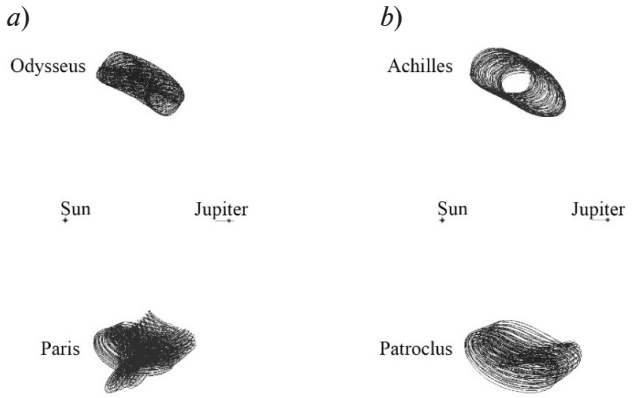


Fig. 1. Libration motion of the Jupiter trojans 1143 Odysseus and 3317 Paris in the time interval between 2022 and 3022 (*a*), libration motion of the Jupiter trojans 588 Achilles and 617 Patroclus in the time interval between 22 and 2022 (*b*)

It should also be noted that in the Earth-fixed moving coordinate systems, any object near the Lagrangian points oscillate in loops along the longitude (e.g. in the frame of the two fixed bodies problem), the size of the loops can vary widely. Sometimes there is a possibility for such objects to "shift" to the C-shaped (horseshoe) orbit, e.g. to cross the unstable equilibrium position $L_3$ and approach a planet from the other side. In some cases, transition to a simple circular orbit is possible, and that is exactly how asteroids 2010 TK7 and 2020 XL5 behave, according to the computer simulation undertaken in the frame of this study.

© Петрова С. Н., Девяткин А. В., Львов В. Н., 2023. Издатель: Санкт-Петербургский политехнический университет Петра Великого.

## 2010 TK7, the first Earth trojan

2010 TK7, the first Earth trojan asteroid, was discovered on October 1, 2010 by the NEOWISE team (with NASA's Wide-field Infrared Survey Explorer (WISE)) [3]. It oscillates around the leading Lagrange point $L_4$, and its estimated diameter is about 0.3 km [9].

The simulation undertaken shows that as the object in question followed a horseshoe orbit, it became the Earth trojan in the middle of the first millennium A.D., it still moves in wide loops to the date and will continue to move in a tadpole orbit for the next several millennia. However, with a high degree of probability, the type of its orbit will then eventually change.

The trajectories of 2010 TK7 relative to two fixed centers (the Sun and the Earth) at two different time intervals are presented in Fig. 2 *a*, *b*.

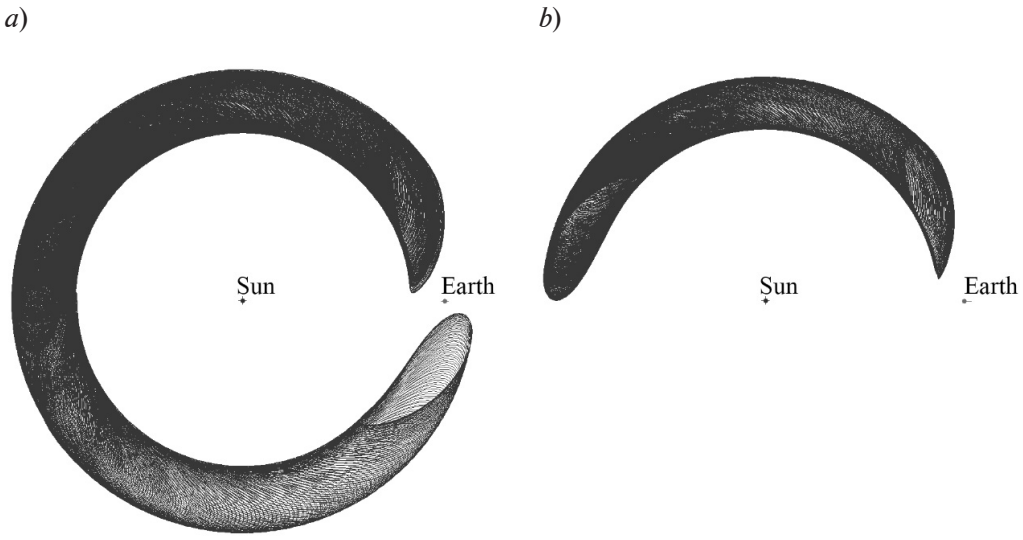


Fig. 2. Trajectory of 2010 TK7 between 22 and 2022 (*a*), trajectory of 2010 TK7 between 2022 and 3022 (*b*)

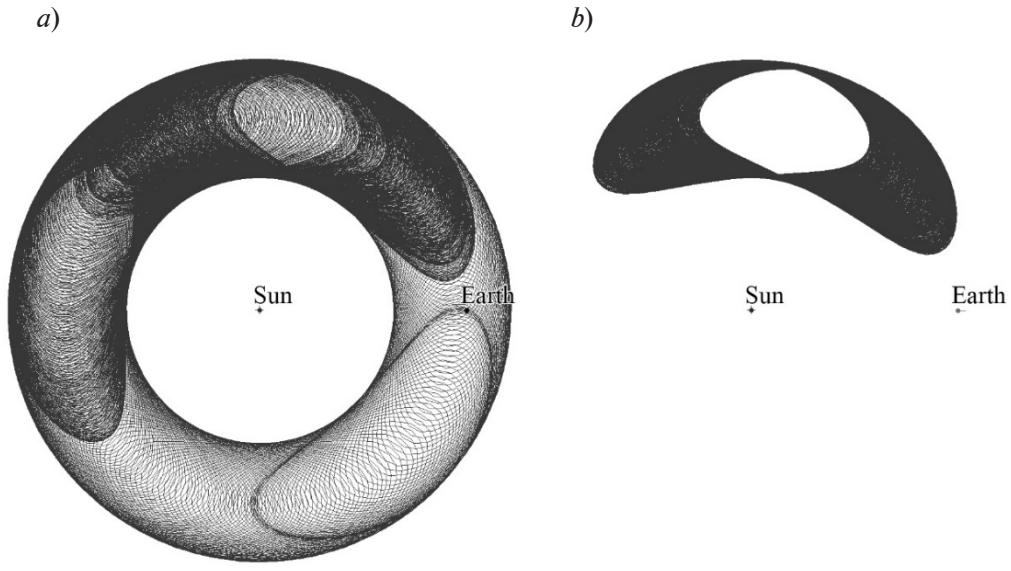


Fig. 3. Trajectory of 2020 XL5 between 1022 and 2022 (*a*), trajectory of 2020 XL5 between 2022 and 3022 (*b*)

### (614689) 2020 XL5, the second Earth trojan

2020 XL5, the second Earth trojan asteroid, was first observed on December, 12, 2020 by the Pan-STARRS 1 survey (Haleakala Observatory, Hawaii) [4]. Like the first one, it oscillates around the leading Lagrange point $L_4$. Its estimated dimeter is about 1.18 ± 0.08 km [10].

The results of the computer modelling of the orbital evolution suggest that asteroid 2020 XL5 has changed three types of orbits over the past thousand years: from a horseshoe orbit, it moved to a circular one, and approximately 400 years ago, it was trapped in the vicinity of $L_4$. The center of the loops is located far enough away from $L_4$, and the scale of the loops is too wide (up to the half of size of a horseshoe orbit), which eventually determines the transition to another type of orbit, but not during the next millennium.

### Conclusion

Although there is not much observational data available for asteroids 2010 TK7 and 2020 XL5 yet, it is possible to model their orbital evolution using the EPOS software package, part of which was developed for simulations of libration motions of the bodies in the neighborhood of the Sun-Earth triangular Lagrange points ($L_4$ and $L_5$) in the frame of the Interplanetary Solar Stereoscopic Observatory (ISSO) project. The results of the simulations, presented in this paper, show that although the Earth trojans are temporarily locked in the vicinity of $L_4$, they have both changed their types of orbits during the previous two millennia and will most likely change them in the future. Thus, the asteroids in question cannot be considered as the members of the compact cluster of matter in the neighbourhood of $L_4$, if it exists.

The discovery of the second Earth trojan in 2020 using the ground-based telescopes proved that ground-based observations can actually be useful for investigations of the Sun−Earth $L_4$ and $L_5$ neighborhoods, so new observational programs of these areas are considered on the base of the Pulkovo Observatory.

## REFERENCES

1. Minor Planet Center. URL: https://minorplanetcenter.net//iau/lists/Trojans.html. Accessed March, 2022.

2. **Chubey M.S., Eroshkin G.I., Pashkevich V.V.**, Space stereoscopic observatory project, Journal of Mathematical Sciences. 128 (2) (2005) 2721−2725.

3. Minor Planet Center. URL: https://minorplanetcenter.net/mpec/K10/K10T45.html. Accessed March, 2022.

4. Minor Planet Center. URL: https://minorplanetcenter.net/mpec/K20/K20XH1.html. Accessed March, 2022.

5. Minor Planet Center. URL: https://minorplanetcenter.net/db_search/show_object?object_id=2010+TK7. Accessed March, 2022.

6. Minor Planet Center. URL: https://minorplanetcenter.net/db_search/show_object?object_id=614689. Accessed April, 2022.

7. **L'vov V.N., Tsekmeister S.D.**, The use of the EPOS software package for research of the Solar System objects, Solar System Research. 46 (2) (2012) 177−179.

8. **Park R.S., Folkner W.M., Williams J.G., Boggs D.H.**, The JPL Planetary and Lunar Ephemerides DE440 and DE441, *The Astronomical Journal.* 161 (105 (2021.

9. NASA's Wide-field Infrared Survey Explorer mission page: https://www.nasa.gov/mission_pages/WISE/news/wise20110727.html. Accessed March, 2022.

10. **Santana-Ros T., Micheli M., Faggioli L., et al.**, Orbital stability analysis and photometric characterization of the second Earth Trojan asteroid 2020 XL5, Nature Communications. 13 (2022) 447.

## THE AUTHORS

**PETROVA Svetlana N.**
stalkered@yandex.ru
ORCID: 0000-0002-1699-4498

**L'VOV Victor N.**
epos-gao@mail.ru
ORCID: 0000-0002-1547-3674

**DEVYATKIN Alexander V.**
a9kin@mail.ru
ORCID: 0000-0001-5095-664X

*Received 28.10.2022. Approved after reviewing 10.11.2022. Accepted 10.11.2022.*

© Peter the Great St. Petersburg Polytechnic University, 2023

Conference materials
UDC 551.590.2
DOI: https://doi.org/10.18721/JPM.161.269

# Long-term effects of solar activity on cyclone tracks in the North Atlantic

S.V. Veretenenko[1]✉, P.B. Dmitriev[1], V.A. Dergachev[1]

[1] Ioffe Institute, St. Petersburg, Russia

✉ s.veretenenko@mail.ioffe.ru

**Abstract.** Long-term changes of extratropical cyclone trajectories in the North Atlantic in cold months (October–March) were analyzed, with the data of Mean Sea Level Pressure archives from Climatic Research Unit, UK (1873–2000) and NCEP/DOE AMIP-II Reanalysis (1979–2021) being used. It was revealed that variations of latitudes of storm tracks in the longitudinal range from 60°W to 10°W are characterized by pronounced periodicities of ~80–90 and ~22 years. This indicates their possible relation to the corresponding periodicities in solar/geomagnetic activity and galactic cosmic ray variations, the secular Gleissberg cycle and the magnetic Hale cycle, respectively. At the maximum of the secular cycle, trajectories of North Atlantic cyclones were found to shift a few degrees south, whereas at the minimum and the descending phase they shift to the north. As North Atlantic cyclones influence significantly weather and climate conditions over Europe, oscillations of their tracks associated with solar activity and related phenomena seem to be of great prognostic importance._

**Keywords:** solar activity, cosmic rays, extratropical cyclones_

**Citation:** Veretenenko S.V., Dmitriev P.B., Dergachev V.A., Long-term effects of solar activity on cyclone tracks in the North Atlantic, St. Petersburg State Polytechnical University Journal. Physics and Mathematics. 16 (1.2) (2023) 454–460. DOI: https://doi.org/10.18721/JPM.161.269

This is an open access article under the CC BY-NC 4.0 license (https://creativecommons.org/licenses/by-nc/4.0/)

Материалы конференции
УДК 551.590.2
DOI: https://doi.org/10.18721/JPM.161.269

# Долговременные эффекты солнечной активности в вариациях траекторий циклонов в Северной Атлантике

С.В. Веретененко [1]✉, П.Б. Дмитриев [1], В.А. Дергачев [1]

[1] Физико-технический институт им. А.Ф. Иоффе РАН, Санкт-Петербург, Россия

✉ s.veretenenko@mail.ioffe.ru

**Аннотация.** Проанализированы долговременные изменения траекторий циклонов в Северной Атлантике в холодные месяцы (октябрь–март) на основе карт среднемесячного приземного давления. Обнаружено, что вариации широты основных траекторий циклонов в области долгот от 60°W до 10°W характеризуются периодичностями ~80–90 и ~22 лет, что указывает на их возможную связь с вариациями солнечной/геомагнитной активности и интенсивности потока галактических космических лучей.

**Ключевые слова:** солнечная активность, космические лучи, внетропические циклоны

**Ссылка при цитировании:** Веретененко С.В., Дмитриев П.Б., Дергачев В.А. Долговременные эффекты солнечной активности в вариациях траекторий циклонов в Северной Атлантике // Научно-технические ведомости СПбГПУ. Физико-математические науки. 2023. Т. 16. № 1.2. С. 454–460. DOI: https://doi.org/10.18721/JPM.161.269

Статья открытого доступа, распространяемая по лицензии CC BY-NC 4.0 (https://creativecommons.org/licenses/by-nc/4.0/)

© Veretenenko S.V., Dmitriev P.B., Dergachev V.A., 2023. Published by Peter the Great St. Petersburg Polytechnic University.

## Introduction

It is well known that cyclonic activity (formation, evolution and movement of extratropical cyclones and anticyclones) is an important factor influencing weather and climate at middle latitudes. Extratropical cyclones from the North Atlantic are responsible for many hazardous weather events over Europe. So, studying influence of solar activity and related disturbances of near-Earth space on cyclone development and trajectories is of significant importance.

Effects of the Sun's activity on extratropical cyclone movement in the North Atlantic were studied in a number of works. Brown and John [1] showed that at sunspot maximum the average latitude of storm tracks in winter months was 2.5° further south than at sunspot minimum. Tinsley [2] revealed that variations of storm track latitudes in the solar cycle may reach ~6° under the west phase of quasibiennial oscillations of the atmosphere. Thus, the aim of this work is to study variations of extratropical cyclone trajectories in the North Atlantic on multidecadal and secular time scales and to compare them with variations of solar activity and related phenomena.

## Temporal variations of storm track latitudes

In this study we used gridded data on mean monthly sea level pressure in the Northern Hemisphere from MSLP (Mean Sea Level Pressure) archives of Climatic Research Unit, UK (1873–2000) [3] and NCEP/DOE AMIP-II Reanalysis (1979–2021) [4]. It is known that North Atlantic cyclones usually arise near the eastern coasts of North America (e.g., [5]). Then they move, as a rule, in the north-eastern direction towards Greenland and Iceland and then towards the Barents Sea. The cyclone movement results in the formation of a region of decreased pressure (baric trough) on monthly maps. This region is extended from the eastern coasts of North America to the Arctic coasts of Eurasia. Fig. 1 demonstrates the distribution of mean monthly SLP in the North Atlantic for cold months when extratropical cyclone activity is most intensive. One can see the examples of positions of baric troughs formed by cyclone motion. The axis of the baric trough (the line of minimal pressure values) shows the main direction of extratropical cyclone movement (storm tracks). It is seen that latitudes of most frequent cyclone passages over a given longitude may vary noticeably.

To study variations of North Atlantic storm tracks, we determined latitudes of pressure minima for the longitudinal range from 60°W to 10°W on monthly maps of SLP. The found values were averaged over cold months (October-March), which is a period of intensive extratropical cyclogenesis. Temporal variations of the mean latitudes of storm tracks in the cold period are presented in Fig. 2 for different longitudes in the North Atlantic.

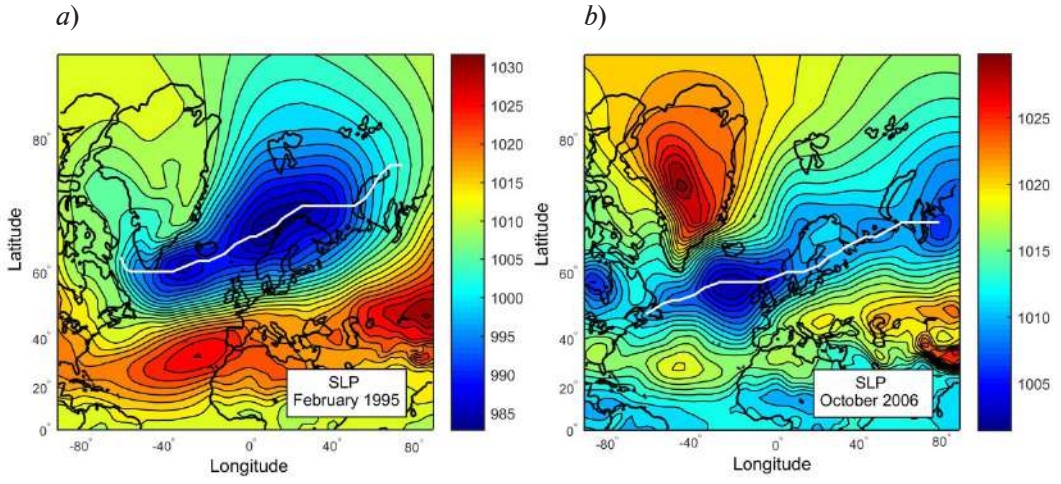


Fig. 1. Maps of mean monthly sea level pressure (in hPa) for February 1995 (*a*) and October 2006 (*b*). White lines show the main direction of cyclone movement (storm track)

© Веретененко С. В., Дмитриев П. Б., Дергачев В. А., 2023. Издатель: Санкт-Петербургский политехнический университет Петра Великого.

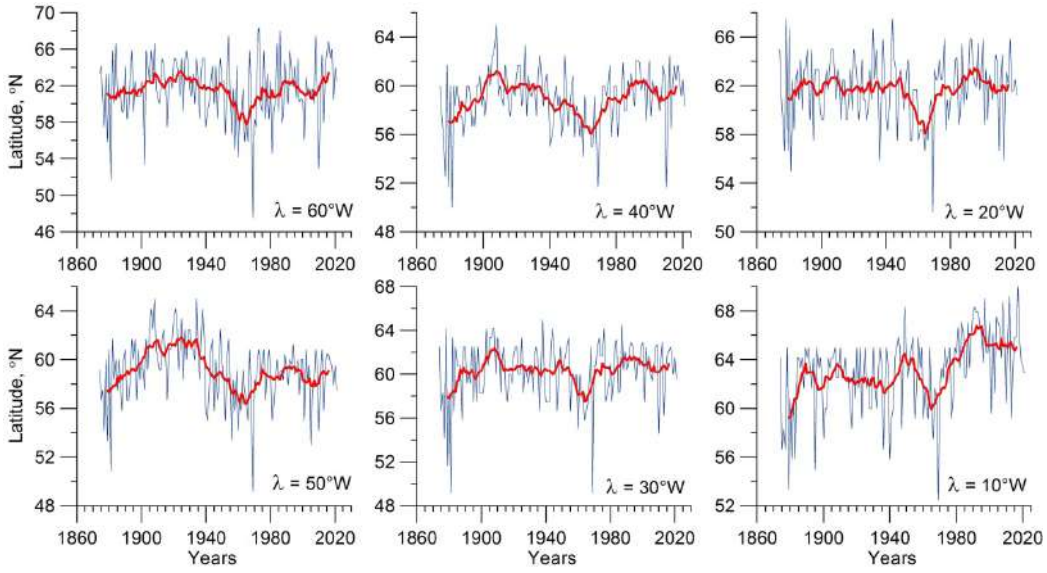


Fig. 2. Temporal variations of the mean latitudes of storm tracks in cold months (October-March) at different longitudes in the North Atlantic. Red lines show 11-yr running averages

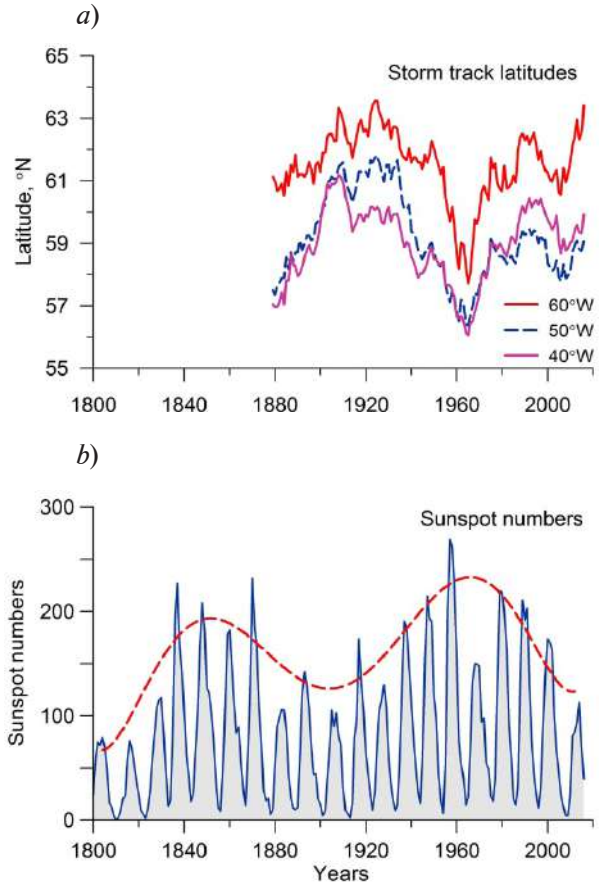


Fig. 3. Long-term changes of storm track latitudes in the western part of the North Atlantic (40–60°W) in the cold half of year (11-yr running averages) (*a*); annual mean sunspot numbers SSN. The dashed line shows the 6$^{th}$ order polynomial approximation of SSN values at maxima of the 11-yr cycle (*b*)

As we can see from Fig. 2, storm track latitudes reveal a pronounced variability both on inter-annual and longer time scales, including multidecadal and secular ones. Long-term variations of storm track latitudes are shown in Fig. 3, *a* for the western part of the North Atlantic, where extratropical cyclones usually form and reach their maximum development. These data are compared with long-term variations of sunspot numbers SSN [6] presented in Fig. 3,*b*. One can see a clear secular variation in the studied cyclone tracks. Maximal values of storm track latitudes were observed in ~1900–1930, which was a period of the secular decrease of solar activity (a minimum of the secular Gleissberg cycle). On the contrary, minimal values took place in ~1950–1960, i.e. at a maximum of the secular cycle. Since ~1960 the secular solar cycle has been at its descending branch and the studied storm track latitudes have been increasing again. Thus, we can suggest that storm tracks in the North Atlantic are influenced by long-term changes of solar activity. Trajectories of North Atlantic cyclones shift a few degrees south at the maximum of the Gleissberg cycle, whereas at the minimum and the descending phase of the cycle, they shift to the north. The peak-to-peak amplitude of secular variations in storm track latitudes is ~5°.

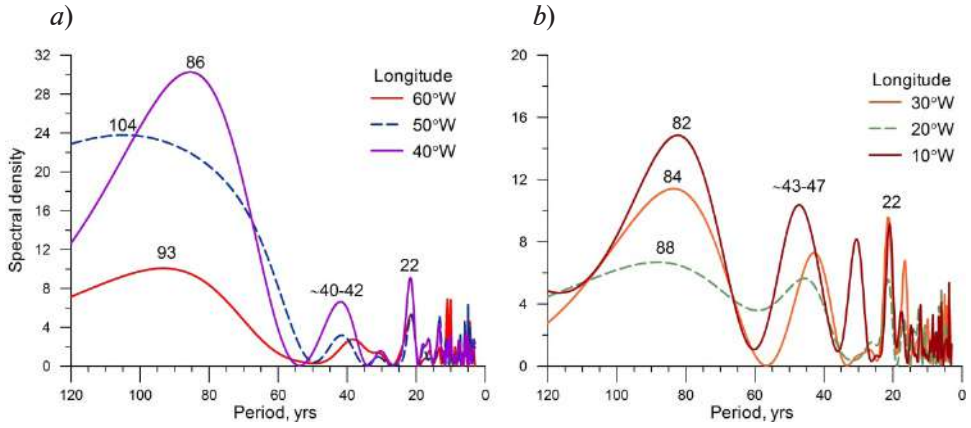


Fig. 4. Sampling estimates of the normalized spectral density of storm track latitudes (initial series) for the western (*a*) and eastern (*b*) parts of the North Atlantic

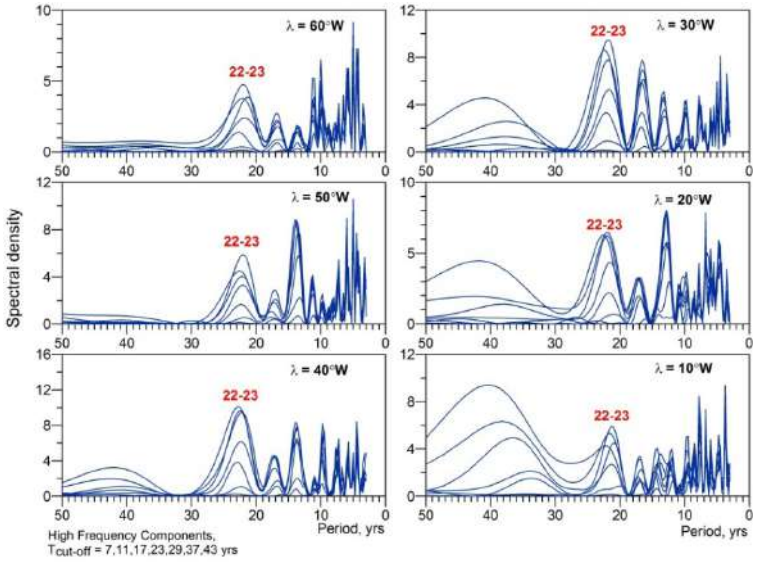


Fig. 5. Sampling estimates of the normalized spectral density of storm track latitudes (high-frequency components with different cut-off parameters $T_{\text{cut-off}}$=7, 11, 17, 23, 29, 37 and 43 years) for the western (left) and eastern (right) parts of the North Atlantic

### Spectral characteristics of storm track latitudes

Let us consider spectral characteristics of the studied storm track latitudes. Spectral analysis was performed using the method of a sampling estimate of the normalized spectral density [7]. To confirm a reliability of the detected periodicities, an additional analysis of high-frequency components (HFC) of the studied time series was carried out, with HFC being calculated using the Blackman-Tukey high-frequency filter with different cut-off frequency parameters ($T_{\text{cut-off}}$) [8].

The results of spectral analysis are presented in Fig. 4 and 5 for the initial time series and high-frequency components, respectively. The data in Fig. 4 demonstrate pronounced secular variations of storm track latitudes both in the western part of the North Atlantic (40–60°W) and its eastern part (10–30°W). One can see that, along with secular variations, cyclone trajectories undergo bidecadal (~22 years) and multidecadal (~40–47 years) oscillations which may also be related to solar variability. The results obtained for HFC of storm track latitudes (Fig. 5) show that there are stable maxima of spectral density at periods ~22–23 years at all the longitudes under study. In the eastern part of the North Atlantic, mulidecadal variations with periods ~40–45 years seem to strengthen.

### Discussion

As it was shown above, long-term changes of storm track latitudes in the North Atlantic reveal oscillations on bidecaldal, multidecadal and secular time scales, which may be linked to solar activity and related phenomena. On a secular time scale, cyclone paths were found to shift further south at the maximum of the Gleissberg cycle compared to the minimum/descending phase of this cycle, with the peak-to-peak amplitude of secular variations in storm tracks reaching ~5°. This effect seems to be similar to those detected in the 11-yr solar cycle [1–2]: the average latitude of winter storm tracks was further south at sunspot maxima than at sunspot minima. Thus, secular variations of solar activity may be responsible for the detected ~80-90-yr periodicities in storm tracks. Let us note that secular variations in storm tracks are the most pronounced in the western part of the North Atlantic (40–60°W), where processes of cyclogenesis (formation and deepening of cyclones) predominate. In the eastern part of the North Atlantic (10-30°W), where filling (destruction) of cyclones gets more frequent, secular variations in storm tracks seem to weaken, whereas multidecadal ones strengthen.

Another characteristic feature of storm track variations seems to be ~22-yr oscillations close to the magnetic (Hale) cycle on the Sun. These oscillations were detected at all the longitudes under study. However, they are the most pronounced at the longitudes 30–40°W, which is a region of the highest temperature contrasts in the Arctic frontal zone forming near the Greenland coasts [9]. In the cold half of year temperature gradients in the layer 1000-500 hPa (~0–5.5 km) in this region were found to undergo strong ~22-yr oscillations [9].

The 22-yr Hale cycle is manifested in magnetic polarity of both sunspots and polar fields on the Sun. It consists of two successive 11-yr cycles with opposite magnetic field polarity. Reversals of solar magnetic fields results in a roughly 22-yr variation in intensity of galactic cosmic rays (GCRs) arriving at Earth. Depending on the overall magnetic field of the Sun, at minima of solar cycles GCR maxima may be flat-topped or peaked [10]. The 22-yr cycle was also revealed in geomagnetic activity [11]. In Fig. 6 one can see the results of spectral analysis of geomagnetic

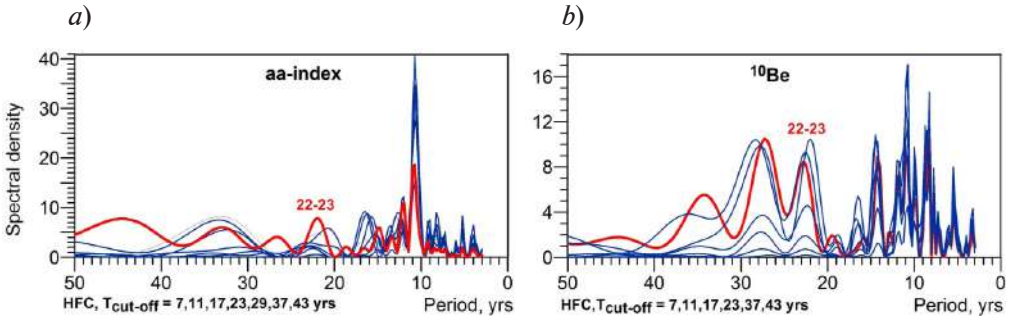


Fig. 6. Sampling estimate of the normalized spectral density of geomagnetic *aa*-index (*a*) and cosmogenic isotope $^{10}$Be concentration in Greenland ice cores (*b*) for the initial series (red lines) and high-frequency components with different cut-off parameters (blue lines)

*aa*-index (detrended values) and concentration of cosmogenic isotope $^{10}$Be produced in the atmosphere by cosmic rays. The data on *aa*-index and $^{10}$Be were taken from [12] and [13], respectively. The data in Fig. 6 demonstrate stable maxima of spectral density at periods ~22–23 years which are related to the solar Hale cycle. Thus, we can suggest that GCR fluxes, as well as geomagnetic activity and related electron precipitations may be involved in the formation of a roughly 22-yr variation in storm tracks.

Spectral characteristics of storm track latitudes (Fig. 4) also demonstrate a noticeable variation of ~40–45 years, which seems to strengthen in the eastern part of the North Atlantic where cyclogenesis processes weaken. Similar variations are observed in solar characteristics, including the North-South asymmetry of sunspot activity (e.g., [14]) and variations of solar cycle length [15]. This allows suggesting that the indicated variation in cyclone trajectories may also be related to solar activity.

The obtained results suggest that possible agents of solar activity influence on cyclone motion may be geomagnetic activity and galactic cosmic ray variations. Extratropical cyclone trajectories are closely related to the mean position of the polar jet stream (a narrow band of strong winds in the upper troposphere) which is influenced by the stratospheric polar vortex (cyclonic circulation forming in the stratosphere in cold months). Under a strong vortex, the polar jet stream tends to strengthen and shift to the north, while under a weak vortex, it slows down and meanders. So, the detected shift of cyclone trajectories to the north with a secular decrease of solar activity may be due to the polar vortex intensification which, in turn, may be associated with an increase of stratospheric ionization produced by cosmic rays. Another factor influencing the state of the polar vortex, and then cyclone trajectories, seems to be geomagnetic activity and related electron precipitations which result in changes of chemical composition and temperature of the polar middle atmosphere. However, the mechanism of solar activity effects on extratropical cyclone movement needs further studies.

### Conclusions

The study revealed noticeable variability of extratropical cyclone trajectories in the North Atlantic on the bidecadal, multidecadal and secular time scales, which may be related to solar activity. Cyclone paths were found to shift south at the maximum of the secular Gleissberg cycle and north at the minimum and the declining phase, with the peak-to-peak amplitude of secular variations of storm tracks reaching ~5°. A distinguished feature of North Atlantic cyclone trajectories is a pronounced ~22-yr variation close to the magnetic Hale cycle on the Sun, which is also observed in geomagnetic activity and galactic cosmic ray intensity. A possible mechanism of solar activity influence on extratropical cyclone movement may involve changes in intensity of the stratospheric polar vortex via ionization changes caused by auroral electrons and galactic cosmic rays.

## REFERENCES

1. **Brown G.M., John J.I.** Solar cycle influences on tropospheric circulation, Journal of Atmospheric and Terrestrial Physics. 41 (1979) 43–52.

2. **Tinsley B.A**. The solar cycle and the QBO influences on the latitude of storm tracks in the North Atlantic, Geophysical Research Letters. 15(5) (1988) 409–412.

3. CRU. URL: https://crudata.uea.ac.uk/cru/data/pressure. Accessed Aug. 08, 2004.

4. NOAA PSL. URL: https://psl.noaa.gov/data/gridded/data.ncep.reanalysis2.surface.html. Accessed Jan. 26, 2022.

5. **Vorobjev V.I.** Synoptic meteorology. Hydrometeoizdat, Leningrad, 1991.

6. WDC-SILSO, Royal Observatory of Belgium. URL: http://www.sidc.be/silso/datafiles. Accessed May 16, 2018.

7. **Jenkins G., Watts D.** Spectral analysis and its application. Holden-Day, San Fransisko, 1968.

8. **Alavi A.S., Jenkins G.M.** An example of digital filtering, Applied Statistics. 14 (1965) 70–74.

9. **Veretenenko S.V., Dergachev V.A., Dmitriyev P.B.** Solar rhythms in the characteristics of the Arctic frontal zone in the North Atlantic, Advances in Space Research. 45(3) (2010) 391–397.

10. **Thomas S.R., Owens M.J., Lockwood M.** The 22-year Hale cycle in cosmic ray flux – evidence for direct heliospheric modulation, Solar Physics. 289 (2014) 407–421.

11. **Cliver E.V., Boriakoff V., Bounar K.H.** The 22-year cycle of geomagnetic and solar wind activity, Journal of Geophysical Research. 101(A12) (1996) 27091–27109.

12. World Data Center for Solar-Terrestrial Physics, Moscow, Russia URL: http://www.wdcb.ru/stp/geomag/geomagn_aa_Aa_ind.html. Accessed Feb. 16, 2022.

13. **Beer J., Blinov A., Bonani G., et al.** Use of $^{10}$Be in polar ice to trace the 11-year cycle of solar activity, Nature. 347 (1990) 164–166.

14. **Obridko V.N., Nagovitsyn Yu.A.** Solar activity, cyclicity and prediction methods. BBM, St. Petersburg, 2017.

15. **Jelbring H**., Analysis of sunspot cycle phase variations – based on D. Justin-Schove's proxy data, Journal of Coastal Research. Special Issue. 17 (1995) 363–369.

## THE AUTHORS

**VERETENENKO Svetlana V.**
s.veretenenko@mail.ioffe.ru
ORCID: 0000-0001-8968-0724

**DERGACHEV Valentin A.**
v.dergachev@mail.ioffe.ru
ORCID: 0000-0003-0734-4933

**DMITRIEV Pavel B.**
paul.d@mail.ioffe.ru
ORCID: 0000-0002-6421-8696

*Received 28.10.2022. Approved after reviewing 08.11.2022. Accepted 09.11.2022.*

© Peter the Great St. Petersburg Polytechnic University, 2023

Conference materials
UDC 524.1
DOI: https://doi.org/10.18721/JPM.161.270

# Kinetic modeling of MHD parameters of mildly-relativistic shocks

V.I. Romansky[1]✉, A.M. Bykov[1], S.M. Osipov[1]

[1] Ioffe Institute, St. Petersburg, Russia

✉ romanskyvadim@gmail.com

**Abstract.** Mildly-relativistic outflows with shocks of velocities 0.1—0.7$c$ were deduced from multiwavelength observations of powerful fast transient sources. These outflows are associated with merging relativistic objects, relativistic supernovae and fast blue optical transients. Relativistic magneto-hydrodynamic (RMHD) models of these objects rely on the equation of state of the fluid, which is a collisionless plasma with a contribution of non-thermal components. In this paper, we present kinetic simulations of mildly-relativistic shocks with Particle-in-Cell and Monte-Carlo techniques to derive the adiabatic index of plasma in the shock downstream directly from the particle distributions, which can be implemented into the RMHD models.

**Keywords:** cosmic rays, shock, MHD, Particle-in-Cell, Monte-Carlo

**Funding:** Modeling by V.I. Romansky and A.M. Bykov at RAS JSCC were supported by RSF grant 21-72-20020. Data analysis by S.M. Osipov was supported by 0040-2019-0025 at Ioffe Institute.

**Citation:** Romansky V.I., Bykov A.M., Osipov S.M., Kinetic modeling of MHD parameters of mildly-relativistic shocks, St. Petersburg State Polytechnical University Journal. Physics and Mathematics. 16 (1.2) (2023) 461—466. DOI: https://doi.org/10.18721/JPM.161.270

This is an open access article under the CC BY-NC 4.0 license (https://creativecommons.org/licenses/by-nc/4.0/)

Материалы конференции
УДК 524.1
DOI: https://doi.org/10.18721/JPM.161.270

# Кинетическое моделирование МГД параметров субрелятивистских ударных волн

В.И. Романский[1]✉, А.М. Быков[1], С.М. Осипов[1]

[1] Физико-технический институт им. А.Ф. Иоффе РАН, Санкт-Петербург, Россия

✉ romanskyvadim@gmail.com

**Аннотация.** Субрелятивистские ударные волны со скоростями 0.1—0.7c обнаружены в мощных транзиентных объектах. Релятивистские магнитогидродинамические модели таких течений используют уравнение состояния вещества при наличии нетепловой компоненты. В этой работе представлены результаты вычисления показателя адиабаты плазмы за фронтом ударной волны с помощью Particle-in-Cell и Монте-Карло моделирования.

**Ключевые слова:** космические лучи, ударные волны, МГД, Particle-in-Cell, Монте-Карло

**Финансирование:** Расчеты Романского В.И. и Быкова А.М. на МСЦ РАН поддержаны грантом РНФ 21-72-20020 Работа Осипова С.М. выполнена в рамках Государственного задания 0040-2019-0025 ФТИ им. Иоффе.

**Ссылка для цитирования:** Романский В.И., Быков А.М., Осипов С.М. Кинетическое моделирование МГД параметров субрелятивистских ударных волн // Научно-технические ведомости СПбГПУ. Физико-математические науки. 2023. Т. 16. № 1.2. С. 461—466. DOI: https://doi.org/10.18721/JPM.161.270

Статья открытого доступа, распространяемая по лицензии CC BY-NC 4.0 (https://creativecommons.org/licenses/by-nc/4.0/)

© Romansky V.I., Bykov A.M., Osipov S.M., 2023. Published by Peter the Great St. Petersburg Polytechnic University.

## Introduction

Recent multiwavelength observations of fast energetic transient sources associated with some classes of supernova and neutron star mergers revealed a presence there of mildly-relativistic outflows with shock waves of velocities faster than 0.1c [1–8]. Analysis of 42 daytimescale-evolving transients detected with Zwicky Transient Facility (ZTF) [9] suggested that most of these objects are likely associated with core-collapse supernovae (SNe). The authors distinguished a few sub-types of the typical events as (i) subluminous SNe of Type Ib or IIb; (ii) luminous Type Ibn or hybrid IIn/Ibn SNe; and (iii) short-duration radio-loud luminous events which prototype is nearby AT2018cow event. While the subluminous SNe events of Type IIb are the most numerous, the AT2018cow like events rate is less than 0.1% of the local corecollapse SNe rate [9]. The multiwavelength data on fast SNe related transients can be generally understood assuming an action of a powerful central engine in the collapsing stars which can launch a relativistic jet-type outflow. The relativistic hydrodynamical simulations performed in [10, 11] illustrated that depending on the time duration of the central engine power activity either a GRB type jet source (for a long enough activity time) or, for a shorter power injection time, a somewhat broader outflow and a radio bright relativistic SN can be produced by a collapsing star. The different energy injection regimes by the central engine result in different energy versus the ejecta speed distributions. The powerful jet breaking through the stellar envelope can form a mildly-relativistic expanding cocoon containing the energy ~$10^{51}$ ergs (see e.g. [12]). The cocoon interacting with the circumstellar winds may emit the synchrotron self-absorbed radio emission observed in the fast optical transients [13]. The physical models of particle acceleration in the fast transients based on the particle in cell simulations of mildly-relativistic shocks in barionic plasma produced by the central engine activity in the fast transients were discussed in [14]. Mildly-relativistic shocks are also determining the transition from the early highly-relativistic to the later time semi-relativistic likely barion-dominated outflows in the gamma-ray burst afterglows (see e.g. [15–17]) where the models can be used to model the non-thermal radiation. Moreover, mildly-relativistic shocks in stellar mass transient sources can be considered as efficient accelerators of cosmic rays well above PeV regime (see [18] and the references therein). The future Large Synoptic Survey Telescope will detect a large amount of fast transients providing good possibilities to of the follow up multiwavelength studies. Therefore, there is a clear need in detailed modeling of different appearances of the semi-relativistic outflows in the transient sources. While to model the global structure of the flows the RMHD simulations are widely used, the collisionless shocks need the microscopic kinetic type of simulations since the collisionless shocks are producing non-thermal components which may influence the equation of state and the macroscopic parameters like the adiabatic indexes of the semi-relativistic plasma. Therefore, we present below the results of simulations of the macroscopic plasma parameters, which can be used in the global RMHD simulations.

## Particle-in-Cell simulations

In this work, we use the particle-in-cell code Smilei [19] for modeling collisionless shocks. The simulation domain is two-dimensional with the reflective wall on the left boundary along the $x$-axis and the plasma flowing in through the right boundary. The boundary conditions along the $y$-axis are periodic.

The simulation parameters are: the initial flow Lorentz factor $\Gamma$ is in interval 1.05–1.5 for different setups, the flow magnetization

$$\sigma = \frac{B^2}{4\pi\Gamma n_0 (m_p + m_e)c^2} = 0.0002,$$

where $B$ is the magnetic field, $m_p$ and $m_e$ are proton and electron masses, $c$ is speed of light. The upstream number density $n_0$ is equal to 1, but all quantities can be easily scaled to different value. The temperature $T = 0.02$ in units of the electron rest energy and the electron mass is increased up to $m_e = m_p/100$. We used setups with different velocities of plasma flow $v_u = \beta_u c$ and inclination angles of magnetic field: $\vartheta$ is angle between the magnetic field and the flow velocity and $\varphi$ is angle of field rotation in perpendicular plane, $\varphi = 0$ corresponds to the magnetic field lying in the simulation plane. Setups and their parameters are listed in Table 2.

© Романский В.И., Быков А.М., Осипов С.М., 2023. Издатель: Санкт-Петербургский политехнический университет Петра Великого.

The spatial grid step is $dx = 0.2c/\omega_p$ and the time step $dt = 0.1/\omega_p$, where

$$\omega_p = \sqrt{\frac{4\pi n_0 e^2}{m_e}}$$

is the plasma frequency, $e$ is the absolute value of the electron charge. The size of the simulation box along the $x$-axis is $L_x = 40000c/\omega_p$ and in the transverse direction $L_y = 100c/\omega_p$. These scales correspond to 200000 and 500 grid points in $x$ and $y$ directions, respectively.

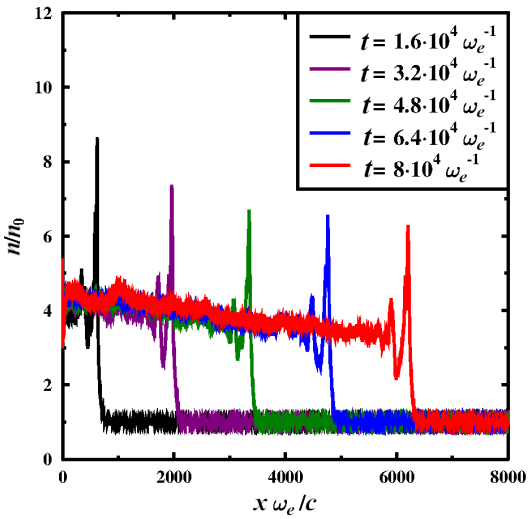


Fig. 1. Time evolution of number density normalized to the far upstream number density in setup B30

We obtain the MHD parameters of the shock from the simulation. The position of the shock front is well defined as shown in Fig. 1 so we can evaluate the shock velocity in the downstream frame $v^d_{sh}$ and $\beta^d_{sh} = v^d_{sh}/c$ The shock velocity in the upstream frame is defined as $\beta_{sh} = (\beta_u + \beta^d_{sh})/(1 + \beta_u \cdot \beta^d_{sh})$ We can find temperature of each particle species behind the shock, minimizing the functional

$$f(T) = \int_{mc^2}^{5mc^2} (F(E) - F_{mj}(E,T))^2 dE,$$

where $F(E)$ is simulated distribution function and $F_{mj}(E,T)$ is Maxwell-Juttner distribution function. Fitting of distribution function is shown in Fig. 2. Also on can see non-thermal tail of distribution, which is cut at level $F(E) \approx 10^{-7}$ to avoid strong statistical fluctuations at high energies. Also, we can derive adiabatic index for every species of particles using definition $\gamma_i = 1 + P/E_k$ where $P$ is the pressure and $E_k$ is the kinetic energy of particles in the plasma rest frame.

$$P = \int F(E) v_x(E,\vartheta) p_x(E,\vartheta) 2\pi \sin(\vartheta) d\vartheta dE,$$

$$\text{and } E_k = \int F(E)(E - mc^2) 2\pi \sin(\vartheta) d\vartheta dE.$$

Also we define $\hat{\gamma}-$ the adiabatic index, evaluated with the same formulae but using the Maxwell-Juttner particle distribution with the corresponding temperature.

Table 1

**Parameters of setups**

| Setup | $\vartheta$ | $\varphi$ | $\beta_u$ | $\beta^d_{sh}$ | $\beta_{sh}$ | $\gamma_p$ | $\gamma_e$ | $T_p$ $10^{10}$K | $T_e$ $10^{10}$K | $\hat{\gamma}_p(T_p)$ | $\hat{\gamma}_e(T_e)$ |
|---|---|---|---|---|---|---|---|---|---|---|---|
| A30 | 30 | 90 | 0.5 | 0.13 | 0.59 | 1.620 | 1.389 | 75.5 | 19.0 | 1.617 | 1.389 |
| A80 | 80 | 90 | 0.5 | 0.16 | 0.61 | 1.601 | 1.396 | 54.7 | 16.3 | 1.629 | 1.397 |
| B30 | 30 | 90 | 0.3 | 0.088 | 0.38 | 1.647 | 1.499 | 14.5 | 4.0 | 1.656 | 1.502 |
| B50 | 50 | 90 | 0.3 | 0.098 | 0.39 | 1.648 | 1.468 | 11.0 | 5.9 | 1.658 | 1.469 |
| C30 | 30 | 0 | 0.3 | 0.088 | 0.38 | 1.647 | 1.502 | 14.4 | 3.9 | 1.656 | 1.504 |
| D30 | 30 | 90 | 0.1 | 0.035 | 0.135 | 1.665 | 1.574 | 1.9 | 1.3 | 1.665 | 1.589 |
| D80 | 80 | 90 | 0.1 | 0.052 | 0.151 | 1.664 | 1.580 | 2.6 | 1.5 | 1.665 | 1.579 |

Notations: $\vartheta$ and $\varphi$ are orientation angles of magnetic field, $\beta_u$ is upstream velocity in units of $c$, $\beta^d_{sh}$ is shock velocity in downstream (laboratory) frame, $\beta_{sh}$ is shock velocity in upstream frame, $\gamma_p$ and $\gamma_e$ are protons and electrons adiabatic indices, $T_p$ and $T_e$ are temperatures of Maxwellian part of distribution and $\hat{\gamma}_p(T_p)$ and $\hat{\gamma}_e(T_e)$ are adiabatic indices, evaluated for Maxwell-Juttner distribution with corresponding temperature.

One can see from Table 1 that the adiabatic index obtained from PIC simulation is smaller than obtained from the simple hydrodynamic theory. It should be taken into account in the MHD simulations. This difference increases when the particle acceleration is more efficient (case of the quasi-parallel shock). Also, the PIC simulation cannot simulate long non-thermal tales of distributions because of it is high computational cost, and other methods, such as hybrid and Monte-Carlo simulation are needed for more precise modeling of the MHD parameters.

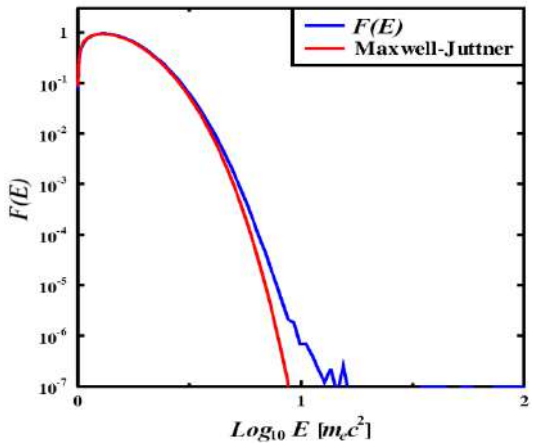


Fig. 2. Fit of the electron distribution in the shock downstream with Maxwell-Juttner distribution, setup B30

## Monte-Carlo simulation

Due to the limited computing power, PIC modeling can be performed only in a small area of the volume of real astrophysical objects. To describe astrophysical objects on their real scales, it is necessary to involve other numerical models. One of such models is the Monte Carlo calculations, which, unlike the PIC calculations, require the introduction of phenomenological laws, such as the mean free path of particles, the growth rates of plasma instabilities.

We develop a nonlinear numerical stationary plane-parallel relativistic Monte Carlo model of particle acceleration by longitudinal collisionless shocks [14]. Particle acceleration occurs by the first-order Fermi mechanism. The particles are scattered by the magnetic fluctuations and repeatedly cross the shock front. In our model, based on an iterative scheme, the conservation laws of energy and momentum fluxes near the shock are fulfilled. The model takes into account the modification of the upstream by the pressure of accelerated particles, the amplification of the magnetic fluctuations due to plasma instabilities caused by the anisotropy of the accelerated particle distribution function in the upstream, the dissipation of turbulent modes, and the turbulent cascade. Particle propagation is organized based on pitch-angle scattering. The particles are divided into accelerated and background. The particle is considered as accelerated if it has crossed the front of the shock at least once from the downstream to the upstream.

Table 2 shows the results of Monte Carlo calculations for different shock velocities $\nu_{sh} = \beta_{sh} c \cdot \gamma_{th}$, $\gamma_{cr}$, $\gamma_{tot}$ are the adiabatic indices of the background plasma, the accelerated particle distribution and the total in the downstream, respectively. $T_{th}$ is the temperature of background protons in the downstream. Other model parameters except $\nu_{sh}$ are the same in all calculations. The free escape boundary of particles is at the coordinate $x_{FEB} = -10 \cdot 5^{14}$ cm, the shock front corresponds to the coordinate $x = 0$. The number density of the background plasma $n_0 = 5 \cdot 10^5$ cm$^{-3}$ in the far unperturbed upstream. The rms turbulent magnetic field $B_{st}(x_{FEB})$ is equal to the constant magnetic field $B_0 = 3 \cdot 10^{-3} G$ in the far unperturbed upstream.

$$B(x) = \sqrt{B_{st}^2(x) + B_0^2} \ .$$

Table 2

**Results of Monte Carlo calculations**

| Setup | $\beta_{sh}$ | $\gamma_{th}$ | $\gamma_{cr}$ | $\gamma_{tot}$ | $T_{th}\, 10^{10} K$ |
|---|---|---|---|---|---|
| MC1 | 0.1 | 1.66 | 1.43 | 1.49 | 0.59 |
| MC2 | 0.3 | 1.66 | 1.42 | 1.49 | 7.11 |
| MC3 | 0.5 | 1.64 | 1.41 | 1.49 | 26.5 |
| MC4 | 0.7 | 1.61 | 1.40 | 1.48 | 82.4 |

Notations: $\beta_{sh}$ is shock velocity in upstream frame in units of $c$, $\gamma_{th}$ is adiabatic index of background plasma, $\gamma_{cr}$ is adiabatic index of accelerated particles, $\gamma_{tot}$ is total adiabatic index and $T_{th}$ is a temperature of background plasma.

Fig. 3 shows the profiles of the background plasma flow velocity and the magnetic field. The turbulent part of the magnetic field is amplified due to plasma instabilities and adiabatically. $r_{g0} = m_p c v_{sh}/eB_0$, where $e$ is elementary charge.

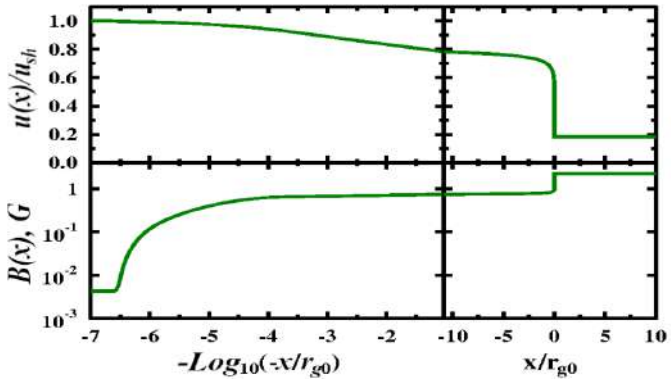


Fig 3. Background plasma velocity profile (upper panel) and magnetic field profile (bottom panel) for the Monte Carlo calculation MC1. Coordinate is shown in units of $r_{g0} = m_p c v_{sh}/eB_0$, where $e$ is elementary charge

The scales achievable in PIC modeling are of the order of several $r_{g0}$, so the PIC modeling can describe a small area near the shock compared to the Monte Carlo modeling (see Fig. 3). Since the maximum energies of accelerated particles strongly depend on the size of the system, in the Monte Carlo calculations, the maximum energies of particles are many orders of magnitude higher than in the PIC calculations. The temperature of the background plasma in the downstream in the Monte Carlo simulation is also affected by the amplification of modes by plasma instabilities associated with the anisotropy of the distribution of the high-energy accelerated particles and the energy dissipation of these modes at the upstream scales.

## Conclusions

Hydrodynamic and RMHD models are constructed to interpret the light-curves and spectra of fast transients (e.g. [20, 10, 5, 21, 22, 13, 23] and the reference therein). Results of kinetic modeling of mildly-relativistic shocks show that adiabatic index of plasma differs from typical values, which are usually used in hydrodynamic models, due to non maxwellian distribution of particles. It should be taken into account during MHD modeling of global structures of mildly-relativistic outflows. Also, Particle-in-Cell modeling provides electrons temperature, which can be useful for hydrodynamic and hybrid modeling.

## Acknowledgments

Modeling by V.I. Romansky and A.M.Bykov at RAS JSCC were supported by RSF grant 21-72-20020. Data analysis by S.M.Osipov were supported by 0040-2019-0025 at Ioffe Institute. Some results of the work were obtained using computational resources of Peter the Great St. Petersburg Polytechnic University Supercomputing Center (http://scc.spbstu.ru).

## REFERENCES

1. **Arcavi I., Wolf W.M., Howell D.A., et al.,** Rapidly Rising Transients in the Supernova—Superluminous Supernova Ga, Astrophysical Journal 819 (2016) 35.

2. **Margutti R., Metzger B.D., Chornock R., et al.,** An Embedded X-Ray Source Shines through the Aspherical AT 2018cow: Revealing the Inner Workings of the Most Luminous Fast-evolving Optical Transients, Astrophysical Journal 872 (2019) 18.

3. **Ho A. Y.Q., Perley D.A., Kulkarni S.R., et al.,** The Koala: A Fast Blue Optical Transient with Luminous Radio Emission from a Starburst Dwarf Galaxy at z = 0.27, Astrophysical Journal 895 (2020) 49.

4. **Nayana A.J., Chandra P.,** uGMRT Observations of a Fast and Blue Optical Transient—AT 2018cow, Astrophysical Journal Letters 912 (2021) L9.

5. **Metzger B.D.,** Kilonovae, Living Reviews in Relativity 23 (2019) 1.
6. **Margutti R., Chornock R.,** First Multimessenger Observations of a Neutron Star Merger, Annual Review of Astronomy and Astrophysics 59 (2021) pp. 155–202.
7. **Kremer K., Lu W., Piro A. L., et al.,** Fast Optical Transients from Stellar-mass Black Hole Tidal Disruption Events in Young Star Clusters, Astrophysical Journal 911 (2021) 104.
8. **Hajela A., Margutti R., Bright J. S., et al.,** Evidence for X-Ray Emission in Excess to the Jet-afterglow Decay 3.5 yr after the Binary Neutron Star Merger GW 170817: A New Emission Component, Astrophysical Journal Letters 927 (2022) L17.
9. **Ho A.Y.Q., Perley D. A., Gal-Yam A., et al.,** The Photometric and Spectroscopic Evolution of Rapidly Evolving Extragalactic Transients in ZTF *arXiv e-prints* arXiv:2105.08811 (2021).
10. **Lazzati D., Morsony B.J., Blackwell C.H., Begelman M.C.,** Unifying the Zoo of Jet-driven Stellar Explosions, Astrophysical Journal 750 (2012) 68.
11. **Corsi A., Lazzati D.,** Gamma-ray burst jets in supernovae, New Astronomy Reviews 92 (2021) 101614.
12. **Piran T., Nakar E., Mazzali P., Pian E.,** Relativistic Jets in Core-collapse Supernovae, Astrophysical Journal Letters 871 (2019) L25.
13. **Gottlieb O., Tchekhovskoy A., Margutti R.,** Shocked jets in CCSNe can power the zoo of fast blue optical transients, Monthly Notices of the Royal Astronomical Society 513 (2022) pp. 3810–3817.
14. **Bykov A., Romansky V., Osipov S.,** Particle Acceleration in Mildly Relativistic Outflows of Fast Energetic Transient Sources, Universe 8 (2022) 32.
15. **Piran T.,** The physics of gamma-ray bursts, Reviews of Modern Pysics 76 (2004) 1143.
16. **Mreszraros P.,** Gamma-ray bursts, Reports on Progress in Physics 69 (2006) 2259–2321.
17. **van Eerten H., van der Horst A., MacFadyen A.,** Gamma-Ray Burst Afterglow Broadband Fitting Based Directly on Hydrodynamics Simulations, Astrophysical Journal 749 (2012) 44.
18. **Bykov A.M., Ellison D.C., Marcowith A., Osipov S. M.,** Cosmic Ray Production in Supernovae, Space Science Reviews 214 (2018) 41.
19. **Derouillat J., Beck A., Prerez F., et al.,** SMILEI: A collaborative, open-source, multi-purpose particle-in-cell code for plasma simulation, Computer Physics Communications 222 (2018) 351–373.
20. **Matzner C.D., McKee C.F.,** The Expulsion of Stellar Envelopes in Core-Collapse Supernovae, Astrophysical Journal 510 (1999) pp. 379–403.
21. **Leung S.C., Blinnikov S., Nomoto K., et al.,** A Model for the Fast Blue Optical Transient AT2018cow: Circumstellar Interaction of a Pulsational Pair-instability Supernova, Astrophysical Journal 903 (2020) 66.
22. **Urvachev E., Shidlovski D., Tominaga N., Glazyrin S., Blinnikov S.,** The Simulation of Superluminous Supernovae Using the M1 Approach for Radiation Transfer, Astrophysical Journal Supplement Series 256 (2021) 8.
23. **Eisenberg M., Gottlieb O., Nakar E.,** Observational signatures of stellar explosions driven by relativistic jets, Monthly Notices of the Royal Astronomical Society 517 (2022) 582.

## THE AUTHORS

**ROMANSKY Vadim I.**
romanskyvadim@gmail.com
ORCID: 0000-0003-1863-2957

**BYKOV Andrei M.**
byk@astro.ioffe.ru
ORCID: 0000-0003-0037-2288

**OSIPOV Sergei M.**
osm2004@mail.ru
ORCID: 0000-0001-8806-0259

*Received 28.10.2022. Approved after reviewing 08.11.2022. Accepted 16.11.2022.*

© Peter the Great St. Petersburg Polytechnic University, 2023

Conference materials
UDC 524.3-59
DOI: https://doi.org/10.18721/JPM.161.271

# Dynamics of quasi-periodic oscillations in the light curve of the GRB 190114C γ-ray burst

V.A. Dranevich, P.B. Dmitriev✉

Ioffe Institute, St. Petersburg, Russia

✉ paul.d@mail.ioffe.ru

**Abstract.** Based on the γ-ray Burst Monitor data of the Fermi space observatory, the light curve time structure of the γ-ray burst GRB 190114C in the energy range from 5 keV to 50 MeV was investigated. It was found that the temporal structure of the emission of this γ-ray burst contains quasi-periodic components with periods of 0.768 s, 1.28 s, 2.24 s, and 3.84 s, determined with an accuracy of up to ±0.064 s where the original data time bin is 0.064 s. We also analyzed the evolution of these quasi-period values during the background radiation intensity, which was recorded within 137 s before and within 354 s after the event. As a result, a systematic decrease with time in the value of the quasi-period of 3.84 s was found, while the value of the quasi-period of 0.768 s at the same time gradually increases. A similar unambiguous result for the quasi-periods of 1.28 s and 2.24 s was not obtained. According to the above estimates, it should be noted that the γ-ray burst itself is located within the time interval when oscillations with quasi-periods of 2.24 s and 3.84 s are in a multiple ratio of ~3/5. Such coincidence can serve as an indication of the significant role of resonance phenomena in the process of formation and flow of a γ-ray burst.

**Keywords:** Gamma-Ray Bursts, GRB 190114C, quasi-periodic oscillations

**Citation:** Dranevich V.A., Dmitriev P.B., Dynamics of quasi-periodic oscillations in the light curve of the GRB 190114C γ-ray burst, St. Petersburg State Polytechnical University Journal. Physics and Mathematics. 16 (1.2) (2023) 467–473. DOI: https://doi.org/10.18721/JPM.161.271

This is an open access article under the CC BY-NC 4.0 license (https://creativecommons.org/licenses/by-nc/4.0/)

Материалы конференции
УДК 524.3-59
DOI: https://doi.org/10.18721/JPM.161.271

# Динамика квазипериодических колебаний кривой блеска γ-всплеска GRB 190114C

В.А. Драневич, П.Б. Дмитриев✉

Физико-технический институт им. А.Ф. Иоффе РАН, Санкт Петербург, Россия

✉ paul.d@mail.ioffe.ru

**Аннотация.** По данным прибора Gamma-ray Burst Monitor космической обсерватории «Fermi» была исследована временная структура световой кривой γ-всплеска GRB 190114C в энергетическом диапазоне от 5 кэВ до 50 МэВ. Было обнаружено, что во временной структуре излучения данного γ-всплеска присутствуют квазипериодические компоненты с периодами 0,768 с, 1,28 с, 2,24 с и 3,84 с. Также была проанализирована эволюция значений этих квазипериодов на протяжении «фоновой» части записи интенсивности излучения длительностью 137 с до и 354 с после события.

**Ключевые слова:** гамма-всплески, GRB 190114C, квазипериодические колебания

© Dranevich V.A., Dmitriev P.B., 2023. Published by Peter the Great St. Petersburg Polytechnic University.

**Ссылка при цитировании:** Драневич В.А., Дмитриев П.Б. Динамика квазипериодических колебаний кривой блеска γ-всплеска GRB 190114C // Научно-технические ведомости СПбГПУ. Физико-математические науки. 2023. Т. 16. № 1.2. С. 467–473. DOI: https://doi.org/10.18721/JPM.161.271

Статья открытого доступа, распространяемая по лицензии CC BY-NC 4.0 (https://creativecommons.org/licenses/by-nc/4.0/)

## Introduction

The question of whether γ-ray bursts are purely stochastic processes, or whether they contain quasi-periodic components, has long been discussed in the scientific literature. From time to time, papers appear in which results are presented on the presence of quasi-periodic oscillations in the structure of the light curves of γ-ray bursts. The periods of these oscillations are usually several seconds [1–7], and quasi-periodic oscillations are observed in a wide energy range from the γ-range up to the visible light one. A detailed review of such observations can be found in [8], where 1160 light curves of γ-ray bursts with duration of more than 3.2 s were analyzed, obtained during observations on the Swift spacecraft. Thanks to these observations, by means of the wavelet analysis method, 34 events with similar oscillations were detected, of which in 21 cases during the events the oscillation period did not change in time, in 10 cases the oscillation frequency increased, and in 3 cases it decreased with time. In 8 events, the simultaneous existence of 2 oscillations was noted, and in 3 events, the simultaneous existence of 3 oscillations, and in each of these events, the oscillation periods were related as integers.

In particular, the authors of [9] studied the light curve of the γ-ray burst GRB 190114C associated with the explosion of a Supernova [10] located at a cosmological distance z equal to 0.425 [11]. Based on the data obtained as a result of observations of this γ-ray burst with the Swift spacecraft, it was found that in the time structure of the light curve of the GRB 190114C exist with a reliability of more than 3σ the quasi-periodic components with periods of 2.24 s and 3.84 s and with a lower confidence value 2σ the quasi-harmonic components with periods of 1.28 s and 0.768 s. The periods of the first two components are related as ~ 3/5 or 7/12, and the two second oscillations can probably be considered as the third harmonics of the first two. A discussion of possible mechanisms for the appearance of quasi-periodic oscillations in the structure of the light curves of γ-ray bursts can be found in [10, 12]. In order to determine which process is responsible for oscillations, it is necessary to know whether they appear during the development of the burst, or whether oscillations that previously existed in the radiation source amplify during the burst. Therefore, in this work, we continued the study of the temporal structure of the GRB 190114C in order to study the behavior of the quasi-harmonic components with time, which were previously identified based on the Swift data [9], but with the involvement of data from a wider energy range obtained by the Fermi spacecraft. To do this, the behavior of the quasi-harmonic oscillations detected during the burst was investigated in the background parts of the radiation intensity record before and after the event.

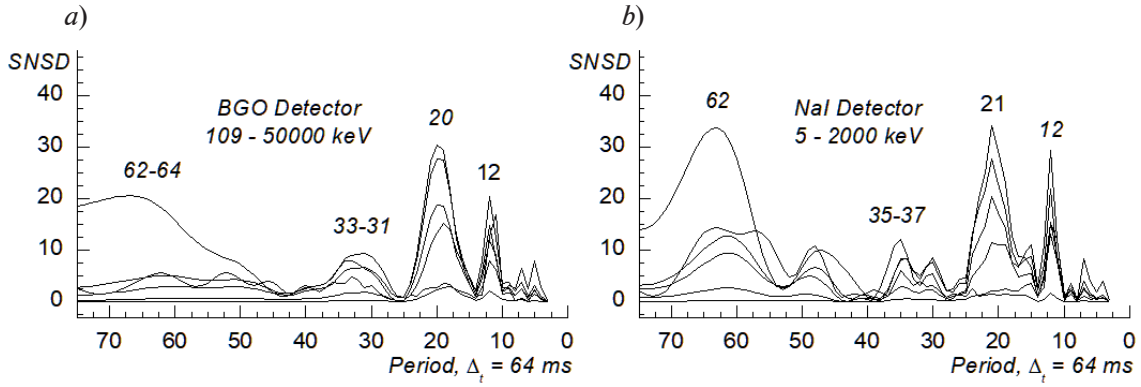


Fig. 1. CSP of the main stage of the GRB 190114C light curve and of light curve high-frequency components with different cutoff parameters ($T_f$ = 7, 17, 29, 37, and 57 $\Delta_t$ = 64 ms) for the BGO (*a*) and the NaI (*b*) detectors

© Драневич В.А., Дмитриев П.Б., 2023. Издатель: Санкт-Петербургский политехнический университет Петра Великого.

## Experimental data and analysis technique

To study the dynamics of quasi-periodic oscillations, data from the Gamma-ray Burst Monitor (GMB) located on board the Fermi space Observatory were used, which are available on the NASA High Energy Astrophysics Science Archive Research Center server [13]. Data from detectors based on NaI crystals (detectors n7 and n8, energy range from 5 to 2000 keV) and BGO crystals (detectors b0 and b1, energy range from 109 keV to 50 MeV) were analyzed. The data files of γ-ray quantum streams of each detector, recorded in the TTE format, were recalculated into even time series in 64 ms increments. Such a time step was chosen according to the sampling value of the time series used to process Swift telescope data [9]. Further, for the convenience of presentation and graphical representation of the source data and the results obtained, the time scale will be displayed, and the time itself will be counted, in units of sampling of the source data: $\Delta_t$ = 64 ms (or 1 bin). Thus, the length of each time series was 8064 $\Delta_t$ or 8064 bins (516.096 s). Fig. 2,*a* and 2,*f* shows graphs of γ-ray quantum fluxes (counts/0.064 s) recorded by detectors based on BGO and NaI crystals within their respective integral energy ranges on the time scale described above. To increase the signal-to-noise ratio, data from two NaI detectors were summed into one row. Similarly, data from two BGO detectors were combined. Further, the records of the time series of observations were divided into two background sections: 2144 bins before and 5522 bins after the burst; and the burst itself, 398 bins long. Then, the section before the burst was divided into seven identical segments with a duration of 536 bins so that each subsequent segment half overlapped the previous one. The section after the burst was divided into nine with duration of 1110 bins in the same way. The power spectrum for each section was calculated separately. For this purpose, the method of constructing a combined spectral periodogram (CSP) was used, which is a modification of the classical spectral analysis method.

A modification of the traditional method of spectral analysis was as follows. A sample normalized spectral density (SNSD) (the Fourier transform of the autocorrelation function of the original signal [14]), of the initial time series was calculated depending on the trial period, which is caused by the formulation of the problem of revealing the hidden periodicity in the initial data [15]. In addition, the initial time series was subjected to preliminary high-frequency filtering [16] with a predetermined filter cut off frequency at half the signal power, which corresponds to the "separation" period $T_f$ in the time domain. The initial data is filtered to eliminate the trend and more powerful low-frequency components from them. Then, for each high-frequency component $T_f$ filtered with its specific value of the parameter $T_f$, the normalized spectral density estimate from the period was again calculated, and all these estimates calculated for different values of the $T_f$ parameter were superimposed on each other on the same field of the graph, forming combined spectral periodogram (CSP). More details about this method can be found in [10, 13].

To assess the statistical significance of the assumed oscillations, a model was constructed that includes 4 sinusoidal oscillations with periods 12, 20, 36, and 60 bins, As a result of calculating the model parameters, the amplitude and statistical significance of each component were estimated.

## Data processing results

The burst flux CSP constructed for the NaI and BGO detector data are shown in Fig. 1. These results, up to the resolution of the CSP (±1 bin), confirm the conclusions made in [9] about the presence of quasi-periodic oscillations with the quasi-periods 12, 20, 35, and 60 bins in the GRB 190114C light curve time structure. The analysis of the periodograms of the background sections of the photon flux recordings was carried out as follows. Starting from the time interval corresponding to the γ-ray burst, the interval in which the periodogram was constructed shifted to the beginning of the analyzed series in increments of 268 bins or to the end of the analyzed data series in increments of 555 bins. Since the time intervals overlapped by half, the signal spectrum of each subsequent section contained elements of the spectrum of the previous section, and therefore, it was possible to trace the evolution of each component of the periodogram. This procedure was repeated until the beginning or the end of the original row was reached. When analyzing the photon background fluxes, it was assumed that the values of the quasi-periods of the existing oscillations would remain unchanged, or would change insignificantly and rather slowly [8]. Therefore, the value corresponding to the peak that was closest to one of the values of the quasi-periods: 12, 20, 35, and 60 bins was chosen from the CSP values of the background data sections. The results

obtained are presented in Fig. 2. It was assumed that the quasi-oscillation periods do not depend on the photon energy and therefore the data from the NaI and BGO detectors are plotted on the same field of the graph. It should be noted that in these graphs, only one point on the time axis corresponds to the length of the 398-bin γ-burst stage.

This method of revealing hidden periodicities in the treatment time series makes it possible to determine the values of the periods of quasi-oscillations only with an accuracy of ±1 bin, and the presence of the cosmic radiation noise component increases the error in estimating these values. Therefore, in order to find out the trend in the behavior of changes in the values of each of the four quasi-periods identified during the burst over the background sections of the light curve before and after the event, the values of the quasi-oscillation periods calculated by the method described above (Fig. 2) were approximated by a linear dependence: $P = A + Bt$ , where $P$ are the values of the quasi-periods, $t$ is the time. The results of this linear fit are shown in the table, from which one can notice a systematic decrease with time in the period of the 60 bins oscillation, while the 12 bins oscillation tends to increase in period values. A similar unambiguous result for oscillations with periods of 35 bins and 20 bins was not obtained. It should be noted that the γ-ray burst itself is located inside the time interval when, according to the estimates, fluctuations with quasi-periods 35 bins and 60 bins are in a multiple ratio of 3/5.

To estimate the amplitudes, initial phases and their standards (assuming their normal distribution) of oscillations, a model consisting of 4 sinusoidal oscillations with periods of 12, 20, 36, and 60 bins was constructed. The amplitude, initial phase and standards of each component were estimated as a result of calculating the parameters of the model under consideration. As a result of such processing the following very unexpected result was revealed. Before the γ-ray burst, there is an increase in the amplitudes (and, accordingly, their standards) of the oscillations characteristic of the main stage of the burst. At the same time, the average value of the background component remained almost unchanged. This is especially noticeable for fluctuations with a period of 12 and 20 bins. During the burst, the amplitude of the first harmonic of the analyzed oscillations increases by more than 2 orders of magnitude. After the main stage of the burst, the amplitude of the oscillations decreases sharply. Then there is a long process of a slow fall in the amplitudes of these oscillations. As noted in [17, 18] in this time interval the energy flux of γ-radiation decreases according to a power law with an exponent of about 1, which is typical for GRB afterglows. At the end of the time series (5000–8064 bins), the analyzed oscillations do not stand out among other noise components of the signal.

At the point of ~6200 bins, an eclipse of the GRB 190114C radiation source occurs by the Earth [17]. At the same time at a time interval of 5000 – 8064 bins we do not see significant changes in the signal spectrum. It should be noted that at the moment of the beginning of the eclipse the average value of the photon flux recorded by the GBM device does not change either.

Table

**Parameters of linear approximation of oscillation periods versus the time: $P = A + Bt$**

| $P$, $\Delta_t$ | Energy range | | | |
|---|---|---|---|---|
| | 5 – 50000 keV | | 109 – 2000 keV | |
| | $A$, $\Delta_t$ | $B*10^4$ | $A$, $\Delta_t$ | $B*10^4$ |
| 12 | 11.96 ± 0.33 | 0.91 ± 0.78 | 11.79 ± 0.30 | 0.27 ± 0.73 |
| 20 | 21.11 ± 0.65 | -1.27 ± 1.59 | 19.50 ± 0.46 | 1.11 ± 1.12 |
| 35 | 36.10 ± 0.65 | -2.13 ± 1.59 | 34.53 ± 0.74 | 2.86 ± 1.81 |
| 60 | 60.18 ± 0.88 | -3.82 ± 2.13 | 61.35 ± 1.08 | -4.44 ± 2.57 |
| Position of the resonance point 3/5 | 380 $\Delta_t$ | | 4116 $\Delta_t$ | |

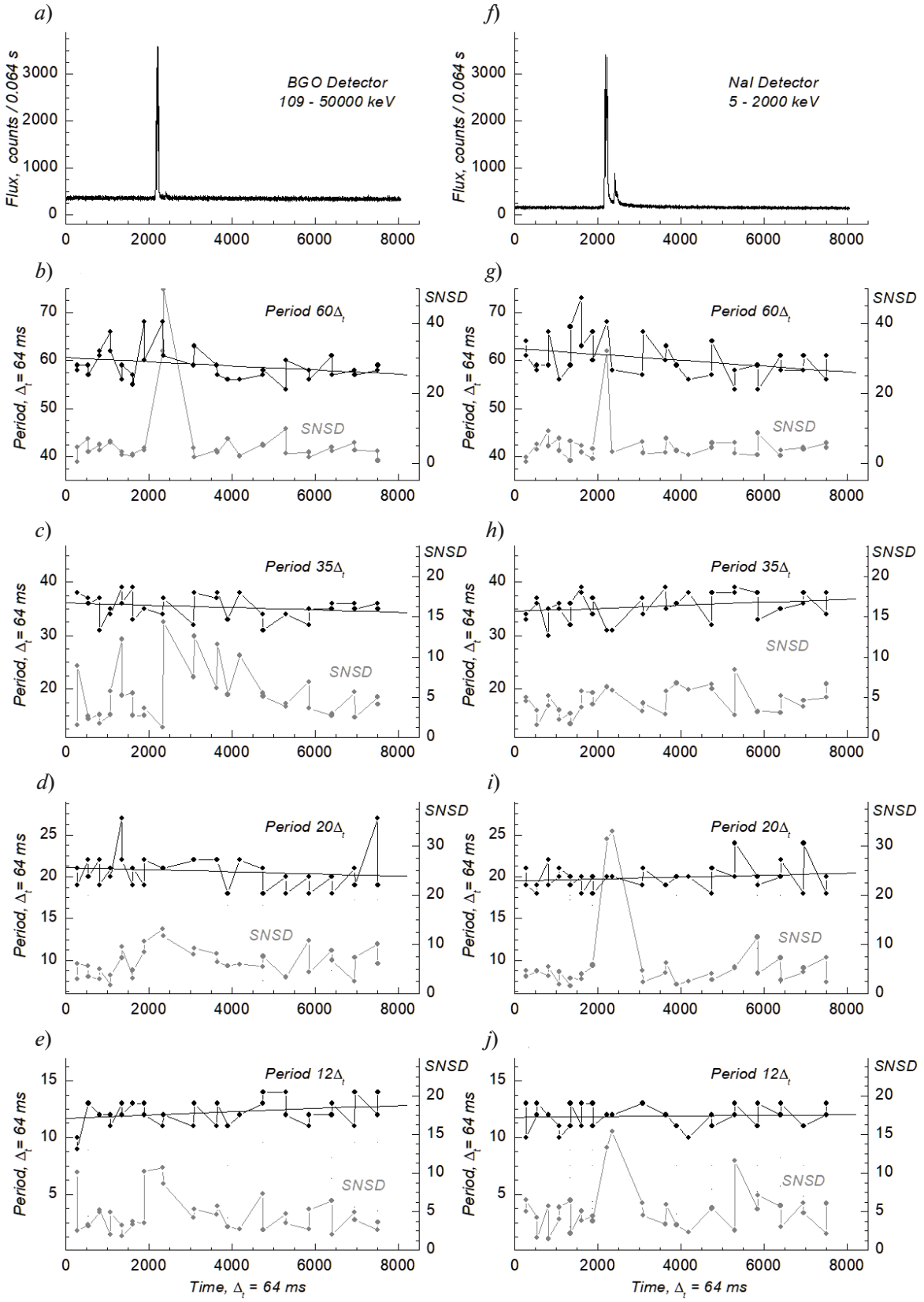


Fig. 2. Change of the oscillation period value and corresponding SNSD value over time for periods: 60 bins (*b*, *g*); 35 bins (*c*, *h*); 20 bins (*d*, *i*), and12 bins (*e*, *j*). The curves on the graphs (*b*–*e*) correspond to the energy range 5–50000 keV, and on the graphs (*g*–*j*) to the energy range 109–2000 keV

Based on the above observations, we can propose the following scenario for the formation of a γ-ray burst GRB 190114C. After a supernova explosion, an accretion disk and jet form around the collapsing core. The oscillation periods of this disk change over time. When the resonance of the oscillations occurs, the amplitude of the oscillations increases significantly, this leads to a significant increase in the flow of matter to the collapsing core. Jet parameters change and conditions arise for generating a γ-ray burst. Such a scenario makes it possible to explain the presence of quasi-periodic fluctuations before the trigger time and after the burst. In this case, the temporal structure of the γ-ray emission reflects the dynamics of the space-time structure of the accretion disk.

**Conclusion**

As a result of this work, it has been established that the oscillatory processes detected on the GRB 190114C light curve also occur in the background areas of this event recordings by the GBM monitor of the Fermi spacecraft. It was hypothesized that the γ-ray burst of GRB 190114C arose due to the resonance of oscillations in the accretion disk around the collapsing Supernova core.

## REFERENCES

1. **Wood K.S., Byram E.T., Chubb T.A., et al.,** A 4.2 second period in the gamma-ray burst of 1977 October 29, ApJ, 247 (1) (1981) 632–638.

2. **Barat C., Hurley K., Niel M., et al.,** 1979 January 13 - an intense gamma-ray burst with a possible associated optical transient, ApJ, 286 (2) (1984) L5–L9.

3. **Kouveliotou C., Desai U.D., Cline T.L., et al.,** A 2.2 second period in the 1984 August 5 gamma-ray burst, ApJ, 330 (2) (1988) L101-L105.

4. **Gehrels N., Norris J.P., Barthelmy S.D., et al.,** A new γ-ray burst classification scheme from GRB060614, Nature, 444 (7122) (2006) 1044–1046.

5. **Crider A.,** A magnetar flare in the BATSE catalog?, arxiv.org/abs/astro-ph/0601019. Accessed January 21, 2022.

6. **Zhilyaev B., Andreev M., Sergeev A. Petkov V.,** Detection of an oscillatory phenomenon in optical transient counterpart of GRB 090522C from observations on peak Terskol, arxiv.org/abs/astro-ph/0711.0038. Accessed January 19, 2022.

7. **Beskin G., Karpov S., Bondar S., et al.,** Fast optical variability of a naked-eye burst - manifestation of the periodic activity of an internal engine, ApJ, 719 (1) (2010) L10–L14.

8. **Tarnopolski M., Marchenko V.,** A comprehensive power spectral density analysis of astronomical time series. II. The Swift/BAT long gamma-ray bursts, ApJ, 911 (1) (2021) 20.

9. **Dranevich V.A., Dmitriyev P.B**., Quasi-periodic oscillation of the γ-ray burst GRB 190114C, Journal of Physics: Conference Series, 1697 (2020) 012012.

10. **Melandri A., Izzo L., D'Avanzo P., et al.**, GRB 190114C: photometric detection of a SN component, GCN Circulars Archive, No. 23983 (2019).

11. **J. Selsing J., Fynbo J.P.U., Heintz K.E., et al.,** GRB 190114C: NOT optical counterpart and redshift, GCN Circulars Archive, No. 23695 (2019).

12. **Dranevich V.A., Dmitriyev P.B., Gnedin Yu.N**., Quasiperiodic oscillations in the light curve of GRB 080319B**,** ApJ, 52 (4) (2009) 534–544.

13. NASA HEASARC. URL: https://heasarc.gsfc.nasa.gov/ FTP/fermi/data/gbm/triggers/ 2019/bn190114873/current/. Accessed Febrary 2, 2021.

14. **Jenkins G.M., Watts D.G.** Spectral Analysis and its Applications, Holden-Day, San Francisco, 1968.

15. **Serebrennikov M.G., Pervozvansky A.A.,** Hidden Periodicity Determination, Nauka, Moscow, 1965.

16. **Alavi A.S., Jenkins G.M.** An example of digital filtering, *Journal of the Royal Statistical Society. Series C (Applied Statistics),* 14 (1) (1965) 70–74.

17. **Ajello M., Arimoto M., Axelsson M., et al.,** Fermi and Swift observations of GRB 190114C: Tracing the evolution of high-energy emission from prompt to afterglow, ApJ, 890 (2020) 9.

18. **Ursi A., Tavani M., Frederiks D. D., et al.,** AGILE and Konus-Wind observations of GRB 190114C: The remarkable prompt and early afterglow phases, ApJ, 904 (2020) 133.

## THE AUTHORS

**DRANEVICH Viacheslav A.**
dranevichva@mail.ru
ORCID: 0000-0002-5145-6206

**DMITRIEV Pavel B.**
paul.d@mail.ioffe.ru
ORCID: 0000-0002-6421-8696

*Received 28.10.2022. Approved after reviewing 08.11.2022. Accepted 08.11.2022.*

© Peter the Great St. Petersburg Polytechnic University, 2023

Conference materials
UDC 52-732
DOI: https://doi.org/10.18721/JPM.161.272

# Search for gamma-ray counterparts to FRBs in Konus-*Wind* data

A.V. Ridnaia[1]✉, D.D. Frederiks[1], D.S. Svinkin[1],
A.L. Lysenko[1], A.E. Tsvetkova[1], M.V. Ulanov[1]

[1] Ioffe Institute, 194021 St. Petersburg, Russia

✉ ridnaia@mail.ioffe.ru

**Abstract.** We report preliminary results of the search in the Konus-*Wind* experiment data for hard X-ray/soft γ-ray emission in coincidence with publicly reported fast radio bursts (FRBs). We find no significant associations for any of the 581 FRBs in our sample and report upper limits to the high-energy fluence/peak flux for three spectral shapes, which generally describe short GRB, long GRB and magnetar giant flare spectra. In addition to study each individual FRB, we perform a stacking analysis of the bursts from each repeating source in our sample and a separate stacking analysis of the bursts from the non-repeating FRBs. We find no statistically significant excess of the cumulative emission over background level for either case.

**Keywords:** fast radio bursts, magnetars, gamma-rays

**Funding:** This study was funded by Russian Science Foundation (RNF) grant number 21-12-00250._

**Citation:** Ridnaia A.V., Frederiks D.D., Svinkin D.S., Lysenko A.L., Tsvetkova A.E., Ulanov M.V., A search for gamma-ray counterparts to FRBs in Konus-*Wind* data, St. Petersburg State Polytechnical University Journal. Physics and Mathematics. 16 (1.2) (2023) 474–479. DOI: https://doi.org/10.18721/JPM.161.272

This is an open access article under the CC BY-NC 4.0 license (https://creativecommons.org/licenses/by-nc/4.0/)

Материалы конференции
УДК 52-732
DOI: https://doi.org/10.18721/JPM.161.272

# Поиск гамма-излучения, сопровождающего быстрые радиовсплески по данным эксперимента Конус-Винд

А.В. Ридная[1]✉, Д.Д. Фредерикс[1], Д.С. Свинкин[1],
А.Л. Лысенко[1], А.Е. Цветкова[1], М.В. Уланов[1]

[1] Физико-технический институт им. А.Ф. Иоффе РАН, Санкт-Петербург, Россия

✉ ridnaia@mail.ioffe.ru

**Аннотация.** В данной работе представлены методика и предварительные результаты архивного поиска гамма-транзиентов вблизи опубликованных быстрых радиовсплесков (FRB) по многолетним данным эксперимента Конус-Винд, осуществляющего непрерывный мониторинг излучения всего неба в диапазоне энергий гамма квантов 20–1500 кэВ. Значимых отождествлений для 581 FRB обнаружено не было и, для каждого события приведены верхние пределы на флюенс/пиковый поток для трех спектральных моделей, описывающих короткие и длинные гамма-всплески и внегалактические магнетарные вспышки. Помимо результатов анализа индивидуальных кривых блеска, проведен анализ усредненных кривых для одиночных событий и отдельно по каждому повторному источнику.

**Ключевые слова:** быстрые радиовсплески, магнетары, гамма-излучение

© Ridnaia A.V., Frederiks D.D., Svinkin D.S., Lysenko A.L., Tsvetkova A.E., Ulanov M.V., 2023. Published by Peter the Great St. Petersburg Polytechnic University.

**Финансирование:** Работа выполнена в рамках гранта Российского научного фонда (РНФ) № 21-12-00250.

**Ссылка при цитировании:** Ридная А.В., Фредерикс Д.Д., Свинкин Д.С., Лысенко А.Л., Цветкова А.Е., Уланов М.В. Поиск гамма-излучения, сопровождающего быстрые радиовсплески по данным эксперимента Конус-Винд // Научно-технические ведомости СПбГПУ. Физико-математические науки. 2023. Т. 16. № 1.2. С. 474–479. DOI: https://doi.org/10.18721/JPM.161.272

Статья открытого доступа, распространяемая по лицензии CC BY-NC 4.0 (https://creativecommons.org/licenses/by-nc/4.0/)

## Introduction

Fast radio burst (FRBs) are bright (~Jy), short-duration (~ms) radio transients of still unknown origin. Since their discovery in 2007, and confirmation as an extragalactic population in 2013, over 600 FRBs, as of 2022 April 27, have been publicly reported (Transient Name Server TNS; http://www.wis-tns.org/). Repeating bursts have been observed from twenty-two FRB sources. Nineteen FRB sources have been localized to arcsecond accuracy and directly associated with a host galaxy, revealing a wide range of galaxy types and local environments surrounding the FRBs [1].

Until now, no clear physical picture of either the central engine that produce an FRB or the mechanism by which the emission is generated has emerged. A wide range of models have been proposed, none of which is able to explain alone the variety of observed events. The most promising models consider magnetars as potential FRB sources. In support of them, an FRB-like event of 2020 April 28 was, for the first time, associated with a known hard X-ray source: the Galactic magnetar SGR 1935+2154 [2,3]. The bright radio burst was accompanied by the simultaneous emission of hard X-rays [4–7], with properties similar to those of short, repeating bursts from Galactic magnetars, except for the peculiarly hard energy spectrum [5].

Like for gamma ray bursts (GRBs) and other classes of astrophysical objects initially detected in a single band, it becomes evident that any progress in our understanding of these enigmatic events could be made only through a coordinated observation campaigns and theoretical efforts in an as wide as possible energy band. The presence or absence of simultaneous or delayed emission corresponding to FRBs in different wavebands can constrain the emission mechanisms and is crucial to identify the FRB progenitor(s).

To date, there have been a number of multiwavelength counterpart searches for FRBs without any significant detection [8–15], however most of them were focused on certain objects or based on small FRB samples available at the time of these publications. In this work, we, taking the advantages of the huge increase in the number of detected FRBs and over 25 years of continuous full-sky observations performed by the Konus-Wind gamma-ray spectrometer (KW), carry out a systematic search for high-energy emission from repeating and non-repeating FRB bursts.

Here, we present preliminary results of the search in KW data for hard X-ray/soft $\gamma$-ray counterparts to over 700 publicly reported FRBs events. The paper is organized as follows. In Section 2 we present an FRB sample used in the search. In Section 3, we briefly describe our technique of the counterpart search and upper limit calculations for individual and stacked events and estimate the KW upper limits. In Section 4 we summarize the results and conclude.

## FRB sample

For our analysis we selected all publicly reported FRBs from the TNS (799 events, accessed on 2022 April 27). Six events had to be discarded due to zero coordinates or times and 25 events due to data gaps in KW. In addition, we decided to preliminarily exclude 14 repeating sources, which have less than six bursts per source and have no accurate localization. So we ended up with the sample of 718 FRB events, including 573 non-repeating FRBs and 145 bursts from eight repeating sources: FRB 20121102A, FRB 20180814A, FRB 20180916B, FRB 20181030A, FRB 20190303A, FRB 20190711A, FRB 20200120E, FRB 20201124A. Fig. 1 shows dispersion measure distributions for the selected FRBs.

© Ридная А.В., Фредерикс Д.Д., Свинкин Д.С., Лысенко А.Л., Цветкова А.Е., Уланов М.В., 2023. Издатель: Санкт-Петербургский политехнический университет Петра Великого.

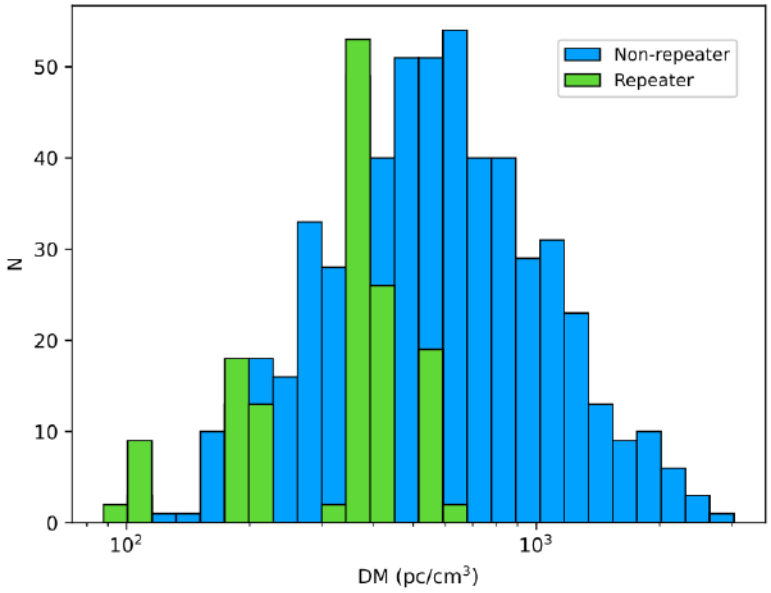


Fig. 1. Dispersion measure (DM) distributions for the selected sample of 581 FRBs: 573 "one-off" events and 145 bursts from 8 repeating sources. For 19 FRB sources associated with host galaxies, luminosity distances spans the range from 3.6 Mpc to 4 Gpc

## Konus-Wind analysis

Konus-*Wind* [16], running successfully since 1994, is a scintillation gamma-ray spectrometer, which consists of two identical NaI (Tl) detectors. It was developed at the Ioffe Institute and mounted on board Wind spacecraft (NASA), which is currently in a Lissajous orbit at the L1 libration point of the Sun-Earth system. The experiment has a unique set of properties, which make it a powerful tool to study hard X-ray/soft gamma-ray transients: stable background, continuous coverage of the full sky, high temporal resolution, and the wide (20 keV–15 MeV) energy range of spectral measurements. The instrument has two operational modes: waiting (continuous) and triggered. The continuous waiting-mode data allow searches for sources that are too weak to trigger KW. In this mode, count rates are recorded in three energy windows G1 (20–80 keV), G2 (80–320 keV), and G3 (320–1300 keV) with 2.944 s time resolution.

To search for FRB counterparts, we first estimate the burst arrival times $T_0$ at the KW position for each FRB. We consider two time corrections: a frequency-dependent delay due to dispersion of the radio frequency with respect to soft γ-rays (infinite frequency) and a propagation delay between KW and the radio telescope site. The calculated time corrections range from ms to hundreds of seconds, with a mean (median) value of 9.2 (4.9) s. We then search for a significant ($> 5\sigma$) high-energy emission increase over the surrounding background level during the 400 s time interval centered on the T0. Since there were no KW triggers in the intervals of interest, the search is performed in the waiting-mode data using six energy channel combinations (G1, G2, G3, G1+G2, G2+G3, and G1+G2+G3) and temporal scales from 2.944 s to 100 s [17]. The background is estimated using two intervals, before ($T_0$ – 1000 s, $T_0$ – 250 s) and after ($T_0$ + 250 s, $T_0$ + 1000 s) the search interval.

For upper limit calculations we apply the standard KW technique [18] using three spectral templates, which generally describe short-GRB, long-GRB, and magnetar giant flares (MGF) spectra: the Band function and two exponentially cut off power laws (CPLs), with the parameters listed in Table 1.

For a possible short event lasting less than 2.944 s and having a typical short GRB or MGF spectrum we provide limit on the 20–1500 keV fluence. For a typical long GRB spectrum we derive a limiting peak flux (20–1500 keV, 2.944 s scale).

In addition to study each individual FRB source, we perform a stacking analysis of background-subtracted KW data on bursts from each repeating source in our sample and a separate stacking analysis of the bursts from the non-repeating FRBs. In either case, we find no statistically significant excess in the cumulative light curve.

Table 1

**Three source spectrum models used in our upper limit calculations**

| Description | Model | Parameters | | |
|---|---|---|---|---|
| | | α | β | $E_p$ (keV) |
| Typical long GRB [19] | Band | –1.0 | –2.5 | 300 |
| Typical short GRB [19] | CPL | –0.5 | … | 500 |
| MGF [20] | CPL | –0.6 | … | 1190 |

## Results and conclusions

For all individual FRBs in our sample, we detect no significant hard X-ray/soft γ-ray emission in 200 s long intervals preceding and following the FRB arrival time. We report upper limits on hard X-ray/soft γ-ray emission in Fig. 2.

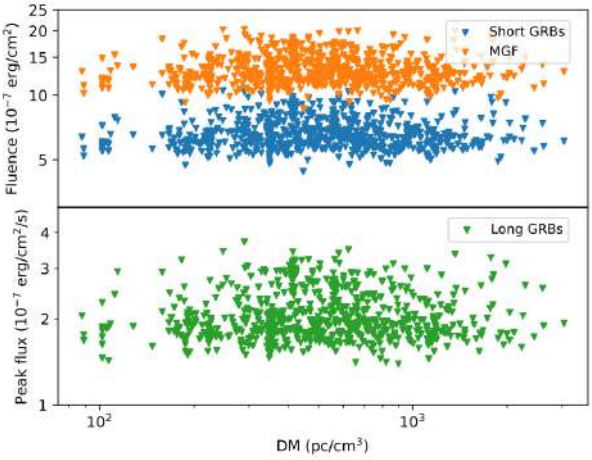


Fig. 2. KW upper limits on FRB high-energy emission (20-1500 keV) of 581 FRBs from our sample. Top panel: upper limits on short-GRB and MGF fluences. Bottom panel: upper limits on a long-GRB peak flux.

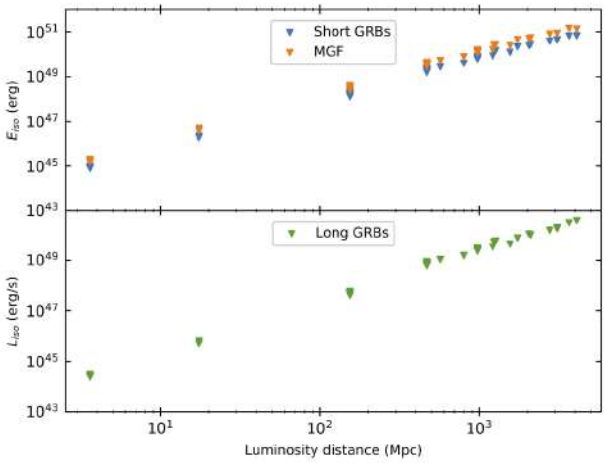


Fig. 3. Upper limits on the total isotropic equivalent energy release and peak luminosity for FRBs with known distances (redshifts)

The obtained individual upper limits are $(5-10)\cdot10^{-7}$ erg cm$^{-2}$ for the short GRB template, $(9-20)\cdot10^{-7}$ erg cm$^{-2}$ for the MGF template, and $(1-4)\cdot10^{-7}$ erg cm$^{-2}$ s$^{-1}$ for long bursts. The stacked data analysis allows us to set about a factor of 20 more stringent than the individual upper limits. For FRBs with measured host distances we estimate upper limits on the total isotropic equivalent energy release $E_{iso}$ and the peak luminosity $L_{iso}$ (see Fig. 3).

The two by far closest FRB repeaters, FRB 20181030A (at 20 Mpc) and FRB 20200120E (at 3.6 Mpc) are promising sources for constraining FRB emission models. The derived upper limits are $E_{iso} < 2.2\cdot10^{46}$ erg and $E_{iso} < 9\cdot10^{44}$ erg for short GRBs from FRB 20181030A and FRB 20200120E, respectively. The harder MGF spectral template results in about a factor of two less stringent upper limits, $E_{iso} < 4.3\cdot10^{46}$ erg and $E_{iso} < 2\cdot10^{45}$ erg, respectively. These limits do not rule out coincident magnetar giant flares, whose $E_{iso}$ range from $10^{44}$ erg to $10^{46}$ erg, as well as less energetic recurrent short and intermediate SGR bursts, with the typical emitted energies below $10^{42}$ erg.

The presented results are preliminary. They can be significantly improved as more distances to FRB sources will be obtained and, hopefully, closer distances will be applicable.

**Acknowledgments**

This study was funded by Russian Science Foundation (RNF) grant 21-12-00250.

## REFERENCES

1. **Heintz K.E., et al.,** Host Galaxy Properties and Offset Distributions of Fast Radio Bursts: Implications for Their Progenitors, The Astrophysical Journal 903 (2) (2020) 152.

2. **Bochenek C.D., Ravi V., Belov K.V., Hallinan G., Kocz J., Kulkarni S.R., McKenna D.L.**, A fast radio burst associated with a Galactic magnetar, Nature 587 (2020) 59–62.

3. **CHIME/FRB Collaboration, et al.,** A bright millisecond-duration radio burst from a Galactic magnetar, Nature 587 (2020) 54–58.

4. **Mereghetti S., et al.,** INTEGRAL Discovery of a Burst with Associated Radio Emission from the Magnetar SGR 1935+2154, The Astrophysical Journal 898 (2) (2020) L29.

5. **Ridnaia A., Svinkin D., Frederiks D., Bykov A., Popov S., Aptekar R., Golenetskii S., Lysenko A., Tsvetkova A., Ulanov M., Cline T.L.**, A peculiar hard X-ray counterpart of a Galactic fast radio burst, Nature Astronomy 5 (2021) 372–377.

6. **Li C.K., et al.,** HXMT identification of a non-thermal X-ray burst from SGR J1935+2154 and with FRB 200428, Nature Astronomy 5 (2021) 378–384.

7. **Tavani M., et al.,** An X-ray burst from a magnetar enlightening the mechanism of fast radio bursts, Nature Astronomy 5 (2021) 401–407.

8. **Tendulkar S.P., Kaspi V. M., Patel C.**, Radio Nondetection of the SGR 1806-20 Giant Flare and Implications for Fast Radio Bursts, The Astrophysical Journal 827 (1) (2016) 59.

9. **Cunningham V., Cenko S. B., Burns E., Goldstein A., Lien A., Kocevski D., Briggs M., Connaughton V., Miller M. C., Racusin J., Stanbro M.**, A Search for High-energy Counterparts to Fast Radio Bursts, The Astrophysical Journal 879 (1) (2019) 40.

10. **Martone R., Guidorzi C., Margutti R., Nicastro L., Amati L., Frontera F., Marongiu M., Orlandini M., Virgilli E.**, A cumulative search for hard X/γ-ray emission associated with fast radio bursts in Fermi/GBM data, Astronomy & Astrophysics 631 (2019) A62.

11. **Anumarlapudi A., Bhalerao V., Tendulkar S. P., Balasubramanian A.**, Prompt X-Ray Emission from Fast Radio Bursts-Upper Limits with AstroSat, The Astrophysical Journal 888 (1) (2020) 40.

12. **Verrecchia F., et al.,** AGILE Observations of Fast Radio Bursts, The Astrophysical Journal 915 (2) (2021) 102

13. **Principe G., Omodei N., Longo F., Di Venere L., Di Lalla N., Fermi-LAT Collaboration**, Hunting the gamma-ray emission from Fast Radio Burst with Fermi-LAT, 37th International Cosmic Ray Conference. 12-23 July 2021. Berlin p 624.

14. **Mereghetti S., Topinka M., Rigoselli M. and GËotz D.**, INTEGRAL Limits on Past High-energy Activity from FRB 20200120E in M81, The Astrophysical Journal 921(1) (2021) L3.

15. **Guidorzi C., et al.,** A search for prompt γ-ray counterparts to fast radio bursts in the Insight-HXMT data, Astronomy & Astrophysics 637 (2020) A69.

16. **Aptekar R.L., Frederiks D.D., Golenetskii S.V., Ilynskii V.N., Mazets E.P., Panov V.N., Sokolova Z.J., Terekhov M.M., Sheshin L.O., Cline T.L., Stilwell D.E.,** Konus-W Gamma-Ray Burst Experiment for the GGS Wind Spacecraft, Space Science Reviews 71 (1-4) (1995) 265–272.

17. **Svinkin D.S., Aptekar R.L., Golenetskii S.V., Frederiks D.D., Ulanov M.V., Tsvetkova A.E.**, Classification of gamma-ray bursts observed with Konus-Wind, Journal of Physics: Conference Series 1400 (2) (2019) 022010.

18. **Ridnaia A., Svinkin D., Frederiks D.**, A search for gamma-ray counterparts to gravitational wave events in Konus-*Wind* data, Journal of Physics: Conference Series 1697 (2020) 012030.

19. **Svinkin D.S., Frederiks D.D., Aptekar R.L., Golenetskii S.V., Pal'shin V.D., Oleynik Ph.P., Tsvetkova A.E., Ulanov M.V., Cline T.L., Hurley K.,** The second Konus-Wind catalog of short gamma-ray bursts, The Astrophysical Journal Supplement series 224 (1) (2016) 10.

20. **Svinkin D., et al.,** A bright γ-ray flare interpreted as a giant magnetar flare in NGC 253, Nature 589 (7841) (2021) 211–213.

## THE AUTHORS

**RIDNAIA Anna V.**
ridnaia@mail.ioffe.ru
ORCID: 0000-0001-9477-5437

**LYSENKO Alexandra L.**
alexandra.lysenko@mail.ioffe.ru
ORCID: 0000-0002-3942-8341

**FREDERIKS Dmitry D.**
fred@mail.ioffe.ru
ORCID: 0000-0002-1153-6340

**TSVETKOVA Anastasia E.**
tsvetkova@mail.ioffe.ru
ORCID: 0000-0003-0292-6221

**SVINKIN Dmitry S.**
svinkin@mail.ioffe.ru
ORCID: 0000-0002-2208-2196

**ULANOV Mikhail V.**
ulanov@mail.ioffe.ru
ORCID: 0000-0002-0076-5228

*Received 28.10.2022. Approved after reviewing 08.11.2022. Accepted 08.11.2022.*

© Peter the Great St. Petersburg Polytechnic University, 2023

Conference materials
UDC 524.1
DOI: https://doi.org/10.18721/JPM.161.273

# Method for gamma-hadron separation according to the experimental data of The Tunka-Grande array

R.D. Monkhoev[1]✉, TAIGA collaboration*

[1] Institute of Applied Physics, Irkutsk State University, Irkutsk, Russia

✉ makaay08@rambler.ru

**Abstract.** The Tunka-Grande array is a part of unified experimental complex, which also includes Tunka-133 and TAIGA-HiSCORE (High Sensitivity COsmic Rays and gamma Explorer) wide-angle Cherenkov arrays, TAIGA-IACT array (Imaging Atmospheric Cherenkov Telescope) and TAIGA-Muon scintillation array. This complex is located in the Tunka Valley (Buryatia Republic, Russia), 50 km from Lake Baikal. It is designed to study the energy spectrum and the mass composition of charged cosmic rays in the energy range 100 TeV–1000 PeV, to search for diffuse gamma rays above 100 TeV and to study local sources of gamma rays with energies above 30 TeV. This report outlines 3 key points. The first is the description of the Tunka-Grande scintillation array. The second one presents the strategy of the search for diffuse gamma rays based on a computer simulation of the Tunka-Grande array. The third one is devoted to the prospects for future research in the field of gamma-ray astronomy using simulation results.

**Keywords:** cosmic rays, extensive air showers, Tunka-Grande array.

**Funding:** The work was performed at the UNU «Astrophysical Complex of MSU-ISU» (agreements EB-075-15-2021-675). The work is supported by the Russian Science Foundation (grant 23-72-00054), the Russian Federation Ministry of Science and High Education (projects FZZE-2023-0004, FZZE-2020-0024, FSUS-2020-0039, FSUS-2022-0015).

**Citation:** Monkhoev R.D., TAIGA collaboration, Method for gamma-hadron separation according to the experimental data of the Tunka-Grande array, St. Petersburg State Polytechnical University Journal. Physics and Mathematics. 16 (1.2) (2023) 480–484. DOI: https://doi.org/10.18721/JPM.161.273

This is an open access article under the CC BY-NC 4.0 license (https://creativecommons.org/licenses/by-nc/4.0/)

Материалы конференции
УДК 524.1
DOI: https://doi.org/10.18721/JPM.161.273

# Метод гамма-адронного разделения по экспериментальным данным сцинтилляционной установки Tunka-Grande

Р.Д. Монхоев[1]✉, TAIGA collaboration*

[1] Иркутский государственный университет, Научно-исследовательский институт прикладной физики, г. Иркутск, Россия

✉ makaay08@rambler.ru

**Аннотация**. Сцинтилляционная установка Tunka-Grande входит в состав астрофизического комплекса TAIGA (Tunka Advanced Instrument for cosmic rays and Gamma Astronomy), который также включает в себя широкоугольные черенковские установки Тунка-133 и TAIGA-HiSCORE (High Sensitivity COsmic Rays and gamma Explorer), сеть атмосферных черенковских телескопов TAIGA-IACT (Imaging Atmospheric Cherenkov Telescope) и сцинтилляционную установку TAIGA-Muon. Данный комплекс располагается в Тункинской долине (республика Бурятия, Россия) в 50 км от озера

© Monkhoev R.D., TAIGA collaboration, 2023. Published by Peter the Great St. Petersburg Polytechnic University.

Байкал и нацелен на изучение энергетического спектра и массового состава космических лучей в диапазоне энергий 100 ТэВ - 1000 ПэВ, поиск диффузного гамма-излучения с энергией выше 100 ТэВ и исследование локальных источников гамма-квантов с энергиями более 30 ТэВ. В работе приведено описание сцинтилляционной установки Tunka-Grande и метода поиска диффузного гамма-излучения на основе проведенного компьютерного моделирования. Также указаны перспективы будущих исследований с использованием результатов этого моделирования.

**Ключевые слова**: Космические лучи, широкие атмосферные ливни, установка Tunka-Grande

**Финансирование**: Работа выполнена на УНУ «Астрофизический комплекс МГУ-ИГУ», поддержана Минобрнауки России (соглашение ЕВ675-2021-15-075-), в рамках тем государственного задания (проекты FZZE0004-2023-, FZZE0024-2020-, FSUS-2020-0039, FSUS0015-2022-), а также при поддержке Российского научного фонда (грант 00054-72-23).

**Ссылка при цитировании:** Монхоев Р.Д., TAIGA collaboration, Метод гамма-адронного разделения по экспериментальным данным сцинтилляционной установки Tunka-Grande // Научно-технические ведомости СПбГПУ. Физико-математические науки. 2023. Т. 16. № 1.2. С. 480–484. DOI: https://doi.org/10.18721/JPM.161.273

Статья открытого доступа, распространяемая по лицензии CC BY-NC 4.0 (https://creativecommons.org/licenses/by-nc/4.0/)

## Introduction

The study of the charged cosmic rays and cosmic gamma rays of high and ultrahigh energies has a great interest for understanding the mechanisms and nature of their origin, which is the most important task of modern astrophysics. The investigation of such radiation is carried out using method, based on the property of primary particles to generate a cascade of secondary particles in the Earth's atmosphere, the so-called extensive air shower (EAS). When an EAS develops, a large number of components arise in it. The electron-photon, hadron, and muon components, as well as the accompanying Cherenkov, ionization, and radio emission reach the observation level within the Earth's atmosphere. All of these components can be used to reconstruct the properties of primary cosmic radiation. Nowadays, the simultaneous detection and the study of many parameters of an EAS with the help of the ground base hybrid systems similar to the experimental complex located in the Tunka Valley, is of major importance.

Astrophysical research in the Tunka Valley has begun in 1993 and for many years was aimed at the study of charged cosmic rays, which continues to this day on the Tunka-133 array [1]. It is known that primary charged particles are deflected by galactic and intergalactic magnetic fields, which lead to the loss of any information about direction to the origin. In many ways, this reason has contributed to the rapid development of experimental gamma-ray astronomy in recent years. Indeed, since gamma rays are electrically neutral, they can be used as a pointer to the astrophysical objects in which they were produced. However, since the gamma-ray flux is low compared to the cosmic-ray flux, the problem arises, how to separate gamma quanta from the background events caused by high-energy charged particles. To solve this non-trivial task, the work has begun on the creation of the TAIGA-HiSCORE [2, 3], Tunka-Grande [4], TAIGA-IACT [5] and TAIGA-Muon [6] arrays in 2012, 2013, 2017 and 2019 respectively.

## Experimental set-up

The Tunka-Grande is designed to detect the charged component of an EAS and is presented as an array of scintillation counters combined in 19 stations on an area of 0.5 km$^2$. Each of them consists of two parts: surface and underground. The first detects all an EAS charged particles at the level of the array and consists of 12 counters covering an area of about 8 m$^2$, while the second, consisting of 8 counters with a total area of about 5 m$^2$, is located under a layer of soil ~1.5 m thick and is designed to detect the muon EAS component. Both parts are near to each other. The scintillation counter [7] has the form of a truncated pyramid whose inner surface is

© Монхоев Р.Д., TAIGA collaboration, 2023. Издатель: Санкт-Петербургский политехнический университет Петра Великого.

covered by a thin diffusely reflecting layer of white enamel. Inside the case there is the NE102A plastic scintillator in the form of a flat plate 800 mm × 800 mm × 40 mm in size and the Philips XP-3462 photomultiplier tube (PMT). Two counters at each station have additional PMTs whose amplification factor is 10 times lower than the standard one, ensuring a wide range of linearity in the measured signals. It should be noted that this type of counters is also currently used in the NEVOD-EAS [8] experiment and has previously been successfully used in the KASCADE-Grande [9] and EAS-TOP [10] experiments.

The electronics of the Tunka-Grande array [11] largely coincide with the electronics of the Tunka-133 array. The stations can send experimental information to central data acquisition system when both the external trigger signal arrives from the nearest cluster of the Tunka-133 array and when the signal arrives from the local trigger of the surface part. The local trigger generation condition of each station is the signal from two relativistic particles at the input of measuring channels of electronics. The count rate of one station in the external trigger mode is about 0.1 Hz and in the local trigger mode is about 10 Hz.

The aim of the Tunka-Grande array is the studying of the energy spectrum and mass composition of charged cosmic rays in the energy range of 10 - 1000 PeV, as well as to search for diffuse gamma rays about in the same energy range.

## Strategy of the search for diffuse gamma rays

Despite more than half a century of work on the search for high-energy diffuse gamma rays, no astrophysical photons with energies above 10 PeV have been detected, and at present only upper limits on their fluxes have been established experimentally. A great contribution to such research in the energy range 10—1000 PeV was made by the EAS-MSU [12] and KASCADE-Grande [13] arrays. According to the experimental data of the Tunka-Grande array, preliminary results were also obtained [14].

Nowadays one of the most promising approaches to separate events from primary gamma rays from the charged cosmic rays background is the studying the muon EAS component, since the number of muons in a shower generated by a gamma quantum is an order of magnitude less than in the hadronic shower. This in turn requires Monte Carlo simulation of EASes, along with selecting and comparing experimental data. For more accurately assess the promise of the Tunka-Grande array in this direction compared to earlier investigating [14], a new two-step computer simulation of the detectors operation was done. At first, the development of an EAS is simulated, second, the detectors response to passage of elementary particles is simulated as well. To solve these tasks, the CORSIKA (Version 7.7401) [15] and Geant4 [16, 17] packages were chosen as the software. EASes were generated from various primary particles (gamma quanta, protons, and iron nuclei) for the energy range $16.5 < lg(E/\text{eV}) < 17.5$ and for an interval of the zenith angle 0—45°. Hadron interactions at low energies were calculated using the GHEISHA model [18], high-energy interactions were processed with the QGSJET-II-04 model [19]. Simulation of the detectors response using the Geant4 package is described in the report [20].

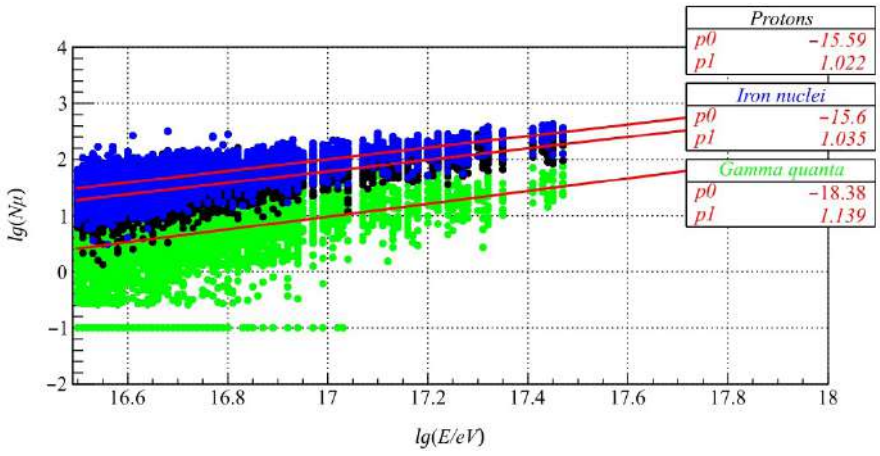


Fig. 1. Simulated distributions of the muon number

The distributions of the muon number versus the energy of primary particles are shown in Fig. 1. The figure presents the sum of detected particles for underground parts of all 19 stations for each EAS initiated by a gamma quantum (green points), proton (black points) and iron nucleus (blue points). The events without any detected muons are plotted with $lg(N\mu) = -1$ to be visible at the logarithmic axis. The distributions are approximated by function:

$$lg(N\mu) = p0 + p1 \cdot lg(E/\text{eV}). \quad (1)$$

It follows from Fig. 1 that, according to the Tunka-Grande experimental data, it is possible to separate gamma-ray candidates from the charged cosmic rays background with an efficiency of no worse than 50%.

### Prospects for the search for diffuse gamma rays

The EAS-MSU and KASCADE-Grande arrays are completed experiments. The Tunka-Grande array is an active experiment and operates around the clock in the data collection regime for almost the entire calendar year over a relatively large total area. Currently, ~240000 EASes with energies of primary particles above 10 PeV and ~2000 EASes with energies above 100 PeV have been detected over ~8900 hours (5 years of operation). The potential of the experiment based on these data will make it possible to detect gamma quanta or to set upper limits no worse than existing in the world.

### Conclusion

The Tunka-Grande array has great prospects for investigating diffuse gamma rays with energies above 10 PeV. Currently, there are experimental data for 5 years of operation of the array. This, together with the use of new computer simulation, will improve existing knowledge in the field of gamma-ray astronomy in the near future

### Acknowledgments

The authors would like to thank Irkutsk Supercomputer Center of SB RAS for providing the access to HPC-cluster “Akademik V.M. Matrosov” (Irkutsk Supercomputer Center of SB RAS, Irkutsk: ISDCT SB RAS; http://hpc.icc.ru).

## REFERENCES

1. **Berezhnev S. F., et al.,** The Tunka-133 EAS Cherenkov light array: status of 2011, Nucl. Instrum. Meth. A 692 (2012) 98—105.

2. **Tluczykont M., et al.,** The HiSCORE concept for gamma-ray and cosmic-ray astrophysics beyond 10 TeV, Astropart. Phys. 56 (2014) 42—53.

3. **Yashin I.I., et al,** The Taiga project, J. Phys. Conf. Ser. 675 (2016) 3, 032037.

4. **Monkhoev R.D., et al.,** The Tunka-Grande experiment: Status and prospects, Bull. Russ. Acad. Sci. 81 (2017) 4, 468—470.

5. **Lubsandorzhiev N., et al.,** The hybrid installation TAIGA: design, status and preliminary results, PoS ICRC729 (2020) 2019.

6. **Monkhoev R.D., et al.,** Tunka-Grande and TAIGA-Muon scintillation arrays: status and prospects, J. Phys. Conf. Ser. 1697 (2020) 1, 012026.

7. **Likiy O.I., et al.,** Investigating the characteristics of scintillation detectors for the NEVOD-EAS experiment, Instrum. Exp. Tech. 59 (2016) 6, 781—788.

8. **Shulzhenko I.A., et al.,** Status of the NEVOD-EAS experiment, Bull. Russ. Acad. Sci. Phys. 79 (2015) 3, 389—391.

9. **Apel W.D., et al.,** The KASCADE-Grande experiment, Nucl. Instrum. Meth. A 620 (2010) 202—216.

10. **Aglietta M., et al.,** UHE cosmic ray event reconstruction by the electromagnetic detector of EAS-TOP, Nucl. Instrum. Meth. A 336 (1993) 310—321.

11. **Monkhoev R.D., et al.,** The Tunka-Grande experiment, JINST 12 (2017) 06, C06019.

12. **Fomin Yu.A., et al.,** Constraints on the flux of ~ ($10^{16}$—$10^{17.5}$) eV cosmic photons from the EAS-MSU muon data, Phys. Rev. D 95 (2017) 12, 123011.

13. **Apel W.D., et al.,** KASCADE-Grande Limits on the Isotropic Diffuse Gamma-Ray Flux between 100 TeV and 1 EeV, Astrophys. J. 848 (2017) 1, 1.

14. **Monkhoev R.D., et al.,** The search for diffuse gamma rays using data from the Tunka-Grande experiment, Bull. Russ. Acad. Sci.: Phys. 83 (2019) 8, 959—61.

15. **Engel R., et al.,** Towards a Next Generation of CORSIKA: A Framework for the Simulation of Particle Cascades in Astroparticle Physics, Comput. Softw. Big Sci. 3 (2019) 1, 2.

16. **Allison J., et al.,** Recent developments in Geant4, Nucl. Instrum. Meth. A 186 (2016) 835—225.

17. **Agostinelli S., et al.,** GEANT4--a simulation toolkit, Nucl. Instrum. Meth. A 506 (2003) 250—303.

18. **Heck D.,** Low energy hadronic interaction models, Nucl. Phys. B Proc. Suppl. 151 (2006) 127—134.

19. **Ostapenko S.,** QGSJET-II: physics, recent improvements, and results for air showers, EPJ Web Conf. 52 (2013) 02001.

20. **Monkhoev R., et al.,** Geant4 simulation of the Tunka-Grande experiment, J. Phys. Conf. Ser. 2103 (2021) 1, 012001.

## THE AUTHORS

**MONKHOEV Roman D.** from TAIGA collaboration
makaay08@rambler.ru
ORCID: 0000-0002-5703-8320

***TAIGA collaboration:**
Astapov I.I., Bezyazeekov P.A., Bonvech E.A., Borodin A.N., Budnev N.M., Bulan A.V., Chernov D.V., Chiavassa A., Dyachok A.N., Gafarov A.R., Garmash A.Yu., Grenebyuk V.M., Gress E.O., Gress O.A., Gress T.I., Grinyuk A.A., Grishin O.G., Ivanova A.D., Ivanova A.L., Ilushin M.A., Kalmykov N.N., Kindin V.V., Kiryukhin S.N., Kokoulin R.P., Kompaniets K.G., Korosteleva E.E., Kozhin V.A., Kravchenko E.A., Kryukov A.P., Kuzmichev L.A., Lagutin A.A., Lavrova M.V., Lemeshev Yu.E., Lubsandorzhiev B.K., Lubsandorzhiev N.B., Malakhov S.D., Mirgazov R.R., Monkhoev R.D., Okuneva E.A., Osipova E.A., Pakhorukov A.L., Pankov L.V., Pan A., Panov A., Petrukhin A.A., Podgrudkov D.A., Popova E.G., Postnikov E.G., Prosin V.V., Ptuskin V.S., Pushnin A.A., Raikin R.I., Razumov A.Yu., Rubtsov G.I., Ryabov E.V., Samoliga V.S., Satyshev I., Sidorenkov A.Yu., Silaev A.A., Silaev A.A., Tarashchansky B.A., Tkachev L.G., Tanaev A.B., Ternovoy M.Yu., Ushakov N.A., Vaidyanathan A., Volchugov P.A., Volkov N.V., Voronin D.M., Zagorodnikov A.V., Zhurov D.P., Yashin I.I.,

*Received 29.10.2022. Approved after reviewing 08.11.2022. Accepted 09.11.2022.*

© Peter the Great St. Petersburg Polytechnic University, 2023

Conference materials
UDC 523.985.3
DOI: https://doi.org/10.18721/JPM.161.274

# Electron acceleration in models with a vertical current sheet

A.N. Shabalin✉, Yu.E. Charikov

Ioffe Institute, St. Petersburg, Russia

✉ ShabalinAN@mail.ioffe.ru

**Abstract.** Model of solar flares with a vertical current sheet and a cusp above the magnetic arcade is considered. In some flares, such magnetic field geometry can be observed directly in the extreme ultraviolet range. According to the model, the relaxation of helmet-like magnetic loops formed due to magnetic field reconnection is supposed. During the relaxation, the magnetic field and the loop length vary with time. Consequently, a betatron acceleration and first-order Fermi electron acceleration appeared. In a kinetic approach the time-dependent kinetic equation for the distribution function of initially accelerated electrons is numerically solved. It is shown that because of such acceleration, the electron energy spectra changes significantly. The proportion of high-energy electrons with energies of more than 200 keV increases by 1–3 orders of magnitude depending on the pitch-angular distribution of accelerated electrons formed in the primary accelerator – the current sheet.

**Keywords:** solar flare, acceleration, magnetic reconnection_

**Citation:** Shabalin A.N., Charikov Yu.E., Electron acceleration in models with a vertical current sheet, St. Petersburg State Polytechnical University Journal. Physics and Mathematics. 16 (1.2) (2023) 485–491. DOI: https://doi.org/10.18721/JPM.161.274

This is an open access article under the CC BY-NC 4.0 license (https://creativecommons.org/licenses/by-nc/4.0/)

Материалы конференции
УДК 523.985.3
DOI: https://doi.org/10.18721/JPM.161.274

# Ускорение электронов в моделях с вертикальным токовым слоем

А.Н. Шабалин✉, Ю.Е. Чариков

Физико-Технический институт им. А.Ф. Иоффе, РАН, Санкт-Петербург, Россия

✉ ShabalinAN@mail.ioffe.ru

**Аннотация.** Модели солнечных вспышек с вертикальным токовым слоем и каспом в области над аркадой замкнутых магнитных петель часто привлекаются при анализе вспышечных событий. В некоторых событиях подобную конфигурацию удается наблюдать непосредственно, в крайнем ультрафиолетовом диапазоне. В подобной геометрии магнитных полей рассматривается процесс релаксации вновь образуемых, после магнитного пересоединения, замкнутых магнитных петель и возникающее, как следствие, вторичное ускорение электронов за счет бетатронного ускорения и ускорения Ферми первого рода. В результате решения нестационарного кинетического уравнения для первично ускоренных электронов показано, что в результате процесса доускорения существенно изменяются со временем их энергетические спектры. Доля высокоэнергичных электронов с энергиями более 200 кэВ возрастает на 1–3 порядка в зависимости от питч-углового распределения ускоренных электронов, сформированного в первичном ускорителе — токовом слое.

**Ключевые слова:** солнечная вспышка, ускорение, магнитное пересоединение_

© Shabalin A.N., Charikov Yu.E., 2023. Published by Peter the Great St. Petersburg Polytechnic University.

**Ссылка при цитировании:** Шабалин А.Н., Чариков Ю.Е. Ускорение электронов в моделях с вертикальным токовым слоем // Научно-технические ведомости СПбГПУ. Физико-математические науки. 2023. Т. 1.2 № .16. С. 485–491. DOI: https://doi.org/10.18721/JPM.161.274

Статья открытого доступа, распространяемая по лицензии CC BY-NC 4.0 (https://creativecommons.org/licenses/by-nc/4.0/)

## Introduction

According to observations and modeling, configurations of magnetic fields with a vertical current sheet and sources on the photosphere are possible in active regions of the atmospheres of flaring stars, in particular the Sun [1–3]. Relaxation of the magnetic structure initially extended in the direction of the current sheet to a closed configuration similar to a dipole is accompanied by a longitudinally - transverse contraction of the magnetic loop. It leads to betatron acceleration and first-order Fermi acceleration [4–6]. The peculiarity of these processes is the angular anisotropy of the energy gained by electrons. Betatron acceleration leads to acceleration in the transverse direction. First-order Fermi acceleration increases the longitudinal component of the particle velocity.

Observational signs of magnetic loops relaxation include, for example, separation of coronal X-ray sources at different energies in height, as well as a decrease in their height with time in the initial phase of the flare [7, 8]. According to the model concepts [9], current sheets have small spatial thicknesses and, therefore, are difficult to observe, especially in the X-ray range. Nevertheless, data at various wavelengths indicate their existence [2, 10–12].

The rate of energy gain by an electron due to the betatron and Fermi acceleration is easily obtained from the conservation of the first (transverse) and the second (longitudinal) adiabatic invariants in a magnetic field. The relative rate of increase of the transverse energy is ~ $(1-\mu^2)$ $d\ln B/dt$, and the longitudinal one is ~ $\mu^2 d\ln L/dt$, where $\mu = \cos(\alpha)$, $\alpha$ is the pitch angle of an electron, $B(t)$ is the magnetic field, $L(t)$ is the length of the loop. Thus, the acceleration depends on the rate of the magnetic field change in the loop during relaxation. In the work within the framework of solving the kinetic equation for the distribution function of accelerated electrons, the calculation of additional (secondary) acceleration of electrons due to the mechanisms of betatron and Fermi acceleration is carried out.

## The modeling of collapsing traps

To solve the problem of additional electron acceleration, we will perform modeling of the kinetics of accelerated electrons in a relaxing magnetic field with a cusp structure. We will consider a time-dependent one-dimensional Fokker–Planck type equation with a model nonstationary magnetic field and a time-variable plasma density along the flare loop. The kinetic equation is considered in detail in [13]. The Fokker-Planck equation can be written in the form [14–17]

$$\frac{\partial f}{\partial t} = -\beta c\mu\frac{\partial f}{\partial s} + \beta c\frac{\partial \ln B}{\partial s}\frac{\partial}{\partial \mu}\left[\frac{(1-\mu^2)}{2}f\right] + C_1\frac{c}{\lambda_0}\frac{\partial}{\partial E}\left(\frac{f}{\beta}\right) + C_2\frac{c}{\lambda_0\beta^3\gamma^2}\frac{\partial}{\partial \mu}\left[(1-\mu^2)\frac{\partial f}{\partial \mu}\right] + \\ + \frac{eY\beta\mu}{m_e c}\frac{\partial f}{\partial E} + \frac{eY}{m_e\beta c}\frac{\partial}{\partial \mu}\left[(1-\mu^2)f\right] + \frac{\partial(\dot{E}f)}{\partial E} + \frac{\partial(\dot{\mu}f)}{\partial \mu} + S(E,\mu,s,t), \quad (1)$$

where $f(E,\mu,s,t)$ is the non-thermal electron distribution function which is defined so that the integrals over variables $E$, $\mu$, $s$ yield the linear density [18], $s$ is the distance along the magnetic field line ($s = 0$ corresponds to the loop top), $t$ is the time, $\mu = \cos(\alpha)$ is the cosine of the pitch angle, $\lambda_0(s) = 10^{24}/n(s)\ln\Lambda$, $n(s)$ is the plasma density; $\Lambda = \frac{3k_B T_e}{2e^2}\left(\frac{k_B T_e}{8\pi e^2 n}\right)^{0.5}$ [19], $k_B$ is the Boltzmann constant, $T_e$ is electron temperature, $e$ is electron charge, $\beta = v/c$, $v$ is non-thermal

© Шабалин А.Н., Чариков Ю.Е., 2023. Издатель: Санкт-Петербургский политехнический университет Петра Великого.

electron speed, $c$ is speed of light, $m_e$ is electron mass, $\gamma = E+1$ is Lorentz factor of the electron, $E$ is the kinetic energy of an electron, expressed in units of the electron rest mass energy, $\tilde{N}_1 = x + \frac{1-x}{2}\frac{\ln \beta^2 g^2 E/\alpha_F^4}{\ln \Lambda}$, $C_2 = \frac{1}{2} + \frac{1+g}{4} C_1$ [20, 21] are the coefficients taking into account the contribution of partially ionized plasma to the energy loss and angular scattering of fast electrons, $\alpha^4_F$ is fine structure constant, $x$ is fraction of ionized hydrogen atoms, $g \sim 1$. The influence of betatron and Fermi processes on the energy and pitch-angles described by the partial derivatives (two terms at the last line of Eq. 1). These terms are considered in more detail in the work [13].

We assume that many episodes of energy release and subsequent "collapses" of magnetic structures occur in the region of the current sheet. However, in this work, we consider the relaxation of one magnetic structure in order to analyze the effects of accumulation of accelerated electrons in a single loop. The collapse times in the range 10–60 s correspond to the possible relaxation times of magnetic loops at sub-Alfven velocities. The paper shows the results for the first 6 seconds, because with a selected collapse time of about 8–10 seconds, the acceleration efficiency is maximum in the initial 6 seconds.

The magnitude of the magnetic field induction at the looptop varied from 20 G to ~200 G. Due to the conservation of the magnetic flux and the number of particles inside the closed magnetic loop, the cross-sectional area of the loop and the plasma density along the loop variates following the change in the magnetic field.

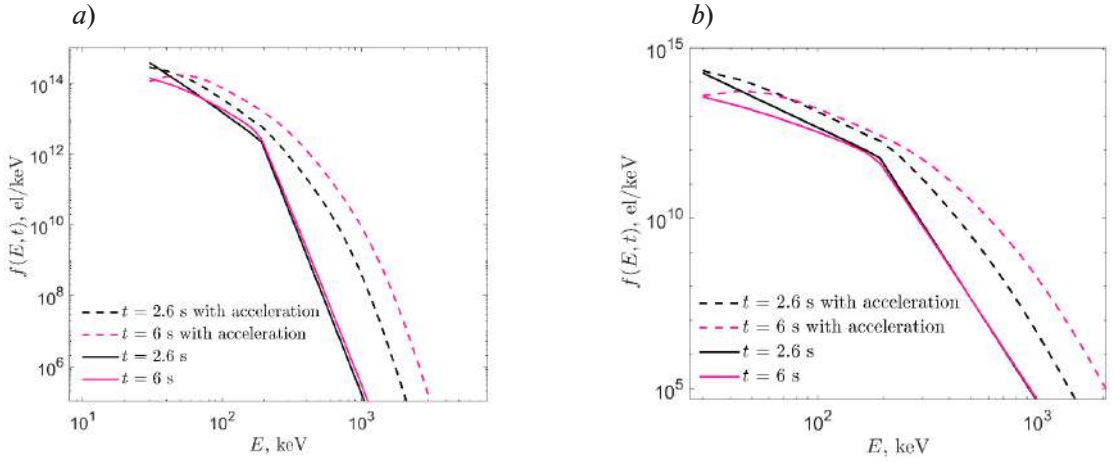


Fig. 1. Looptop energy spectra of accelerated electrons. Left panel: the spectra for the isotropic model S(α) = 1. Right panel: for the anisotropic model $S(\alpha) = \cos^{12}(\alpha)$. The curves are given for two time instants: the injection peak phase at $t$ = 2.6 s and the decay phase at $t$ = 6 s. The spectrum exponents of injected electrons in the models are δ = 3

Thus, at the beginning of the magnetic field relaxation process, the closed loop was an effective trap with a large magnetic ratio of $B_{max}/B_0 = 80$ (20 G at the top and 1.6 kG at the footpoints) for injected electrons accelerated in the current sheet. During the collapse of the magnetic field, the loss cone increases, the plasma density in the coronal part of the loop increases, leading to an increase of Coulomb scattering of accelerated electrons and the effective precipitation of electrons into the chromosphere. In the model the final number density and energy spectrum of accelerated electrons significantly depend on several physical processes – the rate of change of the magnetic field, the Coulomb scattering, the effects of return current, magnetic mirroring, plasma and magnetic field parameters, the pitch angular distribution of accelerated electrons at the injection time.

We consider the effect of betatron and Fermi acceleration on the spectra of accelerated electrons. The rate of energy gain by an accelerated electron during betatron acceleration is determined by the term $\sim(1-\mu^2)d\ln B/dt$ in the kinetic equation, and the term $\sim\mu^2 d\ln L/dt$ determines the efficiency of first-order Fermi acceleration. As can be seen, the pitch--angular dependence of the rate of energy gain in these processes is sharply different: transverse acceleration in betatron acceleration and longitudinal acceleration in the Fermi mechanism.

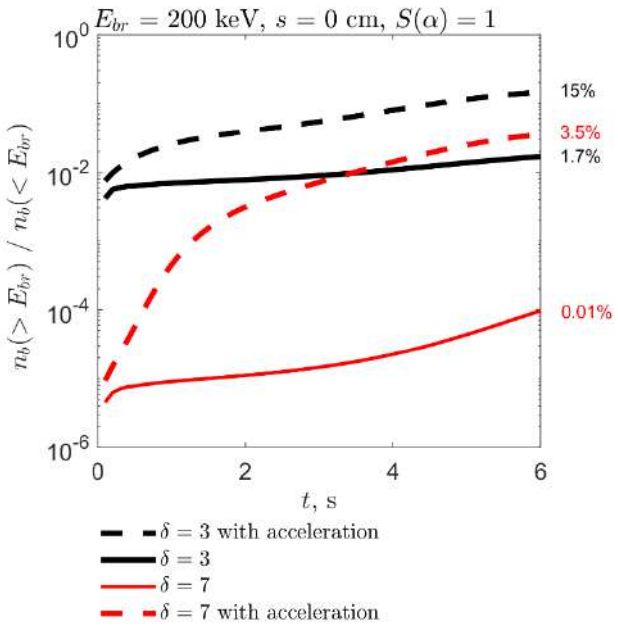


Fig. 2. The dynamics over time of the ratio of the number density of electrons with energy $E > E_{br}$ to electrons with $E < E_{br}$, $E_{br}$ = 200 keV. The ratios are given for the looptop. The pitch-angular distribution of electrons at the injection site is isotropic

The results for two models of accelerated electrons injection into the top of a magnetic loop will be presented below for isotropic model S(α) = 1 and anisotropic one S(α) = $\cos^{12}(\alpha)$. Suppose that at the injection site the energy spectrum is broken power-law with spectrum exponents δ = 3 or 7 in the energy range of 30–200 keV and δ = 10 in the energy range of 200 keV – 10 MeV. The choice of the break point in the spectrum is due to the fact that it is supposed to analyze the efficiency of increasing the number of accelerated electrons with energies that make a predominant contribution to the gyrosynchrotron radiation in the 17–34 GHz range, namely, with energies > 200 keV. The hardness of the emission spectra in the hard X-ray range during flares varies over a wide range. Therefore, variants of the initial soft δ = 7 and hard δ = 3 electron spectra are considered. The angular distribution of accelerated electrons at the moment of injection into the collapsing loop is not known, therefore we considered the limiting cases of isotropic S(α) = 1 and strongly anisotropic S(α) = $\cos^{12}(\alpha)$ distributions of accelerated electrons at the moment of injection.

The initial plasma density at the looptop was set to $7 \cdot 10^8$ cm$^{-3}$ [22, 23]. In the chromosphere, the calculations are performed using height density distribution corresponding to hydrostatic equilibrium [24]. The maximum plasma density at footpoints in the models is $3 \cdot 10^{13}$ cm$^{-3}$. To compare the results, a model with a stationary magnetic field and plasma density at the top of the loop of $10^{10}$ cm$^{-3}$ is also considered.

Fig. 1 shows the spectra of accelerated electrons for a model with permanent distributions of the magnetic field and plasma density (solid curves, hereinafter referred to as the stationary model (S-model)) and a model with longitudinal-transverse compression of the magnetic loop (dashed curves, hereinafter referred to as the non-stationary model (NS-model)). The energy injected by accelerated electrons in both models is $2 \cdot 10^9$ erg cm$^{-2}$s$^{-1}$ for a time period of 6 s. The figure shows that the dashed curves in the NS-model exceed the solid curves of the S-model in the energy range of ~ 45 keV – 8 MeV, which is caused by energy gain due to betatron and Fermi accelerations.

In the range of 30–45 keV, the dashed curves are below the solid curves. This decrease in the number of electrons is explained by more efficient energy losses due to Coulomb interactions with plasma protons, as well as the result of acceleration processes i.e. spectral energy transfer. The spectral energy transfer results in the energy break in the electron injection spectrum in the 200 keV disappears.

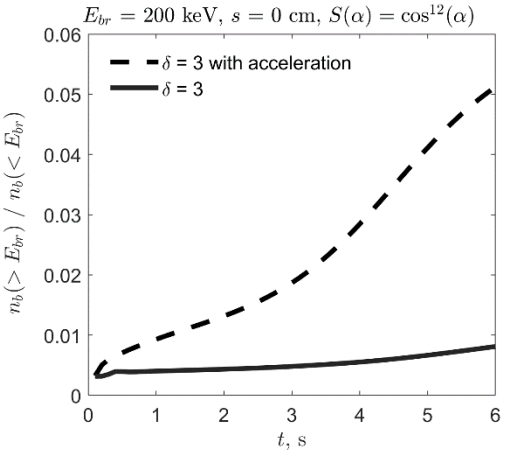


Fig. 3. Same as in Fig. 2 for anisotropic injection of accelerated electrons

The analysis of the observed hard X-ray radiation in the energy range >200 keV by modern spectrometers causes difficulties arising from a sharp decrease in the number of X-ray quanta. Nevertheless, the spectra of high-energy electrons with energies >200 keV determine the gyrosynchrotron radiation at frequencies of ~8–40 GHz [25, 26]. In this regard, let us consider the time dependence of the fraction of electrons accelerated above the energy $E_{br}$ = 200 keV relative to electrons of lower energies. Above-mentioned ratios are shown in Fig. 2 for the isotropic model and in Fig. 3 for the anisotropic model. As in Fig. 1, the dashed curves correspond to the NS-model. The red curves were obtained in a model with a soft electron energy spectrum $\delta = 7$ at the time of injection, and the black curves were obtained in a model with a hard spectrum $\delta = 3$. Figs. 2 and 3 show that the dashed curves significantly exceed the solid curves already starting from the first second from the beginning of injection. At the time $t = 6$ s for the isotropic electron injection with spectrum exponent $\delta = 7$ (Fig. 2) in the NS-model, the proportion of high-energy electrons is 350 times greater than in the S-model. In the case of the injection with a hard spectrum $\delta = 3$, the proportion of high-energy electrons in the NS-model is 5–10 times greater.

Thus, in a model with a vertical current sheet, the proportion of accelerated electrons above the $E_{br}$ energy in a relaxing magnetic field could lead to an increase in hard X-ray, gamma radiation and radio emission at frequencies of 8–40 GHz. We also note that in the analyzed models, according to [13], the additional acceleration of electrons is associated with a higher efficiency of the betatron mechanism in comparison with the first order Fermi acceleration.

## Conclusion

The paper analyzes the efficiency of secondary acceleration of electrons to MeV energies, previously accelerated in a vertical current sheet to energies of hundreds of keV. For this purpose, a time-dependent kinetic equation was numerically solved for accelerated electrons in a magnetoactive plasma, whose parameters change over time as a result of the relaxation process of magnetic structures. The results of calculations show that the additional acceleration resulting from the relaxation of the magnetic field and the processes of betatron acceleration and first-order Fermi increases the proportion of high-energy electrons by 1–3 orders of magnitude. In absolute values, this makes it possible to increase the density of accelerated electrons with energies above 200 keV also by 1–3 orders of magnitude. If we assume that due to the primary acceleration, the number density of accelerated electrons with an energy >200 keV in the magnetic loop is of the order of $10^2$–$10^3$ cm$^{-3}$, then the secondary acceleration considered in the article will lead to an increase in $n_b$ (E>200 keV) to values of the order of $10^4$–$10^6$ cm$^{-3}$. The number density of high-energy electrons ~$10^5$ cm$^{-3}$ is already sufficient to register radiation in the radio band of 8–40 GHz [27]. Thus, the numerical results of electrons propagation in collapsing traps make it possible to significantly lower the requirements for acceleration of highenergy electrons in the primary accelerator — the current sheet.

## REFERENCES


1. **Gary D.E.**, **Chen B.**, **Dennis B.R.**, **Fleishman G.D.**, **Hurford G.J.**, **Krucker S.**, **McTiernan J.M.**, **Nita G.M.**, **Shih A.Y.**, **White S.M.**, **Yu S.**, Microwave and Hard X-Ray Observations of the 2017 September 10 Solar Limb Flare, The Astrophysical Journal, 863 (1) (2018) 83.
2. **Warren H.P.**, **Brooks D.H.**, **Ugarte-Urra I.**, **Reep J.W.**, **Crump N.A.**, **Doschek G.A.**, Spectroscopic Observations of Current Sheet Formation and Evolution, The Astrophysical Journal, 854 (2) (2017) 122.
3. **Jiang C.**, **Zou P.**, **Feng X.**, **Hu Q.**, **Liu R.**, **Vemareddy P.**, **Duan A.**, **Zuo P.**, **Wang Y.**, **Wei F.**, Magnetohydrodynamic Simulation of the X9.3 Flare on 2017 September 6: Evolving Magnetic Topology, The Astrophysical Journal, 869 (1) (2018) 13.
4. **Somov B.V.**, **Kosugi T.**, Collisionless Reconnection and High-Energy Particle Acceleration in Solar Flares, The Astrophysical Journal, 485 (2) (1997) 859–868.
5. **Bogachev S.A.**, **Somov B. V.**, Acceleration of Charged Particles in Collapsing Magnetic Traps During Solar Flares, Astronomy Reports, 45 (2) (2001) 157–161.
6. **Karlicky M.**, **Barta M.**, X-Ray Loop-Top Source Generated by Processes in a Flare Collapsing Trap, The Astrophysical Journal, 647 (2) (2006) 1472–1479.
7. **Veronig A.M., Karlický M., Vršnak B., Temmer M., Magdalenić J., Dennis B.R., Otruba W., Pųtzi W.**, X-ray sources and magnetic reconnection in the X3.9 flare of 2003 November 3, Astronomy & Astrophysics, 446 (2) (2006) 675–690.
8. **Sui L., Holman G.D., Dennis B.R.**, Evidence for Magnetic Reconnection in Three Homologous Solar Flares Observed by RHESSI, The Astrophysical Journal, 612 (1) (2004) 546–556.
9. **Lin J., Forbes T.G.**, Effects of reconnection on the coronal mass ejection process, Journal of Geophysical Research: Space Physics, 105 (A2) (2000) 2375–2392.
10. **Webb D.F., Burkepile J., Forbes T.G., Riley P.**, Observational evidence of new current sheets trailing coronal mass ejections, Journal of Geophysical Research: Space Physics, 108 (A12) (2003) 1440.
11. **Sui L., Holman G.D.**, Evidence for the Formation of a Large-Scale Current Sheet in a Solar Flare, The Astrophysical Journal, 596 (2) (2003) L251–L254.
12. **Ko Y., Raymond J.C., Lin J., Lawrence G., Li J., Fludra A.**, Dynamical and Physical Properties of a Post–Coronal Mass Ejection Current Sheet, The Astrophysical Journal, 594 (2) (2003) 1068–1084.
13. **Shabalin A.N.**, **Charikov Y.E.**, **Sharykin I.N.**, Early-stage Coronal Hard X-Ray Source in Solar Flares in the Collapsing Trap Model, The Astrophysical Journal, 931 (27) (2022) 13.
14. **Hamilton R.J., Lu E.T., Petrosian V.**, Numerical solution of the time-dependent kinetic equation for electrons in magnetized plasma, The Astrophysical Journal, 354 (1990) 726–734.
15. **Zharkova V. V., Kuznetsov A.A., Siversky T. V.**, Diagnostics of energetic electrons with anisotropic distributions in solar flares. I. Hard X-rays bremsstrahlung emission, Astronomy and Astrophysics, 512 (2010) A8.
16. **Filatov L. V., Melnikov V.F., Gorbikov S.P.**, Dynamics of the spatial distribution of electrons and their gyrosynchrotron emission characteristics in a collapsing magnetic trap, Geomagnetism and Aeronomy, 53 (8) (2013) 1007–1012.
17. **Minoshima T., Masuda S., Miyoshi Y.**, Drift-kinetic modeling of particle acceleration and transport in solar flares, The Astrophysical Journal, 714 (1) (2010) 332–342.
18. **McClements K.G.**, The effects of magnetic field geometry on the confinement of energetic electrons in solar flares, Astronomy and Astrophysics, 253 (1992) 261–268.
19. **Ginzburg V.L.**, Theoretical physics and astrophysics. Additional chapters.V.L. Ginzburg.-Moscow:Nauka, (1981) 503 c.
20. **Leach J., Petrosian V.**, Impulsive phase of solar flares. I - Characteristics of high energy electrons , The Astrophysical Journal, 251 (1981) 781.
21. **Emslie A.G.**, The collisional interaction of a beam of charged particles with a hydrogen target of arbitrary ionization level, The Astrophysical Journal, 224 (1978) 241–246.
22. **Vernazza J.E.**, **Avrett E.H.**, **Loeser R.**, Structure of the solar chromosphere. III - Models of the EUV brightness components of the quiet-sun, The Astrophysical Journal Supplement Series, 45 (1981) 635–725.
23. **Masuda S.**, **Kosugi T.**, **Hara H.**, **Tsuneta S.**, **Ogawara Y.**, A loop-top hard X-ray source in a compact solar flare as evidence for magnetic reconnection, Nature, 371 (1994) 495–497.

24. **Mariska J.T.**, **Emslie A.G.**, **Li P.**, Numerical simulations of impulsively heated solar flares, The Astrophysical Journal, 341 (1989) 1067–1074.

25. **Melnikov V.F.**, **Reznikova V.E.**, **Shibasaki K.**, **Nakariakov V.M.**, Spatially resolved microwave pulsations of a flare loop, Astronomy & Astrophysics, 439 (2) (2005) 727–736.

26. **Reznikova V.E.**, **Melnikov V.F.**, **Shibasaki K.**, **Gorbikov S.P.**, **Pyatakov N.P.**, **Myagkova I.N.**, **Ji H.**, 2002 august 24 limb flare loop: dynamics of microwave brightness distribution, The Astrophysical Journal, 697 (1) (2009) 735–746.

27. **Shabalin A.N.**, **Ovchinnikova E.P.**, **Globina V.I.**, **Charikov Y.E.**, Accelerated Electron Propagation Model for the Flare Arcade of the September 23, 2014, Event from RHESSI, SDO, and Nobeyama Radioheliograph Observations, Geomagnetism and Aeronomy, 59 (8) (2019) 1128–1138.

## THE AUTHORS

**SHABALIN Alexander N.**
ShabalinAN@mail.ioffe.ru
ORCID: 0000-0003-3938-0146

**CHARIKOV Yuri E.**
Yuri.Charikov@mail.ioffe.ru
ORCID: 0000-0002-6693-5613

*Received 29.10.2022. Approved after reviewing 08.11.2022. Accepted 08.11.2022.*

© Peter the Great St. Petersburg Polytechnic University, 2023

Conference materials
UDC 523.985.3
DOI: https://doi.org/10.18721/JPM.161.275

# X-ray radiation of partially occulted solar flare of May 13, 2013

E.P. Ovchinnikova[1]✉,

[1]Ioffe Institute, St. Petersburg, Russia

✉elfimovaevgeniya@gmail.com

**Abstract.** The X-ray emission of the SOL2013-05-13T02:12 X1.7-GOES-class flare registered by the RHESSI spectrometer was analyzed. Various models of fitting the X-ray spectrum are applied. The following radiation models are considered: a two-temperature hot plasma model, a combination of a thin target model and a single-temperature plasma model, a combination of a bremsstrahlung model of a thick target and quasi-thermal radiation of a single-temperature plasma. Their validity to the spectra for this event is discussed. Plasma parameters are evaluated: emission measures, temperatures and density.

**Keywords:** Sun, solar flares, X-rays, RHESSI, thin target, thick target, bremsstrahlung.

**Citation:** Ovchinnikova E.P., X-ray radiation of partially occulted solar flare of May 13, 2013, St. Petersburg State Polytechnical University Journal. Physics and Mathematics. 16 (1.2) (2023) 492–498. DOI: https://doi.org/10.18721/JPM.161.275

This is an open access article under the CC BY-NC 4.0 license (https://creativecommons.org/licenses/by-nc/4.0/)

Материалы конференции
УДК 523.985.3
DOI: https://doi.org/10.18721/JPM.161.275

# Рентгеновское излучение частично затенненой солнечной вспышки 13 мая 2013

Е.П. Овчинникова [1] ✉

[1] Физико-технический институт им. А.Ф. Иоффе РАН, Санкт-Петербург, Россия

✉elfimovaevgeniya@gmail.com

**Аннотация.** Проведен анализ рентгеновского излучения вспышки X-1.7GOES класса SOL13-05-2013T02:12, зарегистрированной спектрометром RHESSI. Анализируются модели спектров рентгеновского излучения. Рассматриваются различные модели излучения: двухтемпературная модель горячей плазмы, совокупность модели тонкой мишени и модели однотемпературной плазмы, совокупность модели тормозного излучения (bremsstrahlung) толстой мишени и квазитеплового излучения однотемпературной плазмы. Обсуждается возможность их реализации для данного события. Проводится оценка параметров плазмы: меры эмиссии, температуры и концентрации.

**Ключевые слова:** Солнце, солнечные вспышки, рентгеновское излучение, RHESSI, модель тонкой мишени, модель толстой мишени, тормозное излучение._

**Ссылка при цитировании:** Овчинникова Е.П. Рентгеновское излучение частично затенненой солнечной вспышки 13 мая 2013 // Научно-технические ведомости СПбГПУ. Физико-математические науки. 2023. Т. 16. № 1.2. С. 492–498. DOI: https://doi.org/10.18721/JPM.161.275

Статья открытого доступа, распространяемая по лицензии CC BY-NC 4.0 (https://creativecommons.org/licenses/by-nc/4.0/)

© Ovchinnikova E.P., 2023. Published by Peter the Great St. Petersburg Polytechnic University.

## Introduction

During solar flares, a large amount of stored free energy of the magnetic field is released in the form of heated plasma and charged particles accelerated to energies of at least hundreds of keV. Super-hot plasma with a temperature of tens of MK and accelerated particles emit in the range from radio to gamma-rays [1]. At the same time, the possible acceleration processes have a different nature and can occur in several stages [2]. Subsequently, charged particle beams, during propagation in open and closed magnetic field configurations, undergo significant transformations in the spectrum, pitch-angular distribution due to the influence of many competing processes: secondary acceleration, Coulomb scattering, induced return current, magnetic mirroring, turbulence, magnetic fluctuations, magnetohydrodynamic waves etc [3, 4]. Plasma density and temperature in flaring magnetic structures change as a result of the evaporation effect, the transformation of the magnetic fields themselves [5–7]. All these effects and many others dramatically distort the spectra of accelerated particles, the distribution of temperature and plasma density along the flare loops. Due to the complexity of constructing numerical models that could take into account the listed transport, acceleration, diffusion effects, in the field of spectral analysis of flare phenomena, it is customary to use approximate analysis methods such as one or two temperature models of hot plasma, models of thin, thick and warm targets [8–11]. The use of simplified models can cause ambiguity in the results of the analysis. In this paper, the event is considered which is interesting because due to the partially occulted footpoints of the magnetic arcade, it is possible to observe a coronal source in the hard X-ray range. The analysis of spectra of coronal sources in such events is particularly interesting for assessing the applicability of simplified models of approximation of spectra, since the plasma density during the flare in the coronal part can vary within a sufficiently wide range, which can lead to the appearance of conditions for the implementation of the thick target and thin target models for different populations of accelerated electrons.

## The flare SOL2013-05-13T02:12

The SOL2013-05-13T02:12 flare occurred in the active region AR11748, which was near the Sun's limb on the invisible side, the coronal part and partially the chromospheric part of the magnetic field structure was visible in X-Rays and EUV by The Reuven Ramaty High-Energy Solar Spectroscopic Imager (RHESSI) [12] and by The Atmospheric Imaging Assembly (AIA) on the Solar Dynamics Observatory (SDO) [13]. We will call such an event a partially occulted flare [14], because sometimes radiation from the chromospheric regions of the flare arcade is observed (Fig. 1,*a*). The X-ray source at the looptop is visible in the range of 6-20 keV throughout the entire flare.

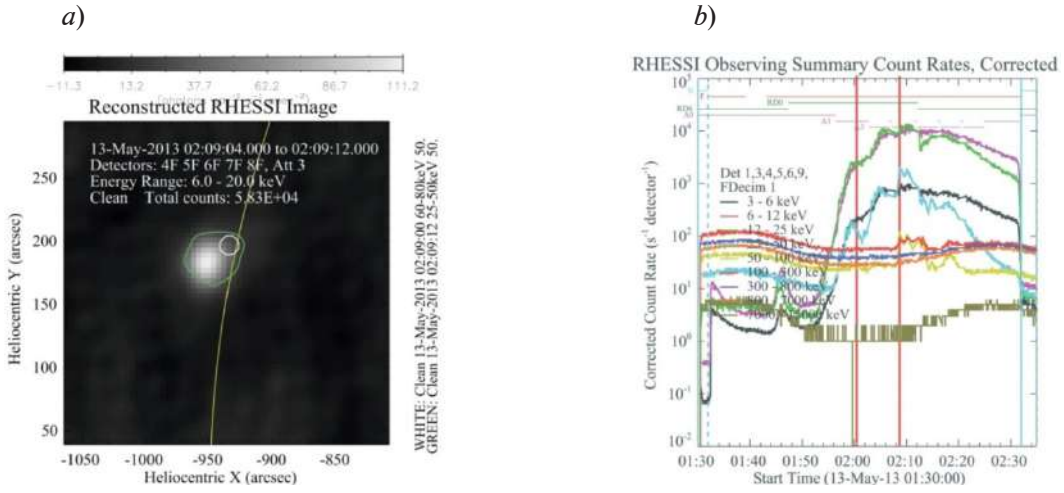


Fig. 1. X-ray image of the flare at 02:09:04 UT, white color - CLEAN 50% contour 6-20 keV, green color 50% contour 25-50 keV, white color 50% contour 60-80 keV, yellow line - Solar limb (*a*) time profile of the flare SOL2013-05-13T02:12 based on RHESSI data, red vertical lines indicate time intervals, which will be analyzed further (*b*)

© Овчинникова Е.П., 2023. Издатель: Санкт-Петербургский политехнический университет Петра Великого.

### X-ray spectra: models of thick and thin targets

Thick target approximation describes the case in which electrons lose all their energy in a hard X-ray source. Thus, at each moment of time, the source contains energetic electrons not only with the injection spectrum, but also with all harder spectra [8].

The thin target approximation is implemented in the case when electrons pass through a small depth, and spectrum changes in the source of hard X-ray radiation can be neglected. Intermediate cases could be described by the characteristic depth of the target or by the characteristic time for electrons to leave the region. The paper [15] gives the following relations for characteristic times: $\tau_e$ is exit time, $\tau_c$ is Coulomb collision time, $\tau_i$ is continuous injection time.

$$\tau_c \le \tau_e \le \tau_i \text{ for thick target approximation}$$

$$\tau_e \le \tau_c \le \tau_i \text{ thin target approximation.}$$

### X-ray spectra

According to the observed spectra and flux power, the flare was nominally divided into two phases: before the main peak and after the main peak in energies ranges 25–50, 50–100 keV (02:08:08) (Fig. 1,*b*). Below are examples of representative spectra from each phase and their analysis (Figs. 2, 3).

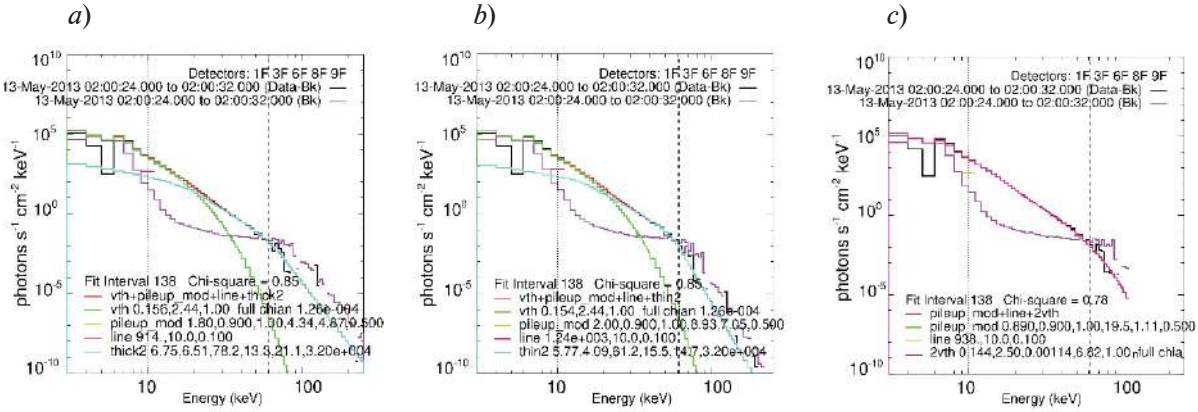


Fig. 2. Three different fitting models for the spectrum at 02:00:24-02:00:32 (before the main peak) vth+pileup_mod+line+thick2 (*a*), vth+pileup_mod+line+thin2 (*b*), 2vth+pileup_mod+line (*c*). Fitting models names according to Object Spectral Executive (OSPEX) [16] package functions in SolarSoft IDL software [17]

Before the main peak, the spectrum extends up to 50–60 keV; after the peak, a characteristic spectrum flattening at 40-100 keV appears in the spectrum, associated with the emission of non-thermal accelerated electrons. For analyzing the X-ray spectrum the following models were considered: thermal radiation of a two-temperature plasma (2vth function), a combination of a thin target (thin2 function), a thick target (thick2 function) with the addition of a single-temperature model of thermal radiation (vth function), auxiliary functions representing a pile-up correction (pileup_mod function), and an instrumentally formed line at 10 keV (line Gaussian function) [18]. A significant difference in the type of spectra in above intervals leads to qualitatively different questions of choosing a fitting model for these intervals.

Before the main peak, the two-temperature plasma model makes it possible to describe the spectrum at 10–60keV by the plasma thermal radiation. This model for the specified time interval well describes spectra by plasma thermal radiation with temperatures ~28MK and ~ 80MK. We consider heating to 80MK is implausible, but do not exclude it from consideration. Therefore, we consider the models with one-temperature approximation as more physically acceptable. The emission measure in these models before the main peak is $\sim 0.15 \cdot 10^{49} \text{cm}^{-3}$. It is worth mentioning that these values of emission measure and temperature 28 MK are obtained for both models with thin and thick targets (Fig. 2, Table 1).

Table 1

**Fits parameters and estimation of density for time interval 2:00:24 - 2:00:32**

| | chi$^2$ | $T_1$ (MK) | EM ($10^{49}$cm$^{-3}$) | $n$ (cm$^{-3}$) | $T_2$ (MK) | EM$_2$ ($10^{49}$cm$^{-3}$) | $\delta_1$ | $E_{break}$ (keV) | $\delta_2$ |
|---|---|---|---|---|---|---|---|---|---|
| 2vth | 0.78 | 29 | 0.14 | $2.7\cdot10^{10}$, $3.6\cdot10^{10}$ | 79 | 0.001 | - | - | - |
| vth+ thin2 | 0.85 | 28 | 0.15 | $2.8\cdot10^{10}$, $3.7\cdot10^{10}$ | - | - | 4.1 | 61 | 14.3 |
| vth+ thick2 | 0.85 | 28 | 0.16 | $2.8\cdot10^{10}$, $3.8\cdot10^{10}$ | - | - | 6.5 | 78 | 13.3 |

Notations: The fitting function is the models from the first column +pileup +line 10keV. Here EM is the emission measure; two density values are obtained for the volume of the emitting region of a sphere and a cylinder, respectively; $E_{break}$ is the break energy in the electron flux distribution; $\delta_1$ and $\delta_2$ are the power-law indices of the electron flux distribution function below and above $E_{break}$, respectively.

After the main peak there is no question about only thermal radiation, the choice of a target for describing the nonthermal part of the spectrum is required. The results for thin and thick targets are shown in Table 2, Fig. 3. The difference in the chi-square for the resulting fits is not significant and it is necessary to rely on the interpretation of physical processes and the resulting parameters of the flare plasma to distinguish between thick and thin targets. The paper [10] discusses a model of a thick warm target for the peak.

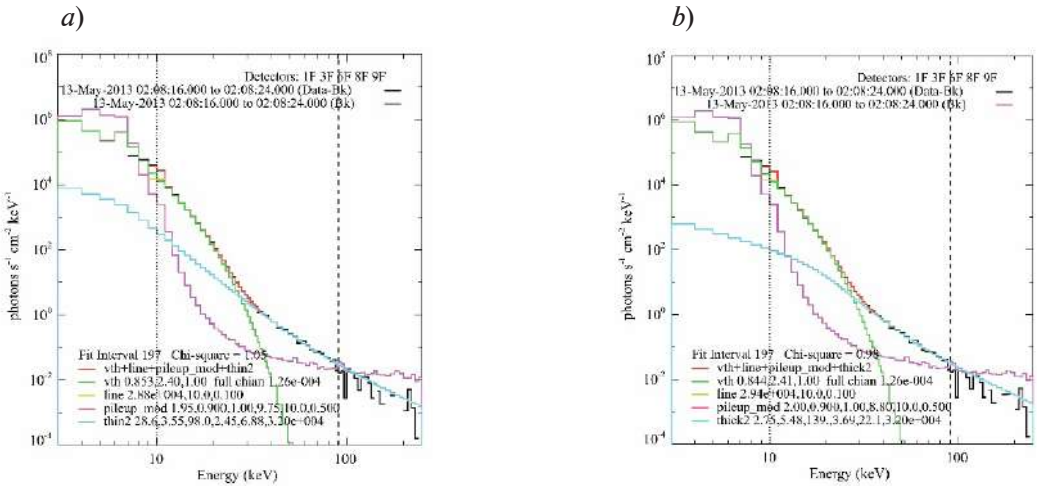


Fig. 3. Two fitting models of spectra at 02:08:16-02:08:24 (after the main peak) vth+pileup_mod+line+thin2 (*a*), vth+pileup_mod+line+thick2 (*b*)

Table 2

**Fits parameters and estimation of density for interval 2:08:16 - 2:08:24**

| | chi$^2$ | EM ($10^{49}$cm$^{-3}$) | $T$ (MK) | $n$ (cm$^{-3}$) | $\delta_1$ | $E_{break}$ (keV) | $\delta_2$ |
|---|---|---|---|---|---|---|---|
| vth+thin2 | 1.05 | 0.85 | 27.8 | $6.7\cdot10^{10}$, $1.1\cdot10^{11}$ | 3.6 | 98.0 | 2.5 |
| vth+thick2 | 0.98 | 0.84 | 28.0 | $6.7\cdot10^{10}$, $1.1\cdot10^{11}$ | 5.5 | 139.0 | 3.7 |

See notations for Table 1.

### X-ray source size and estimation of plasma density

Let us discuss an estimation of a volume and plasma density based on X-ray source size. Two imaging RHESSI reconstruction methods were used: CLEAN (beam factor = 1, contour level 50%), VIS FWDFIT algorithm. The uncertainty in the third invisible spatial parameter leads to an additional inaccuracy in the volume estimation. The volume of the radiating region can be estimated in different ways, assuming the region to be a sphere, a cylinder, or some other shape. Sources of different shapes were obtained by imaging methods: CLEAN makes it closer to a circle, VIS FWDFIT makes a more flattened ellipse, but the characteristic size is the same in both results (see Fig. 4). Using the results of VIS FWDFIT (Table 3), we estimate the volume of the source both as a sphere and as a cylinder.

$V = 4/3\pi \cdot R^3$, $R = 0.5$ major axis, $V = 0.25\pi \cdot D^2 \cdot h$, $h$ = major axis, $D$ = minor axis.

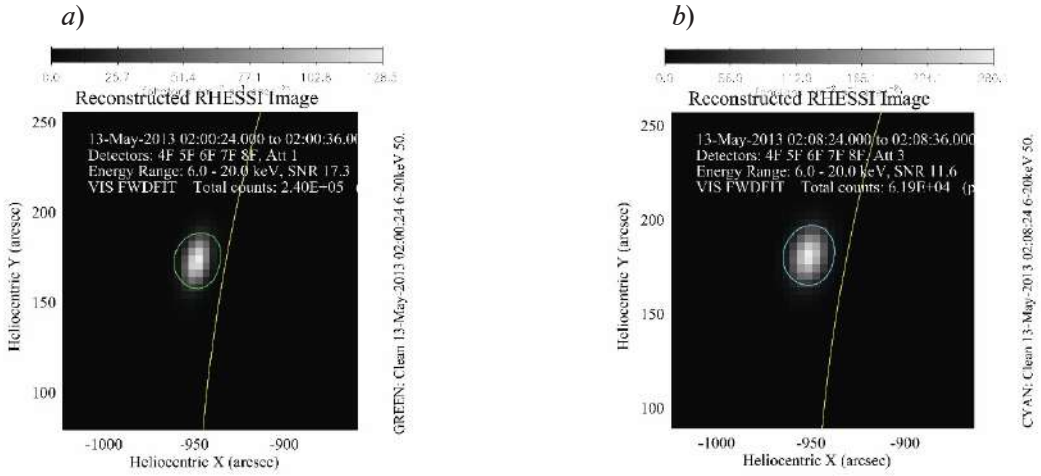


Fig. 4. X-ray images of the flare obtained by VIS FWDFIT and CLEAN methods for two time intervals from different phases of the flare: 2:00:24-2:00:36 (before the main peak) (*a*), 2:08:24-2:08:36 (after the main peak) (*b*)

Table 3

**Source size by VIS FWDFIT and estimation of volume, density and $E_{stop}$**

| | major axis (arcsec) | minor axis (arcsec) | $V_{sphere}$ (cm$^3$) | $V_{cylinder}$ (cm$^3$) | $n_{min}$ (cm$^{-3}$) | $n_{max}$ (cm$^{-3}$) | $E_{stop1}$ (keV) | $E_{stop2}$ (keV) |
|---|---|---|---|---|---|---|---|---|
| 2:00:24 | 21.5 ± 0.5 | 13.2 ± 0.4 | (2.0±0.1) $10^{27}$ | (1.12±0.08) $10^{27}$ | $2.7 \cdot 10^{10}$ | $3.6 \cdot 10^{10}$ | 15 | 17 |
| 2:08:24 | 21.2 ± 0.3 | 10.5 ± 0.2 | (1.9±0.1) $10^{27}$ | (0.69±0.03) $10^{27}$ | $6.5 \cdot 10^{10}$ | $1.1 \cdot 10^{11}$ | 23 | 30 |

For the obtained values, we determine the plasma density $n = (EM \cdot V^{-1})^{1/2}$. The values of the emission measure of thin and thick targets are close, so we do not consider these models separately while finding the plasma parameters. We estimate the minimum and maximum values of density using estimation of volume as a sphere and as a cylinder. Next, $E_{stop}$ is determined as the energy of electrons that lose all their energy due to Coulomb interactions with ions of the surrounding plasma. $E_{stop1}$ and $E_{stop2}$ were obtained using $n_{min}$, $n_{max}$ respectively.

$$E_{stop} = (4\pi \cdot n \cdot e^4 \cdot \Lambda_k \cdot l)^{1/2},$$

where $e$ is elementary charge, $n$ is plasma density, $\Lambda_k$ is the Coulomb logarithm, $l$ is size of a region. VIS FWDFIT estimated size of a region estimated as a major axis of ellipse (Table 3).

For electrons with energies less than $E_{stop}$, the thick target approximation is applicable in the radiation region. The results are shown in table 3. The obtained plasma parameters indicate the choice of a thin target model for this event in the energy range > $E_{stop}$.

**Summary**

The X-ray emission of the SOL2013-05-13T02:12 X1.7-GOES-class flare was analyzed. Before the main peak spectrum was described by the plasma thermal radiation with temperatures 28 MK and 80MK. We consider heating to 80MK is implausible. Spectra could also be represented by models with thin and thick targets before the main peak and after. Worth to mention these approximations are boundary cases in the propagation of high-energy electrons in flare plasma, and might not fully describe the ongoing processes. Thus, intermediate cases are most likely to be implemented. For obtained parameters emission measure, plasma density, source size, volume of emitting region and $E_{stop}$ we evaluated applicability of thin and thick approximations for fixed energy range. Note that, regardless of the choice of the target model, temperature of plasma and emission measure change insignificantly.

The value of $E_{stop}$ mainly depends on the correctness of determining the size of the source and on the unknown filling factor. Let us take a filling factor of 1. Then, before the peak, since the region of transition from thermal to nonthermal radiation is higher than $E_{stop}$ (see Fig. 2, Table 3), nonthermal radiation with energies >20keV could be considered as corresponding to a thin target with parameters indicated in table 1. In case after the peak phase the characteristic energy of transition from a thermal to a nonthermal radiation is also near the ~$E_{stop}$ during this phase, namely between 23–30 keV. Therefore after the peak the thin target model is also applicable to the nonthermal radiation >30 keV.

## REFERENCES

1. **Zharkova V.V., Arzner K., Benz A.O., et al,** Recent Advances in understanding particle acceleration processes in solar flares, Space Science Reviews, 159 (1–4) (2011) 357–420.

2. **Somov B.V., Syrovatskii S.I.,** Physical processes in the solar atmosphere associated with flares, Uspekhi Fizicheskih Nauk, 120 (10) (1976) 217.

3. **Filatov L.V., Melnikov V.F.,** Microwave Emission of a Flare Loop in the Presence of Whistler Turbulence, Geomagnetism and Aeronomy, 60 (8) (2020) 1137–1145.

4. **Shabalin A.N., Ovchinnikova E.P., Globina V.I., Charikov Y.E.,** Accelerated Electron Propagation Model for the Flare Arcade of the September 23, 2014, Event from RHESSI, SDO, and Nobeyama Radioheliograph Observations, Geomagnetism and Aeronomy, 59 (8) (2019) 1128–1138.

5. **Fisher G.H., Canfield R.C., McClymont A.N.,** Flare Loop Radiative Hydrodynamics - Part Six - Chromospheric Evaporation due to Heating by Nonthermal Electrons , The Astrophysical Journal, 289 (1985) 425.

6. **Liu W., Petrosian V., Mariska J.T.,** Combined modeling of acceleration, transport, and hydrodynamic response in solar flares. I. the numerical model, Astrophysical Journal, 702 (2) (2009) 1553–1566.

7. **Karlicky M., Barta M.,** X-Ray Loop-Top Source Generated by Processes in a Flare Collapsing Trap, The Astrophysical Journal, 647 (2) (2006) 1472–1479.

8. **Brown J.C.,** The deduction of energy spectra of non-thermal electrons in flares from the observed dynamic spectra of hard X-ray bursts, Solar Physics, 18 (3) (1971) 489–502.

9. **Brown J.C., Emslie A.G.,** Analytic limits on the forms of spectra possible from optically thin collisional bremsstrahlung source models, The Astrophysical Journal, 331 (1988) 554.

10. **Kontar E.P., Jeffrey N.L.S., Emslie A.G.,** Determination of the Total Accelerated Electron Rate and Power Using Solar Flare Hard X-Ray Spectra , The Astrophysical Journal, 871 (2) (2019) 225.

11. **Syrovatskii S.I., Shmeleva O.P.,** Nagrev plazmy bystrymi elektronami i neteplovoe rentgenovskoe izluchenie pri solnechnyh vspyshkah [Plasma heating by fast electrons and nonthermal X-ray emission during solar flares], Astronomicheskii Zhurnal 49 (1972) 334-347.

12. **Lin R.P., Dennis B.R., Hurford G.J., et al,** The Reuven Ramaty High-Energy Solar Spectroscopic Imager (Rhessi), Solar Physics, 210 (1/2) (2002) 3–32.

13.**Lemen J.R., Title A.M., Akin D.J., et al ,** The Atmospheric Imaging Assembly (AIA) on the Solar Dynamics Observatory (SDO), Solar Physics, 275 (1–2) (2012) 17–40.

14. **Effenberger F., da Costa F.R., Oka M., et al,** Hard X-Ray Emission from Partially Occulted Solar Flares: RHESSI Observations in Two Solar Cycles, The Astrophysical Journal, 835 (2) (2017) 124.

15. **Somov B.V., Syrovatskii S.I.,** Physical processes in the solar atmosphere associated with flares, Uspekhi Fizicheskih Nauk, 120 (10) (1976) 217.

16. OSPEX. URL:http://hesperia.gsfc.nasa.gov/rhessidatacenter/spectroscopy.html
17. SolarSoft IDL software. URL: http://www.lmsal.com/solarsoft/
18. **Phillips K.J.H., Chifor C., Dennis B.R.,** RHESSI Observations of the Solar Flare Iron-Line Feature at 6.7 keV, The Astrophysical Journal, 647 (2) (2006) 1480–1490.

## THE AUTHOR

**OVCHINNIKOVA Evgeniia P.**
elfimovaevgeniya@gmail.com
ORCID: 0000-0001-7892-093X

*Received 02.11.2022. Approved after reviewing 10.11.2022. Accepted 10.11.2022.*

© Peter the Great St. Petersburg Polytechnic University, 2023

conference materials
UDC 524.527.3
DOI: https://doi.org/10.18721/JPM.161.276

# Neutral carbon in the diffuse cold neutral medium

S.A. Balashev[1]✉, D.N. Kosenko[1]

[1] Ioffe Institute, St. Petersburg, Russia

✉ s.balashev@gmail.com

**Abstract**. We discuss the relative abundance of $C_I/H_2$ in the diffuse cold neutral medium. Using semi-analytical formalism, we describe how $C_I/H_2$ depends on the main parameters of the medium: number density, metallicity, strength of the UV field and cosmic ray ionization rate. We show that observed relative abundance of $C_I/H_2$ in the high-redshift damped Lyman alpha systems can be reproduced within our model assuming the typical expected conditions in the diffuse cold medium. We also discuss that the observed relative abundance of $C_I/H_2$, when coupled with data on the population of the fine structure levels of neutral carbon and the rotational levels of molecular hydrogen can be used to derive the cosmic ray ionization rate in the low-metallicity interstellar medium.

**Keywords:** galaxies, interstellar medium, cosmic rays

**Funding:** This work was supported by RSF grant 22-22-00164.

**Citation:** Balashev S.A., Kosenko D.N., Neutral carbon in the diffuse cold neutral medium, St. Petersburg State Polytechnical University Journal. Physics and Mathematics. 16 (1.2) (2023) 499–504. DOI: https://doi.org/10.18721/JPM.161.276

This is an open access article under the CC BY-NC 4.0 license (https://creativecommons.org/licenses/by-nc/4.0/)

Материалы конференции
УДК 524.527.3
DOI: https://doi.org/10.18721/JPM.161.276

# Нейтральный углерод в диффузной фазе холодной нейтральной среды

С.А. Балашев[1]✉, Д.Н. Косенко[1]

[1] Физико-технический институт им. А.Ф. Иоффе РАН, Санкт-Петербург, Россия

✉ s.balashev@gmail.com

**Аннотация.** В работе обсуждается относительная распространенность $C_I/H_2$ в диффузной холодной нейтральной межзвездной среде. Используя полуаналитический формализм, мы описываем, как $C_I/H_2$ зависит от основных параметров в среде: объемной концентрации, металличности, интенсивности УФ поля и скорости ионизации космическими лучами. Показано, что наблюдаемая относительная концентрация $C_I/H_2$ в демпфированных Лайман-альфа системах на больших красных смещениях воспроизводится нашей моделью в предположении типичных условий для холодной диффузной среды. Также обсуждается, что наблюдаемая относительная распространенность $C_I/H_2$ вместе с измеренными населенностями уровней тонкой структуры нейтрального углерода и вращательных уровней молекулярного водорода может использоваться для оценки скорости ионизации космическими лучами в межзвездной среде низкой металличности.

**Ключевые слова:** галактики, межзвездная среда, космические лучи

**Финансирование:** Работа поддержана грантом РНФ № 22-22-00164.

© Balashev S.A., Kosenko D.N., 2023. Published by Peter the Great St. Petersburg Polytechnic University.

**Ссылка при цитировании:** Балашев С.А., Косенко Д.Н. Нейтральный углерод в диффузной фазе холодной нейтральной среды // Научно-технические ведомости СПбГПУ. Физико-математические науки. 2023. Т. 16. № 1.2. С. 499–504. DOI: https://doi.org/10.18721/JPM.161.276

Статья открытого доступа, распространяемая по лицензии CC BY-NC 4.0 (https://creativecommons.org/licenses/by-nc/4.0/)

## Introduction

Cosmic rays are an important component of the interstellar medium, affecting its dynamics, thermal and chemical evolution. In the neutral interstellar medium, low-energy cosmic rays, due to their penetrating power, are the main source of residual ionization, which determines the formation of most molecules. Previously, indirect methods were used to estimate the cosmic ray ionization rate (CRIR), based on the observations of the abundance of a number of molecules that are sensitive to the degree of ionization of the medium. These methods show that there is a large spread in the measured CRIR: from $10^{-17}$ to ~ $10^{-15}$ $s^{-1}$. Such a scatter can be caused by both the natural inhomogeneity of the CRIR in the interstellar medium, associated with the locality of sources and the effects of cosmic ray propagation, and by systematic effects in the methods of estimation used.

To estimate the CRIR one should use the elements sensitive to the ionization state of the medium. There are several molecules (such as $H_3^+$, $OH^+$, $H_2O^+$) used for this in the past (see e.g. [1, 2]) However, these species mostly trace dense molecular gas, while there were few attempts made to constrain CRIR in diffuse gas based on the HD (see [3] and references therein). In turn, the carbon is one of the most abundant elements in the interstellar medium. In neutral diffuse ISM it is mostly present in the ionized form, C II, since the ionization potential of C I is less than H I. However, in the cold phase of neutral ISM the number density and ionization fraction can be sufficiently high to maintain observable fraction of C I, which produced by C II recombinaa tion. Since C II recombination rate can be sensitive to the degree of ionization in the interstellar medium, this may allow constraining on the cosmic ray ionization rate.

The C I chemistry in diffuse ISM was comprehensively considered by e.g. [4, 5]. However, these studies described the observations obtained in our galaxy, i.e., considered only the local ISM. Nevertheless, currently there is a very large number of the observations performed at high-redshift DLAs, i.e., remote galaxies. These observations mostly associated with the low-metallicity gas ($z \leq 0.3$), where one can expect the changes in the ionization and thermal balance (see e.g. [6–8]) which is an important ingredient for the presence of C I.

In this work, we have developed a formalism to describe C I abundance in diffuse ISM. We studied the effect of the metallicity on presence of C I and developed the method for estimating the CRIR based on measuring the relative abundance of neutral carbon, C I, and molecular hydrogen, $H_2$ as well as the population of the fine structure levels of neutral carbon, C I, and the rotational levels of molecular hydrogen, $H_2$

## Relative abundances of C I and $H_2$.

We used a similar formalism to calculate relative C I/$H_2$ abundances as was applied previously for HD/$H_2$ and OH/$H_2$ in [7, 9]. As in mentioned papers we consider the homogeneous (specified by the total hydrogen number density $n_{\rm H}^{\rm tot}$) and isothermal (with temperature $T = 100$ $K$, corresponding to cold diffuse ISM) medium with metallicity, $Z$, that is exposed by the UV field of strength, $\chi$, and cosmic rays with ionization rate, $\zeta$ (the primary ionization rate per hydrogen atom, in units of $\sim 10^{-17}$ $s^{-1}$).

The formalism is based on the analytical description of H I/$H_2$ transition proposed recently by [10, 11], where $H_2$ number density as a function of $H_2$ column density, $N_{H_2}$ can be written as

$$n_{\rm H_2} = n_{\rm H}^{\rm tot} / (\alpha S_{\rm H_2}(N_{\rm H_2}) e^{-\sigma_g (N_{\rm H} + 2N_{\rm H_2})} + 2), \quad (1)$$

© Балашев С.А., Косенко Д.Н., 2023. Издатель: Санкт-Петербургский политехнический университет Петра Великого.

where $N_{\rm H}$ is atomic hydrogen column density, $S_{\rm H_2}$ is self-shielding function, $\sigma_g = 1.9\times10^{-21} Z$ cm$^2$ is the dust Lyman-Werner photon absorption cross-section per hydrogen atom, and $\alpha$ is the ratio of free space $H_2$ photo-dissociation and $H_2$ formation on the dust grains.

The abundance of neutral carbon can be expressed as

$$n_{\rm CI} \approx n_{\rm C}^{\rm tot}(1-f_{\rm C^+}) \equiv n_{\rm H}^{\rm tot} x_c (1-f_{\rm C^+}) \equiv n_{\rm H}^{\rm tot}[{\rm C/H}]_\odot Z d_{\rm C}(1-f_{\rm C^+}), \quad (2)$$

where $x_{\rm C} \equiv [{\rm C/H}]_\odot Z d_{\rm C}$ is a gas phase abundance of carbon, $[{\rm C/H}]_\odot \approx 2.7\times10^{-4}$ is the solar abundance of carbon, $d_{\rm C}$ is depletion of the carbon on dust grains that depends on $Z$, and was taken following [6], and $f_{\rm C}$. is the carbon ionization fraction, i.e., $f_{\rm C^+} \equiv n_{\rm C^+}/n_{\rm C}^{\rm tot}$. The latter can be determined from the balance equation for $C^+$, where it mainly forms by the photoionization of C I and destructed by the recombination with free electrons and dust

$$n_{\rm CI}\chi D_{\rm CI} = n_{\rm C^+} n_e \alpha_{\rm C}^{\rm rec} + n_{\rm C^+} n_{\rm H}^{\rm tot} \alpha_{\rm C}^{\rm gr}, \quad (3)$$

where $n_e$ is an electron density, and $D_{\rm CI} \approx 2.6\cdot10^{-10} e^{-3.76 A_{\rm V}}$ is the neutral carbon photoionization rate determined by [12]. $\alpha_{\rm C}^{\rm rec}$ and $\alpha_{\rm C}^{\rm gr}$ are recombination rates with free electrons [13] and dust, respectively. In terms of $f_{\rm C}$ it can be written as

$$\chi D_{\rm CI}(1-f_{\rm C^+}) = f_{\rm C^+} n_{\rm H}^{\rm tot}(x_e \alpha_{\rm C}^{\rm rec} + \alpha_{\rm C}^{\rm gr}), \quad (4)$$

where electron fraction $x_e \equiv n_e / n_{\rm H}^{\rm tot}$ can be approximated as

$$x_e = f_{\rm H^+} + x_c f_{\rm C^+}, \quad (5)$$

where $f_{\rm H^+}$ is the hydrogen ionization fraction, which can be obtained using the balance equation for $H^+$. We follow the similar description as was presented in [7] except we did not consider the contribution of minor reactions and used the exact form for electron density given in Eq. 5. Then,

$$k_\zeta^{\rm eff}(1-f_{\rm H^+}) = f_{\rm H^+}(x_e \alpha_{\rm H}^{\rm rec} + \alpha_{\rm H}^{\rm gr}), \quad (6)$$

where $\alpha_{\rm H}^{\rm rec}$ and $\alpha_{\rm H}^{\rm gr}$ are recombination rates of H with free electron and dust, respectively, and $k_\zeta^{\rm eff} = k_\zeta^{\rm H}(1-f_{\rm H_2}) + \tilde{k}_\zeta^{\rm H_2} f_{\rm H_2} + k_\zeta^{\rm H_2} f_{\rm H_2}\left(1 + k_1 f_{\rm H_2}/2k_2(1-f_{\rm H_2})\right)^{-1}$, where $k_\zeta^{\rm H} = 1.7\zeta$, $\tilde{k}_\zeta^{\rm H_2} = 0.17\zeta$ and $k_\zeta^{\rm H_2} = 3.4\zeta$ and $k_1 = 2.1\cdot10^{-9}$ and $k_2 = 6.4\cdot10^{-10}$ cm$^3$ s$^{-1}$.

To derive $f_{\rm C^+}$ and $f_{\rm H^+}$ Eqs. (4), (5) and (6) should be solved together numerically, since the $\alpha_{\rm C}^{\rm gr}$ and $\alpha_{\rm H}^{\rm gr}$ are the functions of the combination of the physical parameters (see for example [14]). For $\alpha_{\rm H}^{\rm gr}$ we used parametrization from [14], while for $C^+$ [5] noticed an importance of the $C^+$ recombination with polycyclic aromatic hydrocarbons (PAHs), that lead to significantly (up to 100 times) enhanced grain-assisted recombination coefficients if there is a relatively large fraction of the negatively charged PAHs. The fraction of charged PAHs in turn depends on the physical parameters [5] and should be found self-consistently, but for simplicity, here we assume an intermediate case of $C^+$ recombination rate, that was set to be ten times higher than the rate proposed in [14].

Following presented formalism, $f_{\rm C^+}$ and hence $n_{\rm C^I}$ are functions of the $N_{\rm H_2}$, since the reaction rates in Eqs. (4) and (6) depend on it, i.e., the depth within the cloud. Therefore, one can get the $N_{\rm C^I}$ as a function of $N_{\rm H_2}$ by numerical integration to compare with observational data.

## Results

In Fig. 1 we compare the observed and calculated dependence of C I and $H_2$ column densities. The observed C I and $H_2$ abundances was compiled from the all-known $H_2$-bearing DLAs detected at high redshifts using quasar spectra (see [3, 15, 16] and references therein). For calculated ones we used doubled value of C I column density at half observed $H_2$ column density, i.e., $N_{\rm CI}^{\rm obs} \equiv 2N_{\rm CI}(N_{\rm H_2}/2)$. Such procedure roughly emulates the slab medium of a given $N_{\rm H_2}$ but exposed by radiation field and cosmic rays from both the sides, due to our calculations are based on one-side radiation field models (inherited from formalism by [10]).

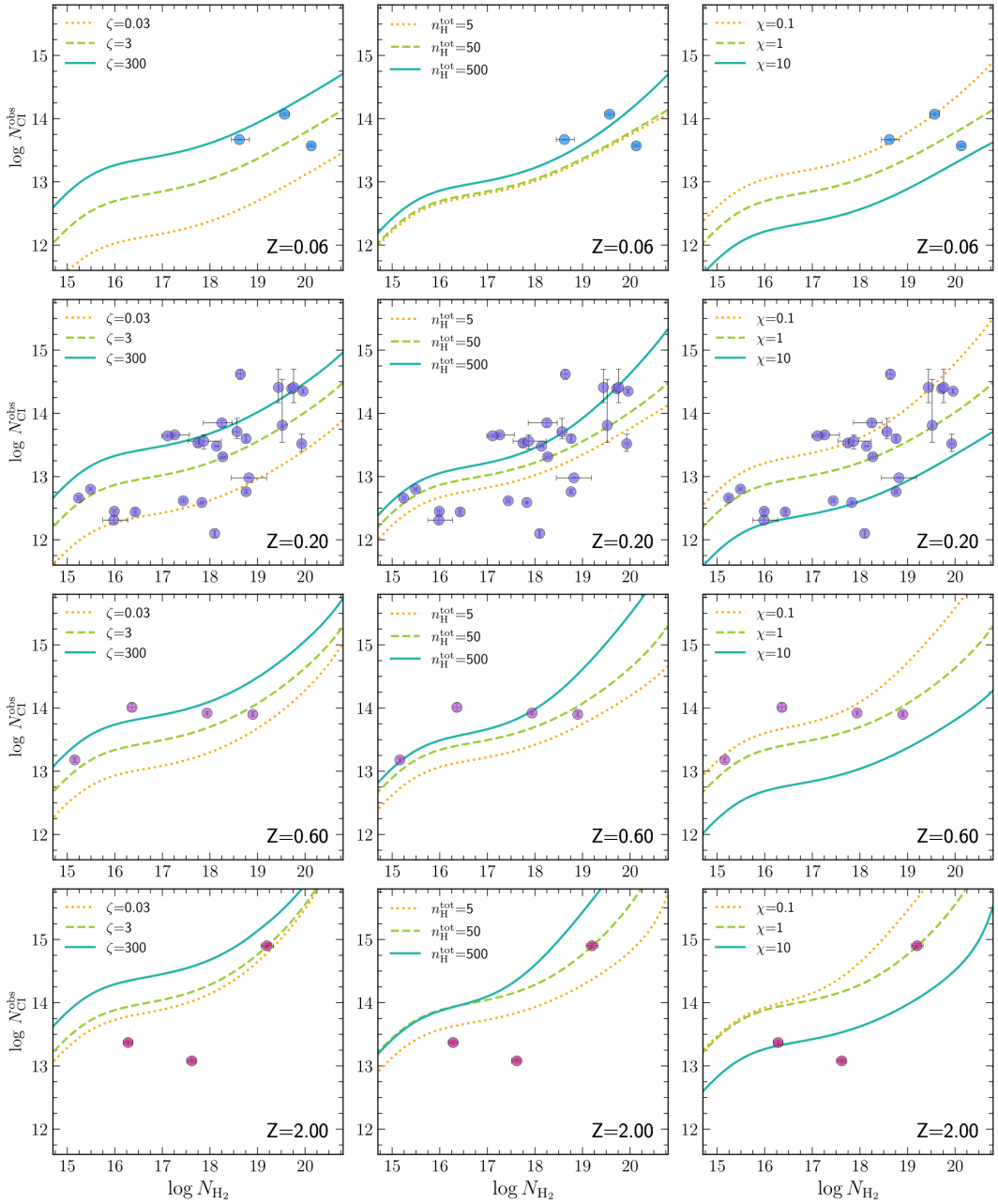


Fig. 1. The dependence of the column densities of C I on $H_2$. The colored points represent an observed abundances in high-redshift DLAs ([15, 16, 3] and references therein) binned by the metallicity, where systems in each bin shown in rows, with mean metallicity within the bin provided in the right bottom corner of the panel. The calculated dependences using described formalism are presented by solid, dashed and dotted lines, that correspond to the variation on one of the parameter from the base model with $n_{\rm H}^{\rm tot} = 50$ cm$^{-3}$, $\zeta = 3$ and $\chi = 1$.

The abundance of C I strongly depends on the metallicity, and it is known that the observational data on the metallicity spans about two orders from log $Z \sim -1.5$ to 0.5. Therefore, to compare the measurements with calculated ones we divide the sample in the four metallicity bins $\approx 0.5$ size and calculate theoretical $N_{\rm CI}^{\rm obs}(N_{\rm H_2})$ profiles for the mean values in the bins. It is also evident that C I abundance depends on the three other global parameters of the cloud: the number density, $n_{\rm H}^{\rm tot}$, CRIR, $\zeta$, and UV field strength, $\chi$. To show the variation on these parameters, we constructed the base model with $n_{\rm H}^{\rm tot} = 50$ cm$^{-3}$, $\zeta = 3$ and $\chi = 1$ and varied independently each of the parameter within two dexs (for CRIR we varied in four dexs, that is motivated by recently obtained quadratic dependence of CRIR on $\chi$ [3]), that correspond to the typical measured variations [3, 16]. The resulted profiles of C I/$H_2$ abundances are shown in Figure 1. One can see that the observed data are reproduced within chosen ranges of the physical parameters relatively well.

One can see that C I/$H_2$ abundance is mostly sensitive to the variation of the UV field at each redshift bin. This is simply because the UV field directly scaled the C I abundance by photoionization. However, for low metallicity medium (corresponding to the most DLAs data), C I/H abundance also becomes quite sensitive to CRIR, since at this metallicity, the C II recombination rate depends on the electron abundance, which in turns depends on the H ionization fraction, which is sensitive to CRIR. Once metallicity approaches solar value, the electron densities start to be determined solely by the carbon abundance (see Equation 5) and hence C I/$H_2$ becomes little sensitive to CRIR (the bottom left panel in Fig. 1). Interestingly, that at low metallicities, C I/$H_2$ abundance becomes almost insensitive to the number density (the top central panel in Fig. 1), at the typically observed number densities $n_{\rm H}^{\rm tot} < \text{few} \times 100 \text{cm}^{-3}$.

## Physical conditions

Since the C I/$H_2$ abundance is sensitive to the physical parameters, the observed values can be used to derive them. However, since the dependence is quite complex, the C I/ $H_2$ abundance alone will provide very vast constraints, and likely on the combination of the parameters, e.g., $\sqrt{\zeta n_{\rm H}^{\rm tot}}/\chi$ for low metallicities. However, since C I/$H_2$ abundances are obtained using absorption line spectroscopy, in most cases (especially, if high-resolution spectrum was used) these data is accompanied with the measurements of the population of C I fine structure and $H_2$ rotational levels. The modelling of these populations may provide tight constraints on the number density, $n_{\rm H}^{\rm tot}$, and UV field strength, $\chi$, see, e.g., [15, 16]). Obviously, these constraints may be exploited to determine CRIR using observed C I/$H_2$ abundances. In other words, C I/$H_2$ abundances coupled with population of C I fine structure and $H_2$ rotational levels will provide tight constrains jointly on the three key main parameters on the diffuse ISM: $n_{\rm H}^{\rm tot}$, $\chi$ and CRIR.

## Conclusions

We describe the semi-analytical formalism to describe the relative abundance of C I/$H_2$ in the diffuse cold neutral medium and its dependence on the physical parameters. We show that it quite well reproduces the observation data on C I/$H_2$ from high-redshift DLAs and may provide the measurement of CRIR using additional constraints comes from the population of C I fine structure and $H_2$ rotational levels. However, we note that these results are sensitive to the value of grain assisted $C^+$ recombination rate. The latter strongly depends on the fraction of the charged PAH, that determines not only by the physical conditions, but also the dependence of the dust (or PAH) abundance on the metallicity, which as shown by recent studies (e.g. [17]) may have non-trivial behaviour and indicate a large natural dispersion. Therefore, to obtain the quantitative comparison with observed data and determine the CRIR from the C I/$H_2$ abundances this formalism needs to be supplemented with a proper modelling of the fraction of the charged PAH, coupled with an assumption of the dependence of the PAH abundance on the metallicity or observational constrains on it.

## REFERENCES


1. **Indriolo N., McCall B. J.**, Investigating the Cosmic-Ray Ionization Rate in the Galactic Diffuse Interstellar Medium through Observations of $H_3^+$, Astroph. J., 2012, vol. 745, 91.
2. **Indriolo N.,** et al, Herschel Survey of Galactic $OH^+$, $H_2O^+$ and $H_3O^+$: Probing the Molecular Hydrogen Fraction and Cosmic-Ray Ionization Rate, Astroph. J., vol. 800, 40.
3. **Kosenko D. N.,** et al, HD molecules at high redshift: cosmic ray ionization rate in the diffuse interstellar medium, MNRAS, 2021, vol. 505, 3810–22.
4. **Liszt H.,** How does $C^+$ recombine in diffuse molecular gas?, 2011, Astron. Astroph., vol. 527, A45
5. **Wolfire M.G.,** et al, Chemical Rates on Small Grains and PAHs: $C^+$ Recombination and $H_2$ Formation, 2008, Astrph. J., vol. 680, 384–97.
6. **Bialy S.**, **Sternberg A.,** Thermal Phases of the Neutral Atomic Interstellar Medium from Solar Metallicity to Primordial Gas, Astroph. J., 2019, vol. 881, 160.
7. **Balashev S.A.,** et al, OH in the diffuse interstellar medium: physical modelling and prospects with upcoming SKA precursor/pathfinder surveys, MNRAS, 2021, vol. 504, 3797–811.
8. **Balashev S.A.,** et al, C I*/C I ratio in high-redshift DLAs: ISM phase separation drives the observed bimodality of [C I] cooling rates, MNRAS, 2022, vol. 509, L26–30.
9. **Balashev S.A.**, **Kosenko D.N.,** $HD/H_2$ ratio in the diffuse interstellar medium, MNRAS, 2020, vol. 492, L45–9.
10. **Sternberg A.** et al, H I-to-$H_2$ Transitions and H I Column Densities in Galaxy Star-forming Regions, Astroph. J., 2014, vol. 790, 10.
11. **Bialy S., Sternberg A.,** Analytic H I-to-$H_2$ Photodissociation Transition Profiles, Astroph. J., 2016, vol. 822, 83.
12. **Heays A.N.,** et al, Photodissociation and photoionisation of atoms and molecules of astrophysical interest, Astron. Astroph., 2017, vol. 602, A105.
13. **Bryans P.,** et al, Molecular Cloud Chemistry and the Importance of Dielectronic Recombination, Astroph. J., 2009, vol. 694, 286–93.
14. **Weingartner J.C., Draine B.T.,** Electron-Ion Recombination on Grains and Polycyclic Aromatic Hydrocarbons**,** Astroph. J., 2001, vol. 563, 842–52.
15. **Balashev S.A.** et al, X-shooter observations of strong $H_2$-bearing DLAs at high redshift, MNRAS, 2019, vol. 490, 2668–78.
16. **Klimenko V.V., Balashev S.A.,** Physical conditions in the diffuse interstellar medium of local and high-redshift galaxies: measurements based on the excitation of $H_2$ rotational and CI fine-structure levels, MNRAS, 2020, vol. 498, 1531–49.
17. **Rumy-Ruyer A.,** et al, Gas-to-dust mass ratios in local galaxies over a 2 dex metallicity range, Astron. Astroph., 2014, vol. 563, A31.


## THE AUTHORS


**BALASHEV Sergei A.**
s.balashev@gmail.com

**KOSENKO Daria N.**
kosenkodn@yandex.ru
ORCID: 0000-0001-7431-8298


*Received 29.10.2022. Approved after reviewing 08.11.2022. Accepted 08.11.2022.*

© Peter the Great St. Petersburg Polytechnic University, 2023

Conference materials
UDC 551.510.535
DOI: https://doi.org/10.18721/JPM.161.277

# Structure and variations of the south-polar ionosphere by GNSS-tomography

D.A. Trofimov[1]✉, S.D. Petrov[2], A.S. Kalishin[2],
V.V. Lukin[2], Yu.A. Serov[2], I.V. Chekunov[3]

[1] St. Petersburg State University, St. Petersburg, Russia;

[2] Arctic and Antarctic Research Institute, St. Petersburg, Russia;

[3] Bauman Moscow State Technical University, Moscow, Russia

✉ d.trofimov@spbu.ru

**Abstract.** The paper is devoted to determination of the total electron content in the vicinity of the South geomagnetic pole using observations by global navigation satellite systems. Observations were carried out at the Russian Antarctic station Vostok in the periods February 2016 – January 2017, February 2018 – February 2019 and February 2020 – January 2021. Observations were made with satellites of GPS and GLONASS systems. Processing of observations was carried out by use of the TEC-suite software. Total electron content series were obtained for the specified time periods. Our results were compared with those of Center for Orbit Determination in Europe, there is a good agreement, based on which we conclude that our data are reliable. For all periods of observation, average daily profiles of changes in the total electron content in winter and summer were plotted. An excess of the winter total electron content measured from global navigation satellite systems observations over the model data provided by Center for Orbit Determination in Europe by about 5 total electron content unit was noted._

**Keywords:** GNSS, ionosphere, total electron content)

**Citation:** Trofimov D.A., Petrov S.D., Kalishin A.S., Lukin V.V., Serov Yu.A., Chekunov I.V., Structure and variations of the south-polar ionosphere by GNSS-tomography, St. Petersburg State Polytechnical University Journal. Physics and Mathematics. 16 (1.2) (2023) 505–510. DOI: https://doi.org/10.18721/JPM.161.277

This is an open access article under the CC BY-NC 4.0 license (https://creativecommons.org/licenses/by-nc/4.0/)

Материалы конференции
УДК 551.510.535
DOI: https://doi.org/10.18721/JPM.161.277

# Структура и вариации южнополярной ионосферы по данным ГНСС-томографии

Д.А. Трофимов[1]✉, С.Д. Петров[1], А.С. Калишин[2],
В.В. Лукин[2], Ю.А. Серов[2], И.В. Чекунов[3]

[1] Санкт-Петербургский государственный университет, Санкт-Петербург, Россия;

[2] Арктический и антарктический научно-исследовательский институт, Санкт-Петербург, Россия;

[3] Московский государственный технический университет им. Н.Э. Баумана, Москва, Россия

✉ d.trofimov@spbu.ru

**Аннотация.** Статья посвящена определению полного электронного содержания в окрестности южного геомагнитного полюса из ГНСС-наблюдений. Наблюдения выполнялись на антарктической станции Восток с февраля 2016 по январь 2017, с февраля 2018 по февраль 2019, с февраля 2020 по январь 2021. Наблюдались спутники

© Trofimov D.A., Petrov S.D., Kalishin A.S., Lukin V.V., Serov Yu.A., Chekunov I.V., 2023. Published by Peter the Great St. Petersburg Polytechnic University.

систем GPS и ГЛОНАСС. Обработка наблюдений проводилась с использованием программного обеспечения TEC-suite. Были получены ряды полного электронного содержания за указанные периоды времени. Наши результаты сравнивались с данными CODE. Для всех периодов наблюдений строились среднесуточные профили изменения полного электронного содержания зимой и летом. Отмечено превышение зимнего полного электронного содержания, измеренного по нашим ГНСС-наблюдениям, над данными, предоставленными CODE, примерно на 5 TECU.

**Ключевые слова:** ГНСС, ионосфера, полное электронное содержание

**Ссылка при цитировании:** Трофимов Д.А., Петров С.Д., Калишин А.С., Лукин В.В., Серов Ю.А., Чекунов И.В. Структура и вариации южнополярной ионосферы по данным ГНСС-томографии // Научно-технические ведомости СПбГПУ. Физико-математические науки. 2023. Т. 16. № 1.2. С. 505–510. DOI: https://doi.org/10.18721/JPM.161.277

Статья открытого доступа, распространяемая по лицензии CC BY-NC 4.0 (https://creativecommons.org/licenses/by-nc/4.0/)

## Introduction

The presented paper is a continuation of the earlier work [1] devoted to estimation of ionospheric parameters from global navigation satellite systems (GNSS) observations at the Antarctic station Vostok. The ionosphere is a layer of the Earth's atmosphere, ionized primarily by solar radiation. It consists of neutral gases and quasi-neutral plasma. Such important branches of human activity as radio communication and radar, radio navigation depend on the state of the ionosphere. There are connections between the processes in the troposphere, tectonic processes and phenomena in the ionosphere. Thus, the study of the ionosphere, the physical processes occurring in it, and their relationship with other geophysical processes is an important scientific task. One of the main characteristics of the ionosphere is the total electron content (TEC), which is the number of free electrons and ions in a cylinder with a cross-sectional area of 1 square meter, oriented along the line of sight. It is measured in total electron content (TECU), 1 TECU = $10^{16}$ electron/m$^2$. One of the most accessible methods for studying the ionosphere under present conditions are GNSS. All modern GNSS are built on similar principles; they transmit the navigation signal over two frequencies, specifically to take into account the signal delay in the ionosphere. Thus, having observations of GNSS satellites at two frequencies, determining the total electron content can be performed according to the method described in the paper [2]. The spread of GNSS, the wide coverage of various networks of scientific and economic importance of large areas provide a huge array of information for determining the total electronic content. However, there are areas where the coverage of GNSS stations is clearly insufficient. One of such areas is Antarctica. The number of stations included in the network of the International GNSS Service (IGS) is only 8. All these stations are located on the coast of Antarctica. In 2016, together with the Department of Astronomy of St. Petersburg State University and the Arctic and Antarctic Research Institute, a GNSS site was organized at the Vostok station. Station coordinates are 78°28′ south latitude and 106°50′ east longitude. The height of the station is 3488 m. This was done to solve several scientific problems, the main ones being the study of the dynamics of the ice shield [3] and the determination of the parameters of the atmosphere and ionosphere near Vostok station. Vostok station is located in the vicinity of the South geomagnetic pole; therefore, the determination of ionospheric parameters in the vicinity of the station is of a special interest.

## Materials and Methods

In this paper, we used GNSS observations made during three expeditions to the Vostok station. The first observation period is from 7 February 2016 to 31 January 2017, the second observation period is from 4 February 2018 to 10 February 2019 and the third observation period is from 7 February 2020 to 01 February 2021. All observations were performed continuously with the Javad Triumph-1 receiver provided by the Department of Astronomy of St. Petersburg State University.

© Трофимов Д.А., Петров С.Д., Калишин А.С., Лукин В.В., Серов Ю.А., Чекунов И.В., 2023. Издатель: Санкт-Петербургский политехнический университет Петра Великого.

The organization of the observation post is described in a previous paper [1]. The receiver used in all observations is the same. Code and phase measurements were performed at two frequencies. GPS and GLONASS satellites were observed, the time resolution of observations was 30 seconds. We also used global ionospheric maps provided by the Center for Orbit Determination in Europe (CODE). This data is provided with a time resolution of 1 hour, on a grid of 2.5° in latitude and 5° in longitude. We also used data on differential code biases (DCB-files) provided by CODE.

## Data processing and results

Data processing was performed using the TEC-suite [4][5] program. With its help, the oblique TEC series were obtained for each observed satellite, both in phase and in code measurements. Subsequently, the slant TEC calculated from the code measurements was corrected for each satellite by DCB, and based on the corrected TEC, the uncertainty for the slant TEC calculated from the phase measurements was eliminated. Based on the slope TEC from the phase measurements, the vertical TEC was calculated using the mapping function. When calculating the mapping function, according to the method described in the paper [2], the height of the thin layer ionosphere was assumed to be H = 450 km. The same height is assumed in the model used to calculate ionospheric map CODE. The vertical TEC for all available satellites was averaged over an hourly interval. Using the method described above, we obtained complete annual series of the total electron content of the ionosphere over Vostok station for all three expedition periods. We compare our TEC series with the TEC provided by CODE to verify our results (see Figs. 1–4).

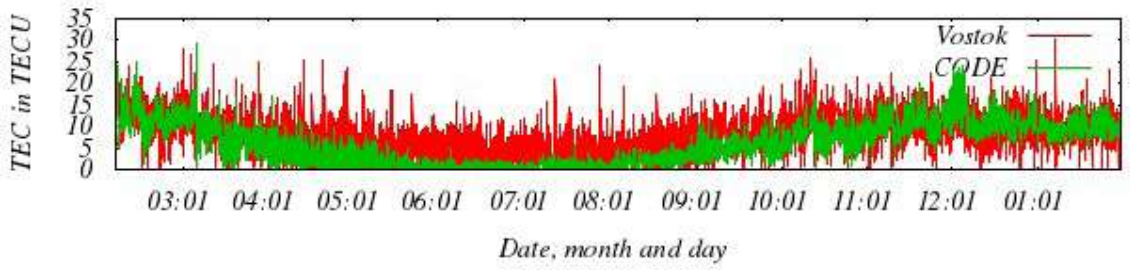


Fig. 1. Total ionospheric electron content over Vostok station according to GNSS observations (red line) of the 2016–2017 expedition in comparison with CODE data (green line). 1.0 (*a*)

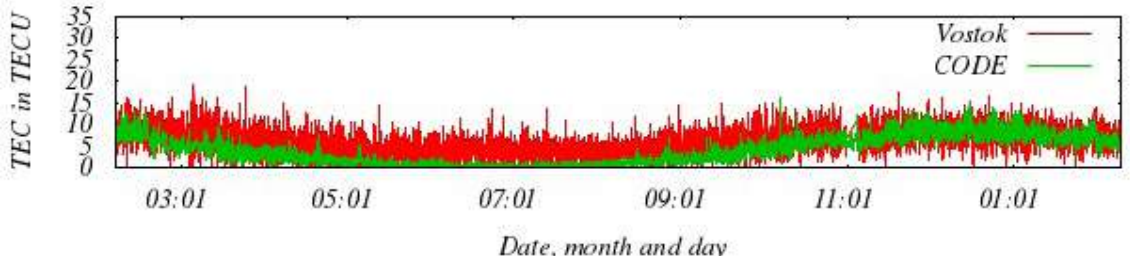


Fig. 2. Total ionospheric electron content over Vostok station according to GNSS observations (red line) of the 2018–2019 expedition in comparison with CODE data (green line) (*a*)

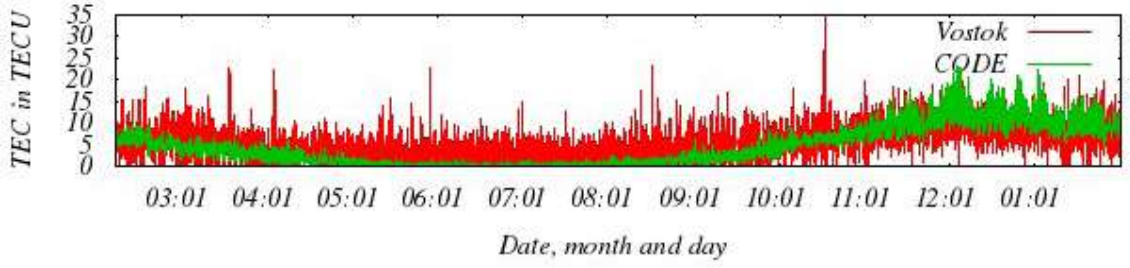


Fig. 3. Total ionospheric electron content over Vostok station according to GNSS observations (red line) of the 2020–2021 expedition in comparison with CODE data (green line) (*a*)

The results obtained by us, as can be seen from the graphs, in general, are in good agreement with the CODE data, which, in our opinion, indicates that the technique we use is correct and we did not make any gross errors in data processing. The results obtained by us are, in general, in good agreement with the CODE data, the seasonal component is clearly visible, which is present both in our series and in the CODE series.

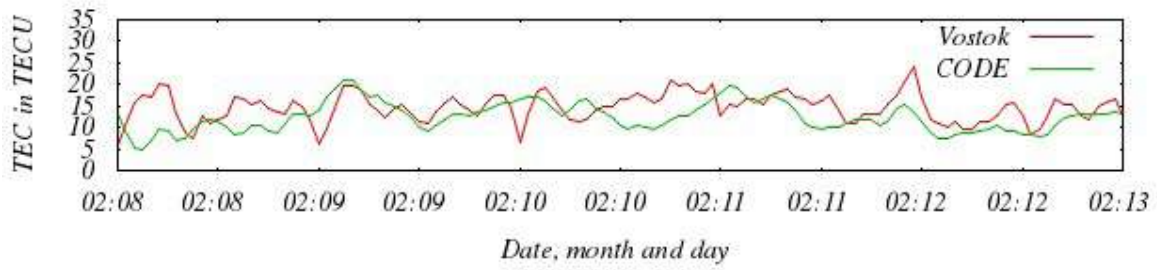


Fig. 4. Total ionospheric electron content over Vostok station according to GNSS observations (red line) 8 – 12 February 2016 in comparison with CODE data (green line)

The accumulated data make it possible to construct daily profiles of the variability of the total electron content of the ionosphere. Graphs of the average daily change in the total electron content for the winter period (in the southern hemisphere this is June-July) and summer periods are given (see Fig. 5–7). The graphs are built separately for each expedition period, 2016-2017, 2018-2019 and 2020-2021. The complete electronic content was built both for all observed satellites and separately for GPS and GLONASS systems. Also for comparison there are graphs constructed according to ionospheric maps from CODE.

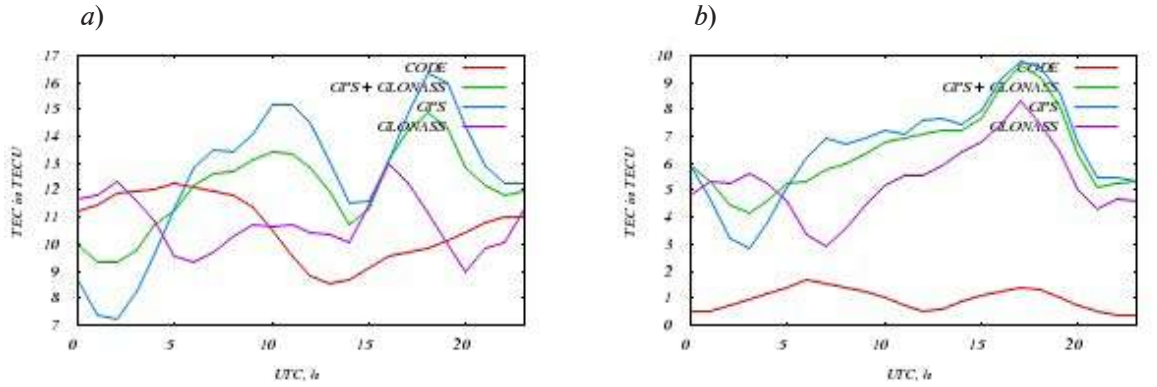


Fig. 5. Average daily TEC profile for June – July 2016 (*a*) and December 2016 – January 2017 (*b*)

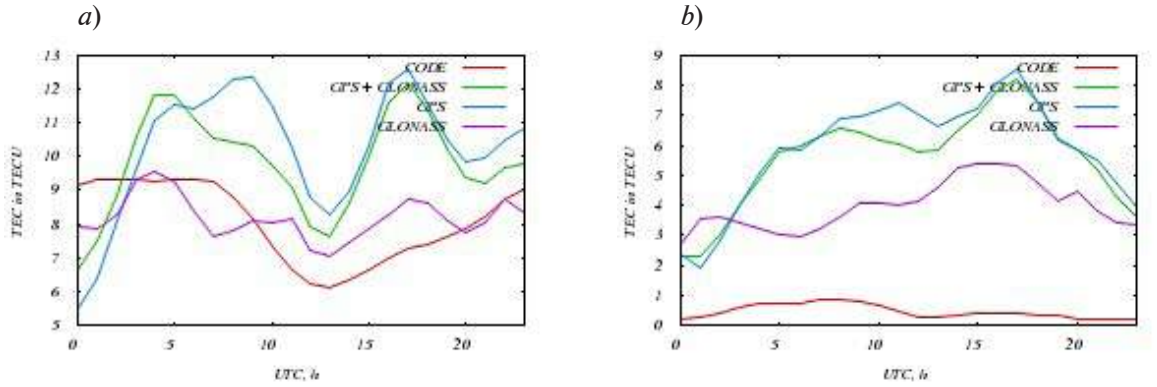


Fig. 6. Average daily TEC profile for June – July 2018 (*a*) and December 2018 – January 2019 (*b*)

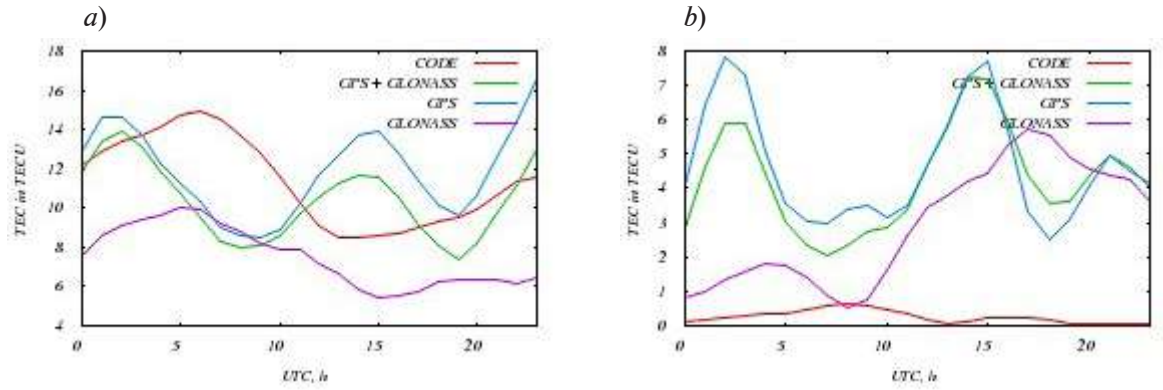


Fig. 7. Average daily TEC profile for June – July 2018 (*a*) and December 2018 – January 2019 (*b*)

As one of the interesting features of the TEC series obtained by us, it should be noted that the TEC values estimated by us in winter are significantly higher than the TEC estimates provided by CODE. The difference is about 5 TECU. This value is significant and needs to be explained. The standard deviation of the vertical TEC value, obtained from one observation epoch is about 3.4 TECU. To obtain one hourly value TEC, we average 120 TEC values, obtained from one epoch each. The difference between our data and CODE data exceeds the standard deviation of the TEC estimation error from one measurment. Consider the possible reasons for such a difference. On the one hand, we can assume that this value is an artifact of observations. As follows from the technique described by us, obtaining the final series of vertical TEC, we average all available observations, but due to the geographical location of our observation point, not a single satellite passes through the zenith, the points of intersection of the satellite-receiver line and the ionosphere are very far from the receiver. Hense, the averaged value The TEC may not display the situation above the receiver. On the other hand, it should be noted that the data, provided by CODE, are built based on available GNSS observations, which are carried out at the coastal stations of the IGS. These stations are located at a great distance from Vostok station and the same statements are true for them that we can make for our observation post. However, it should be noted that in summer the TEC series obtained by us is in good agreement with the CODE data, both at short intervals and at longer intervals, which, in our opinion, indicates that the winter TEC value obtained by us reflects the real physical picture. Perhaps the reason for this phenomenon is the proximity of the south geomagnetic pole of the Earth, near which the Vostok station is located. The ionization of gas in the ionosphere occurs due to the influence of ultraviolet and X-ray radiation from the Sun and due to the influence of charged cosmic particles. Taking into account the proximity of our observation point to the geomagnetic pole, we can assume that there is an additional TEC caused due to gas ionization by the solar wind. However, the question arises as to why this effect is observed only in winter.

## Conclusion

The observations of three expeditions to Vostok station were processed. Annual series of the total electron content of the ionosphere were constructed from phase measurements using the TEC-suite program. The resulting total electron content was compared with data from global ionospheric maps provided by CODE. In general, the series are similar, the same daily and seasonal variations are traced, based on which we can judge the reliability of our data. Typical summer and winter diurnal profiles of the vertical TEC change were estimated with the obtained array of observations. An interesting point was noted that the typical winter TEC value exceeds the TEC value from global ionospheric maps by about 5 TECU. It is concluded that this is a real effect, which cannot be fully explained by the unknown value of the receiver calibration correction. Perhaps there are effects caused by the proximity of the South geomagnetic pole. We are going to continue the study of the causes of this effect in the following publications.

## REFERENCES

**1. Zheltova K.V., Trofimov D. A., Petrov S. D., Smirnov S.S., Chekunov I.V., Serov Yu. A., Troshichev O.A.,** Probing ionospheric TEC near South Geomagnetic Pole by use of GNSS observations, Journal of Physics: Conference Series. 1697. (2020) 012035. 10.1088/1742-6596/1697/1/012035.

**2. Alizadeh M., Wijaya, D., Hobiger, T., Weber R., Schuh H**., Atmospheric Effects in Space Geodesy, Springer Berlin, 2013. 10.1007/978-3-642-36932-2_2.

**3. Trofimov D. A, Serov Y. A., Petrov S. D., Chekunov I. V., Shombina L. A**. 2017. GNSS-observations at the Vostok station, In: Proceedings of Geodesy, cartography, geoinformatics and cadastre. From idea to application, St. Petersburg, Russia, 8 – 10 November 2017, p 74–80.

4. http://www.gnss-lab.org/tec-suite.html

5. https://tec-suite.readthedocs.io/_/downloads/en/latest/pdf/

## THE AUTHORS

**TROFIMOV Dmitrii A.**
d.trofimov@spbu.ru
ORCID: 0000-0001-5119-8510

**LUKIN Valeriy V.**
lukin@aari.ru
ORCID: 0000-0003-1726-7361

**PETROV Sergey D.**
s.d.petrov@spbu.ru
ORCID: 0000-0002-9742-2909

**SEROV Yuri A.**
yuras1981@yandex.ru
ORCID: 0000-0000-0000-0000

**KALISHIN Alexey S.**
askalishin@aari.ru
ORCID: 0000-0001-7299-6546

**CHEKUNOV Ilya V.**
onip4@mail.ru
ORCID: 0000-0000-0000-0000

*Received 30.10.2022. Approved after reviewing 08.11.2022. Accepted 23.11.2022.*

© Peter the Great St. Petersburg Polytechnic University, 2023

Conference materials
UDC 521
DOI: https://doi.org/10.18721/JPM.161.278

# Multiparametric analysis of celestial bodies as sources of space resources

A. O. Andreev[2]✉, Yu. A. Nefedyev[1], N. Y. Demina[1], Yu. A. Kolosov[1], E. P. Korchagina[1]

[1] Kazan Federal University, Kazan, Russia;

[2] Kazan State Power Engineering University, Kazan, Russia

✉ alexey-andreev93@mail.ru

**Abstract.** The work is devoted to the creation of a method based on data from space missions such as LRO (Lunar Reconnaissance Orbiter) and the analysis of possible impactors and meteoroid material for mapping the distribution of minerals on the Moon. In the process of surveys from the Lunar Reconnaissance Orbiter (LRO) spacecraft, the most recent generalized information on the distribution of iron and titanium in the composition of the lunar surface rocks was obtained. To obtain these data, it was necessary to compile a single map from more than 4 thousand images that the LRO spacecraft took during a month of work in a lunar orbit. The processing of the obtained data made it possible to detect areas on the lunar surface containing significant deposits of titanium. The results were calibrated using analyzes of lunar soil samples brought to Earth by the American Apollo missions and Soviet automatic vehicles of the Luna series. Concrete results obtained: Map of mineral distribution gradients depending on selenographic coordinates on the lunar sphere._

**Keywords:** Moon, planetary science, asteroids, space missions

**Funding:** This work was supported by Russian Science Foundation, grant 22-72-10059.

**Citation:** Andreev A.O., Nefedyev Yu.A., Demina N.Y., Kolosov Yu.A., Korchagina E.P., Multiparametric analysis of celestial bodies as sources of space resources, St. Petersburg State Polytechnical University Journal. Physics and Mathematics. 16 (1.2) (2023) 511–516. DOI: https://doi.org/10.18721/JPM.161.278

This is an open access article under the CC BY-NC 4.0 license (https://creativecommons.org/licenses/by-nc/4.0/)

Материалы конференции
УДК 521
DOI: https://doi.org/10.18721/JPM.161.278

# Многопараметрический анализ небесных тел как источников космических ресурсов

А.О. Андреев[2]✉, Ю.А. Нефедьев[1], Н.Ю. Демина[1], Ю.А. Колосов[1], Е.П. Корчагина[1]

[1] Казанский (Приволжский) федеральный университет, г. Казань, Россия;

[2] Казанский государственный энергетический университет, г. Казань, Россия

✉ alexey-andreev93@mail.ru

**Аннотация.** Работа посвящена созданию метода на основе данных космических миссий, таких как LRO (Lunar Reconnaissance Orbiter), и анализу возможных ударников и метеороидного материала для картографирования распределения полезных ископаемых на Луне. В процессе съемок с космического аппарата LRO были получены самые свежие обобщенные сведения о распределении железа и титана в составе пород лунной поверхности.

**Ключевые слова:** Луна, планетология, астероиды, космические миссии_

© Andreev A.O., Nefedyev Yu.A., Demina N.Y., Kolosov Yu.A., Korchagina E.P., 2023. Published by Peter the Great St. Petersburg Polytechnic University.

**Финансирование:** Работа поддержана Российским научным фондом, грант №. 22-72-10059.

**Ссылка при цитировании:** Андреев А.О., Нефедьев Ю.А., Демина Н.Ю., Колосов Ю.А., Корчагина Е.П. Многопараметрический анализ небесных тел как источников космических ресурсов // Научно-технические ведомости СПбГПУ. Физико-математические науки. 2023. Т. 16. № 1.2. С. 511–516. DOI: https://doi.org/10.18721/JPM.161.278

Статья открытого доступа, распространяемая по лицензии CC BY-NC 4.0 (https://creativecommons.org/licenses/by-nc/4.0/)

## Introduction

Currently, researches of useful resources on space bodies are important [1, 2]. In our work, on the basis of the author's multi-parameter method, the simulation of dynamic characteristics was performed, and the parameters of small solar system body (SSSBs) as sources of space resources were determined. Work was carried out to estimate the content of metal atoms in the lunar exosphere. The influence of the kinetics of chemical reactions and SSSBs sizes on the chemical composition of hardened shock vapour delivered to the exosphere of the Moon during SSSBs falls was estimated. Methods were proposed for estimating the abundance of atoms of refractory elements in the exospheres of these celestial bodies, taking into account the condensation of silicates in the impact cloud and the photolysis of impact-formed molecules by solar photons. As part of this study, mapping of the content of helium-3 on the surface of the Moon was also carried out. Studies of the dynamic characteristics of SSSBs were carried out, which included: a) work on estimating the velocity distribution of the main populations of MNTs crossing the Earth's orbit [3]. Asteroids from the main belt [4] fall on the Moon at a lower speed than comets from the regions of Jupiter and the Oort [5–10]. The average impactor velocity decreases from 23 to 14 km/s as the impactor ecliptic latitude increases from 20 to 90 degrees; b) two-color diagrams of asteroid brightness maxima were constructed, the average positions (AP) of groups, root mean square distances of meteoroids from AP and maximum distances to AP were determined. The quantitative and qualitative parameters of the color characteristics of SSSBs with small perihelion distances and their spectral distribution are obtained. It was found that the spectral parameters of the SSSBs are related to the dynamics and chemical composition of celestial bodies. A relationship was also found between the color parameters and the magnitude of the SSSBs, while no dependence on the speed of the asteroid was established [11].

## Materials and Methods

It is believed that the rocks that were formed in the upper regions of the mantle of the Moon and in the lower regions of its crust, went through a stage of differentiation like the terrestrial deep rocks. During the period of active lunar volcanism, these rocks came to the surface in the form of lavas, filling the depressions of the lunar seas. The time sequence of the emergence of marine basalts on the Moon with a step of 0.5 billion years is shown in Fig. 1 [12].

Mapping of the selected areas and their sequence was carried out according to geological analysis, taking into account the frequency analysis of the sizes of craters according to the Lunar Orbiter IV and Clementine spacecraft data. Model ages of basalt deposits were determined using data obtained using images from the narrow and wide-angle cameras of the Lunar Reconnaisance Orbiter (LROC NAC, WAC) and spectral data from the Moon Mineralogy Mapper (M3) [13, 14].

Areas of basalt covers were formed in the period from ~3.9 billion years ago to ~1.1 billion years ago [14]. The maximum active lunar volcanism occurred in the period from 3.8 to 3.1 billion years ago, while the largest volumes of eruptions appeared about 3.5 billion years ago [15]. Most of the basaltic lavas were erupted in the area of the Sea of Clarity approximately 3.7 billion years ago, and in the regions of the Sea of Rains and the Ocean of Storms approximately 3.6 billion years ago [16]. After these most extensive spills of basaltic lavas, the appearance of new marine areas was reduced almost to zero [17].

© Андреев А.О., Нефедьев Ю.А., Демина Н.Ю., Колосов Ю.А., Корчагина Е.П., 2023. Издатель: Санкт-Петербургский политехнический университет Петра Великого.

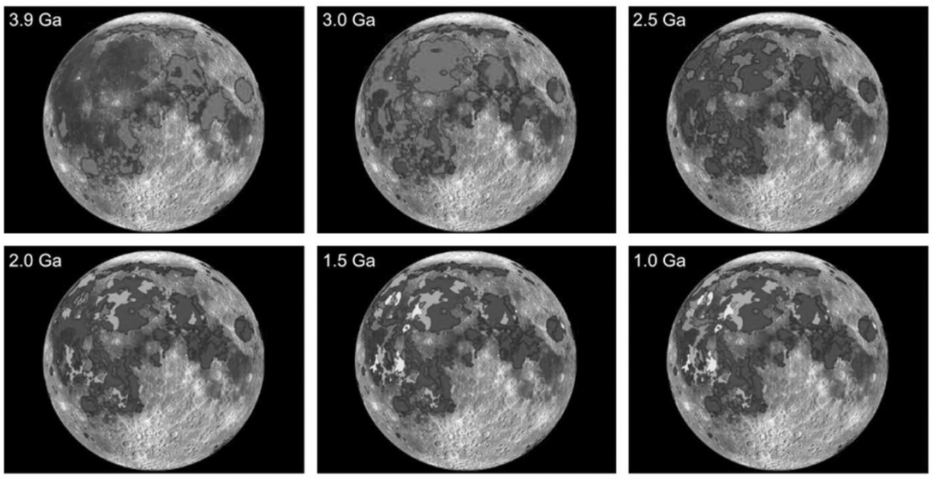


Fig. 1. Time sequence of the emergence of marine basalts on the Moon with a step of 0.5 billion years

The basalts of the lunar seas were formed in the process of crystallization that took place in basalt lavas in layers close to the lunar surface. The main minerals of marine basalts are pyroxenes, plagioclases, ilmenite, and olivines. The rocks that make up the lunar continents consist of anorthosites, norites, and troctolites.

The rocks of the continents are the most ancient and have undergone intense structural changes as a result of a very long impact of meteorite and asteroid bombardment. These rocks are dominated by such minerals as plagioclases and pyroxenes, with minor admixtures of olivine.

Fig. 2 shows distribution maps of the main elements for continental landscapes in the near side of the Moon.

The spectra of the diffuse structure of Reiner Gamma, diffuse structures in the Sea of Moscow and the Sea of Dreams, in the craters of Dufay, Hayford E and Gerasimovich and their vicinities are studied in the optical and near infrared regions according to the data of the M3 instrument.

## Results and Discussion

The study of new images of the lunar regions, made by the Lunar Reconnaissance Orbiter (LRO), has revealed places quite saturated with titanium. In these areas, lava flows that have transformed into lunar stony rocks contain more titanium than the most known deposits of this metal on Earth. It is important that titanium in the future may be in demand for the creation of manned lunar bases and spacecraft.

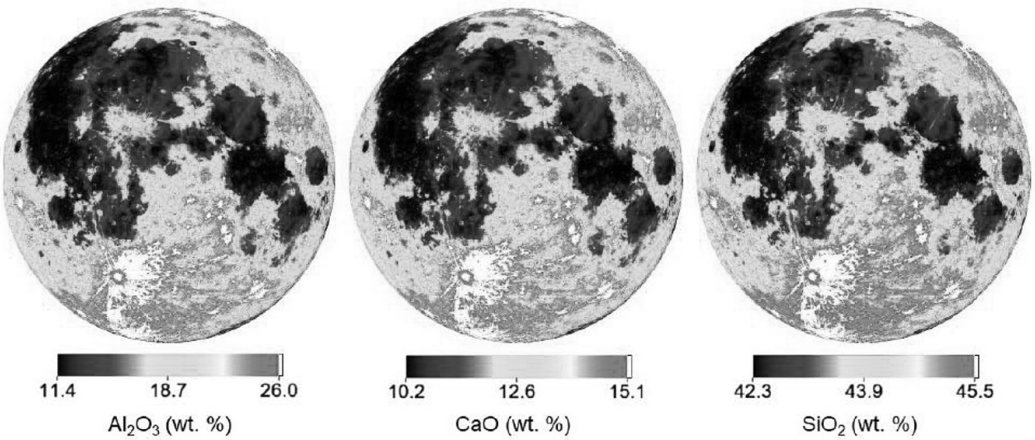


Fig. 2. Distribution maps of the main elements for continental landscapes in the visible hemisphere

According to the results of work performed at the University of Hawaii (USA), analysis of images obtained by the LRO space mission showed that the content of titanium in some "marine" areas of the Moon is 18%, which is 3% more than the content of this metal in deposits on Earth [18].

It should be noted that ilmenites are richest in titanium content on the Moon. Therefore, the areas of the lunar seas marked by the distribution of ilmenite rocks, first of all, may be of interest for obtaining industrial titanium in the future.

When using the simplest research technology, the areas of distribution of ilmenites appear on the images obtained in the process of spectrozonal survey. Such images are the result of observations of the Moon in the visible and ultraviolet ranges of the spectrum. This technique is known to astronomers and has been used more than once in the process of lunar exploration [19, 20].

Determining the frequency of collisions of impactors of various origins (comets and asteroids) with the Moon is important for estimating the influx of meteoroid matter to the Moon and the role of impactors in the formation of a layer of volatile compounds in cold traps at the Moon's poles [21]. Meteoroid matter and volatile compounds at the poles of the Moon, whose main component is water ice, are important minerals on the Moon [22, 23]. For this purpose, the spectral properties of diffuse structures on the Moon were studied using data from the M3 spectrometer of the Indian spacecraft Chandrayaan-1. To estimate the frequency of collisions of comets with the Moon from the data of studying the properties of diffuse structures, it is necessary to carefully study the physical and chemical properties of the upper layer of the lunar regolith and the hydrodynamics of the interaction of the cometary matter of comets approaching the Moon with the lunar surface [24–26]. The analysis of the density of the lunar regolith in diffuse structures was carried out using the original method of mapping the compactness significance factor (CSF) of the regolith.

To solve the problem of using space resources in the future, some projects have been proposed, including those for the utilization of the substance of near-Earth asteroids [21]. Despite the difficulties of capturing, transporting and subsequent development of such an object in space, this method of extracting useful resources seemed technologically possible and economically justified [27]. It has been shown in a number of works that the disposal of asteroidal matter falling on the lunar surface can be technologically simpler and more economically profitable [28].

## Conclusions

One of the results of the work was the relevance of the development of titanium mines on the Moon. The extraction of asteroid origin on the lunar surface is more technologically justified than the capture and delivery of asteroids into the Earth's orbit. Fresh lunar craters are most important if we consider that of the increased content of asteroid origin, the location of which can be determined by analyzing LRO images and by monitoring lunar optical flares. Observable evidence in favor of the formation of a fresh 20-km crater near the craters Copernicus and Kepler after a low-velocity collision of an asteroid with the lunar surface is discussed. The content of metals such as iron, cobalt, nickel, platinum and platinoids, delivered to the lunar surface during low-velocity M and S class asteroid impacts, is estimated. An economic justification for the expediency of using lunar resources is presented. Based on the obtained data, a mapped model of mineral distribution gradients depending on selenographic coordinates on the lunar sphere was constructed.

## Acknowledgments

This work was supported by Russian Science Foundation, grant 22-72-10059.

## REFERENCES


1. **Sato H., Robinson M.S., Lawrence S.J., Denevi B.W., Hapke B., Jolliff B.L., Hiesinger H.**, Lunar mare TiO2 abundances estimated from UV/Vis reflectance, Icarus. 296 (2017) 216–238.

2. **Sanchez J.A., Reddy V., Bottke W.F., Battle A., Sharkey B., Kareta T., Pearson N., Cantillo D.C.,** Physical Characterization of Metal-rich Near-Earth Asteroids 6178 (1986 DA) and 2016 ED85, The Planetary Science Journal. 2 (5) (2021) 1–15.

3. **Sergienko M., Sokolova M., Andreev A., Nefedyev Y.**, Small Meteor Showers Identification with Near-Earth Asteroids, Meteoritics & Planetary Science. 53 (2018) 6165.

4. **Petrova N.K., Nefedyev Y.A., Zagidullin A.A., Andreev A.O.**, Use of an analytical theory for the physical libration of the Moon to detect free nutation of the lunar core, Astronomy Reports. 62 (12) (2018) 1021–1025.

5. **Nefedyev Y.A., Valeev S.G., Mikeev R.R., Andreev A.O., Varaksina N.Y.**, Analysis of data of "CLEMENTINE" and "KAGUYA" missions and "ULCN" and "KSC-1162" catalogues, Advances in Space Research. 50 (11) (2012) 1564–1569.

6. **Williams J.G., Konopliv A.S., Boggs D.H., et al.**, Lunar interior properties from the GRAIL mission, Journal of Geophysical Research: Planets. 119 (7) (2014) 1546–1578.

7. **Nefedyev Y.A., Andreev A.O., Petrova N.K., Demina N.Y., Zagidullin A.A.**, Creation of a global selenocentric coordinate reference frame, Astronomy Reports. 62 (12) (2018) 1016–1020.

8. **Demina N.Y., Andreev A.O., Nefedyev Y.A., Akhmedshina E.N., Demin S.A.**, Analysis of the surfaces and gravitational fields of planets using robust modeling methods, Journal of Physics: Conference Series 1400 (2) (2019) 022019.

9. **Archinal B.A., Rosiek M.R., Kirk R.L., Redding B.L.**, The unified lunar control network 2005, US Geological Survey Open-File Report. 1367 (2006) 18.

10. **Konopliv A.S., Park R.S., Yuan D.N., et al.**, The JPL lunar gravity field to spherical harmonic degree 660 from the GRAIL primary mission, Journal of Geophysical Research: Planets. 118 (7) (2013) 1415–1434.

11. **Binder A.B.**, Lunar prospector: overview, Science. 281 (5382) (1998) 1475–1476.

12. **Andreev A.O., Demina N.Y., Zagidullin A.A., Petrova N.K., Nefedyev Y.A., Demin S.A.**, Analysis of topocentric and gravimetric data from modern space missions, Journal of Physics: Conference Series. 1135 (1) (2018) 012002.

13. **Demin S.A., Panischev O.Y., Nefedyev Y.A.**, Dynamic and spectral X-ray features of the microquasar XTE J1550-564, Kinematics and Physics of Celestial Bodies. 30 (2) (2014) 63–69.

14. **Andreev A.O., Demina N.Y., Nefedyev Y.A., Demin S.A., Zagidullin A.A.**, Modeling of the physical selenocentric surface using modern satellite observations and harmonic analysis methods, Journal of Physics: Conference Series. 1038 (1) (2018) 012003.

15. **Rizvanov N., Nefedjev J.**, Photographic observations of Solar System bodies at the Engelhardt astronomical observatory, Astronomy & Astrophysics. 444 (2) (2005) 625–627.

16. **Nefedjev Y.A., Rizvanov N.G.**, The results of an accurate analysis of EAO charts of the Moon marginal zone constructed on the basis of lunar occultations, Astronomische Nachrichten: Astronomical Notes. 323 (2) (2002) 135–138.

17. **Kronrod E.V., Nefed'ev Y.A., Kronrod V.A., Kuskov O.L., Andreev A.O.**, Selenophysics and models of the lunar three-layered mantle, Uchenye Zapiski Kazanskogo Universiteta. Seriya Fiziko-Matematicheskie Nauki. 161 (1) (2019) 24–38.

18. **Nefedyev Y., Andreev A., Hudec R.**, Isodensity analysis of comets using the collection of digitized Engelhardt Astronomical Observatory photographic plates, Astronomische Nachrichten. 340 (7) (2019) 698–704.

19. **Busarev V.V., Shevchenko V.V.**, Prediction of Lunar Areas Containing Ilmenite Based on Color and Spectrometric Characteristics, Soviet Astronomy. 33 (1989) 304.

20. **Shevchenko V.V., Busarev V.V.**, Ilmenites in Oceanus Procellarum, Second Conference on Lunar Bases and Space Activities of the 21st Century. 652 (1988) 219.

21. **Sokolova M.G., Nefedyev Y.A., Varaksina N.Y.**, Asteroid and comet hazard: Identification problem of observed space objects with the parental bodies, Advances in Space Research. 54 (11) (2014) 2415–2418.

22. **Sokolova M., Nefedyev Y., Sergienko M., Demina N., Andreev A.**, Analysis of the Lyrids' meteor stream structure for long timeslots, Advances in Space Research. 58 (4) (2016) 541–544.

23. **Sergienko M.V., Sokolova M.G., Andreev A.O., Nefedyev Y.A.**, Analysis of the main and small meteor showers, Meteoritics & Planetary Science. 53 (S1) (2018) 6162.

24. **Nefedyev Y.A., Sokolova M.G., Andreev A.O., Sergienko M.V., Demina N.Y.**, The use of the d-criterion method for the analysis of observational data of tunguska event, Meteoritics & Planetary Science. 53(S1) (2018) 6188.

25. **Sokolova M., Sergienko M., Nefedyev Y., Andreev A., Nefediev L.**, Genetic analysis of parameters of near earth asteroids for determining parent bodies of meteoroid streams, Advances in Space Research. 62 (8) (2018) 2355–2363.

26. **Sergienko M.V., Sokolova M.G., Andreev A.O., Nefedyev Y.A.**, Genetic analysis of the meteor showers and asteroids, Journal of Physics: Conference Series. 1400 (2) (2019) 022045.

27. **Sergienko M.V., Sokolova M.G., Kholshevnikov K.V.**, Multifactorial method of search for small bodies in close orbits, Astronomy Reports. 64 (5) (2020) 458–465.

28. **Shirenin A.M., Mazurova E.M., Bagrov A.V.**, Development of a high-precision selenodetic coordinate system for the physical surface of the Moon based on LED beacons on its surface, Cosmic Research. 54 (6) (2016) 452–457.

## THE AUTHORS

**ANDREEV Alexey O.**
alexey-andreev93@mail.ru
ORCID: 0000-0001-8748-3049

**NEFEDYEV Yury A.**
yura.nefedyev@gmail.com
ORCID: 0000-0002-2986-852X

**DEMINA Natalya Y.**
vnu_357@mail.ru
ORCID: 0000-0002-2379-3299

**KOLOSOV Yury A.**
koloyra@gmail.com
ORCID: 0000-0001-7439-731X

**KORCHAGINA Elena P.**
belkalenka2010@yandex.ru
ORCID: 0000-0003-4350-7891

*Received 01.11.2022. Approved after reviewing 24.11.2022. Accepted 26.12.2022.*

© Peter the Great St. Petersburg Polytechnic University, 2023

Conference materials
UDC 521
DOI: https://doi.org/10.18721/JPM.161.279

# Creation of a generalized dynamic model of planetary moons based on an analytical approach for describing the libration processes of their rotation

A.A. Zagidullin[1]✉, N.K. Petrova[2], Yu. A. Nefedyev[1], A. O. Andreev[1,2]

[1] Kazan Federal University, Kazan, Russia;

2 Kazan State Power Engineering University, Kazan, Russia

✉ arhtur.zagidullin@ya.ru

**Abstract.** Our work is devoted to the creation of a generalized dynamic model that describes libration processes in the motion of the natural satellite of the planet, which has been tested on the simulation of the moons rotational parameters(MRPs) of the Earth's Moon and allows adapting description system of MRPs to other celestial objects, having a librational nature of rotation as well.In this case, it is assumed that an analytical approach was used to describe the rotational motion, which, on the one hand, is rather complicated for solving the equations of rotation and has a lower accuracy than the numerical one, but, on the other hand, the resulting analytical representation of MRPs provides a more convenient tool for analyzing the behavior of MRPs with changes in various parameters, determining the rotational dynamics of the satellite.It is with its help that the procedure of flexible computer simulation of the rotation process and the identification of those observational manifestations, which are determined primarily by the parameters of the figure of a celestial body - the laws of distribution of body mass, compression, non-sphericity.

**Keywords:** physical libration, dynamic model of the moon, planets

**Funding:** This work was partially supported by Russian Science Foundation, grant 22-72-10059.

**Citation:** Zagidullin A.A., Petrova N.K., Nefedyev Yu.A., Andreev A.O., Creation of a generalized dynamic model of planets' moons based on an analytical approach for describing the libration processes of their rotation, St. Petersburg State Polytechnical University Journal. Physics and Mathematics. 16 (1.2) (2023) 517–522. DOI: https://doi.org/10.18721/JPM.161.279

This is an open access article under the CC BY-NC 4.0 license (https://creativecommons.org/licenses/by-nc/4.0/)

Материалы конференции
УДК 521
DOI: https://doi.org/10.18721/JPM.161.279

# Создание обобщенной динамической модели естественных спутников планет на основе аналитического подхода для описания либрационных процессов их вращения

А.А. Загидуллин[1]✉, Н.К. Петрова[2], Ю.А. Нефедьев[1], А.О. Андреев[1,2]

[1] Казанский федеральный университет, г. Казань, Россия;

[2] Казанский государственный энергетический университет, г. Казань, Россия

✉ arhtur.zagidullin@ya.ru

**Аннотация.** Работа посвящена созданию обобщенной динамической модели, описывающей либрационные процессы в движении естественного спутника планеты, которая апробирована на моделировании ПВС естественного спутника Земли и позволяет адаптировать систему описания ПВС и на другие небесные объекты, имеющие либрационный характер вращения.

© Zagidullin A.A., Petrova N.K., Nefedyev Yu.A., Andreev A.O., 2023. Published by Peter the Great St. Petersburg Polytechnic University.

**Ключевые слова:** физическая либрация, динамическая модель Луны, планеты

**Финансирование:** Работа поддержана Российским научным фондом, грант №. 22-72-10059.

**Ссылка при цитировании:** Загидуллин А.А., Петрова Н.К., Нефедьев Ю.А., Андреев А.О. Создание обобщенной динамической модели естественных спутников планет на основе аналитического подхода для описания либрационных процессов их вращения // Научно-технические ведомости СПбГПУ. Физико-математические науки. 2023. Т. 16. № 1.2. С. 517–522. DOI: https://doi.org/10.18721/JPM.161.279

Статья открытого доступа, распространяемая по лицензии CC BY-NC 4.0 (https://creativecommons.org/licenses/by-nc/4.0/)

## Introduction

Natural moons systems represent a wide variety of orbital-rotational configurations in the Solar system. [1]. While some of these are clearly the result of tidal processes, others still have largely unknown moons rotational parameters (MRPs) and structural models [1]. At the same time, the knowledge of MRPs makes it possible to study the internal structure of these bodies without expensive, and most often, simply inaccessible space experiments on the lunar surface or its nearby area. Observations of the rotation of the moons of Jupiter, Saturn and the Earth [2–6] made it possible to make the first estimates of their internal structure, the distribution of heat fluxes, and even their chemical composition [7–9]. Of particular interest in this regard are those moons that have passed the stage of tidal evolution and are in stable rotation: so-called libration moons. The physical libration of the Moon (PLM) is the oscillation of a celestial body about the axis of rotation under the influence of perturbing forces. So, for the Moon, when constructing the most accurate theory of libration, it is necessary to take into account the influence of the gravity of the Sun and the Earth on the dynamics of the Moon. For other moons, the influence of the Sun on rotation can most likely be neglected due to the large distance from it. But at the same time, accounting for the central planet, such as Jupiter and Saturn, becomes more significant. Since the influence of the central planet on the moons is very strong, almost all of them have passed the stage of tidal evolution, have a figure strongly elongated towards the planet, and are in stable rotation. Like the Moon, the Galilean moons of Jupiter make one orbit in a period equal to one revolution around the axis. This phenomenon is called orbital - rotational resonance and for these moons is 1:1.

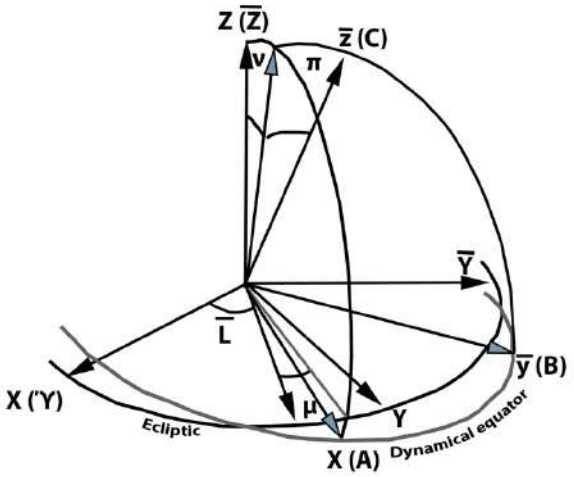


Fig. 1. Selenocentric coordinate systems. *XYZ* is the ecliptic coordinate system. *X*-axis direct to ♈ (the vernal equinox), *Z*-axis direct to the ecliptic pole. $\left(\overline{X},\overline{Y},\overline{Z}\right)$ is a uniformly rotating ecliptic coordinate system

© Загидуллин А.А., Петрова Н.К., Нефедьев Ю.А., Андреев А.О., 2023. Издатель: Санкт-Петербургский политехнический университет Петра Великого.

In this paper, we presented a strategy for solving the physical libration theory of a satellite (PLS) problem based on the method of constructing the theory of the PLM. In practice, for any moon, including the Moon, an important simplification can be introduced: orbital movement does not affect the rotation of the moon in any way.

## Materials and Methods

At the beginning, it was believed that the motion of a celestial body in orbit is described by Newton's second law. However, over time, Lagrange, and then Hamilton, Jacobi and other researchers modified Newton's second law so that the algorithm for solving such a problem would consist of certain stages. In this work, we used the approach proposed by Hamilton. As a result, a system of Hamiltonian differential equations of the first order was obtained, solving which, we obtain the parameters of the PLM theory.

It should be noted that the canonical variables are the transition angles from the inertial coordinate system to the dynamic one (DSC) tied to the principal axes of inertia. In other words, we can say that these are the transition angles from the absolute coordinate system to the rotating one. We have chosen the aircraft angles as such angles, which determine the position of the DSC relative to the ecliptic. The geometric meaning of these angles is described below and shown in Fig. 1. The algorithm for such a transition is as follows:

Rotation around the pole of the ecliptic $Z$ by an angle, $M = \overline{L} + \mu$ from the $X$ axis to the average direction to the Earth $x(A)$;

Rotation around the $\overline{Y}$ axis by an angle $\nu$, until it coincides with the $x(A)$ axis;

Rotation around the $x(A)$ axis by an angle $\pi$, until it coincides with the $y(B)$ axis.

This algorithm can be written using rotation matrices:

$$\begin{pmatrix} x \\ y \\ z \end{pmatrix} = \prod_{x}(-\pi) \times \prod_{\overline{Y}}(\nu) \times \prod_{\overline{Z}}(L+\mu) \begin{pmatrix} X \\ Y \\ Z \end{pmatrix}. \quad (1)$$

It is these libration angles that we have taken as canonical angular variables

$$q_1 = \mu,\ q_2 = \nu, q_3 = \pi.$$

The conjugate canonical moment we define as

$$p_1 = \frac{\partial T}{\partial q_1},\ p_2 = \frac{\partial T}{\partial q_2},\ p_3 = \frac{\partial T}{\partial q_3}.$$

Here $T$ is the kinetic energy of the Moon's rotation, the derivation of the expression for which we describe below.

The expression for the kinetic energy can be written in terms of the Moon's inertia tensor as follows:

$$\mathbf{G} = J\omega = \begin{pmatrix} A & -F & -E \\ -F & B & -D \\ -E & -D & C \end{pmatrix}. \quad (2)$$

Then the kinetic energy of the system will have the form:

$$T = \frac{1}{2}\omega^T J\omega. \quad (3)$$

For the working formula of kinetic energy, it is necessary to determine the projections of the angular velocity for a rotating coordinate system. This is done using simple geometric transformations:

$$\Omega_x = -\dot{M} \times \sin\nu - \dot{\pi},$$
$$q = \Omega_y = -\dot{M} \times \cos\nu \times \sin\pi + \dot{\nu} \times \cos\pi, \tag{4}$$
$$q = \Omega_y = -\dot{M} \times \cos\nu \times \sin\pi + \dot{\nu} \times \cos\pi.$$

After simple transformations, an expression for the kinetic energy is obtained, in which there are no components of the derivatives of the canonical parameters:

$$T = \frac{1}{2}[(1+k_2) \times p_3^2 +$$
$$+(1+k_1)(1+k) \times (p_2 \cos(q_3) - \sec(q_2)(n+p_1-p_3)\sin(q_3))^2] + \tag{5}$$
$$+\frac{1}{2}[p_2 \times \sin(q_3) + \cos(q_3) + ((n+p_1)\sec(q_2) - p_3 \tan(q_2))]^2$$

where $k_1 = \frac{C-B}{B}$, $k_2 = \frac{C-A}{A}$ are expressed in terms of the main parameters of the Moon's inertia; $p_1$, $p_2$, $p_3$ are canonical impulses. Then the system of Hamilton equations in general form will look like this

$$\frac{dq_i}{dt} = \frac{\partial H}{\partial p_i}, \quad \frac{dp_i}{dt} = \frac{\partial H}{\partial q_i}. \tag{6}$$

As a result, equations were obtained that describe the rotation of a celestial body, which can be brought into a general form to expand the gravitational potential of the moon:

$$U(\rho,\theta,\phi) = \frac{GM}{\rho}\left(\begin{array}{l} 1+\left(\frac{a}{\rho}\right)^2 [c_{20}P_2(\cos\theta) + c_{22}\cos(2\lambda)P_{22}(\cos\theta)] + \\ +\sum_{n=3}^{\infty}\sum_{m=0}^{n}\left(\frac{a}{\rho}\right)^n [c_{nm}\cos(m\lambda) + s_{nm}\sin(m\lambda)]P_{nm}(\cos\theta) \end{array}\right). \tag{7}$$

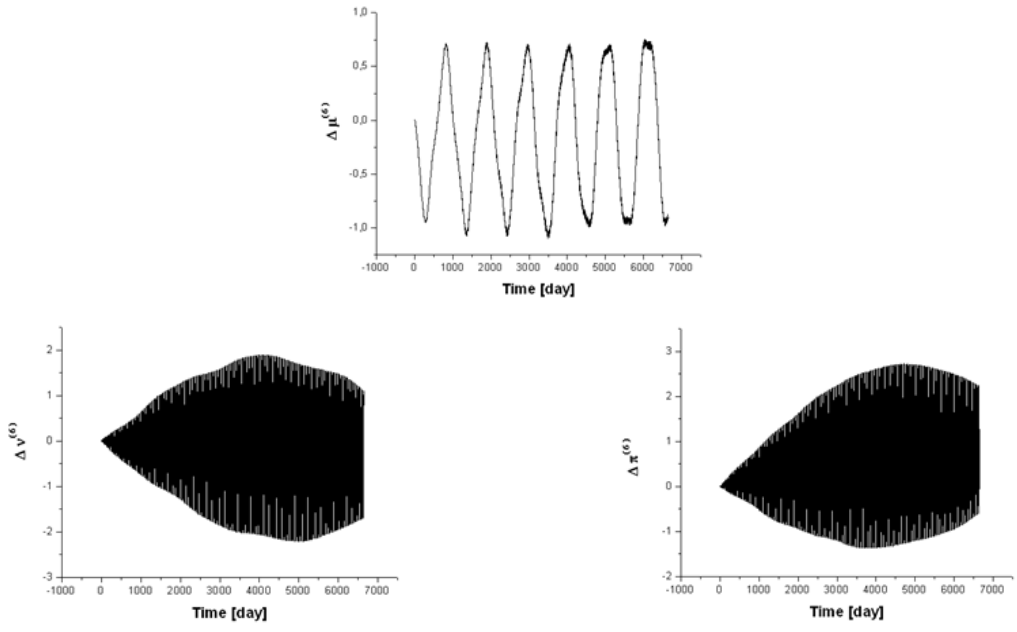


Fig. 2. Residual differences between numerical solution and dynamic ephemeris DE421

## Results and Discussion

In order to assess the accuracy of the theory, a plot of residual differences with respect to the DE421 ephemeris was plotted (Fig. 2). The figure shows the residual differences in libration in longitude and latitude after taking into account all the perturbations included in our model.

In Fig. 2, the scale along the y-axis is expressed in arcseconds.It can be concluded that the amplitudes correspond to the order of one second for all libration angles, and this is a rather large value.If you perform a harmonic analysis of the results to identify the fundamental frequencies, then you get frequencies close to the eigenfrequencies of the system (1047 days, 27.3 days, 68 years). When compared with the theory (DE421), there are significant differences in the process of taking into account various perturbations, such as the lunar core, etc., and in the residual differences, this will manifest itself just at frequencies close to the natural ones.To increase the reliability of the PLM theory, it is possible to subtract the harmonics obtained for the Eigen frequencies of the system.

## Conclusion

Consideration of perturbations from planets for natural satellites is carried out by switching to modern orbital theories of motion DE (dynamic ephemeris) developed at NASA's Jet Propulsion Laboratory, or to the EPM numerical theory developed at IAA RAS [10]. Naturally, the most accurate description of the rotational motion is made for the Moon [11]. If for the majority of moons it is possible to use only second-order harmonics in the expansion of the moon's gravitational field, then for the Moon there are good data for harmonics of the 3rd and higher orders.In our studies, we limited ourselves to the harmonics of the 4th order. In addition, laser ranging data made it possible to estimate the elastic properties of the lunar body [12].This gave us the opportunity to take into account elastic properties of the lunar body in the first approximation.

PLM is not only a tool for constructing a theory of oscillations of a celestial body about the axis of rotation, but also a method for modeling internal processes [13].Already a classic example of considering the process of rotation of a raw and liquid eggs allows us to say that such rotation is greatly influenced by the internal structure of the body itself [14].Therefore, our further research will be aimed at analyzing more subtle effects of the rotational motion of celestial bodies and deriving equations that take into account the presence of the lunar core [15].

The paper presents the result of many years of work on the construction of the theory of PLM, in which all dynamic constants and coefficients in the expansion of the potential were studied, and as a result, a mathematically rigorous theory of the rotation of a celestial body was constructed [16].The results of this work were reported at the All-Russian Astronomical Conference (VAK 2021), and were included in the list of the Scientific Council for Astronomy of the Russian Academy of Sciences as a significant contribution to astronomical research in 2021. All studies carried out in this work are new and performed using the methods developed by the authors. The results obtained can be used in the implementation of space missions to the bodies of the solar system and in the study of exoplanetary systems [17–20].

## Acknowledgments

This work was partially supported by Russian Science Foundation, grant 22-72-10059.

## REFERENCES

1. **Polycarpe W., Saillenfest M., Lainey V., Vienne A., Noyelles B. and Rambaux N.**, Strong tidal energy dissipation in Saturn at Titan's frequency as an explanation for Iapetus orbit, Astronomy and Astrophysics. 619 (2018) A133.

2. **Čadek O., Tobie G., Van Hools T., Massé M., Choblet G., Lefèvre A., Mitri G., Baland R.M., Běhounková M., Bourgeois O., Trinh A.**, Enceladus's internal ocean and ice shell constrained from Cassini gravity, shape, and libration data, Geophyical. Research Letter. 43 (2016) 5653–5660.

3. **Baland R.M., Tobie G., Lefèvre A., Van Hoolst T.**, Titan's internal structure inferred from its gravity field, shape, and rotation state, Icarus. 237 (2014) 29–41.

4. **Gudkova T.V., Zharkov V.N.**, Theoretical free oscillations spectrum for Saturn interior models, Advances in Space Research. 38 (2006) 764–769.

5. **Jolliff B. L., Wieczorek M. A., Shearer C. K. and Neal C. R.**, New views of the Moon, Reviews in Mineralogy & Geochemistry. 60 (2006) 1–119.

6. **Van Hoolst T.**, The libration and interior stucture of large icy satellites and Mercury, Proceedings of the International Astronomical Union. (2014) 91–98.

7. **Baland R.M., Van Hoolst T., Yseboodt M., Karatekin Ö.**, Titan's obliquity as evidence for a subsurface oecan, Astron. Astrophys 530 (2011) A141.

8. **Petrova N., Gusev A., Kawano N., Hanada H.**, Free librations of. the two-layer Moon and the possibilities of their detection, Advances in Space Research. **42** (2008) 1398–1404.

9. **Williams J.G., Boggs D.H., Yoder C.F., Ratcliff J.T., Dickey J.O.**, Lunar core and tides. Journal of Geophysical Research: Planets. 106 (2001) 27933–27968.

10. **Weber R.C., Lin P.Y., Garnero E.J., Williams Q., Lognonné P.**, Seismic detection of the lunar core, Science. 331 (2011) 312–309.

11. **Petrova N., Zagidullin A., Nefedyev Y., Kosulin V. and Andreev A.**, The analytical and numerical approaches to the theory of the Moon's librations: Modern analysis and results, Advances in Space Research. 60 (2017) 2303–2313.

12. **Zagidullin A., Petrova N., Usanin V., Nefedyev Y. and Glushkov M**., Development of the numerical approach in the theory of physical libration within the framework of the "main problem", Uchenye Zapiski Kazanskogo Universiteta. Seriya Fiziko-Matematicheskie Nauki. 159 (546–529 (2017.

13. **Petrova N., Nefedyev Y., Zagidullin A. and Andreev A.**, Use of an Analytical Theory for the Physical Libraton of the Moon to detect Free Nutation of the Lunar Core, Astronomy Reports. 62 (2018) 1021–1025.

14. **Zagidullin A., Petrova N., Usanin V., Andreev A. and Nefedyev Y.**, Analysis of orbital theories for the construction of the numerical theory of the lunar physical librations, Journal of Physics: Conference Series.1038 (2018) 012004.

15. **Petrova N.K., Nefedyev Y.A., Andreev A.O., Zagidullin A.A.**, Lunar-Based Measurements of the Moon's Physical Libration: Methods and Accuracy Estimates, Astronomy Reports. 64 (2020) 1078–1086.

16. **Kronrod E., Nefedyev Y., Kronrod V., Kuskov O. and Andreev A**., Selenophysics and models of the lunar three-layered mantle, Uchenye Zapiski Kazanskogo Universiteta. Seriya Fiziko-Matematicheskie Nauki**.** 161 (2019) 24–38.

17. **Zagidullin A., Usanin V., Petrova N., Nefedyev Y., Andreev A. and Gudkova T.**, Physical Libration of the Moon: An Extended Problem, Astronomy Reports. 64 (2020) 1093–1106.

18. **Zagidullin A., Petrova N., Usanin V., Andreev A. and Nefedyev Y.** Analysis of orbital theories for the construction of the numerical theory of the lunar physical librations, Journal of Physics: Conference Series.1038 **(**2018**)** 012004.

19. **Zagidullin A. A., Usanin V. S., Petrova N. K., Nefedyev Y. A. and Andreev A. O.** Analysis of analytical and numerical dynamic lunar ephemerides, Journal of Physics: Conference Series. 1697 (2020) 012018.

20. **Andreev A., Zagidullin A., Demina N., Petrova N., Nefedyev Y. and Demin S.** Analysis of topocentric and gravimetric data from modern space missions, Journal of Physics: Conference Series. 1135 (2018) 012002.

## THE AUTHORS

**ZAGIDULLIN Arthur A.**
arhtur.zagidullin@ya.ru
ORCID: 0000-0003-4436-9363

**NEFEDYEV Yury A.**
yura.nefedyev@gmail.com
ORCID: 0000-0002-2986-852X

**PETROVA Natalia K.**
nk_petrova@mail.ru
ORCID: 0000-0002-7078-0706

**ANDREEV Alexey O.**
alexey-andreev93@mail.ru
ORCID: 0000-0001-8748-3049

*Received 31.10.2022. Approved after reviewing 08.11.2022. Accepted 09.11.2022.*

© Peter the Great St. Petersburg Polytechnic University, 2023

Conference materials
UDC 521
DOI: https://doi.org/10.18721/JPM.161.280

# ρ-Geminids meteor shower and its connection with near-Earth asteroids

M.V. Sergienko[1]✉, M.G. Sokolova[1], Yu.A. Nefedyev[1], A.O. Andreev[2]

[1] Kazan Federal University, Kazan, Russia;

[2] Kazan State Power Engineering University, Kazan, Russia

✉ maria_sergienko@mail.ru

**Abstract.** In this work, genetic connections (GC) of the small meteor shower ρ-Geminids with near-Earth objects (NEOs) of the Apollo group were studied using the author's multiparameter method. The multiparameter method for determining GC of meteor showers with probable parent bodies is based on the use of a set of criteria for identifying orbits, such as: D-criterion by Drummond, Kholshevnikov's metric, Tisserand's parameter, μ and ν quasi-stationary parameters of the restricted three-body problem, longitude of perihelion π of meteor orbit. The method of identifying meteoroids with asteroids involves computational procedures and the calculation of critical values for each of the criteria used, which increases the reliability of finding the GC for the objects under study. The catalogues of meteor orbits: Meteoroid Orbit Database v3.0, CAMS and EDMOND 5 v.04 of the European Meteor Network were used as source material in the work.

**Keywords:** meteor showers, near-Earth asteroids, orbits of small celestial bodies, genetic relationships between meteor showers and asteroids

**Funding:** This work was partially supported by Russian Science Foundation, grant 22-72-10059.

**Citation:** Sergienko M.V., Sokolova M.G., Nefedyev Yu.A., Andreev A.O., ρ-Geminids meteor shower and its connection with near-earth asteroids, St. Petersburg State Polytechnical University Journal. Physics and Mathematics. 16 (1.2) (2023) 523–529. DOI: https://doi.org/10.18721/JPM.161.280

This is an open access article under the CC BY-NC 4.0 license (https://creativecommons.org/licenses/by-nc/4.0/)

Материалы конференции
УДК 521
DOI: https://doi.org/10.18721/JPM.161.280

# Метеорный поток ρ-гемениды и его связь с околоземными астероидами

М.В. Сергиенко[1]✉, М.Г. Соколова[1], Ю.А. Нефедьев[1], А.О. Андреев[2]

[1] Казанский федеральный университет, г. Казань, Россия;

[2] Казанский государственный энергетический университет, г. Казань, Россия

✉ maria_sergienko@mail.ru

**Аннотация.** В работе были исследованы генетические связи (ГС) малого метеорного потока ρ-Гемениды с околоземными астероидами группы Аполлона с применением авторского многопараметрического метода. Многопараметрический метод установления ГС метеорных потоков с вероятными родительскими телами основан на использовании совокупности критериев отождествления орбит.

**Ключевые слова:** метеорные потоки, околоземные астероиды, орбиты малых небесных тел, генетические связи метеорных потоков и астероидов

© Sergienko M.V., Sokolova M.G., Nefedyev Yu.A., Andreev A.O., 2023. Published by Peter the Great St. Petersburg Polytechnic University.

**Финансирование:** Работа поддержана Российским научным фондом, грант №. 22-72-10059.

**Ссылка при цитировании:** Сергиенко М.В., Соколова М.Г., Нефедьев Ю.А., Андреев А.О. Метеорный поток ρ-гемининды и его связь с околоземными астероидами // Научно-технические ведомости СПбГПУ. Физико-математические науки. 2023. Т. 16. № 1.2. С. ...–... . DOI: https://doi.org/10.18721/JPM.161.280

Статья открытого доступа, распространяемая по лицензии CC BY-NC 4.0 (https://creativecommons.org/licenses/by-nc/4.0/)

## Introduction

For many large meteor showers, parent bodies were identified, while for small meteor showers, the parent body is unknown [1]. Large meteor showers include a great number of meteors, and their orbits can be determined with higher accuracy, while small meteor showers have a low zenithal hourly rate (ZHR) and average orbital elements of the shower are determined with less accuracy [2–5]. Besides, the parent body of a meteor shower can be small, which makes it difficult to observe and, consequently, determine its orbit [6–7]. The orbits of meteoroids and the orbits of the parent bodies evolve rapidly [8], which makes it very difficult to identify the meteoroids of the shower with the orbit of the parent body. The search and identification of possible connections between meteor showers and presumed parent bodies play an important role in the theory of the origin and evolution of meteoroid bodies allowing to understand the mechanism of the decay of the parent body, the process of meteoroid ejection, and to determine potential sources of meteorites [9, 10].

At a moment, it is believed that the formation of meteor showers is possible either due to the decay of the cometary nucleus, or the meteor shower is a derivative of an asteroid. There is also a hypothesis according to which some asteroids are dormant cometary nuclei. The greatest difficulty is the search for methods for separating such objects into comet nuclei, that actually lost their activity, and real asteroids that were formed in the main asteroid belt. Among the ways that can confirm or disprove this hypothesis is a low albedo, a large eccentricity or inclination, but the orbit can be changed under the influence of gravitational perturbations.

According to available data from space missions, the surface of small asteroids is covered with regolith and stones, has splits and cracks, as well as craters. Consequently, at rotation, under the influence of external forces, under the action of centrifugal force and under the influence of the gravitational force of planets, such asteroids can be destroyed, and regolith can be separated from their surface. Under the influence of the tidal force from the Earth, which acts on the asteroid at the moment of their close approach, the shape of the asteroid can change, and the stones and dust located on its surface can be released into interplanetary space. Hoffmeister suggested in 1937 that asteroids produce meteoroids of various size, from dust to large debris. Such asteroids can be extinct comets with low cometary activity as well. Asteroidal meteoroids can also be generated by tidal disruption or asteroid collisions, which can create short and narrow dust trails. The study of these NEOs is important since they pose a danger to our planet having a low tensile strength, but due to their low activity, such small planets are easier to study than the ones of the Jupiter family.

For the first time, Fred Whipple identified an asteroid as the parent body of a meteor shower in 1961; he established that the 3200 Phaeton is associated with the Geminids meteor shower. Recently, 2003 EH1 has been considered the parent body of the Quadrantida meteor shower. The orbits of these objects have a strong orbital inclination about 72°, which excludes their random connection. Later, the minor planet 2003 WY2 was found to be moving in a cometary orbit similar to that of comet D/1819 W1 (Blanpain), this comet was lost, as indicated by the letter D in its name. However, at its appearance, the comet had good activity and its outbursts were accompanied by fragmentation. Thus, it can be assumed that the parent bodies of meteor showers can be searched for among asteroids of near-Earth groups, since among these objects, perhaps, there are extinct comets that lost their volatile component, or fragments of decayed cometary nuclei, and formed bonds are also possible as asteroid-comet complexes.

© Сергиенко М.В., Соколова М.Г., Нефедьев Ю.А., Андреев А.О., 2023. Издатель: Санкт-Петербургский политехнический университет Петра Великого.

## Materials and Methods

The purpose of the study is finding genetic connections the small meteor showers with near-Earth objects. The objectives of the study is investigation the meteor shower ρ-Geminidsand the Apollo group asteroids. The small meteor shower ρ-Geminids (rho Geminids, RGE, #94) was discovered in 1952–1954 by Southworth and Hawkins under the Harvard meteor program. ρ-Geminids are active from December 28 to January 28, the maximum occurs around January 8, the secondary maximum occurs on January 21. The parent body of the shower is not defined. It is a small meteor shower that has a low zenith hourly rate (ZHR): about 20 meteors per hour. In publications, observations and radiants of the ρ-Geminids are given, but there are few publications on the establishment of GC due to its low abundance. Meteoroids were analyzed and their chondrite nature was determined. Chondrites are stone objects interspersed with small chondrules, i.e. spherical formations up to 1 mm in size. Chondrites are the most common group of asteroids.

Optical video observations of meteors began in the 1970s using TVs and VCRs. For the first time this method was used by observers from Netherlands and Japan, and subsequently in connection with the advent of image intensifiers, this method was actively developed. The video method of observation has a number of advantages over the photo method, since it is possible to determine the speed of a meteor and its duration reliably [11].

In addition, in video observations, to determine the initial orbit of the meteoroid, the triangulation method is used and the observation is carried out simultaneously from several stations, which increases the accuracy of a certain orbit. Meteor orbit catalogues were used as source material: Meteoroid Orbit Database v3.0, CAMS (hereinafter CAMS), and EDMOND 5 v.04 of the European Meteor Network (hereinafter EDMOND). The CAMS catalogue includes information on 110521 meteoroid orbits from magnitude $-2^m$ to $+4^m$ (median is $+1.2^m$). Accuracy is $< 2°$ (median is 0.24°) in determining the direction of the radiant and < 10% in determining velocity (median values are 0.31 and 0.51 km/s, approximately 2%). The CAMS catalogue lists errors in measuring the orbital elements of meteoroids.

The version of the EDMOND database (v5.04, February 2018) contains 322,566 meteoroid orbits from 2001 to 2016. There is no information about errors in determining the elements of meteoroid orbits in the catalogue.

Table 1 shows data on the number of selected orbits of ρ-Geminids meteoroids in the catalogues, as well as the elements of average orbits are determined from the orbital characteristics of separate meteoroids and their root mean square errors σ (RMS) (errors and weights are calculated according to the CAMS catalog; according to the EDMOND catalog – excluding them).

To establish a connection between the orbits of meteoroids and their potential parent bodies,

Table 1

**Mean orbits of the ρ-Geminids (angular elements for epoch J2000.0)**

| Catalogue | Number of Orbits | $q\pm\sigma$ (au) | a±σ (au) | e±σ | $i°\pm\sigma°$ | Ω±σ° | ω±σ° | π±σ° |
|---|---|---|---|---|---|---|---|---|
| CAMS | 10 | 0.590 ±0.027 | 2.373 ±0.188 | 0.749 ±0.024 | 2.893 ±0.815 | 279.777 ±3.513 | 266.191 ±3.177 | 289.428 ±3.454 |
| EDMOND | 32 | 0.558 ±0.077 | 2.167 ±0.310 | 0.737 ±0.043 | 2.679 ±1.359 | 264.214 ±47.481 | 242.881 ±1.359 | 185.968 ±1.377 |

Notations. In Table, *q, a, e, i,* Ω, ω, π are perihelion distances, semi-major axis, eccentricities of the orbit, inclination, longitude of the node of the orbit of a small body, argument of perihelion and longitude of perihelion.

we use a multivariate analysis methods described in detail in [1]. For analysis, we use a data sample from two catalogues of meteor orbits CAMS and EDMOND; in calculations, we use the average shower orbit calculated from 10 meteors in the CAMS catalogue and 32 meteors in the EDMOND catalogue (Table 1). To determine the similarity of the orbits, a set of criteria for the proximity of the orbits of small bodies is used. Drummond criterion [2]:

$$D^2 = \left(\frac{e_2 - e_1}{e_2 + e_1}\right)^2 + \left(\frac{q_2 - q_1}{q_2 + q_1}\right)^2 + \left(\frac{I_{21}}{180^\circ}\right)^2 + \left(\frac{e_2 + e_1}{2}\right)^2 + \left(\frac{\theta_{21}}{180^\circ}\right)^2, \quad (1)$$

where $\theta = \arccos\left(\sin\beta_2 \sin\beta_1 + \cos\beta_2 \cos\beta_1 \cos\left(\lambda_2 - \lambda_1\right)\right)$, $\lambda = \Omega + \text{arc tg}(\cos i \,\text{tg}\,\omega)$; 180° is added if cos ω < 0, $\beta = \arcsin\left(\sin i \sin\omega\right)$, where $I$, $e$, $q$ are mutual inclination, eccentricities and perihelion distances of the orbits of two bodies, for which the calculation is carried out.

The Kholshevnikov metric ρ [3], which is defined in the three-dimensional phase factor space as

$$\rho^2 = \left(1 + e_1^2\right) p_1 + \left(1 + e_2^2\right) p_2 - 2\sqrt{p_1 p_2}\left(e_1 e_2 + \cos\left(i_1 - i_2\right)\right), \tag{2}$$

where $p_1$, $p_2$ are focal parameters.

It is believed that the physical dimension of ρ is the root of the length unit, so in what follows we calculate $\rho^2$ (au). Therefore, for the Drummond criterion (1), we calculate $D^2$, since we need a dimensionless quantity. We will accept the hypothesis about the proximity of the orbits of two small bodies $x$ and $y$ if the condition

$$\begin{aligned} D_c^2(x,y) &\le D_c^2, \\ \rho_c^2(x,y) &\le \rho_c^2, \end{aligned} \tag{3}$$

where $D_c$, $\rho_c$ are upper critical values of the Drummond criterion $D$ and the Kholshevnikov metric ρ.

The critical values of and $\rho_c$ are determined as the calculated average values of $D$ (1) and ρ (2) for the pairs of orbits: meteoroid orbit − average shower's orbit [1] (Table 2). Table 2 provides the upper critical values of the Drummond criterion $D_c$ and the Kholshevnikov metric $\rho_c$ and their standard deviations calculated from the CAMS and EDMOND catalogues for ρ-Geminids.

To characterize the dynamics of small bodies, the Tisserand's parameter relative to Jupiter is used. The value of this parameter determines the rate of approach to Jupiter, since this parameter is kept constant in the circular restricted three-body problem. Jupiter has $T_j = 3$. Main belt asteroids have $a < a_j$ and $T_j > 3$.

Table 2

**Critical values of the Drummond criterion $D_c$ and the Kholshevnikov metric $\rho_c$ for ρ-Geminids**

| Catalogue | $D^2_c \pm \sigma$ | $\rho^2_c \pm \sigma\sigma$ |
|---|---|---|
| CAMS | 0.035±0.012 | 0.024±0.009 |
| EDMOND | 0.064±0.027 | 0.011±0.011 |

We also use parameters whose values change insignificantly during the orbital evolution of small bodies: the Tisserand's parameter with respect to Jupiter [4]

$$T = a^{-1} + 0.16860\, a(1 - e^2)^{1/2} \cos i \tag{4}$$

and two quasi-stationary parameters [5, 6]:

$$\mu = \sqrt{a(1 - e^2)}\cos i, \tag{5}$$

$$\nu = \left(1 - e^2\right)\left(0.4 - \sin^2\omega \sin^2 i\right), \tag{6}$$

where $a$, $e$, $i$, ω are semi-major axis, eccentricity, inclination, argument of perihelion and longitude of the node of the orbit of a small body.

Also longitude of perihelion

$$\pi = \omega + \Omega, \tag{7}$$

which also remains constant [11] over long-time intervals. The average values of the parameters $T$, ν, μ, and π for ρ-Geminids are given in Table 3.

Table 3

**Average values of Tisserand's parameter *T*, quasi-stationary parameters μ and ν perihelion longitude π for ρ-Geminids**

| Catalogue | $T\pm\sigma$ | $\mu\pm\sigma$ | $\nu\pm\sigma$ | $\pi\pm\sigma$ |
|---|---|---|---|---|
| CAMS | 3.1030.218± | 1.0140.024± | 0.1740.019± | 185.9681.619± |
| EDMOND | 3.3360.403± | 0.9790.080± | 0.1800.030± | 203.3458.128± |

The selection of asteroids with close orbits is carried out according to the algorithm described in detail in [1]. If condition (3) is observed for a pair of orbits ($x$ is the asteroid's orbit, $y$ is the average shower's orbit), then the Drummond criterion (1) and the Kholshevnikov's metric (2) are assigned the factors $P_1 = 1$, $P_2 = 1$. If condition (3) is satisfied taking into account RMS±σ, ±2σ, etc., then criteria (1) and (2) are fulfilled with the values of the factor $P_1 = 0.9$, $P_2 = 0.9$, $P_1 = 0.8$, $P_2 = 0.8$, etc. respectively.

The fulfillment of criterion (4) on the Tisserand's parameter $T$ for a pair of two orbits is also evaluated on the basis of standard deviation (Table 4) and criterion (4) is fulfilled with the factor $P_3 = 0.9$, $P_3 = 0.8$, etc.

Similarly, the reliability of the fulfillment of criteria (5–7) is assessed based on their RMS (Table 3) with the assignment of factors $P_4$, $P_5$ and $P_6$, respectively. The value of unity is not assigned to the factors $P_3$, $P_4$, $P_5$ and $P_6$, since for criteria (5–7) it is the interval scatter of the values of $T$, μ, ν, π between the asteroid orbits and the average shower's orbit, and not their complete coincidence that is estimated. The overall measure of fulfillment of all criteria (2–7) was estimated as the product $P_i$ of all factors $i = 1, ...,6$.

## Results and Discussion

As a result of all calculations, asteroids were selected for which criteria (2–7) are met with factors $P_i \geq 0.8$ (taking into account rounding to tenths), i.e., the parameters of the criteria do not exceed the 2σ value of their average values. When implementing this approach, the total measure $P_i$ of the fulfillment of all criteria in the aggregate amounted to a value ≥ 0.5 for the two catalogues CAMS and EDMOND. Selected asteroids with close orbits for ρ-Geminids are shown in Table 4, which also presents the results of other sources.

Table 4

**Asteroids with orbits close to the ρ-Geminids (RGE #94)**

| Selected Asteroids | Catalogue | Factor *P* | Data on publications of other authors |
|---|---|---|---|
| 506859 (2007VW137) | CAMS EDMOND | 0.7<br>0.5 | 506859 (2007VW137), 2010 AG30 |
| 2014 XJ3 | CAMS EDMOND | 0.6<br>0.5 | |
| 2010 AG30 | CAMS EDMOND | 0.5<br>0.5 | |

ρ-Geminids meteors were analyzed and identification was carried out using the Southworth-Hawkins $D$ criterion. As a result, asteroids 506859 (2007VW137) ($D_{SH} = 0.09$) and 2010 AG30 ($D_{SH} = 0.13$) were identified. For the $D$ criterion of Southworth-Hawkins, the restriction $D_{SH} < 0.15$ was used, which the authors adopted.

Orbital elements and a number of physical parameters for the asteroids we have chosen are placed in Table 5.

It is assumed that objects with the value of the Tisserand's parameter relative to Jupiter $T < 3.1$ move in cometary orbits, if $T > 3.1$ then in asteroid orbits, and objects with $T \approx 3$ have a transfer orbit. The average orbit of the ρ-Geminids shower has the value of Tisserand's parameter $T_П = 3.273$ for the EDMOND catalog and $T_П = 3.075$ for CAMS, which makes it possible to search for connections between the proximity of orbits among asteroids, since it is impossible to unambiguously determine the type of its orbit, i.e., cometary or asteroid.

Table 5

**Orbital elements (2000.0) and physical parameters of identified asteroids**

| Asteroid | $a$, au | $e$ | $q$, au | $i$° | Ω° | ω° | $T$, year | $T_{jup}$ | Earth MOID, au |
|---|---|---|---|---|---|---|---|---|---|
| 506859 (2007VW137) | 2.229 | 0.739 | 0.581 | 5.943 | 299.655 | 245.071 | 3.327 | 3.212 | 0.039 |
| 2014 XJ3 | 2.134 | 0.727 | 0.582 | 1.223 | 22.312 | 161.671 | 3.118 | 3.317 | 0.020 |
| 2010 AG30 | 2.261 | 0.695 | 0.690 | 2.088 | 103.581 | 84.624 | 3.399 | 3.249 | 0.006 |

All selected asteroids by the value of the Tisserand's parameter have an asteroid type of orbit. The selected asteroids are potentially dangerous, approaching the Earth less than 900 thousand km and, therefore, fall into the sphere of its gravitational influence. There are no data on the size of asteroids and geometric albedo, which does not allow us to assess the degree of their danger to the Earth. There are also no data on the physical and chemical characteristics of asteroids, which makes it difficult to identify them with a meteor shower and requires further additional research.

## Conclusion

In this paper, we searched for possible parent bodies for the poorly studied small meteor shower ρ-Geminids among near-Earth asteroids of the Apollo group. The method of multivariate analysis, described in detail in [12], was applied. As the initial base of meteor orbits, two television catalogues of meteor orbits CAMS [13] and EDMOND [14] were involved, on the basis of which, using the set of the criteria, asteroids 506859 (2007VW137), 2014 XJ3, and 2010 AG30 were selected. Since the ρ-Geminids is a poorly studied meteor shower, only one publication was found on a similar research topic, with which a comparison was made. According to, it should be taken into account that meteoroids are of chondrite nature, which means that the parent body should be searched for in a similar taxonomic class of objects [14]. Since the identified asteroids lack such important parameters as size, geometric albedo, and taxonomic index (Table 5), a more detailed analysis of their relationship with the ρ-Geminids meteor shower is required [15].

To determine the asteroids dangerous for our planet, it is necessary to carry out work to establish genetic relationships between small celestial bodies and meteor showers.

## Acknowledgments

This work was partially supported by Russian Science Foundation, grant 22-72-10059.

## REFERENCES

1. **Sergienko M., Sokolova M. and Kholshevnikov K.,** Multifactorial Method of Search for Small Bodies in Close Orbits , Astronomy Reports. 64(5) (2020) 458–465.

2. **Drummond J.**, A test of comet and meteor shower associations, Icarus. 45 **(**1981**)** 545–553.

3. **Kholshevnikov K., Kokhirova G., Babadzhanov P., Khamroev U.**, Metrics in the space of orbits and their application to searching for celestial objects of common origin, Monthly Notices of the Royal Astronomical Society. 462 **(**2016**)** 2275–2283.

4. **Tisserand F.**, Perturbation des plan`etes d'apr`es la m'ethode de la variation des constantes arbitraires 1 (1889) 1–486.

5. **Lidov M.**, The evolution of orbits of artificial satellites of planets under the action of gravitational perturbations of external bodies, Planetary and Space Science. 9 (1962) 719–759.

6. **Sokolova M., Nefedyev Y., Sergienko M., Demina N. and Andreev A.**, Analysis of the Lyrids' meteor stream structure for long timeslots, Advances in Space Research. 58 (544–541 (2016.

7. **Jenniskens P.**, On the dynamics of meteoroid streams, Earth Planets Space. 50 (1998) 555–567.

8. **Trigo-Rodriguez J.M., et al.**, Asteroid 2002NY40 as a source of meteorite-dropping bolides, Monthly Notices of the Royal Astronomical Society. 382 **(**2007**)** 1933–1939.

9. **Trigo-Rodríguez J.M., Madiedo J.M., Williams I.P., Castro-Tirado A.J., Llorca J., Vitek S. and Jelinek M.**, Observations of a very bright fireball and its likely link with comet C/1919 Q2 Metcalf, Monthly Notices of the Royal Astronomical Society. 394 (576–569 (2009.

10. **Whipple F.L.**, A Comet Model. II. Physical Relations for Comets and Meteors, The Astrophysical Journal. 113 (474–464 (1951.

11. **Sokolova M., Kondratyeva E., Nefedyev Y.**, A comparative analysis of the D-criteria used to determine genetic links of small bodies, Advances in Space Research. 52 (2013) 1217–1220.

12. **Sergienko M., Sokolova M., Andreev A. and Nefedyev Y.**, Genetic analysis of the meteor showers and asteroids, Journal of Physics: Conference Series.1400 (2019) 022045.

13. **Sokolova M., Sergienko M., Nefedyev Y., Andreev A. and Nefediev L.**, Genetic analysis of parameters of near earth asteroids for determining parent bodies of meteoroid streams, Advances in Space Research. 62 (2018) 2355–2363.

14. **Sokolova M., Nefedyev Y. and Varaksina N.,** Asteroid and comet hazard: Identification problem of observed space objects with the parental bodies, Advances in Space Research. 54 (2014) 2415–2418.

15. **Jewitt D**., The active asteroids, The Astronomical Journal. 143 (2012) 1–14.

## THE AUTHORS

**SERGIENKO Maria V.**
maria_sergienko@mail.ru
ORCID: 0000-0003-3447-2500

**NEFEDYEV Yury A.**
yura.nefedyev@gmail.com
ORCID: 0000-0002-2986-852X

**SOKOLOVA Marina G.**
smarina.63@mail.ru
ORCID: 0000-0002-9417-8373

**ANDREEV Alexey O.**
alexey-andreev93@mail.ru
ORCID: 0000-0001-8748-3049

*Received 31.10.2022. Approved after reviewing 21.11.2022. Accepted 21.11.2022.*

© Peter the Great St. Petersburg Polytechnic University, 2023

Conference materials
UDC 521
DOI: https://doi.org/10.18721/JPM.161.281

# Analysis of comet C/1969 Y1 parameters using isophote structural modeling

K.O. Churkin[1]✉, A.O. Andreev[2], Yu.A. Nefedyev[1], Yu.A. Kolosov[1], E.P. Korchagina[1], N.Yu. Demina[1], V.S. Borovskih[3]

[1] Kazan Federal University, Kazan, Russia;

[2] Kazan State Power Engineering University, Kazan, Russia;

[3] Kazan State University of Architecture and Engineering, Kazan, Russia

✉ konstantinch-n87@mail.ru

**Abstract.** This work is devoted to the construction of a brightness structural model of the long-period comet Bennett C/1969 Y1. This comet belongs to the comets of the Jupiter family (JF) and has a Tisserand's parameter T > 2. Determining the brightness characteristics of the comet has been one of the most important goals of cometary observations over the past century. The complexity of such studies lies in the fact that we are dealing with extended sources moving relative to background stars. The problem of obtaining reliable estimates of the distribution of brightness parameters (BPs) for long-period comets also remains especially important, because for many of them observations were made back in the days when high-precision methods, such as CCD-matrices and other technical tools, were not available. At the same time, most of the determined stellar magnitudes of long-period comets were related to the gaseous coma surrounding the comet's nucleus, and not to the comet's nucleus itself. At the same time, cosmic ultraviolet observations of comets in the Lyman-alpha hydrogen lines made it possible to obtain very important data for estimating the emission of $H_2O$ by the cometary nucleus, as well as other types of molecules (e.g. C2, C3, CN, OH). In the presence of dependencies between the productivity of the $H_2O$ cometary nucleus and its brightness characteristics, the determination of BPs of cometary nuclei has acquired a new meaning. However, the dependence of the size of the nucleus on its BPs is not linear, since there is a correlation with the albedo of the surface of the nucleus. In this work, BPs and albedo for comet Bennett C/1969 Y1 are studied. Taking into account the data obtained and the solution of the described problems, we applied the author's isophote method to analyze the structure of the brightness characteristics of Bennett C/1969 Y1.

**Keywords:** comets, planetary science, isophote analysis

**Funding:** This work was supported by Russian Science Foundation, grant no. 22-72-10059.

**Citation:** Churkin K.O., Andreev A.O., Nefedyev Yu.A., Kolosov Yu.A., Korchagina E.P., Demina N.Yu., Borovskih V.S., Analysis of comet C/1969 Y1 parameters using isophote structural modeling, St. Petersburg State Polytechnical University Journal. Physics and Mathematics. 16 (1.2) (2023) 530–535. DOI: https://doi.org/10.18721/JPM.161.281

This is an open access article under the CC BY-NC 4.0 license (https://creativecommons.org/licenses/by-nc/4.0/)

© Churkin K.O., Andreev A.O., Nefedyev Yu.A., Kolosov Yu.A., Korchagina E.P., Demina N.Yu., Borovskih V.S., 2023. Published by Peter the Great St. Petersburg Polytechnic University.

Материалы конференции
УДК 521
DOI: https://doi.org/10.18721/JPM.161.281

# Анализ параметров кометы C/1969 Y1 с использованием метода изофотного структурного моделирования

К.О. Чуркин[1]✉, А.О. Андреев[2], Ю.А. Нефедьев[1], Ю.А. Колосов[1], Е.П. Корчагина[1], Н.Ю. Демина[1], В.С. Боровских[3]

[1] Казанский (Приволжский) федеральный университет, г. Казань, Россия;

[2] Казанский государственный энергетический университет, г. Казань, Россия;

[3] Казанский государственный архитектурно-строительный университет, г. Казань, Россия

✉ konstantinch-n87@mail.ru

**Аннотация.** Настоящая работа посвящена построению структурной модели долгопериодической кометы Bennett C/1969 Y1. Эта комета принадлежит к кометам семейства Юпитера (СЮ) и имеет параметр Тиссерана T > 2. Определение яркостных характеристик кометы было одной из важнейших целей кометных наблюдений в последнее столетие. Сложность таких исследований заключается в том, что мы имеем дело с протяженными источниками, движущимися относительно фоновых звезд. С учетом полученных данных и решения описанных задач мы применили авторский метод изофот для анализа структуры яркостных характеристик Bennett C/1969 Y1.

**Ключевые слова:** кометы, планетология, изофотный анализ

**Финансирование:** Работа поддержана Российским научным фондом, грант №. 22-72-10059.

**Ссылка при цитировании:** Чуркин К.О., Андреев А.О., Нефедьев Ю.А., Колосов Ю.А., Корчагина Е.П., Демина Н.Ю., Боровских В.С. Анализ параметров кометы C/1969 Y1 с использованием метода изофотного структурного моделирования // Научно-технические ведомости СПбГПУ. Физико-математические науки. 2023. Т. 16. № 1.2. С. 530–535. DOI: https://doi.org/10.18721/JPM.161.281

Статья открытого доступа, распространяемая по лицензии CC BY-NC 4.0 (https://creativecommons.org/licenses/by-nc/4.0/)

## Introduction

Comets were seen in ancient times and were considered random incoming objects in the celestial sphere. Comets can be of different types, have different brightness of the nucleus, its size and chemical composition. Comet tails also have differences in their length, width and number of rays. The motion of comets obeys Kepler's laws and they move along orbits with different parameters [1, 2]. Comets also differ in color: they are blue, green, pale orange and yellow. The orbits of comets, unlike the planets, are strongly elongated ellipses; in addition, the planes of the comets' orbits do not coincide with the plane of the planets' orbits [3, 4]. There are short-period (P) comets with a period of less than 300 years and long-period (C) ones [5]. In the names, after indicating the periodicity of the comet, the year is usually indicated, and then a letter characterizing the quarter of the month in which it was discovered is written, then the first discoverers of the comet are indicated in brackets [6, 7].

It is more convenient for astronomers to observe and study large comets, however there is no exact definition of "large comet". It can be said that the approximate brightness of such comets near the perihelion is in absolute terms greater than $6^m - 7^m$ [8]. Their perigee distance is about 0.6 AU, and the distance when passing near the Earth does not exceed 15 million km. Examples of large comets with the longest Earth passing distances are C/1961 T1 (Seki) and C/1996 B2 (Hyakutake), and one of the shortest is D/1770 L1 (Lexell) (2.26 million km) [8].

© Чуркин К.О., Андреев А.О., Нефедьев Ю.А., Колосов Ю.А., Корчагина Е.П., Демина Н.Ю., Боровских В.С., 2023. Издатель: Санкт-Петербургский политехнический университет Петра Великого.

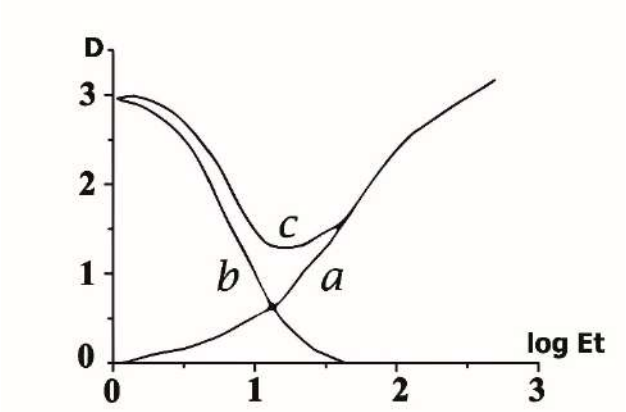


Fig. 1. Curve of the change in the light density of the image (D) on the logarithm of the brightness strength (*Et* is the brightness *E* multiplied by *t*): gradient curve for negative comet image (*a*); gradient curve for positive comet image (b); integrated darkening of the image with the determination of isophotes with the same light density (*c*)

## Materials and Methods

Isophotes are areas that have the same brightness density. The boundaries of isophotes are determined on the basis of the pseudo-solarization law and, in doing so the developed author's automated software package is used. The method is shown in Fig. 1. First, we get a negative image of the comet. After this stage, using the software package, a positive image is created from the negative image of the comet. The method of creating the isophote system consists in the modern interpretation of the method described in [9, 10], and is as follows: To construct isophote regions with specified parameters, the approach of simulating the change in brightness was used (Fig. 1).

## Results and Discussion

Comet Bennett C/1969 Y1 is one of the brightest small celestial bodies. C/1969 Y1 at perihelion was quite close to the Sun (0.54 AU) and its brightness was greater than $0^m$. The comet had a complex tail structure. Around the head of C/1969 Y1 there was a large cloud of hydrogen with a size of more than 12 million km [11]. Parallel to the elongated structure of the comet's head was the comet's tail. The light force at the center of the comet could be as high as $0^m$.

Fig. 2 shows an isophote model of comet Bennett (C/1969 Y1). The first isophote represents the brightest region of the C/1969 Y1 head. The second isophote has a circular structure. Next, come the isophotes that are distorted towards dust emission from the Bennett nucleus. The structural center of the C/1969 Y1 image has an irregular shape. The isophotes are quite close to each other, and the difference in light density between the isophotes is $0.07^m$. The differentiated change in the light density of the first isophote to the ninth is $3.50^m$.

The C/1969 Y1 isophote model proves that the structural elements are sufficiently self-similar. When the comet passed perihelion, the radiation from C/1969 Y1 was quite significant, but the cloud of particles ejected by the comet did not change. One of the hypotheses to explain this effect is that large-scale formations in the structure of comets are a consequence of the radiation of the cometary nucleus under the influence of its rotation. Since comet C/1969 Y1 does not have such cometary material radiation elements, this means that Comet Bennett does not have separate outgassing regions, and the radiation is uniform throughout the cometary nucleus or the radiation sources did not pass through the terminator.

It has been established previously [12] that the emission of dust particles occurs mainly from the side of the comet that is turned towards the Sun, so the next conclusion is that the surface of the cometary nucleus was cleaned at the moment of crossing the perihelion and a large number of emitted particles were formed. At the same time, C/1969 Y1 does not have a pronounced cometary tail, although the emission by cometary head should have captured many dust particles.

## Conclusion

In this work, an isophote model with a clearer structure, compared to previous works, was built. This made it possible to evaluate BPs with higher accuracy and reliability. In addition, we also determined the brightness characteristics of the nucleus, coma, and tail of Comet Bennett (C/1969 Y1). At the same time, there are works in which it was found that large-scale structures in cometary coma lead to significant radiation from nuclei caused by the rotation of the nucleus [12]. In addition, according to the approach described in [13], it can be concluded that $H_2O$ emission from the cometary nucleus is limited.

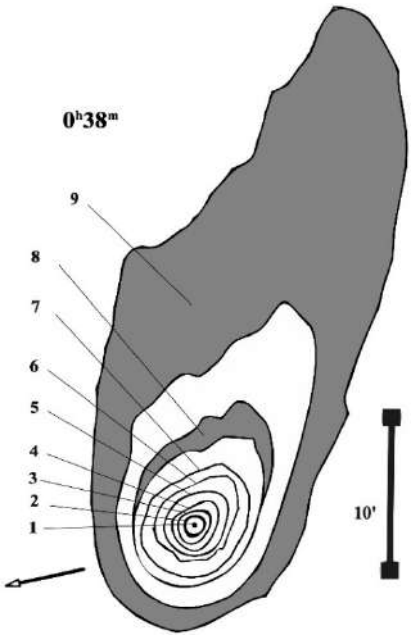


Fig. 2. C/1969 Y1 isophote model

At present, the study of comets has moved to a higher level [14–16]. Space missions are used to observe small bodies of the Solar System [17–22]. The means of processing observations are also being improved [23–24].

It should also be noted that over time, the orbits of comets undergo changes and evolve, as the comet is subjected to various gravitational effects from the planets. This is especially evident when comets pass near giant planets and other celestial bodies, as well as under the influence of non-gravitational effects associated with the fact that comets emit dust and gas. M. Krylikowska (2004) [25] presents the results of an analysis of the influence of non-gravitational effects (NGEs) on the motion of 60 long-period comets, including Bennet (C/1969 Y1). The analysis took into account that water evaporation reaches its maximum a few days before or after the comet passes perihelion [26]. The parameters of NGE were obtained for the model of forced precession with the standard function g(r) for Comet Bennett. All parameters of NGE were determined for 19 comets, of which, for 14, the axes of rotation of the comet nuclei were also determined. For the first time, non-gravitational effect was discovered in the motion of the following comets: /1999 H1 Lee, C/1991 T2 Shoemaker-Levy, C/1999 J3 Linear, C/1975 T1 Mori-Sato-Fujikawa, C/1987W2 Furuyama, C/1991 B1 Shoemaker-Levy [26]. It was also found that the average value of the non-gravitational effect for long-period comets is 10 times greater than the average value of non-gravitational effect determined for short-period ones.

Determining the size of the nucleus is a difficult task, since the size also depends on the surface albedo of the nucleus. Delsemme & Rud (1973) [27] made the first attempt to determine the radius of the nucleus and albedo for comets C/1969 Y1 (Bennett), C/1969 T1 (Tago-Sato-Kosaka) and 2P/Encke using the dependence between the emission velocity of comet H2O near perihelion and the magnitude of the comet's nucleus [28]. Gonzalo Tancredi and a group of researchers analyzed the observed nuclear magnitudes of comets and compiled a catalog for comets of the Jupiter family [14]. The Comet Light Curve Catalog (CLICC) were used, and the research team's own observations were used [14]. The catalog contains comets with a nucleus up to $12.8^m$ (39P/Oterma) and no weaker than $19.3^m$ (45P/Honda-Mrkos-Pajdusakova) [29].

The EAO Digital Library has 2145 digital images of comets and small celestial bodies. The study of these celestial bodies with a new approach will make it possible to build new three-dimensional models and determine the physical parameters of these bodies.

## Acknowledgments

This work was supported by Russian Science Foundation, grant 22-72-10059.

## REFERENCES


1. **Tancredi G., Fernández J.A., Rickman H., Licandro J.**, A catalog of observed nuclear magnitudes of Jupiter family comets, Astronomy and Astrophysics Supplement Series. 146 (1) (2000) 73–90.

2. **DiSanti M.A., Bonev B.P., Russo N. D., et al.**, Hypervolatiles in a Jupiter-family Comet: Observations of 45P/Honda–Mrkos–Pajduľáková Using iSHELL at the NASA-IRTF, The Astronomical Journal. 154 (6) (2017) 246.

3. **A'Hearn M.F., Millis R.L.**, Abundance correlations among comets, The Astronomical Journal. 85 (1980) 1528–1537.

4. **Delsemme A., Rud D.A.**, Albedos and Cross-sections for the Nuclei of Comets 1969 IX, 1970 II and 19711, Astronomy and Astrophysics. 28 (1973) 1.

5. **Dlugach J.M., Ivanova O.V., Mishchenko M.I., Afanasiev V.L.**, Retrieval of microphysical characteristics of particles in atmospheres of distant comets from ground-based polarimetry, Journal of Quantitative Spectroscopy and Radiative Transfer. 205 (2018) 80–90.

6. **Churkin K.O., Andreev A.O., Nefedyev Y.A., Arkhipova A.A., Demina N.Y.**, Structural analysis of the comet 45P/Honda based on isophote modeling, Journal of Physics: Conference Series. 2103 (1) (2021) 012022.

7. **Sokolova M., Nefedyev Y., Sergienko M., Demina N., Andreev A.**, Analysis of the Lyrids' meteor stream structure for long timeslots, Advances in Space Research. 58 (4) (2016) 541–544.

8. **Mobberley M.**, Hunting and Imaging Comets, Springer, New York. (2011) 33–82.

9. **Pennetta M.**, Beach Erosion in the Gulf of Castellammare di Stabia in Response to the Trapping of Longshore Drifting Sediments of the Gulf of Napoli (Southern Italy), Geosciences. 8 (7) (2018) 235.

10. **Breido I., Chebotareva T.**, Ekvidensitometricheskii metod, osnovannyi na fotograficheskom effekte Sabat'e, i ego primenenie k fotometrii tumannostei i komet, Izvestiya GAO. 180 (1966) 159.

11. **Hendrie M. J.**, Comet Bennett 1969i, Journal of the British Astronomical Association. 109 (1999) 14–21.

12. **Orosei R., Capaccioni F., Capria M. T., et al.**, Gas and dust emission from a dusty porous comet, Astronomy and Astrophysics. 301 (1995) 613.

13. **Andreev A., Nefedyev Y., Demina N.**, Kazan virtual observatory, Astronomical and Astrophysical Transactions. 31 (1) (2019) 37–42.

14. **Usanin V., Nefedyev Y., Andreev A.**, Use of long-term nongravitational force models for fitting astrometric observations of comet Encke, Advances in Space Research. 60 (5) (2017) 1101–1107.

15. **Nefedyev Y.A., Valeev S.G., Mikeev R.R., Andreev A.O., Varaksina N.Y.**, Analysis of data of "CLEMENTINE" and "KAGUYA" missions and "ULCN" and "KSC-1162" catalogues, Advances in Space Research. 50 (11) (2012) 1564–1569.

16. **Sokolova M., Sergienko M., Nefedyev Y., Andreev A., Nefediev L.**, Genetic analysis of parameters of near earth asteroids for determining parent bodies of meteoroid streams, Advances in Space Research. 62 (8) (2018) 2355–2363.

17. **Sergienko M.V., Sokolova M.G., Nefedyev Y.A., Andreev A.O.**, The □-Cygnid Meteor Shower and Its Relationship with Near-Earth Asteroids, Astronomy Reports. 64 (12) (2020) 1087–1092.

18. **Usanin V., Nefedyev Y., Andreev A.**, Use of long-term models for analysis of comet Encke's motion, Advances in Space Research. 58 (11) (2016) 2400–2406.

19. **Sokolova M.G., Nefedyev Y.A., Varaksina N.Y.**, Asteroid and comet hazard: Identification problem of observed space objects with the parental bodies, Advances in Space Research. 54 (11) (2014) 2415–2418.

20. **Sokolova M.G., Kondratyeva E.D., Nefedyev Y.A.**, A comparative analysis of the D-criteria used to determine genetic links of small bodies, Advances in Space Research. 52 (7) (2013) 1217–1220.

21. **Andreev A.O., Nefedyev Y.A., Nefediev L.A., Ahmedshina E.N., Demina N.Y., Zagidullin A. A.,** The use of multi-parameter analysis and fractal geometry for investigating the structure of the lunar surface, Uchenye zapiski Kazanskogo universiteta. Seriya Fiziko-Matematicheskie Nauki. 162 (2020) 223–36.

22. **Petrova N., Zagidullin A., Nefedyev Y., Kosulin V., Andreev A.**, The analytical and numerical approaches to the theory of the Moon's librations: Modern analysis and results, Advances in Space Research. 60 (10) (2017) 2303–2313.

23. **Churkin K.O., Andreev A.O., Nefedyev Y.A., Petrova N.K., Demina N.Y.**, Studies of Modern Star Catalogs Based on Photoelectric Observations of Lunar Occultations of Stars, Astronomy Reports. 62 (12) (2018) 1042–1049.

24. **Andreev A.O., Nefedyev Y.A., Demina N.Y., Nefediev L.A., Petrova N.K., Zagidullin A.A.**, Development of methods for navigational referencing of circumlunar spacecrafts to the selenocentric dynamic coordinate system, Astronomy Reports. 64 (9) (2020) 795–803.

25. **Petrova N.K., Nefedyev Y.A., Andreev A.O., Zagidullin A.A.**, Lunar-Based Measurements of the Moon's Physical Libration: Methods and Accuracy Estimates, Astronomy Reports. 64 (12) (2020) 1078–1086.

26. **Varaksina N.Y., Nefedyev Y.A., Churkin K.O., Zabbarova R.R., Demin S.A.**, Selenocentric reference coordinates net in the dynamic system, Journal of Physics: Conference Series. 661 (1) (2015) 012014.

27. **Krylikowska M.**, Long-period comets with non-gravitational effects, Astronomy & Astrophysics. 427 (3) (2004) 1117–1126.

28. **Delsemme A., Rud D.A.**, Albedos and Cross-sections for the Nuclei of Comets 1969 IX, 1970 II and 19711, Astronomy and Astrophysics. 28 (1973) 1.

29. **Stachowski G., Kuligowska E., Kundera T., Dębski B., Bajan K.**, Images of comets on archival photographic plates from the Jagiellonian University Observatory, XXXVIII Polish Astronomical Society Meeting. 7 (2018) 377–379.

## THE AUTHORS

**CHURKIN Konstantin O.**
kchurkin87@gmail.com
ORCID: 0000-0002-5102-8447

**KORCHAGINA Elena P.**
belkalenka2010@yandex.ru
ORCID: 0000-0003-4350-7891

**ANDREEV Alexey O.**
alexey-andreev93@mail.ru
ORCID: 0000-0001-8748-3049

**DEMINA Natalya Yu.**
vnu_357@mail.ru
ORCID: 0000-0002-2379-3299

**NEFEDYEV Yury A.**
yura.nefedyev@gmail.com
ORCID: 0000-0002-2986-852X

**BOROVSKIH Viktor S.**
borovskix@kgasu.ru
ORCID: 0000-0002-3147-4888

**KOLOSOV Yury A.**
koloyra@gmail.com
ORCID: 0000-0001-7439-731X

*Received 01.11.2022. Approved after reviewing 14.11.2022. Accepted 16.11.2022.*

© Peter the Great St. Petersburg Polytechnic University, 2023

# RADIOPHYSICS

Conference materials
UDC 538.975
DOI: https://doi.org/10.18721/JPM.161.282

## Determination of the conductive and structural characteristics of zirconium-containing amorphous nanogranulated composites from the microwave reflection coefficient

I.V. Antonets[1] ✉

[1] Syktyvkar state University the name of Pitirim Sorokin, Syktyvkar, Russia
✉ aiv@mail.ru

**Abstract.** Amorphous nanogranulated composite films $((Co_{45}Fe_{45}Zr_{10})_x(ZrO)_{1-x}$ and $(Co_{45}Fe_{45}Zr_{10})_x(Zr_2O_3)_{1-x})$ were studied experimentally. The film thickness, metal phase concentration, granules size, conductivity, and reflection coefficient of microwave waves at a frequency of 10 GHz were determined. A sequential algorithm for determining the conductive (grain conductivity) and structural (size of grains or gaps between granules, electron mean free path) characteristics from the measured microwave reflection coefficient for amorphous nanogranular composites is given. Using the algorithm and mechanism of intragranular currents based on experimental results, the conductivity of granules, the size of the gaps between the granules and the electron mean free path for zirconium containing series of films $(Co_{45}Fe_{45}Zr_{10})_x(ZrO)_{1-x}$ and $(Co_{45}Fe_{45}Zr_{10})_x(Zr_2O_3)_{1-x}$ were estimated. The dependences of the conductive and structural characteristics of the samples on the microwave reflection coefficient, the concentration of the metal phase and the effective thickness were obtained._

**Keywords:** Amorphous nanogranulated composite films, conductivity of granules, microwave reflection coefficient, mechanism of intragranular currents, electron mean free path

**Funding:** This study was funded by RSF according to the research project 21-72-20048.

**Citation:** Antonets I.V., Determination of the conductive and structural characteristics of zirconium-containing amorphous nanogranulated composites from the microwave reflection coefficient, St. Petersburg State Polytechnical University Journal. Physics and Mathematics. 16 (1.2) (2023) 536–543. DOI: https://doi.org/10.18721/JPM.161.282

This is an open access article under the CC BY-NC 4.0 license (https://creativecommons.org/licenses/by-nc/4.0/)

Материалы конференции
УДК 538.975
DOI: https://doi.org/10.18721/JPM.161.282

## Определение проводящих и структурных характеристик цирконийсодержащих аморфных наногранулированных композитов по коэффициенту отражения СВЧ волн

И.В. Антонец[1] ✉

[1] Сыктывкарский государственный университет имени Питирима Сорокина, г. Сыктывкар, Россия
✉ aiv@mail.ru

**Аннотация**. В работе приведен последовательный алгоритм для определения проводящих (проводимость гранул) и структурных (размеры гранул или промежутки между гранулами, длина свободного пробега электронов) характеристик по измеренному коэффициенту отражения СВЧ волн от цирконийсодержащих аморфных наногранулированных композитов. Используя механизм внутригранулярных токов, на основании результатов экспериментальных исследований коэффициента отражения СВЧ волн оценены проводимость гранул, размеры промежутков между гранулами и длина свободного

© Antonets I.V., 2023. Published by Peter the Great St. Petersburg Polytechnic University.

пробега электронов для серий образцов $(Co_{45}Fe_{45}Zr_{10})_x(ZrO)_{1-x}$ и $(Co_{45}Fe_{45}Zr_{10})_x(Zr_2O_3)_{1-x}$. Приведены зависимости проводящих и структурных характеристик от коэффициента отражения СВЧ волн, удельной проводимости композитов, а также эффективной толщины с учетом содержания металлической фазы.

**Ключевые слова**: Аморфные наногранулированные композитные пленки, проводимость гранул, коэффициент отражения СВЧ, механизм внутригранулярных токов, длина свободного пробега электронов

**Финансирование:** This study was funded by RSF according to the research project 21-72-20048.

**Ссылка при цитировании:** Антонец И.В. Определение проводящих и структурных характеристик цирконийсодержащих аморфных наногранулированных композитов по коэффициенту отражения СВЧ волн // Научно-технические ведомости СПбГПУ. Физико-математические науки. 2023. Т. 16. № 1.2. С. 536–543. DOI: https://doi.org/10.18721/JPM.161.282

Статья открытого доступа, распространяемая по лицензии CC BY-NC 4.0 (https://creativecommons.org/licenses/by-nc/4.0/)

## Introduction

To create the latest small-sized microwave devices, nanostructured composites containing metal granules (for example, iron and cobalt) embedded in a dielectric matrix have been actively studied in recent decades [1–3]. The ferromagnetic metal in such composites causes a giant magnetoresistance [4] and a high level of absorption of microwave radiation [5]. Amorphous nanogranular composites containing zirconium, both in the metallic and dielectric phases, have a number of unique properties. For example, in [6, 7] for $(Co_{45}Fe_{45}Zr_{10})_x(Zr_2O_3)_{1-x}$ films, it was found that the dynamic conductivity in the microwave range can exceed the static conductivity measured at direct current by four orders of magnitude, long before the percolation threshold of the metal phase. It was shown in [8, 9] that the average granule size and the concentration of the metal phase of $(Co_{45}Fe_{45}Zr_{10})_x(ZrO)_{1-x}$ films determine not only the conductive but also the reflective properties of the films in the microwave range. In addition, the magnetic domain structure was visualized in the same films, which is an indicator of the presence of perpendicular magnetic anisotropy in the films and serves as evidence of percolation in the films.

A particularly significant factor is obtaining data about the properties of individual nanostructural elements based on the macroscopic properties of the entire object [10]. So, for modification and obtaining new conductive and structural properties of nanosized granular thin films, the most important parameters are the conductivity of one granule, the size of the granules and the gaps between these granules, and the mean free path of electrons. A numerical estimate of all the above parameters can be obtained based on knowledge of the conductive and reflective properties of the film.

The papers [11, 12] describe the mechanism of intragranular (intracluster) currents, which make the main contribution to the excess of dynamic conductivity over static one. In [13], methods of closed and open circuits of the mechanism of intragranular currents were proposed for calculating the conductive and structural characteristics of nanosized thin-film elements. These methods for describing the structural and conductive characteristics of amorphous granular composite films were tested [7, 10], in particular, on samples of $(Co_{45}Fe_{45}Zr_{10})_x(Al_2O_3)_{1-x}$.

In this work a sequential algorithm for determining the conductive and structural characteristics of amorphous nanogranular composites by means of the mechanism of intragranular currents (closed circuit method) using the size of granules and the reflection coefficient of microwave waves is presented. The gaps between the granules, the conductivity of the granules, and the mean free path of electrons were determined for a series of samples $(Co_{45}Fe_{45}Zr_{10})_x(Zr_2O_3)_{1-x}$ and $(Co_{45}Fe_{45}Zr_{10})_x(ZrO)_{1-x}$.

## Materials and Methods

Composite granulated films of composition $(Co_{45}Fe_{45}Zr_{10})_x(ZrO)_{1-x}$ (thickness 535–1120 nm, $x \sim 0.27$–$0.72$) and $(Co_{45}Fe_{45}Zr_{10})_x(Zr_2O_3)_{1-x}$ (thickness 70–550 nm, $x \sim 0.25$–$0.78$) were obtained in a nitrogen atmosphere at a pressure of 0.024 and 0.080 Pa on a lavsan substrate

© Антонец И. В., 2023. Издатель: Санкт-Петербургский политехнический университет Петра Великого.

0.02 mm in thick. The films were fabricated by ion-beam sputtering at the Voronezh State Technical University. The film thicknesses were determined using a Tescan Vega LMH SEM from electron microscopic images of the cleavage end of the composite film. To determine quantitatively the elemental composition of the film surface, X-ray energy-dispersive spectrometry was used. The surface topography of the samples was studied using an Integra Prima atomic force microscope in semi-contact and contact modes. The reflection coefficient of microwave waves from thin films was measured in the frequency range 8–12 GHz. The device comprised a swept-frequency generator (SFG-61), a voltage standing-wave indicator with an attenuation module (YaSR-67), and a waveguide set of reflectometers. Standing-wave ratio dependencies on frequency were determined from directly on the indicator scale YaSR-67. The conductivity was obtained as the reciprocal of the resistivity measured at a dc current by the two-probe method with the use of the potentiometer substitution method.

**Algorithm for determining conductive and structural characteristics**

Let us consider a thin film composite with a nanogranular structure, in which the reflective properties due to the intrinsic conductivity of the granules. According to the closed circuit mechanism of the model of intragranular currents [11–13], the granule is included in a certain closed circuit, which due to the field of the primary wave contains an EMF source. The internal resistance of the source corresponds to the free space impedance. When an electromagnetic wave falls on a granular film, the electric field of the incident wave excites localized microwave currents inside the metal granules, which create a microwave magnetic field around themselves and form an electromagnetic wave reflected from the film. Due to the currents circulating in the conductive regions, the wave is re-emitted. The presence of conductive regions inside the film that are not in contact with each other increases the microwave reflection coefficient.

If the film consists of flat layers of identical cubic granules, the size of which is g, and the gaps between the granules p, then the reflection coefficient from the granular film at normal wave incidence is [10—15]:

$$R = \left( \left( \left( Z_0 + \frac{2(g+p)}{\sigma_g dg} \right) \frac{(g+p)}{\gamma g Z_0} \right)^{-1} \right)^2, \tag{1}$$

where $\sigma_g$ is the conductivity of the granules, $\gamma = \exp(-p/g)$, $d$ is the film thickness.

At $g \gg p$ the film becomes continuous, $\sigma_g = \sigma$, and the reflection coefficient is determined by the well-known relation [10, 13—15]:

$$R = \left( \left( 1 + \frac{2}{Z_0 \sigma d} \right)^{-1} \right)^2, \tag{2}$$

where $\sigma$ is film conductivity.

To take into account the influence of the metallic phase on the reflection, we introduce the concept of an effective layer. This is the layer that contains only the metal phase in the composite. The thickness of such layer is [8, 13, 14]:

$$d_{\text{eff}} = d \cdot \frac{X, \text{at.}\%}{100\ \%}, \tag{3}$$

where $X$ is the average value of the concentration of the metal phase for each sample (at.%). The effective layer consists of highly conductive granules, so the maximum thickness layer is able to reflect 95% or more of the total incident radiation. From relations (2) and (3) we determine the conductivity of the effective layer $\sigma_{\text{eff}}$ at $R \geq 0.95$, which can be taken as the conductivity of the granules $\sigma_g$:

$$\sigma_{\text{eff}} = \frac{2}{Z_0 d_{\text{eff}}} \frac{\sqrt{R}}{1-\sqrt{R}}. \tag{4}$$

Substituting the obtained values $\sigma_g$ from (4) into (1), using the experimentally measured microwave reflection coefficient $R$, composite thickness $d$ and granules size $g$, we determine the gaps between granules $p$. Solving (1) with respect to $g$ and $p$ we mathematically obtain four possible solutions [10]:

$$(g+p)_{1,2} = \frac{g}{4}\left(\sqrt{\frac{\sigma_g dZ_0\left(8\gamma \pm \sqrt{R}\cdot\sigma_g dZ_0\right)}{\sqrt{R}}} - \sigma_g dZ_0\right), \quad (5)$$

$$(g+p)_{3,4} = -\frac{g}{4}\left(\sqrt{\frac{\sigma_g dZ_0\left(8\gamma \pm \sqrt{R}\cdot\sigma_g dZ_0\right)}{\sqrt{R}}} + \sigma_g dZ_0\right), \quad (6)$$

of which only the first root gives non-negative values. Equations (5), (6) are solved numerically, since on its right side there is a coefficient $\gamma$, depending on $p$.

Finally, using the known relationship for conductivity [10,16]:

$$\sigma = \frac{n e^2 l}{p_F}, \quad (7)$$

where $e$ is electron charge, $n$ is concentration of conduction electrons in the film material, $p_F = 2\pi\hbar\left(\frac{3n}{8\pi}\right)^{1/3}$ is boundary Fermi momentum, and solving (2) and (7) together, we determine the mean free path of electrons $l$ depending on the measured reflection coefficient [10,13,16]:

$$l = \frac{4\pi\hbar}{n\, e^2 Z_0 d}\left(\frac{3n}{8\pi}\right)^{1/3}\frac{\sqrt{R}}{1-\sqrt{R}}. \quad (8)$$

## Results and Discussion

The tables show the measurement results of metal phase concentration, thickness, reflection coefficient at 10 GHz, conductivity, sizes of granules and concentration of conduction electrons of amorphous composite films $(Co_{45}Fe_{45}Zr_{10})_x(ZrO)_{1-x}$ (Table 1) and $(Co_{45}Fe_{45}Zr_{10})_x(Zr_2O_3)_{1-x}$ (Table 2). The values of the conduction electron concentration were obtained from the concentration dependences of the density of states at the Fermi level for various nanocomposites presented in [17].

Fig. 1 shows the experimental dependences of the reflection coefficient $R$ on the concentration of the metal phase $X$. Fig. 2 presents dependences of the measured sizes of granules $g$ on the effective layer thickness $d_{eff}$, and Figs. 3, 4 show calculated dependences of the gaps between the granules $p$, as well as the electron mean free path $l$ on the measured reflection coefficient of microwave waves $R$ of amorphous composite films $(Co_{45}Fe_{45}Zr_{10})_x(ZrO)_{1-x}$ and $(Co_{45}Fe_{45}Zr_{10})_x(Zr_2O_3)_{1-x}$.

As can be seen from Fig. 1 at $X \le 40$ at.% for $(Co_{45}Fe_{45}Zr_{10})_x(ZrO)_{1-x}$ and $X \le 60$ at.% for $(Co_{45}Fe_{45}Zr_{10})_x(Zr_2O_3)_{1-x}$ films the reflection coefficient is less than 1 % and does not depend on $X$. Further, as $X$ increases, the reflection coefficient rapidly increases, and $R$ for $(Co_{45}Fe_{45}Zr_{10})_x(ZrO)_{1-x}$ films 3–5 times higher than $R$ for $(Co_{45}Fe_{45}Zr_{10})_x(Zr_2O_3)_{1-x}$ films in the metal phase concentration range of 60–70 at. %. Finally, in the interval $X \sim 70$–$80$ at.% values of the reflection coefficients are practically equalized and amount to 0.75–0.81. Note that at the same concentrations of the metallic phase, the thickness of the $(Co_{45}Fe_{45}Zr_{10})_x(ZrO)_{1-x}$ films is, on average, 2–2.5 times greater, and the conductivity is one–two orders of magnitude greater than for films $(Co_{45}Fe_{45}Zr_{10})_x(Zr_2O_3)_{1-x}$ (Table 1, 2). Such differences in conductive and reflective properties are achieved due to the different structure of the films. If the effective layer with a maximum thickness of 429 nm for $(Co_{45}Fe_{45}Zr_{10})_x(Zr_2O_3)_{1-x}$ films and 780 nm for $(Co_{45}Fe_{45}Zr_{10})_x(ZrO)_{1-x}$ films (Fig. 2) consisted only of metal granules and reflected 95% and above of incident microwave radiation, then, according to relation (4), the conductivity of the granules is $4.76\cdot10^5$ S/m and $2.62\cdot10^5$ S/m, respectively. This value is only 4.5 times higher than the conductivity of the $(Co_{45}Fe_{45}Zr_{10})_x(ZrO)_{1-x}$ films and more than two orders of magnitude higher than the $(Co_{45}Fe_{45}Zr_{10})_x(Zr_2O_3)_{1-x}$ films. Therefore, at the same values of the reflection

coefficient and thicknesses, the grain sizes for $(Co_{45}Fe_{45}Zr_{10})_x(Zr_2O_3)_{1-x}$ films are 3–4 times larger than for $(Co_{45}Fe_{45}Zr_{10})_x(ZrO)_{1-x}$ films, and the gaps between the granules are 2–3 times less (Fig. 2, 3). Note that, at the maximum $R \sim 0.8$, the gaps between grains for both films are no more than 2–5 nm. Therefore, the reflection from the film is determined precisely by the size of the granules, and the ratio of these sizes becomes close to the ratio of the conductivity of the granules (2.1 and 1.8, respectively).

Table 1

**Metal phase concentration, thickness, reflection coefficient, conductivity, size of granules and concentration of conduction electrons of amorphous composite films $(Co_{45}Fe_{45}Zr_{10})_x(ZrO)_{1-x}$**

| Metal phase concentration $X$, at.% | Thickness $d$, nm | Reflection coefficient $R$ | Conductivity σ, S/m | Size of granules $g$, nm | Concentration of conduction electrons $n \cdot 10^{25}$, m$^{-3}$ |
|---|---|---|---|---|---|
| 27.1 | 570 | $6.9 \cdot 10^{-4}$ | 3.35 | 20±2 | $7.0 \cdot 10^{-3}$ |
| 32.3 | 610 | 0.00138 | 28.2 | 20±2 | $4.2 \cdot 10^{-2}$ |
| 42.6 | 670 | 0.0146 | 119 | 19±2 | 1.3 |
| 48.3 | 670 | 0.186 | 1240 | 21±2 | 1.3 |
| 56.3 | 900 | 0.479 | 1930 | 22±2 | 1.3 |
| 56.8 | 711 | 0.589 | 2290 | 24±2 | 1.3 |
| 58.1 | 772 | 0.676 | 1890 | 23±2 | 1.3 |
| 60.2 | 697 | 0.749 | 6800 | 23±2 | 1.3 |
| 60.8 | 535 | 0.737 | 5300 | 20±2 | 1.3 |
| 61.2 | 900 | 0.577 | 2050 | 23±3 | 1.3 |
| 66.9 | 1030 | 0.729 | 3950 | 32±4 | 1.3 |
| 69.7 | 1120 | 0.791 | 57200 | 44±4 | 1.3 |
| 71.5 | 890 | 0.764 | 49700 | 25±4 | 1.3 |
| 71.9 | 1060 | 0.703 | 43400 | 38±4 | 1.3 |
| 72.5 | 900 | 0.746 | 57200 | 24±4 | 1.3 |

Table 2

**Metal phase concentration, thickness, reflection coefficient, conductivity, size of granules and concentration of conduction electrons of amorphous composite films $(Co_{45}Fe_{45}Zr_{10})_x(Zr_2O_3)_{1-x}$**

| Metal phase concentration $X$, at.% | Thickness $d$, nm | Reflection coefficient $R$ | Conductivity σ, S/m | Size of granules $g$, nm | Concentration of conduction electrons $n \cdot 10^{25}$, m$^{-3}$ |
|---|---|---|---|---|---|
| 25 | 70 | 0.00154 | 0.030 | 33±3 | $4.0 \cdot 10^{-3}$ |
| 38 | 190 | 0.00155 | 0.066 | 37±4 | $3.2 \cdot 10^{-2}$ |
| 54 | 320 | 0.00157 | 0.91 | 70±8 | 1.3 |
| 59 | 280 | 0.00160 | 14.4 | 67±5 | 1.3 |
| 63 | 410 | 0.166 | 25 | 83±7 | 1.3 |
| 65 | 400 | 0.250 | 106 | 84±7 | 1.3 |
| 68 | 420 | 0.591 | 1000 | 86±7 | 1.3 |
| 73 | 390 | 0.562 | 712 | 79±8 | 1.3 |
| 77 | 530 | 0.790 | 3012 | 92±8 | 1.3 |
| 75 | 470 | 0.649 | 3820 | 90±9 | 1.3 |
| 78 | 550 | 0.810 | 4410 | 95±9 | 1.3 |
| 77 | 420 | 0.753 | 4240 | 89±8 | 1.3 |

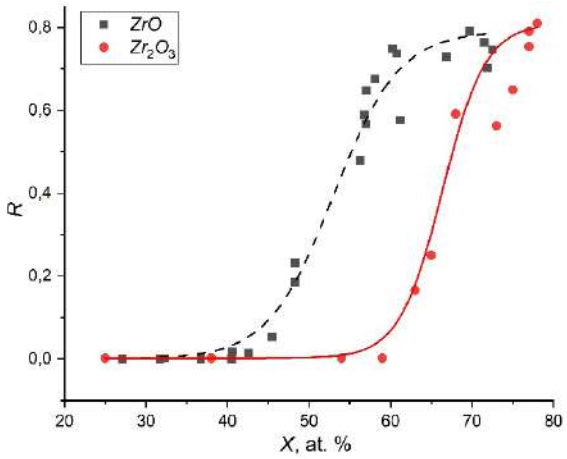


Fig. 1. Dependences of the reflection coefficient on the content of the metal phase

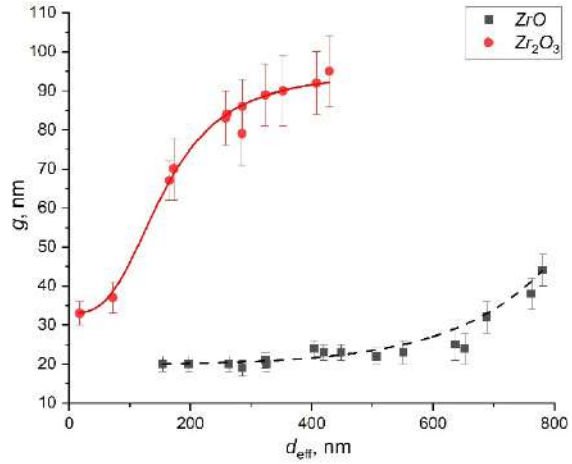


Fig. 2. Dependences of grain sizes on effective film thickness

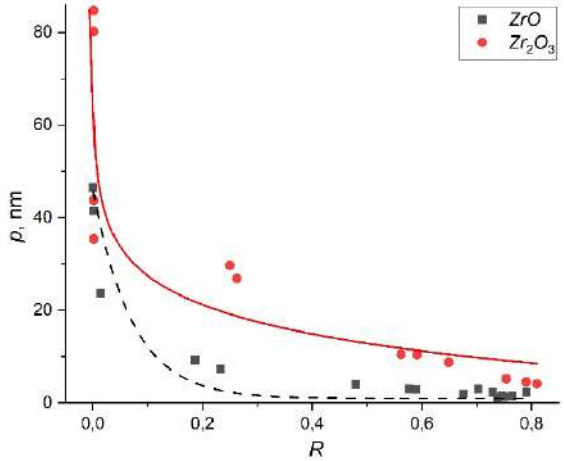


Fig. 3. Dependences of the gaps between the granules on the reflection coefficient

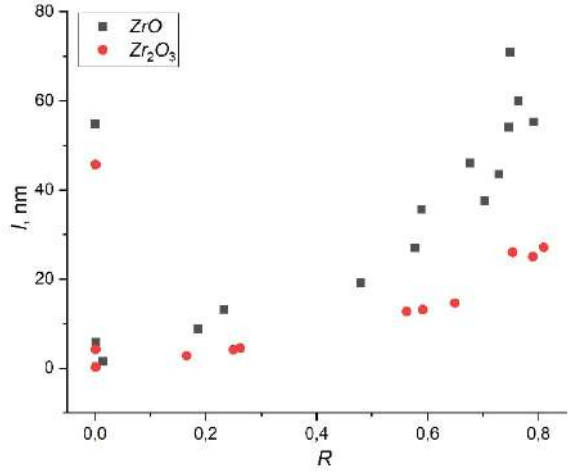


Fig. 4. Dependences of the electron mean free path on the reflection coefficient

From Fig. 4 it can be seen that the mean free path generally increases with the increase in the reflection coefficient. In this case, for $(Co_{45}Fe_{45}Zr_{10})_x(ZrO)_{1-x}$ films at $R = 0.48–0.70$, the mean free path, taking into account the statistical spread, coincides with the grain size. At reflectance values above 0.70, $l$ exceeds the granule size 2–2.5 times. For $(Co_{45}Fe_{45}Zr_{10})_x(Zr_2O_3)_{1-x}$ films on average, the mean free path of electrons is 1.5–2 times less than for $(Co_{45}Fe_{45}Zr_{10})_x(ZrO)_{1-x}$ films for the same $R$.

## Conclusion

The paper presents the results of experimental studies of the thickness, concentration of the metal phase, microwave reflection coefficient, conductivity and grain sizes of amorphous nanogranular composite films $(Co_{45}Fe_{45}Zr_{10})_x(ZrO)_{1-x}$ and $(Co_{45}Fe_{45}Zr_{10})_x(Zr_2O_3)_{1-x}$. Using the closed circuit mechanism of the model of intragranular currents, an algorithm for calculating the conductive and structural characteristics of composites from the measured reflection coefficient is proposed. Using the above algorithm, the results of calculations of the conductivity of granules, gaps between granules and the mean free path of electrons for films $(Co_{45}Fe_{45}Zr_{10})_x(ZrO)_{1-x}$ and $(Co_{45}Fe_{45}Zr_{10})_x(Zr_2O_3)_{1-x}$ were determined. The dependences of the conductive and structural characteristics on the reflection coefficient of microwave waves and the effective thickness of the films are obtained, taking into account the concentration of the metal phase.

## REFERENCES

1. **Vendik I.B, Vendik O.G.**, Metamaterials and their application in microwaves: A review, Tech. Phys. 1(58) (2013) 1–24.

2. **Zolotukhin I.V., Kalinin Yu.E., Ponomarenko A.T., Shevchenko V.G., Sitnikov A.V., Stognei O.V., Figovsky O.**, Metal-dielectric nanocomposites with amorphous structure, J. Nanostructured Polymers and Nanocomposites. 1(2) (2006) 23–34.

3. **Kalinin Yu.E., Remizov A.N., Sitnikov A.V.**, Electrical properties of amorphous $(Co_{45}Fe_{45}Zr_{10})_x(Al_2O_3)_{1-x}$ nanocomposites, Phys. Solid State. 11(46) (2004) 2146–2152.

4. **Gerber A., Milner A., Groisman B., Karpovsky M., Gladkikh A., Sulpice A.**, Magnetoresistance of granular ferromagnets, Phys. Rev. B. 10(55) (1997) 6446–6452.

5. **Kazantseva N.E., Ponomarenko A. T., Shevchenko V.G., Chmutin I.A., Kalinin Yu.E., Sitnikov A.V.**, Phys. and chem. of mater. treat. 1 (2002) 5–11.

6. **Antonets I.V., Kotov L.N., Kalinin Yu.E., Sitnikov A.V., Shavrov V.G., Shcheglov V.I.**, Dynamic Conductivity of Amorphous Nanogranular Films in the Microwave Frequency Range, Tech. Phys. Lett. 7(40) (2014) 584–586.

7. **Antonets I.V., Kotov L.N., Kirpicheva O.A., Golubev E.A., Kalinin Yu.E., Sitnikov A.V., Shavrov V.G., Shcheglov V.I.**, Static and Dynamic Conduction of Amorphous Nanogranulated Metal–Dielectric Composites, J. of Communications Technology and Electronics. 8(60) (2015) 904–914.

8. **Antonets I.V., Kotov L.N., Golubev Ye.A.**, Influence of composition and nanogranular structure of (Co+Fe+Zr)/(ZrO) composite films on conductivity and microwave reflective properties, Mater. Chem. and Phys. 240 (2020) 122097.

9. **Antonets I.V., Kotov L.N., Golubev E.A., Kalinin Yu.E., Sitnikov A.V.**, The structure, conductive properties, and reflective properties of amorphous granulated $(Co_{45}Fe_{45}Zr_{10})_x(ZrO)_{1-x}$ composite films, Tech. Phys. 2(62) (2017) 261–269.

10. **Antonets I.V., Golubev E.A., Shcheglov V.I.**, Algorithm for determining the structural characteristics of amorphous nanogranulated composites from the microwave waves reflection or conductivity, Mater. Chem. and Phys. 290 (2022) 126533.

11. **Antonets I.V., Kotov L.N., Kirpicheva O.A., Golubev E A., Kalinin Yu.E., Sitnikov A.V., Shavrov V.G., Shcheglov V.I.**, Dynamic conductivity mechanism in amorphous nanogranulated "metal-dielectric" films in microwave frequencies, J. of Radio Electronics. 4 (2014) (electronic journal). http://jre.cplire.ru/jre/apr14/12/abstract_e.html

12. **Antonets I.V., Kotov L.N., Golubev E.A., Shavrov V.G., Shcheglov V.I.**, Dynamic conductivity of nanogranulated films "metal-dielectric" on the microwave frequencies, J. of Radio Electronics. 5 (2018) (electronic journal v. 5). http://jre.cplire.ru/jre/may18/2/abstract_e.html

13. **Antonets I.V., Golubev E.A., Shcheglov V.I., Kotov L.N.,** Closed and open circuit methods for calculating the conductive and structural characteristics of thin-film elements by the reflection coefficient of microwave waves, AIP Conf. Proc. 2467 (2022) 00009.

14. **Antonets I.V., Golubev E.A., Shcheglov V.I., Sun S.**, Electromagnetic shielding effectiveness of lightweight and flexible ultrathin shungite plates, Current Appl. Phys. 29 (2021) 97–106.

15. **Golubev Ye.A., Antonets I.V., Shcheglov V.I.**, Static and dynamic conductivity of nanostructured carbonaceous shungite geomaterials, Mater. Chem. and Phys. 226 (2019) 195–203.

16. **Antonets I.V., Kotov L.N., Nekipelov S.V., Shavrov V.G., Shcheglov V I.**, Electrodynamic properties of thin metal films with different thicknesses and morphologies of the film surface, J. of Communications Technology and Electronics. 10(49) (2004) 1164–1170.

17. **Sitnikov A.V.**, Electrical and magnetic properties of nanoheterogeneous metal-dielectric systems. PhD thesis. Voronezh: VSTU, 2010.

## THE AUTHOR

**ANTONETS Igor V.**
aiv@mail.ru
ORCID: 0000-0003-1103-4313

*Received 28.09.2022. Approved after reviewing 08.11.2022. Accepted 08.11.2022.*

© Peter the Great St. Petersburg Polytechnic University, 2023

Conference materials
UDC 533.9
DOI: https://doi.org/10.18721/JPM.161.283

# Ionization wave in air under the action of powerful radiation of the terahertz frequency range

A.V. Sidorov✉, A.P. Veselov, E.I. Rakova, T.V. Barmashova,
A.V. Vodopyanov, A.A. Ananichev. M.Yu. Glyavin

Federal research center "Institute of applied physics RAS", Nizhny Novgorod, Russia

✉ alexsv@ipfran.ru

**Abstract.** Sub-terahertz and terahertz frequency ranges remain the least studied from the point of view of gas discharge physics. Investigation of terahertz gas discharge, sustained by the powerful focused beams of the electromagnetic radiation, has become possible recently due to the development of the powerful sources in this range (FELs and gyrotrons) and is of interest both from a fundamental research and from possible applications. This work presents the results of the studies of the discharge propagation under the action of the focused beam of sub-terahertz (250 GHz) gyrotron. The discharge propagation velocity towards electromagnetic radiation was measured in air in the wide pressure range (0.01 − 1 atm). The focusing system provided the size of the focal spot of (2−3)·λ, which ensured the investigation of discharge phenomena in a wide pressure range. The optical glow of the discharge was recorded with the help of a speed camera. The discharge appeared in the focal spot spread towards heating radiation into the area with the field intensity much less than one in the focal spot. Velocity of the discharge propagation was measured by using photos from speed camera with small exposure (down to 20 ns). It was demonstrated that discharge velocity increase along with pressure decrease and drops with electric field decrease as it moves away from the focal spot.

**Keywords:** terahertz radiation, gas discharge, discharge propagation

**Funding:** This study was funded by Russian Science Foundation, grant 19-72-20166.

**Citation:** Sidorov A.V., Veselov A.P., Rakova E.I., Barmashova T.V., Vodopyanov A.V., Ananichev A.A., Glyavin M.Yu., Ionization wave in air under the action of powerful radiation of the terahertz frequency range, St. Petersburg State Polytechnical University Journal. Physics and Mathematics. 16 (1.2) (2023) 544–549. DOI: https://doi.org/10.18721/JPM.161.283

This is an open access article under the CC BY-NC 4.0 license (https://creativecommons.org/licenses/by-nc/4.0/)

Материалы конференции
УДК 533.9
DOI: https://doi.org/10.18721/JPM.161.283

# Волна ионизации в воздухе под действием мощного излучения терагерцового диапазона частот

А.В. Сидоров✉, А.П. Веселов, Е.И. Ракова, Т.В. Бармашова,
А.В. Водопьянов, А.А. Ананичев, М.Ю. Глявин

Федеральный исследовательский центр «Институт прикладной физика РАН», г. Нижний Новгород, Россия

✉ alexsv@ipfran.ru

**Аннотация.** В работе представлены результаты исследований распространения разряда под действием сфокусированного пучка субтерагерцового (250 ГГц) гиротрона. Скорость распространения разряда навстречу электромагнитному излучению измерялась в воздухе в широком диапазоне давлений (0.01−1 атм). Система фокусировки обеспечивала размер фокального пятна (2−3)·λ, что обеспечивало исследование разрядных явлений в широком диапазоне давлений. Оптическое свечение разряда фиксировалось с помощью камеры контроля скорости. Разряд возникал в фокальном пятне, распространяясь

© Sidorov A.V., Veselov A.P., Rakova E.I., Barmashova T.V., Vodopyanov A.V., Ananichev A.A., Glyavin M.Yu., 2023. Published by Peter the Great St. Petersburg Polytechnic University.

навстречу греющему излучению в область с напряженностью поля, много меньшей, чем в фокальном пятне. Скорость распространения разряда измерялась по фотографиям с камеры контроля скорости с малой экспозицией (до 20 нс). Показано, что скорость разряда увеличивается с уменьшением давления, а падение электрического поля уменьшается по мере его удаления от фокального пятна.

**Ключевые слова:** терагерцовое излучение, газовый разряд, распространение разряда

**Финансирование:** Работа выполнена при поддержке Российского научного фонда, грант № 19-72-20166.

**Ссылка при цитировании:** Сидоров А.В., Веселов А.П., Ракова Е.И., Бармашова Т.В., Водопьянов А.В., Ананичев А.А., Глявин М.Ю. Волна ионизации в воздухе под действием мощного излучения терагерцового диапазона частот // Научно-технические ведомости СПбГПУ. Физико-математические науки. 2023. Т. 16. № 1.2. С. 544–549. DOI: https://doi.org/10.18721/JPM.161.283

Статья открытого доступа, распространяемая по лицензии CC BY-NC 4.0 (https://creativecommons.org/licenses/by-nc/4.0/)

## Introduction

This work is devoted to an experimental study of the propagation of a gas discharge in focused beams of electromagnetic waves of the sub-terahertz band. The discharge propagation in the wave fields is quite well studied at optical and microwave frequencies. It was observed in one of the very first works devoted to the laser spark in gases [1]. It was found that the propagation of the discharge has much in common with the combustion process [2]. As indicated in work 2, the physical reason for this analogy is rooted in the similar nature of the temperature dependence of the main factors that determine the rate of energy release in matter in both cases – the rate of a chemical reaction during combustion and the degree of gas ionization in discharge phenomena. At sufficiently large values of the fields, the propagation, as a rule, has a detonation character. In the case when the field in the beam is less than the breakdown field (when the initial plasma is created by an external source), the discharge can propagate according to the slow combustion principle [2]: thermal ionization of the gas occurs, and heat transfer from the discharge front occurs due to thermal conductivity.

Studies of the propagation of a discharge sustained by microwave radiation were carried out mainly in air [3–7], as a rule, at atmospheric pressure. Interest in this type of discharge, as a rule, was associated with the creation of various microwave plasmatrons [8], and with the fight against parasitic breakdowns in waveguides [3]. In the course of these studies, a number of important features of the discharge propagation were noted in comparison with a laser spark. In particular, the important role of ultraviolet radiation through the discharge front was shown in [5]. Under the action of this radiation ahead of the discharge front (compared to the plasma behind the discharge front) a so-called plasma halo of rarefied density is formed, in which a significant absorption of microwave radiation is possible. At not too high intensities of the incident microwave radiation, this leads to sufficiently strong heating of the gas and its thermal ionization. Thus, the thermal ionization of the gas ahead of the discharge front is maintained not due to thermal conductivity, as in the case of slow combustion [2], but due to the absorption of microwave radiation in the halo. In this case, the discharge propagation velocity is proportional to the incident microwave radiation flux. The discharge propagation has an equilibrium character; the discharge glow repeats the gas temperature distribution. With an increase in the flux of incident microwave radiation, the nature of the discharge propagation becomes non-equilibrium [4]. The structure of the discharge glow repeats the distribution of the electric field strength. In this case, gas heating in the halo leads to a decrease in the breakdown field and the appearance of an independent breakdown ahead of the discharge front. The discharge propagation velocity, as shown by measurements [4], is proportional to the square of the incident microwave radiation flux. It should be noted that interest in the propagation of microwave discharges in air has not weakened so far [9].

© Сидоров А.В., Веселов А.П., Ракова Е.И., Бармашова Т.В., Водопьянов А.В., Ананичев А.А., Глявин М.Ю., 2023. Издатель: Санкт-Петербургский политехнический университет Петра Великого.

This work is devoted to the study of the propagation of a discharge in air, supported by radiation in the sub-terahertz frequency range, in a wide range of gas pressures. The sub-terahertz and terahertz frequency ranges lie between the microwave and optical ranges. The study of discharge phenomena in this range has become possible relatively recently due to significant progress in the creation of powerful sources of radiation in the sub-terahertz and terahertz ranges—gyrotrons and free electron lasers [10–14].

## Experimental setup

A pulsed gyrotron [13] (1 in Fig. 1) generating radiation at a frequency of 250 GHz with a power of up to 250 kW was used as a source of heating radiation. The pulse duration could vary in the range of 20-40 microseconds. The gyrotron radiation was directed into a vacuum discharge chamber using a system of quasi-optical mirrors and focused into a spot with a diameter close to two wavelengths. Maximum power density was 3.5 MW/cm$^2$, which corresponds to the rms electric field density of 35 kV/cm.

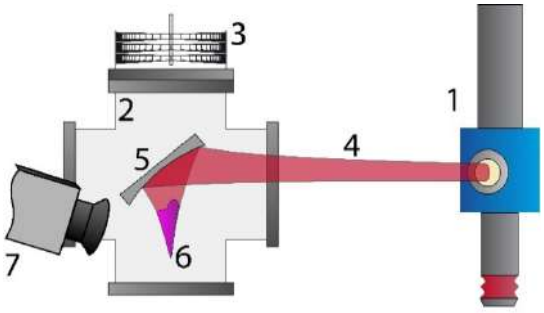


Fig. 1. Scheme of the 250 GHz experimental setup. gyrotron *1*, vacuum chamber *2*, turbomolecular pump *3*, THz beam *4*, focusing mirror *5*, beam waist/discharge plasma *6*, video camera *7*

The discharge glow could be observed through the optical flange of the discharge chamber. The discharge propagation was studied using the Nanogate-24 high-speed camera. The minimum possible frame duration for this camera is 20 ns. During this time, the plasma, at propagation velocities characteristic for this type of the discharge, could move only on a few millimeters or less, so we can assume that the plasma was static during one frame. Numerous photographs were taken with varying delays between the onset of the discharge and the shutter of the camera to calculate the propagation velocity at each point in the propagation path. The discharge propagation speed can be easily calculated as the distance divided by the time between adjacent frames.

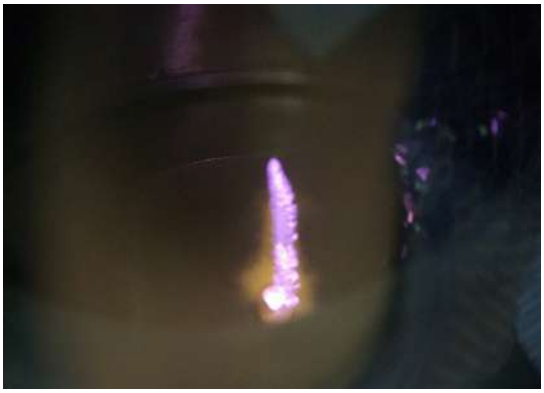

Fig. 2. Photo of the 250 GHz discharge in the air.
Gas pressure is 0.7 atm, gyrotron power is 250 kW

## Experimental results

The discharge appeared at the beam waist and propagated towards heating radiation. From the Fig. 2 one can see the time-integrated photo of the discharge in air. The gyrotron beam power was of 250 kW, gas pressure was 0.7 atm. THz radiation spreads from the top to the bottom. It can be seen that the structure of the discharge repeats the structure of the electric field, which means the non-uniform character of the discharge propagation. Orange halo around the main part of the discharge corresponds to the first positive system of nitrogen which excited by the ultraviolet radiation from the main discharge.

Fig. 3 shows a series of photographs of a discharge in air at the pressure of 1 Torr, taken by a high-speed camera with different delays between the moment of ignition of the discharge and the start of the camera. The delay difference between frames is close to 1 microsecond.

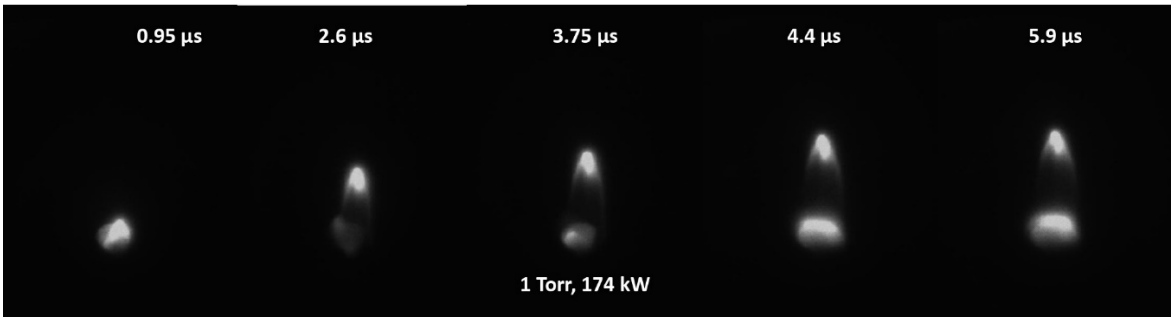


Fig. 3. Series of photographs of a discharge in air at the pressure of 1 Torr, taken by a high-speed camera with different delays between the moment of ignition of the discharge and the start of the camera

Fig. 4 shows the dependence of the discharge front coordinate on time, reconstructed from instantaneous photographs of the discharge. This dependence clearly shows that as the discharge propagates towards the heating radiation, the propagation velocity decreases with a decrease in the field strength in the focused beam. In this case, two characteristic regions of space can be distinguished: with a higher propagation velocity and with a lower one. At present, these two regions of space are associated with the region where the field is higher than the breakdown field (in the absence of plasma), closer to the beam focus, and the region where the field is smaller than the breakdown field, farther from the focus of the heating radiation beam. In the first region, propagation occurs in breakdown fields. In this case, breakdown fields are understood to mean fields sufficient for independent breakdown of the gas in the absence of plasma. In the second area, propagation occurs in pre-breakdown fields. This is most likely related to the fact that the discharge propagation velocity in this region is lower. The same effect was observed in a discharge sustained by a 303 GHz gyrotron in atmospheric pressure air [15].

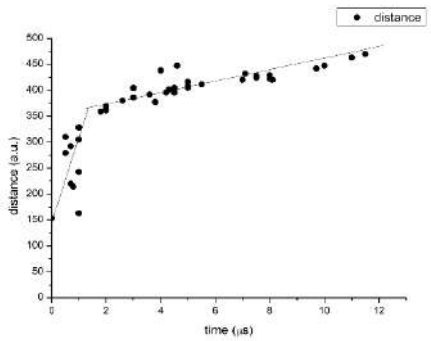


Fig. 4. Dependence of the discharge front coordinate on time. Gas pressure is 95 Torr. Gyrotron power is 215 kW

Fig. 5 shows the dependence of the discharge propagation velocity in the second region on the gas pressure. The pulse power of the gyrotron in this case was 175 kW. It can be seen that the propagation velocity decreases with increasing pressure, from 3.5·105 cm/s to 8·104 cm/s, which is much higher than the speed of sound.

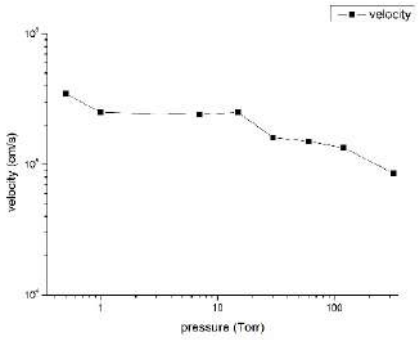


Fig. 5. Dependence of the discharge propagation velocity on the gas pressure. Gyrotron power is 175 kW

Unfortunately, for the first region (breakdown fields), it was not possible to obtain a reliable dependence of the discharge propagation velocity on pressure, which was due to the difficulty of synchronizing the moment of camera start-up and the moment of discharge occurrence at times less than one microsecond. The fact is that even at optimal gas pressures, the moment of the discharge occurrence floats relative to the time of the beginning of the electromagnetic radiation pulse by a value of the order of one microsecond or more. While the propagation velocity in breakdown fields, as measurements show, is quite high, at the level of 106 cm/s, and the size of the region it does not exceed 2–3 cm. As a result, the discharge runs through the first region just in times of the order of a microsecond. As a result, it was not possible to obtain a statistically reliable dependence of the discharge propagation velocity on the gas pressure in this region.

No reliable dependence of the discharge propagation velocity on the power in the gyrotron radiation pulse was found either. Perhaps this was because the range of available powers (to maintain self-discharge in air) was not too wide: 170–250 kW.

## REFERENCES

1. **Ramsden S.A.**, **Davies W.E.,** Physical Review Letters. 13 (1964) 227–228.

2. **Raizer Y.P.,** Laser-Induced Discharge Phenomena, Consultants Bureau, New York, 1977.

3. **Vikharev A.L., Gil'denburg V.B., Golubev S.V., Eremin B.G., Ivanov O.A., Litvak A.G., Stepanov A.N., Yunakovskii A.D.,** Soviet Physics JETP. 67 (1988) 724—728.

4. **Bogatov N.A., Bykov Yu.V., Venediktov N.P., Golubev S.V., Zorin V.G., Eremeev A.G., Semenov V E.,** Soviet Journal Plasma Physics. 12 (1986) 416—423.

5. **Brodskii Yu.Ya., Golubev S.V., Zorin V.G., Luchinin A.G., Semenov V.E.,** JETP. 57 (1983) 989—993.

6. **Golubev S.V., Gritsinin S.I., Zorin V.G., Kossyi I.A., Semenov V.E.**, in High-Frequency Discharge in Wave Fields (in Russian), IPF AN SSSR, Gor'kii, 1988, 136—197.

7. **Cook A.M., Hummelt J.S., Shapiro M.A., Temkin R.J.,** Physics of Plasmas. 18 (2011) 100704.

8. **Rusanov V.D., Fridman A.A., Sholin G.V.,** Soviet Physics Uspkhi. 24 (1981) 447–474.

9. **Artem'ev K.V., Batanov G.M., Berezhetskaya N.K.** et al., JETP Letters. 107 (2018) 219–222.

10. **Glyavin M.Yu., Luchinin A.G., Nusinovich G.S., Rodgers J., Kashyn D.G., Romero-Talamas C.A., Pu R.,** Applied Physics Letters. 101 (2012) 153503.

11. **Bratman V.L., Kalynov Yu.K., Manuilov V.N.,** Physical Review Letters. 102 (2009) 245101.

12. **Glyavin M.Yu.** et al., Review of Scientific Instruments. 86 (2015) 054705.

13. **Denisov G.G.** et al., Review of Scientific Instruments 89 (2018) 084702.

14. **Bolotin V.P.** et al., In Proceedings of the 1st International Conference on Submillimeter Science and Technology, Ahmedabad, India, 2004, 1–8.

15. **Fukunari M., Tanaka S., Shinbayashi R., Yamaguchi Y., Tatematsu Y., Saito T.,** Scientific Reports. 9 (2019) 17972.

## THE AUTHORS

**SIDOROV Alexander V.**
alexsv@ipfran.ru
ORCID: 0000-0002-4826-0114

**VESELOV Alexey P.**
veselov@ipfran.ru
ORCID: 0000-0003-0139-6572

**RAKOVA Elena I.**
eir@ipfran.ru

**BARMASHOVA Tatyana V.**
tanyabarmashova@ipfran.ru

**VODOPYANOV Alexander V.**
avod@ipfran.ru
ORCID: 0000-0001-6136-659X

**ANANICHEV Andrey A.**
a0810@ipfran.ru

**GLYAVIN Mikhail Yu.**
glyavin@ipfran.ru
ORCID: 0000-0002-7896-9212

*Received 25.10.2022. Approved after reviewing 08.11.2022. Accepted 08.11.2022.*

© Peter the Great St. Petersburg Polytechnic University, 2023

# THEORETICAL PHYSICS

Conference materials
UDC 537.9
DOI: https://doi.org/10.18721/JPM.161.284

## Generation of multi-mode velocity of electrons in a Dirac crystal in the monochromatic field

S.V. Kryuchkov[1,2], E.I. Kukhar[1]✉

[1]Volgograd State Technical University, Volgograd, Russia;
[2]Volgograd State Socio-Pedagogical University, Volgograd, Russia
✉ eikuhar@yandex.ru

**Abstract.** Multi-mode dynamics with Zitterbewegung of an electron in 2D Dirac crystal placed in the field of monochromatic radiation is studied. For calculations, a model Hamiltonian taking into account two independent Dirac points has been used. Calculations have shown that the spectrum of electron oscillations contains a series of new (compared to the usual Zitterbewegung) frequencies. The latter, in the case of a high radiation frequency, are a combination of the Zitterbewegung frequency and frequencies that are multiples of the field frequency. In the case when the field frequency is comparable to the Zitterbewegung frequency, the spectrum of electron oscillations is determined by the field amplitude. The character of this dependence has been shown to be changed by variation of the direction of radiation polarization. The possibility of the appearance of a constant component of the electron velocity in the field of monochromatic radiation is also discussed.

**Keywords:** Zitterbewegung, graphene, Dirac crystal, Rabi frequency

**Funding:** This work was funded by the Ministry of Education of the Russian Federation as part of State Task, Project "Propagation and interaction of soliton waves in nanostructures based on Dirac materials".

**Citation:** Kryuchkov S.V., Kukhar E.I., Generation of multi-mode velocity of electrons in a Dirac crystal in the monochromatic field, St. Petersburg State Polytechnical University Journal. Physics and Mathematics. 16 (1.2) (2023) 550–556. DOI: https://doi.org/10.18721/JPM.161.284

This is an open access article under the CC BY-NC 4.0 license (https://creativecommons.org/licenses/by-nc/4.0/)

Материалы конференции
УДК 537.9
DOI: https://doi.org/10.18721/JPM.161.284

## Генерация многомодовой скорости электронов в дираковском кристалле в монохроматическом поле

С.В. Крючков[1,2], Е.И. Кухарь[1]✉

[1]Волгоградский государственный технический университет, г. Волгоград, Россия;
[2]Волгоградский государственный социально-педагогический университет, г. Волгоград, Россия
✉ eikuhar@yandex.ru

**Аннотация.** Исследована многомодовая динамика электрона с учетом Zitterbewegung'а в двумерном дираковском кристалле, помещенном в поле монохроматического излучения. Для расчетов использовался модельный гамильтониан, учитывающий две независимые точки Дирака. Расчеты показали, что спектр колебаний электрона содержит ряд новых (по сравнению с обычным Zitterbewegung'ом) частот. Последние, в случае высокой частоты излучения, представляют собой комбинацию частоты Zitterbewegung'а и частот, кратных частоте поля. В случае, когда частота поля сравнима с частотой Zitterbewegung'а, спектр колебаний электрона определяется амплитудой поля. Показано, что характер этой зависимости меняется при изменении направления поляризации излучения. Обсуждается также возможность появления постоянной составляющей скорости электрона в поле монохроматического излучения.

© Kryuchkov S.V., Kukhar E.I., 2023. Published by Peter the Great St. Petersburg Polytechnic University.

**Ключевые слова:** Дрожащее движение, графен, дираковский кристалл, частота Раби

**Финансирование:** Работа выполнена при финансовой поддержке Министерства просвещения РФ в рамках государственного задания, проект «Распространение и взаимодействие уединенных волн в наноструктурах на основе дираковских материалов».

**Ссылка при цитировании:** Крючков С.В., Кухарь Е.И. Генерация многомодовой скорости электронов в дираковском кристалле в монохроматическом поле // Научно-технические ведомости СПбГПУ. Физико-математические науки. 2023. Т. 16. № 1.2. С. 550–556. DOI: https://doi.org/10.18721/JPM.161.284

Статья открытого доступа, распространяемая по лицензии CC BY-NC 4.0 (https://creativecommons.org/licenses/by-nc/4.0/)

## Introduction

The discovery of new types of 2D crystals constituting the group of so-called Dirac materials (graphene, germanene, silicene, etc.), as well as the study of their electrodynamics properties, determined essentially the development of that part of the physics of solid-state structures that stands at the junction of the condensed matter theory and high energy physics. The point is that the relativistic form of the equations for electron states in 2D hexagonal lattices makes graphene-like materials a convenient platform to study the effects of quantum electrodynamics [1, 2]. The uniqueness of the above materials is explained by the presence of the components relating the momentum of the charge carrier to its pseudospin degree of freedom in the quantum equation. Examples of manifestation of such a relation are topological phase transitions [3–5], transitions of "semi-metal–band insulator" [4, 6, 7] and "Dirac–semi-Dirac material" [8,9] types, as well as the Zitterbewegung (ZB) – fast oscillations of the velocity of free (pseudo)relativistic electron due to the interference of the states with positive and negative energies.

Previously the possibility of electron ZB had been shown theoretically for Dirac crystals [10, 11], for solid state with Rashba/Dresselhaus spin-orbit coupling and the Zeeman splitting [12], and for strained III-V semiconductors [13,14] as well. However for vacuum the experimental realization of ZB is very difficult due to the high frequency (HF) of the corresponding electron oscillations (~$10^{21}$ Hz). The advantage of above solid state structures over the vacuum is a much lower magnitude of ZB frequency, which greatly facilitates its experimental detection in these materials [12,14–16]. In [14] the coherent electron ZB had been shown experimentally to be triggered by initializing an ensemble of electrons in the same spin states. It had been probed in strained *n*-InGaAs as an ac-current at GHz frequencies. In [17, 18] a computer simulation of the damping of ZB oscillations for a wave packet of the Gaussian profile predicted theoretically in [11] had been performed. It should be noted that the study of ZB in Dirac crystals is also of practical importance. So in [19] a path for creating a nanoresonator based on a system of oscillatory circuits that exhibited the properties of an active load if external signal frequencies exceeded the ZB frequency had been outlined. In [20] similar systems had been used in microcircuits, which made it possible to simulate such relativistic quantum effects as the Klein paradox and ZB.

Presently, the problem of controlling the electron ZB in Dirac materials by means of external fields has become topical [21–23]. The possibility of ZB stabilization by a quantizing magnetic field had been shown in [24, 25]. The combination effect from simultaneous allowance of ZB in Dirac structures and an external HF electromagnetic (EM) field had been investigated in [21, 26, 27].

In [27] the so-called multi-mode ZB (electron oscillations induced by an HF electric field) had been studied for free graphene. The spectrum of such oscillations contained new frequencies equal to combinations of the monochromatic field frequency and the ZB frequency. However, the calculations in [27] had not been performed for arbitrary electron momenta: the momentum along the polarization line had been assumed zero. This does not correspond to the real situation, in which the momenta of charge carriers obey 2D statistics. Moreover, in some cases the ac-field amplitude had been assumed sufficiently small. It had allowed solving the equations of motion in the approximation linear in the ac-field amplitude. As a result, the multi-mode ZB spectrum contained only two new frequencies (besides ZB frequency). Below both the rotating wave approximation (RWA) and the approximation of high driving frequency (HDF) are used for calculations as in [27]. However, in contrast to [27] analytical calculations are performed for

© Крючков С. В., Кухарь Е. И., 2023. Издатель: Санкт-Петербургский политехнический университет Петра Великого.

arbitrary ac-field amplitudes and in the case of using HDF for arbitrary electron momenta. For intensive fields the spectrum of the multi-mode ZB is shown to contain a series of new (compared to conventional ZB) frequencies, which are the combination of the ZB frequency and frequencies that are multiples of the pump field frequency. Among other things, the result is generalized to the case of a Hamiltonian model describing two independent Dirac points [8].

**Effect of velocity rectification in monochromatic field**

Let 2D Dirac crystal associated with *xy*-plane is subjected by the monochromatic EM radiation so that electric field oscillates along *Ox* axis. Spinor $\psi$ describing the electron state in this case obeys

$$i\frac{\partial\psi}{\partial t}=\left(\Omega_1\hat{\sigma}_x+\Omega_2\hat{\sigma}_y\right)\psi+e\upsilon_{\mathrm{F}}A(t)\hat{\sigma}_x\psi, \tag{1}$$

where $\hat{\sigma}_{x,y,z}$ are Pauli matrices, $\mathbf{A}(t)$ is vector potential of ac field, $\Omega_1=\upsilon_{\mathrm{F}}p_x$, the form of the term $\Omega_2$ is determined by the crystal model. For the conical model, for instance, one has $\Omega_2=\upsilon_{\mathrm{F}}p_y$. Further we use the model of 2D crystal with displaced Dirac points [8]:

$$\Omega_2=\frac{p_y^2}{2m}-\Delta, \tag{2}$$

and $\Delta > 0$. We note that the change in the sign of the parameter $\Delta$ leads to the transition between semi-metal and band insulator states. In the latter case, the crystal will be of semi-Dirac type. The time dependence of ac-field is assumed to be harmonic: $A(t) = (E_0/\omega)\cos(\omega t + \varphi_0)$. Here $E_0$ is amplitude of the electric field intensity, $\omega$ is its frequency and $\varphi_0$ is its initial phase. Electron ZB is shown below modifies the spectrum of electron velocity oscillations in the monochromatic ac-field. To investigate this modification the initial state in p-representation is assumed to be given by a delta-like wave function: $\psi_0 = \delta(\mathbf{p} - \mathbf{p}')\chi_0$, where $\chi_0$ is eigenspinor of the matrix $\hat{\sigma}_s$ [27]: $\chi_0 = (1\ 0)^{\mathrm{T}}$. Let us note here the next peculiarity of the electron dynamics in Dirac crystals. If $\Omega_2 = 0$, then Eq. (1) admits the exact analytical solution

$$\psi(t)=e^{-i\left(\Omega_1 t+a_0\sin(\omega t+\varphi_0)\right)\hat{\sigma}_x}\psi_0, \tag{3}$$

where $a_0 = \upsilon_{\mathrm{F}}eE_0/\omega^2$. The components of quantum mechanical average velocity of electron which are calculated as the matrix elements $\upsilon_{x,y} = \upsilon_{\mathrm{F}}\langle\psi|\,\hat{\sigma}_{x,y,z}|\psi\rangle$ read

$$\upsilon_x=0,\upsilon_y=-\upsilon_{\mathrm{F}}\sin\left(\Omega_{\mathrm{ZB}}t+2a_0\sin\left(\omega t+\varphi_0\right)\right). \tag{4}$$

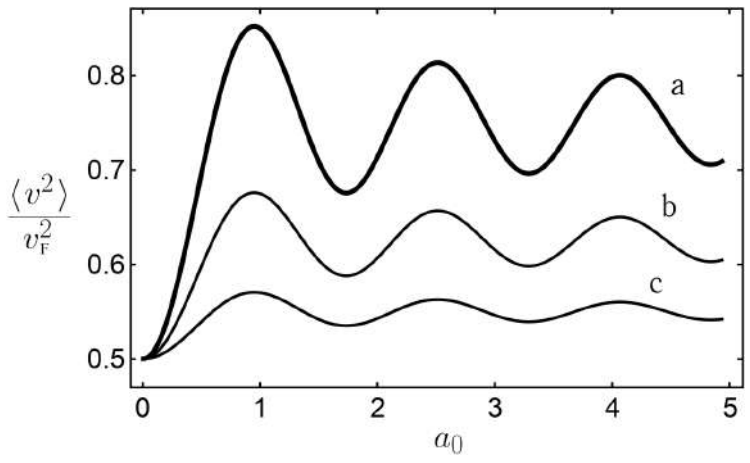


Fig. 1. Intensity of multi-mode Zitterbewegung $\langle\upsilon^2\rangle$ vs. ac-field amplitude: $\Omega_1 = 0$ (*a*); $\Omega_1 = \Omega_2$ (*b*) ; $\Omega_1 : \Omega_2 = 2 : 1$ (*c*)

Here $\Omega_{ZB}$ is ZB frequency in the absence of ac-field. There can be the next situation according to Eq. (4). If $\varphi_0 \neq s\pi$ and ZB frequency is multiples of ac-field frequency, $\Omega_{ZB}=k\omega$ ($s$ and $k$ are integers), then electron velocity acquires the stationary component which reads

$$\left\langle \upsilon_y \right\rangle_t = (-1)^k J_k(2a_0)\upsilon_F \sin k\varphi_0, \tag{5}$$

where $J_k(x)$ is Bessel function of integer order. Particularly in the case when $\varphi_0 = \pi/2$ one can obtain $\left\langle \upsilon_y \right\rangle_t = (-1)^{k+1} J_{2k+1}(2a_0)\upsilon_F$. Such a "velocity rectification" is the nonlinear effect related with the combination of two vibrations of electron in Dirac crystal: ZB existing in the absence of ac-field and forced vibrations arising due to the effect of ac-field.

**Multi-mode ZB in HF electric field**

To analyze the behavior of electron velocity at arbitrary values of $\Omega_2$ it is convenient to use the unitary transformation by means of operator

$$\hat{U} = e^{i\Omega t\hat{\sigma}_0}, \tag{6}$$

where we have define $\hat{\sigma}_0 = \left(\Omega_1\hat{\sigma}_x + \Omega_2\hat{\sigma}_y\right)/\Omega$, $\Omega = \sqrt{\Omega_1^2 + \Omega_2^2}$. In [27] to study the nonlinear dynamics of Dirac electron within the HDF picture the solution of Eq. (1) had been limited by an approximation linear in the ac-field amplitude $a_0$. The unitary operator (6) used here differs from that used in [27] and allows one to obtain analytical results for arbitrary ac-field amplitudes. Having put in Eq. (1) $\psi = \hat{U}^+\chi$, $\hat{\Sigma}_{x,y,z}(t) = \hat{U}\hat{\sigma}_{x,y,z}\hat{U}^+$ and $\varphi_0 = 0$, we arrive at

$$\frac{\partial\chi}{\partial t} = -i\omega a_0 \cos\omega t\hat{\Sigma}_x(t)\chi. \tag{7}$$

Now the condition $\omega \gg \Omega$ (HDF approximation) is assumed to be performed. Then it is easy to verify that the spinor

$$\chi(t) = e^{-ia_0 \sin\omega t\hat{\Sigma}_x(t)}\chi_0 \tag{8}$$

is the solution of Eq. (7). Indeed, terms, which are the result of differentiation of the spinor $\hat{\Sigma}_x(t)\chi_0$ can be neglected, because of they will contain as a multiplier the frequencies which are much less than $\omega$. To prove it let us write the time-derivative for spinor (8) explicitly:

$$\frac{\partial\chi}{\partial t} = -i\omega a_0\left(\cos\omega t\hat{\Sigma}_x + \frac{1}{\omega}\sin\omega t\frac{\partial\hat{\Sigma}_x}{\partial t}\right)\chi. \tag{9}$$

Using the definition (6) one can find that $\dot{\hat{\Sigma}}_x = \Omega_2\hat{\Sigma}_z$. After substitution of latter derivative into Eq. (9) and neglecting of the term containing $\Omega_2/\omega$ ($\Omega_2 \leq \Omega << \omega$) we arrive at Eq. (8). The average quantum mechanical velocity $\upsilon_{x,y} = \upsilon_F\left\langle\chi\middle|\hat{\Sigma}_{x,y}\middle|\chi\right\rangle$ is derived by means of spinor (8). After some algebra one obtains

$$\upsilon_x = \frac{\upsilon_F\Omega_2}{\Omega}\sin 2\Omega t, \tag{10}$$

$$\upsilon_y = -\frac{\upsilon_F\Omega_1}{\Omega}\cos(2a_0\sin\omega t)\sin 2\Omega t - \upsilon_F\sin(2a_0\sin\omega t)\cos 2\Omega t. \tag{11}$$

As expected the velocity vibrations, according to Eq. (11), are not harmonic. To analyze the spectral composition of these vibrations, we expand the right side of Eq. (11) into a Fourier series:

$$\begin{aligned}\upsilon_y = &-\frac{\upsilon_F\Omega_1}{\Omega}J_0(2a_0)\sin 2\Omega t + \frac{\upsilon_F\Omega_1}{\Omega}\sum_{n=1}^{\infty}J_{2n}(2a_0)\left(\sin 2(n\omega-\Omega)t - \sin 2(n\omega+\Omega)t\right) - \\ &-\upsilon_F\sum_{n=0}^{\infty}J_{2n+1}(2a_0)\left(\sin((2n+1)\omega+2\Omega)t + \sin((2n+1)\omega-2\Omega)t\right).\end{aligned} \tag{12}$$

Thus, the spectrum of electron velocity vibrations contains, as the main frequency, the ZB frequency equal to 2Ω, and additional frequencies nω±2Ω, where $n$ is an integer. This type of motion of Dirac electron in a monochromatic field has been called as multi-mode ZB in [27]. If $p_x = 0$ and $a_0 \ll 1$, then, as expected, Eqs. (10) and (12) are transformed into the corresponding formulas from [27]. The multi-mode ZB intensity is proportional to the time-averaged square of the electron velocity $\left\langle \upsilon^2 \right\rangle = \left\langle \upsilon_x^2 \right\rangle + \left\langle \upsilon_y^2 \right\rangle$ [27]. Using Eqs. (10) and (12), we find

$$\left\langle \upsilon^2 \right\rangle = \upsilon_F^2 \left( \frac{\Omega_2^2}{2\Omega^2} + \frac{\Omega_1^2}{2\Omega^2} \left( J_0^2(2a_0) + 2\sum_{n=1}^{\infty} J_{2n}^2(2a_0) \right) + \sum_{n=0}^{\infty} J_{2n+1}^2(2a_0) \right). \tag{13}$$

The dependence of $\langle \upsilon^2 \rangle$ on the dimensionless amplitude of ac-field $a_0$ plotted by Eq. (13) is shown in Fig. 1 for different values of $\Omega_1$ and $\Omega_2$. If $\Omega_2 = 0$ then $\langle \upsilon^2 \rangle$ does not depend on the amplitude $a_0$ and is equal to $\upsilon_F^2 / 2$.

**Rabi frequency**

In this section as in [27] we put $p_x = 0$. However the model (2) is used here instead of conical model of Hamiltonian. RWA allows us to find the solution of Eq. (1) in the case $|2|\Omega_2| - \omega| \dagger \omega$. The components oscillating with frequency $2|\Omega_2| + \omega$ are neglected within RWA. In this situation spectrum of vibrations will still contain three frequencies: $\Omega_R$, $\Omega_R \pm \omega$, where $\Omega_R$ is so called Rabi frequency, which reads

$$\Omega_R = \sqrt{\left(2|\Omega_2| - \omega\right)^2 + \upsilon_F^2 p_0^2}. \tag{14}$$

Here $p_0 = eE_0/\omega$. Rabi frequency is seen from (14) to be determined by three structure parameters $\upsilon_F$, $m$ and $\Delta$ instead one parameter $\upsilon_F$ as it was in conical model [27]. In addition the anisotropy of the Hamiltonian model [8] which takes into account two Dirac points leads to the fact that the character of the dependence of the Rabi frequency on the amplitude of ac-field will be determined by the direction of the polarization of this field in the 2D crystal plane. Now we make sure of this clearly. To do this we change the direction of the field polarization so that it oscillates along the $Oy$ axis. Then instead of Eq. (1) one should write

$$i\frac{\partial \psi}{\partial t} = \Omega_1 \hat{\sigma}_x \psi + \tilde{\Omega}_2 \hat{\sigma}_y \psi + \omega \left( \frac{p_0^2}{4m\omega} \cos 2\omega t + \frac{p_y p_0}{m\omega} \cos \omega t \right) \hat{\sigma}_y \psi, \tag{15}$$

where we define $\tilde{\Omega}_2 = \Omega_2 + p_0^2 / 4m$. Further we put $\tilde{\Omega}_2 = 0$. The latter can be reached if $\Delta > 0$ and $eE_0 < 2\omega\sqrt{m\Delta}$. Then after transformations by means of operator $\hat{S} = e^{i\Omega_1 t \hat{\sigma}_x}$ we arrive at

$$\frac{\partial \chi}{\partial t} = -i\omega \left( a_1 \cos \omega t + a_2 \cos 2\omega t \right) \hat{\Xi}_y \chi. \tag{16}$$

Here $\hat{\Xi}_y = \hat{S}\hat{\sigma}_y\hat{S}^+$, $a_1 = \pm q_0 p_0 / m\omega$, $a_2 = p_0^2 / 4m\omega$, $q_0 = \sqrt{2m\Delta - p_0^2/2}$. To solve Eq. (16) we use RWA, which can be applied in two cases: (a) $|2|\Omega_1| - \omega| \ll \omega$ or (b) $2\|\Omega_1| - \omega| \ll \omega$. In the case (a), we leave in Eq. (16) only terms oscillates with a frequency $2|\Omega_1| - \omega$. As a result we have $\left(a_1 \cos \omega t + a_2 \cos 2\omega t\right) \hat{\Xi}_y \approx \left(a_1 / 2\right) e^{i(2|\Omega_1| - \omega) t \hat{\sigma}_x} \hat{\sigma}_y$. So instead of Eq. (16) one obtains

$$\frac{\partial \chi}{\partial t} = \frac{i\omega a_1}{2} e^{i(2|\Omega_1| - \omega) t \hat{\sigma}_x} \hat{\sigma}_y \chi. \tag{17}$$

After some transformations we write

$$\frac{\partial^2 \chi}{\partial t^2} - i\left(2|\Omega_1| - \omega\right) \hat{\sigma}_x \frac{\partial \chi}{\partial t} + \frac{\omega^2 a_1^2}{4} \chi = 0. \tag{18}$$

Particular solutions of Eq. (18) have the form $\chi_{\pm}(t) = e^{-(i/2)(\omega-2|\Omega_1|\pm\Omega_R)t\hat{\sigma}_x}\chi_0$, where Rabi frequency reads

$$\Omega_R = \sqrt{\left(2|\Omega_1| - \omega\right)^2 + \frac{2\Delta p_0^2}{m}\left(1 - \frac{p_0^2}{4m\Delta}\right)}, \tag{19}$$

In the case $2\|\Omega_1| - \omega| \ll \omega$ only terms oscillates with a frequency $2(|\Omega_1| - \omega)$ should be leaved in Eq. (16). After similar transformations, one obtains for the Rabi frequency the expression

$$\Omega_R = \sqrt{4\left(|\Omega_1| - \omega\right)^2 + \frac{p_0^4}{16m^2}}. \tag{20}$$

The dependence of Rabi frequency on amplitude $p_0 = eE_0/\omega$ is seen from Eqs. (14), (19) and (20), to be different for different polarizations of ac-field. It is explained by the anisotropy of the spectrum of 2D Dirac crystal with the Hamiltonian [8].

## Conclusion

We have considered the nonlinear dynamics of an electron in 2D Dirac crystal placed in AC electric field of monochromatic radiation with frequency ω. In contrast to [27] the model of Hamiltonian [8] used in the above calculations has taken into account the presence of two independent Dirac points and has been characterized by significant anisotropy. Taking into account ZB (oscillations of free Dirac electron) has led to the modification of the spectrum of nonlinear oscillations of an electron in the external ac-field. In HDF approximation, when the external field frequency is much higher than the ZB frequency $\Omega_{ZB}$, this spectrum contains combinations $n\omega \pm 2\Omega_{ZB}$ ($n$ is an integer). It should be mentioned that the multi-mode dynamics of Dirac electron in monochromatic field had been studied earlier in [27], where three frequencies in the spectrum of electron oscillations had been predicted within HDF approximation: $\Omega_{ZB}$ and $\omega \pm 2\Omega_{ZB}$. However, stated in [27] theory had been limited by both 1D motion of an electron and linear approximation of the amplitude of AC field. Here in contrast to [27] we have studied the case of arbitrary directions of the quasi-momentum and arbitrary amplitudes of HF radiation. As a result, the functional dependence of the multi-mode ZB intensity on the amplitude of ac-field $a_0$ has been derived (Fig. 1). Moreover, Eq. (12) allows analytical calculation of dependence of arbitrary $n$-harmonics of multimode ZB on $a_0$.

The spectrum of electron oscillations obtained within RWA, when the frequency of the external ac-field is comparable with ZB frequency, contains, as in [27], three frequencies: $\Omega_R$, $\Omega_R \pm \omega$ ($\Omega_R$ is Rabi frequency). However, in contrast to [27], the dependence of $\Omega_R$ on the amplitude of EM radiation is determined by the direction of its polarization (see Eqs. (14), (19) and (20)). The latter is related to the anisotropy of the Hamiltonian [8] used in the calculations. At the end, we point out the possibility of the appearance of a constant term of electron velocity in 2D Dirac crystal in the field of monochromatic radiation. To this end, it is necessary that ZB frequency be a multiple of the frequency of ac-field. Moreover, according to Eq. (5), the value of such a "rectified" velocity is determined by the amplitude of this field.

## REFERENCES

1. **Katsnelson M.I., Novoselov K.S., Geim. A.K.**, Chiral tunnelling and the Klein paradox in graphene, Nature Physics, 2 (2006) 620–625.

2. **Romanovsky I., Yannouleas C., Landman U.**, Topological effects and particle physics analogies beyond the massless Dirac-Weyl fermion in graphene nanorings, Physical Review B, 87 (2013) 165431.

3. **Ezawa M.**, Valley-Polarized metals and quantum anomalous Hall effect in silicene, Physical Review Letters, 109 (2012) 055502.

4. **Delplace P., Gomez-Leon A., Platero G.**, Merging of Dirac points and Floquet topological transitions in ac-driven graphene, Physical Review B, 88 (2013) 245422.

5. **Usaj G., Perez-Piskunow P. M., Foa Torres L.E.F., Balseiro C.A.**, Irradiated graphene as a tunable Floquet topological insulator, Physical Review B, 90 (2014) 115423.

6. **Oka T., Aoki H.**, Photovoltaic Hall effect in graphene, Physical Review B, 79 (2009) 081406.
7. **Kibis O.V.**, Metal-insulator transition in graphene induced by circularly polarized photons, Physical Review B, 81 (2010) 165433.
8. **Montambaux G., Piéchon F., Fuchs J.-N., Goerbig M.O.**, A universal Hamiltonian for motion and merging of Dirac points in a two-dimensional crystal, The European Physical Journal B, 72 (2009) 509.
9. **Kukhar E.I., Kryuchkov S.V.**, Floquet transitions "Insulator – Semimetal – Insulator" in 2D crystals with displaced Dirac points, Physica E, 134 (2021) 114811.
10. **Cserti J., Dávid G.**, Unified description of Zitterbewegung for spintronic, graphene, and superconducting systems, Physical Review B, 74 (2006) 172305.
11. **Rusin T.M., Zawadzki W.**, Transient Zitterbewegung of charge carriers in mono- and bilayer graphene, and carbon nanotubes, Physical Review B, 76 (2007) 195439.
12. **Tarasenko S.A., Poshakinskiy A.V., Ivchenko E.L., Stepanov I., Ersfeld M., Lepsa M., Beschoten B.**, Zitterbewegung of spin split electrons, JETP Letters, 108 (2018) 326–328.
13. **Schliemann J., Loss D., Westervelt R. M.**, Zitterbewegung of electrons and holes in III–V semiconductor quantum wells, Physical Review B, 73 (2006) 085323.
14. **Stepanov I., Ersfeld M., Poshakinskiy A. V., Lepsa M., Ivchenko E. L., Tarasenko S.A., Beschoten B.**, Coherent electron Zitterbewegung, https://arxiv.org/abs/1612.06190. Accessed April 4, 2022.
15. **Zhang X.**, Observing Zitterbewegung for photons near the Dirac point of a two-dimensional photonic crystal, Physical Review Letters, 100 (2008) 113903.
16. **Iwasaki Y., Hashimoto Y., Nakamura T., Katsumoto S.**, Observation of conductance fluctuation due to Zitterbewegung in InAs 2-dimentional electron gas, Journal of Physics: Conference Series, 864 (2017) 012054.
17. **Gerritsma R., Kirchmair G., Zahringer F., Solano E., Blatt R., Roos C. F.**, Quantum simulation of the Dirac equation, Nature, 463 (2010) 68–71.
18. **Diago-Cisneros L., Serna E., Vargas I.R., Pérez-Álvarez R.**, Pseudospin-dependent Zitterbewegung in monolayer graphene, Journal of Applied Physics, 125 (2019) 203902.
19. **Firsova N.E., Ktitorov S.A.**, Zitterbewegung of electrons and high-frequency conductivity of single-layer graphene at low temperatures, Physics of the Solid State, 63 (2021) 313–317.
20. **Zhang W., Yuan H., He W., Zheng X., Sun N., Di F., Sun H., Zhang X.**, Observation of interaction-induced phenomena of relativistic quantum mechanics, Communications Physics, 4 (2021) 250.
21. **Shi L.-K., Zhang S.-C., Chang K.**, Anomalous electron trajectory in topological insulators, Physical Review B, 87 (2013) 161115.
22. **Ho C.S., Jalil M.B.A., Tan S.G.**, Persistent Zitterbewegung of electron wave packet in time-dependent Rashba system, Europhysics Letters, 108 (2014) 27012.
23. **Reck P., Gorini C., Richter K.**, Steering Zitterbewegung in driven Dirac systems: From persistent modes to echoes, Physical Review B, 101 (2020) 094306.
24. **Rusin T.M., Zawadzki W.**, Zitterbewegung of electrons in graphene in a magnetic field, Physical Review B, 78 (2008) 125419.
25. **Romera E., Roldán J. B., de los Santos F.**, Zitterbewegung in monolayer silicene in a magnetic field, Physics Letters A, 378 (34) (2014) 2582–2585.
26. **Belonenko M.B., Yanyushkina N.N.**, Zitterbewegung in thin-film topological insulators in the presence of a terahertz pulse, Physics of the Solid State, 54 (2012) 2462–2464.
27. **Rusin T.M., Zawadzki W.**, Multimode behavior of electron Zitterbewegung induced by an electromagnetic wave in graphene, Physical Review B, 88 (2013) 235404.

## THE AUTHORS

**KRYUCHKOV Sergei V.**
svkruchkov@yandex.ru
ORCID: 0000-0001-5378-306X

**KUKHAR Egor I.**
eikuhar@yandex.ru
ORCID: 0000-0002-9515-4904

*Received 27.10.2022. Approved after reviewing 08.11.2022. Accepted 10.11.2022.*

© Peter the Great St. Petersburg Polytechnic University, 2023

Conference materials
UDC 534.26
DOI: https://doi.org/10.18721/JPM.161.285

# Structure of acoustic Lauegram on the Ewald circle of reflection for the Rayleigh wave scattering

V.N. Chukov✉

Laboratory of Acoustic Microscopy,
N.M. Emanuel Institute of Biochemical Physics of the RAS, Moscow, Russia

✉ vchukov@mail.ru

**Abstract.** The acoustic Lauegram of the Rayleigh wave the Laue–Bragg–Wulff high-frequency scattering on a rectangle rough band of an isotropic solid, having periodic lattice of an arbitrary number of the roughness discontinuities, is theoretically investigated in details in dependence on the angle of scattering $\varphi_s$ at a fixed ratio of the lattice unit cell size to the wavelength and parameters of the lattice. The Ewald conception of the circle of reflection is used. The problem of an arbitrary number, defined beforehand, of the resonances of scattering, i.e. nodes of the reciprocal lattice, for any $\varphi_s$, defined beforehand, lying on the Ewald circle of reflection, is first solved analytically in the present work in the classical case, i.e. without influence of the amplitude form-factor of the lattice. It is found, that increasing of the number of resonances for any $\varphi_s$ is necessarily accompanied by the increasing of the Ewald circle of reflection radius, i.e. of the Rayleigh wave frequency, at fixed sizes of a discontinuities lattice. It is obtained first, that amplitude form-factor of the discontinuities lattice strongly influences the structure of the acoustic Lauegram: arbitrary number of the resonances of scattering for any $\varphi_s$ can be placed on the Ewald circle of reflection without variation of its radius by using of the appropriate amplitude form-factor of a discontinuities lattice of a solid roughness.

**Keywords:** Rayleigh wave, Laue scattering, Bragg–Wulff reflection

**Funding:** The work is performed under Russian Government order "Investigation of the microstructure and physicochemical properties of the contemporary materials (polymers, composites, bio-composites, nanomaterials) by means of the high-resolution acoustic microscopy methods. Fundamental and applied problems of the micro-acoustic methods and instrumentations of the materials investigations non-destructive control for 2022-2024" (NIOKTR 122041400112-8, theme code FFZR-2022-0012).

**Citation:** Chukov V.N., Structure of acoustic Lauegram on the Ewald circle of reflection for the Rayleigh wave scattering, St. Petersburg State Polytechnical University Journal. Physics and Mathematics. 16 (1.2) (2023) 557–564. DOI: https://doi.org/10.18721/JPM.161.285

This is an open access article under the CC BY-NC 4.0 license (https://creativecommons.org/licenses/by-nc/4.0/)

Материалы конференции
УДК 534.26
DOI: https://doi.org/10.18721/JPM.161.285

# Структура акустической лауэграммы на окружности отражения Эвальда для рассеяния волны Рэлея

В.Н. Чуков✉

Лаборатория Акустической Микроскопии,
Институт Биохимической Физики им. Н.М. Эмануэля РАН, Москва, Россия

✉ vchukov@mail.ru

**Аннотация**. Получены новые закономерности рассеяния Лауэ-Брэгга-Вульфа для поверхностной акустической волны Рэлея в рамках концепции окружности отражения Эвальда.

**Ключевые слова**: волна Рэлея, рассеяние Лауэ, отражение Брэгга-Вульфа

© Chukov V.N., 2023. Published by Peter the Great St. Petersburg Polytechnic University.

**Финансирование**: Работа выполнена в рамках Государственного задания «Исследование микроструктуры и физико-химических свойств современных материалов (полимеров, композитов, биокомпозитов, наноматериалов) методами акустической микроскопии высокого разрешения. Фундаментальные и прикладные проблемы микроакустических методов и средств неразрушающего контроля исследования материалов на 2024-2022гг» (НИОКТР № 122041400112-8, код темы FFZR-2022-0012).

Ссылка при цитировании: Чуков В.Н. Структура акустической лауэграммы на окружности отражения Эвальда для рассеяния волны Рэлея // Научно-технические ведомости СПбГПУ. Физико-математические науки. 2023. Т. 16. № 1.2. С. 557–564. DOI: https://doi.org/10.18721/JPM.161.285

Статья открытого доступа, распространяемая по лицензии CC BY-NC 4.0 (https://creativecommons.org/licenses/by-nc/4.0/)

## Introduction

It is known, that the Bragg-Wulff mirror reflection and the more general Laue scattering of the waves on the periodically arranged inhomogeneities are broadly used in the science and technologies [1—18]. Both these types of the physical phenomena are described by the Bragg-Wulff law of reflection and the Laue conditions of scattering respectively [1—7]. These laws of reflection and scattering are conditions of the phase synchronism of the reflected and scattered waves respectively [7—9]. The great interest is aroused by the phenomena of the wave scattering on the non-perfectly periodic lattices of inhomogeneities, which take place in the real nature [9—13]. Theoretically these physical phenomena are investigated in a frame of the kinematic and dynamic theories of scattering [6, 11]. The first one deals with the Born approximation of the perturbation theory, the second one solves the problems of the multiple scattering of waves on inhomogeneities. The new physical topological [14, 15] laws of scattering were obtained first in [16—18] in a frame of the Born approximation of the perturbation theory in inhomogeneity amplitude. These laws are topological ones [14, 15], since they are the same for the sets of inhomogeneities, having definite configuration properties. They include both the Rayleigh and the Laue–Bragg–Wulff scatterings. It was earlier well-known [5] that the high-frequency Laue–Bragg–Wulff scattering takes place mostly on the medium discontinuities because continuous inhomogeneities are physically smooth for the wave, having the wavelength more less than the character size of inhomogeneity. The periodic space arrangement of the medium discontinuities has the great importance for the conditions of the phase synchronism of the scattered waves according to the Laue–Bragg–Wulff laws [1—7]. But the amplitude form-factor of discontinuities lattice, i.e. dependence of the roughness left and right limit values difference in a point of discontinuity on a number of this discontinuity in a lattice [16—18], was not taken into account [1—13]. As for the Laue–Bragg–Wulff scattering, the new topological laws of scattering reveal the important role of this amplitude form-factor of the discontinuities lattice in a wave scattering, up to violation [16—18] of the Laue–Bragg–Wulff laws [1] of scattering.

It is interesting to investigate the fundamental properties of the acoustic Lauegram of scattering, i.e. dependence of the indicatrix of scattering on the angle of scattering, in the frame of a conception of the Ewald sphere of reflection [3] without influence of the lattice amplitude form-factor on a scattering, for example, when all discontinuities have equal amplitudes, as it is described by the Laue–Bragg–Wulff laws, and with account of this form-factor. The Ewald sphere of reflection conception states that necessary and enough condition that definite angle of scattering corresponds to the resonance of scattering is location of the corresponding node of the reciprocal lattice on the Ewald sphere of reflection. But the conception of the Ewald sphere of reflection does not consider and solve the next problem: what is the radius of the Ewald sphere of reflection, i.e. the frequency of the incident wave, containing arbitrary number, defined beforehand, of resonances for an arbitrary angles of scattering, defined beforehand? This problem is solved first in the present work for the scattering of the surface acoustic Rayleigh wave on a rectangle rough band of an isotropic solid, having periodic lattice of an arbitrary number of the roughness discontinuities [18]. In this case two transverse with respect to direction of the incident

© Чуков В. Н., 2023. Издатель: Санкт-Петербургский политехнический университет Петра Великого.

Rayleigh wave propagation edges of the rough band violate the Laue–Bragg–Wulff law, but all the discontinuities amplitudes of the longitudinal lattice are the same, and so they do not influence the scattering. The scattered Rayleigh wave is cylindrical, so the Ewald sphere of reflection becomes the Ewald circle of reflection. The great influence of the amplitude form-factor of the transverse and longitudinal discontinuities lattices, i.e. of the new topological laws of scattering [16—18], on the solution of this problem is obtained and investigated.

## The statement of the problem and method of a solution

Let us consider the theoretical problem of the surface acoustic Rayleigh wave scattering on a rough finite size part of an isotropic solid in the Laue–Bragg–Wulff case and in a more general case of the new topological laws of scattering [16–18]. The results of this completely concrete problem, obtained from the first principles of the dynamical theory of elasticity [5], give the possibility to understand the general laws of a wave scattering physical phenomena [1–13].

## The problem on the number of the reciprocal lattice nodes, lying on the Ewald circle of reflection

Let the plane surface acoustic Rayleigh wave, propagating along the $x_1$-axis of a free surface of an isotropic homogeneous solid, occupying half-space $x_3 \geq 0$ of the Cartesian coordinates system $(x_1,x_2,x_3)$, is incident on the surface rough region, having the form of a rectangle with the finite sizes $L_1$ and $L_2$ along the $x_1$- and $x_2$-axes respectively. That is the roughness occupies a rectangle region $-L_{1,2}/2 < x_{1,2} < L_{1,2}/2$. It is described by the next function

$$x_3 = f^{(2)}(x_1, x_2) = \delta_0 f_0(x_1, x_2) = \\ = \delta_0 f_\theta(x_1; -L_1/2; L_1/2) f_\theta(x_2; -L_2/2; L_2/2) f_1(x_1) \quad (1)$$

where $\delta_0$ is the roughness amplitude, having dimension of a length; the step function $f_\theta(x,a,b) = 1$ for $a < x < b$ and 0 otherwise; $f_1(x_1)$ is arbitrary dimensionless deterministic (not statistical) function. The problem of the plane Rayleigh wave scattering on the roughness (1) into the cylindrical Rayleigh wave in the Laue–Bragg–Wulff short-wavelength limit $\lambda \ll L_{1,2}$ is solved in [18] in the Rayleigh–Born approximation of the perturbation theory in a roughness amplitude (1). Conditions of the Rayleigh wave scattering resonances are expressed through the wave-vector $\vec{q}$ ((12) in [18]), transmitted from the incident to the scattered Rayleigh wave. This vector is defined uniquely by the absolute value of the wave-vector of incident or scattered wave $k_R$ and the angle of scattering $\varphi_s$. So, two patterns of scattering can be considered. The first one is the frequency spectrum of the indicatrix of scattering, i.e. its dependence on the Laue–Bragg–Wulff parameter $p_{N_l}$ ((10) in [18]) at arbitrary fixed value of the angle of scattering $\varphi_s$. The new topological laws of scattering [16–18] reveal that the frequency spectrum of scattering is always periodic independently on the periodicity or aperiodicity of the discontinuities lattice and on amplitude form-factor of a lattice [17]. The second pattern of scattering, mentioned above, is the structure of the indicatrix of scattering in dependence on the angle of scattering $\varphi_s$ at a constant value of the Laue–Bragg–Wulff parameter $p_{N_l}$. This dependence is known to name the acoustic Lauegram of the surface roughness on the analogy of the X-Rays Lauegrams of a solid surface [1,10]. Let's investigate the fundamental properties of the acoustic Lauegram. The results and designations of [18] are used for this investigation of the present work. The frequency spectrum of scattering contains the resonances of scattering in a general case, but there is not such general case for the Lauegram of scattering. The question about the presence of resonances in the Lauegram is considered by the conception of the Ewald sphere of reflection [3]. The Lauegram contains resonances of scattering if and only if it contains the nodes of the reciprocal lattice in the space of the transmitted wave-vectors $\vec{q}$, corresponding to the scattering lattice and to the conditions of resonances of scattering ((18–21) in [18]). But this conception and result [3] does not consider and solve the analytical problem about the number of such resonances and angles of scattering, corresponding to them. For the cylindrical scattered Rayleigh wave the sphere of reflection becomes the Ewald circle of reflection (Fig. 1). Let us consider and solve the next analytical problem: what is the radius $k_R$ of the Ewald circle of reflection, i.e. the frequency of the incident wave, containing arbitrary number, defined beforehand, of resonances for arbitrary angles of scattering $\varphi_s$, defined beforehand?

Let's investigate this problem in the case without influence of the longitudinal lattice amplitude form-factor, accounting only the presence of the two transverse edges of the lattice (1), [18], violating the classical Laue–Bragg–Wulff law of scattering [18]; and consider the role of the amplitude form-factors of the longitudinal and transverse lattices in the formation of the acoustic Lauegram of scattering.

## Solution of the problem

Let us consider analytical solution of the stated problem.

### The main scattering phase equations on the Ewald circle of reflection

The physical elastic process of the Rayleigh wave scattering corresponds to the circle of the radius $k_R$ in the space of the wave-vectors. Different points on this circle gives the angles of scattering $\varphi_s$. The $\varphi_s = 0$ is the direction of propagation of the incident wave. This circle, constructed in the two-dimensional space of the reciprocal lattice ((18) in [18]), is the Ewald circle of reflection (Fig. 1), [3]. The condition, that the node of the reciprocal lattice $\vec{q}^{\,(r)}(n_1,n_2)$ ((18) in [18]) lies on the Ewald circle of reflection (Fig. 1), having the radius $k_R = p_{Nl}/(L_1/N_l)$, gives the next main scattering phase equations, connecting the Laue–Bragg–Wulff parameter $p_{N_l}$ of the given physical process of scattering and the numbers $(n_1,n_2)$, defining the node of the reciprocal lattice, lying on the Ewald circle of reflection of this process, and consequently the phase of the angular spectrum of scattering, i.e. of the acoustic Lauegram of scattering,

$$\begin{cases} n_1\left(\dfrac{p_{N_l}}{\pi} - n_1\right) = \left(2n_2+1\right)^2 m^{(L)}, \\ \tan\left(\dfrac{\varphi_s}{2}\right) = \pm\dfrac{m_l\left(n_1,n_2\right)}{\sqrt{m^{(L)}}}, \end{cases} \tag{2}$$

where $n_1 = 1, 2, \ldots$; $n_2 = -1/2, 0, 1, 2, \ldots$; $m^{(L)} = \left(L_1/N_l\right)^2/\left(4L_2^2\right)$, $m_l$ is given by (22) in [18]. The second equation of (2) gives the angle of scattering for the resonance $(n_1,n_2)$ ((18–21) in [18]). Since the system (2) connects integer numbers $n_1$ and $2n_2 + 1$, let us consider the next approximation of the real values $p_N/\pi$ and the form parameter $m^{(L)}$ by means of the rational numbers, which are the ratio of any two natural, i.e., positive integer, numbers

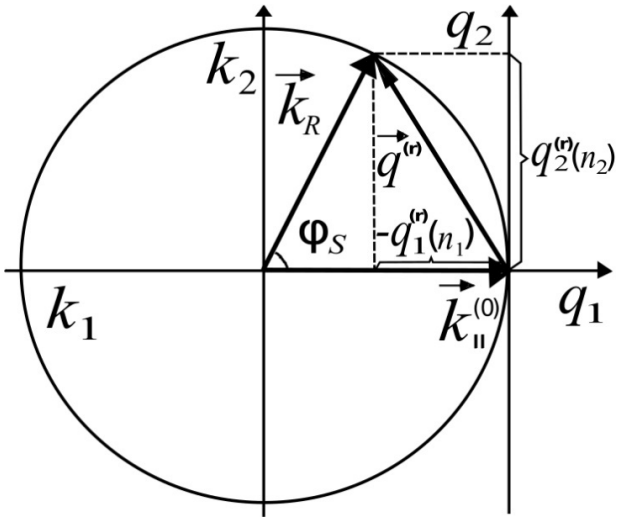


Fig. 1. Ewald circle of reflection. $q_1^{(r)}$, $q_2^{(r)}$ ((18–21) in [18]) are the coordinates of the nodes of the reciprocal lattice in the space $(q_1,q_2)$. $n^{(E)}$ nodes of the reciprocal lattice lie on the Ewald circle, if the angle of scattering $0 < \varphi_s < \pi$. The same amount of the resonance reciprocal lattice nodes, lying on the Ewald circle for the $\pi < \varphi_s < 2\pi$, have positions symmetrical with respect to the $q_1$-axis

$$\frac{p_{N_l}}{\pi} = \frac{m_5}{m_6} C;\ m^{(L)} = \frac{m_7^2}{m_8^2};\ n_1 / m_5 \equiv n_3, \tag{3}$$

where $C, n_3, m_5, m_6, m_7, m_8$ are natural numbers; $p_{N_l} = k_R \left( L_1 / N_l \right)$ is a positive real number. Representation (3) gives the next final system of equations, connecting sought natural numbers $C$, $n_3$, $2n_2 + 1$ with each other and with the angle of scattering $\varphi_s$, instead of the system (2)

$$\begin{cases} m_8^2 m_5^2 n_3 \left( C - m_6 n_3 \right) = \left( 2n_2 + 1 \right)^2 m_7^2 m_6; \\ \tan \dfrac{\varphi_s}{2} = \pm \dfrac{m_l \left( n_1, n_2 \right)}{\sqrt{m^{(L)}}} = \pm \dfrac{m_5 n_3}{\left( 2n_2 + 1 \right)} \dfrac{m_8}{m_7}, \end{cases} \tag{4}$$

where $C$, $n_3$ are natural numbers, $(2n_2 + 1)$ is non-negative integer.

**One possible schema of the solution**

One possible schema of the (4) solution can have the next form

$$\begin{cases} V_1^{(1)^2} \chi_1 m_7^2 m_6^2 + V_1^{(2)^2} \chi_1 = C; \quad V_2^{(1)^2} \chi_2 m_7^2 m_6^2 + V_2^{(2)^2} \chi_2 = C; \quad \ldots \\ \chi_m \left( V_m^{(1)^2} m_7^2 m_6^2 + V_m^{(2)^2} \right) = C; \ \ldots \ V_{n^{(E)}}^{(1)^2} \chi_{n^{(E)}} m_7^2 m_6^2 + V_{n^{(E)}}^{(2)^2} \chi_{n^{(E)}} = C, \end{cases} \tag{5}$$

where $V_m^{(1)}$, $V_m^{(2)}$ are arbitrary natural numbers, $m = 1, 2, \ldots, n^{(E)}$;

$$V_m^{(1)^2} V_m^{(2)^2} \chi_m^2 m_8^2 m_5^2 = \left( 2n_2 + 1 \right)^2, \quad \text{where } m = 1, 2, \ldots, n^{(E)}. \tag{6}$$

It follows from (6), that $V_m^{(1)}$, $V_m^{(2)}$, where $m = 1, 2, \ldots, n^{(E)}$, are arbitrary odd natural numbers. Arbitrary natural number $n^{(E)}$ shows how many nodes of reciprocal lattice lie on the Ewald circle of reflection.

**Results and Discussion**

**The Ewald circle of reflection in a frame of the Laue–Bragg–Wulff laws of scattering**

It follows from the system of equations (5), that sought natural number $C$ is the least common multiple (**lcm**) of the next natural numbers

$$C = \operatorname{lcm} \left\{ V_m^{(1)^2} m_7^2 m_6^2 + V_m^{(2)^2} \right\}, \quad m = 1, 2, \ldots, n^{(E)}. \tag{7}$$

The next relations follow from the (4–6)

$$\begin{gathered} \chi_m = C / \left( V_m^{(1)^2} m_7^2 m_6^2 + V_m^{(2)^2} \right),\ n_3^{(m)} = \chi_m V_m^{(1)^2} m_7^2 m_6, \\ n_1^{(m)} = m_5 n_3^{(m)} = \chi_m V_m^{(1)^2} m_7^2 m_6 m_5, \\ \left( 2n_2^{(m)} + 1 \right) = V_m^{(1)} V_m^{(2)} \chi_m m_8 m_5, \\ m_l^{(m)} = \frac{V_m^{(1)}}{V_m^{(2)}} \frac{m_6}{m_8} m_7^2, \ \ m = 1, 2, \ldots, n^{(E)}. \end{gathered} \tag{8}$$

It follows from (4), (8) that the angles of scattering $\varphi_s^{(m)}$, where $m = 1, 2,..., n^{(E)}$, corresponding to the two nodes of the reciprocal lattice under number $m$, have the next form

$$\tan\frac{\varphi_s^{(m)}}{2} = \pm\frac{V_m^{(1)}}{V_m^{(2)}} m_6 m_7, \quad m = 1, 2, \ldots, n^{(E)} \tag{9}$$

It follows from the solution (9), that predefining of the pairs of arbitrary odd natural numbers $V_m^{(1)}$, $V_m^{(2)}$ means predefining of the arbitrary angles of scattering $\varphi_s^{(m)}$, where $m = 1, 2,..., n^{(E)}$, corresponding to the full resonances of scattering ((18–21) in [18]), lying on the Ewald circle of reflection (Fig. 1), having the next sought radius $k_R = \left(m_5 / m_6\right)\pi C / \left(L_1 / N_l\right)$.

**The new topological laws of scattering and the Ewald circle of reflection**

The new topological laws of scattering [16—18] include first the amplitude form-factor of the discontinuities lattices ((11) in [18]) into the theory of scattering on the basis of the first principles of the dynamical theory of elasticity. Let us consider the influence of the lattice amplitude form-factor on the presence of the resonances of scattering, i.e. nodes of the reciprocal lattice, on the Ewald circle of reflection (Fig. 1), [3]. For the Rayleigh wave scattering on the rectangle periodic lattice of discontinuities (1), ((1) in [18]) with $f_1(x_1)f_2(x_2)$ instead of $f_1(x_1)$, having $N_l^{(1)}$ and $N_l^{(2)}$ unit cells along the $x_1$- and $x_2$- axes respectively, bounded by the discontinuities, located at the next points $l_{m_{1,2}}^{(1,2)} = -L_{1,2}/2 + \tilde{l}_{m_{1,2}}^{(1,2)}$, where $\tilde{l}_{m_{1,2}}^{(1,2)} = \left(m_{1,2} - 1\right)L_{1,2} / N_l^{(1,2)}$, $m_{1,2} = 1, 2, \ldots, N_l^{(1,2)}$, the indicatrix of scattering has the next form analogically to ((10) in [18])

$$I_{\|,3}^{(R)} = \beta^2 \frac{c_R^4}{c_t^4}\frac{p_{N_l}^5}{8\pi R_2^2}\frac{\left(L_2 / L_1\right)^2 A_{1,2}^2\left(x_3\right)}{N_l^{(1)2\left(n_d^{(1)}-3/2\right)} N_l^{(2)2\left(n_d^{(2)}+1\right)}}\times$$
$$\times\frac{\left|\tilde{J}^{(1)}\left(q_1\right)\right|^2\left|\tilde{J}^{(2)}\left(q_2\right)\right|^2\left(1-\cos\varphi_s\right)^2\left(\gamma+\cos\varphi_s\right)^2}{\left(q_1L_1 / N_l^{(1)}\right)^{2\left(n_d^{(1)}+1\right)}\left(q_2L_2 / N_l^{(2)}\right)^{2\left(n_d^{(2)}+1\right)}}, \tag{11}$$

where

$$\left|\tilde{J}^{(1,2)}\left(q_{1,2}\right)\right|^2 = \tilde{F}_0^{(1,2)} + 2\sum\nolimits_{n=1}^{N_l^{(1,2)}}\tilde{F}_n^{(1,2)}\cos\left(q_{1,2}\frac{L_{1,2}}{N_l^{(1,2)}}n\right),$$
$$\tilde{F}_n^{(1,2)} = \sum\nolimits_{m=1}^{N_l^{(1,2)}+1-n} F_m^{(1,2)}F_{m+n}^{(1,2)}, \tag{12}$$
$$F_m^{(1,2)} = L_{1,2}^{n_d^{(1,2)}}\left(\frac{d^{n_d^{(1,2)}}}{d\,x_{1,2}^{n_d^{(1,2)}}}f_{1,2}\left(x_{1,2}\right)\right)\Bigg|_{l_m^{(1,2)}+0}^{l_m^{(1,2)}-0}.$$

$F_m^{(1,2)}$ are dimensionless amplitude form-factors of the longitudinal and transverse lattices, i.e. lattices, arranged along the $x_{1,2}$-axes respectively.

Let us the amplitude form-factors (12) of the lattice have the next form

$$F_{m_{1,2}}^{(1,2)} = 1 + \sum\nolimits_{i=1}^{n_{1,2}^{(a)}}\cos\left(a_i^{(1,2)}m_{1,2}\right),\ m_{1,2} = 1, 2, \ldots, N_l^{(1,2)}. \tag{13}$$

Then the conditions of the full resonances of scattering have the next form [16, 17]

$$q_1L_1 / N_l^{(1)} \pm a_{i_1}^{(1)} = -2\pi n_1,\ q_2L_2 / N_l^{(2)} \pm a_{i_2}^{(2)} = \pm 2\pi n_2,$$
$$n_{1,2} = 1, 2, \ldots;\ i_{1,2} = 1, 2, \ldots, n_{1,2}^{(a)}. \tag{14}$$

It follows from the (14), that the reciprocal resonance lattice with account of the lattice amplitude form-factor (12), (13), i.e. in the frame of the new topological laws (11), [16]-[18], has the next form

$$\vec{q}^{(r)} = -\vec{a}_1^{\left(N_l^{(1)}\right)}\left(2\pi n_1 \pm a_{i_1}^{(1)}\right)\Big/\left(a_1^{\left(N_l^{(1)}\right)}\right)^2 \pm \vec{a}_2^{\left(N_l^{(2)}\right)}\left(2\pi n_2 \mp a_{i_2}^{(2)}\right)\Big/\left(a_2^{\left(N_l^{(2)}\right)}\right)^2, \qquad (15)$$

where $n_{1,2} = 1, 2, \ldots$; $0 \le a_{i_{1,2}}^{(1,2)} \le 2\pi$, $i_{1,2} = 1, 2, \ldots, n_{1,2}^{(a)}$; all the "±" are independent in the (15), but $q_1^{(r)} < 0$ (Fig. 1), ((18), (19) in [18]). The conditions (14) are the system of the linear algebraic equations with respect to the unknowns $a_{i_{1,2}}^{(1,2)}$ (13), defining the amplitude form-factors of the lattice (12), (13).

The radius of the Ewald circle of reflection $k_R$ and the resonance angles of scattering $\varphi_s$ are the parameters of this system. It means that arbitrary number of the resonances of scattering (14), (15) can be placed on the Ewald circle of reflection, i.e. on the acoustic Lauegram of scattering, without increasing of its radius, i.e. the frequency of the Rayleigh wave at fixed sizes of the lattice, contrary to the case (7–10), when the amplitude form-factor of the longitudinal lattice does not influence the scattering, and one of the transverse lattice violates ((18), (21) in [18]) the Laue–Bragg–Wulff law of scattering [1, 2].

## Conclusion

The fundamental properties of the acoustic Lauegram of scattering are obtained in the frame of the new topological laws of scattering [16–18]. These results can be used in the physical research: from the solid state physics up to investigations on the X-Ray and acoustic microscopy materials imaging, and in acoustoelectronic technologies and physics of the acoustic metamaterials [10–13].

## REFERENCES


1. **Bijvoet J.M., Burgers W.G., Hagg G.** (Eds.), Early Papers on Diffraction of X-Rays by Crystals, Vol. I, Springer, 1969; Vol. II, Springer, 1972.
2. **Laue M., Friedrich W., Knipping P.**, in **Bacon G. E.** (Ed.), X-Ray and Neutron Diffraction (in English), Pergamon Press, 1966.
3. **Ewald P.P.,** Acta Cryst. A25 (1969) 103.
4. **Jenkins F.A., White H.E.,** Fundamentals of Optics, McGraw-Hill, 2001.
5. **Biryukov S.V., Gulyaev Yu.V., Krylov V.V., Plesskii V.P.,** Surface Acoustic Waves in Inhomogeneous Media, Springer-Verlag, 1995.
6. **Khapachev Yu.P., Dyshekov A.A.**, Theory of the Dynamic Roentgen Diffraction in Superlattices, Nalchik, Russia, 2002.
7. **Prokhorov A.M.** (Ed.), The Physics Encyclopedia, Moscow, 1988.
8. **Gorodnichev E.E., Dudarev S.I., Rogozkin D.B., Ryazanov M.I.,** Sov. Phys. JETP. 69 (1989) 17.
9. **Savchenkov E.N., Schandarov S.M., et al.,** JETP Letters. 110 (2019) 165.
10. **Miao J., Ishikawa T., Robinson I. K., Murnane M.M.**, Science. 348 (2015) 530.
11. **Lee M.**, X-Ray Diffraction for Materials Research. From Fundamentals to Applications, CRC Press, 2016.
12. **Maev R.G.,** Acoustic Microscopy. Fundamentals and Applications, Wiley-VCH, Weinheim, 2008.
13. **Deymier P.A.** (Ed.), Acoustic Metamaterials and Phononic Crystals, Springer, 2013.
14. **Alexandryan R.A., Mirzahanyan E.A.,** General Topology, Moscow, 1979.
15. **Shapiro I.S., Ol'shanetsky M.A.,** Lectures on Topology for Physicists, Moscow, 2001. ISBN: 5-7029-0311-0.
16. **Chukov V.N.**, Topological Laws of the Rayleigh Wave Scattering, LAP, 2018, ISBN: 978-613-9-84837-9.
17. **Chukov V.N.,** 2020, ISBN: 978-5-7422-7029-4, p. 87, https://acoust-conference.iapras.ru.
18. **Chukov V.N.**, J. Phys.: Conf. Ser. 2103 (2021) 012157.

## THE AUTHOR

**CHUKOV Vitalii N.**
vchukov@mail.ru
ORCID: 0000-0002-7256-5145

*Received 11.11.2022. Approved after reviewing 17.11.2022. Accepted 17.11.2022.*

© Peter the Great St. Petersburg Polytechnic University, 2023

*Journal*

**ST. PETERSBURG STATE POLYTECHNICAL UNIVERSITY JOURNAL: PHYSICS AND MATHEMATICS**

**Vol. 16, No. 1.2, 2023**

Founder and publisher: Peter the Great St. Petersburg Polytechnic University

The journal is registered with the Federal Service for Supervision of Communications, Information Technology and Mass Media (Roskomnadzor).
Certificate ПИ ФС77-51457 issued 19.10.2012.

Editorial Office

Dr. Prof. *V.K. Ivanov*, Editor-in-Chief
Dr. Prof. *A.E. Fotiadi*, Deputy Editor-in-Chief
Dr. Prof.*V.V. Dubov*
Dr. Prof. *P.A. Karaseev*
Dr. Assoc. Prof. *V.M. Kapralova*
*A.S. Kolgatina*, translator
*N.A. Bushmanova*, editorial manager

All papers presented are final author versions
Peer review is under responsibility of the Organizing Committee

Phone 8 (812) 294-22-85

Website https://physmath.spbstu.ru/

E-mail: physics@spbstu.ru

Typesetting by A.S. Kolgatina

Published 15.05.2023. Format 60x84/8. Digital print.
Printer's sheets Print circulation 1000. Order ID